catalysts

Special Issue Reprint

Environmentally Friendly Catalysis for Green Future

Edited by
Zuzeng Qin

mdpi.com/journal/catalysts

MDPI

Environmentally Friendly Catalysis for Green Future

Environmentally Friendly Catalysis for Green Future

Guest Editor

Zuzeng Qin

MDPI

Basel • Beijing • Wuhan • Barcelona • Belgrade • Novi Sad • Cluj • Manchester

Guest Editor
Zuzeng Qin
School of Chemistry and Chemical Engineering
Guangxi University
Nanning
China

Editorial Office
MDPI AG
Grosspeteranlage 5
4052 Basel, Switzerland

This is a reprint of the Special Issue, published open access by the journal *Catalysts* (ISSN 2073-4344), freely accessible at: https://www.mdpi.com/journal/catalysts/special_issues/141778ZDX2.

For citation purposes, cite each article independently as indicated on the article page online and as indicated below:

Lastname, A.A.; Lastname, B.B. Article Title. *Journal Name* **Year**, *Volume Number*, Page Range.

ISBN 978-3-7258-8395-0 (Hbk)
ISBN 978-3-7258-8396-7 (PDF)
https://doi.org/10.3390/books978-3-7258-8396-7

© 2026 by the authors. Articles in this reprint are Open Access and distributed under the Creative Commons Attribution (CC BY) license. The reprint as a whole is distributed by MDPI under the terms and conditions of the Creative Commons Attribution-NonCommercial-NoDerivs (CC BY-NC-ND) license (https://creativecommons.org/licenses/by-nc-nd/4.0/).

Contents

About the Editor . . . . . **vii**

Preface . . . . . **ix**

Zuzeng Qin
Environmentally Friendly Catalysis for Green Future
Reprinted from: *Catalysts* **2026**, *16*, 568, https://doi.org/10.3390/catal16060568 . . . . . **1**

Caressa Munien, Sudesh Rathilal and Emmanuel Kweinor Tetteh
Challenges and Prospects of TiO_2-Based Photocatalysis for Wastewater Treatment: Keyword Analysis
Reprinted from: *Catalysts* **2025**, *15*, 801, https://doi.org/10.3390/catal15090801 . . . . . **4**

Ruofan Xu, Shumeng Qin, Tianguang Lu, Sen Wang, Jing Chen and Zuoli He
Engineering Photocatalytic Membrane Reactors for Sustainable Energy and Environmental Applications
Reprinted from: *Catalysts* **2025**, *15*, 947, https://doi.org/10.3390/catal15100947 . . . . . **32**

Dinh Quang Ho, Van Duy Lai, Quynh Anh Nguyen, D. Duc Nguyen and Duong Duc La
Green Synthesis of TiO_2-CeO_2 Nanocomposites Using Plant Extracts for Efficient Organic Dye Photodegradation
Reprinted from: *Catalysts* **2025**, *15*, 583, https://doi.org/10.3390/catal15060583 . . . . . **82**

Yihan Tang, Yichi Zhang, Ning Jian, Luxi Han, Huage Lin and Weinan Xing
Construction of Sulfur-Doped and Cyanide-Modified Carbon Nitride Photocatalysts with High Photocatalytic Hydrogen Production and Organic Pollutant Degradation
Reprinted from: *Catalysts* **2025**, *15*, 849, https://doi.org/10.3390/catal15090849 . . . . . **98**

Xinlin Huang, Wenting Sun, Rong Bai, Yuchen He, Jingdan Li, Yuwei Pan, et al.
Efficient Degradation of Tetracycline via Cobalt Phosphonate-Activated Peroxymonosulfate: Mechanistic Insights and Catalytic Optimization
Reprinted from: *Catalysts* **2025**, *15*, 580, https://doi.org/10.3390/catal15060580 . . . . . **111**

Jiajia Gao, Siqi Chen, Yun Gao, Wenquan Sun, Jun Zhou, Kinjal J. Shah and Yongjun Sun
Current Developments in Ozone Catalyst Preparation Techniques and Their Catalytic Oxidation Performance
Reprinted from: *Catalysts* **2025**, *15*, 671, https://doi.org/10.3390/catal15070671 . . . . . **128**

Manasik M. Nour, Maha A. Tony, Mai Kamal Fouad and Hossam A. Nabwey
Banana (*Musa sapientum*) Waste-Derived Biochar–Magnetite Magnetic Composites for Acetaminophen Removal via Photochemical Fenton Oxidation
Reprinted from: *Catalysts* **2025**, *15*, 955, https://doi.org/10.3390/catal15100955 . . . . . **150**

M. M. Nour, Maha A. Tony, Mai K. Fouad and Hossam A. Nabwey
Hybrid PK-P/Fe_3O_4 Catalyst Derived from Pumpkin Peel (Bio-Waste) for Synozol Red KHL Dye Oxidation Under Photo-Fenton Reaction
Reprinted from: *Catalysts* **2025**, *15*, 977, https://doi.org/10.3390/catal15100977 . . . . . **176**

Heng Dong, Yuying Qi, Zhenghao Yan, Yimeng Feng, Wenqi Song, Fengxiang Li and Tao Hua
FeCo-LDH/CF Cathode-Based Electrocatalysts Applied to a Flow-Through Electro-Fenton System: Iron Cycling and Radical Transformation
Reprinted from: *Catalysts* **2025**, *15*, 685, https://doi.org/10.3390/catal15070685 . . . . . **201**

Haixiang Shi, Jianming Xu, Xuan Luo and Zuzeng Qin
Progress and Reaction Mechanism of Co-Based Catalysts in the Selective Hydrogenation of α,β-Unsaturated Aldehydes
Reprinted from: *Catalysts* **2025**, *15*, 689, https://doi.org/10.3390/catal15070689 . . . . . **223**

Hanze Zhu, Zeren Zhou, Senhua Ke, Chenyue Mao, Jiannan Song and Wanping Chen
Tribocatalytic Degradation of Organic Dyes by Disk-Shaped PTFE and Titanium: A Powder-Free Catalytic Technology for Wastewater Treatment
Reprinted from: *Catalysts* **2025**, *15*, 754, https://doi.org/10.3390/catal15080754 . . . . . **255**

Zupeng Gong, Shixuan Ding, Mingjie Huang, Wen-da Oh, Xiaohui Wu and Tao Zhou
One-Step Fe/N Co-Doping for Efficient Catalytic Oxidation and Selective Non-Radical Pathway Degradation in Sludge-Based Biochar
Reprinted from: *Catalysts* **2025**, *15*, 934, https://doi.org/10.3390/catal15100934 . . . . . **268**

Ruoxin Li, Jiuhong Wei, Bin Jia, Jun Liu, Xiaoqing Liu, Ying Wang, et al.
Ag-Cu Synergism-Driven Oxygen Structure Modulation Promotes Low-Temperature NO_x and CO Abatement
Reprinted from: *Catalysts* **2025**, *15*, 674, https://doi.org/10.3390/catal15070674 . . . . . **282**

Yiqing Feng and Rui Wang
Non-Noble Metal Catalysts for Efficient Formaldehyde Removal at Room Temperature
Reprinted from: *Catalysts* **2025**, *15*, 723, https://doi.org/10.3390/catal15080723 . . . . . **302**

Jingjing Liu, Guilong Gao and Lu Gan
Metal-Free Cellulose Carbon Nanofiber Supported Graphitic Carbon Nitride for High-Efficient BPA Degradation by Photocatalytic Peroxymonosulfate Activation
Reprinted from: *Catalysts* **2025**, *15*, 788, https://doi.org/10.3390/catal15080788 . . . . . **323**

Qianran Feng, Xiaoting Yu, Jinlian Peng, Siying Du, Liuyun Chen, Xinyuan Xu and Tongming Su
$Zn_{0.8}Cd_{0.2}S$ Photocatalyst Modified with $Ni(OH)_2$ for Enhanced Photocatalytic Hydrogen Production
Reprinted from: *Catalysts* **2025**, *15*, 886, https://doi.org/10.3390/catal15090886 . . . . . **335**

Nan Deng, Yaqi Wu, Yi Sun and Peng Liu
Promotional Effect of Semiconductor-Supported Plasmonic Copper Nanoparticles in Visible-Light-Driven Photocatalytic Oxidative Homocoupling of Alkynes
Reprinted from: *Catalysts* **2025**, *15*, 1045, https://doi.org/10.3390/catal15111045 . . . . . **351**

Xiaoxia Ye, Qiu Wu, Guifang Yang, Yuancai Lv and Minghua Liu
Efficient Water Disinfection via Photocatalytic Oxidation Process Mediated by WO_3/BiOBr@Si Composite
Reprinted from: *Catalysts* **2026**, *16*, 199, https://doi.org/10.3390/catal16020199 . . . . . **368**

Linwei Jiang, Poh Lin Lau, Huaiyuan Kang, Bosong Duan, Aixiang Wang, Hsien-Yi Hsu, et al.
Facile Aqueous Synthesis of High-Entropy Metal Sulfides for Sulfion Oxidation-Assisted Energy-Saving Hydrogen Production
Reprinted from: *Catalysts* **2026**, *16*, 525, https://doi.org/10.3390/catal16060525 . . . . . **389**

About the Editor

Zuzeng Qin

Zuzeng Qin is the Dean at the School of Chemistry and Chemical Engineering, Guangxi University. He completed his PhD studies in Chemical Engineering at Guangxi University in 2009. He recently led 4 NSFC Projects and 4 Key projects for Guangxi. He has published 145 papers in various journals, with 5 of these papers being Highly Cited Papers. His teaching disciplines include chemical engineering and technology, and physical chemistry, and his research interests include environmentally friendly catalytic processes, synthesis and separation of fine chemicals, and resource utilization of low-grade minerals.

Preface

This Reprint centers on environmentally friendly catalysis as a decisive tool for confronting the environmental crises driven by decades of rapid industrialization—including air and water pollution, the greenhouse effect, and climate change. It highlights how tailored catalytic processes, from thermal and electrocatalysis to photocatalysis, enable the conversion of gaseous pollutants (CO_2, VOCs, NO_x, SO_x) and the degradation of organic contaminants and heavy metals in water. The primary goal is to present the latest advances and research hotspots in green catalysis, bridging fundamental theory with practical application. It aims to promote deep collaboration among researchers, accelerate the innovation and scaling-up of sustainable catalytic technologies, and provide actionable references for global environmental governance.

The urgency of this Reprint stems from the accelerating environmental degradation caused by industrial activity and the pressing need for efficient, low-cost, and sustainable catalytic solutions. A clear paradigm shift—toward structure–activity correlation-guided catalyst design and waste-recycling-based material development—is already underway. This Special Issue documents that shift and aims to propel it further.

The Reprint presents 19 contributions—5 review papers and 14 original research articles—spanning a broad spectrum of catalytic technologies. Coverage includes photocatalytic membrane reactors, TiO_2-based wastewater treatment, non-noble metal catalysts for formaldehyde removal, Co-based selective hydrogenation, ozone catalysis, Fenton and Fenton-like systems using bio-waste-derived catalysts, low-temperature NO_x/CO abatement, tribocatalysis, and electro-Fenton systems. Applications range from hydrogen production, water disinfection, and dye degradation to antibiotic removal and gaseous pollutant abatement.

This Reprint is intended for researchers, scientists, and engineers working in catalysis, environmental science, and energy conversion, as well as professionals in academia and industry seeking cutting-edge solutions for environmental sustainability.

Zuzeng Qin
Guest Editor

catalysts

MDPI

Editorial

Environmentally Friendly Catalysis for Green Future

Zuzeng Qin

School of Chemistry and Chemical Engineering, Guangxi Colleges and Universities Key Laboratory of New Chemical Application Technology in Resources, Guangxi University, Nanning 530004, China; qinzuzeng@gxu.edu.cn

Over the past few decades, the advancement of human society and industrialization has led to severe environmental issues, such as air and water pollution, greenhouse effects, and climate change. Environmentally friendly catalysis is crucial in addressing the acute environmental challenges we are currently confronted with. The catalytic conversion of CO_2, VOC, NO_x, SO_x, and other gaseous pollutants is an effective approach for coping with the greenhouse effect and climate change, encompassing thermal catalysis, electrocatalysis, and photocatalysis. Moreover, the catalytic degradation and reduction in organic pollutants and heavy metal ions in water represent advanced technologies that have drawn considerable attention in wastewater treatment.

This Special Issue of Catalysts, entitled "Environmentally Friendly Catalysis for the Green Future", combines the most recent progress and innovations in catalysis that contribute to environmental sustainability. The Special Issue included five review papers covering a range of topics, such as engineering photocatalytic membrane reactors by Zuoli He [Contribution 1], challenges and prospects of TiO_2-based photocatalysis for wastewater treatment by Emmanuel Kweinor Tetteh [Contribution 2], non-noble metal catalysts for efficient formaldehyde removal at room temperature by Rui Wang [Contribution 3], co-based catalysts in the selective hydrogenation of α,β-unsaturated aldehydes by Zuzeng Qin [Contribution 4], and ozone catalyst preparation techniques and their catalytic oxidation performance by Yongjun Sun [Contribution 5]. These studies collectively underscore the critical role of tailored catalyst design in addressing environmental and industrial challenges, particularly through precise control of active sites, surface morphology, and electronic structure. Their methodologies—ranging from atomic-scale metal dispersion to ozone-driven radical generation—highlight a paradigm shift toward structure–activity correlation-guided development.

On the other hand, 14 research papers about catalytic technology in the green future were included. Photocatalysis, as a promising green technology, is a focus of this Special Issue. Related research explores diverse modification strategies to enhance catalytic performance, covering the fields of organic pollutant degradation, hydrogen production, and water disinfection. Specifically, semiconductor-supported plasmonic copper nanoparticles for visible-light-driven alkyne oxidative homocoupling [Contribution 6], $Ni(OH)_2$-modified $Zn_{0.8}Cd_{0.2}S$ composites for significantly improved photocatalytic hydrogen production efficiency [Contribution 7], sulfur-doped and cyanide-modified carbon nitride with dual functionality for hydrogen production and organic pollutant degradation [Contribution 8], metal-free cellulose carbon nanofiber-supported g-C_3N_4 for efficient bisphenol A (BPA) degradation via photocatalytic peroxymonosulfate activation [Contribution 9], green-synthesized TiO_2-CeO_2 nanocomposites using plant extracts for effective organic dye photodegradation [Contribution 10], WO_3/BiOBr@Si composites for photocatalytic oxidation inactivation of *Escherichia coli* to achieve efficient water disinfection [Contribution 11],

and high-entropy metal sulfides for sulfion oxidation-assisted energy-saving hydrogen production [Contribution 12]. All these photocatalytic systems demonstrate excellent catalytic activity, stability, and environmental compatibility, laying a solid foundation for their practical application. Fenton and Fenton-like systems, which are widely used in wastewater treatment, are represented by bio-waste-derived catalysts in this Special Issue, such as pumpkin peel-based PK-P/Fe_3O_4 [Contribution 13] and banana peel-derived biochar-magnetite composites [Contribution 14], which exhibit high efficiency in the degradation of dyes and acetaminophen, respectively. Additionally, Fe/N co-doped sludge-based biochar [Contribution 15] was developed for phenolic pollutant degradation via persulfate activation. These cases emphasize the concept of waste recycling and sustainability while reducing the cost of catalyst preparation. The oxidation-related studies in this Special Issue cover a variety of catalytic systems, including Ag-modified CuSmTi catalysts for the low-temperature abatement of NO_x and CO [Contribution 16] and cobalt phosphonate-activated peroxymonosulfate for efficient tetracycline degradation [Contribution 17], all of which provide effective solutions for the removal of gaseous and antibiotic pollutants. Furthermore, innovative catalytic technologies are also included, such as powder-free tribocatalytic dye degradation using PTFE and titanium disks [Contribution 18] and FeCo-LDH/CF cathode-based electrocatalysts for flow-through electro-Fenton systems [Contribution 19], have been developed, which further expand the scope of eco-friendly catalytic applications and provide new ideas for environmental governance.

This Special Issue comprehensively reflects the latest advances and research hotspots in the field of environmentally friendly catalysis, integrating fundamental theoretical research and practical application exploration, and providing valuable references for addressing global environmental challenges. Looking forward, the exploration and development of efficient, low-cost, and sustainable catalytic materials and technologies will remain a core focus of academic and industrial research. Moreover, future studies should further emphasize the in-depth investigation of structure–activity relationships, the elucidation of reaction mechanisms at the molecular level, and the acceleration of industrial scaling-up of advanced catalytic technologies. It is hoped that this Special Issue will serve as an important academic exchange platform, promoting in-depth cooperation among researchers in related fields, accelerating the innovation and application of environmentally friendly catalysis technologies, and ultimately contributing to the construction of a greener, more sustainable, and healthier future for humanity.

Acknowledgments: As Guest Editor of this Special Issue, I would like to thank all authors for submitting their high-quality reviews and articles and wish all contributors continued success.

Conflicts of Interest: The author declares no conflicts of interest.

List of Contributions

1. Xu, R.; Qin, S.; Lu, T.; Wang, S.; Chen, J.; He, Z. Engineering Photocatalytic Membrane Reactors for Sustainable Energy and Environmental Applications. *Catalysts* **2025**, *15*, 947. https://doi.org/10.3390/catal15100947.
2. Munien, C.; Rathilal, S.; Tetteh, E.K. Challenges and Prospects of TiO_2-Based Photocatalysis for Wastewater Treatment: Keyword Analysis. *Catalysts* **2025**, *15*, 801. https://doi.org/10.3390/catal15090801.
3. Feng, Y.; Wang, R. Non-Noble Metal Catalysts for Efficient Formaldehyde Removal at Room Temperature. *Catalysts* **2025**, *15*, 723. https://doi.org/10.3390/catal15080723.
4. Shi, H.; Xu, J.; Luo, X.; Qin, Z. Progress and Reaction Mechanism of Co-Based Catalysts in the Selective Hydrogenation of α,β-Unsaturated Aldehydes. *Catalysts* **2025**, *15*, 689. https://doi.org/10.3390/catal15070689.

5. Gao, J.; Chen, S.; Gao, Y.; Sun, W.; Zhou, J.; Shah, K.J.; Sun, Y. Current Developments in Ozone Catalyst Preparation Techniques and Their Catalytic Oxidation Performance. *Catalysts* **2025**, *15*, 671. https://doi.org/10.3390/catal15070671.
6. Deng, N.; Wu, Y.; Sun, Y.; Liu, P. Promotional Effect of Semiconductor-Supported Plasmonic Copper Nanoparticles in Visible-Light-Driven Photocatalytic Oxidative Homocoupling of Alkynes. *Catalysts* **2025**, *15*, 1045. https://doi.org/10.3390/catal15111045.
7. Feng, Q.; Yu, X.; Peng, J.; Du, S.; Chen, L.; Xu, X.; Su, T. $Zn_{0.8}Cd_{0.2}S$ Photocatalyst Modified with $Ni(OH)_2$ for Enhanced Photocatalytic Hydrogen Production. *Catalysts* **2025**, *15*, 886. https://doi.org/10.3390/catal15090886.
8. Tang, Y.; Zhang, Y.; Jian, N.; Han, L.; Lin, H.; Xing, W. Construction of Sulfur-Doped and Cyanide-Modified Carbon Nitride Photocatalysts with High Photocatalytic Hydrogen Production and Organic Pollutant Degradation. *Catalysts* **2025**, *15*, 849. https://doi.org/10.3390/catal15090849.
9. Liu, J.; Gao, G.; Gan, L. Metal-Free Cellulose Carbon Nanofiber Supported Graphitic Carbon Nitride for High-Efficient BPA Degradation by Photocatalytic Peroxymonosulfate Activation. *Catalysts* **2025**, *15*, 788. https://doi.org/10.3390/catal15080788.
10. Ho, D.Q.; Lai, V.D.; Nguyen, Q.A.; Nguyen, D.D.; La, D.D. Green Synthesis of TiO_2-CeO_2 Nanocomposites Using Plant Extracts for Efficient Organic Dye Photodegradation. *Catalysts* **2025**, *15*, 583. https://doi.org/10.3390/catal15060583.
11. Ye, X.; Wu, Q.; Yang, G.; Lv, Y.; Liu, M. Efficient Water Disinfection via Photocatalytic Oxidation Process Mediated by WO_3/BiOBr@Si Composite. *Catalysts* **2026**, *16*, 199. https://doi.org/10.3390/catal16020199.
12. Jiang, L.; Lau, P.L.; Kang, H.; Duan, B.; Wang, A.; Hsu, H.-Y.; Yin, Z.; Jia, G. Facile Aqueous Synthesis of High-Entropy Metal Sulfides for Sulfion Oxidation-Assisted Energy-Saving Hydrogen Production. *Catalysts* **2026**, *16*, 525. https://doi.org/10.3390/catal16060525.
13. Nour, M.M.; Tony, M.A.; Fouad, M.K.; Nabwey, H.A. Hybrid PK-P/Fe_3O_4 Catalyst Derived from Pumpkin Peel (Bio-Waste) for Synozol Red KHL Dye Oxidation Under Photo-Fenton Reaction. *Catalysts* **2025**, *15*, 977. https://doi.org/10.3390/catal15100977.
14. Nour, M.M.; Tony, M.A.; Fouad, M.K.; Nabwey, H.A. Banana (*Musa sapientum*) Waste-Derived Biochar–Magnetite Magnetic Composites for Acetaminophen Removal via Photochemical Fenton Oxidation. *Catalysts* **2025**, *15*, 955. https://doi.org/10.3390/catal15100955.
15. Gong, Z.; Ding, S.; Huang, M.; Oh, W.-d.; Wu, X.; Zhou, T. One-Step Fe/N Co-Doping for Efficient Catalytic Oxidation and Selective Non-Radical Pathway Degradation in Sludge-Based Biochar. *Catalysts* **2025**, *15*, 934. https://doi.org/10.3390/catal15100934.
16. Li, R.; Wei, J.; Jia, B.; Liu, J.; Liu, X.; Wang, Y.; Zhao, Y.; Li, G.; Zhang, G. Ag-Cu Synergism-Driven Oxygen Structure Modulation Promotes Low-Temperature NO_x and CO Abatement. *Catalysts* **2025**, *15*, 674. https://doi.org/10.3390/catal15070674.
17. Huang, X.; Sun, W.; Bai, R.; He, Y.; Li, J.; Pan, Y.; Zhang, M.; Wu, G. Efficient Degradation of Tetracycline via Cobalt Phosphonate-Activated Peroxymonosulfate: Mechanistic Insights and Catalytic Optimization. *Catalysts* **2025**, *15*, 580. https://doi.org/10.3390/catal15060580.
18. Zhu, H.; Zhou, Z.; Ke, S.; Mao, C.; Song, J.; Chen, W. Tribocatalytic Degradation of Organic Dyes by Disk-Shaped PTFE and Titanium: A Powder-Free Catalytic Technology for Wastewater Treatment. *Catalysts* **2025**, *15*, 754. https://doi.org/10.3390/catal15080754.
19. Dong, H.; Qi, Y.; Yan, Z.; Feng, Y.; Song, W.; Li, F.; Hua, T. FeCo-LDH/CF Cathode-Based Electrocatalysts Applied to a Flow-Through Electro-Fenton System: Iron Cycling and Radical Transformation. *Catalysts* **2025**, *15*, 685. https://doi.org/10.3390/catal15070685.

Disclaimer/Publisher's Note: The statements, opinions and data contained in all publications are solely those of the individual author(s) and contributor(s) and not of MDPI and/or the editor(s). MDPI and/or the editor(s) disclaim responsibility for any injury to people or property resulting from any ideas, methods, instructions or products referred to in the content.

catalysts

MDPI

Review

Challenges and Prospects of TiO_2-Based Photocatalysis for Wastewater Treatment: Keyword Analysis

Caressa Munien, Sudesh Rathilal and Emmanuel Kweinor Tetteh *

Green Engineering Research Group, Department of Chemical Engineering, Faculty of Engineering and the Built Environment, Durban University of Technology, Durban 4001, South Africa
* Correspondence: ektetteh34@gmail.com or emmanuelk@dut.ac.za

Abstract

Environmental pollution driven by socioeconomic development has intensified the need for advanced and sustainable wastewater treatment technologies. Herein, TiO_2-based photocatalysis emerged as a promising solution due to its oxidative potential, chemical stability, and eco-friendliness but does have unavoidable immobilized recoverability challenges. Therefore, this study explored the challenges and prospects of TiO_2-based photocatalysis for the degradation of emerging contaminants in wastewater. A comprehensive keyword analysis was conducted by using a decade of publications retrieved from Google Scholar, Scopus, and Web of Science (WOS) databases via Preferred Reporting Items for Systematic Reviews and Meta-Analyses (PRISMA) framework. From a pool of 518 refined publications, 318 significant keyword occurrences related to TiO_2-based photocatalysis advanced oxidation processes (AOPs) were revealed. The review delved into various types of AOP mechanisms and catalysts and highlighted the synergistic effect of process parameters and magnetization as recoverability potential for TiO_2-based photocatalysts. Furthermore, emerging strategies including surface modifications, doping, and hybrid AOP integrations were discussed to improve photocatalysis performance and industrial scalability. The study underscores the economic opportunity and environmental sustainability of degrading persistent organic pollutants by integrating a TiO_2-based photocatalytic system with a regenerative magnetic field into the water sector.

Keywords: advanced oxidation process; catalysis; photocatalysis; nanomaterials; wastewater

1. Introduction

The rapid expansion of urbanization and industrialization has produced substantial amounts of organic wastewater, which poses significant and remarkable threats to the environment and human health [1,2]. Notwithstanding the social, economic, and environmental effects of poor sanitation, good water quality is essential for the well-being of all [3]. It is projected that 10 to 20 million individuals die each year due to waterborne and nonfatal contamination. Consistently, around 5000 to 6000 kids die owing to water-related problems of diarrhea [4]. About 0.78 billion individuals globally lack access to potable water resources, causing significant health issues that require drastic measures to meet water needs [5].

Advanced oxidation processes (AOPs) are widely regarded as the most effective technology to alleviate the issues mentioned above and treat high-organic wastewater [6,7]. AOPs have the benefits of a high mineralization efficiency, a rapid oxidation reaction rate, and no secondary contamination [8]. AOPs include hydrogen peroxide (H_2O_2), ozone (O_3),

Fenton, TiO_2, and an ultraviolet radiation agent, which generate highly active radicals that can completely degrade organic pollutants [9,10]. These free radicals have high reactivity and redox capability to react non-selectively with the organic compounds in water [11]. Photocatalysis involving oxidation and reduction reactions occurs under a light source and semiconductor-based nano-photocatalysts, including metallic, non-metallic, and nanomaterials. Titanium dioxide (TiO_2), zinc oxide (ZnO), tin oxide (SnO_2), tungsten oxide (WO_3), cadmium sulfide (CdS), and carbon nitride (C_3N_4) are among the common semiconductor-based nano-photocatalysts that have been studied and applied [12–16]. TiO_2 nanoparticles are among the most promising and fastest growing photocatalysts for purifying water. The mechanism of non-toxicity semiconductor-based photocatalysts, like low-cost TiO_2, includes the production of highly responsive oxidants, like hydroxyl radicals ($OH^{\bullet}$), for removing microorganisms like viruses, algae, fungi, bacteria, among others [17]. TiO_2 has been reported to decrease several waterborne microorganisms such as Pseudomonas aeruginosa, E. coli, fungi, protozoa, and other things after 8 h of simulated exposure to sunlight [14,18,19]. A total inactivation of fecal coliforms under solar irradiation is reported in research expressing the photocatalytic disinfection efficiency of TiO_2 [20].

Titanium dioxide (TiO_2) has been a photocatalyst since the 1970s because of its stable semiconductor properties for natural applications. It has been considered one of the most commonly reported nanomaterials found in consumer products (for example, clothing and food additives). A photocatalysis system happens when a light source meets a semiconductor like TiO_2, prompting or leading to the separation of electrons. Therefore, these electrons scatter on the photocatalyst's surface, which intends to react with external substances, leading to oxidations and reductions [17,21]. The nano-sized particle of TiO_2, with its high surface area, makes it conceivable to achieve high response rates. Recent research shows the action of TiO_2 in degrading typical organic pollutants like methyl orange emanating from textile industries. The outcomes suggest that a synergetic impact between the intensity of the ultraviolet (UV) ratio and electrocatalyst advances the degradation of methyl orange by nearly 90% [22–24]. TiO_2 has additionally demonstrated the ability to adsorb phosphate ions from aqueous solutions within an hour [25].

Iron (III)-doped TiO_2 NPs can also degrade phenol under UV light radiation within 4 h [23]. Another advantage of using this material is that disinfection is commonly unnecessary since UV light helps eliminate microorganisms. However, the significant limitations of this technology are its lower photocatalytic impact within complex organic mixtures and the considerable power consumption needed for longer illumination times in large-scale applications [26,27]. Over the last ten (2013–2023) years, the use of TiO_2 in the fields of environmental management (wastewater treatment, water, and air) and energy production (water splitting) has gained considerable attention from researchers worldwide.

This study analyzed a comprehensive review based on the keywords "Advanced oxidation process" and "TiO_2 photocatalysis" to determine the emerging trends of scientific publications in water and wastewater treatment. This was carried out to reveal current research on AOPs, their mechanisms, and potential opportunities in the water field. Also, it will highlight the challenges and prospects of TiO_2 photocatalysis as a considerable technique for treating emerging contaminants from wastewater due to their prevalence, hazards, and potential risks to human health and the environment.

2. Literature Search Process and Eligibility Criteria

This study employed a well-known published protocol for systematic reviews, the Preferred Reporting Items for Systematic Reviews and meta-analyses (PRISMA). This was driven by investigating recent progress on TiO_2-based photocatalysis and advanced oxidation processes for wastewater treatment. For precise and accurate information gathering,

the Google Scholar, Scopus, and Web of Science (WOS) databases were consulted for publications from 2013 to 30 November 2023. Figure 1 shows the publication trend retrieved from the three databases, whereby, upon screening, cumulative published documents of 13,773, 696, and 468, respectively, were obtained from Google Scholar, Scopus, and WOS. It was deduced that progressive interest in research in photocatalysis had gained attention within the decade.

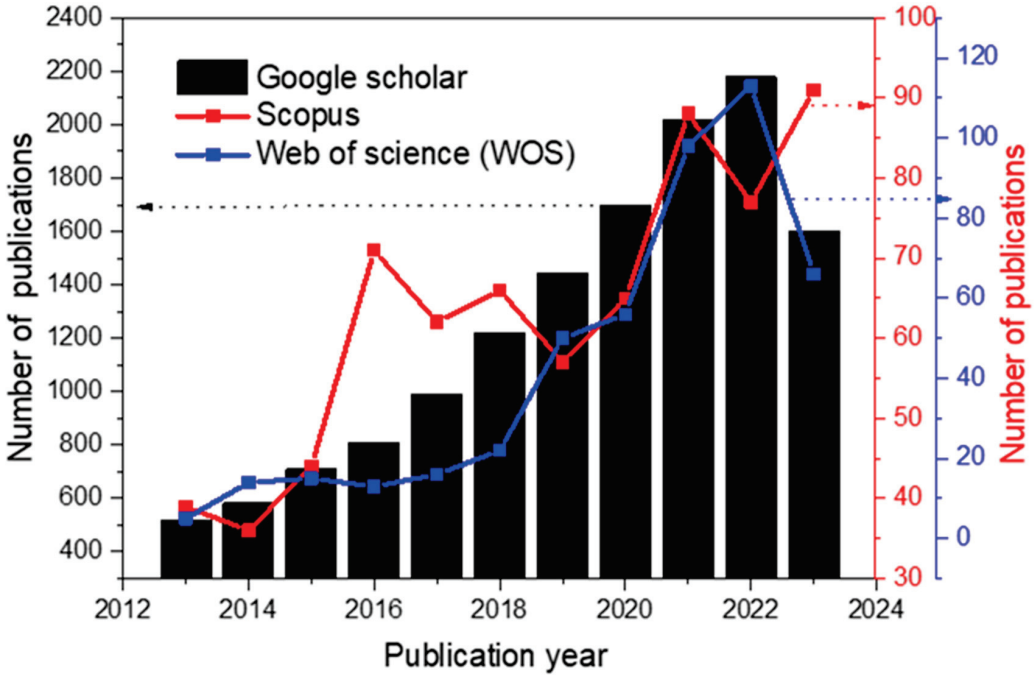


Figure 1. Comparing publications trends from the search engine of the Google Scholar database, Scopus database, and Web of Science to a keyword search of "TiO_2 photocatalysis and advanced oxidation process" from 2013 to 30 November 2023.

Most importantly, between 2020 and 2022, there was a massive increase in publications focusing on addressing emerging contaminants in wastewater settings. The refined database result was obtained by considering the exclusion criteria such as (i) book series and book chapter, (ii) conference proceedings, (iii) non-English language, (iv) publications before 2013, (v) articles in the press, and (vi) articles not open access. The retrieved publications were merged using a common library format (EndNote). In the screening process, duplicated articles were excluded from the database to make them eligible. A database with 518 articles containing titles, abstracts, keywords, and full texts was created using EndNote reference management software Version 21. Some of the potential research areas identified included chemistry (159), environmental science (140), chemical engineering (66), water resources (57), energy (51), and other multidisciplinary (45) fields. The authorship results showed that India is the most affiliated country, with 83 publications linked to 30 countries. India was followed by China (79 publications with 28 linked countries), Spain (79 publications with 20 linked countries), Brazil (58 publications with 18 linked countries), Italy (51 publications with 20 linked countries), USA (51 publications with 15 linked countries), Canada (44 publications with 10 linked countries), Mexico (36 publications with 10 linked countries), South Korea (30 publications with 8 linked countries, and South Africa (7 publications with 5 linked countries). The strong alliance between China and India can be attributed to the number of postgraduate scholarships offered by their academic institutions worldwide. This has significantly impacted their ability to collaborate globally, as evidenced by their diverse research partners and many foreign postgraduates and researchers. By investing in education and research, both countries have

paved the way for advancing knowledge and promoting cross-cultural exchange, making them a force to be reckoned with in the international community. Consequently, 75 articles with research focused on TiO_2-based photocatalytic and AOP activities in the water sector were finally selected and analyzed.

2.1. Research Development and Authors' Keyword Occurrence Network

The co-occurrence analysis of the keyword's appearance concerning the strength of an author's keywords was explored. There were 5491 keywords obtained from the 518 published articles that emerged. Setting the minimum number for a keyword to be repeated with an author's keyword at 10 resulted in 318 keywords linked to others. Figure 2 shows the overlay visualization of the keywords, year of publication, and the link strength. It was found that the average publications with the first 10 high-linked keywords was between 2017 and 2022. "photocatalysis" was the most representative keyword used, with 495 occurrences and 9087 linked strengths to other keywords. The second most linked keyword was "Titanium dioxide", with 485 occurrences and 9475 links to others. Catalysts were the third, with 308 occurrences and 5973 links to others. The rest included "advanced oxidation process" (275 occurrences, 6514 links) > "ultraviolet radiation" (236 occurrences, 5927 links) > "wastewater treatment" (209 occurrences, 4195 links) > "photodegradation "(155 occurrences, 3727 links) > "photolysis" (135 occurrences, 3222 links) > "organic pollutants" (112 occurrences, 3539 links) > "oxidation-reduction" (84 occurrences, 2692 links) and others. Keywords associated with research focused on ozonation, degradation of emerging contaminants (antibiotics), catalyst synthesis (sol–gel process), characterization (surface area, X-ray diffraction, scanning electron microscopy, FTIR, etc.), energy gap, and light sources were observed.

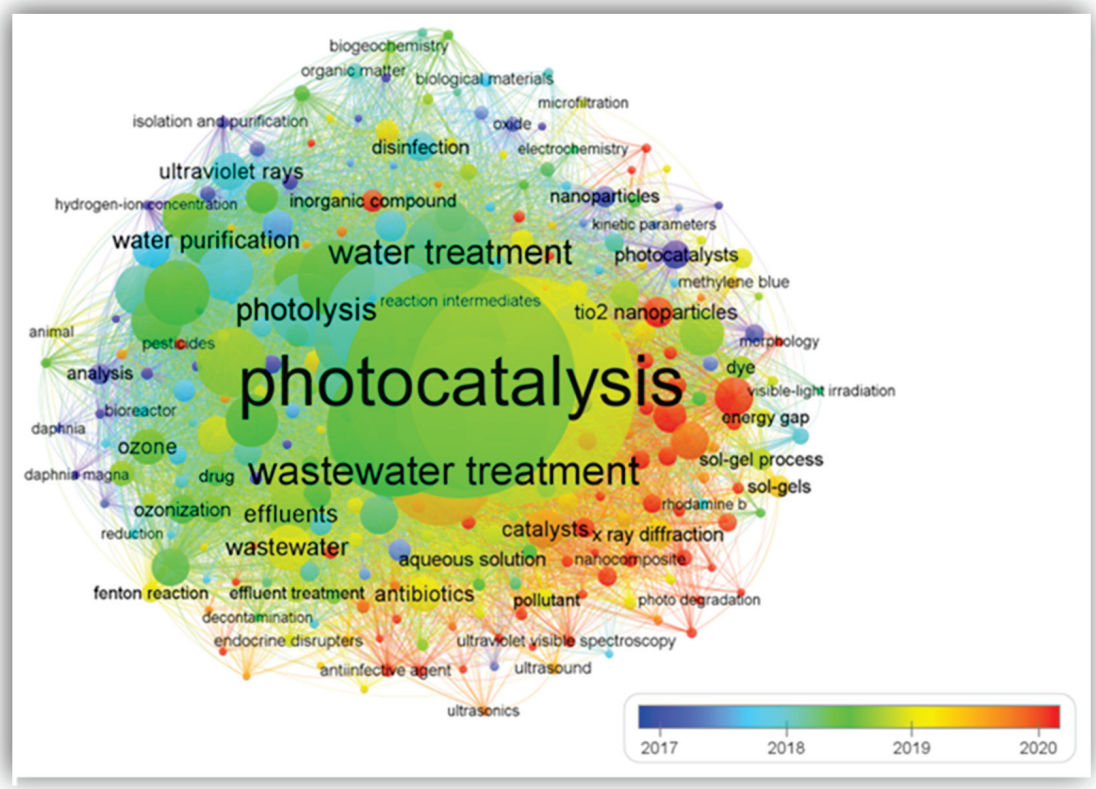


Figure 2. Graphical presentation of the keywords connected to the research field of TiO_2 photocatalysis and advanced oxidation process from 2017 to 2020.

2.2. Research Interest Themes and Keyword Occurrence

TiO_2-based photocatalysis and advanced oxidation processes for wastewater treatment were used as a search string to obtain information. Using the Google Scholar, Scopus, and Web of Science (WOS) databases resulted in cumulative published documents of 13,773, 696, and 468, respectively. Screening and merging of the published articles resulted in 518 articles containing titles, abstracts, keywords, and full texts. Almost 40% of the total publications on this subject under study globally were contributed by China and India, followed by other countries. There were keywords 5491 obtained from the 518 published articles that emerged, whereby 318 keywords were linked to photocatalysis. The keywords obtained were further processed to ascertain themes in connection with wastewater treatment via photocatalysis. As shown in Figure 3, there are five distinct clusters linked to the keywords network.

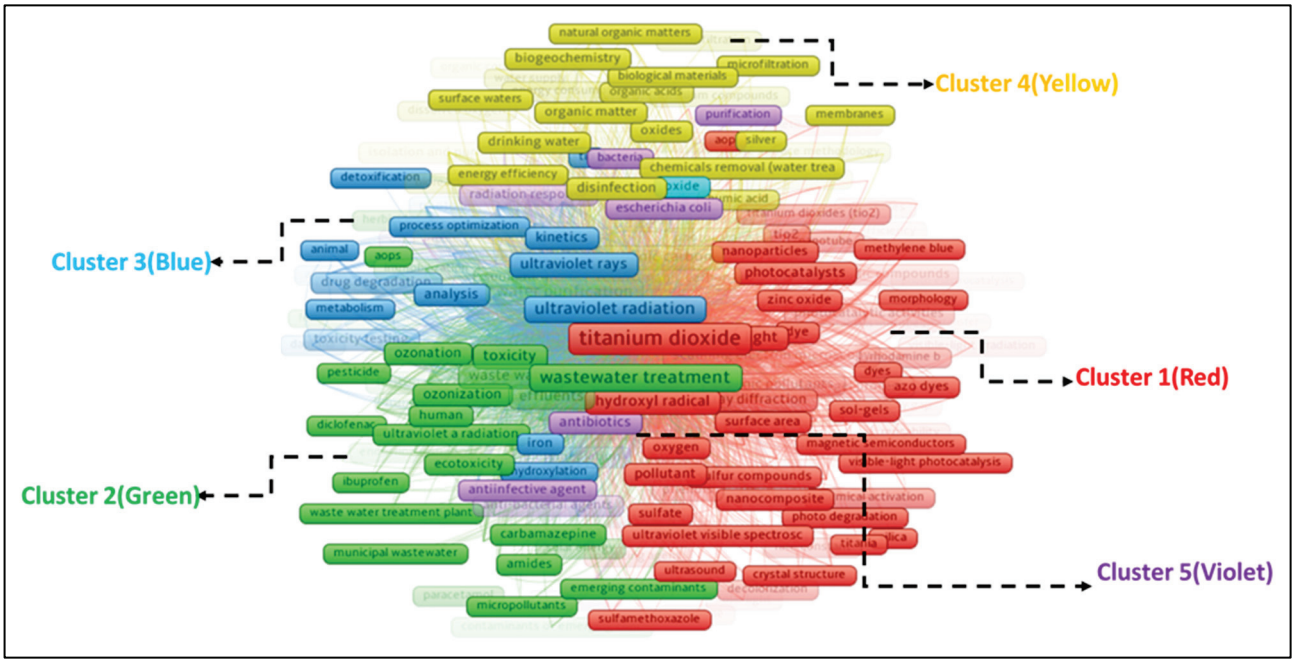


Figure 3. Graphical intersection of keyword networks for research field of TiO_2 photocatalysis and advanced oxidation processes.

Cluster 1 (Red) shows the prevalence of TiO_2-related keywords, which is extensively studied as a photocatalyst in photocatalytic applications. This cluster, with 121 keywords linked to TiO_2, highlights research studies on the drawbacks, synthesis, and characterization approach to producing either photocatalysts or nanocomposites with other narrow band gap semiconductors. The sol–gel approach was the most regularly used method for synthesizing the photocatalysts. Also, the nanoparticle/nanomaterial-related keywords are used in photocatalysis to provide a substantial surface area to enhance adsorption and photocatalytic reactions. It was found that most of the photocatalytic degradation activities were carried out experimentally with the use of UV light and dyes (azo dyes).

Cluster 2 (Green), with 69 keywords linked to wastewater treatment, demonstrated photocatalysis as an effective technique for degrading organic pollutants and emerging contaminants via redox reactions. In wastewater treatment plants, municipal wastewater is usually polluted with pharmaceuticals (ibuprofen, carbamazepine, diclofenac), pesticides, amides, and micropollutants. Aside from photocatalysis, ozonation, and ultraviolet radiation, other keywords for alternative methods for the detoxification of emerging contaminants were observed.

Cluster 3 (Blue), with 56 keywords linked to photocatalysis, highlights the metabolism, process optimization, kinetics, detoxification, and analysis of drugs under ultraviolet radiation. Cluster 4 (Yellow) had 53 keywords linked with photocatalysis using oxides for the degradation of organic matter. Additional techniques such as membranes, microfiltration, chemical treatment, disinfection, and biological processes for wastewater treatment (surface water) for reusability or drinking water are presented.

Cluster 5 (Violet), with 14 keywords linked to photocatalysis, showed that researchers must pay attention to emerging contaminants and wastewater purification. Thus, the presence of antibiotics in wastewater settings contributes to antibacterial resistance. Therefore, emphasis was placed on magnetic photocatalysis to ensure complete mineralization of wastewater organic pollutants.

2.3. Fate of Emerging Contaminants in Wastewater

Nanotechnology-based material industries that do not have centralized systems to mitigate their waste result in the unsustainable management of emerging contaminants in wastewater settings [28]. Nonetheless, the most significant groups of organic pollutants potentially found in wastewater are within the scale of nano- and micropollutants [29]. For example, nanomaterials (photocatalysts) with a minimal size of less than a hundred nanometres (nm), with excellent surface morphology and chemical reactivity, have shown great potential for the removal of contaminants [30–32]. Table 1 presents some nanomaterials and their properties. However, most of the nanomaterials used in petrochemical industries, agrochemicals, textiles, food processing, cosmetics, among others end up in wastewater [30]. Nanoparticles' toxicity is affected by a broad spectrum of factors, including surface properties like coating, reactivity, and area [33]. Also, their chemical composition, shape, and size could likely affect their toxicity. Nanoparticle types with the same chemical composition could have several toxicity levels. This is becoming very alarming due to the industry's successive inability to conduct risk assessment on nanoparticles [11].

Table 1. Types and properties of nanomaterials, adapted from [28].

Examples of Nanomaterials	Novel Properties of Nanomaterials
Carbon nanotubes (CNTs), magnetite, zeolites, TiO_2, and nano-Ag	Photocatalytic activity, high selectivity and permeability, hydrophilicity, low toxicity to humans, intense antimicrobial activity, high chemical and mechanical stability, among others.
Fullerene derivatives and nano-TiO_2	Low cost, high selectivity and stability, low human toxicity, photocatalytic activity in solar spectrum, among others.
CNTs, titanium dioxide (Ag/TiO_2), and nano-silver	Ease of use, high chemical stability, low cost and toxicity, potent antimicrobial activity, among others.
Nanofibers, metal oxide, and nanoscale or CNTs	Easy reuse, tunable surface chemistry, short intraparticle diffusion distance, more adsorption and selective sites, accessible adsorption sites, and high specific surface area.

There is also vast uncertainty about nanoparticle legality and economic and social issues, including the capacity to control nano-risks, the government's right to reject nano-applications, intellectual property, liability, among others [34]. The bioaccumulation of nanoparticles in wastewater streams can result in long-term pathogenic resistance. For instance, published research on carbon nanotubes revealed that they are a causative agent of asbestos-like pathogenicity at the beginning of mesothelioma in test mice. Also, some nanoparticles appear to have the potential for bioaccumulation and biomagnification in the environment [35,36]. Due to this, the United Kingdom's Royal Society, the world's oldest scientific organization, has suggested that the rising proof of serious nanotoxicity risks,

new safety evaluations, and treatability solutions should be considered. Industries should treat nanoparticles with the assumption that they are hazardous and releasing them into the environment ought to be avoided as much as possible.

In essence, emerging contaminants such as nanomaterials, antibiotics, dyes, micropollutants, pharmaceuticals, pesticides, and others directly discharged into wastewater and aquatic environments are detrimental to human health. Removing these recalcitrant pollutants or biotransformation in conventional wastewater treatment plants is very challenging [11]. This necessitates a study on advanced oxidation processes (AOPs), with emphasis on photocatalysis, to provide information that will enhance their complete elimination.

3. Advanced Oxidation Processes (AOPs)

Different types of advanced oxidation processes (AOPs) produce hydroxyl radicals ($OH^{\bullet}$) to remove emerging contaminants from wastewater that have a high chemical balance and limited biodegradability. AOPs have high efficiency in promoting the complete mineralization of pollutants into inorganic compounds, water, and CO_2 [37]. The diversity of AOPs includes chemical oxidation processes (Fe^{2+}/H_2O_2, H_2O_2/O_3, O_3), photocatalysis (photo-Fenton reactions, UV/TiO_2), and photochemical processes (H_2O_2/UV, O_3/UV), which all produce $OH^{\bullet}$ radicals [22–24]. Numerous cutting-edge advanced oxidation systems that are presently being investigated for potential application in wastewater treatment are described in the following sections. These sophisticated, advanced oxidation processes fall into one of two categories: heterogeneous or homogeneous. It is possible to further categorize homogeneous processes into energy-using and non-energy-using processes (Figure 4).

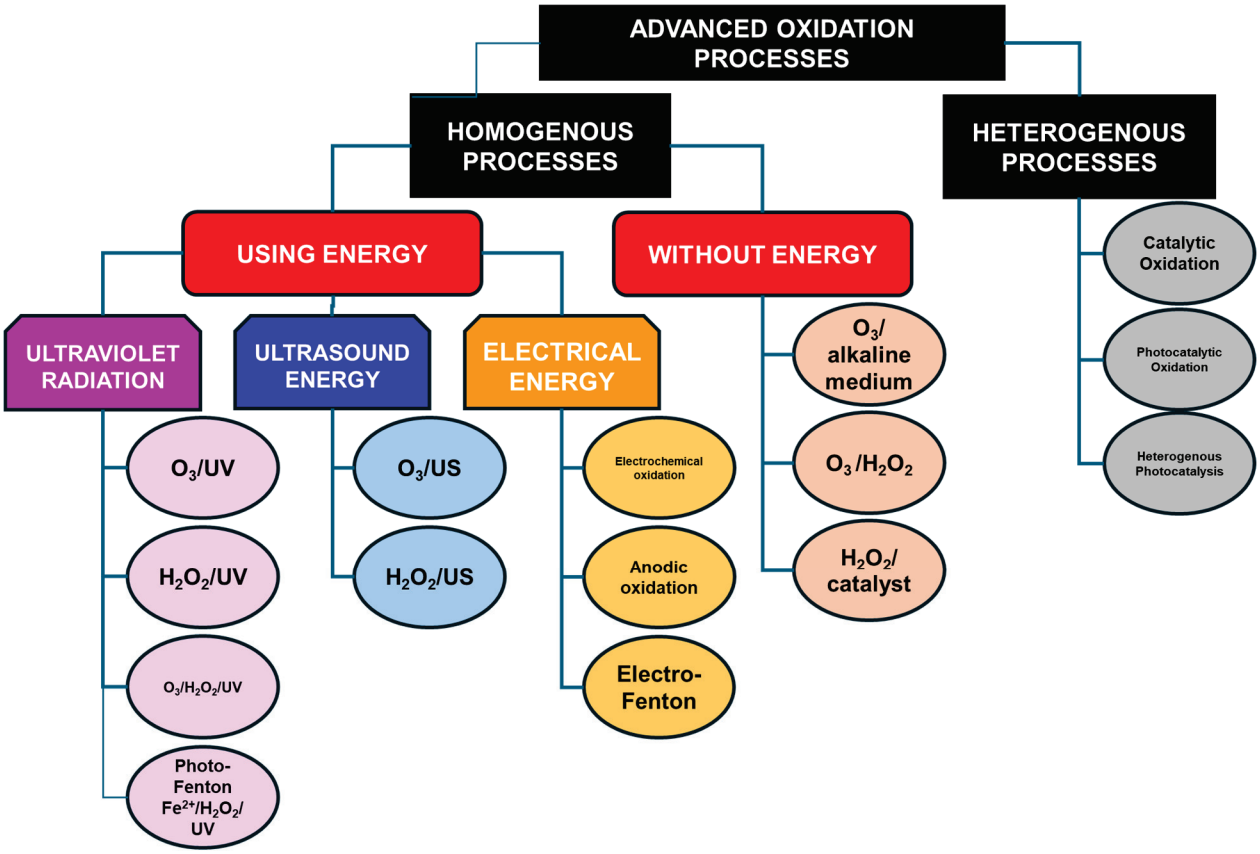


Figure 4. Advanced oxidation process (AOP) classification for wastewater treatment: ozone (O_3), hydrogen peroxide (H_2O_2), ultraviolet radiation (UV), ultrasound (US), and ferrous ions (Fe^{2+}).

3.1. Hydrogen Peroxide Coupled with UV Radiation

This advanced oxidation process entails the formation of hydroxyl radicals generated by the photolysis of H_2O_2 and the corresponding propagation reactions [23]. The photolysis of hydrogen peroxide occurs when UV radiation (hv) is applied, as shown in Equation (1):

$$H_2O_2 \xrightarrow{hv} 2OH^{\bullet} \quad (1)$$

This photolysis rate is not dependent on the pH and increases under more alkaline conditions. This is probably because the wavelength 253.7 nm to the peroxide anion HO^{-2} has an absorption coefficient with a higher value (240 as compared to 18.6 M^{-1} cm^{-1}) [38]. The propagation reactions are expressed in Equations (2)–(4):

$$H_2O_2 + OH^{\bullet} \rightarrow OH_2^{\bullet} + H_2O \quad (2)$$

$$H_2O_2 + OH_2^{\bullet} \rightarrow OH^{\bullet} + O_2 + H_2O \quad (3)$$

$$2OH_2^{\bullet} \rightarrow H_2O_2 + O_2 \quad (4)$$

Hydrogen peroxide decomposes in one way or another, depending on the reaction expressed in Equation (5), and thereafter radicals recombine, as shown in Equation (6):

$$H_2O_2 + OH_2^{-} \rightarrow H_2O + OH^{\bullet} + O_2 \quad (5)$$

$$2OH^{\bullet} \rightarrow H_2O_2 \quad (6)$$

3.2. Photo-Fenton (Fe_2+/H_2O_2/UV)

Hydrogen peroxide (H_2O_2), iron salts, and UV-visible light are the three main components of the photo-Fenton process ($Fe^{2+}/H_2O_2/UV$) of the AOP system that produces hydroxyl radicals ($OH^{\bullet}$). The photo-Fenton AOP requires a wavelength of less than 580 nm, since light in this instance accelerates the processes [23]. The process utilizes solar-powered or UV light for the conversion of Fe (III) oxalate back to Fe (II) oxalate. However, to maintain the iron in the solution, the pH level in the photo-Fenton AOP needs to be kept acidic. The chemicals employed in conventional Fenton reactions are supplemented with UV-visible radiation power in homogenous photo-Fenton reaction processes [39]. In the process of the degradation of pollutants in wastewater, hydrogen peroxide at a wavelength of more than 300 nm can produce hydroxyl radicals to enhance the reaction. The reaction mechanism is expressed in Equations (7)–(9).

$$Fe^{2+} + H_2O_2 \rightarrow Fe^{3+} + OH^{-} + OH^{\bullet} \quad (7)$$

$$Fe^{3+} + H_2O \xrightarrow{hv} Fe^{2+} + H^{+} + OH^{\bullet} \quad (8)$$

$$H_2O_2 \xrightarrow{hv} 2OH^{\bullet} \quad (9)$$

3.3. Electrochemical Oxidation

Fundamentally, electrochemical AOPs are techniques for the remediation of organic compound-contaminated wastewater (emerging contaminants) by producing reactive oxygen species (ROS) in situ, such as hydroxyl radicals ($OH^{\bullet}$) [40]. Electrochemical oxidation occurs via direct and indirect anodic reactions expressed in Equations (10)–(13), producing electron transfers to enhance water purification. In anodic oxidation, a current density is applied to the cell's anode to produce hydroxyl radicals on the anode surface [17,18]. Hydrodynamic parameters, such as the type of cell and electrodes usually incorporated in an electrochemical AOP system, raise concerns about the oxidation capacity and en-

ergy required. This makes the cost of operating electrochemical AOP higher compared to the conventional system. However, it is more efficient if the operating conditions are optimized [23]. A combination of methods has been proposed as a solution to all these drawbacks. To make physicochemical treatments (including electrochemical AOPs) effective and robust, bioremediation, nanotechnology, and other processes are commonly integrated [41]. Consequently, the biodegradable pollutants are degraded via the biological processes, granting the removal of the recalcitrant pollutants via the electrochemical AOPs [39].

[Anode]

$$H_2O \rightarrow H^+ + (OH^\bullet)_{ads} + e^- \quad (10)$$

$$(OH^\bullet)_{ads} \rightarrow (O)_{ads} \text{ or } O_2 + H^+ + e^- \quad (11)$$

$$(O)_{ads} + O_2 \rightarrow O_3 \quad (12)$$

[Cathode]

$$O_2 + 2H^+ + 2e \rightarrow H_2O_2 \quad (13)$$

4. Photocatalysis Process

Photocatalysis has become a viable alternative post-treatment process to conventional water and wastewater treatment technologies. The illumination of photocatalytic semiconductor particles with solar light or UV radiation results in the formation of electron–hole pairs (e^-/h^+) [11]. TiO_2 is classified as a photocatalyst due to its lone electron properties in the particle's outer orbital [42]. The crystal structures of TiO_2 are categorized as rutile (stable at higher temperatures), brookite (usually found in minerals with an orthorhombic crystal structure), and anatase (stable at low temperatures) [43]. A photocatalyst, as described by Umar and Aziz [44], is a material that can be activated by the absorption of a photon and is then capable of speeding up a reaction without itself being consumed in the reaction. TiO_2 can be activated by UV light with a wavelength less than 400 nm, as it has a band gap of 3.2 eV [45]. Table 2 summarizes the bandwidths of various commonly used photocatalysts, as semiconductor bandwidth is a significant factor restricting the wide application of photocatalysts. Table 3 provides a summary of additional research that explains how the photocatalyst dose affects the breakdown of organic contaminants by photocatalysis.

Table 2. Summary of some common photocatalyst band gaps.

Semiconductor	Crystal Structure	Band Gap Structure = 7			Ref.
		Conduction Band (CB)	Valence Band (VB)	Eg/eV	
TiO_2	Anatase	−0.50	2.70	3.20	[46]
ZnO		−0.31	2.89	3.20	[47]
CuO		−1.16	0.85	2.00	[48]
CdS		−0.90	1.50	2.40	[49]
ZnS		−1.04	2.56	3.60	[50]
g-C_3N_4		−1.30	1.40	2.70	[51,52]
g-C_3N_4		−1.53	1.16	2.70	[53]
Ta_3N_5		−0.75	1.35	2.10	[54]

Table 2. *Cont.*

Semiconductor	Crystal Structure	Band Gap Structure = 7			Ref.
		Conduction Band (CB)	Valence Band (VB)	Eg/eV	
TaON		−0.75	1.75	2.50	[55]
Fe_2O_3		0.28	2.48	2.20	[56]
Bi_2O_3		0.33	3.13	2.80	[57]
$BiVO_4$		−0.30	2.10	2.40	[58]
WO_3		−0.10	2.70	2.80	[59]
Ag_3PO_4	Cubic	0.04	2.49	2.45	[60]

Table 3. Summary of research utilizing semiconductor heterojunction photocatalysis at photocatalyst load (0.25–6 g/L) for photocatalytic degradation of several organic compounds.

Photocatalyst	Photocatalyst Load	Irradiation Source	Contaminant	Exposure Time (Minutes)	Photodegradation Efficiency (%)	Ref.
Fe_3O_4@Al_2O_3-PMo	0.5–3 g/L	UV (360 nm)	Cibacron brilliant yellow 3G-P	300	>90	[61]
Pt-TiO_2	0.5–6.0 g/L	UV	Methyl orange	Not given	90.5	[62]
Sn/TiO_2/AC	5.0–15.0 g/L	UV	Orange G	60	99.1	[63]
Cu-doped ZnO	0.1–1 g/L	125 W medium-pressure UVC lamp	Diazinon	120	96.97	[64]
Fe_3O_4@ZnO/PMOs	0.25–1.5 g/L	40 W white LED lamps	Methyl orange	180	98.2	[61]
Fe_3O_4@SiO_2@Ag_2WO_4@Ag_2S	0.5–3 g/L	Xenon + LED lamps (95 W)	Methyl blue	60	99.9	[65]
Bi_2O_3/SnO_2	(20–60) mg/50 mL	350 W Xenon lamp	Bisphenol A	60	93.42	[66]
P-ZnO1.8%	0.5–3 g/L	300 W halogen lamp	Rhodamine B	180	99	[67]
Fe^0@PEDOT\PW_{12}	0.5–3 g/L	Visible light	Oxidative desulfurization	60	98.4	[68]

4.1. TiO_2 Photocatalytic Mechanism

Photo-induced reactions are activated by the absorption of a photon with energy equal to or higher than the band gap energy of the catalyst [69]. This absorption results in charge separation as the electron (e^-) moves from the valence band to the conduction band of the semiconductor catalyst, resulting in a hole (h^+) in the valence band [70]. For the photocatalytic reaction to be favoured, the recombination of the electron and hole must be prevented. This allows for a reaction of electrons with an oxidant, resulting in a reduced product, as well as a hole reacting with a reductant to produce an oxidized product [71]. Hydroxyl radicals produced ($OH^\bullet$) are very reactive species and are therefore able to oxidize a wide variety of organic pollutants in a quick, efficient, and non-selective manner [72]. Akpan and Hameed [69] and Chong et al. [70] explain the series of chain oxidative–reductive reaction equations that take place at the photon-activated surface. The photocatalytic reaction mechanism (Figure 5) indicates that the degradation method is a clean technology and can be applied to the treatment of wastewater, where unwanted organics may exist [73]. These reactions are given by Equations (14)–(20).

$$\text{Photoexcitation}: \quad TiO_2 + hv \rightarrow e^- + h^+ \tag{14}$$

$$\text{Charge} - \text{carrier trapping of } e^-: \quad e^-_{CB} \rightarrow e^-_{TR} \tag{15}$$

$$\text{Charge} - \text{carrier trapping of } h^+ \qquad h^+_{VB} \rightarrow h^+_{TR} \tag{16}$$

$$\text{Electron} - \text{hole recombination :} \qquad e^-_{TR+h^+_{VB}(h^+_{TR})\rightarrow e^-_{CB}+\text{heat}} \tag{17}$$

$$\text{Photoexcited } e^- - \text{scavenging :} \qquad (O_2)_{ads} + e^- \rightarrow O_2^{\bullet -} \tag{18}$$

$$\text{Hydroxyl } h^+ \text{ scavenging :} \qquad OH^- + h^+ \rightarrow OH^{\bullet} \tag{19}$$

$$\text{Photodegradation by } OH^{\bullet} : \qquad R - H + OH^{\bullet} \rightarrow R'^{\bullet} + H_2O \tag{20}$$

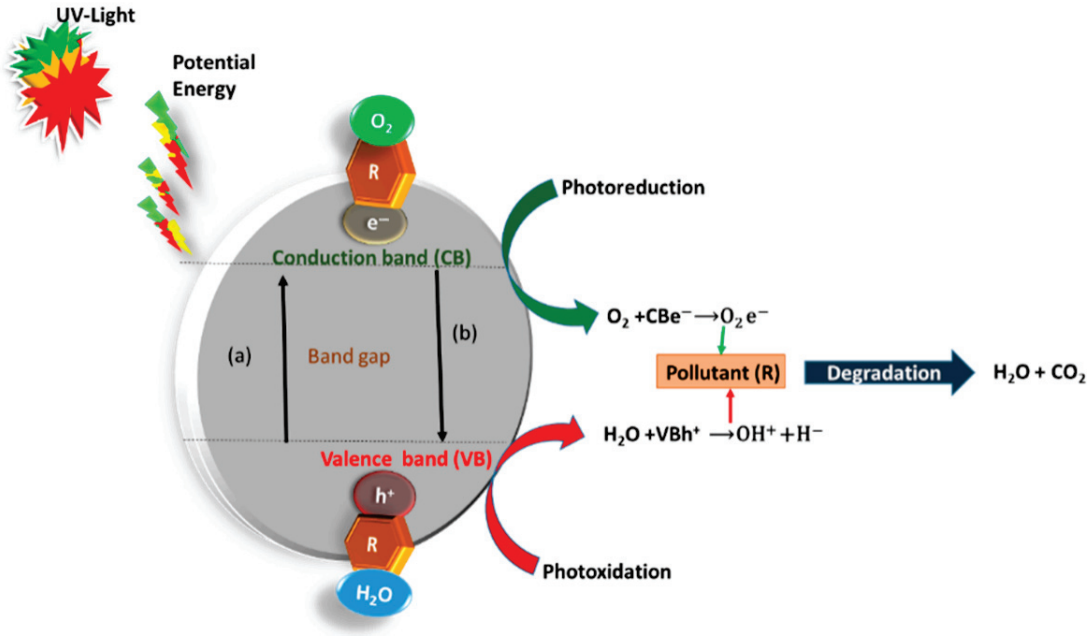


Figure 5. Photocatalytic reaction mechanism over semiconductor material, adapted from Tetteh et al. [74]. (**a**) Conduction band reaction, (**b**) Valence band reaction.

4.2. Factors Affecting Photocatalytic Process

There are a multitude of factors that influence the performance of photocatalytic degradation with TiO_2, which include, but are not limited to, catalyst type and loading, pH of the solution, light intensity or wavelength, the concentration of the photocatalyst, the presence of dissolved oxygen, and reaction time [44,71].

4.2.1. Catalyst Loading

The quantity of catalyst utilized is a major determinant of photodegradation efficiency and total cost. Increasing the TiO_2 load increases the number of e^-/h^+ pairs, which accelerates the reaction rate, in addition to the number of active sites for pollutant adsorption [74]. The rise in TiO_2 loading is proportional to the photocatalytic reaction, and the concentration of catalyst particles affects the reaction rate remarkably, especially in the heterogeneous regime [44]. A higher catalyst concentration means a more significant number of active sites available for adsorption. As catalyst concentration increases above a specific limit, the degradation efficiency decreases [75]. Several researchers have indicated that when catalyst loading exceeds the optimum quantity, a significant reduction in efficiency is observed as excess particles tend to scatter light [76–78]. This could be due to a light scattering effect where light penetration of the effluent was retarded as there was a large number of solid particles present in the solution [79]. The increase in the catalyst amount increases the number of active sites on the photocatalyst surface, thus causing an increase in the formation of several $OH^{\bullet}$ radicals. However, particle–particle interaction or agglomeration

generally takes place at high solid concentrations, which results in a lower surface area for light absorption, thus reducing the degradation efficiency [80].

4.2.2. pH

The effect of pH on the photodegradation process can be attributed to three possible reaction mechanisms. This involves the (i) charge neutralization attack by the photolysis hydroxyl radicals, (ii) the direct oxidation by the positive hole, and (iii) direct reduction by the electron in the conducting band [13,14,17]. The pH effect associated with the surface-charge properties of the photocatalysts could be described at the point of zero charges (PZC). The point of zero charges (PZC) for TiO_2 particles is (pH = 6.8). Therefore, below this value, the photocatalyst surface is positively charged, and above this value, the photocatalyst surface is negatively charged. The surface of the photocatalyst becomes positively charged in an acidic solution or at pH values lower than PZC (pH < 6.8), and vice versa, according to the equations below, where Khan et al. [81] explain that the adsorption of anions is favoured when the pH is less than the point of zero charges (PZC). The pH is known to affect the surface of titania by either protonation or deprotonation, as expressed in Equations (21) and (22).

$$\text{Protonation} \qquad \mathrm{TiOH_{(Surface)} + H^+ \rightarrow TiOH^{2+}{}_{(Surface)}} \tag{21}$$

The adsorbent surface is positively charged when pH is lower than the PZC value, and the surface becomes cation-repelling/anion-attracting.

$$\text{Deprotonation} \qquad \mathrm{TiOH_{(Surface)} + OH^- \rightarrow TiO^-{}_{(Surface)} + H_2} \tag{22}$$

On the contrary, the surface is negatively charged above PZC, and the surface becomes anion-repelling/cation-attracting [82], further iterating that pH is a significant factor influencing the degradation rate. The importance of pH was further emphasized by Saien and Shahrezaei [83], who explain that pH influences the catalyst charge, the pollutant molecule, and the degradation mechanism and generation rate of the hydroxyl radical.

4.2.3. Light Wavelength and Intensity

The photochemical impacts of light sources with various wavelength emission ranges will have a significant effect on the photocatalytic process [84]. The UV light used in the process needs to have sufficient energy to promote electron–hole formation [85]. The corresponding electromagnetic spectrum for UV irradiation is categorized as UV-A, UV-B, and UV-C based on the wavelength of light that it emits [86]. The UV-A range has its light wavelength range from 315 to 400 nm, which corresponds to a (3.10–3.94 eV) band gap [87]. UV-B has a wavelength range of 280–315 nm, which corresponds to a (3.94–4.43 eV) band gap, and the UV-C ranges from 100 to 280 nm, which corresponds to a (4.43–12.4 eV) band gap [88]. In most previous studies, the UV ranges from 254 nm to 315 nm and provides light photons sufficient for the photonic activation of titanium dioxide (TiO_2) [12–14].

TiO_2 has a wide band gap (about 3.2 eV), with optical absorption in the 310–400 nm-wavelength region [66]. A series of modifications to TiO_2 is usually carried out, thereby improving the utilization of visible light by TiO_2 and reducing the photo-generated electron–hole recombination rate on the surface of TiO_2 [89], which is discussed in the next section. However, recombining electron–hole pairs is usually a problem experienced in photocatalysis [66]. Electron–hole pair separation struggles with recombination at a lower light intensity, which decreases the creation of free radicals, and, hence, the degradation of the organic molecules is reduced [86]. The efficiency of isopropanol degradation by TiO_2 nanotubes increased to 56% with increasing UV light intensity from 0 to 3.0 mW/cm^2 [90].

4.2.4. Initial Concentration Nature of Pollutants

The photocatalysis process depends on the adsorption of organic pollutants on the surface of the photocatalyst. This can also be influenced by the rate of photodegradation, the initial concentration of pollutants, nature, and other existing compounds in the wastewater matrix [17]. A high concentration of pollutants in water saturates the TiO_2 surface and hence reduces the photonic efficiency (less radical $OH^{\bullet}$ ions are generated) resulting in the deactivation of the photocatalyst and a smaller degradation percentage. Consequently, the photocatalytic activity of the produced photocatalyst is decreased. Zhu et al. [91] reported that the path length of the photons entering the solution decreases by increasing the initial amount of methyl orange (MO) azo dye, and the opposite effect occurs for the lower amount. Kertèsz et al. [92] studied the effect of different initial amounts of reactive yellow 125 dye on the process of photodegradation, and their results revealed a decrease in degradation efficiency by increasing the amount of dye. This dependence is most likely associated with generating numerous monolayers of the adsorbed dye on the surface of the photocatalyst, which is preferred at high dye concentrations [86]. On the other hand, dye molecules are adsorbed on the photocatalyst surface by increasing the initial concentrations of the dye, and a considerable amount of UV is absorbed by the dye molecules instead of the photocatalyst particles. Consequently, the light penetration decreases on the catalyst surface [21].

4.2.5. Morphology

Surface morphology (surface area, structure, and size of the photocatalyst) is an important physicochemical factor to be considered in the photocatalytic degradation process. The number of photons striking the photocatalyst controls the rate of reaction, which signifies that the reaction takes place only in the absorbed phase of the photocatalyst [93,94]. However, the type of photocatalyst, size, and shape enhance the adsorption capacity and the photocatalytic activity. Additionally, the crystallite size of a catalyst plays a significant role in the photocatalytic process [95,96]. The surface area of the photocatalyst materials also has a significant impact on photocatalytic activity. Thus, a large surface area contains more active sites for the oxidative reactions [97].

The efficiency of the photodegradation of organic molecules is gradually enhanced by raising the temperature. An increase in reaction temperature generally results in increased photocatalytic activity; however, reaction temperature above >80 °C favours the recombination of charge carriers and demotes the adsorption of organic compounds on the titania surface [86]. Also, in the photocatalytic process, increasing the contact time leads to the increasing production of active radicals due to more exposure to the light, thus improving photocatalytic degradation efficiency [98]. Table 4 summarizes some investigations for the photocatalytic degradation of organic pollutants.

Table 4. Different photocatalysts are used in photocatalytic degradation.

Type of Wastewater	Type of Catalyst	Target Pollutant	Operating Conditions	Light Source	Efficiency (%)	Reference
Textile industry wastewater	TiO_2/anthill	Colour	IC (3.01); CL (2.5 g/L); pH (2); T (67 min)	Sunlight	70.92	[99]
Petroleum refinery	TiO_2	COD and SO_4^{2-}	COD: (1226 mg/L); pH (8); CL (1.5 g/L); T (150 min)	UV light	92	[100]
Industrial wastewater	ZnO	Phenol and benzoic acid	IC (50 mg/L); CL (1.0 g/L); T (120 min)	UV light	69.75	[101]
Industrial wastewater	Ce-doped ZnO	Rhodamine B (RhB)	IC (10 mg/L); CL (0.7 g/L); pH (9.0); T (120 min)	Sunlight	97.66	[102]
Textile industry wastewater	ZnO/bentonite	Solophenyl Red 3BL (SR 3BL)	IC (0.75 mg/L); CL (0.75 g/L); pH (6), T (160 min)	Sunlight	92	[103]

Table 4. *Cont.*

Type of Wastewater	Type of Catalyst	Target Pollutant	Operating Conditions	Light Source	Efficiency (%)	Reference
Industrial wastewater	Kaolinite/TiO_2/ZnO	Remazol Red (RR), an anionic azo dye	IC (100 mg/L); CL (100 mg/L); pH (2.5); T (120 min)	Sunlight	98	[104]
Synthetic wastewater	ZnO/RGO	Congo red (CR) and Eosin yellow (EY) contaminate	IC (10 mg/L); CL (0.05 g/L); pH (3.0); T (120 min)	Visible light	51	[105]
Textile industry wastewater	ZnO/pumice composite	Dye-containing wastewater	IC (3.01 mg/L); CL (3.0 g/L); pH (4.01); T (45.04 min)	Sunlight	90.17	[106]
Synthetic wastewater	CuS flowers	Rhodamine B (Rh B)	CL (1 g/L); T (12 min)	Visible light	~99	[107]
Synthetic wastewater	Gelatin–cerium–copper sulfide Ge-Ce-CuS nanoparticles	Malachite green oxalate dye (MGO dye)	IC (3×10^{-4} M); CL (1.5 g/L); pH (9); T (120 min);	Sunlight	90.7	[108]
Pharmaceutical industry treatment	Persulfate Sodium (PPS)	Penicillin G (PG)	IC (5 mg/L); CL (0.8 g/L); t pH (6), (22 °C); MS (500 rpm)	UV light	72.72	[109]
Textile industry wastewater	Lanthanum Vanadate ($LaVO_4$)	Methylene blue (MB)	IC (10 mg/L); CL (0.3 g/L); pH (7)	UV light	91	[110]
Synthetic wastewater	TiO_2/GO graphene oxide composite	Methylene blue (MB)	IC (5 mg/L); CL (0.2 g/L); pH (10); T (4 h).	UV–vis	99	[111]
Pharmaceutical industry treatment	Nanobiocomposite $CoFe_2O_4$@methycellulose (MC)	Metronidazole (MNZ) antibiotic	IC (5 mg/L); CL (0.2 g/L); pH (11); T (120 min)	UV light	85.3	[112]

IC = initial concentration of pollutant; CL = catalyst load; T = expo-*sure time; t = temperature; MS = mixing speed; UV = ultraviolet.

5. Challenges and Prospects of TiO_2-Based Photocatalysis

The photocatalytic process has shown significant promise as a sustainable treatment method in the water and wastewater treatment settings. However, among the various photocatalysts available, TiO_2 is the most extensively studied and utilized due to its cost-saving benefits, non-hazardous properties, and oxidation performance [113,114]. Although many studies have applied TiO_2 photocatalysis in wastewater treatment, TiO_2 possesses several shortcomings that limit its commercial or industrial applications such as wide bandgaps, inability to absorb visible light or visible light utilization from solar sources, stability or poor separation potential (fast electron–hole recombination), recovery, recyclability, and significant attention demand [115]. Figure 6 presents a schematic SWOT (strengths, weaknesses, opportunities, and threats) analysis of TiO_2-based AOPs in the context of wastewater treatment, highlighting critical insights that inform both the current state and future directions of this emerging technology. The SWOT also underscores the need for an integrated research approach that addresses material limitations, process design, environmental implications, and regulatory frameworks. It serves as a roadmap for enhancing the performance, safety, and application of TiO_2-based AOPs in future wastewater treatment solutions. Despite the strong fundamental knowledge of TiO_2 photocatalysis, persistent barriers are hindering its large-scale industrial adoption and successful transformation from laboratory to real-world applications. Table 5 shows a summary of extensive studies on TiO_2-based photocatalysis and future research directions. With continued innovation and research, TiO_2 photocatalysis stands poised to play a critical role in achieving sustainable and efficient water treatment solutions in the 21st century. As shown in Figure 6, visible light activation, recovery techniques (magnetic separation), hybrid system integration, and AI-enhanced optimization were highlighted as future opportunities for TiO_2-based photocatalysis.

Table 5. Summary of knowledge gaps and prospects of TiO_2-based photocatalysis.

Thematic Area	Key Findings	Considerable Remarks	Future Research	Reference
TiO_2 photocatalysis	Synergistic effect of metal-doped TiO_2/AC for efficient visible light-driven cationic dye degradation, Ag-doped TiO_2/AC with enhanced surface functionality, reactivity, and cyclic stability showed 87.25% Rh B degradation.	Advances in environmental remediation using metal-doped TiO_2/AC heterojunctions (e.g., Ag-TiO_2 or TiO_2-ZnO, TiO_2-graphene) for charge separation.	Doping with metals/non-metals to extend visible light activity.	[116]
	Multi-element synergy in photocatalytic material-integrated mechanism–design–preparation strategies	Quantitative analysis of the complex interactions between elements and the integrated design of low-cost materials, elemental doping, and surface plasma.	Immobilization of supports to improve recovery potential. Scalability of eco-friendly synthesis routes (bio-mediated TiO_2 nanostructures).	[117]
	Degradation of antibiotic oxytetracycline using surface-reconstituted TiO_2 photocatalyst	The synergistic effect of co-doping compared to single-component doping.	Understanding of charge transfer mechanism and improving band gap energy reduction under responsive light.	[118]
Advanced oxidation process (AOP)	Commercialization aspects for TiO_2-based indoor air purification	Designing strategies to improve their photon utilization and deactivation resistance, and regeneration of TiO_2-based photocatalysts.	TiO_2-based air purification is proposed to demonstrate the innovative commercialization direction.	[119]
	Application of Uv/O_3/Tio$_2$/hydrogen peroxide-based advanced oxidation processes for wastewater treatment	Hybrid system (UV/TiO_2/O_3) for pollutant removal with pathogen inactivation. Also, ozone-based AOPs are efficient at detoxifying a variety of resistant effluents.	To establish a solid theoretical foundation for the implementation of UV/H_2O_2- and O_3/H_2O_2-based AOPs in wastewater management.	[120]
	Amalgamation of advanced oxidation process with biological techniques for the treatment of tannery wastewater	Pre-treatment of wastewater by AOP converts the recalcitrant organic pollutants to simpler and biodegradable compounds, allowing the wastewater to be treated by subsequent biological treatment.	A cost-effective methodology for the treatment of tannery wastewater to comply with applicable current regulations worldwide must explore the use of AOP coupling with biological treatment technologies.	[121]
	Preparation of the Ti/TiO_2-RNTs/SnO_2–Sb–Ni-La electrode and its electrochemical degradation of oily wastewater	The electrochemical oxidation method is expected to reduce energy loss.	Electrochemical AOPs using renewable energy sources and exploring suitable cost-effective electrode materials.	[122]
Magnetic nanomaterials	Evaluation of photocatalytic degradation of Bisphenol A by reusable Fe_3O_4/SiO_2/TiO_2 magnetic nanocomposite: optimization by response surface methodology	The potential of Fe_3O_4/SiO_2/TiO_2 using both UVA and solar light. Agglomeration and loss of surface activity over time.	Magnetic TiO_2 for easy recovery and reuse with magnetic separation technology. Environmental toxicity and long-term stability have not been fully assessed for scalability applications.	[123]
Emerging materials	Emerging frontiers of nickel–aluminum-layered double hydroxide heterojunctions for photocatalysis	Ni–Al LDH-based heterojunctions in photocatalytic applications, such as H_2 evolution, CO_2 reduction, and pollutant removal.	Exploit new Ni–Al LDH-based heterojunctions for high-performance photocatalytic applications, large surface area, tunable band gap and morphology, abundant reaction sites, and high activity, selectivity, and photostability.	[124]
	ZIF-8 metal–organic frameworks and their hybrid materials: Emerging photocatalysts for energy and environmental applications	Applications of ZIF-8-based photocatalysts in light-driven H_2 evolution, H_2O_2 evolution, CO_2 reduction, and dye and drug degradation.	Developing cost-effective, scalable, and environmentally friendly ZIF-8 composites for industrial applications.	[125]
	Ionic liquids: The emerging "cardiotonic" for photocatalytic materials	Ionic liquids (ILs) and photocatalytic materials (PMs) enhance the properties (hydrogen bonds effect, electrostatic effect, polarity effect, and coordination effect).	Research in high-powered PMs using the strategy of IL modification.	[126]
Environmental relevance	Toward sustainable photocatalysis: Addressing deactivation and environmental impact of anodized and sol–gel photocatalysts	Photocatalytic coating preparation, like chemical sol–gel and electrochemical anodic oxidation, generates the oxide directly from a titanium substrate. Life cycle assessment (LCA) was used to quantify and compare the potential environmental impacts associated with the two different TiO_2 production processes.	Developing more eco-friendly application strategies, like magnetic photocatalysts and synthesis routes (sol–gel photocatalysts). Future research on iron oxide-based composites for environmental remediation.	[127]
AI-integrated process	Artificial intelligence (AI) techniques	Fe_3O_4/TiO_2 nanocomposites were synthesized and optimized for enhanced photocatalytic degradation of organic pollutants. An AI-assisted model was developed to predict removal efficiency based on experimental data.	The potential of integrating AI with advanced photocatalysts for wastewater treatment and suggests a scalable strategy for industrial applications.	[128]

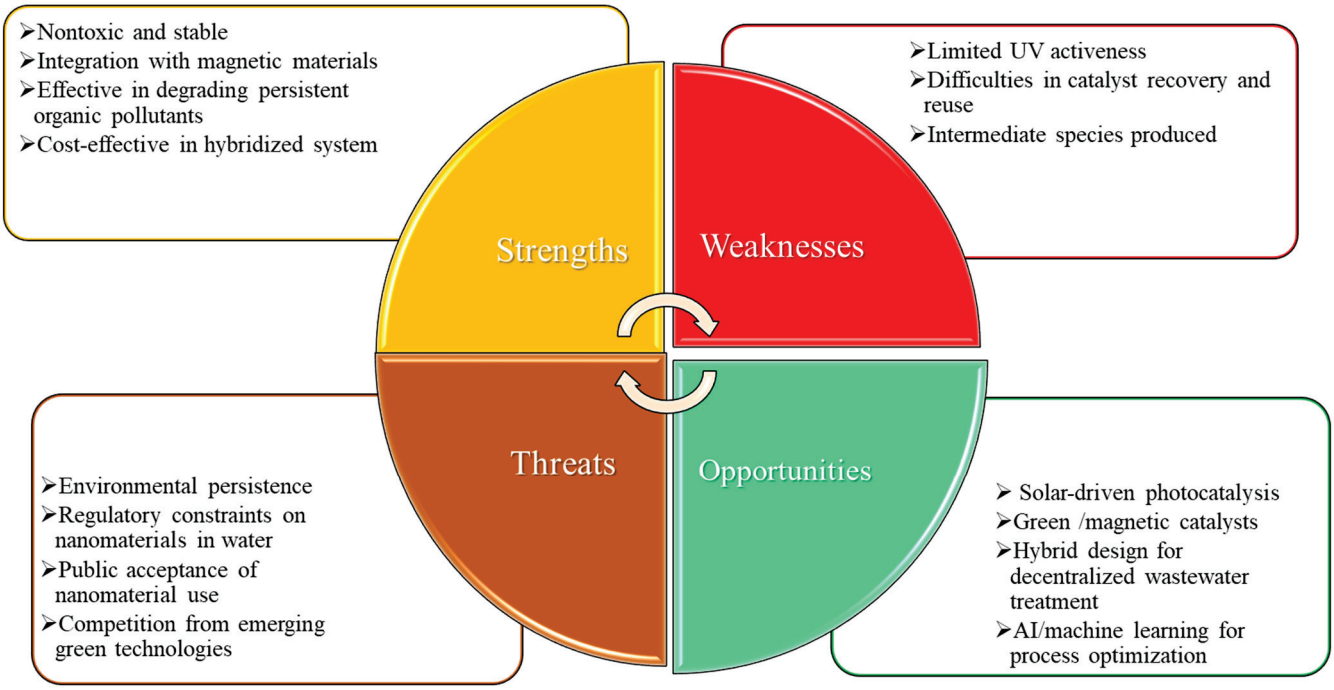


Figure 6. Schematic diagram of strengths, weaknesses, opportunities, and threats (SWOT) analysis of TiO_2-based AOPs in wastewater treatment.

5.1. Challenges of TiO_2's Large Energy Band Gap

Titanium dioxide (TiO_2) is a widely used semiconductor with significant applications in photocatalysis, solar cells, and environmental purification. However, its large energy band gap (~3.2 eV) presents several challenges that limit its practical applications, particularly under visible light. The key challenges of TiO_2's large energy band gap are as follows. (i) Limited Light Absorption: The large band gap of TiO_2 restricts its light absorption to the ultraviolet (UV) region, which constitutes only a small fraction of the solar spectrum. This results in poor utilization of visible light, significantly limiting its efficiency in solar energy applications and photocatalysis [129]. (ii) Low Quantum Efficiency: Due to the wide band gap, TiO_2 exhibits low quantum efficiency. This means that the number of charge carriers generated per photon absorbed is relatively low, reducing the overall efficiency of photocatalytic processes. (iii) High Charge Recombination Rate: TiO_2 suffers from a high rate of recombination of photo-generated electron–hole pairs. This recombination reduces the number of charge carriers available for photocatalytic reactions, further limiting their efficiency [13].

5.1.1. Enhancing TiO_2 Visible/Sunlight and Near-Infrared (NIR) Light Absorption

To enhance the visible/sunlight and near-infrared (NIR) light absorption capacity of titanium dioxide (TiO_2), several strategies have been explored and proven effective. The following are the key approaches:

Doping with Metal and Non-Metal Elements

(i) Metal Doping: Incorporating metal elements such as copper (Cu), iron (Fe), and manganese (Mn) into TiO_2 can significantly improve its visible light absorption. For instance, Cu substitution in TiO_2 has been shown to enhance visible light absorption, especially when combined with an applied electric field [130]. Fe doping broadens the light absorption spectrum and improves charge separation, enhancing photocatalytic performance [131]. Mn-doped TiO_2 nanotubes also demonstrate improved visible light absorption and efficient separation of photo-generated electron–hole pairs [132]. (ii) Non-

Metal Doping: Non-metal elements like nitrogen (N), sulfur (S), and carbon (C) can also be used to extend the absorption edge of TiO_2 into the visible region. N, S-co-doped TiO_2 nanoparticles exhibit strong visible light absorption and enhanced photocatalytic activity [133]. Anion doping with elements such as nitrogen and carbon in TiO_2 nanotube membranes has been shown to improve light absorption and efficiency in solar-to-fuel conversion [134].

Creating Oxygen Vacancies, Defects, and Introducing Dopants

(i) Oxygen Vacancies: Introducing oxygen vacancies in TiO_2 narrows its band gap, enhancing light absorption in the NIR region. Techniques such as laser ablation in liquid (LAL) can create abundant oxygen vacancies efficiently [135]. (ii) Ti^{3+} Defects: Introducing Ti^{3+} defects in TiO_2 can make it responsive to visible light. A novel approach involves generating surface Ti^{3+} sites without creating oxygen vacancies, which significantly enhances visible light response [136]. (ii) Photon Localization Effects: Utilizing photonic crystals to localize photons can enhance light harvesting efficiency. For example, coupling SiO_2 opal photonic crystals with Fe-doped TiO_2 films improves N_2 photo-fixation performance [133].

Combining with Conjugated Polymers

Polymer Composites: Using conjugated polymers with TiO_2 nanoparticles can extend light absorption to the visible range and enhance photocatalytic reactions. For instance, PVA/TiO_2 composites with a porous morphology show efficient degradation of phenol under visible light [137].

Structural and Morphological Modifications

(i) Nanostructuring: Creating nanostructures such as nanotubes, nanorods, and aerogels can increase the surface area and improve light absorption. For example, nitrogen-doped TiO_2 aerogels loaded with palladium nanoparticles show significant enhancement in visible light-driven H_2 production [138]. (ii) Core–Shell Nanostructures: Creating core–shell nanostructures, such as $NaYF_4$:b, Tm@$NaYF_4$:b, Nd@TiO_2, can enhance NIR absorption and energy transfer, improving the overall photocatalytic performance [139]. (iii) Plasmonic Nanostructures: Integrating metallic plasmonic nanostructures like aluminum and gold with TiO_2 can activate the structures plasmonically, increasing optical absorption in the visible and NIR spectral range [140]. Embedding plasmonic nanostructures such as silver nanoplates (Ag NPLs) into TiO_2 can significantly enhance NIR absorption. The surface plasmon resonance (SPR) effect of Ag NPLs generates additional photo-generated carriers and improves the separation of electron–hole pairs, thus enhancing the overall light absorption [141].

Co-Doping and Synergistic Effects

Co-doping: Combining multiple dopants can synergistically enhance light absorption and photocatalytic activity. For instance, co-doping with phosphorus (V) and titanium (III) in a leaf-architectured TiO_2 structure significantly enhances visible light harvesting and solar photocatalysis [142].

Hydrogenation and Phase Transformation

(i) Hydrogenation: Hydrogenating TiO_2 to form hydrogenated TiO_2 (H-TiO_2) improves its absorption in the Vis-NIR region. This process can be achieved through a one-step hydrogen reduction, which also enhances the material's magnetic and photoconversion properties [143]. (ii) Phase Transformation: Using pulsed laser irradiation to induce phase transformations in TiO_2 can create defect-engineered black TiO_2, which shows improved light absorption in the visible and NIR regions [144].

Up-Conversion Materials

Rare-Earth Doping: Incorporating rare-earth-doped luminescent materials that perform NIR-to-UV-VIS spectral conversion can enhance the photocatalytic activity of TiO_2. This approach leverages the energy from NIR radiation to drive photocatalytic reactions [145,146].

5.2. Complex Oxidizable Organic Substrates

The critical challenge identified as a constraint for photocatalysis application is the treatment scope for contaminants. Jiang et al. [147] reported that obtaining selective oxidation of the target pollutant or pollutants in the presence of other oxidizable organic substrates is relatively complex, which has become a significant setback for photocatalysis systems. It is challenging to oxidize benzene or other BTEX chemicals selectively in the presence of a high concentration of DOM (dissolved organic matter) [27,148]. Also, the intermediates of some emerging contaminants (antibiotics, phenols, pharmaceuticals, etc.) can result in antibiotic resistance and environmental risks [149]. Consequently, future technical research should focus on the intermediate formed as well as increasing the material efficiency [150–152].

5.3. Energy-Intensive/Recovery, Recyclability, and Reusability

The conventional method for the use of TiO_2 involves slurry suspension, where the TiO_2 nanoparticle powder is dispersed in contaminated water in the form of a slurry or suspension. However, the TiO_2 particles in the form of a slurry can utilize the maximum light absorption and mass transfer of pollutants. The method has some major drawbacks, such as the power consumption needed for continuous mixing to keep the particles suspended during photolysis [153–155]. After the photocatalytic process, the TiO_2 nanoparticles are difficult to separate, which affects the sustainability of the environment. The post-photocatalysis separation of the TiO_2 particles usually requires complex and high-energy-consuming processes such as ultrafiltration, ultracentrifugation, and adequate precipitation [19]. The main flaw associated with the slurry suspension method is that photocatalytic water treatment processes are not receiving widespread acceptance in practical applications [153,156–158]. An approach such as the immobilization of titanium dioxide onto supporting materials in a solid matrix has become an intriguing alternative to avoid the challenge of coagulation and the drawbacks of the slurry suspension method [159–161].

Furthermore, TiO_2 photocatalysts can be enhanced using dye sensitization supports, magnetization, and surface modification by doping with non-metals, metals, and transition metals, as well as coupling with other semiconductors [162,163]. The TiO_2 ternary/quaternary-based composites and hybrid materials are also a major trend, primarily to attain higher photonic efficiency by synergistically modifying physical, chemical, and electronic properties [164]. Researchers have used various substrates or other uncommon materials, such as microporous cellulosic membranes, alumina clays, ceramic membranes, monoliths, zeolites, and even stainless steel, as a support for TiO_2 [165–167]. The recyclability of catalysts is one of the critical steps toward the sustainable application of photocatalysts and the development of heterogeneous photocatalysis technology for water and wastewater treatment [168]. Recently, several studies have demonstrated satisfactory recyclability of nanomagnetic nanoparticles via magnetic separation processes using a magnetic field [169]. Krishna et al. [170] reported the reusability of the $CoFe_2O_4/TiO_2$ nanocatalysts for acid blue 113 (AB113) dye degradation through magnetic separation, where their photocatalytic activity was found to be retained up to six consecutive cycles without considerable loss of photocatalytic activity and stability.

5.4. Industrial/Large-Scale Application of Semiconductor Photocatalysts

The relatively slow transfer of photocatalysis treatment techniques from bench to industrial scale is likely due to the system's design currently used in water treatment [114,171]. A disadvantage of large-scale applications could be an unsuitable choice of catalyst for pollutant degradation, such as utilizing a photocatalyst that is ineffective or incompatible with the contaminants [114]. This necessitates the modification of the photocatalyst's structure to adjust its band gap and effectively harness visible light irradiation. The primary obstacle to large-scale photocatalysis is the retrieval of the photocatalyst after each cycle. For instance, powdered photocatalysts tend to settle at the bottom of the tank, making their full recovery unfeasible [172]. However, further research should be carried out, as the upscaling of photocatalytic processes may be challenging without adequate studies on more economical and available materials. Also, the design of more reliable photocatalysts through coating or doping on fixed supports would allow for the simultaneous degradation and separation of contaminants from the effluent stream [114].

5.5. The Challenges and Prospects of Magnetized TiO_2-Based Photocatalysts

Magnetic photocatalytic systems have emerged as a promising route for environmental remediation due to its dual advantages of photocatalytic degradation and magnetic recoverability. However, the stability of core–shell magnetic photocatalysts (Fe_3O_4-TiO_2) under real wastewater conditions has some setbacks. For instance, under extreme pH, high ionizing strength, and oxidizing conditions, leaching of semiconductors and corrosive ions (Cl and SO_4) can occur. The exposure to the magnetic core diminishes the structural integrity and the catalytic performance, thereby rendering the magnetic serration ineffective. The environmental and health concerns due to the potential ecotoxicological impacts of leached magnetic nanomaterials require research attention.

Consequently, ongoing research work is being conducted on the application of TiO_2-based photocatalysis. However, its industrial applications and efficient use of sunlight to mitigate its energy challenge are still limited. Table 6, therefore, presents an action plan to develop reusable and regenerative photocatalysts with an affordable, environmentally friendly, and non-toxic precursor. Moreover, doping of tunable materials for suitable morphological structures via a synthetic route has a bottleneck. Hence, adapting optimization and life cycle assessment (LCA) concepts may aid in developing environmentally friendly and sustainable green synthesis techniques. Although laboratory-based research has demonstrated efficient magnetic recovery, the costs associated with rare-earth magnetics, the energy required to generate a magnetic field, and the complexity of sludge handling pose substantial barriers for commercial implementation.

Table 6. Action plan to improve TiO_2-based photocatalyst challenges.

Conditions	Current Challenges	Prospective Way Forward
Cost-effective synthesis route	* Nanomaterials required to improve TiO_2 production * Cheap design method * Synthesis route with eco-friendly and non-toxic precursors	* Developing and optimizing cost-effective TiO_2 synthesis methods to maximize production yield * Regenerative and reusable photocatalyst approach
Morphology control	* Synthesis of nanoparticles with good crystallinity, surface area, and small particle size	* Develop a synthesis method to maximize morphology * Develop a kinetic model for the predictive morphology of photocatalysts
Visible light absorption	* Modification with cheap co-catalysts * Concentration of doped materials	* Develop and optimize a cost-effective modification process
Product selectivity and optimization	* Sensitivity and selectivity of nanomaterials to improve product yield* Optimizing the selective product	* Tuning the band structure and accumulation of illumination * TiO_2 modification and regeneration * Optimizing the synthesis process, multi-factors, or operating conditions

Table 6. *Cont.*

Conditions	Current Challenges	Prospective Way Forward
Charge separation efficiency	* Difficult to separate photocatalysts after being used	* Develop semiconductors with suitable band positions to couple with TiO_2 * Develop magnetized TiO_2 to enhance magnetic separation and regeneration usability
Cost-effective photocatalytic reactor design	* Design of a suitable photocatalytic reactor	* Establishment of hybridized solar/UV–photocatalytic reactor * Commercialization of reactors

Furthermore, the operational and economic viability of magnetic separation systems requires a higher loading of the magnetic core, which is photocatalytically inert. Hence, proposing reactor design and development of ion-resistant coatings to enhance material stability, establishing testing protocols for metal leaching and toxicity under realistic wastewater matrices, and integrating magnetic photocatalysis with complementary technologies such as membrane, filtration, adsorption, or electrochemical systems come in handy. These interdisciplinary efforts are needed to bridge the gap between material synthesis and reactor engineering to ensure that promising laboratory materials can be translated into scalable and robust treatment solutions.

6. Conclusions

This study provides insight into the research trends, challenges, and prospects of advanced oxidation processes and photocatalysis in wastewater treatment. A comprehensive review was conducted using the Preferred Reporting Items for Systematic Reviews and Meta-Analyses (PRISMA) approach. The keyword occurrence and research interest assessment revealed the research gap and prospects of TiO_2-based photocatalysis on emerging contaminants. Moreover, to improve TiO_2 photocatalytic efficiency, energy band gap, morphology, recyclability, and reusability, schemes such as metal, non-metal, magnetic, and plasma doping can be employed via optimized sol–gel techniques. Also, the integration of photocatalysis with biological processes was found to be very favourable than other conventional methods of mitigating recalcitrant pollutants. Also, studies on the life cycle assessment of photocatalysts at the preparatory and application stages should be intensified. Multidisciplinary and application-driven research can unlock the full potential of TiO_2-based photocatalysis in wastewater treatment. Future research should explore more of the following:

- Magnetic nanocomposite photocatalysis, which involves coupling TiO_2 with magnetic materials (Fe_3O_4), allows for easy recovery and regeneration of the catalyst with a magnetic field and enhances its practical applicability.
- TiO_2 doped with emerging materials such as nitrogen, ionic liquids, sulfur, metal ions, carbon, and hybrid systems with carbon-based materials can increase the photocatalytic activity under visible light response systems.
- The adoption of environmentally friendly synthesis methods of TiO_2 nanoparticles with plant or biodegradable-based materials can contribute to the broader goals of sustainable nanotechnology.
- The integration of TiO_2 photocatalysis with biological treatment, electrocatalysis, or membrane systems offers multifunctional effects to enhance overall treatment performance.
- The development of standard testing protocols, regulatory frameworks, and environmental risk assessments is critical to support the safe and responsive implementation of TiO_2-based photocatalysis.

Author Contributions: Conceptualization, C.M. and E.K.T.; methodology, E.K.T.; writing—original draft preparation, C.M. and E.K.T.; writing—review and editing, C.M., S.R., and E.K.T.; supervision, S.R. and E.K.T. All authors have read and agreed to the published version of the manuscript.

Funding: This research received no external funding.

Data Availability Statement: No new data were created or analyzed in this study. Data sharing is not applicable to this article.

Acknowledgments: The authors are thankful to Jaafar Mohammed and the Green Engineering Research Group, Department of Chemical Engineering, Durban University of Technology, for their support. The authors declare that the use of AI tools, such as Grammarly software, were employed to improve the grammar of the write-up. After using these tools/services, the authors reviewed and edited the content as needed and take full responsibility for the content of the publication.

Conflicts of Interest: The authors declare no conflicts of interest.

References

1. Karri, R.R.; Ravindran, G.; Dehghani, M.H. Wastewater—Sources, toxicity, and their consequences to human health. In *Soft Computing Techniques in Solid Waste and Wastewater Management*; Elsevier: Amsterdam, The Netherlands, 2021; pp. 3–33.
2. Bao, H.; Wu, M.; Meng, X.; Han, H.; Zhang, C.; Sun, W. Application of electrochemical oxidation technology in treating high-salinity organic ammonia-nitrogen wastewater. *J. Environ. Chem. Eng.* **2023**, *11*, 110608. [CrossRef]
3. United Nations Sustainable Development. Goal 6: Ensure Access to Water and Sanitation for All. Available online: https://www.un.org/sustainabledevelopment/water-and-sanitation/ (accessed on 10 July 2024).
4. Siraj, K.T.; Rao, P. Review on current world water resources scenario and water treatment technologies and techniques. *Int. J. Appl. Res.* **2016**, *2*, 262–266.
5. Bilal, H.; Li, X.; Iqbal, M.S.; Mu, Y.; Tulcan, R.X.S.; Ghufran, M.A. Surface water quality, public health, and ecological risks in Bangladesh—A systematic review and meta-analysis over the last two decades. *Environ. Sci. Pollut. Res.* **2023**, *30*, 1–19. [CrossRef]
6. Liu, L.; Chen, Z.; Zhang, J.; Shan, D.; Wu, Y.; Bai, L.; Wang, B. Visible-light-promoted peroxymonosulfate activation for ACE degradation: Overlooked role of photogenerated hole. *Appl. Catal. B Environ. Energy* **2025**, *365*, 124881.
7. Krishnan, S.; Rawindran, H.; Sinnathambi, C.M.; Lim, J.W. Network capture effect-driven enhanced activation of peroxymonosulfate by iron-doped carbon quantum dots derived from ferrous gluconate for efficient ciprofloxacin degradation: DFT calculations and mechanism analysis. *J. Mater. Chem. A* **2025**, *26*, 1–16.
8. Liu, L.; Chen, Z.; Zhang, J.; Shan, D.; Wu, Y.; Bai, L.; Wang, B. Treatment of industrial dye wastewater and pharmaceutical residue wastewater by advanced oxidation processes and its combination with nanocatalysts: A review. *J. Water Process Eng.* **2021**, *42*, 102122. [CrossRef]
9. Krishnan, S.; Rawindran, H.; Sinnathambi, C.; Lim, J. Comparison of various advanced oxidation processes used in remediation of industrial wastewater laden with recalcitrant pollutants. *IOP Conf. Ser. Mater. Sci. Eng.* **2017**, *206*, 012089. [CrossRef]
10. Srivastav, M.; Gupta, M.; Agrahari, S.K.; Detwal, P. Removal of refractory organic compounds from wastewater by various advanced oxidation process-a review. *Curr. Environ. Eng.* **2019**, *6*, 8–16. [CrossRef]
11. Kweinor Tetteh, E.; Opoku Amankwa, M.; Armah, E.K.; Rathilal, S. Fate of COVID-19 occurrences in wastewater systems: Emerging detection and treatment technologies—A review. *Water* **2020**, *12*, 2680. [CrossRef]
12. Abbood, N.S.; Ali, N.S.; Khader, E.H.; Majdi, H.S.; Albayati, T.M.; Saady, N.M.C. Photocatalytic degradation of cefotaxime pharmaceutical compounds onto a modified nanocatalyst. *Res. Chem. Intermed.* **2023**, *49*, 43–56. [CrossRef]
13. López, J.; Rey, A.; Viñuelas-Zahinos, E.; Álvarez, P.M. Preparation of a new green magnetic Fe_3O_4@TiO_2-P25 photocatalyst for solar advanced oxidation processes in water. *J. Environ. Chem. Eng.* **2023**, *11*, 109999. [CrossRef]
14. Mohod, A.V.; Momotko, M.; Shah, N.S.; Marchel, M.; Imran, M.; Kong, L.; Boczkaj, G. Degradation of Rhodamine dyes by Advanced Oxidation Processes (AOPs)–Focus on caviatation and photocatalysis-A critical review. *Water Resour. Ind.* **2023**, *30*, 100220. [CrossRef]
15. Yang, J.; Wang, H.; Jiang, L.; Yu, H.; Zhao, Y.; Chen, H.; Yuan, X.; Liang, J.; Li, H.; Wu, Z. Defective polymeric carbon nitride: Fabrications, photocatalytic applications and perspectives. *Chem. Eng. J.* **2022**, *427*, 130991. [CrossRef]
16. Jiang, L.; Yang, J.; Zhou, S.; Yu, H.; Liang, J.; Chu, W.; Li, H.; Wang, H.; Wu, Z.; Yuan, X. Strategies to extend near-infrared light harvest of polymer carbon nitride photocatalysts. *Coord. Chem. Rev.* **2021**, *439*, 213947. [CrossRef]
17. Fu, R.; Zhang, P.-S.; Jiang, Y.-X.; Sun, L.; Sun, X.-H. Wastewater treatment by anodic oxidation in electrochemical advanced oxidation process: Advance in mechanism, direct and indirect oxidation detection methods. *Chemosphere* **2023**, *311*, 136993. [CrossRef] [PubMed]

18. Panizza, M.; Cerisola, G. Direct and mediated anodic oxidation of organic pollutants. *Chem. Rev.* **2009**, *109*, 6541–6569. [CrossRef]
19. Pattnaik, A.; Sahu, J.; Poonia, A.K.; Ghosh, P. Current perspective of nano-engineered metal oxide based photocatalysts in advanced oxidation processes for degradation of organic pollutants in wastewater. *Chem. Eng. Res. Des.* **2023**, *190*, 667–686. [CrossRef]
20. Gelover, S.; Gómez, L.A.; Reyes, K.; Leal, M.T. A practical demonstration of water disinfection using TiO_2 films and sunlight. *Water Res.* **2006**, *40*, 3274–3280. [CrossRef]
21. Kaswan, V.; Kaur, H. A comparative study of advanced oxidation processes for wastewater treatment. *Water Pract. Technol.* **2023**, *18*, 1233–1254. [CrossRef]
22. Zawrah, M.; Snousy, M.G. Environmental Challenges of Nanotechnology in Subsurface. In *Environmental Science and Engineering*; Studium Press LLC: Houston, TX, USA, 2017; Volume 10, pp. 379–416.
23. Chakraborty, A.; Ruzimuradov, O.; Gupta, R.K.; Cho, J.; Prakash, J. TiO_2 nanoflower photocatalysts: Synthesis, modifications and applications in wastewater treatment for removal of emerging organic pollutants. *Environ. Res.* **2022**, *212*, 113550. [CrossRef]
24. Kaur, K.; Badru, R.; Singh, P.P.; Kaushal, S. Photodegradation of organic pollutants using heterojunctions: A review. *J. Environ. Chem. Eng.* **2020**, *8*, 103666. [CrossRef]
25. Kong, X.; Bai, R.; Wang, S.; Wu, B.; Zhang, R.; Li, H. Recovery of phosphorus from aqueous solution by magnetic TiO_2*/Fe_3O_4 composites. *Chem. Phys. Lett.* **2022**, *787*, 139234. [CrossRef]
26. Binas, V.; Venieri, D.; Kotzias, D.; Kiriakidis, G. Modified TiO_2 based photocatalysts for improved air and health quality. *J. Mater.* **2017**, *3*, 3–16.
27. Coha, M.; Farinelli, G.; Tiraferri, A.; Minella, M.; Vione, D. Advanced oxidation processes in the removal of organic substances from produced water: Potential, configurations, and research needs. *Chem. Eng. J.* **2021**, *414*, 128668. [CrossRef]
28. Amin, M.T.; Alazba, A.A.; Manzoor, U. A review of removal of pollutants from water/wastewater using different types of nanomaterials. *Adv. Mater. Sci. Eng.* **2014**, *2014*, 825910. [CrossRef]
29. Marimuthu, S.; Antonisamy, A.J.; Malayandi, S.; Rajendran, K.; Tsai, P.-C.; Pugazhendhi, A.; Ponnusamy, V.K. Silver nanoparticles in dye effluent treatment: A review on synthesis, treatment methods, mechanisms, photocatalytic degradation, toxic effects and mitigation of toxicity. *J. Photochem. Photobiol. B Biol.* **2020**, *205*, 111823. [CrossRef]
30. Boccuni, F.; Rondinone, B.; Petyx, C.; Iavicoli, S. Potential occupational exposure to manufactured nanoparticles in Italy. *J. Clean. Prod.* **2008**, *16*, 949–956. [CrossRef]
31. Lyons, K. Nanotechnology: Transforming food and the environment. *Food First Backgrounder* **2010**, *16*, 1–4.
32. Kerry, R.G.; Rout, J.R.; Das, G.; Fraceto, L.F.; Paramithiotis, S.; Patra, J.K. Applications of nanotechnology in food and agriculture. In *Food Molecular Microbiology*; CRC Press: Boca Raton, FL, USA, 2019; pp. 223–249.
33. Ahmad, F.; Salem-Bekhit, M.M.; Khan, F.; Alshehri, S.; Khan, A.; Ghoneim, M.M.; Wu, H.-F.; Taha, E.I.; Elbagory, I. Unique properties of surface-functionalized nanoparticles for bio-application: Functionalization mechanisms and importance in application. *Nanomaterials* **2022**, *12*, 1333. [CrossRef]
34. Bukht, R. Responsibility, Regulation and the Construction of Markets of Nanotechnologies in Food and Food Packaging: The Cases of Canada and India. Ph.D. Thesis, The University of Manchester (United Kingdom), Manchester, UK, 2016.
35. Henshaw, D.L.; O'Carroll, M.J. Scientific Committee on Emerging and Newly Identified Health Risks (SCENIHR). Opinion on Possible Effects of Electromagnetic Fields (EMF) on Human Health. 2009. Available online: https://citeseerx.ist.psu.edu/document?repid=rep1&type=pdf&doi=31882392b69b95d2a7dfc4c61d83c8862f53b52f (accessed on 15 August 2025).
36. Samaras, T.; Leitgeb, N.; Auvinen, A.; Danker-Hopfe, H.; Mild, K.H.; Mattsson, M.-O.; Norppa, H.; Rubin, G.J.; Scarfi, M.R.; Schüz, J. Scientific Committee on Emerging and Newly Identified Health Risks. Opinion on Potential Health Effects of Exposure to Electromagnetic Fields. *Bioelectromagnetics* **2015**, *36*, 480–484.
37. Castellar, J.A.; Torrens, A.; Buttiglieri, G.; Monclus, H.; Arias, C.A.; Carvalho, P.N.; Galvao, A.; Comas, J. Nature-based solutions coupled with advanced technologies: An opportunity for decentralized water reuse in cities. *J. Clean. Prod.* **2022**, *340*, 130660. [CrossRef]
38. Poyatos, J.M.; Muñio, M.M.; Almecija, M.C.; Torres, J.C.; Hontoria, E.; Osorio, F. Advanced Oxidation Processes for Wastewater Treatment: State of the Art. *Water Air Soil Pollut.* **2010**, *205*, 187–204. [CrossRef]
39. Tetteh, E.K.; Amo-Duodu, G.; Rathilal, S. Anaerobic Digested Wastewater CO_2 Sequestration Using a Biophotocatalytic System with a Magnetized Photocatalyst (Fe-TiO_2). *Molecules* **2022**, *27*, 5213. [CrossRef]
40. Martinez-Huitle, C.A.; Ferro, S. Electrochemical oxidation of organic pollutants for the wastewater treatment: Direct and indirect processes. *Chem. Soc. Rev.* **2006**, *35*, 1324–1340. [CrossRef]
41. Tetteh, E.K.; Rathilal, S. Biophotocatalytic reduction of CO_2 in anaerobic biogas produced from wastewater treatment using an integrated system. *Catalysts* **2022**, *12*, 76. [CrossRef]
42. Dlamini, C.P. Evaluation of Micro-Scaled TiO_2 on Degradation and Recovery of mTiO_2 from Treated Drinking Water. Ph.D. Thesis, Durban University of Technology, Durban, South Africa, 2016.

43. Janzeer, Y. Surface Modification of Titanium and Titanium Alloys to Enhance Bone Healing. Ph.D. Thesis, King's College London, London, UK, 2013.
44. Umar, M.; Aziz, H.A. Photocatalytic Degradation of Organic Pollutants in Water. *Intech* **2013**, *8*, 196–197. [CrossRef]
45. Laoufi, N.A.; Tassalit, D.; Bentahar, F. The degradation of phenol in water solution by TiO_2 photocatalysis in a helical reactor. *Glob. NEST J.* **2008**, *10*, 404–418.
46. Liu, H.; Zhang, Z.-G.; He, H.-W.; Wang, X.-X.; Zhang, J.; Zhang, Q.-Q.; Tong, Y.-F.; Liu, H.-L.; Ramakrishna, S.; Yan, S.-Y. One-step synthesis heterostructured g-C_3N_4/TiO_2 composite for rapid degradation of pollutants in utilizing visible light. *Nanomaterials* **2018**, *8*, 842. [CrossRef] [PubMed]
47. Sun, N.; Si, X.; He, L.; Zhang, J.; Sun, Y. Strategies for enhancing the photocatalytic activity of semiconductors. *Int. J. Hydrogen Energy* **2024**, *58*, 1249–1265. [CrossRef]
48. de Jongh, P.E.; Vanmaekelbergh, D.; Kelly, J.J. Cu_2O: A catalyst for the photochemical decomposition of water? *Chem. Commun.* **1999**, *12*, 1069–1070. [CrossRef]
49. Finlayson, M.F.; Wheeler, B.L.; Kakuta, N.; Park, K.H.; Bard, A.J.; Campion, A.; Fox, M.A.; Webber, S.E.; White, J.M. Determination of flat-band position of cadmium sulfide crystals, films, and powders by photocurrent and impedance techniques, photoredox reaction mediated by intragap states. *J. Phys. Chem.* **1985**, *89*, 5676–5681. [CrossRef]
50. Zheng, N.-C.; Ouyang, T.; Chen, Y.; Wang, Z.; Chen, D.-Y.; Liu, Z.-Q. Ultrathin CdS shell-sensitized hollow S-doped CeO_2 spheres for efficient visible-light photocatalysis. *Catal. Sci. Technol.* **2019**, *9*, 1357–1364. [CrossRef]
51. Wang, X.; Maeda, K.; Thomas, A.; Takanabe, K.; Xin, G.; Carlsson, J.M.; Domen, K.; Antonietti, M. A metal-free polymeric photocatalyst for hydrogen production from water under visible light. *Nat. Mater.* **2009**, *8*, 76–80. [CrossRef] [PubMed]
52. Zhang, J.; Chen, X.; Takanabe, K.; Maeda, K.; Domen, K.; Epping, J.D.; Fu, X.; Antonietti, M.; Wang, X. Synthesis of a carbon nitride structure for visible-light catalysis by copolymerization. *Angew. Chem. Int. Ed.* **2010**, *49*, 441–444. [CrossRef] [PubMed]
53. Yan, S.; Lv, S.; Li, Z.; Zou, Z. Organic–inorganic composite photocatalyst of gC_3N_4 and TaON with improved visible light photocatalytic activities. *Dalton Trans.* **2010**, *39*, 1488–1491. [CrossRef]
54. Chun, W.-J.; Ishikawa, A.; Fujisawa, H.; Takata, T.; Kondo, J.N.; Hara, M.; Kawai, M.; Matsumoto, Y.; Domen, K. Conduction and valence band positions of Ta_2O_5, TaON, and Ta_3N_5 by UPS and electrochemical methods. *J. Phys. Chem. B* **2003**, *107*, 1798–1803. [CrossRef]
55. Memar, A.; Phan, C.M.; Tade, M.O. Influence of surfactants on Fe_2O_3 nanostructure photoanode. *Int. J. Hydrogen Energy* **2012**, *37*, 16835–16843. [CrossRef]
56. Li, Z.-Q.; Chen, X.-T.; Xue, Z.-L. Microwave-assisted synthesis and photocatalytic properties of flower-like Bi_2WO_6 and Bi_2O_3–Bi_2WO_6 composite. *J. Colloid Interface Sci.* **2013**, *394*, 69–77. [CrossRef]
57. Cai, L.; Kisch, H. Visible light induced photoelectrochemical properties of n-$BiVO_4$ and n-$BiVO_4$/p-Co_3O_4. *J. Phys. Chem. C* **2008**, *112*, 548–554.
58. Hardee, K.L.; Bard, A.J. Semiconductor electrodes: X. Photoelectrochemical behavior of several polycrystalline metal oxide electrodes in aqueous solutions. *J. Electrochem. Soc.* **1977**, *124*, 215. [CrossRef]
59. Yi, Z.; Ye, J.; Kikugawa, N.; Kako, T.; Ouyang, S.; Stuart-Williams, H.; Yang, H.; Cao, J.; Luo, W.; Li, Z. An orthophosphate semiconductor with photooxidation properties under visible-light irradiation. *Nat. Mater.* **2010**, *9*, 559–564. [CrossRef] [PubMed]
60. Doshi, J.; Reneker, D.H. Electrospinning process and applications of electrospun fibers. *J. Electrost.* **1995**, *35*, 151–160. [CrossRef]
61. Ammar, S.H.; Abdulnabi, W.A. Synthesis, characterization and environmental remediation applications of polyoxometalates-based magnetic zinc oxide nanocomposites (Fe_3O_4@ZnO/PMOs). *Environ. Nanotechnol. Monit. Manag.* **2020**, *13*, 100289. [CrossRef]
62. Huang, M.; Xu, C.; Wu, Z.; Huang, Y.; Lin, J.; Wu, J. Photocatalytic discolorization of methyl orange solution by Pt modified TiO_2 loaded on natural zeolite. *Dye. Pigment.* **2008**, *77*, 327–334. [CrossRef]
63. Sun, J.; Wang, X.; Sun, J.; Sun, R.; Sun, S.; Qiao, L. Photocatalytic degradation and kinetics of Orange G using nano-sized Sn(IV)/TiO_2/AC photocatalyst. *J. Mol. Catal. A Chem.* **2006**, *260*, 241–246. [CrossRef]
64. Shirzad-Siboni, M.; Jonidi-Jafari, A.; Farzadkia, M.; Esrafili, A.; Gholami, M. Enhancement of photocatalytic activity of Cu-doped ZnO nanorods for the degradation of an insecticide: Kinetics and reaction pathways. *J. Environ. Manag.* **2017**, *186*, 1–11. [CrossRef]
65. Jabbar, Z.H.; Ebrahim, S.E. Highly efficient visible-light-driven photocatalytic degradation of organic pollutants by using magnetically separable supported heterogeneous nanocomposites (SiO_2/Fe_3O_4/Ag_2WO_4). *Environ. Nanotechnol. Monit. Manag.* **2021**, *16*, 100554. [CrossRef]
66. Chen, D.; Cheng, Y.; Zhou, N.; Chen, P.; Wang, Y.; Li, K.; Huo, S.; Cheng, P.; Peng, P.; Zhang, R. Photocatalytic degradation of organic pollutants using TiO_2-based photocatalysts: A review. *J. Clean. Prod.* **2020**, *268*, 121725. [CrossRef]
67. Saffari, R.; Shariatinia, Z.; Jourshabani, M. Synthesis and photocatalytic degradation activities of phosphorus containing ZnO microparticles under visible light irradiation for water treatment applications. *Environ. Pollut.* **2020**, *259*, 113902. [CrossRef]

68. Ammar, S.H.; Salman, M.D.; Shafi, R.F. Keggin-and Dawson-type polyoxotungstates immobilized on poly (3, 4-ethylenedioxythiophene)-coated zerovalent iron nanoparticles: Synthesis, characterization and their catalytic oxidative desulfurization activity. *J. Environ. Chem. Eng.* **2021**, *9*, 104904. [CrossRef]
69. Akpan, U.G.; Hameed, B.H. Parameters affecting the photocatalytic degradation of dyes using TiO2-based photocatalysts: A review. *J. Hazard. Mater.* **2009**, *170*, 520–529. [CrossRef]
70. Chong, M.N.; Jin, B.; Chow, C.W.; Saint, C. Recent developments in photocatalytic water treatment technology: A review. *Water Res.* **2010**, *44*, 2997–3027. [CrossRef] [PubMed]
71. Gaya, U.I.; Abdullah, A.H. Heterogeneous photocatalytic degradation of organic contaminants over titanium dioxide: A review of fundamentals, progress and problems. *J. Photochem. Photobiol. C: Photochem. Rev.* **2008**, *9*, 1–12. [CrossRef]
72. Konstantinou, I.K.; Albanis, T.A. TiO2-Assisted Photocatalytic Degradation of Azo Dyes in Aqueous Solution: Kinetic and Mechanistic Investigations: A Review. *Appl. Catal. B Environ.* **2004**, *49*, 1–14. [CrossRef]
73. Corrêa, A.X.R.; Tiepo, E.N.; Somensi, C.A.; Sperb, R.M.; Radetski, C.M. Use of Ozone-Photocatalytic Oxidation O_3 /UV/TiO_2 and Biological Remediation for Treatment of Produced Water from Petroleum Refineries. *J. Environ. Eng.* **2010**, *136*, 40–45. [CrossRef]
74. Tetteh, E.K.; Rathilal, S.; Asante-Sackey, D.; Chollom, M.N. Prospects of synthesized magnetic TiO_2-based membranes for wastewater treatment: A review. *Materials* **2021**, *14*, 3524. [CrossRef]
75. Diya'uddeen, B.H.; Daud, W.M.A.W.; Aziz, A.A. Treatment technologies for petroleum refinery effluents: A review. *Process Saf. Environ. Prot.* **2011**, *89*, 95–105. [CrossRef]
76. Naeem, K.; Feng, O. Effect of calcination on photocatalytic activity of Fe^{3+}-doped TiO_2 nanoparticles for degradation of phenol under UV irradiation. In Proceedings of the 2009 4th IEEE International Conference on Nano/Micro Engineered and Molecular Systems, Shenzhen, China, 5–8 January 2009; pp. 348–352.
77. Fahad, S.; Sönmez, O.; Saud, S.; Wang, D.; Wu, C.; Adnan, M.; Arif, M. *Engineering Tolerance in Crop Plants Against Abiotic Stress*; CRC Press: Boca Raton, FL, USA, 2021.
78. Begum, S.; Mishra, S.R.; Ahmaruzzaman, M. Fabrication of ZnO–SnO_2 nanocomposite and its photocatalytic activity for enhanced degradation of Biebrich scarlet. *Environ. Sci. Pollut. Res.* **2022**, *29*, 87347–87360. [CrossRef]
79. Zangeneh, H.; Zinatizadeh, A.; Habibi, M.; Akia, M.; Isa, M.H. Photocatalytic oxidation of organic dyes and pollutants in wastewater using different modified titanium dioxides: A comparative review. *J. Ind. Eng. Chem.* **2015**, *26*, 1–36. [CrossRef]
80. Ahmed, S.; Rasul, M.; Martens, W.N.; Brown, R.; Hashib, M. Heterogeneous photocatalytic degradation of phenols in wastewater: A review on current status and developments. *Desalination* **2010**, *261*, 3–18. [CrossRef]
81. Khan, M.M.; Adil, S.F.; Al-Mayouf, A. Metal oxides as photocatalysts. *J. Saudi Chem. Soc.* **2015**, *19*, 462–464. [CrossRef]
82. Das, L.; Dutta, M.; Basu, J.K. Photocatalytic degradation of phenol from industrial effluent using titania-zirconia nanocomposite catalyst. *Int. J. Environ. Sci.* **2013**, *4*, 415–431.
83. Saien, J.; Shahrezaei, F. Organic pollutants removal from petroleum refinery wastewater with nanotitania photocatalyst and UV light emission. *Int. J. Photoenergy* **2012**, *2012*, 703074. [CrossRef]
84. Molinari, R.; Lavorato, C.; Argurio, P. Visible-light photocatalysts and their perspectives for building photocatalytic membrane reactors for various liquid phase chemical conversions. *Catalysts* **2020**, *10*, 1334. [CrossRef]
85. Ameta, S.C.; Ameta, R. *Advanced Oxidation Processes for Wastewater Treatment: Emerging Green Chemical Technology*; Academic Press: Cambridge, MA, USA, 2018.
86. Rafiq, A.; Ikram, M.; Ali, S.; Niaz, F.; Khan, M.; Khan, Q.; Maqbool, M. Photocatalytic degradation of dyes using semiconductor photocatalysts to clean industrial water pollution. *J. Ind. Eng. Chem.* **2021**, *97*, 111–128. [CrossRef]
87. Boltersdorf, J.; King, N.; Maggard, P.A. Flux-mediated crystal growth of metal oxides: Synthetic tunability of particle morphologies, sizes, and surface features for photocatalysis research. *CrystEngComm* **2015**, *17*, 2225–2241. [CrossRef]
88. Janssens, R.; Cristóvão, B.M.; Bronze, M.R.; Crespo, J.G.; Pereira, V.J.; Luis, P. Photocatalysis using UV-A and UV-C light sources for advanced oxidation of anti-cancer drugs spiked in laboratory-grade water and synthetic urine. *Ind. Eng. Chem. Res.* **2019**, *59*, 647–653. [CrossRef]
89. Zhang, F.; Wang, X.; Liu, H.; Liu, C.; Wan, Y.; Long, Y.; Cai, Z. Recent advances and applications of semiconductor photocatalytic technology. *Appl. Sci.* **2019**, *9*, 2489. [CrossRef]
90. Hou, W.-M.; Ku, Y. Enhanced photocatalytic decomposition of gaseous isopropyl alcohol in a polymer electrolyte cell. *Aerosol Air Qual. Res.* **2013**, *13*, 1570–1581. [CrossRef]
91. Zhu, H.; Jiang, R.; Fu, Y.; Guan, Y.; Yao, J.; Xiao, L.; Zeng, G. Effective photocatalytic decolorization of methyl orange utilizing TiO_2/ZnO/chitosan nanocomposite films under simulated solar irradiation. *Desalination* **2012**, *286*, 41–48. [CrossRef]
92. Kertèsz, S.; Cakl, J.; Jiránková, H. Submerged hollow fiber microfiltration as a part of hybrid photocatalytic process for dye wastewater treatment. *Desalination* **2014**, *343*, 106–112. [CrossRef]
93. Zhou, H.; Qu, Y.; Zeid, T.; Duan, X. Towards highly efficient photocatalysts using semiconductor nanoarchitectures. *Energy Environ. Sci.* **2012**, *5*, 6732–6743. [CrossRef]

94. Neaţu, Ş.; Maciá-Agulló, J.A.; Garcia, H. Solar light photocatalytic CO_2 reduction: General considerations and selected bench-mark photocatalysts. *Int. J. Mol. Sci.* **2014**, *15*, 5246–5262. [CrossRef] [PubMed]
95. Li, D.; Song, H.; Meng, X.; Shen, T.; Sun, J.; Han, W.; Wang, X. Effects of particle size on the structure and photocatalytic performance by alkali-treated TiO_2. *Nanomaterials* **2020**, *10*, 546. [CrossRef]
96. Rani, A.; Reddy, R.; Sharma, U.; Mukherjee, P.; Mishra, P.; Kuila, A.; Sim, L.C.; Saravanan, P. A review on the progress of nanostructure materials for energy harnessing and environmental remediation. *J. Nanostructure Chem.* **2018**, *8*, 255–291. [CrossRef]
97. Tian, J.; Zhao, Z.; Kumar, A.; Boughton, R.I.; Liu, H. Recent progress in design, synthesis, and applications of one-dimensional TiO_2 nanostructured surface heterostructures: A review. *Chem. Soc. Rev.* **2014**, *43*, 6920–6937. [CrossRef]
98. Azmoon, P.; Farhadian, M.; Pendashteh, A.; Tangestaninejad, S. Adsorption and photocatalytic degradation of oilfield produced water by visible-light driven superhydrophobic composite of MIL-101(Cr)/Fe_3O_4-SiO_2: Synthesis, characterization and optimization. *Appl. Surf. Sci.* **2023**, *613*, 155972. [CrossRef]
99. Yusuff, A.S.; Olateju, I.I.; Adesina, O.A. TiO_2/anthill clay as a heterogeneous catalyst for solar photocatalytic degradation of textile wastewater: Catalyst characterization and optimization studies. *Materialia* **2019**, *8*, 100484. [CrossRef]
100. Tetteh, E.K.; Ezugbe, E.O.E.; Rathilal, S.; Asante-Sackey, D. Removal of COD and SO_4^{2-} from oil refinery wastewater using a photo-catalytic system—Comparing TiO_2 and zeolite efficiencies. *Water* **2020**, *12*, 5–14. [CrossRef]
101. Benhebal, H.; Chaib, M.; Salmon, T.; Geens, J.; Leonard, A.; Lambert, S.D.; Crine, M.; Heinrichs, B. Photocatalytic degradation of phenol and benzoic acid using zinc oxide powders prepared by the sol–gel process. *Alex. Eng. J.* **2013**, *52*, 517–523. [CrossRef]
102. Hu, B.; Sun, Q.; Zuo, C.; Pei, Y.; Yang, S.; Zheng, H.; Liu, F. A highly efficient porous rod-like Ce-doped ZnO photocatalyst for the degradation of dye contaminants in water. *Beilstein J. Nanotechnol.* **2019**, *10*, 1157–1165. [CrossRef] [PubMed]
103. Boutra, B.; Trari, M. Solar photodegradation of a textile azo dye using synthesized ZnO/Bentonite. *Water Sci. Technol.* **2017**, *75*, 1211–1220. [CrossRef] [PubMed]
104. Hasan, A.M.; Dey, S.C.; Rahman, M.M.; Zakaria, A.M.; Sarker, M.; Ashaduzzaman, M.; Shamsuddin, S.M. A kaolinite/TiO_2 TiO_2/ZnO-based novel ternary composite for photocatalytic degradation of anionic azo dyes. *Bull. Mater. Sci.* **2020**, *43*, 27. [CrossRef]
105. Ravi, K.; Mohan, B.S.; Sree, G.S.; Raju, I.M.; Basavaiah, K.; Rao, B.V. ZnO/RGO nanocomposite via hydrothermal route for photocatalytic degradation of dyes in presence of visible light. *Int. J. Chem. Stud.* **2018**, *6*, 20–26.
106. Yusuff, A.S.; Taofeek Popoola, L.; Aderibigbe, E.I. Solar photocatalytic degradation of organic pollutants in textile industry wastewater by ZnO/pumice composite photocatalyst. *J. Environ. Chem. Eng.* **2020**, *8*, 103907. [CrossRef]
107. Srinivas, B.; Kumar, B.G.; Muralidharan, K. Stabilizer free copper sulphide nanostructures for rapid photocatalytic decomposition of rhodamine B. *J. Mol. Catal. A Chem.* **2015**, *410*, 8–18. [CrossRef]
108. Meena, K.; Shanthi, M. Eco-Friendly Gelatin–Cerium–Copper Sulphide Nanoparticles for Enhanced Sunlight Photocatalytic Activity. *Sustainability* **2022**, *14*, 15325. [CrossRef]
109. Berkani, M.; Smaali, A.; Kadmi, Y.; Almomani, F.; Vasseghian, Y.; Lakhdari, N.; Alyane, M. Photocatalytic degradation of Penicillin G in aqueous solutions: Kinetic, degradation pathway, and microbioassays assessment. *J. Hazard. Mater.* **2022**, *421*, 126719. [CrossRef]
110. Samy, M.; Ibrahim, M.G.; Alalm, M.G.; Fujii, M. Modeling and optimization of photocatalytic degradation of methylene blue using lanthanum vanadate. In *Materials Science Forum*; Trans Tech Publications, Ltd.: Baech, Switzerland, 2020; pp. 97–103.
111. Kurniawan, T.A.; Mengting, Z.; Fu, D.; Yeap, S.K.; Othman, M.H.D.; Avtar, R.; Ouyang, T. Functionalizing TiO_2 with graphene oxide for enhancing photocatalytic degradation of methylene blue (MB) in contaminated wastewater. *J. Environ. Manag.* **2020**, *270*, 110871. [CrossRef]
112. Nasiri, A.; Tamaddon, F.; Mosslemin, M.H.; Gharaghani, M.A.; Asadipour, A. New magnetic nanobiocomposite $CoFe_2O_4$@methycellulose: Facile synthesis, characterization, and photocatalytic degradation of metronidazole. *J. Mater. Sci. Mater. Electron.* **2019**, *30*, 8595–8610. [CrossRef]
113. Sikiru, S.; Abiodun, O.A.; Sanusi, Y.K.; Sikiru, Y.A.; Soleimani, H.; Yekeen, N.; Haslija, A.A. A comprehensive review on nanotechnology application in wastewater treatment a case study of metal-based using green synthesis. *J. Environ. Chem. Eng.* **2022**, *10*, 108065. [CrossRef]
114. Amakiri, K.T.; Angelis-Dimakis, A.; Ramirez Canon, A. Recent advances, influencing factors, and future research prospects using photocatalytic process for produced water treatment. *Water Sci. Technol.* **2022**, *85*, 769–788. [CrossRef]
115. Arora, I.; Chawla, H.; Chandra, A.; Sagadevan, S.; Garg, S. Advances in the strategies for enhancing the photocatalytic activity of TiO_2: Conversion from UV-light active to visible-light active photocatalyst. *Inorg. Chem. Commun.* **2022**, *143*, 109700. [CrossRef]
116. Zia, A.; Akhter, P.; Nazir, A.; Hussain, M.; Park, Y.-K. Synergistic effect of metal-doped TiO_2/AC for efficient visible light driven cationic dye degradation. *Sep. Purif. Technol.* **2025**, *361*, 131402. [CrossRef]
117. Qi, Z.; Li, G.; Guo, X. Multi-Element Synergy in Photocatalytic Materials Integrated Mechanism-Design-Preparation Strategies. *Mater. Res. Express* **2025**, *12*, 062001.

118. You, C.-S.; Noh, J.-Y.; Choi, Y.; Jung, S.-C. Degradation of antibiotic oxytetracycline using surface reconstituted TiO_2 photocatalyst. *Appl. Surf. Sci.* **2025**, *687*, 162244. [CrossRef]
119. Ayappan, C.; Kannan, S.K.; Ochiai, T.; Zhang, X.; Xing, R.; Liu, S.; Fujishima, A. Commercialization aspects for TiO_2-based indoor air purification. *Trends Chem.* **2025**, *7*, 134–148. [CrossRef]
120. Rastinifard, N.; Tota-Maharaj, P. Application of $Uv/O_3/TiO_2$/Hydrogen Peroxide-Based Advanced Oxidation Processes for Wastewater Treatment (Focused on Constructed Wetlands): A Review. Available online: https://papers.ssrn.com/sol3/papers.cfm?abstract_id=5220953 (accessed on 15 August 2025).
121. Gopal, S.; Jayabalan, J.; Jayaraman, D.; Perumal, M.; Santhi, V.M. Amalgamation of Advanced Oxidation Process with Biological Techniques for Treatment of Tannery Wastewater. *Phys. Chem. Earth Parts A/B/C* **2025**, *138*, 103883. [CrossRef]
122. Cen, Y.; Zhou, Y.; Zhu, M.; Zheng, K.; Zhou, S. Preparation of the Ti/TiO_2-RNTs/SnO_2–Sb–Ni-La Electrode and Its Electrochemical Degradation of Oily Wastewater. *Langmuir* **2025**, *41*, 8766–8780. [CrossRef]
123. Aghel, S.; Bahramifar, N.; Younesi, H.; Tanha Ziyarati, M. Evaluation of Photocatalytic Degradation of Bisphenol A by Reusable $Fe_3O_4/SiO_2/TiO_2$ Magnetic Nanocomposite: Optimization by Response Surface Methodology. *Int. J. Environ. Res.* **2025**, *19*, 77. [CrossRef]
124. Li, C.; Ding, G.; Wang, P.; Liu, K.; Yang, B.; Liao, G. Emerging frontiers of nickel–aluminium layered double hydroxide heterojunctions for photocatalysis. *Dalton Trans.* **2025**, *54*, 889–897. [CrossRef] [PubMed]
125. Behera, D.; Priyadarshini, P.; Parida, K. ZIF-8 metal–organic frameworks and their hybrid materials: Emerging photocatalysts for energy and environmental applications. *Dalton Trans.* **2025**, *54*, 2681–2708. [CrossRef] [PubMed]
126. He, B.; Zhong, S.; Li, K.; Wei, S.; Li, M.; Liu, R. Ionic liquids: The emerging "cardiotonic" for photocatalytic materials. *Coord. Chem. Rev.* **2025**, *529*, 216461. [CrossRef]
127. Diamanti, M.V.; Shinnur, M.V.; Pedeferri, M.; Ferrari, A.M.; Rosa, R.; Meroni, D. Toward Sustainable Photocatalysis: Addressing Deactivation and Environmental Impact of Anodized and Sol–Gel Photocatalysts. *Adv. Sustain. Syst.* **2025**, *9*, 2401017. [CrossRef]
128. Gholizadeh, A.; Shabani, A. Artificial intelligence techniques. *Results Chem.* **2025**, *15*, 102276. [CrossRef]
129. Khaki, M.R.D.; Shafeeyan, M.S.; Raman, A.A.A.; Daud, W.M.A.W. Application of doped photocatalysts for organic pollutant degradation-A review. *J. Environ. Manag.* **2017**, *198*, 78–94. [CrossRef] [PubMed]
130. Li, L.; Li, W.; Yang, J.-F.; Mao, L.-F. The impact of the location of Cu substitutions and electric field on visible light absorption in defective titanium dioxide: Ab initio calculations. *J. Optoelectron. Adv. Mater.* **2018**, *20*, 56–60.
131. Xu, Y.-M.; Chen, S.; Chen, S.-L.; Wang, A.-J. Improved N_2 photo-fixation performance of nanocrystalline TiO_2 films by photon localization effects and Fe doping. *New J. Chem.* **2024**, *48*, 6494–6504. [CrossRef]
132. Xu, Z.; Li, C.; Fu, N.; Li, W.; Zhang, G. Facile synthesis of Mn-doped TiO_2 nanotubes with enhanced visible light photocatalytic activity. *J. Appl. Electrochem.* **2018**, *48*, 1197–1203. [CrossRef]
133. Lv, Y.; Ding, Y.; Zhou, J.; Xiao, W.; Feng, Y. Preparation, characterization, and photocatalytic activity of N, S-codoped TiO_2 nanoparticles. *J. Am. Ceram. Soc.* **2009**, *92*, 938–941. [CrossRef]
134. Ding, Y.; Nagpal, P. Standalone anion-and co-doped titanium dioxide nanotubes for photocatalytic and photoelectrochemical solar-to-fuel conversion. *Nanoscale* **2016**, *8*, 17496–17505.
135. Chen, X.; Meng, C.; Wang, Y.; Zhao, Q.; Li, Y.; Chen, X.M.; Zhou, Y. Laser-synthesized rutile TiO_2 with abundant oxygen vacancies for enhanced solar water evaporation. *ACS Sustain. Chem. Eng.* **2020**, *8*, 1095–1101. [CrossRef]
136. YCao, Y.; Zhou, P.; Tu, Y.; Liu, Z.; Dong, B.-W.; Azad, A.; Ma, D.; Wang, D.; Zhang, X.; Yang, Y.; et al. Modification of TiO_2 nanoparticles with organodiboron molecules inducing stable surface Ti^{3+} complex. *IScience* **2019**, *20*, 195–204.
137. Song, Y.; Zhang, J.; Yang, L.; Cao, S.; Yang, H.; Jiang, L.; Dan, Y.; Le Rendu, P.; Nguyen, T. Photocatalytic activity of TiO_2 based composite films by porous conjugated polymer coating of nanoparticles. *Mater. Sci. Semicond. Process.* **2016**, *42*, 54–57. [CrossRef]
138. Kwon, J.; Choi, K.; Schreck, M.; Liu, T.; Tervoort, E.; Niederberger, M. Gas-phase nitrogen doping of monolithic TiO_2 nanoparticle-based aerogels for efficient visible light-driven photocatalytic H_2 production. *ACS Appl. Mater. Interfaces* **2021**, *13*, 53691–53701. [CrossRef]
139. Su, Y.; Liu, L.; Wen, S. Broadband $NaYF_4$: Yb, Tm@$NaYF_4$: Yb, Nd@TiO_2 nanoparticles anchored on SiO_2/carbon electrospun fibers for photocatalytic degradation of organic pollutants. *ACS Appl. Nano Mater.* **2021**, *4*, 12576–12587. [CrossRef]
140. Daskalova, D. Combined Structural and Plasmonic Enhancement of Nanometer-Thin Film Photocatalysis for Solar-Driven Wastewater Treatment. *ACS Appl. Nano Mater.* **2023**, *6*, 5204–15212. [CrossRef]
141. Hou, W.; Xiao, Y.; Han, G.; Lin, J.-Y. Stable and near-infrared absorption enhanced dye-sensitized solar cell based on silver nanoplates@silica nanocrystals. *Mater. Res. Bull.* **2018**, *104*, 164–172. [CrossRef]
142. Wu, L.; Guo, C.; Feng, R.; Zhang, H.; Shi, N.; Li, Y.; Su, H.; Cui, X.; Song, F. Co-doping of P (V) and Ti (III) in leaf-architectured TiO_2 for enhanced visible light harvesting and solar photocatalysis. *J. Am. Ceram. Soc.* **2021**, *104*, 5719–5732. [CrossRef]
143. Wang, M.; Deng, K.; Lü, W.; Deng, X.; Li, K.; Shi, Y.; Ding, B.; Cheng, Z.; Xing, B.; Han, G.; et al. Rational design of multifunctional Fe@γ-Fe_2O_3@H-TiO_2 nanocomposites with enhanced magnetic and photoconversion effects for wide applications: From photocatalysis to imaging-guided photothermal cancer therapy. *Adv. Mater.* **2018**, *30*, 1706747. [CrossRef]

144. Nair, P.R.; Ramirez, C.R.S.; Pelaes, R.F.C.; Krishnan, B.; Martínez, J.A.A.; Avellaneda, D.A.; Pinilla, M.A.G.; Shaji, S. IR laser induced defects and morphology in titania nanoparticles as black titania for environmental remediation. *Appl. Surf. Sci.* **2025**, *709*, 163827. [CrossRef]
145. Méndez-Ramos, J.; Borges, M.; Torres-García, S.; Medina-Alayón, M.; Acosta-Mora, P.; Del-Castillo, J.; Menéndez-Velázquez, A.; García-Delgado, A.; Mullins, C.; Esparza, P. There is plenty of energy at the bottom": A spectral conversion approach for upconversion-powered water-splitting PEC cell. *J. Power Sources* **2025**, *625*, 235668. [CrossRef]
146. Jiang, L.; Zhou, S.; Yang, J.; Wang, H.; Yu, H.; Chen, H.; Zhao, Y.; Yuan, X.; Chu, W.; Li, H. Near-infrared light responsive TiO_2 for efficient solar energy utilization. *Adv. Funct. Mater.* **2022**, *32*, 2108977. [CrossRef]
147. Jiang, D.; Otitoju, T.A.; Ouyang, Y.; Shoparwe, N.F.; Wang, S.; Zhang, A.; Li, S. A review on metal ions modified TiO_2 for photocatalytic degradation of organic pollutants. *Catalysts* **2021**, *11*, 1039. [CrossRef]
148. Giannakis, S.; Lin, K.-Y.A.; Ghanbari, F. A review of the recent advances on the treatment of industrial wastewaters by Sulfate Radical-based Advanced Oxidation Processes (SR-AOPs). *Chem. Eng. J.* **2021**, *406*, 127083. [CrossRef]
149. Umar, K.; Ibrahim, M.N.M.; Ahmad, A.; Rafatullah, M. Synthesis of Mn-doped TiO_2 by novel route and photocatalytic mineralization/intermediate studies of organic pollutants. *Res. Chem. Intermed.* **2019**, *45*, 2927–2945. [CrossRef]
150. Santos, F.; Azevedo, E.; Dezotti, M. Photocatalysis as a tertiary treatment for petroleum refinery wastewaters. *Braz. J. Chem. Eng.* **2006**, *23*, 451–460. [CrossRef]
151. Li, G.; An, T.; Nie, X.; Sheng, G.; Zeng, X.; Fu, J.; Lin, Z.; Zeng, E.Y. Mutagenicity assessment of produced water during photoelectrocatalytic degradation. *Environ. Toxicol. Chem. Int. J.* **2007**, *26*, 416–423. [CrossRef]
152. Gouma, P.; Lee, J. Photocatalytic nanomats clean up produced water from fracking. *Transl. Mater. Res.* **2014**, *1*, 025002. [CrossRef]
153. Islam, M.T.; Dominguez, A.; Turley, R.S.; Kim, H.; Sultana, K.A.; Shuvo, M.; Alvarado-Tenorio, B.; Montes, M.O.; Lin, Y.; Gardea-Torresdey, J. Development of photocatalytic paint based on TiO_2 and photopolymer resin for the degradation of organic pollutants in water. *Sci. Total Environ.* **2020**, *704*, 135406. [CrossRef]
154. Nakata, K.; Fujishima, A. TiO_2 photocatalysis: Design and applications. *J. Photochem. Photobiol. C Photochem. Rev.* **2012**, *13*, 169–189. [CrossRef]
155. Stylidi, M.; Kondarides, D.I.; Verykios, X.E. Pathways of solar light-induced photocatalytic degradation of azo dyes in aqueous TiO_2 suspensions. *Appl. Catal. B Environ.* **2003**, *40*, 271–286. [CrossRef]
156. Tugaoen, H.O.N.; Garcia-Segura, S.; Hristovski, K.; Westerhoff, P. Compact light-emitting diode optical fiber immobilized TiO_2 reactor for photocatalytic water treatment. *Sci. Total Environ.* **2018**, *613*, 1331–1338. [CrossRef] [PubMed]
157. Szczepanik, B. Photocatalytic degradation of organic contaminants over clay-TiO_2 nanocomposites: A review. *Appl. Clay Sci.* **2017**, *141*, 227–239. [CrossRef]
158. Lee, C.-G.; Javed, H.; Zhang, D.; Kim, J.-H.; Westerhoff, P.; Li, Q.; Alvarez, P.J. Porous electrospun fibers embedding TiO_2 for adsorption and photocatalytic degradation of water pollutants. *Environ. Sci. Technol.* **2018**, *52*, 4285–4293. [CrossRef]
159. Shoneye, A. Photocatalytic Mineralisation of Toxic Chlorophenols and Removal of Cr (VI) in Aqueous Solution Using Cocatalyst Decorated TiO_2. Ph.D. Thesis, UCL (University College), London, UK, 2021.
160. Pillai, S.C.; McGuinness, N.B.; Byrne, C.; Han, C.; Lalley, J.; Nadagouda, M.; Falaras, P.; Kontos, A.G.; Gracia-Pinilla, M.A.; OShea, K. Photocatalysis as an effective advanced oxidation process. *Adv. Oxid. Process. Water Treat. Fundam. Appl.* **2017**, *16*, 333–381. [CrossRef]
161. Kumar, M.; Sridharan, S.; Sawarkar, A.D.; Shakeel, A.; Anerao, P.; Mannina, G.; Sharma, P.; Pandey, A. Current research trends on emerging contaminants pharmaceutical and personal care products (PPCPs): A comprehensive review. *Sci. Total Environ.* **2023**, *859*, 160031. [CrossRef]
162. Sun, Q.; Hou, P.; Wu, S.; Yu, L.; Dong, L. The enhanced photocatalytic activity of Ag-Fe_2O_3-TiO_2 performed in Z-scheme route associated with localized surface plasmon resonance effect. *Colloids Surf. A Physicochem. Eng. Asp.* **2021**, *628*, 127304. [CrossRef]
163. Xu, K.; Liu, Z.; Qi, S.; Yin, Z.; Deng, S.; Zhang, M.; Sun, Z. The quaternary system of Ag_2S/ZnS co-modified ZnO/TiO_2 nanotree arrays: Excellent photocatalysis and photoelectrochemistry performance. *Appl. Surf. Sci.* **2021**, *538*, 148044. [CrossRef]
164. Zhao, Y.; Nie, L.; Yang, H.; Song, K.; Hou, H. Tailored fabrication of TiO_2/In_2O_3 hybrid mesoporous nanofibers towards enhanced photocatalytic performance. *Colloids Surf. A Physicochem. Eng. Asp.* **2021**, *629*, 127455. [CrossRef]
165. Ali, H.M.; Roghabadi, F.A.; Ahmadi, V. Solid-supported photocatalysts for wastewater treatment: Supports contribution in the photocatalysis process. *Sol. Energy* **2023**, *255*, 99–125. [CrossRef]
166. Joseph, A.; Vijayanandan, A. Review on support materials used for immobilization of nano-photocatalysts for water treatment applications. *Inorganica Chim. Acta* **2022**, *255*, 121284. [CrossRef]
167. Srikanth, B.; Goutham, R.; Narayan, R.B.; Ramprasath, A.; Gopinath, K.; Sankaranarayanan, A. Recent advancements in supporting materials for immobilised photocatalytic applications in waste water treatment. *J. Environ. Manag.* **2017**, *200*, 60–78. [CrossRef]
168. Mapossa, A.B.; Mhike, W.; Adalima, J.L.; Tichapondwa, S. Removal of organic dyes from water and wastewater using magnetic ferrite-based titanium oxide and zinc oxide nanocomposites: A review. *Catalysts* **2021**, *11*, 1543. [CrossRef]

169. Gupta, V.K.; Eren, T.; Atar, N.; Yola, M.L.; Parlak, C.; Karimi-Maleh, H. $CoFe_2O_4$@TiO_2 decorated reduced graphene oxide nanocomposite for photocatalytic degradation of chlorpyrifos. *J. Mol. Liq.* **2015**, *208*, 122–129. [CrossRef]
170. Krishna, S.; Sathishkumar, P.; Pugazhenthiran, N.; Guesh, K.; Mangalaraja, R.; Kumaran, S.; Gracia-Pinilla, M.; Anandan, S. Heterogeneous sonocatalytic activation of peroxomonosulphate in the presence of $CoFe_2O_4/TiO_2$ nanocatalysts for the degradation of Acid Blue 113 in an aqueous environment. *J. Environ. Chem. Eng.* **2020**, *8*, 104024.
171. Loeb, S.K.; Alvarez, P.J.; Brame, J.A.; Cates, E.L.; Choi, W.; Crittenden, J.; Dionysiou, D.D.; Li, Q.; Li-Puma, G.; Quan, X. The technology horizon for photocatalytic water treatment: Sunrise or sunset? *Environ. Sci. Technol.* **2018**, *53*, 2937–2947. [CrossRef] [PubMed]
172. Cao, S.; Piao, L. Considerations for a more accurate evaluation method for photocatalytic water splitting. *Angew. Chem. Int. Ed.* **2020**, *59*, 18312–18320. [CrossRef] [PubMed]

Disclaimer/Publisher's Note: The statements, opinions and data contained in all publications are solely those of the individual author(s) and contributor(s) and not of MDPI and/or the editor(s). MDPI and/or the editor(s) disclaim responsibility for any injury to people or property resulting from any ideas, methods, instructions or products referred to in the content.

catalysts

MDPI

Review

Engineering Photocatalytic Membrane Reactors for Sustainable Energy and Environmental Applications

Ruofan Xu [1,2], Shumeng Qin [1,2], Tianguang Lu [3,*], Sen Wang [4,*], Jing Chen [5,*] and Zuoli He [1,2,*]

[1] Shandong Key Laboratory of Water Pollution Control and Resource Reuse, Shandong Key Laboratory of Environmental Processes and Health, School of Environmental Science and Engineering, Shandong University, Qingdao 266237, China
[2] Weihai Research Institute of Industrial Technology of Shandong University, Shandong University, Weihai 264209, China
[3] State Key Laboratory of Microbial Technology, Microbial Technology Institute, Shandong University, Qingdao 266237, China
[4] School of Electrical Engineering, Shandong University, Jinan 250061, China
[5] The Key Laboratory for Surface Engineering and Remanufacturing in Shaanxi Province, School of Chemical Engineering, Xi'an University, Xi'an 710065, China
* Correspondence: tlu@sdu.edu.cn (T.L.); wangsen@sdu.edu.cn (S.W.); jingchen@xawl.edu.cn (J.C.); zlhe@sdu.edu.cn (Z.H.)

Abstract

Photocatalytic membrane reactors (PMRs), which combine photocatalysis with membrane separation, represent a pivotal technology for sustainable water treatment and resource recovery. Although extensive research has documented various configurations of photocatalytic-membrane hybrid processes and their potential in water treatment applications, a comprehensive analysis of the interrelationships among reactor architectures, intrinsic physicochemical mechanisms, and overall process efficiency remains inadequately explored. This knowledge gap hinders the rational design of highly efficient and stable reactor systems—a shortcoming that this review seeks to remedy. Here, we critically examine the connections between reactor configurations, design principles, and cutting-edge applications to outline future research directions. We analyze the evolution of reactor architectures, relevant reaction kinetics, and key operational parameters that inform rational design, linking these fundamentals to recent advances in solar-driven hydrogen production, CO_2 conversion, and industrial scaling. Our analysis reveals a significant disconnect between the mechanistic understanding of reactor operation and the system-level performance required for innovative applications. This gap between theory and practice is particularly evident in efforts to translate laboratory success into robust and economically feasible industrial-scale operations. We believe that PMRs will realize their transformative potential in sustainable energy and environmental applications in future.

Keywords: photocatalyst; membrane; reactors; water treatment; reaction kinetics

1. Introduction

The merging of rapid urbanization and industrialization has led to increased environmental pollution and energy insecurity, presenting major global challenges. A key sign of these pressures is the rising demand for clean water, which has attracted widespread international concern. Solar-driven photocatalytic processes have been recognized as a highly promising technological solution for addressing these interconnected issues [1,2].

The capacity of photocatalytic processes to be driven by either solar or artificial light positions them as a paradigm of sustainable technology. By leveraging renewable solar energy, photocatalysis facilitates the complete mineralization of recalcitrant pollutants and the effective inactivation of viruses [3–6]. Consequently, owing to its inherent environmentally benign nature and demonstrated efficacy, this technology has garnered substantial interest and is recognized as one of the most promising solutions for environmental remediation. It also allows for splitting water into hydrogen and oxygen, highlighting its potential in sustainable energy applications [7–10]. From a semiconductor photochemistry perspective, photocatalysis works by initiating or speeding up specific redox reactions through the irradiation of semiconductor materials. The core mechanism begins when a photocatalyst absorbs light energy equal to or exceeding its band gap. By utilizing free sunlight to drive strong redox reactions, photocatalytic technology has demonstrated unique advantages and broad prospects in the field of environmental remediation, in terms of both pollution control and energy generation. The mechanistic pathway of photoreduction is contingent upon its specific application, predominantly proceeding via a single-electron transfer process in domains such as organic synthesis, environmental remediation, and solar energy conversion [11–13]. Alternatively, it can proceed through more complex multi-electron transfers, such as in the reduction of water (H_2O) or protons (H^+) to produce hydrogen (H_2) fuel [14]. This process relies on exciting semiconductor catalysts with photons whose energies match or surpass their band gaps, causing electrons to move from the valence band to the conduction band, leaving behind holes. These photogenerated holes are strongly oxidizing, capable of withdrawing electrons from nearby molecules. Upon migration to the catalyst surface, interfacial redox reactions are initiated; the photo-generated electrons, possessing reduction potentials between +0.5 and −1.5 V vs. NHE, mediate the reduction of electron acceptors, while the holes, with oxidation potentials ranging from +1.0 to +3.5 V vs. NHE, drive the oxidation of electron donors [15]. The consequent generation of highly reactive oxygen species (ROS), notably hydroxyl and superoxide radicals, possessing potent oxidizing capabilities, is instrumental in the degradation of a wide spectrum of aqueous contaminants. The photoreduction process can happen through various pathways, which might involve single-electron transfer, common in organic synthesis, environmental cleanup, and solar energy conversion. For applications such as producing hydrogen (H_2) fuel from water (H_2O) or protons (H^+), the process can proceed via more complex multi-electron transfers. One major advantage of photocatalytic technology is its natural sustainability. It operates under mild conditions and does not require chemical additives. By effectively utilizing sunlight as a renewable energy source, photocatalysis stands out as a key technology for sustainable environmental management.

Photocatalytic technology is increasingly acknowledged for its profound potential in water treatment, primarily owing to its capacity for the comprehensive degradation of persistent pollutants [4,5,16]. The efficacy of this photoelectron-driven process is underscored by a compelling suite of advantages, including its potent oxidizing capabilities, facile operational control under ambient temperature conditions, extended operational stability, and the negligible formation of secondary pollutants [12]. These attributes, combined with its cost-effectiveness, culminate in superior water purification efficacy [13]. However, widespread industrial use of this technology faces several ongoing challenges [14]. A primary issue is the rapid recombination of photogenerated electrons and holes, which significantly reduces quantum efficiency. Additionally, the small size of photocatalysts makes their separation from treated water difficult, hindering reuse. The nanoscale dimensions of these particles further complicate recovery and increase operational costs [15]. Conventional photoreactor designs often suffer from poor light-harvesting efficiency, which limits overall performance and economic feasibility. In response to these limitations, the strategic

evolution of photocatalytic technology has led to the development of PMRs. This innovative approach, which integrates the photocatalytic process with membrane separation technology, has proven particularly effective in surmounting the aforementioned obstacles and represents a significant advancement in reactor engineering (Figure 1). In this setup, the membrane acts as a physical support for immobilizing photocatalyst nanoparticles, directly solving catalyst separation and recovery problems. Simultaneously, the photocatalyst degrades contaminants and organic foulants at the membrane surface, reducing membrane fouling—a common operational problem in conventional filtration [17]. This combined approach not only solves separation issues but also improves degradation efficiency by ensuring prolonged, close contact between pollutants and catalytic sites, representing a promising direction for advanced water purification [16]. The primary thrust of research in this field has been directed toward two principal avenues: the enhancement of photocatalyst efficiency and the innovation of reactor design. While considerable scientific effort has been dedicated to the synthesis and characterization of novel catalyst materials with superior properties, a notable disparity is evident in the literature [18–20]. Specifically, rigorous and systematic investigations focusing on comprehensive reactor modeling and process optimization have received comparatively less attention, representing a critical knowledge gap that may hinder the scalable implementation of this technology. Developing photocatalytic reactors that boost catalytic efficiency and minimize separation steps has thus become an urgent technical goal. The integration of inorganic photocatalyst nanoparticles with organic polymeric matrices to fabricate composite photocatalytic membranes represents a particularly effective strategy [21]. This approach capitalizes on the proven versatility and efficiency of membrane separation technology, a cornerstone of water purification that has achieved widespread commercial acceptance [17]. In this synergistic configuration, the degradation of contaminants at the membrane surface is mediated by the immobilized photocatalyst nanoparticles, which concurrently mitigate membrane fouling while ensuring intimate contact with pollutants to enhance degradation efficiency. Such progress in catalyst fabrication and reactor engineering is pivotal for resolving these persistent operational challenges [22].

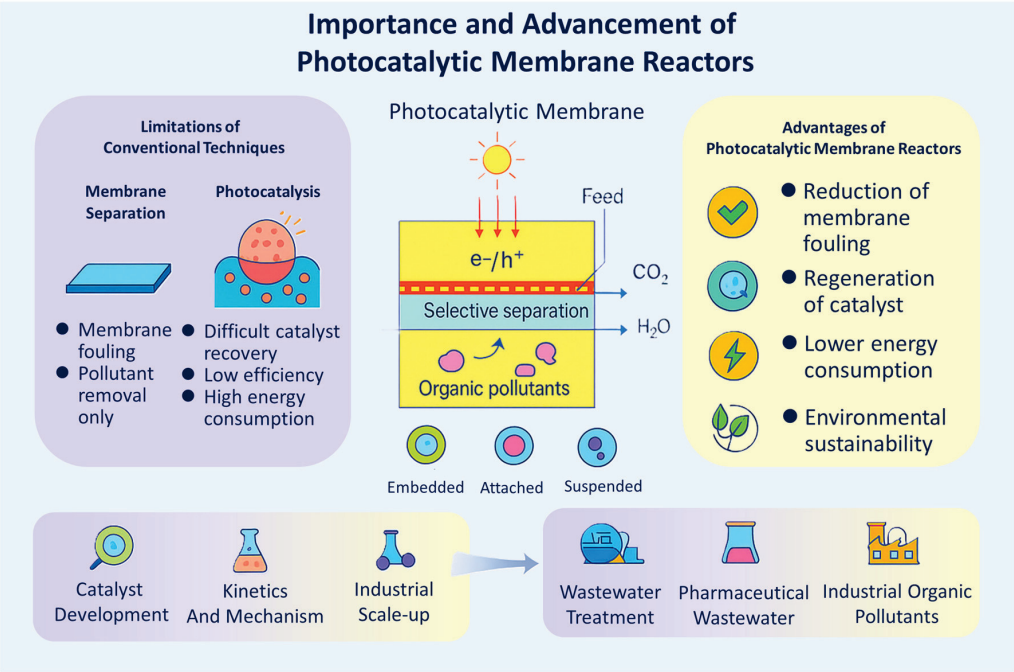


Figure 1. Synergistic integration of photocatalysis and membrane filtration in PMRs: mechanisms, advantages, and applications.

The integration of membrane filtration with photocatalysis represents a significant advancement in developing energy-efficient and sustainable wastewater treatment methodologies. Photocatalytic membranes (PMs) have been extensively studied due to the sustainability and environmental friendliness of solar energy in an eco-friendly manner [23]. Historically, the synergy between photocatalysis and membrane technology was principally confined to the downstream separation and recovery of photocatalyst nanoparticles from suspension [24]. However, the practical implementation of photocatalytic systems for water treatment necessitates a more sophisticated approach to reactor design, where multiple critical parameters must be simultaneously optimized. Effective photoreactor engineering must address the optimization of catalyst performance, the maximization of light energy utilization, the mitigation of mass transmission limitations, and the efficiency of catalyst retention. The central challenge in reactor design lies in creating a system that concurrently achieves high catalytic activity and rapid pollutant degradation. This imperative has driven the development and optimization of PMRs, which are a key innovation in advanced photocatalytic systems [25]. By immobilizing the photocatalyst directly onto or within the membrane structure, PMRs not only resolve the issue of catalyst recovery but also facilitate more effective control of membrane fouling. Ultimately, rigorous research and development in reactor design are crucial for transitioning these processes from laboratory-scale experiments to industrially viable applications. Advanced PM technologies have garnered considerable attention for their high efficiency and energy-saving potential [26]. This innovative system is predicated on the synergistic integration of photocatalysis with membrane separation, a concept developed in the early 21st century to achieve the dual objectives of contaminant degradation and physical filtration [27]. A key advantage of the PMR configuration lies in its ability to address the persistent challenge of catalyst recovery encountered in conventional slurry-based systems. By immobilizing or confining the photocatalyst, the membrane module ensures its retention within the reactor, which prevents catalyst loss and maintains the continuous stability of the system [23,28]. In addition, this integration enhances the interfacial contact area between the catalyst and pollutants, thereby leading to a significant improvement in degradation efficiency. Compared to traditional water treatment methods, PMRs offer simplified operation, lower energy consumption, high reaction efficacy, and a substantially reduced risk of secondary pollution [29].

A substantial body of review literature has documented the progress of PMRs, providing a solid theoretical foundation for the field. Early reviews systematically described various configurations of photocatalytic-membrane hybrid processes and their potential applications in water treatment [30]. Subsequent research has delved deeper into process optimization, particularly using multivariate analysis to determine optimal operating parameters to maximize photo-oxidation performance [31,32]. A significant portion of subsequent literature has been dedicated to membrane fouling, a critical bottleneck for practical applications. Currently, the application scope of PMRs has expanded significantly beyond pollutant degradation to encompass emergent fields, including visible light implementation. Related reviews systematically summarize the evolution, types, and consequences of membrane fouling [33]; deeply explore the influence of photocatalytic reaction conditions on fouling behavior; and compare and analyze physical cleaning strategies, such as aeration and membrane oscillation. Simultaneously, the application areas of PMRs have expanded from their initial focus on pollutant degradation to a wider range [34], encompassing cutting-edge areas such as visible light-based water splitting for hydrogen production, selective synthesis of organic compounds (such as phenol and vanillin), and air purification of volatile organic compounds (VOCs) and nitrogen oxides (NO_x) [35]. In addition, some reviews have examined the technology from a more macro perspective. For example, one work systematically reviewed the evolution of PMRs over the past two decades, fo-

cusing on their progress in reducing membrane material degradation, improving catalyst reusability, enhancing visible light catalytic activity, and improving synthetic reaction selectivity [36,37]. Other studies have focused on the fundamental principles of reactor design, aiming to decouple the intrinsic kinetic properties of catalysts from reactor performance, providing theoretical guidance for establishing a standardized evaluation system [38]. Despite the extensive coverage provided by these reviews, the reviews have predominantly focused on discrete aspects of PMR technology—such as membrane fouling, catalyst development, or specific applications—while existing literature often examines specific aspects—such as membrane fouling, catalyst development, or particular applications—in relative isolation [39]. Specifically, the key question of how the intrinsic properties of the catalyst, the multi-physics coupling within the reactor (such as the light field, flow field, and mass transmission), and the microscopic mechanisms of membrane fouling synergistically influence the overall performance and long-term stability of the reactor remains underdeveloped [40]. Despite the demonstrated advantages of PMRs, including their capacity for high-efficiency separation [41], in situ catalyst recovery [42], and continuous operation [43], their transition from laboratory-scale proof-of-concept to industrial-scale application is impeded by several critical scientific questions [44]. A significant challenge lies in bridging the pronounced gap between laboratory success and viable industrial implementation, an issue often defined as the scale-up challenge. The present review is therefore motivated by the need to bridge this gap. Concurrently, an intrinsic trade-off frequently exists between maximizing catalytic efficiency for broad-spectrum pollutant degradation and achieving high selectivity toward specific target contaminants [35,45]. Furthermore, the suboptimal energy utilization efficiency of many current PMR configurations remains a substantial barrier to their sustainable and cost-effective deployment. Therefore, a focused investigation into these limitations is imperative [46]. This paper is motivated by the necessity to address these unresolved issues, aiming to elucidate key mechanisms and propose novel strategies that will advance the practical application of PMRs in environmental remediation. We will systematically review the research progress of PMRs; discuss their structural design, performance influencing factors, and deep-rooted mechanisms, as well as the challenges in practical applications; and look forward to the future development trend.

2. Principles and Developments of PMRs

The integration of photocatalysis with membrane separation has enabled the development of multifunctional composite systems that overcome the intrinsic limitations of each technology when employed independently. Membrane separation, a well-established technology in modern water treatment, owing to its high efficiency and compact configuration, is nevertheless hindered by fouling [47]. The accumulation of foulants on the membrane surface causes a progressive decline in permeate flux, an increase in transmembrane pressure, and a reduction in service life, thereby elevating operational costs. In addition, conventional membrane processes generate a concentrated retentate stream that necessitates secondary treatment [48,49]. PMRs provide a transformative approach by shifting from passive separation to active, in situ remediation. Their operation relies on immobilized semiconductor photocatalysts that, under light irradiation, generate ROS [50]. These ROS mineralize adsorbed organic macromolecules and microbial biofilms—the principal contributors to fouling—into harmless end products such as carbon dioxide and water. The continuous, light-driven self-cleaning process alleviates pore blocking and cake layer formation while simultaneously eliminating the retentate stream, converting potential waste into purified effluent [51–53]. Practical implementation of PMRs has been achieved through three main fabrication strategies: incorporation of photocatalyst nanoparticles into the membrane matrix during phase inversion, deposition or grafting of a photocatalytic

layer onto pre-formed membranes, and confinement of a photocatalyst suspension using a membrane barrier [54,55]. Each configuration entails distinct trade-offs among catalyst stability, mass transmission efficiency, and light utilization. By embedding contaminant degradation directly within the separation process, PMRs shift fouling control from reactive measures such as pre-treatment or chemical cleaning toward an integrated, preventive solution [56]. This coupling of separation and degradation processes represents a significant step toward the realization of sustainable and high-performance technologies for environmental remediation.

Recent advancements in PMRs have concentrated on three principal areas: the development of novel catalyst materials, the optimization of membrane structures, and the innovation of reactor configurations (Figure 2). The integration of photocatalysis with membrane technology has emerged as a promising approach to sustainable wastewater treatment [23]. Since their conceptualization around 2000, PMRs have been predominantly investigated for water purification applications, leveraging solar-driven photocatalysis to degrade recalcitrant organic pollutants [57]. Solar-driven photocatalysis has garnered considerable attention, with significant efforts directed toward catalyst innovation and reactor design [58]. Integrating catalytic materials into non-thermal plasma reactors, while challenging, has opened new avenues for performance enhancement [59]. Significant research efforts have been directed toward the synthesis of high-performance photocatalysts, such as graphitic carbon nitride, and their effective integration with advanced membrane materials [40]. The reactor configuration, which fundamentally comprises a light source, the photocatalytic membrane, and the reaction vessel, is a critical determinant of overall system efficiency [60]. Innovations in reactor design, such as the development of split-type PMRs, have been pivotal in enhancing mass transmission, light distribution, and pollutant removal efficacy. A typical PMR comprises a light source, a membrane, and a photocatalyst, underscoring the critical role of reactor configuration in system performance [61]. Future research should prioritize the development of novel, low-cost adsorption materials for the removal of hazardous pollutants [62]. Innovations in photocatalysis-membrane separation reactors have emphasized advancements in membrane materials, reactor design, and integration with complementary technologies [63]. The overarching objective is to transition PMR technology from a laboratory-scale concept to a practical and sustainable solution for environmental remediation [64].

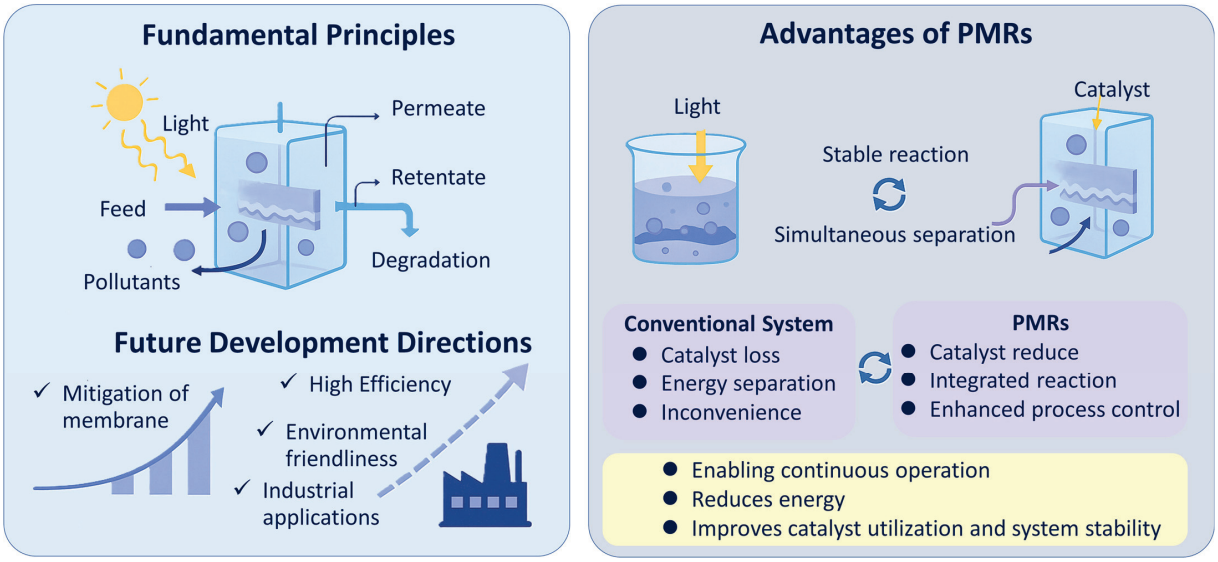


Figure 2. Comparative illustration of PMRs versus conventional systems, highlighting operating principles, key advantages, and future development directions.

The integrated nature of PMRs confers significant operational advantages over conventional photoreactors, including the capacity for continuous operation, in situ catalyst recovery and reuse, and simultaneous substance separation. The modularity and scalability of PMR designs have consequently spurred considerable research interest. However, the transition of this technology from controlled laboratory settings to industrial-scale applications is impeded by several formidable scientific and engineering challenges [65]. The catalytic efficiency and long-term stability of the system can be significantly compromised by the competitive adsorption of inorganic salts and the fouling effects of natural organic matter, factors often excluded from idealized laboratory assessments. This challenge is directly coupled to the critical issues of scalability and economic feasibility. At present, PMR development remains largely confined to laboratory research and small-scale experimental studies, with limited industrial applications [66]. Despite this, PMRs exhibit several advantages that surpass conventional advanced oxidation and separation technologies, such as simultaneous photocatalytic degradation and separation, along with complete retention of the photocatalyst. Despite significant progress in PMR technology, its application in wastewater treatment remains fraught with challenges and uncertainties. A key issue is the incomplete understanding of reaction kinetics during PMR operation, particularly in complex wastewater systems [48]. Additionally, there is a lack of systematic quantification of the interactions between chemical reaction pathways and catalyst activity. Most existing studies have primarily focused on performance evaluation under controlled laboratory conditions, often overlooking the influence of real-world factors, such as water complexity, fluctuations in pollutant types and concentrations, and the competing adsorption of inorganic salts and organic compounds [67]. These external factors can significantly reduce the catalytic efficiency of PMRs and undermine the long-term stability and fouling resistance of the membrane. Another critical challenge is the scalability and economic feasibility of PMR technology [62]. While some studies have explored low-cost catalytic materials and modular designs, achieving stable and efficient performance in large-scale operations at high flow rates remains a significant technical hurdle. In addition, optimizing the energy efficiency of light sources and addressing the overall energy consumption in large-scale engineering applications are essential for the widespread adoption of PMR systems. Laboratory-scale studies often rely on idealized conditions that may not accurately reflect the challenges encountered during scale-up, such as catalyst deactivation, membrane fouling, and uneven light distribution [68]. The uniform distribution of photons, the management of hydrodynamics to mitigate mass transmission limitations, and the maintenance of membrane integrity and catalyst activity over extended operational periods represent significant technical hurdles in large-scale systems. Accordingly, future research must prioritize a holistic approach to reactor design and process optimization. This necessitates the development of robust kinetic models that account for complex water chemistry and the optimization of reactor configurations to enhance light-harvesting efficiency, potentially through the strategic use of low-energy light sources such as LEDs or natural sunlight [69]. In addition, energy efficiency and economic feasibility must be integral components of reactor design, particularly in selecting and distributing light sources (e.g., natural light or LEDs) [70]. The goal should be to balance uniform light intensity distribution with overall energy control [71]. Furthermore, advancing the scalability of PMRs is predicated on the development of multifunctional, integrated systems that may combine photocatalysis with complementary processes, such as adsorption or biological treatment. The overarching objective is the creation of robust, energy-efficient, and economically viable systems capable of operating effectively at an industrial scale.

The evolution of PMRs is driven by advances in materials and membrane technology and pressing environmental demands. The efficacy of these systems arises from a pro-

found synergy between photocatalysis and membrane separation [72]. By confining the photocatalyst, the membrane establishes a microenvironment with a high catalyst concentration, which optimizes photon utilization and promotes the complete mineralization of pollutants [73]. Reciprocally, the photocatalytic process provides a continuous self-cleaning mechanism that mitigates membrane fouling; however, this potent oxidative environment concurrently raises concerns about the long-term stability of the membrane material [74]. Therefore, a comprehensive understanding of this bidirectional interaction is crucial for the rational design and optimization of advanced PMR systems. Overall, PMRs effectively address many of the limitations associated with traditional photocatalytic technologies. They significantly enhance resource utilization efficiency, simplify operational processes, and reduce operating costs. By integrating photocatalysis with membrane separation, PMRs provide an optimal pathway for efficient photocatalyst recovery and sustainable system operation. Owing to their broad application potential in modern environmental management, PMRs have emerged as a promising and innovative technological direction (Figure 3).

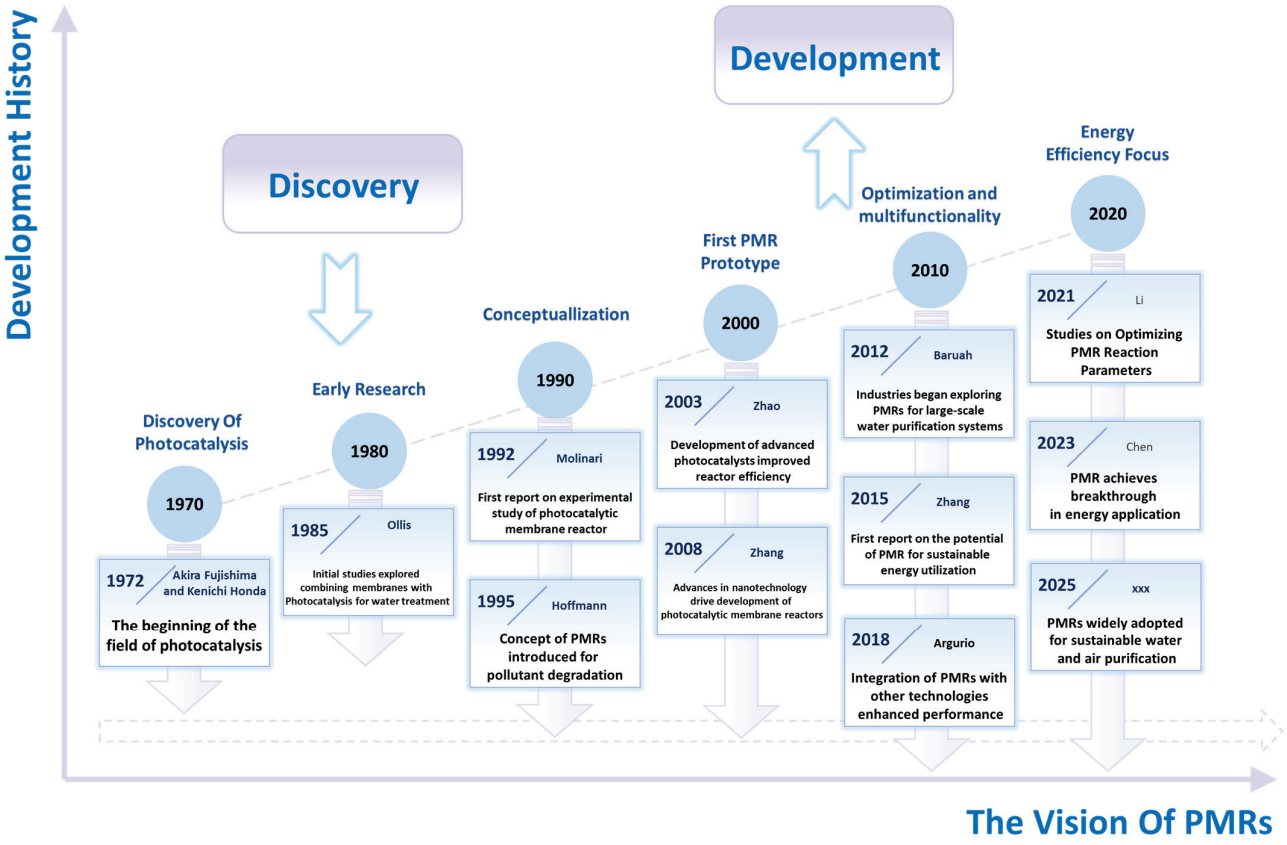


Figure 3. Historical trajectory of PMRs, illustrating a strategic shift from systems for environmental remediation to multifunctional platforms for the sustainable water-energy nexus.

3. Photocatalytic Membrane Reactors

The progression of photocatalytic technology toward industrial-scale commercialization is contingent upon the design and implementation of highly efficient photoreactors. Judicious reactor engineering is paramount, as it can substantially enhance the quantum yield of reactive oxygen species, thereby maximizing the efficient utilization and conversion of photonic energy [75]. Among the various advanced reactor configurations, the photocatalytic membrane reactor (PMR) has emerged as a particularly innovative technology [30]. This system synergistically integrates photocatalysis and membrane separation within a single unit, a design conceived to address the critical challenges of catalyst recovery and

the management of photodecomposition products. Within this integrated framework, the photocatalytic component facilitates the mineralization of organic pollutants into benign substances, such as carbon dioxide and water. Concurrently, the membrane module serves a dual purpose: it acts as a physical barrier for the complete retention of the photocatalyst, enabling its recovery and reuse, and as a selective filter for the treated effluent [76]. Attributable to its high efficiency, operational simplicity, and inherently sustainable design, the PMR exhibits considerable promise as a viable and advanced technology for water and wastewater treatment [61]. Therefore, the design and development of efficient PMRs have emerged as a focal area of research, garnering significant attention in the field [61].

PMRs offer distinct operational and efficiency advantages over conventional photocatalytic slurry systems, primarily due to the synergistic integration of photocatalysis and membrane separation [77]. Through the action of membrane components, PMRs can confine the photocatalyst to a specific region during the reaction process while allowing the treated products to selectively permeate the membrane, thus realizing an efficient separation of the catalyst from the products [78]. This design facilitates a highly controlled reaction environment where the photocatalyst is physically confined, while the treated effluent selectively permeates the membrane [79], further enhancing the system's economy and applicability [30]. Furthermore, the operational stability and process control are significantly improved within a PMR. The membrane module provides a defined reaction zone, which helps to optimize reaction kinetics by regulating the residence time of reactants and intermediates. In PMR systems, photocatalysts can be present in a variety of forms, including loaded on the surface or inside of the membrane matrix, and directly mixed in the reaction medium [33]. This integrated system enables continuous operation with superior catalyst reusability, mitigating the catalyst loss that is often unavoidable in conventional reactor designs. An additional key advantage is the mitigation of membrane fouling. The photocatalytic activity at or near the membrane surface can degrade adsorbed organic foulants, creating a self-cleaning mechanism that extends the operational lifespan and preserves the performance stability of the membrane. This design is particularly suitable for the degradation and separation of environmental pollutants, as it allows for multi-step operation within a single system, thereby simplifying the process flow. The structural design of the PMR also has potential additional advantages. The structural configuration of the reactor extends membrane longevity and enhances performance stability, which is a critical attribute for the long-term treatment of complex wastewater streams. Furthermore, when compared to conventional treatment processes, PMRs exhibit a significantly reduced physical footprint and lower energy consumption, underscoring their potential for widespread industrial application.

3.1. Classifications

The efficacy of a photocatalytic process is fundamentally dictated by the photoreactor's design and the specific mode of catalyst deployment [80]. Critical design parameters that govern overall performance include the nature of the irradiation source (e.g., natural sunlight versus artificial lamps), its spatial configuration relative to the reaction medium (i.e., submerged or external), and the physical form of the catalyst, which may be deployed as a suspended slurry or immobilized on a solid support [32]. Possessing distinctive structural and functional attributes, PMRs can be classified according to multiple criteria. This inherent versatility allows for tailored optimization of the system across a diverse range of application scenarios.

Depending on the mode of operation, PMRs can be categorized into two types: continuous flow and intermittent flow (Figure 4a,b). The integration of continuous flow operation with multiphase photocatalysis is a particularly promising strategy for the development

of sustainable chemical processes. Although conventional filled-bed reactors have been widely used in industrial catalytic applications, they encounter limitations related to energy transfer in photocatalytic systems [81]. Continuous photocatalytic reactors, which operate on the principle that photocatalysts absorb light energy to stimulate a chemical reaction, have a significant advantage over conventional discrete reactors in that they achieve continuous feed and product discharge. This design not only enables stable operation for a long period of time but also significantly enhances the reaction rate, thus providing a novel alternative to conventional synthesis and reaction chemistry [82]. For instance, a continuous fixed-bed photoreactor employing Bi_2WO_6 photocatalysts coated on silica sand was reported to achieve a degradation efficiency of 95.40% for sodium isobutylxanthate within 70 min under optimal conditions [83]. However, despite these advantages, the industrial-scale implementation of continuous PMRs is often hindered by challenges related to scale-up, potential for catalyst deactivation, and overall operating costs. In addition, photochemical reactions conducted in microchannels (inner diameter < 1 mm) demonstrate significantly shorter reaction time due to higher and uniform photon fluxes, while reducing by-product generation induced by over-irradiation, a phenomenon that is more common in conventional intermittent flow reactors. Batch reactors with intermittent flow have traditionally been used for small-scale studies to explore reaction mechanisms and conversion efficiencies. A significant limitation of conventional batch reactors is the non-uniform distribution of light intensity, which typically attenuates from the reactor wall toward the center, resulting in reduced reaction rates and uneven irradiation. Nevertheless, intermittent operation can be strategically advantageous in certain PMR configurations [84]. In contrast, intermittent flow reactors exhibit unique advantages in small-volume reactions due to their simplicity of fabrication, ease of operation, and higher residence times [71]. However, standard intermittent flow reactors, typically on the centimeter scale in diameter, suffer from uneven distribution of light intensity, which attenuates significantly from the vessel wall toward the center of the reaction mixture, resulting in reduced reaction rates and uneven irradiation [84]. In an effort to address such limitations, Ahmad et al. fabricated a partially coated TiO_2 (pc-TiO_2) layer on a porous Al_2O_3 membrane substrate for application in a photocatalytic membrane reactor designed for the treatment of organic dye pollutants; low-cost polyvinyl chloride (PVC) was utilized to generate interstitial voids. Their investigation revealed that intermittent flow membrane filtration markedly enhanced the photocatalytic activity of both uncoated (uc) and pc-TiO_2 composite membranes when compared to the performance of bare Al_2O_3 membranes [85]. Furthermore, different PMR configurations can be distinguished based on different locations of the light source. In particular, the radiation source may be (i) above/inside the container containing the feed solution; (ii) above/inside the cell containing the membrane; and (iii) above/inside an additional container that may be located between the feed tank and the cell containing the membrane (Figure 4c–f) [86].

The most common classification method is based on whether the catalyst is dispersed in a slurry or immobilized on a carrier. PMRs can be designed in two main configurations, as shown in Figure 5: (i) reactors characterized by the suspension of the photocatalyst within the reaction mixture are designated as slurry PMRs and (ii) PMRs with photocatalysts immobilized in/on a substrate material used as a photocatalytic membrane (IPMR). Both configurations have specific advantages and limitations depending on the specific application [69].

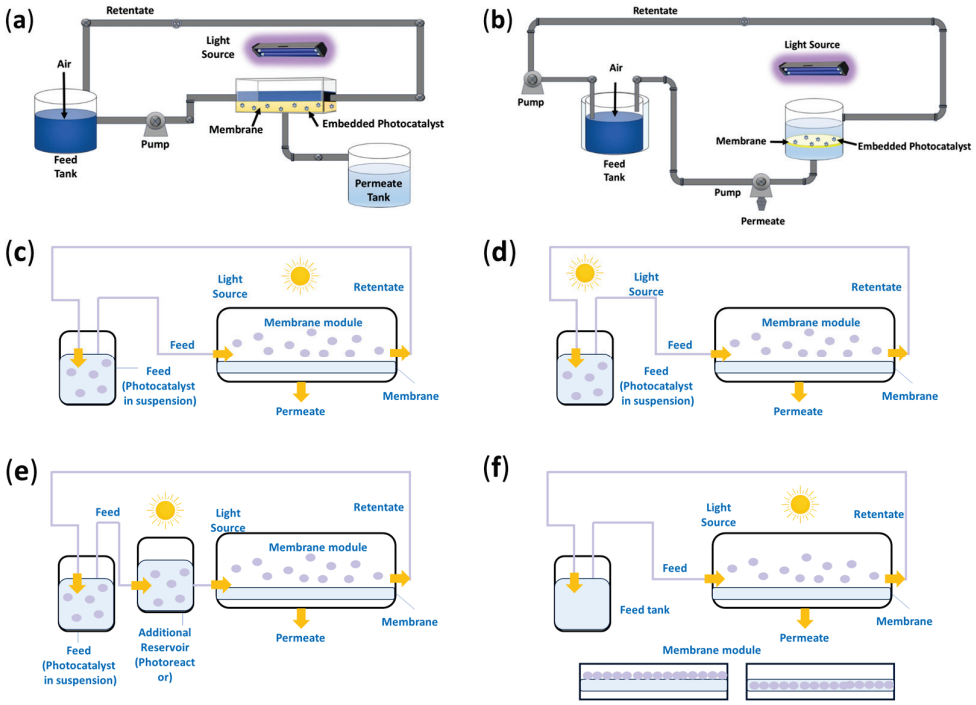


Figure 4. Classification of PMRs: (**a**) continuous flow and (**b**) intermittent flow according to the mode of operation. Reprinted with permission from Ref. [54]. Copyright (2021), Elsevier. (**c**–**f**) different light sources location. Reprinted with permission from Ref. [30]. Copyright (2010), Elsevier.

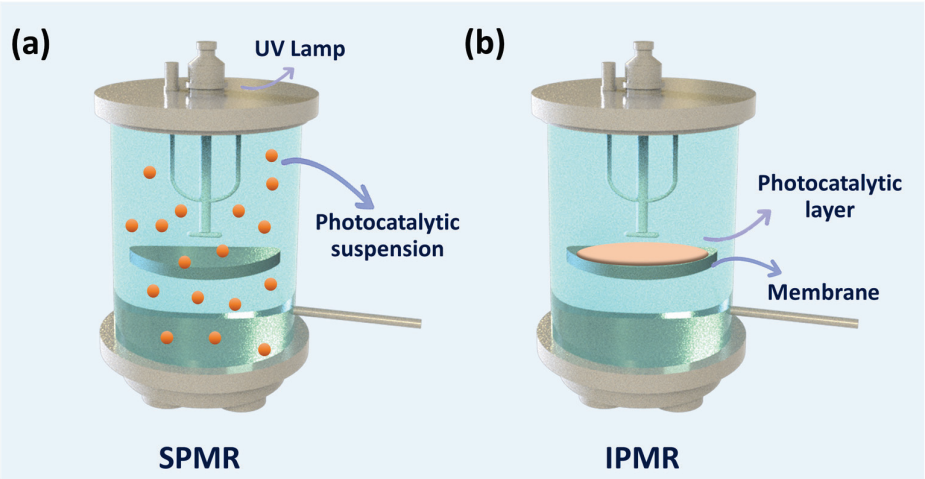


Figure 5. Classification of PMRs: The catalysts are categorized according to their state as (**a**) slurry and (**b**) immobilized. Reprinted with permission from Ref. [54]. Copyright (2021), Elsevier.

3.1.1. Slurry Photocatalytic Membrane Reactor (SPMR)

While photocatalytic membranes with immobilized catalysts offer a promising route for simultaneous pollutant degradation and fouling mitigation, ensuring sufficient and uniform irradiation of the catalyst layer on the membrane surface remains a significant engineering challenge. However, how to ensure that the membrane surface receives sufficient light remains a critical issue to be solved. As a practical alternative, the slurry photocatalytic membrane reactor (SPMR) configuration has been widely investigated. The slurry photocatalytic membrane reactor, a type of photoreactor in which the photocatalyst is dispersed in the feed solution, effectively increases the chance of contact between the pollutant and the photocatalyst. The system utilizes the excellent separation performance of the separation membrane to achieve efficient separation and recovery of photocatalytic particles. This

design confers several distinct advantages. The suspended nature of the catalyst provides a very large specific surface area for reaction and mitigates mass transmission limitations, which can significantly accelerate photocatalytic degradation rates [87]. Significantly, the membrane acts as an absolute barrier, ensuring the complete retention and recovery of the photocatalyst particles. Simultaneously, the application of dispersed particles increased the number of suspended photocatalysts, thus accelerating the photocatalytic degradation process and further improving the treatment efficiency.

The SPMR represents a prevalent configuration wherein the photocatalyst is maintained as a suspension within the reaction medium. This design is intended to capitalize on the superior mass transmission characteristics inherent to slurry-based systems, where the high specific surface area of the dispersed nano- or micro-sized catalyst particles optimizes reaction kinetics and pollutant degradation rates. Furthermore, the turbulence induced by mechanical agitation or aeration serves a dual purpose: it mitigates the deposition of foulants on the membrane surface and enhances the mass transmission of dissolved oxygen, which acts as a critical electron scavenger, thereby improving the overall process efficiency. However, excessive bubble formation can scatter light, which may reduce photocatalytic reaction efficiency [25]. Slurry photocatalytic systems are widely recognized for their superior mass transmission performance and high photocatalytic efficiency. Semiconductor photocatalysts, typically in the nanometer or micrometer size range, enhance mass transmission rates and optimize reaction conditions. Slurry-type reactors have been extensively employed to address mass transmission limitations due to their ability to enhance efficiency and reduce residence time [88]. A primary limitation is the phenomenon of light scattering by the suspended particles, which can impede uniform photon distribution throughout the reactor and adversely affect the overall quantum yield [89]. SPMRs have been developed to overcome these limitations by integrating catalyst separation and recycling mechanisms. Concurrently, the membrane module itself is susceptible to two distinct operational issues: potential material degradation resulting from prolonged exposure to UV irradiation and a decline in permeate flux due to the deposition of the catalyst nanoparticles themselves, which can form a resistive cake layer on the membrane surface. In parallel, prolonged operation may expose the membrane to UV radiation, potentially causing damage. This issue can be addressed by incorporating an opaque baffle between the light source and the membrane. Alternatively, placing the membrane outside the reactor can protect it from UV damage, though this arrangement may increase the pressure drop and cause fluctuations in catalyst concentration within the reactor [65]. The design of slurry-based reactors involves optimizing the balance between mass transmission and radiation. The convective movement of catalyst particles can cause significant light scattering, which affects light distribution within the reactor and subsequently impacts reaction efficiency [71]. Numerous studies have demonstrated that PMRs with slurry photocatalysts generally achieve higher efficiencies compared to those with immobilized photocatalysts. Submerging the membrane directly within the photoreactor offers a simplified and compact system, although protective measures such as opaque baffles may be necessary to shield the membrane from direct irradiation [57]. Conversely, positioning the membrane in an external loop effectively protects it from UV degradation but can introduce hydraulic complexities, including increased pressure drop and potential fluctuations in catalyst concentration within the reactor. As an illustration of the former configuration, a suspended catalyst in an SPMR was developed by Gomaa et al., utilizing ZnO as the photocatalyst and an immersed LED-UV lamp as the irradiation source. This system demonstrated approximately 86% dye decolorization efficiency in the treatment of methylene blue (MB) and achieved nearly complete oil-water separation, showcasing its dual functionality for simultaneous pollutant degradation and physical separation [90].

SPMRs are principally classified into two configurations based on the spatial relationship between the photoreaction and membrane separation modules: immersed and split-type systems [36]. In the immersed configuration, the membrane module is submerged directly within the slurry photoreactor, creating a highly integrated and compact unit. This design minimizes the system footprint and hydraulic resistance, thereby reducing capital and operational expenditures. Typically, inorganic or polymer membranes are submerged in a slurry-based photocatalytic reactor for operation [91]. In this system, the membrane module is submerged directly in the photocatalytic reactor, preventing catalyst loss and maintaining a stable catalyst concentration in the reactor. This design provides greater operational stability than other reactor types. In addition, the compact structure of the immersed reactor can shorten the pipeline length and reduce the system resistance loss, which in turn significantly reduces the investment and maintenance costs [92]. The direct immersion ensures complete catalyst retention, which promotes a stable catalyst concentration and high operational stability. Early iterations of this design, such as the system developed by Zhang et al. for sodium dodecylbenzene sulfonate surfactant degradation, utilized a PMR with a silica/titania nanorods/nanotubes composite photocatalytic membrane [93]. While this ensured intimate contact between the catalyst and photons, it lacked a dedicated catalyst recovery mechanism. Subsequent innovations have addressed this limitation [94]. The filtration mechanism relied on a dynamic filter cake layer, making it particularly suitable for handling larger particles of suspended pollutants. However, this system did not include a catalyst recovery method, and the internal placement of the UV light source ensured close interaction with the catalyst, thereby enhancing the excitation and efficiency of the photocatalytic reaction. Building on this approach, Li et al. introduced a novel enhancement by integrating an external magnetic field into the submerged photocatalytic reactor system, enabling efficient recovery of the catalyst. They proposed a photo-Fenton catalytic system, the submerged magnetic separation photocatalytic membrane reactor, which combined photocatalysis and Fenton oxidation processes [95]. The synthesized TiO_2-Fe_3O_4 composite catalyst demonstrated exceptional degradation performance, particularly for the removal of amoxicillin, significantly improving photocatalytic reaction efficiency and catalyst reusability. Extending the application of PMR technology, Zeitoun et al. designed a system combining a polyvinylidene fluoride (PVDF) membrane with TiO_2 and an ultraviolet light source. This PVDF-TiO_2 system exhibited notable hydrophobicity and high filtration precision, making it especially effective for treating dye wastewater and other high-pollution-load effluents [96]. The direct immersion ensures complete catalyst retention, which promotes a stable catalyst concentration and high operational stability. The slurry photocatalytic membrane reactor by Janssens et al. treated secondary wastewater with anticancer drugs, retaining TiO_2. This indicates PMRs are promising for advanced water treatment, but a catalyst for real wastewater is still needed [97]. While this ensured intimate contact between the catalyst and photons, it lacked a dedicated catalyst recovery mechanism. Subsequent innovations have addressed this limitation. Immersed PMR integrates membrane materials and light sources into one system, which can adapt to a variety of treatment scenarios by changing different membrane materials or operating modes. In contrast, split reactors consist of two distinct units for photocatalytic reaction and membrane separation, connected via piping to form an integrated system. The photocatalytic module and the membrane separation module are connected via piping to form a coordinated system [98]. The external structure of this design has the advantages of clear operation, easy assembly, and low maintenance. The split photocatalytic membrane reactor with an external membrane separation module can be operated in continuous mode. In this case, the permeate is discharged as a treated effluent, and the photocatalyst is returned to

the reactor for reuse; in the batch mode, both the permeate and the concentrate are returned to the photoreactor to maintain a constant volume of the reaction system [99,100].

From an industrial application perspective, the choice between immersed and split-slurry PMR configurations is often governed by specific operational priorities. Immersed systems are generally favored for applications where high reaction efficiency and a compact footprint are paramount. Slurry-based systems are inherently advantageous as they can minimize the mechanical shear stress on catalyst particles and reduce the potential for pump abrasion and clogging [101]. Despite these advantages, slurry-based PMRs require aeration, which can result in significant energy consumption [102]. Therefore, optimizing the aeration rate, along with the size and distribution of bubbles, is crucial for improving efficiency [103]. Parallel to reactor configuration, the selection of the membrane material is a pivotal design decision. Organic polymeric membranes represent a more economical option, whereas inorganic ceramic membranes are distinguished by their superior chemical, thermal, and mechanical stability [104]. A primary research challenge associated with polymeric membranes is enhancing their long-term stability and resistance to degradation by photogenerated reactive oxygen species. Conversely, while ceramic membranes are inherently more robust, a significant body of research has been dedicated to leveraging photocatalysis for the effective mitigation of biofouling on their surfaces.

3.1.2. Immobilized Photocatalytic Membrane Reactor (IPMR)

Photocatalysts in suspended form are widely used in PMRs, but the complexity of their recovery from the reaction system has become a major challenge in realizing large-scale applications. To cope with this problem, the research focus in recent years has shifted to photocatalytic membrane technology, in which the catalyst recovery challenges are effectively avoided by immobilizing the photocatalyst on the membrane surface or inside [104]. Immobilized PMRs (IPMRs) are designed by fixing the photocatalyst directly on the membrane surface or embedding it in its porous structure, which effectively eliminates the need for downstream catalyst recovery processes. This approach is further motivated by the inherent limitations of conventional photoreactors, which often suffer from low surface-area-to-volume ratios and non-uniform light distribution, thereby constraining overall quantum efficiency. The immobilization of photocatalysts on polymeric membrane carriers, thus utilizing membrane reactors to carry out the reaction, is a promising and efficient solution. The efficacy of the immobilized PMRs concept is well-illustrated by a study from Biao et al. on the removal of microplastic fibers from synthetic laundry wastewater. This system was designed to harness the synergistic effects of photocatalytic degradation by the Ag-TiO_2 layer, enhanced by the plasmonic effect of the silver nanoparticles, and physical rejection of the microfibers by the membrane support. The study demonstrated the significant potential of immobilized PMRs as a scalable and effective technology for mitigating pollution from emerging contaminants [105]. The method combines photocatalytic degradation with membrane filtration to effectively reject and degrade fibrous MPs, thereby reducing their environmental impact.

The integration of the photocatalyst with the membrane support, accomplished via either surface anchoring or matrix entrapment, yields a bifunctional composite. This architecture enables the membrane to serve the dual purpose of a catalytic reaction platform and a selective separation barrier [106]. The preeminent advantage of this design is the complete elimination of the catalyst recovery and recirculation loop required in slurry-based systems. Although the immobilization of the catalyst may introduce mass transmission resistances that can potentially lower the apparent reaction kinetics, this limitation is frequently offset by the substantial gains in operational stability, catalyst reusability, and

process simplification. These attributes are instrumental for the development of continuous, long-term, and sustainable photocatalytic processes for environmental remediation.

In PMRs, the immobilization of the catalyst onto a support is a key strategy to overcome the limitations inherent to slurry-based systems. In this approach, the photocatalyst is anchored to the membrane, forming an integrated, bifunctional unit that performs both catalytic degradation and physical separation [25]. Systems with a split design can effectively isolate the photocatalytic and membrane units, thus avoiding potential damage to the membrane material from UV irradiation and photogenerated reactive oxygen species. This design fundamentally obviates the challenges associated with the recovery, agglomeration, and potential loss of suspended nanoparticles [57]. Photocatalysts can be deposited on commercial membranes by surface loading or embedding, and the resulting catalytic membranes prepared are capable of simultaneous pollutant separation and photocatalytic degradation [107]. In this configuration, the function of the membrane can be categorized into two types: only as a carrier for the photocatalyst, or both separation and immobilization of the catalyst. In the latter case, the membrane not only acts as a selective barrier to confine the pollutant to be degraded to the reaction environment, but also assumes the role of a photocatalyst carrier [65]. Integrated PMRs (IPMRs) are considered an advanced solution. Although suspended photocatalysts exhibit high pollutant degradation efficiencies due to the large specific surface area of their nanoparticles, the difficulty of their separation and recycling is their main limitation. In addition, the tendency of nanoparticles to agglomerate may further reduce the reaction efficiency. By immobilizing the photocatalyst on a support material, these problems can be alleviated to a certain extent, as embodied in the design of the IPMR. In addition, membrane contamination triggered by photocatalyst deposition in suspended PMRs (SPMRs) is a pressing issue. Based on the concept of process enhancement, the application of immobilized photocatalysts avoids the subsequent recovery step of the catalyst and can effectively mitigate the fouling caused by photocatalysts and contaminants [65]. In the reactor with immobilized catalysts, since the catalysts are immobilized in the form of membranes, the light scattering effect can be neglected, which simplifies the modeling process of the radiation field. Therefore, the focus of the study is more concentrated on internal and external mass transmission phenomena [108].

The morphology of the photocatalytic membranes and the distribution of nanoparticles largely depend on the specific synthesis method used to incorporate the photocatalysts into the membranes [57]. In recent years, the focus of research has gradually shifted to stationary PMRs, aiming to overcome their lack of efficiency through appropriate catalyst modification [47]. An immobilized photocatalytic membrane reactor can be further divided into the following two categories according to the different photocatalytic membrane preparation methods: (1) photocatalysts are deposited into the membrane structure; (2) photocatalysts are loaded on the surface of the membrane material [88]. The photocatalytic membrane can not only serve as a physical barrier to achieve efficient separation but also degrade the organic pollutants attached to the membrane surface or through the membrane pores through photocatalysis. This dual functionality positions photocatalytic membranes as an innovative water treatment solution that is both efficient and sustainable.

3.1.3. Other Types

Submerged Photocatalytic Membrane

In slurry systems, the flow of photocatalytic particles may cause mechanical damage to the membrane surface, thus shortening the lifetime of the membrane [109]. For slurry-based PMRs, the permeation of photocatalysts may reduce the permeate quality during the early stages of filtration [110]. Although slurry reactors can provide higher mass transmission efficiencies and reaction rates, significantly improving treatment performance, additional

separation steps are required to remove suspended catalyst from the treated water [111]. Conversely, the suspended catalyst reactor exhibits a larger mass transmission area and a higher reaction rate for the same catalyst dose. However, this design faces an inherent challenge in that the catalyst particles must be recovered from the treated water [112]. When the catalyst is loaded onto the carrier material in an immobilized form, this usually leads to a significant reduction in the accessibility of the photocatalytic active surface, which weakens the photocatalytic performance [113]. A primary operational constraint is the necessity for a downstream separation unit to recover the catalyst, a requirement that invariably elevates operational expenditures. Internally, the system's performance is often compromised by two phenomena: particle agglomeration at elevated catalyst loadings, which diminishes the effective specific surface area, and the light-scattering effect induced by suspended particles, which impedes uniform photon penetration and reduces the overall quantum yield. Although photocatalytic membrane systems (PMSs) with suspended catalysts have shown significant advantages in mitigating membrane contamination, the effective recovery and regeneration of the catalysts remain an urgent challenge [25]. Insights from existing theoretical models and slurry system experiments indicate that compact "membrane-type" configurations are generally more effective for achieving high treatment efficiency. By contrast, bulk water treatment demands extended or sequential photocatalytic reactors to maintain adequate reaction efficiency [75]. In response to these limitations, submerged photocatalytic membranes have been proposed as a promising alternative. A submerged photocatalytic membrane reactor is a hybrid system integrating photocatalysis and membrane filtration, which effectively overcomes the difficulty of separating catalysts from wastewater in traditional processes. In this system, the suspended photocatalyst can significantly improve the pollutant removal efficiency due to its large specific surface area and the generation of highly active free radicals. However, the separation of suspended catalysts and the continuous operation of the system face certain challenges. To solve these problems, a submerged photocatalytic membrane reactor was developed. The submerged photocatalytic membrane reactor represents a more compact and structurally integrated configuration when compared to conventional split-loop designs. In the submerged photocatalytic membrane reactor, the core function of the membrane is to act as a barrier, both to prevent the loss of catalyst and to separate the products and by-products generated during the photocatalytic oxidation process. In this system, the core function of the membrane, typically a microfiltration or ultrafiltration module, is to serve as a dynamic barrier. Its role extends beyond the mere retention of suspended catalyst particles to include the separation of products and by-products generated during the photocatalytic oxidation process. Furthermore, the membrane can be engineered to selectively sequester target pollutants, a functionality that allows for the precise regulation of their residence time within the photoreactive zone, thereby enhancing the overall degradation efficiency [114]. Studies have demonstrated that catalyst particles deposited on the membrane surface can further enhance photocatalytic reactions, and optimization of membrane loading and catalyst concentration is critical for improving system performance [115]. In addition, submerged membrane filtration technology, which is widely used in conventional membrane bioreactors, is cost-effective in mitigating particle deposition [116]. Another advantage of combining photocatalysis with submerged membranes is that photocatalytic degradation of contaminants and physical separation through membranes can be achieved simultaneously in a single device. However, the problem of membrane contamination significantly reduces membrane permeability, which in turn shortens membrane lifetime, increases operating costs, and weakens system performance. Especially in a submerged photocatalytic membrane reactor, the deposition of photocatalysts on the membrane surface not only leads to a decrease in membrane permeability but may also affect the photocat-

alytic efficiency [39]. In recent years, several research groups have made important progress in submerged photocatalytic membrane reactors. Jiang et al. investigated the potential of a membrane photocatalytic reactor (MPR) for degrading soluble extracellular organic matter (SEOM), achieving over 60% removal at a hydraulic retention time of 140 min (Figure 6a). This was largely due to the synergistic effect of adsorption and photocatalysis on the TiO_2 surface, showcasing the foundational benefits of integrating membrane filtration with photocatalysis for pollutant degradation [117]. Building on this foundation, Wang et al. developed a submerged membrane photocatalytic reactor (SMPR) specifically tailored for the treatment of p-nitrophenol (PNP) wastewater. Their system not only achieved a high PNP removal rate of 91.6% under simulated sunlight but also demonstrated a significant advantage over slurry systems by ensuring a 100% retention rate of the catalyst on the MF membrane, thus preventing catalyst loss and secondary pollution, which are common issues in slurry reactors [118] (Figure 6b). Further advancing this concept, Li et al. introduced a submerged ceramic membrane photocatalytic reactor (SCMPR) that utilized suspended TiO_2 for antibiotic removal. The antifouling ceramic membrane with its hollow structure facilitated efficient catalyst separation, offering stability and high removal efficiency for amoxicillin across a broad pH range. This design exemplifies how submerged reactors can handle complex, pH-sensitive pollutants more effectively than slurry systems by providing a stable environment for catalyst activity [119]. Lastly, Kertèsz et al. took the submerged PMR approach to optimize dye wastewater treatment with a hollow fiber microfiltration photocatalytic membrane reactor (Figure 6c). Their system not only achieved complete catalyst separation from the treated water but also operated at a sustainable permeate flux, emphasizing the importance of balancing the photocatalytic and membrane separation capacities for enhanced system performance. This study further underscores the advantage of submerged PMRs in maintaining catalyst integrity and enhancing treatment efficiency compared to slurry reactors, where catalyst recovery is more challenging [120]. In aggregate, these studies illustrate a progressive enhancement in submerged PMR technology, from basic pollutant removal to sophisticated treatment of specific contaminants like dyes and antibiotics, offering clear advantages in catalyst retention, pollutant degradation, and system sustainability over traditional slurry photocatalytic systems.

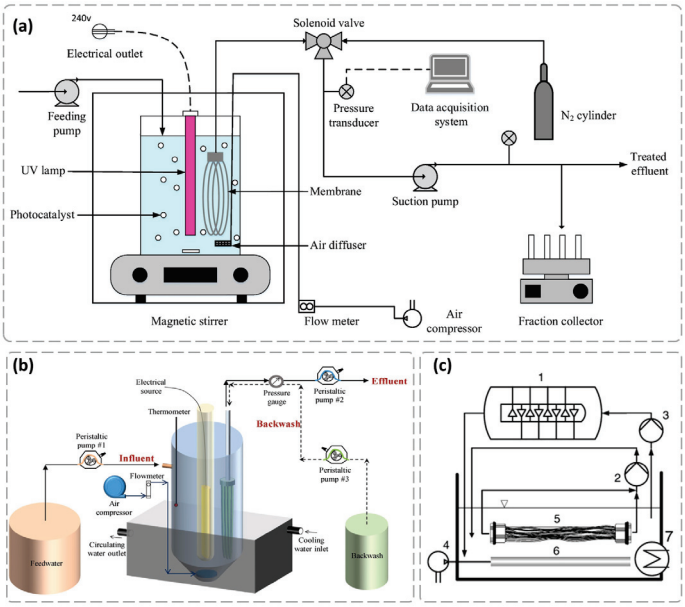


Figure 6. For the defects of slurry type of PMR improvement with (**a**) Submerged PMR used for the treatment of secondary effluents. Reprinted with permission from Ref. [117]. Copyright (2016), Elsevier.

(**b**) Submerged PMR. Reprinted with permission from Ref. [118]. Copyright (2021), Elsevier. (**c**) Submerged PMR. Reprinted with permission from Ref. [120]. Copyright (2014), Elsevier. for the defects of immobilized type of PMR improvement.

Oscillating Photocatalytic Membrane

The operation of photocatalysts in PMRs using immobilized photocatalysts also presents several challenges, such as the leaching and settling of the catalysts, as well as the process of separating and recycling the catalysts from the treated water, which are complex, time-consuming, and costly. In addition, the absorption and scattering of light by the catalyst can limit the depth of light penetration [89]. Nevertheless, the deposition of photocatalyst nanoparticles (NPs) on the membrane surface triggers a decrease in flux, while the fouling problem due to light scattering remains a major limiting factor in the performance of such membrane photoreactors [36]. It has been shown that the introduction of oscillatory motion can effectively reduce the deposition of particles on the membrane surface [89].

In submerged photocatalytic reactors without oscillations, the transverse osmotic flow directs catalyst particles to the membrane surface, leading to the formation of a particle/filter cake layer on the membrane surface. This deposit not only increases the pressure drop across the membrane but also reduces the fraction of catalyst in suspension, which decreases the photocatalytic efficiency of the system. In contrast, membrane oscillation can provide significant advantages in terms of membrane cleaning and photocatalytic efficiency. This is due to the development of vortices, especially during shear reversal, which may dominate most of the oscillation cycle. In addition, enhanced shear dynamic filtration (DF) systems have been recognized as an effective means of improving the hydrodynamic conditions of membrane separation systems and reducing membrane contamination [121]. This method creates high shear forces at the membrane surface by generating relative motion between the membrane and the neighboring fluid, such as rotational or oscillatory motion. This mechanism not only reduces membrane contamination and increases system flux but also achieves separation of the permeate stream from the surface shear, thus providing additional flexibility to optimize the reactor residence time to suit the photocatalytic reaction kinetics. The application of oscillatory motion has further demonstrated its significant effect in reducing membrane contamination and promoting catalyst suspension in PMRs (Figure 7) [111]. It has been shown that ZnO exhibits excellent photocatalytic activity by virtue of its excellent UV light absorption and unique crystal structure. These properties make ZnO an efficient photogenerated electron capture site, which significantly enhances charge separation while reducing the need for oxygen as an electron acceptor [112].

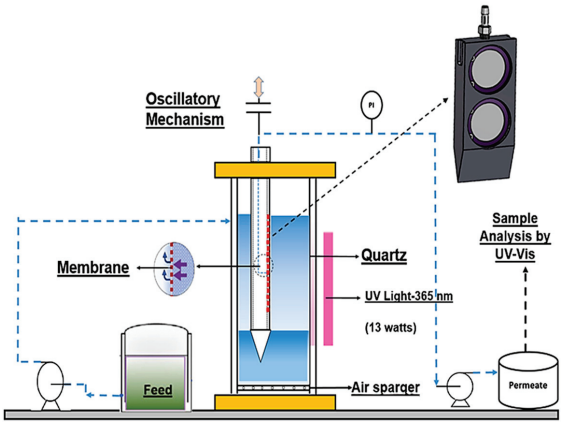


Figure 7. For the defects of slurry type of PMR improvement with oscillating PMR. Reprinted with permission from Ref. [111]. Copyright (2021), Elsevier.

3.2. Kinetics in PMRs

The study of reaction kinetics in PMRs is particularly important because it determines the reaction rate, conversion efficiency, and reactor design and operating conditions. As shown in Figure 8, photocatalytic reaction kinetics is the study of the rates, pathways, and influencing factors of chemical reactions of reactants on the surface of photocatalysts, which can help predict and optimize the performance of photocatalytic reactors.

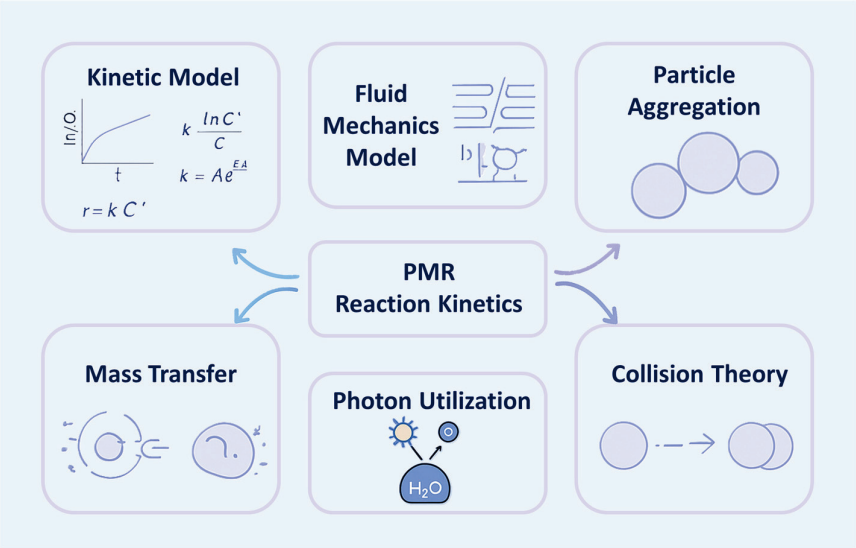


Figure 8. Schematic overview of the reaction kinetics in PMR.

3.2.1. Kinetic Model

A quantitative understanding of reaction kinetics is fundamental to the design, optimization, and scale-up of PMRs. The heterogeneous photocatalytic degradation of organic pollutants in PMRs is most frequently described by the Langmuir–Hinshelwood (L–H) kinetic model, which accounts for reactant adsorption on catalytic sites, surface photochemical reactions, and subsequent desorption of intermediates and products. Under conditions of low initial substrate concentration, the L-H model can often be simplified to an apparent pseudo-first-order kinetic model. The determination of the apparent rate constant, k, is therefore a central objective in experimental and modeling studies, as it provides a quantitative metric for evaluating and comparing system performance. The magnitude of this rate constant is a complex function of multiple interdependent variables. These include intrinsic catalyst properties, such as specific surface area and surface activity; external operational parameters, including incident light intensity (photon flux), pH, and temperature; and the mass transmission characteristics of the system, which are governed by the initial reactant concentration and the hydraulic properties of the membrane module. A thorough understanding of these kinetic relationships is thus indispensable for elucidating reaction mechanisms, identifying rate-limiting steps, and systematically optimizing the operational parameters of the reactor for maximal degradation efficiency. The rate of the photocatalytic reaction can be expressed by the following reaction equation, as shown in Equation (1):

$$r = \frac{kKC}{1 + KC}, \tag{1}$$

where r is the reaction rate, k is the apparent reaction rate constant, K is the adsorption equilibrium constant, and C is the concentration of the reactants. The model shows that the reaction rate is proportional to the reactant concentration at low concentrations and saturates at high concentrations. The apparent kinetic parameters of photodegradation in

immobilized PMR systems are determined by the kinetics of pollutants and intermediates to and from the immobilized photocatalysts on or in the photocatalytic membrane. Most of the degradation reactions in immobilized PMRs follow the proposed first-order kinetics [122]. The rate constant (k) is an important factor affecting the reaction rate and conversion (in this case, degradation efficiency). In most studies, the kinetic rate constant takes into mass transmission effects in the reactor. Therefore, it has been reported that the kinetic constant usually varies with size, stirring speed [71]. The kinetics of pollutant degradation in aqueous multiphase catalytic reactions were investigated using the Langmuir-Hinshelwood model and power law [123]. The reaction kinetics provide information about the reaction rate and the mechanism of pollutant removal. The Langmuir-Hinshelwood model is commonly used in multiphase reaction kinetic studies, such as photocatalytic processes using TiO_2 nanoparticles. The general form of the model is shown in Equation (2):

$$R = -\frac{dC_L}{dt} = \frac{k_{L-H} K_{ads} C_L}{1 + K_{ads} C_L}, \quad (2)$$

where C_L denotes the concentration of leachate COD at each time, k_{L-H} is the Langmuir-Hinshelwood reaction constant for the removal of COD, and K_{ads} is the equilibrium constant for the adsorption of organic matter onto TiO_2 nanoparticles.

3.2.2. Fluid Mechanics Model

The integration of kinetic, hydrodynamic, and radiative transfer models enables a priori prediction of photocatalytic reactor performance and provides a foundation for systematic optimization. In order to allow for appropriate development and scale-up strategies for PMR design, it is important to understand the interaction effects of hydrodynamic and colloidal forces on catalyst particle aggregation [121]. Despite its importance, a significant gap persists in the literature concerning the analytical and numerical modeling of these interactions, a deficit that is especially pronounced for advanced configurations such as DF systems. Dynamic filtration is an advanced operational strategy engineered to mitigate membrane fouling by inducing high shear at the membrane surface, typically through rotational or oscillatory motion of the membrane or an adjacent component [124]. Beyond the effective mitigation of concentration polarization and cake layer formation, a salient advantage of DF is the decoupling of the permeate flux from the cross-flow hydrodynamics. This decoupling provides an independent degree of freedom for the precise control of the reactor residence time, a parameter dictated by the intrinsic kinetics of the photocatalytic reaction [121].

3.2.3. Particle Aggregation

The degradation kinetics within slurry PMR systems are profoundly influenced by the interplay between initial substrate concentration and the prevailing hydrodynamic conditions [125]. Particularly in photocatalytic reactors, particle aggregation can negatively affect semiconductor photocatalytic activity by reducing the production of hydroxyl radicals and reactive oxygen species [121]. This phenomenon, known as the inner filter effect, diminishes the quantum efficiency of the process by reducing the rate of electron-hole pair generation. Conversely, operation at lower substrate concentrations, particularly when coupled with higher flow rates, has been demonstrated to yield superior degradation efficiency. This enhanced performance is attributable not only to the mitigation of the inner filter effect, which increases photon availability for the catalyst, but also to the improved mass transmission of reactants to the catalyst surface under conditions of increased turbulence [71].

3.2.4. Mass Transmission

In PMRs, the integration of a physical separation barrier introduces complex mass transmission phenomena that can become the rate-determining step for the overall process. Consequently, the observed degradation rate is frequently governed not by the intrinsic kinetics of the surface photochemical reaction, but by the transport of reactants and products to and from the active catalytic sites. A comprehensive analysis of mass transmission limitations within a PMR must consider several distinct transport resistances. The first is external mass transmission, which involves the convective-diffusive transport of pollutant molecules from the bulk fluid across the hydrodynamic boundary layer to the exterior surface of the photocatalyst or the catalytic membrane. The second is internal mass transmission, or intraparticle diffusion, which pertains to the diffusion of reactants within the porous structure of the photocatalyst or the catalytically active membrane layer. Finally, transmembrane mass transmission—the transport of molecules through the membrane pores—is also a critical factor, influenced by membrane properties, such as pore size and surface chemistry, and by operational conditions that dictate the formation of polarization layer. A rigorous understanding of these coupled transport processes is therefore a prerequisite for the accurate kinetic modeling and rational design of high-performance PMRs.

3.2.5. Photon Utilization

A pivotal performance metric for any photocatalytic system is the photon utilization efficiency, which is defined as the fraction of incident photons that are productively absorbed by the catalyst and result in the desired chemical transformation. This parameter provides an integrated measure of the system's capacity to convert light energy into chemical potential, inherently accounting for losses due to reflection, transmission, and scattering. In kinetic investigations, the photon utilization efficiency is an indispensable parameter for quantifying and comparing the intrinsic activity of different photocatalytic materials. Its magnitude is fundamentally dictated by the inherent optoelectronic properties of the semiconductor, most notably its band gap energy and spectral absorption characteristics, as well as the degree of spectral overlap with the emission profile of the irradiation source. From a reactor engineering standpoint, the maximization of this efficiency is a primary design objective. This requires the careful optimization of the reactor geometry, the catalyst loading, and the system hydrodynamics to ensure a uniform radiation field and to minimize non-productive light absorption and scattering.

3.2.6. Collision Theory

Within the porous architecture of photocatalytic membranes, where pore diameters typically range from nanometers to several micrometers, the internal fluid dynamics are characterized by Stokes flow. Under this low-Reynolds-number regime, the transport of micropollutants to the catalytically active pore walls is governed predominantly by radial diffusion. ROS are subsequently generated at these surfaces through the interaction of adsorbed pollutants with the immobilized photocatalyst. Within the porous architecture of photocatalytic membranes, where pore diameters typically range from nanometers to several micrometers, the internal fluid dynamics are characterized by Stokes flow. A reduction in pore size to the nanometer or sub-nanometer scale can markedly enhance the apparent reaction kinetics, primarily due to the significant shortening of the diffusional path length required for reactant molecules to access active sites. In such highly confined spaces, the distinction between aqueous-phase and absorbed-phase reactions becomes effectively negligible, as interactions between pollutants, ROS, and the catalytic surface occur almost instantaneously at the solid–liquid interface [126].

Collision theory provides a robust framework for characterizing the rate of homogeneous reactions and serves as an effective tool for assessing the performance and mechanical limitations of PMRs. According to collision theory, reactants must collide to undergo a chemical reaction; however, only a fraction of these collisions lead to successful reactions. For a reaction to occur, the colliding molecules must possess sufficient energy to overcome the activation energy barrier, enabling the breaking of existing bonds and the formation of new ones. An increase in reactant concentration enhances the number of collisions within a given timeframe, thereby increasing the reaction rate. This relationship underscores the importance of collision frequency in determining reaction kinetics. The collision frequency is intrinsically linked to the reaction rate constant, k (mol L^{-1} s^{-1}), as described by the Arrhenius equation, which quantitatively connects the reaction rate to the temperature and activation energy of the system (Equation (3)).

$$k = Zexp\left(\frac{-E_a}{R_g T}\right), \tag{3}$$

where Z (mol L^{-1} s^{-1}) corresponds to the product of the concentrations of the reacting species. The activation energy, E_a (J mol^{-1}), represents the minimum energy required for a reaction to occur, while R_g (J K^{-1} mol^{-1}) denotes the universal gas constant, and T is the absolute temperature. $exp\left(\frac{-E_a}{R_g T}\right)$ signifies the fraction of molecular collisions with sufficient energy to overcome the activation energy barrier, thereby facilitating a chemical reaction. Characterizing the reaction kinetics in a PMR based on collision theory requires the identification and quantification of ROS generated during the process. Assuming that a minimal quantity of micropollutants, such as nanogram-per-liter concentrations of steroid hormones, participates in the quenching of singlet oxygen ($^1O_2$), the concentration of ROS generated can be determined based on three key factors: (i) the absorbed photon flux (φ_{abs}, V), (ii) the lifetime or self-decay rate of the ROS, and (iii) the photon conversion efficiency, represented by the quantum yield (Φ_Δ), as expressed in Equation (4).

$$[^1O_2] = \frac{\varphi_{abs,\, v}\varnothing_\Delta}{k_\Delta + k_q[MP]N_{avo}} \approx \frac{\varphi_{abs,\, v}\varnothing_\Delta}{k_\Delta N_{avo}} \tag{4}$$

where k_Δ (μs^{-1}) is the rate constant of $^1O_2$ decay (inverse of the $^1O_2$ lifetime), k_q (L mol^{-1} s^{-1}) is the bimolecular rate constant of $^1O_2$ quenching by micropollutant molecules, and $[MP]$ (mol L^{-1}) is the molar concentration of micropollutants. When the micropollutant concentration is very low ($[MP] \ll k_\Delta / k_q$ $[MP]$), the condition $k_\Delta \gg k_q$ $[MP]$ is satisfied. The quantum yield (Φ_Δ) of $^1O_2$ generation is defined as the ratio of the number of ROS formed to the number of photons absorbed. Palladium (II)-containing porphyrins exhibit a Φ_Δ for $^1O_2$ generation, attributed to their ability to significantly enhance spin–orbit coupling. This enhancement facilitates intersystem crossing, thereby increasing the efficiency of porphyrins in generating $^1O_2$.

The operational flow rate is a critical parameter that profoundly influences the performance of a photocatalytic membrane reactor by governing two key factors: the convective mass transport of pollutants and the hydraulic residence time. An increase in the flow rate enhances the molar flux of micropollutants to the catalytically active surfaces, which can alleviate external mass transmission limitations. Concurrently, however, this elevated flow rate corresponds to a diminished hydraulic residence time, thereby reducing the contact time available for the photocatalytic degradation to occur. The interplay between these opposing effects gives rise to a characteristic kinetic profile, wherein the overall degradation rate is observed to increase with flow rate up to a distinct threshold, beyond which the rate either plateaus or declines. This behavior reflects transitions between reaction regimes: at

low flow rates, performance is restricted by mass transmission to catalytic sites, whereas at higher flow rates, this limitation is alleviated, and degradation improves. Beyond the optimal range, however, the system becomes kinetically controlled, with insufficient residence time rendering the intrinsic surface photochemical reaction the rate-determining step.

Previous conceptual frameworks have sought to rationalize the photodegradation efficiency within porous photocatalytic membranes by invoking the qualitative concept of "contact". This concept correlates the hydraulic residence time with the characteristic "mixing time"—the average time required for a micropollutant to diffuse across the pore radius. While this heuristic provides a rudimentary explanation for performance variations with respect to pore size and flow rate, its utility is fundamentally limited, as it fails to quantitatively account for the specific reaction locus or for critical system parameters such as photon flux, light penetration depth, photosensitizer concentration, and the intrinsic reactivity of the target micropollutants. In contrast, the application of a framework grounded in collision theory represents a significant conceptual advancement by offering a more fundamental and comprehensive approach to describing these nanoscale reactive events. The adaptation of collision theory to describe reactions within highly confined nanoporous environments is a novel approach that is anticipated to provide a more rigorous and quantitative understanding of the kinetic interplay between pollutants and catalytic sites within PMRs.

3.3. Factors Affecting PMR Performances

The operational advantages of PMRs over conventional photoreactor configurations are substantial, arising from the synergistic integration of reaction and separation. This unified approach facilitates the complete retention of the photocatalyst within the reaction environment, affords precise control over molecular residence times, and enables the continuous removal of products [113]. Despite these intrinsic merits, the practical implementation of PMR technology is encumbered by several persistent challenges. These include suboptimal pollutant degradation efficiencies under certain conditions, insufficient long-term membrane durability, a pronounced susceptibility to severe membrane fouling, and the limited availability of robust, recyclable membrane materials [77]. The overall performance of any PMR system is dictated by a complex interplay of physicochemical and engineering parameters. As shown in Figure 9, the key variables influencing the reaction chemistry include the photocatalyst loading, the intensity and wavelength of the irradiation source, the nature and concentration of the target pollutant, and the bulk solution properties, such as temperature, pH, and the presence of inorganic salts. Concurrently, reactor-specific parameters, such as the light intensity distribution, hydraulic residence time, and the mode of catalyst deployment (i.e., suspended or immobilized), are critical determinants of the overall process efficiency [71].

Increased catalyst loading implies a more significant surface area available for adsorption and degradation of target compounds. Nonetheless, overloading of the catalyst will increase operating costs and may lead to a decrease in pollutant removal efficiency by impeding light penetration in the native solution [30]. This phenomenon was exemplified in a study on the degradation of amoxicillin (AMX) within a submerged ceramic membrane photocatalytic reactor (SCMPR), which employed a TiO_2 photocatalyst. They used a TiO_2 photocatalyst and Ceraflo CF-3604-DH hollow plate ceramic membrane in the SCPMR. The results showed that the TiO_2 catalyst (average particle size of 1.4 μm) could be easily separated by the ceramic membrane (pore size less than 500 nm). Although membrane contamination was observed during operation, it was effectively resolved by backwashing. The effect of TiO_2 loading was also investigated, and it was found that excess TiO_2 resulted in decreased degradation efficiency due to light blocking and scattering effects [119].

Hairom et al. successfully synthesized four different types of ZnO nanoparticles using oxalic acid and zinc acetate solutions by precipitation and constructed them into a PMR system to investigate the effect of ZnO nanoparticles on the treatment of Congo red (CR) dye in the MPR. The effect of the ZnO nanoparticles on the optimum photocatalyst loading for the MPR system was found to be 0.3 g/L^{-1} at an initial dye concentration of 20 mg/L^{-1} at pH 7, due to the effective surface area of ZnO-PVP-St and adsorption of UV light. It can be concluded that the optimum dosage of ZnO-PVP-St nanoparticles in the MPR for the treatment of industrial dye effluent has a great potential for very low NF membrane contamination [127]. Sakhaie et al. investigated and developed a zirconium-doped titanium dioxide-coated silicon carbide (Zr/TiO_2-SiC) photocatalytic membrane and activated it with an ultraviolet light-emitting diode (UV-LED) to establish the optimum conditions for photocatalytic synthesis and immobilization. The photocatalytic membrane was applied to the degradation of rhodamine B, a typical pollutant in textile wastewater. The design and operating parameters of zirconium molar ratio, photocatalyst loading, and UV-LED irradiance all affected the performance of the photocatalytic membrane. The results showed that zirconium doping increased the photocatalytic activity by more than 20% at an optimal concentration of 10% [128]. Shen et al. designed a continuous-flow fixed-bed photoreactor for the degradation of sodium isobutyl xanthate (SIBX) under visible-light irradiation using a Bi_2WO_6 photocatalyst coated on silica sand. After 30 min of visible light irradiation, the catalyst loading increased from 27.54% to 52.79% as it increased from 30% to 100%. These results indicate that the increase in catalyst loading improved the photodegradation of SIBX. This is due to the utilization of light energy to produce active substances, which are gradually utilized to reach the maximum degradation efficiency after the start of the photoreaction. The increase in catalyst loading leads to an increase in the ratio of [total catalyst surface area]/[SIBX molecules] [83]. Heredia et al. investigated the effect of the thickness of the coated catalysts and proposed a model capable of explaining this effect. Nine photocatalytic nanofiltration ceramic membranes with thicknesses ranging from 0.26 to 21.9 μm were prepared and evaluated. The function of these photocatalytic membranes was experimentally investigated in a one-way dead-end membrane reactor for the decolorization of methylene blue [129]. The obtained surface reaction rate constants indicated that the multilayers provided enhanced reactivity compared to the individual catalytic layers.

The initial and determinative step in a heterogeneous photocatalytic system is the photoexcitation of the catalyst surface, a process fundamentally governed by the quantum efficiency of the incident photons. Consequently, the overall reaction rate is intrinsically dependent on the specific type and concentration of the photocatalyst employed [130]. A significant constraint on the widespread implementation of photocatalytic reactors, particularly PMRs, for wastewater treatment is the requisite availability of large quantities of photocatalyst material and the limited diversity of effective photocatalyst composites [101]. For instance, TiO_2 is the most extensively utilized photocatalyst in slurry PMR systems, a preference attributable to its exceptional photochemical stability in aqueous media, robust catalytic activity, relatively long electron-hole pair lifetime, low cost, and minimal toxicity. A notable limitation of this material, however, is its inactivity under visible light irradiation. Its wide bandgap restricts its absorption profile to the UV portion of the solar spectrum, which constitutes only approximately 5% of the total solar radiation [61]. The efficacy of a photocatalytic process is contingent upon the band gap energy of the semiconductor, which determines its ability to drive chemical reactions. Within this framework, innovative strategies for catalyst modification have been developed to enhance performance. Yin et al. reported a strategy to deposit a Pd-Cu alloy on titanium dioxide bonded to a polyvinylidene difluoride membrane to improve membrane permeability and resistance

to contamination and to achieve a high humic acid (HA) rejection efficiency (100%). Detailed characterization revealed a dual functionality of the PdCu-TiO_2 alloy: it provided paired Pd-Cu sites that facilitated enhanced HA adsorption and electron transfer, thereby improving photocatalytic removal, while simultaneously inducing a photothermal effect via carrier damping that directly augmented the membrane's permeation flux. The remarkable performance of these functionalized membranes validates the significance of the alloying effect for the treatment of aqueous organic pollutants. Notwithstanding these advancements, photocatalyst deactivation remains a critical impediment to the widespread industrial application of photocatalytic degradation technologies. Research on this issue has focused on catalyst lifetime, deactivation mechanisms, and regeneration strategies. In an investigation of the continuous photocatalytic degradation of methyl orange (MO) within a PMR, the lifetime, deactivation causes, and regeneration of Degussa P25 TiO_2 were examined. The study concluded that photocatalyst deactivation had occurred once the concentration of MO in the PMR effluent reached a stable plateau, signifying a cessation of degradation activity [131].

The performance and reaction kinetics of integrated processes, such as CO_2 capture and its subsequent conversion to formic acid, have been evaluated using combined membrane contactor and photocatalytic systems. In such configurations, the rate of CO_2 photoreduction to formic acid was identified as the rate-limiting step, highlighting the necessity for further process optimization [132]. Among the operational variables, the solution pH is a pivotal parameter that profoundly influences photodegradation efficiency. Variations in pH significantly alter the surface charge of the photocatalyst and the speciation of contaminants, thereby governing adsorption behavior and overall degradation performance [83,133]. The pH also affects catalyst aggregation in suspension and the interaction of reactive species with the catalyst surface, making it a decisive factor in process efficiency [31]. Investigations of membrane fouling in PMRs across various pH levels have shown that operation under highly alkaline conditions (e.g., pH = 12) can minimize the membrane contact angle and reduce the deposition of TiO_2 particles [114]. Wang et al. [134] investigated membrane fouling of PMRs at several pH values (3, 6, 9, and 12) and reported that the membranes had the smallest contact angle and the lowest deposition of TiO_2 particles when operated at pH = 12. The effect of pH on fouling is intricate, and the optimal pH must be determined through preliminary studies for specific applications. Generally, alkaline conditions are favored to enhance photocatalytic degradation and optimize the interactions between TiO_2 particles and the membrane. However, the ideal pH is also contingent on the feed composition [33]. When investigating the effect of feed composition and pH on membrane contamination, it was found that the presence of Cl^- and $SO_4{}^{2-}$ ions adversely affected the permeate flux. They also reported that the highest permeate flux was achieved when a near-neutral pH was used [135].

PMRs have become one of the most effective technologies for the treatment of contaminated water. A significant operational constraint, however, is the unilateral irradiation of the membrane, which utilizes only a single side for photo-activation. As shown by Mathieu et al., a reactor was developed where the membrane can be irradiated on both sides to overcome this problem. Polyacrylonitrile membranes incorporating up to 60% TiO_2 nanoparticles were fabricated by electrospinning and subsequently applied in a 3D-printed staggered-flow photocatalytic membrane reactor for the degradation of methylene blue under various light conditions. Utilizing both membrane surfaces substantially enhanced photocatalytic activity, leading to improved decolorization efficiency of methylene blue in water [136]. Further progress was achieved by Le et al., who designed visible light-responsive TiO_2@polydopamine (TiO_2@PDA) core–shell structures for integration into polyvinylidene difluoride (PVDF) membranes. Better dispersion of TiO_2@PDA in mixed-

matrix membranes (MMMs) resulted in higher photodegradation performance compared to surface-coated membranes. At comparable TiO_2 loading (3.5–4.0%), the MMMs degraded 95.1% of the dye, while the surface-coated membrane degraded 89.2%. This performance differential underscores the critical role of intra-pore degradation, which was found to constitute 72% of the total degradation rate in surface-coated membranes and was the predominant mechanism within the MMMs [137].

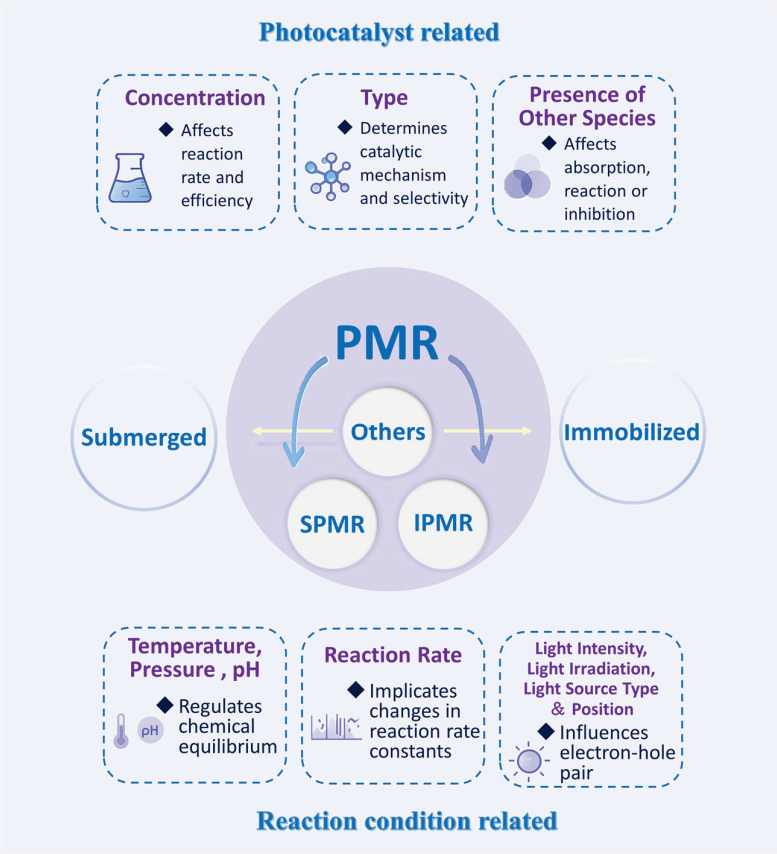


Figure 9. Key parameters influencing the performance of PMR, categorized by photocatalyst properties, operating conditions, and reactor configuration.

Incident light serves as the primary energy input for any photocatalytic reaction, as the absorption of photons is responsible for the generation of electron-hole pairs within the photocatalyst, thereby initiating the degradation process. In a photoreactor, the catalyst must be activated by the incident light [104]. In general, the reaction rate increases with augmenting light intensity until a plateau is reached, whereupon the system becomes limited by mass transmission. The relationship between the reaction rate and light intensity is distinctly non-linear and can be delineated into three regimes. At low light intensities, typically in the range of 0–20 $mW \cdot cm^{-2}$, a first-order relationship is observed where the reaction rate is directly proportional to the intensity. This is attributable to the fact that the generation of electron-hole pairs is the rate-determining step, with recombination being negligible. As the light intensity increases to a moderate level (~25 $mW \cdot cm^{-2}$), the reaction rate becomes a function of the square root of the intensity. This dependency arises from the competitive kinetics between electron-hole pair formation and their recombination. At high light intensities (>25 $mW \cdot cm^{-2}$), the reaction rate becomes independent of this parameter, as the catalyst surface becomes saturated with photons and the overall process is constrained by other factors, such as the rate of mass transmission of the pollutant to the catalyst surface [30,36]. In practical operation, moderate irradiation intensities typically

promote higher pollutant degradation rates while reducing membrane fouling [33], as increased light intensity supports both electron–hole formation and recombination, whereas at low intensities, formation predominates without significant recombination [101]. The effect of light transmission also plays a critical role, since in most photoreactor designs, light must traverse fluids, gases, or transparent walls before reaching the catalyst, with partial absorption occurring along the path [104]. Experimental studies conducted under conditions free from transmission losses have consistently shown that reaction rates follow dependence on light intensity at values exceeding the solar equivalent. Conversely, at sufficiently low intensities (depending on the catalyst), the rate is first order in intensity. Because photon absorption is linear with respect to light intensity, quantum efficiency (molecules converted per absorbed photon) remains constant at low levels but decreases significantly at higher intensities, often to values between 0.7 and 0.5. This decline reflects efficiency loss under strong artificial irradiation or concentrated solar energy. Overall, increasing light intensity enhances volumetric reaction rates until the mass transmission limit becomes the controlling factor [82]. As reported in previous studies, photons with energies equal to or greater than the bandgap energy can be absorbed in the photocatalytic activity, leading to the production of electron-hole pairs. Consequently, the performance of a photocatalytic system is intrinsically linked to the spectral characteristics and intensity of the incident irradiation. For maximal quantum efficiency, a significant overlap between the emission spectrum of the light source and the absorption spectrum of the photocatalyst is required. This principle has driven considerable research into visible-light-responsive photocatalysts, which are of particular interest for developing environmentally sustainable and economically viable PMR systems [138]. Mercury lamps are among the most widely used sources, available in low-pressure and medium-pressure forms. At comparable power levels and without catalyst suspension, LP lamps were shown to induce higher degradation rates of cyclophosphamide than MP lamps, owing to their shorter emission wavelength of approximately 254 nm [139,140]. Upon irradiation, photons with energies greater than or equal to the band gap promote electrons from the valence band to the conduction band, initiating redox reactions through electron–hole pair formation. Since synthesized photocatalysts exhibit varying band gap energies, optimization of the light source is a critical parameter for enhancing performance [101]. Both the type and intensity of irradiation significantly affect photocatalytic efficiency. In multiphase systems, incident photons excite electrons, generating electron–hole pairs and subsequent free radicals [141]. The efficiency of this process depends on the wavelength and intensity of the applied light, while electron–hole generation itself is constrained by the intrinsic band gap of the photocatalyst material. Light introduction into photocatalytic systems typically follows two approaches: external illumination, with lamps positioned on the reactor wall or axis, and internal illumination, where lamps are immersed directly in the reaction medium [71]. Many evidences indicate that the reaction rate constant (k) is related to the illumination intensity (I) and wavelength according to the power law: $k = \kappa I^{\alpha}$, where κ is the irradiance constant and α the exponent. At low intensities ($I < 200\ W \cdot m^{-2}$), the rate constant increases linearly with intensity ($\alpha \approx 1$). In the intermediate range (200–250 $W \cdot m^{-2}$), the dependence weakens ($\alpha \approx 0.5$), while at very high intensities, the reaction rate becomes independent of illumination ($\alpha = 0$). Beyond intensity, the spectral characteristics of the light source are equally critical, as optimal quantum efficiency requires a strong overlap between the emission spectrum of the lamp and the absorption spectrum of the photocatalyst. From a reactor engineering perspective, these principles emphasize the necessity of delivering photons efficiently and uniformly to catalytically active surfaces. This requirement dictates careful consideration of reactor design, particularly light source placement, such as the placement of the light source—either via external illumination or internal immersion within

the fluid, to maximize irradiation efficiency while minimizing scattering and parasitic absorption losses.

The chemical composition of the feedwater matrix is a critical determinant of PMR performance, with various co-solutes exerting either inhibitory or synergistic effects on the degradation process and membrane stability. A key consideration is the nature of the oxidant employed; for instance, peroxymonosulfate (PMS) exists in aqueous solutions as an acidic oxidant in the form of HSO_5^- and SO_5^{2-} ions. To enhance the efficacy of PMR systems, novel catalytic membranes have been developed. In one such study, 5CoMIL-88B(Fe) catalysts were synthesized in situ on an Al_2O^3 carrier, creating a specialized membrane for phenol degradation. A comparative analysis revealed that both the base MRS-MIL-88B(Fe)@Al_2O_3 and the cobalt-doped MRS-5CoMIL-88B(Fe)@Al_2O_3 membranes demonstrated superior phenol removal efficiency under illumination compared to dark conditions, confirming their photo-responsive characteristics. The introduction of PMS into the MRS-5CoMIL-88B(Fe)@Al_2O_3 membrane system further augmented the degradation efficiency. Notably, a direct correlation was observed between increasing PMS concentration and improvements in both degradation rates and permeate flux, indicative of enhanced reactivity. Conversely, the presence of certain inorganic and organic constituents in the feedwater can adversely affect PMR operation [142]. Darowna et al. systematically examined the influence of feedwater composition—specifically the concentration of inorganic anions (SO_4^{2-}, HPO_4^{2-}, HCO_3^-), solution pH, and the presence of humic acids (HAs)—on the fouling behavior and stability of commercial polyethersulfone (PES) ultrafiltration membranes in PMRs. Their findings revealed that elevated concentrations of inorganic anions reduced permeate flux and diminished the photocatalytic degradation efficiency of humic acids, largely as a result of ionic hole and hydroxyl radical scavenging. Conversely, in the absence of inorganic salts, adsorption of HAs onto TiO_2 particles played a significant role in enhancing treatment performance within the PMR system [109]. The presence of inorganic salts in the solution also has an effect on the treatment effect of PMR. A significant decline in membrane flux was observed with increasing NaCl concentration, a phenomenon attributed to ionic strength-dependent conformational changes in HA molecules. At low ionic strengths, HA molecules adopt a more linear structure with pronounced intermolecular repulsion, leading to the formation of a looser deposition layer on the membrane surface and consequently higher permeate flux. Conversely, at high ionic strengths, electrostatic shielding effects diminish both intermolecular repulsion and the electrostatic repulsion between the membrane and HA molecules. This induces a more coiled conformation in the HA molecules, resulting in the formation of a dense cake layer that exacerbates membrane fouling and leads to a more pronounced flux decline [98]. Molinari et al. reported a decrease in the flux of humic acids in a saline solution due to the presence of ROS in the oxidizing environment. However, it is crucial to note that configurations employing photocatalysts immobilized directly on the membrane surface can render the polymer susceptible to photodegradation, as the membrane itself is directly irradiated to facilitate contaminant degradation on its surface or within its pores. Beyond their role in fouling, co-solutes can also modulate the efficiency of target pollutant degradation [143]. Petsi et al. investigated the reduction of nitrate in a photocatalytic membrane reactor in the presence of organic acids. A systematic study was carried out in a laboratory pilot PMR using a hybrid TiO_2/UV-A catalytic-ultrafiltration process using formic acid as the most favorable cavity scavenger for nitrate reduction, and the results showed the superior performance of formic acid in nitrate reduction [144]. Peñas-Garzón et al. conducted a comprehensive evaluation of graphitic carbon nitride immobilized on polymeric membranes (CN/F) within a continuous-flow planar reactor for the removal

of pharmaceutical mixtures, including venlafaxine, citalopram, carbamazepine, tramadol, ketoprofen, and diclofenac (3 μM each) [145].

The integration of novel photocatalytic materials with innovative reactor configurations is a promising strategy for enhancing PMR performance. When incorporated into a specially designed slant plate photocatalytic reactor, this system demonstrated the rapid and effective degradation of Rhodamine B from simulated wastewater, while also facilitating the efficient, loss-free recovery of the photocatalyst [146]. The development of bifunctional composite membranes, capable of concurrent physical separation and chemical degradation, represents a significant advancement in membrane science. These membranes are capable of simultaneously achieving efficient oil-in-water emulsion separation and photocatalytic degradation of organic dyes in wastewater. To enhance degradation capacity without compromising separation efficiency, strategies combining photocatalytic active nanoparticles with hydrophilic membrane matrices have been widely adopted in water treatment research [147]. Li et al. prepared a bifunctional separation membrane through PVDF/PEMA electrospinning followed by in situ deposition of anatase TiO_2 nanoparticles containing Ti^{3+} sites and oxygen vacancies. The resulting composite membranes exhibited superior hydrophilicity (WCA = 15.65°), strong underwater oleophobicity (UOCA = 156.69°), and excellent photocatalytic activity [148]. Furthermore, the reactor configuration itself is a critical determinant of performance. Yang et al. developed three flat-plate immobilized PMRs based on Bi_2WO_6-g-C_3N_4/PVDF photocatalytic membranes and evaluated their performance in atrazine (ATZ) removal under simulated sunlight. The vertical PMR configuration achieved 78.98% degradation of ATZ within 6 h and maintained stable removal efficiency (~65%) under continuous-flow operation for 18 h [149].

4. Advances of PMRs in Different Applications

PMRs have been instrumental in various areas of environmental remediation, playing a significant role in the green energy transition, carbon neutrality, and the development of a circular economy. Current research focuses primarily on high-efficiency, laboratory-scale applications. Innovations in nanomaterials and membrane architectures have achieved impressive pollutant degradation and conversion efficiencies under highly optimized, albeit energy-intensive, conditions. However, translating these promising laboratory results to industrial-scale applications remains a daunting challenge, requiring overcoming key hurdles such as designing efficient large-scale illumination systems, in-depth integration and optimization of reaction kinetic models, mitigating persistent membrane fouling, and establishing stable, cost-effective operation. Premature scale-up, prioritizing cost reduction at the expense of catalytic efficiency, can lead to degraded system performance and inefficient energy utilization. Therefore, the future direction of PMR technology is to achieve the ideal of high performance at an industrial scale, a goal that requires a shift from simple pollutant removal to more complex functional models. A comprehensive four-quadrant overview of PMR development, as depicted in Figure 10, offers an in-depth comparative analysis of various PMR types based on existing applications. This comprehensive summary, based on existing applications, provides an in-depth comparative analysis of the various types of PMRs within each category, summarizing representative research and applicable scenarios, and guides the selecting of the appropriate PMR type. These advanced applications include leveraging the membrane's selective separation capabilities to guide reactions to valuable products, integrating PMRs with processes such as adsorption or biological treatment to create synergistic hybrid systems, and facilitating the recovery of valuable resources from wastewater streams. Achieving this vision relies on key engineering and design innovations, such as the adoption of modular reactor

configurations for enhanced scalability, the implementation of AI-driven operational control optimization, and the development of coupled photoelectrochemical systems. Ultimately, the successful deployment of PMRs in environmental remediation requires bridging the gap between laboratory feasibility and industrial practicality, supported by rigorous techno-economic evaluations and a sustained focus on maximizing energy efficiency and process robustness.

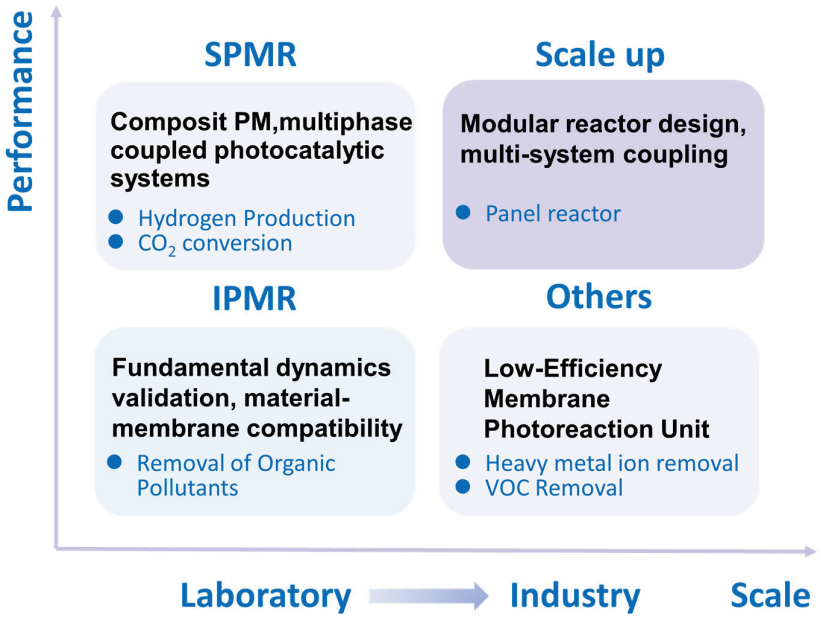


Figure 10. Four-quadrant diagram for PMR Research.

4.1. Photocatalytic Water Splitting to Produce Hydrogen

As a green, clean, and highly efficient advanced oxidation technology, photocatalysis shows great potential for photocatalytic hydrogen production in water. A variety of innovative strategies, including nanostructure control, doping, co-catalyst integration, and bandgap and defect engineering, have been proposed to enhance photocatalyst performance. Nevertheless, significant challenges persist in photocatalytic hydrogen production, notably charge recombination, limited light absorption, and insufficient catalyst stability, which currently impede large-scale implementation. Therefore, reactor design is crucial for scaling up photocatalytic hydrogen production. The development of photocatalytic reactors for hydrogen evolution has garnered considerable attention, primarily due to their potential for efficient solar energy utilization, which balances material use, light capture, and reaction efficiency, thereby offering a pathway to reduce hydrogen production costs. PMRs have emerged as a particularly effective technology for sustainable hydrogen production. By inhibiting the deleterious back-reaction between H_2 and O_2, PMRs facilitate the generation of pure hydrogen in a single step, obviating the need for downstream purification processes. Foundational work in this area demonstrated a TiO_2-Nafion-Pt based membrane system (Figure 11a) where, under UV irradiation and without an external bias, methanol oxidation on the TiO_2 side drives proton transport across the Nafion membrane for subsequent reduction to H_2 on a Pt surface, achieving a hydrogen production rate of up to 69 $\mu L\ h^{-1}\ cm^{-2}$ [150]. Building upon this principle, subsequent research has focused on enhancing system stability and efficiency. Building on this, Tsydenov et al. proposed an innovative approach by modifying porous polymer membranes with Pt and TiO_2 for hydrogen production through ethanol dehydrogenation. This system not only exhibited excellent physicochemical stability under illumination but also incorporated PTFE filters with polypropylene modifications to improve mechanical robustness, thereby enhancing

the durability and practical viability of PMRs for hydrogen production [151,152]. Further advancing the field, a sophisticated dual-fiber optic setup has been introduced, integrating LED light sources with optical fibers coated with a Metal–Organic Framework (MOF) catalyst (Figure 11b), specifically POF-MIL-101(Fe). This advanced configuration, coupled with a re-oxygenated hollow membrane fiber, was engineered not only for efficient H_2 evolution but also for the simultaneous, high-yield production of hydrogen peroxide, showcasing a significant progression toward multi-functional photoreactor systems where performance is optimized through sophisticated light delivery and catalyst integration [153].

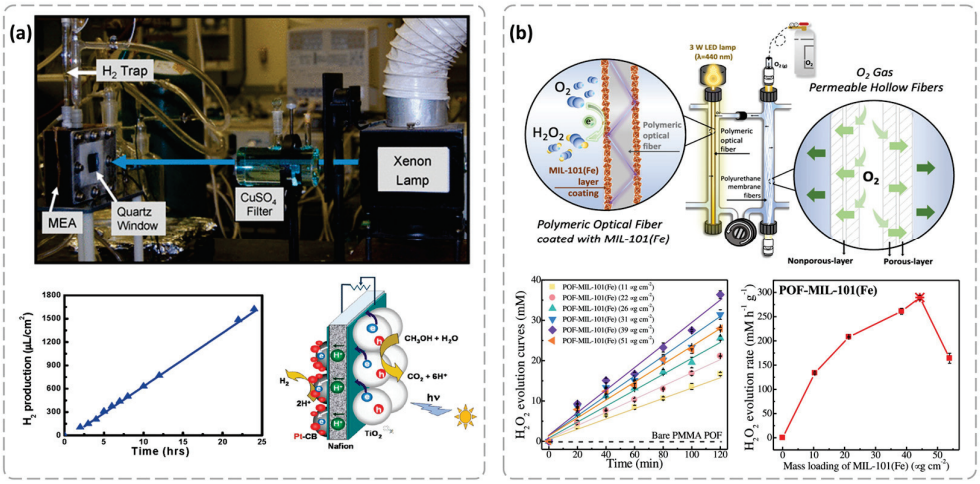


Figure 11. Advances in PMRs in hydrogen production: (**a**) photoelectrocatalysis cell setup and performance in producing hydrogen. Reprinted with permission from Ref. [150]. Copyright (2009), American Chemical Society. (**b**) Schematic illustration of photocatalytic H_2O_2 production in a dual-fiber system and H_2O_2 evolution and evolution rates. Reprinted with permission from Ref. [153]. Copyright (2023), American Chemical Society.

While the immense terrestrial solar flux presents a compelling resource for sustainable hydrogen production, a conspicuous disparity persists between laboratory-scale potential and tangible, large-scale implementation [154]. Historically, the research impetus in photocatalytic overall water splitting (POWS) has been overwhelmingly directed toward the synthesis of novel materials to overcome quantum efficiency limitations, a strategy justified when solar-to-hydrogen (STH) efficiencies remained well below the benchmark for commercial viability. However, the recent advent of photocatalysts achieving STH efficiencies approaching the 10% threshold signals a critical inflection point [155]. This progress indicates that the primary impediment to practical deployment is no longer solely the intrinsic activity of the photocatalyst, but rather the absence of sophisticated reactor engineering, mandating a paradigm shift in research priorities. The critical challenge now resides in translating high-efficiency materials into functional systems, a goal for which the holistic design of PMRs is paramount [156]. Future efforts must therefore prioritize the engineering of these integrated systems, where photon management, mass transport, and in situ product separation are co-optimized to bridge the gap between fundamental material discovery and industrial-scale solar hydrogen production.

Progress in solar hydrogen production is marked by the successful translation of nanoscale photocatalytic principles into progressively larger and more robust reactor systems. At the laboratory scale, performance is enhanced through the engineering of composite nanoreactors that exploit localized photothermal effects; silver sulfide quantum dots on carbon nitride nanovesicles, for example, create thermal hotspots that accelerate reaction kinetics. A critical step towards scalable architectures is demonstrated by hydrogen-bonded organic frameworks (HOFs), where engineering micropore-confined

exciton transfer has led to exceptional apparent quantum yields (>25%) [157]. This principle has been successfully embodied in a 0.5 m^2 flexible panel reactor, achieving a notable hydrogen productivity of over one mole per square meter per day [44]. The ultimate validation of this technology's potential resides in meter-scale demonstrations under real-world conditions, where a panel reactor utilizing immobilized mesoporous carbon nitride has proven its long-term viability by maintaining stable operation over one month under natural sunlight, reaching a maximum solar-to-hydrogen conversion of 0.12% [158]. This developmental trajectory—from engineering nanoscale thermal effects to achieving meter-scale operational stability—delineates a viable pathway for translating fundamental photocatalyst design into practical solar hydrogen technologies. As a clean and efficient advanced oxidation process, photocatalysis holds significant promise for hydrogen production from water. To enhance photocatalyst performance, strategies such as nanostructure engineering, elemental doping, co-catalyst integration, and bandgap or defect engineering have been extensively explored. Despite these advances, key limitations persist, including rapid charge recombination, restricted light absorption, and insufficient catalyst stability. Overcoming these challenges is essential for translating photocatalytic hydrogen production into large-scale sustainable energy systems.

4.2. Removal of Organic Pollutants from Water

Advanced oxidation process (AOP), represented by photocatalysis, has been considered as an effective approach for the removal and degradation of a broad spectrum of non-biodegradable organic pollutants in water bodies [159] (Figure 12a). It has been popularized for its mild reaction conditions, absence of secondary pollution, and low operational cost. However, a significant challenge remains in the separation and recovery of catalysts, especially in large-scale water treatment applications. The photocatalytic membrane reactor, which combines photocatalysis and membrane separation processes, can effectively solve this problem and has been applied to the removal of organic pollutants in water many times. Zhang et al. utilized TiO_2 as a photocatalyst and ultraviolet (UV) light as the irradiation source to treat wastewater contaminated with the azo dye Acid Red B in a slurry photocatalytic membrane reactor (Figure 12b). The reactor design included a dual-layer cylindrical photocatalytic reaction zone and a plate-and-frame membrane separation section. The study demonstrated that the combined photocatalytic and ultrafiltration processes effectively degraded Acid Red B from textile wastewater, highlighting the potential of this system for treating azo dye-contaminated wastewater [160]. To overcome the energy cost limitations associated with UV-dependent systems, subsequent research has shifted focus toward visible-light-driven photocatalysis. Building on this, Nur et al. shifted the focus towards visible light photocatalysis by incorporating ZnO nanoparticles in an MPR (Figure 12c) to treat Congo Red dye, enhancing the treatment capability and addressing membrane fouling, thus offering an improvement over UV-dependent systems by potentially using a broader light spectrum. The results indicated that the optimal dosage of ZnO-PVP-St nanoparticles significantly enhanced the MPR's capability to treat industrial dye wastewater while minimizing fouling of the nanofiltration (NF) membranes. The ZnO-PVP-St nanoparticle formulation enhanced pollutant removal efficiency while mitigating nanofiltration membrane fouling, thereby improving performance compared with UV-dependent systems [127].

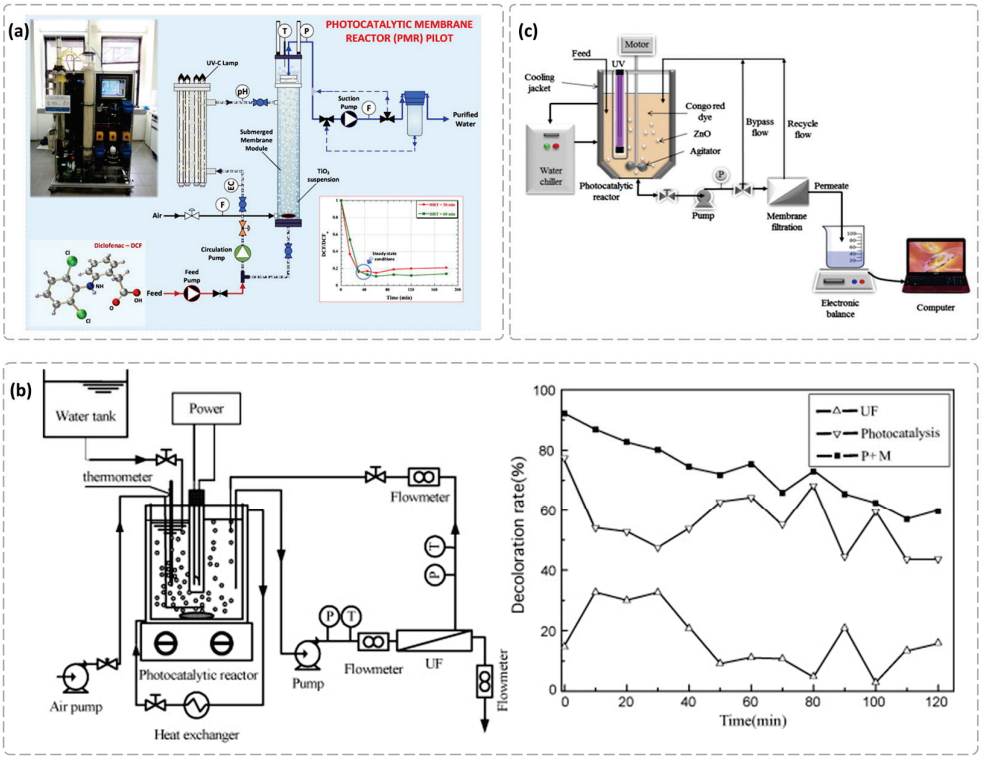


Figure 12. Advances in PMRs in removal of organic pollutants from water: (**a**) A Novel pilot-scale continuous photocatalytic membrane reactor. Reprinted with permission from Ref. [159]. Copyright (2015), Elsevier. (**b**) Schematic diagram of the experiment and contribution of different parts in the photocatalytic membrane reactor. Reprinted with permission from Ref. [160]. Copyright (2010), Elsevier. (**c**) Schematic diagram of the laboratory-scale MPR. Reprinted with permission from Ref. [127]. Copyright (2014), Elsevier.

Hu et al. further expanded the scope of PMR applications by evaluating an Al_2O_3 hollow fiber membrane photoreactor (Figure 13a) for the degradation of mixed pollutants, including methylene blue (MB), methyl orange, and phenol. The Al_2O_3 substrate exhibited high thermal and chemical stability, making it suitable for photocatalyst deposition and advanced hollow fiber membrane reactor design [161]. In pursuit of more sustainable materials, Hu et al. also reported a metal-free photocatalyst, phosphorus-doped g-C_3N_4 (PCN), coated on Al_2O_3 hollow fiber membranes. This visible-light-driven PMR achieved efficient and stable removal of MB, methyl orange, phenolic compounds, and their mixtures [162]. Catalyst modification has also been explored to enhance performance under simulated solar irradiation. Ashar et al. developed PMRs by growing undoped and Fe^{3+}-doped ZnO nanoparticles on polyester fabrics using a low-temperature hydrothermal method. The ZnO/PMR and Fe^{3+}@ZnO/PMR achieved maximum degradation rates of 88.89% and 98.34%, respectively, for the reactive dye RB5 under simulated sunlight (D65, 72 W) irradiation within 180 min (Figure 13b). Subsequent experiments revealed that the photocatalytic efficiency of the Fe^{3+}@ZnO/PMR slightly decreased after eight cycles of continuous operation [163]. Concurrently, efforts to mitigate membrane fouling have led to the development of photocatalytic membranes (PMs) with anti-fouling properties. Sahar et al. developed a photocatalytic membrane (PM) by coating a silicon carbide membrane with a Zr/TiO_2 sol. The degradation performance of various concentrations of humic acids was evaluated under UV irradiation (275 nm and 365 nm). The results demonstrated that the PM effectively reduced fouling formation while efficiently degrading humic acids, thus mitigating the loss of membrane permeability [128].

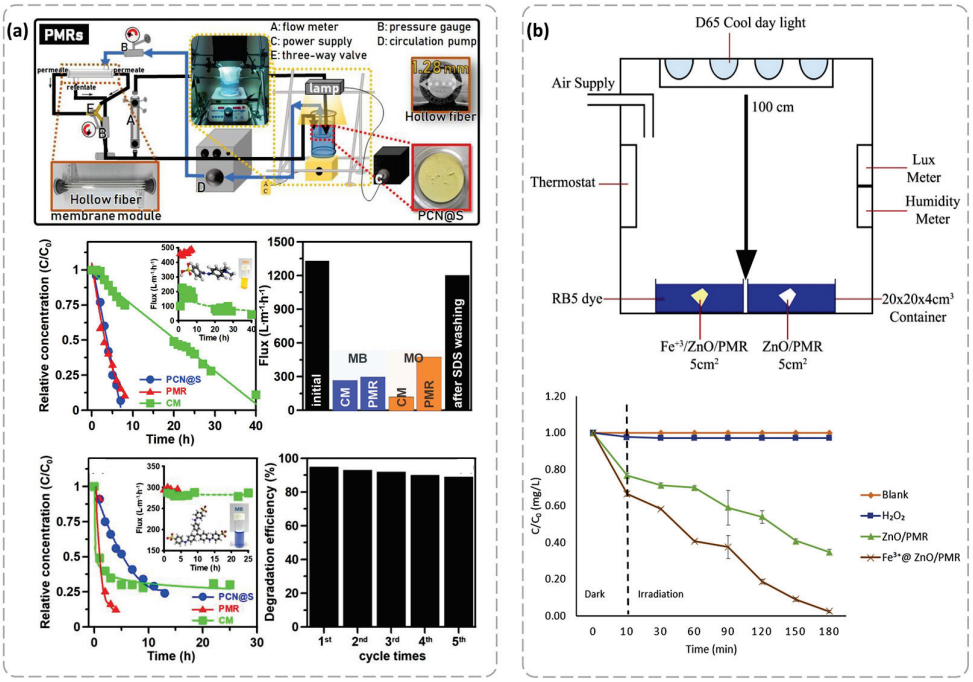


Figure 13. Advances in PMRs in removal of organic pollutants from water: (**a**) Schematic diagram of the PMR system integrated with inorganic Al_2O_3 hollow fiber membrane module and PCN@S and MB degradation and reusability test. Reprinted with permission from Ref. [161]. Copyright (2019), Elsevier. (**b**) Determination of the extent of photocatalytic degradation (C/C_0) of RB5 using ZnO/PMR and Fe^{3+}@ ZnO/PMR with respect to time. Reprinted with permission from Ref. [163]. Copyright (2020), Elsevier.

4.3. Heavy Metal Ion Removal

Typical industrial methods employed in conventional heavy metal-containing wastewater treatment, including adsorption, chemical precipitation, ion exchange, ozonation, biological methods, and activated carbon electrochemical methods, often struggle to effectively reduce metal concentrations in water to levels that meet regulatory standards. Photocatalysis has emerged as a promising alternative for heavy metal remediation [164], primarily owing to its high versatility and the ability to convert toxic, high-valence heavy metal ions into their less toxic, low-valence counterparts [165]. The primary mechanisms governing the photocatalytic removal of heavy metal ions include the direct reduction of metal ions by photogenerated electrons from the conduction band and the indirect reduction of highly oxidized metal species by photogenerated intermediates. For direct photocatalytic reduction to be thermodynamically feasible, the conduction band energy level of the semiconductor must be more negative than the reduction potential of the target metal ion couple (M^{n+}/M). Innovations in membrane technologies, such as those based on nanoparticles, carbon nanotubes, or graphene, have demonstrated significant potential for heavy metal ion removal due to properties like high water permeability [166]. Recent innovations in membrane technologies incorporating nanoparticles, carbon nanotubes, and graphene have demonstrated notable potential for heavy metal ion removal due to their high water permeability and functional versatility. However, only nanocomposite membranes have been scaled up and commercialized for heavy metal ion removal [167], while other membranes are still in the basic research and development stage [168]. An advanced strategy for wastewater treatment is the integration of photocatalysis with membrane filtration, forming PMRs. In this configuration, the membrane functions as a selective barrier, while the immobilized photocatalyst provides active sites for contaminant degradation or reduction. This dual action not only enhances pollutant removal but also mitigates

membrane fouling, a major operational limitation. For example, Silva et al. reported that a recycled reverse osmosis membrane modified with a graphene oxide–titanium dioxide (GO–TiO_2) nanocomposite effectively polished petroleum refinery effluent. Under UV irradiation, the membrane exhibited self-cleaning behavior, reducing flux decline by degrading surface foulants while simultaneously improving the removal of organic pollutants (Figure 14a). The underlying mechanism—the generation of reactive photogenerated electrons at the membrane surface—can also be applied to heavy metal remediation. These electrons enable the reduction of toxic high-valence metal ions to less harmful lower-valence states. Thus, PMRs offer a promising route to achieve efficient heavy metal removal while maintaining membrane performance through photocatalytic self-cleaning [169]. Building on this foundation, as shown in Figure 14b, Rathna et al. advanced the concept by synthesizing TiO_2-WO_3 nanoparticles through hydrothermal methods and integrating them into polyaniline (PANI) membranes for chromium (VI) removal from aqueous solutions (Figure 14b). They varied the concentration of the photocatalyst within the membrane, which not only enhanced the photocatalytic activity under visible light but also introduced a self-cleaning mechanism due to the combined photoanode and cathode system within the membrane. This approach not only demonstrates a step towards multifunctional membranes that can both degrade and reduce heavy metals but also shows the versatility of PMRs in handling different forms of pollutants in various media, from gas to liquid. These studies collectively illustrate a clear technological progression from foundational, gas-phase applications to more sophisticated, multifunctional liquid-phase systems that employ advanced composite materials, thereby significantly broadening the scope of PMR technology for heavy metal remediation [170].

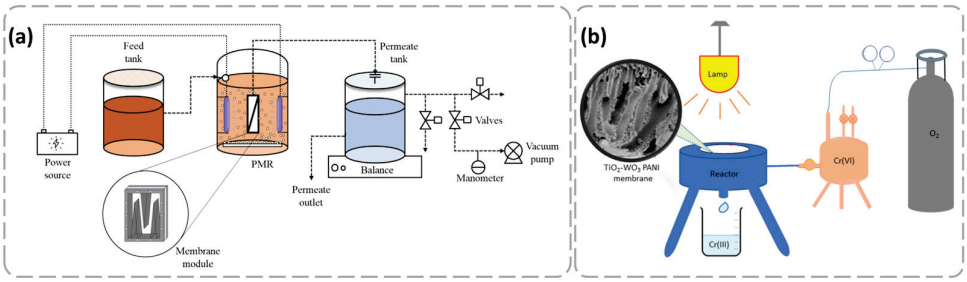


Figure 14. Advances in PMRs in heavy metal ion removal: (**a**) The experimental schematic of a wet photocatalytic membrane bioreactor. Reprinted with permission from Ref. [169]. Copyright (2025), Elsevier. (**b**) Fabrication of visible-light-assisted TiO_2-WO_3-PANI membrane for effective reduction of chromium (VI) in photocatalytic membrane reactor. Reprinted with permission from Ref. [170]. Copyright (2021), American Chemical Society.

4.4. CO_2 Reduction

The capture and subsequent utilization of carbon dioxide (CO_2) are now recognized as crucial strategies for advancing sustainable development [171]. Within this context, photocatalytic processes represent a promising technology for the reduction of CO_2 emissions and the concurrent production of energy-containing compounds [172]. Membrane reactor technology, in particular, offers a viable solution for the integrated capture and conversion of CO_2 into valuable products, with PMRs being especially well-suited for this application [173]. While PMRs can maintain high product yields and selectivity by controlling reaction pathways and preventing reverse reactions, their efficiency has historically been constrained by limitations in electron and proton mobility, as well as by mass transmission issues. The enhancement of proton transport and mass transmission is therefore critical to realizing the full potential of membrane reactors for the photocatalytic conversion of CO_2 into fuels. Initial investigations into this application, such as the work by Sellaro et al.,

demonstrated the fundamental feasibility of using TiO_2-Nafion composite membranes for the continuous conversion of CO_2 to methanol. Building upon this, Brunetti et al. developed more advanced membranes incorporating a C_3N_4-TiO_2 heterojunction photocatalyst, which exhibited enhanced efficiency for CO_2 reduction. However, Brunetti et al. took this further by exploring coupled reactions, embedding a C_3N_4-TiO_2 photocatalyst in a dense Nafion matrix, showcasing high efficiency in continuous CO_2 reduction to methanol, thus expanding on the initial idea of membrane-catalyzed CO_2 conversion [129]. They designed a dual-function Janus membrane, integrating a CO_2 concentration layer (gas separation) and a photocatalytic reaction layer. This membrane demonstrated the ability to directly convert trace CO_2 from air into CH_4. The structure of the gas separation layer and the CO_2 conversion efficiency were optimized by incorporating amine-functionalized graphene oxide, while graphene was introduced into the photocatalytic reaction layer to effectively inhibit electron-hole recombination and enhance the likelihood of excited electron collisions with CO_2 [129]. Building upon these foundational studies, Cheng et al. introduced a novel approach with a photofluidic membrane microreactor. This system leverages photofluidic technology to enhance photon and mass transport, coated with TiO_2 on carbon paper treated with PTFE for hydrophobicity. Their reactor achieved an unprecedented methanol production rate from CO_2 reduction, establishing a new benchmark in yield and efficiency, demonstrating a significant leap in reactor design for CO_2 photocatalytic conversion. The performance of the membrane was evaluated in terms of its ability to reduce CO_2, yielding a maximum methanol production of 111.0 mmol/g-cat/h at a flow rate of 25 mL/min and a light intensity of 8 mW/cm^2. This result represents the highest reported yield to date, demonstrating the effectiveness and superiority of the proposed photofluidic membrane microreactor for CO_2 photocatalytic reduction (Figure 15a) [174]. Liu et al. approached the challenge from a different angle by focusing on CO_2 separation alongside conversion. They synthesized branched polyethyleneimine (PEI)-functionalized UiO-66 for mixed matrix membranes (MMMs), which not only separated CO_2 from CH_4 but also facilitated CO_2 conversion through reversible amine reactions, achieving high selectivity and permeability, thus broadening the application scope of PMRs to include both separation and conversion processes. The UiO-66-PEI MMMs exhibited optimal performance at a filler concentration of 15 wt%, achieving a CO_2 permeability of 28.23 Barrer and a high CO_2/CH_4 selectivity of 56.49% [175] (Figure 15b). Saleh et al. addressed the challenge of CO_2 conversion by immobilizing TiO_2 photocatalysts on PTFE membranes (Figure 15c) to enhance stability and reusability. The PTFE membrane surface was modified through defluorination and grafting with carboxylic acid, achieving a high grafting degree of 8.5% using 30 wt% acetic acid. TiO_2 was successfully immobilized (11.32 wt%), confirmed by FESEM-EDX and TGA [173]. Although leaching tests showed 59% TiO_2 loss after 4 days, the membrane demonstrated good reusability over 5 cycles. The photocatalytic CO_2 reduction in a rich amine medium produced methanol, albeit at a lower yield (7 μmol/g·h) compared to slurry systems (134.5 μmol/g·h), attributed to reduced surface area and light exposure. This study highlights the potential of immobilized systems for sustainable CO_2 conversion while addressing catalyst recovery challenges. Taken together, this body of research illustrates a clear and progressive evolution of PMR technology for CO_2 conversion, from foundational proof-of-concept studies to the development of highly sophisticated, multifunctional reactor systems.

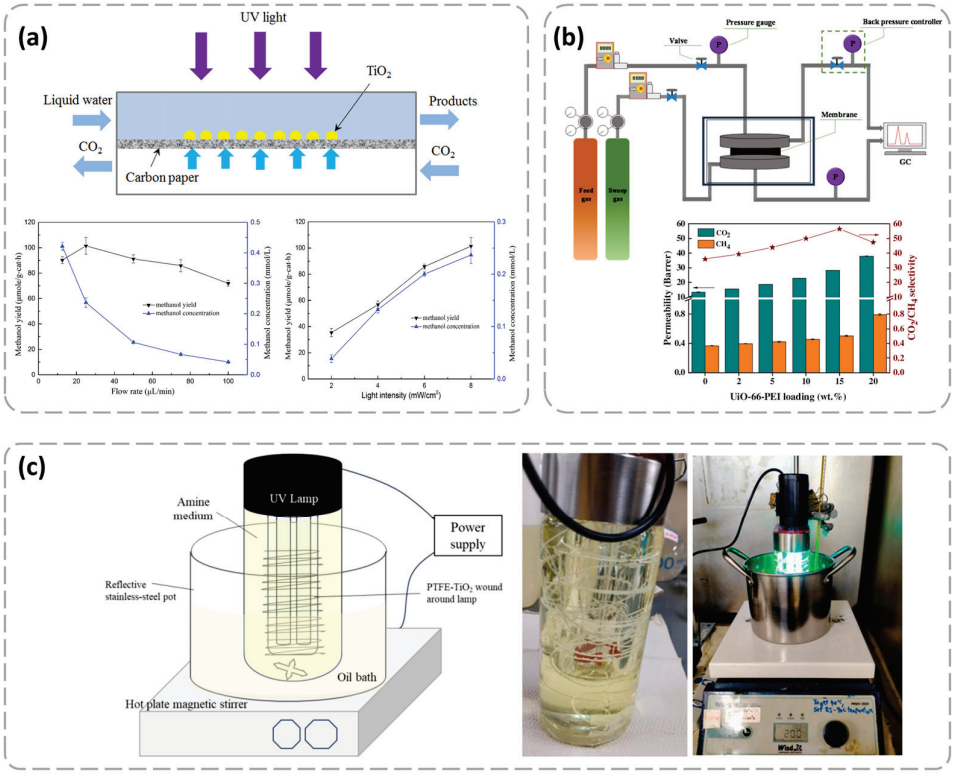


Figure 15. Advances in PMRs in CO_2 reduction: (**a**) Schematic of the optofluidic membrane microreactor for photocatalytic reduction of CO_2. Effect of the liquid water flow rate and light intensity on the methanol concentration and yield. Reprinted with permission from Ref. [174]. Copyright (2016), Elsevier. (**b**) CO_2 breakthrough curves of the 30PEI-UiO-66 at five consecutive CO_2 adsorption–desorption cycles and gas permeability and CO_2/CH_4 selectivity of MMMs with different UiO-66-PEI loadings. MMM, mixed-matrix membrane; PEI, polyethyleneimine. Reprinted with permission from Ref. [175]. Copyright (2020), Wiley. (**c**) Schematic diagram of the batch reactor setup for photocatalytic CO_2 reduction wherein TiO_2-immobilized PTFE membranes were wound around the UVC light source. The batch reactor filled with CO_2–rich amine medium, and the UVC light source switched on to test the photocatalyst performance for CO_2 reduction in the amine. Reprinted with permission from Ref. [173]. Copyright (2024), Elsevier.

4.5. VOC Removal

With the great progress in photocatalytic materials, photocatalytic reactor design has a broad prospect and urgency [176]. The use of PMRs for the treatment of volatile organic compounds (VOCs) has become a promising measure due to their high efficiency, sustainability, and flexible operation. By combining selective membrane separation with photocatalytic oxidation, PMRs can achieve the complete mineralization of a wide range of VOCs to CO_2 and H_2O, thereby minimizing the formation of hazardous byproducts and the risk of secondary pollution. A distinct advantage of this technology is its ability to operate at ambient temperature and pressure, which confers a significant energy-saving benefit over conventional, high-temperature abatement methods such as thermal or catalytic combustion. The photocatalytic membrane reactor can be operated at ambient temperature and pressure, offering significant energy-saving advantages over other energy-intensive thermal decomposition or catalytic combustion technologies. In addition, its modular design is easy to expand and can be adapted to different waste gas treatment needs. The treatment of low concentration VOCs is usually a difficult issue in environmental engineering, while the photocatalytic membrane reactor can maintain good degradation performance at low VOC concentrations through the selective separation of the membrane and the high activity of photocatalysis [177]. A particularly promising strategy for the

treatment of low-concentration VOCs, a persistent challenge in environmental engineering, is the coupling of photocatalysis with dense, selective polymer membranes. Toshinori et al. laid the groundwork by synthesizing porous titanium dioxide (TiO_2) membranes via the sol–gel method, with pore sizes tailored for the effective degradation of methanol and ethanol. Their setup allowed for unidirectional flow through the membrane, where oxidation occurred both on the surface and within the pores, achieving near-complete oxidation of methanol at high concentrations. The oxidation reactions occurred both on the TiO_2 membrane surface and within its pores, while the reactants flowed unidirectionally through the membrane. The Pt-modified TiO_2 membrane demonstrated near-complete oxidation of methanol, even at concentrations up to 10,000 ppm, with a feed flow rate of 500×10^{-6} m^3/min [68]. However, this approach primarily focused on the membrane's physical structure and catalyst placement. Further pushing the boundaries, Khalilzadeh et al. employed a jet reactor system with modified TiO_2 nanoparticles, which demonstrated high efficiency in VOC removal (Figure 16a) [178]. This method shifted from static membrane systems to a dynamic one, suggesting improvements in mass transmission and catalytic exposure, thus enhancing the removal efficiency. Lastly, Favre et al. explored an integration of dense polymer membranes with photocatalytic processes by placing the catalyst within the permeation chamber, aiming at low-concentration VOC removal, like n-hexane from air. Their configuration not only improved the membrane's separation efficiency but also achieved complete mineralization of hexane under UV-A light, illustrating a significant step forward in combining photocatalysis with membrane technology for trace contaminant removal (Figure 16b). Experimental results demonstrated that the coupled device significantly enhanced membrane separation efficiency for hexane concentrations as low as 1 ppm. Moreover, complete mineralization of hexane was achieved under various UV-A light irradiation conditions (W/m^2) [179]. Together, these studies illustrate a progression from basic catalyst-membrane interaction, through the enhancement of photocatalytic activity with novel materials, to dynamic reactor designs, and finally to sophisticated integration of photocatalysis with dense membrane systems for low-level contaminant removal, each study adding layers of complexity and efficiency to the application of PMRs in VOC abatement.

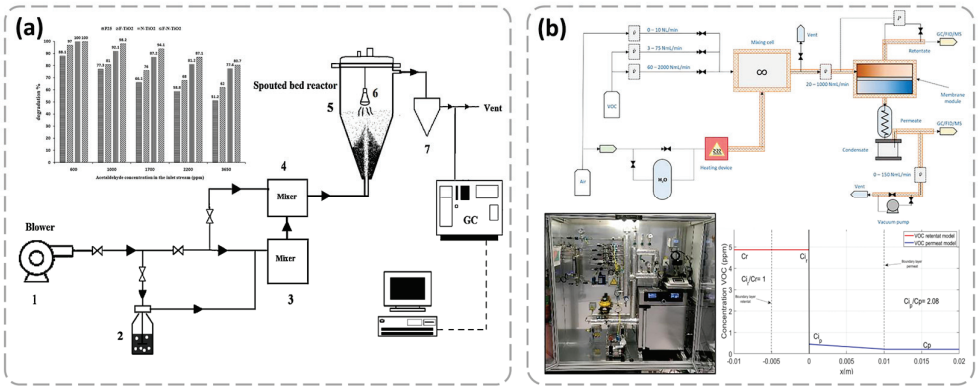


Figure 16. Advances in PMRs in VOC removal: (**a**) Experimental setup for photocatalytic oxidation and photocatalytic activity of different samples in a spouted bed reactor under 80 W Hg light. Reprinted with permission from Ref. [178]. Copyright (2016), Elsevier. (**b**) Experimental gas permeation setup. Reprinted with permission from Ref. [179]. Copyright (2021), Elsevier.

4.6. Amplification of Photocatalytic Reactors

The scaling-up of photocatalytic reactors represents a technically and economically viable process [180]. To facilitate the transition of PMRs from laboratory-scale research to industrial applications, the development and utilization of scale-up strategies are essen-

tial. Investigating the changes in reaction kinetics during the transition from small-scale experiments to industrial-scale systems is critical. This process necessitates a comprehensive understanding of how key performance-determining factors, such as hydrodynamic regimes, mass transmission phenomena, and the distribution of the radiation field, evolve with increasing reactor size and complexity. The primary objective of reactor scale-up is the design of amplified photoreactors that can process large volumetric flow rates while maintaining high energy efficiency and catalytic performance. A significant challenge in this endeavor is the issue of low solar energy utilization in many photocatalytic systems. Amplified photocatalytic reactors play a crucial role in translating laboratory-scale photocatalytic reactions into industrial applications. These reactors improve the efficiency of light energy utilization and accelerate reaction rates by optimizing key parameters, including light source, reactor design, catalyst support, and fluid dynamics [70]. The primary advantages of amplified photoreactors lie in their ability to maximize light energy utilization, streamline operation, and reduce costs, making them highly applicable in areas such as environmental remediation, energy conversion, and hazardous substance treatment. In recent years, the integration of amplified photocatalytic reactors into PMRs has gained significant attention, particularly in the context of sustainable development goals. The introduction of amplified photoreactors in the design of PMRs offers substantial benefits. By immobilizing catalysts on membrane materials and optimizing light sources, photocatalytic efficiency can be significantly enhanced, particularly for the treatment of high pollutant concentrations or large-scale water treatment applications [181]. Unlike conventional photoreactors, which often face challenges such as uneven light distribution, oversized reactor volumes, and inconsistent catalyst distribution, amplified photoreactors address these limitations through a systematic design approach. These improvements enable the treatment of larger wastewater or gas flows without compromising efficiency. In the pursuit of enhancing photocatalytic efficiency and scalability, several innovative approaches have been explored for PMRs. Starting with the fundamental challenge of low energy utilization in solar-driven photocatalysis, Dittmeyer et al. at Karlsruhe Institute of Technology developed a cost-effective, highly efficient, and easily manufacturable panel-type photochemical reactor (Figure 17a). This reactor addresses the issues of low photocatalytic efficiency (typically around 1% energy utilization) and high costs through its simplicity, mass production potential using polymers, and adaptability to various photocatalysts [182]. Building on this foundation, Yoon's group at the Korea Institute of Energy Research took a step further by comparing rotary and flat-type photoreactors for treating emerging contaminants in water under UV or solar irradiation. Their studies demonstrated significant improvements in solar-driven photocatalytic efficiency by optimizing reactor geometry and light source configurations, tackling the challenges of photocatalyst recovery and low photon utilization (Figure 17b) [183]. Advancing the design complexity, Spasiano et al. conducted comparative analyses of different photoreactor types, including parabolic trough collectors (PTCs), non-concentrating collectors (NCCs), and compound parabolic collectors (CPCs) [184]. His findings suggest that by rationally designing the light distribution and hydrodynamic parameters, photocatalytic performance can be significantly enhanced, which is crucial for scaling up PMRs for both environmental remediation and improving catalyst recovery and reactor stability [58]. Pushing the boundaries of reactor design, Hyeon's research team at the Center for Nanoparticle Research, Institute for Basic Science (IBS) in Seoul, Korea, proposed a novel floating photocatalytic platform based on a porous elastomer-hydrogel nanocomposite [185]. This platform, which operates at the air-water interface, offers advantages like efficient light transmission, ease of gas separation, and reduced hydrogen oxidation, making it particularly scalable for photocatalytic applications [186]. To bridge the gap between laboratory-scale materials

and industrial applications, a highly photostable organic-inorganic membrane catalyst has been engineered to address key challenges in scaling up solar fuel production. This robust design integrates CdS@SiO_2-Pt composites into durable PVDF membranes, demonstrating exceptional recyclability and achieving 0.68% efficiency in solar-to-hydrogen conversion (Figure 17c). This successful transition from novel materials to larger integrated panel-scale H_2O to H_2 conversion systems provides a viable pathway for the scalable implementation of photocatalytic membrane reactor technology [187].

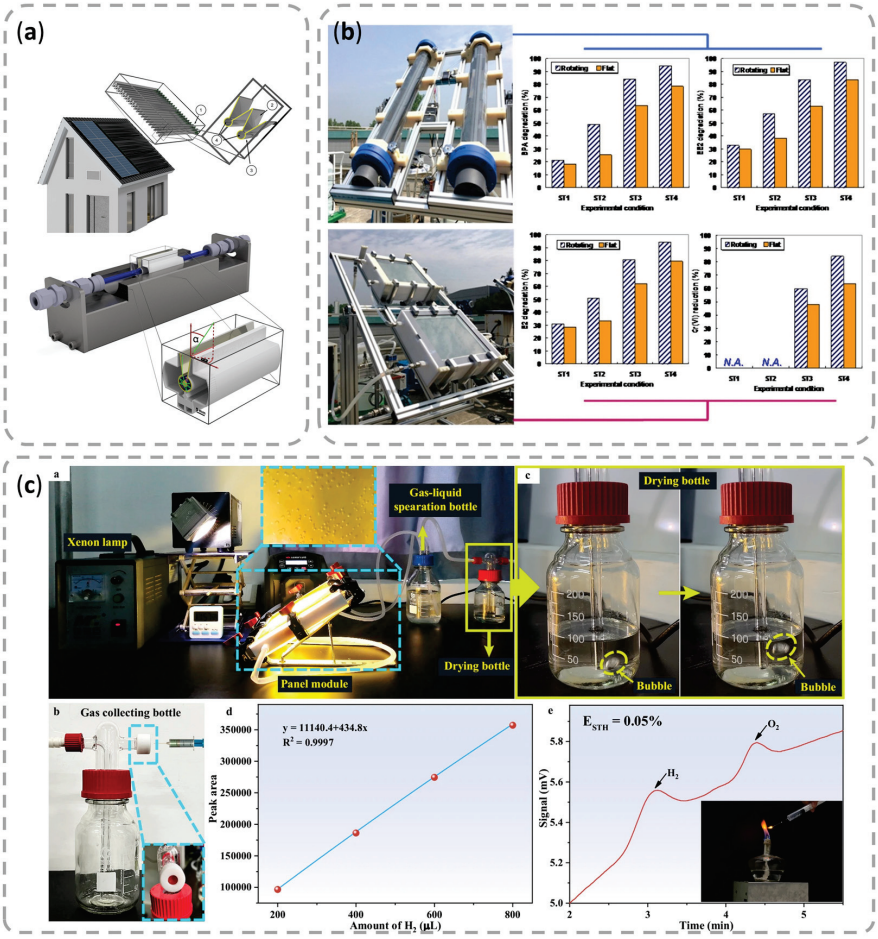


Figure 17. Advances in PMRs in large-scale PMR: (**a**) Potential application of the proposed low-cost, high-efficiency photoreactors on the rooftop of a low-energy house and computer-aided design (CAD) model rendering of the single-channel lab photoreactor employed for the demonstration of the proposed photoreactor concept. Reprinted with permission from Ref. [182]. Copyright (2023), Elsevier. (**b**) Photographs of photocatalytic reactors, including nanotubular TiO_2 (NTT); Small (**left**) and scale-up (**right**) flat-type reactor, small (**left**) and scale-up (**right**) rotating-type reactor. Reprinted with permission from Ref. [183]. Copyright (2017), Elsevier. (**c**) The panel water-splitting reaction system and photocatalytic mechanism. Reprinted with permission from Ref. [187]. Copyright (2024), Springer Nature.

Fu et al. designed a scalable photocatalytic membrane reactor system for solar-driven water splitting by spatially separating H_2 and O_2 evolution using a $MoSe_2$-loaded perovskite photocatalyst ($FAPbBr_{34}I_4$) and NiFe-LDH/$BiVO_4$, connected via an I_3^-/I^- redox shuttle (Figure 18a). The system achieved 2.47% solar-to-hydrogen efficiency in lab tests and maintained 1.21% efficiency in a 692.5 cm^2 outdoor demonstration while effectively suppressing back-reactions through its modular design. This approach demonstrates the feasibility of large-scale photocatalytic hydrogen production through reaction decoupling and redox mediation [188]. Lee et al. developed a floatable photocatalytic hydrogel

nanocomposite that achieves a high hydrogen evolution rate of 163 mmol h^{-1} m^{-2} using Pt/TiO_2 aerogel (Figure 18b). The system's air-water interface design enhances light absorption and gas separation while suppressing back-oxidation. When scaled to 1 m^2, it produces 79.2 mL H_2/day under natural sunlight and maintains performance in seawater and turbid conditions. The platform also enables PET photo-reforming (0.154 L h^{-1} m^{-2}) and demonstrates scalability to 100 m^2, offering a practical solution for large-scale solar hydrogen production [185]. Together, these studies reflect a progressive journey from addressing basic efficiency and cost challenges in photocatalytic reactors to exploring advanced, scalable designs that enhance both the application spectrum and the economic viability of PMRs in environmental remediation.

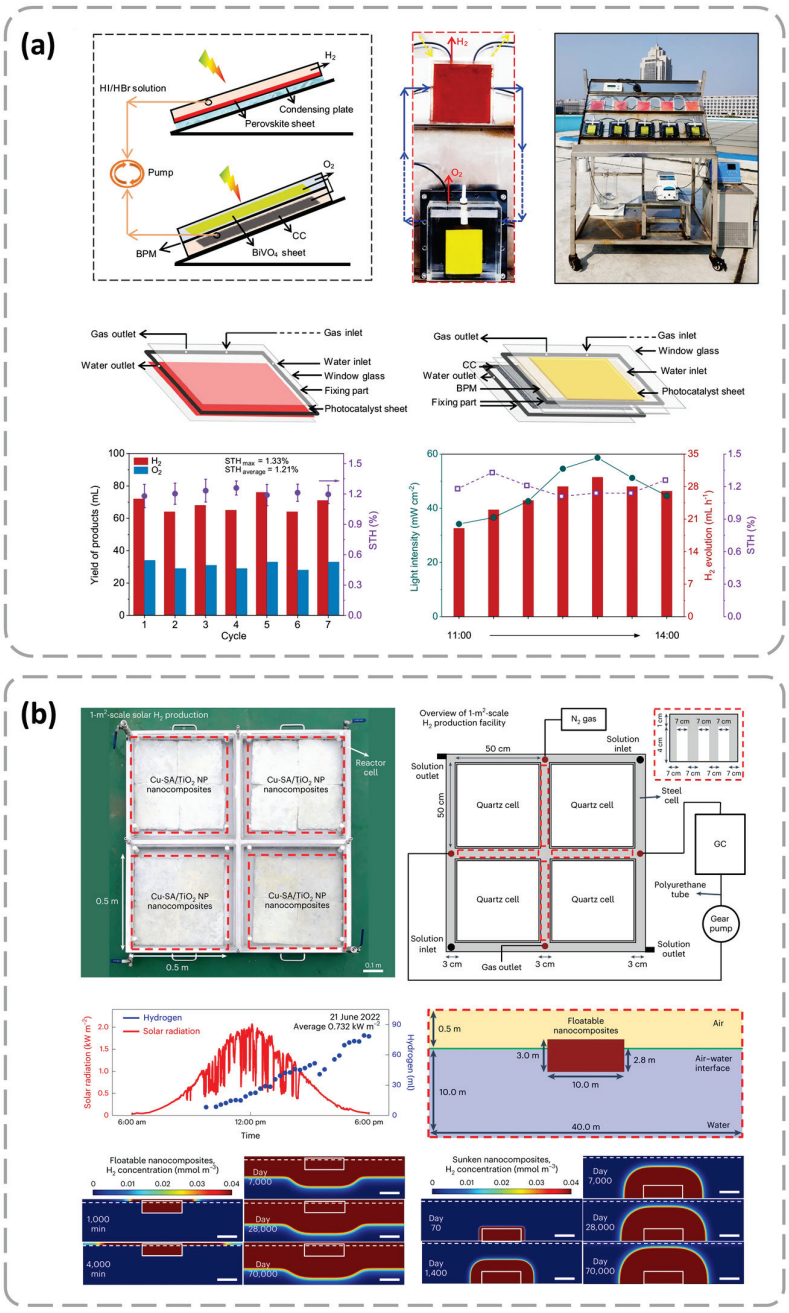


Figure 18. Advances in PMRs in large-scale up PMR: (**a**) Scale up of the nanocomposites. Reprinted with permission from Ref. [188]. Copyright (2025), Springer Nature. (**b**) Panel system for large-scale outdoor water splitting. Reprinted with permission from Ref. [185]. Copyright (2023), Springer Nature.

5. Conclusions and Outlooks

This review traced the development of photocatalytic membrane reactors (PMRs), highlighting their potential to extend beyond conventional water purification by integrating membrane separation with solar-driven catalytic conversion. This synergistic combination allows PMRs to not only efficiently remove pollutants but also transform waste streams into valuable chemical feedstocks and energy carriers. Based on a comparative evaluation, we systematically categorized PMR configurations according to their functional characteristics and optimal application scenarios. Slurry-type PMRs (SPMRs) are particularly suitable for high-value-added applications at the laboratory scale. The suspended catalyst particles offer extensive surface areas for reactions, which is critical for achieving the high catalytic efficiencies required in emerging fields such as solar-driven hydrogen production and photocatalytic CO_2 conversion into fuels and chemicals. These systems represent the most promising architecture for energy-focused applications. Immobilized PMRs (IPMRs) provide indispensable platforms for fundamental research where system stability and reproducibility are essential. They are primarily used for removing persistent organic pollutants under well-controlled conditions, enabling precise validation of reaction kinetics, performance evaluation of novel photocatalysts, and rigorous assessment of material-membrane compatibility over prolonged operation.

PMR technology progresses toward industrial adoption, and modular high-performance designs—exemplified by panel-type reactors—are envisioned to bridge the gap between laboratory success and scalable deployment. This approach facilitates a systematic increase in processing capacity without compromising catalytic efficiency, making it particularly suitable for demanding industrial environmental and energy applications. Despite significant progress in material design and reactor engineering, a considerable gap remains between laboratory achievements and the demands of industrial-scale implementation. A primary challenge is attaining high performance at scale—an objective that entails more than simply enlarging reactor dimensions. It requires a paradigm shift toward viewing PMRs as multifunctional platforms for resource recovery, sustainable energy production, and waste valorization. Balancing manufacturing cost with catalytic efficiency ensure that scaling up does not undermine energy utilization or overall performance—core aspects of the technology's value proposition. The next generation of PMRs should be designed not as static reaction-separation units but as adaptive systems capable of continuous adjustment, multifunctionality, and resource integration. Realizing this vision will depend on merging advances in photocatalytic materials with system-level design strategies that enable predictive control of photon, mass, and fouling dynamics. Digital modeling and real-time process monitoring can provide the basis for moving beyond empirical optimization, paving the way for reactors that are efficient, resilient, and scalable.

PMRs should be regarded as nexus technologies that interconnect water treatment, solar hydrogen production, CO_2 conversion, and resource recovery. In this expanded role, they directly support decarbonization and circular economy goals. Embedding sustainability from the design phase—through recyclable catalysts, regenerable membranes, and low-energy manufacturing routes—will be essential to minimize both economic and environmental costs. Integrating PMRs into renewable-energy-powered distributed treatment networks could further amplify their impact, transforming them into decentralized infrastructures capable of delivering both clean water and clean energy.

Author Contributions: Conceptualization, R.X., J.C. and Z.H.; Writing—original draft preparation, R.X. and S.Q.; Writing—review and editing, J.C., T.L., S.W. and Z.H.; Supervision, T.L. and Z.H.; Funding acquisition, T.L. and Z.H. All authors have read and agreed to the published version of the manuscript.

Funding: This research was supported under the framework of the National Natural Science Foundation of China (No. U22B20102 and No. 22278245), Future Young Scholars Program of Shandong University (No. 61440089964189).

Data Availability Statement: No new data were created or analyzed in this study. Data sharing is not applicable to this article.

Conflicts of Interest: The authors declare no conflicts of interest.

References

1. Xiao, L.; Zhang, J.; Lu, T.; Zhou, G.; Ren, Y.; Zheng, Z.; Yuan, X.; Wang, S.; He, Z. High-strength TiO_2/TPU composite fiber based textiles for organic pollutant removal. *npj Clean Water* **2024**, *7*, 98. [CrossRef]
2. Feng, Y.; Yu, H.; Lu, T.; Zheng, Z.; Tian, S.; Xiang, L.; Zhao, S.; Wang, S.; He, Z. Synergistic Cu single-atoms and clusters on tubular carbon nitride for efficient photocatalytic performances. *Rare Met.* **2024**, *43*, 5891–5904. [CrossRef]
3. Zheng, Z.Y.; Tian, S.; Feng, Y.X.; Zhao, S.; Li, X.; Wang, S.G.; He, Z.L. Recent advances of photocatalytic coupling technologies for wastewater treatment. *Chin. J. Catal.* **2023**, *54*, 88–136. [CrossRef]
4. Bai, Y.; Xu, S.; Chen, J.; Sun, X.; Zhao, S.; Chang, J.; He, Z. Ti_3C_2@g-C_3N_4/TiO_2 ternary heterogeneous photocatalyst for promoted photocatalytic degradation activities. *Coatings* **2023**, *13*, 655. [CrossRef]
5. Qu, K.; Li, H.; Sun, J.; Wang, S.; He, Z.; Wang, S. Rationally designed assembled FeV_3O_8/g-C_3N_4 heterojunction improve carrier transport separation and efficiently promote the degradation of 2,4,6-TCP by photo-activated peroxymonosulfate. *Mater. Sci. Semicond. Process.* **2025**, *194*, 109541. [CrossRef]
6. Qin, S.; Xu, R.; Jin, Q.; Wang, S.; Ren, Y.; Huang, Y.; Zheng, Z.; Xiao, L.; Zhai, D.; Wang, S.; et al. Efficient photocatalytic reduction of hexavalent chromium by $NiCo_2S_4$/BiOBr heterogeneous photocatalysts. *Coatings* **2024**, *14*, 1492. [CrossRef]
7. Zhang, J.; Li, X.; Guo, J.; Zhou, G.H.; Xiang, L.; Wang, S.G.; He, Z.L. Novel TiO_2/TPU composite fiber-based smart textiles for photocatalytic applications. *Mater. Adv.* **2022**, *3*, 1518–1526. [CrossRef]
8. He, Z.; Kim, C.; Lin, L.H.; Jeon, T.H.; Lin, S.; Wang, X.C.; Choi, W. Formation of heterostructures via direct growth CN on h-BN porous nanosheets for metal-free photocatalysis. *Nano Energy* **2017**, *42*, 58–68. [CrossRef]
9. Zhang, S.; He, Z.; Li, X.; Zhang, J.; Zang, Q.; Wang, S. Building heterogeneous nanostructures for photocatalytic ammonia decomposition. *Nanoscale Adv.* **2020**, *2*, 3610–3623. [CrossRef]
10. Dai, M.; He, Z.; Zhang, P.; Li, X.; Wang, S. $ZnWO_4$-$ZnIn_2S_4$ S-scheme heterojunction for enhanced photocatalytic H_2 evolution. *J. Mater. Sci. Technol.* **2022**, *122*, 231–242. [CrossRef]
11. Li, X.; Chang, J.; Zhang, S.; Xiao, L.; Wu, X.; He, Z. Microcystis@TiO_2 nanoparticles for photocatalytic reduction reactions: Nitrogen fixation and hydrogen evolution. *Catalysts* **2021**, *11*, 1443. [CrossRef]
12. Xiao, L.H.; Li, X.; Zhang, J.; He, Z.L. MgB_4 MXene-like nanosheets for photocatalytic hydrogen evolution. *ACS Appl. Nano Mater.* **2021**, *4*, 12779–12787. [CrossRef]
13. Dai, M.; He, Z.; Cao, W.; Zhang, J.; Chen, W.; Jin, Q.; Que, W.; Wang, S. Rational construction of S-scheme BN/MXene/$ZnIn_2S_4$ heterojunction with interface engineering for efficient photocatalytic hydrogen production and chlorophenols degradation. *Sep. Purif. Technol.* **2023**, *309*, 123004. [CrossRef]
14. Cao, W.R.; He, Z.L.; Dai, M.; Wang, G.Z.; Huang, G.H.; Wang, S.G. Electronic structure modulation of bimetallic sulfides for efficient sacrificial-agent-free photocatalytic H_2 evolution. *ACS Appl. Energy Mater.* **2023**, *6*, 4715–4723. [CrossRef]
15. Wang, H.; Zhang, L.; Chen, Z.; Hu, J.; Li, S.; Wang, Z.; Liu, J.; Wang, X. Semiconductor heterojunction photocatalysts: Design, construction, and photocatalytic performances. *Chem. Soc. Rev.* **2014**, *43*, 5234–5244. [CrossRef]
16. Dai, M.; Yu, H.; Chen, W.; Qu, K.; Zhai, D.; Liu, C.; Zhao, S.; Wang, S.; He, Z. Boosting photocatalytic activity of $CdLa_2S_4$/$ZnIn_2S_4$ S-scheme heterojunctions with spatial separation of photoexcited carries. *Chem. Eng. J.* **2023**, *470*, 144240. [CrossRef]
17. Zhang, J.; Ma, H.; Ma, J.; Hu, M.; Li, Q.; Chen, S.; Ning, T.; Ge, C.; Liu, X.; Xiao, L.; et al. Cone shaped surface array structure on an alkaline polymer electrolyte membrane improves fuel cell performance. *Acta Phys.-Chim. Sin.* **2023**, *39*, 2111037. [CrossRef]
18. Sun, J.; Ren, Y.; Dai, M.; Li, H.; Yu, H.; Wang, S.; He, Z.; Wang, S. Efficient photocatalytic degradation of sulfamethazine by carboxylic CNT-decorated Bi_2O_3/Bi_2WO_6 heterojunction catalysts. *Chem. Res. Chin. Univ.* **2025**. [CrossRef]
19. Hong, F.; Jing, T.; Wang, S.; He, Z. Defect engineering of $ZnIn_2S_4$ photocatalysts for enhanced hydrogen evolution reaction. *Coatings* **2025**, *15*, 1061. [CrossRef]
20. Chen, W.; Dai, M.; Xiang, L.; Zhao, S.; Wang, S.; He, Z. Assembling S-scheme heterojunction between basic bismuth nitrate and bismuth tungstate with promoting charges' separation for accelerated photocatalytic sulfamethazine degradation. *J. Mater. Sci. Technol.* **2024**, *171*, 185–197. [CrossRef]
21. Zhao, X.; Qiu, H.; Shao, Y.; Wang, P.; Yu, S.; Li, H.; Zhou, Y.; Zhou, Z.; Ma, L.; Tan, C. Silver nanoparticle-modified 2D MOF nanosheets for photothermally enhanced silver ion release antibacterial treatment. *Acta Phys.-Chim. Sin.* **2023**, *39*, 2211043. [CrossRef]

22. Cheng, K.; Liu, C.; Wang, Y.; Jiang, Q.; Zheng, T.; Li, X.; Xia, C. Design of noble metal catalysts and reactors for the electrosynthesis of hydrogen peroxide. *Acta Phys.-Chim. Sin.* **2025**, *41*, 100112. [CrossRef]
23. Zhang, J.; Wu, H.; Shi, L.; Wu, Z.; Zhang, S.; Wang, S.; Sun, H. Photocatalysis coupling with membrane technology for sustainable and continuous purification of wastewater. *Sep. Purif. Technol.* **2024**, *329*, 125225. [CrossRef]
24. Romanos, G.E.; Athanasekou, C.P.; Likodimos, V.; Aloupogiannis, P.; Falaras, P. Hybrid ultrafiltration/photocatalytic membranes for efficient water treatment. *Ind. Eng. Chem. Res.* **2013**, *52*, 13938–13947. [CrossRef]
25. Zhang, H.R.; Wan, Y.H.; Luo, J.Q.; Darling, S.B. Drawing on membrane photocatalysis for fouling mitigation. *ACS Appl. Mater. Interfaces* **2021**, *13*, 14844–14865. [CrossRef]
26. Peng, L.; Zhang, Y.; He, R.; Xu, N.; Qiao, J. Research advances in electrocatalysts, electrolytes, reactors and membranes for the electrocatalytic carbon dioxide reduction reaction. *Acta Phys.-Chim. Sin.* **2023**, *39*, 2302037. [CrossRef]
27. Wu, C.-J.; Valerie Maggay, I.; Chiang, C.; Chen, W.; Chang, Y.; Hu, C.; Venault, A. Removal of tetracycline by a photocatalytic membrane reactor with MIL-53(Fe)/PVDF mixed-matrix membrane. *Chem. Eng. J.* **2023**, *451*, 138990. [CrossRef]
28. Xu, S.; Wu, Q.; Lu, B.-A.; Tang, T.; Zhang, J.-N.; Hu, J.-S. Recent advances and future prospects on industrial catalysts for green hydrogen production in alkaline media. *Acta Phys.-Chim. Sin.* **2023**, *39*, 2209001. [CrossRef]
29. Jin, H.G.; Zhao, P.C.; Qian, Y.Y.; Xiao, J.D.; Chao, Z.S.; Jiang, H.L. Metal-organic frameworks for organic transformations by photocatalysis and photothermal catalysis. *Chem. Soc. Rev.* **2024**, *53*, 9378–9418. [CrossRef]
30. Mozia, S. Photocatalytic membrane reactors (PMRs) in water and wastewater treatment. A review. *Sep. Purif. Technol.* **2010**, *73*, 71–91. [CrossRef]
31. Chong, M.N.; Jin, B.; Chow, C.W.K.; Saint, C. Recent developments in photocatalytic water treatment technology: A review. *Water Res.* **2010**, *44*, 2997–3027. [CrossRef]
32. Molinari, R.; Marino, T.; Argurio, P. Photocatalytic membrane reactors for hydrogen production from water. *Int. J. Hydrogen Energy* **2014**, *39*, 7247–7261. [CrossRef]
33. Zhang, W.X.; Ding, L.H.; Luo, J.Q.; Jaffrin, M.Y.; Tang, B. Membrane fouling in photocatalytic membrane reactors (PMRs) for water and wastewater treatment: A critical review. *Chem. Eng. J.* **2016**, *302*, 446–458. [CrossRef]
34. Molinari, R.; Lavorato, C.; Argurio, P. Recent progress of photocatalytic membrane reactors in water treatment and in synthesis of organic compounds. A review. *Catal. Today* **2017**, *281*, 144–164. [CrossRef]
35. Hassnain, M.; Ali, A.; Azhar, M.R.; Abutaleb, A.; Mubashir, M. Challenges and perspectives on photocatalytic membrane reactors for volatile organic compounds degradation and nitrogen oxides treatment. *Glob. Chall.* **2025**, *9*, 2500035. [CrossRef] [PubMed]
36. Argurio, P.; Fontananova, E.; Molinari, R.; Drioli, E. Photocatalytic membranes in photocatalytic membrane reactors. *Processes* **2018**, *6*, 162. [CrossRef]
37. Molinari, R.; Lavorato, C.; Argurio, P. The evolution of photocatalytic membrane reactors over the last 20 years: A state of the art perspective. *Catalysts* **2021**, *11*, 775. [CrossRef]
38. Visan, A.; van Ommen, J.R.; Kreutzer, M.T.; Lammertink, R.G.H. Photocatalytic reactor design: Guidelines for kinetic investigation. *Ind. Eng. Chem. Res.* **2019**, *58*, 5349–5357. [CrossRef]
39. Gupta, S.; Gomaa, H.; Ray, M.B. Fouling control in a submerged membrane reactor: Aeration vs membrane oscillations. *Chem. Eng. J.* **2022**, *432*, 134399. [CrossRef]
40. Mendret, J.; Brosillon, S. Advances in photocatalytic membrane reactor. *Membranes* **2023**, *13*, 541. [CrossRef]
41. Zhang, J.; Miao, Y.; Huo, Y.; Li, H. Development of photocatalysis-membrane separation reactor systems for aqueous pollutant removal. *PhotoMat* **2023**, 1–21. [CrossRef]
42. Fu, L.; Chen, X.; Xiang, Y.; Zeng, G. Integrated catalytic membranes for advanced antibiotic wastewater treatment: Synergistic separation-degradation mechanisms and next-generation design. *Sep. Purif. Technol.* **2025**, *372*, 133440. [CrossRef]
43. Zheng, X.; Shen, Z.; Shi, L.; Cheng, R.; Yuan, D. Photocatalytic Membrane Reactors (PMRs) in Water Treatment: Configurations and Influencing Factors. *Catalysts* **2017**, *7*, 224. [CrossRef]
44. Zhou, Q.; Guo, Y.; Zhu, Y. Photocatalytic sacrificial H_2 evolution dominated by micropore-confined exciton transfer in hydrogen-bonded organic frameworks. *Nat. Catal.* **2023**, *6*, 574–584. [CrossRef]
45. Li, J.; Wu, X.; Liu, S. Fluorinated TiO_2 hollow photocatalysts for photocatalytic applications. *Acta Phys.-Chim. Sin.* **2021**, *37*, 2009038.
46. Le, C.C.; Wismer, M.K.; Shi, Z.C.; Zhang, R.; Conway, D.V.; Li, G.; Vachal, P.; Davies, I.W.; MacMillan, D.W.C. A general small-scale reactor To enable standardization and acceleration of photocatalytic reactions. *ACS Cent. Sci.* **2017**, *3*, 647–653. [CrossRef]
47. Tripathi, A.; Dhanda, A.; Raj, R.; Ghangrekar, M.M.; Surampalli, R.Y. Graphene-based photocatalytic membrane application for the remediation of organic dye pollutants: A review. *Groundw. Sustain. Dev.* **2024**, *26*, 101214. [CrossRef]
48. Tsuru, T.; Kan-no, T.; Yoshioka, T.; Asaeda, M. A photocatalytic membrane reactor for gas-phase reactions using porous titanium oxide membranes. *Catal. Today* **2003**, *82*, 41–48. [CrossRef]
49. Yang, J.; Liu, B.; Zhao, X. A visible-light-active Au-Cu(I)@$Na_2Ti_6O_{13}$ nanostructured hybrid pasmonic photocatalytic membrane for acetaldehyde elimination. *Chin. J. Catal.* **2017**, *38*, 2048–2055. [CrossRef]

50. Athanasekou, C.P.; Romanos, G.E.; Katsaros, F.K.; Kordatos, K.; Likodimos, V.; Falaras, P. Very efficient composite titania membranes in hybrid ultrafiltration/photocatalysis water treatment processes. *J. Membr. Sci.* **2012**, *392*, 192–203. [CrossRef]
51. Bortot Coelho, F.E.; Gionco, C.; Paganini, M.C.; Calza, P.; Magnacca, G. Control of membrane fouling in organics filtration using Ce-doped zirconia and visible light. *Nanomaterials* **2019**, *9*, 534. [CrossRef] [PubMed]
52. El Batouti, M.; Alharby, N.F.; Elewa, M.M. Review of new approaches for fouling mitigation in membrane separation processes in water treatment applications. *Separations* **2021**, *9*, 1. [CrossRef]
53. Hazaraimi, M.H.; Goh, P.S.; Lau, W.J.; Ismail, A.F.; Hashim, N.; Kerishnan, N.D.K.; Yahaya, N.K.E.M.; Mamat, R.B.R. Advancing photocatalytic membrane for efficient endocrine disrupting compounds removal: Progresses and challenges. *J. Water Process Eng.* **2024**, *68*, 106338. [CrossRef]
54. Nasrollahi, N.; Ghalamchi, L.; Vatanpour, V.; Khataee, A. Photocatalytic-membrane technology: A critical review for membrane fouling mitigation. *J. Ind. Eng. Chem.* **2021**, *93*, 101–116. [CrossRef]
55. Ping, M.-M.; Qiu, S.-J.; Wei, G.-J.; Liu, J.-X.; Wang, Z.-J.; Wang, S.-T.; An, C.-H. Monolith free-standing plasmonic PAN/Ag/AgX (X = Br, I) nanofiber mat as easily recoverable visible-light-driven photocatalyst. *Rare Met.* **2019**, *38*, 361–368. [CrossRef]
56. Bortot Coelho, F.E.; Deemter, D.; Candelario, V.M.; Boffa, V.; Malato, S.; Magnacca, G. Development of a photocatalytic zirconia-titania ultrafiltration membrane with anti-fouling and self-cleaning properties. *J. Environ. Chem. Eng.* **2021**, *9*, 106671. [CrossRef]
57. Chen, L.; Xu, P.; Wang, H. Photocatalytic membrane reactors for produced water treatment and reuse: Fundamentals, affecting factors, rational design, and evaluation metrics. *J. Hazard. Mater.* **2022**, *424*, 127493. [CrossRef]
58. Zhang, H.; Liu, Y.F.; Liu, N.; Kang, S.F. Understanding the interface properties of photocatalytic reactors for rational engineering applications. *Chem. Eng. J.* **2023**, *472*, 145057. [CrossRef]
59. Rosa, V.; Cameli, F.; Stefanidis, G.D.; Van Geem, K.M. Integrating materials in non-thermal plasma reactors: Challenges and opportunities. *Acc. Mater. Res.* **2024**, *5*, 1024–1035. [CrossRef]
60. Esfandiaribayat, M.; Binazadeh, M.; Sabbaghi, S.; Mohammadi, M.; Ghaedi, S.; Rajabi, H. Tetracycline removal from wastewater via g-CN loaded RSM-CCD-optimised hybrid photocatalytic membrane reactor. *Sci. Rep.* **2024**, *14*, 1163. [CrossRef]
61. Binazadeh, M.; Rasouli, J.; Sabbaghi, S.; Mousavi, S.M.; Hashemi, S.A.; Lai, C.W. An overview of photocatalytic membrane degradation development. *Materials* **2023**, *16*, 3526. [CrossRef]
62. Ahmed, M.; Mavukkandy, M.O.; Giwa, A.; Elektorowicz, M.; Katsou, E.; Khelifi, O.; Naddeo, V.; Hasan, S.W. Recent developments in hazardous pollutants removal from wastewater and water reuse within a circular economy. *npj Clean Water* **2022**, *5*, 12. [CrossRef]
63. Fei, H.; Zhao, T.; Guo, W.; Wang, X.; Zhang, J.; Fei, Z.; Feng, Z.; Liu, G. Strategies for enhancing activities of typical piezo-photocatalytic material and its applications in environmental remediation: A review. *J. Environ. Chem. Eng.* **2024**, *12*, 111650. [CrossRef]
64. Santana, H.S.; Silva, J.L.; Aghel, B.; Ortega-Casanova, J. Review on microfluidic device applications for fluids separation and water treatment processes. *SN Appl. Sci.* **2020**, *2*, 395. [CrossRef]
65. Romay, M.; Diban, N.; Rivero, M.J.; Urtiaga, A.; Ortiz, I. Critical issues and guidelines to improve the performance of photocatalytic polymeric membranes. *Catalysts* **2020**, *10*, 570. [CrossRef]
66. Zhang, G.; Yao, L.; Wang, L.; Zhang, J.; Xu, L.; Fan, Z. Photocatalytic membrane reactor used for water and wastewater treatment. *Recent Pat. Eng.* **2012**, *6*, 127–136. [CrossRef]
67. Sabouni, R.; Gomaa, H.G. Comparative analysis of aeration and oscillation in a suspended catalyst photocatalytic membrane reactor. *Chem. Eng. Res. Des.* **2021**, *173*, 55–62. [CrossRef]
68. Huang, X.; Meng, Y.; Liang, P.; Qian, Y. Operational conditions of a membrane filtration reactor coupled with photocatalytic oxidation. *Sep. Purif. Technol.* **2007**, *55*, 165–172. [CrossRef]
69. Molinari, R.; Lavorato, C.; Argurio, P.; Szymanski, K.; Darowna, D.; Mozia, S. Overview of photocatalytic membrane reactors in organic synthesis, energy storage and environmental applications. *Catalysts* **2019**, *9*, 239. [CrossRef]
70. Rehm, T.H.; Gros, S.; Renken, A.; Löb, P. Photocatalysis with visible light–optimization and scale-up for the falling-film microreactor. *Chem. Ing. Tech.* **2016**, *88*, 1334–1335. [CrossRef]
71. Binjhade, R.; Mondal, R.; Mondal, S. Continuous photocatalytic reactor: Critical review on the design and performance. *J. Environ. Chem. Eng.* **2022**, *10*, 107746. [CrossRef]
72. Alvey, J.; Dev, S.; Quiñones, O.; Dickenson, E.; Aggarwal, S.; Dotson, A. Photocatalytic membrane reactor utilizing immobile photocatalytic active layer on membranes for the removal of micropollutants. *ACS EST Water* **2023**, *3*, 1050–1059. [CrossRef]
73. Hu, Z.Y.; Liu, T.; Yang, Y.R.; An, A.K.; Liew, K.M.; Li, W.W. Binder-free immobilization of photocatalyst on membrane surface for efficient photocatalytic H_2O_2 production and water decontamination. *Nanomicro. Lett.* **2025**, *17*, 301. [CrossRef] [PubMed]
74. Kakhki, R.M. Beyond photosynthesis: Engineering self-healing photocatalytic systems for sustainability. *Colloid. Interface Sci. Commun.* **2025**, *67*, 100842. [CrossRef]
75. Wang, D.W.; Mueses, M.A.; Márquez, J.A.C.; Machuca-Martínez, F.; Grcic, I.; Moreira, R.P.M.; Li Puma, G. Engineering and modeling perspectives on photocatalytic reactors for water treatment. *Water Res.* **2021**, *202*, 117421. [CrossRef]
76. Szymański, K.; Morawski, A.W.; Mozia, S. Humic acids removal in a photocatalytic membrane reactor with a ceramic UF membrane. *Chem. Eng. J.* **2016**, *305*, 19–27. [CrossRef]

77. Feng, X.; Long, R.; Liu, C.; Liu, X. Novel dual-heterojunction photocatalytic membrane reactor based on Ag_2S/NH_2-MIL-88B(Fe)/poly(aryl ether nitrile) composite with enhanced photocatalytic performance for wastewater purification. *Chem. Eng. J.* **2023**, *454*, 139765. [CrossRef]
78. Heredia Deba, S.A.; Wols, B.A.; Yntema, D.R.; Lammertink, R.G.H. Transport and surface reaction model of a photocatalytic membrane during the radical filtration of methylene blue. *Chem. Eng. Sci.* **2022**, *254*, 117617. [CrossRef]
79. Jung, J.T.; Lee, W.H.; Kim, J.O. Photodegradation and permeability of conventional photocatalytic reactor and two different submerged membrane photocatalytic reactors for the removal of humic acid in water. *Desalin. Water Treat.* **2016**, *57*, 26765–26772. [CrossRef]
80. Tahir, B.; Tahir, M.; Amin, N.S. Performance analysis of monolith photoreactor for CO_2 reduction with H_2. *Energy Convers. Manag.* **2015**, *90*, 272–281. [CrossRef]
81. Allasia, N.; Nevskyi, O.; Marelli, M.; Plazl, I.; Albertazzi, J.; Busini, V.; Castiglione, F.; Rossi, F.; Vilé, G. Bijel-based mesophotoreactor with integrated carbon nitride for continuous-flow photocatalysis. *Chem. Eng. J.* **2024**, *499*, 155885. [CrossRef]
82. Ollis, D.F.; Pelizzetti, E.; Serpone, N. Destruction of water contaminants. *Environ. Sci. Technol.* **1991**, *25*, 1522–1529. [CrossRef]
83. Shen, M.W.; Zhang, G.Q.; Liu, J.Y.; Liu, Y.H.; Zhai, J.Y.; Zhang, H.C.; Yu, H.S. Visible-light-driven photodegradation of xanthate in a continuous fixed-bed photoreactor: Experimental study and modeling. *Chem. Eng. J.* **2023**, *461*, 141833. [CrossRef]
84. Sambiagio, C.; Noël, T. Flow photochemistry: Shine some light on those tubes! *Trends Chem.* **2020**, *2*, 92–106. [CrossRef]
85. Ahmad, R.; Lee, C.S.; Kim, J.H.; Kim, J. Partially coated TiO_2 on Al_2O_3 membrane for high water flux and photodegradation by novel filtration strategy in photocatalytic membrane reactors. *Chem. Eng. Res. Des.* **2020**, *163*, 138–148. [CrossRef]
86. Kayvani Fard, A.; McKay, G.; Buekenhoudt, A.; Al Sulaiti, H.; Motmans, F.; Khraisheh, M.; Atieh, M. Inorganic Membranes: Preparation and Application for Water Treatment and Desalination. *Materials* **2018**, *11*, 74. [CrossRef]
87. Lee, S.A.; Choo, K.H.; Lee, C.H.; Lee, H.I.; Hyeon, T.; Choi, W.; Kwon, H.H. Use of ultrafiltration membranes for the separation of TiO_2 photocatalysts in drinking water treatment. *Ind. Eng. Chem. Res.* **2001**, *40*, 1712–1719. [CrossRef]
88. Corredor, J.; Perez-Peña, E.; Rivero, M.J.; Ortiz, I. Performance of rGO/TiO_2 photocatalytic membranes for hydrogen production. *Membranes* **2020**, *10*, 218. [CrossRef]
89. Horovitz, I.; Avisar, D.; Baker, M.A.; Grilli, R.; Lozzi, L.; Di Camillo, D.; Mamane, H. Carbamazepine degradation using a N-doped TiO_2 coated photocatalytic membrane reactor: Influence of physical parameters. *J. Hazard. Mater.* **2016**, *310*, 98–107. [CrossRef]
90. Gomaa, H.G. Hydrodynamics and energy analysis in suspended catalyst photocatalytic membrane reactors. *Chem. Eng. Process.* **2023**, *193*, 109563. [CrossRef]
91. Yan, G.; Zuo, B.; Liu, S.; Wang, T.; Wang, R.; Bao, J.; Zhao, Z.; Chu, F.; Li, Z.; Yamauchi, Y.; et al. Opportunities and challenges of capacitive deionization for uranium extraction from seawater. *Acta Phys.-Chim. Sin.* **2025**, *41*, 100032. [CrossRef]
92. Chin, S.S.; Lim, T.M.; Chiang, K.; Fane, A.G. Factors affecting the performance of a low-pressure submerged membrane photocatalytic reactor. *Chem. Eng. J.* **2007**, *130*, 53–63. [CrossRef]
93. Zhang, H.; Quan, X.; Chen, S.; Zhao, H.; Zhao, Y. The removal of sodium dodecylbenzene sulfonate surfactant from water using silica/titania nanorods/nanotubes composite membrane with photocatalytic capability. *Appl. Surf. Sci.* **2006**, *252*, 8598–8604. [CrossRef]
94. Horng, R.Y.; Huang, C.P.; Chang, M.C.; Shao, H.; Shiau, B.L.; Hu, Y.J. Application of TiO_2 photocatalytic oxidation and non-woven membrane filtration hybrid system for degradation of 4-chlorophenol. *Desalination* **2009**, *245*, 169–182. [CrossRef]
95. Li, Q.L.; Kong, H.; Jia, R.R.; Shao, J.H.; He, Y.L. Enhanced catalytic degradation of amoxicillin with TiO_2-Fe_3O_4 composites via a submerged magnetic separation membrane photocatalytic reactor (SMSMPR). *RSC Adv.* **2019**, *9*, 12538–12546. [CrossRef]
96. Madadi Avargani, V.; Zendehboudi, S.; Osfouri, S.; Rostami, A. Performance evaluation of a solar nano-photocatalytic reactor for wastewater treatment applications: Reaction kinetics, CFD, and scale-up perspectives. *J. Clean. Prod.* **2023**, *421*, 138240. [CrossRef]
97. Janssens, R.; Hainaut, R.; Gillard, J.; Dailly, H.; Luis, P. Performance of a slurry photocatalytic membrane reactor for the treatment of real secondary wastewater effluent polluted by anticancer drugs. *Ind. Eng. Chem. Res.* **2021**, *60*, 2223–2231. [CrossRef]
98. Shao, J.H.; Hou, J.A.; Song, H.C. Comparison of humic acid rejection and flux decline during filtration with negatively charged and uncharged ultrafiltration membranes. *Water Res.* **2011**, *45*, 473–482. [CrossRef]
99. Sarasidis, V.C.; Plakas, K.V.; Patsios, S.I.; Karabelas, A.J. Investigation of diclofenac degradation in a continuous photo-catalytic membrane reactor. Influence of operating parameters. *Chem. Eng. J.* **2014**, *239*, 299–311. [CrossRef]
100. Iglesias, O.; Rivero, M.J.; Urtiaga, A.M.; Ortiz, I. Membrane-based photocatalytic systems for process intensification. *Chem. Eng. J.* **2016**, *305*, 136–148. [CrossRef]
101. Molinari, R.; Severino, A.; Lavorato, C.; Argurio, P. Which configuration of photocatalytic membrane reactors has a major potential to be used at an industrial level in tertiary sewage wastewater treatment? *Catalysts* **2023**, *13*, 1204. [CrossRef]
102. Vaiano, V.; Sacco, O.; Pisano, D.; Sannino, D.; Ciambelli, P. From the design to the development of a continuous fixed bed photoreactor for photocatalytic degradation of organic pollutants in wastewater. *Chem. Eng. Sci.* **2015**, *137*, 152–160. [CrossRef]
103. Shi, H.B.; Magaye, R.; Castranova, V.; Zhao, J.S. Titanium dioxide nanoparticles: A review of current toxicological data. *Part. Fibre Toxicol.* **2013**, *10*, 15. [CrossRef]

104. Van Gerven, T.; Mul, G.; Moulijn, J.; Stankiewicz, A. A review of intensification of photocatalytic processes. *Chem. Eng. Process.* **2007**, *46*, 781–789. [CrossRef]
105. Biao, W.; Awanis Hashim, N.; Rabuni, M.F.B.; Lide, O.; Ullah, A. An innovative strategy for polyester microplastic fiber elimination from laundry wastewater via coupled separation and degradation using TiO_2-based photocatalytic membrane reactor. *Sep. Purif. Technol.* **2025**, *356*, 129929. [CrossRef]
106. Rezaei, M.; Rashidi, F.; Royaee, S.J.; Jafarikojour, M. Performance evaluation of a continuous flow photocatalytic reactor for wastewater treatment. *Environ. Sci. Pollut. R.* **2014**, *21*, 12505–12517. [CrossRef]
107. Li, N.; Lu, X.K.; He, M.T.; Duan, X.G.; Yan, B.B.; Chen, G.Y.; Wang, S.B. Catalytic membrane-based oxidation-filtration systems for organic wastewater purification: A review. *J. Hazard. Mater.* **2021**, *414*, 125478. [CrossRef]
108. Yang, L.P.; Liu, Z.Y.; Shi, H.W.; Hu, H.; Shangguan, W.F. Design consideration of photocatalytic oxidation reactors using TiO_2-coated foam nickels for degrading indoor gaseous formaldehyde. *Catal. Today* **2007**, *126*, 359–368. [CrossRef]
109. Darowna, D.; Wróbel, R.; Morawski, A.W.; Mozia, S. The influence of feed composition on fouling and stability of a polyethersulfone ultrafiltration membrane in a photocatalytic membrane reactor. *Chem. Eng. J.* **2017**, *310*, 360–367. [CrossRef]
110. Gao, B.; Chen, W.P.; Liu, J.D.; An, J.J.; Wang, L.; Zhu, Y.; Sillanpää, M. Continuous removal of tetracycline in a photocatalytic membrane reactor (PMR) with $ZnIn_2S_4$ as adsorption and photocatalytic coating layer on PVDF membrane. *J. Photochem. Photobiol. A Chem.* **2018**, *364*, 732–739. [CrossRef]
111. Gupta, S.; Gomaa, H.; Ray, M.B. A novel submerged photocatalytic oscillatory membrane reactor for water polishing. *J. Environ. Chem. Eng.* **2021**, *9*, 105562. [CrossRef]
112. Zhang, C.Y.; Sabouni, R.; Shao, Y.; Gomaa, H.G. Performance of submerged oscillatory membrane photoreactor for water treatment. *J. Environ. Chem. Eng.* **2017**, *5*, 3330–3336. [CrossRef]
113. Mozia, S.; Tomaszewska, M.; Morawski, A.W. A new photocatalytic membrane reactor (PMR) for removal of azo-dye Acid Red 18 from water. *Appl. Catal. B Environ. Energy* **2005**, *59*, 131–137. [CrossRef]
114. Vatanpour, V.; Darrudi, N.; Sheydaei, M. A comprehensive investigation of effective parameters in continuous submerged photocatalytic membrane reactors by RSM. *Chem. Eng. Process.-Process Intensif.* **2020**, *157*, 108144. [CrossRef]
115. Trinh, T.H.T.; Samhaber, W.M. The coupling of catalysis with submerged ceramic MF membrane for hybrid water treatment process. *Chem. Eng. Trans.* **2016**, *47*, 247–252.
116. Fu, J.F.; Ji, M.; Wang, Z.; Jin, L.N.; An, D.N. A new submerged membrane photocatalysis reactor (SMPR) for fulvic acid removal using a nano-structured photocatalyst. *J. Hazard. Mater.* **2006**, *131*, 238–242. [CrossRef] [PubMed]
117. Jiang, L.; Choo, K. Photocatalytic mineralization of secondary effluent organic matter with mitigating fouling propensity in a submerged membrane photoreactor. *Chem. Eng. J.* **2016**, *288*, 798–805. [CrossRef]
118. Wang, Q.; Wang, P.; Xu, P.; Hu, L.M.; Wang, X.J.; Qu, J.H.; Zhang, G.S. Submerged membrane photocatalytic reactor for advanced treatment of p-nitrophenol wastewater through visible-light-driven photo-Fenton reactions. *Sep. Purif. Technol.* **2021**, *256*, 117783. [CrossRef]
119. Li, Q.L.; Jia, R.R.; Shao, J.H.; He, Y.L. Photocatalytic degradation of amoxicillin via TiO_2 nanoparticle coupling with a novel submerged porous ceramic membrane reactor. *J. Clean. Prod.* **2019**, *209*, 755–761. [CrossRef]
120. Kertèsz, S.; Cakl, J.; Jiránková, H. Submerged hollow fiber microfiltration as a part of hybrid photocatalytic process for dye wastewater treatment. *Desalination* **2014**, *343*, 106–112. [CrossRef]
121. Gomaa, H.G. Interaction forces and suspension characteristics in an oscillatory membrane photocatalytic reactor. *Chem. Eng. Res. Des.* **2022**, *185*, 301–308. [CrossRef]
122. Leong, S.W.; Razmjou, A.; Wang, K.; Hapgood, K.; Zhang, X.W.; Wang, H.T. TiO_2 based photocatalytic membranes: A review. *J. Membr. Sci.* **2014**, *472*, 167–184. [CrossRef]
123. Mesgari, Z.; Saien, J. Pollutant degradation over dye sensitized nitrogen doped titania substances in different configurations of visible light helical flow photoreactor. *Sep. Purif. Technol.* **2017**, *185*, 129–139. [CrossRef]
124. Chen, T.; Xue, X.; Li, J.; Cui, M.; Hao, Y.; Xue, M.; Xiao, H.; Ge, J.; Wang, P. Membrane-anchoring nanoengineered carbon dots as a pyroptosis amplifier for robust tumor photodynamic-immunotherapy. *Acta Phys.-Chim. Sin.* **2025**, *41*, 100113. [CrossRef]
125. Liu, S.Q.; Edara, P.C.; Schäfer, A.I. Influence of organic matter on the photocatalytic degradation of steroid hormones by TiO_2-coated polyethersulfone microfiltration membrane. *Water Res.* **2023**, *245*, 120438. [CrossRef] [PubMed]
126. Nguyen, M.N.; Raota, C.S.; Turshatov, A.; Richards, B.S.; Schäfer, A.I. Collision theory and membrane photocatalysis: Steroid hormones meet singlet oxygen in palladium-porphyrin-coated polytetrafluoroethylene membranes. *Chem. Eng. J.* **2024**, *501*, 157582. [CrossRef]
127. Hairom, N.H.H.; Mohammad, A.W.; Kadhum, A.A.H. Effect of various zinc oxide nanoparticles in membrane photocatalytic reactor for Congo red dye treatment. *Sep. Purif. Technol.* **2014**, *137*, 74–81. [CrossRef]
128. Sakhaie, S.; Taghipour, F. Highly durable zirconium/titanium dioxide-silicon carbide photocatalytic membrane for water and wastewater treatment. *J. Environ. Chem. Eng.* **2023**, *11*, 110142. [CrossRef]
129. Heredia Deba, S.A.; Wols, B.A.; Yntema, D.R.; Lammertink, R.G.H. Advanced ceramics in radical filtration: TiO_2 layer thickness effect on the photocatalytic membrane performance. *J. Membr. Sci.* **2023**, *672*, 121423. [CrossRef]

130. Li, W.X.; Zhao, W.X.; Zhu, H.Y.; Li, Z.J.; Wang, W.L. State of the art in the photochemical degradation of (micro)plastics: From fundamental principles to catalysts and applications. *J. Mater. Chem. A* **2023**, *11*, 2503–2527. [CrossRef]
131. Yan, X.J.; Li, J.Y.; Ma, C.; Tang, Y.; Kong, X.J.; Lu, J.F. Study on the lifetime of photocatalyst by photocatalytic membrane reactors (PMR). *Water Sci. Technol.* **2020**, *81*, 131–137. [CrossRef] [PubMed]
132. Astuti, A.R.A.; Saputera, W.H.; Ariono, D.; Wenten, I.G.; Sasongko, D. Membrane contactor-photocatalytic hybrid system for carbon dioxide capture and conversion to formic acid. *Results Eng.* **2024**, *22*, 102085. [CrossRef]
133. Khataee, A.; Honarnezhad, R.; Fathinia, M. Degradation of sodium isopropyl xanthate from aqueous solution using sonocatalytic process in the presence of chalcocite nanoparticles: Insights into the degradation mechanism and phyto-toxicity impacts. *J. Environ. Manag.* **2018**, *211*, 225–237. [CrossRef] [PubMed]
134. Wang, P.H.; Fane, A.G.; Lim, T.T. Evaluation of a submerged membrane vis-LED photoreactor (sMPR) for carbamazepine degradation and TiO_2 separation. *Chem. Eng. J.* **2013**, *215*, 240–251. [CrossRef]
135. Xue, X.D.; Fu, J.F.; Zhu, W.F.; Guo, X.C. Separation of ultrafine TiO_2 from aqueous suspension and its reuse using cross-flow ultrafiltration (CFU). *Desalination* **2008**, *225*, 29–40. [CrossRef]
136. Grandcolas, M.; Oudin, E. Enhanced photocatalytic activity of electrospun TiO_2/polyacrylonitrile membranes in a crossflow reactor using dual lights. *Environ. Chem. Lett.* **2022**, *21*, 633–638. [CrossRef]
137. Le, T.M.H.; Wang, Y.N.; Li, C.; Wang, R.; Sairiam, S. Durable PVDF photocatalytic membranes with TiO_2@PDA incorporated into/onto for dye degradation under visible-light. *Chem. Eng. J.* **2024**, *499*, 156215. [CrossRef]
138. Athanasekou, C.P.; Moustakas, N.G.; Morales-Torres, S.; Pastrana-Martínez, L.M.; Figueiredob, J.L.; Faria, J.L.; Silva, A.M.T.; Dona-Rodriguez, J.M.; Romanos, G.E.M.; Falaras, P. Ceramic photocatalytic membranes for water filtration under UV and visible light. *Appl. Catal. B Environ.* **2015**, *178*, 12–19. [CrossRef]
139. Kim, I.; Yamashita, N.; Tanaka, H. Photodegradation of pharmaceuticals and personal care products during UV and UV/H_2O_2 treatments. *Chemosphere* **2009**, *77*, 518–525. [CrossRef]
140. Kim, I.; Tanaka, H. Photodegradation characteristics of PPCPs in water with UV treatment. *Environ. Int.* **2009**, *35*, 793–802. [CrossRef]
141. Phan, D.D.; Babick, F.; Nguyen, M.T.; Wessely, B.; Stintz, M. Modelling the influence of mass transfer on fixed-bed photocatalytic membrane reactors. *Chem. Eng. Sci.* **2017**, *173*, 242–252. [CrossRef]
142. Hou, L.B.; Catherine, H.N.; Harada, K.; Yoshida, M.; Chen, Y.L.; Hu, C.C. Reactive seeding growth of cobalt-doped MIL-88B(Fe) on Al_2O_3 membrane for phenol removal in a photocatalytic membrane reactor. *J. Membr. Sci.* **2023**, *680*, 121730. [CrossRef]
143. Molinari, R.; Palmisano, L.; Drioli, E.; Schiavello, M. Studies on various reactor configurations for coupling photocatalysis and membrane processes in water purification. *J. Membr. Sci.* **2002**, *206*, 399–415. [CrossRef]
144. Petsi, P.N.; Sarasidis, V.C.; Plakas, K.V.; Karabelas, A.J. Reduction of nitrates in a photocatalytic membrane reactor in the presence of organic acids. *J. Environ. Manag.* **2021**, *298*, 113526. [CrossRef] [PubMed]
145. Peñas-Garzón, M.; Sampaio, M.J.; Chávez, A.M.; Silva, A.M.T.; Silva, C.G.; Faria, J.L. Film-immobilized carbon nitride for the degradation of pharmaceuticals: A continuous flow photoreactor performance upheld by excitation-emission matrix fluorescence spectroscopy. *Chem. Eng. J.* **2024**, *500*, 157384. [CrossRef]
146. Tian, J.; Zhang, Y.; Qian, F.; Cao, M.; Cheng, Y.; Li, J.; Tian, M.; Li, W.; Wang, L. The design of novel swash plate photocatalytic reactor with PAN/BiInOCl membrane photocatalyst for excellent RhB degradation. *J. Alloys Compd.* **2023**, *968*, 171894. [CrossRef]
147. Liu, N.; Zhang, W.F.; Li, X.Y.; Qu, R.X.; Zhang, Q.D.; Wei, Y.; Feng, L.; Jiang, L. Fabrication of robust mesh with anchored Ag nanoparticles for oil removal and in situ catalytic reduction of aromatic dyes. *J. Mater. Chem. A* **2017**, *5*, 15822–15827. [CrossRef]
148. Li, C.C.; Yu, H.W.; Huang, B.; Liu, G.J.; Guo, Y.H.; Zhu, H.L.; Yu, B. Fabrication of anatase TiO_2/PVDF composite membrane for oil-in-water emulsion separation and dye photocatalytic degradation. *Membranes* **2023**, *13*, 364. [CrossRef]
149. Yang, C.Y.; Zhang, Z.H.; Wang, P.; Xu, P.; Shen, T.Y.; Xin, Y.J.; Zhang, G.S. A novel vertical immobilized photocatalytic membrane reactor based on Bi_2WO_6-g-C_3N_4/PVDF for enhanced removal of atrazine, anti-fouling performance and long-term stability. *Chem. Eng. J.* **2023**, *471*, 144672. [CrossRef]
150. Seger, B.; Kamat, P.V. Fuel cell geared in reverse: Photocatalytic hydrogen production using a TiO_2/Nafion/Pt membrane assembly with No applied bias. *J. Phys. Chem. C* **2009**, *113*, 18946–18952. [CrossRef]
151. Tsydenov, D.E.; Parmon, V.N.; Vorontsov, A.V. Toward the design of asymmetric photocatalytic membranes for hydrogen production: Preparation of TiO_2-based membranes and their properties. *Int. J. Hydrogen Energy* **2012**, *37*, 11046–11060. [CrossRef]
152. Zhang, Y.; Li, B.; Wu, L. GO-assisted supramolecular framework membrane for high-performance separation of nanosized oil-in-water emulsions. *Acta Phys.-Chim. Sin.* **2024**, *40*, 2305038. [CrossRef]
153. Wang, T.H.; Chen, M.J.; Lai, Y.S.; Doong, R.A.; Westerhoff, P.; Rittmann, B. High-efficiency photocatalytic H_2O_2 production in a dual optical- and membrane-fiber system. *ACS Sustain. Chem. Eng.* **2023**, *11*, 6465–6473. [CrossRef]
154. Hisatomi, T.; Domen, K. Reaction systems for solar hydrogen production via water splitting with particulate semiconductor photocatalysts. *Nat. Catal.* **2019**, *2*, 387–399. [CrossRef]
155. Zhou, P.; Navid, I.A.; Ma, Y.; Xiao, Y.; Wang, P.; Ye, Z.; Zhou, B.; Sun, K.; Mi, Z. Solar-to-hydrogen efficiency of more than 9% in photocatalytic water splitting. *Nature* **2023**, *613*, 66–70. [CrossRef]

156. Han, X.; Qian, A.; Ye, L.; Fan, M.; Yu, J.; Zhang, C.; Zheng, Y.; Yang, Q. Photocatalytic materials and reactors for hydrogen production: A review. *Mol. Chem. Eng.* **2025**, *1*, 100001. [CrossRef]
157. Sun, X.; Chen, Z.; Shen, Y.; Lu, J.; Shi, Y.; Cui, Y.; Guo, F.; Shi, W. Plasmonic coupling-boosted photothermal nanoreactor for efficient solar light-driven photocatalytic water splitting. *J. Colloid. Interface Sci.* **2023**, *652*, 1016–1027. [CrossRef] [PubMed]
158. Schröder, M.; Kailasam, K.; Borgmeyer, J.; Neumann, M.; Thomas, A.; Schomäcker, R.; Schwarze, M. Hydrogen Evolution Reaction in a Large-Scale Reactor using a Carbon Nitride Photocatalyst under Natural Sunlight Irradiation. *Energy Technol.* **2015**, *3*, 1014–1017. [CrossRef]
159. Plakas, K.V.; Sarasidis, V.C.; Patsios, S.I.; Lambropoulou, D.A.; Karabelas, A.J. Novel pilot scale continuous photocatalytic membrane reactor for removal of organic micropollutants from water. *Chem. Eng. J.* **2016**, *304*, 335–343. [CrossRef]
160. Jiang, H.B.; Zhang, G.L.; Huang, T.; Chen, J.Y.; Wang, Q.D.; Meng, Q. Photocatalytic membrane reactor for degradation of acid red B wastewater. *Chem. Eng. J.* **2010**, *156*, 571–577. [CrossRef]
161. Hu, C.; Wang, M.-S.; Chen, C.-H.; Chen, Y.-R.; Huang, P.-H.; Tung, K.-L. Phosphorus-doped g-C_3N_4 integrated photocatalytic membrane reactor for wastewater treatment. *J. Membr. Sci.* **2019**, *580*, 1–11. [CrossRef]
162. Zou, Q.; Zhang, Z.P.; Li, H.F.; Pei, W.K.; Ding, M.N.; Xie, Z.L.; Huo, Y.N.; Li, H.X. Synergistic removal of organic pollutant and metal ions in photocatalysis-membrane distillation system. *Appl. Catal. B Environ.* **2020**, *264*, 118463. [CrossRef]
163. Ashar, A.; Bhatti, I.A.; Ashraf, M.; Tahir, A.A.; Aziz, H.; Yousuf, M.; Ahmad, M.; Mohsin, M.; Bhutta, Z.A. Fe^{3+}@ ZnO/polyester based solar photocatalytic membrane reactor for abatement of RB5 dye. *J. Clean. Prod.* **2020**, *246*, 119010. [CrossRef]
164. Gao, X.Y.; Meng, X.C. Photocatalysis for heavy metal treatment: A review. *Processes* **2021**, *9*, 1729. [CrossRef]
165. Liu, Z.L.; Zhang, C.; Liu, L.Z.; Zhang, T.S.; Wang, J.; Wang, R.; Du, T.; Yang, C.Y.; Zhang, L.; Xie, L.X.; et al. A conductive network and dipole field for harnessing photogenerated charge kinetics. *Adv. Mater.* **2021**, *33*, 2104099. [CrossRef]
166. Fouda-Mbanga, B.G.; Prabakaran, E.; Pillay, K. Carbohydrate biopolymers, lignin based adsorbents for removal of heavy metals (Cd^{2+}, Pb^{2+}, Zn^{2+}) from wastewater, regeneration and reuse for spent adsorbents including latent fingerprint detection: A review. *Biotechnol. Rep.* **2021**, *30*, e00609. [CrossRef]
167. Arshad, F.; Al Momani, D.E.; de Vos, W.M.; Zou, L.D. Nanocomposite membrane for simultaneous removal of dye and heavy metal ions from wastewater. *J. Environ. Manag.* **2024**, *371*, 123242. [CrossRef]
168. Subramani, A.; Jacangelo, J.G. Emerging desalination technologies for water treatment: A critical review. *Water Res.* **2015**, *75*, 164–187. [CrossRef]
169. dos Anjos Silva, G.R.; do Espírito Santo, A.S.S.; Tomaz, G.S.; Moreira, V.R.; de Oliveira Machado, C.P.; Viana, M.M.; Amaral, M.C.S. Photocatalytic modified membranes with dopamine and GO-TiO_2 applied to petroleum refinery wastewater treatment. *Sep. Purif. Technol.* **2025**, *361*, 131621. [CrossRef]
170. Rathna, T.; PonnanEttiyappan, J.; RubenSudhakar, D. Fabrication of visible-light assisted TiO_2-WO_3-PANI membrane for effective reduction of chromium (VI) in photocatalytic membrane reactor. *Environ. Technol. Innov.* **2021**, *24*, 102023. [CrossRef]
171. Chen, J.J.; Oh, P.C.; Saleh, S.B.M. Recent development on photocatalysts and membrane processes for photoreduction of CO_2 into C1 solar fuels. *Korean J. Chem. Eng.* **2024**, *41*, 609–637. [CrossRef]
172. de Richter, R.K.; Ming, T.Z.; Caillol, S. Fighting global warming by photocatalytic reduction of CO_2 using giant photocatalytic reactors. *Renew. Sustain. Enrergy Rev.* **2013**, *19*, 82–106. [CrossRef]
173. Mohd Saleh, S.; Oh, P.C.; Zain, M.M.; Quek, V.C.; Zulkifli, A.S.; Chew, T.L. Revolutionizing CO_2 reduction with TiO_2 photocatalyst immobilized on polytetrafluoroethylene (PTFE) membrane. *J. Ind. Eng. Chem.* **2024**, *131*, 230–239. [CrossRef]
174. Cheng, X.; Chen, R.; Zhu, X.; Liao, Q.; He, X.; Li, S.; Li, L. Optofluidic membrane microreactor for photocatalytic reduction of CO_2. *Int. J. Hydrogen Energy* **2016**, *41*, 2457–2465. [CrossRef]
175. Liu, B.; Li, D.; Yao, J.; Sun, H. Enhanced CO_2 selectivity of polyimide membranes through dispersion of polyethyleneimine decorated UiO-66 particles. *J. Appl. Polym. Sci.* **2020**, *137*, 49068. [CrossRef]
176. Moulis, F.; Krysa, J. Photocatalytic degradation of several VOCs (-hexane, -butyl acetate and toluene) on TiO_2 layer in a closed-loop reactor. *Catal. Today* **2013**, *209*, 153–158. [CrossRef]
177. Debono, O.; Hequet, V.; Le Coq, L.; Locoge, N.; Thevenet, F. VOC ternary mixture effect on ppb level photocatalytic oxidation: Removal kinetic, reaction intermediates and mineralization. *Appl. Catal. B Environ.* **2017**, *218*, 359–369. [CrossRef]
178. Khalilzadeh, A.; Fatemi, S. Spouted bed reactor for VOC removal by modified nano-TiO_2 photocatalytic particles. *Chem. Eng. Res. Des.* **2016**, *115*, 241–250. [CrossRef]
179. Gérardin, F.; Cloteaux, A.; Simard, J.; Favre, É. A photodriven energy efficient membrane process for trace VOC removal from air: First step to a smart approach. *Chem. Eng. J.* **2021**, *419*, 129566. [CrossRef]
180. McCullagh, C.; Skillen, N.; Adams, M.; Robertson, P.K.J. Photocatalytic reactors for environmental remediation: A review. *J. Chem. Technol. Biotechnol.* **2011**, *86*, 1002–1017. [CrossRef]
181. Deepracha, S.; Atfane, L.; Ayral, A.; Ogawa, M. Simple and efficient method for functionalizing photocatalytic ceramic membranes and assessment of its applicability for wastewater treatment in up-scalable membrane reactors. *Sep. Purif. Technol.* **2021**, *262*, 118307. [CrossRef]

182. Kant, P.; Liang, S.Z.; Rubin, M.; Ozin, G.A.; Dittmeyer, R. Low-cost photoreactors for highly photon/energy-efficient solar-driven synthesis. *Joule* **2023**, *7*, 1347–1362. [CrossRef]
183. Kim, S.; Cho, H.; Joo, H.; Her, N.; Han, J.; Yi, K.; Kim, J.O.; Yoon, J. Evaluation of performance with small and scale-up rotating and flat reactors; photocatalytic degradation of bisphenol A, 17β-estradiol, and 17α-ethynyl estradiol under solar irradiation. *J. Hazard. Mater.* **2017**, *336*, 21–32. [CrossRef]
184. Spasiano, D.; Marotta, R.; Malato, S.; Fernandez-Ibanez, P.; Di Somma, I. Solar photocatalysis: Materials, reactors, some commercial, and pre-industrialized applications. A comprehensive approach. *Appl. Catal. B Environ.* **2015**, *170–171*, 90–123. [CrossRef]
185. Lee, W.H.; Lee, C.W.; Cha, G.D.; Lee, B.-H.; Jeong, J.H.; Park, H.; Heo, J.; Bootharaju, M.S.; Sunwoo, S.-H.; Kim, J.H.; et al. Floatable photocatalytic hydrogel nanocomposites for large-scale solar hydrogen production. *Nat. Nanotechnol.* **2023**, *18*, 754–762. [CrossRef] [PubMed]
186. Hu, C.C.; Chen, Y.C.; Ajebe, E.G.; Tsai, M.C.; Tsai, H.C.; Lee, K.R.; Lai, J.Y. A study on photocatalytic Janus membrane reactor for direct conversion of low concentration carbon dioxide in air to methane: Effects of combination of two-dimensional carbon nanosheets. *Chem. Eng. J.* **2023**, *478*, 147358. [CrossRef]
187. Li, W.; Duan, W.; Liao, G.; Gao, F.; Wang, Y.; Cui, R.; Zhao, J.; Wang, C. 0.68% of solar-to-hydrogen efficiency and high photostability of organic-inorganic membrane catalyst. *Nat. Commun.* **2024**, *15*, 6763. [CrossRef]
188. Fu, H.; Wu, Y.Q.; Guo, Y.H.; Sakurai, T.; Zhang, Q.Q.; Liu, Y.Y.; Zheng, Z.K.; Cheng, H.F.; Wang, Z.Y.; Huang, B.B.; et al. A scalable solar-driven photocatalytic system for separated H_2 and O_2 production from water. *Nat. Commun.* **2025**, *16*, 990. [CrossRef]

Disclaimer/Publisher's Note: The statements, opinions and data contained in all publications are solely those of the individual author(s) and contributor(s) and not of MDPI and/or the editor(s). MDPI and/or the editor(s) disclaim responsibility for any injury to people or property resulting from any ideas, methods, instructions or products referred to in the content.

catalysts

MDPI

Article

Green Synthesis of TiO_2-CeO_2 Nanocomposites Using Plant Extracts for Efficient Organic Dye Photodegradation

Dinh Quang Ho [1], Van Duy Lai [2], Quynh Anh Nguyen [1], D. Duc Nguyen [3,4,*] and Duong Duc La [5,*]

[1] School of Chemistry, Biology and Environment, Vinh University, 182 Le Duan Street, Vinh 43100, Vietnam; hodinhquang@vinhuni.edu.vn (D.Q.H.); anhnq@vinhuni.edu.vn (Q.A.N.)
[2] Institute of Materials Science, Vietnam Academy of Science and Technology, 18 Hoang Quoc Viet Street, Cau Giay District, Hanoi 10000, Vietnam
[3] Department of Civil & Energy Systems Engineering, Kyonggi University, Suwon 15442, Republic of Korea
[4] School of Engineering & Technology, Duy Tan University, Da Nang 50217, Vietnam
[5] Institute of Materials, Biology and Environment, 17 Hoang Sam, Nghia Do, Cau Giay District, Hanoi 10000, Vietnam
* Correspondence: dinhduc.nguyen@kyonggi.ac.kr (D.D.N.); duc.duong.la@gmail.com (D.D.L.)

Abstract: The growing presence of hazardous organic pollutants in wastewater poses severe environmental and health risks, necessitating sustainable and efficient treatment solutions. Traditional remediation methods have limitations, highlighting the need for innovative approaches. A green synthesis method was developed to produce TiO_2-CeO_2 nanocomposites using Cleistocalyx operculatus leaf extract. The photocatalytic efficiency of the synthesized nanocomposites was evaluated under simulated sunlight by degrading Methylene Blue (MB) dye. Various compositions were tested to determine the optimal performance. The 0.1% TiO_2-CeO_2 nanocomposite achieved the highest degradation efficiency (95.06% in 150 min) with a reaction rate constant (k) of 18.5×10^{-2} min^{-1}, outperforming commercial TiO_2 (P25, 74.85%, $k \approx 3.7 \times 10^{-2}$ min^{-1}). Additionally, the material maintained excellent stability over eight consecutive cycles with only a slight decrease in efficiency from 95.85% to 93.28%. The enhanced photocatalytic activity is attributed to the synergistic effects of CeO_2 incorporation, which enhances charge separation, extends visible light absorption, and promotes reactive oxygen species (ROS) generation. These findings highlight the potential of green-synthesized TiO_2-CeO_2 nanocomposites as a cost-effective and sustainable solution for wastewater treatment.

Keywords: sustainable photocatalysis; TiO_2-CeO_2 nanocomposite; green synthesis; photocatalytic; wastewater treatment; environmental remediation

1. Introduction

In recent years, the rapid development of industrialization has led to the extensive use of organic compounds in water that pose a risk to our health as well as the environment. Out of the organic compounds, Methylene Blue (MB) is one of the most common dyes that is widely used in dying process of cotton fabrics, silk, and wood [1]. Moreover, MB has potential applications in various industrial fields, such as in testing the freshness of milk and dairy products and treating some fish's diseases [2]. However, MB is regarded as a biologically toxic compound to the environment and life on the earth due to its ability to damage to the nervous system and eyes [1]. Further, like other synthetic dyes that have a complex aromatic molecular structure, MB is stable and hard to degrade naturally. Therefore, MB dye needs to be removed from wastewater.

Many methods have been reported for the removal of MB dye. Although diverse traditional treatment approaches, such as chemical (reduction [3], ozonation [4], precipitation [5], coagulation [6], ion exchange [7]), physical (adsorption [8], selective filters [9], membrane separation [10]), and biological (decomposition by microorganisms [11] such as algae [12] and bacteria [13]) procedures have been effectively applied to clean and treat the wastewater. However, these methods often face several limitations as they operate in specific conditions, produce poisonous byproducts, and require expensive equipment [14]. In addition, due to the presence of aromatic rings in the chemical structure of MB compounds, this dye is highly stable towards sunlight and is also resistant against high temperatures, some oxidizing reagents and microbial disintegration. Thus, it is necessary to develop more useful and advanced techniques to remove or degrade MB dye in water.

Photocatalyst degradation appears to be a promising alternative for dye removal in wastewater due to its simple, cost-effective operation and environment-friendly [15] by quickly converting organic pollutants under light irradiation into simple gases like CO_2, H_2O, or other harmless smaller molecules [15]. In this regard, a nanoparticles-based semiconducting photocatalyst is an attractive candidate for the removal of organic contaminants in wastewater treatment due to their huge surface area, high reactivity, and other dependent features [16]. On account of the photocatalytic activity of semiconductors, the absorbed light with higher energy than the semiconductor band gap will produce electrons and holes, which then can accelerate the redox reactions to degrade the organic pollutants.

Several semiconductor nanomaterials, such as TiO_2 [17], ZnO [18], CuO [19], WO_3 [20], Ag_3PO_4 [21], and CdS [22], have been found to be good photocatalysts for organic dye photodecomposition. In particular, a TiO_2-based photocatalyst is the most popular catalyst for dye degradation owing to its inert chemical properties, high stability, low toxicity and relative availability at low cost [23]. Unfortunately, the optical bandgap of TiO_2 is relatively broad (3.0–3.2 eV), limiting its usage only under UV light with the absorption below 360 nm and affecting its photocatalytic efficiency due to the easy electron–hole recombination [24]. In order to improve its photocatalytic activity, many solutions were proposed. Among them, modification with other materials is an attractive solution because it can improve the lifetime of the photogenerated charges and enhance the spectra response in the visible absorption region. The integration of TiO_2 with various metal oxides such as SnO_2/TiO_2 [25], ZnO/TiO_2 [26], WO_3/TiO_2 [1], Bi_2O_3/TiO_2 [27] and In_2O_3/TiO_2 [28] were reported to have an improved catalytic activity compare to the intrinsic material alone.

Among different metal oxides, cerium (IV) oxide (CeO_2) has attracted much more attention because of its high electrical conductivity and thermal stability, high UV absorption ability, non-toxic, low cost and biocompatibility [29]. Recently, the photocatalytic performance over a CeO_2-based photocatalyst has been widely studied in various applications, such as solar cells, CO_2 conversion and organic pollutant degradation [30]. The most outstanding properties of this metal oxide that facilitate the photoreactions are primarily derived from its high oxygen storage capacity with abundant oxygen vacancies and Ce^{3+} defect sites in the structure of CeO_2 due to its easy transition between the Ce(IV) and Ce(III) oxidation states with the corresponding displacement from CeO_2 and Ce_2O_3 under redox condition that occurs in this particle [31]. The oxygen released by CeO_2 plays an important role in the oxidation reactions. CeO_2 can store oxygen from an aqueous solution and transfer this adsorbed oxygen to TiO_2, these oxygen species are necessary in the oxidation of organic pollutants and also act as electron scavengers which reduce the recombination rate of electron–hole pairs in TiO_2 composites. In addition, various oxidation states of Ce (Ce^{3+} and Ce^{4+}) could favor electron transfer and enhance the charge separation. Thus, these findings suggest that coupling TiO_2 with CeO_2 could lengthen

the lifespan of the photogenerated electron and holes, resulting in an enhancement in the photocatalytic activity.

Recently, cerium dioxide (CeO_2) has attracted considerable attention as a photocatalyst for the degradation of MB, a common dye in wastewater. Due to the face-centered cubic structure of cerium oxide, there are a large number of oxygen vacancies on its surface and body. The existence of these oxygen vacancies makes CeO_2 suitable for applications in adsorption and catalytic remediation of water pollution [32]. For example, Wu et al. prepared CeO_2 for the efficient degradation of volatile organic compounds under vacuum ultraviolet light [33]. In addition, Thanh Tuyen et al. [32] showed that the incorporation of CeO_2 into TiO_2-NTs enhanced the photocatalytic activity in the visible light region. CeO_2/TiO_2-NTs are stable and have potential as visible light photocatalysts for the degradation of organic substances in aqueous solutions.

The photocatalytic performance of TiO_2-CeO_2 nanocomposites is highly dependent on the synthesis method, which significantly influences crystal structure, particle size, and surface characteristics. Various strategies have been employed to enhance their activity [34]. For instance, CeO_2–TiO_2 synthesized via mechanochemical grinding exhibited ~63% degradation of Rhodamine B under visible light after 240 min, attributed to its structural stability and reusability potential [35]. A green synthesis approach using Cleome chelidonii leaf extract resulted in superior MB degradation (95% within 150 min under UV–Vis irradiation), due to reduced band gap, enhanced surface adsorption, and suppressed electron–hole recombination [36]. Moreover, core/shell TiO_2/CeO_2 nanostructures with low CeO_2 content demonstrated remarkable photocatalytic and photoelectrochemical performance, achieving 71% MB degradation and a high photoconversion efficiency of 0.70%, ascribed to efficient charge separation [37]. Notably, a modified sol–gel method produced TiO_2-CeO_2 nanocomposites with a mixed anatase–fluorite heterojunction, ultrasmall particle size (~10 nm), and high BET surface area, leading to enhanced visible light absorption and up to 95% MB degradation under simulated solar irradiation [38]. Among these methods, chemical preparation is the most popular approach to synthesizing nano-photocatalysts, but it requires specific synthetic conditions and toxic chemical precursors that restrict the applications of the products due to serious eco-toxicological concerns.

In this respect, the sustainable green method using natural plant extracts as the precursors to produce nanomaterials is a promising solution because this approach avoids the use of chemicals as well as the toxicity of the products. This process is also more cost-effective because plant materials are abundant in nature. In addition, organic compounds in the plant extract can act as capping or chelating reagents to avoid agglomeration in nanoparticles [39]. To the best of our knowledge, the use of green TiO_2-CeO_2 synthesized from plant extract as a catalyst for dye photodegradation has not been reported before in the literature.

This study aimed to develop a novel green synthesis of TiO_2-CeO_2 nanocomposites using Cleistocalyx operculatus leaf extract and assess their efficacy in removing organic waste, marking a significant advancement in eco-friendly nanomaterial production. The innovative use of ultrasonic solvent extraction—optimized with an ethanol–water ratio of 1/20, a raw material–solvent ratio of 5/30 (g/mL), and a 30 min extraction time—eliminates the need for toxic chemicals, setting a new standard for sustainable synthesis methods. This plant-based approach not only ensures environmentally safe production but also actively supports ecosystem preservation, distinguishing it as a novel, green alternative to conventional chemical-intensive techniques.

The results indicate that TiO_2-CeO_2 nanocomposites are highly effective in decomposing MB under simulated sunlight, achieving up to 95.06% degradation in 150 min—a performance markedly superior to commercial TiO_2 (P25) at 74.85%. The material's feasi-

bility and stability were further validated through photocatalytic recycling experiments, underscoring its strong potential for water pollution treatment using natural sunlight. These findings highlight the novelty of leveraging green-synthesized semiconductor oxides, offering a sustainable, high-performance solution for environmental remediation and advancing the field of photocatalytic wastewater treatment.

2. Results and Discussion

2.1. Morphological and Microstructural Characterization

FESEM images clearly show the change in morphology of TiO_2-CeO_2 nanocomposite materials through two processing stages. In the SEM images at positions (a–c)—the material after synthesis but not through the calcination process—the TiO_2-CeO_2 particles have a dense cloud structure, tightly linked into a regular network without forming individually.

After calcination at 500 °C for 2 h, the TiO_2-CeO_2 nanoparticles exhibited an ill-defined morphology, as illustrated in Figure 1d–f, in contrast to the more dispersed and spherical structures observed in the as-synthesized samples. The cloud-like architecture was retained, with the formation of tightly bonded and agglomerated clusters, indicating partial structural rearrangement and densification induced by thermal treatment.

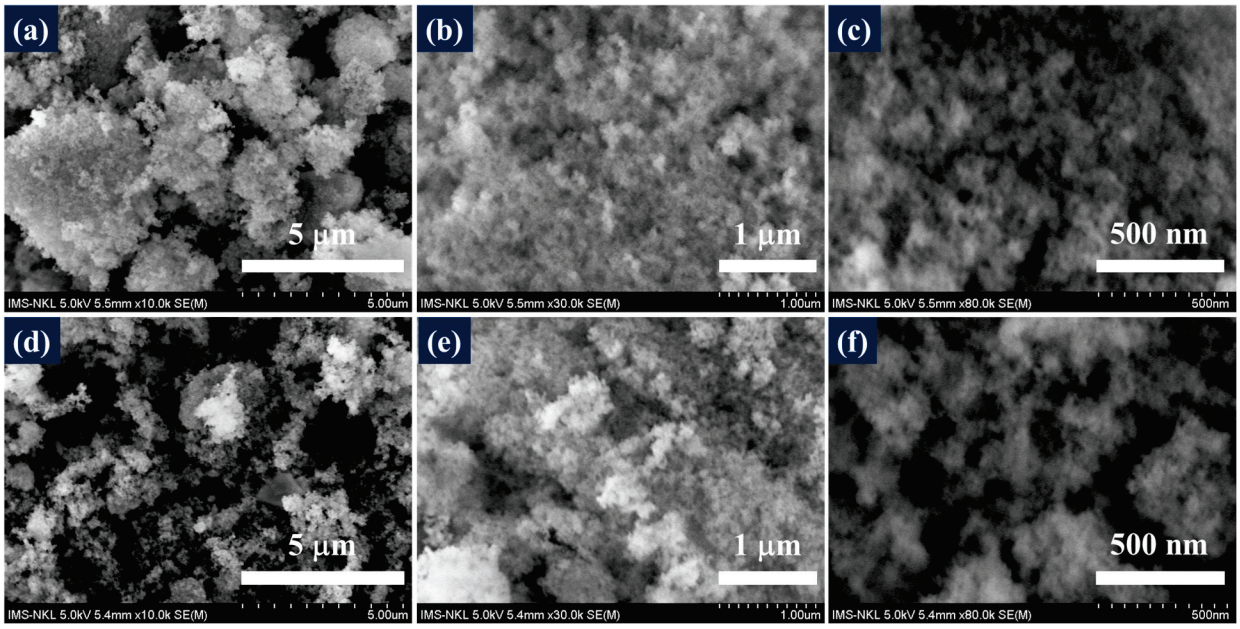


Figure 1. SEM images of 0.1% TiO_2-CeO_2 nanocomposites synthesized via the green method: (**a**–**c**) as-synthesized; (**d**–**f**) annealed at 500 °C for 2 h in air.

Compared to pure TiO_2 nanoparticles (Figure S1, Supporting Information), which exhibit a well-defined spherical morphology, the TiO_2-CeO_2 nanocomposites demonstrated substantial changes in surface texture and particle organization. This morphological evolution underscores the significant role of the Cleistocalyx operculatus leaf extract in the synthesis process. The extract not only serves as a reducing agent but also acts as a stabilizing agent during nanoparticle formation. Specifically, polyphenolic compounds present in the extract are responsible for reducing titanium (Ti^{4+}) and cerium (Ce^{3+}) ions, facilitating the formation of TiO_2-CeO_2 nanostructures. Moreover, these biomolecules likely act as complexing ligands, promoting the formation of interconnected nanoclusters rather than discrete particles.

This bio-assisted synthesis route contributes to enhanced interaction and intimate contact between TiO_2 and CeO_2 domains, which may improve charge separation efficiency and increase photocatalytic performance under light irradiation.

The crystal structures of TiO_2-CeO_2 catalysts were studied via X-ray diffraction (XRD), as shown in Figure 2a. Firstly, all the black-labeled diffraction peaks observed in the XRD pattern align well with the anatase TiO_2 structure (JCPDS card no 21-1272). The pattern displays diffraction peaks corresponding to the (101), (004), (200), (105) and (215) crystal planes of TiO_2 in heterostructure, with a particularly high crystallinity observed on the (101) plane. Secondly, the green labeled in the XRD pattern clearly indicates diffraction on the (111), (200), (220), (311), (222) and (331) crystal planes of CeO_2 in the heterostructure, all of which match the pure cubic structure of CeO_2 (JCPDS card no 34-0394) [40,41]. In addition, no diffraction peaks from other phases were detected, confirming the successful preparation of the TiO_2-CeO_2 heterostructure. Furthermore, the CeO_2 peak in the figure is neither as sharp nor as intense as that of TiO_2, suggesting that CeO_2 has lower crystallinity compared to TiO_2.

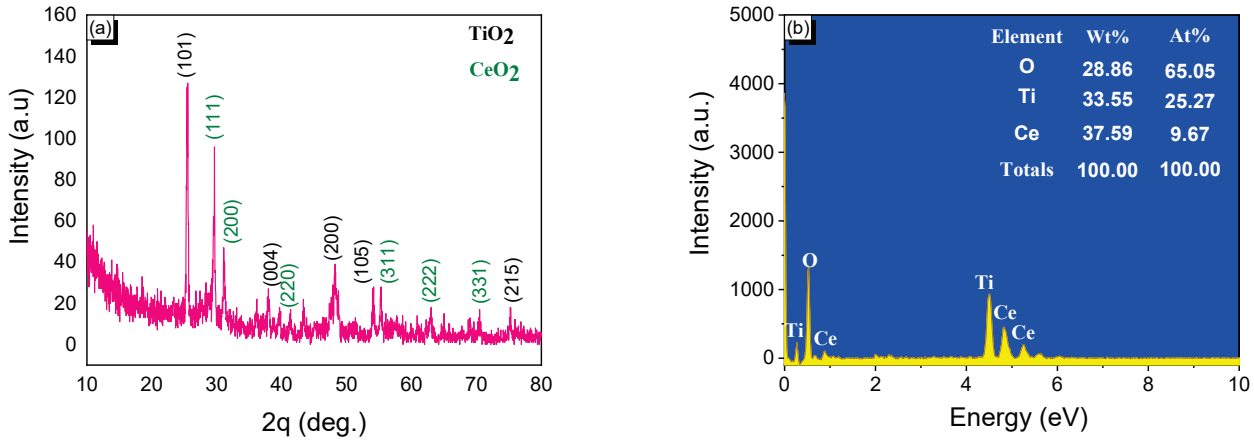


Figure 2. (**a**) XRD pattern and (**b**) EDS spectra of 0.1% TiO_2-CeO_2 nanocomposites.

The average crystallite size (D) of nanocomposite was calculated based on their most intense diffraction peak using the Debye–Scherrer equation:

$$DB = K \cdot \lambda / \beta cos\theta \quad (1)$$

where K is Scherrer's constant (0.9), λ is the wavelength of X-ray diffraction (λ = 1.5406 Å), β is full width at half maximum (FWHM), and θ is the Bragg's angle. The estimated mean grain size of the TiO_2-CeO_2 composite was 0.47 nm, and the diffraction pattern exhibited no obvious impurity peaks.

Energy-dispersive X-ray spectroscopy (EDS) was used to analyze the composition of the TiO_2-CeO_2 composite. As shown in Figure 2b, the spectra confirm the presence of Titanium (Ti), cerium (Ce) and oxygen (O) in the nanocomposite. The atomic ratio of (Ti + Ce)/O was approximately ½, suggesting the formation of TiO_2-CeO_2 composite structure [40].

Figure 3 presents the Raman spectrum of the TiO_2-CeO_2 nanocomposite, where the anatase phase of TiO_2 is identified by characteristic peaks near 148, 195, 395, 514, and 639 cm^{-1}. Additionally, the band at 450 cm^{-1} corresponds to the F_{2g} vibrational mode of CeO_2's cubic fluorite structure [42,43]. The broadening of the spectral peaks in the synthesized samples can be attributed to factors such as small particle size, surface stress, particle size distribution heterogeneity, and non-harmonic effects induced by high temperatures, which collectively cause shifts and variations in the peak positions [44].

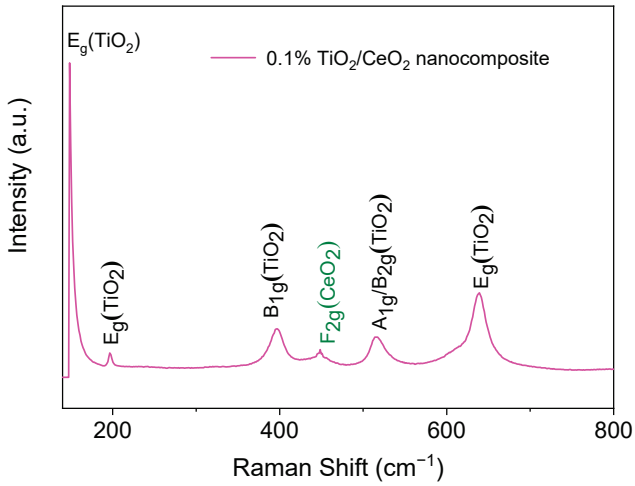


Figure 3. Raman spectra of 0.1% TiO_2-CeO_2 nanocomposites.

The BET analysis of the TiO_2-CeO_2 nanocomposite (Figure 4) revealed a type IV nitrogen adsorption isotherm, characteristic of mesoporous materials, accompanied by a type H3 hysteresis loop as per the IUPAC classification. The measured BET surface area was 29.01 m^2/g, with an average pore volume of 0.23 cc/g and a mean pore diameter of 1.90 nm. The presence of the H3 hysteresis loop suggests the formation of a heterogeneous porous structure, attributed to the capillary condensation process. In mesoporous materials, the disparity between adsorption and desorption isotherms typically indicates complex interactions occurring within the capillary network [43,45].

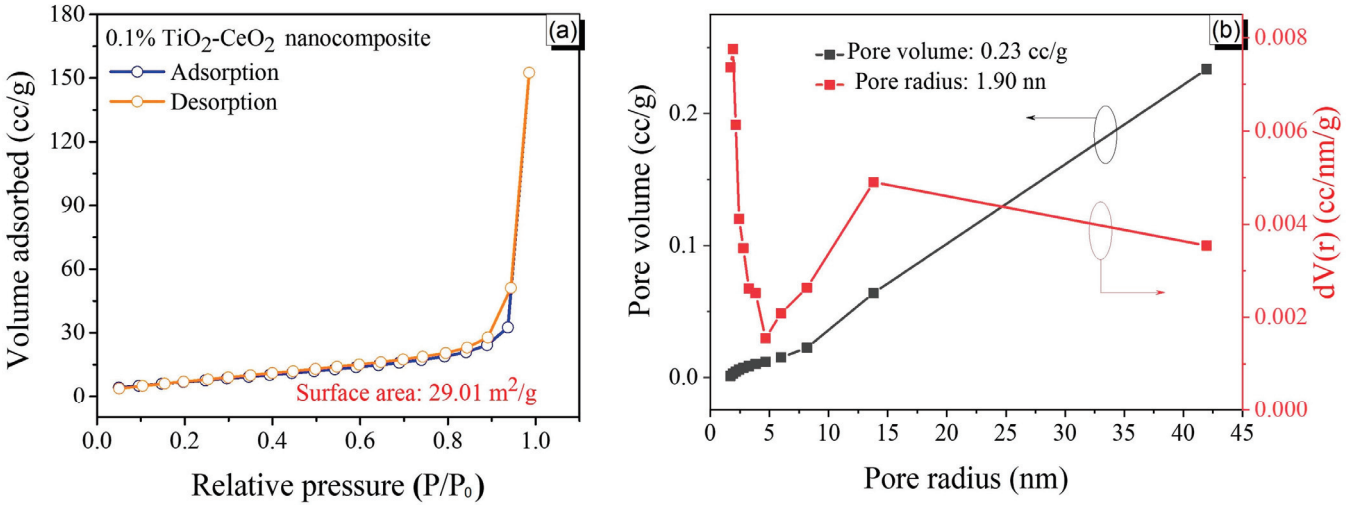


Figure 4. (**a**) Nitrogen adsorption/desorption characterization, and (**b**) pore size and volume of 0.1% TiO_2-CeO_2 nanocomposites.

The UV–Vis diffuse reflectance spectra of pure TiO_2 and TiO_2-CeO_2 nanocomposites (Figure 5a,c) reveal significant optical absorption from the UV to the visible region. Pure TiO_2 exhibits an absorption edge around 400 nm, consistent with its intrinsic band gap (~3.15 eV), while the TiO_2-CeO_2 nanocomposite shows a red-shifted absorption edge approaching 450 nm, indicating improved light harvesting in the visible region [14,40].

The Tauc plots (Figure 5b,d) further quantify this red shift, showing a decrease in the direct band gap energy from 3.15 eV for pure TiO_2 to 2.57 eV for the TiO_2-CeO_2 nanocomposite [40]. This notable band gap narrowing suggests a modification of the electronic structure due to CeO_2 incorporation. Specifically, the presence of cerium in

mixed valence states (Ce^{4+}/Ce^{3+}) plays a critical role in introducing localized impurity states within the TiO_2 band gap.

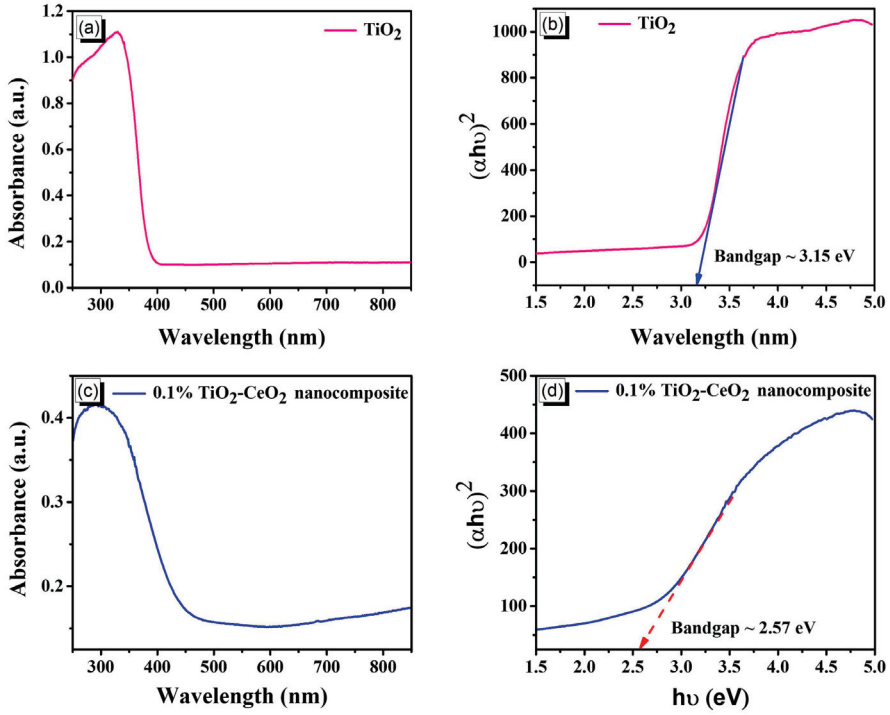


Figure 5. UV–Vis diffuse reflectance spectra and Tauc plots for band gap estimation of pure TiO_2 (**a**,**b**) and (**c**,**d**) 0.1% TiO_2-CeO_2 nanocomposites.

From a physicochemical standpoint, the Ce^{4+}/Ce^{3+} redox couple introduces oxygen vacancies and intermediate energy levels that facilitate electron excitation under lower-energy visible light. The Ce^{3+} species, formed via partial reduction of Ce^{4+}, generates localized 4f states below the conduction band of TiO_2, thereby creating a cascade of electronic states that effectively bridge the TiO_2 band gap. These defect states act as shallow traps for charge carriers, improving charge separation and extending the photoresponse into the visible spectrum.

Moreover, the intimate interfacial contact between TiO_2 and CeO_2 in the composite enhances charge transfer dynamics. Electrons photoexcited in TiO_2 can be efficiently transferred to the CeO_2 phase, where Ce^{4+} can act as an electron sink, being reduced to Ce^{3+}. This process not only mitigates charge recombination but also regenerates Ce^{4+} sites, enabling continuous redox cycling that is beneficial for photocatalytic activity.

2.2. Evaluation of the Photocatalytic Degradation Efficiency of TiO_2-CeO_2 Nanoparticles on Methylene Blue

Photocatalytic degradation experiments of MB were conducted using TiO_2-CeO_2 nanocomposites with different CeO_2 loadings (0.1%, 0.2%, and 1%) under simulated sunlight and compared with commercial TiO_2 (P25) as a reference. Over time, UV–Vis spectra of the MB solution were recorded to monitor the reduction in absorbance intensity, allowing the estimation of degradation efficiency.

The UV–Vis spectra revealed that MB exhibits strong absorption between 500 and 750 nm, with a peak at 664 nm. As shown in Figure 6, the absorbance peak at 664 nm progressively decreased with irradiation time, indicating effective photocatalytic degradation

of MB by TiO_2-CeO_2 nanocomposites. The degradation efficiency (H) was calculated using the formula:

$$H = (C0 - Ct)/C0 \times 100\% \quad (2)$$

where C_0 and C_t are the initial and time-dependent concentrations of MB (mg/L), respectively.

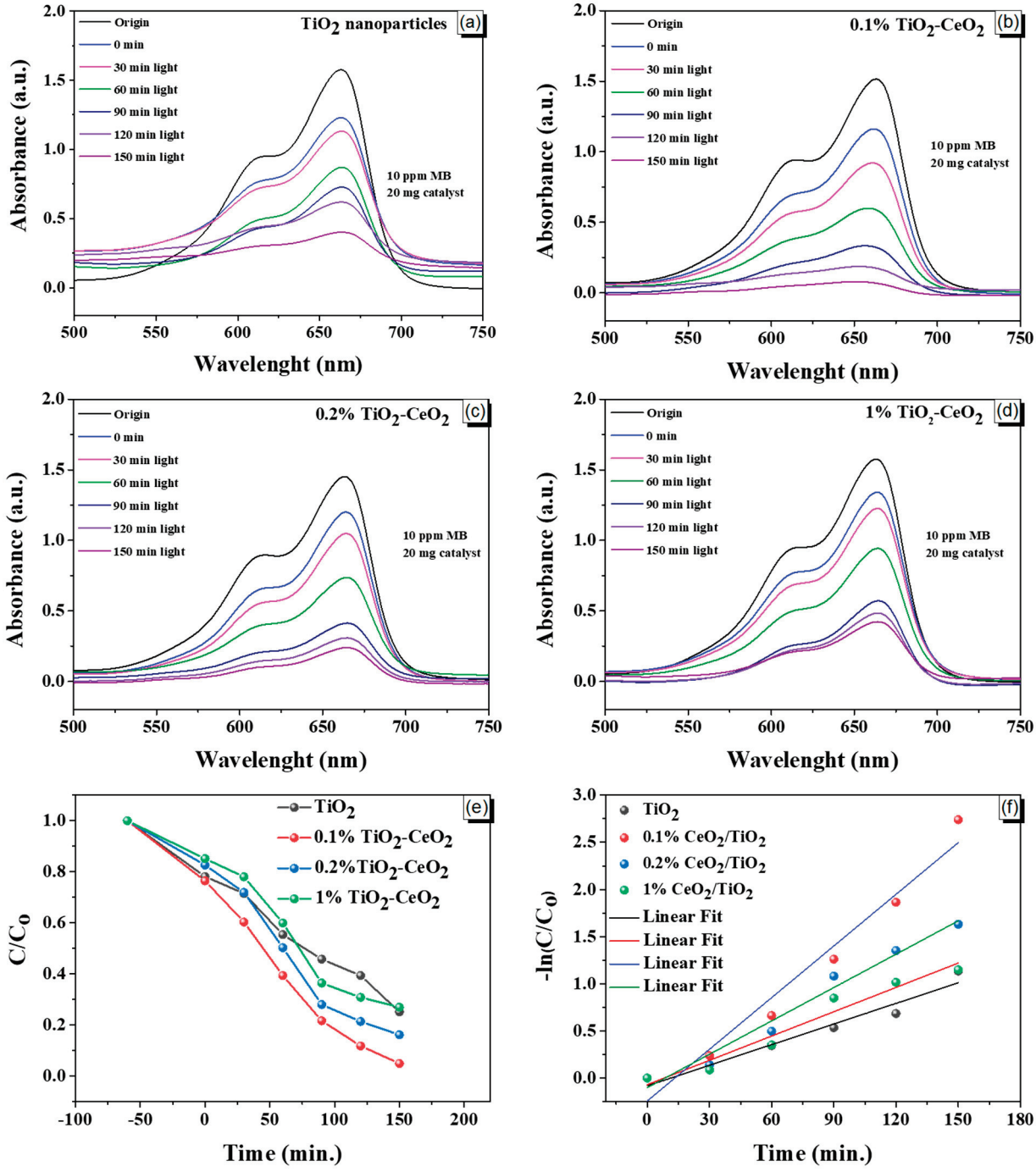


Figure 6. (**a**) UV–Vis absorption spectra of methylene blue degraded by TiO_2 nanoparticles; (**b**–**d**) UV–Vis absorption spectra of methylene blue degraded by (1%, 0.1%, 0.2%) CeO_2/TiO_2 nanocomposite; (**e**) concentration of methylene blue (C/C_0) over time for different photocatalysts; and (**f**) over time for different photocatalysts ($-\ln(C/C_0)$ vs. time) for Methylene Blue degradation.

Figure 6e clearly demonstrates that the photocatalytic activity of TiO_2-CeO_2 nanocomposites (0.1%, 0.2%, and 1%) was superior to that of P25. After 150 min of irradiation, the MB degradation rates for P25, 0.1% TiO_2-CeO_2, 0.2% TiO_2-CeO_2, and 1% TiO_2-CeO_2 were

74.85%, 95.06%, 83.82%, and 73.01%, respectively. The results indicate that under simulated sunlight, the 0.1% TiO_2-CeO_2 nanocomposite achieved the highest MB degradation of approximately 95.06% after 150 min, with a reaction rate constant $k \approx 18.5 \times 10^{-2}$ phút^{-1}. In contrast, P25 showed a degradation efficiency of 74.85% with a lower reaction rate constant $k \approx 3.7 \times 10^{-2}$ phút^{-1}. This superior performance of the 0.1% TiO_2-CeO_2 nanocomposite can be attributed to its optimal CeO_2 loading, which enhances light absorption and electron–hole pair separation, thereby improving photocatalytic efficiency.

The photocatalytic performance of TiO_2-CeO_2, as shown in Table 1, surpasses that of many other catalyst systems, including pure CeO_2, CeO_2 doped with metal oxides, precious metals, and graphene oxide (GO). This system effectively degrades MB under Xenon lamp irradiation, reducing the required catalyst amount while optimizing reaction volume. Compared to systems reliant on UV lamps, TiO_2-CeO_2 is more environmentally friendly and cost-effective, especially when used with a Xenon lamp or sunlight. UV lamps consume more energy and pose potential health risks, whereas this method lowers operating costs, minimizes environmental impact, and enhances sustainability. However, its performance is influenced by factors such as solution concentration, catalyst dosage, and irradiation time. Despite Table 1 being for reference purposes, TiO_2-CeO_2 remains a promising candidate for environmental remediation due to its high efficiency, low cost, and eco-friendly nature.

Table 1. Comparative Analysis of Methylene Blue Photodegradation Efficiency by TiO_2-CeO_2 Nanocomposites.

Photocatalyst	Weight of Catalyst	Volume of MB Solution	Initial MB Solution Concentration	Degr. Time (min)	Light Source	Photo Degr. Effic. (%)	Ref.
CeO_2 NPs	60 mg	250 mL	20 mg/L	90	UV light	90.84	[46]
CeO_2 NPs	0.10 g	50 mL	20 mg/L	90	Visible light, (Xenon arc lamp, 300 W)	98	[47]
Ag/CeO_2	10 mg	100 mL	30 mg/L	120	Visible light (Xenon lamp, 400 nm)	94	[48]
CeO_2-NPs/GO	2.5 mg	10 mL	5 mg/L	90	UV-A light	90	[49]
0.1% CeO_2–TiO_2	3 g	100 mL	10 µmol/L	60	UV light (15 W)	95	[50]
CeO_2–TiO_2 (5CeTiO)	10 mg		20 mg/L	150	UV–Vis light	95	[36]
TiO_2/CeO_2	40 mg		40 mg/L	40	UV light	71	[37]
SnO_2/CeO_2		100 mL	20 mg/L	120	UV light (40 W)	80	[51]
TiO_2/SnO_2/CeO_2	200 mg	50 mL	10 mg/L	120	UV lamp (254 nm)	85.5	[52]
0.1% TiO_2-CeO_2 nanocomposite	30 mg	20 mL	10 mg/L	150	Xenon lamp (350 W)	95.06	This work

Stability is an important factor when evaluating the practicality of photocatalytic materials. The photocatalytic performance of 0.1% TiO_2-CeO_2 nanocomposites was tested over eight consecutive reuse cycles. After each degradation cycle, the material was recovered by centrifugation and washed with ethanol. As shown in Figure 7, under simulated sunlight, the removal efficiency of MB only slightly decreased from 95.85% to 93.28% after eight cycles. This indicates that the TiO_2-CeO_2 nanocomposites maintain stable photocatalytic activity, highlighting their potential for sustainable use in practical applications.

Figure 8 illustrates the effects of reactive species scavengers on the photocatalytic degradation of MB, aiming to elucidate the predominant active species involved in the degradation mechanism over 0.1% TiO_2-CeO_2 nanocomposites. p-Benzoquinone (BQ), isopropyl alcohol (IPA), and ammonium oxalate (AO) were employed as selective scavengers for superoxide radicals ($O_2^{-\bullet}$), hydroxyl radicals ($OH^\bullet$), and photogenerated holes (h^+), respectively. The introduction of all scavengers led to a significant suppression of

MB degradation efficiency, indicating the involvement of multiple reactive species in the photocatalytic process.

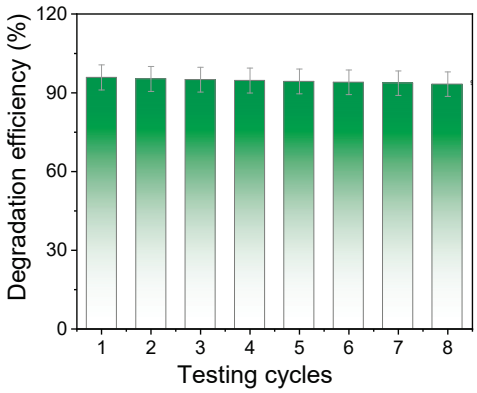


Figure 7. The stability of 0.1% TiO_2-CeO_2 nanocomposites photocatalytic activity for the degradation of MB.

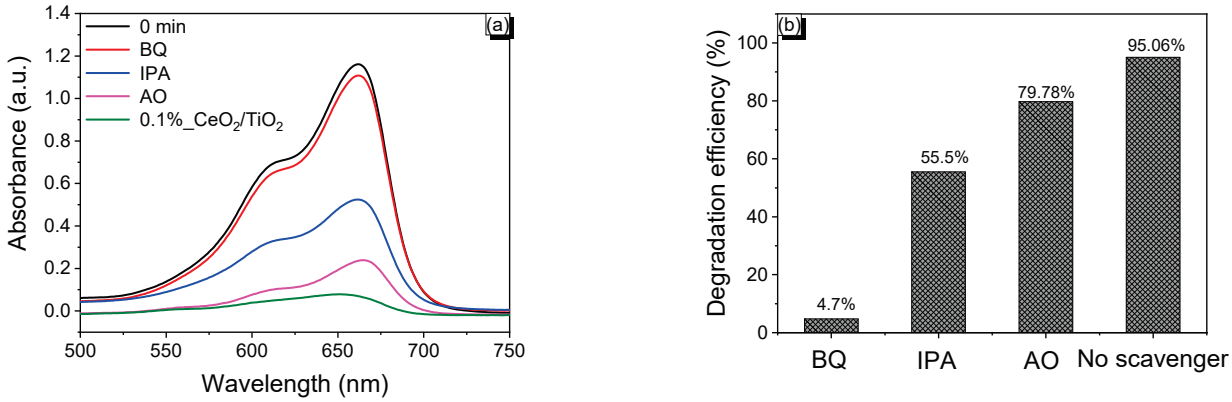


Figure 8. Influence of various radical scavengers on the photocatalytic degradation of MB over 0.1% TiO_2-CeO_2 composites: (**a**) UV–Vis absorption spectra and (**b**) degradation efficiencies.

Specifically, the degradation efficiency decreased to 4.7%, 55.5%, and 79.8% in the presence of BQ, IPA, and AO, respectively. Notably, the most pronounced inhibition was observed with BQ, highlighting the dominant role of superoxide radicals ($O_2^{-\bullet}$) in the photocatalytic mechanism. These findings suggest that ($O_2^{-\bullet}$) species primarily drive the oxidative degradation pathway of MB, while $OH^\bullet$ and h^+ also contribute to a lesser extent. Based on these results, a plausible photocatalytic degradation mechanism involving the generation and participation of these reactive species is proposed for the 0.1% TiO_2-CeO_2 composite system.

Figure 9 illustrates the proposed mechanism of MB photocatalytic reaction over TiO_2-CeO_2 catalyst. Upon light irradiation, both CeO_2 and TiO_2 absorb photon, exciting electrons to their respective conduction bands (CB), leaving behind holes in their valence band (VB). Since the CB energy of CeO_2 is more negative than that of TiO_2, electrons in the CB of CeO_2 can easily jumped to TiO_2's CB. These electrons interact with O_2 molecules, forming various reactive oxygen radical such as superoxide radicals (O_2^{*-}) and hydroxyl radical ($OOH^\bullet$/$OH^\bullet$) on the surface of nanocomposite catalyst. Simultaneously, holes are transferred from the VB of TiO_2 to the VB of CeO_2, where they react with H_2O molecules to generate additional hydroxyl radicals. These active species on the surface of catalyst initiate the dye degradation reaction, and then convert the MB molecules into CO_2, H_2O and

inorganic anions. The possible photodegradation reactions for TiO_2-CeO_2 are described below [32,37,53]:

$$TiO_2\text{-}CeO_2 + h\lambda \rightarrow h^+ + e^- \quad (3)$$

$$h^+ + H_2O \rightarrow H^+ + OH^\bullet \quad (4)$$

$$e^- + O_2 \rightarrow O_2^{-\bullet} \quad (5)$$

$$O_2^{-\bullet} + H_2O \rightarrow OOH^\bullet + OH^- \quad (6)$$

$$2OOH^\bullet \rightarrow H_2O_2 + O_2 \quad (7)$$

$$H_2O_2 + e^- \rightarrow OH^- + OH^\bullet \quad (8)$$

$$Ce^{4+} + e^- \rightarrow Ce^{3+} \quad (9)$$

$$Ce^{3+} + O_2 \rightarrow Ce^{4+} + O_2^{-\bullet} \quad (10)$$

$$(OH^\bullet,\ O_2^{-\bullet} + MB \rightarrow \text{products}) \quad (11)$$

It has been suggested that the enhanced photocatalytic performance of TiO_2-CeO_2 catalyst could be attributed to the extended charge lifetime due to the presence of Ce^{3+} species within the composites. When the catalyst is exposed to light, the photogenerated electrons are captured by Ce^{4+}, reducing it to Ce^{3+}, which may induce charge imbalance or strain, leading to the formation of oxygen vacancies. The Ce^{3+} was then reoxidized to Ce^{4+} by adsorbed oxygen in this system. The coexistence of Ce^{4+} and Ce^{3+}, along with oxygen vacancies in the composite, causes the 4f band to split into occupied and unoccupied energy levels just below the CB of TiO_2. This inter-band transition from Ce^{3+} promotes interfacial charge transfer, reducing the band gap and thus enhancing photocatalytic degradation.

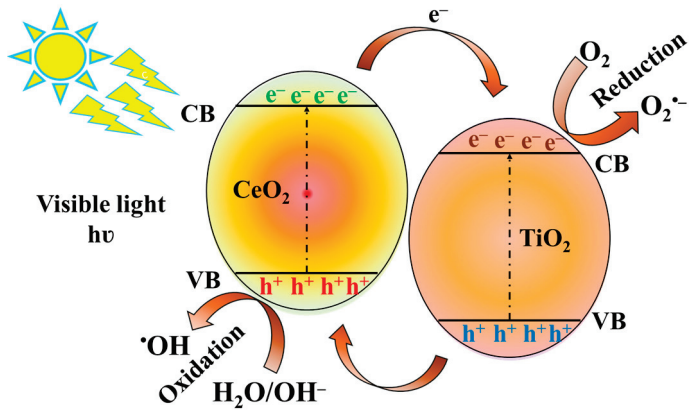


Figure 9. Proposed photocatalytic mechanism of TiO_2-CeO_2 composites under simulated sunlight illumination.

3. Materials and Methods

3.1. Materials

The synthetic materials, including Xeri nitrat hexahydrat ($Ce(NO_3)_3 \cdot 6H_2O$, ≥99.0%) and Ethanol (C_2H_5OH, ≥99.8%) were supplied by Sigma-Aldrich (St. Louis, MO, USA), while Titanium oxide (TiO_2, 99%) was purchased from Xilong (Shantou, China). Deionized (DI) water was used to dissolve the chemicals and remove impurities during the measurement.

3.2. Synthesis of Cleistocalyx Operculatus Leaf Extract

The synthesis process of *Cleistocalyx operculatus* leaf extract is described in (Figure 10A). Leaves of CE (*Cleistocalyx operculatus*) were collected in Ha Tay Province, Vietnam, and identified. The CE leaves were dried and ground in powder form. Dried CE leaves (5 g) were heated and constantly stirred in 30 mL of ethanol at a temperature of 50–60 °C for 2 h. Finally, the mixture was filtered using a vacuum filtration system to remove solid residues, yielding a clear, concentrated extract ready for further analysis.

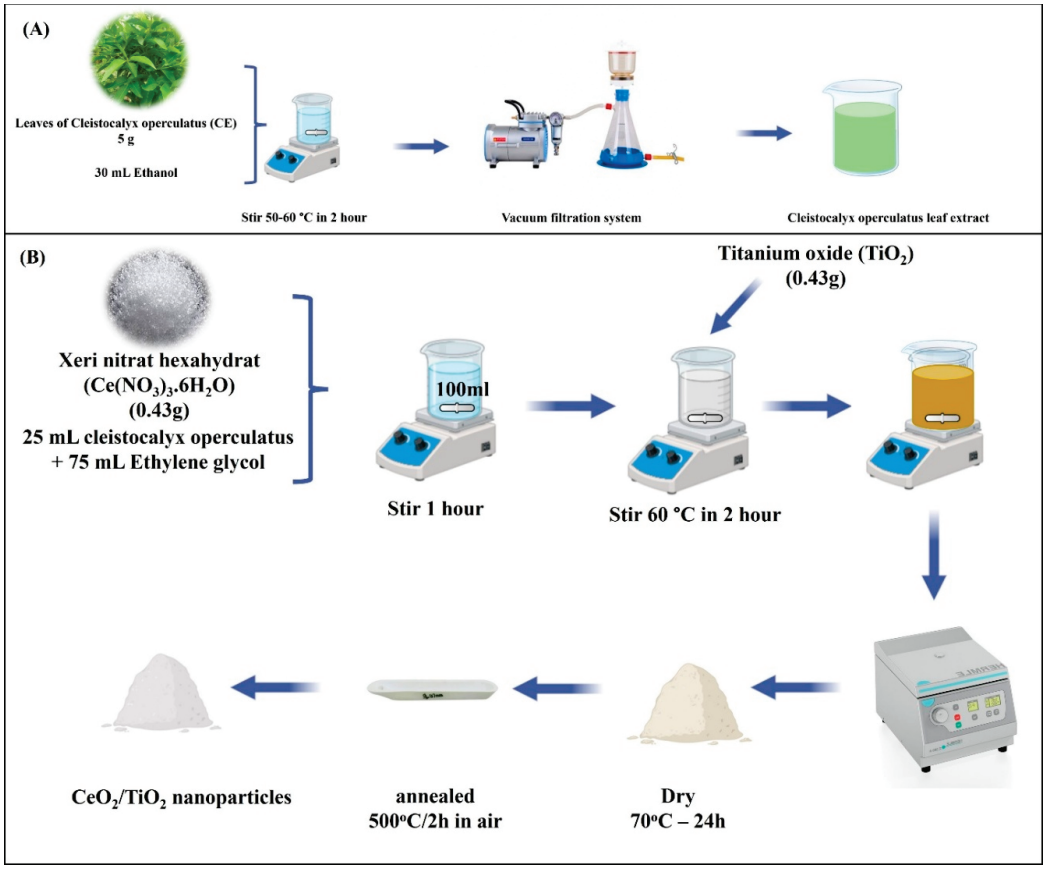


Figure 10. The schematic diagram of synthesis (**A**) extraction of *Cleistocalyx operculatus* leaf; (**B**) TiO_2-CeO_2 nanoparticles.

3.3. Synthesis of TiO_2-CeO_2 Nanoparticles

The procedure is schematized in (Figure 10B). The TiO_2-CeO_2 nanocomposite particles were fabricated using a straightforward, template-free sol–gel method as follows: Initially, 0.2%, 0.1%, and 1% molar ratios of cerium nitrate solution ($Ce(NO_3)_3 \cdot 6H_2O$) were dissolved in a solution of 25 mL of *Cleistocalyx operculatus* extract and 75 mL of ethylene glycol, and then continuously stirred with a magnetic stirrer at 600 rpm for 1 h. Then, 0.43 g of TiO_2 was added, and the mixture was heated to 60 °C to promote hydrolysis, resulting in a light yellow-brown gel after 2 h of stirring. After aging the gel for 2 days, the gel was filtered and washed three times with distilled water and twice with ethanol. Finally, the gel was dried at 70 °C for 24 h and calcined in air at 500 °C for 2 h to produce TiO_2-CeO_2 nanocomposites.

3.4. Material Characterization

The nanomaterials were characterized using various techniques: field-emission scanning electron microscopy (JEOL 7600F, Akishima, Japan), powder X-ray diffraction (Advance D8, Bruker, Billerica, MA, USA, with a Cu-$K_{\alpha 1}$ radiation source, $\lambda = 1.54056$ Å), energy-dispersive X-ray spectroscopy, and high-resolution transmission electron mi-

croscopy (JEOL 2100F). Optical absorption spectra were collected using a UV−Vis spectrophotometer (Shanghai Yoke Instrument Co., Ltd., Shanghai, China). The bonding nature of the materials was investigated through Raman spectroscopy with a Renishaw inVia confocal micro-Raman system. Fourier transform infrared spectroscopy was performed with a FT/IR-4600 type A spectrometer (JASCO, Hachioji, Japan). Finally, the specific surface area and pore size distribution were determined using Brunauer–Emmett–Teller (BET) analysis (Micromeritics Gemini VII 2390, Norcross, GA, USA) based on nitrogen adsorption/desorption isotherms.

3.5. Photocatalytic Experiments

The photocatalytic performance of the synthesized samples was evaluated by degrading MB dyes under simulated sunlight provided by a 350 W Xenon lamp (Shenzhen Anhongda, Shenzhen, China). For each test, 30 mg of catalyst was stirred in a 10 ppm MB solution (20 mL, pH 7). The solution was initially allowed to reach an adsorption equilibrium in the dark on a magnetic stirrer for 1 h before exposure to the Xenon lamp, positioned 30 cm away, to initiate the photocatalytic process. At specified intervals, aliquots of the solution were withdrawn, centrifuged, and filtered to separate the catalyst. The residual MB concentration was determined using a Cary 5000 UV–Vis–NIR spectrophotometer (Yoke Instrument Co., Ltd., Shanghai, China) at a maximum absorption wavelength of 664 nm. Experiments comparing MB degradation efficiency were conducted with two types of catalysts, TiO_2 and TiO_2-CeO_2, to evaluate and compare the photocatalytic ability of each material.

4. Conclusions

This study successfully demonstrated the green synthesis of TiO_2-CeO_2 nanocomposites using Cleistocalyx operculatus leaf extract, presenting an eco-friendly and highly efficient approach for photocatalytic degradation of MB. The results demonstrated that CeO_2 incorporation significantly enhanced photocatalytic efficiency, achieving 95.06% degradation in 150 min under simulated sunlight. The improved performance is attributed to the efficient charge transfer between CeO_2 and TiO_2, driven by the Ce^{3+}/Ce^{4+} redox cycle, which promotes interfacial charge separation and suppresses electron–hole recombination. The formation of reactive oxygen species, including $OH^{\bullet}$, $O_2{}^{-\bullet}$, and $OOH^{\bullet}$, played a crucial role in breaking down MB into CO_2, H_2O, and inorganic ions. Additionally, the coexistence of Ce^{3+}/Ce^{4+} species and oxygen vacancies facilitated the bandgap reduction, enhancing visible light absorption. The catalyst also exhibited excellent reusability, maintaining over 93% efficiency after eight cycles. These findings suggest that TiO_2-CeO_2 nanocomposites synthesized via green methods highlight industrial relevance for scalability, emphasizing their potential as a sustainable, cost-effective solution for environmental remediation and wastewater treatment.

Supplementary Materials: The following supporting information can be downloaded at: https://www.mdpi.com/article/10.3390/catal15060583/s1, Figure S1: SEM image of TiO_2 nanoparticles.

Author Contributions: Conceptualization, D.D.N., D.D.L. and D.Q.H.; methodology, D.D.L. and D.D.N.; software, V.D.L.; investigation, D.Q.H. and V.D.L.; data curation, Q.A.N.; writing—original draft, D.Q.H. and D.D.L.; writing—reviewing scientific contents and editing, D.D.N. and D.D.L. All authors have read and agreed to the published version of the manuscript.

Funding: This research was financially supported by the Ministry of Education and Training (MOET) under Project No. B2023-TDV-04.

Data Availability Statement: The original contributions presented in this study are included in the article/Supplementary Material. Further inquiries can be directed to the corresponding authors.

Conflicts of Interest: The authors declare no conflicts of interest.

References

1. Din, M.I.; Khalid, R.; Najeeb, J.; Hussain, Z. Fundamentals and photocatalysis of methylene blue dye using various nanocatalytic assemblies- a critical review. *J. Clean. Prod.* **2021**, *298*, 126567. [CrossRef]
2. Aruchamy, K.; Sudarsan, D.; Ajith, M.; Sreekumar, A.A.M.; Ayyasamy, U.M.; Manickam, S. Enhanced photocatalytic activity of V_3O_7/V_2O_5—Reduced graphene oxide nanocomposite towards methylene blue dye degradation. *Environ. Sci. Pollut. Res.* **2024**, *31*, 20983–20998. [CrossRef] [PubMed]
3. Begum, R.; Najeeb, J.; Sattar, A.; Naseem, K.; Irfan, A.; Al-Sehemi, A.G.; Farooqi, Z.H. Chemical reduction of methylene blue in the presence of nanocatalysts: A critical review. *Rev. Chem. Eng.* **2020**, *36*, 749–770. [CrossRef]
4. Oladoye, P.O.; Ajiboye, T.O.; Omotola, E.O.; Oyewola, O.J. Methylene blue dye: Toxicity and potential elimination technology from wastewater. *Results Eng.* **2022**, *16*, 100678. [CrossRef]
5. Roguai, S.; Djelloul, A. Structural, microstructural and photocatalytic degradation of methylene blue of zinc oxide and Fe-doped ZnO nanoparticles prepared by simple coprecipitation method. *Solid State Commun.* **2021**, *334–335*, 114362. [CrossRef]
6. Ho, Y.-C.; Chua, S.-C.; Chong, F.-K. *Coagulation-Flocculation Technology in Water and Wastewater Treatment*; IGI Global: Hershey, PA, USA, 2020. [CrossRef]
7. Bashir, A.; Malik, L.A.; Ahad, S.; Manzoor, T.; Bhat, M.A.; Dar, G.N.; Pandith, A.H. Removal of heavy metal ions from aqueous system by ion-exchange and biosorption methods. *Environ. Chem. Lett.* **2018**, *17*, 729–754. [CrossRef]
8. Santoso, E.; Ediati, R.; Kusumawati, Y.; Bahruji, H.; Sulistiono, D.O.; Prasetyoko, D. Review on recent advances of carbon based adsorbent for methylene blue removal from waste water. *Mater. Today Chem.* **2020**, *16*, 100233. [CrossRef]
9. Li, N.; Lu, X.; He, M.; Duan, X.; Yan, B.; Chen, G.; Wang, S. Catalytic membrane-based oxidation-filtration systems for organic wastewater purification: A review. *J. Hazard. Mater.* **2021**, *414*, 125478. [CrossRef] [PubMed]
10. Pronk, W.; Ding, A.; Morgenroth, E.; Derlon, N.; Desmond, P.; Burkhardt, M.; Wu, B.; Fane, A.G. Gravity-driven membrane filtration for water and wastewater treatment: A review. *Water Res.* **2019**, *149*, 553–565. [CrossRef]
11. Saravanan, A.; Kumar, P.S.; Varjani, S.; Jeevanantham, S.; Yaashikaa, P.R.; Thamarai, P.; Abirami, B.; George, C.S. A review on algal-bacterial symbiotic system for effective treatment of wastewater. *Chemosphere* **2021**, *271*, 129540. [CrossRef]
12. Aditya, L.; Mahlia, T.M.I.; Nguyen, L.N.; Vu, H.P.; Nghiem, L.D. Microalgae-bacteria consortium for wastewater treatment and biomass production. *Sci. Total Environ.* **2022**, *838*, 155871. [CrossRef] [PubMed]
13. Chan, S.S.; Khoo, K.S.; Chew, K.W.; Ling, T.C.; Show, P.L. Recent advances biodegradation and biosorption of organic compounds from wastewater: Microalgae-bacteria consortium—A review. *Bioresour. Technol.* **2022**, *344*, 126159. [CrossRef] [PubMed]
14. Malekkiani, M.; Ravari, F.; Heshmati Jannat Magham, A.; Dadmehr, M.; Groiss, H.; Hosseini, H.A.; Sharif, R. Fabrication of Graphene-Based TiO_2@CeO_2 and CeO_2@TiO_2 Core–Shell Heterostructures for Enhanced Photocatalytic Activity and Cytotoxicity. *ACS Omega* **2022**, *7*, 30601–30621. [CrossRef]
15. Al-Mamun, M.R.; Kader, S.; Islam, M.S.; Khan, M.Z.H. Photocatalytic activity improvement and application of UV-TiO_2 photocatalysis in textile wastewater treatment: A review. *J. Environ. Chem. Eng.* **2019**, *7*, 103248. [CrossRef]
16. Natarajan, T.S.; Thampi, K.R.; Tayade, R.J. Visible light driven redox-mediator-free dual semiconductor photocatalytic systems for pollutant degradation and the ambiguity in applying Z-scheme concept. *Appl. Catal. B Environ.* **2018**, *227*, 296–311. [CrossRef]
17. Sari, Y.; Gareso, P.L.; Armynah, B.; Tahir, D. A review of TiO_2 photocatalyst for organic degradation and sustainable hydrogen energy production. *Int. J. Hydrog. Energy* **2024**, *55*, 984–996. [CrossRef]
18. Güell, F.; Galdámez-Martínez, A.; Martínez-Alanis, P.R.; Catto, A.C.; da Silva, L.F.; Mastelaro, V.R.; Santana, G.; Dutt, A. ZnO-based nanomaterials approach for photocatalytic and sensing applications: Recent progress and trends. *Mater. Adv.* **2023**, *4*, 3685–3707. [CrossRef]
19. Ahmaruzzaman, M. Metal oxides (ZnO, CuO and NiO)-based nanostructured materials for photocatalytic remediation of organic contaminants. *Nanotechnol. Environ. Eng.* **2022**, *8*, 219–235. [CrossRef]
20. Liu, W.; Liu, N.; Song, K.; Zeng, M.; Lu, Z. Fabrication of WO_3 photocatalyst by plasma assisted ball milling under different discharge atmospheres. *Vacuum* **2024**, *220*, 112809. [CrossRef]
21. Zhang, C.; Feng, C.; Yuan, J.; Wang, Z.; Wang, Y.; Zhou, S.; Gu, P.; Li, Y. Extended construction strategies of Ag_3PO_4-based heterojunction photocatalysts for robust environmental applications. *J. Environ. Chem. Eng.* **2023**, *11*, 110705. [CrossRef]
22. Ren, Y.; Li, Y.; Pan, G.; Wang, N.; Xing, Y.; Zhang, Z. Recent progress in CdS-based S-scheme photocatalysts. *J. Mater. Sci. Technol.* **2024**, *171*, 162–184. [CrossRef]
23. Guo, Q.; Zhou, C.; Ma, Z.; Yang, X. Fundamentals of TiO_2 Photocatalysis: Concepts, Mechanisms, and Challenges. *Adv. Mater.* **2019**, *31*, 1901997. [CrossRef]
24. Sharma, P.K.; Cortes, M.A.L.R.M.; Hamilton, J.W.J.; Han, Y.; Byrne, J.A.; Nolan, M. Surface modification of TiO_2 with copper clusters for band gap narrowing. *Catal. Today* **2019**, *321–322*, 9–17. [CrossRef]

25. Etshindo, L.A.; Sousa, C.; Tamiasso-Martinhon, P.; Colaço, M.V.; Camara, A.R.; Rocha, A.S. SnO_2-TiO_2 materials for photocatalytic degradation of cationic dye under UV and visible light and a chitosan composite film investigation. *Catal. Today* **2025**, *444*, 114995. [CrossRef]
26. Ghamarpoor, R.; Fallah, A.; Jamshidi, M. A Review of Synthesis Methods, Modifications, and Mechanisms of ZnO/TiO_2-Based Photocatalysts for Photodegradation of Contaminants. *ACS Omega* **2024**, *9*, 25457–25492. [CrossRef]
27. Ma, B.; Zha, Y.; Xu, R.; Li, J.; Guo, Y.; Liu, J.; Wang, S.; Yan, B.; Lan, Y.; Zhao, B.; et al. Hollow α-Bi_2O_3/TiO_2 nanotube arrays hierarchical heterojunction with strong interface interaction for efficient photocatalytic ciprofloxacin degradation. *J. Water Process Eng.* **2024**, *60*, 105134. [CrossRef]
28. Alamgir; Ullah, R.; Talha, K.; Yang, H.; Mushtaq, N.; Ahmad, A.; Fan, L.; Li, L.; Zhao, G.; Wang, X.; et al. MOF-derived In_2O_3/TiO_2 S-scheme heterojunction for efficient photocatalytic degradation of tetracycline. *J. Alloys Compd.* **2024**, *1002*, 175398. [CrossRef]
29. Ma, R.; Zhang, S.; Wen, T.; Gu, P.; Li, L.; Zhao, G.; Niu, F.; Huang, Q.; Tang, Z.; Wang, X. A critical review on visible-light-response CeO_2-based photocatalysts with enhanced photooxidation of organic pollutants. *Catal. Today* **2019**, *335*, 20–30. [CrossRef]
30. Hoque, K.A.; Sathi, S.A.; Akter, F.; Akter, T.; Ahmed, T.; Ullah, W.; Arafin, K.; Rahaman, M.S.; Shahadat, H.M.; Imran, A.B.; et al. Recent advances on photocatalytic CO_2 reduction using CeO_2-based photocatalysts: A review. *J. Environ. Chem. Eng.* **2024**, *12*, 113487. [CrossRef]
31. Wan, Y.; Wang, H.; Liu, J.; Liu, X.; Song, X.; Zhou, W.; Zhang, J.; Huo, P. Enhanced degradation of polyethylene terephthalate plastics by CdS/CeO_2 heterojunction photocatalyst activated peroxymonosulfate. *J. Hazard. Mater.* **2023**, *452*, 131375. [CrossRef]
32. Tuyen, L.T.T.; Quang, D.A.; Tam Toan, T.T.; Tung, T.Q.; Hoa, T.T.; Mau, T.X.; Khieu, D.Q. Synthesis of CeO_2/TiO_2 nanotubes and heterogeneous photocatalytic degradation of methylene blue. *J. Environ. Chem. Eng.* **2018**, *6*, 5999–6011. [CrossRef]
33. Wu, M.; Zhang, Y.; Szeto, W.; Pan, W.; Huang, H.; Leung, D.Y.C. Vacuum ultraviolet (VUV)-based photocatalytic oxidation for toluene degradation over pure CeO_2. *Chem. Eng. Sci.* **2019**, *200*, 203–213. [CrossRef]
34. Stefa, S.; Lykaki, M.; Fragkoulis, D.; Binas, V.; Pandis, P.K.; Stathopoulos, V.N.; Konsolakis, M. Effect of the Preparation Method on the Physicochemical Properties and the CO Oxidation Performance of Nanostructured CeO_2/TiO_2 Oxides. *Processes* **2020**, *8*, 847. [CrossRef]
35. Kumar Mandal, R.; Kumar Pradhan, S. Enhanced photocatalytic performance of cauliflower-like CeO_2-TiO_2 nanocomposite for the RhB dye degradation under visible light. *Mater. Today Proc.* **2022**, *66*, 3307–3314. [CrossRef]
36. SenthilKumar, S.; Lellala, K.; Ashok, M.; Priyadharsan, A.; Sanjeeviraja, C.; Rajendran, A. Green synthesis of CeO_2–TiO_2 compound using Cleome chelidonii leaf extract for excellent photocatalytic activity. *J. Mater. Sci. Mater. Electron.* **2018**, *29*, 14022–14030. [CrossRef]
37. Ramakrishnan, K.; Gayathri, V.; Aravinthkumar, K.; Ramachandran, K.; Ajitha, B.; Rameshbabu, M.; Sasiflorence, S.; Karazhanov, S.; Praba, K.; Raja Mohan, C. TiO_2/CeO_2 Core/Shell nanostructures for photocatalytic and photo electrochemical applications. *Inorg. Chem. Commun.* **2022**, *144*, 109842. [CrossRef]
38. Cano-Franco, J.C.; Álvarez-Láinez, M. Effect of CeO_2 content in morphology and optoelectronic properties of TiO_2-CeO_2 nanoparticles in visible light organic degradation. *Mater. Sci. Semicond. Process.* **2019**, *90*, 190–197. [CrossRef]
39. Ying, S.; Guan, Z.; Ofoegbu, P.C.; Clubb, P.; Rico, C.; He, F.; Hong, J. Green synthesis of nanoparticles: Current developments and limitations. *Environ. Technol. Innov.* **2022**, *26*, 102336. [CrossRef]
40. Wandre, T.M.; Gaikwad, P.N.; Tapase, A.S.; Garadkar, K.M.; Vanalakar, S.A.; Lokhande, P.D.; Sasikala, R.; Hankare, P.P. Sol–gel synthesized TiO_2-CeO_2 nanocomposite: An efficient photocatalyst for degradation of methyl orange under sunlight. *J. Mater. Sci. Mater. Electron.* **2015**, *27*, 825–833. [CrossRef]
41. Wang, J.; Zhou, G.; He, R.; Huang, W.; Zhu, J.; Mao, C.; Wu, C.; Lu, G. Experimental preparation and optical properties of CeO_2/TiO_2 heterostructure. *J. Mater. Res. Technol.* **2020**, *9*, 9920–9928. [CrossRef]
42. Abdel-Mageed, A.M.; Cisneros, S.; Mosrati, J.; Atia, H.; Vuong, T.H.; Rockstroh, N.; Wohlrab, S.; Brückner, A.; Rabeah, J. Controlling Activity of Heterogeneous Cu Single-Atom Catalysts by Fine-Tuning the Redox Properties of CeO_2-TiO_2 Supports. *ChemCatChem* **2023**, *15*, e202201669. [CrossRef]
43. Kumar, P.; Kaur, R.; Verma, S.; Singh, S.; Štangar, U.L. Tuning the catalytic active sites of TiO_2/CeO_2 interactions to improve oxygen vacancy and lattice parameters for CO_2 conversion to green fuel additive. *Catal. Today* **2024**, *433*, 114652. [CrossRef]
44. Wang, J.; Meng, F.; Xie, W.; Gao, C.; Zha, Y.; Liu, D.; Wang, P. TiO_2/CeO_2 composite catalysts: Synthesis, characterization and mechanism analysis. *Appl. Phys. A* **2018**, *124*, 645. [CrossRef]
45. Sarvari, N.; Mohammadi, M.R. Influence of photoanode architecture on light scattering mechanism and device performance of dye-sensitized solar cells using TiO_2 hollow cubes and nanoparticles. *J. Taiwan Inst. Chem. Eng.* **2018**, *86*, 81–91. [CrossRef]
46. Kusuma, K.B.; Manju, M.; Ravikumar, C.R.; Raghavendra, N.; Amulya, M.A.S.; Nagaswarupa, H.P.; Murthy, H.C.A.; Kumar, M.R.A.; Shashi Shekhar, T.R. Photocatalytic degradation of Methylene Blue and electrochemical sensing of paracetamol using Cerium oxide nanoparticles synthesized via sonochemical route. *Appl. Surf. Sci. Adv.* **2022**, *11*, 100304. [CrossRef]

47. Hkiri, K.; Elsayed Ahmed Mohamed, H.; Ghotekar, S.; Maaza, M. Green synthesis of cerium oxide nanoparticles using *Portulaca oleracea* Extract: Photocatalytic activities. *Inorg. Chem. Commun.* **2024**, *162*, 112243. [CrossRef]
48. Ahmad, A.; Javed, M.S.; Khan, S.; Almutairi, T.M.; Mohammed, A.A.A.; Luque, R. Green synthesized Ag decorated CeO_2 nanoparticles: Efficient photocatalysts and potential antibacterial agents. *Chemosphere* **2023**, *310*, 136841. [CrossRef]
49. Kalaycıoğlu, Z.; Özuğur Uysal, B.; Pekcan, Ö.; Erim, F.B. Efficient Photocatalytic Degradation of Methylene Blue Dye from Aqueous Solution with Cerium Oxide Nanoparticles and Graphene Oxide-Doped Polyacrylamide. *ACS Omega* **2023**, *8*, 13004–13015. [CrossRef]
50. Kılıç Dokan, F.; Kuru, M. A new approach to optimize the synthesis parameters of TiO_2 microsphere and development of photocatalytic performance. *J. Mater. Sci. Mater. Electron.* **2020**, *32*, 640–655. [CrossRef]
51. Paramarta, V.; Taufik, A.; Saleh, R. Photocatalytic degradation of methylene blue (MB) by UV-light irradiation using SnO_2/CeO_2 modified nanographene platelets (NGP). *J. Phys. Conf. Ser.* **2020**, *1442*, 012005. [CrossRef]
52. Husna, R.A.; Suherman; Natsir, T.A. Enhancing photocatalytic degradation of methylene blue by mixed oxides $TiO_2/SnO_2/CeO_2$ under visible light. *Results Eng.* **2023**, *19*, 101253. [CrossRef]
53. Khatibnezhad, H.; Ettouil, F.B.; Moreau, C. Photoactive Ce-doped TiO_2 and CeO_2-TiO_2 composite coatings deposited by suspension/solution plasma spray. *Mater. Res. Bull.* **2023**, *166*, 112346. [CrossRef]

Disclaimer/Publisher's Note: The statements, opinions and data contained in all publications are solely those of the individual author(s) and contributor(s) and not of MDPI and/or the editor(s). MDPI and/or the editor(s) disclaim responsibility for any injury to people or property resulting from any ideas, methods, instructions or products referred to in the content.

catalysts

MDPI

Article

Construction of Sulfur-Doped and Cyanide-Modified Carbon Nitride Photocatalysts with High Photocatalytic Hydrogen Production and Organic Pollutant Degradation

Yihan Tang [1], Yichi Zhang [1], Ning Jian [1], Luxi Han [1], Huage Lin [1] and Weinan Xing [1,2,*]

[1] College of Ecology and Environment, Co-Innovation Center for the Sustainable Forestry in Southern China, Nanjing Forestry University, Nanjing 210037, China; tangyihan3239@163.com (Y.T.); yichizhang2021@163.com (Y.Z.); gorillaj2004@163.com (N.J.); hlucy0812@163.com (L.H.); linhuage2001@163.com (H.L.)

[2] National Positioning Observation Station of Hung-tse Lake Wetland Ecosystem in Jiangsu Province, Huai'an 223100, China

* Correspondence: xingwn@njfu.edu.cn

Abstract

Element doping and functional group modification engineering serve as efficient approaches that contribute to the improvement of the functional efficiency in graphitic carbon nitride (CN) materials. A CN photocatalyst co-modified with sulfur (S) and cyano moieties was prepared through thermal condensation polymerization. The introduced S species modulated the band structure, increased charge carrier mobility, and significantly promoted charge separation and transport. Additionally, the introduction of cyano groups extended light absorption range and improved the material's selective adsorption of reactant molecules. The as-prepared sulfur-modified CN photocatalyst obtained after a 6 h thermal treatment, which was capable of degrading organic pollutants and producing hydrogen (H_2) efficiently and stably, exhibited excellent catalytic performance. The photocatalyst's photocatalyst exhibited a significantly enhanced photocatalytic activity, with a Rhodamine B (RhB) removal efficiency reaching 97.3%. Meanwhile, the H_2 production level reached 1221.47 μmol $h^{-1}g^{-1}$. Based on four-cycle experiments, the photocatalyst exhibited excellent recyclability and stability in both H_2 production processes and photocatalytic organic pollutant degradation. In addition, mechanistic studies confirmed the dominant role of ·OH and $\cdot O_2^-$ as active species responsible for the reaction system's performance. This study highlights that the co-decoration of heteroatoms and functional groups can markedly enhance the photocatalytic performance of CN-based materials, offering considerable potential for future applications in energy conversion and environmental remediation.

Keywords: carbon nitride; photocatalytic; sulfur doping; cyano; photodegradation; hydrogen production

1. Introduction

The rapid expansion of the global economy and the steady rise in population have intensified the conflict between rising energy demands and the need for environmental protection [1,2]. Finding a sustainable energy supply method and an effective means of environmental pollution control has become the focus of global attention [3]. Photocatalytic processes harness solar energy to drive reactions like hydrogen (H_2) production via water

splitting and the breakdown of organic contaminants [4–6]. Effectively coupling pollutant degradation with H_2 production requires the deliberate construction of high-performance photocatalysts [7,8]. Among various photocatalytic materials, graphitic carbon nitride (CN) is particularly appealing due to its desirable combination of economic viability, appropriate energy band gap, ease of synthesis, and superior chemical stability [9,10].

Although promising, CN demonstrates limited light-harvesting efficiency and rapid charge recombination, hindering practical applications [11,12]. To address these limitations, the photocatalytic capability of CN can be significantly improved via multiple modification routes, including morphology engineering, heterojunction, homojunction, metal/non-metal element doping, etc. [13–15]. Heteroatom incorporation into CN frameworks represents a particularly efficient modification strategy, simultaneously optimizing electronic band structure, suppressing charge recombination, and extending visible-light response [16–18]. Notably, sulfur (S) stands out among dopant elements due to its relatively large atomic radius, low electronegativity, high electron density, and its ability to form diverse covalent bonding configurations [19,20]. In a notable contribution, Luo's team synthesized thin, S-modified CN sheets with controlled porosity using precursor-directed thermal condensation, where thiocyanuric acid served as both S donor and structure-directing agent. A hydrogen production rate of 6225.4 μmol $g^{-1}h^{-1}$ was obtained [21]. S doping enhances light absorption and suppresses charge recombination, thereby significantly improving the H_2 production photoactivity. Like heteroelement doping, rational modification by such as cyano group was regarded as one of strategies to modulate the activity of CN. The abundant presence of cyano groups facilitates enhanced light harvesting, promotes more efficient separation of charge carriers, and increases the availability of active sites on the catalyst surface [22,23]. In this study, Lee et al. used SiO_2 clusters as templates to prepare cyano-bonded mesoporous graphitic carbon nitride nanoclusters as highly active photocatalysts, which completely degraded tetracycline solution within 30 min [24]. While the modification of CN through cyano group functionalization and elemental doping has been widely recognized as an effective approach in photocatalysis, limited research has explored the potential synergistic effects of combining these two strategies to further improve photocatalytic activity.

Herein, we developed a new strategy based on synergistic effect to co-modify CN with S and cyano groups (denoted as CNS) to enhance the photodegradation ability and photocatalytic H_2 production. The obtained CNS-*X* has significantly improved RhB degradation and H_2 production performance. CNS-6 showed superior photocatalytic behavior. Multiple characterization techniques confirmed the successful synergistic modification of S atoms and cyano groups. This dual modification induces an active structure with an electron compensation effect and spatial coordination advantage. It shows a significant synergistic catalytic mechanism in regulating the electron density of metal centers, constructing efficient reaction sites, stabilizing key intermediates, and optimizing reaction pathways. Our work provides a strategy to achieve the co-decoration of CN with heteroelements and functional groups.

2. Results and Discussion

2.1. Material Characterizations and Structural Model Optimization

The nanoscale architecture of the as-prepared samples was investigated through scanning electron microscopy (SEM) and transmission electron microscopy (TEM). The SEM image in Figure 1a shows that CN has a thick bulk structure. However, after thermal reaction, the thickness of the obtained CNS-6 is greatly reduced, showing a porous flake structure (Figure 1b). All the prepared CNS samples showed a layered structure from TEM observation. In Figure 2a, CNS-6 presents nanoscale-layered morphology. The sample

surface is a loose and diffuse thin layer with abundant pores. The TEM image shown in Figure 2b also clearly indicates that CNS-6 possess macropores and presents an ultra-thin layer structure that is almost transparent. Further observations show that there are abundant planar nanopores of a few nanometers, proving the formation of porous CNS-6 sheets (Figure 2c). Furthermore, both CNS-4 and CNS-8 exhibited porous structures (Figure S1).

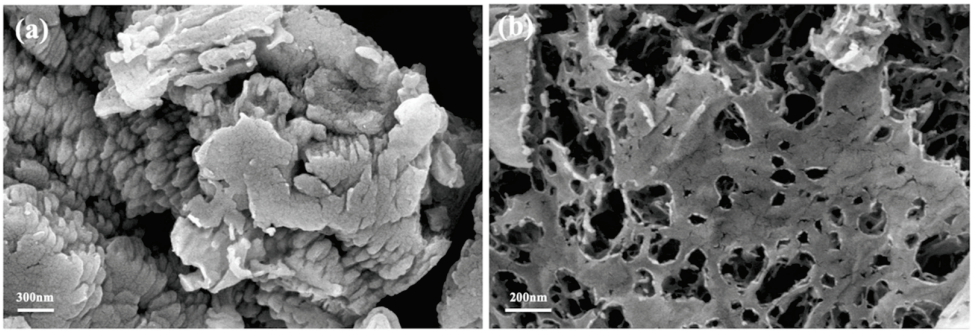


Figure 1. SEM images of (**a**) CN and (**b**) CNS-6.

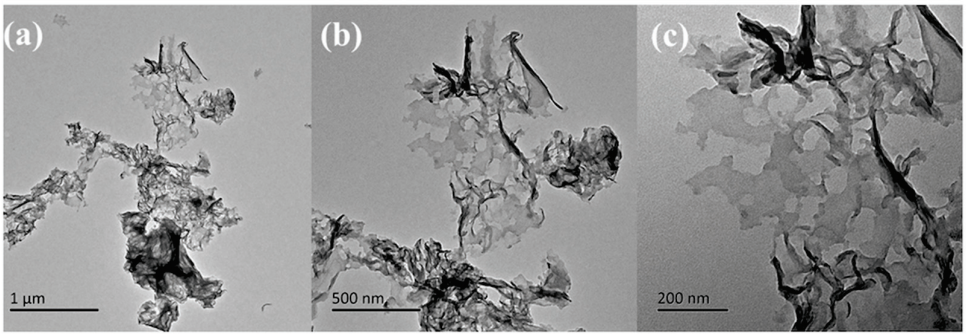


Figure 2. TEM images of (**a**–**c**) CNS-6.

As shown in Figure 3a, the specific surface area (BET) and pore volume of CNS-6 are 109 cm^2/g and 0.683 cm^3/g, respectively (Table S1). The BET and pore volume of CNS-6 are significantly larger than those of CN. The increased BET provides more active sites and reaction interfaces, which is beneficial for improving catalytic activity. Figure 3b presents the X-ray diffraction (XRD) profiles of CN and CNS-X. Layered CN presents two distinct diffraction peaks around 13° and 27°, corresponding, respectively, to the (100) in-plane packing and (002) interlayer π-π stacking pattern of the heptazine structure [25,26]. For CNS-X, the main peaks are still near 13° and 27°, indicating that their main structure is CN. Moreover, the magnified image shows that the diffraction peak assigned to the (002) plane of CNS-6 changes to a higher diffraction angle, indicating that there is a strong van der Waals attraction between adjacent heptaquinone unit layers, resulting in a reduction in the stacking distance between π-π layers. The (002) plane of the sample becomes weaker and wider, indicating that the morphology of CNS-6 becomes thinner. This observation aligns with previous TEM images. As shown in Figure 3c, the functional groups present in both CN and CNS were characterized via Fourier transform infrared (FT-IR). Furthermore, the broad absorption region at 1200–1700 cm^{-1} can be attributed to the characteristic skeletal vibrations of aromatic structures, including C=C stretching in benzene rings and C-N heterocycles [27,28]. Specifically, the peaks at 1241–1242 cm^{-1} correspond to C-N-C and C-N stretching vibrations [29]. Broad absorption features observed between 3100 and 3500 cm^{-1} originate from stretching modes of -NH and -OH functional groups, resulting, respectively, from terminal amine functionalities and surface-bound water species. Notably, characteristic -C≡N stretching vibrations appear at 2160–2180 cm^{-1} in CNS-X materials,

confirming cyano group incorporation [30], which likely emerge due to the deprotonation of amino groups during thermal treatment. To further illustrate the structural stability of the catalyst, thermogravimetric analysis was performed. As shown in Figure S2, CNS exhibits almost no mass loss at 520 °C, indicating that it is stable at this temperature.

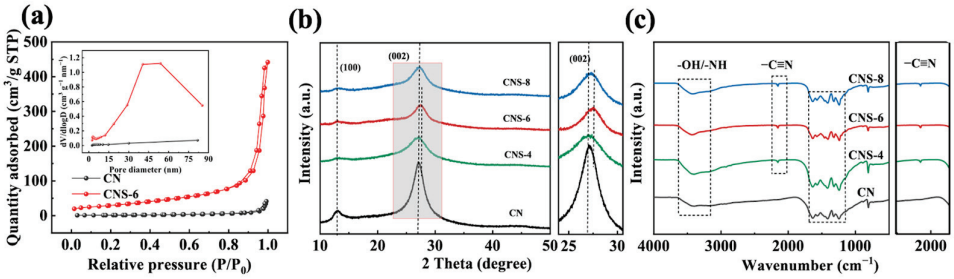


Figure 3. The N_2 adsorption–desorption isotherm (**a**) of CN and CNS-6. XRD and (**b**) FT-IR spectra (**c**) of pristine CN and CNS-X.

X-ray photoelectron spectroscopy (XPS) analysis provides definitive evidence of both elemental constituents and their bonding configurations. The scanning survey results (Figure 4a) fully explains that the original CN contains carbon (C), nitrogen (N), and oxygen (O). In parallel with C, N, and O, CNS-6 contains S elements, and CNS-4 (Figure S3) and CNS-8 (Figure S4) also contain them. This shows that S atoms are successfully doped into CN. Figure 4b shows two significant peaks at 284.6 eV and 288.8 eV, which correspond to adventitious carbon (C=C) and sp^2-hybridized C atom bonded to N (N-C=N) [31]. Compared with the original CN, the observed peak shifts in the CNS-6 further confirm the breaking of heterocyclic bonds and the generation of cyano-related defects within the aromatic framework during the thermal treatment of N-C=N linkages [32]. The samples reveal four distinct binding energy signals centered at 398.5, 400.8, and 401.2 eV, along with a higher-energy feature attributed to π^* excitation (Figure 4c). The presence of the π^* signal in the XPS spectrum is likely associated with the delocalized π-electron system inherent to the conjugated structure of the photocatalyst. Characteristic peaks of the π^* excitation state may emerge in the N 1s spectrum as a result of the electronic transition of this excited state. The various N chemical conditions are represented by these peaks. The 398.5 eV signal in pristine CN is characteristic of C=N-C coordination, with additional features at 400.8 eV and 401.2 eV corresponding to N-$(C)_3$ and C-N-H moieties. With regard to CNS-6, a comparable peak is detected, with a slight shift in the N-$(C)_3$ component. The creation of cyano groups, whose binding energy falls between that of N-$(C)_2$ and N-$(C)_3$ configurations, is probably responsible for this change [33]. According to the findings displayed in Figure 4d, the peak at 164.4 eV corresponds to C-S bonding, suggesting the substitution of N atoms by S within the CN framework. To reconfirm the successful introduction of sulfur atoms, we tested the sulfur content in CNS-6 using organic elemental analysis (Table S2). These findings provide solid evidence for the formation of defective CN simultaneously modified with S-doped and cyano groups.

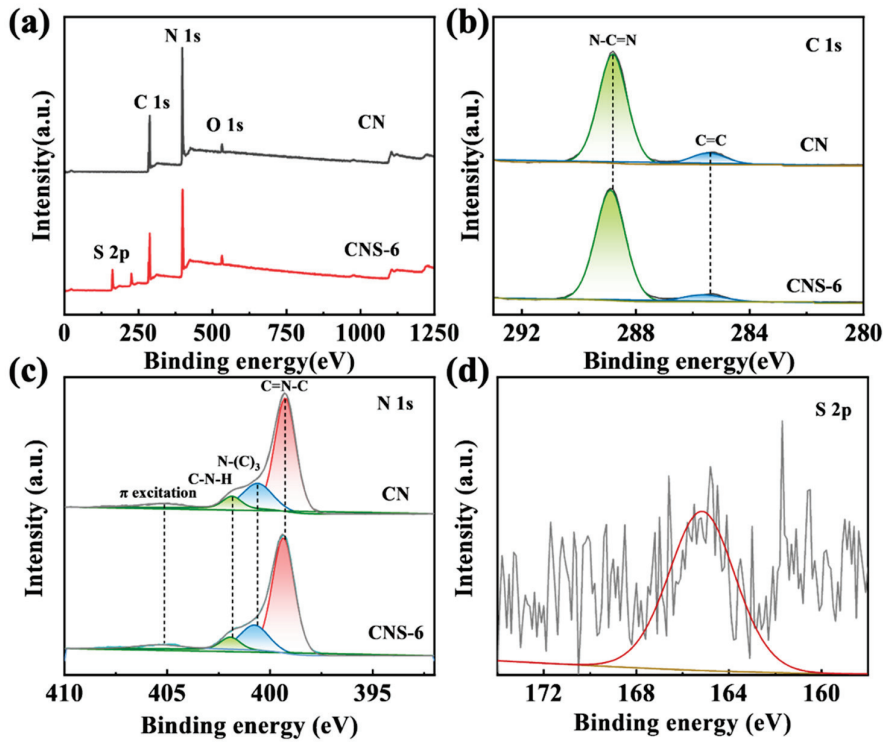


Figure 4. XPS spectra of pristine CN and CNS-6. (**a**) Full survey, (**b**) C 1s, (**c**) N 1s, and (**d**) S 2p.

2.2. Photocatalytic Properties

2.2.1. Optical Properties and Band Structures

Figure 5a clearly demonstrates that the optical properties of CN and CNS-6 and their light capture ability were systematically studied through ultraviolet–visible diffuse reflectance spectroscopy (UV–vis DRS). Because of its π-π electron transition, the CN sample shows a distinct absorption edge at roughly 474 nm, suggesting a typical band gap absorption feature. This indicates the restricted absorption capacity of CN in the visible-light region. In contrast, CNS-6 shows a broader and enhanced absorption range, especially showing a significant red shift. This improvement is attributed to the incorporation of S atoms and cyano groups, which help to regulate its electronic structure, expand the π conjugated system, and reduce the energy required for π-π transitions, thereby effectively broadening the photoresponse range. The increased absorption intensity suggests that CNS-6 is more efficient in harvesting sunlight and utilizing photogenerated charge carriers. As shown in Figure 5b, from the Kubelka–Munk equation $\alpha h\nu = A\,(h\nu - Eg)^{2}$, the bandgap energies of the CN and CNS-6 samples are obtained to be 2.89 eV and 2.87 eV. Obviously, functional group modification and element doping have an important influence on the band gap of semiconductors. Figure 5c presents the valence band (VB) spectra obtained by XPS. The VBs are determined to be 2.08 eV for CN and 2.21 eV for CNS-6. The formula Eg = $E_{VB} - E_{CB}$ was used. Combined with the Eg value, the conduction bands (CBs) of CN and CNS-6 are inferred to be -0.79 eV and -0.68 eV. The position of E_{VB} and E_{CB} is the decisive factor affecting the catalytic redox ability. Figure 5d shows the band diagrams of CN and CNS-6. Compared with the original CN, the positions of CB and VB in CNS-6 shift downward, indicating that CNS-6 has a stronger oxidation ability.

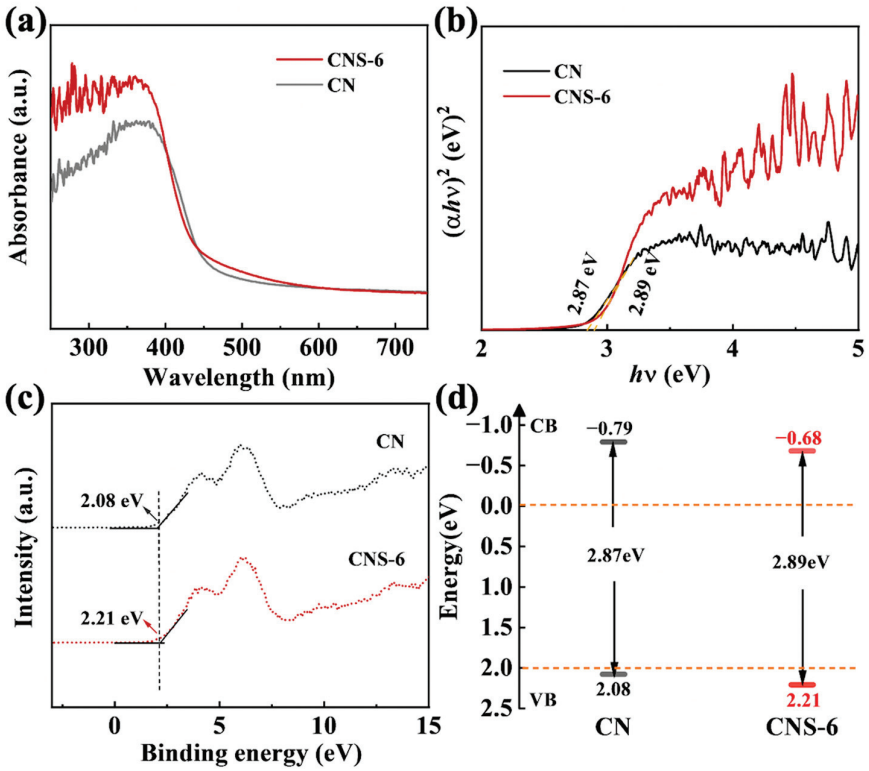


Figure 5. UV–vis DRS, (**a**) bandgap values, (**b**) XPS-VB spectra, and (**c**) the band structures of (**d**) CN and CNS-6.

2.2.2. Characterization of Charge Separation

To investigate the impact of S doping and cyano groups on charge carrier dynamics, we conducted transient photocurrent measurements and Nyquist plot analysis. The experimental consequents show that CNS-6 exhibits a sensitive photocurrent response in the on/off lighting cycle (Figure 6a). Compared with other catalysts, CNS-6 exhibits the strongest signal, indicating that CNS-6 has a smaller carrier migration impedance and a higher photogenerated charge transfer efficiency [34]. The experimental data plotted in Figure 6b indicate that the smallest arc radius in EIS for CNS-6 compared to other catalysts suggests indicating that its charge transfer resistance is significantly reduced [35]. It is obvious that CN has the weakest carrier separation efficiency. It can be seen from Figure 6c that the sample has a PL emission peak at 475 nm, and CNS-6 has a lower fluorescence emission intensity. These findings further demonstrate that S doping and cyano group introduction regulate the electronic configuration of CN, thus facilitating more effective spatial separation of photoinduced charge carriers within CNS.

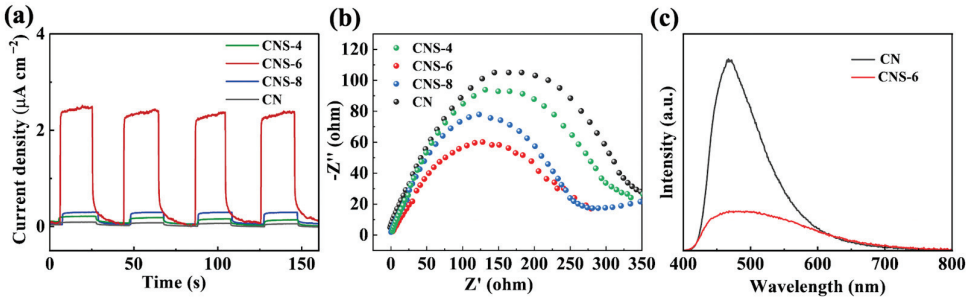


Figure 6. Photocurrent responses curves and (**a**) EIS of (**b**) CN and CNS-X. PL spectra (**c**) of CN and CNS-6.

2.3. Photocatalytic Activity

2.3.1. Photocatalytic H_2 Generation Performance

The visible-light-induced H_2 evolution reaction was performed to evaluate the catalytic performance of CN and CNS-X. As shown in Figure 7a, CNS-6 exhibits a remarkably enhanced activity compared to the pristine CN, with the highest H_2 production rate reaching 1221.47 μmol $h^{-1}g^{-1}$. Compared with other catalysts, it has better hydrogen production performance (Table S3). The experiments indicated the hierarchical porous structure of CNS-6 effectively reduces electron–hole recombination and consequently shortens migration path of charge carriers. This is consistent with the large specific surface area of CNS-6, which facilitates the provision of more active sites. The durability of CNS-6 in H_2 evolution was further confirmed, showing minimal performance loss after four consecutive cycles (Figure 7b). These findings indicate that CNS-6 possesses excellent photostability.

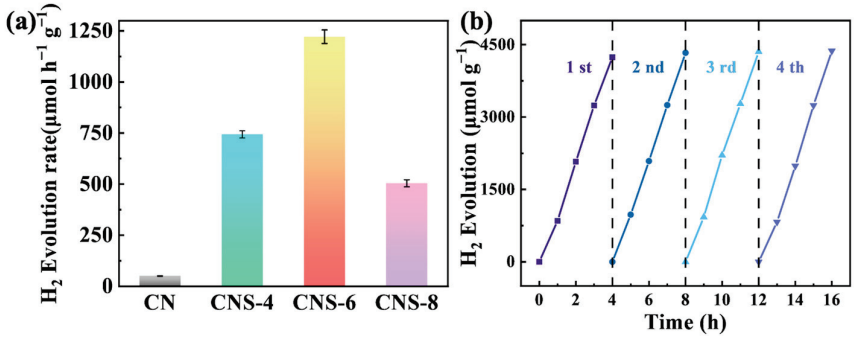


Figure 7. Photocatalytic H_2 evolution rates of (**a**) CN and CNS-X. (**b**) Stability testing of H_2 evolution of CNS-6.

2.3.2. Photocatalytic Degradation of RhB

The photocatalytic degradation capability of CN and CNS-X was systematically investigated using RhB dye under visible-light illumination. Different samples were subjected to dark adsorption treatment for 60 min, and the adsorption equilibrium was reached at 30 min (Figure S5). The RhB concentration at 30 min was selected as the initial concentration for the experiment. Compared with other photocatalysts (Figure 8a), CNS-6 achieved a removal efficiency of up to 97.3% for RhB by heating for 6 h, which is also higher than other catalysts reported before (Table S4). This is consistent with CNS-6 having a more positive valence band potential, which confers a stronger oxidative capacity. S doping in CNS enhances electron utilization by accelerating electron transfer to the target RhB, thereby achieving a higher degradation efficiency. Figure 8b,c show the fitting of the degradation data using the Equation (2). It can be seen from the figure that the CNS-6 photocatalyst shows the best rate constant of 0.03250 min^{-1}. Table S5 showed the experimental error values of Rhb degradation by different catalysts. The modified CNS-6 has better degradation performance than other catalysts. The data obtained here strongly suggest that doping S in CNS consistently increases the oxidative capacity of CNS and thus markedly increases the degradation rate of RhB. The stability of the CNS-6 sample was also tested (Figure 8d). After four cycles for a total of 8 h, the stability of the CNS-6 photocatalyst still maintained an extremely high degradation rate, indicating that CNS-6 has recyclability and excellent stability. At the same time, photolysis experiments were carried out under the same irradiation conditions but without the addition of a photocatalyst. Figure S6 shows that under visible light conditions, the degradation of RhB is negligible.

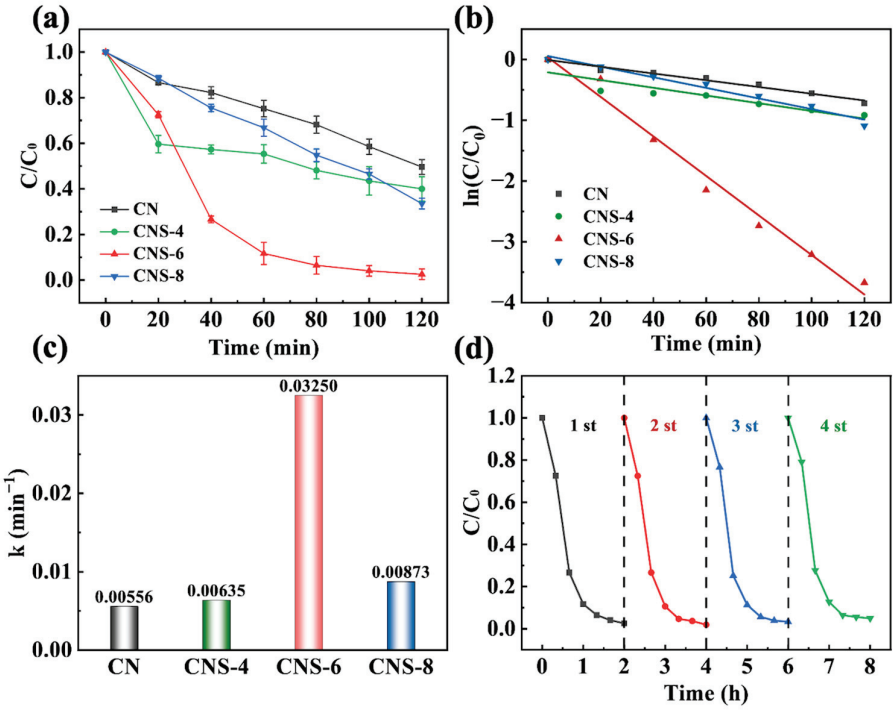


Figure 8. (**a**) Photodegradation curves, (**b**) corresponding reaction kinetics as a function of time, and (**c**) histogram of the best reaction rate constants for degradation of RhB using CN and CNS-X. (**d**) Reusability of CNS-6 for RhB degradation (experimental conditions: RhB concentration = 10 mg/L).

2.3.3. Photocatalytic Mechanism

In order to determine the dominant oxidative species responsible for the photocatalytic decomposition mechanism, radical trapping investigations were carefully carried out. Disodium ethylenediamine tetraacetic acid (EDTA-2Na), isopropyl alcohol (IPA), and 1,4-benzoquinone (BQ) were used as used as quenchers for holes (h^+), hydroxyl radicals (OH), and superoxide radicals (O_2^-), respectively. Figure 9a,b clearly illustrates that the photocatalytic process of CNS-6 degrading RhB with different quenchers. When EDTA-2Na was added to the system, no significant impact on degradation efficiency was observed, suggesting that h^+ is not an active species for RhB degradation. The introduction of BQ led to significant decreases in degradation efficiency, with reductions of 68.72%, respectively. Therefore, it is inferred that O_2^- plays the major role. OH plays a role, not by directly oxidizing bulk water but through surface -OH oxidation or intermediate O_2^-/H_2O_2 conversion. Due to the simultaneous action of other ROS (such as H^+ and O_2^-), IPA capture only partially inhibits degradation [36].

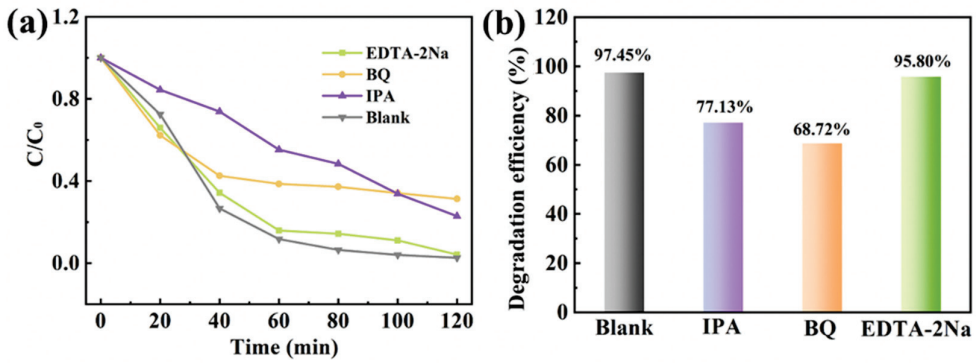


Figure 9. (**a**,**b**) Active species trapping experiments of CNS-6 based on different scavengers.

3. Experimental Section

3.1. Materials

All materials were obtained at analytical reagent (AR) grade and applied without further processing. Melamine ($C_3H_6N_6$), trithiocyanuric acid ($C_3H_3N_3S_3$), acetonitrile (C_2H_3N), and triethanolamine (TEOA) were purchased Shanghai McLean Biochemical Technology Co. (Shanghai, China). Isopropyl alcohol (C_3H_8O), ethanol (C_2H_5OH), and sodium sulfate (Na_2SO_4) were purchased from Sinopharm Chemical Reagent Co. (Shanghai, China).

3.2. Preparation of Photocatalysts

3.2.1. Synthesis of CN

For CN synthesis, 2.0 g of $C_3H_6N_6$ was calcined in a muffle furnace using the following program: heating at 2 °C/min to 520 °C with a 2 h plateau. The sample obtained was labeled as CN.

3.2.2. Synthesis of S-Doped and Cyanide-Modified Carbon Nitride Photocatalysts

In total, 2.0 g of $C_3H_3N_3S_3$ was heated in a ceramic crucible at 2 °C/min until reaching 520 °C in a muffle furnace, with subsequent thermal treatments maintained for 4, 6, or 8 h, respectively. The product was cooled and set aside for use. By changing the heating time during the preparation process, a series of samples with different defects were obtained, named CNS-X. The products are named CNS-4, CNS-6, and CNS-8 according to their time gradient.

3.3. Experimental

3.3.1. Characterizations

Scanning electron microscopy (SEM, JSM-7600F, JEOL, Tokyo, Japan) and transmission electron microscopy (TEM, JEM-1400, 120 kV, JEOL, Tokyo, Japan) were used to study the morphology. Fourier transform infrared spectroscopy (FT-IR) was employed to identify functional groups in the samples. X-ray diffraction (XRD) patterns were measured on the Ultima IV instrument (Rigaku, Tokyo, Japan) using Cu-Kα radiation. Fourier transform infrared (FT-IR) spectrum was acquired on Bio-Rad 575c FTIR spectrometer (Bio-Rad Laboratories, Hercules, CA, USA). X-ray photoelectron spectroscopy (XPS) was conducted using a ESCALAB 250Xi (Thermo Fisher Scientific, Waltham, MA, USA, Al-Kα = 1486.6 eV). UV–vis diffuse reflectance spectra (DRS) were measured with a Lambda 950 UV–vis spectrophotometer (PerkinElmer, Waltham, MA, USA). Photoluminescence (PL) spectra were captured by a HITACHI F-7100 instrument (Tokyo, Japan) with a Xe lamp.

3.3.2. Electrochemical Testing

The electrochemical impedance spectroscopy (EIS) and transient photocurrent response (I-T) curves were obtained using a conventional three-electrode system on the CHI760 electrochemical workstation. Anhydrous sodium sulfate was used as the electrolyte. In total, 5 mg of photocatalyst was added to ethanol, sonicated and mixed, and then dropped uniformly on the FTO glass. It was dried at 60 °C and subsequently used as working electrode. In addition, Pt foil was used as counter electrode, and Ag/AgCl was used as reference electrode. I-T measurements were conducted under a 300 W Xe lamp. The EIS was tested under identical conditions over a frequency range of 10 Hz to 1.0 kHz with a 1.6 V sweep frequency.

3.3.3. Photocatalytic Performance Experiments

Photocatalytic H_2 production: 20 mg of photocatalyst was added to 50 mL of deionized water, along with TEOA and Pt. Air was removed from the reactor using a vacuum pump. A 300 W xenon lamp (420 nm $\leq \lambda \leq$ 780 nm) was used as the light source. H_2 production was measured using a gas chromatograph (GC 7920, argon carrier gas, TCD detector, Beijing China Education Au-light Co., Ltd., Beijing, China) with online detection. Stability testing requires re-preparing the sacrificial agent solution with the same concentration, resetting the apparatus, and re-evacuating the reactor for 4–10 cycles.

Rhodamine B (RhB) degradation: 10 mg of photocatalyst was added to a 10 mg/L RhB solution and sonicated. To eliminate adsorption effects, the solution was stirred in the dark for 30 min. Subsequently, samples were collected and filtered every 20 min under visible light. UV–visible absorbance was measured at the RhB maximum absorption peak (λmax = 554 nm). The degradation rate is defined as below in Equation (1):

$$Degradation\ rate = \left(1 - \frac{C}{C_0}\right) * 100\% \quad (1)$$

The catalytic kinetics of the RhB degradation process was analyzed using a pseudo-first-order kinetic model. The specific method is Equation (2):

$$ln\frac{C}{C_0} = kt \quad (2)$$

In this equation, C denotes the real-time concentration of RhB, C_0 denotes the initial concentration of RhB, and k represents the reaction rate constant. Stability experiments were then conducted. After each cycle, the RhB solution was completely replaced with an equal volume and concentration. The catalyst was recovered and repeated multiple times, with data from each cycle analyzed.

4. Conclusions

In summary, CNS with S-modified and endowed with cyano-functionalization was successfully prepared to achieve efficient photocatalytic degradation and decomposition of water for H_2 evolution. The results show that S atoms and cyano groups synergistically regulate, which not only modulates the band structure of samples but also enhances their oxidation capacity, improves visible-light absorption, and promotes the efficient separation of photogenerated charge carriers. The numerical results indicate that CNS-6 exhibits a degradation rate of 97.30% for RhB and H_2 yield of 1221.47 μmol $h^{-1}g^{-1}$. The findings of this work highlight the significant promise of CN in photocatalysis and offer a foundation for advancing novel CN-derived photocatalytic materials.

Supplementary Materials: The following are available online at https://www.mdpi.com/article/10.3390/catal15090849/s1, The characterizations and photocatalytic performance experiments [37–50]. Figure S1. TEM images of (a) CNS-4 and (b) CNS-8. Table S1. The physical properties of CN and CNS-6. Figure S2. TGA curves of the condensation process of CNS-6 in air at a heating rate of 10 °C/min. Table S2. The elemental analysis of CNS-6. Figure S3. XPS spectra of CNS-4. (a) Full survey, (b) C 1s, (c) N 1s, and (d) S 2p. Figure S4. XPS spectra of CNS-8. (a) Full survey, (b) C 1s, (c) N 1s, and (d) S 2p. Figure S5. In the dark environment, the degradation kinetics of RhB by different catalysts. Figure S6. Photolysis test of RhB. Table S3. Comparison with other CN-based photocatalysts reported previously. Table S4. The RhB degradation efficiency of different catalysts. Table S5. Data for kinetic fitting models.

Author Contributions: Conceptualization, formal analysis, and writing—original draft were carried out by Y.T.; methodology and data curation were carried out by Y.Z.; investigation and data curation

were carried out by N.J., L.H. and H.L.; investigation, supervision, funding acquisition, and writing—review and editing were carried out by W.X. All authors have read and agreed to the published version of the manuscript.

Funding: This work was financially supported by the National Natural Science Foundation of China (22478195); the authors also would like to thank Scientific Compass (https://www.shiyanjia.com) for help with testing.

Data Availability Statement: The data presented in this study are available on request from the corresponding author.

Conflicts of Interest: The authors declare that they have no known competing financial interests or personal relationships that could have appeared to influence the work reported in this paper.

References

1. Wang, J.; Wang, S. A critical review on graphitic carbon nitride (g-C_3N_4)-based materials: Preparation, modification and environmental application. *Coord. Chem. Rev.* **2022**, *453*, 214338. [CrossRef]
2. Qi, M.-Y.; Conte, M.; Anpo, M.; Tang, Z.-R.; Xu, Y.-J. Cooperative coupling of oxidative organic synthesis and hydrogen production over semiconductor-based photocatalysts. *Chem. Rev.* **2021**, *121*, 13051–13085. [CrossRef] [PubMed]
3. Liu, Z.; Liu, C.; Chen, Z.; Huang, H.; Liu, Y.; Xue, L.; Sun, J.; Wang, X.; Xiong, P.; Zhu, J. Recent advances in two-dimensional materials for hydrovoltaic energy technology. In *Exploration*; Wiley Online Library: Hoboken, NJ, USA, 2023; Volume 3, p. 20220061.
4. Ma, X.; Cheng, H. Self-introduction of carbon nitride quantum dots into carbon nitride planar structure for enhanced photocatalytic hydrogen production. *Appl. Catal. B Environ.* **2023**, *339*, 123101. [CrossRef]
5. Zhu, X.; Yang, F.; Liu, J.; Zhou, G.; Chen, D.; Liu, Z.; Fang, J. Design and Architecture of PO Co-Doped Porous g-C_3N_4 by Supramolecular Self-Assembly for Enhanced Hydrogen Evolution. *Catalysts* **2022**, *12*, 1583. [CrossRef]
6. Idrees, F.; Dillert, R.; Bahnemann, D.; Butt, F.K.; Tahir, M. In-situ synthesis of Nb_2O_5/g-C_3N_4 heterostructures as highly efficient photocatalysts for molecular H2 evolution under solar illumination. *Catalysts* **2019**, *9*, 169. [CrossRef]
7. Lange, T.; Reichenberger, S.; Ristig, S.; Rohe, M.; Strunk, J.; Barcikowski, S.; Schlögl, R. Zinc sulfide for photocatalysis: White angel or black sheep? *Prog. Mater. Sci.* **2022**, *124*, 100865. [CrossRef]
8. Tao, X.; Zhou, H.; Zhang, C.; Ta, N.; Li, R.; Li, C. Triclinic-Phase Bismuth Chromate: A Promising Candidate for Photocatalytic Water Splitting with Broad Spectrum Ranges. *Adv. Mater.* **2023**, *35*, 2211182. [CrossRef]
9. Nguyen, T.-B.; Huang, C.; Doong, R.-a.; Chen, C.-W.; Dong, C.-D. Visible-light photodegradation of sulfamethoxazole (SMX) over Ag-P-codoped g-C_3N_4 (Ag-P@ UCN) photocatalyst in water. *Chem. Eng. J.* **2020**, *384*, 123383. [CrossRef]
10. Wang, X.; Qin, Y.; Lu, J.; Qin, W.; Teng, H. Incorporation of benzene rings and nickel atoms into g-C_3N_4 framework with enhanced spatial charge transfer for efficient photocatalysis. *Sep. Purif. Technol.* **2025**, *362*, 131659. [CrossRef]
11. Liu, W.; Song, C.; Kou, M.; Wang, Y.; Deng, Y.; Shimada, T.; Ye, L. Fabrication of ultra-thin g-C_3N_4 nanoplates for efficient visible-light photocatalytic H_2O_2 production via two-electron oxygen reduction. *Chem. Eng. J.* **2021**, *425*, 130615. [CrossRef]
12. An, W.; Ma, C.; Lu, J.; Wang, H.; Li, G.; Cui, W. Single-electron effects regulate the electronic structure of carbon nitride to enhance photocatalytic hydrogen peroxide generation and pollutant degradation performance. *J. Colloid Interface Sci.* **2025**, *696*, 137869. [CrossRef]
13. He, F.; Wang, Z.; Li, Y.; Peng, S.; Liu, B. The nonmetal modulation of composition and morphology of g-C_3N_4-based photocatalysts. *Appl. Catal. B Environ.* **2020**, *269*, 118828. [CrossRef]
14. Liu, Y.; Lu, S.; Wang, S.; Tang, Z.; Bahnemann, J.; Liu, Y.; Chen, H.; Jiang, F. Conductive polymer/sulfur-doped graphitic carbon nitride with π-π conjugated structure for photocatalytic degradation of tetracycline in high and low salinity aquatic systems: Unveiling switching between free radical and non-radical pathways. *J. Colloid Interface Sci.* **2025**, *692*, 137548. [CrossRef]
15. Li, H.; Zhang, N.; Zhao, F.; Liu, T.; Wang, Y. Facile fabrication of a novel Au/phosphorus-doped g-C_3N_4 photocatalyst with excellent visible light photocatalytic activity. *Catalysts* **2020**, *10*, 701. [CrossRef]
16. Khan, I.; Khan, S.; Shayan, M.; Ullah, R.; Rizwan, M.; Khan, A.; Alodhayb, A.N.; Iqbal, A.; Iqbal, K.; Ullah, S. Simultaneous dopants and defects synergistically modulate the band structure of CN in Z-scheme heterojunctional photocatalysts for simultaneous HER and OER production. *Carbon* **2024**, *229*, 119451. [CrossRef]
17. Peng, X.; Chen, X.; Pang, R.; Cheng, L.; Chen, F.; Lu, W. The Impact of Polymerization Atmosphere on the Microstructure and Photocatalytic Properties of Fe-Doped g-C_3N_4 Nanosheets. *Catalysts* **2024**, *14*, 520. [CrossRef]
18. Ning, J.; Zhang, B.; Siqin, L.; Liu, G.; Wu, Q.; Xue, S.; Shao, T.; Zhang, F.; Zhang, W.; Liu, X. Designing advanced S-scheme CdS QDs/La-Bi_2WO_6 photocatalysts for efficient degradation of RhB. In *Exploration*; Wiley Online Library: Hoboken, NJ, USA, 2023; Volume 3, p. 20230050.

19. Chen, J.; Wang, Y.; Yu, Y.; Wang, J.; Liu, J.; Ihara, H.; Qiu, H. Composite materials based on covalent organic frameworks for multiple advanced applications. In *Exploration*; Wiley Online Library: Hoboken, NJ, USA, 2023; Volume 3, p. 20220144.
20. Mohammad, A.; Chandra, P.; Khan, M.E.; Choi, C.-H.; Yoon, T. Sulfur-doped graphitic carbon nitride: Tailored nanostructures for photocatalytic, sensing, and energy storage applications. *Adv. Colloid Interface Sci.* **2023**, *322*, 103048. [CrossRef] [PubMed]
21. Luo, L.; Gong, Z.; Ma, J.; Wang, K.; Zhu, H.; Li, K.; Xiong, L.; Guo, X.; Tang, J. Ultrathin sulfur-doped holey carbon nitride nanosheets with superior photocatalytic hydrogen production from water. *Appl. Catal. B Environ.* **2021**, *284*, 119742. [CrossRef]
22. Cui, Y.; Li, X.; Yang, C.; Xiao, B.; Xu, H. K–I co-doped crystalline carbon nitride with outstanding visible light photocatalytic activity for H_2 evolution. *Int. J. Hydrogen Energy* **2022**, *47*, 12569–12581. [CrossRef]
23. Zhao, B.; Gao, D.; Liu, Y.; Fan, J.; Yu, H. Cyano group-enriched crystalline graphitic carbon nitride photocatalyst: Ethyl acetate-induced improved ordered structure and efficient hydrogen-evolution activity. *J. Colloid Interface Sci.* **2022**, *608*, 1268–1277. [CrossRef] [PubMed]
24. Razavi-Esfali, M.; Mahvelati-Shamsabadi, T.; Fattahimoghaddam, H.; Lee, B.-K. Highly efficient photocatalytic degradation of organic pollutants by mesoporous graphitic carbon nitride bonded with cyano groups. *Chem. Eng. J.* **2021**, *419*, 129503. [CrossRef]
25. Dong, S.; Lee, G.; Zhou, R.; Wu, J.J. Synthesis of g-C_3N_4/$BiVO_4$ heterojunction composites for photocatalytic degradation of nonylphenol ethoxylate. *Sep. Purif. Technol.* **2020**, *250*, 117202. [CrossRef]
26. Liu, C.; Dong, S.; Chen, Y. Enhancement of visible-light-driven photocatalytic activity of carbon plane/g-C_3N_4/TiO_2 nanocomposite by improving heterojunction contact. *Chem. Eng. J.* **2019**, *371*, 706–718. [CrossRef]
27. Fu, J.; Zhu, B.; Jiang, C.; Cheng, B.; You, W.; Yu, J. Hierarchical porous O-doped g-C_3N_4 with enhanced photocatalytic CO_2 reduction activity. *Small* **2017**, *13*, 1603938. [CrossRef]
28. Zhao, H.; Li, G.; Tian, F.; Jia, Q.; Liu, Y.; Chen, R. g-C_3N_4 surface-decorated $Bi_2O_2CO_3$ for improved photocatalytic performance: Theoretical calculation and photodegradation of antibiotics in actual water matrix. *Chem. Eng. J.* **2019**, *366*, 468–479. [CrossRef]
29. Chen, Q.; Gao, G.; Guo, H.; Wang, S.-A.; Wang, Q.; Fang, Y.; Hu, X.; Duan, R. Boron-doped polymeric carbon nitride co-modified with carbon-ring and carboxyl for efficient photocatalytic overall water-splitting. *Chem. Eng. J.* **2023**, *470*, 144199. [CrossRef]
30. Zhang, Q.; Chai, Y.; Cao, M.; Yang, F.; Zhang, L.; Dai, W.-L. Facile synthesis of ultra-small Ag decorated g-C_3N_4 photocatalyst via strong interaction between Ag^+ and cyano group in monocyanamide. *Appl. Surf. Sci.* **2020**, *503*, 143891. [CrossRef]
31. Du, R.; Xiao, K.; Li, B.; Han, X.; Zhang, C.; Wang, X.; Zuo, Y.; Guardia, P.; Li, J.; Chen, J. Controlled oxygen doping in highly dispersed Ni-loaded g-C_3N_4 nanotubes for efficient photocatalytic H_2O_2 production. *Chem. Eng. J.* **2022**, *441*, 135999. [CrossRef]
32. Luo, Y.; Deng, B.; Pu, Y.; Liu, A.; Wang, J.; Ma, K.; Gao, F.; Gao, B.; Zou, W.; Dong, L. Interfacial coupling effects in g-C_3N_4/$SrTiO_3$ nanocomposites with enhanced H_2 evolution under visible light irradiation. *Appl. Catal. B Environ.* **2019**, *247*, 1–9. [CrossRef]
33. Liu, Q.; Cui, K.; Cui, M.; Liu, X.; Zhang, Q. Co-modification of carbon and cyano defect in g-C_3N_4 for enhanced photocatalytic peroxymonosulfate activation: Combined experimental and theoretical analysis. *Sep. Purif. Technol.* **2023**, *316*, 123844. [CrossRef]
34. Liao, Z.; Li, C.; Shu, Z.; Zhou, J.; Li, T.; Wang, W.; Zhao, Z.; Xu, L.; Shi, L.; Feng, L. K–Na co-doping in crystalline polymeric carbon nitride for highly improved photocatalytic hydrogen evolution. *Int. J. Hydrogen Energy* **2021**, *46*, 26318–26328. [CrossRef]
35. Lei, J.; Chen, B.; Lv, W.; Zhou, L.; Wang, L.; Liu, Y.; Zhang, J. Robust photocatalytic H_2O_2 production over inverse opal g-C_3N_4 with carbon vacancy under visible light. *ACS Sustain. Chem. Eng.* **2019**, *7*, 16467–16473. [CrossRef]
36. Li, L.; Zeng, H.; Zhong, L.; Wu, H.; Zheng, J.; Zhou, Z.; Liu, J.; Tang, R.; Deng, Y.; Huang, Y. Tailoring a donor-acceptor structure in oxygen and cyano group co-modified carbon nitride for enhanced photocatalytic imidacloprid degradation. *Chem. Eng. J.* **2025**, *518*, 164671. [CrossRef]
37. Lin, Y.; Yang, Y.; Guo, W.; Wang, L.; Zhang, R.; Liu, Y.; Zhai, Y. Preparation of double-vacancy modified carbon nitride to greatly improve the activity of photocatalytic hydrogen generation. *Appl. Surf. Sci.* **2021**, *560*, 150029. [CrossRef]
38. Lin, Q.; Li, Z.; Lin, T.; Li, B.; Liao, X.; Yu, H.; Yu, C. Controlled preparation of P-doped g-C_3N_4 nanosheets for efficient photocatalytic hydrogen production. *Chin. J. Chem. Eng.* **2020**, *28*, 2677–2688. [CrossRef]
39. Liang, G.; Waqas, M.; Yang, B.; Xiao, K.; Li, J.; Zhu, C.; Zhang, J.; Duan, H. Enhanced photocatalytic hydrogen evolution under visible light irradiation by p-type MoS_2/n-type Ni_2P doped g-C_3N_4. *Appl. Surf. Sci.* **2020**, *504*, 144448. [CrossRef]
40. Li, J.; Ma, W.; Chen, J.; An, N.; Zhao, Y.; Wang, D.; Mao, Z. Carbon vacancies improved photocatalytic hydrogen generation of g-C_3N_4 photocatalyst via magnesium vapor etching. *Int. J. Hydrogen Energy* **2020**, *45*, 13939–13946. [CrossRef]
41. Qi, K.; Lv, W.; Khan, I.; Liu, S.-y. Photocatalytic H_2 generation via CoP quantum-dot-modified g-C_3N_4 synthesized by electroless plating. *Chin. J. Catal.* **2020**, *41*, 114–121. [CrossRef]
42. Yu, M.; Lin, H.; Zhang, Y.; Shu, W.; Wu, G.; Xing, W. Frustrated Lewis pairs on hollow flower-liked carbon nitride by phosphorous and tungsten co-doping to enhance photocatalytic performance. *J. Mol. Struct.* **2025**, *1319*, 139510. [CrossRef]
43. Jang, D.; Lee, S.; Kwon, N.H.; Kim, T.; Park, S.; Jang, K.Y.; Yoon, E.; Choi, S.; Han, J.; Lee, T.-W. Preparation of carbon nitride nanotubes with P-doping and their photocatalytic properties for hydrogen evolution. *Carbon* **2023**, *208*, 290–302. [CrossRef]
44. Gu, Y.; Han, Y.; Li, Y.; Zhang, L.; Wang, Z.; Li, Z. Phosphorylation promotes liquid-phase proton transfer and carrier separation for boosted photocatalytic hydrogen evolution over g-C_3N_4. *Chem. Eng. J.* **2024**, *502*, 158084. [CrossRef]

45. Zhang, H.; Zhu, C.; Cao, J.; Tang, Q.; Li, M.; Kang, P.; Shi, C.; Ma, M. Ultrasonic-Assisted Synthesis of 2D α-Fe_2O_3@g-C_3N_4 Composite with Excellent Visible Light Photocatalytic Activity. *Catalysts* **2018**, *8*, 457. [CrossRef]
46. Venkatachalam, A.; Martin Mark, J.A.; D, D.; J, R.; Jesuraj, J.p. Sunlight active photocatalytic studies of Fe_2O_3 based nanocomposites developed via two-pot synthesis technique. *Inorg. Chem. Commun.* **2021**, *124*, 108417. [CrossRef]
47. Lu, X.; Wang, Q.; Cui, D. Preparation and Photocatalytic Properties of g-C_3N_4/TiO_2 Hybrid Composite. *J. Mater. Sci. Technol.* **2010**, *26*, 925–930. [CrossRef]
48. Kolesnyk, I.; Kujawa, J.; Bubela, H.; Konovalova, V.; Burban, A.; Cyganiuk, A.; Kujawski, W. Photocatalytic properties of PVDF membranes modified with g-C_3N_4 in the process of Rhodamines decomposition. *Sep. Purif. Technol.* **2020**, *250*, 117231. [CrossRef]
49. Tahir, M.B.; Sagir, M.; Zubair, M.; Rafique, M.; Abbas, I.; Shakil, M.; Khan, I.; Afsheen, S.; Hasan, A.; Ahmed, A. WO_3 Nanostructures-Based Photocatalyst Approach Towards Degradation of RhB Dye. *J. Inorg. Organomet. Polym. Mater.* **2018**, *28*, 1107–1113. [CrossRef]
50. Chen, Y.; Li, J.; Zhai, B.; Liang, Y. Enhanced photocatalytic degradation of RhB by two-dimensional composite photocatalyst. *Colloids Surf. A Physicochem. Eng. Asp.* **2019**, *568*, 429–435. [CrossRef]

Disclaimer/Publisher's Note: The statements, opinions and data contained in all publications are solely those of the individual author(s) and contributor(s) and not of MDPI and/or the editor(s). MDPI and/or the editor(s) disclaim responsibility for any injury to people or property resulting from any ideas, methods, instructions or products referred to in the content.

catalysts

MDPI

Article

Efficient Degradation of Tetracycline via Cobalt Phosphonate-Activated Peroxymonosulfate: Mechanistic Insights and Catalytic Optimization

Xinlin Huang [1], Wenting Sun [1], Rong Bai [1], Yuchen He [1], Jingdan Li [1], Yuwei Pan [1], Ming Zhang [1] and Guangyu Wu [1,2,*]

[1] College of Ecology and the Environment, Co-Innovation Center for the Sustainable Forestry in Southern China, Nanjing Forestry University, Nanjing 210037, China; huangxinlin2127@163.com (X.H.); swt13181610959@163.com (W.S.); bairongrourou@163.com (R.B.); hyc76523466@163.com (Y.H.); jdanli@126.com (J.L.); panyw@njfu.edu.cn (Y.P.); mzhang925@njfu.edu.cn (M.Z.)

[2] Guangxi Key Laboratory of Petrochemical Resource Processing and Process Intensification Technology, School of Chemistry and Chemical Engineering, Guangxi University, Nanning 530004, China

* Correspondence: gywuchem@njfu.edu.cn

Abstract: The persistent contamination of aquatic systems by antibiotics, particularly tetracycline (TC), which induces antibiotic resistance genes and chronic toxicity to aquatic organisms, necessitates advanced oxidation processes. Herein, cobalt phosphonate (CoP) nanosheets with tailored Co/P ratios were synthesized to activate peroxymonosulfate (PMS) for TC degradation under visible light. Through a controlled-variable approach, the reaction parameters were systematically optimized. The refined CoP-3 system achieved 90.7% TC removal within 6 min, with the optimal degradation parameters determined as 0.1 g/L CoP-3 and 0.2 g/L PMS. Based on liquid chromatography–tandem mass spectrometry (LC-MS/MS) analysis, three degradation pathways were inferred. The toxicity of TC and its intermediates was assessed using quantitative structure–activity relationships (QSARs) via the Toxicity Estimation Software Tool (T.E.S.T). The results demonstrated reduced acute toxicity in intermediates compared to the parent compound. In practical applications, the catalyst achieved 64.7% and 80.8% TC removal rates in livestock wastewater and river water, respectively, while maintaining stable activity over four cycles. This demonstrates significant potential for engineering applications. The results were verified by free radical quenching experiments and were attributed to enhanced charge separation and an h^+-dominated non-free radical pathway. This work provides a sustainable strategy for antibiotic remediation based on transition metal phosphonates.

Keywords: cobalt phosphonate; peroxymonosulfate activation; TC degradation; visible-light photocatalysis

1. Introduction

Tetracycline (TC) antibiotics pose escalating global threats to ecosystems and public health due to their widespread misuse and environmental persistence [1,2]. Recent data reveal that over 30,000 tons of TC class antibiotics are consumed annually worldwide, with agricultural runoff and pharmaceutical wastewater being primary contamination sources. Advanced monitoring studies detected alarming TC concentrations exceeding 1200 μg/L in hospital effluents and 85 mg/kg in manure-amended soils [3]. These residues drive antimicrobial resistance crises, with cutting-edge metagenomics identifying TC exposure as being responsible for 12–18 fold increases in resistant pathogens carrying tet

(X) and other novel resistance genes [4,5]. The ecological impacts are equally severe; TC disrupts microbial communities at concentrations as low as 50 μg/L, impairing critical nutrient cycling functions [6]. Human health risks now include verified links to dysbiosis, heightened allergy susceptibility, and potential endocrine disruption. According to the Global Water Quality Monitoring Report, TC contamination has been detected in 76% of freshwater samples worldwide. Developing effective remediation strategies has become an urgent One Health priority.

Currently, the mainstream emerging antibiotic wastewater treatment technologies, both domestically and internationally, include coupled biological treatment methods [7], physical–chemical methods, membrane separation technology [8] and advanced oxidation technology [9]. The coupled biological treatment method has the advantages of reducing the use of chemical agents, avoiding secondary pollution, and having low operating costs. However, the presence of antibiotics inhibits microbial growth [10], thereby affecting the degradation efficiency of antibiotics in wastewater. Physical–chemical wastewater treatment methods do not rely on microbial metabolism and are suitable for treating high-concentration, difficult-to-degrade, or toxic wastewater. Membrane separation technology, as a key technique for treating antibiotic wastewater, efficiently removes antibiotic pollutants through mechanisms such as physical sieving, charge effects, and catalytic degradation. Sun et al. reported a strategy for preparing a series of inorganic–organic hybrid nanosheets based on pillar-supported aryl-embedded MXene nanosheets [11], where the membrane was formed through vacuum-assisted filtration. The prepared membrane demonstrated relatively high retention rates and stability when treating water containing antibiotics. However, the reusability of the membrane requires further discussion.

Advanced oxidation processes (AOPs) are a class of chemical oxidation methods that efficiently degrade organic pollutants by generating strong oxidizing radicals such as hydroxyl radicals ($^{\bullet}OH$) and sulfate radicals ($SO_4^{\bullet-}$). Although $^{\bullet}OH$ is the primary radical, its non-selective nature and stringent pH requirements lead to more severe consumption when multiple pollutants are present in water, thereby reducing its effectiveness in degrading antibiotics. Advanced oxidation technologies based on $SO_4^{\bullet-}$ (SR-AOPs) are considered viable alternatives to traditional AOPs due to their high redox potential (2.5–3.1 V) [12,13], which is close to that of $^{\bullet}OH$ (2.8 V), and their long half-life in the mineralization of organic pollutants. Additionally, $SO_4^{\bullet-}$ is more adaptable to a wide range of environmental pH values and exhibits greater selectivity, avoiding excessive degradation [14].

The integration of photocatalysis with peroxymonosulfate (PMS) activation represents a breakthrough in tetracycline antibiotic degradation, combining the advantages of both advanced oxidation processes [15–18]. This hybrid system generates multiple reactive oxygen species including $^{\bullet}OH$, $SO_4^{\bullet-}$, holes (h^+), and singlet oxygen through synergistic mechanisms, enabling mineralization of persistent tetracycline molecules under mild conditions [19,20]. Recent advances in catalyst design have significantly enhanced the efficiency of these systems, with cobalt-doped carbon nitride demonstrating a remarkable 99.2% tetracycline removal within 20 min by facilitating interfacial electron transfer between the photocatalyst and PMS [21]. Cobalt-based metal-organic frameworks have shown particular promise while maintaining excellent structural stability with minimal metal leaching [22]. Novel biomass-derived carbon materials with nitrogen and sulfur co-doping have exhibited exceptional performance, displaying reaction kinetics 5.3 times faster than conventional photocatalysis alone due to their unique defect-mediated activation pathways [23]. These innovative materials address the long-standing challenges of traditional water treatment methods by simultaneously improving light absorption, charge separation efficiency, and PMS utilization while demonstrating superior stability for practical applications [24,25].

Transition metal phosphonates (TMPs) have emerged as highly effective catalysts for pollutant degradation due to their unique electronic properties and exceptional stability. Recent studies demonstrate their remarkable performance in advanced oxidation processes, particularly for degrading persistent organic contaminants [26,27]. For instance, Ni2P-modified photocatalysts exhibit superior tetracycline degradation efficiency, achieving complete mineralization within 60 min by simultaneously enhancing charge separation and activating PMS [28]. Similarly, FeP nanoparticles demonstrate outstanding stability in acidic conditions while effectively decomposing various pharmaceuticals through radical and non-radical pathways [29]. These materials overcome key limitations of conventional catalysts, offering both high activity and long-term durability for water treatment applications. The synergistic effects between their metallic conductivity and catalytic sites enable efficient pollutant degradation while minimizing secondary contamination, making TMPs promising candidates for sustainable environmental remediation [30,31].

The main lines of this study are as follows: (1) characterization of the synthesized CoP-3 by SEM, TEM, EDS, XRD, XPS, and FT-IR spectra; (2) comparison of different cobalt–phosphorus feedstock molar ratios in terms of the TC degradation effect; (3) analysis of the effect of optimized experimental conditions (including TC concentration, PMS concentration, and catalyst dosage) on the degradation of CoP-3/PMS for comparison; (4) investigation of the interference effects of anions, organic compounds, and real water matrices to assess the practical viability of this degradation system; (5) identification of three degradation pathways through liquid chromatography–mass spectrometry (LC-MS) analysis, and toxicological simulations of the intermediate products; (6) comparison of the catalytic properties and the types of the main acting radicals by radical quenching experiments; and (7) evaluation of the application prospects of the materials from the perspectives of stability, reusability, and applicability.

In this study, five transition metal phosphonate catalysts were synthesized in different ratios using cobalt nitrate and phenylphosphonic acid as feedstock. Under visible-light conditions, the degradation of TC was evaluated through PMS activation, and the results showed that all five catalysts exhibited effective catalytic activity. The excellent performance is attributed to the optimized catalyst structure, which promotes efficient PMS activation and rapid generation of active species. Additionally, the catalysts demonstrated excellent cycling stability, maintaining activity across multiple reaction cycles. By systematically elucidating the synergistic interaction between TMPs and PMS activation, we established a new paradigm for efficient pollutant mineralization through radical and non-radical coupled pathways, providing fundamental mechanistic insights for the rational design of high-performance photocatalytic systems for environmental remediation. These findings significantly advance the current understanding of PMS-mediated photocatalysis, particularly highlighting the dual functions of TMPs as both an electron mediator and a catalytic active site. The demonstrated material durability and pH adaptability address key limitations in traditional advanced oxidation processes. Furthermore, the revealed structure–activity relationships lay the scientific foundation for developing next-generation catalysts through targeted atomic engineering.

2. Results and Discussion

2.1. Characterization of Catalysts

The morphology of CoP-X was examined using SEM and TEM. As illustrated in Figure 1a,b, the SEM images of CoP-3 reveal a leaf-like lamellar structure. According to literature reports, polar solvents influence the crystallization direction of complexes [32]. The observed morphology of the catalyst may be attributed to the use of DMF during the preparation process. Figure 1c,d display the TEM images of CoP-3, which confirm the

lamellar morphology observed in the SEM images. Furthermore, energy-dispersive X-ray spectroscopy (EDS) analysis was conducted to examine the surface elemental composition of CoP-3. The results, presented in Figure 1e–j, demonstrate a uniform distribution of C, N, O, Co, and P elements across the catalyst.

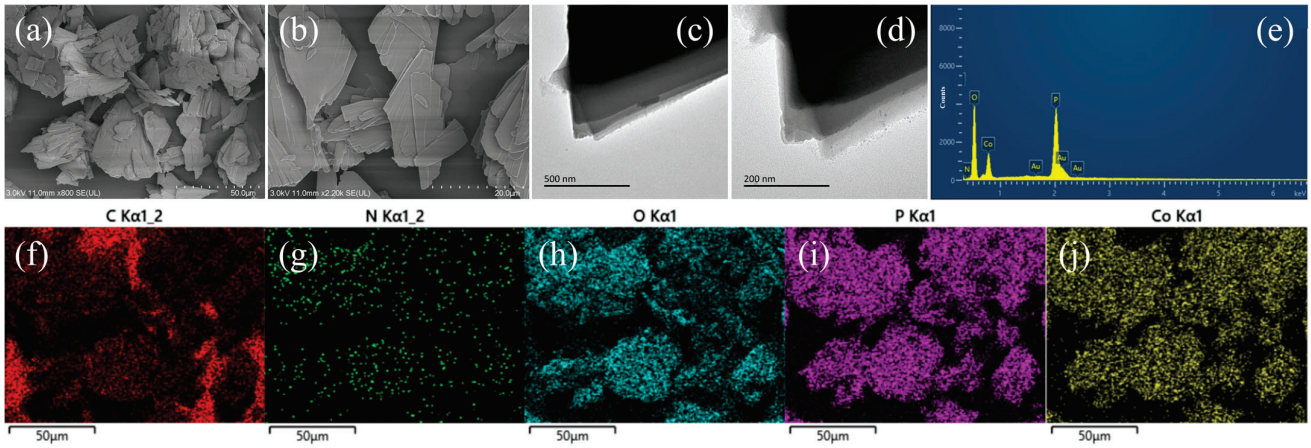


Figure 1. (**a**,**b**) SEM image of CoP-3; (**c**,**d**) TEM images of CoP-3; (**e**–**j**) EDS image of CoP-3.

The crystal structure of CoP-X was determined by XRD, as shown in Figure 2a. The results showed that all CoP-X samples exhibited good crystalline morphology. Despite the differences in the crystallinity of the catalysts with different ratios, all of them observed strong characteristic diffraction peaks at 2θ = 12.02, and the characteristic peaks of CoP appeared at 2θ ≈ 31.6° (200) and 36.3° (210), indicating the successful synthesis of the cobalt–phosphorus compounds [33–36]. Among them, the intensity of diffraction peaks of CoP-3 was significantly higher than that of other samples, indicating its better crystallinity.

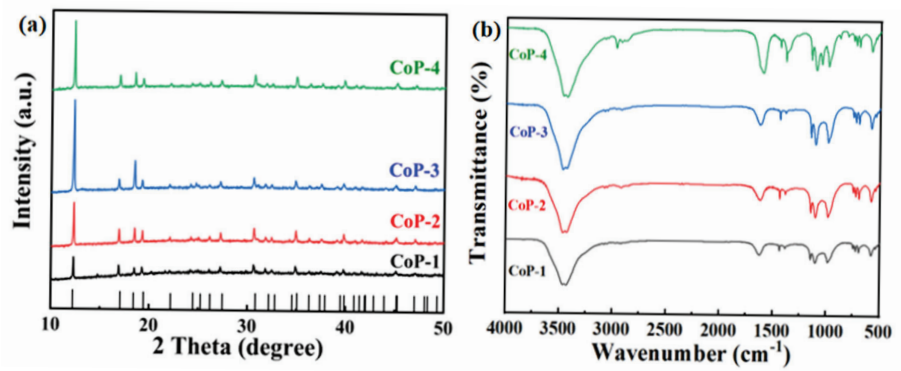


Figure 2. (**a**) XRD and (**b**) FT-IR spectra of CoP-X with different proportions.

To further identify the functional groups present in CoP-X, infrared absorption spectroscopy was performed, as illustrated in Figure 2b. The peak positions across all materials are generally consistent. A strong absorption peak at 3466 cm^{-1} corresponds to the C-H bond in the benzene ring, while the peak at 1608 cm^{-1} is attributed to the bending vibration mode of water molecules [37]. The absorption peak at 1437 cm^{-1} represents skeletal vibrations of the benzene ring, and the peak at 1053 cm^{-1} is characteristic of Co-O-P bonds [35]. Peaks between 900 and 1142 cm^{-1} are associated with the bending modes of tetrahedral CPO_3 groups, and the band below 900 cm^{-1} likely relates to Co-O stretching vibrations [38]. These results confirm that the functional groups present in CoP-X align with the expected structural composition.

Based on the infrared spectroscopy analysis, XPS was conducted to further investigate the bonding modes of elements in CoP-X, as shown in Figure 3a. The wide-spectrum

XPS data confirm the presence of C (1s), O (1s), P (2p), N (1s), and Co (2p) in all CoP-X samples. From the high-resolution Co 2p spectrum (Figure 3b), the binding energy of Co in CoP-2 is observed at 780.8 eV and 796.7 eV, indicating that cobalt exists in the CoP catalyst as Co^{2+} [39–42]. Notably, the binding energy in CoP-2 decreases compared to that in CoP-1, suggesting a higher electron density in CoP-2. Conversely, compared to CoP-3, CoP-2 exhibits higher binding energy, indicating a lower electron density than CoP-3. The electron density differences influence the catalytic behavior: higher electron density facilitates the generation of $SO_4^{\bullet -}$ by donating electrons to PMS, whereas lower electron density promotes the attraction of electrons, favoring the formation of $^1O_2$ [43]. The high-resolution spectrum of P 2p (Figure 3c) reveals that phosphorus predominantly exists as phosphorus–oxygen bonds [44,45], further confirming the chemical composition and crystal structure of the prepared samples. The XPS characterization results are consistent with those obtained from other techniques, providing insights into the valence states and charge transfer directions within the catalysts.

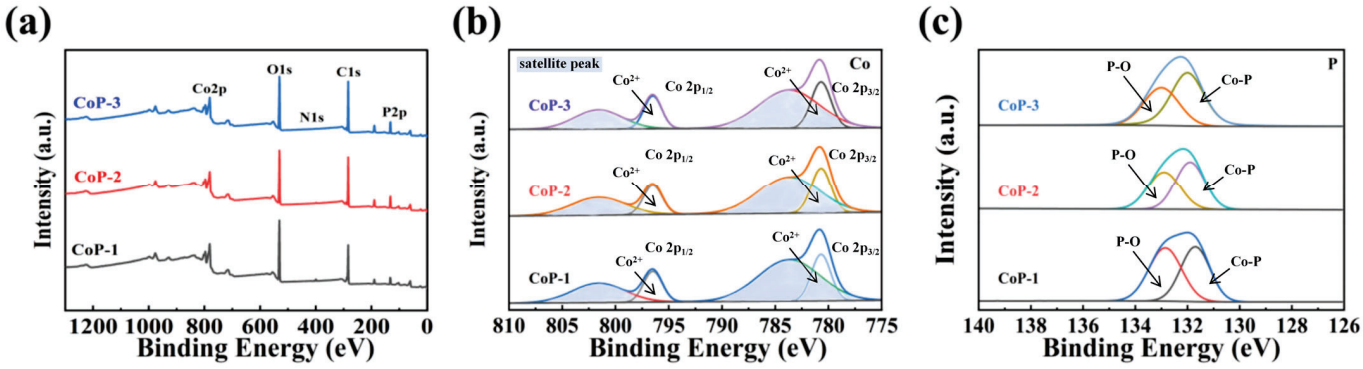


Figure 3. (**a**) XPS patterns of CoP-X with different proportions; (**b**) Co 2p and (**c**) P 2p XPS spectra of CoP-X with different proportions.

The optical properties of CoP-X were analyzed using UV-Vis DRS, as shown in Figure S1. CoP-X exhibits strong absorption in both the ultraviolet and visible regions, with notable peaks at approximately 275 nm and 540 nm, indicating high visible-light absorption efficiency across all samples.

The charge migration behavior in CoP-X catalysts was investigated through photoelectric current response experiments. As shown in Figure 4a, under visible-light irradiation, CoP-1 and CoP-3 exhibited significant photoelectric current responses during multiple on-off cycles. CoP-3 demonstrated a higher photoelectric current density than CoP-1, indicating superior separation and transfer capabilities of photogenerated electron-hole pairs in CoP-3 [46,47]. Furthermore, the photoelectric current remained stable under prolonged illumination, reflecting the continuous ability of CoP-3 to generate and transfer electrons and holes. The electrochemical impedance spectrum further corroborates the enhanced electron transfer capability of CoP-3. As shown in Figure 4b, the arc radius of CoP-3 is smaller than that of CoP-1, indicating lower electron transfer impedance and faster electron diffusion rates. The CoP-X catalysts effectively inhibit the recombination of photogenerated electron–hole pairs while promoting their separation and transfer, with CoP-3 demonstrating the most efficient performance among the samples [48].

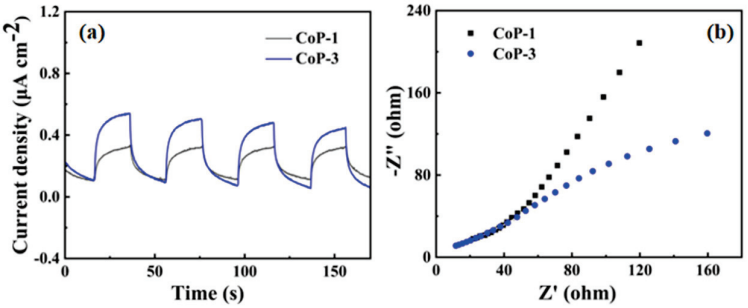


Figure 4. (**a**) Photocurrent response diagram; (**b**) EIS spectra of CoP-1 and CoP-3 samples.

2.2. Photocatalytic Activity of CoP Catalysts with Different Proportions

The photocatalytic activity of CoP-X catalysts with varying proportions of precursors under visible-light irradiation was evaluated using PMS for the degradation of TC as the target pollutant. After a 20 min dark reaction, the TC concentration decreased by 1.5%, indicating that the material has low adsorption performance. A quantity of 5.0 mg of PMS was introduced to the system, and the pollutant degradation rate was monitored, as shown in Figure 5a,b. The results reveal that, under the synergistic effect of PMS, all five catalysts significantly enhanced the TC degradation rate. Among these, the CoP-3 catalyst synthesized with 3 mmol phenylphosphonic acid ($n[C_6H_7O_3P]$:n = 3:2) exhibited the highest degradation efficiency, achieving a TC degradation rate of 65.5% within 6 min with a corresponding rate constant of 0.503 min^{-1}. These findings are consistent with the catalyst characterization results.

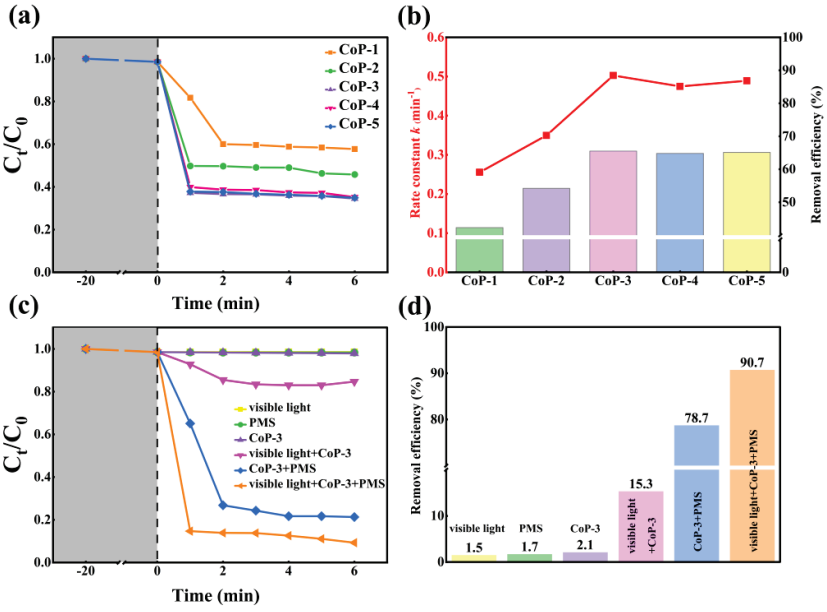


Figure 5. (**a**) Degradation performance and (**b**) removal rate and corresponding first-order degradation rate constant of TC with different catalysts by visible light (0.1 mg/L catalysts, 0.1 mg/L PMS, 10 mg/L TC); (**c**) degradation performance and (**d**) removal efficiency of TC in different catalytic systems (0.1 mg/L catalysts, 0.2 mg/L PMS, 10 mg/L TC).

2.3. Catalytic Activity of CoP-3 Catalyst

The system was tested for the removal of TC under six conditions: visible light, PMS, and CoP-3 alone, and visible light + CoP-3, PMS + CoP-3 and visible light + CoP-3 + PMS. As shown in Figure 5c, d, the results indicate that the degradation rate in the presence of visible light, PMS, and CoP-3 alone is low and almost negligible. Under the conditions of visible light + CoP-3, PMS + CoP-3, and visible light + CoP-3 + PMS, the TC removal

rates were 15.3%, 78.7% and 90.7%, respectively, which indicated that the material had certain light-responsive properties and substantially improved the degradation efficiency with the addition of PMS, and the combination of visible light and PMS improved the TC removal efficiency.

2.4. Optimization of Experimental Parameters in the CoP-3/PMS/Vis System

2.4.1. Influence of Catalyst Dosage

The role of catalyst dosage in TC degradation was investigated using a fixed TC concentration of 10.0 mg/L. Following a 20 min dark reaction, 5.0 mg of PMS was added, and the effects of varying catalyst dosages (2.5, 5.0, 10.0, 15.0, and 20.0 mg) were assessed, as shown in Figure 6a,b. The results demonstrate a strong correlation between catalyst dosage and degradation efficiency. For a dosage of 2.5 mg of CoP-3, the TC degradation rate reached 70.5% within 6 min, which slightly increased to 70.2% when the dosage was raised to 5.0 mg, with a rate constant of 1.148 min^{-1}. The higher doses (10.0–20.0 mg) all showed degradation rates of more than 60.0% within 6 min, which was slightly lower than the TC removal rate at a catalyst of 5.0 mg, probably due to the competition of activation sites of the catalyst for PMS molecules. The experimental results showed that the optimal catalyst dose of 5.0 mg (equivalent to a concentration of 0.1 g/L) achieved the best degradation performance under this experimental condition.

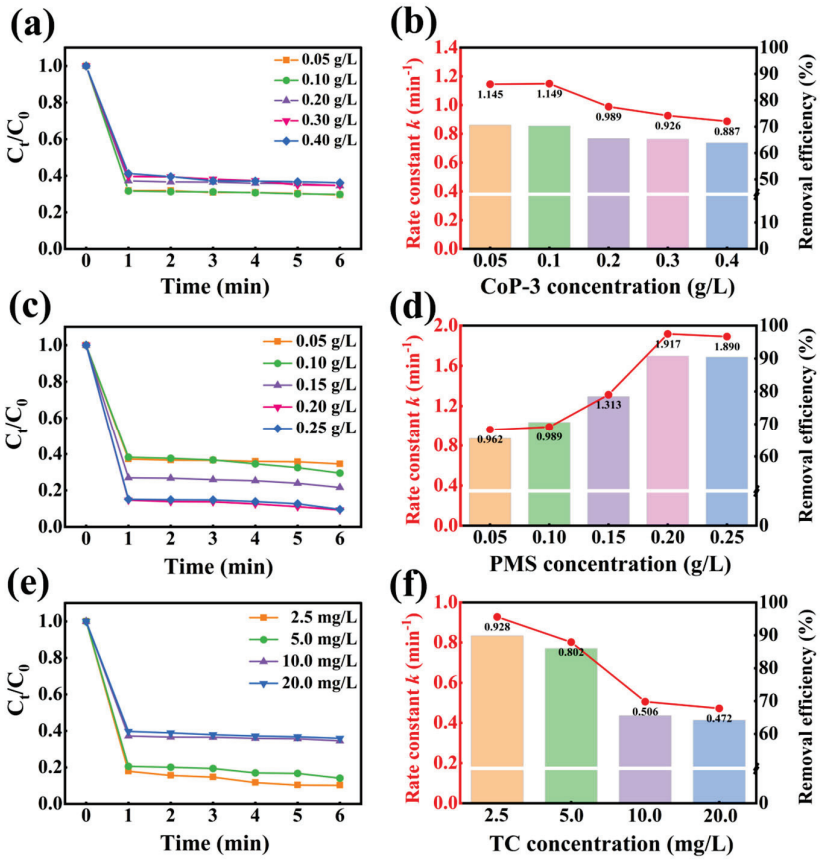


Figure 6. Effects of (**a**,**b**) catalyst concentration, (**c**,**d**) PMS concentration, and (**e**,**f**) TC concentration on TC degradation performance, removal rate, and corresponding first-order degradation rate constant.

2.4.2. Influence of PMS Concentration

In order to investigate the effect of PMS concentration on TC degradation, the catalyst dose was fixed at 5.0 mg in the experiment, and the TC concentration was set at 10.0 mg/L. The PMS concentration was varied between 2.5 and 12.5 mg, and the results are shown in Figure 6c,d. The degradation rate was gradually increased with the increase in the

PMS concentration, which indicated that the PMS provided free radicals for the whole reaction system [49]. At the PMS concentration of 0.20 g/L, the degradation effect did not change much and tended to stabilize around 90% with a rate constant of 1.917 min^{-1}. When the PMS concentration was further increased to 0.25 g/L, the degradation rate decreased slightly, which may be due to the generation of less reactive substances by the secondary reaction (e.g., $SO_5^{\bullet -}$), as described in Reactions (1) and (2) [50]. In addition, the limited number of active sites on the catalyst surface restricted further acceleration of the degradation reaction. Therefore, the optimum PMS concentration for the system was determined to be 0.20 g/L.

$$HSO_5 + SO_4^{\bullet -} \rightarrow SO_5^{\bullet -} + HSO_4 \quad (1)$$

$$HSO_5 + {}^{\bullet}OH \rightarrow SO_5^{\bullet -} + H_2O \quad (2)$$

2.4.3. Influence of TC Concentration

The effect of varying TC concentrations (2.5, 5.0, 10.0, and 20.0 mg/L) on degradation efficiency was investigated under conditions of 5.0 mg catalyst and 10 mg PMS, as shown in Figure 6e,f. The degradation rates for TC concentrations of 2.5, 5.0, 10.0, and 20.0 mg/L were 89.8%, 85.9%, 65.5%, and 64.1%, respectively. After 6 min, the degradation rate for 5.0 mg/L TC reached 85.9%, indicating the highest degradation efficiency. Higher TC concentrations resulted in slower degradation rates, which could be attributed to the limited quantity of free radicals produced by the quantitative catalyst activation of PMS and the limited amount of TC that could be degraded [51]. However, the system exhibited effective TC degradation at all concentrations tested.

2.5. Response of the CoP-3/PMS/Vis Degradation System to External Disturbances

Exploring the effect of anions on the system, Figure 7a,b show that the solution with the addition of HCO_3^- was the most obviously inhibited, with a TC removal rate of only 13.3%, and CO_3^{2-}, $H_2PO_4^-$, and Cl^-, in that order, had a decreasing effect on the removal rate of the system, with degradation rates of 69.7%, 76.5%, and 76.8%. At the same time, by adding HA to the system to simulate the effect of organic matter on the degradation process, it can be clearly seen that the degradation effect is inhibited, and the degradation rate compared with the blank experimental group decreased by 60.4%. The organic matter competes with the pollutants for the active radicals in the degradation process, resulting in a decrease in the TC degradation rate [52].

In this experiment, TC was added to four water samples (Xuanwu Lake, Chaohu Lake, Yangtze River, and animal husbandry wastewater) at a concentration of 10 mg/L (Figure 7c,d). Compared with the blank group, the system showed good catalytic degradation performance in Yangtze River and Chaohu Lake samples, and the removal rate of TC reached 79.9%. 79.9%, and 80.8%, which is attributed to the fact that these two water systems are natural water systems with less interference of substances. In contrast, the TC removal rate in Xuanwu Lake was slightly lower than in the previous two samples, because Xuanwu Lake is an artificial lake, and there is a certain concentration of N/P content interference. Livestock farming wastewater from suburban livestock and poultry breeding bases, which has a high content of organic matter and anions, is affected by various factors, and the removal rate of TC in it is 64.7%. The actual water samples' interference experiments demonstrated that the degradation system has a certain degree of feasibility in practical applications, with good degradation effect, which is stable at more than 64%.

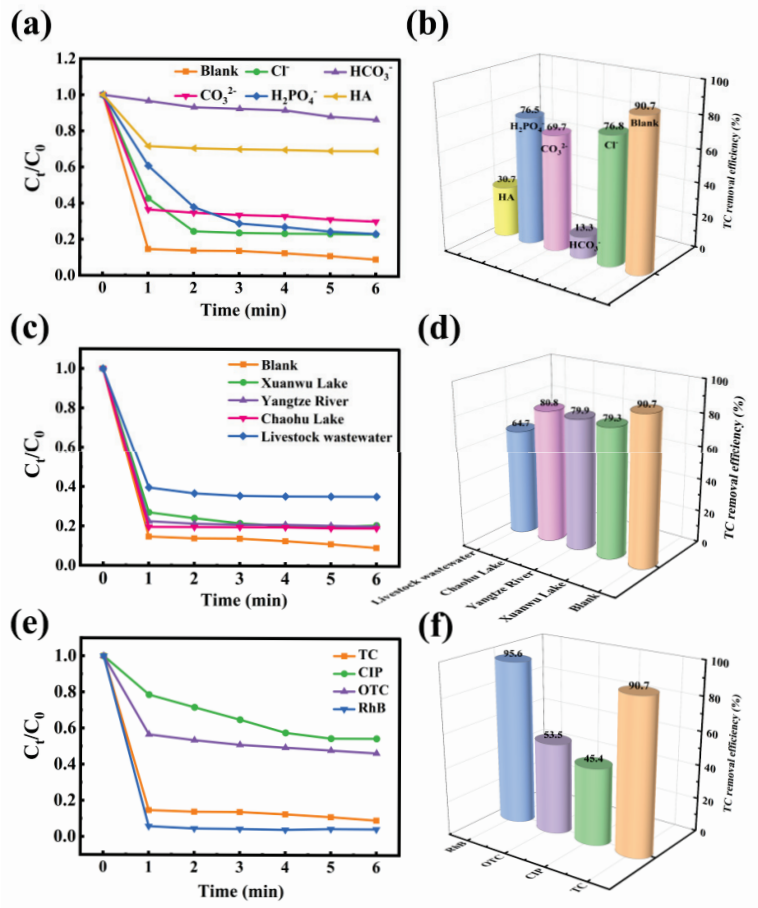


Figure 7. (**a**) Effects of Cl^-, HCO_3^-, CO_3^{2-}, $H_2PO_4^-$ ions, and HA on TC degradation; (**b**) TC removal rates in the presence of different anions; (**c**,**d**) degradation and removal rates of TC by the CoP-3/PMS/Vis system in different water matrices (including Yangtze River, Chaohu Lake, Xuanwu Lake, and livestock wastewater); (**e**,**f**) degradation efficiency and removal rates of various pollutants by the CoP-3/PMS/Vis system.

To investigate whether the degradation system can remove other pollutants, this study examined the degradation of three pollutants, oxytetracycline (OTC), ciprofloxacin (CIP), and Rhodamine B (RhB), by the CoP-3/PMS/visible-light system. The results are shown in the Figure 7e,f. During antibiotic degradation, CIP and OTC were partially degraded with removal rates of 45.4% and 53.5%, respectively, significantly lower than that of the tetracycline system. The lowest removal rate for CIP may be attributed to its nature as a fluoroquinolone antibiotic [53], which is notoriously difficult to degrade. In contrast, RhB achieved a removal rate of 95.6%, demonstrating excellent catalytic degradation performance.

2.6. Free Radical Analysis

The role of reactive radicals in PMS activation for TC degradation under visible-light irradiation was examined using quenching experiments. For free radical quenching experiments, $^{\bullet}OH$, superoxide radicals ($O_2^{\bullet-}$), and h^+ were quenched by the addition of IPA (200 mM), BQ (10 mM), and EDTA (10 mM), respectively [54–56].

Figure 8 shows that the degradation rate constant in the absence of quenchers was 0.989 min^{-1}, while the addition of EDTA as a quencher reduced the rate constant to 0.475 min^{-1}, with a degradation efficiency of about 38.5%. In contrast, the addition of BQ and IPA reduced degradation efficiencies to 47.2% and 60.0%. The results showed that EDTA had the greatest effect on the CoP-3/PMS system, inhibiting the TC degradation rate by 41.1%, indicating that h^+ quenched by EDTA plays a dominant role in the

CoP-3/PMS/Vis degradation system. It is inferred that a radical chain reaction exists in the system.

$$Co(II) + HSO_5^- \rightarrow Co(III) + SO_4^{\cdot-} + OH^- \quad (3)$$

$$Co(III) + HSO_5^- \rightarrow Co(II) + SO_5^{\cdot-} + H^+ \quad (4)$$

$$SO_5^{\cdot-} + SO_5^{\cdot-} \rightarrow {}^1O_2 + 2SO_4^{2-} \quad (5)$$

$$2SO_5^{\cdot-} + H_2O \rightarrow 1.5\,{}^1O_2 + 2HSO_4^- \quad (6)$$

$$O_2^{\cdot-} + \cdot OH \rightarrow {}^1O_2 + OH^- \quad (7)$$

$$HO_2^{\cdot-} + SO_4^{\cdot-} \rightarrow {}^1O_2 + HSO_5^- \quad (8)$$

$$SO_4^{\cdot-} + H_2O \rightarrow SO_4^{2-} + \cdot OH + H^+ \quad (9)$$

$$SO_4^{\cdot-} + OH^- \rightarrow SO_4^{2-} + \cdot OH \quad (10)$$

$$HSO_5^- + H_2O \rightarrow H_2O_2 + HSO_4^- \quad (11)$$

$$\cdot OH + H_2O_2 \rightarrow HO_2^{\cdot-} + H_2O \quad (12)$$

$$HO_2^{\cdot-} \rightarrow H^+ + O_2^{\cdot-} \quad (13)$$

$$SO_4^{\cdot-}/O_2^{\cdot-}/\cdot OH/{}^1O_2 + CIP \rightarrow \text{Intermediates} + CO_2 + H_2O \quad (14)$$

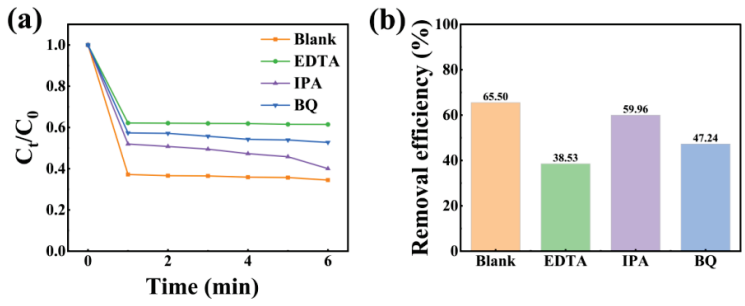


Figure 8. Effects of different quenchers on the degradation of TC in the system: (**a**) degradation rate; (**b**) rate constant.

2.7. Transformation Pathways of TC Degradation

To elucidate potential intermediates generated during the degradation process of this system, we analyzed the intermediates in the degradation process by liquid chromatography–mass spectrometry (Figure S2). Three proposed pathways are illustrated in the Figure 9. In Pathway 1, TC was fragmented to P1 (m/z = 427) by the dehydration process, starting with ROS attacking the -N(CH_3)$_2$ group to generate P2 (m/z = 399). P2 was converted to P3 (m/z = 318) by deamination reaction, and P3 was degraded to P4 (m/z = 274) by combined demethylation [57]. In Pathway 2, subsequently, it was further oxidized to P5 (m/z = 359), before losing hydroxyl and opening the ring to form P6 (m/z = 245). According to the HOME and Fukui index, C29–C30 on the benzene ring was attacked via nucleophilic reaction and further opened, as well as hydroxylation, to produce P7 (m/z = 157) [58]. Furthermore, as displayed in Path 3, after demethylation, TC was gradually decomposed, and P9 (m/z = 397) was subsequently decomposed into P10 (m/z = 297) through deamination, demethylation, and dehydroxylation. Then, P6 (m/z = 195) was generated from P10 (m/z = 297) via dehydroxylation and the destruction of C–C bonds [59].

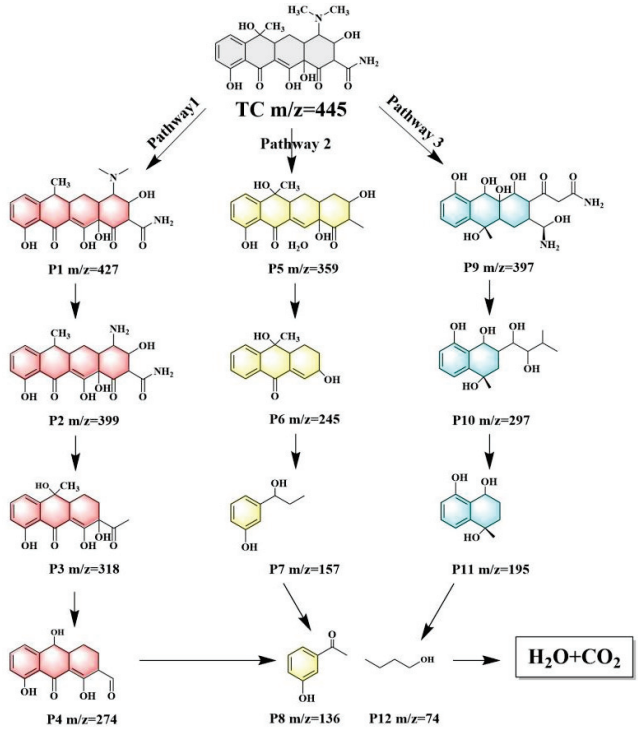


Figure 9. Potential pathway for the transformation of TC degradation in CoP-3/PMS/Vis system.

Finally, product m/z values of P8 (m/z = 136) and P12 (m/z = 74) were obtained via further cleavage of the ring along with hydroxylation [60,61].

The toxicity of the intermediates was simulated by T.E.S.T (5.1.2) toxicity analysis software in terms of developmental toxicity and biological toxicity (LC50 of fathead ninnow and Daphnia magna). The results are presented in Figure 10. The analyses showed that all the biological toxicity was reduced except for that of P1, P2, P4 and P5; in particular, the toxicity of P8/P10 was lower, and the liquid-plasmid results showed that P8 was also largely converted to P7. In the results, P8 was also converted to a large amount, and the degradation process was green and safe in terms of developmental toxicity [62].

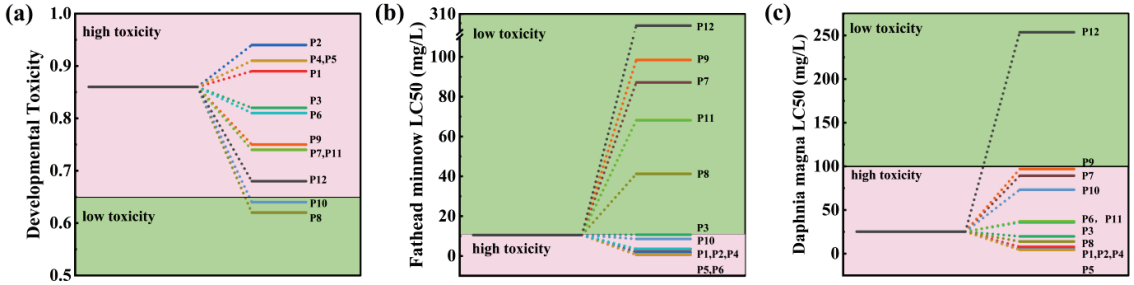


Figure 10. (**a**) Developmental toxicity, (**b**) fathead minnow LC50 (96 h), (**c**) Daphnia magna LC 50, for CIP and intermediate products.

In the LC50 simulation of two aquatic organisms, fathead ninnow and Daphnia magna, P12 showed low toxicity. A small amount of P12 generation was detected at six minutes of reaction time. However, the toxicity of P1/P2/P4/P5 was similar to that of TC, which did not significantly reduce the toxicity of TC; however, due to the short existence time, it was easily converted into other low-toxicity substances. It can be concluded that the degradation reaction process, which can reduce the toxicity of TC, has good ecological safety.

2.8. Catalyst Stability

The stability of the CoP-3 catalyst was evaluated through cyclic experiments under conditions of 5.0 mg catalyst, 10.0 mg PMS, and 10.0 mg/L TC, as shown in Figure 11. After four cycles, the TC degradation rate was maintained at about 70%, indicating stable catalyst activity without significant performance loss, thus confirming its high stability and favoring reproducibility in future practical applications [63,64].

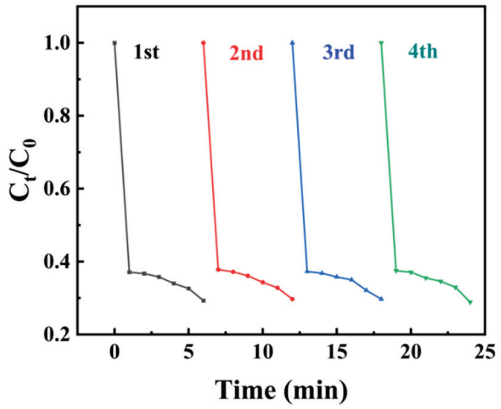


Figure 11. Stability of CoP-3 catalysts.

2.9. Catalyst Performance Comparison

To investigate the superior catalytic efficiency of CoP-3 in this experiment, a comparison was made with relevant catalysts reported in previous literature, as shown in Table S1 [63,65–68]. It can be clearly observed that the degradation time in our system is shorter and the reaction rate constant is significantly higher than those in other catalytic systems, reached 0.989 min^{-1}. This system efficiently removes TC from wastewater while requiring a smaller amount of catalyst, offering significant cost advantages.

3. Materials and Methods

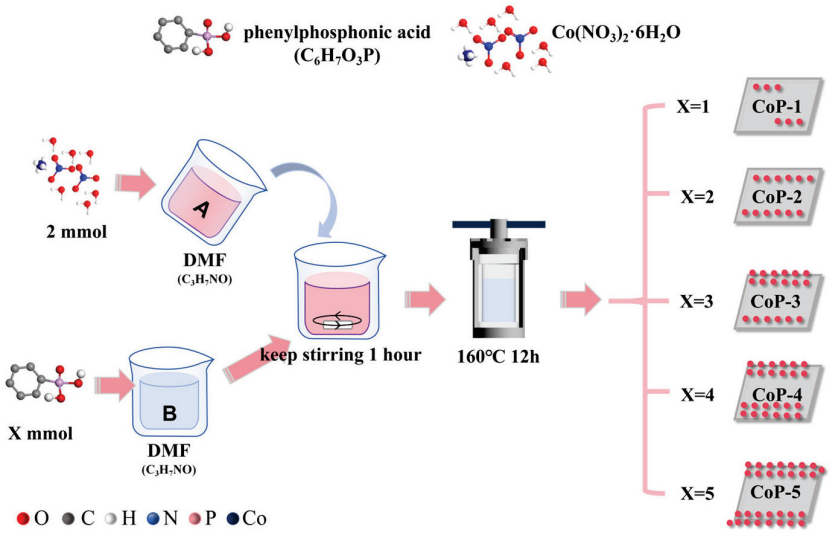
3.1. Chemicals and Reagents

The materials in this paper are shown in Supporting Information.

3.2. Synthesis of Catalysts

The preparation process is illustrated in Scheme 1. First, 2 mmol of cobalt nitrate was dissolved in 10 mL of N, N-Dimethylformamide (DMF) to prepare solution A. Separately, a specific amount of phenylphosphonic acid was dissolved in 15 mL of DMF to prepare solution B. After complete dissolution, solution A was slowly added to solution B under continuous stirring. The resulting mixture was stirred for 1 h using a magnetic stirrer, then transferred to a 50 mL reactor and heated in an oven at 160 °C for 12 h. After the reaction, the obtained samples were washed with ethanol, dried in an oven, and stored for subsequent use.

The amount of phenylphosphonic acid used was varied (1 mmol, 2 mmol, 3 mmol, 4 mmol, and 5 mmol) to synthesize different materials. The resulting catalysts were designated as CoP-X (X = 1, 2, 3, 4, or 5), where X represents the amount of phenylphosphonic acid employed in the synthesis process.



Scheme 1. Synthesis steps of CoP-X.

3.3. Characterization Techniques and Degradation Testing

Comprehensive details regarding the characterization apparatus and the TC degradation assessment are presented in the Supporting Information.

4. Conclusions

A series of CoP photocatalysts with tailored precursor ratios were synthesized and extensively characterized to establish structure–performance relationships. The optimized CoP-3 catalyst demonstrated exceptional photocatalytic activity, achieving rapid TC degradation (90.7% in 6 min) under visible light and the PMS system, attributed to its superior crystallinity, electronic structure, and efficient charge transfer capabilities. Systematic optimization of reaction parameters identified the ideal conditions for maximizing degradation efficiency: 0.1 g/L CoP-3 and 0.2 g/L PMS. Mechanistic investigations revealed that the generation of h^+ and its synergy with active species significantly enhanced catalytic performance, offering new insights into PMS activation pathways. This study establishes a robust framework for designing advanced CoP-based photocatalysts, advancing their application in environmental remediation.

Supplementary Materials: The following supporting information can be downloaded at: https://www.mdpi.com/article/10.3390/catal15060580/s1, the reuse studies, Figure S1: UV-vis DRS spectra of CoP-X samples; Figure S2: Mass spectra of TC and transformation products at 0 min, 1.0 min, 6.0 min; Table S1: Comparison of catalytic effects among homogeneous catalysts.

Author Contributions: Conceptualization, methodology and formal analysis were conducted by X.H.; material preparation and characterization were conducted by W.S., R.B., Y.H., J.L., Y.P. and M.Z.; writing–original draft preparation, manuscript review, supervision and funding acquisition were conducted by G.W. All authors have read and agreed to the published version of the manuscript.

Funding: This work was financially supported by the Opening Project of Guangxi Key Laboratory of Petrochemical Resource Processing and Process Intensification Technology (2023K004), Natural Science Foundation of Jiangsu Province in China (BK20230410), Natural Science Research of Jiangsu Higher Education Institution of China (23KJB610010), The National College Students Innovation and Entrepreneurship Training Program (202210298069Z, 202410298096Z). Thanks to Shiyanjia Lab (https://www.shiyanjia.com, access on 7 June 2025) for help with testing.

Data Availability Statement: The data presented in this study are available on request from the corresponding author.

Conflicts of Interest: The authors declare no conflicts of interest.

References

1. Li, X.Y.; Lai, C.Y.; Zhao, H.P. A Novel Oxygen-Based Manganese Oxides Modified Membrane Reactor for TC Oxidative Degradation. *J. Water Process Eng.* **2024**, *59*, 104978. [CrossRef]
2. Li, Y.; Jia, Z.; Xu, L.; Sheng, G.; Wan, C. Synergistic Removal of Tetracycline Hydrochloride by Nano-MnO_x/NCF Composite Fiber (MNCs) Catalysts via Heterogeneous Peroxymonosulfate (PMS) Activation. *Inorg. Chem. Commun.* **2025**, *172*, 113682. [CrossRef]
3. Lyu, J.; Yang, L.; Zhang, L.; Ye, B.; Wang, L. Antibiotics in Soil and Water in China–a Systematic Review and Source Analysis. *Environ. Pollut.* **2020**, *266*, 115147. [CrossRef]
4. Chu, G.; Qi, W.; Chen, W.; Zhang, Y.; Gao, S.; Wang, Q.; Gao, C.; Gao, M. Metagenomic Insights into the Nitrogen Metabolism, Antioxidant Pathway, and Antibiotic Resistance Genes of Activated Sludge from a Sequencing Batch Reactor under Tetracycline Stress. *J. Hazard. Mater.* **2024**, *462*, 132788. [CrossRef]
5. Zhu, Y.G.; Johnson, T.A.; Su, J.Q.; Qiao, M.; Guo, G.X.; Stedtfeld, R.D.; Hashsham, S.A.; Tiedje, J.M. Diverse and Abundant Antibiotic Resistance Genes in Chinese Swine Farms. *Proc. Natl. Acad. Sci. USA* **2013**, *110*, 3435–3440. [CrossRef]
6. Larsson, D.G.J.; Flach, C.F. Antibiotic Resistance in the Environment. *Nat. Rev. Microbiol.* **2022**, *20*, 257–269. [CrossRef]
7. Ding, Y.; Liang, B.; Jiang, W.; Han, J.; Guadie, A.; Yun, H.; Cheng, H.; Yang, R.; Liu, S.J.; Wang, A.; et al. Effect of Preferential UV Photolysis on the Source Control of Antibiotic Resistome during Subsequent Biological Treatment Systems. *J. Hazard. Mater.* **2021**, *414*, 125484. [CrossRef]
8. Zhang, S.; Zhang, X.; Shen, X.; Lu, X.; Guo, Y.; Li, Y.; Han, X.; Liu, R.; Chen, F.; Sun, C. Research Status of Membrane Separation Technology in the Treatment of Antibiotic Wastewater. *Environ. Sci. Water Res. Technol.* **2025**, *11*, 1386–1400. [CrossRef]
9. Zhang, X.; Zhu, G.; Xiao, B.; Geng, J.; Yang, Y.; Wang, D.; Li, J.; Wang, J.; Zhu, Y. Iron-Based Resin Heterogeneous Photo-Self-Fenton System for Efficient Photocatalytic Degradation of Antibiotic Wastewater. *Sep. Purif. Technol.* **2024**, *330*, 125338. [CrossRef]
10. Uddin, T.M.; Chakraborty, A.J.; Khusro, A.; Zidan, B.R.M.; Mitra, S.; Emran, T.B.; Dhama, K.; Ripon, M.d.K.H.; Gajdács, M.; Sahibzada, M.U.K.; et al. Antibiotic Resistance in Microbes: History, Mechanisms, Therapeutic Strategies and Future Prospects. *J. Infect. Public Health* **2021**, *14*, 1750–1766. [CrossRef]
11. Sun, Y.; Yi, F.; Li, R.; Min, X.; Qin, H.; Cheng, S.; Liu, Y. Inorganic–Organic Hybrid Membrane Based on Pillararene-intercalated MXene Nanosheets for Efficient Water Purification. *Angew. Chem. Int. Ed.* **2022**, *61*, e202200482. [CrossRef] [PubMed]
12. Liu, S.; Zhang, Z.; Huang, F.; Liu, Y.; Feng, L.; Jiang, J.; Zhang, L.; Qi, F.; Liu, C. Carbonized Polyaniline Activated Peroxymonosulfate (PMS) for Phenol Degradation: Role of PMS Adsorption and Singlet Oxygen Generation. *Appl. Catal. B* **2021**, *286*, 119921. [CrossRef]
13. Feng, S.; Xie, T.; Wang, J.; Yang, J.; Kong, D.; Liu, C.; Chen, S.; Yang, F.; Pan, M.; Yang, J.; et al. Photocatalytic Activation of PMS over Magnetic Heterojunction Photocatalyst $SrTiO_3/BaFe_{12}O_{19}$ for Tetracycline Ultrafast Degradation. *Chem. Eng. J.* **2023**, *470*, 143900. [CrossRef]
14. Xu, Y.; Guo, M.; Ge, C.; Zhang, P.; Xu, W.; Zhang, L.; Zhou, S.; Liao, J. Cu Single Atoms/O Doping g-C_3N_4 Mediated Photocatalytic Activation of Peroxymonosulfate for Ultrafast Carbamazepine Removal via High $^1O_2$ Yield. *Appl. Surf. Sci.* **2023**, *640*, 158290. [CrossRef]
15. Shi, W.; Hao, C.; Fu, Y.; Guo, F.; Tang, Y.; Yan, X. Enhancement of Synergistic Effect Photocatalytic/Persulfate Activation for Degradation of Antibiotics by the Combination of Photo-Induced Electrons and Carbon Dots. *Chem. Eng. J.* **2022**, *433*, 133741. [CrossRef]
16. Hu, J.; Tian, J.; Yang, Y.; Li, S.; Lu, J. Enhanced Antibiotic Degradation via Photo-Assisted Peroxymonosulfate over Graphitic Carbon Nitride Nanosheets/$CuBi_2O_4$: Highly Efficiency of Oxygen Activation and Interfacial Charge Transfer. *J. Colloid Interface Sci.* **2024**, *661*, 68–82. [CrossRef]
17. Gao, X.; Zhang, Y.; Wang, X.; Zhou, Y.; Wu, W.D.; Chen, X.D.; Wu, Z. Unraveling the Photocatalytic Activation of Peroxymonosulfate on Anatase/Rutile Homojunctions: Efficacy and Mechanism Study. *Chem. Eng. J.* **2023**, *476*, 146804. [CrossRef]
18. Jiang, X.; Li, J.; Li, J.; Xu, W.; Liu, Z. Visible-Light-Driven Peroxymonosulfate Activation for Accelerating Tetracycline Removal Using Co-TiO_2 Nanospheres. *Catalysts* **2023**, *13*, 836. [CrossRef]
19. Cui, M.; Cui, K.; Liu, X.; Zhang, Y.; Chen, X.; Chen, Y.; Sun, S.; Liu, J.; Hu, Z. Peroxymonosulfate Conversion to Singlet Oxygen over π-Electron Delocalized Carbon Nitride for Selective Degradation of Emerging Contaminants. *J. Environ. Chem. Eng.* **2023**, *11*, 111494. [CrossRef]
20. Xiang, W.; Liao, Y.; Cui, J.; Fang, Y.; Jiao, B.; Su, X. Room-Temperature Synthesis of Fe/Cu-BTC for Effective Removal of Tetracycline Antibiotic from Aquatic Environments. *Inorg. Chem. Commun.* **2024**, *167*, 112728. [CrossRef]
21. Wang, Y.; Bai, Y.; Han, C.; Li, Z.; Lun, X.; Zhang, C. Photocatalysis-PMS Oxidation System Based on CQDs-Doped Carbon Nitride Nanosheets for Degradation of Residual Drugs in Water. *Environ. Sci. Pollut. Res.* **2023**, *30*, 108538–108552. [CrossRef] [PubMed]

22. Zhao, W.; Shen, Q.; Nan, T.; Zhou, M.; Xia, Y.; Hu, G.; Zheng, Q.; Wu, Y.; Bian, T.; Wei, T.; et al. Cobalt-Based Catalysts for Heterogeneous Peroxymonosulfate (PMS) Activation in Degradation of Organic Contaminants: Recent Advances and Perspectives. *J. Alloys Compd.* **2023**, *958*, 170370. [CrossRef]
23. Xian, L.; Fan, G. N,S,O Triply-Doped Carbon with Nanotubes-Interwoven Nanosheets Encapsulated Co Nanoparticles for Robust Antibiotic Destruction via Activating Peroxymonosulfate. *Environ. Res.* **2024**, *248*, 118259. [CrossRef] [PubMed]
24. Long, X.; Feng, C.; Ding, D.; Chen, N.; Yang, S.; Chen, H.; Wang, X.; Chen, R. Oxygen Vacancies-Enriched $CoFe_2O_4$ for Peroxymonosulfate Activation: The Reactivity between Radical-Nonradical Coupling Way and Bisphenol a. *J. Hazard. Mater.* **2021**, *418*, 126357. [CrossRef]
25. Ren, T.; Yin, M.; Chen, S.; Ouyang, C.; Huang, X.; Zhang, X. Single-Atom Fe-N_4 Sites for Catalytic Ozonation to Selectively Induce a Nonradical Pathway toward Wastewater Purification. *Environ. Sci. Technol.* **2023**, *57*, 3623–3633. [CrossRef]
26. Shen, M.; Zhang, X.; Zhao, S.; Wang, S. gCN-P: A Coupled g-C_3N_4/Persulfate System for Photocatalytic Degradation of Organic Pollutants under Simulated Sunlight. *Environ. Sci. Pollut. Res.* **2022**, *29*, 23280–23291. [CrossRef]
27. Du, M.; Li, D.; Liu, S.F.; Yan, J. Transition Metal Phosphides: A Wonder Catalyst for Electrocatalytic Hydrogen Production. *Chin. Chem. Lett.* **2023**, *34*, 108156. [CrossRef]
28. Yan, X.; An, H.; Chen, Z.; Yang, G. Significantly Enhanced Charge Transfer Efficiency and Surface Reaction on NiP_2/g-C_3N_4 Heterojunction for Photocatalytic Hydrogen Evolution. *Chin. J. Chem. Eng.* **2022**, *43*, 31–39. [CrossRef]
29. Xu, L.H.; Che, P.C.; Zhang, X.J.; Cosnier, S.; Shan, D. FeP Nanoparticles Highly Dispersed on N,P-Doped Petaloid Carbon Nanosheet: Interface Engineering and Boosted Intrinsic ORR Activity. *Appl. Surf. Sci.* **2023**, *620*, 156770. [CrossRef]
30. Zhang, W.; Chen, Y.; Ma, Z.; Sun, Z.; Wang, J.; Feng, J.; Yan, W.; Wang, H. Challenges and Strategies of Transition Metal Phosphides Applied in Oxygen Evolution Reaction of Electrocatalytic Water Splitting: A Review. *Fuel* **2024**, *369*, 131741. [CrossRef]
31. Sushma; Kumari, M.; Saroha, A.K. Performance of Various Catalysts on Treatment of Refractory Pollutants in Industrial Wastewater by Catalytic Wet Air Oxidation: A Review. *J. Environ. Manag.* **2018**, *228*, 169–188. [CrossRef] [PubMed]
32. Cheng, X.; Zhai, Y.; Wang, X.; Cao, X.; Guan, D.; Zhang, H.; Zhu, Q.; Fang, S.; Wang, L. Polar Solvent-Mediated Direct Room Temperature Synthesis of Pure-Red-Emitting Perovskite Nanocrystals. *J. Lumin.* **2024**, *271*, 120610. [CrossRef]
33. Zhang, K.; Zhang, G.; Ji, Q.; Qu, J.; Liu, H. Arrayed Cobalt Phosphide Electrocatalyst Achieves Low Energy Consumption and Persistent H_2 Liberation from Anodic Chemical Conversion. *Nano-Micro Lett.* **2020**, *12*, 154. [CrossRef] [PubMed]
34. Chen, J.B.; Ying, J.; Xiao, Y.X.; Tian, G.; Dong, Y.; Shen, L.; Córdoba De Torresi, S.I.; Symes, M.D.; Janiak, C.; Yang, X.-Y. Directed Mass and Electron Transfer Promoted by Hierarchical Porous Co–P–O Leads to Enhancement of the Overall Water Splitting Efficiency. *ACS Catal.* **2023**, *13*, 14802–14812. [CrossRef]
35. Zhang, Y.; Diao, Z.; Wei, J.; Luo, M.; Xie, L.; Huang, L.; Ren, J.; Ai, N.; Li, L.; Guo, H.; et al. Bifunctional Synergistic CoP/Coral-like g-C_3N_4 Catalyst: Boosting the Photocatalytic Water Splitting Hydrogen Evolution and Appreciation of Anisalcohol at Same Time. *Appl. Surf. Sci.* **2023**, *614*, 156187. [CrossRef]
36. Luo, R.; Liu, C.; Li, J.; Wang, J.; Hu, X.; Sun, X.; Shen, J.; Han, W.; Wang, L. Nanostructured CoP: An Efficient Catalyst for Degradation of Organic Pollutants by Activating Peroxymonosulfate. *J. Hazard. Mater.* **2017**, *329*, 92–101. [CrossRef]
37. Kohantorabi, M.; Giannakis, S.; Moussavi, G.; Bensimon, M.; Gholami, M.R.; Pulgarin, C. An Innovative, Highly Stable Ag/ZIF-67@GO Nanocomposite with Exceptional Peroxymonosulfate (PMS) Activation Efficacy, for the Destruction of Chemical and Microbiological Contaminants under Visible Light. *J. Hazard. Mater.* **2021**, *413*, 125308. [CrossRef]
38. Zhang, Z.; Zhang, Y.; Chen, X.; Huang, Z.; Zou, Z.; Zheng, H. Co_3O_4-ZnO/rGO Catalyst Preparation and Rhodamine B Degradation by Sulfate Radical Photocatalysis. *J. Zhejiang Univ.-Sci. A* **2023**, *24*, 710–721. [CrossRef]
39. Liu, Y.; Zou, H.; Ma, H.; Ko, J.; Sun, W.; Andrew Lin, K.; Zhan, S.; Wang, H. Highly Efficient Activation of Peroxymonosulfate by MOF-Derived CoP/CoO_x Heterostructured Nanoparticles for the Degradation of Tetracycline. *Chem. Eng. J.* **2022**, *430*, 132816. [CrossRef]
40. Chen, Y.; Kang, J.; Li, Z.; Zhu, M.; Yin, R. Activation of Peroxymonosulfate by Co_2P via Interfacial Radical Pathway for the Degradation and Mineralization of Carbamazepine. *Surf. Interfaces* **2023**, *40*, 103045. [CrossRef]
41. Li, Y.; Chen, L.; Zhang, J.; Zhu, C.; Liu, L. Synergistic Photocatalytic Degradation of TC-HCl by Mn^{3+}/Co^{2+}/Bi_2O_3 and PMS. *Inorg. Chem. Commun.* **2023**, *150*, 110468. [CrossRef]
42. Chen, X.; Zhang, H.; Xu, S.; Du, X.; Zhang, K.; Hu, C.P.; Zhan, S.; Mi, X.; Oh, W.D.; Hu, X.; et al. A Recyclable Co-Fe Bimetallic Immobilized Cellulose Hydrogel Bead (CoFeO@CHB) to Boost Singlet Oxygen Evolution for Tetracycline Degradation. *Catalysts* **2023**, *13*, 1150. [CrossRef]
43. Ren, X.; Xu, P.; Tian, K.; Cao, M.; Shi, F.; Zhang, G. Peroxymonosulfate Activation by CuO-Fe_2O_3-Modified Ni Foam: A $^1O_2$ Dominated Process for Efficient and Stable Degradation of Tetracycline. *Catalysts* **2023**, *13*, 329. [CrossRef]
44. Xu, D.; Yang, T.; Dong, Y.; Wang, Q.; Zhu, J.; Zhang, G.; Lv, L.; Xia, Y.; Ren, Z.; Wang, P. Activation of Peroxymonosulfate by CoP@Co_2P Heterostructures via Radical and Non-Radical Pathways for Antibiotics Degradation. *Ceram. Int.* **2023**, *49*, 16999–17007. [CrossRef]

45. Fu, X.; Lin, Y.; Yang, C.; Wu, S.; Wang, Y.; Li, X. Peroxymonosulfate Activation via CoP Nanoparticles Confined in Nitrogen-Doped Porous Carbon for Enhanced Degradation of Sulfamethoxazole in Wastewater with High Salinity. *J. Environ. Chem. Eng.* **2022**, *10*, 107734. [CrossRef]
46. Huang, X.; Li, G.; Liu, L.; He, Y.; Su, X.; Pan, Y.; Xing, W.; Wu, G.; Zhang, M. Boosting Peroxymonosulfate Activation over Co-N-C@Co_9S_8 Double-Shelled Nanocages for Ciprofloxacin Degradation: Insights into Catalytic Performance, Degradation Mechanism and Routes. *Sep. Purif. Technol.* **2025**, *359*, 130662. [CrossRef]
47. Zhang, H.; Xu, J.; Yuan, Y.; Guo, Y.; Tan, X.; Wang, H.; Hu, X.; Tang, C. Highly Conductive Ti_3C_2 MXene Reinforced G-C_3N_4 Heterojunction Photocatalytic for the Degradation of Ciprofloxacin: Mechanism Insight. *Sep. Purif. Technol.* **2024**, *330*, 125520. [CrossRef]
48. Meng, X.; Yang, J.; Xu, S.; Zhang, C.; Ma, B.; Ding, Y. Integrating Mo_2B_x (x = 1, 4) with CdS for Efficient Photocatalytic Hydrogen Production. *Chem. Eng. J.* **2021**, *410*, 128339. [CrossRef]
49. Zhang, J.; Xie, J.F.; Yang, J.-C.E.; Li, D.; Zhong, L.B.; Zheng, Y.M. Ultra-Fast Degradation of Ciprofloxacin by the Peroxymonosulfate Activation Using a Co/Al-LDH Decorated Magnetic Hydrochar: Structural Design, Catalytic Performance and Synergistic Effects. *Chem. Eng. J.* **2023**, *477*, 146961. [CrossRef]
50. Wang, F.; Zhang, Y.; Peng, Y.; Xiao, W.; Yu, W.; Wang, H.; Bian, Z. Continuous Peroxymonosufate Activation for Antibiotics Degradation via Fluorine-Free-Ti_3C_2Tx-$CoFe_2O_4$ Hydrogel Beads: Performance, Mechanism and Application. *Appl. Catal. B* **2024**, *358*, 124441. [CrossRef]
51. Sun, Q.; Wang, X.; Liu, Y.; Zhang, Y.; Xia, S.; Zhao, J. Visible-Light-Driven g-C_3N_4 Doped $CuFe_2O_4$ Floating Catalyst Enhanced Peroxymonosulfate Activation for Sulfamethazine Removal via Singlet Oxygen and High-Valent Metal-Oxo Species. *Chem. Eng. J.* **2023**, *455*, 140198. [CrossRef]
52. Shen, Q.; Song, X.; Fan, J.; Chen, C.; Guo, Z. Degradation of Humic Acid by UV/PMS: Process Comparison, Influencing Factors, and Degradation Mechanism. *RSC Adv.* **2024**, *14*, 22988–23003. [CrossRef] [PubMed]
53. Klein, E.Y.; Impalli, I.; Poleon, S.; Denoel, P.; Cipriano, M.; Van Boeckel, T.P.; Pecetta, S.; Bloom, D.E.; Nandi, A. Global Trends in Antibiotic Consumption during 2016–2023 and Future Projections through 2030. *Proc. Natl. Acad. Sci. USA* **2024**, *121*, e2411919121. [CrossRef] [PubMed]
54. Fan, Y.H.; Li, Y.Q.; Hayat, F.; Liu, C.; Li, J.; Chen, M. Multi-Targeted Removal of Coexisted Antibiotics in Water by the Synergies of Radical and Non-Radical Pathways in PMS Activation. *Sep. Purif. Technol.* **2023**, *305*, 122475. [CrossRef]
55. Lv, H.; Yu, W.; Li, Y.; Sun, X.; Hou, X.; Bian, Z.; Wang, H.; Wei, Y. Cyclodextrin-Supported Sulfide Zero-Valent Iron as PMS Activator for Simultaneous Removing Norfloxacin and ARGs in Reclaimed Water: Activation and Controlled Release of Active Components. *Chem. Eng. J.* **2025**, *505*, 159656. [CrossRef]
56. Chen, L.; Fu, W.; Hou, C.; Yang, Y.; Zhang, X. A Comprehensive Assessment of Catalytic Performances of Mn_2O_3 Nanoparticles for Peroxymonosulfate Activation during Bisphenol A Degradation. *Catalysts* **2021**, *11*, 993. [CrossRef]
57. Wang, C.; Chang, L.; Zhang, X.; Chai, H.; Huang, Y. Promoting Oxygen Vacancies Utility for Tetracycline Degradation via Peroxymonosulfate Activation by Reduced Mg-Doped Co_3O_4: Kinetics and Key Role of Electron Transfer Pathway. *Environ. Res.* **2024**, *252*, 118892. [CrossRef]
58. Ma, R.; Chen, Z.; Xu, W.; Yu, R.; Zhang, Y.; Chen, F.; Peng, X.; Ni, B.-J.; Qian, J. Fe-MOFs/CuS Nanocomposite-Mediated Peroxymonosulfate Activation for Tetracycline Degradation: Boosted Dual Redox Cycles. *J. Clean. Prod.* **2024**, *442*, 140885. [CrossRef]
59. Huo, Y.; Zhou, G.; Guan, Y.; Meng, X.; Yan, W.; Hu, J.; Jiang, Y.; Xu, Y.; Yin, J.; Zhang, L. Inducing Oxygen Vacancies in ZnO/Co_3O_4 via g-C_3N_4 Carrier for Enhanced Universality and Stability in TC Degradation. *Colloids Surf. A* **2024**, *683*, 132974. [CrossRef]
60. Li, Z.; He, J.; Ma, H.; Zang, L.; Li, D.; Guo, S.; Ci, Y. Preparation of Heterogeneous TiO_2/g-C_3N_4 with a Layered Mosaic Stack Structure by Use of Montmorillonite as a Hard Template Approach: TC Degradation, Kinetic, Mechanism, Pathway and DFT Investigation. *Appl. Clay Sci.* **2021**, *207*, 106107. [CrossRef]
61. Jahanshahi, M.; Afsharipour, R.; Mirhosseini Rayen, N.A. Fabrication of a Spirulina Algae-$CuFeS_2$/$CuWO_4$ Composite for Effective Photo-Fenton Degradation of TC and RhB with Environmental Assessment. *J. Environ. Manag.* **2025**, *381*, 125340. [CrossRef] [PubMed]
62. You, Y.; Song, L.; Guo, Y.; Zhang, X.; Hu, S. Coupled Homogeneous-Heterogeneous Fenton-like System to Highly Efficiently Degrade Tetracycline in Water at Circumneutral pH: Mechanism and Toxicity Evaluation. *J. Water Process Eng.* **2025**, *72*, 107569. [CrossRef]
63. Chen, P.; Cheng, Z.; Zhang, X.; Yan, C.; Wei, J.; Qiu, F.; Liu, Y. Fe–Mn Bimetallic Catalyst to Activate Peroxymonosulfate (PMS) for Efficient Degradation of Tetracycline: Mechanism Insights and Application for Pharmaceutical Wastewater. *J. Clean. Prod.* **2024**, *445*, 141365. [CrossRef]
64. Nie, L.; Fang, C.; Xin, S.; Yang, Y.; Chen, H.; Chen, X.; Li, X. Effective Removal of Tetracycline Hydrochloride from Wastewater over Porous Co_3O_4@NC/Honeycomb Ceramics by Fenton-like Catalysis. *Inorg. Chem. Commun.* **2025**, *171*, 113598. [CrossRef]

65. Xing, H.; Gao, S.; Zhang, J.; Xu, Y.; Du, H.; Zhu, Z.; Wang, J.; Yao, Y.; Zhang, S.; Ren, L. Ultrasound-Assisted Synthesized $BiFeO_3$ as $FeOH^+$ Promoted Peroxymonosulfate Activator for Highly Efficient Degradation of Tetracycline. *J. Alloys Compd.* **2021**, *854*, 157281. [CrossRef]
66. Su, L.; Long, L.; Wang, W.; Kuang, Z.; Zhou, X.; Chen, C.; Xu, M.; He, Y.; Yang, G. Mn-Enhanced Cobalt Silicate-Activated Peroxymonosulfate for Tetracycline Degradation: Inheriting Merit and Offsetting Deficiency of Oxygen Vacancies. *ACS EST Eng.* **2023**, *3*, 1614–1625. [CrossRef]
67. Lu, S.; You, S.; Hu, J.; Li, X.; Li, L. Magnetic $MnFe_2O_4$ /ZIF-67 Nanocomposites with High Activation of Peroxymonosulfate for the Degradation of Tetracycline Hydrochloride in Wastewater. *RSC Adv.* **2024**, *14*, 7528–7539. [CrossRef]
68. Zhang, X.; Xu, B.; Wang, S.; Li, X.; Wang, C.; Liu, B.; Han, F.; Xu, Y.; Yu, P.; Sun, Y. Tetracycline Degradation by Peroxymonosulfate Activated with CoN_x Active Sites: Performance and Activation Mechanism. *Chem. Eng. J.* **2022**, *431*, 133477. [CrossRef]

Disclaimer/Publisher's Note: The statements, opinions and data contained in all publications are solely those of the individual author(s) and contributor(s) and not of MDPI and/or the editor(s). MDPI and/or the editor(s) disclaim responsibility for any injury to people or property resulting from any ideas, methods, instructions or products referred to in the content.

catalysts

MDPI

Review

Current Developments in Ozone Catalyst Preparation Techniques and Their Catalytic Oxidation Performance

Jiajia Gao, Siqi Chen, Yun Gao, Wenquan Sun, Jun Zhou, Kinjal J. Shah and Yongjun Sun *

College of Urban Construction, Nanjing Tech University, Nanjing 211816, China; gao123@njtech.edu.cn (J.G.)
* Correspondence: sunyongjun@njtech.edu.cn

Abstract

Through the use of heterogeneous catalysts, catalytic ozone oxidation technology, an effective and eco-friendly advanced oxidation process (AOP), facilitates the breakdown of ozone into reactive oxygen species (like ·OH) and greatly increases the mineralization efficiency of pollutants. This study examines the development of heterogeneous ozone catalysts through a critical evaluation of the five primary preparation techniques: ion exchange, sol–gel, coprecipitation, impregnation, and hydrothermal synthesis. Each preparation method's inherent qualities, benefits, drawbacks, and performance variations are methodically investigated, with an emphasis on how they affect the breakdown of different resistant organic compounds. Even though heterogeneous catalysts are more stable and reusable than homogeneous catalysts, they continue to face issues like active component leaching, restricted mass transfer, and ambiguous mechanisms. In order to determine the key paths for catalyst selection in catalytic ozone treatment going forward, the main goal of this review is to provide an overview of the accomplishments in the field of the heterogeneous ozone catalyst treatment of wastewater that is difficult to degrade.

Keywords: ozone catalysts; heterogeneous catalytic ozonation; ozonation; preparation methods; refractory organics

1. Introduction

More than 420 billion tons of organic wastewater are released into rivers, lakes, and oceans annually worldwide due to the rapidly expanding pharmaceutical, chemical, printing and dyeing, and metallurgical-related industries [1]. These wastewaters contain organic pollutants like dyes, detergents, pharmaceuticals, personal care items, pesticides, carboxylic acids, and aromatic compounds [2]. Long-term exposure to these organic wastewaters will harm the water body's ecology and reduce its dissolved oxygen content, but it will also endanger human health due to the food chain and biological deposition enrichment effect [3]. Physical (adsorption, precipitation), biological (biofilm, activated sludge), and chemical (coagulation, UV disinfection) methods are currently the conventional treatment methods for these organic wastewaters [4], but they typically have clear limitations and are unable to effectively remove organics that are difficult to degrade in wastewater [5]. Due to its high efficiency and environmentally friendly qualities, ozone oxidation, an advanced oxidation process (AOP), exhibits significant promise for use in the treatment of wastewater that is challenging for biodegradation.

With a redox potential of 2.07 V in alkaline solutions [6], ozone is a potent oxidizing agent that can either directly oxidize pollutants or react with them indirectly through the production of -OH during ozone decomposition [7]. Ozone oxidation by itself, however,

has drawbacks, including low ozone utilization, high energy consumption, low pollutant mineralization, a high pH effect, and certain organic byproducts that could pollute water bodies more severely [8]. Because of its quick rate of organic pollutant degradation, low operating costs, stable and dependable operation, and capacity to function across a broad pH range, the catalytic ozone oxidation process can significantly offset the drawbacks of individual ozone oxidation. A higher pollutant removal efficiency can be attained by adding ozone catalysts, which can also encourage the breakdown of ozone and the production of reactive free radicals, increasing the degree of organic pollutant mineralization [9]. Depending on the kind of catalyst, catalytic ozone oxidation is typically divided into two categories: homogeneous and non-homogeneous. Common homogeneous catalysts include transition metals Fe^{2+}, Mn^{2+}, Cu^{2+}, Ni^{2+}, Ag^{+}, and others. In homogeneous catalytic ozone oxidation, the catalyst typically exists in a dissolved state [10], which can be evenly distributed in the aqueous solution and has a higher reaction efficiency; however, the catalysts and wastewater share common characteristics, making it difficult to recycle the catalysts. Additionally, the high concentration of metal ion residue in the wastewater can easily lead to the secondary pollution of the water body, which restricts its use in real-world applications [11].

In order to overcome the drawbacks of homogeneous catalysts, which are hard to recycle and prone to secondary pollution, heterogeneous catalytic ozone oxidation typically uses a stable solid catalyst to catalyze the ozone oxidation of organic matter. It also offers the benefits of superior catalytic performance, reusability, and large-scale preparation and production, and is frequently used to treat wastewater that is hard to degrade [12]. Non-homogeneous catalysts can be broadly divided into three categories based on their active ingredients: loaded catalysts, metal-based catalysts, and carbon-based catalysts. Non-homogeneous catalysts can significantly accelerate the breakdown of ozone to create reactive oxygen species (ROS), including ·OH, $\cdot O^{2-}$, etc. Consequently, organic matter in wastewater is degraded, and the rate of ozone utilization is somewhat increased. Nowadays, impregnation, coprecipitation, sol–gel, hydrothermal, and ion exchange techniques are the primary techniques used to prepare non-homogeneous catalysts. Additionally, various catalysts have a significant impact on the cost of treatment and the efficiency of catalytic oxidation during the reaction process. Therefore, the key to implementing catalytic ozone oxidation technology to lower treatment costs and increase ozone utilization efficiency is to find a heterogeneous ozone catalyst that is both affordable and environmentally friendly. The preparation techniques of widely used catalysts in heterogeneous ozone oxidation in recent years, as well as their uses in the mineralization and degradation of organic pollutants in water that are difficult for biodegradation, are reviewed in this paper. The difficulties and potential future directions of this technology are also suggested, which will serve as a foundation for the creation of new high-efficiency ozone catalysts.

2. Heterogeneous Catalytic Ozone Oxidation Mechanism

The process of heterogeneous catalytic ozone oxidation is extremely complicated and involves three-phase reactions in gas, liquid, and solid phases. These reactions include the mass transfer of O_3 to the liquid phase, adsorption of O_3 and pollutants on the catalyst, diffusion of active species on the catalyst surface to the liquid phase, and interaction between O_3 and active species and the pollutants. In Figure 1, the heterogeneous catalytic ozone oxidation mechanism is depicted. Currently, the main mechanisms for the degradation of pollutants by heterogeneous catalytic ozone oxidation are as follows:

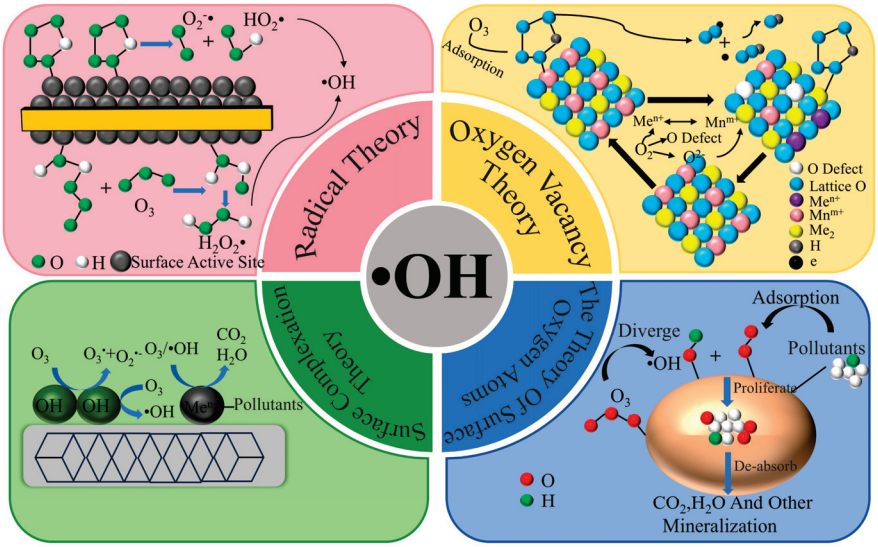


Figure 1. Mechanism of heterogeneous catalytic ozone oxidation.

(1) Free radical theory. This theory holds that ozone adsorbed on the catalyst catalytic activity center decomposes to produce stronger oxidizing hydroxyl radicals (·OH), superoxide anion radicals ($\cdot O^{2-}$), and other active substances, which in turn triggers a free-radical chain reaction on the catalyst surface and in the solution of the decomposition of organic matter [13]. The catalytic activity center is the catalyst surface of the active species in the catalyst surface and diffusion to the liquid phase, as well as active species attacks on the pollutants and other processes. Where ozone splits and transforms into radicals on the catalyst surface is the epicenter of catalytic activity. Ozone breaks down more quickly to produce ·OH when it is adsorbed on the catalyst surface with H_2O, creating surface hydroxyl groups. Water-soluble O_3 adsorbs on the surface of a semiconductor-type heterogeneous catalyst in a heterogeneous reaction system, where it breaks down to release free radicals. Following their attack on organic compounds, these free radicals result in ring-opening and chain-breaking reactions. Numerous small organic molecules are produced by the destroyed organic compounds, and free radicals then cause these small organic molecules to mineralize into inorganic ones. As a result, free radicals in the reaction system are crucial for increasing catalytic oxidation's efficiency.

(2) Oxygen vacancy theory. One particular instance of radical theory is the oxygen vacancy theory. The decomposition pathway of ozone on catalysts is significantly impacted by the numerous lattice defects that are frequently present on the surface of oxides. Using CeO_2 as an example, it has a high capacity for both storing and releasing oxygen. Ce easily changes from Ce^{4+} to Ce^{3+}. Oxygen vacancies are created following high-temperature reduction. A portion of the Ce^{4+} changes into Ce^{3+} when oxygen levels are low, and vice versa when oxygen levels are high. Oxygen vacancies on the catalyst surface are crucial for the catalytic breakdown of organic compounds by ozone, which is more effective when the Ce^{3+}/Ce^{4+} ratio on the CeO_2 surface rises [14]. Through a heavy metallization reaction that submerges zero-valent iron particles in $Cu(NO_3)_2$ to achieve the controlled decomposition and formation of ·OH, ref. [15] indirectly confirmed that O_3 can use CFO NPs in aqueous solutions to synthesize CFO NPs. They also suggested that the Cu(II)/Cu(I) and Fe (III)/Fe(II) redox pairs which activated O_3 are the source of the high catalytic activity of CFO NPs. O_3 interacts with hydroxyl radicals to form $Cu(I)_2O$–OH–O_3 precursors. Cu(I) oxidizes to Cu(II) while reducing the lattice's oxygen to O_2, resulting in surface oxygen vacancies. The aforementioned statement makes clear that the amount of oxygen vacancies in metal oxides has a direct impact on their catalytic activity. Therefore, the restoration of oxygen vacancies depends critically on the timely breakdown of the peroxides on the

catalyst surface. The catalyst will gradually deactivate if they are unable to be restored because they will not be able to take part in the subsequent reaction process. The average oxidation state of the metal oxide will rise as a result of O_2^{2-}, which cannot be broken down into other free radicals, being transformed into lattice oxygen [16].

(3) The complexation theory of surface coordination. According to the surface coordination complexation theory, transition metals with empty electron orbitals form metal–organic complexes with organic matter. These complexes are subsequently adsorbed on the catalyst surface, where ozone molecules oxidize and decompose them. There are two general categories into which this mechanism can be divided. The first is that organic matter is adsorbed onto the catalyst's surface via chemical bonding, and the second is that coordination complexation is the sole mechanism involved. The other is that organic matter and ozone are adsorbed on the catalyst's surface, and the redox reaction is propelled by electron transfer [17]. Zhang and associates [18] examined the outcomes of ozone-catalyzed oxidation and used Ce-doped TiO_2 nanoparticles to break down humic acid. They suggested that ozone can react directly with complex products formed by organic compounds adhering to the surface of heterogeneous catalysts. The radical mechanism pathway is not dominant when the pH is acidic, which is necessary for the complexation pathway to function. Ozone has a redox potential of 2.07 eV, making it a potent oxidizing agent that can directly react with organic matter to break it down into aldehydes or carboxylic acids through redox reactions. However, the full mineralization of organic pollutants is severely limited because neither of these pathways reacts with ozone oxygen. Furthermore, the degree of mineralization of organic matter is further decreased by the selective and comparatively slow reaction between ozone and organic matter [19].

(4) The theory of the surface oxygen atom. Bulanin was the first to propose the function of surface oxygen atoms in heterogeneous catalytic oxidation. On the surface of n-type transition metal oxides, O_3 adsorbs and produces *O, an intermediate between O_3 and ·OH with an oxidation potential of 2.42 eV. As a result, *O has a greater oxidizing effect than direct ozone oxidation; however, it is less capable of mineralizing than ·OH. In heterogeneous catalytic ozone oxidation technology, in situ Raman spectroscopy is thought to be a useful technique for clarifying the production and transformation of *O [20]. *O is created when O_3 combines with the Pd surface's active sites on the PdO/CeO_2 bimetallic catalyst. The organic matter adsorbed on Ce(IV) is oxidized and degraded by *O after some *O reacts with some of the O_3 to produce intermediate products, surface peroxides ($*O_2$), and the active sites on the Pb surface are reduced once more. Most people think that *O is not a single product in the reaction; instead, it frequently collaborates with ·OH to finish the oxidation process. O_3 molecules have a tendency to catalyze dissociation into *O and free peroxides ($*O_2$) in investigations involving surface oxygen atoms. Quenching tests and in situ EPR spectroscopy demonstrate that *O either directly targets adsorbed organic matter or produces ·OH free radicals by reacting with nearby water and oxygen molecules.

3. Preparation and Application of Heterogeneous Catalyst

3.1. Impregnation

The method of impregnation is to introduce the carrier into a liquid or gas containing the active substances, which are gradually adsorbed on the surface of the carrier, and then drying, cooking, activation, etc. This method of impregnation has the following advantages: catalytic carriers of different shapes and sizes are commercially available, which eliminates the need for catalyst molding steps; suitable carriers can provide a more suitable specific surface area, pore size, mechanical strength, etc., for the physical structure characteristics required for catalytic converters; the active substance is not only loaded on the surface, which is important for rare metal catalysts; and it is highly used and low cost. The dormant

method is particularly suited for the manufacture of rare earths catalysts, catalysts with a low active ingredient content, and catalysts with high mechanical strength.

During the impregnation process, the metal was modified by physically filling the pores on the surface of the carrier, which resulted in an increase in pore volume and pore diameter, significantly increasing the specific surface area necessary for adsorption [21]. Among these, iron-based catalysts and their composites demonstrated exceptional efficacy in treating a range of pollutants, including Fe_3O_4-MnO_2 magnetic composites (Table 1). The impregnation method was used to prepare the materials: $KMnO_4$ solution was added dropwise at a 4:1 Fe/Mn ratio to a mixture of $FeSO_4 \cdot 7H_2O$/PVP/NaOH, reacted for two hours at 70 °C, and then processed to yield the end product. Characterization using Brunauer–Emmett–Teller (BET), scanning electron microscopy (SEM), X-ray photoelectron spectroscopy (XPS), vibrating sample magnetometer (VSM), and X-ray diffraction (XRD) techniques verified its mesoporous structure, high specific surface area (127.26 m^2/g), amorphous MnO_2 shell rich in Mn^{4+} active sites, and superparamagnetic properties (26.82 emu/g). This material significantly outperforms single-component catalysts in the catalytic ozone degradation of bisphenol A (BPA): at 100 mg/L catalyst, 100 mL/min O_3, and pH 7.0, the removal rate reaches 97.0% within 30 min and maintains 88.8% high efficiency and stability after five cycles [22], while Fe_3Ce_2/NaY catalysts achieved 99.14% of 90 mg/L quinoline in 30 min [23], demonstrating effective removal of nitrogen-containing heterocyclic pollutants. These authors list the catalysts produced by the impregnation method and their catalytic properties, which include transition metal composite catalysts such as Cu-Fe-O nanoparticles [15] and Mn-Cu/Al_2O_3 [24]. Cu-Fe-O nanocatalysts (CFO NPs) are made by forming a composite structure through a displacement reaction with zero-valent iron (ZVI) and Cu $(NO_3)_2$ as precursors (Cu/Fe molar ratio = 1:1). In order to create a $(Cu_2O)_0$ composite, hydrothermal synthesis was conducted at 120 °C, precipitation at pH 8, and calcination at 600 °C for four hours. For the composite of CuO-α-FeO_3, its spherical nanostructure (SEM), surface rich in Cu^+ active sites (Cu(I) make up 50–5% of the XPS-Cu 2p), and low metal leaching (Fe < 0.03 mg/L, Cu = 0.49 mg/L) were all confirmed by characterization using XRD/SEM/XPS/BET. With a TOC removal rate of 50.1% (as opposed to 18.6% with ozone alone), DMP was fully broken down in 20 min at 100 mg/L catalyst, 1.8 mg/min O_3, and pH 5.7. The activity stayed above 95% after five reuses. Although the degradation rate of DMP by the Cu-Fe-O nanocatalyst is close to 100%, its active metal Cu^{2+} leaching is 0.49 mg/L, which is 10 times higher than the drinking water standard. The synthesis of Mn-Cu/Al_2O_3 was accomplished by ultrasonic impregnation. The oxidation states of the metal oxides (Mn^{3+}/Mn^{4+} and Cu^+/Cu^{2+}) changed in tandem with the formation of oxygen vacancies, according to XPS analysis, which greatly accelerated the breakdown of ozone and the production of ROS. The degradation rate of PCMC reached 100% in 30 min under ideal experimental conditions, which included an initial pH of 7, a catalyst dosage of 15 g/L, and an ozone dosage of 4–0 mg/min. Mn-Cu/AlO_3 has outstanding stability, reusability, and industrial application potential, according to reusability tests. According to mechanistic research, the ozone catalytic system greatly benefits from the contributions of O_2 and $1O_2$. Furthermore, possible degradation pathways were deduced from the intermediate products found using LC-MS. In conclusion, ozone catalyzed by Mn-Cu/AlO_3 is a successful technique for breaking down PCMC in wastewater. Although the degradation rates of DMP and PCMC by Cu-Fe-O and Mn-Cu/Al_2O_3 catalysts are close to 100%, under long-term operation or changes in environmental conditions (such as pH fluctuations), the leaching of supported metals from the catalyst surface poses a serious risk of secondary pollution and potential environmental toxicity, which is a matter of concern.

Table 1. Catalyst prepared by impregnation method and its performance.

Catalyst	Pollutants	Experimental Condition	Catalytic Performance	Reusability	References
Iron-based catalyst	Industrial wastewater	[Cat] = 200 g/L $[O_3]$ = 5 mg/min $[Pull]_0$ = 69.3 mg/L pH = 6.8	TOC removal rate 78.7%	After 50 uses, the TOC above 60%	[21]
Fe_3O_4-MnO_2 magnetic composite	Bisphenol A (BPA)	[Cat] = 0.1 g/L $[O_3]$ = 0.1 L/min $[Pull]_0$ = 0.05 mg/L pH = 7.0	BPA removal rate was 97%	After five cycles, the degradation efficiency of BPA was 88.8%.	[22]
Fe_3Ce_2/NaY	Quinoline	[Cat] = 0.5 g/L $[O_3]$ = 2.19 g/h $[Pull]_0$ = 0.05 mg/L pH = 7.0	Quinoline removal rate was 99.14%	The COD removal efficiencies were nearly same during four cycles	[23]
Cu-Fe-O nanoparticles	Dimethyl phthalate (DMP)	[Cat] = 75 mg/L $[O_3]$ = 1.8 mg/min $[Pull]_0$ = 50 mg/L pH = 5.7	DMP degradation rate close to 100%	After three cycles, the degradation rate of DMP was close to 100%.	[15]
Mn-Cu/Al_2O_3	4-chloro-3-methylphenol (PCMC)	[Cat] = 15 mg/L $[O_3]$ = 4.0 mg/min $[Pull]_0$ = 100 mg/L pH = 7.0	PCMC removal rate near 100%	After five reuses, the PCMC removal rate decreased from 100% to 90.8%.	[24]
Co/Al_2O_3	Pyruvic acid (PA)	[Cat] = 5 g/L $[O_3]$ = 40 mg/min $[Pull]_0$ = 0.1 g/L pH = 4.0	PA removal rate was 94.4%	/	[25]
Mn-CeO_x/γ-Al_2O_3	Bromaminic acid (BAA)	[Cat] = 1 g/L $[O_3]$ = 20 mg/L $[Pull]_0$ = 50 mg/L pH = 6.8	BAA almost completely degraded	After three reuses, the TOC removal rate dropped to 57.2%.	[26]
C/Cu-Al_2O_3	High-salt petrochemical wastewater	[Cat] = 400 g/L $[O_3]$ = 12 mg/L $[Pull]_0$ = 100 mg/L pH = 7.8	COD removal of pollutants was 62.5%	After 20 reuses, its COD removal rate for pollutants exceeds 53%.	[27]
Fe_3O_4/MWCNTs	Sulfamethizole (SMT)	[Cat] = 0.5 g/L $[O_3]$ = 9 mg/min $[Pull]_0$ = 20 mg/L pH = 4.0	TOC removal rate of SMT was 39.1%	/	[28]
Cu-Ce@Az	Purified terephthalic acid (PTA)	[Cat] = 86 g/L $[O_3]$ = 2 g/h $[Pull]_0$ = 178.6 mg/L pH = 8.0	COD removal rate of PAT was 84.2%	After 30 reuses, the COD removal rate of PTA wastewater was 68.2%.	[29]
Mn-Cu/γ-Al_2O_3	Tannery wastewater	[Cat] = 2 g/L $[O_3]$ = 0.3 g/h $[Pull]_0$ = 5200 mg/L pH = 7.0	COD removal rate of tannery wastewater was 88%	/	[30]

Similarly, Fe-Mn-O loading on granular activated carbon (GAC) by impregnation [31] significantly enhanced the mineralization efficiency of Reactive Black 5 in water by catalytic

ozone oxidation, with an 18% increase in TOC removal compared to unmodified GAC [32], suggesting that the synergistic effect of the bimetal significantly enhances the hydroxyl radical generation efficiency. Al_2O_3 has become a widely used carrier material by virtue of its porous structure, stable mechanical properties, and ability to provide more active sites for the reactants [33]. The 94.4% removal of pyruvic acid by Co/Al_2O_3 under acidic conditions (pH = 4) [25], and the Mn-CeO_x/γ-Al_2O_3 Ce^{3+}/Ce^{4+} redox pair was introduced, which enhanced the concentration of oxygen vacancies on the catalyst surface, promoted ozone adsorption and dissociation on the catalyst surface, and shifted the degradation pathway of bromoacetic acid (BAA) from direct ozone oxidation to a free radical-dominated reaction [26], which revealed the synergistic effect between the acidic sites on the carrier surface and the active revealing the synergistic mechanism between the acidic sites on the carrier surface and the active components. In our earlier research, we used the impregnation method to create a Cu-Ce@γ-Al_2O_3 catalyst that effectively treated chemically concentrated wastewater from reverse osmosis (RO) membranes. Fourier transform infrared spectroscopy (FTIR) and SEM/BET/XRD/XPS/X-ray fluorescence (XRF) are used to thoroughly characterize the catalyst, exposing its microstructure, elemental composition, and crystal structure. The following were found to be the ideal reaction conditions: a reactor aspect ratio of 5:1, an initial pH of 9.0, a catalyst loading rate of 10%, and an ozone dosage of 8 mg/L/min. The catalytic ozone treatment's chemical oxygen demand (COD) removal efficiency under these circumstances was 63.04% [34]. Although Al_2O_3 is widely used as a carrier due to its porous structure and stability, and studies on Mn-CeO_x/γ-Al_2O_3 show that there is a synergistic effect between the acidic sites of the carrier and the active components (such as Ce^{3+}/Ce^{4+} pair), or that Cu-Ce@γ-Al_2O_3 can achieve 63.04% COD removal under specific conditions, these synergistic mechanisms are usually poorly described, and the carrier itself may introduce new restrictions or costs. The degradation process of the above catalysts is presented in Figure 2. Although the active components of the impregnation method are distributed on the carrier surface, which is conducive to the reaction, and the production method is simple, with a high production capacity and low cost, which is suitable for mass production, the leaching toxicity of the metal elements on the surface of the loaded metal catalysts will be harmful to the environment, resulting in secondary pollution, and the agglomeration of the metal particles in the process of calcination will lead to the deterioration of the performance of the catalytic carriers, which, together with the surface of the solid–liquid phase between the diffusion between solid and liquid phases, results in poor mass transfer efficiency and other problems that need to be solved.

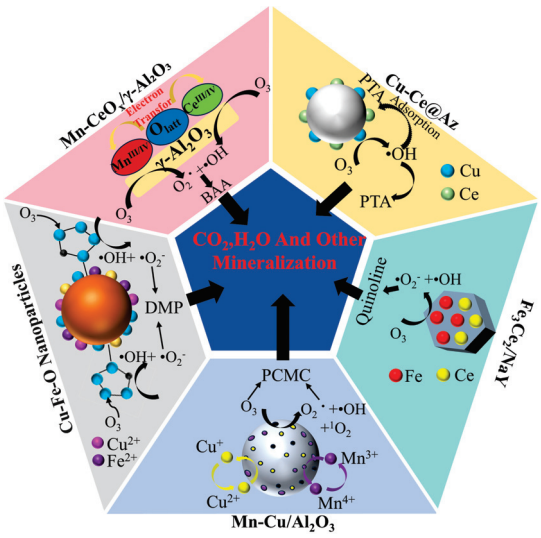


Figure 2. The process of catalyst degradation by impregnation.

3.2. Coprecipitation

When creating an ultrafine powder of composite oxides with two or more metal elements, coprecipitation is a crucial technique. Coprecipitation has the following benefits: first, it creates nanopowder materials with a consistent chemical composition directly through a variety of chemical reactions in solution; second, it makes it easier to prepare materials with uniform distribution and small particle sizes. One of the primary techniques for creating nanoparticles, nanocomposites, and catalysts is coprecipitation, which works well for creating multi-component catalysts.

Table 2 lists the catalysts prepared by the coprecipitation method and their catalytic performance. Among them, iron-based catalysts exhibit good catalytic activity under acidic conditions. For example, the $Ce_{0.1}Fe_{0.9}OOH$ catalyst was synthesized using $Fe(NO_3)_3$ and $Ce(NO_3)_3$ as precursors (Fe:Ce = 9:1). The mixed solution (total metal concentration 0.53 M) was reacted with 2 M NaOH, followed by aging at 60 °C for 15 days to form needle-like structures (SEM showed lengths of 1–2 μm and widths of 0.1–0.4 μm). Characterization via XRD/SEM/EDS confirmed that the synthesized catalyst exhibits a single needle hematite phase without CeO_2 impurities, with uniform elemental doping (Fe:Ce atomic ratio ≈ 9:1, as determined by EDS). Under conditions of 0.2 g/L catalyst, 15 mg/L O_3, and pH 7.0, the TOC removal rate of sulfamethoxazole (SMT) reached 42% after 120 min (compared to 27.8% with ozone alone) [35]. α-$Fe_{0.9}Mn_{0.1}OOH$ achieves an 87.6% removal rate for iopamidol under neutral conditions [36], indicating that Mn doping optimizes the surface electronic structure of the catalyst and enhances its ability to generate reactive oxygen species (ROS) from ozone decomposition. Similarly, $FeCl_3/FeSO_4/MnCl_2$ was coprecipitated with activated carbon (AC) (Fe:Mn = 1:11.2) to create the $Mn_xFe_YO_2$/AC catalyst. This was then aged for two hours at 70 °C and calcined at 600 °C. According to BET/SEM/XPS characterization, the synthesized catalyst has a uniform distribution of Mn/Fe/O, an ultra-high specific surface area (819.3 m^2/g), and outstanding recovery performance. The degradation rate of Sulfadiazine (SMZ) reached 90.5% (64.8% with ozone alone) in 8 min at a catalyst concentration of 0.05 g/L, 50 mL/min O_3, and pH 6.1. After five cycles, the activity stayed at 77.5%. Transition metal oxides and composite catalysts have a synergistic effect on the catalytic ozone oxidation process [37]. $CuMn_2O_4/g\text{-}C_3N_4$ increased the degradation rate constant of benzophenone-4 (BP-4) to three times that of ozone oxidation alone at pH = 6.4 [38], indicating that the $g\text{-}C_3N_4$ carrier promotes electron transfer and enhances ozone activation. Additionally, Ag-La-Co nano-metal oxides achieve a TOC removal rate of up to 95% for Active Black 5 (RB5) under neutral conditions [39], indicating that the synergistic effect of noble metals (Ag) and rare earth metals (La) significantly enhances the ozone mineralization capacity. Although the introduction of supports (such as AC, $g\text{-}C_3N_4$) or specific doping (such as Mn optimized electronic structure, Ce/La enhanced stability) has been reported to improve the catalytic performance, the synergistic mechanism (such as charge transfer, active site formation) is usually inadequate or too simplified. The limitations of the carrier itself have not been fully discussed and may bring additional costs or complexity.

Table 2. Catalyst prepared by coprecipitation method and its performance.

Catalyst	Pollutants	Experimental Condition	Catalytic Performance	Reusability	References
$Ce_{0.1}Fe_{0.9}OOH$	Sulfamethazine (SMT)	[Cat] = 0.4 g/L $[O_3]$ = 15 mg/L $[Pull]_0$ = 40 mg/L pH = 3.0	SMT removal rate was 42%	/	[35]
α-$Fe_{0.9}Mn_{0.1}OOH$	Iohexol	[Cat] = 100 mg/L $[O_3]$ = 0.8 mg/L $[Pull]_0$ = 1 mg/L pH = 7.0	Iohexol removal rate was 87.6%	After three cycles, the mineralization rate of TOC still reached 71.7%.	[36]
$Mn_xFe_yO_z$/AC	Sulfadiazine (SMZ)	[Cat] = 0.05 g/L $[O_3]$ = 50 mL/min $[Pull]_0$ = 10 mg/L pH = 6.1	SMZ removal rate was 90.5%	After five reuses, the removal rate of SMZ decreased from 90.5% to 77.5%.	[37]
$CuMn_2O_4$/g-C_3N	Benzophenone (BP-4)	[Cat] = 0.25 g/L $[O_3]$ = 20 mg/L $[Pull]_0$ = 0.084 mmol/L pH = 6.4	BP-4 removal rate was 87%	/	[38]
Ag-La-Co nano-metal oxide	Reactive Black 5 (RB5)	[Cat] = 1 g/L $[O_3]$ = 30 L/h $[Pull]_0$ = 100 mg/L pH = 7.0	TOC removal rate of RB5 was 95%	After three reuses, the catalytic activity does not decrease significantly.	[39]
CeO_2@HSZSM-5	Sulfamethoxazole (SMX)	[Cat] = 0.4 g/L $[O_3]$ = 9.3 mg/min $[Pull]_0$ = 20 mg/L pH = 7.0	TOC removal rate of SMX was 80.4%	After five cycles, the TOC removal rate decreased by only 7.3%.	[40]
Fe_3O_4/GO nanohybrid material	Acid Red 88 (AR88)	[Cat] = 0.25 g/L $[O_3]$ = 6 mg/min $[Pull]_0$ = 150 mg/L pH = 4.5	COD removal rate of AR88 was 69%	After five cycles of reuse, the degradation efficiency of AR88 remains high.	[41]
Fe_3O_4/ZnO	1-Hexyl-3-methylimidazole bromide ($HMIM_{Br}$)	[Cat] = 0.25 g/L $[O_3]$ = 36 mL/min $[Pull]_0$ = 150 mg/L pH = 9.0	$HMIM_{Br}$ removal rate was 90.5%	After five cycles of reuse, the degradation efficiency of $[HMIM]_{Br}$ can still reach 90%.	[42]
Cu-Al LDHs	Ciprofloxacin (CIP)	[Cat] = 0.79 g/L $[O_4]$ = 62 mg/min $[Pull]_0$ = 10 mg/L pH = 9.0	CIP removal rate was 96%	After five cycles, the TOC removal rate remained at approximately 70%.	[43]
Zn-Cu-Ni composite silicate	Ciprofloxacin (CIP)	[Cat] = 0.5 g/L $[O_3]$ = 1.5 mg/L $[Pull]_0$ = 3 mg/L pH = 7.0	COD removal of PAT was 84.2%	/	[44]

Compared to carbon-based materials, mesoporous molecular sieves, although possessing advantages such as a large adsorption capacity and adjustable pore size, lack protonic acid and Lewis acid centers, and thus generally lack catalytic activity [45]. Therefore, introducing rare earth dopant elements such as Ce and La can significantly enhance ozone utilization efficiency and catalyst stability. The CeO_2@HSZSM-5 catalyst was prepared using cerium nitrate as the precursor, which was mixed with high-silica ZSM-5 (SiO_2/Al_2O_3 = 500), followed by ultrasonic aging, ammonia precipitation (pH = 10), and calcination at 500 °C. Characterization using SEM/High Resolution Transmission Electron Microscope (HRTEM)/XPS/BET/Hydrogen Temperature-Programmed Reduction (H_2-TPR) confirmed that it possesses a high specific surface area (348–395 m^2/g), small grain size (8.2–33.5 nm), and abundant surface oxygen vacancies (Ce^{3+} accounts for 68.59%). This material exhibits excellent performance in the catalytic ozone degradation of sulfamethoxazole (SMX): under conditions of 0.4 g/L catalyst, 9.3 mg/(min·L) O_3, and pH 7.0, the TOC removal rate of sulfamethoxazole (SMX) reached 80.4% after 180 min, significantly outperforming ozonation alone (40%). After five cycles, the efficiency decreased by only 7.3%, and the cerium leaching amount was negligible (<0.016 mg/L) [40]. In contrast, Fe_3O_4/GO achieved a COD removal rate of 69% for acidic red dye (AR88) at pH = 4.5 [41], indicating that while the introduction of graphene (GO) enhances electron conductivity, acidic conditions may limit the decomposition efficiency of ozone. Additionally, magnesium–aluminum layered double hydroxide (MgAl-LDH) nanoparticles were prepared using a simple and rapid coprecipitation method and used as a catalyst for the ozone oxidation of PNA. The structure of the synthesized MgAl-LDH was investigated using X-ray diffraction patterns and field emission scanning electron microscopy–energy dispersive spectroscopy. Under optimal conditions of an initial PNA concentration of 162.5 mg/L, pH of 8.25, LDH loading of 750 mg/L, and reaction time of 70 min, the PNA removal rate reached 91.5% [46]. Some catalysts exhibit excellent performance under alkaline conditions (pH = 9), such as Fe_3O_4/ZnO, which achieves a removal rate of 96% for the ionic liquid HMIMBr [42], and Cu-Al LDHs, which achieve a removal rate of 72% for ciprofloxacin (CIP) [43], indicating that alkaline conditions may promote the generation of hydroxyl radicals (·OH), thereby enhancing the oxidative capacity. The performance of different catalysts is highly pH dependent (e.g., Fe_3O_4/ZnO and Cu-Al LDHs are better in alkaline solution). This not only increases the complexity of process control, but also limits the applicability of catalysts in the treatment of practical wastewater with large pH fluctuations. Additionally, Zn-Cu-Ni composite silicates were prepared using the chemical coprecipitation method. The prepared catalyst was characterized using SEM, XRD, XPS, nitrogen adsorption–desorption, and Fourier transform infrared analysis (FTIR). The catalyst exhibits a high specific surface area (308.137 m^2/g) and an irregular morphology, with a particle size of 7.6 μm, and contains Si-O-Si, Ni-O-Si, and Zn-O-Si. Under optimal conditions (pH 7.0, CIP 3.0 mg/L, ozone 1.5 mg/L), the removal rates of CIP and total organic carbon (TOC) were increased by 51.09% and 18.72%, respectively, compared to using ozone alone [44]. Figure 3 illustrates the degradation process of the aforementioned catalysts. Although the coprecipitation method has advantages such as simple operation, cost-effectiveness, practical preparation process, uniform component distribution, relatively low reaction temperature, controllable particle size and composition of the product, and typically no involvement of organic solvents, it also has limitations such as a high sensitivity to reaction preparation conditions, and the prepared catalysts generally have small specific surface areas and a low probability of contact with organic matter [47].

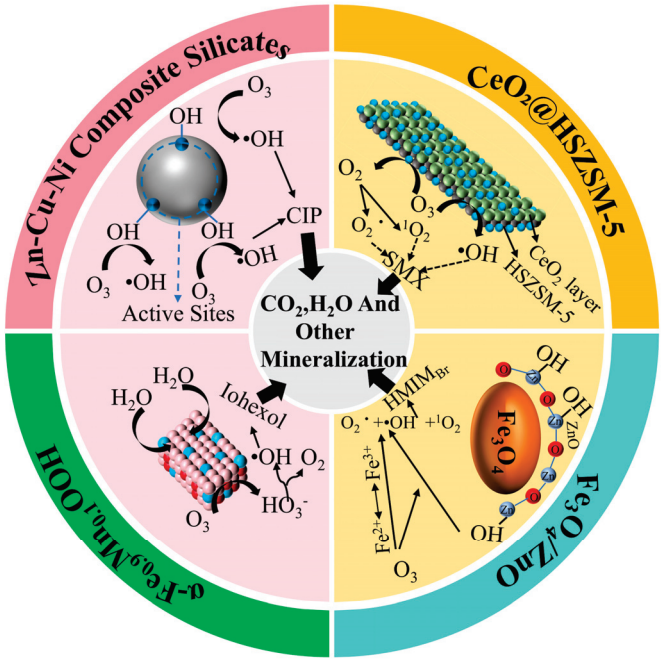


Figure 3. Process of catalyst degradation through coprecipitation.

3.3. Sol–Gel Method

Using solutions, sols, and gels to solidify metal–organic or inorganic compounds, followed by heat treatment to create oxides or other solid compounds, is known as the sol–gel method. The sol–gel method has the following benefits: first, it can quickly achieve molecular-level uniformity; second, trace elements can be easily and quantitatively incorporated through the solution reaction step, achieving molecular-level uniform doping; and third, chemical reactions are simpler to perform and only require lower synthesis temperatures than solid-phase reactions.

A high specific surface area, homogeneous composition, controllable pore structure, and composite or doped components—such as metal oxides, composite oxides, noble metal-supported catalysts, porous materials, and doped catalysts—can all be prepared using the sol–gel method. Because the sol–gel process is performed in solution, specific structural elements can be customized. The sol–gel catalysts and their catalytic performance are listed in Table 3. Bimetallic/polymeric metal catalysts have been thoroughly investigated in heterogeneous catalytic ozone systems due to their high stability, diverse oxidation states, and high catalytic activity. The Fe-Mn/PAC catalyst was prepared using the sol–gel method: PAC was added to a precursor solution of iron nitrate/manganese nitrate/citric acid at a Fe/Mn molar ratio of 1:1, followed by ultrasonic dispersion, ethylene glycol cross-linking, drying, and calcination (400 °C). The catalyst was then pressed into shape using PTFE as a binder (diameter 1 cm). Characterization by XPS/FT-IR/XRD/BET confirmed the successful loading of the bimetallic catalyst (Fe 11.9 wt%, Mn 9.3 wt%), rich in C=O/C-OH surface functional groups, and retention of a mesoporous structure (specific surface area 682.14 m^2/g, pore size 3–5 nm). Under conditions of 50 mg/L ozone and 1 g/L catalyst, the removal efficiencies for COD and phenol reached 79% and 95%, respectively, and the COD removal efficiency remained at 74% after continuous operation for 100 days [48]. By encouraging ozone adsorption and dissociation through surface hydroxyl groups and efficiently preventing the leaching of active components (Fe-Cu alloy), the SiO_2 shell in Fe-Cu@SiO_2 core–shell catalysts raises the TOC removal rate of salicylic acid to 88% (as opposed to 35% with ozone alone) [49]. Although the core–shell structure can reduce leaching, the SiO_2 shell may hinder mass transfer and increase the complexity of synthesis; further, it has poor reproducibility and is difficult to scale up. Similarly, the ozone treatment

of N,N-dimethylacetamide (DMAC) was studied by introducing Cu-Fe bimetallic elements to create $CuFe_2O_4$ magnetic nanoparticles. The TOC removal rate was only 22.3%, despite the $CuFeO_4/O_3$ process achieving a degradation rate of 95.4% for DMAC. This suggests that intermediate products accumulated, requiring bimetallic site design to optimize the mineralization pathway [50]. Furthermore, doping the catalyst with certain noble metals can improve its stability and ozone activation effectiveness. A series of well-crystallized silver-doped $MnFe_2O_4$ catalysts with a spinel structure were synthesized using the sol–gel method. The substitution of Ag for Mn in the structure was confirmed by SEM, EDS, and XRD, and the alteration of the oxygen coordination environment was determined by XPS. This stable and reusable magnetic porous material efficiently catalyzes the ozone treatment of DBP, with 0.5% Ag doping (relative to Mn) increasing the apparent rate constant by a factor of three [51]. Although the introduction of noble metals (such as Ag doping) can improve the apparent activity, the cost of precious metals is high and resources are scarce, and it is doubtful whether the activity improvement of trace doping (0.5%) can offset its economic and environmental costs.

Table 3. Catalyst prepared by sol–gel method and its performance.

Catalyst	Pollutants	Experimental Condition	Catalytic Performance	Reusability	References
Fe-Mn/PAC	phenolic compounds	[Cat] = 4 g/L $[O_3]$ = 50 mg/L $[Pull]_0$ = 700 mg/L pH = 7.5	Phenol removal rate was 95%	Over 50 operating days, the COD removal rate remained stable at around 74%.	[48]
Fe-Cu@SiO_2	Salicylic acid (SA)	[Cat] = 0.1 g/L $[O_3]$ = 4.6 mg/L $[Pull]_0$ = 11.2 mg/L pH = 7.0	TOC removal rate of SA was 88%	/	[49]
$CuFe_2O_4$	N,N-Dimethylacetamide (DMAC)	[Cat] = 30 g/L $[O_3]$ = 0.06 L/min $[Pull]_0$ = 200 mg/L pH = 6.8	DMAC removal rate was 95.4%	After five reuses, the removal rate of DMAC did not decrease.	[50]
Ag/$MnFe_2O_4$	Butyl phthalate (DBP)	[Cat] = 10 mg/L $[O_3]$ = 20 mg/L $[Pull]_0$ = 0.5 mg/L pH = 7.3	DBP removal rate was 75.3%	/	[51]
Nano TiO_2	Nitrobenzene (NB)	[Cat] = 0.1 g/L $[O_3]$ = 15 mg/L $[Pull]_0$ = 20 mg/L pH = 7.0	NB removal rate was 75.3%	/	[52]
CeO_2-T	Phenol	[Cat] = 0.1 g/L $[O_3]$ = 172.8 mg/L $[Pull]_0$ = 100 mg/L pH = 7.8	Phenol removal rate was 91.7%	/	[53]
CeO_2	4-Nitrophenol (PNP)	[Cat] = 0.4 g/L $[O_3]$ = 1.6 mg/min $[Pull]_0$ = 25 mg/L pH = 5.7	TOC removal rate of PNP was 86%	After three reuses, the TOC removal rate decreased from 86.14% to 75.38%.	[54]

A Nobel Prize winning nano-tio-oxide prepared by the solvent method was used to catalyze the oxidation of nitrobenzene to ozone. Studies show that TiO_2 increases the formation of ·OH radicals and thus significantly increases the removal efficiency of nitrobenzene [52]. In addition, certain mesoporous materials may increase the mineralization capacity of pollutants by virtue of catalytic synergies. A large specific surface area and an ordered pore structure of the mesoporous CeO_2-T significantly increases the adsorption capacity of the phenol, while the oxygen vacancies on the surface promote the oxidation of the ozone to OH, with a phenol removal rate of 91.7% [53]. Likewise, CeO_2-OCNT composite materials were made by the sol–gel method, which involved using carbon nanotubes (OCNT) as the carrier and hydrothermally reacting the precursor $Ce(NO_3)_3{\cdot}6H_2O$ in a NaOH solution for 24 h at 100 °C, then calcining the mixture at 300 °C. Its mesoporous structure (average pore size 12.6 nm), high dispersion, high specific surface area, and effective Ce^{3+}/Ce^{4+} redox cycling were all confirmed by characterization using XRD/SEM/XPS/TPR-H_2/BET. Within 60 min, the phenol mineralization rate (TOC removal) reached 96% under the conditions of 0–10 g/L catalyst, 12 mg/L O_3, and pH 6.2. After five cycles, the rate remained at a 94% high stability [55]. Figure 4 illustrates the degradation process of the aforementioned catalysts. For the time being, the solvent–gel preparation process for supported nanocatalysts and the theories of reaction kinetics and thermodynamics in the system need to be clarified.

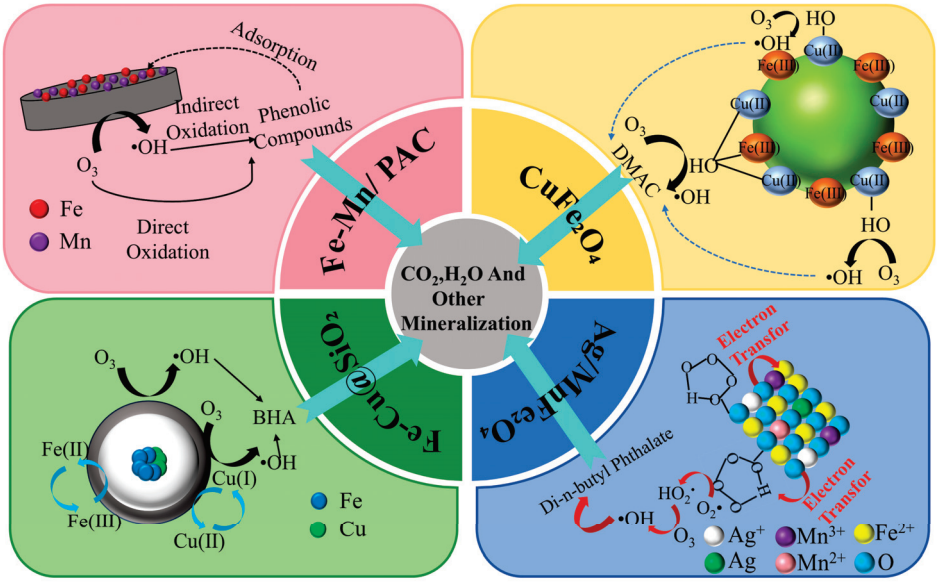


Figure 4. Sol–gel method of catalyst degradation.

3.4. Hydrothermal Method

The hydrothermal method refers to the process of preparing the material in a sealed pressure vessel with water as a solvent, in which the powder is dissolved and subsequently re-treated. Compared with other powder preparations, hydrothermal-produced powders show good crystalline development, small particle size, homogeneous distribution, minimal agglomeration, the possibility of using relatively cheap raw materials, and ease of achieving the appropriate stoichiometry and crystal morphology. The hydrothermal method can be used for the preparation of single component microcrystals and of specialized compound compounds of two or more components. It is used for preparing powdered materials such as metals, oxides, and powdered waxes. The size range of particles in the resulting powder materials usually ranges from 0.1 micrograms to several micrometers, some of them reaching up to several tens of nanometers.

Table 4 lists several catalysts synthesized using the hydrothermal method and their catalytic performance. Among these, transition metal oxides such as α-MnO_2 and $CoFe_2O_4$ exhibit excellent catalytic performance in ozone systems. For example, the combination of α-MnO_2 and ozone can achieve removal rates exceeding 99.5% for metoprolol (MET) and ibuprofen (IBU) within 30 min [56]. Similarly, rGO achieved a nearly 100% removal efficiency for p-hydroxybenzoic acid (PHBA) under acidic conditions, with its high efficiency potentially attributed to the high specific surface area and abundant active sites of graphene materials [57]. Similarly, Luo et al. [58] synthesized a petal-shaped δ-MnO_2 microsphere via the hydrothermal method and tested its performance in the catalytic ozonolysis degradation of bisphenol A (BPA) and IBU. The experimental results showed that the degradation efficiency reached over 68% within 20 min, outperforming both ozone treatment alone and commercial MnO_2 catalysts, demonstrating the broad-spectrum degradation capability of metal oxide catalysts for pharmaceutical pollutants. In a similar manner, the hydrothermal method was utilized to prepare the Cl/S-CN catalyst. Melamine and cyanuric acid were employed as precursors, which formed hexagonal prisms through hydrogen bonding. Following an 8 h hydrothermal reaction at 180 °C, the material was calcined for 4 h at 520 °C in a nitrogen atmosphere to yield carbon nanotubes (CN); HCl/H_2SO_4 was then added to achieve Cl/S co-doping. Its ordered nanotube structure (tube diameter 56 nm), high specific surface area (65.78 m^2/g), mesoporous properties, broad visible light response (absorption edge at 494 nm), and optimized band structure (CB = −0.96 eV, VB = 1.46 eV) were all confirmed by XRD/SEM/XPS/BET/UV-Vis characterization. In the O_3/visible light/Cl/S-CN system, tetracycline (TC) attained a 90.1% degradation rate in 10 min and a 78% TOC removal rate in 30 min at a concentration of 100 mg/L. After five cycles, the TC degradation efficiency dropped by less than 5% [59]. Transition metal oxides such as $CoFe_2O_4$ [60] and $MnFe_2O_4$@Co_3S_4 [61] exhibit high TOC removal rates (80%) and color removal rates (93.55%) for black ink and methylene blue (MB), respectively, indicating that they enhance degradation efficiency by promoting ozone decomposition to generate strong oxidative free radicals (such as ·OH). However, some catalysts, such as Fe-MCM-48, exhibit low TOC removal efficiency for diclofenac (DCF) (49.9%), which may be attributed to the complexity of the pollutant structure or insufficient accessibility of the catalyst's active sites [62].

Table 4. Catalyst prepared by hydrothermal method and its performance.

Catalyst	Pollutants	Experimental Condition	Catalytic Performance	Reusability	References
α-MnO_2	Metoprolol (MET) Ibuprofen (IBU)	[Cat] = 0.1 g/L $[O_3]$ = 1 mg/min $[Pull]_0$ = 10 mg/L pH = 7.0	MET removal rate was 99.62%; IBU removal rate was 99.51%	After four reuses, there was no significant decrease in pollutant removal efficiency.	[56]
rGO	4-Hydroxybenzoic acid (PHBA)	[Cat] = 0.05 g/L $[O_3]$ = 20 mg/L $[Pull]_0$ = 20 mg/L pH = 3.5	PHBA removal rate close to 100%	After five reuses, the inactivation phenomenon continues.	[57]
$CoFe_2O_4$	Melanoidin	[Cat] = 0.1 g/L $[O_3]$ = 10 mL/min $[Pull]_0$ = 300 mg/L pH = 6.85	TOC removal rate of Melanoidin was 80%	/	[60]

Table 4. *Cont.*

Catalyst	Pollutants	Experimental Condition	Catalytic Performance	Reusability	References
$MnFe_2O_4$@Co_3S_4	Methylene Blue (MB)	[Cat] = 0.6 g/L [O_3] = 2.5 mg/L [Pull]$_0$ = 50 mg/L pH = 6.6	MB removal rate was 93.55%	After five cycles of reuse, the degradation rate of MB dropped to 90.02%.	[61]
Fe-MCM-48	Diclofenac (DCF)	[Cat] = 0.15 g/L [O_3] = 100 mg/h [Pull]$_0$ = 15 mg/L pH = 7.0	TOC removal rate of DCF was 49.9%	/	[62]
Fe_2O_3/Al_2O_3@SBA-15	Ibuprofen (IBU)	[Cat] = 1.5 g/L [O_3] = 30 mg/L [Pull]$_0$ = 10 mg/L pH = 7.0	TOC removal rate of IBU was 49.9%	/	[63]
Ag/MCM-41	p-chlorobenzoic acid (p-CBA)	[Cat] = 1 g/L [O_3] = 100 mg/h [Pull]$_0$ = 10 mg/L pH = 4.2	TOC removal rate of p-CBA was 84%	The TOC removal rate decreased by only 4% after four reuses.	[64]
Cu_2S/Ni_4S_2@NF	4-Nitrophenol (PNP)	[Cat] = 3 pcs [O_3] = 2 mg/min [Pull]$_0$ = 100 mg/L pH = 7.8	PNP removal rate was 99.9%	After five cycles of reuse, the removal rate of PNP decreased to only 90.1%.	[65]
MnO_2-NH_2-GO	Cefalexin (CLX)	[Cat] = 25 g/L [O_3] = 0.12 mg/L [Pull]$_0$ = 1 mg/L pH = 4.2	CLX removal rate was 55.6%	/	[66]
MgO	P-chlorophenol (4-CP)	[Cat] = 1 g/L [O_3] = 5 mg/L [Pull]$_0$ = 100 mg/L pH = 6.2	4-CP removal rate was 95.1%	During the 7.5 h of operation, the removal rate remained at around 99.0%.	[67]
Sludge carbon/TiO_2	Bisphenol A (BPA)	[Cat] = 0.2 g/L [O_3] = 40 mL/min [Pull]$_0$ = 10 mg/L pH = 7.0	BPA removal rate was 75%	/	[68]
$ZnAl_2O_4$	5-Sulfosalicylic acid (SSal)	[Cat] = 0.2 g/L [O_3] = 10 mg/min [Pull]$_0$ = 500 mg/L pH = 7.0	SSal removal rate was 64.8%	After three reuses, the removal rate of SSal was 64.8–59.7%.	[69]

Additionally, the design of the support material significantly influences catalytic efficiency. For example, the preparation of Fe_2O_3/Al_2O_3@SBA-15 composite materials was conducted via the hydrothermal method: using $AlCl_3$ and $FeCl_3$ as precursors, Al_2O_3 and Fe_2O_3 were sequentially loaded onto the mesoporous SBA-15 carrier, yielding an optimal catalyst with a 12 wt% Fe loading. Characterization via XRD/TEM/XPS/pyridine adsorption FTIR confirmed that the material retains the ordered mesoporous structure of SBA-15, with Al_2O_3 and Fe_2O_3 exhibiting excellent high dispersion; the bimetallic catalyst exhibits the highest Lewis acid sites (264.3 μmol/g) and a near-neutral zero charge

point (pH_{pzc} = 7.25). Under conditions of 1.5 g/L catalyst, 30 mg/L ozone, and pH 7.0, the TOC removal rate for IBU reached 90% after 60 min (compared to 26% with ozone alone), with stable activity and no metal leaching after six cycles [63]. Ag/MCM-41 achieved the efficient mineralization of p-chlorobenzoic acid (p-CBA) (84%) by leveraging the synergistic effect of silver nanoparticles [64]. Notably, some studies have optimized reactor designs, such as Cu_2S/Ni_3S_2@NF using plate-shaped catalysts to achieve the rapid degradation of p-nitrophenol (PNP) (99.9%) [65], but high catalyst loading (e.g., MnO_2-NH_2-GO requires 25 g/L) may limit their practical application [66]. Figure 5 illustrates the degradation processes of the aforementioned catalysts. Although the hydrothermal method is a synthesis method with low pollution, simple operation, good product dispersion, and high performance, it requires raw materials with high purity, resulting in relatively higher costs. Since the reaction occurs in a sealed container, operators cannot observe the reaction process in real-time and must adjust the process based on the characterization results of the products, which introduces a certain degree of lag. Overall, compared to other preparation methods, the hydrothermal method is more suitable for laboratory research or the preparation of small quantities (trace amounts) of solid materials requiring high purity [70].

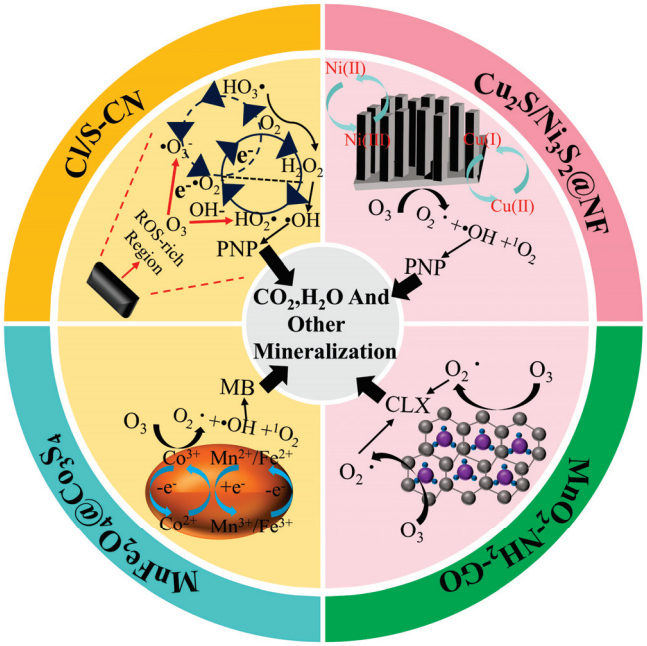


Figure 5. Process of catalyst degradation by hydrothermal methods.

3.5. Ion Exchange Method

The ion exchange process makes use of the exchangeable ions on the carrier's surface. Under certain conditions, these ions may exchange with metal ions, resulting in the carrier's initial loading. After additional processing stages like filtration and drying, a catalyst with a corresponding reaction activity can be created. The ion exchange method is commonly applied to carriers that have exchangeable ions on their surfaces, such as molecular sieves and ion exchange resins. Two characteristics of catalysts produced using this method are high catalytic activity and a good dispersion of active ingredients. Among other things, this method is effective for producing acid–base catalysts, catalysts with a low component content, catalysts with high utilization rates, and catalysts made of precious metals [71].

When designing nanocatalytic materials, ion exchange offers special benefits as a highly effective method of controlling the shape and structure of catalytic active sites. Figure 6 illustrates its mechanism of degradation. Mass transfer efficiency and the degree

of catalytic active center exposure can be greatly increased by carefully regulating the loading form and distribution state of metal species through ion exchange reactions. Using catalysts based on zeolite as an example, Rutkowska et al., through ion exchange, added iron species to ZSM-5 and Y-type zeolites [72]. They discovered that the Y-type zeolite's larger pore size promotes the formation of oligomeric or single-nuclear iron species, which leads to a noticeably higher N_2O decomposition activity than the ZSM-5 system. Further demonstrating the crucial role of the carrier pore structure in the dispersion state of metals, the stability of iron species is only slightly affected by the calcination temperature. By contrasting Mn/ZSM-5 catalysts made by impregnation and ion exchange techniques, it was discovered that the former produces a molecular-level dispersion of MnOx species, greatly increasing the concentration of surface adsorbed oxygen. This confirms the technical benefits of the ion exchange technique in enhancing metal dispersion. Zhang and colleagues [73] increased the method's applicability by successfully creating hierarchical porous Ag_2ZnGeO_4 microspheres at room temperature by stepwise exchanging GeO_3^{2-} colloids with Zn^{2+}/Ag^+. Their ordered crystalline structure and high specific surface area (>150 m^2/g) enhanced Rhodamine B's degradation efficiency by 53% when compared to the original germanate, demonstrating the method's potential for creating intricate nanostructures. The ion exchange technique is noteworthy because it not only successfully prevents metal particle agglomeration (e.g., forming isolated Fe or Mn active sites) [74], but it also makes it possible to regulate the coordination environment to prepare unique morphologies like hollow and core–shell structures [75], offering fresh perspectives on creating sophisticated catalysts with robust and high activity.

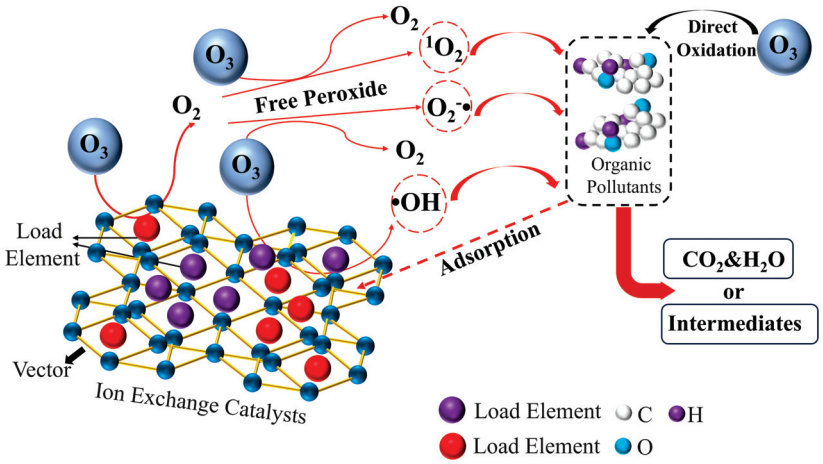


Figure 6. Catalyst degradation mechanism by ion exchange method.

4. Conclusions and Future Perspective

This review highlights the unique benefits and drawbacks of recent developments in heterogeneous ozone catalyst preparation methods, including impregnation, coprecipitation, sol–gel, hydrothermal synthesis, and ion exchange. Although impregnation is inexpensive and scalable, it has drawbacks such as pore blockage and metal leaching. Coprecipitation produces materials with a limited surface area but allows for uniform multi-component catalysts. While hydrothermal techniques produce high crystallinity but have trouble scaling up to the industrial level, the sol–gel method offers precise structural control at the cost of complex synthesis. Although it greatly relies on carrier compatibility, ion exchange produces remarkable active-site dispersion. Through catalysis, metal oxides (e.g., supported composites and FeO_4, MnO_2, and CeO_2) improve the breakdown of ozone into reactive oxygen species (e.g., ·OH), greatly increasing the mineralization efficiency of a variety of refractory pollutants, including industrial contaminants and pharmaceuticals.

Notwithstanding advancements, significant obstacles still exist, such as unclear reaction mechanisms, restrictions on mass transfer, metal leaching, and catalyst deactivation. Practical implementation is hampered by these problems, especially in intricate wastewater matrices with high salinity or organic loads. Advanced catalyst design and process innovation are two interrelated fronts that need to be given top priority in future research. Non-precious multi-metal oxides should be the main focus of material development (e.g., Fe-Mn-Ce), with engineered acid–base sites, oxygen vacancies, and hierarchical porosity to improve accessibility, inhibit leaching, and increase stability. Meanwhile, mechanistic research employing in situ methods is necessary to clarify degradation pathways and radical pathways (e.g., Raman, EPR). New reactor designs are necessary for process optimization (e.g., systems with high gravity) and hybrid technologies (e.g., ozonation–photocatalysis) to maximize synergy and move past obstacles to mass transfer. In the end, combining sustainable methods—like catalysts made from waste and standardized stability tests—will connect lab advancements with real-world uses. By addressing these issues, catalytic ozonation will be promoted as a reliable, environmentally friendly method of treating stubborn wastewater, supporting international objectives for environmental sustainability and water security.

Author Contributions: Conceptualization, J.G. and Y.S.; methodology, J.G., S.C., Y.G. and J.Z.; resources, Y.S. and W.S.; data curation, J.G.; writing—original draft preparation, J.G. and Y.S.; writing—review and editing, J.G., W.S., K.J.S. and Y.S.; supervision, W.S. and Y.S.; project administration, W.S. and Y.S.; funding acquisition, W.S. and Y.S. All authors have read and agreed to the published version of the manuscript.

Funding: This research was supported by National Key Research and Development Program of China (No. 2024YFB4105502-4), National Natural Science Foundation of China (No. 51508268), and Natural Science Foundation of Jiangsu Province in China (No. BK20201362).

Data Availability Statement: The original contributions presented in this study are included in the article. Further inquiries can be directed to the corresponding authors.

Conflicts of Interest: The authors declare no conflicts of interest.

Abbreviations

The following abbreviations are used in this manuscript:

AOP	Advanced oxidation process
ROS	Reactive oxygen species
BPA	Bisphenol A
DMP	Dimethyl phthalate
PCMC	4-chloro-3-methylphenol
PA	Pyruvic acid
BAA	Bromaminic acid
SMT	Sulfamethizole
PTA	Purified terephthalic acid
SMT	Sulfamethazine
SMZ	Sulfadiazine
BP-4	Benzophenone
RB5	Reactive Black 5
SMX	Sulfamethoxazole
AR88	Acid Red 88
HMIMBr	1-Hexyl-3-methylimidazole bromide

CIP	Ciprofloxacin
SA	Salicylic acid
DMAC	N,N-Dimethylacetamide
DBP	Butyl phthalate
NB	Nitrobenzene
PNP	4-Nitrophenol
MET	Metoprolol
IBU	Ibuprofen
PHBA	4-Hydroxybenzoic acid
MB	Methylene Blue
DCF	Diclofenac
p-CBA	p-chlorobenzoic acid
CLX	Cefalexin
SSal	5-Sulfosalicylic acid
XRD	X-ray diffraction
SEM	scanning electron microscopy
XPS	X-ray photoelectron spectroscopy
VSM	vibrating sample magnetometer
BET	Brunauer–Emmett–Teller
XRF	X-ray fluorescence
HRTEM	High Resolution Transmission Electron Microscope
H_2-TPR	Hydrogen Temperature-Programmed Reduction

References

1. Connor, R.; United Nations Economic; South Commission for Women in Asia; South Commission in Asia; Pacific Task Force; United Nations Economic Commission for Latin America; Caribbean Task Force. The united nations world water development report 2017: Wastewater: The untapped resource. *Future Food J. Food Agric. Soc.* **2017**, *5*, 80–81.
2. Ghuge, S.P.; Saroha, A.K. Catalytic ozonation for the treatment of synthetic and industrial effluents—Application of mesoporous materials: A review. *J. Environ. Manag.* **2018**, *211*, 83–102. [CrossRef]
3. Malakootian, M.; Shahesmaeili, A.; Faraji, M.; Amiri, H.; Martinez, S.S. Advanced oxidation processes for the removal of organophosphorus pesticides in aqueous matrices: A systematic review and meta-analysis. *Process. Saf. Environ.* **2020**, *134*, 292–307. [CrossRef]
4. Sun, X.Z.; Jin, L.L.; Zhou, F.Y.; Jin, K.; Wang, L.C.; Zhang, X.X.; Ren, H.Q.; Huang, H. Patent analysis of chemical treatment technology for wastewater: Status and future trends. *Chemosphere* **2022**, *307*, 135802. [CrossRef] [PubMed]
5. Petrie, B.; Barden, R.; Kasprzyk-Hordern, B. A review on emerging contaminants in wastewaters and the environment: Current knowledge, understudied areas and recommendations for future monitoring. *Water Res.* **2015**, *72*, 3–27. [CrossRef]
6. Wang, Y.J.; Yu, G. Challenges and pitfalls in the investigation of the catalytic ozonation mechanism: A critical review. *J. Hazard. Mater.* **2022**, *436*, 129157. [CrossRef]
7. Real, F.J.; Acero, J.L.; Benitez, F.J.; Matamoros, E. Elimination of neonicotinoids by ozone-based advanced oxidation processes: Kinetics and performance in real water matrices. *Sep. Purif. Technol.* **2022**, *301*, 121975. [CrossRef]
8. Esposito, S. "Traditional" Sol-Gel Chemistry as a Powerful Tool for the Preparation of Supported Metal and Metal Oxide Catalysts. *Materials* **2019**, *12*, 668. [CrossRef]
9. Li, Z.X.; Jing, J.X.; Gao, K.C.; Ren, G.M.; Zhang, J.W.; Jiao, W.Z.; Liu, Y.Z. Degradation of nitrobenzene by high-gravity intensified heterogeneous catalytic ozonation with Mn-Fe/ZSM-5 catalysts. *Chem. Eng. Process.* **2021**, *169*, 108642. [CrossRef]
10. Kolosov, P.; Peyot, M.L.; Yargeau, V. Novelmaterials for catalytic ozonation of wastewater for disinfection and removal of micropollutants. *Sci. Total Environ.* **2018**, *644*, 1207–1218. [CrossRef]
11. Zhang, Y.; Zhao, P.; Li, J.; Hou, D.Y.; Wang, J.; Liu, H.J. A hybrid process combining homogeneous catalytic ozonation and membrane distillation for wastewater treatment. *Chemosphere* **2016**, *160*, 134–140. [CrossRef] [PubMed]
12. Wei, X.Y.; Shao, S.J.; Ding, X.; Jiao, W.Z.; Liu, Y.Z. Degradation of phenol with heterogeneous catalytic ozonation enhanced by high gravity technology. *J. Clean. Prod.* **2020**, *248*, 119179. [CrossRef]
13. Yu, G.F.; Wang, Y.X.; Cao, H.B.; Zhao, H.; Xie, Y.B. Reactive Oxygen Species and Catalytic Active Sites in Heterogeneous Catalytic Ozonation for Water Purification. *Environ. Sci. Technol.* **2020**, *54*, 5931–5946. [CrossRef] [PubMed]
14. Orge, C.A.; Orfao, J.J.M.; Pereira, M.F.R.; de Farias, A.M.D.; Fraga, M.A. Ceria and cerium-based mixed oxides as ozonation catalysts. *Chem. Eng. J.* **2012**, *200*, 499–505. [CrossRef]

15. Liu, Y.; Wu, D.L.; Peng, S.H.; Feng, Y.; Liu, Z.G. Enhanced mineralization of dimethyl phthalate by heterogeneous ozonation over nanostructured Cu-Fe-O surfaces: Synergistic effect and radical chain reactions. *Sep. Purif. Technol.* **2019**, *209*, 588–597. [CrossRef]
16. Jia, J.; Zhang, P.; Chen, L. Catalytic decomposition of gaseous ozone over manganese dioxides with different crystal structures. *Appl. Catal. B Environ.* **2016**, *189*, 210–218. [CrossRef]
17. Huang, Y.X.; Sun, Y.R.; Xu, Z.H.; Luo, M.Y.; Zhu, C.L.; Li, L. Removal of aqueous oxalic acid by heterogeneous catalytic ozonation with MnOx/sewage sludge-derived activated carbon as catalysts. *Sci. Total Environ.* **2017**, *575*, 50–57. [CrossRef]
18. Zhang, H.F.; Wang, J.Y. Catalytic Ozonation of Humic Acids by Ce-Ti Composite Catalysts. *Kinet. Catal.* **2017**, *58*, 734–740. [CrossRef]
19. Nawrocki, J.; Kasprzyk-Hordern, B. The efficiency and mechanisms of catalytic ozonation. *Appl. Catal. B Environ.* **2010**, *99*, 27–42. [CrossRef]
20. Wang, Y.X.; Chen, L.L.; Chen, C.M.; Xi, J.X.; Cao, H.B.; Duan, X.G.; Xie, Y.B.; Song, W.Y.; Wang, S.B. Occurrence of both hydroxyl radical and surface oxidation pathways in N-doped layered nanocarbons for aqueous catalytic ozonation. *Appl. Catal. B Environ.* **2019**, *254*, 283–291. [CrossRef]
21. Li, X.F.; Chen, W.Y.; Ma, L.M.; Wang, H.W.; Fan, J.H. Industrial wastewater advanced treatment via catalytic ozonation with an Fe-based catalyst. *Chemosphere* **2018**, *195*, 336–343. [CrossRef] [PubMed]
22. Zhang, H.; He, Y.L.; Lai, L.D.; Yao, G.; Lai, B. Catalytic ozonation of Bisphenol A in aqueous solution by Fe_3O_4-MnO_2 magnetic composites: Performance, transformation pathways and mechanism. *Sep. Purif. Technol.* **2020**, *245*, 116449. [CrossRef]
23. Li, X.Y.; Li, G.; He, R.F. Degradation of quinoline by ozone oxidation using Fe3Ce2/NaY catalyst. *Microporous Mesoporous Mater.* **2025**, *392*, 113630. [CrossRef]
24. Wang, Y.C.; Liu, H.Q.; Zhang, Y.; Sun, W.Q.; Liu, Z.Y.; Lu, X.; Sun, Y.J.; Xu, Y.H. Efficient catalytic ozonation of 4-chloro-3-methylphenol by Mn-Cu/Al2O3: Performance, mechanism, and degradation pathways. *J. Water Process. Eng.* **2025**, *71*, 107325. [CrossRef]
25. Alvarez, P.M.; Beltrán, F.J.; Pocostales, J.P.; Masa, F.J. Preparation and structural characterization of Co/Al_2O_3 catalysts for the ozonation of pyruvic acid. *Appl. Catal. B Environ.* **2007**, *72*, 322–330. [CrossRef]
26. Wu, Z.W.; Zhang, G.Q.; Zhang, R.Y.; Yang, F.L. Insights into Mechanism of Catalytic Ozonation over Practicable Mesoporous Mn-CeOx/γ-Al2O3 Catalysts. *Ind. Eng. Chem. Res.* **2018**, *57*, 1943–1953. [CrossRef]
27. Chen, J.J.; Qin, J.H.; Tu, Y.M.; Shao, G.Y.; Liu, F.; Zhou, Z.Y.; Tian, S.C.; Ren, Z.Q. Catalytic ozonation with carbon-coated copper-based core-shell catalysts ($C/Cu\text{-}Al_2O_3$) for the treatment of high-salt petrochemical wastewater. *J. Environ. Chem. Eng.* **2024**, *12*, 112303. [CrossRef]
28. Bai, Z.Y.; Yang, Q.; Wang, J.L. Catalytic ozonation of sulfamethazine antibiotics using Fe_3O_4/multiwalled carbon nanotubes. *Environ. Prog. Sustain. Energy* **2018**, *37*, 678–685. [CrossRef]
29. Lu, X.; Xie, S.Q.; Li, S.; Zhou, J.; Sun, W.Q.; Xu, Y.H.; Sun, Y.J. Treatment of Purified Terephthalic Acid Wastewater by Ozone Catalytic Oxidation Method. *Water* **2021**, *13*, 1906. [CrossRef]
30. Huang, G.D.; Pan, F.; Fan, G.F.; Liu, G.G. Application of heterogeneous catalytic ozonation as a tertiary treatment of effluent of biologically treated tannery wastewater. *J. Environ. Sci. Health A* **2016**, *51*, 626–633. [CrossRef]
31. Alhassan, S.I.; He, Y.J.; Huang, L.; Wu, B.C.; Yan, L.J.; Deng, H.Y.; Wang, H.Y. A review on fluoride adsorption using modified bauxite: Surface modification and sorption mechanisms perspectives. *J. Environ. Chem. Eng.* **2020**, *8*, 104532. [CrossRef]
32. He, H.P.; Wu, D.L.; Lv, Y.P.; Ma, L.M. Enhanced mineralization of aqueous Reactive Black 5 by catalytic ozonation in the presence of modified GAC. *Desalination Water Treat.* **2016**, *57*, 14997–15006. [CrossRef]
33. Wei, K.J.; Cao, X.X.; Gu, W.C.; Liang, P.; Huang, X.; Zhang, X.Y. Ni-Induced $C\text{-}Al_2O_3$-Framework (NiCAF) Supported Core-Multishell Catalysts for Efficient Catalytic Ozonation: A Structure-to-Performance Study. *Environ. Sci. Technol.* **2019**, *53*, 6917–6926. [CrossRef]
34. Sun, W.Q.; Wang, Y.; Yang, X.W.; Wang, Z.R.; Zhu, H.Q.; Zhou, J.; Sun, Y.J. Catalytic ozone oxidation of chemical RO membrane concentrate wastewater by a $Cu\text{-}Ce@\gamma\text{-}Al_2O_3$ ozone catalyst. *Water Environ. Res.* **2025**, *97*, e70034. [CrossRef]
35. Bai, Z.Y.; Yang, Q.; Wang, J.L. Catalytic ozonation of sulfamethazine using $Ce_{0.1}Fe_{0.9}OOH$ as catalyst: Mineralization and catalytic mechanisms. *Chem. Eng. J.* **2016**, *300*, 169–176. [CrossRef]
36. Yan, P.W.; Shen, J.M.; Zhou, Y.C.; Yuan, L.; Kang, J.; Wang, S.Y.; Chen, Z.L. Interface mechanism of catalytic ozonation in an $\alpha\text{-}Fe_{0.9}Mn_{0.1}OOH$ aqueous suspension for the removal of iohexol. *Appl. Catal. B Environ.* **2020**, *277*, 119055. [CrossRef]
37. Liu, X.H.; Zhu, W.X.; Yang, Z.G.; Yang, Y.; Li, H.P. Efficient ozone catalysis by manganese iron oxides/activated carbon for sulfamerazine degradation. *J. Water Process. Eng.* **2022**, *49*, 103050. [CrossRef]
38. Liu, Y.; Song, Z.L.; Wang, W.H.; Wang, Z.B.; Zhang, Y.T.; Liu, C.; Wang, Y.P.; Li, A.; Xu, B.B.; Qi, F. A $CuMn_2O_4/g\text{-}C_3N_4$ catalytic ozonation membrane reactor used for water purification: Membrane fabrication and performance evaluation. *Sep. Purif. Technol.* **2021**, *265*, 118268. [CrossRef]
39. Chokshi, N.P.; Ruparelia, J.P. Synthesis of Nano Ag-La-Co Composite Metal Oxide for Degradation of RB 5 Dye Using Catalytic Ozonation Process. *Ozone Sci. Eng.* **2021**, *44*, 182–195. [CrossRef]

40. Zuo, X.T.; Ma, S.L.; Wu, Q.Y.; Xiong, J.; He, J.J.; Ma, C.; Chen, Z.B. Nanometer CeO_2 doped high silica ZSM-5 heterogeneous catalytic ozonation of sulfamethoxazole in water. *J. Hazard. Mater.* **2021**, *411*, 125072. [CrossRef]
41. Fahadi, M.; Nabavi, S.R.; Chaichi, M.J. Mesoporous Fe_3O_4/graphene oxide nanohybrid for catalytic Ozonation: Preparation, characterization and process modeling by neural network. *J. Taiwan Inst. Chem. E* **2022**, *134*, 104278. [CrossRef]
42. Tian, J.; Wei, J.Y.; Liang, Y.P.; Guo, R.X.; Li, B.B.; Qu, R.J.; Zhou, D.M.; Wang, Z.Y.; Sun, P. Catalytic ozonation of an imidazole ionic liquid via Fe_3O_4/ZnO nanocomposites: Performance, products and reaction mechanism. *J. Environ. Chem. Eng.* **2022**, *10*, 108726. [CrossRef]
43. Xu, R.J.; Li, L.; Fu, X.J.; Yu, L.; Jin, Y.J.; Li, L.D. Catalytic Ozonation of Ciprofloxacin with Cu-Al Layered Double Hydroxides Based on Response Surface Analysis. *J. Environ. Eng.* **2022**, *148*, 04022010. [CrossRef]
44. Liu, Y.; Guo, R.; Li, J.; Cheng, Y.Z.; Wang, C.M.; Wang, W.Q.; Zheng, H.F. Enhanced Ciprofloxacin Ozonation Degradation by an Aqueous Zn-Cu-Ni Composite Silicate: Degradation Performance and Surface Mechanism. *Separations* **2025**, *12*, 15. [CrossRef]
45. Ikhlaq, A.; Brown, D.R.; Kasprzyk-Hordern, B. Catalytic ozonation for the removal of organic contaminants in water on ZSM-5 zeolites. *Appl. Catal. B Environ.* **2014**, *154*, 110–122. [CrossRef]
46. Malakootian, M.; Shahamat, Y.D.; Mahdizadeh, H. Optimization and modeling of p-nitroaniline removal from aqueous solutions in heterogeneous catalytic ozonation process using MgAl-layered double hydroxides (MgAl-LDH COP). *Desalination Water Treat.* **2021**, *223*, 114–127. [CrossRef]
47. Dong, H.X.; Koenig, G.M. A review on synthesis and engineering of crystal precursors produced via coprecipitation for multicomponent lithium-ion battery cathode materials. *Crystengcomm* **2020**, *22*, 1514–1530. [CrossRef]
48. Jothinathan, L.; Cai, Q.Q.; Ong, S.L.; Hu, J.Y. Fe-Mn doped powdered activated carbon pellet as ozone catalyst for cost-effective phenolic wastewater treatment: Mechanism studies and phenol by-products elimination. *J. Hazard. Mater.* **2022**, *424*, 127483. [CrossRef]
49. Chen, W.R.; Bao, Y.X.; Li, X.K.; Huang, J.; Tang, Y.M.; Li, L.S. Mineralization of salicylic acid via catalytic ozonation with Fe-Cu@SiO_2 core-shell catalyst: A two-stage first order reaction. *Chemosphere* **2019**, *235*, 470–480. [CrossRef]
50. Zhang, H.; Ji, F.Z.; Zhang, Y.H.; Pan, Z.C.; Lai, B. Catalytic ozonation of N,N-dimethylacetamide (DMAC) in aqueous solution using nanoscaled magnetic $CuFe_2O_4$. *Sep. Purif. Technol.* **2018**, *193*, 368–377. [CrossRef]
51. Wang, Z.M.; Ma, H.; Zhang, C.; Feng, J.; Pu, S.Y.; Ren, Y.M.; Wang, Y. Enhanced catalytic ozonation treatment of dibutyl phthalate enabled by porous magnetic Ag-doped ferrospinel MnFe2O4 materials: Performance and mechanism. *Chem. Eng. J.* **2018**, *354*, 42–52. [CrossRef]
52. Yang, Y.X.; Ma, J.; Qin, Q.D.; Zhai, X.D. Degradation of nitrobenzene by nano-TiO_2 catalyzed ozonation. *J. Mol. Catal. A Chem.* **2007**, *267*, 41–48. [CrossRef]
53. Zhang, L.H.; Zhou, J.; Liu, Z.Q.; Guo, J.B. Mesoporous CeO_2 Catalyst Synthesized by Using Cellulose as Template for the Ozonation of Phenol. *Ozone Sci. Eng.* **2019**, *41*, 166–174. [CrossRef]
54. Afzal, S.; Quan, X.; Lu, S. Catalytic performance and an insight into the mechanism of CeO_2 nanocrystals with different exposed facets in catalytic ozonation of p-nitrophenol. *Appl. Catal. B Environ.* **2019**, *248*, 526–537. [CrossRef]
55. Wang, J.; Quan, X.; Chen, S.; Yu, H.T.; Liu, G.B. Enhanced catalytic ozonation by highly dispersed CeO_2 on carbon nanotubes for mineralization of organic pollutants. *J. Hazard. Mater.* **2019**, *368*, 621–629. [CrossRef]
56. He, Y.; Wang, L.J.; Chen, Z.; Shen, B.; Wei, J.S.; Zeng, P.; Wen, X.H. Catalytic ozonation for metoprolol and ibuprofen removal over different MnO_2 nanocrystals: Efficiency, transformation and mechanism. *Sci. Total Environ.* **2021**, *785*, 147328. [CrossRef]
57. Wang, Y.X.; Xie, Y.B.; Sun, H.Q.; Xiao, J.D.; Cao, H.B.; Wang, S.B. Efficient Catalytic Ozonation over Reduced Graphene Oxide for p-Hydroxylbenzoic Acid (PHBA) Destruction: Active Site and Mechanism. *ACS Appl. Mater. Interfaces* **2016**, *8*, 9710–9720. [CrossRef]
58. Luo, K.; Zhao, S.X.; Wang, Y.F.; Zhao, S.J.; Zhang, X.H. Synthesis of petal-like δ-MnO_2 and its catalytic ozonation performance. *New J. Chem.* **2018**, *42*, 6770–6777. [CrossRef]
59. Zhu, B.J.; Jiang, G.F.; Chen, S.H.; Liu, F.; Wang, Y.Q.; Zhao, C.C. Multifunctional Cl-S double-doped carbon nitride nanotube unit in catalytic ozone oxidation synergistic photocatalytic system: Generation of ROS-rich region and effective treatment of organic wastewater. *Chem. Eng. J.* **2022**, *430*, 132843. [CrossRef]
60. de Oliveira, J.S.; Salla, J.D.; Kuhn, R.C.; Jahn, S.L.; Foletto, E.L. Catalytic Ozonation of Melanoidin in Aqueous Solution over $CoFe_2O_4$ Catalyst. *Mater. Res. Ibero Am. J. Mater.* **2019**, *22*, e20180405. [CrossRef]
61. Xiang, T.X.; Zhong, D.J.; Zhou, Y.X.; Xu, Y.L.; Tang, D.L.; Li, W.T.; Yang, Y.F.; Fan, C.M.; Chen, J.S. Degradation of Methylene Blue by Ozone Oxidation Catalyzed by the Magnetic $MnFe_2O_4$@Co_3S_4 Nanocomposite. *Langmuir* **2025**, *41*, 2699–2713. [CrossRef]
62. Li, X.K.; Chen, W.R.; Tang, Y.M.; Li, L.S. Relationship between the structure of Fe-MCM-48 and its activity in catalytic ozonation for diclofenac mineralization. *Chemosphere* **2018**, *206*, 615–621. [CrossRef]
63. Bing, J.S.; Hu, C.; Nie, Y.L.; Yang, M.; Qu, J.H. Mechanism of Catalytic Ozonation in Fe_2O_3/Al_2O_3@SBA-15 Aqueous Suspension for Destruction of Ibuprofen. *Environ. Sci. Technol.* **2015**, *49*, 1690–1697. [CrossRef]

64. Pan, Z.Q.; Zeng, J.Y.; Lan, B.Y.; Li, L.S. Catalytic Activity of Argentum-loaded MCM-41 for Ozonation of p-Chlorobenzoic Acid (p-CBA) in Aqueous Solution. *J. Adv. Oxid. Technol.* **2015**, *18*, 139–146. [CrossRef]
65. Zhu, L.J.; Zhou, S.Y.; Cheng, H.; Ma, J.F.; Imanova, G.; Komarneni, S. Cu_2S/Ni_3S_2 nanosheets combined with nickel foam substrate for efficient catalytic ozonation of p-nitrophenol in wastewater. *J. Environ. Chem. Eng.* **2024**, *12*, 113591. [CrossRef]
66. Xu, J.; Li, Y.; Qian, M.Q.; Pan, J.; Ding, J.; Guan, B.H. Amino-functionalized synthesis of MnO_2-NH_2-GO for catalytic ozonation of cephalexin. *Appl. Catal. B Environ.* **2019**, *256*, 117797. [CrossRef]
67. Chen, J.; Tian, S.H.; Lu, J.; Xiong, Y. Catalytic performance of MgO with different exposed crystal facets towards the ozonation of 4-chlorophenol. *Appl. Catal. A Gen.* **2015**, *506*, 118–125. [CrossRef]
68. Athalathil, S.; Erjavec, B.; Kaplan, R.; Stüber, F.; Bengoa, C.; Font, J.; Fortuny, A.; Pintar, A.; Fabregat, A. TiO_2-sludge carbon enhanced catalytic oxidative reaction in environmental wastewaters applications. *J. Hazard. Mater.* **2015**, *300*, 406–414. [CrossRef]
69. Dai, Q.Z.; Zhang, Z.; Zhan, T.T.; Hu, Z.T.; Chen, J.M. Catalytic Ozonation for the Degradation of 5-Sulfosalicylic Acid with Spinel-Type $ZnAl_2O_4$ Prepared by Hydrothermal, Sol-Gel, and Coprecipitation Methods: A Comparison Study. *ACS Omega* **2018**, *3*, 6506–6512. [CrossRef]
70. Xu, T.; Jiang, M.H.; Mao, X.H.; Sher, F.; Ren, T.L.; Xin, K.; Hussain, I.; Hua, H.L.; Wang, X. Design of high-performance ozone catalysts by identifying and modulating anchoring sites for metal on γ-Al_2O_3 spheres. *Appl. Catal. B Environ.* **2025**, *372*, 125321. [CrossRef]
71. Wang, H.; Yu, Z.; Sun, Y.J.; Zhou, J.H.; Yang, Y.X.; Yang, Y.M.; Chen, X.F.; Chen, F.T.; Lu, W.Y. Preparation of porous $La_{0.9}Ce_{0.1}CoO_3$ and its application in enhancing catalytic ozonation for nitrobenzene degradation in aqueous solution. *J. Environ. Chem. Eng.* **2025**, *13*, 116814. [CrossRef]
72. Rutkowska, M.; Chmielarz, L.; Jablonska, M.; Van Oers, C.J.; Cool, P. Iron exchanged ZSM-5 and Y zeolites calcined at different temperatures: Activity in N_2O decomposition. *J. Porous Mater.* **2014**, *21*, 91–98. [CrossRef]
73. Zhang, N.; Ouyang, S.X.; Kako, T.; Ye, J.H. Synthesis of hierarchical Ag2ZnGeO4 hollow spheres for enhanced photocatalytic property. *Chem. Commun.* **2012**, *48*, 9894–9896. [CrossRef]
74. Liu, J.; Yuan, X.J.; Dong, H.Y.; Sans, C. Progress in MnO_2/MnO_2-based materials catalytic ozonation process for water and wastewater treatment. *J. Environ. Manag.* **2025**, *383*, 125493. [CrossRef]
75. Yan, C.L.; Rosei, F. Hollow micro/nanostructured materials prepared by ion exchange synthesis and their potential applications. *New J. Chem.* **2014**, *38*, 1883–1904. [CrossRef]

Disclaimer/Publisher's Note: The statements, opinions and data contained in all publications are solely those of the individual author(s) and contributor(s) and not of MDPI and/or the editor(s). MDPI and/or the editor(s) disclaim responsibility for any injury to people or property resulting from any ideas, methods, instructions or products referred to in the content.

catalysts

MDPI

Article

Banana (*Musa sapientum*) Waste-Derived Biochar–Magnetite Magnetic Composites for Acetaminophen Removal via Photochemical Fenton Oxidation

Manasik M. Nour [1], Maha A. Tony [2,3], Mai Kamal Fouad [4] and Hossam A. Nabwey [1,*]

[1] Department of Mathematics, College of Science and Humanities in Al-Kharj, Prince Sattam bin Abdulaziz University, Al-Kharj 11942, Saudi Arabia
[2] Basic Engineering Science Department, Faculty of Engineering, Menoufia University, Shebin El-Kom 32511, Egypt; dr.maha.tony@gmail.com
[3] Advanced Materials/Solar Energy and Environmental Sustainability (AMSEES) Laboratory, Faculty of Engineering, Menoufia University, Shebin El-Kom 32511, Egypt
[4] Chemical Engineering Department, Faculty of Engineering, Cairo University, Giza 12613, Egypt
* Correspondence: h.mohamed@psau.edu.sa

Abstract

Recently, researchers have been focused on the recycling as well as transforming of bio-waste streams into a valuable resource. Banana peels are promising for such application, due to their wide availability. In this context, the integration of banana peel-derived biochar with environmentally benign magnetite has significantly broadened its potential applications as a solar photocatalyst compared to the conventional photocatalysts. The materials are mixed in varied proportions of Ban-Char500-Mag@-(0:1), Ban-Char500@Mag-(1:1) and Ban-Char500@Mag-(2:1) and characterized using X-ray diffraction (XRD) and scanning electron microscopy (SEM) augmented with dispersive X-ray spectroscopy (EDX). Such modification is leading to an improvement in its application as a solar photocatalyst using the photochemical solar collector facility. The study discusses the factors controlling acetaminophen removal from aqueous effluent within 30 min of solar illumination time. Furthermore, the highlighted optimum parameters are pH 3.0, using 10 mg/L of the Ban-Char500@Mag-(1:1) catalyst and 100 mg/L of the hydrogen peroxide as a Fenton combination system for removing a complete acetaminophen from wastewater (100% oxidation). Also, the temperature influence in the oxidation system is studied and the high temperature is unfavorable, which verifies that the reaction is exothermic in nature. The catalyst is signified as a sustainable (recoverable, recyclable and reusable) substance, and showed a 72% removal even though it was in the six cyclic uses. Further, the kinetic study is assessed, and the experimental results revealed the oxidation process is following the first-order kinetic reaction. Also, the kinetic–thermodynamic parameters of activation are investigated and it is confirmed that the oxidation is exothermic and non-spontaneous in nature.

Keywords: acetaminophen; photocatalysis; Fenton; solar energy; banana peels

1. Introduction

Globally, rapid industrial growth has been accompanied by a substantial increase in water consumption, resulting in massive discharges of wastewater from various industrial activities [1,2]. Among these, the pharmaceutical industry is one of the fastest expanding

sectors [3,4]. Pharmaceuticals encompass a wide range of compounds, including antibiotics, anti-inflammatory drugs, lipid regulators, and other therapeutic agents [5–11]. The discharge of pharmaceuticals into aquatic systems is particularly concerning, as they are increasingly recognized as emerging pollutants (EPs) due to their low biodegradability, high persistence, and potential for bioaccumulation [12–16]. Pharmaceutical effluents are released at different stages of their life cycle [17,18], from production to disposal, and their persistence in aquatic environments poses risks to both human health and ecosystems [19–27]. Consequently, considerable research efforts have been directed toward addressing these emerging pollutants [28–33]. Various treatment strategies—such as advanced oxidation processes, flotation, electrochemical techniques, and biological methods—have been proposed to mitigate pharmaceutical contamination in aquatic ecosystems [34–39]. However, many of these approaches face limitations, including high operational and maintenance costs, as well as the potential formation of secondary toxic by-products.

The existence of pharmaceuticals is widespread in the modern societies as emerging chemicals [15–19], and could be as a result of several activities [20–27]. Therefore, such pharmaceutical effluent discharge is a challenge, from their production to their elimination [26–28]. Moreover, their presence in the aqueous system is a global issue that might cause damage to human beings as well as numerous wildlife species [29,31]. Hence, ever-increasing efforts have been devoted to enable the emergence of those EPs [32]. Various systems have been suggested to treat such pharmaceuticals contaminating the ecosystem, such as oxidation, flotation, electrochemical techniques and biological managements [33,34]. Nevertheless, such methods are not convenient because of expensive operating or maintenance charges or generating secondary excess toxic contaminants.

Advanced oxidation processes (AOPs) are promising treatment candidates due to their advantages, including simple operation, cost-effectiveness, and high efficiency in both removing and mineralizing pollutants [35–42]. The current compilation in research is looking for sustainable treatment facilities to better signify the frontiers in such a field [17,39]. Fenton oxidation, which uses iron oxides, is suitable for AOP treatment because pollutants can be oxidized and completely mineralized into harmless end products, such as carbon dioxide and water, upon activation with H_2O_2. However, although the reaction commonly requires a relatively short reaction time, homogenous Fenton process forms iron sludge as a secondary pollutant, and it is essential to deal with it prior to final disposal [43]. Further, not only is such sludge a drawback, but also the acidic pH, losing the iron activity and thereby reducing the oxidation efficiency [44,45]. To avoid such parameters that hinder the system and to attain a high removal efficiency, solar radiation might be combined with the Fenton oxidation to increase the system activity and reach a higher mineralization compared to the solo Fenton treatments. It is noteworthy that the operational cost of the Fenton system can be reduced by using renewable solar energy [46]. To sum up, chemical precursors of the Fenton system are still behind the cost of the process.

Nevertheless, most published studies on the Fenton reaction do not utilize waste-derived materials as a catalyst source. This gap highlights the novelty of the present work, where waste is utilized as a functional material and applied for wastewater remediation, thereby promoting sustainable resource use. Thus, to reach an economic sustainable Fenton oxidation using waste sources as an ecological catalyst source coupled with magnetite nanoparticles is essential for a substitute of metal oxides that is signified as the backbone of the Fenton reaction [47,48]. Banana peels (*Musa sapientum*) generated in millions of tons annually as agro-industrial by-products from beverage factories, local shops, and households, represent a significant waste challenge [49–51]. Although various techniques are dealing with such banana peel management, the common handling facility is dumping or landfilling, so as to be an organic fertilizer, or may be to be used as animal feed [11,52–54].

Converting banana peels into functional catalysts offers a win–win strategy to simultaneously address solid waste management and water pollution

In this work, we introduce a novel approach that integrates naturally abundant agricultural waste with magnetite to create a recyclable catalyst for solar photo-Fenton applications. Specifically, biochar derived from *Musa sapientum* was functionalized with environmentally benign magnetite via a simple co-precipitation route. This hybrid material, serving as a cost-effective and sustainable photocatalyst, was thoroughly characterized and subsequently applied for the oxidation of acetaminophen in wastewater. The novelty of this study lies in the synergistic utilization of waste-derived biochar, its integration with magnetite, and the solar collector that assisted photo-Fenton processes to enhance solar energy harvesting for efficient pharmaceutical wastewater remediation.

2. Results and Discussion

2.1. Structural and Morphological Characterization of Ban-Char500 Samples

XRD

XRD, X-ray diffraction patterns of magnetite and composite magnetite/biochar are displayed in Figure 1. As exhibited in Figure 1a, the magnetite crystal structure XRD data (JCPDS No. 89-4319) [14] appears in the pattern. The XRD pattern exhibits well-defined sharp diffraction peaks. The peaks appear at the 2θ values of 30.15, 35.61, 43.20, 57.71, and 62.81, which correspond to the plans of (220), (311), (400), (422), and (620), respectively. Also, it is noteworthy to mention that the most intensive magnetite peaks appear in the two samples of (b) Char500@Mag-(1:1) and (d) Ban-Char500@Mag-(2:1), with well-defined sharp diffraction peaks that exhibit good crystalline phase. That verifies the well distributed magnetite nanoparticles in the composites, without causing damage to the magnetite nanoparticle crystal structure. However, XRD examination of the composite containing banana biochar, (b) Ban-Char500@Mag-(1:1), (c) Ban-Char500@Mag-(2:1) and (d) Ban-Char500@Mag-(1:0) reveals broad peaks indicative of an amorphous carbon layer, suggesting the predominantly amorphous nature of the banana peel material. Furthermore, the inclusion of banana peel into magnetite mostly does not result in alterations to the crystallinity or phase of the magnetite material. However, an observable change is evident in the introduction of banana biochar into the magnetite material consequences in a reduction in peak intensity within the XRD pattern of the composite of Ban-Char500@Mag-(1:1) or Ban-Char500@Mag-(2:1) materials. This could be due to the fact that banana biochar, which is signified as a carbon-based material, does not reveal diffraction peaks in XRD patterns [4]. As peak intensity in XRD patterns reflects the extent of diffraction at a specific angle, the addition of banana biochar to magnetite in different proportions could potentially reduce the concentration of magnetite in the material campsite, due to the mixing ratios, thereby leading to a deduction in the peak intensity represented in the XRD pattern [4–6]. Additionally, the XRD pattern of Ban-Char500@Mag-(1:0) in Figure 1d signifies the diffraction peaks observed at 2θ values of 23° and 42.5°, corresponding to the (002) and (101) planes of graphitic carbon, respectively, confirming the carbonaceous structure of the biochar.

FTIR

The FTIR result of the prepared composite Ban-Char500@Mag-(1:1) is illustrated in Figure 2. The data clearly confirms the presence of magnetite in the composite. Specifically, magnetite nanoparticles (Fe_3O_4) are signified by their characteristic Fe–O stretching bands at 585 and 460 cm^{-1}, while, simultaneously, surface O–H stretching is observed at 3400 cm^{-1}, together with the H–O–H bending mode of adsorbed water at 1635 cm^{-1}. Furthermore, organic bands, including aliphatic C–H stretching at 2920–2850 cm^{-1}, a carbonyl band around 1715 cm^{-1}, and aromatic C=C vibrations near 1600–1510 cm^{-1}, as well as strong C–O/C–O–C vibrations in the 1260–1030 cm^{-1} region, are also present in the

composite. Altogether, the coexistence of Fe–O bands with biochar-derived functionalities therefore provides evidence of successful coating and anchoring of magnetite on the carbonaceous surface. Hence, such results are consistent with interfacial interactions such as hydrogen bonding and electrostatic effect between surface hydroxyl/carboxyl groups and Fe sites.

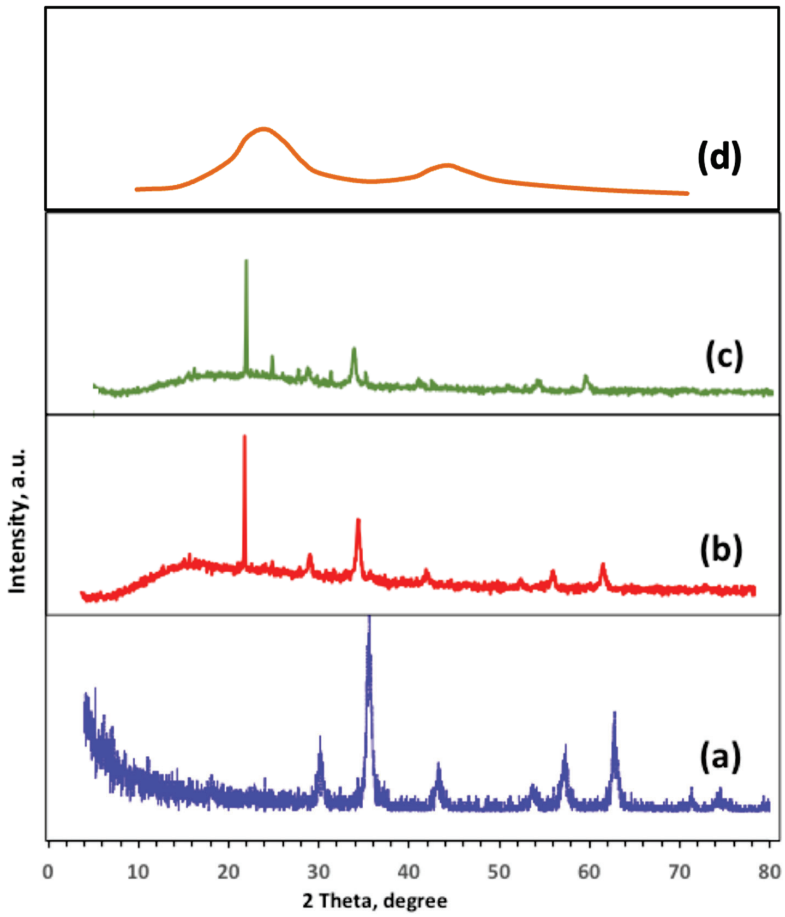


Figure 1. XRD of magnetite and banana biochar composites: (**a**) Ban-Char500@Mag-(0:1), (**b**) Ban-Char500@Mag-(1:1), (**c**) Ban-Char500@Mag-(2:1) and (**d**) Ban-Char500@Mag-(1:0).

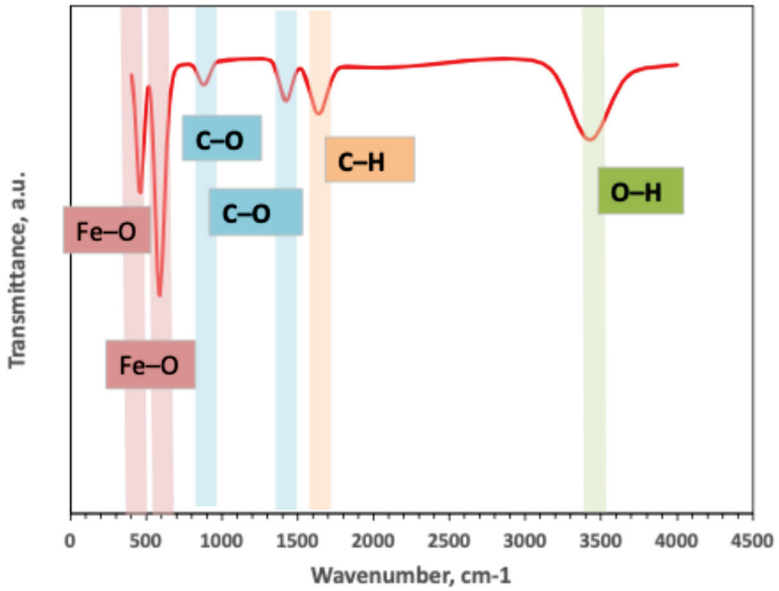


Figure 2. FTIR analysis of Ban-Char500@Mag-(1:1) composite material.

SEM and particle size distribution:

The SEM graph displayed in Figure 3a represents the magnetite nanoparticles and magnetite augmented with banana biochar with different proportions of (c) Ban-Char500@Mag-(1:1) and (e) Ban-Char500@Mag-(2:1). Ban-Char500@Mag-(0:1), which is related to magnetite nanoparticles, shows semi-spherical particle aggregates with a particle size distribution (Figure 3b) in an average of 6.8 nm. However, the images displayed in Figure 3c,e showed scattered grains with rough texture, as well as the presence of small semi-spherical-like particles that maintained the same particles of magnetite. Also, the particle size distribution is observed to be 9.77 nm (Figure 3d) and 10.42 nm (Figure 3f) for Ban-Char500@Mag-(1:1) and 6.83 nm for (e) Ban-Char500@Mag-(2:1), respectively. Thus, such images verify the presence of magnetite. Despite the presence of magnetite with Ban-Char500 biochar, the molecules are retaining their shape.

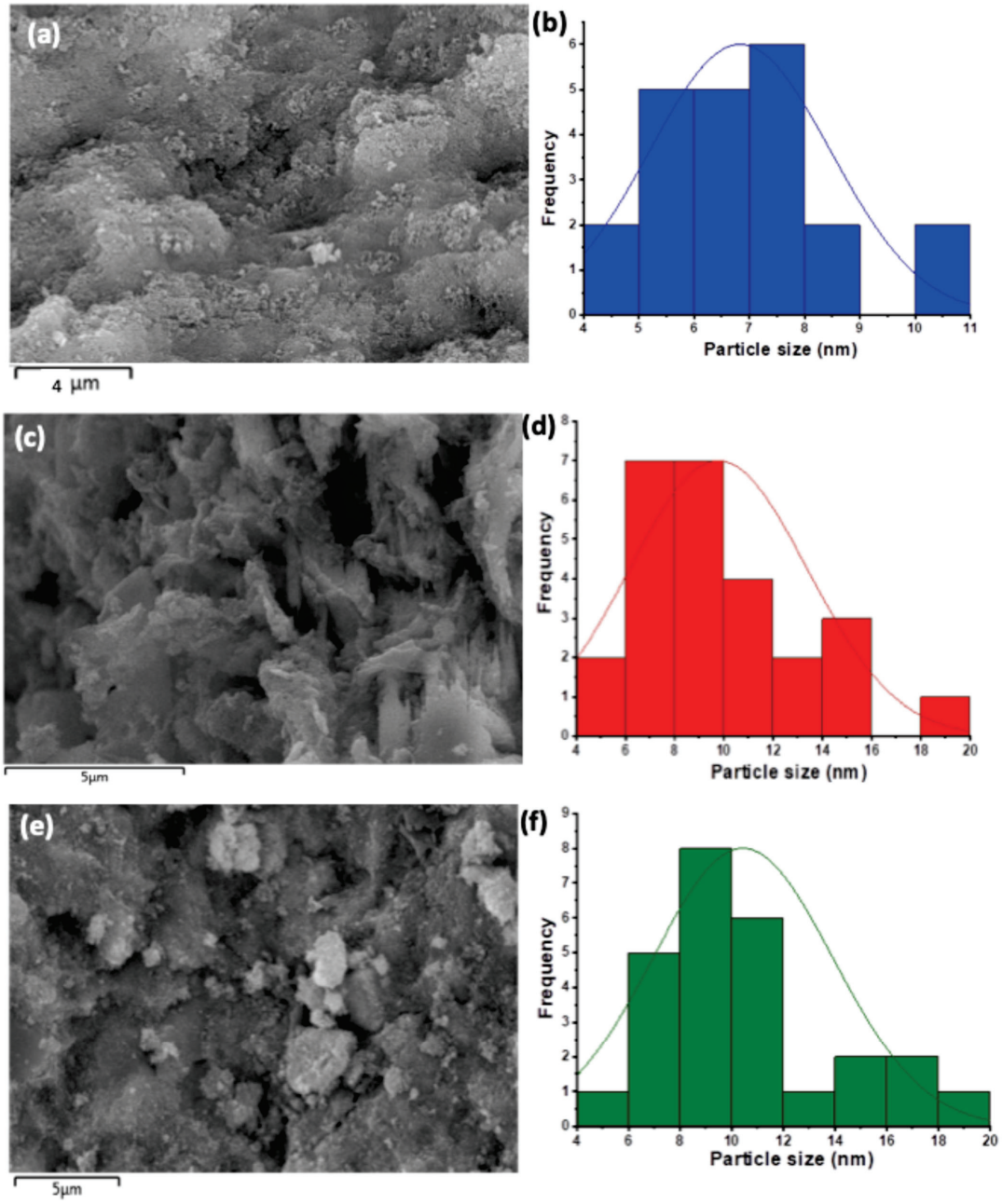
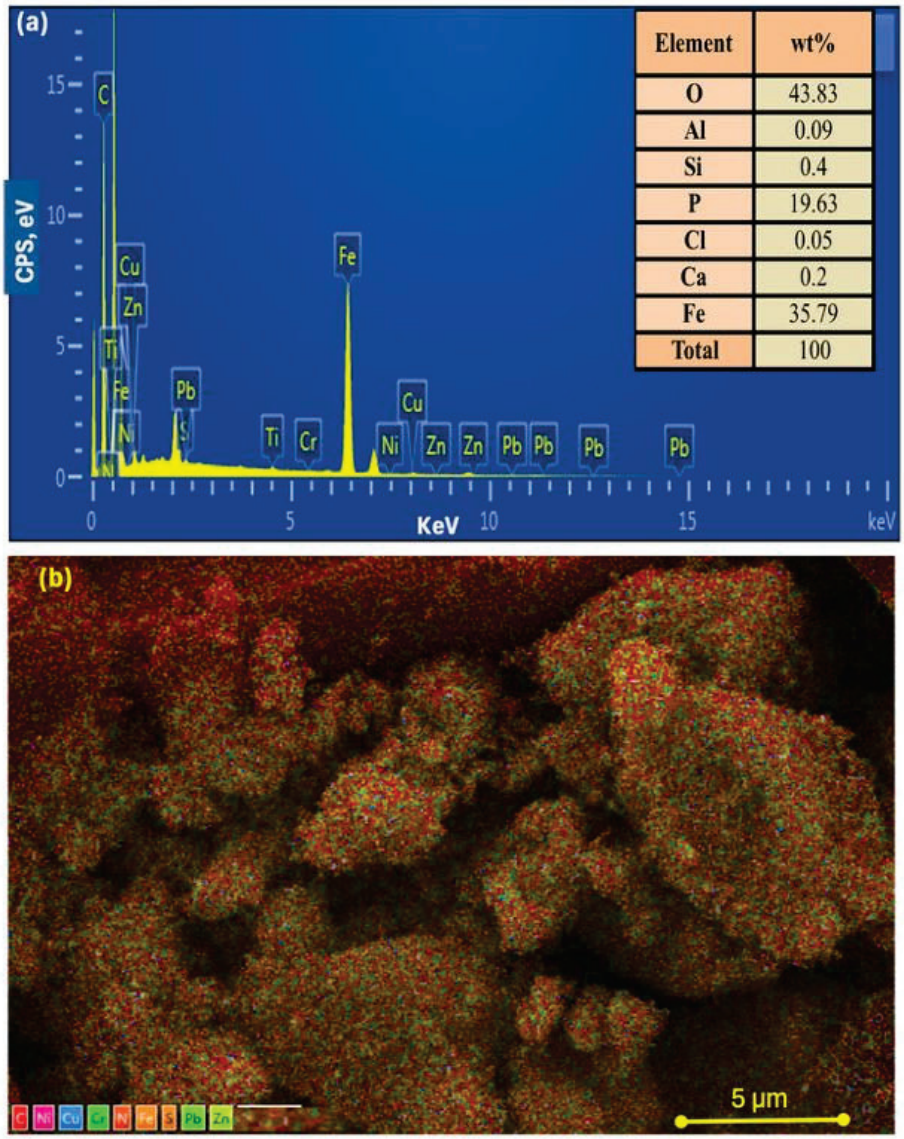


Figure 3. SEM images and particle size distribution of (**a**,**b**) Ban-Char500@Mag-(0:1), (**c**,**d**) Ban-Char500@Mag-(1:1) and (**e**,**f**) Ban-Char500@Mag-(2:1).

EDX and mapping

The Fe content in the composites was estimated using SEM–EDX analysis, which provides semi-quantitative values based on localized surface probing. As displayed in Figure 4a,c and their corresponding mapping graph of Figure 4b,d, the energy-dispersive X-ray spectroscopy (EDX) analysis of a selected area of the Ban-Char500@Mag-(1:1) and Ban-Char500@Mag-(2:1), respectively, verified the occurrence of O and Fe, elements found in magnetite, as well as the nitrogenous base and/or sugar elements (C, N, O) present. The corresponding EDX spectrum readily identified the presence of O and Fe, with the iron emission energy observed at 6.405 keV, which corresponds to the Kα 1 peak. The assenting occurrence of all the above-mentioned elements in the synthesized Ban-Char500@Mag suggests the successful incorporation of magnetite with the banana-based biochar. Furthermore, the existence of Cl on the Ban-Char500@Mag-(1:1) sample in a low amount (0.05%) is most likely due to unreacted iron (II) and (III) chloride residues (i.e., magnetite precursors). Notably, such an amount might be trapped in the nanoparticle crystalline lattice during the co-precipitation synthesis.



Element	wt%
O	43.83
Al	0.09
Si	0.4
P	19.63
Cl	0.05
Ca	0.2
Fe	35.79
Total	100

Figure 4. *Cont.*

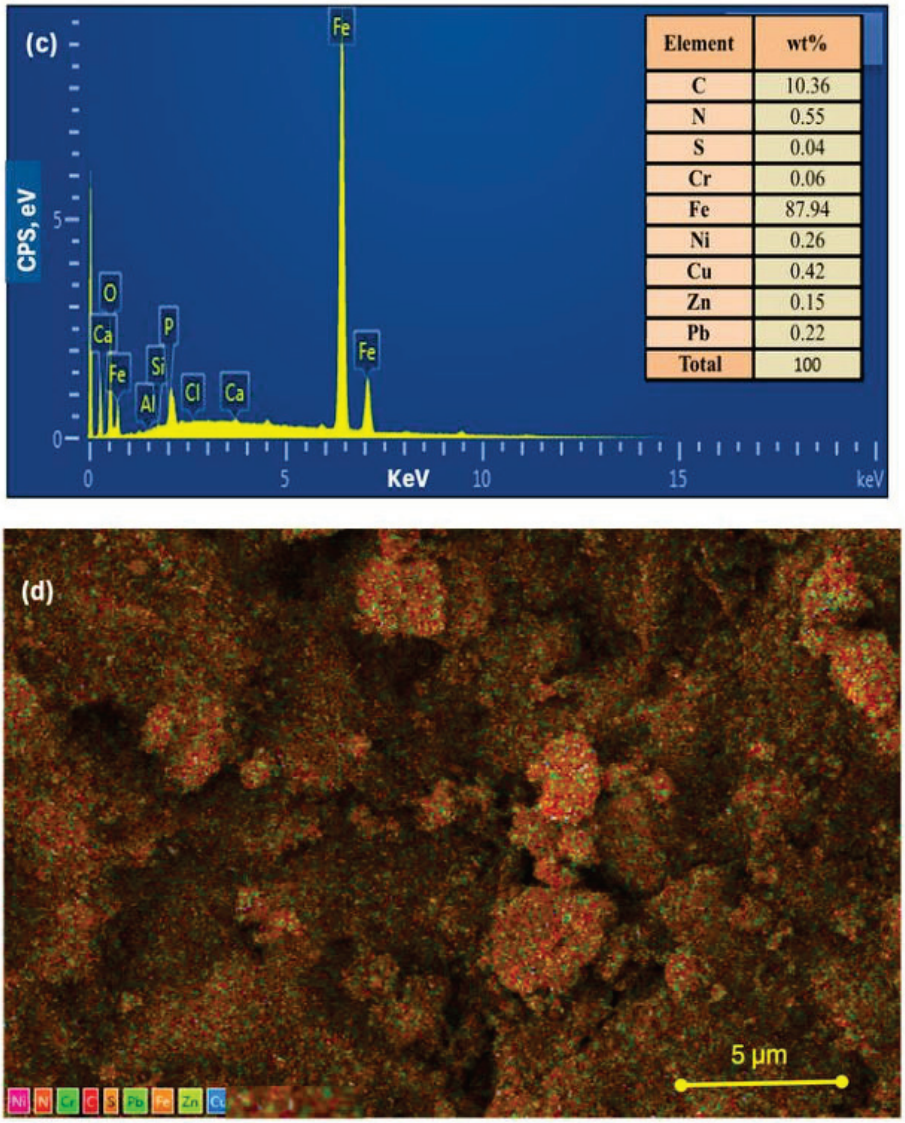


Figure 4. (**a**,**b**) Ban-Char500@Mag-(1:1) and (**c**,**d**) Ban-Char500@Mag-(2:1) EDS mapping graphs.

2.2. Solar Radiation and Collector Analysis

The parabolic trough solar collector represents the active constituent of the ultraviolet initiation technique that transfers the initiation process into the tubular reactor. A typical parabolic trough-collector type is used in this current work, as illustrated in the above-mentioned sections. The collector was placed facing south-west, according to the geographic location, and a tilt on the horizontal with an angle of 32° that suits the location. Results are from directly measured solar energy radiation intensity, in the place of experiment, during the summer season. Figure 5 illustrates that the maximum incident solar radiation recorded during the study reached 1015 W/m^2, representing the average solar intensity over the experimental period.

In the meantime, the ambient temperature is recorded through the study, to verify the solar intensity values. It is noteworthy to mention that temperatures and the solar intensity increases from the early morning to reach their maximum values around the solar noon. But the increased solar intensity begins to decline again later in the afternoon. Thus, the favorable conducting experimental time is around the solar noon [24].

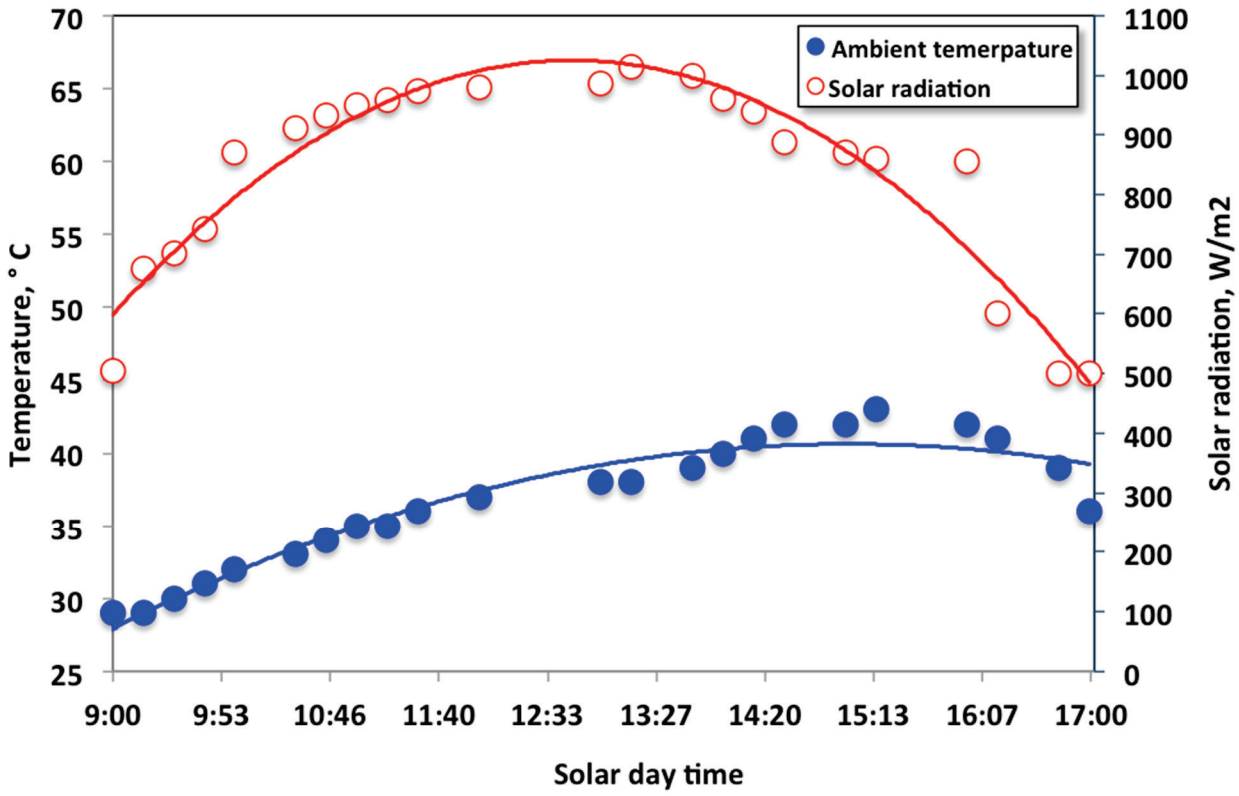


Figure 5. Thermal analysis of the photochemical parabolic trough collector versus time, showing the temperature profile and the solar intensity radiation.

2.3. Solar-Fenton Oxidation

2.3.1. Comparison of Illumination Time for Various Oxidation and Adsorption Systems

Initially, to evaluate and assess the suggested novel system, it is essential to compare it with various oxidation systems, and the data is displayed in Figure 6. To properly evaluate the proposed Char500@Mag-based solar-Fenton system, its performance was compared with adsorption and different oxidation pathways, as shown in Figure 6. The systems tested included the solo adsorption with Char500 biochar or adsorption with magnetite alone, dark Fenton (without irradiation), H_2O_2/solar, Mag/solar, and the complete solar-Fenton system (Char500@Mag/H_2O_2/solar).

Acetaminophen removal is introduced for removing a pharmaceutical contaminate from aqueous effluent. Experiments were executed at various irradiance and oxidation times for all introduced systems including H_2O_2/solar, Mag/solar, and solar-Fenton based Ban-Char500@Mag-(1:1), and compared with the dark Fenton (without ultraviolet illumination), and the oxidation effectiveness rates were assessed. The data exhibited in Figure 6 at a natural wastewater pH condition (pH 6.8) revealed the effectiveness of the dual treatment represented in the Fenton (dual oxidation) system, augmenting solar photons as a source of initiation UV. The data represented a higher removal efficiency, corresponding to 95% of the solar-Fenton system in comparison to 45, 30 and 14% for the H_2O_2/solar, dark Fenton and Mag/solar systems, respectively. Such results verified both the roles of the solar system and the newly supplied Fenton source in conducting the oxidation reaction. Also, the reaction time that is required is only 60 min. However, it is noteworthy to mention that the first rapid rate of oxidation is identified within the initial 10 min of oxidation time. Afterwards, a steady oxidation rate within the next oxidation reaction is achieved.

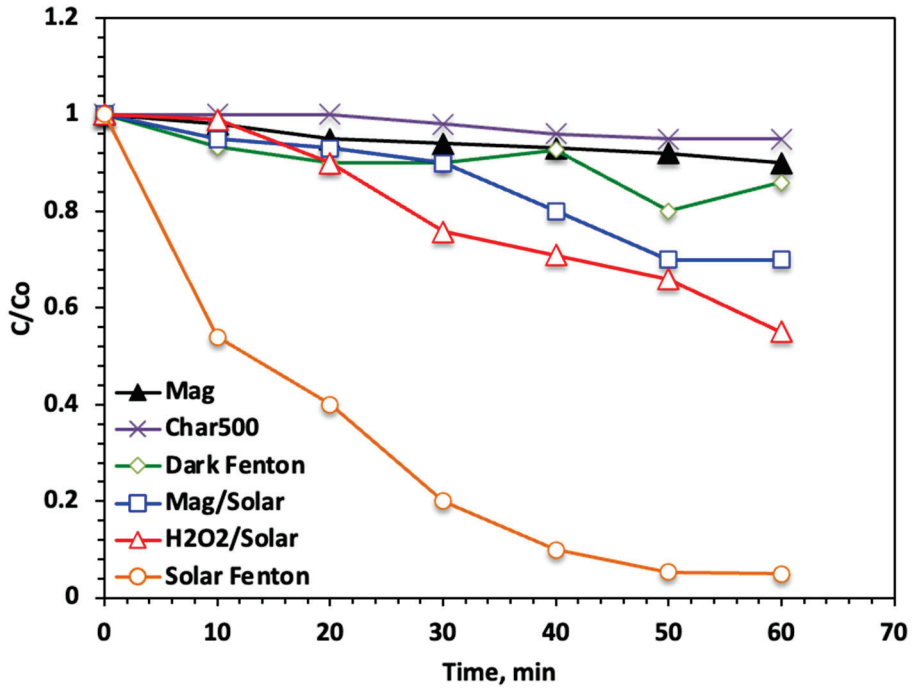


Figure 6. Effect of various oxidation and adsorption systems on the acetaminophen reaction time (Char500@Mag-(1:1) 10 mg/L; H_2O_2 400 mg/L and pH 3.0).

The results presented in Figure 6 demonstrate that even though the dark Fenton showed a considerable low oxidation efficiency (30%) within one hour of reaction time, it could still oxidize acetaminophen. However, the solar-Fenton reaction could reach 95%, verifying the role of the presence of solar radiation. Also, the oxidation is stopped, and no further oxidation could occur; hydrogen peroxide is consumed through the reaction time and, thereby, no further •OH radicals are produced. This could be attributed to extra •OH radicals being generated in the dual solar-Fenton system. Furthermore, it is noteworthy to mention that the presence of Ban-Char500@Mag also helps in the acetaminophen molecules adsorption, as well as oxidation, since the presence of carbon acts as an adsorbent material. Consequently, when the vacant active sites of the Ban-Char500@Mag substance are saturated with the acetaminophen molecules, the propensity of the Char500@Mag material to adsorb more molecules is minimized. Such data are in accordance with the previously reported data in the literature, treating wastewater containing dye adsorption using a magnetite catalyst and adsorbent material. To sum up, the superior oxidation tendency is achieved within the initial reaction time, which might be linked to •OH radicals' speciation [28]. •OH radicals are traced through the catalytic decomposition of the H_2O_2 reagent by the Char500@Mag material.

Additionally, the results indicate that adsorption alone, whether with Char500 or magnetite, led to only limited acetaminophen removal (<10% within 60 min), confirming that physical uptake cannot account for the high removal observed in the composite system. It should be noted, however, that adsorption was evaluated only for 60 min under the present experimental conditions for direct comparison with the oxidation reactions. Extending the contact time, together with optimizing operational parameters (e.g., pH, dosage, and catalyst loading), could potentially enhance the adsorption performance and lead to higher acetaminophen removal efficiency.

Hence, the effective destruction of the acetaminophen molecules, which attacked through •OH radicals [55]. Consequently, the Char500@Mag composite containing magnetite possesses the advantage of being a sustainable recoverable solar photocatalyst material.

2.3.2. Effect of Char500@Mag Composite Type

In the light of selecting the superior composite combination activity, it is essential to evaluate the ideal combination between magnetite and Char500-activated biochar biopolymer, Ban-Char500-Mag@-(1:0), Ban-Char500-Mag@-(0:1), Ban-Char500@Mag-(1:1) and Ban-Char500@Mag-(2:1)-based solar reaction, applied as as a source of the Fenton system. Hydrogen peroxide is supplemented to initiate the Fenton reaction. Various oxidation combinations' efficacy was assessed in terms of acetaminophen oxidation. Consequently, the initial doses are the catalyst in 10 mg/L and hydrogen peroxide of 100 mg/L, which were added to the wastewater at acidic wastewater pH conditions (pH 3.0), since the Fenton reaction might work at acidic conditions, as a modified solar-Fenton oxidation test, and the aqueous solution is subjected for solar irradiance in the photochemical reactor. The experiments are conducted around the solar noon at the time of the study.

The results displayed in Figure 7 validate that a high % of the acetaminophen removal is attained in the all applied systems, with a superior and shorter reaction time recorded for the corresponding system-based Ban-Char500@Mag-(1:1) system. It is essential to report that the initial oxidation time in all systems reveals greater oxidation effectiveness compared to exceeding the illumination time. The superiority of the solar-based catalyst is in the order of Ban-Char500@Mag-(1:1) >> Ban-Char500@Mag-(2:1) >> Ban-Char500@Mag-(0:1) >> Ban-Char500-Mag@-(1:0), which recorded 100, 98, 90 and 50%, respectively. This behavior can be explained by the influence of magnetite content in the reaction medium, as Fe^{2+}/Fe^{3+} ions present in the composite act as the key reagents driving the solar-Fenton process. The banana peel-derived biochar serves as an effective adsorbent, and its combination with magnetite enhances the overall surface area of the material [18]. However, when the composite contains a higher proportion of biochar, adsorption becomes more dominant, while the catalytic role of magnetite is reduced. Consequently, the Ban-Char500@Mag (1:1) catalyst generates an excess of ·OH radicals, which synergistically supports both adsorption and oxidation, thereby improving system performance. In contrast, Ban-Char500@Mag (0:1), containing only biochar without magnetite, relies solely on ·OH radical generation in the reaction medium, which results in lower efficiency compared to the combined oxidation–adsorption mechanism [44]. Thus, in the absence of magnetite, the composite functions primarily as a biochar $–H_2O_2$ system, where the degradation relies largely on hydrogen peroxide alone. This results in lower oxidation efficiency compared to systems incorporating magnetite, which play a crucial role in enhancing radical generation and overall performance.

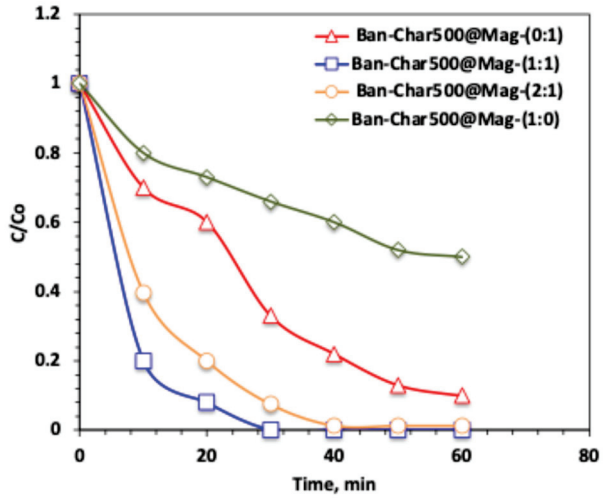


Figure 7. Effect of various Char500@Mag composites on the solar-Fenton oxidation system on acetaminophen removal.

2.3.3. Effect of Acetaminophen Loading

For catching the real scalar field applications, it is essential to study the pollutant loading on the performance of the solar oxidation suggested Ban-Char500@Mag-(1:1)-based Fenton oxidation. The initial acetaminophen concentration is varied to evaluate the pollutant loading on the performance of the solar catalytic-modified classical Fenton oxidation system. In this regard, the loading of acetaminophen is tested to examine H_2O_2/Ban-Char500@Mag/solar system oxidation capabilities. Figure 8 presents the effect of the modified Fenton oxidation process on acetaminophen at concentrations ranging from 50 to 200 ppm, while maintaining constant operating conditions (catalyst 10 mg/L, H_2O_2 100 mg/L, and pH 3.0). The maximal acetaminophen removal efficacy is extended to a complete (100%) acetaminophen removal for the low concentrations, i.e., 50 ppm; when reached, it declines from 96 to 58 when the acetaminophen is increased gradually, from 100 to 200 ppm, respectively. This can be explained by the fact that the amounts of catalyst and H_2O_2 were kept constant in all experiments, while the acetaminophen load was progressively increased. As a result, the generated ·OH radicals were insufficient to achieve complete oxidation at higher pollutant concentrations.

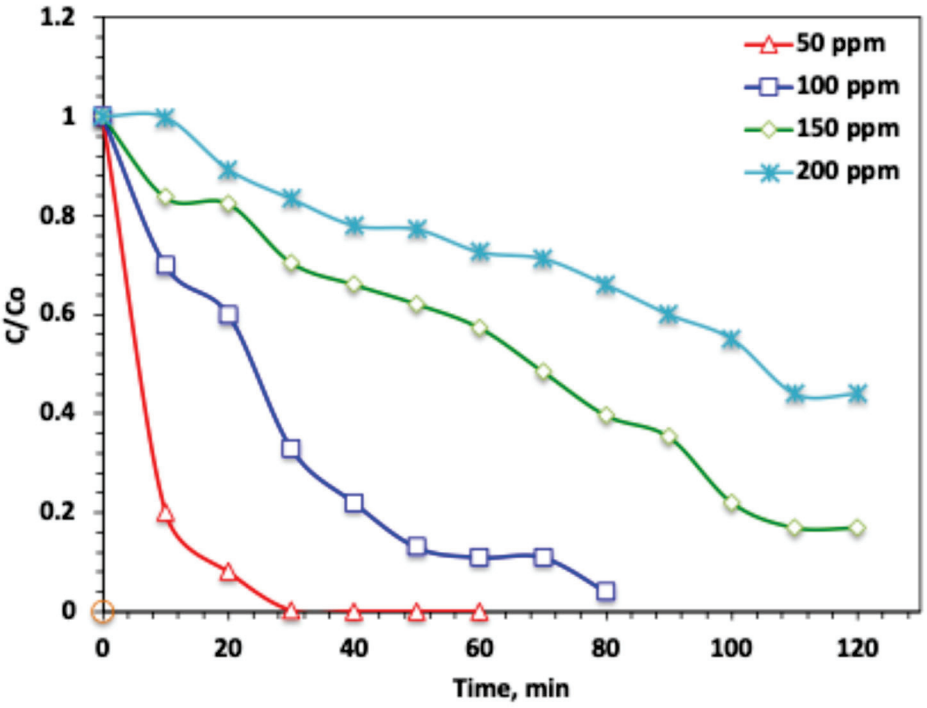


Figure 8. Effect of acetaminophen dose on the modified Char500@Mag Fenton oxidation system.

Additionally, the available active vacant adsorbent sites on the composite of Mag (magnetite) and Ban-Char500@Mag (Banana biochar) are not sufficient to adsorb higher acetaminophen molecules. Additionally, the high acetaminophen molecules adsorbed on the Ban-Char500@Mag composite active sites might be causing the decline of the efficient hydroxyl radical's species' quantity. A similar exploration was previously reported in the literature by [19] in oxidizing organics through Fenton, initiated by the ultraviolet system.

2.3.4. Catalyst Effect on Modified Solar-Fenton System

It is essential to investigate Char500@Mag as a catalyst and hydrogen peroxide (H_2O_2) reagent validity on the oxidation of acetaminophen by the suggested Fenton reaction, to proceed with an optimal reagent. Initially, Char500@Mag concentration is investigated, and the results are displayed in Figure 9. The effect of the dosage of Char500@Mag-(1:1)

on the oxidation of acetaminophen was studied in the range of 5–40 mg/L. As the data illustrated in Figure 9 revealed a Char500@Mag increase from 5 to10 mg/L, the corresponding oxidation efficacy of acetaminophen increased from 67 to 100%, respectively, through 30 min of solar irradiance time. However, the further increase in adding Char500@Mag in the reaction medium results in a decline in the overall oxidation to 52 and 37% for 30 and 40 mg/L, respectively. The amount of Char500@Mag elevated is possibly postulated by extra active species for acetaminophen oxidation, and hence the results are an improvement in the oxidation proficiency.

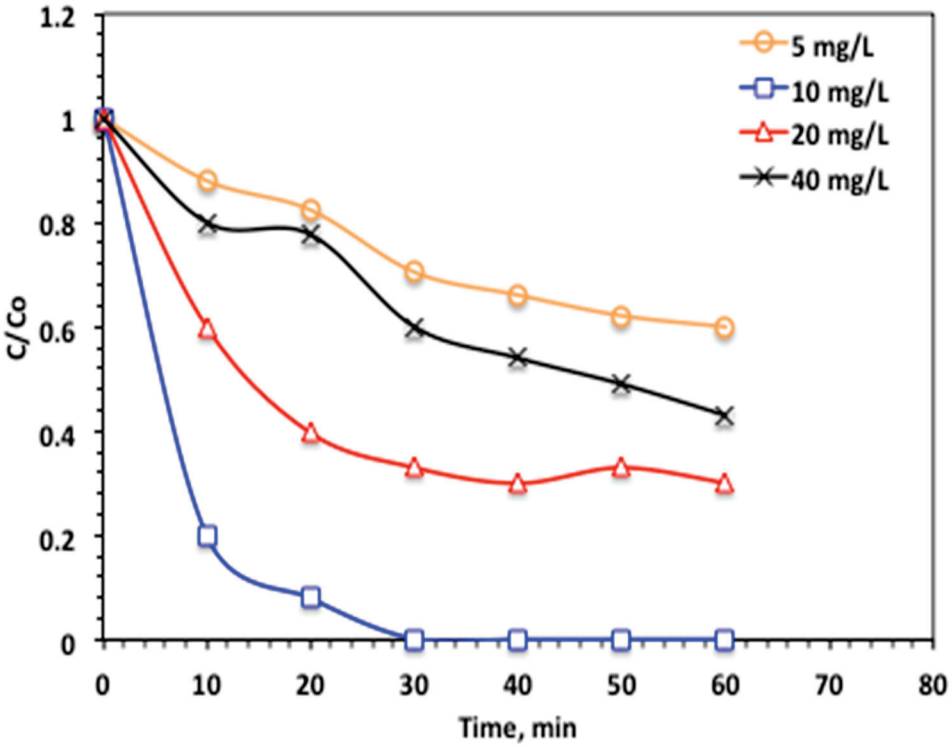


Figure 9. Effect of catalyst dose on the modified Char500@Mag Fenton oxidation system (H_2O_2 100 mg/L and pH 3.0).

However, when the Char500@Mag dosage is increased beyond a certain threshold (10 mg/L), the catalyst may precipitate in the reaction medium instead of effectively reacting with H_2O_2 to generate ·OH radicals. In addition, excess Char500@Mag particles can hinder the penetration of solar UV light into the medium, thereby reducing light absorption and diminishing oxidation efficiency. For this reason, a catalyst dosage of 10 mg/L was selected and applied in the subsequent experiments. This observed trend is consistent with previous reports involving various pollutants [24,33].

2.3.5. H_2O_2 Effect on Modified Solar-Fenton System

The influence of hydrogen peroxide on the oxidation of acetaminophen by the modified Fenton reaction catalyzed by Char500@Mag is exhibited in Figure 10. H_2O_2 increase results in an advance in the acetaminophen oxidation efficiency, resulting in a complete removal when the hydrogen peroxide is elevated from 50 to 100 mg/L. The mineralization rate reaches 100% of complete acetaminophen oxidation within 30 min of solar irradiance time. But this further increase, rather than 100 mg/L, is not favorable. Although the H_2O_2 is the source of the •OH radicals, in the Char500@Mag/H_2O_2/solar-Fenton system, notably, the elevation of the H_2O_2 reagent concentration from 100 to 400 mg/L results in a decline

in acetaminophen oxidation that reaches 96 and 93% when the peroxide dose is increased to 200 and 400 mg/l, respectively.

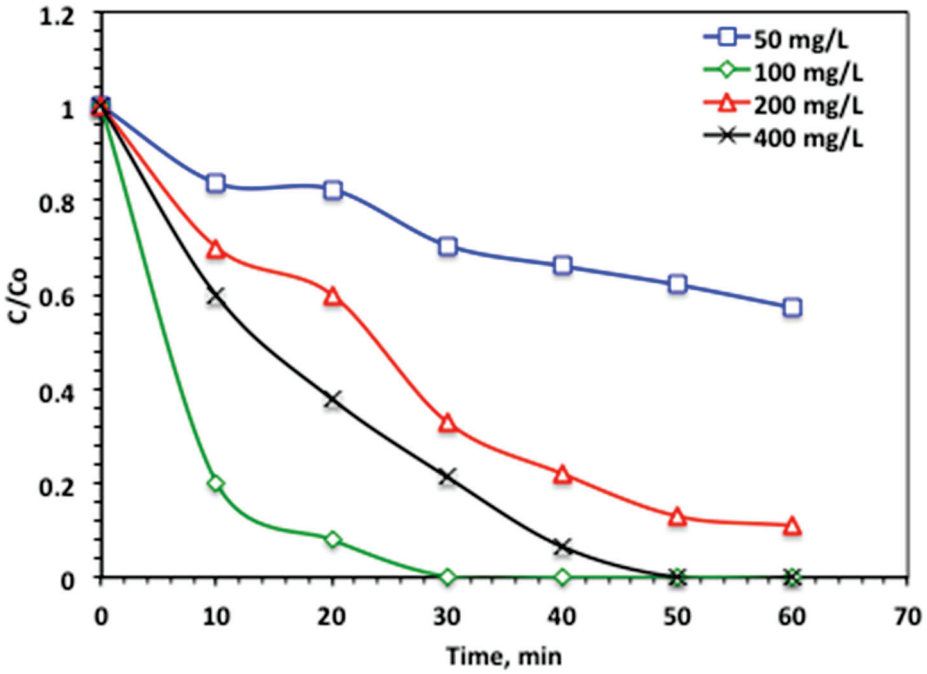


Figure 10. Effect of hydrogen peroxide dose on the modified Char500@Mag Fenton oxidation system (Char500@Mag-(1:1) 10 mg/L and pH 3.0).

This trend can be attributed to the enhanced generation of reactive species, particularly hydroxyl radicals (·OH), at certain concentrations where the balance between catalyst activity and oxidant availability favors radical production. However, when the H_2O_2 dose is further increased from 100 to 400 mg/L, additional radicals such as $O_2\bullet^-$ and $^\bullet HO_2$ are formed in the reaction medium. These species exhibit significantly lower oxidation potentials compared to ·OH radicals, leading to a reduction in overall acetaminophen degradation efficiency. These findings are consistent with observations reported in previous studies [36,55]. Therefore, 100 mg/L can be considered the optimum H_2O_2 dosage for effective acetaminophen oxidation and removal from aqueous media.

2.3.6. pH Effect on Modified Solar-Fenton System

The effect of the operating pH on acetaminophen oxidation was examined by varying the initial pH of the aqueous medium from 3.0 to 8.0, while maintaining 100 mg/L hydrogen peroxide and 10 mg/L Char500@Mag catalyst under solar irradiation. The data exhibited in Figure 11 revealed that the acetaminophen oxidation rate is improved by a decline in pH value and when the optimal operating pH value is in acidic (3.0) conditions. But increasing the pH value results in a reduction in the acetaminophen oxidation rate. In particular, higher pH values in the alkaline range were found to be unfavorable, as they reduced the oxidation efficiency to only 78%. Notably, at pH 5.0, the system exhibited the lowest performance, with an oxidation rate of just 52% after 30 min of reaction.

Such an oxidation change, which is related to the pH value, can be clarified by the surface charge of the Char500@Mag catalyst. According to the previous work cited, the point of zero charge of Char500@Mag composite is recorded at about pH 7.2. The surface of the Char500@Mag catalyst might be charged in a negative or positive charge, due to the dissociation of the basic character of the catalyst at the point of zero charge. Hence, the change in the medium pH affects the surface charge of the catalyst, and thereby

affects the catalytic and adsorption tendency. Hence, this could be illustrated by the presence of low electrostatic interactions among molecules of acetaminophen and the corresponding Char500@Mag molecules at the alkaline pH medium, whereby the oxidation rate is deduced [45,53].

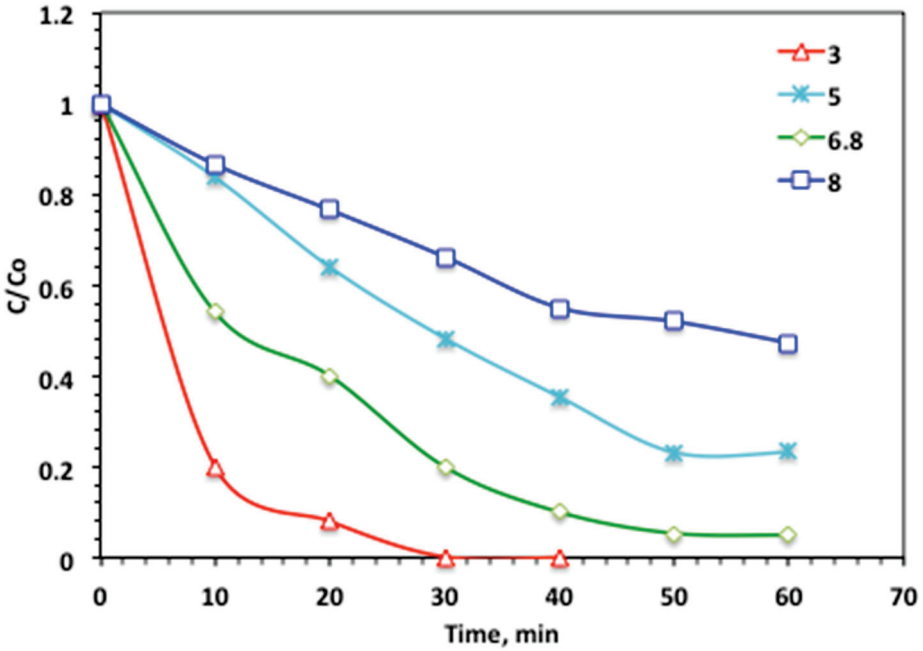


Figure 11. Effect of pH on the modified Char500@Mag Fenton oxidation system (Char500@Mag-(1:1) 10 mg/L and H_2O_2 100 mg/L).

2.3.7. Temperature Effect on Modified Solar-Fenton System

To accomplish a real-life practical world, it is necessary to attain the effect of temperature, since it affects reaction rates, and the aqueous effluent might be discharged in various rates. From such a demonstration, the aqueous acetaminophen solution temperature is increased from 26 to 60 °C in the studied range, to evaluate the temperature influence on the oxidation reaction. The experimental data exposed in Figure 12 illustrated a reduction in the acetaminophen oxidation rate with the temperature elevation. A 100%, complete acetaminophen removal is achieved in almost 30 min of solar irradiance time at 26 °C. But further temperature elevation results in a decline in acetaminophen removal, ranging from 89 and 77 to 63%, with the gradual temperature increase of 40, 50 and 60 °C, respectively. Thus, at higher temperatures, there is a decline in the OH radicals rather than the low 26 °C room-temperature value. At elevated temperatures, a decline in hydroxyl radical production occurs, which negatively impacts the pollutant oxidation. This effect is further compounded by the thermal decomposition of H_2O_2 into O_2 and H_2O, thereby reducing the overall reaction rate. While some studies [23,33] have reported that higher temperatures promote ·OH radical formation, and consequently enhance oxidation efficiency, other investigations suggest that temperature exerts only a marginal influence on Fenton-based systems compared with other operational parameters. Therefore, it is verified by the literature that the higher reaction rate for the Fenton system is around room temperature (17–38 °C), which produces high-oxidative species.

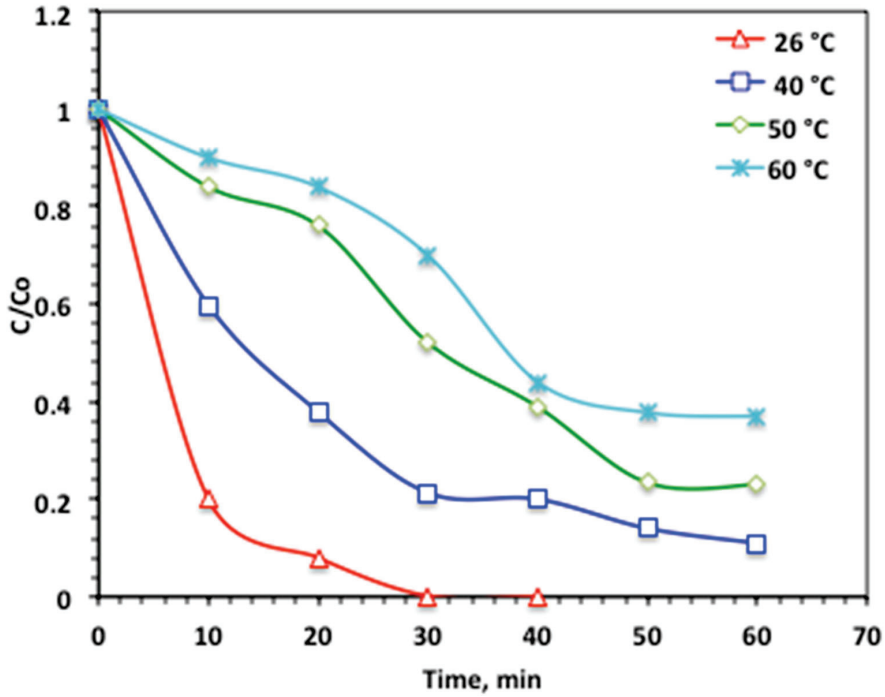


Figure 12. Effect of temperature on the modified Char500@Mag Fenton oxidation system.

2.3.8. Oxidation Kinetics

For further examining the oxidation reaction through the modified Char500@Mag-based solar-Fenton system, the oxidation kinetics is assessed. The kinetics calculations are accommodating an assessment of reactor design and system control that is essential for real-life applications. Thereby, it is assessing both underlying capital and operating expenses, to evaluate the total cost of treatment. Due to the heterogeneous nature of the Char500@Mag/H_2O_2 system for acetaminophen oxidation and the complexity of the intermediates generated during the reaction, it is not feasible to perform a detailed kinetic analysis for each individual pathway. Hence, the kinetic study represents the overall acetaminophen elimination. Acetaminophen removal as a function of time data through varied temperatures is fitted to the linear integrated equations forms for the three common kinetic models of 0th-, 1st-, and 2nd-order kinetics, according to their equations tabulated in Table 1. Such a plot is displayed in Figure 13, and the attained data is also displayed in Table 1.

Table 1. Parameters of kinetic models for acetaminophen oxidation by Char500@Mag-based solar-Fenton.

Kinetic Model	Parameters	Values			
		T, °C			
		26 °C	**40 °C**	**50 °C**	**60 °C**
Zero-order ($C_t = C_o - k_0 t$)	k_0 (min^{-1})	0.62	0.67	0.71	0.56
	$t_{1/2}$ (min)	40.32	37.314	35.21	44.64
	R^2	0.53	0.81	0.95	0.96
Pseudo-First-order ($C_t = C_o - e^{k_1 t}$)	k_1 (min^{-1})	0.204	0.039	0.022	0.018
	$t_{1/2}$ (min)	38.5	31.5	17.76	3.39
	R^2	0.95	0.96	0.95	0.96
Pseudo-Second-order ($\left(\frac{1}{C_t}\right) = \left(\frac{1}{C_0}\right) - k_2 t$)	k_2 ($L.mg^{-1}.min^{-1}$) $\times 10^{-2}$	0.4009	0.0027	0.0013	0.0006
	$t_{1/2}$ (min)	0.049	7.41	15.38538	33.34
	R^2	0.62	0.67	0.71	0.56

where C_o and C_t are the concentrations at time 0 and time t; k_0, k_1 and k_2 are the kinetic constants of zero-and first- and second-order kinetics, respectively.

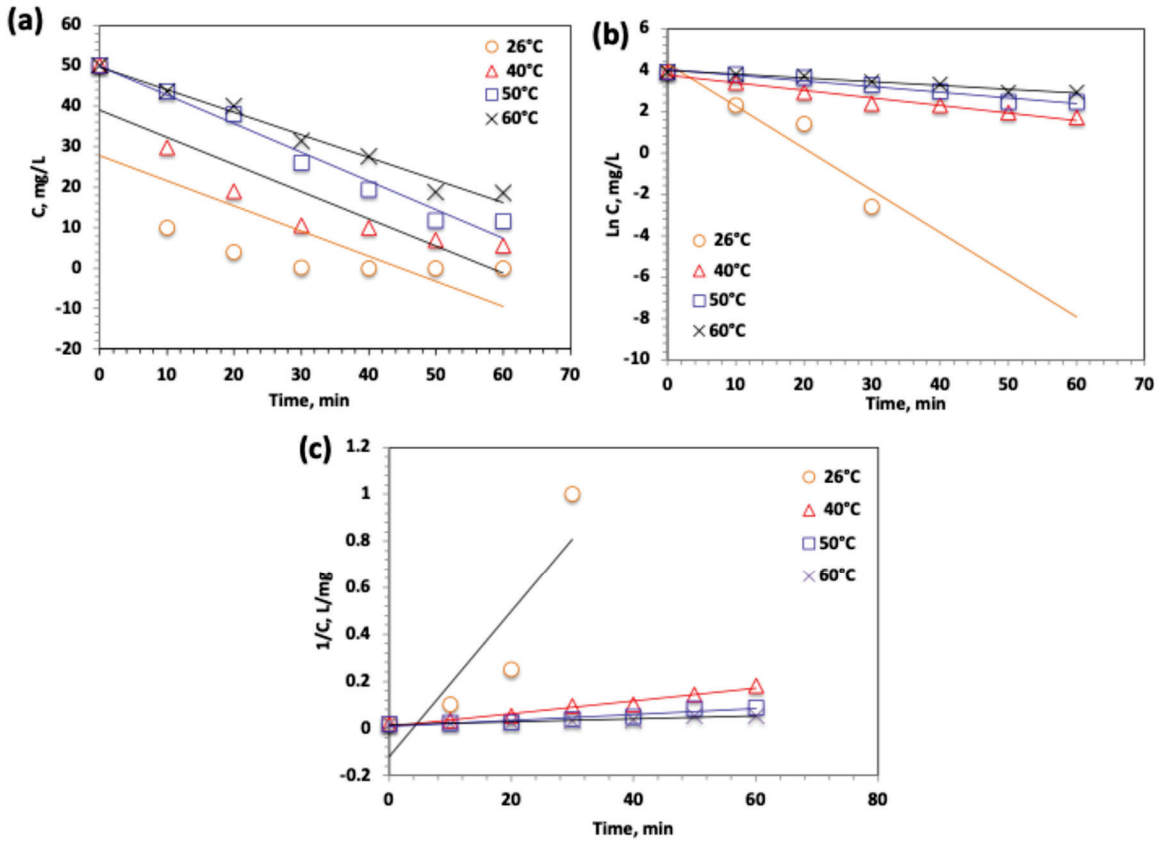


Figure 13. Plot of kinetic models of (**a**) Zero-order, (**b**) Pseudo-First-order and (**c**) Pseudo-Second-order for the modified Char500@Mag Fenton oxidation system.

Based on the comparison of correlation coefficients (R^2) from the kinetic plots, acetaminophen oxidation was found to follow first-order kinetics, as indicated by the highest R^2 values (0.95–0.96) compared to other kinetic models. Furthermore, the calculated half-life times ($t_1/_2$) for the first-order model, as presented in Table 1, showed close agreement with the experimental results. These findings are consistent with previously reported studies [42], which also demonstrated that Fenton-based systems typically follow first-order reaction kinetics.

2.3.9. Activation Parameter Determination

To elucidate the influence of temperature on the oxidation process, activation parameters were assessed based on kinetic–thermodynamic analysis, and were evaluated based on the 1st-order kinetic model. Two complementary approaches were employed: the Arrhenius equation analysis for determining the apparent activation energy (E_a), and the Eyring transition state theory for estimating activation enthalpy ($\Delta H'$), entropy ($\Delta S'$), and Gibbs free energy ($\Delta G'$) [52]. The linearized form of the Arrhenius equation is given according to the following equation:

$$Lnk_1 = lnA - \frac{E_a}{RT} \quad (1)$$

where A is the pre-exponential factor constant; E_a is the energy of activation (kJ mol^{-1}); R is the gas constant (8.314 J mol^{-1} K^{-1}); and T is temperature (K). The plot in Figure 14 displays

the lnk_1 versus 1/T that is giving a linear relation, whereas its slope is corresponding to $-E_a/R$. In addition, the Eyring equation was applied:

$$k_1 = \frac{k_B T}{h} e^{\left(-\frac{\Delta G'}{RT}\right)} \quad (2)$$

where *kB* is Boltzmann's constant and *h* is Planck's constant. From this relation, the enthalpy of activation was obtained using the following relation:

$$\Delta H' = E_a - RT \quad (3)$$

Moreover, the entropy of activation was derived from Equation (4):

$$\Delta S' = \left(\Delta H' - \Delta G'\right)/T \quad (4)$$

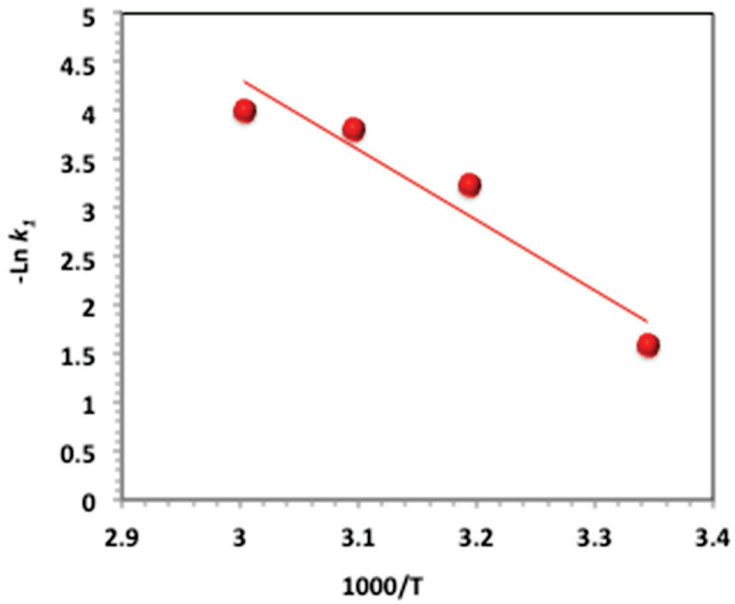


Figure 14. Plot of $(-\mathrm{Ln}\ K_1)$ vs. 1000/T.

Then, from the above-mentioned relations, the kinetic–thermodynamic data are calculated, and the data are tabulated in Table 2.

Table 2. Activation parameters for acetaminophen oxidation by Char500@Mag-based solar-Fenton.

Parameter	T, °C			
	26 °C	**40 °C**	**50 °C**	**60 °C**
$\Delta G'$ (kJ/mol)	77.18	85.22	89.57	92.98
$\Delta H'$ (kJ/mol)	57.71	57.60	57.51	57.43
$\Delta S'$ (J/mol K)	−65.11	−88.26	−99.23	−106.75
Ea (kJ/mol)	60.20			

Based on these relations, the kinetic–thermodynamic activation parameters were independently evaluated at each temperature, and the results are summarized in Table 2. Minor variations in $\Delta H'$ and $\Delta S'$ across temperatures arise because the parameters were calculated separately for each experimental condition, reflecting the sensitivity of the Eyring relation to experimental data rather than true temperature dependence.

The results revealed that the Gibbs free energy of activation ($\Delta G'$) values were positive, as expected for chemical reactions, indicating the presence of an activation barrier that

must be overcome for the reaction to proceed. The positive enthalpy of activation ($\Delta H'$) suggests an endothermic activation step, while the negative entropy of activation ($\Delta S'$) implies that the transition state is more ordered than the reactants. These findings are consistent with earlier reports on heterogeneous Fenton-like oxidation systems [45,52].

Although the overall oxidation of acetaminophen by the Char500@Mag/H_2O_2 system is thermodynamically feasible and exothermic, the observed decline in removal efficiency at elevated temperatures indicates that the process is not solely controlled by thermodynamics. Instead, kinetic factors (such as shorter residence times of reactive species) and mass transfer limitations may become dominant at higher temperatures, thereby reducing the net photocatalytic activity.

2.3.10. Stability and Sustainability Assays

To verify the catalyst sustainability of Ban-Char500@Mag Fenton, the catalyst reuse is evaluated. Hence, after the oxidation test, the Ban-Char500@Mag is collected and then filtered prior to washing and cleaning with distilled water, with successive washes. The recovered catalyst is then oven-dried at 150 °C for one hour using an electric furnace. The successive use of the catalyst showed its sustainability for several cycles that could reach six cyclic uses. The data displayed in Figure 15 revealed that, compared to 100 removals for the fresh Ban-Char500@Mag use, continuing the oxidation under solar radiation reached 74% for the sixth cyclic use. Such a result is a considerably reasonable removal. This may be attributed to acetaminophen molecules occupying the active sites of the composite, thereby hindering further oxidation reactions. Previous cited data [33] are in accordance with such an investigation.

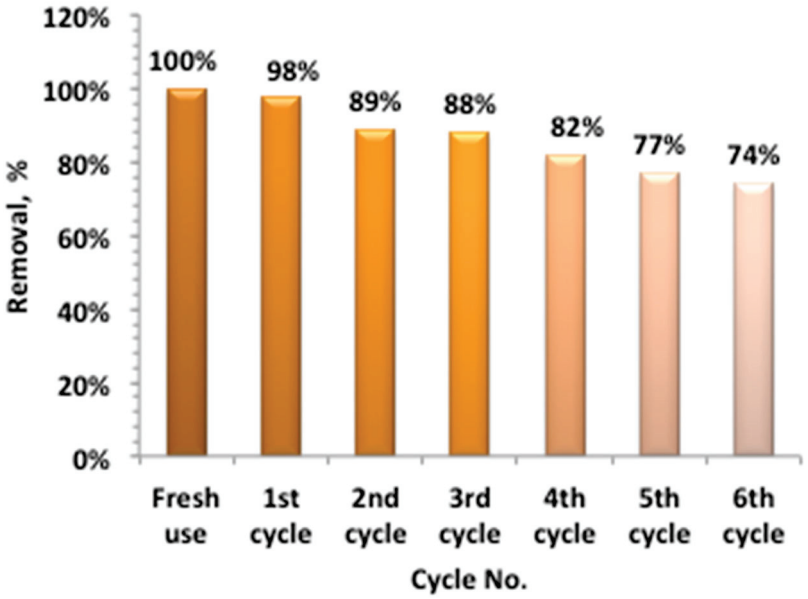


Figure 15. Catalyst recyclability activity on acetaminophen oxidation.

2.3.11. Study Compared with the Literature

The previously related cited work is compared to the current work; the comparison data is summarized in Table 3. The comparison is based on the operating time and the initiation source of activation of the Fenton system-type system for various pharmaceutical types contaminating aqueous media. The literature articles are examined, and the previous work is based on the dark Fenton or initiated systems through electro Fenton and/or ultraviolet initiation. Although the studies are based on the ultraviolet initiation, there is a lack of literature in using the renewable solar energy for initiation. Table 3 demonstrates

that the solar-Fenton oxidation system in the present study achieved the complete removal of contaminants. Similar investigations reported in the literature have also shown high removal efficiencies in degrading various classes of pharmaceuticals, including antibiotics, anti-inflammatory drugs, and lipid-regulating (antilipemic) agents, effectively transforming them into non-toxic end-products. While alternative oxidation processes have likewise exhibited high efficiencies in eliminating such compounds, the solar-Fenton system remains a particularly effective and sustainable approach. It is significant to mention that the current work is based on a renewable costless energy-system facility in lesser reaction time. Hence, using solar energy exhibited a dual economically wise system and a clean renewable-energy efficient source. Additionally, it is noteworthy to mention that the introduced study suggests the use of a Fenton-based biochar/magnetite catalyst as a recoverable and recyclable material for sustainable use, since it is based on waste biochar material.

Table 3. Comparison of different Fenton systems for treating varied pharmaceuticals' wastewater.

Fenton's Reaction Type/Catalyst *	Pharmaceutical Category	Oxidation (%)	Operating Conditions	Ref.
Electro/UV/Fenton/MSWCNTs–$FeCl_2$	Anti-Inflammatory	71%	pH: 5, MSWCNTs–$FeCl_2$: 0.05 M, oxidation time: 2 h	[55]
UV/Fenton (Fe/Cu/TiO_2)	Anti-Inflammatory	41%	Cu/Fe: 1 g/L, oxidation time: 1 h	[56]
Dark Fenton/Fe-POM	Antibiotics	97%	Fe-POM: 1 g/L, oxidation time: 0.2 h	[57]
Electro/UV/Fenton/$CuFeS_2$	Antibiotics	100%	pH: 3.0, $CuFeS_2$: 0.05 g/L, oxidation time: 0.25 h	[58]
Dark Fenton/MOF-Fe	Antilipemic agent	62%	pH: 5.1, MOF-Fe: 0.05 g/L, oxidation time: 4 h	[59]
Electro/UV/Fenton/ZVI/C	Lipid-regulating	94%	pH: 6.0, ZVI: 0.05 M, oxidation time: 1 h	[59]
Dark/Fe/C	Antibiotics	95%	pH: 6.0, Fe/C: 1.0 g/L, oxidation time: 0.2 h	[60]
Electro/UV/Fenton/Fe	Antibiotics	98%	pH: 3.0, Fe: 0.01 M, oxidation time: 1 h	[61]
Electro/UV/Fenton/Fe/C	Antibiotics	70%	pH: 5.0, Fe/C: 0.05 M, oxidation time: 2 h	[62]
Electro/UV/Fenton/FeS_2	Antibiotics	99%	pH: 3.0, FeS_2: 0.05 M, oxidation time: 0.3 h	[63]
Electro/UV/Fenton/Fe_2O_3	Antibiotics	98%	pH: 3.0, Fe_2O_3: 0.01 M, oxidation time: 1 h	[64]
Electro/Fenton/FeS_2	Antibiotic	86%	pH: 4.0, FeS_2: 0.02 M, oxidation time: 6 h	[49]
Solar-Fenton/Ban-Char500@Mag-(1:1)	Antibiotic	92%	pH: 3.0, Ban-Char500@Mag-(1:1): 10 mg/L, oxidation time: 0.5 h	Current work

* ZVI: Zero Valent Iron; MOF: Metal Organic Frame; MSWCNTs: Metallic Single-Walled Carbon Nanotubes.

3. Materials and Methods

3.1. Materials

Wastewater:

Acetaminophen (AC) is selected to be a pharmaceutical model wastewater pollutant simulating the pharmaceutical discharge. The acetaminophen stock solution was prepared by dissolving the 1000 mg of the powder in one liter of distilled water, which is then further diluted to the desired concentrations. Acetaminophen raw material is supplied by the Sigma-Aldrich Company. Sulfuric acid and/or sodium hydroxide is used to adjust the pH of the drug solution. All the used reagents and chemicals are of analytical grade and used as received, without further purification or treatment.

Organic waste:

Musa sapientum, which refers to banana peels, are collected from a local juice factory in Egypt. The material is transferred to the laboratory and then rinsed with water to remove any debris. Afterwards, it is left for air-drying prior to treatment.

3.2. Magnetic/Biochar from Musa Sapientum

Banana peel biochar was prepared according to the previously described method [54], with some modifications. The material was washed with distilled water to remove any dust or impurities during the air-drying. Next, the material was then put in an oven at 80 °C overnight, to verify the complete dryness. Afterwards, the dried material was exposed for soaking overnight with phosphoric acid (60%). Then, the soaked material was subjected to an electrical furnace for semi-carbonization at a temperature of 200 °C for 4 h. The resultant dried biomass was cooled to room temperature and then carbonized in a furnace at 500 °C for 2 h for activation. The activated powder was then successively washed with distilled water to remove any remaining phosphoric acid in it by measuring the pH of the washing liquor that should reach neutral. Finally, the carbonized biochar was washed with 0.1 M NaOH solution followed by distilled water rinsing, to neutralize residual acidic groups, remove surface impurities, and enhance the exposure of active functional sites on the biochar surface. The subsequent material was dried overnight in an oven (105 °C) and exposed to ball mill-size reduction. The resultant treated and activated biochar is signified as Ban-Char500.

Consistently, the co-precipitation routine as a simple, economic, and high-yield method is applied to prepare the environmentally benign magnetite nanoparticles. In such a technique, 2 mol of $Fe_2(SO_4)_3$ and 1 mol of $Fe(SO_4)$ are used as a precursor to prepare such a substance. The two salts were mixed, then dissolved in 1.5 L of distilled water. About 8 mol of NaOH solution was added dropwise, while stirring till the pH of the solution reached 12.0 (alkaline pH). Subsequently, the mixture was exposed for stirring through heating (80 °C) and then a precipitate of nanoparticles formed. Subsequently, attained nanoparticles were then repeatedly washed using distilled water, in order to reach the neutral pH 7.0. The nanoparticles were then collected and exposed to electrical oven drying at 60 °C overnight. The resultant powder was labelled as "Mag".

Afterwards, mixed biochar with magnetite as a sustainable catalyst was prepared by mixing the biochar with the prepared magnetite nanoparticles and referred to as Ban-Char500@Mag. The mixture was added at different ratios, of 0:1, 1:1 and 2:1, and was signified as Ban-Char500-Mag@(0:1), Ban-Char500@Mag-(1:1) and Ban-Char500@Mag-(2:1), respectively. Consequently, the powder was stored in hermetic plastic bags till use. The preparation step is illustrated in the graphical illustration in Figure 16.

3.3. Experimental Methodology and Analytical Determination

A 1000 mL aliquot of the AC-water sample (at the studied concentrations in the range of 50 to 200 ppm) was exposed for stirring and left to stand under solar illumination in the solar photochemical reactor, to assure the Fenton photo oxidation reaction after the addition of the catalyst and hydrogen peroxide, to initiate the oxidation system. The pilot-scale experimental setup is mounted at the latitude (30°58′ N) and longitude (31°01′ E), which maximizes the solar radiation. The location generally enjoys dry mild and sunny days, especially in the summer season.

The photochemical reactor in a pilot-scale manner is designed with a parabolic trough collector to increase the parallel ray's incident solar radiation, and designed with a reflective sheet of stainless steel. The collector is framed facing the south, inclined from the ground according to the latitude of the location of study in Egypt (32°). Such a reactor consists of a tubular glass tube fabricated from silica glass fixed on a focal line of a collector to receive

the reflected radiation from the parabola trough. The tubular reactor is connected to a feeding tank that includes the aliquot with the catalyst and hydrogen peroxide (30% w/v, supplied Alpha chemicals) to initiate the Fenton reaction. Then, the mixture is pumped to the reactor using a peristaltic dosing pump in a flow rate of 1800 mL/min. The schematic representation of the system is exhibited in Figure 17. Also, the solar radiation intensity is monitored using a solar meter (type: Eppley Black and White, Model: 8-48), which is placed closest to the parabolic trough collector at the time of the experiment.

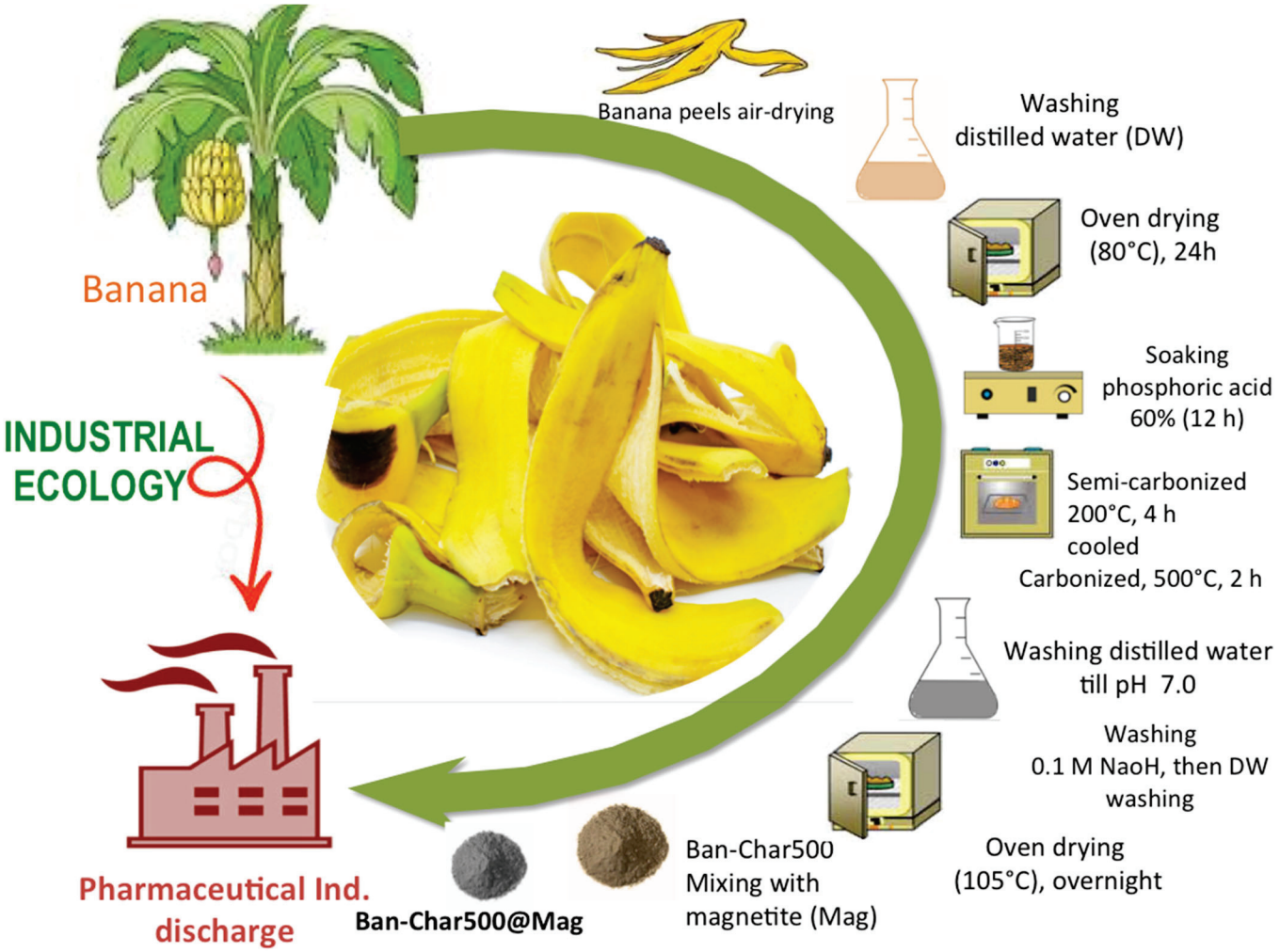


Figure 16. Schematic representation of the banana biochar/magnetite catalyst Ban-Char500-Mag.

The AC-water concentrations prior to and after the solar oxidation process were assessed through spectrophotometric analysis (UV–visible spectrophotometer type, model Unico UV-2100 spectrophotometer, UNICO, New York, NY, USA) at the corresponding maximum wavelength of AC at 243 nm, at specific time intervals. All the experiments were performed on a pilot scale in the laboratory, the data collection is conducted in a triplicate manner, and the displayed results are the average of the three replicates.

Kinetic experiments were also conducted in a thermostatically controlled batch reactor (26–60 °C) equipped with a magnetic stirrer to ensure uniform mixing. A water-circulation system connected to a thermostatic bath was used to maintain the reaction temperature within ±1 °C at the desired set points. The initial acetaminophen concentration is 50 mg/L, whereas the fixed Char500@Mag-(1:1) dosage is 10 mg/L, and H_2O_2 at 10 mg/L. The initial solution pH was adjusted to 3.0, using dilute NaOH or H_2SO_4, prior to reaction. Then, samples were withdrawn at regular intervals and analyzed by UV–Vis spectropho-

tometry at regular intervals (0–60 min). Each experiment was repeated in triplicate, and mean values are reported. The experimental concentration-time data were evaluated by applying the integrated linear forms of zero-order, first-order, and second-order kinetic models, and the rate constants, correlation coefficients (R^2), and half-life values (t½) were calculated accordingly.

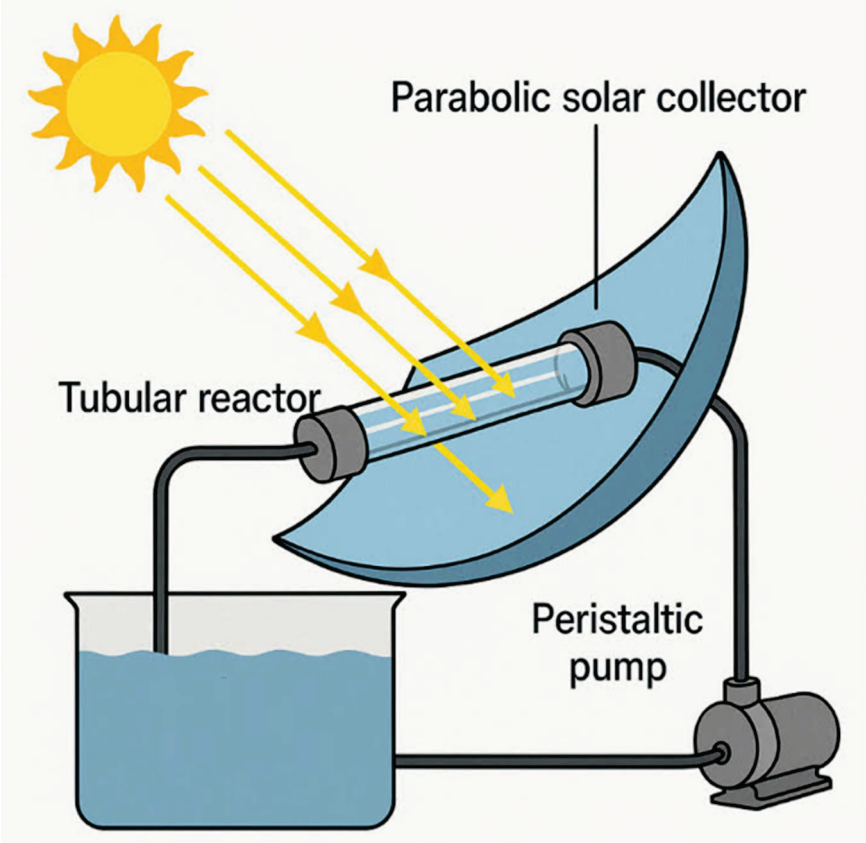


Figure 17. Schematic representation of the pilot-scale solar–photochemical oxidation system.

3.4. Ban-Char500-Mag Catalyst Characterizations

The prepared Ban-Char500 samples were described through X-ray diffraction (XRD, D8-Find, Bruker, with CuKα radiation (1.5418 Å), Madison, WI, USA), working at a current of 40 MA, voltage of 40 kV, and step filter of 0.01° for crystalline nature. Furthermore, the morphology of such sample is also described by field emission–scanning electron microscopy (FE-SEM), using Quanta FEG 250, FEI Company, Hillsboro, OR, USA. Also, the dispersive X-ray spectroscopy (EDX) for elemental analysis is supplied using such an instrument (Quanta FEG 250). Also, Fourier-transform infrared (FTIR) analysis was performed in the region of 400–4000 cm^{-1} wavenumber, using a Jasco FTIR-4100 spectrometer.

4. Conclusions

The Ban-Char500@Mag nanoparticle composite was synthesized through a straightforward route using waste banana peels as the precursor for biochar, augmented with the environmentally benign material magnetite. The composites were prepared at different magnetite-to-biochar ratios: Ban-Char500@Mag(0:1), Ban-Char500@Mag(1:1), and Ban-Char500@Mag(2:1). Structural and morphological analyses, confirmed by XRD diffractograms and SEM micrographs, revealed a moderately uniform distribution of magnetite nanoparticles on the Ban-Char500 biochar matrix. The resulting hybrid materials demonstrated multifunctional solar–photocatalytic activity, achieving up to 100% removal of

acetaminophen, a model pharmaceutical contaminant, from aqueous effluents. Complete oxidation of acetaminophen was attained within only 30 min of solar irradiation in a photochemical reactor. Key operating parameters were optimized, and the reaction kinetics and thermodynamics were systematically investigated. The kinetic study showed that the oxidation system followed a first-order kinetic model with a global activation energy of 60.20 kJ/mol. Furthermore, recyclability tests confirmed the efficient recovery and sustained catalytic performance of the composite. Overall, this work highlights a green, cost-effective, and sustainable strategy for wastewater remediation, demonstrating the potential of waste-derived magnetite–biochar composites as highly efficient solar photocatalysts.

Author Contributions: Conceptualization, M.M.N., M.A.T., M.K.F. and H.A.N.; methodology, M.A.T.; investigation, M.A.T. and M.K.F.; writing—original draft, M.M.N. and H.A.N.; writing—review and editing, M.M.N., M.A.T., M.K.F. and H.A.N.; visualization, M.M.N. and H.A.N.; supervision, H.A.N. All authors have read and agreed to the published version of the manuscript.

Funding: The authors extend their appreciation to Prince Sattam bin Abdulaziz University for funding this research work through the project number (PSAU/2025/01/35045).

Data Availability Statement: Data available upon request.

Conflicts of Interest: The authors declare no conflicts of interest.

References

1. Basheer, A.A. Chemical chiral pollution: Impact on the society and science and need of the regulations in the 21st century. *Chirality* **2018**, *30*, 402–406. [CrossRef]
2. Bashir, A.; Malik, L.A.; Ahad, S.; Manzoor, T.; Bhat, M.A.; Dar, G.N.; Pandith, A.H. Removal of heavy metal ions from aqueous system by ion–exchange and biosorption methods. *Environ. Chem. Lett.* **2019**, *17*, 729–754. [CrossRef]
3. Bosio, G.N.; García Einschlag, F.S.; Carlos, L.; Mártire, D.O. Recent Advances in the Development of Novel Iron–Copper Bimetallic Photo Fenton Catalysts. *Catalysts* **2023**, *13*, 159. [CrossRef]
4. Lai, Y.J.; Lee, D.J. Solid Mediator Z–Scheme Heterojunction Photocatalysis for Pollutant Oxidation in Water: Principles and Synthesis Perspectives. *J. Taiwan Inst. Chem. Eng.* **2021**, *125*, 88–114. [CrossRef]
5. Zolfaghari, G.; Esmaili-Sari, A.; Anbia, M.; Younesi, H.; Ghasemian, M.B. A zinc oxide-coated nanoporous carbon adsorbent for lead removal from water: Optimization, equilibrium modeling, and kinetics studies. *Int. J. Environ. Sci. Technol.* **2013**, *10*, 325–340. [CrossRef]
6. Beni, A.A.; Esmaeili, A. Biosorption, an efficient method for removing heavy metals from industrial effluents: A review. *Environ. Technol. Innov.* **2020**, *17*, 100503. [CrossRef]
7. Muthusamy, S.; Charles, J. Metal–organic framework of nanostructured polypyrrole incorporated with TiO_2 nanoparticles for supercapacitor electrode. *J. Mater. Sci. Mater. Electron.* **2021**, *32*, 7349–7365. [CrossRef]
8. Ribeiro, E.; Plantard, G.; Teyssandier, F.; Maury, F.; Sadiki, N.; Chaumont, D.; Goetz, V. Activated-carbon/TiO_2 composites preparation: An original grafting by milling approach for solar water treatment applications. *J. Environ. Chem. Eng.* **2020**, *8*, 104115. [CrossRef]
9. Muthukannan, V.; Praveen, K.; Natesan, B. Fabrication and characterization of magnetite/reduced graphene oxide composite incurred from iron ore tailings for high performance application. *Mater. Chem. Phys.* **2015**, *162*, 400–407. [CrossRef]
10. Zhang, M.H.; Dong, H.; Zhao, L.; Wang, D.-X.; Meng, D. A Review on Fenton Process for OrganicWastewater Treatment Based on Optimization Perspective. *Sci. Total. Environ.* **2019**, *670*, 110–121. [CrossRef]
11. Abdollahzadeh, H.; Fazlzadeh, M.; Afshin, S.; Arfaeinia, H.; Feizizadeh, A.; Poureshgh, Y.; Rashtbari, Y. Efficiency of activated carbon prepared from scrap tires magnetized by Fe_3O_4 nanoparticles: Characterisation and its application for removal of reactive blue19 from aquatic solutions. *Int. J. Environ. Anal. Chem.* **2020**, *102*, 1911–1925. [CrossRef]
12. Tony, M.A.; Ali, I.A. Mechanistic implications of redox cycles solar reactions of recyclable layered double hydroxides nanoparticles for remazol brilliant abatement. *Int. J. Environ. Sci. Technol.* **2021**, *19*, 9843–9860. [CrossRef]
13. Channei, D.; Thammaacheep, P.; Jannoey, P. Utilizing banana peel in conjunction with TiO_2 photocatalyst for the efficient decolorization of malachite green. *Chem. Phys. Impact* **2024**, *8*, 100629. [CrossRef]
14. Morales, A.E.; Mora, E.S.; Pal, U. Use of diffuse reflectance spectroscopy for optical characterization of un-supported nanostructures. *Rev. Mex. Física* **2007**, *53*, 18–22.

15. Maroudas, A.; Pandis, P.K.; Chatzopoulou, A.; Davellas, L.-R.; Sourkouni, G.; Argirusis, C. Synergetic decolorization of azo dyes using ultrasounds, photocatalysis and photo-fenton reaction. *Ultrason. Sonochemistry* **2021**, *71*, 105367. [CrossRef]
16. Zhao, Y.Q.; Yang, Y. Extending the use of dewatered alum sludge as a P-trapping material in effluent purification: Study on two separate water treatment sludges. *J. Environ. Sci. Health Part A* **2010**, *45*, 1234–1239. [CrossRef]
17. Tony, M.A.; Lin, L.-S. Iron Coated-Sand from Acid Mine Drainage Waste for Being a Catalytic Oxidant Towards Municipal Wastewater Remediation. *Int. J. Environ. Res.* **2021**, *15*, 191–201. [CrossRef]
18. Wu, H.F.; Wang, J.P.; Duan, E.G.; Feng, Y.F.; Wan, Z.Y.; Wu, Y.X.; Lu, Y.Q. Study on the preparation of granular alum sludge adsorbent for phosphorus removal. *Water Sci. Technol.* **2019**, *79*, 2378–2386. [CrossRef]
19. Abdou, K.A.; Mohammed, A.N.; Moselhy, W.; Farghali, A.A. Assessment of modified rice husk and sawdust as bio-adsorbent for heavy metals removal using nano particles in fish farm. *Asian J. Anim. Vet. Adv.* **2018**, *13*, 180–188. [CrossRef]
20. Foroughi, M.; Chavoshi, S.; Bagheri, M.; Yetilmezsoy, K.; Samadi, M.T. Alum-based sludge (AbS) recycling for turbidity removal in drinking water treatment: An insight into statistical, technical, and health-related standpoints. *J. Mater. Cycles Waste Manag.* **2018**, *20*, 1999–2017. [CrossRef]
21. Yin, Z.; Li, Y.; Song, T.; Bao, M.; Li, Y.; Lu, J.; Li, Y. Preparation of superhydrophobic magnetic sawdust for effective oil/water separation. *J. Clean. Prod.* **2020**, *253*, 120058. [CrossRef]
22. Tony, M.A. Paradigms of homo/heterogonous Fenton systems incorporating 'Solar Energy' based on 'Emerging Pollutants' removal–challenges, advancements and visualized bibliometric analysis. *Int. J. Environ. Anal. Chem.* **2021**, *103*, 7877–7908. [CrossRef]
23. Nabwey, H.A.; Tony, M.A. Thermal energy storage using a hybrid composite based on technical-grade paraffin-AP25 wax as a phase change material. *Nanomaterials* **2023**, *13*, 2635. [CrossRef]
24. Hilder, M.; Winther-Jensen, O.; Winther-Jensen, B.; MacFarlane, D.R. Graphene/zinc nano-composites by electrochemical co-deposition. *Phys. Chem. Chem. Phys.* **2012**, *14*, 14034–14040. [CrossRef]
25. Tauc, J. *Amorphous and Liquid Semiconductors*; Springer Science & Business Media: New York, NY, USA, 2012.
26. Kulkarni, S.A.; Sawadh, P.S.; Palei, P.K.; Kokate, K.K. Effect of synthesis route on the structural, optical and magnetic properties of Fe_3O_4 nanoparticles. *Ceram. Int.* **2014**, *40*, 1945–1949. [CrossRef]
27. Amir, M.; Baykal, A.; Güner, S.; Güngüneş, H.; Sözeri, H. Magneto-optical investigation and hyperfine interactions of copper substituted Fe3O4 nanoparticles. *Ceram. Int.* **2016**, *42*, 5650–5658. [CrossRef]
28. Bachan, N.; Asha, A.; Jeyarani, W.J.; Kumar, D.A.; Shyla, J.M. A Comparative investigation on the structural, optical and electrical properties of SiO2–Fe3O4 core–shell nanostructures with their single components. *Acta Metall. Sin. (Engl. Lett.)* **2015**, *28*, 1317–1325. [CrossRef]
29. Ge, J.; Zhang, Q.; Zhang, T.; Yin, Y. Core–satellite nanocomposite catalysts protected by a porous silica shell: Controllable reactivity, high stability, and magnetic recyclability. *Angew. Chem.* **2008**, *120*, 9056–9060. [CrossRef]
30. Ahangaran, F.; Hassanzadeh, A.; Nouri, S. Surface modification of Fe_3O_4@SiO_2 microsphere by silane coupling agent. *Int. Nano Lett.* **2013**, *3*, 23. [CrossRef]
31. Zhang, H.; Niu, Z.; Liu, Z.; Wen, Z.; Li, W.; Wang, X.; Wu, W. Equilibrium, kinetic and thermodynamic studies of adsorption of Th (IV) from aqueous solution onto kaolin. *J. Radioanal. Nucl. Chem.* **2015**, *303*, 87–97. [CrossRef]
32. Aroke, U.O.; Abdulkarim, A.; Ogubunka, R.O. Fourier-transform infrared characterization of kaolin, granite, bentonite and barite. *ATBU J. Environ. Technol.* **2013**, *6*, 42–53.
33. Chang, C.-F.; Wu, Y.-L.; Hou, S.-S. Preparation and characterization of superparamagnetic nanocomposites of aluminosilicate/silica/magnetite. *Colloids Surf. A Physicochem. Eng. Asp.* **2009**, *336*, 159–166. [CrossRef]
34. Chen, C.-W. *Magnetism and Metallurgy of Soft Magnetic Materials*; Courier Corporation: Chelmsford, MA, USA, 2013.
35. James, R.D. Magnetic alloys break the rules. *Nature* **2015**, *521*, 298–299. [CrossRef]
36. Guo, S.; Dan, Z.; Duan, N.; Chen, G.; Gao, W.; Zhao, W. Zn (II), Pb (II), and Cd (II) adsorption from aqueous solution by magnetic silica gel: Preparation, characterization, and adsorption. *Environ. Sci. Pollut. Res.* **2018**, *25*, 30938–30948. [CrossRef]
37. Raut-Jadhav, S.; Pinjari, D.V.; Saini, D.R.; Sonawane, S.H.; Pandit, A.B. Intensification of degradation of methomyl (carbamate group pesticide) by using the combination of ultrasonic cavitation and process intensifying additives. *Ultrason. Sonochem.* **2016**, *31*, 135–142. [CrossRef]
38. Nichela, D.A.; Berkovic, A.M.; Costante, M.R.; Juliarena, M.P.; Einschlag, F.S.G. Nitrobenzene degradation in Fenton-like systems using Cu (II) as catalyst. Comparison between Cu (II)-and Fe (III)-based systems. *Chem. Eng. J.* **2013**, *228*, 1148–1157. [CrossRef]
39. Singh, C.; Chaudhary, R.; Gandhi, K. Preliminary study on optimization of pH, oxidant and catalyst dose for high COD content: Solar parabolic trough collector. *Iran. J. Environ. Health Sci. Eng.* **2013**, *10*, 13. [CrossRef]
40. Shanmugam, B.K.; Easwaran, S.N.; Mohanakrishnan, A.S.; Kalyanaraman, C.; Mahadevan, S. Biodegradation of tannery dye effluent using Fenton's reagent and bacterial consortium: A biocalorimetric investigation. *J. Environ. Manag.* **2019**, *242*, 106–113. [CrossRef]

41. Toosi, F.S.; Hosseiny, M.; Joghataei, A.; Toosi, F.S. The application of SiO_2 nanoparticles for anionic dye removal from aqueous solution. *Arch. Hyg. Sci.* **2017**, *6*, 136–144. [CrossRef]
42. Buthiyappan, A.; Raman, A.A.A.; Daud, W.M.A.W. Development of an advanced chemical oxidation wastewater treatment system for the batik industry in Malaysia. *RSC Adv.* **2016**, *6*, 25222–25241. [CrossRef]
43. Ahmadi, M.; Behin, J.; Mahnam, A.R. Kinetics and thermodynamics of peroxydisulfate oxidation of Reactive Yellow 84. *J. Saudi Chem. Soc.* **2016**, *20*, 644–650. [CrossRef]
44. Do, Q.C.; Kim, D.-G.; Ko, S.-O. Catalytic activity enhancement of a Fe_3O_4@SiO_2 yolk-shell structure for oxidative degradation of acetaminophen by decoration with copper. *J. Clean. Prod.* **2018**, *172*, 1243–1253. [CrossRef]
45. Huang, X.; Nan, Z. Formation of octahedron-shaped $ZnFe_2O_4$/SiO_2 with yolk–shell structure. *J. Phys. Chem. Solids* **2020**, *141*, 109410. [CrossRef]
46. Phan, T.T.N.; Nikoloski, A.N.; Bahri, P.A.; Li, D. Facile fabrication of perovskite-incorporated hierarchically mesoporous/macroporous silica for efficient photoassisted-Fenton degradation of dye. *Appl. Surf. Sci.* **2019**, *491*, 488–496. [CrossRef]
47. Nour, M.M.; Tony, M.A.; Nabwey, H.A. Heterogeneous fenton oxidation with natural clay for textile levafix dark blue dye removal from aqueous effluent. *Appl. Sci.* **2023**, *13*, 8948. [CrossRef]
48. Hassan, E.A.; Tony, M.A.; Nabwey, H.A.; Awad, M.M. Potential of the Biomass Waste Originating from Saccharum officinarum as a Fenton Precursor for the Efficient Oxidation of Azo Dye from an Aqueous Stream. *Processes* **2023**, *11*, 1394. [CrossRef]
49. Ye, Z.; Schukraft, G.E.; L'Hermitte, A.; Xiong, Y.; Brillas, E.; Petit, C.; Sirés, I. Mechanism and stability of an Fe-based 2D MOF during the photoelectro-Fenton treatment of organic micropollutants under UVA and visible light irradiation. *Water Res.* **2020**, *184*, 115986. [CrossRef]
50. Hassan, E.A.; Tony, M.A.; Nabwey, H.A.; Awad, M.M. Management of Agricultural Water Containing Acetimidothioic Acid Pesticide through Catalytic Oxidation to Facilitate Reclaimed Water Recycling for Sustainable Food Production. *Processes* **2023**, *11*, 792. [CrossRef]
51. Shoorangiz, M.; Nikoo, M.R.; Salari, M.; Rakhshandehroo, G.R.; Sadegh, M. Optimized electro-Fenton process with sacrificial stainless steel anode for degradation/mineralization of ciprofloxacin. *Process Saf. Environ. Prot.* **2019**, *132*, 340–350. [CrossRef]
52. Thiam, A.; Salazar, R.; Brillas, E.; Sirés, I. In-situ dosage of Fe^{2+} catalyst using natural pyrite for thiamphenicol mineralization by photoelectro-Fenton process. *J. Environ. Manag.* **2020**, *270*, 110835. [CrossRef]
53. Soliman, E.M.; Ahmed, S.A.; Fadl, A.A. Adsorptive removal of oil spill from sea water surface using magnetic wood sawdust as a novel nano-composite synthesized via microwave approach. *J. Environ. Health* **2020**, *18*, 79–90. [CrossRef]
54. Srinivasakannan, C.; Bakar, M.Z.A. Production of activated carbon from rubber wood sawdust. *Biomass Bioenergy* **2004**, *27*, 89–96. [CrossRef]
55. Sadeghi, M.; Mehdinejad, M.H.; Mengelizadeh, N.; Mahdavi, Y.; Pourzamani, H.; Hajizadeh, Y.; Zare, M.R. Degradation of diclofenac by heterogeneous electro-Fenton process using magnetic single-walled carbon nanotubes as a catalyst. *J. Water Process Eng.* **2019**, *31*, 100852. [CrossRef]
56. Tamuly, C.; Saikia, I.; Hazarika, M.; Das, M. Reduction of aromatic nitro compounds catalyzed by Biogenic CuO nanoparticles. *RSC Adv.* **2014**, *4*, 53229–53236. [CrossRef]
57. Jiang, J.; Wang, X.; Liu, Y.; Ma, Y.; Li, T.; Lin, Y.; Xie, T.; Dong, S. Photo-Fenton degradation of emerging pollutants over Fe-POM nanoparticle/porous and ultrathin g-C3N4 nanosheet with rich nitrogen defect: Degradation mechanism, pathways, and products toxicity assessment. *Appl. Catal. B Environ.* **2020**, *278*, 119349. [CrossRef]
58. Collins, D.; Luxton, T.; Kumar, N.; Shah, S.; Walker, V.K.; Shah, V. Assessing the impact of copper and zinc oxide nanoparticles on soil: A field study. *PLoS ONE* **2012**, *7*, e42663. [CrossRef]
59. Midander, K.; Cronholm, P.; Karlsson, H.L.; Elihn, K.; Mo, L.; Leygraf, C.; Wallinder, I.O. Surface characteristics, copper release, and toxicity of nano- and micrometer-sized copper and copper(II) oxide particles: A cross-disciplinary study. *Small* **2009**, *5*, 389–399. [CrossRef]
60. Scherrer, P. Bestimmung der Grösseundderinneren Struktur von Kolloidteilchen mittels Röntgenstrahlen. *Nachr. Ges. Wiss. Göttingen* **1918**, *26*, 98–100.
61. Nguyen, T.T.; Huynh, K.A.; Padungthon, S.; Pranudta, A.; Amonpattaratkit, P.; Tran, L.B.; Phan, P.T.; Nguyen, N.H. Synthesis of natural flowerlike iron-alum oxide with special interaction of Fe-Si-Al oxides as an effective catalyst for heterogeneous Fenton process. *J. Environ. Chem. Eng.* **2021**, *9*, 105732. [CrossRef]
62. Molina, C.B.; Sanz-Santos, E.; Boukhemkhem, A.; Bedia, J.; Belver, C.; Rodriguez, J.J. Removal of emerging pollutants in aqueous phase by heterogeneous Fenton and photo-Fenton with Fe_2O_3-TiO_2-clay heterostructures. *Environ. Sci. Pollut. Res.* **2020**, *27*, 38434. [CrossRef]

63. Droguett, C.; Salazar, R.; Brillas, E.; Sirés, I.; Carlesi, C.; Marco, J.F.; Thiam, A. Treatment of antibiotic cephalexin by heterogeneous electrochemical Fenton-based processes using chalcopyrite as sustainable catalyst. *Sci. Total Environ.* **2020**, *740*, 140154. [CrossRef] [PubMed]
64. Kalantary, R.R.; Farzadkia, M.; Kermani, M.; Rahmatinia, M. Heterogeneous electro-Fenton process by Nano-Fe_3O_4 for catalytic degradation of amoxicillin: Process optimization using response surface methodology. *J. Environ. Chem. Eng.* **2018**, *6*, 4644. [CrossRef]

Disclaimer/Publisher's Note: The statements, opinions and data contained in all publications are solely those of the individual author(s) and contributor(s) and not of MDPI and/or the editor(s). MDPI and/or the editor(s) disclaim responsibility for any injury to people or property resulting from any ideas, methods, instructions or products referred to in the content.

catalysts

MDPI

Article

Hybrid PK-P/Fe_3O_4 Catalyst Derived from Pumpkin Peel (Bio-Waste) for Synozol Red KHL Dye Oxidation Under Photo-Fenton Reaction

M. M. Nour [1], Maha A. Tony [2,3], Mai K. Fouad [4] and Hossam A. Nabwey [1,*]

[1] Department of Mathematics, College of Science and Humanities in Al-Kharj, Prince Sattam bin Abdulaziz University, Al-Kharj 11942, Saudi Arabia
[2] Basic Engineering Science Department, Faculty of Engineering, Menoufia University, Shebin El-Kom 32511, Egypt; dr.maha.tony@gmail.com
[3] Advanced Materials/Solar Energy and Environmental Sustainability (AMSEES) Laboratory, Faculty of Engineering, Menoufia University, Shebin El-Kom 32511, Egypt
[4] Chemical Engineering Department, Faculty of Engineering, Cairo University, Giza 12613, Egypt
* Correspondence: eng_hossam21@yahoo.com or h.mohamed@psau.edu.sa

Abstract

This study introduces a novel photocatalyst derived from pumpkin peel bio-waste, calcined at 200 °C and incorporated with magnetite nanoparticles to form a hybrid PK-P/Fe_3O_4 catalyst. The material was characterized using X-ray diffraction (XRD), diffuse reflectance spectra (DRS), and scanning electron microscopy (SEM) with energy-dispersive X-ray spectroscopy (EDX) mapping to confirm its structure and elemental distribution. The catalyst was applied for the photo-Fenton degradation of Synozol Red KHL dye under natural solution conditions (pH 5.7). Optimal parameters were achieved with a 20 mg/L catalyst and 200 mg/L H_2O_2, resulting in complete dye removal within 25 min of irradiation. The PK-P/Fe_3O_4 catalyst exhibited excellent reusability, retaining 72% removal efficiency after 10 successive cycles. Kinetic analysis confirmed a first-order model, while thermodynamic evaluation revealed a non-spontaneous, endothermic process with a low activation energy barrier, indicating energy-efficient dye degradation. These findings highlight the potential of bio-waste-derived PK-P/Fe_3O_4 as a sustainable, low-cost, and highly effective catalyst for treating dye-polluted wastewater under photo-Fenton conditions.

Keywords: Synozol Red KHL; catalysis; photo-Fenton; pumpkin peel; bio-waste

1. Introduction

The release of industrial wastewater discharge into natural ecosystems represents a major source of pollution and poses serious ecological and aesthetic threats to both human beings and aquatic environments [1,2]. Such discharges also create risks of bioaccumulation [3], whereby contaminants enter the food chain and ultimately affect human health. Certain pollutants are associated with severe outcomes, including allergies and cancer [4,5]. Therefore, wastewater must be treated before discharge to safeguard both the environment and public health.

One of the industrial sectors producing massive amounts of contaminated aqueous effluent is the textile industry. The discharge of textile dyes into the environment poses serious ecological and health challenges due to their complex aromatic molecular structures, high stability, and resistance to biodegradation [6]. Dye-containing effluents are often highly colored, reducing light penetration in water bodies and thereby disrupting

photosynthetic activity in aquatic plants and algae [7]. Many dyes and their degradation by-products are toxic, mutagenic, or even carcinogenic, posing risks to aquatic organisms and, through bioaccumulation, to humans as well [8]. In addition, untreated textile wastewater typically contains high levels of chemical oxygen demand (COD), total dissolved solids (TDS), and heavy metals, which further deteriorate water quality and harm aquatic ecosystems [9]. Persistent contamination can destabilize food chains, reduce biodiversity, and impair ecosystem balance, while also limiting the usability of water resources for drinking, irrigation, and industrial purposes. These impacts highlight the urgent need for sustainable and effective wastewater treatment strategies to mitigate the environmental burden caused by textile dye effluents.

Wastewater treatment typically relies on conventional methods such as physical, chemical, and biological processes, including adsorption on activated carbon, membrane filtration, coagulation–flocculation, and biological degradation [10,11]. While these techniques are effective in removing suspended solids, turbidity, and biodegradable organics, they often face significant drawbacks when applied to recalcitrant pollutants such as synthetic dyes, pharmaceuticals, and aromatic compounds. For example, adsorption only transfers contaminants to another medium without degradation, biological treatments are ineffective against non-biodegradable compounds, and chemical coagulation generates large amounts of sludge that pose secondary disposal issues [12,13]. To overcome these limitations, advanced oxidation processes (AOPs) have been developed, which rely on the generation of highly reactive hydroxyl radicals (•OH) capable of non-selectively oxidizing and mineralizing a wide range of persistent organic pollutants [14,15]. Among AOPs, the Fenton reaction, which is based on the catalytic decomposition of hydrogen peroxide (H_2O_2) in the presence of ferrous ions (Fe^{2+}), has received particular attention due to its simplicity, high efficiency, and ability to operate under mild conditions [16]. The Fenton process not only achieves rapid decolorization and degradation of complex dye molecules but also reduces toxicity by converting pollutants into less harmful intermediates, thereby offering a promising and sustainable alternative to conventional treatment methods [17].

Despite its proven efficiency, the conventional Fenton process suffers from several limitations that restrict its large-scale applications. One major drawback is its requirement for an acidic medium (optimal pH is always in the acidic range 2.5–3.0), which necessitates continuous pH adjustment and increases operational costs [18]. In addition, the process generates large amounts of iron-rich sludge due to the reaction between Fe^{2+} and Fe^{3+}, creating secondary disposal and environmental challenges [19]. Furthermore, the narrow working pH range, difficulty in catalyst recovery, and relatively high operating costs hinder its industrial-scale adoption. Moreover, the requirement for fresh chemicals, particularly ferrous salts and hydrogen peroxide, adds to the overall cost of treatment, making the process less economically viable for long-term or large-volume wastewater treatment [20]. These limitations have driven interest in modified systems such as photo-Fenton, electro-Fenton, and heterogeneous Fenton, which aim to reduce chemical use, reduce sludge generation, widen the applicable pH range, and improve overall process sustainability [21].

On the other hand, porous carbon-based substances have gained significant attention due to their high surface area, shortened diffusion pathways, and reduced diffusion limitations [22]. Recently, the fabrication of porous carbon materials from diverse biomass precursors—including cotton pulp, lignin, silk, fruit waste, and peanut shells—has become a prominent research direction in the wastewater treatment field [23,24]. These biomass-derived carbons generally exhibit high efficiency in removing contaminants from wastewater. When subjected to pyrolysis at elevated temperatures (700–900 °C), such materials develop hydroxyl and carboxyl functional groups on their surfaces [25–29]. These groups enhance adsorption capacity and may promote selective pollutant uptake [26,30–32]. Therefore, porous

carbon electrodes derived from biomass not only deliver improved treatment performance but also offer the advantages of low cost and reduced environmental toxicity.

Efficient biowaste management plays a crucial role in the industrial sector, as its utilization can deliver environmental and economic merits while enhancing the overall value of production [27,33]. By-products from fruit and vegetable processing, as well as from juice and jam manufacturing, are especially noteworthy since they serve as valuable sources of compounds. Non-edible portions of fruits, such as peels and seeds, are often rich in phenolic and bioactive compounds [34–39]. Pumpkin peel contains high levels of these molecules and, in addition to its well-recognized antioxidant activity, has been identified as a promising natural preservative [30,40–43]. Recent investigations have also shown that waste materials can be modified into functional adsorbents and catalysts for wastewater treatment [31,44–48]. Bio-char is highly porous, enriched with hydroxyl and carboxyl functional groups [49], and well-suited for applications in adsorption [50], catalyst support, and wastewater treatment. This highlights their potential use in the wastewater management industry as natural alternatives to synthetic substances, contributing to safer and more sustainable strategies.

Biomass materials investigated so far face major limitations for large-scale industrial application due to the scarcity and high cost of raw materials, uneven geographical distribution, and challenges related to cultivation, transportation, and storage. But pumpkins waste peels stand out as a more suitable precursor due to their availability worldwide. They are abundant in sugars and starches and offer favorable properties for global production as porous carbon-based substances with outstanding properties characteristics [51–54].

Herein, the current investigation deals with the converting biomass waste pumpkin peels (PK-P) into a valuable substance with specific characteristics. The material is valorized through simple techniques. Next, magnetite is prepared as an environmentally benign material and added to PK-P as a composite photocatalyst. Further, the composite characterization is also assessed using XRD and SEM morphology. Synozol Red KHL is oxidized, and the removal efficiency related to the operating variables is investigated. Hence, the suggested system is introduced as a modified Fenton system to overcome the demerits of conventional Fenton oxidation to reach a win-win ecological system.

2. Results and Discussion

2.1. Catalyst Characterization

Crystalline structure:

The X-ray diffraction (XRD) spectra of PK-P-bio-char/magnetite and pristine magnetite nanoparticles were obtained using an X-ray diffractometer (XRD, D8-Find, Bruker, Madison, WI, USA) with CuKα radiation (1.5418 Å), operating at a current of 40 mA and voltage of 40 kV, and a step filter of 0.01° to analyze the crystalline nature. The data is presented in Figure 1. As shown in Figure 1a, the diffraction peaks correspond well to the magnetite crystal structure (JCPDS No. 89-4319) [46]. Also, Figure 1b represents magnetite augmented with PK-P-bio-char/magnetite.

In both graphs (a) and (b) in Figure 1, the patterns of the same spinel phase appear, which signifies the presence of magnetite nanoparticles. The characteristic reflections appear at the 2 theta values of 30.2°, 35.5°, 43.2°, 57.0°, and 62.6° 2θ, which index to the corresponding planes of (220), (311), (400), (511), and (440) of the cubic spinel lattice. The magnetite XRD pattern (Figure 2a) reflects a sharp intense peak on low background evidence, which reflects a good crystallinity as well as a relatively large crystallite size. Figure 2b, which represents the XRD graph of the PK-P-bio-char/magnetite pattern, exhibits the same peak positions as exhibited for magnetite (Figure 1a), but a more pronounced broadening, lower intensity, and a higher diffuse background [47]. Furthermore, a notable

weak hump near the 2 thetas of 20–30° might indicate the presence of an amorphous component, increased microstrain, or poorly crystalline structures. Such amorphous components might be referred to as the carbon matrix or poorly ordered phase. However, it is notable that there are no additional peaks attributable to impurity iron oxides. Thus, the results verify phase purity [48]. It is worth noting that the crystallinity is retained and decreases in the composite PK-P-bio-char/magnetite material.

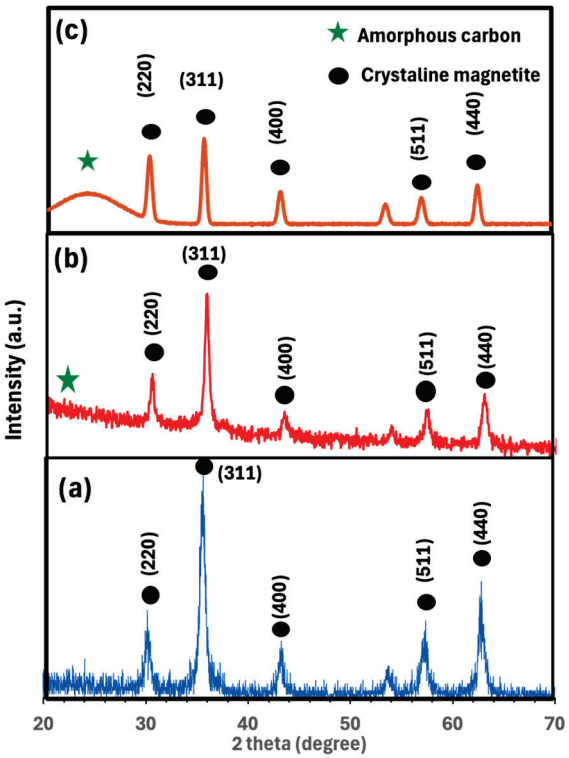


Figure 1. XRD of (**a**) magnetite, (**b**) PK-P-bio-char/magnetite, and (**c**) PK-P-bio-char/magnetite after loading with dye for cyclic use.

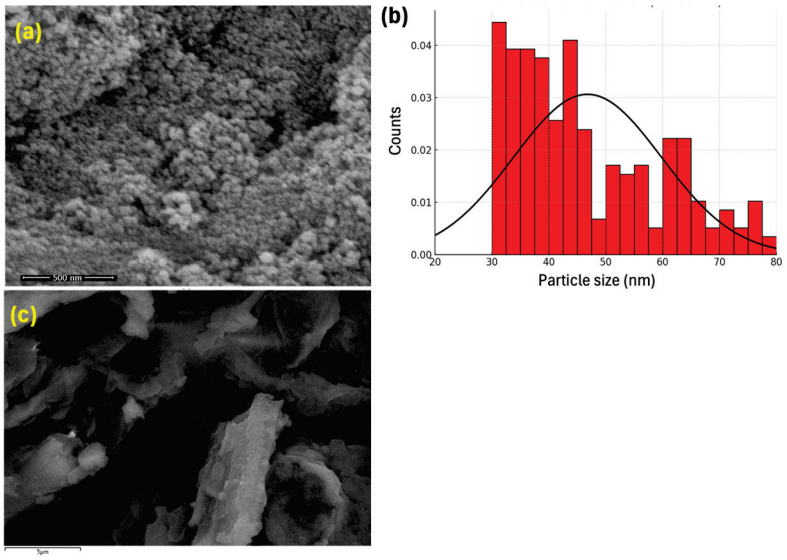


Figure 2. SEM image of (**a**) magnetite and its (**b**) particle size distribution analysis and (**c**) SEM image of PK-P-bio-char/magnetite nanocomposite.

Moreover, the XRD pattern of the PK-P-bio-char/magnetite material after dye loading and cyclic use is displayed in Figure 1c. It is clear from the graph that the magnetite

peaks still appear at the same 2θ positions, but their heights decrease. When the PK-P-bio-char/magnetite was loaded with Synozol Red, the XRD pattern retained the characteristic reflections of magnetite at 2θ ≈ 30.1°, 35.5°, 43.1°, 53.5°, 57.1°, and 62.7°, confirming the presence of the crystalline phase of Fe_3O_4, which remained intact and integrated with the PK-P-bio-char in the material. However, a noticeable decrease in the relative peak heights was observed, accompanied by a slight broadening of the diffraction peaks. This attenuation in intensity can be attributed to the coverage of magnetite crystallites by the amorphous dye layer, which absorbs and scatters incident X-rays, thereby lowering the diffracted signal. In addition, the baseline of the diffractogram was slightly elevated with the appearance of a broad hump around 22–26°, corresponding to the amorphous contribution from the bio-char matrix and the adsorbed organic dye molecules [48,49]. These changes indicate that dye loading does not alter the crystalline structure of magnetite but introduces additional amorphous content and surface disorder, consistent with the successful adsorption of Synozol Red onto the composite surface.

Morphological characterization:

The SEM micrograph in Figure 2 displays the morphological characteristics of the bio-char-derived material incorporated with magnetite nanoparticles. The morphology was imaged by field emission scanning electron microscopy (FE-SEM) using Quanta FEG 250 (FEI Company, Hillsboro, OR, USA). Also, dispersive X-ray spectroscopy (EDX) for elemental analysis was performed using the same instrument (Quanta FEG 250).

The SEM micrograph of magnetite nanoparticles (Figure 2a) exhibits a dense, cauliflower-like carpet of near-spherical nanoparticles. Also, it is notable that they are agglomerated into larger clusters. The particles possess a rough surface with a non-faceted texture and non-uniform ordering. The pronounced aggregation is associated with the magnetically driven properties. During material drying, a porous hierarchical texture forms, providing a high external surface area that is beneficial for wastewater adsorption or catalytic oxidation.

Furthermore, the average particle size was measured to be approximately 45 nm, which is signifies a narrow size distribution, reinforcing their classification as nanocomposites (<100 nm) (Figure 2b).

The composite image exhibits a heterogeneous and irregular surface with a wrinkled texture, and visible layered and fragmented sheet-like structures (Figure 3). Such morphology indicates the occurrence of a highly porous material, which is a characteristic feature of bio-char-derived materials. The sheet-like and wrinkled texture supports a large specific surface area and, thereby, abundant active sites. Hence, the material could be categorized as favorable for adsorption and catalytic applications.

Also, dark regions appear in the micrograph, signifying the presence of microporous and mesoporous cavities, whereas the brighter areas correspond to denser carbon-rich or possibly iron-rich spheres. Furthermore, it is notable that the rough and fractured appearance improves the potential of the material to act as an efficient catalyst support substance, because it facilitates the uniform dispersion and incorporation of magnetite nanoparticles. Notably, visible structural defects, cracks, and pores signify that the pyrolysis and composite preparation processes are successful in developing a porous carbonaceous matrix. This porous nature not only endorses better mass transfer and dye contaminants diffusion in polluted aqueous effluents but also enhances the accessibility of reactive sites. Therefore, such reactive sites are highly beneficial for photo-Fenton catalytic reactions, and the performance of the modified Fenton reaction is maximized.

Overall, the SEM image verifies that the prepared PK-P-bio-char-incorporated magnetite nanocomposite retains the desirable surface roughness and porosity essential for high-performance wastewater treatment applications.

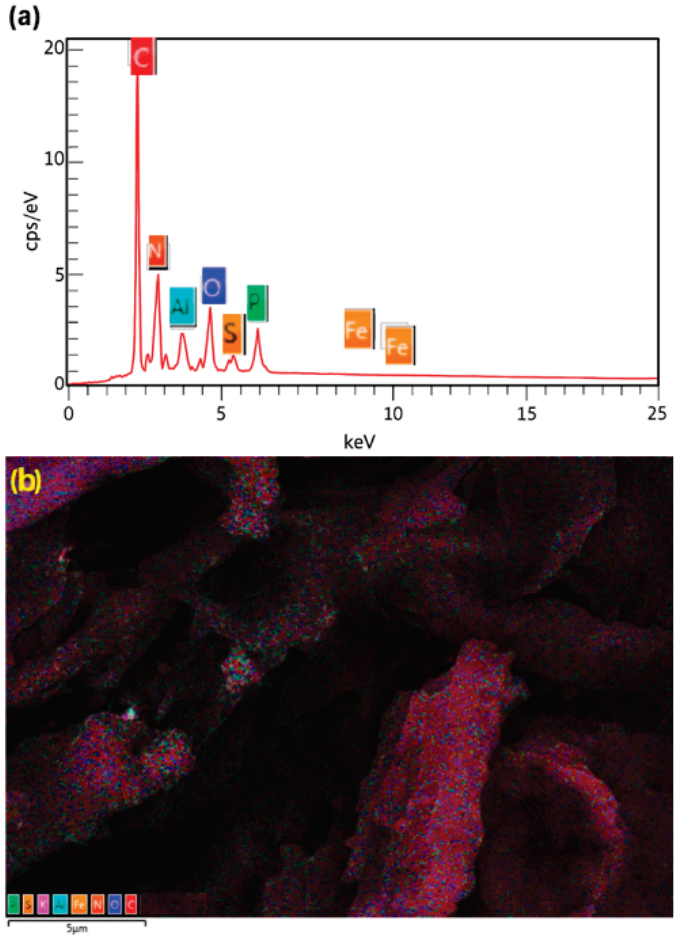


Figure 3. (a) Elemental analysis of EDX and (**b**) mapping of PK-P-bio-char/magnetite nanocomposite.

Elemental Composition:

An energy-dispersive X-ray spectroscopy (EDS) spectrum that illustrates the elemental composition of the PK-P-bio-char/magnetite nanocomposite was also obtained to investigate the material's composition. The data displayed in Figure 3a indicate the intensity of the detected X-rays from the material. Notably, sharp peaks are observed, corresponding to specific elements, verifying the presence of specific material derived from the pumpkin peel treatment and pyrolysis. The spectrum reveals prominent peaks for carbon (C), nitrogen (N), oxygen (O), aluminum (Al), sulfur (S), phosphorus (P), and iron (Fe). It is noteworthy that the most intense peak corresponds to carbon, indicating that carbon is the dominant element in the PK-P-bio-char/magnetite nanocomposite. In contrast, nitrogen, oxygen, and other detected elements were present in lower concentrations. However, it is essential to mention that the notable presence of aluminum, sulfur, phosphorus, and iron suggests the possibility of the existence of possible inorganic compounds or complex substances in the material. Overall, the EDS analysis confirms the multi-elemental nature of the prepared sample, with a high carbon content, validating the successful incorporation of bio-char in the composite material.

EDX elemental mapping was also obtained, and the data is displayed in Figure 3b. Different colors in the displayed image correspond to the spatial distribution of specific elements in the PK-P-bio-char/magnetite nanocomposite sample. The legend at the bottom of Figure 3b represents the occurrence of identified elements: phosphorus (P), sulfur (S), potassium (K), aluminum (Al), iron (Fe), nitrogen (N), oxygen (O), and carbon (C). Notably, a red signal, representing carbon, dominates the image, suggesting that the sample is primarily a carbon-rich material; this observation is consistent with the carbonaceous or

possibly organic-based nature of the substance. Other elements also appear, including oxygen (blue) and nitrogen (orange), which are distributed in patches. Such distribution indicates surface oxidation or the incorporation of heteroatoms. Notably, iron (pink) appears more sparsely but in localized regions, which could correspond to embedded nanoparticles or possible mineral inclusions. Nevertheless, the overall mapping exhibits a heterogeneous distribution. It is worth mentioning that the carbon matrix serves as the main structural component, whereas other elements are dispersed or clustered in specific regions, reflecting the complex multiphase composition.

Diffuse reflectance spectra, DRS:

The absorption spectrum of the PK-P-bio-char/magnetite composite is presented in Figure 4. The DRS profile of the PK-P-bio-char/magnetite composite shows broad absorption in the visible region (approximately 400–800 nm), which is a characteristic feature of magnetite nanoparticles. The initial absorption plateau around 350–400 nm can be attributed to charge transfer transitions in the Fe–O bonds. A slight incline near 500 nm indicates scattering effects or overlapping transitions, while the strong increase in absorption above 600 nm reflects the narrowing of the optical band gap induced by the incorporation of magnetite into the pumpkin peel-derived composite. Additionally, the optical absorption spectra were analyzed using a plot of $\left(F(R)hv\right)^{\frac{1}{2}}$ as a function of the energy of a photon (hv), where $F(R)$ follows the Kubelka–Munk relation [54]. This relation is expressed as $F(R) = \left(1 - R\right)^2/2R$, where R is the diffuse reflectance. The band gap energy (E_g) was estimated by extrapolating the absorption edge to the photon energy (hv) axis through a linear fit. The optical band gap was determined to be approximately 2.49 eV.

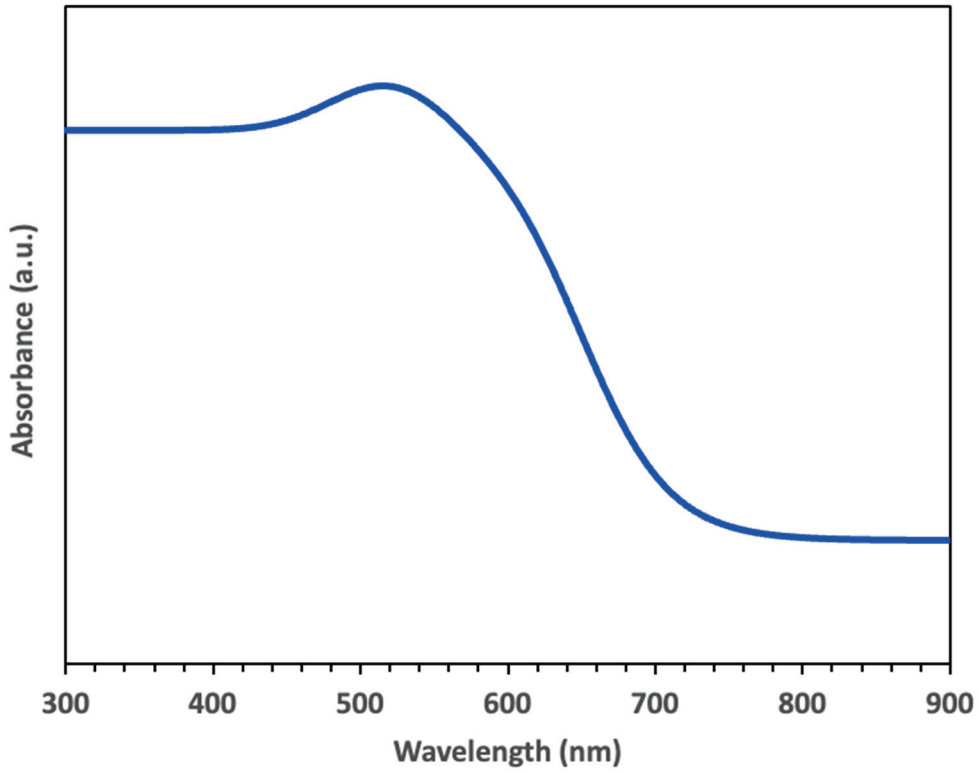


Figure 4. UV–vis diffuse reflectance spectrum graph for PK–Fe_3O_4 (magnetite-based composite).

2.2. Dye-Containing Wastewater Oxidation

2.2.1. Effects of Different Treatment Systems

To evaluate the performance of the proposed novel system, various Synozol Red KHL treatment systems were compared simultaneously to investigate their oxidation perfor-

mance as well as the time of reaction. Such a comparison verifies the efficiency of the proposed system with the conventional process, and the data exhibited in Figure 5. PK-P-bio-char/magnetite, as a novel catalyst, was subjected to degradation experiments under the initiation of the ultraviolet source. The data exhibited in the graph reveal that the H_2O_2/UV, PK-P-bio-char/magnetite/UV, and photo-Fenton PK-P-bio-char/magnetite/H_2O_2/UV were compared, and the experimental results showed that the highest efficiency was achieved by the combined photo-Fenton system PK-P-bio-char/magnetite/H_2O_2/UV. The results clearly demonstrate that the dual treatment achieved superior removal efficiency, reaching 95% under the experimental conditions (pH 5.7, catalyst 10 mg/L, and hydrogen peroxide 100 mg/L).

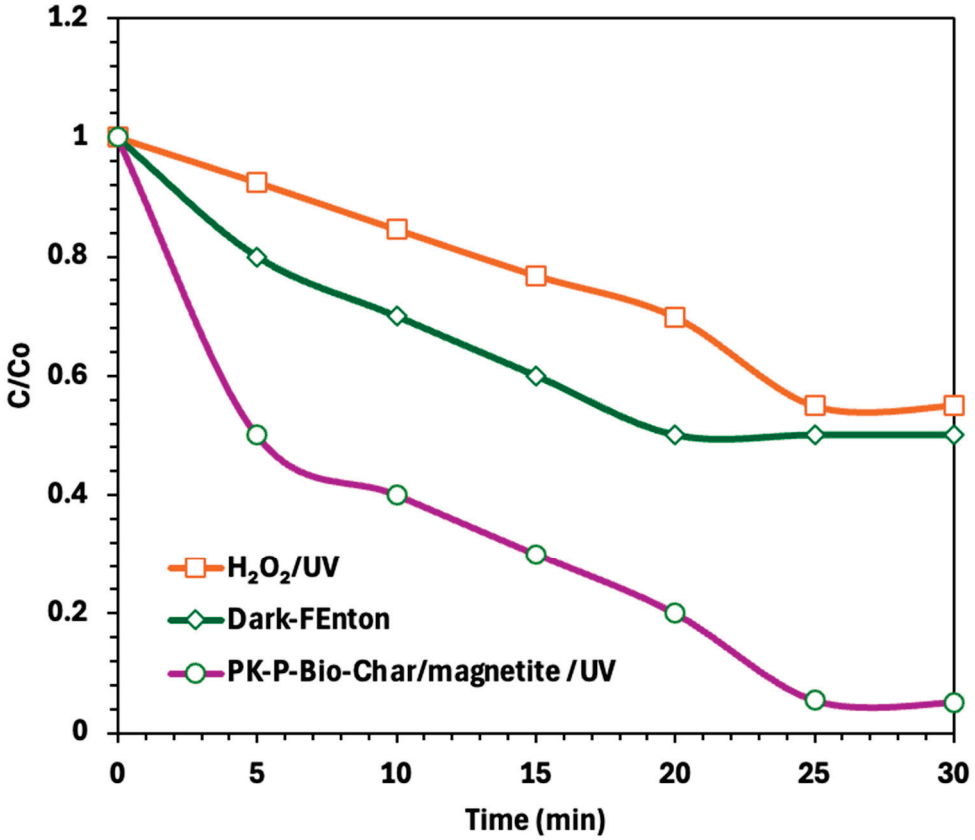


Figure 5. Comparison of oxidation systems based on the Synozol Red KHL dye reaction time.

The plot shows that oxidation time is approximately 30 min under UV irradiance for all the applied systems: dark Fenton, H_2O_2/UV, and the PK-P-bio-char/magnetite/UV photo-Fenton catalyst. It is noteworthy that the hybrid PK-P-bio-char/magnetite/UV curve drops steeply within the initial 5 min of irradiance, followed by a gradual drop in oxidation efficiency. Also, the pronounced early drop and slower oxidation for the PK-P-bio-char/magnetite/UV system are associated with the strong synergistic effect between UV irradiation and the magnetite photo-Fenton reaction supported on bio-char derived from PK-P waste. Furthermore, the system is superior compared to other oxidation systems and might be linked to the higher OH radical yield associated with the Fenton reaction.

The system was compared to hydrogen peroxide and the solo magnetite system. It is noteworthy that the combined system benefits from rapid adsorption/pre-concentration, efficient •OH generation, and sustained redox cycling. However, the other routes are limited by slower radical generation. This data is in accordance with the previous data in the literature on treating various contaminants in wastewater [14,33].

2.2.2. Effect of Photo-Fenton Operating Parameters

Effect of Hydrogen Peroxide:

Hydrogen peroxide may also decompose prematurely under non-optimal conditions, reducing efficiency. In addition, the process sometimes achieves incomplete mineralization, producing toxic intermediates that require further treatment. Hydrogen peroxide concentration was varied from 50 to 300 mg/L to investigate its effect on the oxidation and removal of Synozol Red KHL dye, whereas all other parameters—including 50 ppm dye concentration, 20 mg/L of the catalyst, and the original pH of 5.7 of the dye solution—were kept constant. The results are displayed in Figure 6. All experiments displayed a superior oxidation tendency during the initial period of irradiation, with a fast drop within the first 5–10 min. Subsequently, a slower plateau approach was commonly observed, consistent with Fenton/photo-Fenton oxidation for Synozol Red KHL dye removal. It is noteworthy that adsorption and oxidation reactions occur simultaneously due to the presence of the bio-char/magnetite catalyst. Notably, as the reaction proceeds, hydrogen peroxide is consumed, and thereby the rate of oxidation decreases.

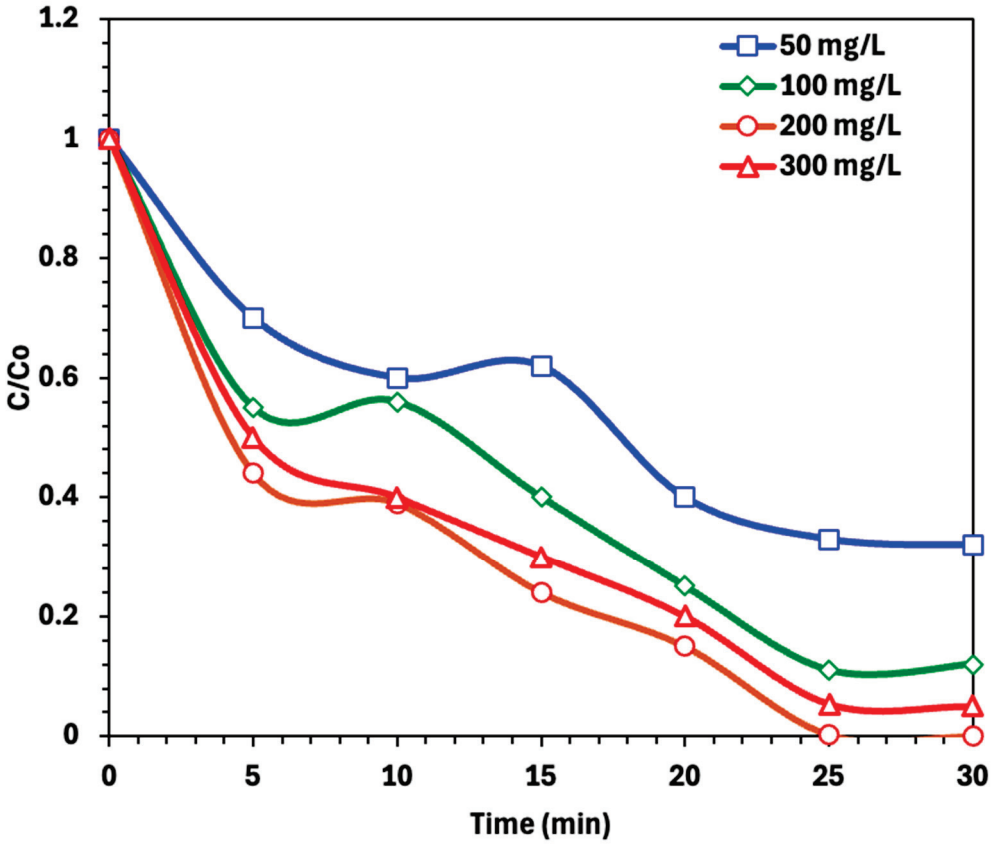


Figure 6. Effect of hydrogen peroxide on the photo-Fenton reaction for Synozol Red KHL dye oxidation.

PK-P-Bio-Char/Fe_3O_4 catalyst:

The impact of the PK-P-bio-char/Fe_3O_4 catalyst on the photo-Fenton reaction was assessed by varying its concentration in the oxidation system reaction. Figure 7 illustrates the effect of the catalyst in Fenton's oxidation. The catalyst concentration ranged from 5 to 30 mg/L. The data show a drop in pollutant concentration during the initial oxidation period, followed by a slower decline. This is linked to the increase in the catalyst concentration, which results in superior oxidation efficiency, which increased from 40 to 100% removal with the catalyst increasing from 5 to 20 mg/L. This could be attributed to the active sites of the substance being filled, with intermediates accumulating in the reaction medium rather than oxidizing the pollutants. When •OH radicals are generated at an opti-

mal value, it leads to higher removal efficiency. However, a further increase in the catalyst concentration to 30 mg/L results in a decline in the oxidation efficiency. This is attributed to the radicals/active sites becoming limiting and light screening or mass-transfer effects appearing. The available data aligns with the expectation that a high concentration of hydrogen peroxide will produce a significant amount of •OH radicals [44], thereby enhancing the dye removal rate up to a point, beyond which hydrogen peroxide contributes minimally. Thus, this investigation confirms that H_2O_2 must be optimized for best performance.

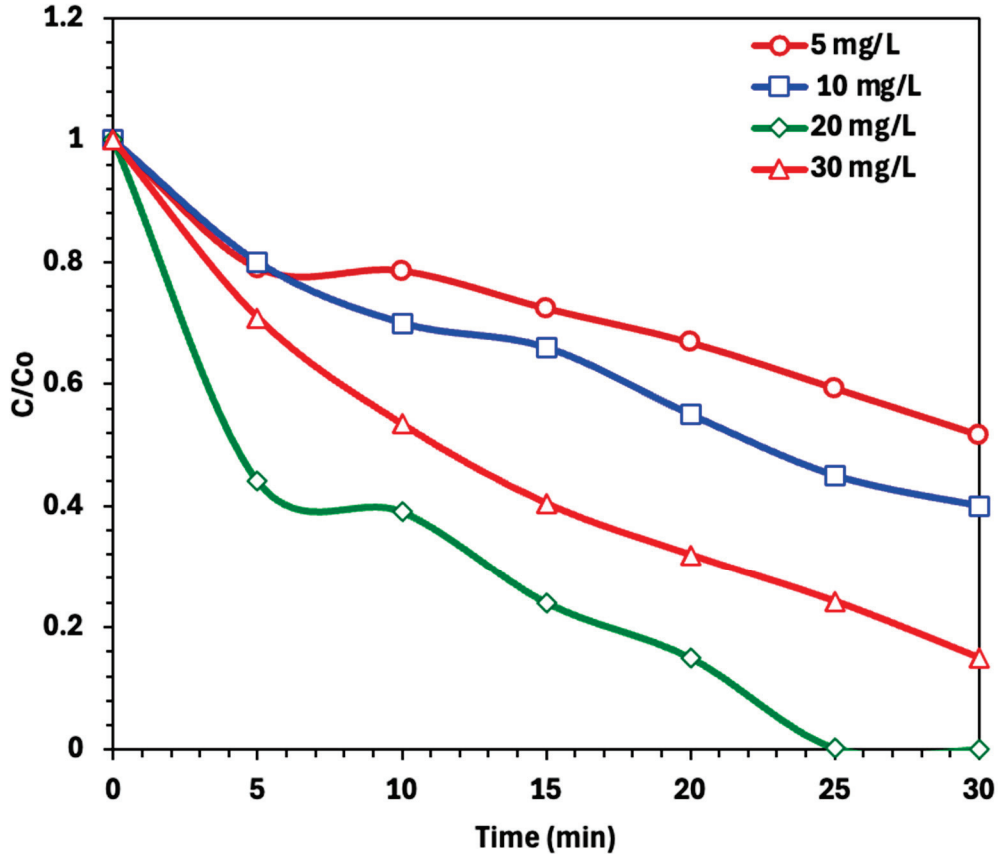


Figure 7. Effect of PK-P-bio-char/Fe_3O_4 on the photo-Fenton reaction for Synozol Red KHL dye oxidation.

pH-value effect:

pH is signified as a worthy adjustable variable in the photo-Fenton reaction, since the pH in the reaction is considered to influence the H_2O_2 reagent decomposition and the hydrolytic speciation of metal ions. In this regard, the pH value in the system is varied to evaluate the best operating performance, whereas the hydrogen peroxide value (200 mg/L) and PK-P-bio-char/Fe_3O_4 catalyst (20 mg/L) are kept constant in all pH conditions of the systems. The data displayed in Figure 8 exhibited a strong pH dependence of Synozol Red KHL dye oxidation and thereby removal in the photo-Fenton system. The process is superior and reaches complete dye removal (100%) when the pH is the natural pH of the dye (5.7). Also, the acidic pH offers superior efficiency that also achieves almost complete removal of the dye (99%). This might be attributed to the Fenton chemistry where Fe^{2+}/Fe^{3+} cycling and •OH production is maximized, and iron remains soluble under the given pH value. At pH 5.7, the curve drops very quickly in the first 5–10 min. Similarly, the adsorption could take place onto the bio-char support, demonstrating that near-neutral operation is feasible. However, at neutral pH 7.0, Synozol Red KHL dye oxidation markedly declines and becomes slower due to the Fe^{3+} hydroxy species precipitating. Thereby, the result is a reduction in the photo-Fenton activity and limited surface redox cycling. Also,

when the pH is raised to the alkaline range 8.0, the reaction is strongly inhibited due to iron precipitation. Also, new intermediates appeared in the reaction medium that could be scavenging the •OH radicals such as OH^- species [12,33]. Furthermore, H_2O_2 could be decomposed into the less reactive $HO_2^-/O_2\bullet^-$ pathway that leads to the formation of the hydroperoxide ($\bullet HO_2$) inactive radical [22]. The hydroperoxide radical and the superoxide radical anion are signified as the strongest reaction inhibitors that neutralize the oxidizing forms of metal cations in aquatic solution. Overall, acidic conditions yield the highest radical flux and the fastest mineralization. Also, near-neutral pH benefits from adsorption plus heterogeneous photo-Fenton. But the alkaline pH conditions suppress the process. The data exhibited for the experiment runs verifies that even though natural dye pH or acidic pH is favorable, it is noteworthy that the oxidation could be efficient at varied pH ranges. This investigation is in accordance with the previous work [17,20] that confirmed the pH dependence of Fenton's reaction and other work [22] that reported that carbon-based treatment is also significant with respect to the pH value.

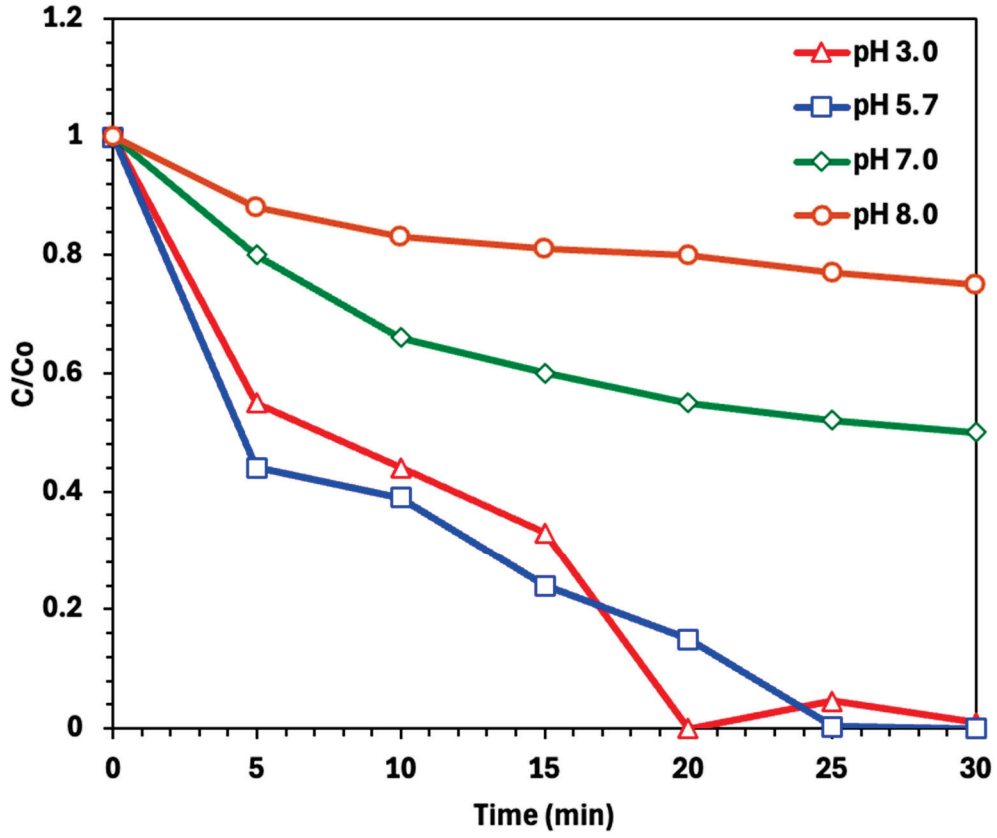


Figure 8. Effect of the pH value on the photo-Fenton reaction for Synozol Red KHL dye oxidation.

Temperature effect

To achieve effective treatment of textile effluents and ensure real-life applicability, it is crucial to evaluate the impact of temperature to understand its effectiveness in the oxidation system. Since discharged effluents may vary in temperature, the temperature influence is investigated by varying the temperature from room temperature (32 °C) to 40, 50, and 60 °C, whereas the hydrogen peroxide value (200 mg/L) and PK-P- bio-char/Fe_3O_4 catalyst (20 mg/L) are kept constant at pH 5.7. The data displayed in Figure 9 revealed that at all temperatures, the dye concentration drops sharply within the initial 5 min of oxidation time. This fast drop in the preliminary irradiance time suggests a high availability of active sites and/or OH hydroxyl radical species in the initial step of the oxidation process. Also, the oxidation tendency increases as the temperature increases. Complete dye removal is

achieved (100%) with oxidation of Synozol Red KHL dye, and when the temperatures 60 °C, the oxidation is completed within only 20 min compared to 25 min at room temperature, with notable residual concentration even at 15 min. Notably, all temperature systems reached full degradation by 25–30 min, but higher temperatures significantly accelerated the oxidation rate. This could be associated with the enhanced molecular collisions as well as the increased oxidative •OH radical yield, which increases at high temperature. Thus, the data revealed that operating at elevated temperatures can markedly improve treatment efficiency, though energy considerations should be addressed for large-scale applications. These data are in accordance with previous work [44] using dual adsorption and Fenton reaction with activated carbon and Fe^{3+} composite, which addressed the influence of temperature on such treatment.

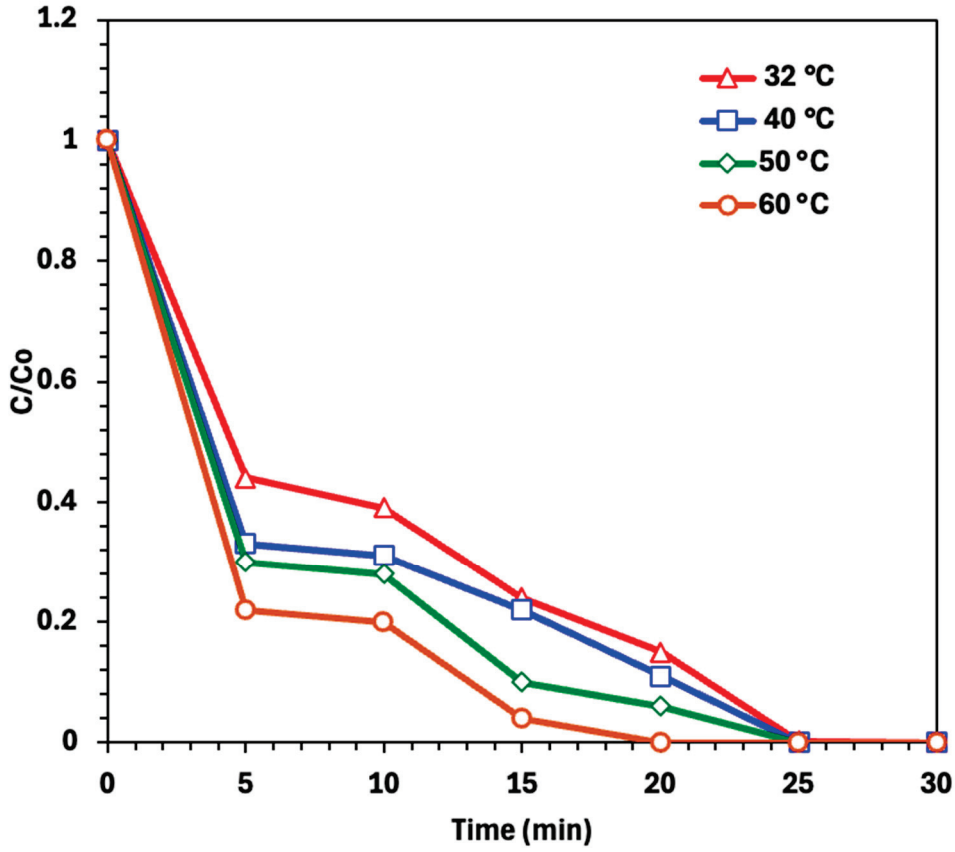


Figure 9. Temperature effect on photo-Fenton reaction for Synozol Red KHL dye oxidation.

Dye loading:

Synozol Red K-HL dye oxidation is influenced by the initial dye concentration, and it is essential to study this effect since, in the real world, industrial effluents might be discharged at varied loads. In this context, the dye concentration ranging from 20 to 200 mg/L is investigated, whereas all other operational parameters are kept constant (hydrogen peroxide value at 200 mg/L, PK-P-bio-char/Fe_3O_4 catalyst at 20 mg/L, and pH 5.7). The photo-Fenton-based PK-P-bio-char/Fe_3O_4 oxidation process is evaluated at different dye concentrations. The experimental data displayed in Figure 10 reveals that at low dye concentrations of 20 ppm and 40 ppm, the oxidation rate is significantly high and proceeds at a rapid rate, achieving complete removal within 25 and about 40 min, respectively. However, at the high dye load of 80 ppm, the removal is significantly slower compared to low loads, with only partial oxidation of 25% after 60 min of irradiance time. Nevertheless, at the highest concentration of 200 ppm dye load, the process revealed the lowest efficiency, with over 50% of the dye persisting even after 60 min.

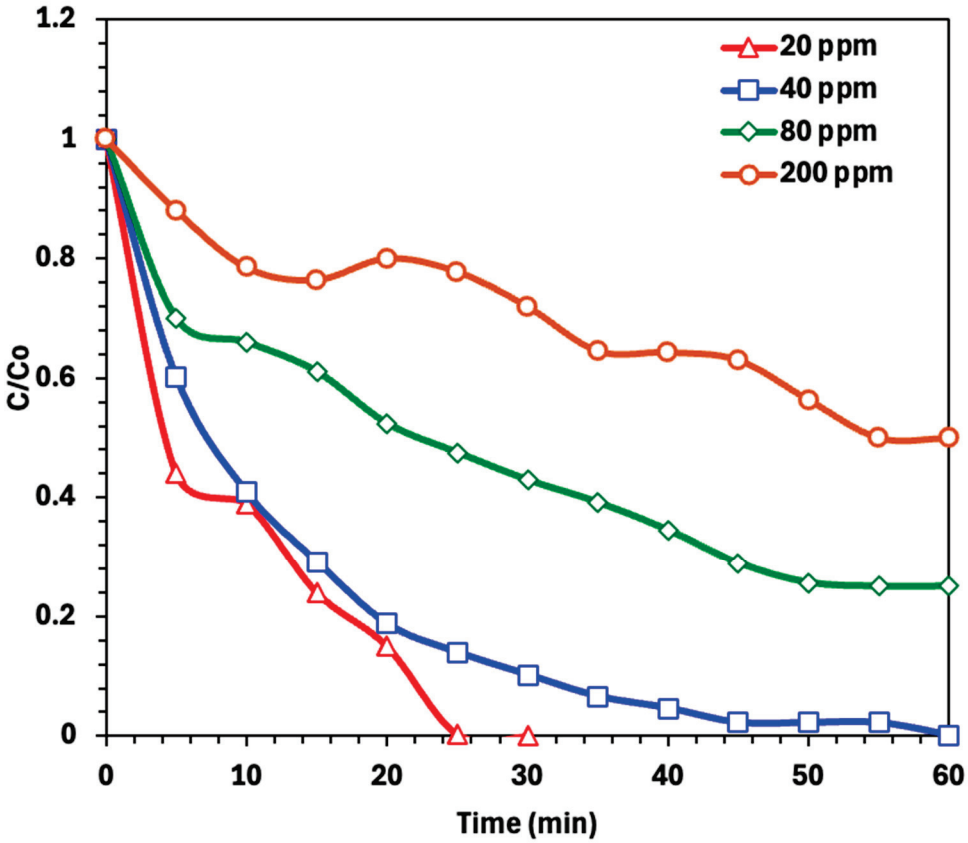


Figure 10. Synozol Red KHL dye concentration effect on photo-Fenton-based PK-P-bio-char/Fe_3O_4 composite catalyst.

This above-mentioned observation indicates that higher dye concentrations hinder oxidation efficiency. Such a trend might be due to the insufficient radical availability relative to dye molecules at higher concentrations since the same amounts of Fenton reagent are added even though the dye load is low or high. Thus, the same quantity of •OH radicals is produced, and the dye molecules increase [24]. Moreover, radical scavenging effects could occur, whereas extra dye molecules compete with intermediates, thereby decreasing the effective oxidation [22,44]. Furthermore, several researchers [13,25,44] have mentioned that the possibility of ultraviolet light penetration into the reaction medium is reduced due to the shadowing effect of the dye in the solution at high loads. Also, mass transfer resistance persists at high concentrations, limiting the oxidation reaction from occurring efficiently. These findings highlight that optimal performance is achieved at moderate dye concentrations, while sufficient •OH radical species are available in the reaction medium, ensuring a rapid and complete oxidation rate. Thus, this investigation emphasizes the importance of dose optimization in practical wastewater treatment applications.

2.3. Comparative Investigation with Cited Literature

Synozol Red K-HL dye oxidation was investigated in the current work and compared with the available literature. According to the data exhibited in Table 1, although the homogeneous Fenton (Fe^{2+} /H_2O_2) remains one of the most superior processes, achieving a high rate of dye oxidation within minimal time (>90%)—with reaction times ranging from 30 to 60 min—it possesses some limitations. Its drawbacks include the requirement for a strictly acidic pH medium and by-product sludge formation. But heterogeneous catalysts, including Fe_3O_4 nanoparticles and Fe-doped TiO_2, afford comparable removal efficiencies (80–90%), with the advantage of easier recovery and reusability opportunities, although at the expense of longer reaction times. ZnO nanoparticles exhibit similar performance

under solar/UV irradiation, suggesting a sustainable alternative; nevertheless, stability and photo-corrosion remain challenges.

Table 1. Comparison of various types of wastewater loaded with Synozol Red KHL dye treatment-based catalysis reactions.

Type of Process/ Catalyst	Removal Efficiency	Operating Conditions	Oxidation Time	Reference
Heterogeneous photo-Fenton/Fe_3O_4 nanoparticles	80%	pH 3–4, UV irradiation, H_2O_2 100 mg/L, catalyst 0.5 g/L	60–90 min	[35]
Photocatalysis/Fe-doped TiO_2	86%	pH 5.0–7.0, UV light, catalyst 0.5 g/L	120 min	[42]
Photocatalysis/ZnO nanoparticles	83%	pH 6.0, solar/UV light, catalyst 1.0 g/L	90–120 min	[43]
Adsorption + Fenton/ activated carbon/ Fe^{3+} composite	81–94%	pH 3.0, H_2O_2 50–80 mg/L, catalyst 1.0 g/L	40–70 min	[44]
Biomass-derived photo-Fenton/pumpkin peel–Magnetite (PK-P/Fe_3O_4)	100%	pH 5.7, H_2O_2 100 mg/L, UV irradiation, catalyst 10 mg/L	25 min	Current work

Activated carbon/Fe^{3+} composites provide a dual treatment of adsorption and oxidation reactions. Hence, the removal yield is high and could reach a removal efficiency of more than 85–95% due to the synergistic effect. However, it is worth mentioning that regeneration of the adsorbent might be costly. Notably, the biomass-derived PK-P/Fe_3O_4 material demonstrates efficient removal, achieving complete dye removal comparable to previous conventional systems. Moreover, the current system offers the advantages of low cost, sustainability, and valorization of agricultural waste. Thus, such a study highlights the potential of integrating bio-waste-derived catalysts with photo-Fenton processes as an environmentally friendly alternative to traditional techniques of wastewater treatment.

2.4. Oxidation Mechanism

Synozol Red KHL dye oxidation by applying the modified photo-Fenton system using pumpkin peel–magnetite (PK-P/Fe_3O_4) is investigated through the reaction mechanism (as displayed in Figure 11). In such a reaction, the photocatalytic oxidation and degradation pathway of the dye (Synozol Red KHL)-contaminated wastewater is proposed by the use of pumpkin peel–magnetite (PK-P/Fe_3O_4) as a heterogeneous catalyst under ultraviolet assisted photo-Fenton environments. Primarily, Synozol Red KHL dye molecules are adsorbed onto the porous prepared bio-char-based bio-waste material incorporated with magnetite nanoparticles (PK-P-bio-char/Fe_3O_4) through electrostatic interactions and hydrogen bonding, which improves the Synozol Red KHL contaminant loading near catalytic sites. Under ultraviolet illumination, the exposed H_2O_2 peroxide might decompose, either directly or via catalytic Fe^{2+}/Fe^{3+} redox cycling on the PK-P/Fe_3O_4 surface, thereby producing highly reactive oxidative radical species. These radicals include hydroxyl radicals (•OH) and hydroperoxyl radicals (•HO_2). These radicals attack the Synozol Red KHL molecules, cleaving azo bonds and aromatic rings; the result is fast decolorization due to the dye molecules' reduction. Subsequent oxidation converts intermediate compounds into low molecular weight organic acids and eventually into CO_2, H_2O, and inorganic ions species such as SO_4^{2-} and NO_3^-. The porous bio-char matrix of PK-P-bio-char not only improves the adsorption and electron transfer, but also helps produce Fe^{2+} from

Fe^{3+}, thus sustaining the catalytic cycle. Finally, after the oxidation treatment reaction, the magnetite-based composite can be easily separated magnetically for reuse. Thus, this catalyst demonstrates an efficient, eco-friendly solution that aligns with the 3 R criteria of "Recover, Recycle and Reuse" as a sustainable option for wastewater treatment.

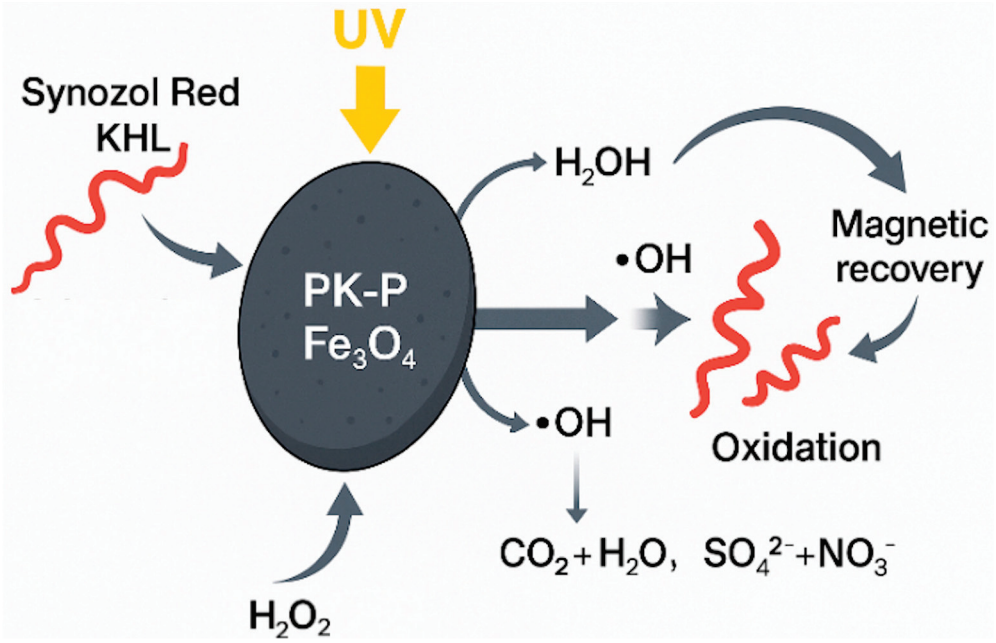


Figure 11. Oxidation mechanism of the photo-Fenton reaction-based PK-P-bio-char/Fe_3O_4 composite catalyst.

2.5. Oxidation Kinetics

Generally, real-life industrial applications require process design aspects for reactor design and system control, which can be evaluated through the study of system kinetic modeling. Hecne, in this contextt, the oxidation of Synozol Red KHL dye-containing wastewater is considered a function of time under various temperatures. Three general kinetic models—0th-, 1st-, and 2nd-order [51,52]—are applied by transforming their equations into linearized forms, as displayed in Table 2.

R^2 values (correlation coefficients) were applied to assess the fit of the compared models of 0th-, 1st-, and 2nd-order kinetics. The best-fitting model is determined by the highest correlation coefficient value between the empirical and theoretical data. Initially, the relationship between various operating temperatures and time for 0th-, 1st-, and 2nd-order reaction rates was plotted, and the data is displayed in Figure 12a, b, and c, respectively. Furthermore, the relationship between various operating temperatures and time for 0th-, 1st-, and 2nd-order oxidation rates were investigated (Table 2).

According to the data tabulated in Table 2 and the graphs exhibited in Figure 12, to identify the best-fit kinetic model, the correlation coefficients were compared. The compared models of 0th-, 1st-, and 2nd-order kinetics models were evaluated, and the 0th- and 2nd-order models were excluded due to their relatively low correlation coefficient values (0.58–0.85 and 0.51–0.88 for 0th and 2nd order, respectively). But the values of 0.87–0.96, which are comparatively higher, correspond to the 1st-order model.

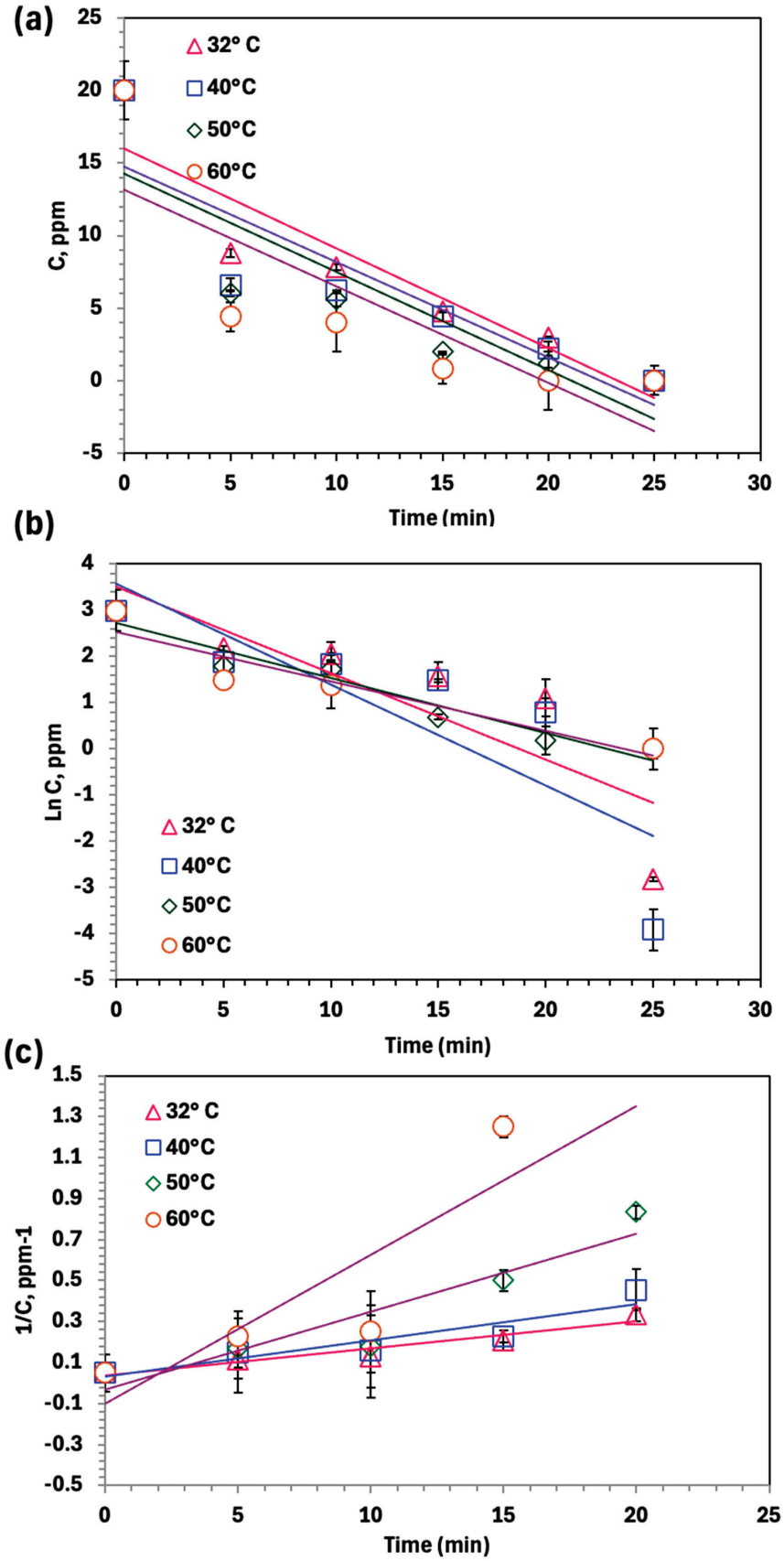


Figure 12. Plots of the (**a**) 0th-, (**b**) 1st-, and (**c**) 2nd-order kinetic models for Synozol Red KHL dye oxidation through modified PK-P-bio-char/Fe_3O_4-based photo-Fenton at different operating temperatures.

As presented in Table 2, k_1 decreased to 0 as the temperature increased from 32 °C to 60 °C, and the half-lives of the reaction time also declined with the rise in temperature. These findings suggest that the oxidation process is strongly influenced by temperature. This indicates that the reaction rate accelerates as the temperature rises, consistent with the temperature relationship. Similar findings have been reported by different researchers, who stated that 1st-order kinetics in Fenton oxidation has been observed for dyes such as Reactive Red SBE [51], highlighting that the reaction order may vary depending on the dye structure and system conditions, while other studies have reported that the follows 2nd-order kinetic models [52,53].

Table 2. Kinetic models and their parameter values for the PK-P-bio-char/Fe_3O_4-based photo-Fenton oxidation kinetics.

Model and Equation *	Model Parameters	Values			
		T, °C			
		32 °C	**40 °C**	**50 °C**	**60 °C**
0th-order model $C_t = C_0 - k_0 t$	k_0 (min^{-1})	0.68	0.65	0.67	0.66
	$t_{1/2}$ (min)	14.70	15.38	14.92	15.15
	R^2	0.85	0.78	0.58	0.73
1st-order model $C_t = C_0 - e^{k_1 t}$	k_1 (min^{-1})	0.064	0.0211	0.015	0.0103
	$t_{1/2}$ (min)	67.28	46.2	32.84	10.82
	R^2	0.93	0.96	0.95	0.87
2nd-order model $\left(\frac{1}{C_t}\right) = \left(\frac{1}{C_0}\right) - k_2 t$	k_2 ($L \cdot mg^{-1} \cdot min^{-1}$)	0.0123	0.0382	0.0185	0.0177
	$t_{1/2}$ (min)	4.065	1.31	2.70	2.82
	R^2	0.88	0.86	0.51	0.79

* C_0 and C_t are the concentration at time 0 and time t; k_0, k_1, and k_2 are the kinetic constants of 0th, 1st and 2nd orders, respectively.

2.6. Thermodynamic Investigation

To evaluate the feasibility of implementing the photo-Fenton oxidation reaction for system design, a thermodynamic investigation was conducted. The key thermodynamic parameters were predicated to investigate the nature of the reaction. The Arrhenius equation, based on the 1st-order rate constant $k_1 = Ae^{\frac{-E_a}{RT}}$ was linearized by taking its natural logarithm and then plotted, as displayed in Figure 12, where A is the pre-exponential factor, E_a is the activation energy ($kJ \cdot mol^{-1}$), R is the gas constant (8.314 $J \cdot mol^{-1} \cdot K^{-1}$), and T is the absolute temperature (K). The linear plot (Figure 13) estimates the activation energy, which was determined to be 43.22 $kJ \cdot mol^{-1}$. This relatively low E_a confirms that the oxidation of the dye via the photo-Fenton process proceeds with a minimal energy barrier.

To gain deeper insight into the temperature effect, other thermodynamic parameters, including the Gibbs free energy of activation (ΔG′), activation enthalpy (ΔH′), and activation entropy (ΔS′), were also investigated, with the results summarized in Table 3. The variation of these parameters with temperature highlighted the dependence of the system-based photo-Fenton oxidation on the 1st-order kinetic constants. The Gibbs free energy of activation (ΔG′) was calculated using Eyring's equation, $k_1 = \frac{k_B T}{h} e^{(-\frac{\Delta G'}{RT})}$, where k_B and h are Boltzmann and Planck's constants, respectively. Additionally, the activation enthalpy (ΔH′) and entropy (ΔS′) were derived from the relations $\Delta H' = E_a - RT$ and $\Delta S' = (\Delta H' - \Delta G')/T$. These findings provide a comprehensive understanding of the thermodynamic behavior of the system, offering valuable insights into the design and optimization of the photo-Fenton oxidation process.

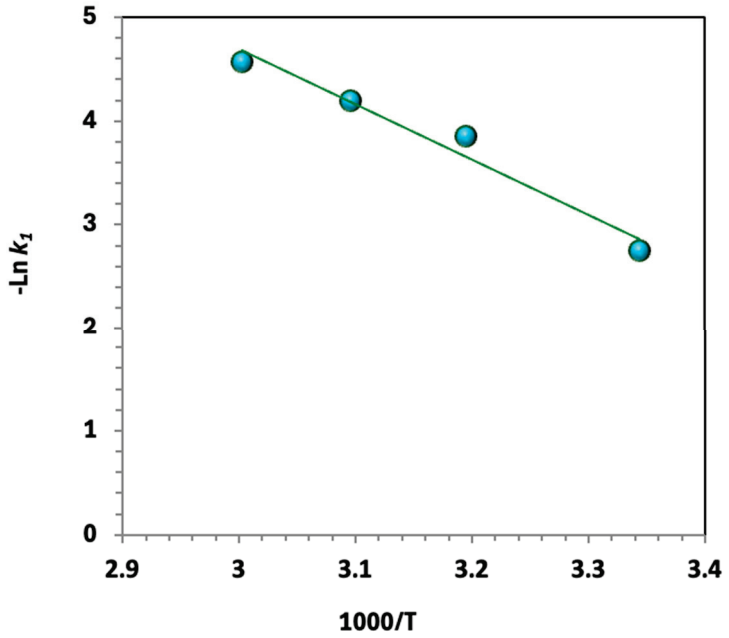


Figure 13. Plot of the Arrhenius relation.

Table 3. Thermodynamic parameters for Synozol Red KHL dye oxidation for the PK-P-bio-char/Fe_3O_4-based photo-Fenton.

Temperature, °C	Ln k_2	E_a, kJ mol^{-1}	$\Delta G'$, kJ mol^{-1}	$\Delta H'$, kJ mol^{-1}	$\Delta S'$, J mol^{-1}
32	−2.74	43.22	80.06	40.74	−131.51
40	−3.85		86.82	40.63	−147.5
50	−4.199		90.59	40.54	−154.95
60	−4.57		94.52	40.46	−162.35

As summarized in Table 3, the positive Gibbs free energy values indicate that the PK-P-bio-char/Fe_3O_4-based photo-Fenton oxidation process is a non-spontaneous type of oxidation, with the degree of non-spontaneity increasing at higher temperatures. However, the lowest Gibbs free energy values were observed at ambient temperature, suggesting greater molecular freedom of the dye and more effective interaction with hydroxyl radicals (•OH). These findings confirm that increasing the temperature up to 60 °C improves the degradation efficiency of Synozol Red KHL dye. Additionally, the positive activation enthalpy values reveal that the oxidation reaction is endothermic in nature, while the negative activation entropy values further support the non-spontaneous characteristics of the PK-P-bio-char/Fe_3O_4-based photo-Fenton system.

2.7. Reusability and Sustainability

To verify the catalyst sustainability, PK-P-bio-char/magnetite as a based photo-Fenton system is evaluated by catalyst recovery through filtration, thoroughly washing it with distilled water to remove residual impurities, and then oven-drying at 150 °C for one hour. The catalyst is thereafter used for successive cycles of oxidation. The data are exhibited in Figure 14. The results demonstrated that the catalyst maintained effective performance over multiple uses, sustaining high activity for up to 10 consecutive cycles. This data verifies the catalyst stability and potential for repeated applications. The fresh catalyst achieved 100% removal efficiency, which slightly decreased to 98% in the first cycle and 93% in the second cycle, indicating minimal loss of activity during early reuse. However, a gradual decline in performance was observed with successive cycles, dropping to 82% by the fifth cycle and 70% by the tenth cycle. However, it is essential to mention that, although the oxidation rate

remains high even with cyclic use, there is a reasonable reduction in the activity of PK-P-bio-char/Fe_3O_4 material due to partial deactivation or loss of active sites, since the surface is filled with the dye molecules and minor leaching of active components occurs during repetitive catalyst use. Despite this reduction, maintaining 70% efficiency after 10 cycles highlights the catalyst's superior stability and recyclability, supporting it as a highly promising candidate for cost-efficient and sustainable wastewater treatment applications.

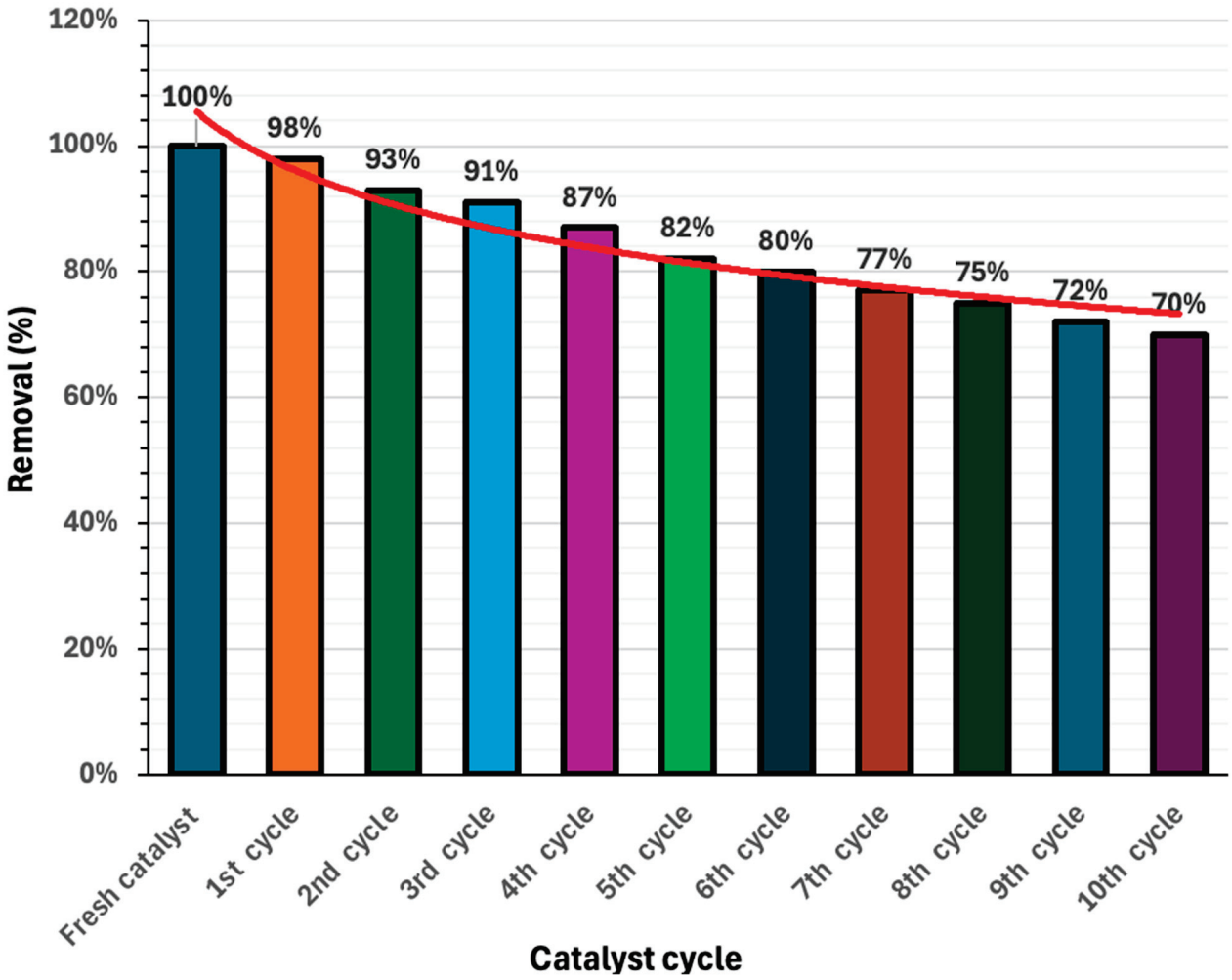


Figure 14. PK-P-bio-char/Fe_3O_4 composite catalyst reusability.

Furthermore, the kinetic investigation across cycles (fresh, 1st to 10th cycle) is conducted. The concentration profiles for representative cycles fit well to the first-order model according to the correlation coefficient values, and the data is tabulated in Table 4. The first-order kinetic rate constant decreased with the reuse cycle. This behavior is attributed to progressive surface coverage by reaction intermediates and minor loss of accessible iron sites, which collectively slow •OH generation and substrate access. This data reflects a gradual deactivation of the catalyst surface during successive runs. Also, the observed decline in k_1 values, as displayed in Table 4, is primarily attributed to the progressive surface coverage by reaction intermediates, which limits the availability of active sites and the minor loss of accessible Fe sites [54]. Thus, overall, the oxidation reaction has reduced efficiency in hydroxyl radical (•OH) generation. Nevertheless, the catalyst retained appreciable activity even after 10 cycles, confirming its potential for repeated use despite reduced efficiency.

Table 4. First-order kinetic model and its parameter values for the cyclic PK-P-bio-char/Fe_3O_4-based photo-Fenton oxidation use.

Cycle	Removal (%)	k_1 (min^{-1})	R^2
Fresh use	100	0.064	0.93
1st cycle	98	0.056	0.94
2nd cycle	93	0.053	0.91
3rd cycle	91	0.046	0.92
4th cycle	87	0.040	0.90
5th cycle	82	0.034	0.87
6th cycle	80	0.030	0.86
7th cycle	77	0.027	0.91
8th cycle	75	0.026	0.93
9th cycle	72	0.022	0.88
10th cycle	70	0.018	0.96

2.8. Radical Scavenging Test

Overall, hydroxyl (•OH) and hydroperoxyl (HO_2•) radicals are the most quantitatively significant reactive species in the catalytic oxidation system. In particular, the hydroxyl radical (•OH) is known to be a highly effective oxidant for a wide range of pollutant molecules. Thus, in order to verify the significant effects and the role of these radicals and other charge carriers in the oxidation process, radical scavenging experiments were performed using specific quenching agents: isopropyl alcohol (IPA) as an •OH scavenger, ammonium oxalate (AO) as a hole (h^+) scavenger, and silver nitrate ($AgNO_3$) as an electron (e^-) scavenger for Synozol Red KHL dye [2].

Figure 15 presents the results of the scavenger experiments performed under the optimal operating conditions of the PK-P/Fe_3O_4 based photo-Fenton system. When isopropyl alcohol (IPA) was introduced as an •OH scavenger, the degradation efficiency of Synozol Red KHL dye dropped drastically from nearly 100% to 40%. This sharp decline highlights the dominant role of hydroxyl radicals (•OH) in the oxidation of Synozol Red KHL dye over PK-P/Fe_3O_4. In comparison, the addition of electron ($AgNO_3$) and hole (AO) scavengers produced less pronounced effects, lowering the efficiency to 56% and 59%, respectively. These results confirm that although multiple reactive species are involved, •OH radicals are the primary contributors in Synozol Red KHL dye degradation within our system. This could be attributed to the fact that the PK-P/Fe_3O_4 composite generates multiple reactive species during the oxidation process, with •OH radicals dominating the oxidation of Synozol Red KHL. However, the photogenerated holes (h^+) exert a minimal influence on dye oxidation. The scavenger experiments clearly demonstrate that hydroxyl radicals (•OH) are the predominant reactive species responsible for the degradation of Synozol Red KHL dye in the PK-P/Fe_3O_4-based photo-Fenton system. Although electrons (e^-) and photogenerated holes (h^+) also participate in the process, their contributions are comparatively minor. These findings confirm that the superior oxidation performance of PK-P/Fe_3O_4 is mainly attributed to its ability to effectively generate •OH radicals, which drive the rapid breakdown of the dye molecules.

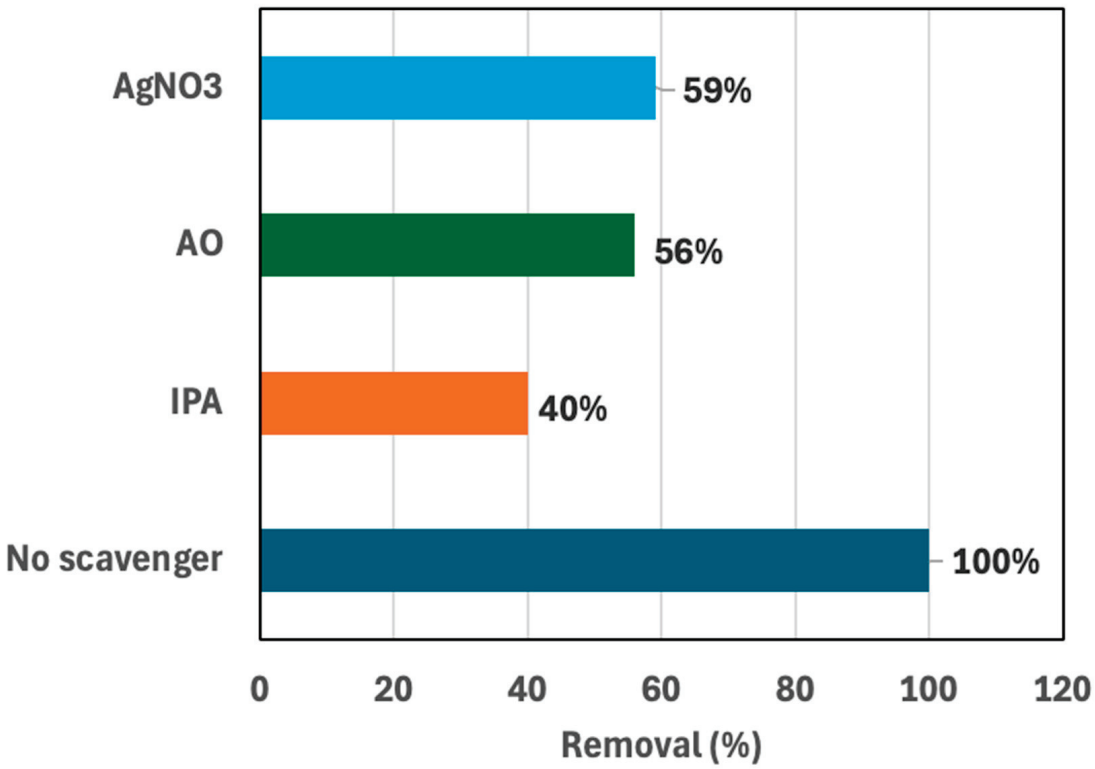


Figure 15. Comparative impact of radical scavengers on dye oxidation efficiency.

3. Materials and Methodology Investigation

3.1. Materials

Wastewater

A synthetic and commercial type of textile dye is introduced in the current work to simulate industrial discharges. An aqueous dye solution is initially prepared though 1000 ppm of stock solution from such dye by dissolving a certain amount in distilled water. Next, a subsequent dilution is carried out to investigate the effects of different concentrations of the dye on the oxidation efficiency in the range of 100–500 ppm. The pH of the wastewater is signified as the natural pH of the effluent and recorded at 5.7. However, to adjust the pH (using a digital pH meter, ADWA, Szeged, Hungary) of such wastewater into different values, successive diluted concentrations of H_2SO_4 and NaOH are used to adjust the solution according to the studied values. All the chemicals used were of analytical grade and applied as purchased without further purification.

PK-P-Bio-Char/Fe_3O_4

Pumpkin-derived bio-char is prepared by simple treatments of pumpkin peels (PK-P). The treatment is designed to convert bio-waste into a porous, carbon-rich substance. Primarily, pumpkin PK-P peel residue peels were collected from a local shop. Subsequently, they were initially washed thoroughly with distilled water to remove any dirt or impurities on its surface. Thereafter, the material is was air-dried for 7 days. Then, the material obtained was rinsed with distilled water again to remove any dust prior to being subjected to oven drying at 80 °C until a constant weight was achieved.

The dried material was ground using a pestle and mortar to attain small particles and then sieved to achieve a uniform size, which enhances the efficiency of subsequent carbonization. Next, the powdered biomass was subjected to calcination. To illustrate, the dried powder was gradually calcined to the desired temperature of 400 °C at a heating rate of 10 °C/min in a furnace. The pyrolysis was continued for 2 h to ensure complete carbonization. The resultant material is referred to as pumpkin peel bio-char, PK-P-bio-char.

The co-precipitation method is applied as a simple, cost-effective, and high yield process. In the procedure, the molar stoichiometric ratio of 1:2 from the sources of $Fe_2(SO_4)_3$ and $FeSO_4$ are added and employed by dissolving in distilled water. The pH is elevated to 12.0 by the gradual addition of sodium hydroxide solution under continuous stirring at 80 °C. The result is a precipitate of magnetite nanoparticles. Next, the attained substance of precipitate is exposed to successive washing with distilled water until it reaches the neutral water pH of 7.0. The collected nanoparticles are then dried overnight in an electric oven at 60 °C. Then, the resultant magnetite is mixed with the prepared pumpkin peel bio-char. Then, the material is characterized using X-ray diffraction (XRD, D8-Find, Bruker, with CuKα radiation (1.5418 Å), Madison, WI, USA) and scanning electron microscopy ((FE-SEM), using Quanta FEG 250, FEI Company, Hillsboro, OR, USA) techniques augmented with energy-dispersive X-ray spectroscopy (EDX) analysis, and their corresponding mapping is conducted to verify its structural and chemical properties.

3.2. Experimental Methodology

A certain amount (100 mL) of the model synthetic dye solution is poured into the jar test. When the pH adjustment to a certain level is required in such a case, it is adjusted using acid/base prior to being poured into the experiment. Then, a certain amount of catalyst reagent PK-P-bio-char/Fe_3O_4 is added to the reaction and subjected to ultrasonic dispersion before the hydrogen peroxide reagent is added to initiate the reaction. Afterwards, the mixture is exposed to ultraviolet UV radiation emitting 254 nm illumination while stirring is continued. The graphical representation of the experimental set-up is displayed in Figure 16.

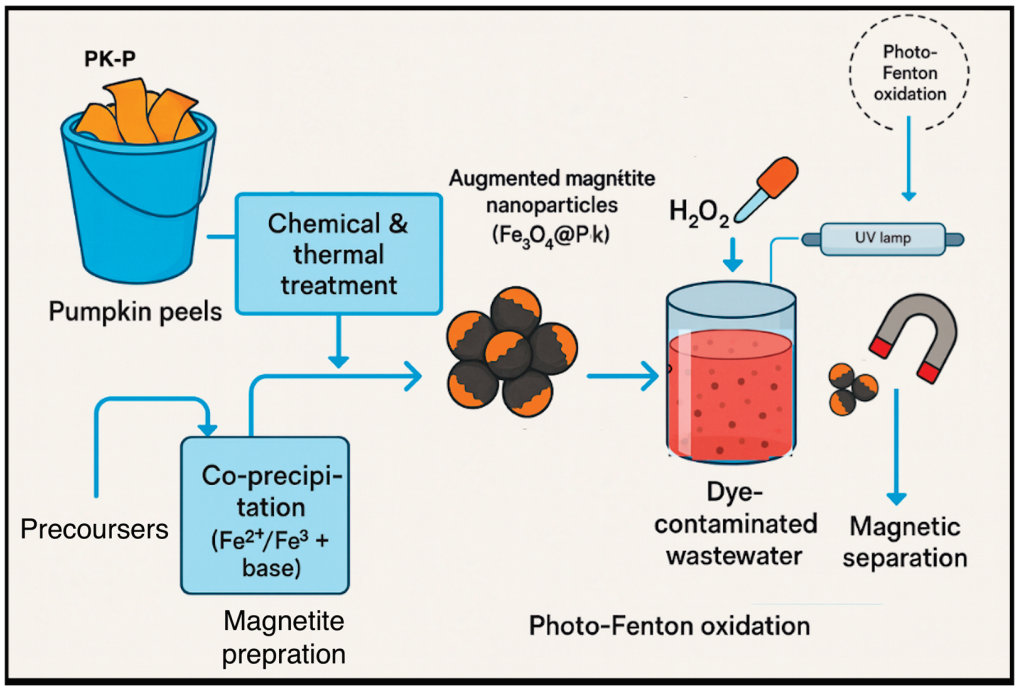


Figure 16. Schematic representation of the treatment steps.

Through the experiments, the samples are taken periodically for the object of analysis. The samples initially are filtered through a micro-filter and then exposed for spectrophotometric analysis using a Unico UV-2100 spectrophotometer (UNICO, Dayton, NJ, USA) model, with some modification.

For the kinetic experiments, a series of batch experiments were conducted in a thermostatically controlled reactor at different temperatures (32, 40, 50, and 60 °C) to examine the

influence of thermal variation on the reaction rate. The initial concentration of the Synozol Red KHL solution was fixed at 20 ppm, and the catalyst dosage and oxidant concentration were maintained constant throughout the tests to ensure comparability. During each run, aliquots of the reaction mixture were withdrawn at regular time intervals (5 min) for subsequent analysis using a UV–vis spectrophotometer at the maximum absorbance wavelength of the dye. The concentration at each time point was calculated using a pre-established calibration curve. To ensure reproducibility, all experiments were carried out in triplicate, and the reported values represent the average of three independent trials with standard deviations. Kinetic data were then evaluated according to different models.

4. Conclusions

A novel PK-P/Fe_3O_4 hybrid photocatalyst derived from pumpkin peel bio-waste and magnetite nanoparticles was successfully applied for the photo-Fenton oxidation of Synozol Red KHL dye. The catalyst demonstrated rapid and complete dye removal, excellent stability, and significant reusability, confirming its promise for repeated applications. Kinetic and thermodynamic evaluations further supported its efficiency, showing first-order behavior and an energy-efficient endothermic process. These findings establish bio-waste-derived PK-P/Fe_3O_4 as a sustainable, low-cost, and highly effective material for wastewater treatment. Thus, this work demonstrates that pumpkin peel-derived PK-P/Fe_3O_4 is a sustainable, low-cost, and energy-efficient photocatalyst with strong potential for scalable solar-driven wastewater treatment. Hence, future studies should focus on pilot-scale validation and the utilization of renewable solar irradiation to enhance the practicality and environmental benefits of this approach.

Author Contributions: Conceptualization, M.A.T., M.K.F. and H.A.N.; Methodology, M.M.N. and M.A.T.; Validation, M.A.T.; Formal analysis, M.K.F.; Writing—original draft, M.M.N., M.A.T. and H.A.N.; Writing—review and editing, M.M.N., M.A.T., M.K.F. and H.A.N.; Visualization, M.M.N. and H.A.N.; Supervision, H.A.N. All authors have read and agreed to the published version of the manuscript.

Funding: Prince Sattam bin Abdulaziz University through project number PSAU/2025/01/35045.

Data Availability Statement: Data available upon request.

Acknowledgments: The authors extend their appreciation to Prince Sattam bin Abdulaziz University for funding this research work through project number PSAU/2025/01/35045.

Conflicts of Interest: The authors declare no conflicts of interest.

References

1. Bidira, F.; Al-Senani, G.M.; Bekele, E.A.; Garomsa, F.S.; Vigneshwaran, S.; Al-Qahtani, S.D.; Asaithambi, P. Synergistic pollutant removal from brewery wastewater using electrocoagulation-assisted pumpkin seed-activated carbon. *Process Saf. Environ. Prot.* **2025**, *200*, 107429. [CrossRef]
2. Mangood, A.H.; Salama, E.S.; El Sayed, I.E.T.; Fouad, M.K.; Tony, M.A. Efficient Augmentation of Superparamagnetic Ferrite with Alum Sludge as a Sustainable Nanoadsorbent Matrix for Promoting Dye Removal: Preparation, Characterization and Application. *Int. J. Environ. Res.* **2025**, *19*, 1–23. [CrossRef]
3. Kızıl, Y.; Benek, V.; Teğin, İ.; Önal, Y.; Erol, K.; Alacabey, I. Reactive Blue 19 Adsorption on Activated Carbon from Pumpkin (Cucurbita Pepo) Seed Waste: Kinetic, Isotherm and Thermodynamic Studies, Journal of Environmental Research. *Eng. Manag.* **2024**, *80*, 7–20. [CrossRef]
4. Nour, M.M.; Tony, M.A.; Lee, W.H.; Nabwey, H.A. Opportunities of aluminum sludge dredging with soft magnetic conditioner for dewaterability enrichment. *Sci. Rep.* **2025**, *15*, 7796. [CrossRef]
5. Robinson, T.; McMullan, G.; Marchant, R.; Nigam, P. Remediation of dyes in textile effluent: A critical review. *Bioresour. Technol.* **2001**, *77*, 247–255. [CrossRef]
6. Forgacs, E.; Cserháti, T.; Oros, G. Removal of synthetic dyes from wastewaters: A review. *Environ. Int.* **2004**, *30*, 953–971. [CrossRef] [PubMed]

7. Zollinger, H. *Color Chemistry: Syntheses, Properties, and Applications of Organic Dyes and Pigments*; Wiley-VCH: Zurich, Switzerland, 2003.
8. Daneshvar, N.; Aber, S.; Dorraji, M.S.; Khataee, A.R.; Rasoulifard, M.H. Photocatalytic degradation of the insecticide diazinon in the presence of prepared nanocrystalline ZnO powders under irradiation of UV-C light. *Sep. Purif. Technol.* **2007**, *58*, 91–98. [CrossRef]
9. Ali, H. Biodegradation of synthetic dyes—A review. *Water Air Soil. Pollut.* **2010**, *213*, 251–273. [CrossRef]
10. Raji, F.; Maghool, S.; Shayesteh, H.; Rahbar-Kelishami, A. Effective adsorptive removal of Pb2+ ions from aqueous solution using functionalized agri-waste biosorbent: New green mediation via Seidlitzia rosmarinus extract. *Chemosphere* **2024**, *363*, 142759. [CrossRef]
11. Bhatnagar, A.; Minocha, A.K. Conventional and non-conventional adsorbents for removal of pollutants from water-A review. *Indian J. Chem. Technol.* **2006**, *13*, 203–217.
12. Fu, F.; Wang, Q. Removal of heavy metal ions from wastewater: A review. *J. Environ. Manag.* **2011**, *92*, 407–418. [CrossRef]
13. Al-Kdasi, A.; Idris, A.; Saed, K.; Guan, C.T. Treatment of textile wastewater by advanced oxidation processes. *Glob. Nest Int. J.* **2004**, *6*, 222–230.
14. Nour Manasik, M.; Tony, M.A.; Nabwey, H.A. Heterogeneous fenton oxidation with natural clay for textile levafix dark blue dye removal from aqueous effluent. *Appl. Sci.* **2023**, *13*, 8948. [CrossRef]
15. Pignatello, J.J.; Oliveros, E.; MacKay, A. Advanced oxidation processes for organic contaminant destruction. *Crit. Rev. Environ. Sci. Technol.* **2006**, *36*, 1–84. [CrossRef]
16. Nabwey Hossam, A.; Maha, A.T. Dewatered Sludge Decorated with Nanoparticles for Alum Sludge Conditioning towards the Concept of "End-of-Waste". *Nanomaterials* **2023**, *13*, 2903. [CrossRef]
17. Neyens, E.; Baeyens, J. A review of classic Fenton's peroxidation as an advanced oxidation technique. *J. Hazard. Mater.* **2003**, *98*, 33–50. [CrossRef] [PubMed]
18. Bautista, P.; Mohedano, A.F.; Casas, J.A.; Zazo, J.A.; Rodriguez, J.J. An overview of the application of Fenton oxidation to industrial wastewaters. *J. Chem. Technol. Biotechnol.* **2008**, *83*, 1323–1338. [CrossRef]
19. Deng, Y.; Englehardt, J.D. Treatment of landfill leachate by Fenton process. *Water Res.* **2006**, *40*, 3683–3694. [CrossRef]
20. Zhao, Q.; Yang, J.; Xia, J.; Zhao, G.; Yang, Y.; Zhang, Z.; Li, J.; Wei, F.; Song, W. Biomass Cellulose-Derived Carbon Aerogel Supported Magnetite-Copper Bimetallic Heterogeneous Fenton-like Catalyst Towards the Boosting Redox Cycle of ≡Fe(III)/≡Fe(II). *Nanomaterials* **2025**, *15*, 614. [CrossRef]
21. Wang, S.; Wang, J. Recent advances in heterogeneous Fenton-like catalysis for water treatment. *Chem. Eng. J.* **2019**, *373*, 624–641.
22. Sevilla, M.; Fuertes, A.B. The production of carbon materials by hydrothermal carbonization of cellulose. *Carbon* **2009**, *47*, 2281–2289. [CrossRef]
23. Chen, Q.; Tan, X.; Liu, Y.; Liu, S.; Li, M.; Gu, Y.; Zhang, P.; Ye, S.; Yang, Z.; Yang, Y. Biomass-derived porous graphitic carbon materials for energy and environmental applications. *J. Mater. Chem. A* **2020**, *8*, 5773–5811. [CrossRef]
24. Gillani, Q.F.; Bakbolat, B.; Tatykayev, B.; Sultanov, F.; Mentbayeva, A. Biomass-derived carbon materials for hydrogen storage: Structure-performance relationships and design strategies. *J. Energy Storage* **2025**, *135*, 118401. [CrossRef]
25. Bai, S.; Tan, G.; Li, X.; Zhao, Q.; Meng, Y.; Wang, Y.; Zhang, Y.; Xiao, D. Pumpkin-derived porous carbon for supercapacitors with high performance. *Chem. Asian J.* **2016**, *11*, 1869–1873. [CrossRef] [PubMed]
26. Vandana, T.U.; Tripathy, B.K.; Mishra, R.K.; Sharma, A.; Mohanty, K. A review on waste biomass-derived biochar: Production, characterisation, and advanced analytical techniques for pollutants assessment in water and wastewater. *Process Saf. Environ. Prot.* **2025**, *201*, 107505. [CrossRef]
27. Leichtweis, M.G.; Molina, A.K.; Petropoulos, S.A.; Carocho, M.; Pires, T.C.S.P.; Dias, M.I.; Calhelha, R.; Oliveira, M.B.P.P.; Pereira, C.; Barros, L. Valorization of Pumpkin Peel as a Source of Bioactive Compounds: Optimization of Heat- and Ultrasound-Assisted Extraction. *Molecules* **2023**, *28*, 3168. [CrossRef]
28. Añibarro-Ortega, M.; Pinela, J.; Ćirić, A.; Martins, V.; Rocha, F.; Soković, M.D.; Barata, A.M.; Carvalho, A.M.; Barros, L.; Ferreira, I.C.F.R. Valorisation of table tomato crop by-products: Phenolic profiles and in vitro antioxidant and antimicrobial activities. *Food Bioprocess. Technol.* **2020**, *124*, 307–319. [CrossRef]
29. Salami, A.; Asefi, N.; Kenari, R.E.; Gharekhani, M. Extraction of pumpkin peel extract using supercritical CO2and subcritical water technology: Enhancing oxidative stability of canola oil. *J. Food Sci. Technol.* **2021**, *58*, 1101–1109. [CrossRef]
30. Kang, S.F.; Liao, C.H.; Po, S.T. Decolorization of textile wastewater by photo-Fenton oxidation technology. *Chemosphere* **2000**, *41*, 1287–1294. [CrossRef]
31. Gavril Rațu, R.N.; Stoica, F.; Lipșa, F.D.; Constantin, O.E.; Stănciuc, N.; Aprodu, I.; Râpeanu, G. Pumpkin and Pumpkin By-Products: A Comprehensive Overview of Phytochemicals, Extraction, Health Benefits, and Food Applications. *Foods* **2024**, *13*, 2694. [CrossRef] [PubMed] [PubMed Central]

32. Nour, M.M.; Tony, M.A.; Nabwey, H.A. Immobilization of magnetic nanoparticles on cellulosic wooden sawdust for competitive Nudrin elimination from environmental waters as a green strategy: Box–Behnken design optimization. *Int. J. Environ. Res. Public. Health* **2022**, *19*, 15397. [CrossRef]
33. Tony, M.A.; Lin, L.-S. Iron recovery from acid mine drainage sludge as a Fenton source for municipal wastewater treatment. *Int. J. Environ. Anal. Chem.* **2020**, *100*, 1071–1083. [CrossRef]
34. Tolkou, A.K.; Tsoutsa, E.K.; Kyzas, G.Z.; Katsoyiannis, I.A. Sustainable use of low-cost adsorbents prepared from waste fruit peels for the removal of selected reactive and basic dyes found in wastewaters. *Environ. Sci. Pollut. Res. Int.* **2024**, *31*, 14662–14689. [CrossRef] [PubMed]
35. Yun Wang, Xiao-hui Xu, Juan Han, Yong-sheng Yan, Separation/enrichment of trace tetracycline antibiotics in water by [Bmim]BF_4–$(NH_4)2SO_4$ aqueous two-phase solvent sublation. *Desalination* **2011**, *266*, 114–118. [CrossRef]
36. Shamshad, J.; Ur Rehman, R. Innovative approaches to sustainable wastewater treatment: A comprehensive exploration of conventional and emerging technologies. *Environ. Sci. Adv.* **2025**, *4*, 189–222. [CrossRef]
37. Zhang, T. Sustainable wastewater treatment and the circular economy. *Water* **2025**, *17*, 335. [CrossRef]
38. Hung, Y.-T. Advances in biotechnologies for water and wastewater treatment. *Water* **2025**, *17*, 509. [CrossRef]
39. Lee, C.; Lin, L.-S.; Martínez-Huitle, C.A.; Pensini, E. Towards decentralized and sustainable water and wastewater treatment technologies. *Sci. Rep.* **2025**, *15*, 14331. [CrossRef]
40. Islam, F.A.S. Advanced wastewater treatment technologies in addressing future water scarcity through resource recovery and reuse. *J. Eng. Res. Rep.* **2025**, *27*, 370–398. [CrossRef]
41. Rossi, S.; Capson-Tojo, G.; Sànchez-Zurano, A.; Carecci, D.; Batstone, D.J.; Acièn-Fernandez, G.F.; Ficara, E. Recent advances and challenges in mechanistic modelling of photosynthetic processes for wastewater treatment. *Water Res.* **2025**, *278*, 123216. [CrossRef]
42. Chiang, P.C.; Chang, E.E.; Liang, C.H. NOM characteristics and treatabilities of ozonation processes. *Chemosphere* **2002**, *46*, 929–936. [CrossRef]
43. Daneshvar, N.; Salari, D.; Khataee, A.R. Photocatalytic degradation of azo dye acid red 14 in water on ZnO as an alternative catalyst to TiO_2. *J. Photochem. Photobiol. A: Chem.* **2004**, *162*, 317–322. [CrossRef]
44. Bhatnagar, A.; Sillanpää, M. Utilization of agro-industrial and municipal waste materials as potential adsorbents for water treatment—A review. *Chem. Eng. J.* **2010**, *157*, 277–296. [CrossRef]
45. Thiam, A.; Salazar, R.; Brillas, E.; Sirés, I. In-situ dosage of Fe2+ catalyst using natural pyrite for thiamphenicol mineralization by photoelectro-Fenton process. *J. Environ. Manag.* **2020**, *270*, 110835. [CrossRef] [PubMed]
46. Jain, A.; Ong, S.P.; Hautier, G.; Chen, W.; Richards, W.D.; Dacek, S.; Cholia, S.; Gunter, D.; Skinner, D.; Ceder, G.; et al. Commentary: The Materials Project—A Materials Genome Approach to Accelerating Materials Innovation. *APL Mater.* **2013**, *1*, 011002. [CrossRef]
47. Wu, C.-C.; Chen, D.H. Spontaneous Synthesis of Gold Nanoparticles on Gum-Arabic–Modified Magnetic Nanoparticles. *Nanoscale Res. Lett.* **2012**, *7*, 182. [CrossRef]
48. Donadel, K.; Felisberto, M.D.; Laranjeira, M.C. Preparation and characterization of hydroxyapatite-coated iron oxide particles by spray-drying technique. *Acad Bras Cienc* **2009**, *81*, 179–186. [CrossRef] [PubMed]
49. Li, H.; Dong, X.; da Silva, E.B.; de Oliveira, L.M.; Chen, Y.; Ma, L.Q. Mechanisms of metal sorption by biochars: Biochar characteristics and modifications. *Chemosphere* **2017**, *178*, 466–478. [CrossRef]
50. Thommes, M.; Kaneko, K.; Neimark, A.V.; Olivier, J.P.; Rodriguez-Reinoso, F.; Rouquerol, J.; Sing, K.S.W. Physisorption of gases, with special reference to the evaluation of surface area and pore size distribution (IUPAC Technical Report). *Pure Appl. Chem.* **2015**, *87*, 1051–1069. [CrossRef]
51. Haddad, M.; Regti, A.; Laamari, M.R.; Mamouni, R.; Saffaj, N. Use of Fenton reagent as advanced oxidative process for remov-ing textile dyes from aqueous solutions. *J. Mater. Environ. Sci.* **2014**, *5*, 667–674.
52. Youssef, N.S.; Shaban, A.; Ibrahim, F.A.; Mahmoud, A.S. Degradation of methyl orange using Fenton catalytic reaction. *Egy. J. Pet.* **2016**, *25*, 317–321. [CrossRef]
53. Xu, H.; Lu, G. On-line spectrophotometric method for decolourizing reaction kinetics of reactive black 5 by Fenton oxidation. *Asian J. Chem.* **2013**, *25*, 7989–7992. [CrossRef]
54. Thabet, R.H.; Fouad, M.K.; El Sherbiny, S.A.; Tony, M.A. Construction of a hetero-junction recyclable composite photocatalyst from aluminum-based waste/magnetite for efficient carbamate insecticide oxidation. *Environ. Sci. Water Res. Technol.* **2022**, *8*, 1874–1894. [CrossRef]

Disclaimer/Publisher's Note: The statements, opinions and data contained in all publications are solely those of the individual author(s) and contributor(s) and not of MDPI and/or the editor(s). MDPI and/or the editor(s) disclaim responsibility for any injury to people or property resulting from any ideas, methods, instructions or products referred to in the content.

catalysts

MDPI

Article

FeCo-LDH/CF Cathode-Based Electrocatalysts Applied to a Flow-Through Electro-Fenton System: Iron Cycling and Radical Transformation

Heng Dong, Yuying Qi, Zhenghao Yan, Yimeng Feng, Wenqi Song, Fengxiang Li * and Tao Hua *

Key Laboratory of Pollution Process and Environmental Criteria, Ministry of Education, China Tianjin Engineering Center of Environmental Diagnosis and Contamination Remediation, College of Environmental Science and Engineering, Nankai University, 38 Tongyan Road, Tianjin 300350, China
* Correspondence: lifx@nankai.edu.cn (F.L.); huatao@nankai.edu.cn (T.H.)

Abstract

In this investigation, a hierarchical FeCo-layered double hydroxide (FeCo-LDH) electrochemical membrane material was prepared by a simple in situ hydrothermal method. The prepared material formed a 3D honeycomb-structured FeCo-LDH-modified carbon felt (FeCo-LDH/CF) catalytic layer with uniform open pores on a CF substrate with excellent catalytic activity and was served as the cathode in a flow-through electro-Fenton (FTEF) reactor. The electrocatalyst demonstrated excellent treatment performance (99%) in phenol simulated wastewater (30 mg L^{-1}) under the optimized operating conditions (applied voltage = 3.5 V, pH = 6, influent flow rate = 15 mL min^{-1}) of the FTEF system. The high removal rate could be attributed to (i) the excellent electrocatalytic oxidation performance and low interfacial charge transfer resistance of the FeCo-LDH/CF electrode as the cathode, (ii) the ability of the synthesized FeCo-LDH to effectively promote the conversion of H_2O_2 to •OH under certain conditions, and (iii) the flow-through system improving the mass transfer efficiency. In addition, the degradation process of pollutants within the FTEF system was additionally illustrated by the •OH dominant ROS pathway based on free radical burst experiments and electron paramagnetic resonance tests. This study may provide new insights to explore reaction mechanisms in FTEF systems.

Keywords: Heterogeneous Electro-Fenton; FeCo-layered double hydroxide; redox cycle; electrocatalysis; phenol

1. Introduction

At present, phenol, exemplified by phenol, have garnered considerable attention on account of their deleterious effects on humans and the environment. Phenol undergoes selective hydrogenation to yield a range of valuable by-products, including hexanone and cyclohexanol. In addition to this, it is a crucial raw material particularly in the production of bisphenol A [1,2]. Estimates suggest that each year a significant volume of phenolic waste is released into the environment without undergoing treatment. Studies have demonstrated that prolonged human exposure to phenol at lethal levels can evoke a series of physiological effects, including breathing distress and injury to brain tissues [1,3–6], in addition to impacts on water, soil, and air as a result of its solubility when released. Furthermore, the release of it into the environment can have detrimental effects on water, soil, and air due to its solubility. In recent years, current wastewater treatment technologies for phenol-containing wastewater have faced a number of challenges. These include low treatment efficiency, high

energy consumption, and expensive operating costs. Balancing efficiency and cost become challenging when relying solely on one treatment technology. As a case in point, membrane separation technology boasts a number of key advantages, including low chemical use, high scalability, and a compact equipment footprint. However, it should be noted that the retention and adsorption of membrane modules can limit the removal of organic pollutants, and these modules are prone to fouling problems during operation; furthermore, the traditional Fenton has the problems of slow Fe^{2+} regeneration and low utilization rate of H_2O_2, and the utilization rate of H_2O_2 can reach 99.7% [7]. Electrochemical advanced oxidation processes (EAOPs) generate free radicals with strong oxidizing capacity, which can mineralize organic matter, thus exhibiting excellent pollutant removal ability. Batool et al. studied the MnO_2-CC electrocatalytic system, and the mineralization rate of TCS was over 99% [8]. It must be emphasized, however, that EAOPs inherently demand significant energy input and are vulnerable to the formation of toxic by-products and other drawbacks. Consequently, it is imperative to select a treatment technology that is highly efficient in the removal of phenolics.

Electro-Fenton (EF), a subset of advanced oxidation processes (AOPs), relies on a functional cathode to produce H_2O_2 via a two-electron oxygen reduction reaction ($2e^-$ORR) (Equations (1) and (2), where * represents the unoccupied active site while HOO^* signifies the formation of the single adsorption intermediate) [9–11]. Subsequently, H_2O_2 reacts with Fe^{2+} to produce •OH radicals (Equation (3)), which degrade organic pollutants. Meanwhile, the cathode continuously regenerates Fe^{2+} via reduction (Equation (4)). Within the EF system, pollutant removal relies on the non-selective reactivity of •OH radicals. Consequently, boosting •OH concentration and optimizing H_2O_2 conversion are imperative to elevate the degradation efficiency of phenol [12–14]. Flow-through electro-Fenton (FTEF), an enhanced variant of the conventional Fenton process, operates by applying an external electric field. This architecture facilitates the cyclic regeneration of Fe^{2+} ions, consequently minimizing the formation of iron-based sludge and curbing the consumption of iron-based reagents [15]. Electrodes featuring a high specific surface area and serving as dual-function filtration media [16], have demonstrated improved mass transfer efficiency for pollutants. These electrodes are widely regarded for their high efficiency. Notwithstanding its merits, the technology is hampered by two key drawbacks: the low generation efficiency of •OH, the dominant reactive agent in EF [17], and the sluggish Fe^{3+} reduction to Fe^{2+}, where Fe^{2+} depletion happens at a rate roughly three orders of magnitude faster than its renewal. Further enhancements are imperative to augment the permeate flux across electrodes and fabricate electrodes with elevated electroactive surface areas in FTEF systems [18].

$$M + H_2O \rightarrow M(\bullet OH) + H^+ + e^- \quad (1)$$

$$HOO^* + H^+ + e^- \rightarrow H_2O_2^* \quad (2)$$

$$Fe^{2+} + H_2O_2 \rightarrow Fe^{3+} + \bullet OH + OH^- \quad (3)$$

$$Fe^{3+} + e^- \rightarrow Fe^{2+} \quad (4)$$

In recent decades, transition metal-based materials, such as Ni-, Fe- and Co-based compounds, have emerged as highly promising catalysts owing to their adjustable electronic structure and diverse nanoscale architectures. Recent studies highlight that Fe-Co-based and Co-containing base metal electrocatalysts have shown notable efficacy in key green reactions. Kuznetsova et al. and Zhou et al. both demonstrated such catalysts' effectiveness in nitrate-related sustainable processes [19,20]. And extensive studies have confirmed that the CoFe-LDH cathode exhibits a wide range of anion tolerance and pH adaptability. Their layered structure exhibits stability in a variety of ionic environments due to selec-

tive oxygen anion adsorption and pH-buffered anion exchange, while surface hydroxyl groups (-OH) enable efficient H_2O_2 activation under acidic to alkaline conditions by acting as pH-dependent charge regulators [21–23]. Among them, layered double hydroxide (LDHs) materials consisting of coplanar octahedral MO_6 layers have drawn significant attention due to their large specific surface area (>100 $m^2\ g^{-1}$) and fast anion transfer channels [24], and moreover, the catalytic performance is significantly enhanced by the synergistic effect of the laminar metal elements, which have been verified as efficient for Oxygen Evolution Reaction (OER) [25–28]. It has been shown that Fe- and Co-based LDHs materials exhibit excellent pollutant mineralization in the electro-Fenton system, and the $Fe^{II}Fe^{III}$-LDH cathode degraded the antibiotic sulfamethoxazole with an efficiency of up to 98% (120 min) [29]. However, the inherent poor conductivity characteristic of LDHs restricts the enhancement of their electrocatalytic performance and application [30–32], and in order to obtain higher electrocatalytic performance, the augmentation of active site quantity (specific surface area), regulation of electronic properties, and modification of surface properties are imperative for electrocatalysts. In the previous literature, the FeCo-LDH system demonstrated a dual reaction center mechanism, where the Co site was able to enhance the $2e^-$ORR selectivity to more than 85% by optimizing the *OOH adsorption free, while the Fe site significantly promoted H_2O_2 activation by accelerating the Fe^{2+}/Fe^{3+} redox cycle (kobs = 0.67 s^{-1}) (Equations (3) and (4)). The synergistic interaction between the two metals led to a 3.2-fold enhancement in the apparent rate constant for phenol degradation relative to the monometallic system [33]. Notably, Fe substantially boosted the catalytic activity of the Co-based material (Equations (5)–(7)) [31].

$$Co^{3+} + e^- \rightarrow Co^{2+} \quad (5)$$

$$Fe^{3+} + Co^{2+} \rightarrow Fe^{2+} + Co^{3+} \quad (6)$$

$$Co^{2+} + H_2O_2 \rightarrow Co^{3+} + \bullet OH + OH^- \quad (7)$$

In this study, FeCo-LDH/CF electrochemical membrane was prepared by a simple in situ hydrothermal method. In this experiment, this was used as the membrane electrode material and applied in an FTEF to investigate the operation mechanism with the goal of improving the degradation performance and exploring the mechanism. The morphology of the cathode membrane electrode was characterized using scanning electron microscopy (SEM), combined with X-ray photoelectron spectroscopy (XPS), X-ray diffraction (XRD), and Fourier-transform infrared spectrometry (FT-IR); the synthesized electrochemical membranes were characterized for their electrochemical performances using an electrochemical workstation (CHI660E), and the system was also studied through the stability analysis, versatility analysis, and energy consumption analysis performance studies. Quenching experiments, electron paramagnetic resonance (EPR), and free radical trapping assays were employed to identify Reactive Oxygen Species (ROS) and elucidate the phenol degradation mechanism in the Fenton system. The results indicated that hydroxyl radicals served as the dominant oxidizing radicals in the system. The system's design integrates a flow-through architecture to enhance interfacial mass transfer rates, alongside electrochemical membranes with high active site loading to optimize filtration electrocatalytic oxidation and free radical conversion. To further boost degradation performance, the reaction mechanism from reactants, intermediates to products were comprehensively studied.

2. Results and Discussion

2.1. The Electrode Structure Enables Catalytic Activity

The morphology of the materials synthesized under various conditions was obtained by SEM, and the SEM photographs of the virgin CF, FeCo-LDH powder, and FeCo-LDH/CF composites synthesized at 70 °C, 90 °C, and 120 °C for 12 h are presented in Figure 1. The carbon fibers of the pristine CF have a cross-packed pore structure (Figure 1a,b). A large number of FeCo-LDH showing anisotropic growth appeared on the CF produced by solvothermal synthesis, and the FeCo-LDH/CF synthesized at different temperatures showed different morphological and structural characteristics. When the synthesis temperature was 70 °C, FeCo-LDH showed an agglomerated but interstitial particle morphology on the CF substrate (Figure 1c,f), which indicated that only the LDH particles nucleated at this temperature [32]. Upon raising the synthesis temperature to 90 °C, FeCo-LDH with a lamellar hexagonal morphology grew perpendicularly on CF (Figure 1d,g), forming a 3D honeycomb structure with uniformly open pores, which can provide abundant reaction sites for the catalytic reaction. While some studies have shown that FeCo-LDH can achieve higher density growth on CF substrates at 120 °C than at 70 °C and 90 °C [27,34,35], but in this study, after the synthesis temperature was increased to 120 °C, the FeCo-LDH grown on CF was in the form of fragmented flakes or filaments, where the FeCo-LDH underwent intensive growth. After that, the honeycomb structure began to collapse. The structure of FeCo-LDH powder generated at 120 °C further illustrates the collapse of the honeycomb structure (Figure 1e). The data indicate that this temperature may compromise structural integrity. Crucially, XRD results (Figure 2a) provide complementary evidence that samples synthesized at 120 °C exhibit broadened diffraction peaks and reduced crystallinity, indicating lattice disorder and degraded crystal quality. This morphological deterioration correlates directly with diminished electrochemical performance. Thus, 90 °C is optimal for preserving the performance-critical honeycomb structure under these synthesis conditions. At this point, a portion of hexagonal flaky FeCo-LDH is still present, but its structure changes from a honeycomb to a rod or filamentary sea urchin structure [36]. The FeCo-LDH powder obtained by Imran Shakir et al. synthesized at 130 °C for 10 h has an intercalated structure of varying sizes [37]. The FeCo-LDH powder obtained by synthesizing at 90 °C for 7 h was a dense sea urchin-like structure, and the FeCo-LDH powder obtained by synthesizing at 90 °C for 21 h has the same structure, but a slight collapse was observed at 50 μm scale, and the degradation rate of the sea urchin-like structure dropped after the first cycle (11%), and the degradation rate exceeded 60% after the seventh cycle, which presents that the sea urchin-like structure is less effective than the sea urchin structure in the electrocatalytic field, which is not better than the honeycomb structure. Energy dispersive X-ray (EDX) spectral results (Figure 1i–l) showed the homogeneous distribution of O, C, Fe, and Co elements over FeCo-LDH/CF.

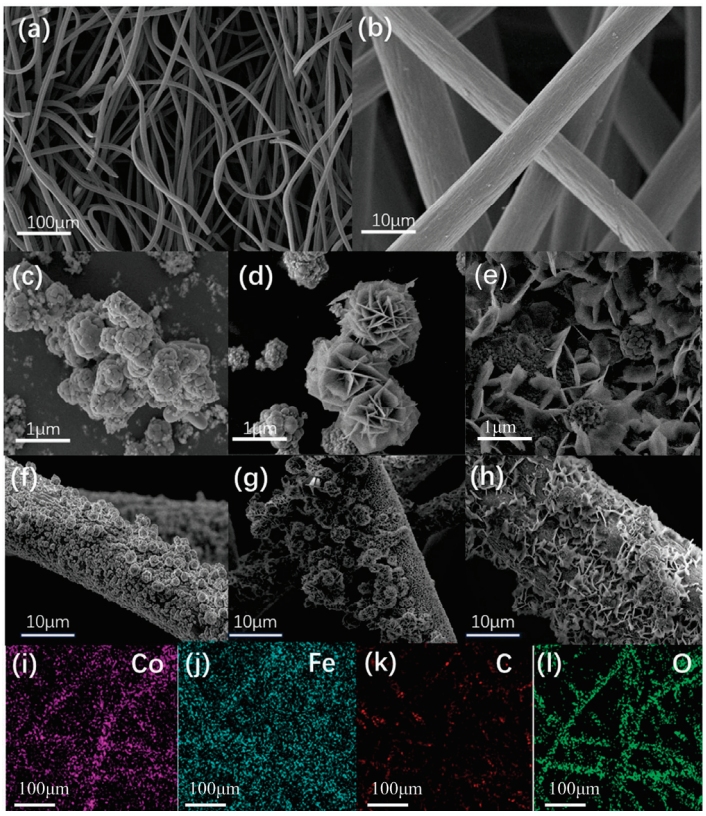


Figure 1. SEM and EDX results of the materials: (**a**,**b**) are the SEM images of the pristine carbon mats; (**c**–**e**) are the SEM images of FeCo-LDH powders prepared by synthesizing the powders at 70 °C, 90 °C, and 120 °C for 12 h, respectively; (**f**–**h**) are the SEM images of FeCo-LDH/CF prepared by synthesizing the powders at 70 °C, 90 °C, and 120 °C for 12 h, respectively; (**i**–**l**) EDX analysis of FeCo-LDH/CF prepared by 12 h of synthesis at 90 °C, respectively.

To further analyze the synthesis of FeCe-LDH as well as the crystalline grains, the XRD patterns of FeCo-LDH powders obtained by synthesizing them for 12 h at temperatures of 70 °C, 90 °C, and 120 °C, separately, were tested (Figure 2a), the XRD patterns were analyzed using MDI Jade software (9.0) with the ICDD PDF-2 database (MDI-500.csd internal index), and all the samples showed characteristic diffraction peaks at 11.9°, 23.7°, 34.3°, 35.4°, 46.5°, and 61.1°, which are in good agreement with the reported FeCo-LDH characteristic lattice planes (003), (006), (012), (009), (018), and (113) in good agreement [27,38], which indicates the successful synthesis of FeCo-LDH on CF substrate, and sharp (003)/(006) XRD peaks confirm highly ordered stacking of 90 °C-synthesized FeCo-LDH. Notably, peak positions across all samples remain largely unchanged, though their intensities exhibit temperature-dependent variations. Specifically, samples synthesized at 120 °C show diminished characteristic peak intensity compared to those prepared at lower temperatures. The intensity of characteristic peaks in the samples decreased, while the diffraction peaks originally located at 61.1° and 64.7° vanished completely, indicating that the temperature affects both the lattice parameters and crystallization of FeCo-LDH [27,35]. Additional crystalline phases were identified, while the LDH phase supported on the CF substrate showed typical purity. FTIR spectroscopy (Figure 3a) unveiled functional groups in FeCo-LDH synthesized at varying temperatures, with a characteristic hydroxyl stretching band observed between 2500 cm^{-1} and 3900 cm^{-1} in the typical LDH structure. The FTIR spectra of FeCo-LDH prepared at 70 °C and 90 °C exhibit subtle peak variations near 3500 cm^{-1}, which stem from stretching and bending deformation of M•OH (M=Fe, Co). On the contrary, the absorption bands at 33,258.79 cm^{-1}, 3321.70 cm^{-1}, and 3498.64 cm^{-1} in FeCo-LDH are associated with stretching vibrations of hydrogen-bonded O-H groups, which arise from water molecules

adsorbed on the surface or within interlayers. [39]. At 1640.92 cm^{-1} and 1644.71 cm^{-1}, the observed absorption bands relate to H-O-H bending vibrations in water molecules held by hydrogen bonding [35]. A strong absorption band observed at 1500.84 cm^{-1} in the FTIR spectrum of FeCo-LDH synthesized at 120 °C is attributed to the N-O stretching vibration of nitrate anions adsorbed on the surface and in interlayer spaces, exposing more active sites. While conventional synthesis (120–150 °C) typically promotes nitrate intercalation, our XRD data reveal compromised crystallinity at 120 °C (broadened peaks in Figure 2a) and our catalytic results, strongly suggesting the predominant species is surface-bound organic nitro (-NO_2) rather than intercalated nitrate [40]. These anions are derived from the nitrate salts (i.e., $Co(NO_3)_2 \cdot 6H_2O$ and $Fe(NO_3)_3 \cdot 9H_2O$) incorporated during material preparation [34]. In addition, due to the adsorption of CO_2 gas from the atmosphere or CO_2 from the decomposition of urea added during the hydrothermal reaction in the interlayers of the LDH structure, stretching vibrations belonging to the CO_3^{2-} at 1053.16 cm^{-1}, 1382.80 cm^{-1}, and 1384.18 cm^{-1}, separately, appeared [41]. The absorption peaks detected in the lower wavenumber regions (699.67 cm^{-1} and 836.75 cm^{-1}, 700.67 cm^{-1} and 809.26 cm^{-1}, 693.04 cm^{-1}, and 831.23 $cm^{-1,}$ respectively) can be assigned to the stretching vibrations of M-O or O-M-O bonds (M=Fe, Co) in FeCo-LDH [27].

To confirm the chemical environments of elements, XPS measurements were carried out on FeCo-LDH powders prepared via 12 h synthesis at 70 °C, 90 °C, and 120 °C. The recorded spectra included the full scan, along with high-resolution scans of C 1s, O 1s, Fe 2p, and Co 2p. In the samples the elements Co, Fe, C, O and F were detected (Figure 2b), respectively, and the element F appeared in comparison with the EDS test results, which was probably introduced by the ammonium fluoride used in the synthesis process and the possible role of F is to neutralize the excess positive charge in the LDH layer [34]. The highest peak of F was found in the sample synthesized at 90 °C, which may be a result of the better synthesis of LDH. Split-peak fitting of C1s showed three characteristic signal peaks (Figure 2c): the characteristic peaks of C-C at 284.80 eV, C-O at 285.55 eV, and C=O at 288.69 eV, respectively, with C-C having the highest relative abundance. The O1s spectra (Figure 2d) show three distinct peaks: those at 530.31 eV and 531.62 eV correspond to lattice oxygen and unsaturated oxygen (i.e., M-O and M•OH, M=Fe, Co), respectively, while the peak at 532.31 eV is assigned to physically and chemically adsorbed H2O in the FeCo-LDH nanostructure [42]. It is clear that the intensity of M•OH bonds increases significantly with increasing temperature, but the intensity of peaks associated with M-O decreases significantly at 120 °C, whereas the highest content of M-O and M•OH is found in the material obtained at 90 °C, suggesting that at this time, FeCo-LDH contains more oxygen-containing compounds associated with the catalytic reaction [43]. The Fe 2p profiles (Figure 2e) of FeCo-LDH obtained at both 70 °C and 90 °C showed two main peaks at 711.86 eV and 724.96 eV, corresponding to Fe $2p_{1/2}$ and Fe $2p_{3/2}$, respectively, whereas the peaks at 718.92 eV and 734.41 eV belonged to the satellite peaks, which indicated that a high spin was present in the LDH material. In summary, FeCo-LDH/CF synthesized at 90 °C exhibits structural advantages due to its honeycomb structure (Figure 1d,g), high crystallinity (XRD, Figure 2a), and bimetallic synergism (XPS, Figure 2e,f). In the following section, the catalytic mechanism and performance limits will be further revealed by combining electrochemical tests (CV, EIS) and the optimization of system operating parameters.

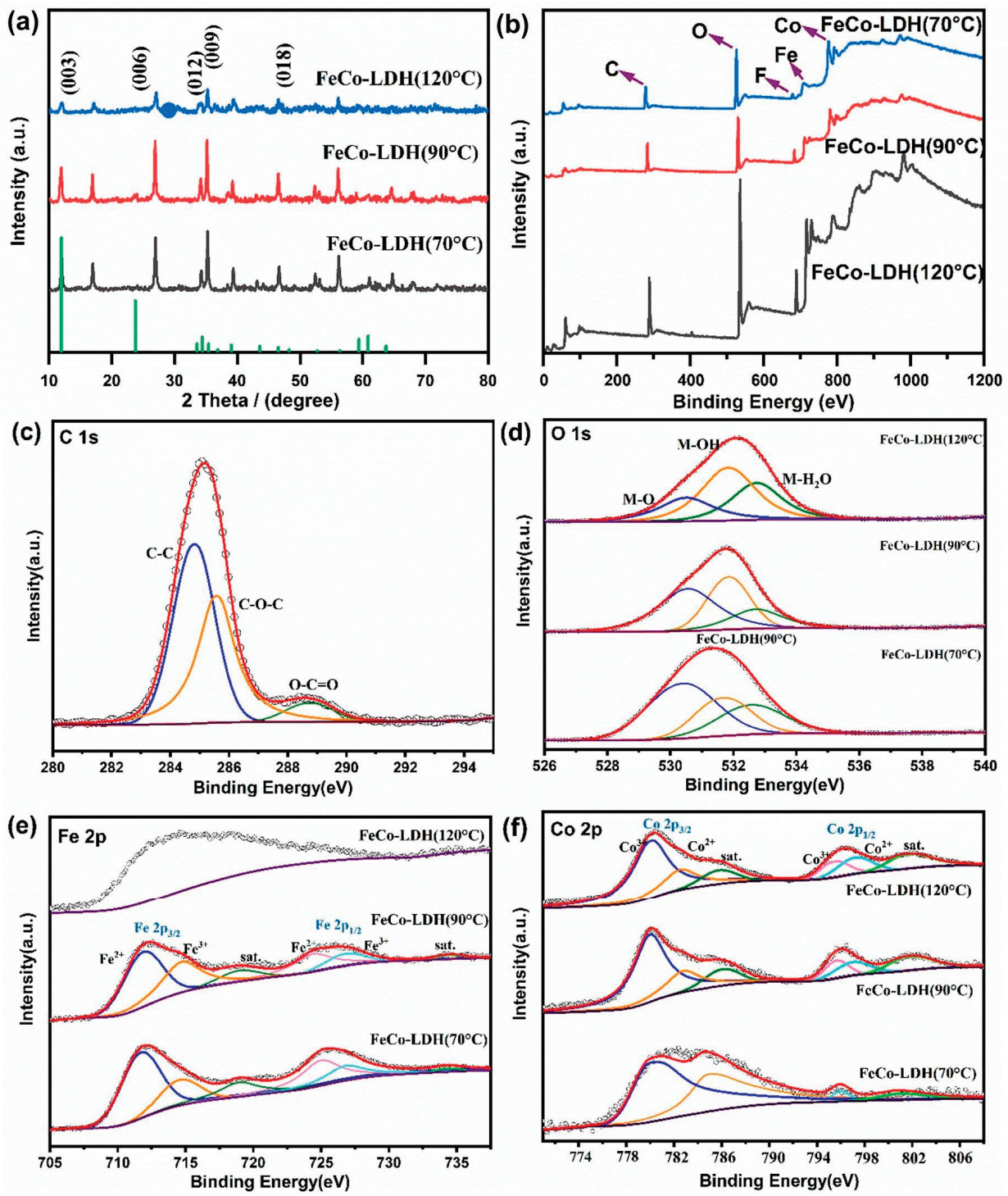


Figure 2. XRD and XPS spectra of the synthesized materials under different conditions (**a**) XRD images of FeCo-LDH powders prepared by synthesizing at 70 °C, 90 °C, and 120 °C for 12 h (phase identification was performed using the ICDD PDF-2 database, with the matched PDF card number 50-0235). (**b**) XPS full spectrum of FeCo-LDH powders synthesized at 70 °C, 90 °C, and 120 °C. (**c**) C 1s high-resolution spectrum. (**d**) O 1s high-resolution spectrum. (**e**) Fe 2p high-resolution spectrum. (**f**) Co 2p high-resolution spectrum.

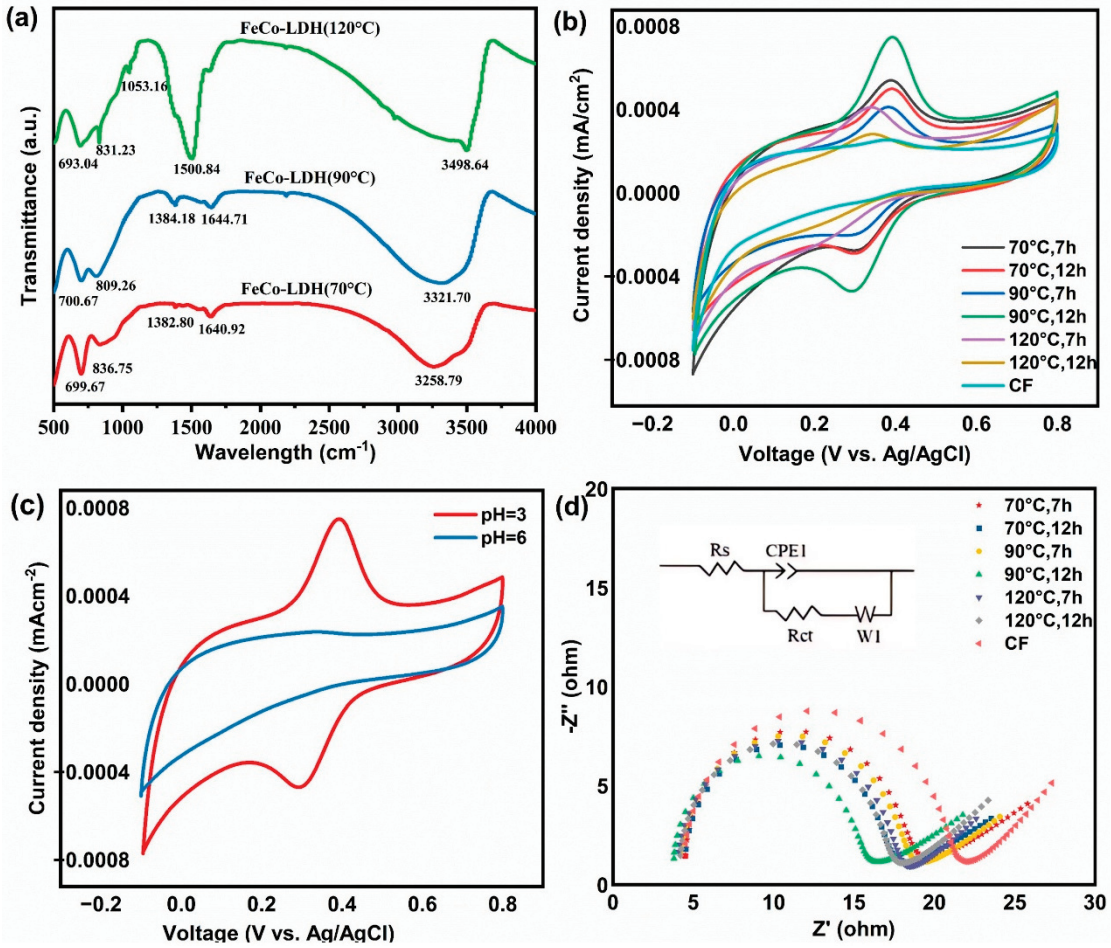


Figure 3. FTIR profiles and electrochemical properties of materials synthesized under different conditions: (**a**) FTIR profiles of FeCo-LDH powders fabricated at 70 °C, 90 °C, and 120 °C for 12 h, individually. (**b**) CV tests of different FeCo-LDH/CF and CF films in O_2-saturated 50 mM Na_2SO_4 electrolyte at pH = 3, with a scanning rate of 10 mV/s and a potential range of −0.1 to 0.8 V (vs. Ag/AgCl). (**c**) CV profiles of FeCo-LDH/CF (synthesized at 90 °C for 12 h) in O_2-saturated 50 mM Na_2SO_4 electrolyte under pH 3 and pH 6 conditions, with a scanning rate of 10 mV/s and a potential range of −0.1 to 0.8 V (vs. Ag/AgCl). (**d**) EIS curves of different FeCo-LDH/CF and CF films in O_2-saturated 50 mM Na_2SO_4 electrolyte, measured at open circuit potential with a frequency range of 0.01 to 1,000,000 Hz and an AC amplitude of 0.01 V.

2.2. Optimization of System Performance

Building on the structural characterization in Section 3.1, cyclic voltammetry (CV) and electrochemical impedance spectroscopy (EIS) were employed to access the electrochemical properties of FeCo-LDH/CF. This aimed to elucidate how the material structure influences catalytic activity. The CV curves of FeCo-LDH/CF in 50 mM Na_2SO_4 obtained under different treatment conditions are shown in Figure 3b,c; for the CF film, no obvious reversible oxidation/reduction peaks were found. The FeCo-LDH/CF integral area was significantly larger than that of the other materials, indicating that the materials have more active surface sites. However, to further test the electrocatalytic performance of the material in different pH environments, a CV curve test was added for pH = 6 (Figure 3c), at which time there was no obvious redox peak. A short-term appearance of obvious reversible oxidation/reduction peaks at pH = 3 suggests that there was a leaching of Fe^{3+}, and Co^{2+} into solution under acidic conditions, exposing more active sites and thus briefly increasing the electrochemical activity. Many studies have proved that initial leaching of transition metals can generate vacancies or defects, transiently enhancing activity by

exposing underlying active sites [42]. Metal ion leaching may induce alterations in the microenvironment of the electrode interface, thereby promoting side reactions. Additionally, LDH exhibits lower stability under strongly acidic conditions. The metal leaching measurement further verified this analysis, while further analysis is needed to observe the trend of current density and CV peak shape with time, as well as to further validate the activation effect and side-reaction interference (excluding metal ion contribution). Jia et al. explored the level of cobalt leaching under neutral water conditions [44]. Ganiyu et al. observed that the peak current rose as the pH value decreased, and there was no significant redox peak at pH 5.83 due to the stability of the material [34]. The lack of distinct redox peaks at pH = 6 demonstrates the coating's high stability [34,45]. The electrochemical impedance spectroscopy (EIS) technique was employed to assess the electrical conductivity of the prepared electrochemical membranes, as illustrated in Figure 3d. The obtained EIS data were fitted using an equivalent circuit model, in which RS represents the series resistance, primarily associated with the solution resistance; RCT denotes the interfacial charge transfer resistance; CPE1 serves as the non-ideal capacitive element applied in the fitting process; and W1 indicates the Warburg impedance. Notably, the diameter of the semicircle in the EIS plot corresponds to the actual magnitude of RCT. The RCT values of the pure CF material and the material obtained from the synthesis condition of 90 °C for 12 h are 21.6 Ω and 15.9 Ω, respectively. The FeCo-LDH coating enhances the conductivity of CF, and with the incorporation of electrode materials, the charge transfer resistance decreases, leading to enhanced charge transfer efficiency and an accelerated electrochemical reaction rate. This phenomenon indicates a high density of active sites within the material. The above electrochemical tests showed that FeCo-LDH/CF has excellent ORR activity and electron transfer efficiency. In order to further evaluate its potential for practical applications, this study conducted a systematic investigation into the impacts of operational parameters on the phenol degradation rate.

The FeCo-LDH/CF composite served as the cathode in an FTEF system, where phenol was employed as a model contaminant to evaluate phenol elimination efficiency and system-wide H_2O_2 generation. Experiments were conducted under conditions of 100 mM Na_2SO_4 electrolyte, a 3.5 V applied potential, and pH = 6 (Figures S3 and S4). It was shown that the average concentration of H_2O_2 generated by FeCo-LDH/CF at 90 °C for 12 h of synthesis conditions was lower than that of CF, which was only 65 μmol L^{-1}, but 100% degradation rate could be achieved [27,46]. It stems from its ordered structural superiority and bimetallic center, which significantly promotes H_2O_2 transformation [22,40]. Within 20 min from the beginning of the reaction, the H_2O_2 yields of all the materials were low due to mass transfer limitations. After experimental observation, when the CF membrane was used as the electrode, the phenol removal was only 49% after 150 min of reaction, which could not be carried out due to the lack of catalyst Fenton reaction. At this time, the phenol removal was contributed by the anodic oxidation, and the average concentration of the generated H_2O_2 in the system was 96 μmol L^{-1}. It is noteworthy that, after the addition of FeCo-LDH to the FTEF system, three cathodic membranes showed slightly lower removal efficiencies of phenol than the CF cathodic membrane in the first 30 min of the reaction, which may be attributed to the agglomeration phenomenon of the catalysts on the three cathodic membranes or the higher thickness of the loaded catalytic layer, which increased the mass-transfer resistance and resulted in a slower catalytic rate for the generation of •OH from H_2O_2. However, after 30 min, the degradation efficiency of all FeCo-LDH/CF membranes for phenol exceeded that of CF membranes, which could be ascribed to the abundance of electroactive sites in the FeCo-LDH catalytic layer. Of the average concentrations of H_2O_2 generated by FeCo-LDH/CF at 90 °C, 12 h, and 120 °C, 12 h synthesis conditions were lower than that of CF, especially FeCo-LDH/CF at 90 °C,

12 h, which was only 65 μmol L^{-1}. This phenomenon can be ascribed to the mesoporous hydrotalcite structure of the material, which imparts a larger electrochemical surface area to it. Such a structure provides abundant active sites for heterogeneous catalytic reactions, aligning well with the SEM, CV, and EIS results. These characterizations revealed robust electrocatalytic performance, enabling rapid decomposition of pollutants by in situ generated H_2O_2 and efficient electron cycling starting from the 20th minute of the reaction. FeCo-LDH/CF membranes obtained at a synthesis temperature of 70 °C produced on average 207 μmolL^{-1} of hydrogen peroxide, but the phenol removal performance was poor, probably because at lower temperatures, FeCo-LDH showed a blocky agglomeration on the CF substrate and lacked sufficient catalytically active sites, which was consistent with the SEM results.

The stability and degradation activity of the FTEF system was determined across a broad pH ranging from 3 to 9 (Figure 4a). The present framework showed 91%, 100% and 78% phenol removal after 150 min of reaction at pH = 3, 6, and 9, respectively. It has been shown that the non-homogeneous Fenton reaction takes place on the surface of the FeCo-LDH catalyst. This mechanism extends the operational pH range of the Fenton course with no or very little Fe/Co sludge generation. At pH = 3, when there is Fe^{3+}/Co^{2+} leaching, phenol removal is good, as shown in the CV curves of Figure 3b, and the ICP-MS analysis of the reaction effluent shows that the amount of leaching of Fe and Co is higher, 0.57 mg L^{-1} and 0.63 mg L^{-1}, and that the EF reaction occurs in the native solution, respectively. Phenol degradation was attributed to the synergistic action of heterogeneous oxidation on the cathode surface and homogeneous oxidation in the bulk solution [34]. As the pH shifted toward alkalinity, the FeCo-LDH catalyst exhibited enhanced stability. Specifically, the leaching amount of Fe decreased to 0.28 mg L^{-1} and that of Co was 0.39 mg L^{-1} at pH = 6, while the amount of Fe leaching quantity was only 0.05 mg L^{-1} and that of Co was 0.05 mg L^{-1} at pH = 9. Concurrently, the phenol removal efficiency increased, suggesting that phenol degradation under alkaline conditions was primarily driven by the heterogeneous Fenton reaction occurring on the catalyst surface. The reason for the reduction in phenol elimination rate after the pH was elevated to the alkaline region was that the alkaline environment affected the oxidizing ability of the free radicals and the generation of the active species, for example, the generation of HO_2^- instead of H_2O_2 (Equation (8)) [18,27].

$$O_2 + H_2O + 2e^- \rightarrow HO_2^- + OH^- \quad (8)$$

The feed concentration affects the loading of the system and the mass transfer resistance of the solution. The influence of feed concentration on phenol removal from water by the FTEF system was investigated under an applied voltage of 3.5 V, an electrolyte concentration of 100 mM, pH = 6, and an influent flow rate of 15 mL min^{-1} as depicted in Figure 4b. Phenol removal efficiency declined as the feed concentration increased. At a feed concentration of 10 mg L^{-1}, complete phenol removal was attained exclusively within the initial 30 min of the reaction. When the feed concentration was increased to 30 mg L^{-1} and 50 mg L^{-1}, the phenol removal rates were 93% and 88%, respectively. When the feed concentration was further elevated, the phenol removal rate dropped sharply to about 70%, at which time the high concentration of phenol molecules increased the mass transfer resistance, affected the electron transport rate, and even caused the blockage of membrane pores [47]. In addition, the increase in phenol concentration also means the increase in degradation by-products, which increase the consumption of •OH [48]. The influence of influent flow rate on phenol removal from water by the FTEF system was also investigated by conducting several trials under a phenol concentration of 30 mg L^{-1}, an electrolyte concentration of 100 mM, pH = 6, and an applied voltage of 3.5 V. The outcomes are presented in Figure 4c. As the flow rate was elevated from 1.6 mL min^{-1} to 20 mL min^{-1}, the

phenol removal efficiency rose from 61% to 99% following 150 min of reaction because the open voids of the honeycomb structure can reduce the mass transfer resistance and support efficient reaction at high flow rates. Compared to conventional electrochemical filters with limited contact area between membrane electrodes and feed solution, which need to be operated at a lower flow rate to ensure pollutant removal [35,49,50], a recirculation reaction mode was adopted in this study, and the increased fluid velocities not only imply an increase in the number of circulations of simulated wastewater through the FTEF system, but also enhance the mass transfer process. In addition, the flow rate directly determines the contact time between the oxidant (e.g., •OH, SO_4^{-}•) and the target molecules, and increasing the flow rate accelerates the process of solute molecules reaching the active sites present on the surface of the electrochemical membrane and increases the number of contacts between solute molecules and the surface-active sites of the membrane [18,47].

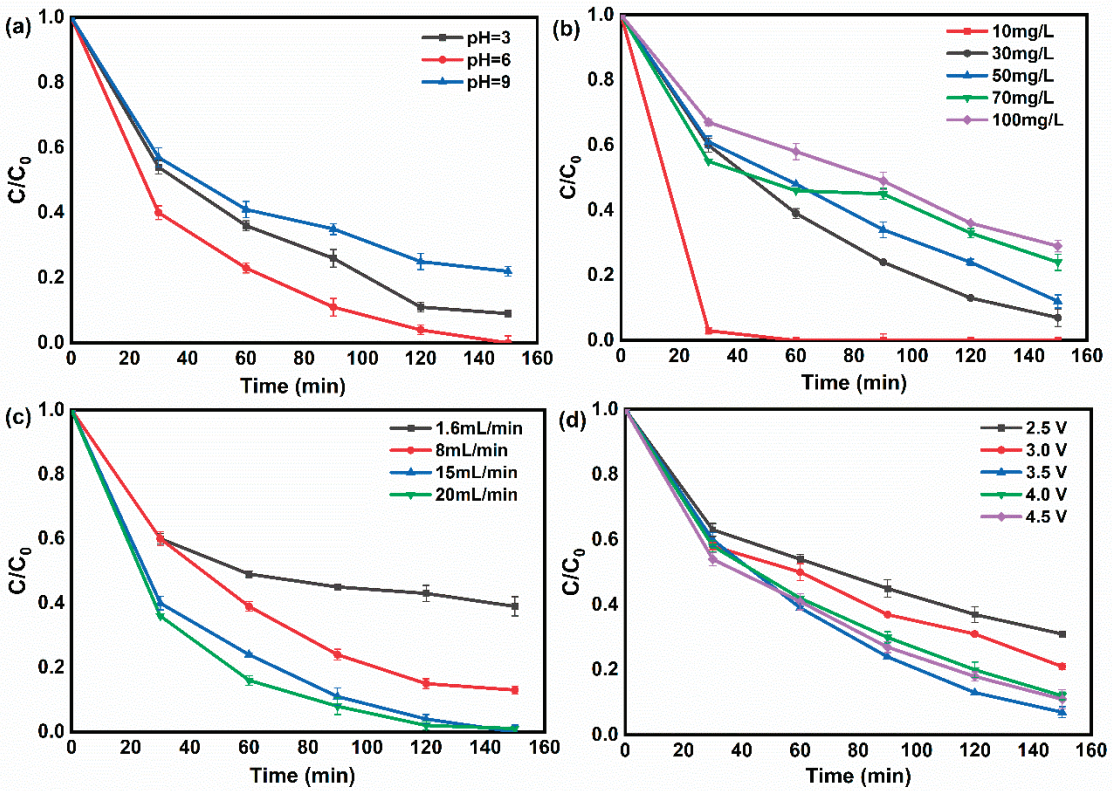


Figure 4. (**a**) Effect of pH on phenol removal rate with reaction time under the conditions of phenol concentration 30 mg L^{-1}, applied voltage 3.5 V, electrolyte concentration 100 mM, and influent flow rate 15 mL min^{-1}. (**b**) Effect of feed concentration with reaction time on phenol removal rate under the conditions of applied voltage 3.5 V, electrolyte concentration 100 mM, pH = 6, and influent flow rate 15 mL min^{-1}. (**c**) Effect of influent flow rate on phenol removal rate under the conditions of phenol concentration 30 mg L^{-1}, electrolyte concentration 100 mM, pH = 6, and applied voltage 3.5 V. (**d**) Effect of applied voltage on phenol removal rate with reaction time under the conditions of phenol concentration 30 mg L^{-1}, electrolyte concentration 100 mM, pH = 6, and influent flow rate 15 mL min^{-1}.

Figure 4d shows the exploration of how applied voltage affects the system's treatment of organic pollutants. The system was operated at a concentration of 30 mg L^{-1} of phenol. The effect of the magnitude of the applied voltage on the phenol removal by the FTEF system was investigated with a phenol concentration of 30 mg L^{-1}, an electrolyte concentration of 100 mM, pH = 6, and an influent flow rate of 15 mL min^{-1} (Figure 4d). The phenol removal by the system increased with increasing the applied voltage from 2.5 V to 3.5 V, 69% and 79%, respectively, and the highest phenol removal (93%) was achieved at 3.5 V.

The system was able to remove phenol from the water with the increase in applied voltage from 2.5 V to 3.5 V, respectively. This is attributed to the fact that increasing the voltage over a range increases the yield of H_2O_2. However, when the voltage was further increased, the phenol removal rate decreased instead, while during the experiment, a large number of bubbles were found to appear near the cathode electrode, which was the occurrence of the side reaction 4e$^-$ORR (Equation (9)), and as the concentration of H_2O_2 buildup decreased, the decomposition reaction of H_2O_2 was generated on the electrode surface (Equations (11) and (12)), and hydrogen precipitation reaction (Equations (10) and (11)), which leads to a decrease in pH in the vicinity of the electrode, thus disrupting the Fenton reaction in the system [51]. Similarly, in the study it was found that the hydrogen peroxide accumulation decreases after increasing with increasing current [27]. On one hand, the production of H_2O_2 was reduced, and on the other hand, the conversion of H_2O_2 to •OH [18,52] was affected, which consequently influenced phenol degradation in the FTEF system. Based on the optimization of the operating parameters, the stability of FeCo-LDH/CF in long-term operation was further investigated to verify its engineering practicality.

$$O_2 + 4H^+ + 4e^- \rightarrow 2H_2O \quad (9)$$

$$2H^+ + 2e^- \rightarrow H_2 \quad (10)$$

$$H_2O_2 + 2H^+ + 2e^- \rightarrow 2H_2O \quad (11)$$

$$H_2O_2 + HO_2^- \rightarrow H_2O + O_2 + OH^- \quad (12)$$

Owing to their inherent stability, the materials enabled the system to undergo six consecutive contaminant removal cycles. Evaluation of the membrane electrodes' reusability was conducted under operational conditions: 30 mg L^{-1} phenol concentration, 3.5 V applied voltage, 100 mM electrolyte, pH = 6, and 15 mL min^{-1} influent flow rate, with each cycle lasting 150 min. Following each experiment, the cathode was carefully rinsed and refreshed with fresh phenol solution. Phenol removal efficiencies of more than 90% were achieved in the first four cycles (Figure 5a), but with a slight decrease: from 99% in the first cycle to 93% in cycle4, and 89% and 85% at the end of the fifth cycle and the sixth cycle, respectively. Despite prolonged continuous operation inducing pore blockage and partial deactivation of membrane electrode active sites, the FTEF system maintained effective pollutant removal during the initial 750 min (i.e., up to the fifth cycle). By the end of six cycles, the system retained a stable TOC removal rate of approximately 70%, as shown in Figure 5b. SEM characterization of the FeCo-LDH/CF was carried out after 900 min of operation (Figure 5c). After a long period of operation, the catalyst on the membrane electrodes showed slight detachment phenomenon, but basically no fouling phenomenon, and the typical honeycomb structure was maintained, which indicated that the FeCo-LDH/CF electrochemical membrane had good mechanical and chemical stability. The ICP-MS results were analyzed for the effluent after each cycle (Table S6), and there was no significant increase in metal leaching from the cathode membrane after 900 min of continuous operation. The system's long-term operational viability is supported by its structural stability and minimal leaching.

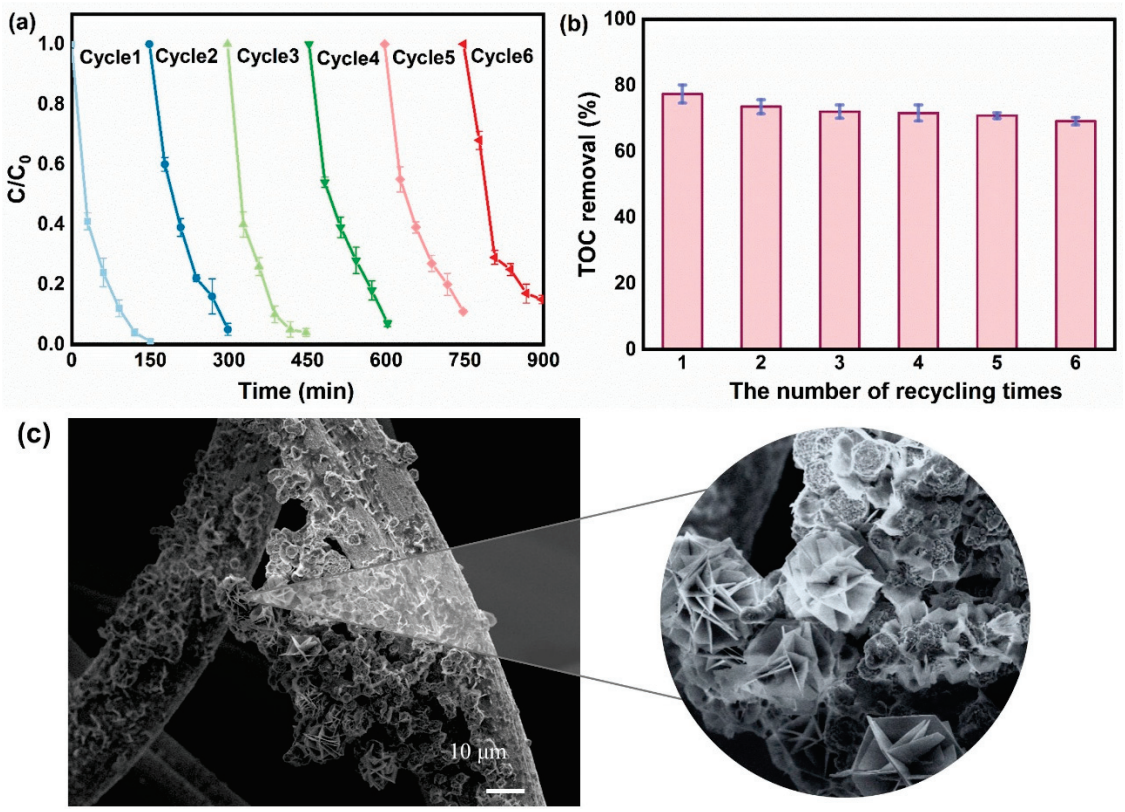


Figure 5. (**a**) Phenol removal rate of 6 cycles of continuous operation of the flow-through electric Fenton system; (**b**) TOC removal rate of the flow-through electro-Fenton system after 6 cycles of continuous operation and (**c**) SEM images of the FeCO-LDH/CF electrode after 900 min of continuous operation. The experiments were conducted under the conditions of phenol concentration 30 mg L^{-1}, applied voltage 3.5 V, electrolyte concentration 100 mM, pH = 6, influent flow rate 15 mL min^{-1}; each experimental cycle was 150 min.

2.3. Multi-Scale Analysis of Degradation Mechanisms and Pathways

Phenol degradation experiments were performed in filtration mode, conventional intermittent mode, and flow-through electrolysis mode (Figure 6a) to assess the impact of mass transfer patterns on organic matter removal. In the filtration-only mode, the phenol removals of CF and FeCo-LDH/CF membranes were very low, only 12% and 16%, when the adsorption interception of the membranes was playing a role in the system. Adding an electric field, the phenol removal of CF and FeCo-LDH/CF membranes were 46% and 61%, respectively, providing electrochemical oxidation to promote phenol degradation, in which the electric field was able to act synergistically with the membranes: the FeCo-LDH/CF membranes adsorbed the pollutant molecules and enhanced the interaction of phenol molecules with the oxidizing free radicals formed on the electrodes surface; as a consequence, the removal efficiency was increased [53]. In the flow-through electrolysis mode, the phenol removal rates of CF and FeCo-LDH/CF membranes were as high as 67% and 99%, which may be ascribed to the enhanced interfacial mass transfer efficiency of the flow-through configuration, which increased the contact opportunities between the contaminants and the strong oxidants, and even the uncatalyst-modified CF electrode achieved higher phenol removal rates than the FeCo-LDH/CF electrode in the conventional intermittent mode. In addition, the continuous passage of influent water through the membrane allowed the contaminants to reach not only the membrane surface or nearby degradation, but also the membrane surface or membrane pores, between which the deposited FeCo-LDH had a 3D honeycomb structure, which could provide abundant reactive active sites, thus improving the phenol removal rate. The phenol degradation

efficiency was only 28% by using a Ti mesh cathode instead of FeCo-LDH/CF membrane cathode (Figure 6b). In addition, the improvement of the mass transfer process in the circulation model was further analyzed by studying the phenol degradation kinetics and CA curves in different models. The fitting results of zero-, one-, and two-stage kinetic models (Table S4) showed that the phenol degradation process in both intermittent mode and circulation electrolysis mode conformed to quasi-one-stage kinetics. In contrast to conventional intermittent operation, flow-through electrolysis mode exhibited a marked enhancement in phenol removal efficiency, with the reaction rate constant (k) approximately 5-fold higher than that of the intermittent mode (Figure 6c) [54].

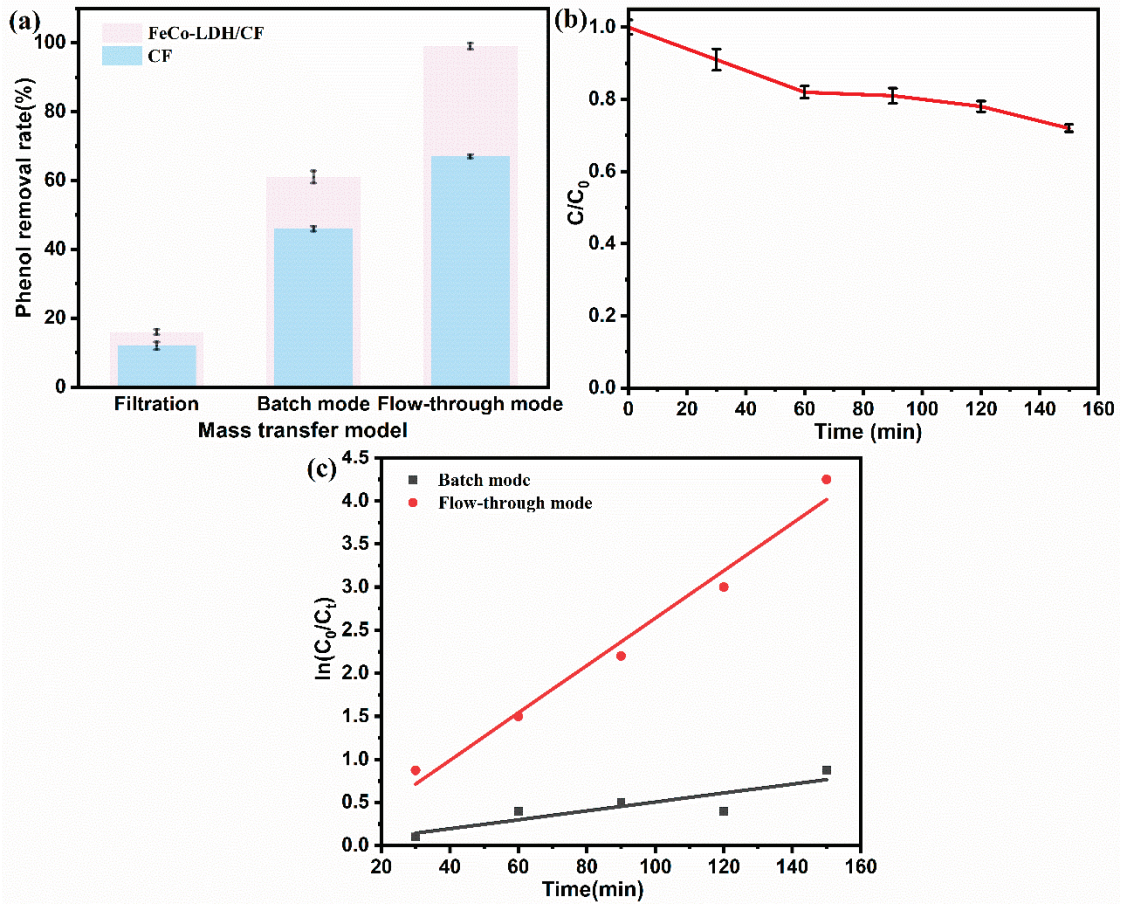


Figure 6. (**a**) Phenol removal from CF and FeCo-LDH/CF membranes in different operation modes. (**b**) Phenol removal from Ti mesh as cathode. (**c**) First-stage kinetic fitting for phenol removal process.

The previous section provides a cursory assessment of the reasons for the increased efficiency of the system in treating pollutants, and further elaboration of the mechanism of action of the system, i.e., the substances that produce the action, is needed. To explore the types of ROS produced in the FeCo-LDH/CF electro-filtration system, free radical quenching experiments were conducted by adding different bursting agents (tert-butanol, methanol, and furfuryl alcohol) to the system. As illustrated in Figure 7a, the introduction of an adequate quantity of furfuryl alcohol exerted negligible influence on organic matter removal, while the addition of methanol reduced the phenol removal to 61%, and the addition of sufficient amount of tertiary butanol severely limited the removal of phenol in this system to 37%. Bursting experiments preliminarily indicated that •OH was the dominant ROS in the FeCo-LDH/CF electro-filtration system, while SO_4^{-}• also played a role, with •OH contributing about 63% of the phenol degradation rate. EPR analysis with DMPO as the •OH trapping agent was employed to further characterize ROS generated

during phenol oxidation. As depicted in Figure 7b, the FeCo-LDH/CF system exhibited four characteristic peaks with an intensity ratio of 1:2:2:1, which matched the signature of the DMPO•OH adduct. In addition, the characteristic peaks of DMPO•OH disappeared after the addition of a sufficient amount of tert-butanol, and these phenomena further confirmed the presence of •OH. The pathway and mechanism of phenol degradation by the FeCo-LDH/CF cathodic electro-Fenton system are shown in Figure S6. In addition to the initial addition of a small amount of hydrogen peroxide initiating reactant, hydrogen peroxide was also generated during the process, and the source of •OH was guessed to be oxygen, for which experiments were carried out to investigate the contribution of cathodic fluxed O_2 in phenol removal. The experimental findings are depicted (Figure 7c). The phenol degradation rate is lower than 60% when oxygen is not passed through the FTEF system; at this time, the system can only utilize the dissolved oxygen inherent in the solution as well as the dissolved oxygen entering from the air, and the adsorption energy of the cathode material for oxygen is still limited, and the adsorption of oxygen has been improved way of the study of Yu et al. [27]. After constant aeration to the influent water with the air passed through the cathode material, the system obtains sufficient O_2 for H_2O_2 production, and a phenol removal rate of 99% was obtained, which shows that the FeCo-LDH/CF electrode has limited efficiency in utilizing the oxygen inherent in the solution, and that oxygen has a decisive role in the production of •OH. As a functional positive electrode, the CF component in FeCo-LDH/CF serves as a highly active and stable $2e^-$ORR catalyst, critically influencing •OH generation. In contrast, FeCo-LDH alone exhibits a significantly high energy barrier for oxygen adsorption, leading to minimal H_2O_2 production due to its intrinsic properties [27]. This experiment did not verify the relationship between the amount of oxygen passed through and the amount of H_2O_2 produced, and the amount of oxygen dissolved is yet to be investigated, with the electrocatalytic cathode sufficiently adsorbing oxygen. Following the confirmation of •OH presence, the SA method was employed to indirectly quantify the •OH yield in the FeCo-LDH/CF electro-filtration system [55], where SA was able to capture •OH to produce stable 2,3-DHBA and 2,5-DHBA, and the sum of the contents of the two products was roughly equal to the content of •OH. The variation in •OH content in this system is shown in Figure 7d, and the content of OH increases gradually with the reaction time, from the initial 0.013 mmol to 0.50 mmol after 150 min.

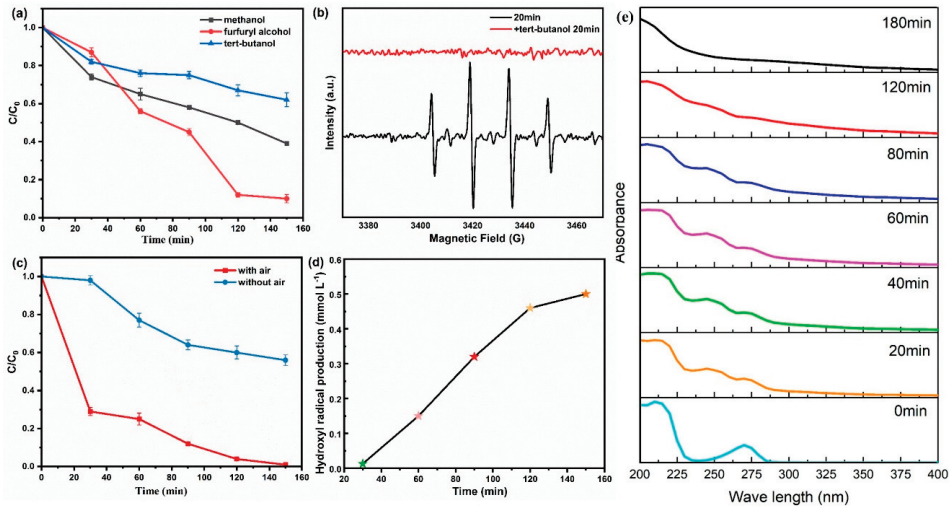


Figure 7. (**a**) Phenol removal after addition of different bursting agents. (**b**) EPR spectra of DMPO•OH without and with the addition of tert-butanol. (**c**) Effect of O_2 content on phenol removal. (**d**) •OH yield of the FTEF system. (**e**) UV spectral absorption spectra of phenol after different reaction durations.

Next, the pathway of phenol degradation and the pathway of ROS generation action were analyzed, and the material changes during phenol degradation were analyzed by UV-Vis's absorption spectroscopy (Figure 7e). The characteristic absorption peaks of phenol were concentrated at 210–215 nm and 270–275 nm, and the intensities of the peaks at these two locations gradually decreased until disappeared with the increase in degradation time. Thirty minutes after reaction initiation, a new characteristic peak was observed at 245–250 nm, assignable to the formation of benzoquinone with an absorption wavelength of λ_{max} = 248 nm. By 120 min, the characteristic peaks at 210–215 nm and 245–50 nm were weakened, while the characteristic peaks at 270–275 nm disappeared, which might be due to the further degradation of the intermediates, catechol and hydroquinone. Until 180 min later, all the characteristic peaks disappeared and no new peaks appeared, indicating that phenol might be completely degraded to CO_2 and H_2O at this time, which is in accordance with Figure 6a results. It was also observed that the color of the effluent solution of the phenol-simulated wastewater underwent a process of changing from dark brown to light yellow and finally was colorless as the reaction proceeded. Although the flow-through electrochemical system in this study achieved more than 90% phenol removal, the TOC removal of the effluent was less than 80%, suggesting that other organic intermediates were generated during the phenol removal process. With a view to analyze the degradation products of phenol, the effluent water from the FTEF system was tested by HPLC at different time intervals. By comparing the results with the retention time of standard samples, the degradation products of phenol were hydroquinone, catechol, maleic acid, and glycolic acid (Table S5). After 20 min, hydroquinone began to accumulate; after 40 min, catechol appeared; after 60 min, cisbutylene dioic acid began to accumulate; as the reaction proceeded, the peak areas of hydroquinone and catechol decreased dramatically in the second half of the reaction; after 150 min, phenol showed a very low peak area, and cisbutylene dioic acid disappeared. The formation of ethanedioic acid, however, was detected. This suggests that hydroxylation of reactive phenol occurs as a rapid step, whereas the ring-opening reaction (maleic acid → ethanedioic acid) serves as the rate-determining step. It can be speculated that the appearance of hydroquinone and catechol during phenol degradation indicates hydroxylation of phenol under the attack of OH [56]; these intermediates open the conjugated structure of the benzene ring under the strong oxidation of •OH and SO_4^{-}• to produce maleic acid; as the oxidation reaction proceeds, maleic acid was decomposed into the simpler structure of ethanedioic acid, which was eventually converted to CO_2 and H_2O. The degradation process of the system is shown in Figure 8.

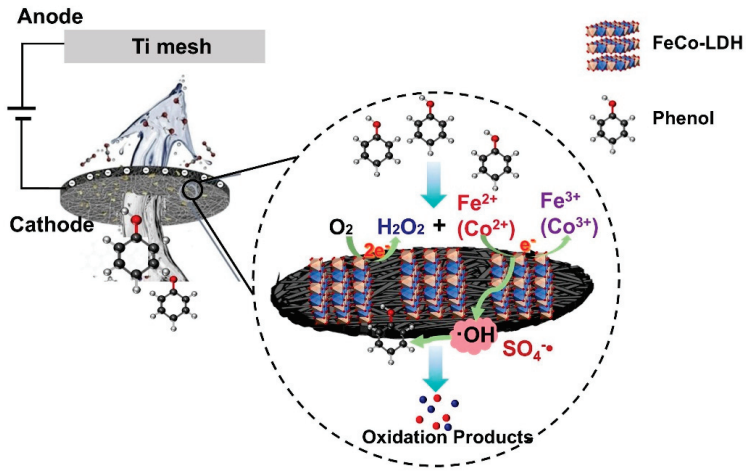


Figure 8. Schematic diagram of the degradation of phenol by a flow-through electrochemical system with FeCo-LDH/CF electrochemical membrane as cathode.

3. Materials and Methods

3.1. Reagents and Materials

Phenol(C_6H_6O), methylene blue ($C_{16}H_{18}ClN_3S$), cobalt nitrate hexahydrate ($Co(NO_3)_2{\cdot}6H_2O$), ferric nitrate nonahydrate ($Fe(NO_3)_2{\cdot}9H_2O$), urea ($O = C(NH_2)_2$), ammonium fluoride (NH_4F), tert-butyl alcohol, ethanol, furfuryl alcohol, methyl orange, ammonia, potassium ferrocyanide,4-aminoantipyrine, anhydrous sodium sulfate, 5,5-dimethyl-1-pyrrolidinium-N-oxide, 2,3-dihydroxybenzoic acid, and 2,5-dihydroxybenzoic acid used are analytically pure and can be used without further purification, acetonitrile is chromatographically pure, and can be used without further purification, and acetonitrile is color spectroscopically pure. The chemicals and materials used in the experiments were counted (Tables S1 and S2), and the determination of organic substances during the experiments (Text S1 and Figure S2).

3.2. Synthesis of Electrodes

FeCo-LDH-modified CF electrodes were fabricated via an in situ hydrothermal method. Specifically, NH_4F (0.125 M), $Co(NO_3)_2{\cdot}6H_2O$, $CO(NH_2)_2$ (0.5 M), and $Fe(NO_3)_2{\cdot}9H_2O$ were dissolved in deionized water, where Co: Fe = 2:1 (n/n). The mixture was transferred to a stainless-steel autoclave equipped with a Teflon liner after being stirred vigorously for 30 min to ensure homogeneity. The original CF was first treated with concentrated HNO_3 and then successively washed in an ultrasonic bath for 15 min using deionized water, acetone, ethanol, and deionized water in sequence. The clean CF was placed into the autoclave with the growth solution and hydrothermally treated at temperatures of 70 °C, 90 °C, and 120 °C for 7 h and 12 h cycles, respectively. Reactions during the hydrothermal process mainly involved decomposition reactions of NH_4F and $CO(NH_2)_2$ (Equations (13) and (14)). The alkaline solution generated by Equation (15) triggers homogeneous nucleation, crystallization, and the growth of metal hydroxides directly on CF substrates. During immersion in the growth solution, CFs serve as nucleation sites that facilitate the formation and growth of LDH structures [34]. Following the reaction, the LDH-coated substrates were rinsed exhaustively with deionized water. The solid LDH was then isolated from the suspension via filtration. Both the coated substrates and the filtered precipitate were dried in an oven at 45 °C, completing the synthesis of FeCo-LDH.

$$NH_4F + H_2O \rightarrow NNH_4{}^+ + OH^- + HF \quad (13)$$

$$CO(NH_2)_2 + 3H_2O \rightarrow 2NH_4{}^+ + 2OH^- + CO_2 \quad (14)$$

$$Co^{2+} + Fe^{3+} + OH^- \rightarrow FeCo - LDH \quad (15)$$

3.3. Evaluation of Electrode Morphology and Performance

To characterize the structural and morphological features of the electrodes, as well as their electrochemical properties, they were evaluated using the following methods. Structural, morphological, and particle size analyses of the samples were performed with a scanning electron microscope (SEM, TESCAN MIRA LMS, Brno, Czech Republic). Elemental composition characterization of the membrane electrodes was performed via X-ray photoelectron spectroscopy (XPS, Thermo Scientific ESCALAB 250Xi, Waltham, MA, USA) and X-ray diffraction (XRD, Rigaku Miniflex 600, Tokyo, Japan). Fourier transform infrared spectroscopy (FTIR, Thermo Scientific Nicolet iS2, Waltham, MA, USA) was utilized to assess the morphology of membrane materials, while an electrochemical workstation (CHI660E, Chenhua Instruments, Shanghai, China) was adopted to appraise the electrochemical properties of the synthesized electrochemical membranes. The electrode materials were evaluated via comprehensive photoelectrochemical measurements, including cyclic

voltammetry (CV) and electrochemical impedance spectroscopy (EIS). CV scans were conducted at a rate of 10 mV s^{-1} and a scan voltage of −0.1–0.8 V (vs. Ag/AgCl), while EIS spectra were recorded at an open-circuit potential with an AC amplitude of 0.01 V in the frequency range of 0.01–10^6 Hz (Text S3).

3.4. Experiments on Phenol Degradation by FeCo-LDH/CF FTEF System

A 150 mL glass vessel was used to construct an FTEF system (Text S2 and Figure S1) with the prepared modified FeCo-LDH/CF electrochemical membrane as the cathode and titanium mesh as the anode. For the purpose of investigating the FeCo-LDH/CF cathode-based FTEF system's capability in degrading pollutants, phenol was chosen as the target compound, Na_2SO_4 was used as the electrolyte, and the system was operated by maintaining an air flux of 300 mL min^{-1}, plus the voltage provided by a DC power supply, and the degradation efficiency of the system on phenol was measured. For a deeper analysis of individual factor impacts, the execution of the FTEF system under changing operating scenarios was systematically compared and analyzed, such as feed concentration (10–100 mg L^{-1}), applied voltage (2.5–4.5 V), solution pH (3.0, 6.0, and 9.0), and influent flow rate (1.6 mL min^{-1}, 8.0 mL min^{-1}, 15.0 mL min^{-1}, and 20.0 mL min^{-1}); and the performance of the FTEF system was investigated through the analysis of stability, versatility, and energy consumption. The system performance was investigated by stability analysis, versatility analysis, and energy consumption analysis (Texts S4 and S5 and Table S3); and the treatment mechanism of phenol in the Fenton system was explored through quenching experiments, EPR tests, and ROS identification via free radical trapping experiments.

4. Conclusions

This study utilized FeCo-LDH/CF electrochemical membranes and a novel FTEF system to overcome the limitations of the traditional EF technology, which effectively improved the problems of the traditional EF technology in terms of low yield of electroactive substances, poor mass transfer efficiency, narrow reaction pH range, and large production of iron sludge, etc. In this study, the FeCo-LDH/CF electrochemical membranes with abundant catalytic active sites were prepared and used as the cathode to construct an FTEF system. In this study, a FeCo-LDH/CF electrochemical membrane with abundant catalytic sites was prepared and used as the cathode to construct an FTEF system, and the performance of the system in the removal of organic pollutants was investigated in depth. The FeCo-LDH/CF electrochemical membrane is a 3D honeycomb structure, which can effectively promote the conversion of H_2O_2 to •OH, while the flow-through design of the system allows convective transfer of influent water, which increases the reaction rate by 5 times compared to the intermittent mode on the basis of higher steady state current, and is capable of achieving 40% higher phenol removal rate. The FeCo-LDH/CF system was able to achieve 78–100% phenol removal over a wide operating pH range, maintain 85% phenol removal and 70% TOC removal after six cycles of use, thus FeCo-LDH has great potential for practical wastewater treatment. The present study demonstrates the bimetallic synergy assisted by positively charged LDH for in situ generation and stabilization of radical ROS, which provides a new strategy for maximizing the performance of a non-homogeneous Fenton-like system with low chemical input and high mineralization efficiency, and provides a basis for further optimization of the conventional EF. Although this study has successfully developed an efficient FTEF system, there are still shortcomings. For example, the oxidation reaction may be kinetically limited at higher water fluxes. In order to optimize the system performance for practical applications, in-depth explorations on practical wastewater treatment evaluation, system stability and effluent safety are still

needed. However, this experiment can still provide a reference for further enhancing the EF degradation efficiency by modifying the cathode with membrane filtration.

Supplementary Materials: The following supporting information can be downloaded at https://www.mdpi.com/article/10.3390/catal15070685/s1. Text S1: Methods for the determination of organic matter; Text S2: Assembly of the system; Text S3: Specific operational conditions for the characterization of materials; Text S4: Calculation of the removal rate of organic matter and analysis of energy consumption; Text S5: Energy consumption analysis; Text S6: Identification of ROS; Figure S1: Schematic diagram of the structure of the FTEF device and its working flow diagram; Figure S2: (a) Absorbance standard curve of 2,3-DHBA; (b) Absorbance standard curve of 2,5-DHBA; Figure S3: H_2O_2 concentrations with different FeCo-LDH/CF and CF electrode stacks (reaction conditions: 100 mM Na_2SO_4 electrolyte, 3.5 V applied voltage, pH = 6); Figure S4: Degradation of phenol by different FeCo-LDH/CF and CF as cathodes of FTEF systems (reaction conditions: phenol initial concentration of 30 mg L^{-1}, electrolyte of 100 mM Na_2SO_4, applied voltage of 3.5 V, pH = 6, inlet flow rate of 15 mL min^{-1}); Figure S5: FTEF system for (a) phenol removal and (b) TOC removal in different water matrices; (c) removal rates of different types of pollutants; (d) removal rate of mixed contaminants and TOC; Table S1: Main materials and instruments required in the catalyst synthesis process; Table S2: Main reagents required in the catalyst synthesis process; Table S3: Comparison of the performance of different electrochemical filtration systems; Table S4: Simulation results of phenol degradation process kinetics under different modes; Table S5: Detection results of phenol degradation products. Table S6: The flow-through electric Fenton system operates continuously for 6 cycles of Fe and Co leaching. References [56–62].

Author Contributions: Conceptualization, F.L. and T.H.; methodology, F.L., T.H., H.D. and Y.Q.; software, H.D.; validation, H.D. and Y.Q.; formal analysis, F.L., T.H., H.D., Y.Q., Z.Y., Y.F. and W.S.; investigation, H.D. and Y.Q.; resources, F.L. and T.H.; data curation, H.D. and Y.Q.; writing—original draft preparation, Y.Q.; writing—review and editing, H.D.; visualization, H.D. and Y.Q.; project administration, F.L. and T.H.; funding acquisition, F.L. and T.H. All authors have read and agreed to the published version of the manuscript.

Funding: This work was supported by the National Natural Science Foundation of China (32171615).

Data Availability Statement: The generated data are available from the corresponding author upon request.

Conflicts of Interest: The authors declare no conflicts of interest.

References

1. Xue, G.; Yin, L.; Shao, S.; Li, G. Recent Progress on Selective Hydrogenation of Phenol toward Cyclohexanone or Cyclohexanol. *Nanotechnology* **2022**, *33*, 072003. [CrossRef]
2. Chen, H.; Sun, J. Selective Hydrogenation of Phenol for Cyclohexanone: A Review. *J. Ind. Eng. Chem.* **2021**, *94*, 78–91. [CrossRef]
3. Raza, W.; Lee, J.; Raza, N.; Luo, Y.; Kim, K.-H.; Yang, J. Removal of Phenolic Compounds from Industrial Waste Water Based on Membrane-Based Technologies. *J. Ind. Eng. Chem.* **2019**, *71*, 1–18. [CrossRef]
4. Pavithra, K.G.; Rajan, P.S.; Arun, J.; Brindhadevi, K.; Le, Q.H.; Pugazhendhi, A. A Review on Recent Advancements in Extraction, Removal and Recovery of Phenols from Phenolic Wastewater: Challenges and Future Outlook. *Environ. Res.* **2023**, *237*, 117005. [CrossRef] [PubMed]
5. Enguita, F.J.; Leitão, A.L. Hydroquinone: Environmental Pollution, Toxicity, and Microbial Answers. *BioMed Res. Int.* **2013**, *2013*, 542168. [CrossRef]
6. Chouhan, S.; Yadav, S.K.; Prakash, J.; Swati; Singh, S.P. Effect of Bisphenol A on Human Health and Its Degradation by Microorganisms: A Review. *Ann. Microbiol.* **2014**, *64*, 13–21. [CrossRef]
7. Liu, J.; Hu, Y.; Li, X.; Liu, Y.; Chen, Y.; Cheng, J.; Zhu, X.; Wang, G.; Xie, J. Unlocking the Power of Manganese-Doped MoS_2 Hollow Nanotubes: A Game-Changing Fenton Co-Catalyst for Ciprofloxacin Degradation. *Chem. Eng. J.* **2025**, *511*, 162009. Available online: https://www.sciencedirect.com/science/article/pii/S1385894725028359 (accessed on 12 July 2025). [CrossRef]
8. Batool, A.; Shao, S.; Majhi, K.C.; Mushtaq, A.; Jiang, Y.; Ho, W.; Tsang, Y.F.; He, Y.; Yee Leung, K.M.; Lam, J.C. MnO_2-Catalyzed Electrocatalytic Mineralization of Triclosan in Chlorinated Wastewater. *Environ. Sci. Ecotechnol.* **2025**, *25*, 100559. Available online: https://www.sciencedirect.com/science/article/pii/S2666498425000377 (accessed on 12 July 2025). [CrossRef]

9. Siahrostami, S.; Verdaguer-Casadevall, A.; Karamad, M.; Deiana, D.; Malacrida, P.; Wickman, B.; Escudero-Escribano, M.; Paoli, E.A.; Frydendal, R.; Hansen, T.W.; et al. Enabling Direct H_2O_2 Production through Rational Electrocatalyst Design. *Nat. Mater.* **2013**, *12*, 1137–1143. [CrossRef]
10. Nørskov, J.K.; Rossmeisl, J.; Logadottir, A.; Lindqvist, L.; Kitchin, J.R.; Bligaard, T.; Jónsson, H. Origin of the Overpotential for Oxygen Reduction at a Fuel-Cell Cathode. *J. Phys. Chem. B* **2004**, *108*, 17886–17892. [CrossRef]
11. Viswanathan, V.; Hansen, H.A.; Rossmeisl, J.; Nørskov, J.K. Unifying the $2e^-$ and $4e^-$ Reduction of Oxygen on Metal Surfaces. *J. Phys. Chem. Lett.* **2012**, *3*, 2948–2951. [CrossRef]
12. Yan, B.; Shi, Z.; Lin, J.; Zhang, L.; Han, L.; Shi, X.; Yang, Q. Boosting Heterogeneous Fenton Reactions for Degrading Organic Dyes via the Photothermal Effect under Neutral Conditions. *Environ. Sci. Nano* **2022**, *9*, 532–541. [CrossRef]
13. Jain, B.; Singh, A.K.; Kim, H.; Lichtfouse, E.; Sharma, V.K. Treatment of Organic Pollutants by Homogeneous and Heterogeneous Fenton Reaction Processes. *Environ. Chem. Lett.* **2018**, *16*, 947–967. [CrossRef]
14. Liu, X.; Zhou, Y.; Zhang, J.; Luo, L.; Yang, Y.; Huang, H.; Peng, H.; Tang, L.; Mu, Y. Insight into Electro-Fenton and Photo-Fenton for the Degradation of Antibiotics: Mechanism Study and Research Gaps. *Chem. Eng. J.* **2018**, *347*, 379–397. [CrossRef]
15. Zeng, H.; Zhang, G.; Ji, Q.; Liu, H.; Hua, X.; Xia, H.; Sillanpää, M.; Qu, J. pH-Independent Production of Hydroxyl Radical from Atomic H*-Mediated Electrocatalytic H_2O_2 Reduction: A Green Fenton Process without Byproducts. *Environ. Sci. Technol.* **2020**, *54*, 14725–14731. [CrossRef] [PubMed]
16. Ly, Q.V.; He, K.; Maqbool, T.; Sun, M.; Zhang, Z. Exploring the Potential Application of Hybrid Permonosulfate/Reactive Electrochemical Ceramic Membrane on Treating Humic Acid-Dominant Wastewater. *Sep. Purif. Technol.* **2022**, *286*, 120513. [CrossRef]
17. Zhang, S.; Sun, M.; Hedtke, T.; Deshmukh, A.; Zhou, X.; Weon, S.; Elimelech, M.; Kim, J.-H. Mechanism of Heterogeneous Fenton Reaction Kinetics Enhancement under Nanoscale Spatial Confinement. *Environ. Sci. Technol.* **2020**, *54*, 10868–10875. [CrossRef]
18. Hakizimana, I.; Zhao, X.; Wang, C.; Mutabazi, E.; Zhang, C. Insights into the Flow-through Electrochemical System in Water and Wastewater Treatment: Influential Factors, Advantages, Challenges, and Perspective. *Sep. Purif. Technol.* **2024**, *331*, 125533. [CrossRef]
19. Zhou, Y.; Wang, M.; Zhang, L.; Li, N.; Qian, T.; Yan, C.; Lu, J. Quaternary Medium-Entropy Alloy Metallene with Strong Charge Polarization for Highly Selective Urea Electrosynthesis from Carbon Dioxide and Nitrate. *ACS Nano* **2025**, *19*, 7273–7282. [CrossRef]
20. Kuznetsova, I.; Kultin, D.; Lebedeva, O.; Nesterenko, S.; Murashova, E.; Kustov, L. Intermetallic Compound and Solid Solutions of Co75Me25 (Me: Si, Fe, Cr) as Catalysts for the Electrochemical Reaction of Nitrate Conversion to Ammonia. *Int. J. Mol. Sci.* **2025**, *26*, 1650. [CrossRef]
21. Yin, Q.; Rao, D.; Zhang, G.; Zhao, Y.; Han, J.; Lin, K.; Zheng, L.; Zhang, J.; Zhou, J.; Wei, M. CoFe–Cl Layered Double Hydroxide: A New Cathode Material for High-Performance Chloride Ion Batteries. *Adv. Funct. Mater.* **2019**, *29*, 1900983. Available online: https://advanced.onlinelibrary.wiley.com/doi/full/10.1002/adfm.201900983 (accessed on 11 July 2025). [CrossRef]
22. Liu, P.F.; Yang, S.; Zhang, B.; Yang, H.G. Defect-Rich Ultrathin Cobalt-Iron Layered Double Hydroxide for Electrochemical Overall Water Splitting. *ACS Appl. Mater. Interfaces* **2016**, *8*, 34474–34481. [CrossRef] [PubMed]
23. Yu, J.M.; Song, J.; Kim, Y.K.; Oh, J.; Kim, K.Y.; Noh, W.Y.; Byun, W.J.; Lee, J.U.; Yang, C.; Jang, J.W.; et al. High-Performance Electrochemical and Photoelectrochemical Water Splitting at Neutral pH by Ir Nanocluster-Anchored CoFe-Layered Double Hydroxide Nanosheets. *Nano Lett.* **2023**, *23*, 5092–5100. Available online: https://pubs.acs.org/doi/10.1021/acs.nanolett.3c01024?ref=PDF (accessed on 11 July 2025). [CrossRef] [PubMed]
24. Wang, L.; Xu, S.-M.; Yang, X.; He, S.; Guan, S.; Waterhouse, G.I.N.; Zhou, S. Exploiting Co Defects in CoFe-Layered Double Hydroxide (CoFe-LDH) Derivatives for Highly Efficient Photothermal Cancer Therapy. *ACS Appl. Mater. Interfaces* **2020**, *12*, 54916–54926. [CrossRef] [PubMed]
25. Liu, Z.; Liu, Y.; Zhong, Y.; Cui, L.; Yang, W.; Razal, J.M.; Barrow, C.J.; Liu, J. Facile Construction of $MgCo_2O_4$@CoFe Layered Double Hydroxide Core-Shell Nanocomposites on Nickel Foam for High-Performance Asymmetric Supercapacitors. *J. Power Sources* **2021**, *484*, 229288. [CrossRef]
26. Paramanik, L.; Mohapatra, L.; Choi, D.Y.; Yoo, S.H. Enhanced Photocatalytic Performance of MXene-Modified Cation-Exchanged CoFe-LDH/$CoFeCrO_4$ Heterostructure for Antibiotic Degradation and Hydrogen Production through Synergistic Charge Dynamics. *Compos. Part B Eng.* **2024**, *278*, 111416. [CrossRef]
27. Yu, D.; He, J.; Wang, Z.; Pang, H.; Li, L.; Zheng, Y.; Chen, Y.; Zhang, J. Mineralization of Norfloxacin in a CoFe–LDH/CF Cathode-Based Heterogeneous Electro-Fenton System: Preparation Parameter Optimization of the Cathode and Conversion Mechanisms of H_2O_2 to OH. *Chem. Eng. J.* **2021**, *417*, 129240. [CrossRef]
28. Liu, R.; Wang, Y.; Liu, D.; Zou, Y.; Wang, S. Water-Plasma-Enabled Exfoliation of Ultrathin Layered Double Hydroxide Nanosheets with Multivacancies for Water Oxidation. *Adv. Mater.* **2017**, *29*, 1701546. [CrossRef]

29. Ganiyu, S.O.; Thi, X.H.L.; Bechelany, M.; Oturan, N.; Papirio, S.; Esposito, G.; van Hullebusch, E.; Cretin, M.; Oturan, M.A. Electrochemical Mineralization of Sulfamethoxazole over Wide pH Range Using $Fe^{II}Fe^{III}$ LDH Modified Carbon Felt Cathode: Degradation Pathway, Toxicity and Reusability of the Modified Cathode. *Chem. Eng. J.* **2018**, *350*, 844–855. [CrossRef]
30. Yuan, F.; Zhang, E.; Liu, Z.; Yang, K.; Zha, Q.; Ni, Y. Hollow CoSx Nanoparticles Grown on FeCo-LDH Microtubes for Enhanced Electrocatalytic Performances for the Oxygen Evolution Reaction. *ACS Appl. Energy Mater.* **2021**, *4*, 12211–12223. [CrossRef]
31. Sohrabi, H.; Khataee, A.; Ghasemzadeh, S.; Majidi, M.R.; Orooji, Y. Layer Double Hydroxides (LDHs)-Based Electrochemical and Optical Sensing Assessments for Quantification and Identification of Heavy Metals in Water and Environment Samples: A Review of Status and Prospects. *Trends Environ. Anal. Chem.* **2021**, *31*, e00139. [CrossRef]
32. Hameed, A.; Batool, M.; Liu, Z.; Nadeem, M.A.; Jin, R. Layered Double Hydroxide-Derived Nanomaterials for Efficient Electrocatalytic Water Splitting: Recent Progress and Future Perspective. *ACS Energy Lett.* **2022**, *7*, 3311–3328. [CrossRef]
33. Yang, F.; Sliozberg, K.; Sinev, I.; Antoni, H.; Bähr, A.; Ollegott, K.; Xia, W.; Masa, J.; Grünert, W.; Cuenya, B.R.; et al. Synergistic Effect of Cobalt and Iron in Layered Double Hydroxide Catalysts for the Oxygen Evolution Reaction. *ChemSusChem* **2017**, *10*, 156–165. [CrossRef]
34. Ganiyu, S.O.; Huong Le, T.X.; Bechelany, M.; Esposito, G.; Van Hullebusch, E.D.; Oturan, M.A.; Cretin, M. A Hierarchical CoFe-Layered Double Hydroxide Modified Carbon-Felt Cathode for Heterogeneous Electro-Fenton Process. *J. Mater. Chem. A* **2017**, *5*, 3655–3666. [CrossRef]
35. Yang, L.; Xu, D.; Yang, H.; Luo, X.; Liang, H. Structurally-Controlled FeNi LDH/CNTs Electro-Fenton Membrane for In-Situ Electro-Generation and Activation of Hydroxyl Radicals toward Organic Micropollutant Treatment. *Chem. Eng. J.* **2022**, *432*, 134436. [CrossRef]
36. Shakir, I.; Almutairi, Z.; Shar, S.S. Fabrication of Nanostructured Iron-Cobalt Layered Double Hydroxide: An Innovative Approach for the Facile Synthesis. *J. Saudi Chem. Soc.* **2022**, *26*, 101500. [CrossRef]
37. Li, R.; Zhang, D.; Chen, H.; Wang, S.; Ling, Y.; Fang, C. Morphological and Electronic Regulation of Zn,S-Incorporated FeCo–LDH Nanosheets for Boosting the Bi-Electrocatalytic Oxygen Evolution and Urea Oxidation Reactions. *ACS Sustain. Chem. Eng.* **2023**, *11*, 16098–16107. [CrossRef]
38. Abedi, H.; Mehrpooya, M. Synthesis of Three-Metal Layered Double Hydroxide and Dual Doped Graphene Oxide Composite as a Novel Electrocatalyst for Oxygen Reduction Reaction. *J. Alloys Compd.* **2021**, *875*, 160047. [CrossRef]
39. Understanding Catalyst Poisoning in Precious Metal Catalysts: Causes, Problems, and Solutions. Available online: https://www.samaterials.com/content/catalyst-poisoning-in-precious-metal-catalysts-causes-problems-and-solutions.html (accessed on 12 July 2025).
40. Ma, Q.; Nengzi, L.; Li, B.; Wang, Z.; Liu, L.; Cheng, X. Heterogeneously Catalyzed Persulfate with Activated Carbon Coated with CoFe Layered Double Hydroxide (AC@CoFe-LDH) for the Degradation of Lomefloxacin. *Sep. Purif. Technol.* **2020**, *235*, 116204. [CrossRef]
41. Sun, H.; Zhang, W.; Li, J.-G.; Li, Z.; Ao, X.; Xue, K.-H.; Ostrikov, K.K.; Tang, J.; Wang, C. Rh-Engineered Ultrathin NiFe-LDH Nanosheets Enable Highly-Efficient Overall Water Splitting and Urea Electrolysis. *Appl. Catal. B Environ.* **2021**, *284*, 119740. [CrossRef]
42. Jia, W.; Li, Y.; Chen, C.; Wu, Y.; Liang, Y.; Du, J.; Feng, X.; Wang, H.; Wu, Q.; Guo, W.-Q. Unveiling the Fate of Metal Leaching in Bimetal-Catalyzed Fenton-like Systems: Pivotal Role of Aqueous Matrices and Machine Learning Prediction. *J. Hazard. Mater.* **2024**, *477*, 135291. [CrossRef]
43. Feng, C.; Wang, F.; Liu, Z.; Nakabayashi, M.; Xiao, Y.; Zeng, Q.; Fu, J.; Wu, Q.; Cui, C.; Han, Y.; et al. A Self-Healing Catalyst for Electrocatalytic and Photoelectrochemical Oxygen Evolution in Highly Alkaline Conditions. *Nat. Commun.* **2021**, *12*, 5980. Available online: https://www.nature.com/articles/s41467-021-26281-0 (accessed on 12 July 2025). [CrossRef] [PubMed]
44. Yang, W.; Zhou, M.; Oturan, N.; Bechelany, M.; Cretin, M.; Oturan, M.A. Highly Efficient and Stable $Fe^{II}Fe^{III}$ LDH Carbon Felt Cathode for Removal of Pharmaceutical Ofloxacin at Neutral pH. *J. Hazard. Mater.* **2020**, *393*, 122513. [CrossRef] [PubMed]
45. Ma, X.; Wang, S.; Wang, H.; Ding, J.; Liu, S.; Huang, Z.; Sun, W.; Liu, G.; Wang, L.; Xu, W. Construction of High-Performance Asymmetric Supercapacitor Based on FeCo-LDH@C_3N_4 Composite Electrode Material with Penetrating Structure. *J. Energy Storage* **2022**, *56*, 106034. [CrossRef]
46. Lin, S.; Zhou, Z.; Wu, H.; Yin, S.; Wang, Y. Electrochemical Oxidation of Aniline Using a High-Flux CNT Filter. *J. Water Process Eng.* **2022**, *46*, 102536. [CrossRef]
47. Shi, C.; Yu, S.; Li, C. Fabrication of Aligned Carbon Nanofiber Doped with SnO_2-Sb for Efficient Electrochemical Removal of Tetracycline. *Chem. Eng. J.* **2022**, *441*, 136052. [CrossRef]
48. Guo, D.; Liu, Y.; Ji, H.; Wang, C.-C.; Chen, B.; Shen, C.; Li, F.; Wang, Y.; Lu, P.; Liu, W. Silicate-Enhanced Heterogeneous Flow-Through Electro-Fenton System Using Iron Oxides under Nanoconfinement. *Environ. Sci. Technol.* **2021**, *55*, 4045–4053. [CrossRef]
49. Li, Z.; Shen, C.; Liu, Y.; Ma, C.; Li, F.; Yang, B.; Huang, M.; Wang, Z.; Dong, L.; Wolfgang, S. Carbon Nanotube Filter Functionalized with Iron Oxychloride for Flow-through Electro-Fenton. *Appl. Catal. B Environ.* **2020**, *260*, 118204. [CrossRef]

50. Kong, L.; Guo, J.; Li, Y.; Shao, J.; Ren, L.; Jia, J.; Ying, D. Using Flow-through Reactor to Enhance Ferric Ions Electrochemical Regeneration in Electro-Fenton for Wastewater Treatment. *Process Saf. Environ. Prot.* **2024**, *191*, 907–916. [CrossRef]
51. Ghasemi, M.; Khataee, A.; Gholami, P.; Cheshmeh Soltani, R.D. Template-Free Microspheres Decorated with Cu-Fe-NLDH for Catalytic Removal of Gentamicin in Heterogeneous Electro-Fenton Process. *J. Environ. Manag.* **2019**, *248*, 109236. [CrossRef]
52. Lin, L.; Zhang, F.; Hou, X.; Wang, L.; Wu, W.; Wang, L.; Li, Y.; Xie, H. Fe@Fe_2O_3/Etched Carbon Felt as a Cathode for Efficient Bisphenol a Removal in a Flow-through Electro-Fenton System: Electron Transfer Pathway and Underlying Mechanism. *Sep. Purif. Technol.* **2024**, *334*, 125982. [CrossRef]
53. Zhou, X.; Liu, S.; Xu, A.; Wei, K.; Han, W.; Li, J.; Sun, X.; Shen, J.; Liu, X.; Wang, L. A Multi-Walled Carbon Nanotube Electrode Based on Porous Graphite-RuO_2 in Electrochemical Filter for Pyrrole Degradation. *Chem. Eng. J.* **2017**, *330*, 956–964. [CrossRef]
54. Gui, L.; Chen, Z.; Chen, B.; Song, Y.; Yu, Q.; Zhu, W.; Hu, Q.; Liu, Y.; Zheng, Z.; Ze, L.; et al. Preparation and Characterization of ZnO/PEG-Co(II)-PbO_2 Nanocomposite Electrode and an Investigation of the Electrocatalytic Degradation of Phenol. *J. Hazard. Mater.* **2020**, *399*, 123018. [CrossRef]
55. Ma, J.; Li, H.; Yang, Y.; Li, X. Influence of Water Matrix Species on Persulfate Oxidation of Phenol: Reaction Kinetics and Formation of Undesired Degradation Byproducts. *Water Sci. Technol.* **2018**, *2017*, 340–350. [CrossRef]
56. Fu, X.; Han, Y.; Xu, H.; Su, Z.; Liu, L. Electrochemical Study of a Novel High-Efficiency PbO_2 Anode Based on a Cerium-Graphene Oxide Co-Doping Strategy: Electrodeposition Mechanism, Parameter Optimization, and Degradation Pathways. *J. Hazard. Mater.* **2022**, *422*, 126890. [CrossRef]
57. Zhao, Y.; Sun, M.; Wang, X.; Wang, C.; Lu, D.; Ma, W.; Kube, S.A.; Ma, J.; Elimelech, M. Janus Electrocatalytic Flow-through Membrane Enables Highly Selective Singlet Oxygen Production. *Nat. Commun.* **2020**, *11*, 6228. [CrossRef]
58. Guo, D.; Wang, Y.; Lu, P.; Liu, J.; Liu, Y. Flow-through Electro-Fenton Using Nanoconfined Fe-Mn Bimetallic Oxides: Ionization Potential-Dependent Micropollutants Degradation Mechanism. *Appl. Catal. B Environ. Energy* **2023**, *328*, 122538. [CrossRef]
59. Jia, X.; Cao, P.; Qin, X.; Chen, S.; Yu, H.; Quan, X. High-Efficiency Electrochemical Activation of H_2O_2 into OH Enabled by Flow-through FeOCl-Modified Carbon Electrode for Organic Pollutants Degradation. *Sep. Purif. Technol.* **2022**, *295*, 121279. [CrossRef]
60. Liu, F.; Liu, Y.; Yao, Q.; Wang, Y.; Fang, X.; Shen, C.; Li, F.; Huang, M.; Wang, Z.; Sand, W.; et al. Supported Atomically-Precise Gold Nanoclusters for Enhanced Flow-through Electro-Fenton. *Environ. Sci. Technol.* **2020**, *54*, 5913–5921. [CrossRef] [PubMed]
61. Wang, X.; Zhang, Q.; Jing, J.; Song, G.; Zhou, M. Biomass Derived S, N Self-Doped Catalytic Janus Cathode for Flow-through Metal-Free Electrochemical Advanced Oxidation Process: Better Removal Efficiency and Lower Energy Consumption under Neutral Conditions. *Chem. Eng. J.* **2023**, *466*, 143283. [CrossRef]
62. Zheng, J.; Ma, J.; Wang, Z.; Xu, S.; Waite, T.D.; Wu, Z. Contaminant Removal from Source Waters Using Cathodic Electrochemical Membrane Filtration: Mechanisms and Implications. *Environ. Sci. Technol.* **2017**, *51*, 2757–2765. [CrossRef]

Disclaimer/Publisher's Note: The statements, opinions and data contained in all publications are solely those of the individual author(s) and contributor(s) and not of MDPI and/or the editor(s). MDPI and/or the editor(s) disclaim responsibility for any injury to people or property resulting from any ideas, methods, instructions or products referred to in the content.

catalysts

MDPI

Review

Progress and Reaction Mechanism of Co-Based Catalysts in the Selective Hydrogenation of α,β-Unsaturated Aldehydes

Haixiang Shi, Jianming Xu, Xuan Luo and Zuzeng Qin *

School of Chemistry and Chemical Engineering, Key Laboratory of Applied New Technology in Resource Chemical Engineering of Guangxi Universities and Colleges, Guangxi University, Nanning 530004, China
* Correspondence: qinzuzeng@gxu.edu.cn

Abstract

In recent years, Co-based catalysts have attracted considerable attention in research on selective hydrogenation reactions because of their mild activities and favorable selectivities for producing intermediate products, especially in the selective hydrogenation of α,β-unsaturated aldehydes (UAL). However, the low activity of Co-based catalysts for activating hydrogen limits their application in industry, and the diversity of forms and electronic states of Co-based catalysts also leads to the development of complex products and hydrogenation mechanisms at Co active sites. This review provides a comprehensive and systematic overview of recent progress in the selective hydrogenation of UAL over Co-based catalysts, where the preparation methods, hydrogenation properties, and UAL hydrogenation mechanisms of Co-based catalysts are carefully discussed. The influences of nanosize effects, electronic effects, and coordination effects on Co metal and Co oxides are investigated. In addition, the different reaction mechanisms at Co active sites are compared, and their strengths and weaknesses for C=O hydrogenation are further proposed. Finally, the outlook and challenges for the future development of Co-based hydrogenation catalysts are highlighted.

Keywords: α-unsaturated aldehyde; hydrogenation; Co-based catalyst; mechanism

1. Introduction

Compared with traditional homogeneous hydrogenation technology, the selective hydrogenation of α,β-unsaturated aldehydes (ULAs) is still an important process for producing unsaturated alcohols (ULOs) in industry because of its advantages in terms of being environmentally friendly and simple [1–3]. In the fine chemical industry, catalytic hydrogenation technology is widely applied in the fabrication of numerous valuable products, such as flavors, drugs, dyes, perfumery, and functional polymers [4–7]. The hydrogenation pathways of UAL are shown in Figure 1A. The selective hydrogenation of UAL with conjugated double bonds is a complicated reaction because it involves various hydrogenation products, such as unsaturated alcohol (UOL), saturated aldehyde (SAL), and saturated alcohol (SOL), in which UOL is most difficult to obtain because of the disadvantage of C=O hydrogenation regarding both thermodynamics and kinetics. In addition, the byproducts of acetals and ethers may be generated by strong acid sites, leading to complicated products [8–10]. Thus, efforts to achieve highly efficient hydrogenation in order to produce UOL still face severe challenges.

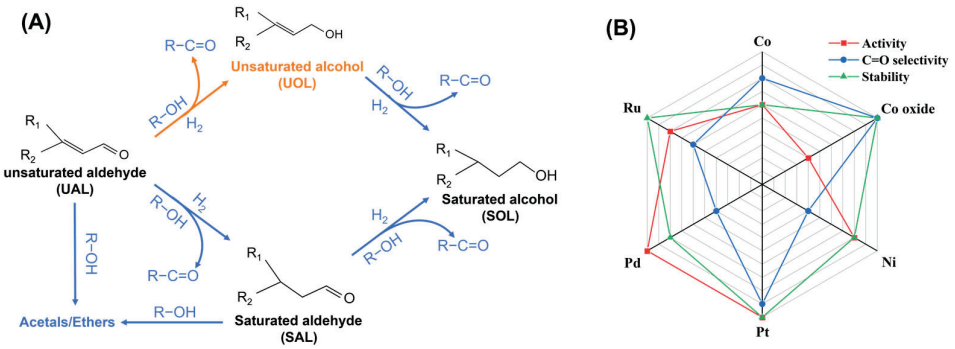


Figure 1. (**A**) Illustration of potential reaction routes of UAL during hydrogenation. (**B**) Comparison of activity, UOL hydrogenation, and stability of Co-based catalysts and noble metal catalysts for UAL hydrogenation on basis of reported studies.

Two main pathways for the selective hydrogenation of UAL via heterogeneous catalysis have been reported: H_2 dissociation hydrogenation and catalytic transfer hydrogenation using H_2 and organic alcohols as hydrogen donors, respectively [11]. Traditional H_2 dissociation hydrogenation relies on H_2 pyrolysis to activate H species at the metal center, and the hydrogenation process usually follows the Horiuti–Polanyi mechanism [12–14]. Although noble metals, such as Pt, Pd, and Au, have superior activity in UAL hydrogenation [15–19], the drawbacks of high cost and non-renewability limit their development in the future. Thus, researchers are concentrated on studying nonnoble metal catalysts and overcoming the problem of disequilibrium in terms of catalytic and hydrogenation selectivity.

As another hydrogenation pathway of UAL, catalytic transfer hydrogenation is a safe and convenient technology for producing UOL because it circumvents the use of H_2 under high-pressure conditions or the use of other hydride-containing reducing agents [20]. As shown in Figure 1A, hydrogenation and dehydrogenation products are generated simultaneously in the transfer hydrogenation pathway, which is similar to homogeneous hydrogenation via Meerwein–Ponndorf–Verley (MPV) reduction via an isopropanol hydrogen donor [21–23]. Organic alcohols work as both solvents and hydrogen donors, resulting in a significant solvent effect on transfer hydrogenation. However, the transfer hydrogenation mechanism and the changes in the reaction interface over catalysts remain controversial and unclear.

In recent years, nonnoble metal catalysts, including Ni, Co, Cu, and Fe, have been widely used in UAL hydrogenation because they are more economical and sustainable than noble catalysts [24–28]. In addition, several design principles for hydrogenation catalysts have been proposed in previous reviews, including turning the electronic structure, the nanosize effect, metal–support interaction, and the steric effect of metal catalysts [29–32], which are beneficial and practical for most supported-metal catalysts. In addition, metal oxides play an important role in UAL hydrogenation because of the abundant Lewis acid sites originating from M–O structures and the potential synergistic effect of the M^0 and $M^{\delta+}$ sites. Moreover, many transition metal oxides and derivative catalysts, such as Co [33–37], Al [38,39], Mg [3,40], and Zr [41–43], have been reported for their catalytic activity in transfer hydrogenation. Among them, Co is usually introduced into hydrogenation catalysts as a second metal or assistant for enhancing the C=O hydrogenation properties. When Co is used as the primary active component in selective hydrogenation, it has mild activity and high affinity for C=O in UAL hydrogenation because its special d-band structure is similar to that of noble metals, and Co has seven d-electrons and larger d-bandwidths than other nonnoble metals [44]. Furthermore, Co_3O_4 catalysts are reported to have a selectivity for UOL of more than 90% in UAL transfer hydrogenation [33,34]. As shown in Figure 1B, Co and Co oxide catalysts have satisfactory hydrogenation selectivity

for C=O compared with Pt, Pd and Ru noble metal catalysts. In particular, Co oxide catalysts exhibit more than 90% selectivity for UOL in transfer hydrogenation and are regarded as promising alternatives to replace noble metal catalysts. Although numerous studies have been conducted to improve the preparation and modification methods of Co-based catalysts, they still face the problems of poor activity and stability, restricting their large-scale application in industry. With the gradual maturation of advanced characterization and theoretical calculation methods, a deeper understanding of the process from catalyst preparation to the hydrogenation mechanism is essential and meaningful for Co-based catalysts applied in the hydrogenation industry.

Many researchers have comprehensively reviewed the design strategies, reaction properties, and applications of supported metal catalysts in recent years [11,29–32,45,46], but overall discussions of the preparation, reactivity, and mechanism of Co-based catalysts are incomplete and unclear. Therefore, this review focuses on the strengths, shortcomings, and size scale of the particles in different synthesis methods for Co-based catalysts. The characteristics of UAL-selective hydrogenation on various Co-based catalysts were subsequently discussed and summarized. More attention has been given to the design principles and modification methods of Co metal and Co oxide catalysts. In addition, the main hydrogenation pathways and mechanisms, including H_2 dissociation and catalytic transfer hydrogenation, are highlighted. Finally, ongoing challenges and opportunities for the future development of Co-based hydrogenation catalysts are discussed.

2. Preparation Methods and Size Scales for Co-Based Catalysts

The methods used to prepare Co-based catalysts have crucial effects on the dispersion, particle size and crystal characteristics of Co and Co_3O_4 nanoparticles (NPs). For the hydrogenation activities of metal particles, a theoretical study suggested that the chemical nature of the particle size effect may result in a mutation in hydrogenation reactions when the metal size reaches the cluster scale, but the mechanism of the size effect remains a matter of study [47]. As shown in Figure 2, the nanosize effect may affect the hydrogenation selectivity by changing the adsorption modes of the substrates. With increasing Co NP size, the electronic structure of the Co metal gradually varies from the positively charged ($M^{\delta+}$) state to the metallic state (M^0) due to different levels of metal–support interactions. The size of Co NPs can be approximately distinguished at the nanoscale (5~100 nm), cluster scale (0.5~5 nm), and atomic scale [48]. Owing to the difference in structure and the number of aggregated atoms of metal oxides, the size of cobalt oxide clusters has not been clearly defined. Usually, the size and exposed crystal plane of Co NPs can be observed and analyzed via X-ray diffraction (XRD) and transmission electron microscopy (TEM), but metal clusters may not be directly detected and observed via the present analysis methods. Currently, traditional preparation methods and many advanced methods are widely studied and developed, and the strengths, shortcomings and particle scales of different preparation methods are summarized in Table 1.

Table 1. Various preparation methods for Co-based catalysts.

Synthesis Method	Co Species	Advantages	Disadvantages	Scale
Impregnation method	Co NPs	Operational convenience; facile operation; economy	Need pretreatment; aggregation of particles	Nanoscale
Precipitation method	Co NPs, Co_3O_4	Economy; simple equipment/process; facile operation	Poor uniformity	Nanoscale

Table 1. *Cont.*

Synthesis Method	Co Species	Advantages	Disadvantages	Scale
Solvothermal methods	Co_3O_4	Operational convenience; controllable size; good dispersion	Low production; dependence on equipment;	Nanoscale
Sol–gel method	Co NPs, Co_3O_4, composite oxides	Mild preparation conditions; controllable structure; anti-deactivation	Long preparation cycle	Cluster scale
Pyrolysis method	Co_3O_4; Co complexes	Good dispersion; atomic control	Rely on substrate material; long preparation cycle	Atomic or cluster scale

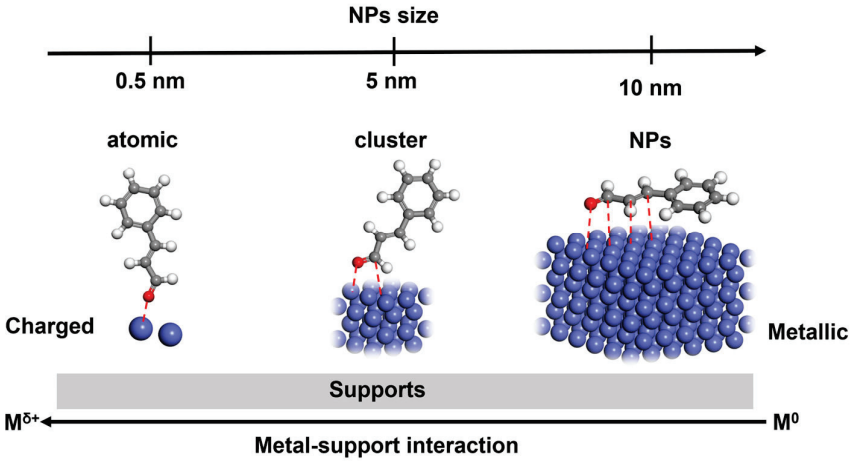


Figure 2. Illustration of nanosize effect over supported Co NP catalysts for selective hydrogenation of conjugated double bonds.

2.1. Impregnation Method

As the most facile and widely used method to prepare hydrogenation catalysts in industry, the impregnation method has the advantages of operational convenience and economy [32,49]. For supported catalysts, the substrates are first dispersed in a solution with metal ions, which are adsorbed on the supports by surface tension and solvation effects, and the solvents are removed to obtain the Co catalyst precursor. Typically, Ma et al. prepared a series of Pd/CNT, Co/CNT, and $Pd_{0.1}$Co/CNT catalysts via an improved impregnation method [50], in which Pd/CNT and Co/CNT catalysts prepared by the equal-volume impregnation method had particle sizes of approximately 10.9 ± 12.6 nm and 5.3 ± 1.5 nm, respectively. The $Pd_{0.1}$Co/CNT catalysts prepared via the successive impregnation method, co-impregnation- method, and deep eutectic solvent impregnation method presented similar particle sizes of approximately 11.2 ± 3.0, 9.4 ± 2.9, and 10.4 ± 3.0 nm, respectively. In addition, the limited structures can easily regulate the size of Co particles via the impregnation method; for example, the pores of MOFs can restrict the growth of Co particles to an average size of 9.0 nm [51]. Modification of the impregnation conditions can control the dispersal of metal particles on the support at the nanoscale. The impregnation method is appropriate for preparing most supported catalysts, but weak metal–support interactions may result in the migration and aggregation of metal NPs.

2.2. Precipitation Method

As one of the widely used production methods in industry, the precipitation method has advantages of economy, simple equipment/processing, and facile operation. In the precipitation method, precipitants, such as ammonia, ammonium, carbonates, and alkalis, are used to immobilize the metal ions on the supports, and the catalysts are finally obtained

after the following calcination and reduction procedures [52–56]. The pure Co_3O_4 NPs with a cubic spinel structure prepared via the precipitation method with a NaOH precipitant have a particle size of 3~29 nm, which can be controlled by varying the synthesis conditions [57,58]. Although Co_3O_4 catalysts sintered at high temperatures may have larger particle sizes [59], the introduction of surfactants and thermostable supports efficiently prevents the agglomeration of Co NPs [60,61].

The precipitation method is also the simplest method for preparing multimetal catalysts and composite oxide catalysts because most nonnoble metals can be deposited in basic environments. A familiar case is Co-Ni bimetallic catalysts [56,62–65], which are widely studied and applied in heterogeneous hydrogenation. Yang et al. prepared a CoNi-LDH hydrotalcite precursor bimetallic catalyst supported on Al_2O_3 by a precipitation method using a mixture of $NaCO_3$ and NaOH, and the sediments were further calcined and reduced with H_2 to obtain a Co-Ni/Al_2O_3 catalyst [62], in which the average size of the particles was 8.6 nm for Ni_2Co_1/Al_2O_3 and 11.4 nm for Co/Al_2O_3 (Figure 3), demonstrating that the precipitation method is feasible for synthesizing small NPs. A similar particle size of Ni-Co also existed on the NiCo/MgAlO catalyst with a uniform particle size of 14.1 nm, and the study revealed that the particle size further increased with increasing calcination time and significantly affected the hydrogenation properties of FAL [56]. In addition, the Ni-Co alloy may form during calcination and improve the interaction of Ni with Co, preventing the loss and aggregation of metals [63]. Although the precipitation method for preparing Co-based catalysts has obvious advantages in industrial production, the poor uniformity of sediments and particles due to the continuous change in systematic concentration results in regional differences in catalyst properties.

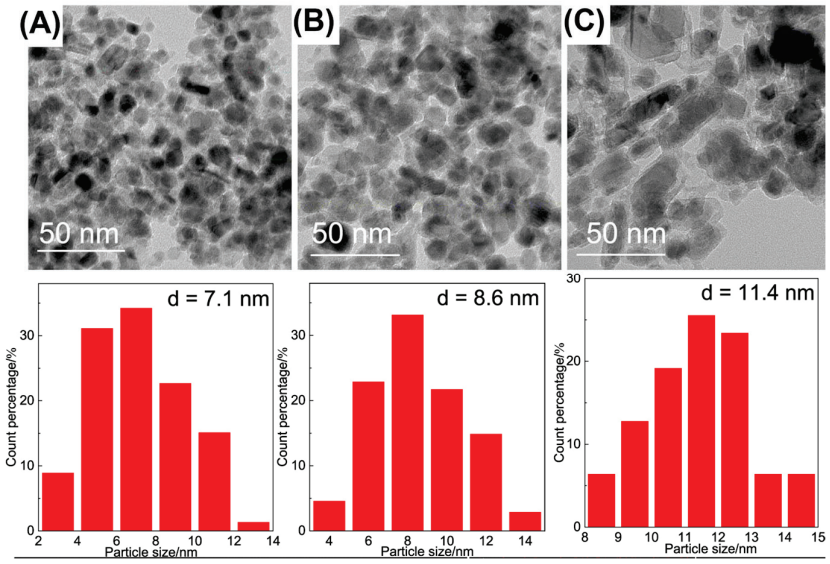


Figure 3. TEM micrographs and particle distributions of Ni_xCo_y/Al_2O_3 with diverse Ni/Co molar ratios: (**A**) Ni/Al_2O_3; (**B**) Ni_2Co_1/Al_2O_3; (**C**) Co/Al_2O_3. Reprinted with permission from ref. [62], 2024, KeAi Communications.

2.3. Solvothermal Method

The solvothermal method is another important synthesis technology for preparing Co-based catalysts; it uses an aqueous solution system with metal ions, complexing agents, precipitants and surfactants and creates internal high-temperature and high-pressure reactors [35,66,67]. The solvothermal method usually involves several processes, including preparing the solution system, dispersing templates or supports, adjusting the pH of the solution, performing a solvothermal reaction, washing and drying the obtained sediments,

and calcining. Because the main products of the solvothermal method are cobalt oxides, the reduction of Co catalysts by H_2 or borohydrides before use is necessary to form active metal sites or metal/metal oxide interfaces [68].

Compared with the precipitation method and impregnation method, the solvothermal process can produce more uniform particles of Co oxides. As shown in Figure 4A, the Ru/Co_3O_4 catalyst was synthesized through co-precipitation, followed by the hydrothermal method, where the Co hydroxides were oxidized under mild hydrothermal conditions at 120 °C and formed Co_3O_4 particles [69]. According to the HRTEM and particle size distribution results (Figure 4B–E), the exposed crystal facets of Ru/Co_3O_4 suggest that spinel cubic oxide single-crystalline phases are present in a sample with frequently separated lattice fringes of 0.24, 0.44, 0.23, and 0.28 nm belonging to Co_3O_4 oxide, and the Co_3O_4 particles have an intensive distribution in the range of 10~22 nm, with an average value of 17.5 nm, which is close to the Co particle size calculated via the Scherer equation. To obtain smaller Co_3O_4 NPs, different solvents are used to create additional interactions between Co_3O_4 NPs [70]. For example, Yun et al. prepared a $Co@SiO_2$ catalyst via a solvothermal process using ethanol as the solvent, followed by a calcination process [71]. The $Co@SiO_2$ catalyst has an average particle size of approximately 10 nm, suggesting that ethanol may inhibit the growth of cobalt nuclei.

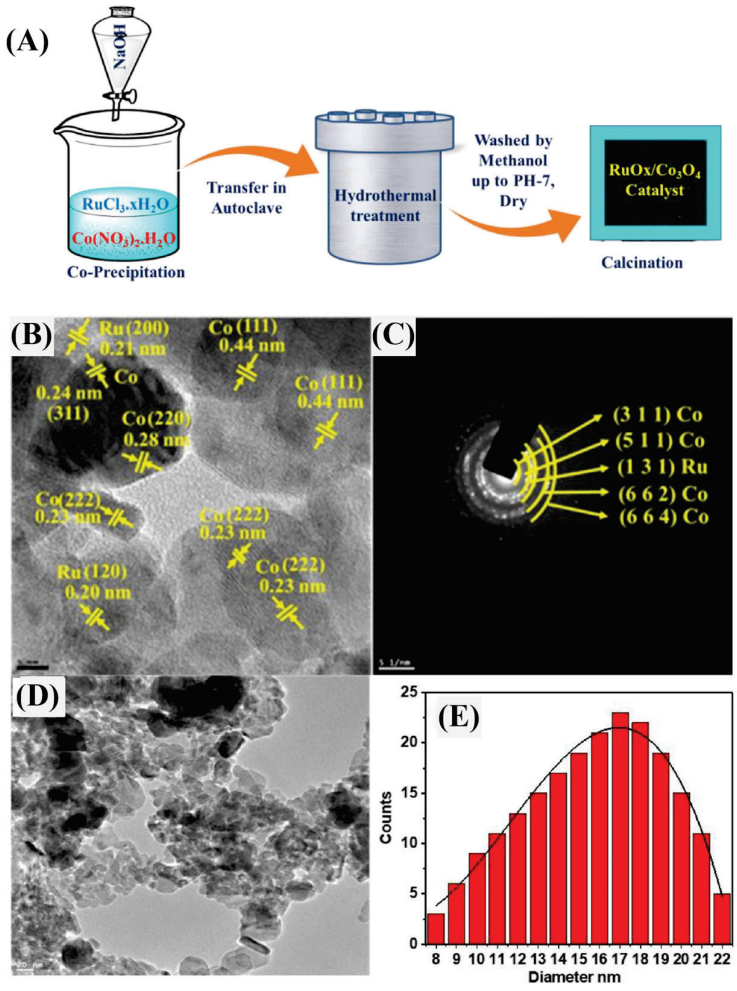


Figure 4. (**A**) Schematic representation of synthesis of $Ru\text{-}Co_3O_4$. (**B**) HR-TEM image of 2.9 wt.% $Ru\text{-}Co_3O_4$ showing different fringes. (**C**) SAED pattern of 2.9 wt.% $Ru\text{-}Co_3O_4$ catalyst. (**D**) HR-TEM image of 2.9 wt.% $Ru\text{-}Co_3O_4$ catalyst at 20 nm scale. (**E**) Particle size of 2.9 wt.% $Ru\text{-}Co_3O_4$ catalyst. Reprinted with permission from ref. [69], 2024, Elsevier.

In addition, the morphology of Co_3O_4 can be controlled by alkali additives during the hydrothermal process, helping to generate Co hydroxides or complexes and further resolve Co oxides. Sharad et al. synthesized Co_3O_4 cubes, rods, and sheets via different additives of NaOH, Na_2CO_3, and ammonia [66]. The characterization results revealed that although the crystal structure, surface composition, and reducibility of Co_3O_4 catalysts with different morphologies are highly similar, Co_3O_4 with reactive (110) planes has superior catalytic activity for CO_2 hydrogenation compared with other structures, indicating that the nanostructure and specific exposed facets of Co_3O_4 can improve catalytic activity. In addition, the hydrothermal conditions and solution composition also influence the exposed crystal facet and interface of Co_3O_4, which has been demonstrated as one of the core problems for its catalytic activity [66,68,72].

2.4. Sol–Gel Method

As an advanced method for synthesizing inorganic materials, the sol–gel technique has many advantages in catalyst preparation because of its mild preparation conditions, controllable microstructure of active components, thermal stability, and anti-deactivation ability. The sol–gel method is a wet chemical method used to prepare metal catalysts by forming homogeneous gels, which results in a high dispersion of metal precursors at the cluster level and even at the atomic level, especially for the preparation of mesoporous nanomaterials [73]. The preparation of Co-based catalysts by the sol–gel method can be briefly summarized in three steps: hydrolysis and polymerization of Co active monomers to form sol, evaporation of the solvent and drying gel, and further calcination or reduction to produce a Co catalyst. Furthermore, several key factors for the synthesis of metal catalysts by sol–gel methods need to be considered, including pH, reactant stoichiometry, gelation temperature, solvent, drying and pretreatment conditions [74].

In recent years, the sol–gel technique has been applied to prepare Co-based composite oxides [17,75–78]. For example, a Co-Al spinel catalyst is prepared via a low-temperature sol–gel method [76], and a schematic illustration of this process is shown in Figure 5A, where the Co and Al nitrates are fully dissolved in ethanol with propylene oxide as a chelating agent and stirred until a Co–Al gel is formed. After aging, the Co-Al gel was dried and calcined under N_2 or air to obtain the Co-Al spinel catalyst. The in situ XRD patterns revealed that the Co-Al gel existed in an amorphous state and that the $CoAl_2O_4$ phase was generated during high-temperature calcination (Figure 5B,C). Finally, the $CoAl_2O_4$ particles of SPN-A (calcined in air) had an average size of 8.5 nm. Mitran et al. used different complexing agents, including citric acid, malic acid, oxalic acid, and urea, to prepare $CoAl_2O_4$ spinels via the sol–gel method and studied their influence on their properties and catalytic activities [79]. The XRD patterns of a series of Co-Al spinels showed similar diffraction peaks for the $CoAl_2O_4$ and Co_3O_4 phases, and the crystallite size of $CoAl_2O_4$ calculated via the Scherrer equation was in the range of 10~19 nm. The influence of using different complexing agents may be reflected in the Co^{3+}/Co^{2+} ratio and Co^{2+}/Al^{3+} ratio, where a good relationship between the Co^{3+}/Co^{2+} ratio and acetophenone hydrogenation conversion was observed. The sample prepared with oxalic acid had the largest Co^{3+}/Co^{2+} ratio of 1.23 and Co^{2+}/Al^{3+} ratio of 4.72, indicating the best hydrogenation activity. Thus, the complexing agents affect the content of high-valence Co sites for Co-Al spinel, which are potential active sites for selective hydrogenation. The sol–gel method has been widely studied and successfully used for preparing uniform composite oxides and derived catalysts. However, gel formation and various procedures for postprocessing lead to longer recycling of catalyst synthesis and high operation costs, restricting industrial production.

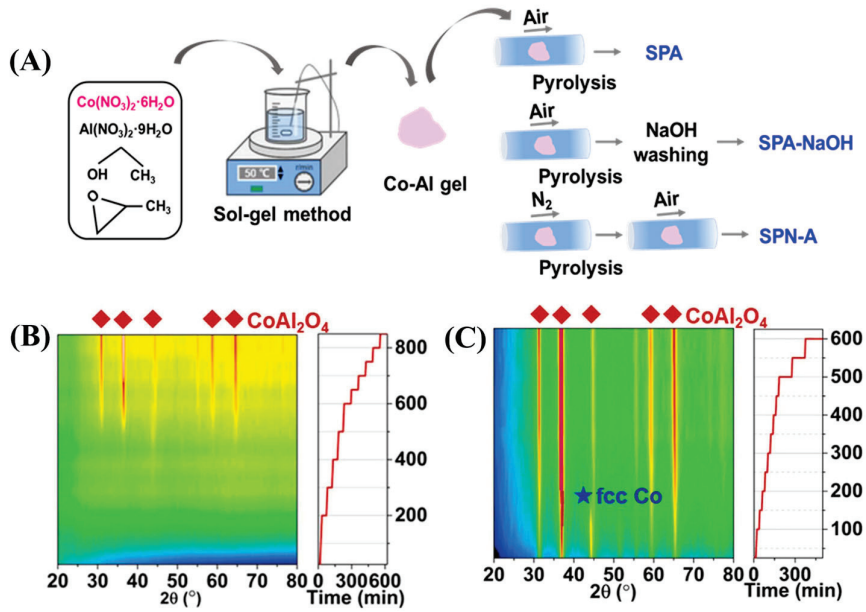


Figure 5. (**A**) Schematic illustrations of preparation process of different $CoAl_2O_4$ catalysts. In situ XRD patterns of (**B**) Co-Al precursor in air and (**C**) SPN (calcined in N_2) in air. ★fcc Co represents the face-centered cubic structure. Reprinted with permission from ref. [76], 2024, Elsevier.

2.5. Pyrolysis Method

The pyrolysis method is based on the use of some functional materials or templates to prepare Co catalyst precursors and further form Co catalysts with special structures by thermolysis, which can construct highly dispersed Co or Co_3O_4 NPs and modify their coordination structure to enhance their hydrogenation properties. Thus, the pyrolysis method is usually used in combination with other methods. Typically, the pyrolysis of MOF-based Co precursors results in the formation of a carbon network with anchored Co species, such as ZIF-67 and ZIF-8 [26,35,51,80–83]. As shown in Figure 6A, the Co-N/C catalyst was first synthesized from the Co-ZIF-67 precursor, which was further pyrolyzed at high temperature to generate Co NPs with an average size of approximately 6–10 nm and many single-atom sites in the carbon network [81]. Furthermore, the use of a surfactant-assisted pyrolysis strategy for Co-based MOFs can further inhibit the agglomeration of Co during the pyrolysis process and afford abundant active CoN_x species and metallic Co clusters (10.8 nm) [83]. Compared with traditional methods, the pyrolysis method results in stronger interactions between the substrate and Co NPs; thus, the prepared Co catalysts have superior reaction properties. In addition, the Co@ZIF-8 (C) catalyst derived from the pyrolysis of the Co@ZIF-8 precursor has a smaller particle size (<2 nm) than Co-ZIF-67 does, indicating that controlling the scale of derived Co particles to reach the cluster or atomic scale by exploring various MOF structures is promising. Moreover, the pyrolysis strategy can also be applied in the template method to realize steric effects and anchoring of metal atoms by physical constraints, and the size of Co metal can be efficiently limited by controlling the structure of the template agents. As shown in Figure 6B, in the synthesis of Co_3O_4 supported on mesoporous carbon, Co^{2+} was first introduced into the polymer gel product by ion exchange, and then Co_3O_4 NPs and the mesoporous carbon network formed simultaneously during the reduction and mild oxidation processes. Ultimately, Co_3O_4 NPs with a mean particle size of approximately 3 nm can be restricted to mesoporous structures [33]. The pyrolysis method for preparing Co-based catalysts has remarkable advantages in terms of steric effects and metal–support interactions, which benefit the dispersion and atomic control of Co metal. However, the catalyst structure after

pyrolysis highly relies on the framework and characteristics of the substrate material, and its application in industry may be limited by the long preparation cycle.

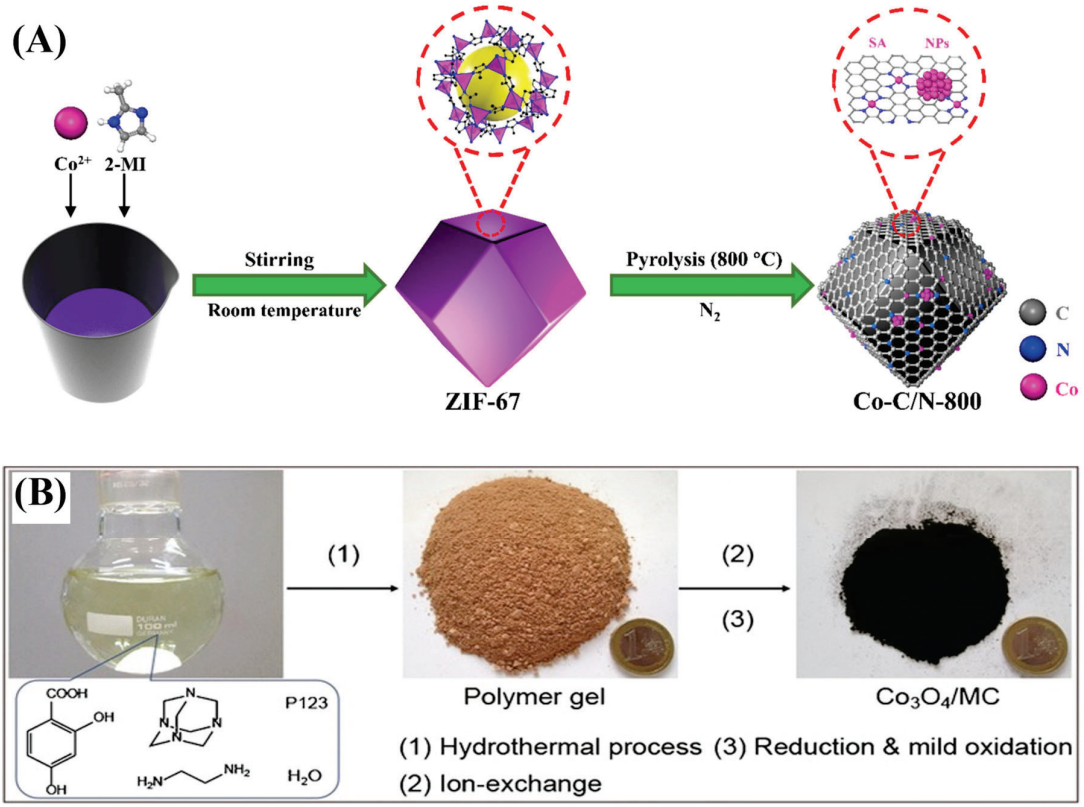


Figure 6. (**A**) Schematic diagram of synthesis procedure of the Co-C/N-800 catalyst. Reprinted with permission from ref. [81], 2024, Elsevier. (**B**) Synthesis of Co_3O_4/MC catalyst. Reprinted with permission from ref. [33], 2024, Wiley.

3. Hydrogenation Properties of Co-Based Catalysts for UAL

The hydrogenation of UAL is a complicated process over Co-based catalysts because of the diversity of Co species, supports, and interfaces, resulting in complicated intermediates and products. It has been reported that Co^0 sites and Co single-atom sites have catalytic activity to dissociate H_2 [44,84,85]. Co_3O_4 has been found to catalyze the transfer hydrogenation of UAL with hydrogenous solvents [86], which mainly finishes the transfer of H atoms by forming annular intermediates. In addition, whether other Co-based compounds have hydrogenation activity remains to be studied. The adsorption mode and hydrogenating direction of the substrate are determined by the geometric and electronic properties of the active center [30]. Thus, the catalytic performance of Co-based and Co oxide catalysts in the selective hydrogenation of typical UAL, including cinnamaldehyde (CAL) to cinnamyl alcohol (COL) and furfural (FAL) to furfuryl alcohol (FOL), are summarized in Table 2 to compare the inherent properties, nanoscale effects, and interfacial effects of Co-based catalysts.

Table 2. Hydrogenation properties of UAL compared to several advanced Co-based catalysts in recent years.

Entry	Catalyst	Loading (wt %)	Reactant	Product	Reaction Condition				X (%)	S_{UOL} (%)	Ref.
					T (°C)	P (MPa)	t (h)	Solvent			
				H_2 dissociation hydrogenation							
1	Co/TiO_2	15.0	CAL	COL	120	1.0	1.0	Methanol	47.4	58.0	[87]
2	CoAl	11.7	CAL	COL	150	-	5.0	Propylene carbonate	51.0	57.0	[88]
3	ε-Co_{NP}/G_{OX}	4.5	CAL	COL	120	2.0	4.0	Dioxane	45.1	100.0	[89]
4	Co-C-500	56.0	CAL	COL	90	2.0	4.0	Ethanol + H_2O	85.3	51.5	[90]
5	Co@NPC	69.8	CAL	COL	80	0.5	5.0	H_2O	85.5	79.1	[91]
6	Co-NC-450	80.0	FAL	FOL	110	1.5	2.0	H_2O	92.0	99.0	[92]
7	Co/NC-700	55.0	FAL	FOL	120	2.0	0.5	Methanol	83.0	100.0	[93]
8	$Co/CoN_x/C$	48.9	CAL	COL	30	2.0	13.0	methylbenzene	94.0	93.0	[26]
9	$Co\text{-}N\text{-}C@F127_{0.3}$	29.1	FAL	FOL	140	1.0	2.0	2-POL	97.2	92.5	[83]
10	$Co@L2N@b\text{-}TiO_2$–N-7	3.13	CAL	COL	100	2.0	6.0	2-POL	59.0	97.0	[94]
11	Co@BN/BN-600	8.5	CAL	COL	120	0.4	11.0	Ethanol	83.3	81.3	[95]
12	$Co_2Al\text{-}H_2$-400	NA	CAL	COL	100	2.0	2.0	H_2O	97.0	73.6	[96]
13	$Co/ZrLa_{0.2}O_x$	8.8	FAL	FOL	80	2.0	2.0	H_2O	95.0	92.0	[97]
14	CuCo/MgO-0.04	5.0	FAL	FOL	100	2.0	0.7	2-POL	82.4	92.7	[98]
15	CuCo/NC	39.3	FAL	FOL	100	3.0	6.0	Ethanol	35.6	94.3	[82]
16	$CoZnB/Nb_2CT_x$	9.5	CAL	COL	100	3.5	2.0	2-POL	91.4	72.6	[99]
17	Co-Fe-1%Zn-B	60.7	CAL	COL	130	2.0	1.0	Ethanol	97.7	100.0	[100]
18	Co-Fe/ACBT	8.3	CAL	COL	120	2.0	5.0	Methanol	90.5	86.8	[101]
19	$Fe_{0.5}Co@NC$	46.8	CAL	COL	80	2.0	5.0	Water	95.1	91.7	[102]
				Catalytic transfer hydrogenation							
20	$Co_3O_4@NC$	3.5	CAL	COL	180	1.0	12.0	2-POL	81.1	94.1	[35]
21	Co_3O_4/MC	15.0	FAL	FOL	160	1.0	6.0	2-POL	100.0	98.0	[33]
22	$Co_3O_4/NCNF$	22.0	CAL	COL	160	-	5.0	2-POL	100.0	95.0	[34]
23	$CoO_x@Co\text{-}500$	15.6	CAL	COL	120	-	8.0	2-POL	97.5	90.1	[37]
24	$ZIF\text{-}67@SiO_2\text{-}CPTEOS$	17.4	CAL	COL	180	1.0	12.0	2-POL	84.6	95.0	[103]
25	$Co_3O_4\text{-}Al_2O_3$	45.8	FAL	FOL	150	-	6.0	2-POL	76.3	97.0	[104]
26	$CoCrO_x$ (1:2)-CN	8.6	CAL	COL	120	1.0	12.0	2-POL	97.5	95.3	[105]
27	$Co_{1.5}Mg_{1.5}Al_1$-LDO-500	15.5	FAL	FOL	160	-	6.0	2-POL	99.7	95.9	[106]

3.1. Metal Catalysts

3.1.1. Monometallic Co-Based Catalysts

Monometallic Co catalysts are simple and efficient catalysts for producing UOCs because of their natural hydrogenation selectivity for C=O. To investigate the inherent hydrogenation activity of Co, a series of monometallic Co catalysts supported on Al_2O_3, SiO_2, and TiO_2 were prepared via the conventional impregnation method for CAL hydrogenation [87], where the Co/TiO_2 catalyst showed the highest CAL conversion of 47.4% and selectivity of 58% for COL, suggesting that the Co NPs preferentially hydrogenated C=O, followed by C=C hydrogenation. Even for the $Co\text{-}CoO@SiO_2$-500 catalyst with a core–shell structure, the selectivity of COL ultimately reaches approximately 65% under steric effects [67]. The above monometallic Co catalysts prepared via a simple method usually generate typical hexagonal close-packed (hcp) Co, which mainly exposes (1 1 $\bar{2}$ 0)-type facets and has higher hydrogenation activity than face-centered cubic (fcc) Co and epsilon (ε) Co. Notably, ε-Co NPs have been successfully prepared, which have an average particle size of 6.5 nm and exhibit superior selectivity to COL (100%), but the ε phase of Co cannot stably exist under the reaction conditions [89].

It is well known that reducing the size of metal particles can increase the specific surface area and the exposed metal sites of catalysts and thus improve their catalytic performance [30,107]. However, it seems that the smaller size of Co NPs is not always beneficial for C=O hydrogenation. For example, a CoAl spinel catalyst derived from layered double hydroxide (LDH) precursors has smaller Co NPs than 3 nm after H_2 reduction [88], which results in moderate selectivity for UOL (~60%) because the adsorption of both C=O and C=C may be allowed simultaneously on small particles of Co, although the adsorption

of the C=O bond is predominant. For another hydrotalcite-derived Co_2Al-400 catalyst [96], Co NPs with a mean size of 7.0 nm showed a higher conversion of 97.0% and selectivity of 73.6% for COL in H_2O, suggesting that Co NPs have a significant size effect on their hydrogenation activity. For larger particles over the Co/NC catalyst, Co NPs have an average size of 12.8 nm, which results in better performance in terms of both conversion (83%) and selectivity (>99%) for producing UOL [93], suggesting that smaller Co particles are not necessarily better for hydrogenation. The same nanosize effect also occurs for the adsorption and conversion of other substrates on Co NPs [47,76]. Thus, according to the above discussion, the size of Co NPs should have an appropriate range of approximately 6~20 nm close to the cluster or subnanometer scale for hydrogenation.

To enhance the hydrogenation properties of monometallic Co catalysts, an effective strategy is to introduce functional supports to adjust the size and electronic properties of Co NPs at the same time. Owing to the natural electronic structure of Co metal, its ability to dissociate H_2 can be improved by the use of electron-rich supports to increase the d-electron intensity of Co NPs. For example, Tian et al. prepared a Co NP catalyst supported on a carbon material derived from the MOF precursor Co-BTC [90]. Compared with the other monometallic Co catalysts, the Co-C-500 catalyst resulted in greater conversion of CAL (85.3%) at a low reaction temperature of 90 °C, which was attributed to the uniform dispersion of Co NPs on the carbon support, with an average diameter of 11.3 nm. Furthermore, the doped elements are introduced into the carbon material to modify the electronic structure of the Co NPs. For example, nitrogen is introduced into MOF-derived $Co/CoN_x/C$ catalysts to enhance C=O hydrogenation over Co-N_x active sites [26]. As shown in Figure 7A–D, the Co NPs were uniformly anchored on the derived carbon network with a mean diameter of 6~7 nm, and the $Co/CoN_x/C$-600 catalyst showed improved selectivity for COL (>90%). The Raman and XPS spectra of the catalyst revealed possible N-bonds over $Co/CoN_x/C$ (Figure 7E), indicating that the Co-N_x sites may work as active centers or promote electron transfer. The electronic effect of doped N has also been reported for other derived carbon materials [91–93] and boron nitride materials [95,108], demonstrating that it is a widely practicable strategy for the design of Co-based catalysts. As mentioned above, monometallic Co catalysts are widely used in C=O-selective hydrogenation, and the selectivity for UOL can reach 90% when some functional materials are used as supports. In addition, Co NPs have a size effect, which is reflected by the remarkable decrease in activity and C=O selectivity in UAL hydrogenation when their size is less than 6 nm.

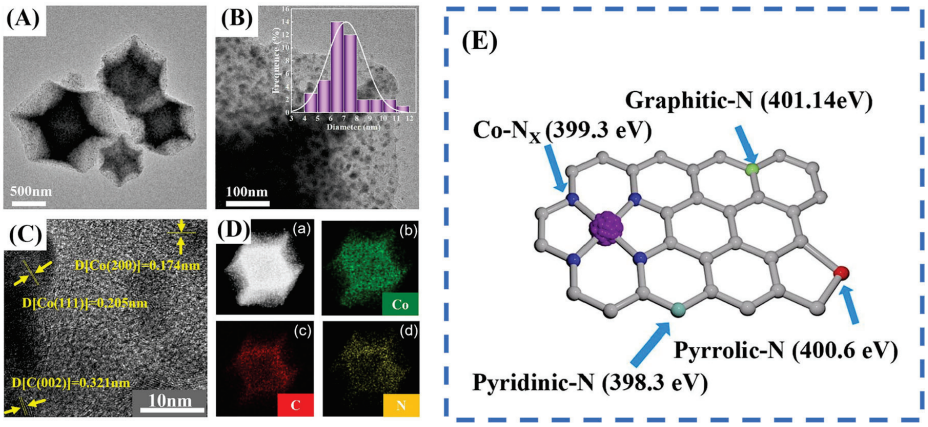


Figure 7. (**A**–**C**) HRTEM image of $Co/CoN_x/C$-600. (**D**) HAADF-STEM images of individual NPs (a) and corresponding elemental mappings of Co (b), C (c), and N (d) in $Co/CoN_x/C$-600. (**E**) Schematic representation of possible N-bond configurations. Reprinted with permission from ref. [26], 2024, Elsevier.

3.1.2. Bimetallic Co-Based Catalysts

Co is usually introduced as an assistant to noble metals, such as Pt, Pd, and Ni, to improve their C=O hydrogenation properties, and the promoting role of Co has been sufficiently discussed in previous reviews [29,30,46]. In this section, the roles of Co and second metals in the structural effect and electronic effect are concentrated. On the basis of the above discussion, monometallic Co catalysts have moderate catalytic activity and preferentially attack C=O, followed by C=C hydrogenation. Therefore, second metals are introduced to further enhance their catalytic properties, which mainly play a role in two aspects: modifying the properties of Co metal and forming synergistic effects with Co via additional functional sites.

In general, Co combined with some nonnoble metals, such as Cu [82,98], Fe [101,102], and Zn [99], may have synergistic effects. For example, a CuCo/MgO bimetallic catalyst synthesized by simple impregnation and calcination methods has different electronic effects on Co and Cu [98], where the electron-rich Cu sites play a role in H_2 dissociation, and the d-band center of the CuCo/MgO catalyst moves upward from −2.4756 eV to −2.4350 eV (Figure 8A,B), resulting in a more pronounced adsorption capacity of the Cu sites for H_2 and intermediate, ultimately resulting in an increasing conversion of 82.4% and selectivity of 92.7% compared with those of the monometallic catalyst. In addition, Xu et al. demonstrated that the improved catalytic performance of the CuCo system was due to the high dispersion of the Cu-related species on the Co NPs, confinement effect of the N-doped carbon supports and synergistic effect [82]. The DFT results suggested that the energy of H_2 dissociation was only 0.003 eV for the CoCu/NC catalyst, and the barrier to the hydrogenation of C=O by active H atoms also decreased (Figure 8C). Importantly, the rate-determining step of UAL hydrogenation over a Co-based bimetallic catalyst may involve the activation of reactants and a progressive hydrogenation process.

The large d-bandwidth of Co and its role in C=O hydrogenation have been proven by many studies. However, Co sites lack the ability to inhibit the adsorption of C=C, resulting in complicated reaction products. In our previous work, the effect of a dilute alloy on a CoZnB/Nb_2CT_x catalyst was studied, where Zn was introduced to modify the coordination and electronic states of CoB NPs [99]. As shown in Figure 9, Zn worked as a dispersing agent and restricted the growth of CoB NPs, and the enhanced activity of CoZnB/Nb_2CT_x at low temperatures (from 15.2% to 91.4%) was attributed to the smaller particle size (reduced from ~40 nm to ~15 nm) and electron transfer effect, which promoted the adsorption and activation of H_2 and C=O at the Co and B sites, respectively. This size effect of metal atoms via the distributed arrangement of multimetal atoms also occurred for Co-Fe [101,102] and Co-Fe-Zn systems [100], which not only weakened the concentrated adsorption of nonpolar C=C on adjacent Co-Co sites but also inhibited side reactions involving solvent effects. For Co-based catalysts, the reductive etherification and aldolization of aldehydes and alcohols can be catalyzed by cobalt and Lewis acid cooperative sites [8,10,109]; thus, decreasing the coordination number and bond length of Co-Co with a second metal efficiently reduces the number of byproducts.

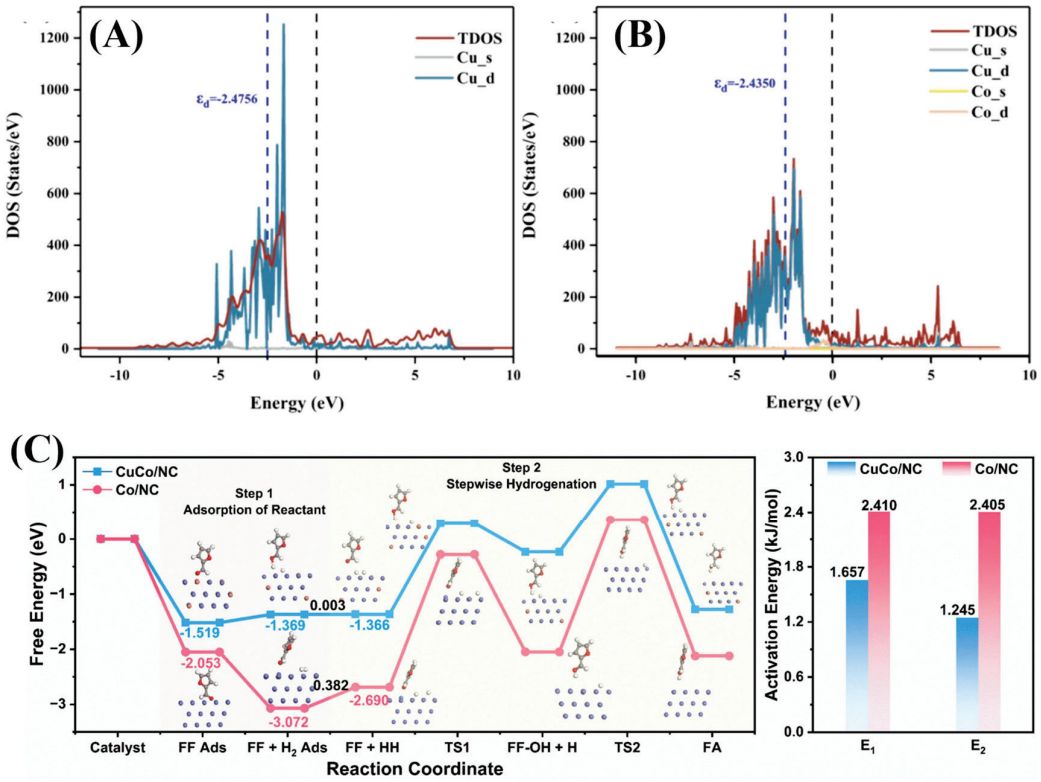


Figure 8. Total density of states (TDOS) and partial density of states (PDOS) of (**A**) Cu/MgO surface and (**B**) CuCo/MgO-0.04 interface; vertical black-dashed lines represent the Fermi level. Reprinted with permission from ref. [98], 2024, Elsevier. (**C**) Gibbs free energy pathway of FF-selective hydrogenation reaction catalyzed by Co/NC and CuCo/NC. Reprinted with permission from ref. [82], 2025, Elsevier.

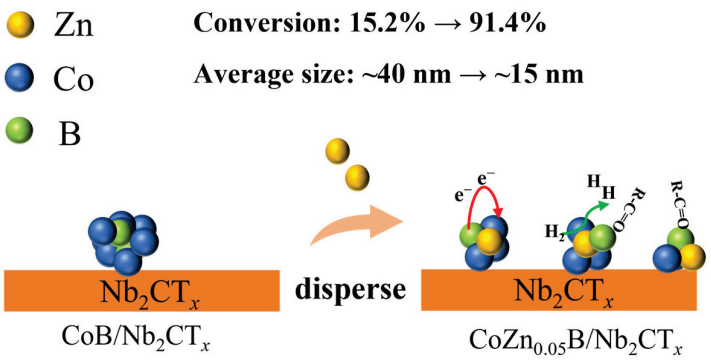


Figure 9. Mechanistic diagram of how Zn improved catalyst performance. Reprinted with permission from ref. [99], 2025, Elsevier.

3.2. Co-Based Oxide Catalysts

Co oxide components widely exist in all Co-based catalysts, and their role in catalytic reactions is easily overlooked. It has been reported that the synergistic effect of Co^0 and $Co^{\delta+}$ sites over the Co^0/CoO_x interface can remarkably improve the process of H_2 dissociation and activate hydrogen transfer to substrates [110]. In addition, Co_3O_4 NPs are highly selective catalysts for transfer hydrogenation via the use of organic alcohols as hydrogen sources [33,86]; therefore, Co_3O_4 NPs are safer than traditional H_2 hydrogenation methods under high pressure. Compared with H_2 dissociation hydrogenation, transfer hydrogenation of UAL on Co-based catalysts shows significant differences in two aspects. On the one hand, catalytic activity is determined by the protonation and proton transfer ability of the catalyst for organic alcohols. On the other hand, the solvent effect has a more

marked effect on the hydrogenation selectivity. In this section, the catalytic performances of Co-based oxide catalysts are briefly reviewed.

3.2.1. Co Oxide Catalysts

Compared with Co NPs, pure Co_3O_4 NPs have natural properties for transfer hydrogenation and show greater selectivity for C=O. Wang et al. prepared Co_3O_4 NPs (~3 nm) supported on mesoporous carbon (Co_3O_4/MC), which have 95% selectivity toward UOL at full conversion, higher than that of most Co metal catalysts [33]. Notably, a size effect of Co_3O_4 NPs has been reported for CO_2 [111] and acetone [47] hydrogenation, but its influence on the hydrogenation selectivity of UAL is still poorly understood. For FAL and 5-hydroxymethylfurfural hydrogenation, Co_3O_4-6 nm, Co_3O_4-17 nm, and Co_3O_4-nanocasting catalysts are introduced for comparison with Co_3O_4/MC. As shown in Figure 10A,B, the Co_3O_4/MC catalyst with an average Co_3O_4 NP size of 3 nm is more active than the other Co_3O_4 catalysts. In addition, Co_3O_4-6 nm exhibited the best reaction rate (2.29 mmol/(g_{cata}·h)) at 120 °C compared with Co_3O_4-17 nm (0.26 mmol/(g_{cata}·h)) and Co_3O_4-nanocasting (0.32 mmol/(g_{cata}·h)) samples without support [33], suggesting that smaller Co_3O_4 NPs may increase the hydrogenation rate.

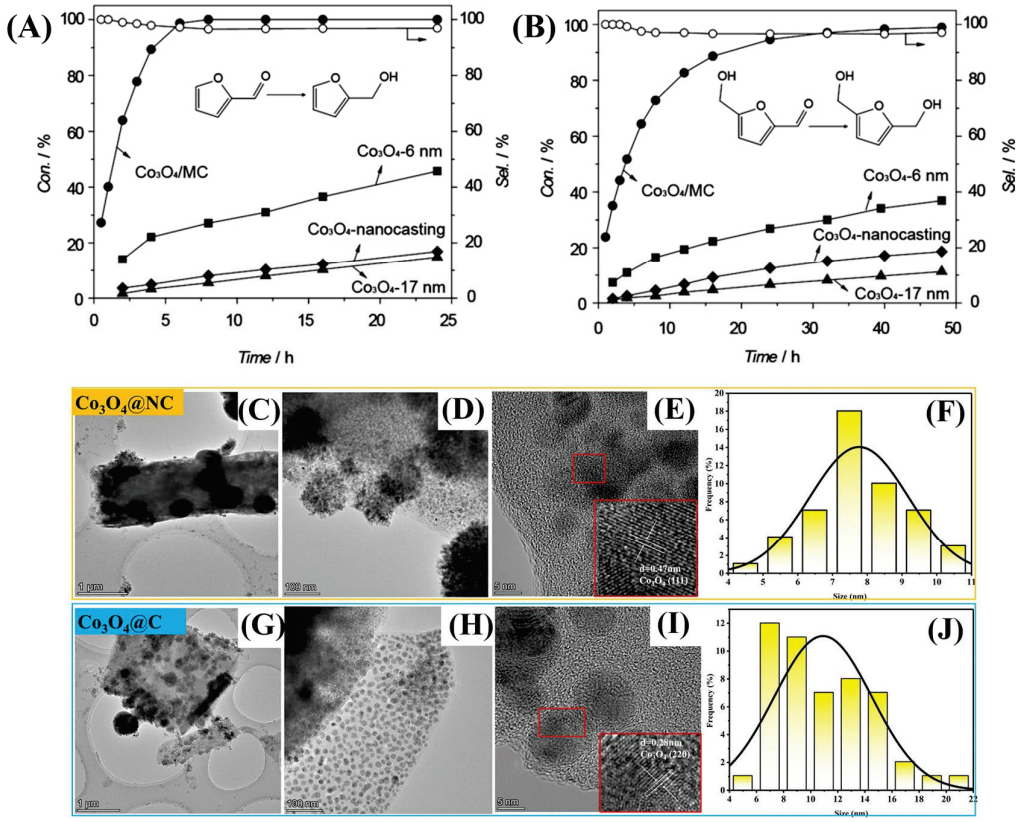


Figure 10. Catalytic performance in the transfer hydrogenation of (**A**) FAL to FOL and (**B**) HMF to BHMF at 120 °C over Co_3O_4/MC, Co_3O_4-nanocasting, Co_3O_4-6 nm, and Co_3O_4-17 nm. Reaction conditions: 1 mmol of substrate, 10 mL of 2-propanol, 50 mg of Co_3O_4/MC, 25 mg of Co_3O_4-nanocasting, Co_3O_4-6 nm, and Co_3O_4-17 nm. Reprinted with permission from ref. [33], 2016, Wiley. TEM images of (**C**,**D**) Co_3O_4@NC and (**G**,**H**) Co_3O_4@C; HRTEM images of (**E**) Co_3O_4@NC and (**I**) Co_3O_4@C; particle size distributions of (**F**) Co_3O_4@NC and (**J**) Co_3O_4@C. Reprinted with permission from ref. [35], 2023, Elsevier.

Furthermore, Co_3O_4 NPs are more resistant to agglomeration and do not suffer from oxidative deactivation, resulting in better reaction stability than Co NPs under reaction conditions. Although the Co_3O_4 NPs showed superior C=O selectivity in UAL hydrogenation,

their poor activity led to strict reaction conditions and a low turnover frequency. Thus, the main factors and modification methods used to promote the intrinsic and total activities of Co_3O_4 catalysts have been studied. For Co-based catalysts supported on carbon materials, N doping is a widely used strategy to improve the interaction between catalysts and substrates [34,91–93,112]. For example, Cui et al. successfully synthesized MOF-derived Co_3O_4@NC catalysts for the transfer hydrogenation of CAL [35]. As shown in Figure 10C–J, the Co_3O_4 NPs were uniformly dispersed on the carbon networks derived from the MOFs, and the average particle size distribution of Co_3O_4@NC was 7.5 nm, whereas it was 10 nm for Co_3O_4@C, suggesting that the introduction of N in the MOFs reduced the aggregation of Co_3O_4 NPs. In terms of their hydrogenation properties, the conversion of CAL increased 41.2% after N doping with 95.9% selectivity to COL, which was attributed not only to the change in Co_3O_4 NP size but also to the intervention of functional N sites in the hydrogenation process. In general, doped N sites or functional groups containing N act as basic sites to adsorb active H species or intermediates on solid catalysts [35,113]. Moreover, a specific Co-N_x can modify the electronic structure of Co sites [26,114], ultimately resulting in the promotion of Co-based catalysts.

In addition, the composition and valence state of Co oxides affect their hydrogenation performance. Gong et al. synthesized a simple shell-core structured CoO_x@Co catalyst for UAL hydrogenation to UOL with a selectivity over 90% [37]. As shown in Figure 11A–C, a clear interface of Co^0/CoO can be observed in the TEM images, with a concentrated distribution of Co in the core. The XPS spectra further verified the reduction of Co oxides and the generation of the Co^0 core (Figure 11D,E). Moreover, a synergistic effect of Co^0–$Co^{\delta+}$ sites over the CoO_x@Co catalyst was revealed by DFT calculations. As shown in Figure 11F, CAL had an adsorption energy of −1912 kJ/mol on the CoO (111) surface, suggesting that the low activity of Co oxides in transfer hydrogenation may be ascribed to extremely strong adsorption, resulting in a decreased turnover frequency and possible hydrogenation of C=C. The internal Co^0 sites of the CoO_x@Co catalyst can facilitate weak adsorption toward C=O, suggesting that an optimal CoO_x composition is required to simultaneously achieve efficient conversion and high selectivity. This influence of the chemical composition of Co oxides on selective hydrogenation properties lays the foundation for the design of Co-based composite oxide catalysts.

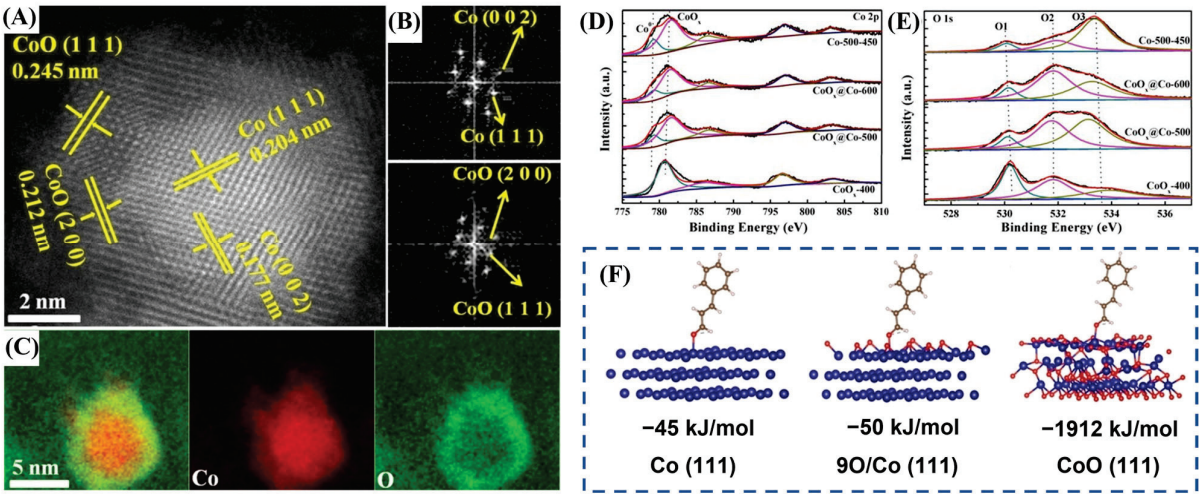


Figure 11. (**A**) HRTEM image, (**B**) FFT image, and (**C**) EELS elemental maps of one particle of CoO_x@Co-500 catalyst. (**D**) Co 2p and (**E**) O 1s spectra of CoO_x-400, CoO_x@Co-500, CoO_x@Co-60 and Co-500-450. (**F**) Optimized geometry for most stable configuration of CAL on Co (111), Co (111), and CoO (111) surfaces. Blue, red, brown, and white spheres represent cobalt, oxygen, carbon and hydrogen atoms, respectively. Reprinted with permission from ref. [37], 2019, Wiley.

3.2.2. Co-Based Composite Oxide Catalysts

Similarly to Co-based bimetallic catalysts, the drawback of low activity for Co oxide catalysts is overcome by the formation of composite oxide catalysts, including mixed metal oxides and multimetal oxides. As shown in Table 2 entries 24–27, the required reaction conditions for Co-based composite oxide catalysts are milder, while the transformation rate and selectivity for C=O are also superior to those of pure Co oxide catalysts. Mixed or supported metal oxide catalysts are easily obtained via simple impregnation methods and precipitation methods. For example, a hydrotalcite-derived Co_3O_4-Al_2O_3 catalyst was synthesized via the co-precipitation method [104], which showed good activity for FAL transfer hydrogenation and 97% selectivity for C=O at low temperatures. The introduction of Al_2O_3 may provide crucial basic sites for transfer hydrogenation via the MPV reaction. However, the formation of side products derived from the acetalization and etherification pathways is also observed at various temperatures because of the presence of several strong acid or basic sites [8–10].

Another strategy to construct Co-based composite oxide catalysts is to dope other metals into the spinel structure of Co_3O_4. For example, CoMgAl composite oxide (LDO) catalysts are derived from Co-based ternary layered hydroxides for transfer hydrogenation of FAL [106]. As shown in Figure 12A,B, the characteristic diffraction peaks of the LDH precursor basically disappeared after calcination, new diffraction peaks belonging to Co_3O_4 spinel appeared, and the intensity gradually increased, suggesting that Mg and Al did not exist as independent oxides. The surface acidity and basicity of $Co_{1.5}Mg_{1.5}Al_1$-LDO-500 significantly increased compared with those of the Mg_3Al_1-LDO-500 catalyst (Figure 12C,D), in which the basic site (O^{2-} site) and Lewis acid sites ($Co^{\delta+}$) promoted the deprotonation of isopropanol and the activation adsorption of FAL via the MPV route, resulting in an improved hydrogenation activity of 99% conversion and 95% selectivity to FOL. In addition, Mao et al. successfully prepared a $CoCrO_x$ spinel catalyst supported on N-doped carbon via the sol–gel method and revealed the influence of interfacial electron migration and N-doped carbon on the acid–base synergy of the $CoCrO_x$ catalyst [105], in which $CoCrO_x$(1:2)-CN showed a 95.3% yield of COL and an activation energy of 69.2 kJ/mol for CAL transfer hydrogenation lower than those of other samples (Figure 13A), demonstrating that the Co–Cr spinel phase is more active for transfer hydrogenation. Furthermore, the effects of the Co/Cr ratio and doped N on the acidity and basicity were investigated. As shown in Figure 3B,C, CO_2-TPD and NH_3-TPD profiles revealed that strong acid and basic sites near 597.1 °C and 582.7 °C, respectively, were generated when the Co/Cr ratio increased to 1:1, suggesting the interaction of Co and Cr. After the introduction of N into carbon, both the surface acidity and basicity significantly increased (Figure 13D), indicating that N sites not only provided surface basic sites for the catalyst but also promoted the exposed acid sites from $CoCrO_x$ spinel. Co oxides and Co-based composite oxides seem to be promising catalysts for transfer hydrogenation because of their safe reaction conditions without high-pressure hydrogen and superior selectivity to UOL. However, the effects of the Co oxide composition, interface, and weak interactions of the substrate need more in-depth investigation.

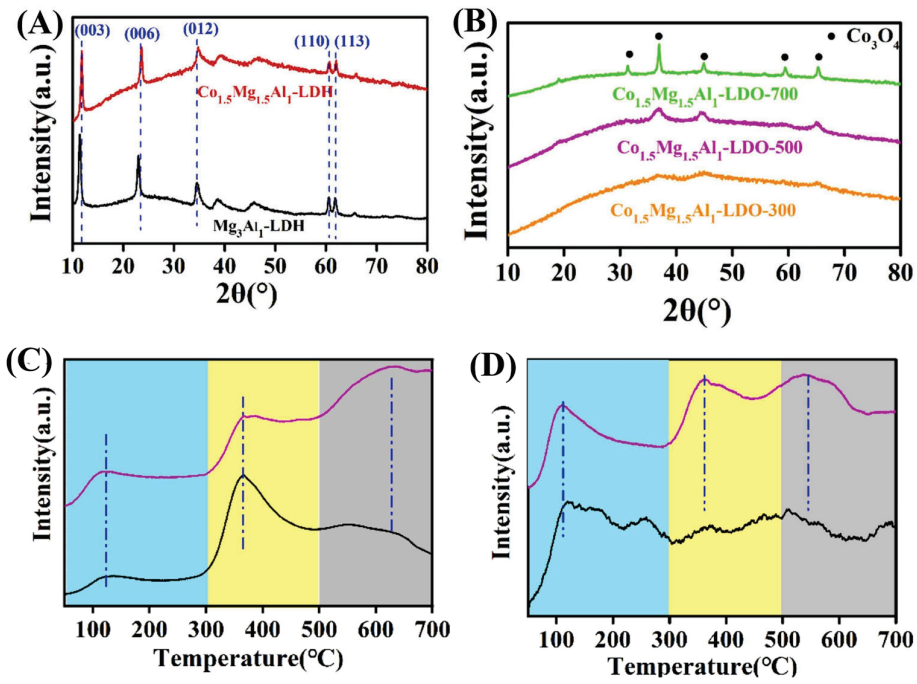


Figure 12. (**A**) XRD patterns of Mg_3Al_1-LDH and $Co_{1.5}Mg_{1.5}Al_1$-LDH. (**B**) XRD patterns of $Co_{1.5}Mg_{1.5}Al_1$-LDO at different calcination temperatures. (**C**) NH_3-TPD and (**D**) CO_2-TPD spectra of Mg_3Al_1-LDO-500 (black line) and $Co_{1.5}Mg_{1.5}Al_1$-LDO-500 (pink line), where the blue dotted line represents the rough position of desorption peaks. Reprinted with permission from ref. [106], 2024, Elsevier.

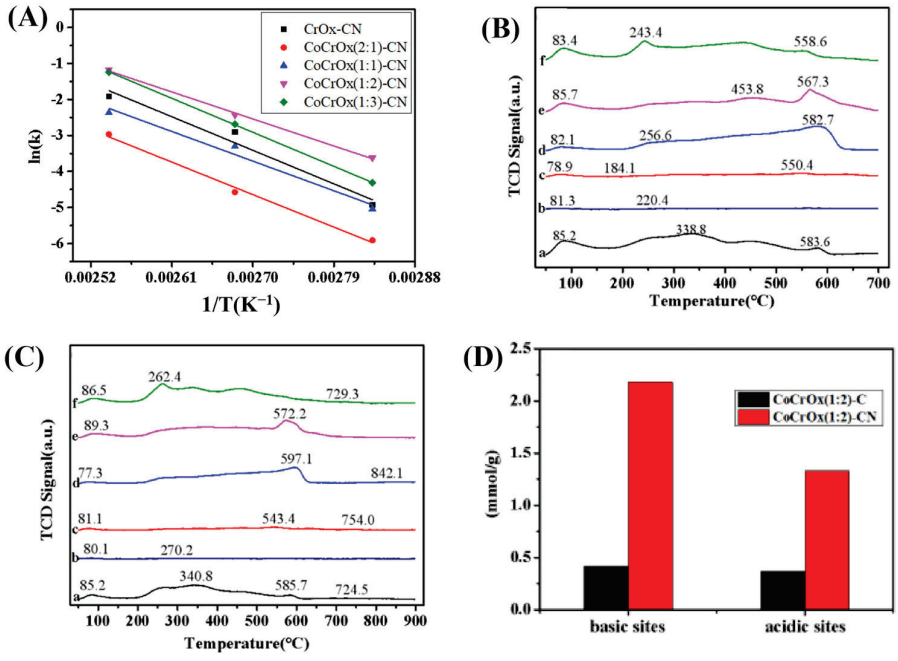


Figure 13. (**A**) ln(k) vs. reciprocal of reaction temperature in CTH of CMA. (**B**) CO_2-TPD and (**C**) NH_3-TPD curves of catalysts: (a) CrO_x-CN, (b) CoO_x-CN, (c) $CoCrO_x$ (2:1)-CN, (d) $CoCrO_x$ (1:1)-CN, (e) $CoCrO_x$ (1:2)-CN and (f) $CoCrO_x$ (1:3)-CN. (**D**) Number of basic and acidic sites. Reprinted with permission from ref. [105], 2022, Elsevier.

4. Reaction Mechanisms of UAL over Co Active Sites

On the basis of differences in hydrogen donors, the hydrogenation of UAL to produce UOL can be conducted via two pathways: H_2 dissociation hydrogenation and catalytic

transfer hydrogenation. As shown in Figure 14, H_2 dissociation hydrogenation usually follows the Horiuti–Polanyi mechanism over a metal center, where H_2 and UAL are adsorbed and activated on adjacent metal sites simultaneously, and the selectivities of products are determined by the adsorption model of conjugated double bonds. The transfer hydrogenation pathway mainly followed the MPV mechanism, in which the C=O of UAL and the hydroxy of organic alcohol can form a ring intermediate and further finish the hydrogenation of C=O by Lewis acid sites. In both hydrogenation pathways, solvents have a crucial effect on the reaction process. On the one hand, solvents play a role in promoting mass transfer and increasing the contact surface area of reactants in direct H_2 hydrogenation [115,116], where alcohols do not participate in hydrogenation. On the other hand, transfer hydrogenation using solvents as hydrogen resources can occur by altering the catalyst and reaction conditions, where the hydroxyl hydrogen of alcohol is activated and transferred to C=O or C=C and generates aldehyde or ketone products. In addition, side reactions between alcohols and aldehydes, such as aldolization [9,10] and reductive etherification [117], may occur during both hydrogenation pathways. Thus, the reaction process, solvent effect, and several potential hydrogenation mechanisms for UAL hydrogenation over Co-based catalysts are reviewed and discussed in this section.

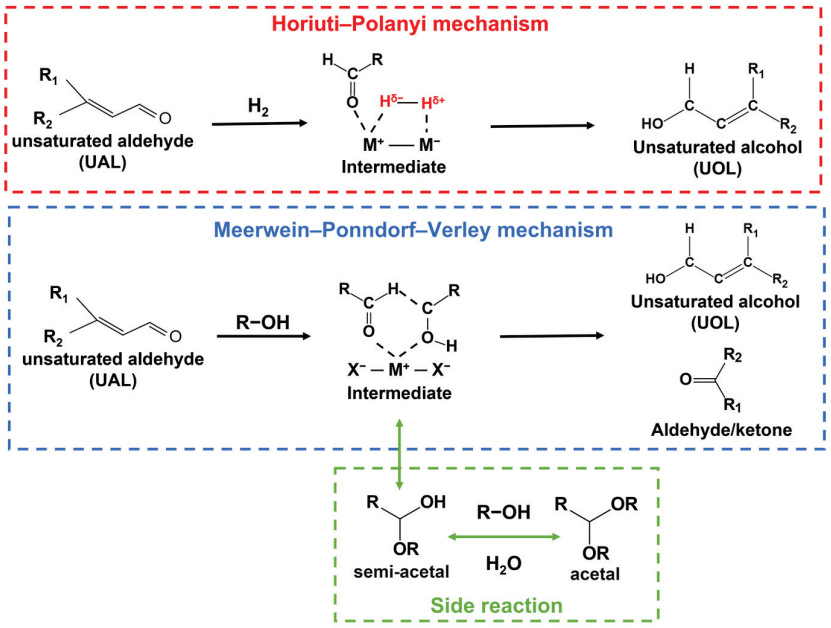


Figure 14. Illustration of Horiuti–Polanyi and MPV mechanisms with potential side reaction pathways for UAL hydrogenation.

4.1. Hydrogen Dissociation Hydrogenation

Thermocatalytic H_2 dissociation hydrogenation is still one of the most typical and widely applied technologies for modern industry and pharmaceutical applications [118,119] and relies on H_2 pyrolysis to activate H species on active metal centers, metal-base sites, and frustrated Lewis pair (FLP) sites [12,120,121]. As shown in Figure 15, for Co-based catalysts, H_2 can be activated at adjacent Co–M (M = Co or second metal) sites and Co–X (X = base site) sites by homolytic dissociation or heterolytic dissociation. Moreover, the adsorption and desorption behavior of UAL at the active center markedly affects the hydrogenation selectivity and catalytic activity of catalysts [30]. In this section, the characteristics and characteristics of H_2 dissociation hydrogenation of UAL over different Co active sites are summarized.

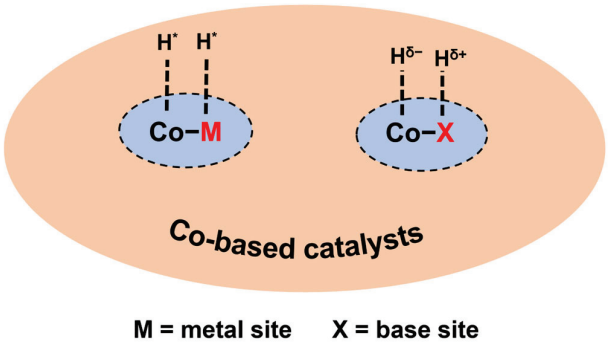


Figure 15. Illustration of H_2 dissociation over Co-based catalysts.

The H_2 dissociation efficiency usually determines the total catalytic rate of catalysts in hydrogenation. For the Co NPs, the DFT calculations revealed that the dissociation barriers of H_2 on Co(311), Co(111), and Co(110) are 13.0, 2.7, and 14.5 kJ/mol, respectively, which are all lower than their desorption energies, indicating that H_2 is likely activated at the Co active center and that Co(111) is more active for H_2 pyrolysis to activate hydrogen [122]. Furthermore, the influences of the particle size and crystal structure of Co NPs are reviewed. First, the different H_2 dissociation energies that rely on the size of the fcc Co NPs are shown in Figure 16A, in which the H_2 activation efficiency of the Co NPs in the particle size range of 3.5~40 nm according to H–D exchange analyses demonstrated that the more facile HD formation at lower temperatures is, the larger the Co particles become [47], indicating that large Co NPs benefit H_2 dissociation. The influence of the Co NP crystal structure can subsequently be explained by their H_2 desorption ability. As shown in Figure 16B, hcp Co exhibited an obvious desorption peak of H_2 near 100 °C, which was not observed for fcc Co. The amount of H_2 released from hcp Co (21.0 μmol/g) was up to two times greater than that released from fcc Co (9.7 μmol/g) [123], resulting in better H_2 activation efficiency for hcp Co. The activation of H_2 by Co centers may be related to the bond length and structure of the exposed Co–Co sites, indicating differences in the hydrogenation properties of Co NPs with various particle sizes and crystal structures.

On the basis of the discussion above, H_2 can be dissociated by dual active sites in principle. However, it is exceptional for single-atom catalysts. For example, Cao and coworkers prepared a single-atom Co catalyst with a g-C_3N_4 template and adjusted its coordination structure via P-doping [113]. As shown in Figure 16C, the single-atom Co_1-N-C and Co_1-N/P-C catalysts had H_2 desorption temperatures of 535 K and 697 K, respectively, which are higher than those of the other Co NP catalysts, indicating that the stronger interaction and activation of H_2 are related to the coordination environment of the single-atom Co sites. Furthermore, the dissociation processes and energies of H_2 over Co_1-N-C and Co_1-N/P-C catalysts are calculated via DFT simulation, where one of the H atoms attaches to the Co center while the other H atom transfers to the neighboring N atom or P atom, and the dissociation energy barriers are only 2.06 eV and 0.71 eV for the Co_1-N-C and Co_1-N/P-C catalysts, respectively (Figure 16D). It seems that H_2 activation over Co_1–N_4 or Co_1–N_2P_2 sites followed the Lewis acid-base principle; the greater the charge difference between acid–base sites was, the easier the dissociation of H_2 was. Although single-atom Co catalysts exhibit superior activity in hydrogenation, their application in UAL hydrogenation has not been reported.

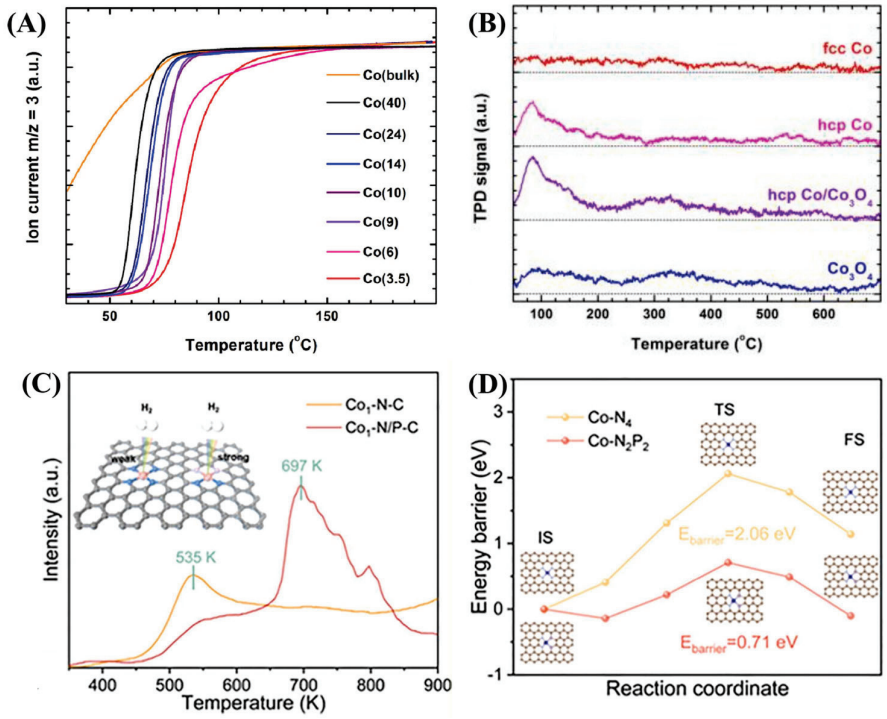


Figure 16. (**A**) Formation of HD over the Co/C3N4 catalysts and bulk fcc Co during temperature-programmed H2–D2 exchange. Reprinted with permission from ref. [47], 2024, American Chemical Society. (**B**) H2 TPD profiles of Co catalysts. Reprinted with permission from ref. [123], 2024, Elsevier. (**C**) H2-TPD tests of Co1-N-C and Co1-N/P-C. (**D**) Energy barriers of H2 dissociation on Co1-N-C and Co1-N/P-C. Reprinted with permission from ref. [113], 2024, Elsevier.

The adsorption structures of CAL on Co sites are shown in Figure 17A,B, where a vertical configuration can be observed on the Co (111) and CoO (200) planes with adsorption energies of −0.58 eV and −5.64 eV, respectively [91], indicating that the Co oxides have relatively strong adsorption on CAL, resulting in possible overhydrogenation. The moderate adsorption of C=O on Co (111) allowed the COL product to desorb. However, unmodified Co NPs also adsorb C=C via concentrated Co–Co sites, leading to a horizontal adsorption configuration of UAL and the imperfect selectivity of the target UOL product [124]. The doped N can efficiently improve the interaction between Co NPs and C=O. As shown in Figure 17C, differential charge density analysis revealed that the N-doped carbon support provided more electrons to transfer from the N to the Co NPs, resulting in an electron-rich state and a negative charge on the Co NPs [26]. Furthermore, the $Co/CoN_X/C$-600 catalyst showed a lower energy barrier for the first hydrogenation of C=O (0.07 eV) than for C=C hydrogenation (0.39 eV) and C=O hydrogenation over the Co/C catalyst (0.43 eV) (Figure 17D,E), ultimately resulting in an enhanced low-temperature activity of 100% conversion and 78% selectivity for C=O.

In addition, H_2 and UAL hydrogenation are simultaneously activated at the Co active center, which increases the difficulty of the highly selective hydrogenation of C=O. Therefore, the M (M = second metal) and X (base site) sites are introduced to form dual metal sites with Co, and this change in structure and electronic structure directly influences the H_2 dissociation activity and adsorption mode of substrates over the Co center. As shown in Figure 8C, the dual Co–Cu site had a lower energy barrier for H_2 dissociation and the migration of H to C=O, whereas a stronger vertical configuration of C=O (1680 cm^{-1}) and two negligible characteristic peaks of the furan ring (1580 cm^{-1} and 1450 cm^{-1}) were observed in the in situ FTIR spectra of the Cu-Co catalyst than in those of the single Cu catalyst (Figure 18), indicating that the introduction of Co into Cu inhibited the production

of byproducts. The enhanced performance of CuCo catalysts is due mainly to electron transfer between Co and Cu [82,98], which results in the formation of new bimetallic sites with different electronegativities favoring the heterolytic dissociation of hydrogen [12]. The same electronic effect is appropriate for other electropositive metals, such as In and Ga, which lose their electrons and serve as active sites for activating polarized C=O groups [124].

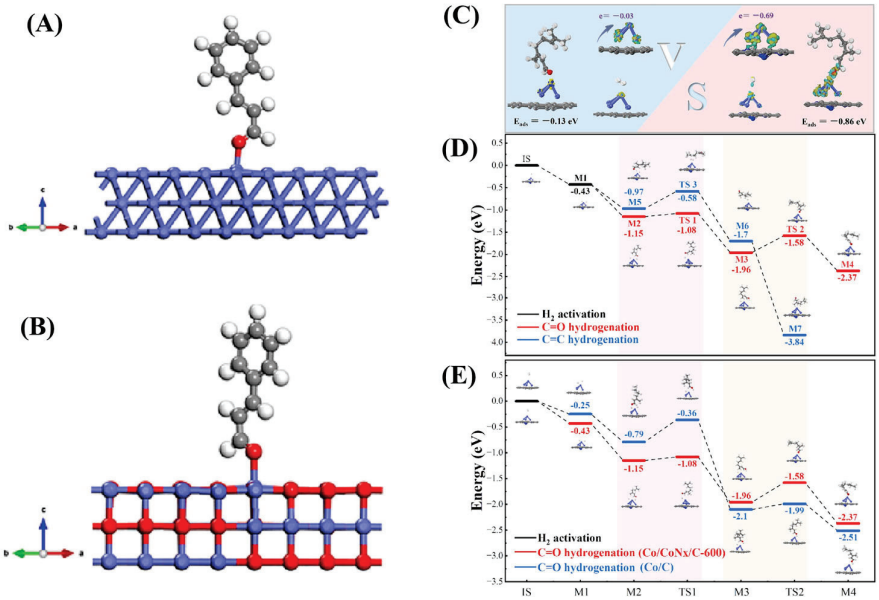


Figure 17. DFT-optimized geometries for absorption of CAL on (**A**) Co (111) surface and (**B**) CoO (200) surface. Blue, gray, red, and white spheres represent Co, C, O and H, respectively. Reprinted with permission from ref. [91], 2023, Elsevier. (**C**) Direct adsorption of citral over Co/C and Co/CoN$_X$/C-600 catalysts (geometry of the corresponding adsorption energies (Eads)); (**D**) potential energy distribution of citral hydrogenation on Co/CoN$_X$/C-600; (**E**) potential energy distribution of C=O bond hydrogenation on Co/C and Co/CoN$_X$/C-600 in citral. Reprinted with permission from ref. [26], 2024, Elsevier.

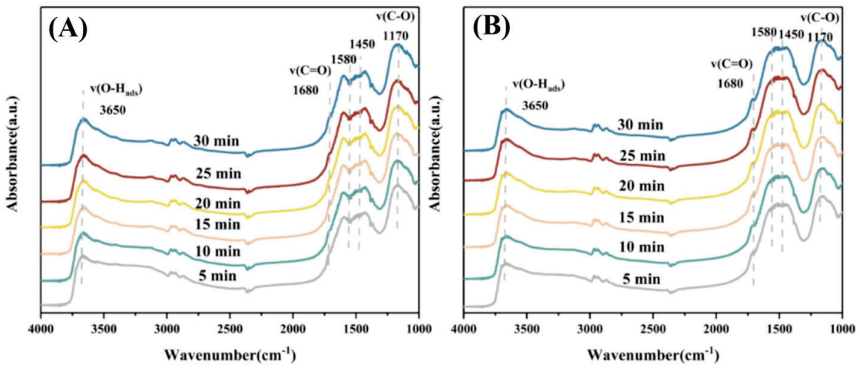


Figure 18. In situ infrared characterization of FAL on (**A**) Cu/MgO and (**B**) CuCo/MgO-0.04. Reprinted with permission from ref. [98], 2024, Elsevier.

The hydrogenation dissociation mechanisms at Co–X sites are quite different from those at Co–M sites because of the lack of adjacent metal–metal bonds. When the neighboring atom of a metal center is replaced with a nonmetal atom or ligand, H_2 may be activated via a dihydrogen complex pathway to form active H species. First, the electron transfers from the filled σ orbital of H_2 to the empty d_σ orbital of the metal center to form a two-electron, three-center orbital bonding over all three atoms [125,126]. Then, a dihydride complex ($H^{\delta-}$–M–$H^{\delta+}$) is generated by the dissociation of H_2 because the d_π electron of transition metals is donated back to the σ^* antibonding orbital of hydrogen [125,127],

ultimately resulting in a proton–hydride pair ($M–H^{\delta-}/X–H^{\delta+}$) consisting of a metal center (Lewis acid) and a Lewis base with heterolytic dissociation of H_2 [128]. This heterolytic process is similar to the hydrogenation mechanism in FLP systems [120,129–131].

For Co NPs, the UAL is easily adsorbed on the electropositive site via polarized C=O, whereas the active H can be dissociated on dual metal sites and directly attack C=O to form an intermediate, leading to a decrease in the energy barrier. In addition, the Co–X sites on the surface or interface of catalysts can promote the spatial separation of the adsorption site of UAL from the H_2 dissociation site, which allows good tunability of the reaction selectivity. However, the reduced density of exposed active sites may be the cost of high hydrogenation selectivity, leading to poor low-temperature activity for Co-based bimetallic catalysts and metal-based catalysts compared with Co-NP catalysts (Table 2).

4.2. Catalytic Transfer Hydrogenation

The catalytic transfer hydrogenation of UAL over metal catalysts mainly abides by the acid–base catalysis principle for organic alcohols and unsaturated compounds, which results in superior properties for C=O-selective hydrogenation [21,42]. Because organic alcohols are used as hydrogen donors, the key step for the transfer hydrogenation mechanism is the activation of hydroxy groups and the generation of activated intermediates from organic alcohols and UAL.

Unlike H_2 dissociation hydrogenation, catalytic transfer hydrogenation mainly occurs over Co oxide catalysts, where the $Co^{\delta+}$ sites work as active centers [34,37]. Cui et al. carried out DFT calculations to study the differences in potential active sites over the Co_3O_4@NC catalyst for transfer hydrogenation, confirming the energy profiles of the CAL hydrogenation pathways on Co_3O_4 (111), N-Co_3O_4 (111), Co_3O_4 (111)-O_v, Co. . .N FLP sites, and Co. . .O FLP sites (Figure 19A,B) [35]. The Co_3O_4 (111) surface and unliganded Co (111)-O_v site had a higher energy barrier for CAL transfer hydrogenation but markedly decreased at the unliganded Co. . .O FLP site. Furthermore, the Co. . .N FLP site exhibited a lower activation energy than the Co. . .O FLP site did, indicating that stronger basic sites can promote the dissociation of O–H and the formation of intermediates [34]. Moreover, the catalytic transfer hydrogenation over Co–O and Co–N sites seems to follow the Meerwein–Ponndorf–Verley (MPV) pathway [20,21], as shown in Figure 19C. The C=O group of CAL and the OH group of the organic alcohol may be adsorbed on the $Co^{\delta+}$ site simultaneously and form a cyclic six-membered intermediate. Furthermore, Cui et al. revealed the transformation process of similar cyclic six-membered intermediates on Co–N centers over a Co-based MOF catalyst [103]. As shown in Figure 19E, the H_a in isopropanol first transferred to the adjacent N from the Co–N bond, and then the Co–N was broken. Subsequently, another H_b in isopropanol is transferred to C_a in CAL, and isopropanol forms acetone. Finally, a new isopropanol was adsorbed on the Co center and provided its H_a to O_a in CAL to generate a target product of COL. Another pathway involves the adsorption of C=O and OH groups on adjacent M–O–M sites [105,106]. For example, Cheng et al. proposed a potential hydrogenation pathway for CoMgAl-LDO mixed oxide catalysts [106]. As shown in Figure 19D, the H atom of the organic alcohol is adsorbed on the Lewis basic site (O^{2-}), thus weakening the O–H bond, and the Lewis acid site ($Co^{\delta+}$) can directly activate C=O. Proton transfer from alcohol to O^{2-} subsequently promotes the formation of a six-membered intermediate between Co, isopropanol, and FAL. This six-membered ring mechanism of UAL transfer hydrogenation over Co-oxide catalysts revealed the direct effect of C=O on the Lewis acid site, which is responsible for the high hydrogenation selectivity to C=O.

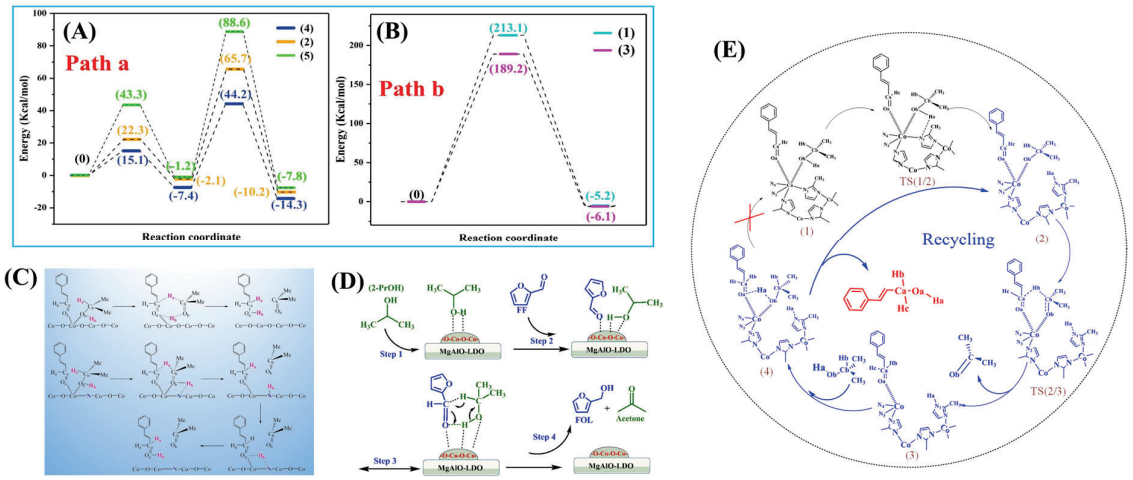


Figure 19. (**A**,**B**) CAL hydrogenation pathways on the surface of ideal Co_3O_4 (111) (1), ideal N-Co_3O_4 (111) (2), Co_3O_4 (111)-O_v (3), Co. . .N FLP sites (4), and Co. . .O FLP sites (5), where Path a is the transfer hydrogenation on Co–N or Co–O dual sites, and Path b represents the transfer hydrogenation on single Co sites. (**C**) Proposed mechanism for CAL transfer hydrogenation to COL over Co_3O_4 and Co_3O_4@NC. Reprinted with permission from ref. [35], 2023, Elsevier. (**D**) The proposed pathways for the catalytic transfer hydrogenation of FF to FOL over the CoMgAl-LDO-500 catalyst. Reprinted with permission from ref. [106], 2024, Elsevier. (**E**) Proposed mechanism involving the formation of cinnamyl alcohol over Co–N_4. Reprinted with permission from ref. [103], 2020, Elsevier.

Compared with H_2 dissociation hydrogenation, catalytic transfer hydrogenation over Co-based catalysts showed superior hydrogenation selectivity to C=O due to the strong interaction of C=O and Lewis acid sites. However, the Co oxides showed poor activity for catalytic transfer hydrogenation at low temperatures. Tuning the coordination structure of Co centers to further adjust the surface acid–base sites of Co-based catalysts may be an effective strategy to increase their activity for catalytic transfer hydrogenation. In summary, H_2 dissociation hydrogenation and catalytic transfer hydrogenation of UAL over Co-based catalysts have significant differences as well as some similarities. On the one hand, H_2 and organic alcohol as hydrogen donors are activated to produce active H species on the Co–Co sites and Co–X sites, respectively, with different energy barriers and reaction conditions. On the other hand, C=O is similarly adsorbed and activated on Co centers or Lewis acid sites, determining the direction of hydrogenation. In addition, the synergistic effect of Co^0 and Co–X may further enhance the hydrogenation performance [37,110,114], but new aspects of hydrogenation mechanisms require further understanding.

4.3. Solvent Effects and Side Reactions

In this section, the influences of solvents are briefly discussed to further understand the hydrogenation process and potential side reactions. In general, UAL hydrogenation reactions commonly use low-carbon organic alcohols as solvents, including methanol, ethanol, and isopropanol, because of their better capacity for dispersing substrates and proton transfer than other solvents [132]. The hydrogenation properties are involved in the polarity of the solvent molecules. First, protic solvents with strong polarity have high H2 solubility and a lower barrier for exchanging hydrogen [14,115]. For example, a series of protic solvents sorted according to their polarity, i.e., water > methanol > ethanol > isopropanol, were investigated for their influence on polarity over Co-Fe catalysts supported on acidic bentonite [101], in which the methanol group resulted in higher conversion and selectivity for C=O, demonstrating that the high polarity of the solvent is beneficial for H_2 hydrogenation at Co^0 active sites. Moreover, when a solvent molecule with a long carbon structure is adsorbed on the catalyst surface, it may have a steric effect and reduce the

interaction between UAL and the active sites, leading to poor hydrogenation activity of the catalyst [133]. With respect to transfer hydrogenation, the solvent effect showed the opposite trend [34,105,106]. For example, Wang et al. studied the influence of hydrogen donors on the transfer hydrogenation of CAL, where the reaction activity decreased with decreasing polarity of C_2–C_5 alcohols over an Al_2O_3 catalyst, which was attributed to weaker alcohol–CMA and alcohol–catalyst interactions in low-polarity solvents [38]. For the CoMgAl mixed oxide catalysts, as shown in Figure 20A, with increasing carbon chain length, both the conversion and C=O selectivity increased in FAL transfer hydrogenation [106], indicating that a specific polarity may favor the catalytic transfer hydrogenation reaction for C=O.

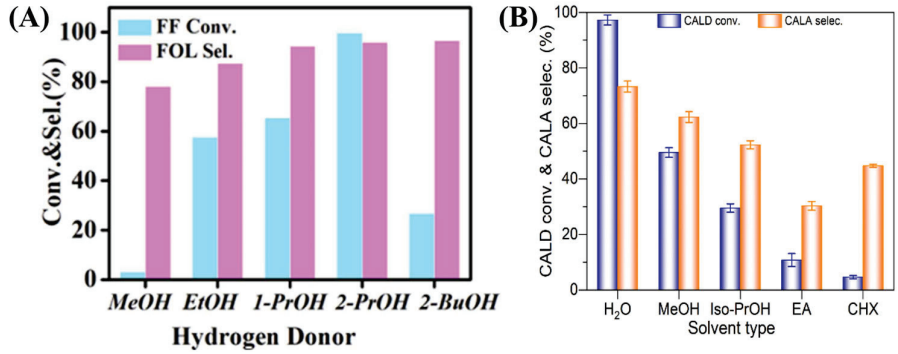


Figure 20. (**A**) Influence of different hydrogen sources on catalytic transfer hydrogenation of FF to FOL. Reaction conditions: catalyst (0.1 g), FF (1.2 mmol), 2-PrOH (20 mL), 160 °C, 6 h. Reprinted with permission from ref. [106], 2024, Elsevier. (**B**) Effects of solvent on CAL conversion and product yields over Co_2Al-H_2-400 catalyst. Reaction conditions: 200 μL CAL, 10 mL solvent, 30 mg catalyst, 100 °C, 2 MPa H_2. Reprinted with permission from ref. [96], 2024, Elsevier.

Furthermore, the influence of solvent polarity on the selectivity of hydrogenation was investigated. It has been reported that nonpolar solvents prefer to activate nonpolar C=C, and polar solvents benefit from attacking C=O [134]. To further reveal the relationship between solvent and selectivity over Co-based catalysts, Gao and coworkers studied the performance of Co_2Al-H_2 catalysts with different solvents [96]. As shown in Figure 20B, the C=O selectivity of the catalyst obviously increased with increasing solvent polarity, which revealed that strongly polar protic solvents promoted proton migration and intermolecular hydrogen bonding, resulting in increased UOL productivity. However, this regularity of protic solvents was not distinct over the Co@Pd–Co core–shell catalyst, where the hydrogenation selectivity was similar when H_2O, methanol, ethanol, and isopropanol were used [50]. This may be because the adsorption of solvent is weak on the catalyst surface; thus, the hydrogenation properties are mainly determined by the interaction of reactants and catalysts [83].

Moreover, water is a particular solvent for UAL hydrogenation. On the one hand, water can be easily activated and transfer protons to produce UOL due to its extremely strong polarity compared with that of organic alcohols; meanwhile, some side reactions involving organic alcohols can be avoided [10]. On the other hand, UAL is difficult to dissolve in water, resulting in a lower mass transfer rate of H_2 and a smaller contact area between the reactant and the catalyst. Thus, using a mixed solvent with an appropriate proportion of water can enhance the selective hydrogenation of UAL [109,133]. According to the above results, although the nature of the solvent clearly influences the hydrogenation performance of Co-based catalysts, the magnitude of the solvent effect on hydrogenation is strongly dependent on the catalyst identity, hydrogenation pathways, and nature of the solvent employed, which may result in different interactions between the adsorbed solvent and unsaturated double bonds in the reactant and transition states on the metal surfaces.

Another important impact of the solvent effect is side reactions involving organic alcohols and UAL, including aldolization and reductive etherification. The unstable aldehyde functional group can be catalyzed by acid sites to form acetals via organic alcohols [9], which protects the aldehyde group from hydrogenation and reduces the hydrogenation rate. Therefore, unsaturated acetals and saturated acetals from UAL and SAL may be produced on surface acid catalysts during hydrogenation [10,135–137]. For organic alcohols, methanol and ethanol are preferable for the formation of acetals because polarized hydroxyl groups are easily broken and dehydrated. The pure Co^0 or Co–O–Co active sites cannot catalyze side reactions, but the synergy of Co and Lewis acid sites will occur [8,77]. On the mixed Co-based catalysts, aldolization easily occurs on metal Lewis acid sites from surface acid supports and the metal–support interface because the simultaneous adsorption of C=O and hydroxy groups on acid sites is necessary for producing acetals, making it easier to compete with transfer hydrogenation.

In recent years, side reactions during UAL hydrogenation involving organic alcohol solvents have been reported, but the mechanism and its relationship with the structure and active sites of catalysts remain ambiguous. To avoid the production of byproducts, several solutions have been proposed. First, because the side reactions of aldolization and reductive etherification are reversible, appropriate reaction conditions, such as increasing the concentration of substrates and H_2 pressure, are selected to enhance the hydrogenation reaction. Second, a mixed solvent of alcohol–water was prepared, where the appropriate amount of water can reduce the contact between UAL and alcohols and promote the hydrolysis of acetals. Third, the use of solvents with long carbon structures results in steric effects, which can weaken the adsorption of solvents on the surface of catalysts.

5. Conclusions and Perspectives

In summary, Co-based catalysts play a pivotal role in the C=O-selective hydrogenation of UAL to produce UOL due to the special electronic structure of Co metal. Thus, the preparation methods, hydrogenation properties, and UAL hydrogenation mechanisms of Co-based catalysts are carefully summarized in this review. The discussions suggest the crucial role of particle size, bimetallic synergistic effect, and coordination structure for Co NPs and Co oxide catalysts. First, the strengths and shortcomings of different preparation processes and the corresponding particle scale and nanosize effects on the hydrogenation properties of Co NPs are considered, where the optimal range of Co particle sizes for obtaining high conversion and selectivity simultaneously is approximately 6~20 nm. A value either above or below this range may result in the loss of catalytic activity or C=O selectivity for Co-based catalysts. Second, the coordination structure and electronic properties of Co can be regulated by introducing a second metal or ligand, further enhancing the catalytic activity and interaction of C=O over Co^0 and $Co^{\delta+}$ sites. Third, the UAL hydrogenation mechanism of H_2 dissociation hydrogenation and catalytic transfer hydrogenation over Co-based catalysts are summarized, which suggests the key role of Co active sites in the adsorption and transformation of hydrogen donors and UAL.

Moreover, in light of these two hydrogenation mechanisms, the key factors and following strategies are proposed to improve Co-based catalysts. As shown in Figure 21, for the Co NP catalyst, the first mechanism regulates the particle size of the metal in an appropriate range of approximately 6~20 nm because of the nanosize effect. The second mechanism modifies the electronic structure of the Co metal to achieve an electronic effect by introducing a second metal or ligand. Finally, the steric structure around the Co center should be controlled to restrict the adsorption of C=C and the benzene skeleton. For the Co oxide catalyst, catalytic transfer hydrogenation also had a nanosize effect on both the hydrogenation activity and selectivity. The solvent effect is remarkable for catalytic

transfer hydrogenation due to the strong interaction of the catalyst and solvents, which is related to the polarity of organic alcohols. Finally, tuning the surface acid and base sites is essential because the Lewis acid–base effect simultaneously affects the transfer hydrogenation activity and the side reactions of aldolization and reductive etherification.

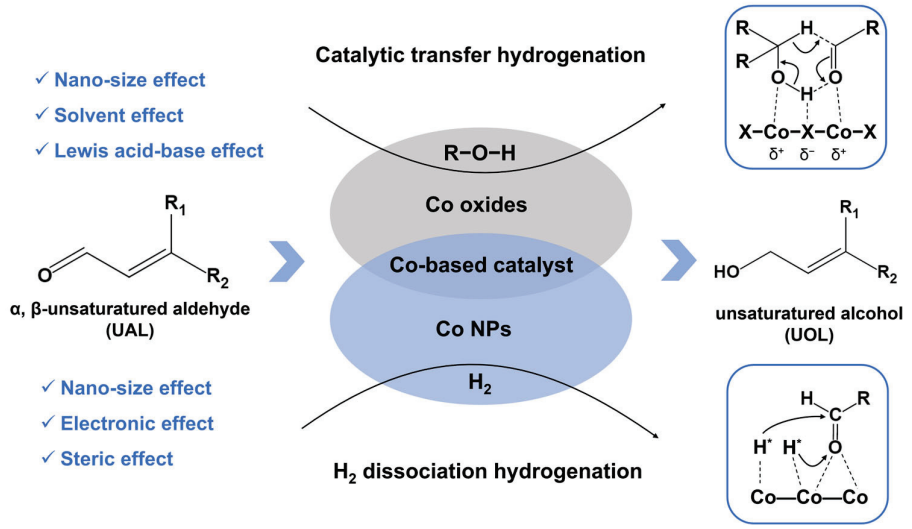


Figure 21. Illustration of main factors and hydrogenation mechanisms of Co-based catalysts, where H* represents the active hydrogen species.

Co-based catalysts are promising for replacing noble metal catalysts because of their high hydrogenation selectivity, but many practical problems and challenges need to be solved. First, the poor activity of Co-based catalysts at low temperatures results in higher production costs and longer production cycles. Although many advanced Co-based catalysts, such as single-atom catalysts and intermetallic components, have been rapidly developed in recent years, Co-based catalysts lag behind noble metal catalysts. Thus, improving the intrinsic catalytic activity of Co centers is crucial in the future. Furthermore, the study of the hydrogenation mechanism over Co-based catalysts is insufficient, especially for the catalytic transfer hydrogenation of UAL, which constrains researchers' ability to design high-performance catalysts. The complexity of the hydrogenation process involving solvents and the role of the Co/CoO_x interface require further investigation via advanced in situ and operando characterization techniques. Finally, the stability of Co active sites should be carefully considered when designing catalysts because of the agglomeration, loss, and poisoning of metal and metal oxide NPs. The construction of functional supports for forming strong metal–support interactions and protective structures may be an efficient strategy to improve the stability of Co active sites.

Author Contributions: H.S.: investigation, data curation, writing—original draft, conceptualization. J.X.: data curation, formal analysis. X.L.: writing—original draft, resources, formal analysis. Z.Q.: writing—review and editing, writing—original draft, supervision, resources, project administration, methodology. All authors have read and agreed to the published version of the manuscript.

Funding: This research was funded by the Opening Project of the Guangxi Key Laboratory of Petrochemical Resource Processing and Process Intensification Technology (2023K002).

Data Availability Statement: Data will be made available upon request.

Conflicts of Interest: The authors declare no conflicts of interest.

References

1. Zahid, M.; Ismail, A.; Khan, M.F.; Ali, N.; Bakhtiar, S.H.; El Jery, A.; Al Alwan, B.; Ullah, R.; Raziq, F.; He, W.; et al. Understanding the working principle of sustainable catalytic materials for selective hydrogenation of carbonyls bond in α, β-unsaturated aldehydes. *Coord. Chem. Rev.* **2025**, *525*, 216295. [CrossRef]
2. Zhou, S.; Yang, Y.; Shen, T.; Yin, P.; Wang, L.; Ren, Z.; Zheng, L.; Wang, B.; Yan, H.; Wei, M. Highly Selective Hydrogenation of Unsaturated Aldehydes in Aqueous Phase. *ACS Appl. Mater. Interfaces* **2024**, *16*, 13685–13696. [CrossRef]
3. Zhang, P.; Chen, T.; Liu, Y.-Y.; Sun, Z.; Wang, Y.; Wang, A. Transfer hydrogenation of cinnamaldehyde to cinnamyl alcohol over SnO-MgO composite catalysts. *Chem. Eng. J.* **2025**, *512*, 162483. [CrossRef]
4. Ma, M.; Li, L.; Li, X.; Wang, Q.; Huang, T.; Geng, Z.; Tian, G.; Li, G. Stabilization of unique $Zr^{>4+}$ species in $NiFe_2O_4$ nanocrystals for unprecedented catalytic transfer hydrogenation reaction. *Appl. Catal. B-Environ. Energy* **2024**, *350*, 123905. [CrossRef]
5. Zhong, L.; Liao, X.; Huang, H.; Cui, H.; Huang, J.; Luo, H.a.; Pei, Y.; Lv, Y.; Liu, P. B, N Codoped Defective Reduced Graphene Oxide as a Highly Efficient Frustrated Lewis Pairs Catalyst for the Selective Hydrogenation of α,β-Unsaturated Aldehydes to Unsaturated Alcohols. *J. Am. Chem. Soc.* **2025**, *147*, 3840–3854. [CrossRef]
6. Liang, Y.; He, J.; An, Y.; Zhang, J.; Park, G.-S.; Zhao, L.; Oh, R.; Huang, X.; Dong, J.; Liu, L. Boosting selective hydrogenation of α,β-unsaturated aldehydes through constructing independent Pt and Fe active sites on support. *Chem. Eng. J.* **2024**, *484*, 149670. [CrossRef]
7. Yang, X.; Huang, Z.; Liu, W.; Li, X.; Su, S.; Peng, H.; Fang, Y.; Dong, J.; Sun, Q. Regioselective Upgrading of Furfural into 2-Methyl Furan over Cobalt Confined in Microporous Carbon Spheres. *ACS Catal.* **2025**, *15*, 6199–6208. [CrossRef]
8. Liu, B.; Li, Y.; Liu, Q. Cobalt/Lewis acid cooperative catalysis for reductive etherification of ketones and aldehydes with alcohols. *Chem Catal.* **2022**, *2*, 883–897. [CrossRef]
9. Lashdaf, M.; Tiitta, M.; Venäläinen, T.; Österholm, H.; Krause, A.O.I. Ruthenium on beta zeolite in cinnamaldehyde hydrogenation. *Catal. Lett.* **2004**, *94*, 7–14. [CrossRef]
10. Zhang, X.B.; Zhang, Y.J.; Chen, F.; Xiang, Y.Z.; Zhang, B.; Xu, L.Y.; Zhang, T.R. Efficient selective hydrogenation of cinnamaldehyde over zeolite supported cobalt catalysts in water. *React. Kinet. Mech. Catal.* **2015**, *115*, 283–292. [CrossRef]
11. Gong, W.; Ma, J.; Chen, G.; Dai, Y.; Long, R.; Zhao, H.; Xiong, Y. Unlocking the catalytic potential of heterogeneous nonprecious metals for selective hydrogenation reactions. *Chem. Soc. Rev.* **2025**, *54*, 960–982. [CrossRef]
12. Aireddy, D.R.; Ding, K. Heterolytic Dissociation of H2 in Heterogeneous Catalysis. *ACS Catal.* **2022**, *12*, 4707–4723. [CrossRef]
13. Yang, B.; Gong, X.-Q.; Wang, H.-F.; Cao, X.-M.; Rooney, J.J.; Hu, P. Evidence To Challenge the Universality of the Horiuti–Polanyi Mechanism for Hydrogenation in Heterogeneous Catalysis: Origin and Trend of the Preference of a Non-Horiuti–Polanyi Mechanism. *J. Am. Chem. Soc.* **2013**, *135*, 15244–15250. [CrossRef] [PubMed]
14. Qiao, M.; Wang, Y.; Gao, S.; Fu, Q.; Wang, X.; Qin, R.; Zheng, N. Ligand Modification-Induced Electronic Effects and Synergistic Protic Solvent Effects Promote C=O Bond Hydrogenation. *ACS Catal.* **2024**, *14*, 11468–11476. [CrossRef]
15. Li, X.; Liu, J.; Wu, J.; Zhang, L.; Cao, D.; Cheng, D. Constructing a Highly Active Pd Atomically Dispersed Catalyst for Cinnamaldehyde Hydrogenation: Synergistic Catalysis between Pd–N_3 Single Atoms and Fully Exposed Pd Clusters. *ACS Catal.* **2024**, *14*, 2369–2379. [CrossRef]
16. Zhang, S.; Xia, Z.; Li, W.; Wang, Y.; Zou, Y.; Zhang, M.; Gong, Z.; Cui, Y.; Qu, Y. In-situ reconstruction of single-atom Pt on Co_3O_4 for hydrogenation. *Nano Res.* **2022**, *16*, 6507–6511. [CrossRef]
17. Wang, Z.; Hu, R.; Wang, L.; Zhou, S. Enhanced Selective Hydrogenation of Cinnamaldehyde to Cinnamyl Alcohol over Silica-Coated Pt–Co_xO_y Hybrid Nanoparticles. *ACS Appl. Mater. Interfaces* **2023**, *16*, 924–932. [CrossRef]
18. Wang, S.; Wu, B.; Zhang, Q.; Li, Y.; Zhu, L.; Yu, H.; Yin, H. Design of Pt@Sn core–shell nanocatalysts for highly selective hydrogenation of cinnamaldehyde to prepare cinnamyl alcohol. *Chem. Eng. J.* **2024**, *488*, 151019. [CrossRef]
19. Lu, Y.; Chen, Q.; Zhang, Y.; Wei, Y.; Hou, X.; Huang, R.; Deng, D. Accelerating Semihydrogenation of Cinnamaldehyde by Water over a Au/α-MoC Catalyst. *ACS Catal.* **2024**, *14*, 10113–10121. [CrossRef]
20. Farrar-Tobar, R.A.; Dell'Acqua, A.; Tin, S.; de Vries, J.G. Metal-catalysed selective transfer hydrogenation of α,β-unsaturated carbonyl compounds to allylic alcohols. *Green Chem.* **2020**, *22*, 3323–3357. [CrossRef]
21. Zhu, Y.; Chuah, G.; Jaenicke, S. Selective Meerwein–Ponndorf–Verley reduction of α,β-unsaturated aldehydes over Zr-zeolite beta. *J. Catal.* **2006**, *241*, 25–33. [CrossRef]
22. Plessers, E.; Fu, G.; Tan, C.; De Vos, D.; Roeffaers, M. Zr-Based MOF-808 as Meerwein–Ponndorf–Verley Reduction Catalyst for Challenging Carbonyl Compounds. *Catalysts* **2016**, *6*, 104. [CrossRef]
23. Liu, S.H.; Jaenicke, S.; Chuah, G.K. Hydrous Zirconia as a Selective Catalyst for the Meerwein–Ponndorf–Verley Reduction of Cinnamaldehyde. *J. Catal.* **2002**, *206*, 321–330. [CrossRef]
24. Fan, Y.; Li, S.; Wang, Y.; Zou, X.; Zhuang, C. Size-Dependent Fe-Based Catalysts for the Catalytic Transfer Hydrogenation of α,β-Unsaturated Aldehydes. *Inorg. Chem.* **2025**, *64*, 3101–3110. [CrossRef]

25. Sheng, Q.; Wang, Y.; Zhang, P.; Jiang, Y.; Zhang, J.; Liu, Q.; Chang, Q.; Yao, Y.; Liao, X.; Li, Z.; et al. Highly dispersed Ni on defective carbon with metal-support interaction for efficient and selective cinnamaldehyde hydrogenation. *Appl. Surf. Sci.* **2024**, *666*, 160369. [CrossRef]
26. Zhu, Y.; Zhang, B.; Shi, S.; Bo, Z.; Yuan, M.; Xu, Y.; Xiao, W.; Wang, S.; Chen, C. Targeted electron transfer effect of enzyme-like Co-N_X catalysts for enhanced C = O hydrogenation. *Chem. Eng. J.* **2024**, *488*, 151199. [CrossRef]
27. Zhang, J.; Yang, X.; Jia, Z.; Han, Q.; Yu, S.; Liu, S.; Li, L.; Wu, Q.; Yu, H.; Liu, Y.; et al. Bi-functional active sites Cu/MgO-La_2O_3 catalysts the selective hydrogenation of furfural to furfuryl alcohol. *Chem. Eng. J.* **2024**, *500*, 157400. [CrossRef]
28. Ngan, H.T.; Sautet, P. Tuning the Hydrogenation Selectivity of an Unsaturated Aldehyde via Single-Atom Alloy Catalysts. *J. Am. Chem. Soc.* **2024**, *146*, 2556–2567. [CrossRef]
29. Wang, X.; Liang, X.; Geng, P.; Li, Q. Recent Advances in Selective Hydrogenation of Cinnamaldehyde over Supported Metal-Based Catalysts. *ACS Catal.* **2020**, *10*, 2395–2412. [CrossRef]
30. Shi, H.; Su, T.; Qin, Z.; Ji, H. Role of catalyst surface-active sites in the hydrogenation of α,β-unsaturated aldehyde. *Front. Chem. Sci. Eng.* **2024**, *18*, 64. [CrossRef]
31. Lan, X.; Wang, T. Highly Selective Catalysts for the Hydrogenation of Unsaturated Aldehydes: A Review. *ACS Catal.* **2020**, *10*, 2764–2790. [CrossRef]
32. Ren, Y.; Yang, Y.; Wei, M. Recent Advances on Heterogeneous Non-noble Metal Catalysts toward Selective Hydrogenation Reactions. *ACS Catal.* **2023**, *13*, 8902–8924. [CrossRef]
33. Wang, G.H.; Deng, X.; Gu, D.; Chen, K.; Tüysüz, H.; Spliethoff, B.; Bongard, H.J.; Weidenthaler, C.; Schmidt, W.; Schüth, F. Co_3O_4 Nanoparticles Supported on Mesoporous Carbon for Selective Transfer Hydrogenation of α,β-Unsaturated Aldehydes. *Angew. Chem. Int. Ed.* **2016**, *55*, 11101–11105. [CrossRef]
34. Zhou, S.; Qi, H. A sustainable natural nanofibrous confinement strategy to obtain ultrafine Co_3O_4 nanocatalysts embedded in N-enriched carbon fibers for efficient biomass-derivative in situ hydrogenation. *Nanoscale* **2020**, *12*, 17373–17384. [CrossRef] [PubMed]
35. Cui, H.; Liao, X.; Ren, Y.; Zhou, Y.; Xiao, J.; Deng, R.; Lv, Y.; Liu, H.; Liu, P.; Yang, H. Highly selective transfer hydrogenation of α,β-unsaturated aldehydes by frustrated Lewis pairs (FLPs) on oxygen-defect-rich Co_3O_4@NC. *J. Catal.* **2023**, *428*, 115126. [CrossRef]
36. Krishnaveni, T.; Lakshmi, K.; Kaveri, M.V.; Kadirvelu, K. Chemoselective transfer hydrogenation of aromatic and heterocyclic aldehydes by green chemically prepared cobalt oxide nanoparticles. *Mol. Catal.* **2020**, *496*, 111180. [CrossRef]
37. Gong, W.B.; Han, M.M.; Chen, C.; Lin, Y.; Wang, G.H.; Zhang, H.M.; Zhao, H.J. CoO_X@Co Nanoparticle-based Catalyst for Efficient Selective Transfer Hydrogenation of α,β-Unsaturated Aldehydes. *ChemCatChem* **2020**, *12*, 1019–1024. [CrossRef]
38. Wang, H.; Liu, B.; Liu, F.; Wang, Y.; Lan, X.; Wang, S.; Ali, B.; Wang, T. Transfer Hydrogenation of Cinnamaldehyde Catalyzed by Al_2O_3 Using Ethanol as a Solvent and Hydrogen Donor. *ACS Sustain. Chem. Eng.* **2020**, *8*, 8195–8205. [CrossRef]
39. Xu, X.; Li, L.; Han, W.; Luo, J.; Zhang, D.; Wang, Y.; Li, G. Crystalline/amorphous Al/Al_2O_3 core/shell nanospheres as efficient catalysts for the selective transfer hydrogenation of α,β-unsaturated aldehydes. *Catal. Commun.* **2018**, *109*, 50–54. [CrossRef]
40. Gliński, M.; Ulkowska, U. Description of the structure-chemoselectivity relationship in the transfer hydrogenation of α,β-unsaturated aldehydes and ketones with alcohols in the presence of magnesium oxide. *Appl. Catal. A-Gen.* **2018**, *554*, 117–124. [CrossRef]
41. Cui, H.; Zhong, L.; Lv, Y.; Hao, F.; Liu, P.; Xiong, W.; Xiong, S.; Liu, H.; Luo, H. A facile synthesis of in-situ formed amorphous zirconia catalysts for efficient transfer hydrogenation of unsaturated aldehydes. *Fuel* **2022**, *317*, 123551. [CrossRef]
42. Zhong, L.; Liao, X.; Cui, H.; Luo, H.; Lv, Y.; Liu, P. Highly Efficient Hydrogenation of α,β-Unsaturated Aldehydes to Unsaturated Alcohols over Defective MOF-808 with Constructed Frustrated Lewis Pairs. *ACS Catal.* **2024**, *14*, 857–873. [CrossRef]
43. Zhong, L.; Liao, X.; Cui, H.; Luo, H.; Lv, Y.; Liu, P. Hydrogenation of α,β-unsaturated aldehydes over defective UiO-66 with Frustrated Lewis Pairs: Modulation of densities of defect sites via tailoring ligand-vacancies. *Appl. Catal. B-Environ. Energy* **2024**, *342*, 123421. [CrossRef]
44. Singh, U.K.; Vannice, M.A. Liquid-Phase Citral Hydrogenation over SiO_2-Supported Group VIII Metals. *J. Catal.* **2001**, *199*, 73–84. [CrossRef]
45. Dong, C.; Li, Y.; Cheng, D.; Zhang, M.; Liu, J.; Wang, Y.-G.; Xiao, D.; Ma, D. Supported Metal Clusters: Fabrication and Application in Heterogeneous Catalysis. *ACS Catal.* **2020**, *10*, 11011–11045. [CrossRef]
46. Luneau, M.; Lim, J.S.; Patel, D.A.; Sykes, E.C.H.; Friend, C.M.; Sautet, P. Guidelines to Achieving High Selectivity for the Hydrogenation of α,β-Unsaturated Aldehydes with Bimetallic and Dilute Alloy Catalysts: A Review. *Chem. Rev.* **2020**, *120*, 12834–12872. [CrossRef]
47. Yang, H.; Goldbach, A.; Wei, J.; Shen, W. Size-Dependent Hydrogenation Activity of Cobalt Nanoparticles. *ACS Catal.* **2024**, *14*, 7444–7455. [CrossRef]
48. Liu, L.; Corma, A. Metal Catalysts for Heterogeneous Catalysis: From Single Atoms to Nanoclusters and Nanoparticles. *Chem. Rev.* **2018**, *118*, 4981–5079. [CrossRef]

49. Galhardo, T.S.; Braga, A.H.; Arpini, B.H.; Szanyi, J.; Gonçalves, R.V.; Zornio, B.F.; Miranda, C.R.; Rossi, L.M. Optimizing Active Sites for High CO Selectivity during CO_2 Hydrogenation over Supported Nickel Catalysts. *J. Am. Chem. Soc.* **2021**, *143*, 4268–4280. [CrossRef]
50. Ma, X.; Zhu, Z.; Dong, Q.; Kong, T.; Li, X.; Su, T.; Huang, B.; Lü, H.; Yang, K. Co@Pd–Co Core–Shell Nanoparticles as Catalysts for the Selective Hydrogenation of Furfural to Furfuryl Alcohol. *ACS Appl. Nano Mater.* **2024**, *7*, 26825–26835. [CrossRef]
51. Zhang, Z.; Chi, Y.; Guo, M.; Wang, L.; Zhang, X.; Li, G. Active cobalt nanoparticles confined in porous N-doped carbon shell for selective hydrogenation of nitroarenes. *Mol. Catal.* **2024**, *555*, 113911. [CrossRef]
52. Din, I.U.; Shaharun, M.S.; Naeem, A.; Tasleem, S.; Ahmad, P. Revalorization of CO_2 for methanol production via ZnO promoted carbon nanofibers based Cu-ZrO_2 catalytic hydrogenation. *J. Energy Chem.* **2019**, *39*, 68–76. [CrossRef]
53. Neethu, P.P.; Venkatachalam, G.; Venkatesha, N.J.; Joseph, D.; Sakthivel, A. Cobalt-Based Hydrotalcite: A Potential Non-Noble Metal-Based Heterogeneous Catalyst for Selective Hydrogenation of Aromatic Aldehydes. *Ind. Eng. Chem. Res.* **2023**, *62*, 4976–4986. [CrossRef]
54. Duan, L.; Huang, Z.; Chen, G.; Liu, M.; Liu, X.; Ma, R.; Zhang, N. $CoWO_4$ nanoparticles with dual active sites for highly efficient ammonia synthesis. *Nanoscale Horiz.* **2025**, *10*, 1096–1106. [CrossRef] [PubMed]
55. Chen, M.; Liu, H.; Wang, Y.; Zhong, Z.; Zeng, Y.; Jin, Y.; Ye, D.; Chen, L. Cobalt catalyzed ethane dehydrogenation to ethylene with CO_2: Relationships between cobalt species and reaction pathways. *J. Colloid Interface Sci.* **2024**, *660*, 124–135. [CrossRef] [PubMed]
56. Gong, X.; Li, N.; Li, Y.; Hu, R. The catalytic hydrogenation of furfural to 2-methylfuran over the Mg-Al oxides supported Co-Ni bimetallic catalysts. *Mol. Catal.* **2022**, *531*, 112651. [CrossRef]
57. Sadasivan, S.; Bellabarba, R.M.; Tooze, R.P. Size dependent reduction–oxidation–reduction behaviour of cobalt oxide nanocrystals. *Nanoscale* **2013**, *5*, 11139. [CrossRef]
58. Uddin, M.K.; Baig, U. Synthesis of Co_3O_4 nanoparticles and their performance towards methyl orange dye removal: Characterisation, adsorption and response surface methodology. *J. Clean. Prod.* **2019**, *211*, 1141–1153. [CrossRef]
59. Abdallah, A.M.; Awad, R. Study of the Structural and Physical Properties of Co_3O_4 Nanoparticles Synthesized by Co-Precipitation Method. *J. Supercond. Nov. Magn* **2019**, *33*, 1395–1404. [CrossRef]
60. Alzaid, M.; Abu-Dief, A.M.; Hadia, N.M.A.; Ezzeldien, M.; Mohamed, W.S. Synthesis and characterization study of spinel Co_3O_4 nanoparticles synthesized via the facial co-precipitation route for optoelectronic application. *Opt. Quantum Electron.* **2024**, *56*, 1156. [CrossRef]
61. Zhang, M.; Su, X.; Ma, L.; Khan, A.; Wang, L.; Wang, J.; Maloletnev, A.S.; Yang, C. Promotion effects of halloysite nanotubes on catalytic activity of Co_3O_4 nanoparticles toward reduction of 4-nitrophenol and organic dyes. *J. Hazard. Mater.* **2021**, *403*, 123870. [CrossRef]
62. Yang, J.; Zhang, J.; Benassi, E.; Li, X.; Liu, H.; Fang, W.; Tian, J.; Xia, C.; Huang, Z. NiCo/Al_2O_3 nanocatalysts for the synthesis of 5-amino-1-pentanol and 1,5-pentanediol from biomass-derived 2-hydroxytetrahydropyran. *Green Chem. Eng.* **2024**, *5*, 119–131. [CrossRef]
63. Zhao, L.; An, H.; Zhao, X.; Wang, Y. Effect of Ni/Co mass ratio and NiO–Co_3O_4 loading on catalytic performance of NiO–Co_3O_4/Nb_2O_5–TiO_2 for direct synthesis of 2-propylheptanol from n-valeraldehyde. *RSC Adv.* **2021**, *11*, 1736–1742. [CrossRef]
64. Zhu, Y.; Ma, H.; Qian, W.; Zhang, H.; Zhang, H.; Ying, W. Co- and Ni-promoted indium oxide for CO_2 hydrogenation to methanol. *Catal. Sci. Technol.* **2024**, *14*, 3771–3783. [CrossRef]
65. Philippov, A.A.; Nasokhov, D.E.; Prosvirin, I.P.; Martyanov, O.N. Bimetallic Ni-Co catalyst for improving selectivity in transfer hydrogenation of phenolic compounds. *Mol. Catal.* **2024**, *561*, 114200. [CrossRef]
66. Gupta, S.; Jain, P.; Jagadeesan, D.; Vinod, C.P. Morphology-Dependent Catalysis by Co3O4 Nanostructures in Atmospheric Pressure Carbon Dioxide Hydrogenation. *J. Phys. Chem. C* **2023**, *127*, 13055–13064. [CrossRef]
67. Bustamante, T.M.; Fraga, M.A.; Fierro, J.L.G.; Campos, C.H.; Pecchi, G. Cobalt SiO_2 core-shell catalysts for chemoselective hydrogenation of cinnamaldehyde. *Catal. Today* **2020**, *356*, 330–338. [CrossRef]
68. Li, K.; Zhang, D.; Guo, H.; Yang, X.; Liang, C.; Wu, X.; Wang, Q.; Li, D.; Jia, L. Insight into crystal-plane-dependent of cobalt catalysts for ethylene glycol amination. *Mol. Catal.* **2025**, *570*, 114655. [CrossRef]
69. Bankar, B.D.; Naikwadi, D.R.; Tayade, R.J.; Biradar, A.V. Direct hydrogenation of CO_2 to formic acid using Ru supported Co_3O_4 oxide as an efficient heterogeneous catalyst. *Mol. Catal.* **2023**, *535*, 112875. [CrossRef]
70. Yang, F.; Zhang, T.; Zhao, J.; Xiao, J.; Zhou, W. Tuning selectivity of CO_2 hydrogenation over Co catalysts by surface decoration of Sn. *J. Catal.* **2024**, *429*, 115242. [CrossRef]
71. Yun, M.; Chen, T.; Zhao, N.; Li, Z. Enhanced fischer-tropsch synthesis performance on Co@SiO_2 catalyst with core-shell structure. *Mol. Catal.* **2025**, *572*, 114749. [CrossRef]
72. Wang, X.; Yang, Y.; Wang, T.; Zhong, H.; Cheng, J.; Jin, F. In Situ Formed Metal Oxide/Metal Interface Enhanced C–C Coupling in CO_2 Reduction into CH_3COOH over Hexagonal Closed-Packed Cobalt. *ACS Sustain. Chem. Eng.* **2021**, *9*, 1203–1212. [CrossRef]
73. Yu, H.; Liu, M.; Lu, Q.; Yu, Y.; Zhao, D.; Li, X. Mesoporous Metal Oxides. *J. Phys. Chem. C* **2024**, *128*, 19945–19961. [CrossRef]

74. Israf Ud, D.; Nasir, Q.; Garba, M.D.; Alharthi, A.I.; Alotaibi, M.A.; Usman, M. A Review of Preparation Methods for Heterogeneous Catalysts. *Mini-Rev. Org. Chem.* **2022**, *19*, 92–110. [CrossRef]
75. Guo, S.; Li, Z.; Yin, R.; Li, J.; Zeng, Z.; Hu, Z.; Luo, G.; Lv, J.; Huang, S.; Wang, Y.; et al. Oxygen Vacancy over $CoMnO_x$ Catalysts Boosts Selective Ethanol Production in the Higher Alcohol Synthesis from Syngas. *ACS Catal.* **2023**, *13*, 14404–14414. [CrossRef]
76. Li, Y.; Zhao, Z.; Zhao, M.; Zhu, H.; Ma, X.; Li, Z.; Lu, W.; Chen, X.; Ying, L.; Lin, R.; et al. Oxygen-vacancy induced structural changes of Co species in $CoAl_2O_4$ spinels for CO_2 hydrogenation. *Appl. Catal. B-Environ. Energy* **2024**, *347*, 123824. [CrossRef]
77. Jia, S.; Yang, W.; Liu, H.; Chen, X.; Luo, J.; Liang, C. Regulation of sol-gel derived Cu-M/Al_2O_3 by metal additives for the selective catalytic transfer hydrogenation of furfural. *Catal. Today* **2025**, *445*, 115078. [CrossRef]
78. Gao, J.; Jiang, B.; Ni, C.; Qi, Y.; Zhang, Y.; Oturan, N.; Oturan, M.A. Non-precious Co_3O_4-TiO_2/Ti cathode based electrocatalytic nitrate reduction: Preparation, performance and mechanism. *Appl. Catal. B Environ.* **2019**, *254*, 391–402. [CrossRef]
79. Mitran, G.; Nguyen, T.L.P.; Seo, D.-K. The influence of complexing agents on the cobalt-based catalysts properties and activities. *J. Ind. Eng. Chem.* **2022**, *114*, 446–455. [CrossRef]
80. Miao, Y.; Gu, Y.; Zhou, J.; Chen, L.; Xie, Y. Cobalt-and-Nitrogen-Doped Carbon Nanoparticle Catalysts for Selective Hydrogen Transfer Reactions. *ACS Appl. Nano Mater.* **2024**, *7*, 10130–10136. [CrossRef]
81. Qi, H.; Wang, X.; Lei, M.; Fan, W.; Huang, S.; Zhu, L.; Tang, H. Highly efficient catalytic hydrogenation of nitrobenzene on cobalt-immobilized nitrogen-doped carbon: A dual-sites synergistic effect between cobalt single atoms and cobalt nanoparticles. *Chem. Eng. J.* **2024**, *500*, 157057. [CrossRef]
82. Xu, J.; Han, X.; Zhu, L.; Wang, W.; Ruan, L.; Yang, Z.; Ye, H.; Chen, B.H. Revealing the intrinsic relationship between nano/electronic structure of CuCo/NC (NC drived from ZIF-67) and their catalytic performance for furfural selective hydrogenation. *J. Catal.* **2025**, *447*, 116140. [CrossRef]
83. Huai, M.; Li, X.; Zhang, Y.; Qin, X.; Zhang, Y.; Qin, X.; Liu, Y.; Liang, X.; Li, G.; Zhao, J. Boosting Furfural Hydrogenation Performance of Confined Co-Based Composites Derived From ZIF-67 via a Surfactant-Assisted Pyrolysis Strategy. *ChemCatChem* **2024**, *17*, e202401651. [CrossRef]
84. Lin, Y.; Nie, R.; Li, Y.; Wu, X.; Yu, J.; Xie, S.; Shen, Y.; Mao, S.; Chen, Y.; Lu, D.; et al. Highly efficient and anti-poisoning single-atom cobalt catalyst for selective hydrogenation of nitroarenes. *Nano Res.* **2022**, *15*, 10006–10013. [CrossRef]
85. Liu, X.; Wang, C.; Meng, J.; Yue, X.; Wang, Q.; Lu, J.; Wang, J.; Wang, X.; Zong, Y.; Jiang, X. Single-atom cobalt catalysts for chemoselective hydrogenation of nitroarenes to anilines. *Chin. Chem. Lett.* **2023**, *34*, 108745. [CrossRef]
86. Jagadeesh, R.V.; Banerjee, D.; Arockiam, P.B.; Junge, H.; Junge, K.; Pohl, M.-M.; Radnik, J.; Brückner, A.; Beller, M. Highly selective transfer hydrogenation of functionalised nitroarenes using cobalt-based nanocatalysts. *Green Chem.* **2015**, *17*, 898–902. [CrossRef]
87. Joseph Antony Raj, K.; Prakash, M.G.; Elangovan, T.; Viswanathan, B. Selective Hydrogenation of Cinnamaldehyde over Cobalt Supported on Alumina, Silica and Titania. *Catal. Lett.* **2011**, *142*, 87–94. [CrossRef]
88. Rudolf, C.; Dragoi, B.; Ungureanu, A.; Chirieac, A.; Royer, S.; Nastro, A.; Dumitriu, E. NiAl and CoAl materials derived from takovite-like LDHs and related structures as efficient chemoselective hydrogenation catalysts. *Catal. Sci. Technol.* **2014**, *4*, 179–189. [CrossRef]
89. Yi, D.; Min, Y.; Muzzi, B.; Marty, A.; Romana, I.; Fazzini, P.F.; Blon, T.; Viau, G.; Serp, P.; Soulantica, K. Epsilon Cobalt Nanoparticles as Highly Performant Catalysts in Cinnamaldehyde Selective Hydrogenation. *ACS Appl. Nano Mater.* **2022**, *5*, 5498–5507. [CrossRef]
90. Tian, F.; Zhang, X.; Sheng, Y.; Chen, X.; Wang, X.; Liang, C. Metal-organic framework-derived Co-C catalyst for the selective hydrogenation of cinnamaldehyde to cinnamic alcohol. *Chin. J. Chem. Eng.* **2023**, *62*, 46–56. [CrossRef]
91. Shen, Y.; Chen, C.; Zou, Z.; Hu, Z.; Fu, Z.; Li, W.; Pan, S.; Zhang, Y.; Zhang, H.; Yu, Z.; et al. Geometric and electronic effects of Co@NPC catalyst in chemoselective hydrogenation: Tunable activity and selectivity via N,P co-doping. *J. Catal.* **2023**, *421*, 65–76. [CrossRef]
92. Pan, H.; Li, Z.; Ma, Q.; Zhang, Y.; Zheng, Y.; Gao, Y. Cobalt catalyst encapsulated by N-doped carbon for selective hydrogenation of aldehyde to alcohol. *Mol. Catal.* **2024**, *553*, 113752. [CrossRef]
93. Yogita; Anjana, P.N.; Kumar, P.M.; Rao, K.T.V.; Subrahmanyam, C.; Lingaiah, N. Studies on Cobalt Nano Particles Supported on Nitrogen-Doped Carbon Catalysts for Selective Hydrogenation of Biomass Derived Furfural. *Catal. Lett.* **2025**, *155*, 137. [CrossRef]
94. Mishra, J.; Mrugesh, P.; Subramanian, P.S.; Pratihar, S. Co–Ti Bimetallic Complex-Induced Phase Modulation of Co@Black TiO_2 for Catalytic Hydrogenation of Cinnamaldehyde. *Inorg. Chem.* **2024**, *63*, 10423–10433. [CrossRef]
95. Zhang, R.; Wang, L.; Ren, J.; Hu, C.; Lv, B. Effect of boron nitride overlayers on Co@BNNSs/BN-Catalyzed aqueous phase selective hydrogenation of cinnamaldehyde. *J. Colloid Interface Sci.* **2023**, *630*, 549–558. [CrossRef] [PubMed]
96. Gao, X.; Ma, Y.; Ruan, Y.; Zhang, W.; Zhang, S.; Xiong, W.; Tian, D.; Yang, S.; Fan, P.; Yang, Y.; et al. Water-promoted selective hydrogenation of cinnamaldehyde over hydrotalcite-derived Co catalysts. *Mol. Catal.* **2024**, *559*, 114096. [CrossRef]
97. Ma, Y.; Xu, G.; Wang, H.; Wang, Y.; Zhang, Y.; Fu, Y. Cobalt Nanocluster Supported on $ZrREnO_x$ for the Selective Hydrogenation of Biomass Derived Aromatic Aldehydes and Ketones in Water. *ACS Catal.* **2018**, *8*, 1268–1277. [CrossRef]

98. Zhang, J.; Liu, Y.; Jia, Z.; ShitaoYu; Liu, S.; Li, L.; Wu, Q.; Yu, H.; Liu, Y.; Jiang, X.; et al. Selective hydrogenation of furfural to furfuryl alcohol over copper-cobalt bimetallic catalyst. *Chem. Eng. J.* **2024**, *490*, 151677. [CrossRef]
99. Shi, H.; Li, Q.; Su, T.; Luo, X.; Qin, Z.; Ji, H. $CoZn_yB/Nb_2CT_x$ (MXene) for cinnamaldehyde hydrogenation to cinnamyl alcohol: Effects of Zn. *Appl. Catal. A-Gen.* **2025**, *689*, 120024. [CrossRef]
100. Jia, A.; Yao, X.; Feng, L.; Ma, Z.; Li, F.; Wang, Y. Synthesis of Hierarchically Porous Amorphous Alloy Hollow Sphere with High Surface Area as Effective and Selective Catalysts for Cinnamaldehyde Hydrogenation. *Eur. J. Inorg. Chem.* **2020**, *2020*, 1184–1191. [CrossRef]
101. Shi, H.; Xu, Y.; Su, T.; Luo, X.; Xie, X.; Qin, Z.; Ji, H. Co–Fe catalyst supported on acidified bentonite for selective hydrogenation of cinnamaldehyde. *Catal. Sci. Technol.* **2024**, *14*, 1181–1190. [CrossRef]
102. Lv, Y.; Han, M.; Gong, W.; Wang, D.; Chen, C.; Wang, G.; Zhang, H.; Zhao, H. Fe-Co Alloyed Nanoparticles Catalyzing Efficient Hydrogenation of Cinnamaldehyde to Cinnamyl Alcohol in Water. *Angew. Chem. Int. Ed.* **2020**, *59*, 23521–23526. [CrossRef]
103. Cui, H.; Liu, S.; Lv, Y.; Wu, S.; Wang, L.; Hao, F.; Liu, P.; Xiong, W.; Luo, H. Transfer hydrogenation of cinnamaldehyde to cinnamyl alcohol in hydrophobically modified core–shell MOFs nanoreactor: Identification of the formed metal–N as the structure of an active site. *J. Catal.* **2020**, *381*, 468–481. [CrossRef]
104. Ramos, R.; Peixoto, A.F.; Arias-Serrano, B.I.; Soares, O.S.G.P.; Pereira, M.F.R.; Kubička, D.; Freire, C. Catalytic Transfer Hydrogenation of Furfural over $Co_3O_4-Al_2O_3$ Hydrotalcite-derived Catalyst. *ChemCatChem* **2020**, *12*, 1467–1475. [CrossRef]
105. Mao, W.; Liu, J.; Yin, B.; Miao, S.; Li, Y.; Kong, D.; Wang, F. Co-Cr composite oxides efficiently catalyzed transfer hydrogenation of α, β-unsaturated aldehydes via N-doped carbon and interfacial electron migration. *Mol. Catal.* **2022**, *524*, 112257. [CrossRef]
106. Cheng, S.; Ding, J.; Chen, Y.; Pan, G.; Feng, X.; Xu, X.; Xu, J. Enhanced catalytic transfer hydrogenation of biomass-based furfural into furfuryl alcohol over Co_3O_4-based mixed oxide catalysts from hydrotalcite. *Appl. Catal. A-Gen.* **2024**, *684*, 119909. [CrossRef]
107. Yang, Y.; Ren, Z.; Zhou, S.; Wei, M. Perspectives on Multifunctional Catalysts Derived from Layered Double Hydroxides toward Upgrading Reactions of Biomass Resources. *ACS Catal.* **2021**, *11*, 6440–6454. [CrossRef]
108. Zhang, R.; Wang, L.; Yang, X.; Tao, Z.; Ren, X.; Lv, B. The role of surface N-H groups on the selective hydrogenation of cinnamaldehyde over Co/BN catalysts. *Appl. Surf. Sci.* **2019**, *492*, 736–745. [CrossRef]
109. Li, J.; Xi, Y.; Qiao, Y.; Zhao, Z.; Liu, J.; Li, F. Solvent Effects on Heterogeneous Catalysis for the Selective Hydrogenation. *ChemCatChem* **2024**, *16*, e202400120. [CrossRef]
110. Liu, S.; He, Y.; Fu, W.; Chen, J.; Ren, J.; Liao, L.; Sun, R.; Tang, Z.; Mebrahtu, C.; Zeng, F. Hetero-site cobalt catalysts for higher alcohols synthesis by CO_2 hydrogenation: A review. *J. CO2 Util.* **2023**, *67*, 102322. [CrossRef]
111. Chen, Y.; Wang, S.; Chen, Z.; Ding, Y.; Zhang, L.; Lv, L.; Wang, Y.; Xu, D.; Wang, S. Synthesis of Co_3O_4 nanoparticles with controllable size and their catalytic properity. *Solid State Sci.* **2018**, *82*, 78–83. [CrossRef]
112. Xie, H.; Guo, T.; Zhang, Y.; Huang, Z.; Hu, H.; He, Q.; Gan, T. Mechanical activation assisted synthesis of atomically dispersed cobalt catalysts supported on N, P co-doped cellulose-derived carbon for nitrobenzene hydrogenation. *Appl. Surf. Sci.* **2025**, *685*, 162020. [CrossRef]
113. Cao, F.; Ni, W.; Zhao, Q.; Wang, L.; Xue, S.; Li, Y.; Kong, D.; Wu, M.; Zhi, L. Precisely manipulating the local coordination of cobalt single-atom catalyst boosts selective hydrogenation of nitroarenes. *Appl. Catal. B-Environ. Energy* **2024**, *346*, 123762. [CrossRef]
114. Li, J.; Yan, X.; Ren, Y.; Liu, T.; Li, K.; Wei, H. Synergy of metallic Co and Co-N species in highly dispersed Co based catalyst for enhanced nitroarene hydrogenation. *Fuel* **2024**, *375*, 132567. [CrossRef]
115. Mohammadi, M.-R.; Hadavimoghaddam, F.; Atashrouz, S.; Abedi, A.; Hemmati-Sarapardeh, A.; Mohaddespour, A. Modeling hydrogen solubility in alcohols using machine learning models and equations of state. *J. Mol. Liq.* **2022**, *346*, 117807. [CrossRef]
116. Gao, X.; Tian, S.; Jin, Y.; Wan, X.; Zhou, C.; Chen, R.; Dai, Y.; Yang, Y. Bimetallic PtFe-Catalyzed Selective Hydrogenation of Furfural to Furfuryl Alcohol: Solvent Effect of Isopropanol and Hydrogen Activation. *ACS Sustain. Chem. Eng.* **2020**, *8*, 12722–12730. [CrossRef]
117. Li, X.-L.; Zhang, K.; Chen, S.-Y.; Li, C.; Li, F.; Xu, H.-J.; Fu, Y. A cobalt catalyst for reductive etherification of 5-hydroxymethylfurfural to 2,5-bis(methoxymethyl)furan under mild conditions. *Green Chem.* **2018**, *20*, 1095–1105. [CrossRef]
118. Zhang, Y.; Zhang, R.; Lyu, S.; Ren, X.; Liu, G.; Wang, L. Highly dispersed Pd nanoparticles supported on SBA-15@derived C from RF resin for hydrogenation of 2-ethylanthraquinone. *AlChE J.* **2025**, *71*, e18862. [CrossRef]
119. Zhao, M.; Yuan, K.; Wang, Y.; Li, G.; Guo, J.; Gu, L.; Hu, W.; Zhao, H.; Tang, Z. Metal–organic frameworks as selectivity regulators for hydrogenation reactions. *Nature* **2016**, *539*, 76–80. [CrossRef]
120. Stephan, D.W. Frustrated Lewis Pairs: From Concept to Catalysis. *Acc. Chem. Res.* **2014**, *48*, 306–316. [CrossRef]
121. Li, S.; Wu, Q.; You, X.; Ren, X.; Du, P.; Li, F.; Zheng, N.; Shen, H. Anchoring Frustrated Lewis Pair Active Sites on Copper Nanoclusters for Regioselective Hydrogenation. *J. Am. Chem. Soc.* **2024**, *146*, 27852–27860. [CrossRef]
122. Yu, M.; Liu, L.; Wang, Q.; Jia, L.; Hou, B.; Si, Y.; Li, D.; Zhao, Y. High coverage H_2 adsorption and dissociation on fcc Co surfaces from DFT and thermodynamics. *Int. J. Hydrogen Energy* **2018**, *43*, 5576–5590. [CrossRef]
123. Yang, H.; Goldbach, A.; Shen, W. Acetone hydrogenation over face-centered cubic and hexagonal close-packed cobalt. *Int. J. Hydrogen Energy* **2024**, *51*, 1360–1372. [CrossRef]

124. Yang, Y.; Rao, D.; Chen, Y.; Dong, S.; Wang, B.; Zhang, X.; Wei, M. Selective Hydrogenation of Cinnamaldehyde over Co-Based Intermetallic Compounds Derived from Layered Double Hydroxides. *ACS Catal.* **2018**, *8*, 11749–11760. [CrossRef]
125. Kubas, G.J. Molecular hydrogen complexes: Coordination of a. sigma. bond to transition metals. *Acc. Chem. Res.* **1988**, *21*, 120–128. [CrossRef]
126. Kubas, G.J. Activation of dihydrogen and coordination of molecular H_2 on transition metals. *J. Organomet. Chem.* **2014**, *751*, 33–49. [CrossRef]
127. Crabtree, R.H. Dihydrogen complexes: Some structural and chemical studies. *Acc. Chem. Res.* **1990**, *23*, 95–101. [CrossRef]
128. Crabtree, R.H. Dihydrogen Complexation. *Chem. Rev.* **2016**, *116*, 8750–8769. [CrossRef]
129. Welch, G.C.; San Juan, R.R.; Masuda, J.D.; Stephan, D.W. Reversible, Metal-Free Hydrogen Activation. *Science* **2006**, *314*, 1124–1126. [CrossRef]
130. Ghuman, K.K.; Hoch, L.B.; Wood, T.E.; Mims, C.; Singh, C.V.; Ozin, G.A. Surface Analogues of Molecular Frustrated Lewis Pairs in Heterogeneous CO_2 Hydrogenation Catalysis. *ACS Catal.* **2016**, *6*, 5764–5770. [CrossRef]
131. Riddhi, R.K.; Penas-Hidalgo, F.; Chen, H.; Quadrelli, E.A.; Canivet, J.; Mellot-Draznieks, C.; Solé-Daura, A. Experimental and computational aspects of molecular frustrated Lewis pairs for CO_2 hydrogenation: En route for heterogeneous systems? *Chem. Soc. Rev.* **2024**, *53*, 9874–9903. [CrossRef]
132. Hongyun, Y.; Jingjun, L.; Kaiyue, H.; Riyang, S.; Zhipeng, T.; Chao, W.; Ying, C. Mechanism of solvent effect on hydrogenation of lignin-derived phenolic compounds. *CIESC J.* **2022**, *73*, 4498–4506. [CrossRef]
133. Lu, Q.; Wang, H.; Sun, J.; Wei, X.-Z.; Zhang, Q.; Zhang, X.; Chen, L.; Liu, J.; Chen, Y.; Ma, L. Solvent effect in selective hydrogenation of cinnamaldehyde over Pd–Ni nanoclusters encapsulated within siliceous zeolite. *Microporous Mesoporous Mater.* **2024**, *367*, 112979. [CrossRef]
134. Yamada, H.; Goto, S. The Effect of Solvents Polarity on Selective Hydrogenation of Unsaturated Aldehyde in Gas-Liquid-Solid Three Phase Reactor. *J. Chem. Eng. Jpn.* **2003**, *36*, 586–589. [CrossRef]
135. Lashdaf, M.; Nieminen, V.-V.; Tiitta, M.; Venäläinen, T.; Österholm, H.; Krause, O. Role of acidity in hydrogenation of cinnamaldehyde on platinum beta zeolite. *Microporous Mesoporous Mater.* **2004**, *75*, 149–158. [CrossRef]
136. Hou, Z.; Zhu, Y.; Chi, H.; Zhao, L.; Wei, H.; Xi, Y.; Ma, L.; Feng, X.; Lin, X. Silica-modified Pt/TiO_2 catalysts with tunable suppression of strong metal–support interaction for cinnamaldehyde hydrogenation. *Chin. J. Chem. Eng.* **2024**, *70*, 189–198. [CrossRef]
137. Bai, Y.; Cherkasov, N.; Huband, S.; Walker, D.; Walton, R.; Rebrov, E. Highly Selective Continuous Flow Hydrogenation of Cinnamaldehyde to Cinnamyl Alcohol in a Pt/SiO_2 Coated Tube Reactor. *Catalysts* **2018**, *8*, 58. [CrossRef]

Disclaimer/Publisher's Note: The statements, opinions and data contained in all publications are solely those of the individual author(s) and contributor(s) and not of MDPI and/or the editor(s). MDPI and/or the editor(s) disclaim responsibility for any injury to people or property resulting from any ideas, methods, instructions or products referred to in the content.

catalysts

MDPI

Article

Tribocatalytic Degradation of Organic Dyes by Disk-Shaped PTFE and Titanium: A Powder-Free Catalytic Technology for Wastewater Treatment

Hanze Zhu, Zeren Zhou, Senhua Ke, Chenyue Mao, Jiannan Song and Wanping Chen *

School of Physics and Technology, Wuhan University, Wuhan 430072, China
* Correspondence: wpchen@whu.edu.cn

Abstract

Tribocatalysis is receiving more and more attention for its great potential in environmental remediation. In this study, a special tribocatalysis was explored as a powder-free catalytic technology for the degradation of organic dyes. Polytetrafluoroethylene (PTFE) and titanium (Ti) disks were first assembled as magnetic rotary disks and then driven to rotate through magnetic stirring in dye solutions in beakers with PTFE, Ti, and Al_2O_3 disks coated on bottoms separately. PTFE and Ti generated dynamic friction with the disks on the beaker bottoms in the course of magnetic stirring, from which some interesting dye degradations resulted. Among those dynamic frictions generated, 40 mg/L rhodamine b (RhB), 30 mg/L methyl orange (MO), and 20 mg/L methylene blue (MB) were effectively degraded by the one between PTFE and PTFE, the one between Ti and Ti, and the one between PTFE and Ti, respectively. Hydroxyl radicals and superoxide radicals were detected for two frictions, one between PTFE and PTFE and the other between Ti and Ti. It is proposed that Ti in friction increases the pressure in blocked areas through deformation and then catalyzes reactions under high pressure. Mechano-radicals are formed by PTFE through deformation, and are responsible for dye degradation. This work demonstrates a powder-free tribocatalysis for organic pollutant degradation and suggests an especially eco-friendly catalytic technology to wastewater treatment.

Keywords: tribocatalysis; powder-free; PTFE; titanium; wastewater; dye degradation

1. Introduction

With various invaluable merits, many organic chemicals are used in huge amounts in industry, agriculture, and our daily life [1–3]. Unfortunately, many of them appear as major harmful organic pollutants in wastewater, such as organic dyes [4], pharmaceuticals [5], phenols [6], biphenyls [7], pesticides [8], fertilizers [9], plasticizers [10], detergents [11], and carbohydrates [12]. They inflict serious harms to human health and environmental ecosystems if not treated properly [1,13,14]. For instance, organic dyes can alter the physical properties of water bodies [15], produce toxicity [16], and affect photosynthesis in aquatic plants [17], thus destroying the ecological balance and stability of water bodies. They also affect soil fertility [18] and nutrient cycling [19] through irrigation or run-off. Many organic pollutants are known as persistent organic pollutants (POPs), whose molecules need to be destroyed through chemical oxidation [20]. Currently, some oxidizing chemicals, such as Fenton [21] and hydrogen peroxide [22], are used in large amounts in wastewater treatment to eliminate these POPs completely from the environment [23]. The application

of these chemicals in wastewater treatment not only increases costs but also results in secondary pollution [24]. Alternative green oxidation methods are highly desirable for wastewater treatment.

A well-known green technology in wastewater treatment is photocatalysis, in which solar light induces redox reactions in wastewater via semiconductor nanoparticles suspended in water [25–27]. Another newly emerging appealing technology in wastewater treatment is tribocatalysis, in which mechanical energy is absorbed by powder in water through friction and is converted into chemical energy [28–31]. For photocatalysis, wastewater should be relatively transparent for light to reach the semiconductor nanoparticles suspended in it. While for tribocatalysis, there is no such limitation, and it is more attractive for treating wastewater of low transparency than photocatalysis [32]. A mechanism based on the excitation of electron–hole pairs in semiconductor particles by mechanical energy has been proposed for tribocatalysis, which is quite similar to that for photocatalysis [33–36]. Though photocatalysis and tribocatalysis both make good use of clean energies in wastewater treatment, their dependence on particles suspended in water to absorb these clean energies actually faces some challenges for practical large-scale wastewater treatment, including catalyst recovery and secondary pollution.

With particles like TiO_2 [37], ZnO [38], NiO [39], and Co_3O_4 [40] as catalysts, tribocatalysis has been successfully applied to the degradation of organic dyes and to the conversion of H_2O and CO_2. It is worth noting that, besides this typical tribocatalysis with particles as catalysts, another novel form of powder-free tribocatalysis has emerged for the conversion of H_2O and CO_2 into flammable gases [41,42]. Specifically, Cui et al. assembled copper (Cu) disks as Cu magnetic rotary disks, which were driven to rotate through magnetic stirring in reactors enclosed with H_2O and CO_2. Without any powders, the dynamic friction between Cu magnetic rotary disks and reactor bottoms catalyzed the conversion of H_2O and CO_2 into flammable gases [41]. Similarly, nickel (Ni) disks were employed to catalyze the conversion from H_2O and CO_2 into chemical fuels through friction [42]. It was shown that Ni exhibited significant catalytic effects during friction, and its chemical stability was maintained. Thus, these findings demonstrated the great potential of disk-shaped metals to catalyze important chemical reactions through friction without powders. In this study, a powder-free tribocatalytic degradation of organic dyes was successfully explored for disk-shaped polytetrafluoroethylene (PTFE) and titanium (Ti). Mounted as parts of magnetic rotary disks, disk-shaped PTFE and Ti were driven through magnetic stirring to generate friction with beaker bottoms in solutions of rhodamine b (RhB), methylene blue (MB), and methyl orange (MO) separately, which are widely studied as model organic pollutants in photocatalysis [43–45]. To our great surprise, all three kinds of organic dyes degraded through magnetic stirring without the participation of any powders. It has thus clearly extended powder-free tribocatalysis from the conversion of H_2O and CO_2 to the degradation of organic pollutants, which is especially attractive for wastewater treatment prospects regarding powder-related secondary pollution. To our knowledge, this is the first report of a powder-free catalytic technology for the degradation of organic pollutants, which is especially attractive for wastewater treatment in view of powder-related secondary pollution.

2. Results and Discussion

2.1. Organic Dyes Degradation

Figure 1 shows the results obtained for the PTFE magnetic rotary disk, which was driven to rotate through magnetic stirring in solutions of 40 mg/L RhB, 20 mg/L MB, and 30 mg/L MO contained in glass beakers with Ti, aluminum oxide (Al_2O_3), and PTFE coatings separately. PTFE from the magnetic rotary disk generated dynamic friction with

the bottoms of beakers in the course of magnetic stirring and the friction pairs are termed as PTFE@Ti, PTFE@Al_2O_3, and PTFE@PTFE, respectively. As shown in Figure 1a, for 40 mg/L RhB in a Ti-coated beaker, the characteristic peak at 554 nm decreased significantly while remaining observable after 180 min of magnetic stirring. It can also be seen from the inset that the dye color faded from red to pink rather than to colorless. As shown in Figure 1b, for 40 mg/L RhB in an Al_2O_3-coated beaker, the characteristic peak decreased with magnetic stirring time much slower than that in Figure 1a, and after 180 min of magnetic stirring, the peak was still rather high, and the solution was still rather bright in color. Encouragingly, for 40 mg/L RhB in a PTFE-coated beaker, the characteristic peak completely disappeared and the solution became colorless after 180 min of magnetic stirring, as shown in Figure 1c, which form sharp contrasts with those in Figure 1a,b. Obviously, the frictions between PTFE and the coatings of the beakers in the course of magnetic stirring resulted in the observed RhB degradations, and the best result was obtained for the beaker with PTFE coating. Namely, the friction between PTFE and PTFE was most effective for RhB degradation.

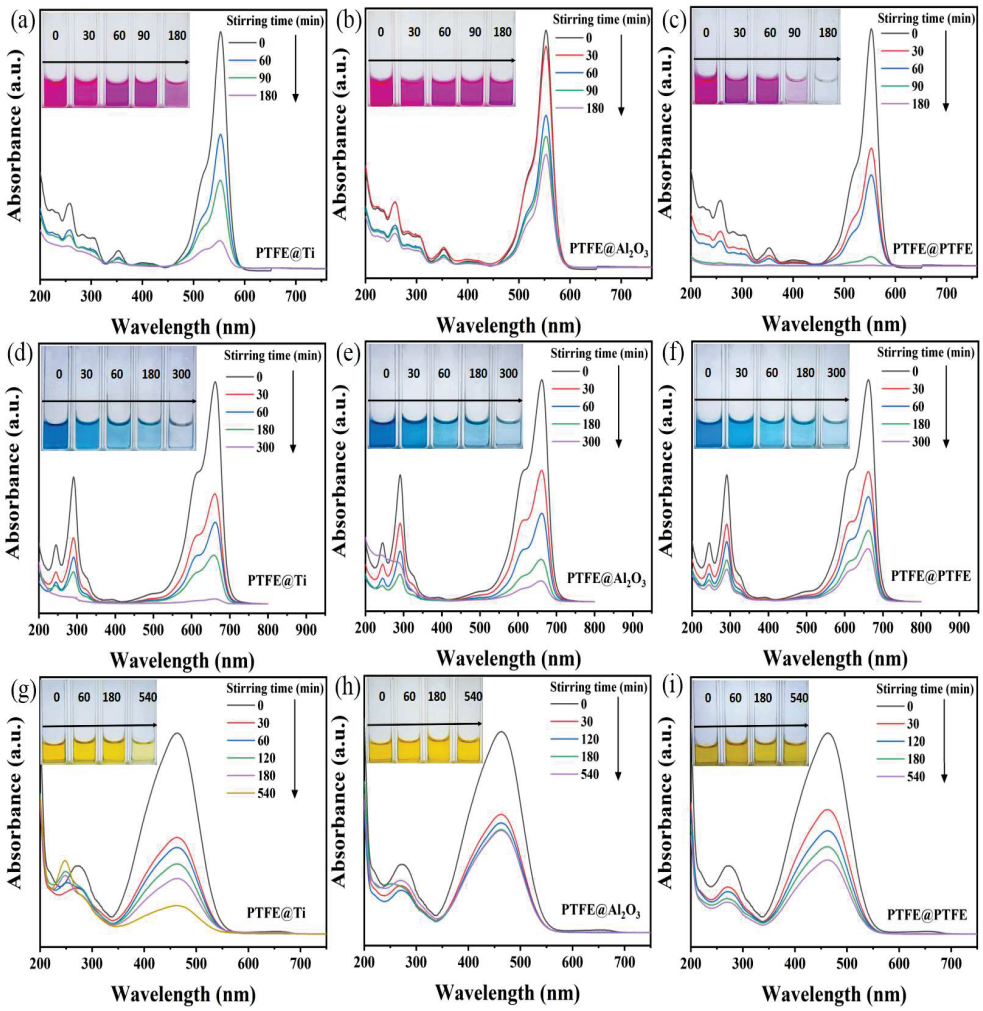


Figure 1. UV–Vis absorption spectra of organic dye solutions contained in glass beakers with Ti, Al_2O_3, and PTFE coatings separately and stimulated through a PTFE magnetic rotary disk that was driven to rotate by magnetic stirring (inset: solution color change): (**a**) RhB (40 mg/L) in a Ti-coated beaker; (**b**) RhB (40 mg/L) in an Al_2O_3-coated beaker; (**c**) RhB (40 mg/L) in an PTFE-coated beaker; (**d**) MB (20 mg/L) in a Ti-coated beaker; (**e**) MB (20 mg/L) in an Al_2O_3-coated beaker; (**f**) MB (20 mg/L) in a PTFE–coated beaker; (**g**) MO (30 mg/L) in a Ti-coated beaker; (**h**) MO (30 mg/L) in an Al_2O_3-coated beaker; (**i**) MO (30 mg/L) in a PTFE-coated beaker.

The results for the degradation of 20 mg/L MB are shown in Figure 1d–f. At the initial stage of magnetic stirring, the characteristic peak at 665 nm decreased readily with magnetic stirring time for all three kinds of coatings. After 180 min of magnetic stirring, however, the decreasing speed of the peak began to slow down for Al_2O_3 and PTFE coatings. After 300 min of magnetic stirring, a complete degradation was only obtained for the Ti coating. Namely, the peak completely disappeared, and the solution almost became colorless, as shown in Figure 1d. It is clear that the friction between PTFE and Ti is most effective for the degradation of MB.

For 30 mg/L MO, the peak at 464 nm decreased rather slowly with magnetic stirring time for all three kinds of coatings. Even after 540 min of magnetic stirring, the peak did not disappear and the solution was not colorless for all the three coatings, as shown in Figure 1g–i. It seems that the PTFE magnetic rotary disk was less effective for the degradation of MO than for those of RhB and MB.

The results obtained for the Ti magnetic rotary disk are shown in Figure 2. In sharp contrast with the PTFE magnetic rotary disk, the Ti disk was found especially effective in degrading MO. For both Ti and Al_2O_3 coatings, the characteristic peak of MO at 464 nm completely disappeared and the solution also became colorless after 120 min of magnetic stirring, as shown in Figure 2a,b. It should be pointed out that a new peak appeared at 247 nm, which has been observed in previous studies and suggests that MO molecules have been broken into some less harmful small molecules [46,47]. However, for PTFE coating, the characteristic peak and the bright orange color were still observed even after 540 min of magnetic stirring, as shown in Figure 2c. Together with the results shown in Figure 1g–i, it is clear that PTFE is not effective for degrading MO through friction either as a magnetic rotary disk or as a coating.

The results obtained for the degradation of 20 mg/L MB solution by the Ti disk are shown in Figure 2d–f. As shown in Figure 2d, the degradation in the Ti-coated beaker was relatively slow. The characteristic peak at 665 nm was decreased by 70% and the solution color was changed from dark blue to light blue after 540 min of magnetic stirring. As for 20 mg/L MB in the Al_2O_3-coated beaker, the Ti disk induced a nearly 100% degradation and the solution became colorless after 540 min of magnetic stirring, as shown in Figure 2e. A dynamic friction between PTFE and Ti occurred for the PTFE rotary disk in the Ti-coated beaker, and also for the Ti rotary disk in the PTFE-coated beaker. In both cases, 20 mg/L MB was effectively degraded, as shown in Figures 1d and 2f. In short, both the PTFE and Ti magnetic rotary disks were very successful in degrading 20 mg/L MB through friction.

Although the Ti magnetic rotary disk was very successful for the degradation of MO and MB, it was found quite incompetent for the degradation of RhB through friction. As shown in Figure 2g–i, even after 360 min of magnetic stirring, the peak at 554 nm did not disappear and the solution was still rather red for all three coatings. It is worth noting that though the friction between PTFE and PTFE was very effective for degrading RhB, as shown in Figure 1c, the friction between PTFE and Ti was far less effective for the degradation of RhB, as shown in both Figures 1a and 2i.

Figure 3 shows the relationship between C/C_0 and magnetic stirring time for the three dye solutions in this study. As shown in Figure 3a, for 40 mg/L RhB, the fastest degradation was observed for PTFE@PTFE, while the slowest one was observed for Ti@Ti, which roughly suggests that PTFE is much more effective than Ti in degrading RhB through friction.

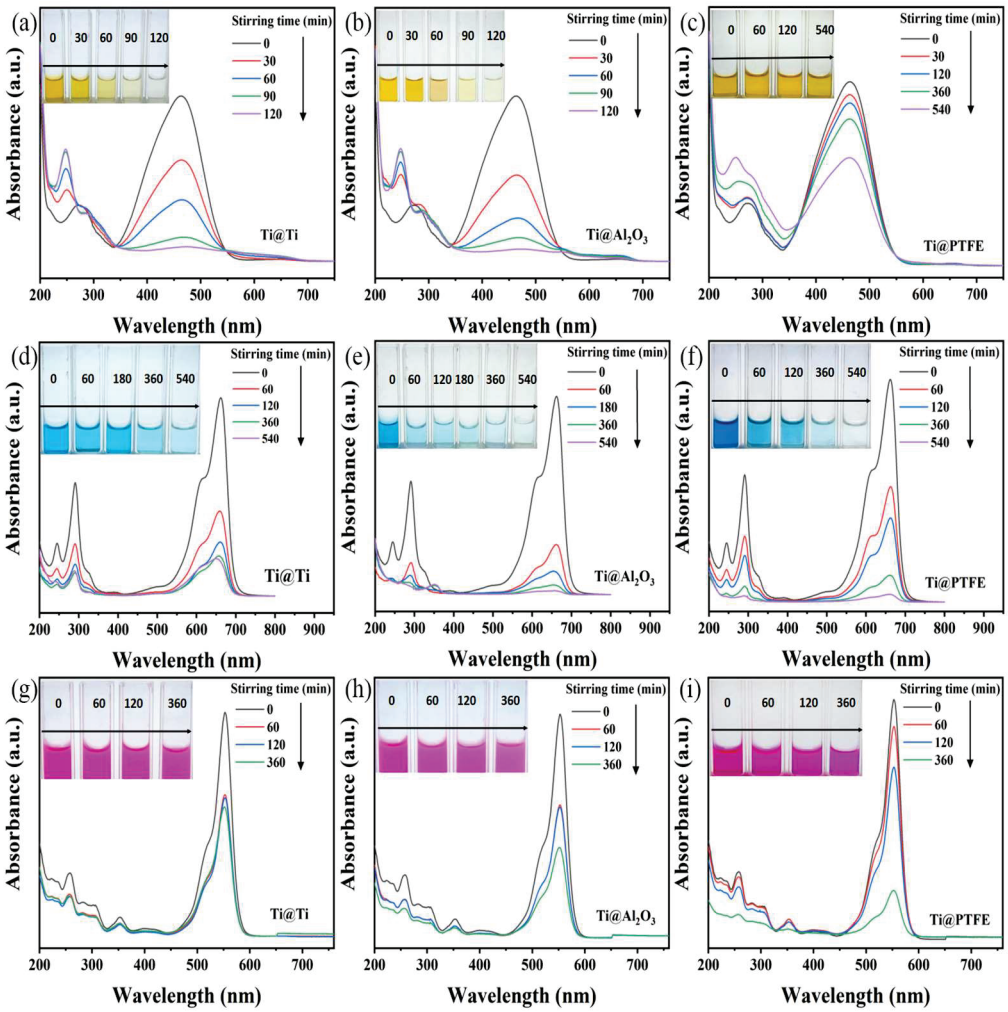


Figure 2. UV–Vis absorption spectra of organic dye solutions contained in glass beakers with Ti, Al_2O_3, and PTFE coatings separately and stimulated through a Ti magnetic rotary disk that was driven to rotate by magnetic stirring (inset: solution color change): (**a**) MO (30 mg/L) in a Ti-coated beaker; (**b**) MO (30 mg/L) in an Al_2O_3-coated beaker; (**c**) MO (30 mg/L) in a PTFE-coated beaker; (**d**) MB (20 mg/L) in a Ti-coated beaker; (**e**) MB (20 mg/L) in an Al_2O_3-coated beaker; (**f**) MB (20 mg/L) in a PTFE-coated beaker; (**g**) RhB (40 mg/L) in a Ti-coated beaker; (**h**) RhB (40 mg/L) in an Al_2O_3-coated beaker; (**i**) RhB (40 mg/L) in a PTFE-coated beaker.

For the 20 mg/L MB shown in Figure 3b, almost 100% degradation was observed for three friction pairs, namely PTFE@Ti, Ti @PTFE, and Ti@Al_2O_3. It seems that the friction between PTFE and Ti is especially useful for the degradation of MB.

Among the results obtained for the 30 mg/L MO shown in Figure 3c, two friction pairs, namely Ti@Ti and Ti@Al_2O_3, were much better than all the others in degrading MO. As two hard materials happened to appear only in these two friction pairs, it seems that for Ti, friction with a hard material is necessary for the degradation of MO. On the other hand, as PTFE is present in all the other friction pairs that are not effective for the degradation of MO, in view of the efficiency of PTFE in degrading RhB, this suggests that PTFE is less effective in degrading MO than RhB through friction.

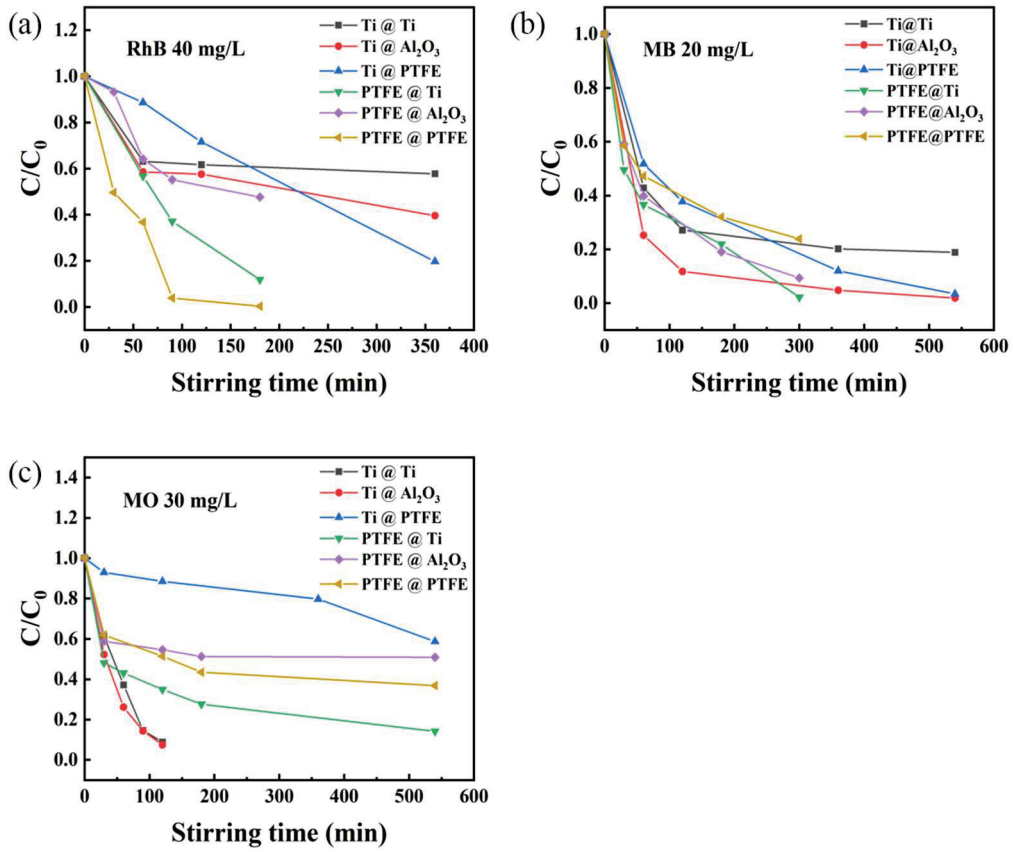


Figure 3. Relationship between C/C_0 and stirring time for the degradation of three kinds of dye solutions in this study: (**a**) 40 mg/L RhB; (**b**) 20 mg/L MB; (**c**) 30 mg/L MO.

Though only three kinds of disk-shaped materials (PTFE, Ti, and Al_2O_3) were employed to take part in the friction pairing in this study, the results obtained are highly surprising in several ways. Firstly, all the model dye solutions in this study, namely 40 mg/L RhB, 20 mg/L MB, and 30 mg/L MO, were successfully degraded in a relatively short period of time by these materials stimulated through magnetic stirring. As a matter of fact, the concentrations of these solutions were actually so high that they were challenging to be degraded by photocatalysts under solar light irradiation. Secondly, for the same organic dye, different materials showed highly different capabilities to degrade through friction. For example, PTFE was much more competent than Ti at degrading RhB, while Ti was much more competent than PTFE at degrading MO. It is thus expected that many other organic pollutants can be degraded in this way after many more kinds of materials have been investigated and chosen to take part in friction pairing. Therefore, it can be expected that many other organic pollutants can be degraded in this way once a wider range of materials for use in friction pairs is investigated and selected. Thirdly, the power of magnetic stirring in this study was below 10 W, which indicates that this powder-free technology is scalable for large-scale wastewater treatment. While this powder-free tribocatalysis first appeared for the conversion of H_2O and CO_2 [41,42], it should be especially appealing for large-scale wastewater treatment in which powder-related secondary pollution has long been a major concern.

2.2. Mechanism Analysis

There are two special friction pairs in this study, namely PTFE@PTFE and Ti@Ti, whose two materials in friction are of the same kind. Since some highly surprising results have been observed for them, the radicals that were generated by their dynamic frictions

have been investigated in depth. Terephthalic acid (TA) and nitrotetrazolium blue chloride (NBT) have been used as molecule probes, as the reaction of TA with ·OH produced 2-hydroxyterephthalic acid (TAOH) with a fluorescence response at 425 nm [48], and the reaction of NBT with $\cdot O_2^-$ caused the absorption peak of NBT at 259 nm to gradually decrease [49]. For a PTFE magnetic rotary disk rotated in 0.5 mM TA and 2 mM NaOH contained in a PFTE-coated beaker, as shown in Figure 4a, the fluorescence intensity of TAOH gradually increased with magnetic stirring time, which indicates that ·OH was continuously generated through the friction of PTFE@PTFE. On the other hand, the characteristic peak of NBT at 259 nm gradually decreased with magnetic stirring time and finally disappeared within 120 min, as shown in Figure 4b, indicating that superoxide radicals ($\cdot O_2^-$) were continuously generated through the friction of PTFE@PTFE. For a Ti magnetic rotary disk rotating in a Ti-coated beaker, both radicals were generated in much greater amounts through the friction of Ti@Ti than their counterparts through the friction of PTFE@PTFE separately, as shown in Figure 4c,d.

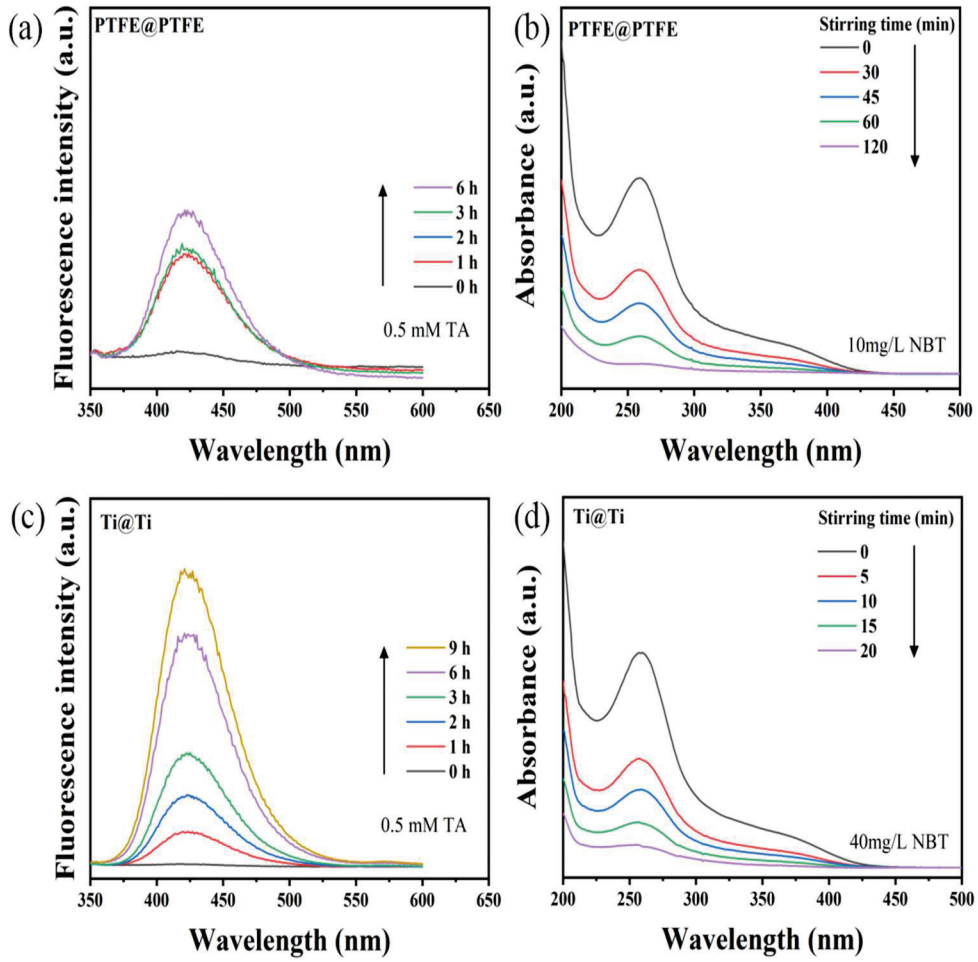


Figure 4. A PTFE magnetic rotary disk rotating in a PTFE-coated beaker: (**a**) fluorescence intensity spectra for 0.5 mM TA and 2 mM NaOH; (**b**) UV–Vis absorption spectra for 10 mg/L NBT. A Ti magnetic rotary disk rotating in a Ti-coated beaker: (**c**) fluorescence intensity spectra for 0.5 mM TA and 2 mM NaOH; (**d**) UV–Vis absorption spectra for 40 mg/L NBT.

As a matter of fact, a mechanism has been proposed for the tribocatalytic conversion from H_2O and CO_2 to chemical fuels by Cu and Ni, in which hydroxyl radicals have been detected as intermediate products [41,42]. These metals first increase the pressure in blocked holes in friction surface through elastic deformation and then exert their catalytic role under elevated pressures. Similarly, this mechanism can be adopted to explain the dye

degradation induced by the Ti magnetic rotary disk. When Ti forms dynamic friction with another hard material, including Ti, small holes in the friction surface can be blocked and squeezed by Ti through elastic deformation, and Ti catalyzes dye degradation under high pressures. As catalytic reactions, it is common for hydroxyl and super oxygen radials to be detected as intermediate products.

As for the dye degradations induced by the PTFE magnetic rotary disk, quite similar results were reported by Grzybowski et al. in 2012 [50]. As they observed that some polymers are able to induce redox reactions in surrounding solutions merely through mechanical deformation, they proposed that mechano-radicals created by mechanically stressed polymers are responsible for the reactions. Though the nature of mechano-radicals needs further investigations, we would like to tentatively explain the degradations induced by PTFE in this study in the same way. Specifically for the friction between PTFE and PTFE, PTFE is deformed in some local areas under friction, as shown in Figure 5. Mechano-radials are created by deformed PTFE and subsequently induce dye degradation.

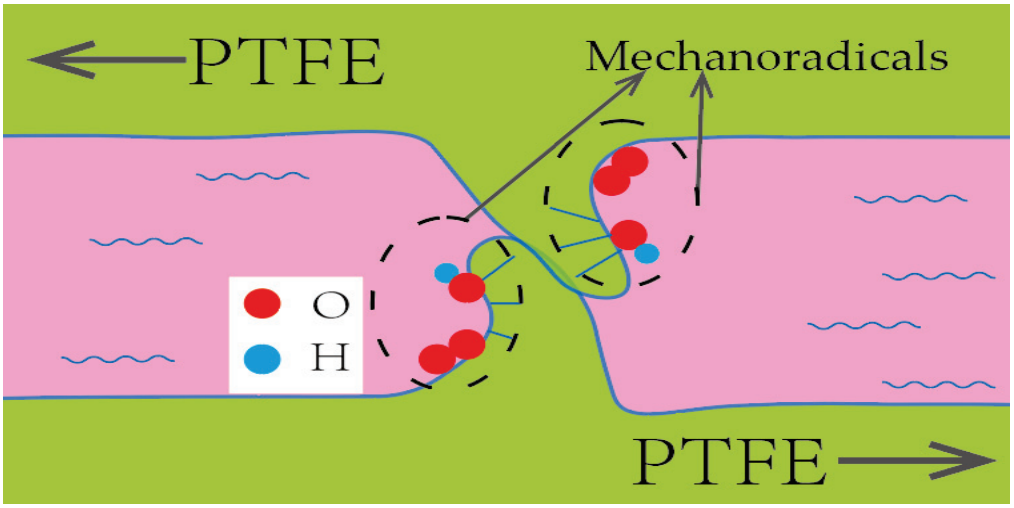


Figure 5. A schematic drawing for PTFE deformation in friction between PTFE and PTFE disks, and the creation of mechano-radicals from deformed PTFE.

Many interesting results obtained in this study deserve further in-depth exploration. For instance, the friction between PTFE and PTFE was especially effective for degrading RhB, while the friction between Ti and Ti was especially effective for degrading MO. The mechanisms behind them are important not only for wastewater treatment but also for the development of tribocatalysis as a whole.

3. Materials and Methods

3.1. PTFE and Ti Disks Assembled as Magnetic Rotary Disks

A PTFE disk, ϕ 35 mm × 5 mm, was assembled as a PTFE magnetic rotary disk by mounting 18 magnets, ϕ 5 mm × 5 mm, on its back, which were then encapsulated with epoxy. The fabrication of PTFE magnetic rotary disks was described in detail in a previous paper [39].

Four Ti disks, ϕ 10 mm × 3 mm, were mounted symmetrically on a PTFE disk, ϕ 35 mm × 5 mm, as shown in Figure 6a. A total of 18 magnets, ϕ 5 mm × 5 mm, were placed into the recess of a PFTE disk, ϕ 35 mm × 8 mm. These two PTFE disks were bound together with strong glue, as shown in Figure 6b. Driven through magnetic stirring, this Ti magnetic rotary disk will rotate, and its Ti disks will form dynamic friction with the beaker bottom.

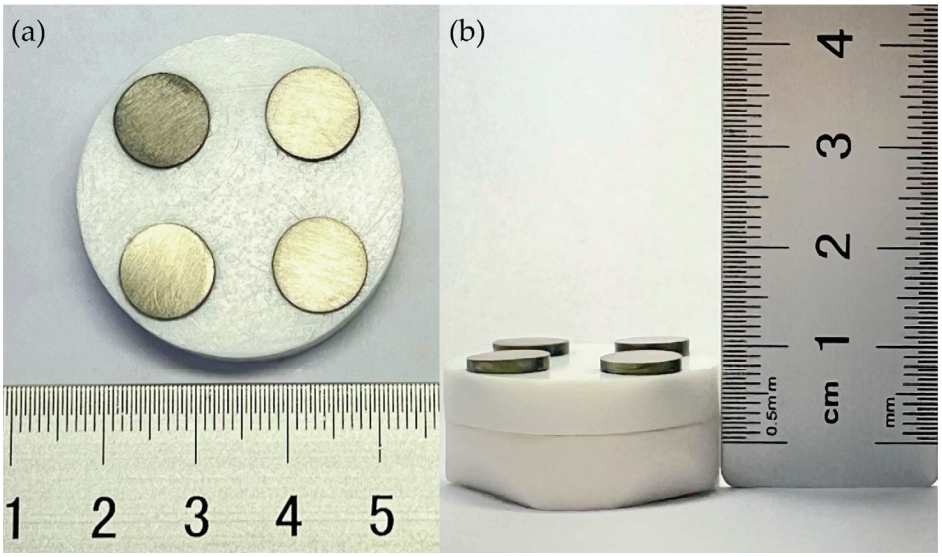


Figure 6. Images of a Ti magnetic rotary disk: (**a**) front surface; (**b**) side surface.

3.2. Modifying Glass Beakers with PTFE, Ti, and Al_2O_3 Disks on Their Bottoms

Commercially available flat-bottomed quartz glass beakers (ϕ 50 mm × 75 mm, 150 mL) were modified through coating disks of PTFE, Ti, and Al_2O_3 on their bottoms separately. This approach resulted in beakers with bottoms of PTFE, Ti, and Al_2O_3, prepared separately for further investigation.

3.3. Degradation of Organic Dyes Through Magnetic Stirring

As in a typical experiment, a PTFE or a Ti magnetic rotary disk was placed in a beaker that contained 20 mL of 20 mg/L MB, 30 mg/L MO, or 40 mg/L RhB solution. The magnetic rotary disk was driven to rotate at 400 rpm in the solution through a magnetic stirrer (HO3-A, Shanghai Meiyingpu Instrument manufacturing Co., Shanghai, China), as shown by an example in Figure 7, the room temperature was kept at 25 °C, and the beaker was kept in dark environment. Samples of 2 mL were collected at specified intervals. The absorbance spectra for MB, MO, and RhB were recorded with a UV–Vis spectrophotometer (UV-2550; Shimadzu, Kyoto, Japan). The efficiency of organic dye degradation was typically calculated using the equation $D = 1 - A/A_0$, with A_0 and A denoting the initial and remaining absorbance at the dye's characteristic peak (RhB: 554 nm; MO: 464 nm; MB: 665 nm), respectively.

3.4. Detection for Hydroxyl Radicals and Superoxide Radicals

A PTFE magnetic rotary disk was first placed in a PTFE-coated beaker, and a Ti magnetic rotary disk was first placed in a Ti-coated beaker. For the detection of hydroxyl radicals (·OH), 20 mL of a mixture of 0.5 mM terephthalic acid (TA) and 2 mM NaOH was added to the PTFE-coated beaker and the Ti-coated beaker separately. The magnetic rotary disks in the beakers were driven to rotate at 400 rpm in darkness and 2 mL of samples was collected at certain time intervals, and their fluorescence spectra were measured on a fluorescence luminescence spectrophotometer (FL-F4600, Hitachi, Tokyo Japan) using 315 nm excitation light. For the detection of superoxide radicals ($\cdot O_2^-$), 20 mL of 10 mg/L NBT solution was added to the PTFE-coated beaker and 20 mL of 40 mg/L NBT solution was added to the Ti-coated beaker. Magnetic stirring was conducted similarly, and 2 mL of samples was also collected at certain time intervals, whose absorption spectra were determined through a UV–Vis spectrophotometer (UV-2550; Shimadzu, Kyoto, Japan).



Figure 7. Image of the experimental setup for tribocatalytic degradation of organic dyes in this study: a Ti magnetic rotary disk was placed in MB solution contained in a PTFE-coated beaker.

4. Conclusions

PTFE and Ti magnetic rotary disks were separately assembled from their disks with magnets, and were placed in dye solutions contained in separate beakers with PTFE, Ti, and Al_2O_3 disks coated on their bottoms. The magnetic rotary disks were driven to rotate in the dye solutions through magnetic stirring, which resulted in some highly surprising dye degradations. Among them, 99.7% of 40 mg/L RhB was degraded after 3 h of magnetic stirring for PTFE@PTFE, 100% of 30 mg/L MO was degraded after 2 h of magnetic stirring for Ti@Ti, and 95% of 20 mg/L MB was degraded after 5 h of magnetic stirring for PTFE@Ti. The tribocatalytic performance of Ti is explained in terms of its catalytic role under high pressures, and that of PTFE is explained in terms of the formation of mechano-radicals by deformed polymers. These findings clearly demonstrate an appealing powder-free technology to utilize mechanical energy for wastewater treatment.

Author Contributions: Conceptualization, H.Z. and W.C.; methodology, H.Z. and C.M.; formal analysis, H.Z.; investigation, H.Z., S.K. and J.S.; data curation, H.Z. and Z.Z.; writing—original draft preparation, H.Z.; writing—review and editing, W.C.; visualization, H.Z., Z.Z. and C.M.; supervision, W.C.; project administration, W.C.; funding acquisition, W.C. All authors have read and agreed to the published version of the manuscript.

Funding: This research was partially supported by Jiangsu Engineering Research Center of New Materials for Adsorptive Separation in Chemical Industry and Environmental Treatment, Suzhou, 215123, China (Grant No. SDGC2424).

Data Availability Statement: Data are contained within the article.

Conflicts of Interest: The authors declare no conflicts of interest.

References

1. Topinka, J.; Rossner, P.; Milcová, A.; Schmuczerová, J.; Pěnčíková, K.; Rossnerová, A.; Ambrož, A.; Štolcpartová, J.; Bendl, J.; Hovorka, J.; et al. Day-to-day variability of toxic events induced by organic compounds bound to size segregated atmospheric aerosol. *Environ. Pollut.* **2015**, *202*, 135–145. [CrossRef] [PubMed]
2. Jones, K.C. Persistent Organic Pollutants (POPs) and Related Chemicals in the Global Environment: Some Personal Reflections. *Environ. Sci. Technol.* **2021**, *55*, 9400–9412. [CrossRef] [PubMed]
3. Habesoglu, S.; Atici, A.A. Assessment of pollution indices and human health risk related to 13 heavy metal contents in surface water of Sihke Pond (Van), Turkey. *Spectrosc. Lett.* **2022**, *55*, 464–477. [CrossRef]
4. Tkaczyk, A.; Mitrowska, K.; Posyniak, A. Synthetic organic dyes as contaminants of the aquatic environment and their implications for ecosystems: A review. *Sci. Total Environ.* **2020**, *717*, 137222. [CrossRef]
5. Zhuang, W.; Hachem, K.; Bokov, D.; Javed Ansari, M.; Taghvaie Nakhjiri, A. Ionic liquids in pharmaceutical industry: A systematic review on applications and future perspectives. *J. Mol. Liq.* **2022**, *349*, 118145. [CrossRef]
6. Motamedi, M.; Yerushalmi, L.; Haghighat, F.; Chen, Z. Recent developments in photocatalysis of industrial effluents: A review and example of phenolic compounds degradation. *Chemosphere* **2022**, *296*, 133688. [CrossRef]
7. Yasir, M.W.; Siddique, M.B.A.; Shabbir, Z.; Ullah, H.; Riaz, L.; Nisa, W.U.; Shafeeq, U.R.; Shah, A.A. Biotreatment potential of co-contaminants hexavalent chromium and polychlorinated biphenyls in industrial wastewater: Individual and simultaneous prospects. *Sci. Total Environ.* **2021**, *779*, 146345. [CrossRef]
8. Mdeni, N.L.; Adeniji, A.O.; Okoh, A.I.; Okoh, O.O. Analytical Evaluation of Carbamate and Organophosphate Pesticides in Human and Environmental Matrices: A Review. *Molecules* **2022**, *27*, 618. [CrossRef]
9. Diacono, M.; Persiani, A.; Testani, E.; Montemurro, F.; Ciaccia, C. Recycling Agricultural Wastes and By-products in Organic Farming: Biofertilizer Production, Yield Performance and Carbon Footprint Analysis. *Sustainability* **2019**, *11*, 3824. [CrossRef]
10. Almeida, S.; Ozkan, S.; Gonçalves, D.; Paulo, I.; Queirós, C.S.G.P.; Ferreira, O.; Bordado, J.; Santos, R.G.D. A Brief Evaluation of Antioxidants, Antistatics, and Plasticizers Additives from Natural Sources for Polymers Formulation. *Polymers* **2022**, *15*, 6. [CrossRef]
11. Chen, X.; Wang, Y.; Bai, Z.; Ma, L.; Strokal, M.; Kroeze, C.; Chen, X.; Zhang, F.; Shi, X. Mitigating phosphorus pollution from detergents in the surface waters of China. *Sci. Total Environ.* **2022**, *804*, 150125. [CrossRef] [PubMed]
12. Silvello, M.A.C.; Gonçalves, I.S.; Azambuja, S.P.H.; Costa, S.S.; Silva, P.G.P.; Santos, L.O.; Goldbeck, R. Microalgae-based carbohydrates: A green innovative source of bioenergy. *Bioresour. Technol.* **2022**, *344*, 126304. [CrossRef]
13. Morra, P.; Lisi, R.; Spadoni, G.; Maschio, G. The assessment of human health impact caused by industrial and civil activities in the Pace Valley of Messina. *Sci. Total Environ.* **2009**, *407*, 3712–3720. [CrossRef]
14. Zhou, X.; Zhou, X.; Wang, C.; Zhou, H. Environmental and human health impacts of volatile organic compounds: A perspective review. *Chemosphere* **2022**, *313*, 137489. [CrossRef]
15. Bal, G.; Thakur, A. Distinct approaches of removal of dyes from wastewater: A review. *Mater. Today Proc.* **2022**, *50*, 1575–1579. [CrossRef]
16. Shanker, U.; Rani, M.; Jassal, V. Degradation of hazardous organic dyes in water by nanomaterials. *Environ. Chem. Lett.* **2017**, *15*, 623–642. [CrossRef]
17. Al-Tohamy, R.; Ali, S.S.; Li, F.; Okasha, K.M.; Mahmoud, Y.A.-G.; Elsamahy, T.; Jiao, H.; Fu, Y.; Sun, J. A Critical Review on the Treatment of dye-containing wastewater: Ecotoxicological and Health Concerns of Textile Dyes and Possible Remediation Approaches for Environmental Safety. *Ecotoxicol. Environ. Saf.* **2022**, *231*, 113160. [CrossRef]
18. Annamalai, S.; Santhanam, M.; Selvaraj, S.; Maruthamuthu, S.; Pandian, K.; Pazos, M. 'Green technology': Bio-stimulation by an electric field for textile reactive dye contaminated agricultural soil. *Sci. Total Environ.* **2018**, *624*, 1649–1657. [CrossRef] [PubMed]
19. Wan, L.; Cao, L.; Song, C.; Cao, X.; Zhou, Y. Regulation of the Nutrient Cycle Pathway and the Microbial Loop Structure by Different Types of Dissolved Organic Matter Decomposition in Lakes. *Environ. Sci. Technol.* **2022**, *57*, 297–309. [CrossRef]
20. Liu, Z.; Ren, X.; Duan, X.; Sarmah, A.K.; Zhao, X. Remediation of environmentally persistent organic pollutants (POPs) by persulfates oxidation system (PS): A review. *Sci. Total Environ.* **2022**, *863*, 160818. [CrossRef]
21. Dapaah, M.F.; Niu, Q.; Yu, Y.Y.; You, T.; Liu, B.; Cheng, L. Efficient persistent organic pollutant removal in water using MIL-metal–organic framework driven Fenton-like reactions: A critical review. *Chem. Eng. J.* **2022**, *431*, 134182. [CrossRef]
22. Luo, M.; Zhou, H.; Zhou, P.; Lai, L.; Liu, W.; Ao, Z.; Yao, G.; Zhang, H.; Lai, B. Insights into the role of in-situ and ex-situ hydrogen peroxide for enhanced ferrate (VI) towards oxidation of organic contaminants. *Water Res.* **2021**, *203*, 117548. [CrossRef]
23. Liu, Y.; Zhao, Y.; Wang, J. Fenton/Fenton-like processes with in-situ production of hydrogen peroxide/hydroxyl radical for degradation of emerging contaminants: Advances and prospects. *J. Hazard. Mater.* **2021**, *404*, 124191. [CrossRef] [PubMed]
24. Zhang, S.; Gao, F.; Fang, M.; Liu, B.; Zhang, B.; Zhong, Z.; Yu, L.; Zhang, Y.; Tan, X.; Wang, X. Catalyst-Free Extraction of U (VI) in Solution by Tribocatalysis. *Adv. Sci.* **2024**, *11*, 2404397. [CrossRef]

25. Macak, J.M.; Zlamal, M.; Krysa, J.; Schumuki, P. Self-Organized TiO_2 Nanotube Layers as Highly Efficient Photocatalysts. *Small* **2007**, *3*, 300–304. [CrossRef]
26. Nishiyama, H.; Yamada, T.; Nakabayashi, M.; Maehara, Y.; Yamaguchi, M.; Kuromiya, Y.; Nagatsuma, Y.; Tokudome, H.; Akiyama, S.; Watanabe, T.; et al. Photocatalytic solar hydrogen production from water on a 100-m^2 scale. *Nature* **2021**, *598*, 304–307. [CrossRef] [PubMed]
27. Kang, D.; Young, J.B.; Lim, H.; Klein, W.M.; Chen, H.; Xi, Y.; Gai, B.; Deutsch, T.G.; Yoon, J. Printed assemblies of GaAs photoelectrodes with decoupled optical and reactive interfaces for unassisted solar water splitting. *Nat. Energy* **2017**, *2*, 17043. [CrossRef]
28. Duan, C.; Qin, X.; Wang, X.; Feng, X.; Yu, H.; Dai, L.; Wang, W.; Zhao, W. Simultaneous mechanical refining and phosphotungstic acid catalysis for improving the reactivity of kraft-based dissolving pulp. *Cellulose* **2019**, *26*, 5685–5694. [CrossRef]
29. Domen, K.; Ikeda, S.; Takata, T.; Tanaka, A.; Hara, M.; Kondo, J.N. Mechano-catalytic overall water-splitting into hydrogen and oxygen on some metal oxides. *Appl. Energy* **2000**, *67*, 159–179. [CrossRef]
30. Hara, M.; Komoda, M.; Hasei, H.; Yashima, M.; Ikeda, S.; Takata, T.; Kondo, J.N.; Domen, K. A Study of Mechano-Catalysts for Overall Water Splitting. *J. Phys. Chem. B* **2000**, *104*, 780–785. [CrossRef]
31. Takata, T.; Ikeda, S.; Tanaka, A.; Hara, M.; Kondo, J.N.; Domen, K. Mechano-catalytic overall water splitting on some oxides (II). *Appl. Catal. A Gen.* **2000**, *200*, 255–262. [CrossRef]
32. Xu, X.; Mao, C.; Ke, S.; Song, J.; Gu, Y.; Li, N.; Chen, W. Greatly enhanced tribocatalytic degradation of organic dyes by Fe_2O_3 nanoparticles through Ti and Al_2O_3 coatings. *J. Mater. Sci.* **2025**, *60*, 7333–7342. [CrossRef]
33. Che, J.; Gao, Y.; Wu, Z.; Ma, J.; Wang, Z.; Liu, C.; Jia, Y.; Wang, X. Review on tribocatalysis through harvesting friction energy for mechanically-driven dye decomposition. *J. Alloys Compd.* **2024**, *1002*, 175413. [CrossRef]
34. Hu, J.; Ma, W.; Pan, Y.; Cheng, Z.; Yu, S.; Gao, J.; Zhang, Z.; Wan, C.; Qiu, C. Insights on the mechanism of Fe doped ZnO for tightly-bound extracellular polymeric substances tribo-catalytic degradation: The role of hydration layers at the interface. *Chemosphere* **2021**, *276*, 130170. [CrossRef]
35. Hu, J.; Ma, W.; Pan, Y.; Chen, Z.; Zhang, Z.; Wan, C.; Sun, Y.; Qiu, C. Resolving the Tribo-catalytic reaction mechanism for biochar regulated Zinc Oxide and its application in protein transformation. *J. Colloid Interface Sci.* **2021**, *607*, 1908–1918. [CrossRef] [PubMed]
36. Li, P.; Wu, J.; Wu, Z.; Jia, Y.; Ma, J.; Chen, W.; Zhang, L.; Yang, J.; Liu, Y. Strong tribocatalytic dye decomposition through utilizing triboelectric energy of barium strontium titanate nanoparticles. *Nano Energy* **2019**, *63*, 103832. [CrossRef]
37. Mao, C.; Lei, H.; Guo, Z.; Jia, X.; Cui, X.; Huang, J.; Fei, L.; Jia, Y.; Chen, W. Exceptional tribo-catalytic degradation of concentrated methyl orange and methylene blue solutions by DXN-RT30 TiO^2 nanoparticles. *Ceram. Int.* **2023**, *50*, 4737–4745. [CrossRef]
38. Lei, H.; Cui, X.; Jia, X.; Qi, J.; Wang, Z.; Chen, W. Enhanced Tribocatalytic Degradation of Organic Pollutants by ZnO Nanoparticles of High Crystallinity. *Nanomaterials* **2022**, *13*, 46. [CrossRef]
39. Lei, H.; Jia, X.; Wang, H.; Cui, X.; Jia, Y.; Fei, L.; Chen, W. Tribo-Catalytic Conversions of H_2O and CO_2 by NiO Particles in Reactors with Plastic and Metallic Coatings. *Coatings* **2023**, *13*, 396. [CrossRef]
40. Jia, X.; Wang, H.; Lei, H.; Mao, C.; Cui, X.; Liu, Y.; Jia, Y.; Yao, W.; Chen, W. Boosting tribo-catalytic conversion of H_2O and CO_2 by Co_3O_4 nanoparticles through metallic coatings in reactors. *J. Adv. Ceram.* **2023**, *12*, 1833–1843. [CrossRef]
41. Cui, X.; Wang, H.; Lei, H.; Jia, X.; Jiang, Y.; Fei, L.; Jia, Y.; Chen, W. Surprising tribo-catalytic conversion of H_2O and CO_2 into flammable gases utilizing frictions of copper in water. *ChemistrySelect* **2023**, *8*, e202204146. [CrossRef]
42. Lei, H.; Wu, Z.; Wang, H.; Mao, C.; Guo, Z.; Fei, L.; Chen, W. Converting H_2O and CO_2 into chemical fuels by nickel via friction. *Surf. Interfaces* **2024**, *46*, 104203. [CrossRef]
43. Barrocas, B.; Monteiro, O.C.; Nunes, M.R.; Silvestre, A.J. Influence of Re and Ru doping on the structural, optical and photocatalytic properties of nanocrystalline TiO_2. *SN Appl. Sci.* **2019**, *1*, 556. [CrossRef]
44. Patil, S.S.; Mali, M.G.; Hassan, M.A.; Patil, D.R.; Kolekar, S.S.; Ryu, S.-W. One-Pot in Situ Hydrothermal Growth of $BiVO_4$/Ag/rGO Hybrid Architectures for Solar Water Splitting and Environmental Remediation. *Sci. Rep.* **2017**, *7*, 8404. [CrossRef]
45. Vale, M.; Barrocas, B.T.; Serôdio, R.M.; Oliveira, M.C.; Lopes, J.M.; Marques, A.C. Robust Photocatalytic MICROSCAFS® with Interconnected Macropores for Sustainable Solar-Driven Water Purification. *Int. J. Mol. Sci.* **2024**, *25*, 5958. [CrossRef]
46. Cui, X.; Guo, Z.; Lei, H.; Jia, X.; Mao, C.; Ruan, L.; Zhou, X.; Wang, Z.; Chen, F.; Chen, W. Tribo-Catalytic Degradation of Methyl Orange Solutions Enhanced by Silicon Single Crystals. *Coatings* **2023**, *13*, 1804. [CrossRef]
47. Zhou, Z.; Luo, R.; Mao, C.; Hu, Y.; Chen, W. Contrasting tribocatalytic degradations of organic dyes by two different commercial silicon powders. *J. Adv. Dielectr.* **2024**, *15*, 2450025. [CrossRef]
48. Guo, J.; Wang, Y.; Zhao, M. 3D flower-like ferrous(II) phosphate nanostructures as peroxidase mimetics for sensitive colorimetric detection of hydrogen peroxide and glucose at nanomolar level. *Talanta* **2018**, *182*, 230–240. [CrossRef]

49. Liu, R.; Fu, Y.; Zhan, H. Spectrophotometric Determination of Superoxide Anion Radical with Nitroblue Tetrazolium. *J. Instrum. Anal.* **2008**, *27*, 355.
50. Baytekin, B.; Baytekin, H.T.; Grzybowski, B.A. What Really Drives Chemical Reactions on Contact Charged Surfaces? *J. Am. Chem. Soc.* **2012**, *134*, 7223–7226. [CrossRef]

Disclaimer/Publisher's Note: The statements, opinions and data contained in all publications are solely those of the individual author(s) and contributor(s) and not of MDPI and/or the editor(s). MDPI and/or the editor(s) disclaim responsibility for any injury to people or property resulting from any ideas, methods, instructions or products referred to in the content.

catalysts

MDPI

Article

One-Step Fe/N Co-Doping for Efficient Catalytic Oxidation and Selective Non-Radical Pathway Degradation in Sludge-Based Biochar

Zupeng Gong [1], Shixuan Ding [1], Mingjie Huang [1,*], Wen-da Oh [2], Xiaohui Wu [1] and Tao Zhou [1,*]

[1] Hubei Key Laboratory of Multi-Media Pollution Cooperative Control in the Yangtze Basin, School of Environmental Science and Engineering, Huazhong University of Science and Technology, Wuhan 430074, China; zupenggong@hust.edu.cn (Z.G.); shihhsuanding@163.com (S.D.); xhwoo@hust.edu.cn (X.W.)
[2] School of Chemical Sciences, Universiti Sains Malaysia, Gelugor 11800, Penang, Malaysia; ohwenda@usm.my
* Correspondence: mingjiehuang@hust.edu.cn (M.H.); zhoutao@hust.edu.cn (T.Z.)

Abstract

This study presents the preparation of iron and nitrogen co-doped sludge-based biochar (FeCN-MSBC) and iron oxide-doped biochar (FeO-MSBC) by ball milling municipal sludge with different iron precursors ($K_3Fe(CN)_6$ and Fe_2O_3), followed by pyrolysis. These biochars were utilized to activate persulfate (PMS) for the degradation of phenolic pollutants. The results demonstrate that FeCN-MSBC, formed by the introduction of $K_3Fe(CN)_6$, contains Fe/N phases, with surface Fe sites exhibiting a lower oxidation state, which significantly enhances PMS activation efficiency. In contrast, FeO-MSBC, due to the aggregation of Fe_2O_3/Fe_3O_4, shows relatively lower catalytic activity. The FeCN-MSBC/PMS system degrades pollutants via a synergistic mechanism involving non-radical pathways mediated by $^1O_2$ and electron transfer processes (ETP) catalyzed by surface Fe. Electrochemical oxidation and quenching experiments confirm that ETP is the dominant pathway. FeCN-MSBC, prepared at a pyrolysis temperature of 600 °C and an Fe loading of 3 mmol/g TSS, exhibited the best performance, achieving a phenol degradation rate constant (k_{obs}) of 0.127 min^{-1}, 4.5 times higher than that of undoped biochar (MSBC). FeCN-MSBC/PMS maintained high efficiency across a wide pH range and in complex water matrices, exhibiting excellent stability over multiple cycles, demonstrating strong potential for practical applications. This study provides an effective strategy for simultaneous Fe and N doping in sludge-derived biochar and offers mechanistic insights into Fe/N synergistic activation of PMS for practical water treatment.

Keywords: biochar; advanced oxidation processes (AOPs); sludge; peroxymonosulfate

1. Introduction

Biological treatment is the most widely employed process in wastewater management due to its low cost and high efficiency [1,2]. However, wastewater sludge, a solid byproduct generated during biological treatment, contains a variety of potentially hazardous substances such as pathogenic microorganisms, heavy metals, and refractory organic compounds, posing risks to both human health and the environment [3]. Conventional sludge disposal methods, including landfilling, incineration, and composting, often suffer from drawbacks such as high costs and the potential for secondary environmental pollution [4,5]. Therefore, it is of great importance to explore innovative approaches for sludge management. In recent years, pyrolysis for converting sludge into sludge-derived biochar has

attracted increasing attention, as it not only ensures the safe disposal of sludge but also enables its resource recovery while effectively reducing greenhouse gas emissions [6–8].

Compared with conventional water treatment methods, persulfate-based advanced oxidation processes (PS-AOPs) have attracted increasing attention as an efficient strategy for advanced wastewater remediation, particularly in the degradation of organic pollutants [9,10]. Early studies focused on Fenton and Fenton-like processes driven by •OH [11], followed by the rise in persulfate-based AOPs around 2010, which expanded the role of both radical and non-radical species [12–14]. In recent years, biochar has attracted growing attention as a sustainable catalyst, with heteroatom and transition-metal doping strategies shown to significantly enhance its catalytic performance [15]. The surface of biochar, enriched with abundant active sites (e.g., C=O, C–O, –COO, C–N), can effectively activate persulfate to generate diverse reactive oxygen species (ROS), including •OH, $SO_4^{\bullet-}$, $O_2^{\bullet-}$, and $^1O_2$. These ROS enable efficient degradation of organic pollutants through both direct oxidation and indirect pathways mediated by electron transfer processes (ETP) [16–18]. Feng et al. prepared sludge-based biochar (BS900) by pyrolyzing sludge from a municipal wastewater treatment plant and employed it to activate PMS for the degradation of tetracycline (TC). Graphitic nitrogen and Fe^0 served as electron mediators, reducing charge transfer resistance and facilitating the activation of PMS to generate $O_2^{\bullet-}$ and $^1O_2$ for the degradation of pollutants [19]. Wang et al. prepared sludge-based biochar (SBC) using a one-step pyrolysis method and employed it to activate PMS for the degradation of triclosan (TCS). The dominant active species were •OH, $SO_4^{\bullet-}$, and singlet oxygen ($^1O_2$). The carbon backbone defects and oxygen-containing functional groups were identified as key factors in PMS activation [20].

Biochar materials prepared directly from raw sludge as precursors exhibit limited activation efficiency for persulfate (PS) due to factors such as the high content of inorganic components, and low levels of non-metallic elements, as well as transition metals [21,22]. In fact, nitrogen doping has been found to significantly enhance the catalytic performance of biochar by modulating spin density and charge distribution [23,24]. Specifically, it has been reported that graphitic-N species play a crucial role in the activation of PMS, as the positive charge on the carbon material leads to strong interactions with PMS [24]. Similarly, edge nitrogen species, such as pyridinic-N, have been identified as key reactive sites within biochar [25]. Byambaa et al. prepared nitrogen-doped biochar (HTNBC) by mixing wastewater sludge with ammonium nitrate, followed by hydrothermal pretreatment and high-temperature pyrolysis. This biochar was used to degrade pollutants such as sulfamethoxazole (SMX), 4-chlorophenol (4-CP), and carbamazepine (CBZ). Graphitic nitrogen, pyridinic nitrogen, and carbonyl groups were identified as the primary active sites responsible for PMS activation [26]. The incorporation of transition metals can further modify sludge-based biochar materials. The valence conversion between metals can trigger redox reactions, thereby increasing the generation pathways of reactive oxygen species (ROS) [27]. Iron, a non-toxic transition metal, is abundant in environmental protection areas and is an ideal metal for doping. Wang et al. prepared iron-containing biochar (FeBC) from residual sludge and used it to activate PMS and H_2O_2, generating free radicals (such as $SO_4^{\bullet-}$, •OH, and $^1O_2$) for the degradation of pharmaceutical wastewater. Fe(II) activated PMS to produce $SO_4^{\bullet-}$ and •OH (radical pathway), while the graphitic structure on the biochar surface facilitated the generation of $^1O_2$ (non-radical pathway) [28]. Existing literature on the introduction of Fe sources mainly focuses on endogenous Fe in sludge, while exogenous Fe reagents, such as $FeCl_3$, Fe_2O_3, and $FeSO_4$, are also commonly used [29–31]. For nitrogen sources, chemical reagents such as urea and melamine are typically introduced [32,33], requiring stepwise doping, which complicates practical operations. Additionally, the clustering of Fe leads to low utilization efficiency of Fe,

mainly due to the easy hydrolysis of Fe ions during the preparation process [34]. In the case of current single-atom catalysts, Fe precursors usually require coupling with ligands, such as iron acetylacetonate and iron phthalocyanine [35,36]. To prevent Fe clustering, the loading amount of Fe is usually less than 1 wt% [37], which significantly restricts the further enhancement of catalytic performance in Fe-doped biochar.

In this study, $K_3Fe(CN)_6$ was introduced as the Fe source for sludge-based biochar. Fe was efficiently mixed with the biochar through a simple ball milling method, followed by pyrolysis to prepare Fe and N co-doped sludge-based biochar (FeCN-MSBC), which was used for activating PMS to efficiently degrade phenolic pollutants. This method allows for the simultaneous doping of Fe and N, and due to the strong coordination between -CN and Fe, it ensures the effective dispersion of Fe, thereby enhancing its utilization. Quenching experiments, radical capture tests, and electrochemical oxidation tests revealed that, unlike other sludge-based biochar/PMS-AOPs systems, the electron transfer process (ETP) mediated by FeCN-MSBC/PMS was identified as the primary pathway for pollutant degradation. This provides a new approach for the efficient utilization of sludge-derived biochar.

2. Results and Discussion

2.1. Characterizations of MSBC with Different Fe Ball Milling Treatment

Scanning electron microscopy (SEM) and transmission electron microscopy (TEM) were performed on the three biochar materials obtained at 600 °C (MSBC, FeCN-MSBC, and FeO-MSBC) (Figure 1a–c). Distinct morphological differences were observed among the samples. MSBC exhibited relatively large, bulky spherical particles with heterogeneous particle sizes. FeO-MSBC displayed irregular block-like structures, where the crystallites predominantly existed in aggregated and stacked forms. Due to the incorporation of Fe_2O_3, pronounced surface aggregation and clustering of iron oxides were evident. In contrast, FeCN-MSBC showed well-defined and uniformly sized particles, with no obvious clustering phenomena compared to the other materials. Elemental mapping obtained from TEM-EDS analysis further confirmed that the constituent elements were uniformly distributed across the material surface (Figure 1d–r).

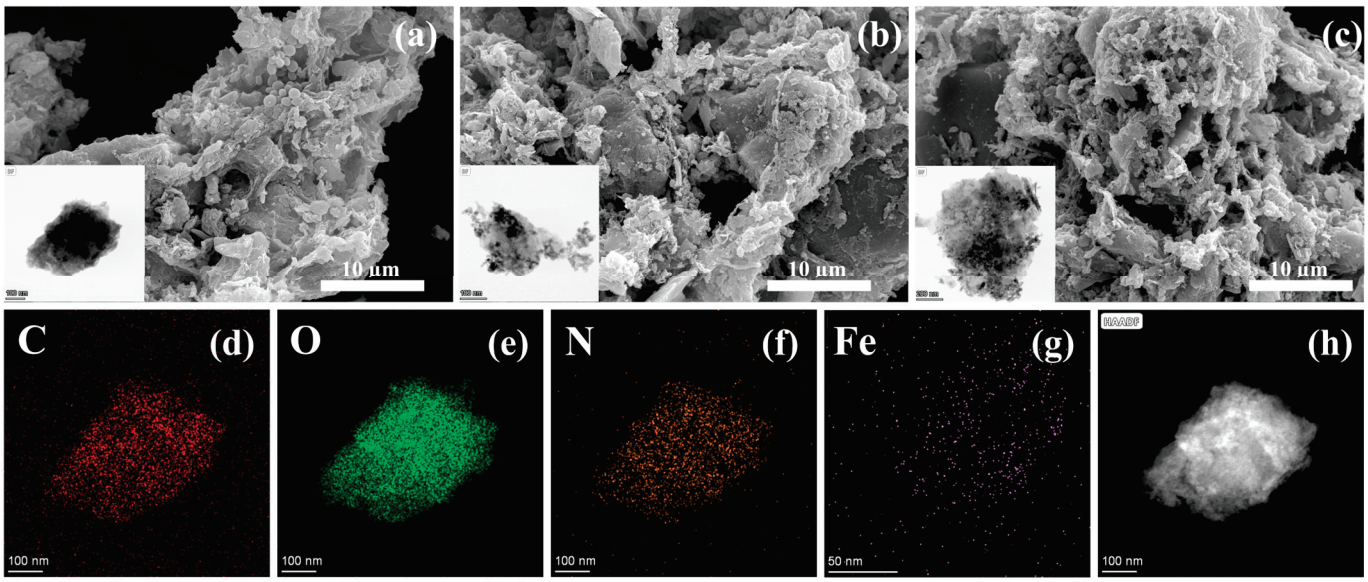


Figure 1. *Cont.*

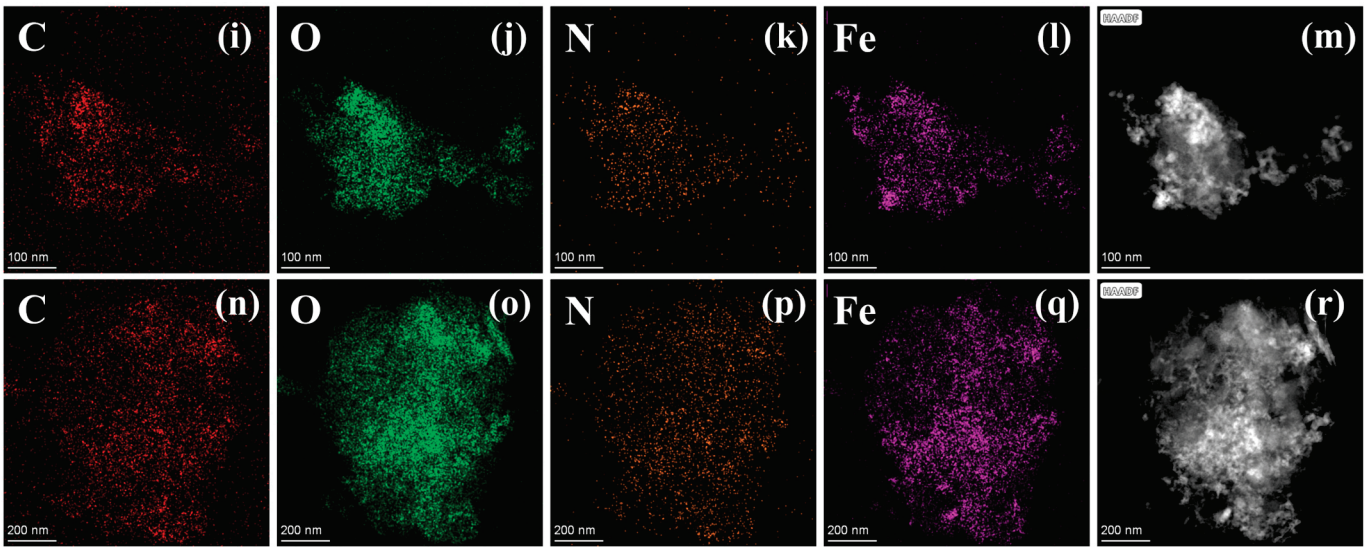


Figure 1. SEM, TEM (**a**–**c**), and TEM-Mapping (**d**–**r**) of MSBC, FeCN-MSBC, and FeO-MSBC.

XRD analysis revealed that the surface Fe species of the biochars prepared by ball milling MSBC-400 with different Fe precursors ($K_3Fe(CN)_6$ and Fe_2O_3) varied significantly (Figure 2a). Compared with MSBC, distinct Fe_2N signals were detected in FeCN-MSBC, whereas Fe in FeO-MSBC predominantly existed in the forms of Fe_2O_3 and Fe_3O_4 [38]. In addition, characteristic diffraction peaks of graphitic carbon were observed in all three biochars, indicating that the sludge biomass underwent graphitization during pyrolysis, leading to the formation of structurally stable biochar materials. These differences in Fe speciation and graphitization degree are expected to play a crucial role in determining the catalytic activity of the biochars [39,40]. Raman spectroscopy results demonstrated that FeCN-MSBC exhibited a lower I_D/I_G ratio (I_D/I_G = 2.36) compared with MSBC (I_D/I_G = 2.57) and FeO-MSBC (I_D/I_G = 2.58) (Figure 2b). The D band (I_D), typically located at ~1300 cm^{-1}, is associated with lattice defects of carbon atoms, whereas the G band (I_G), appearing at ~1580 cm^{-1}, corresponds to the in-plane stretching vibration of sp^2-hybridized C–C bonds [41]. A lower I_D/I_G ratio generally indicates fewer structural defects and a higher degree of graphitization in the biochar [42]. In addition, the specific surface areas of the three biochars followed the order: FeCN-MSBC < FeO-MSBC < MSBC, while the average pore size was the largest for FeCN-MSBC (12.9 nm). Evidently, the incorporation of $K_3Fe(CN)_6$ reduced the surface area but enlarged the average pore size of the biochar. The UV–Vis DRS results (Figure 2d) indicate that, compared with MSBC and FeO-MSBC, the incorporation of $K_3Fe(CN)_6$ facilitates bandgap narrowing in the biochar material, which is more favorable for electron shuttling. Such structural changes may influence the exposure of active sites and mass transfer efficiency, thereby affecting the catalytic performances of the biochars, which will be further investigated.

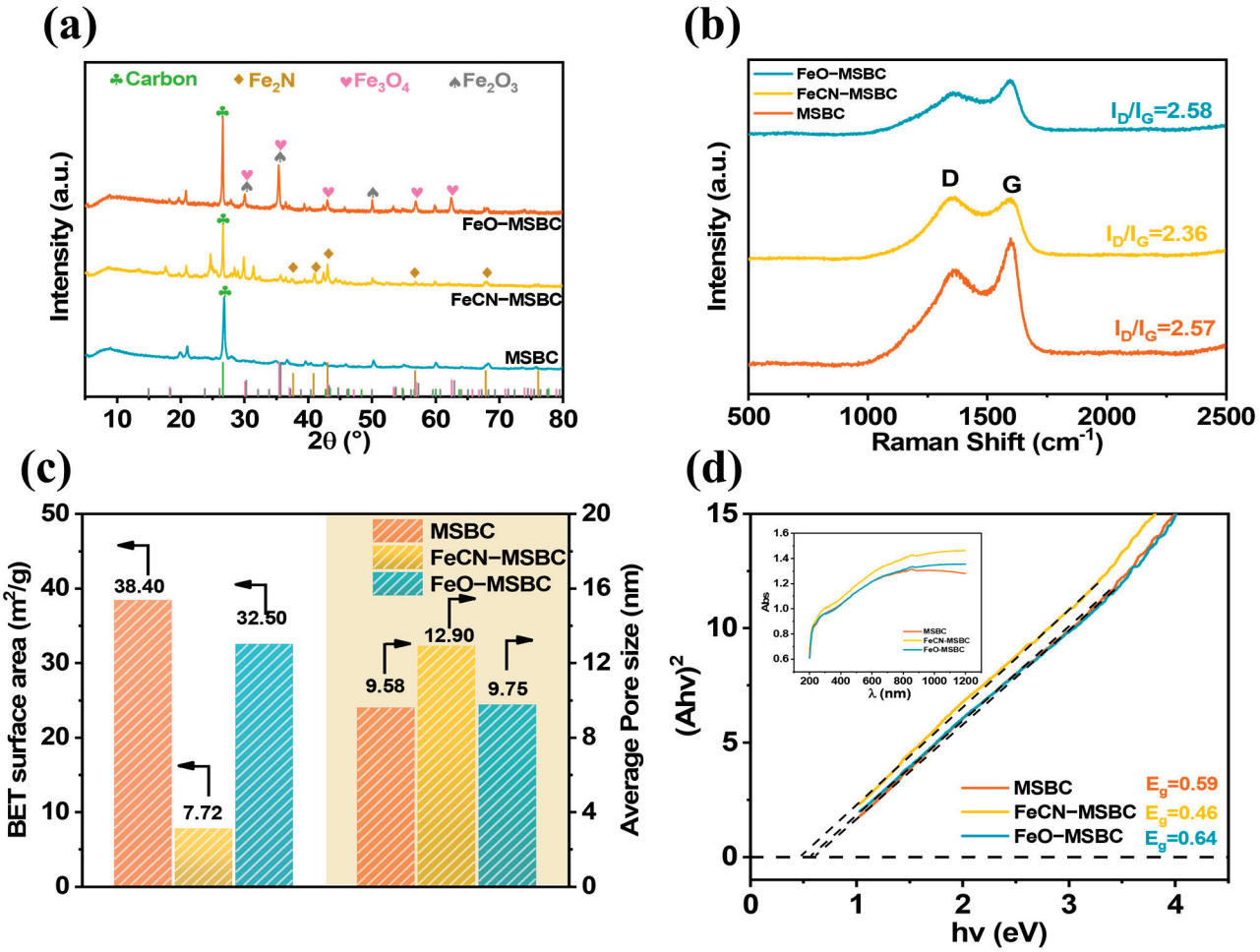


Figure 2. XRD (**a**), Raman spectrum (Peak G: Located at approximately 1580 cm^{-1}, it represents the stretching vibration within the carbon atom plane, reflecting the degree of graphite formation and orderliness of the material. Peak D: Located at approximately 1350 cm^{-1}, it represents the vibration mode induced by disorder, used to characterize the degree of defects in the material) (**b**), BET (The arrow indicates the data reference axis) (**c**), and UV-Vis DRS (**d**) characterizations of MSBC, FeCN-MSBC, and FeO-MSBC.

2.2. Distinguishing Key Factors Affecting the Phenol Degradation in the MSBC/PMS Systems

The time-dependent degradation of phenol in the MSBC/PMS, FeCN-MSBC/PMS, and FeO-MSBC/PMS systems was investigated, and the results are shown in Figure 3a. As observed, the phenol degradation rate (pseudo-first-order kinetics) in the FeCN-MSBC/PMS system (k_{obs} = 0.127 min^{-1}) was significantly higher than that in the MSBC/PMS system (k_{obs} = 0.028 min^{-1}), whereas the FeO-MSBC/PMS system exhibited a markedly reduced degradation rate (k_{obs} = 0.016 min^{-1}). These findings indicate that the type of Fe precursor has a pronounced effect on PMS activation, with the incorporation of $K_3Fe(CN)_6$-derived Fe species being more favorable for PMS activation. This trend is consistent with the structural characterization results, where the formation of Fe_2N in FeCN-MSBC enhanced PMS activation, while the dominance of Fe_2O_3/Fe_3O_4 in FeO-MSBC was less effective. Further investigations were conducted on two key parameters affecting the catalytic activity of FeCN-MSBC, namely pyrolysis temperature and the dosage of $K_3Fe(CN)_6$. As the pyrolysis temperature increased from 500 to 900 °C, the catalytic activity of FeCN-MSBC first increased and then declined. Since pyrolysis temperature typically influences the degree of graphitization and the specific surface area of biochar [43], the results indicated that FeCN-MSBC exhibited the highest catalytic activity at 600 °C. Simi-

larly, the catalytic activity of FeCN-MSBC as a function of $K_3Fe(CN)_6$ loading also followed a volcano-type trend, suggesting that an appropriate Fe doping level is more favorable for enhancing the catalytic performance [44]. Specifically, FeCN-MSBC synthesized at 600 °C with an Fe loading of 3 mmol/g TSS showed the optimum catalytic activity. Unless otherwise specified, FeCN-MSBC mentioned hereafter refers to the material prepared under these conditions.

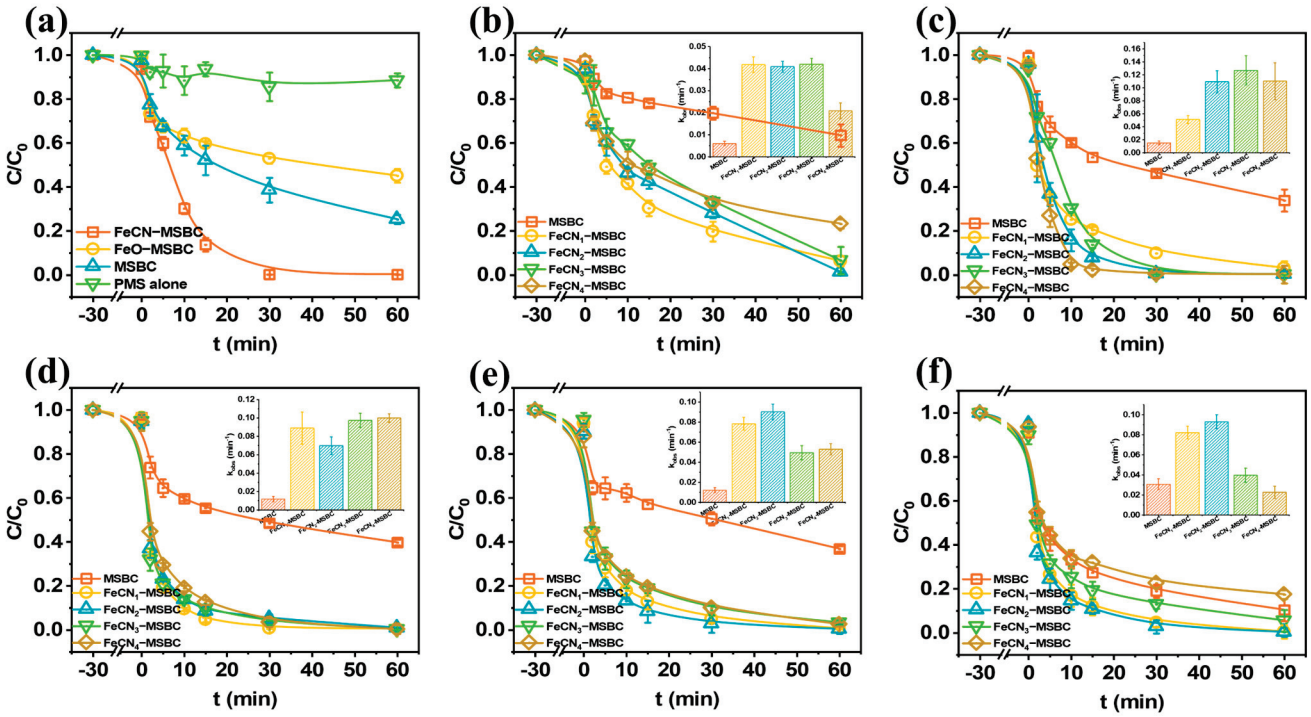


Figure 3. MSBC, FeCN-MSBC, and FeO-MSBC/PMS degradation rate of Phenol (**a**), the effect of pyrolysis temperature on $FeCN_x$-MSBC/PMS degradation rate of Phenol (**b**–**f**): 500 °C (**b**), 600 °C (**c**), 700 °C (**d**), 800 °C (**e**), 900 °C (**f**). Reaction conditions: $[Phenol]_0$ = 50 mg/L; $[PMS]_0$ = 500 mg/L $[materials]_0$ = 0.5 g/L; pH = 6.5.

2.3. Examinations of the Dominant Reactive Species in FeCN-MSBC/PMS System

Radical quenching experiments were conducted to identify the dominant reactive oxygen species (ROS) in the FeCN-MSBC/PMS system (Figure 4a). Four common scavengers were employed, namely methanol (MeOH), tert-butanol (TBA), furfuryl alcohol (FFA), and PMSO [45]. As shown in Figure 3a, MeOH, TBA, and PMSO only exerted slight inhibitory effects on phenol degradation, whereas the presence of FFA almost completely suppressed the reaction. This finding indicates that $^1O_2$, rather than •OH, $SO_4^{\bullet-}$, or Fe(IV)=O, is the primary ROS in this system. In addition, the introduction of 1.0 mM 1,10-phenanthroline (1,10-Phen) into the FeCN-MSBC/PMS system resulted in a pronounced inhibition of phenol degradation, suggesting that surface Fe sites of FeCN-MSBC serve as the major catalytic centers for PMS activation [46]. This observation is consistent with the XRD results, implying that the Fe_2N phase formed in FeCN-MSBC plays a crucial role in PMS activation and $^1O_2$ generation.

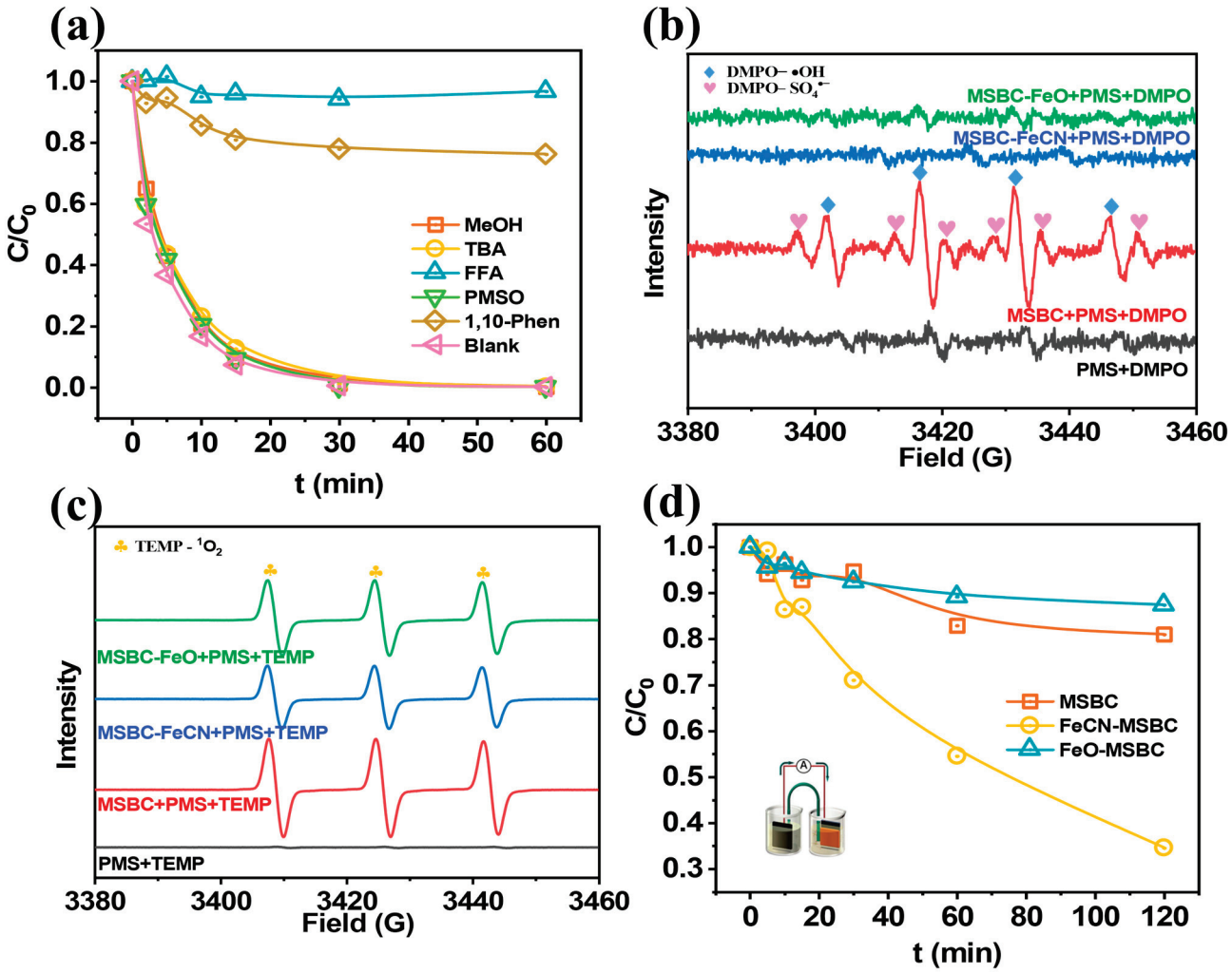


Figure 4. Reaction rate constant of FeCN-MSBC/PMS/Phenol quenching experiment (**a**), removal of Phenol in the galvanic oxidation process (GOP); the inset is a diagram of the GOP (**b**), EPR spectrum of DMPO trapped radical adducts in MSBC/FeCN-MSBC/FeO-MSBC/PMS systems (**c**), and TEMP trapped $^1O_2$ in MSBC/FeCN-MSBC/FeO-MSBC/PMS systems (**d**). Reaction conditions: $[Phenol]_0$ = 50 mg/L; $[PMS]_0$ = 500 mg/L $[materials]_0$ = 0.5 g; pH = 6.5.

To further verify the ROS, electron paramagnetic resonance (EPR) analysis was performed using two spin-trapping solutions: PMS + DMPO + H_2O and PMS + TMPO + H_2O, which are commonly employed for the quantitative detection of $\bullet OH/SO_4^{\bullet-}$ and $^1O_2$, respectively [47]. As shown in Figure 4b,c, distinct $\bullet OH/SO_4^{\bullet-}$ and $^1O_2$ signals were observed in the MSBC/PMS system, indicating that both species could act as dominant ROS. This may be attributed to graphitic defects and oxygen-containing functional groups in the biochar, which facilitate electron transfer and promote ROS generation via radical or non-radical pathways. In contrast, the FeCN-MSBC/PMS and FeO-MSBC/PMS systems showed negligible $\bullet OH/SO_4^{\bullet-}$ signals, and the $^1O_2$ signals were weaker than those in MSBC/PMS. Considering the higher catalytic rate of FeCN-MSBC/PMS, this suggests the presence of additional catalytic pathways.

To explore the potential electron transfer catalysis (ETP) pathway, a galvanic oxidative process (GOP) experiment was conducted, in which PMS and phenol were placed in two separate reactors connected via wires and a salt bridge (Figure 4) [48]. Significant phenol degradation was observed in the FeCN-MSBC/PMS system, whereas no electron transfer catalysis occurred in the MSBC/PMS or FeO-MSBC/PMS systems. Collectively, these results demonstrate that the high catalytic activity of FeCN-MSBC arises from a

combination of $^1O_2$-mediated oxidation and surface Fe-catalyzed electron transfer, with Fe_2N phases playing a key role in facilitating both pathways.

2.4. Key Factors Affecting the Catalytic Mechanism of the FeCN-MSBC/PMS System

The strong inhibitory effect of 1,10-phenanthroline indicates that surface Fe sites of FeCN-MSBC serve as the key catalytic centers. To further investigate the influence of $K_3Fe(CN)_6$ and Fe_2O_3 doping on the coordination environment of surface Fe, X-ray photoelectron spectroscopy (XPS) analysis was conducted on MSBC, FeCN-MSBC, and FeO-MSBC (Figure 5a–c). XPS analysis was conducted to elucidate the chemical states and coordination environment of Fe, N, and O in the biochars. The Fe 2p spectra show that the peaks at 709.2 eV and 722.8 eV correspond to Fe^{2+} $2p_{3/2}$ and $2p_{1/2}$, respectively, while the peaks at 711.2 eV and 724.8 eV are assigned to Fe^{3+} $2p_{3/2}$ and $2p_{1/2}$ [49,50]. These results indicate that Fe in FeCN-MSBC exhibits a lower oxidation state compared with FeO-MSBC, which can be attributed to the lower electronegativity of nitrogen in Fe–CN and Fe–N bonds relative to oxygen in Fe–O bonds. The Fe oxidation state is considered a key factor mediating the electron transfer catalysis (ETP) pathway.

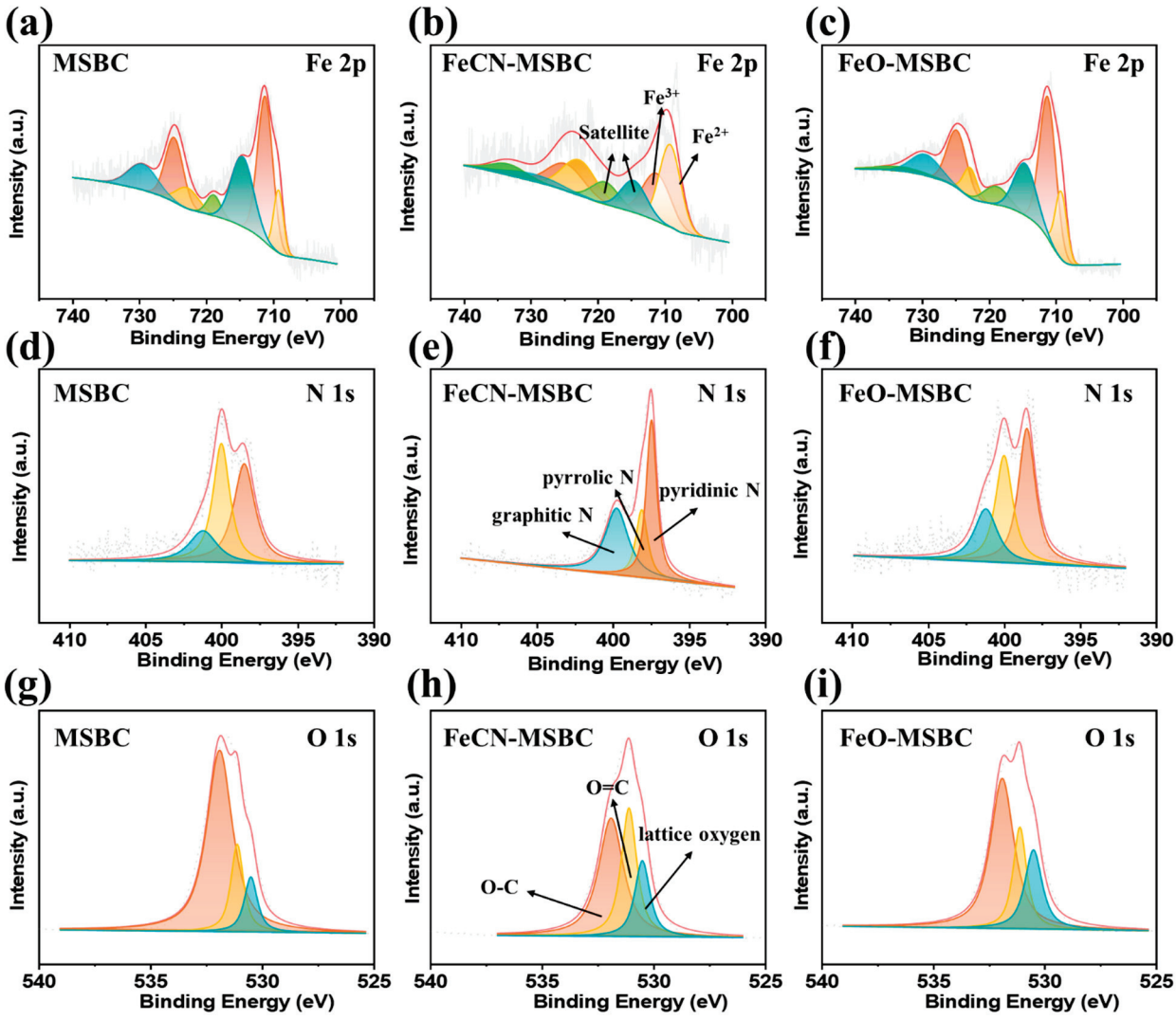


Figure 5. XPS spectra of Fe 2p (**a**–**c**), N 1s (**d**–**f**), and O 1s (**g**–**i**) for MSBC/FeCN-MSBC/FeO-MSBC.

N 1s analysis further revealed that FeCN-MSBC contains a higher proportion of pyridinic nitrogen compared with MSBC and FeO-MSBC. Pyridinic N is regarded as the key nitrogen species responsible for forming Fe–N coordination sites. Meanwhile, O 1s

spectra indicated that FeCN-MSBC possesses a higher content of lattice oxygen, which is considered to facilitate electron transfer processes during the catalytic reaction.

Collectively, these observations suggest that the formation of Fe–N active sites, with Fe in a relatively low oxidation state coordinated to pyridinic N, together with abundant lattice oxygen, plays a crucial role in promoting PMS activation and the ETP pathway in the FeCN-MSBC/PMS system.

2.5. Application of FeCN-MSBC/PMS in Complex Water Matrices

To further evaluate the catalytic activity of FeCN-MSBC/PMS under complex water matrices, phenol degradation experiments were conducted at different initial pH values (pH = 3, 5, 7, 9, 11) (Figure 6a). The results indicated that FeCN-MSBC/PMS maintained high catalytic activity over a wide pH range (pH 3–9) with $k_{obs} > 0.12$ min^{-1} and still exhibited considerable activity under strongly alkaline conditions (pH 11, $k_{obs} > 0.03$ min^{-1}).

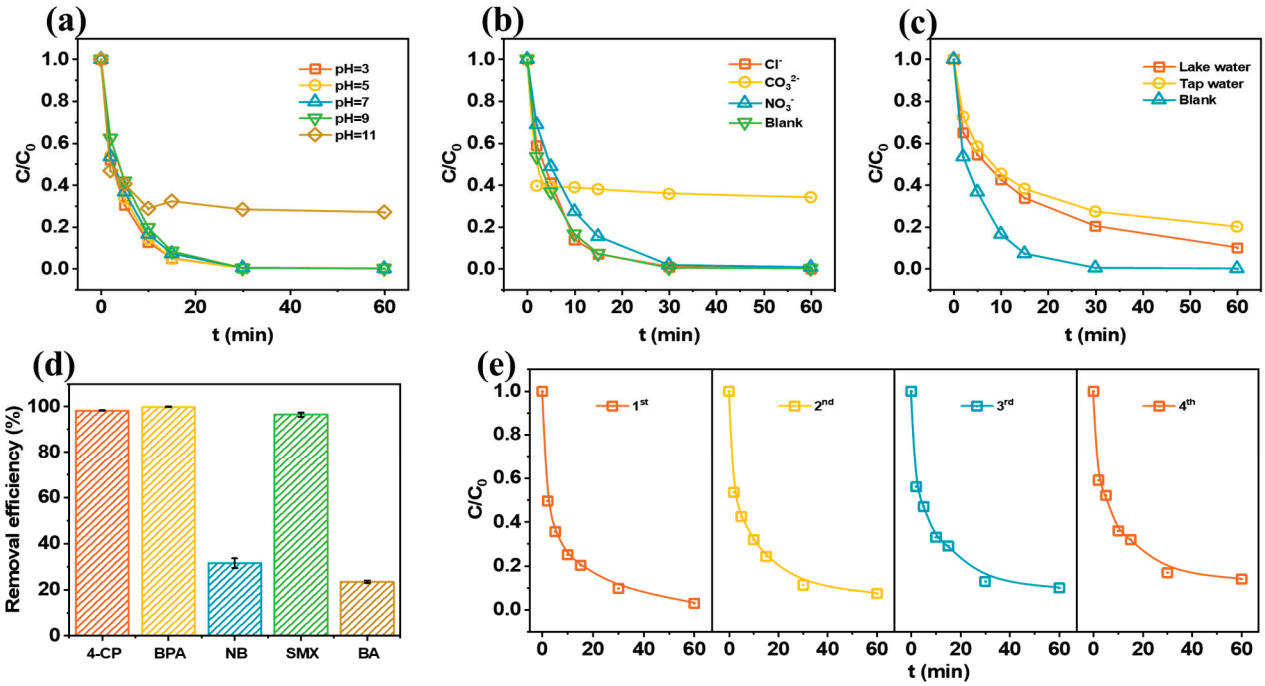


Figure 6. The effect of initial pH on Phenol degradation (**a**), common anion interference experiment (**b**), natural water body interference experiment (**c**), degradation performance of different phenolic pollutants (**d**), and FeCN-MSBC cycle stability experiment (**e**). Reaction conditions: $[Pollutant]_0$ = 50 mg/L; $[PMS]_0$ = 500 mg/L $[materials]_0$ = 0.5 g; pH = 6.5.

The influence of common anions (Cl^-, CO_3^{2-}, NO_3^-) and natural water matrices (lake water, tap water) on phenol degradation was also investigated (Figure 6b,c). FeCN-MSBC/PMS displayed strong tolerance toward these interferences, which can be attributed to the non-radical pathway dominated by $^1O_2$ and the electron transfer catalysis (ETP) process [51].

To further explore the applicability of FeCN-MSBC/PMS for a broader range of pollutants, the degradation of various phenolic contaminants, including 4-chlorophenol (4-CP), bisphenol A (BPA), nitrobenzene (NB), sulfamethoxazole (SMX), and benzoic acid (BA), was examined. The results showed that electron-rich pollutants, such as 4-CP, BPA, and SMX, were removed with high efficiency (removal rate > 96%). The results of the cycle stability experiment demonstrate that the catalyst retains over 86.1% of its initial activity after four cycles, indicating good reusability and durability, demonstrating the potential of FeCN-MSBC/PMS for practical water treatment applications.

3. Materials and Methods

3.1. Chemicals and Reagents

All chemicals used were of analytical grade and used without further purification. $K_3Fe(CN)_6$ (≥99.0%), α-Fe_2O_3 (150 nm, 99.9%), NaOH (≥99.0%), H_2SO_4 (≥99.0%), PMS ($2KHSO_5 \bullet KHSO_4 \bullet K_2SO_4$), phenol (PhOH), p-chlorophenol (4-CP), benzoic acid (BA), bisphenol A (BPA), nitrobenzene (NB), sodium chloride (NaCl), sodium bicarbonate ($NaHCO_3$), Sodium nitrate ($NaNO_3$), methanol (MeOH), tert-butyl alcohol (TBA, ≥ 99%), furfuryl alcohol (FFA ≥ 99.9%), 1,10-phenanthroline (1,10-Phen), methyl phenyl sulfoxide (PMSO) were all purchased from Sinopharm Chemical Reagent Co, Shanghai, China. 5,5-dimethyl-pyrroline-oxide (DMPO ≥ 97%), 2,2,6,6-tetramethyl-1-piperidinyloxy (TEMP) and sulfamethoxazole (SMX) were purchased from Aladdin Co., Shanghai, China. All solutions were prepared in deionized water.

The biochemical sludge used in this study was taken from a local municipal wastewater treatment plant (WWTP). The basic characteristics and inorganic components of the sludge are listed in Table 1.

Table 1. Characteristics of the raw sludge.

Date of Drawing	TSS g/L	VSS g/L	Moisture Content	pH	CST s L/g
20 February 2024	31.56	24.12	93.5%	6.53	6.3

3.2. Preparation of Biochars

Municipal sludge was employed as the precursor for biochar production. The dried sludge was first pyrolyzed at 400 °C for 2 h in a tubular furnace to obtain MSBC-400. Subsequently, MSBC-400 was doped with $K_3Fe(CN)_6$ or Fe_2O_3 at Fe loadings of 1, 2, 3, and 4 mmol/g, followed by ball milling (PM 100, RETSCH, Haan, Germany) at 600 $r \cdot min^{-1}$ for 1 h. The resulting mixtures were further pyrolyzed at 500–900 °C (heating rate: 10 °C min^{-1}) for 2 h under N_2 atmosphere. The products were ground, washed three times with ultrapure water, and dried at 60 °C, and were designated as $FeCN_x$-MSBC (x = 1, 2, 3, 4) and FeO-MSBC, respectively. Unless otherwise specified, FeCN-MSBC refers to the sample prepared at a pyrolysis temperature of 600 °C with an Fe loading of 3 mmol/g TSS (denoted as $FeCN_3$-MSBC). For comparison, sludge biochar prepared under identical conditions without Fe additives was denoted as MSBC.

3.3. Degradation Experiments

Degradation experiments using phenol as the model pollutant were conducted in 100 mL glass beaker reactors. To assess the catalytic performance of the synthesized biochars, a simulated phenol solution (50 mg L^{-1}) was introduced into the reactors under continuous magnetic stirring. The dosage of biochar materials (MSBC, FeCN-MSBC, and FeO-MSBC) was fixed at 0.5 g L^{-1}. Prior to reaction initiation, the suspensions were equilibrated for 30 min to establish adsorption–desorption equilibrium. The reactions were then initiated by adding PMS at the prescribed dosages. At predetermined time intervals, aliquots were withdrawn, filtered through 0.22 μm membranes, and analyzed.

3.4. Analytical Methods

Scanning electron microscopy (SEM, JSM-6330F-FEI/Quanta 400, Tokyo, Japan) and X-ray diffraction analysis (XRD, X'Pert PRO X-ray diffractometer, Almelo, Netherlands) were used to characterize the morphological and crystal structure of the biochars, respectively. X-ray photoelectron spectroscopy (XPS, Thermo Scientific, Waltham, MA, USA) was used to characterize the element valence state of the materials surface, Brunauer–Emmett–Teller

analysis (BET, Micromeritics ASAP2460, Norcross, GA, USA) was conducted to test the specific surface area and pore size of the material. The PFRs of the material surface were characterized by EPR spectrometer (Bruker EMX nano, Billerica, MA, USA), CST of sludge was measured with a 304M CST instrument (Triton Electronics, Great Dunmow, UK), the pH of the solution was measured with a Rex laboratory pH meter (PH400F, Shanghai, China), the concentrations of Phenol, BPA, SMX, 4-CP, NB and BA were determined by High Performance Liquid Chromatography (HPLC) combined with UV detector and 18 chromatographic column (4.6 × 25 cm). The mobile phase consisted of 0.1% (*v*/*v*) acetic acid and 100% acetonitrile, and the ratio of the two solutions was 40%:60% (*v*/*v*). The flow rate was 0.6 mL/min, and the sample volume was 20 μL. The detection wavelength was 270 nm and the column temperature was 35 °C.

4. Conclusions

In this work, Fe and N co-doped sludge-based biochar (FeCN-MSBC) and iron oxide-doped biochar (FeO-MSBC) were successfully prepared by ball milling municipal sludge with $K_3Fe(CN)_6$ or Fe_2O_3, followed by pyrolysis. FeCN-MSBC exhibited superior catalytic activity for PMS activation and phenolic pollutant degradation, attributed to the formation of Fe/N phases, the low oxidation state of surface Fe sites. Mechanistic investigations revealed that FeCN-MSBC/PMS degrades pollutants via a synergistic pathway involving $^1O_2$-mediated non-radical oxidation and surface Fe-catalyzed electron transfer (ETP). Optimal FeCN-MSBC, prepared at 600 °C with 3 mmol/g Fe loading, achieved a phenol degradation rate constant (k_{obs}) of 0.127 min^{-1}, 4.5 times higher than undoped biochar, while maintaining high activity under diverse pH conditions, common anion interferences, and natural water matrices. Furthermore, the material demonstrated good reusability, retaining over 86% of its activity after four cycles. This study provides a practical and efficient approach for the resource recovery of sludge via one-step Fe and N co-doping and elucidates the multi-pathway mechanism of Fe/N synergistic PMS activation, offering a promising strategy for advanced wastewater treatment applications.

Author Contributions: Z.G.: Investigation, data curation, writing—original draft. S.D.: investigation, data curation. M.H.: data curation, visualization. W.-d.O.: writing—editing. X.W.: writing–editing. T.Z.: paper design, writing—review and editing. All authors have read and agreed to the published version of the manuscript.

Funding: This study is financially supported by the National Key Technical Research and Development Program of China (2023YFC3207204), the National Natural Science Foundation of China (Nos. 22106159 and 21677055), and the Leading Plan for Scientific and Technological Innovation of High-Tech Industries in Hunan Province (2021GK4060). Huazhong University of Science and Technology's Analytic and Testing Center is thanked for its advanced analytical operations.

Data Availability Statement: The datasets used or analyzed during the current study are available from the corresponding author upon reasonable request.

Conflicts of Interest: The authors declare no conflicts of interest.

References

1. Samer, M. Biological and Chemical Wastewater Treatment. In *Wastewater Treatment Engineering*; InTech: Rijeka, Croatia, 2015; pp. 1–50.
2. Tang, J.; Zhang, C.; Shi, X.; Sun, J.; Cunningham, J.A. Municipal wastewater treatment plants coupled with electrochemical, biological and bio-electrochemical technologies: Opportunities and challenge toward energy self-sufficiency. *J. Environ. Manag.* **2019**, *234*, 396–403. [CrossRef]
3. Mantis, I.; Voutsa, D.; Samara, C. Assessment of the environmental hazard from municipal and industrial wastewater treatment sludge by employing chemical and biological methods. *Ecotoxicol. Environ. Saf.* **2005**, *62*, 397–407. [CrossRef]

4. Deleris, S.; Geaugey, V.; Camacho, P.; Debellefontaine, H.; Paul, E. Minimization of sludge production in biological processes: An alternative solution for the problem of sludge disposal. *Water Sci. Technol.* **2002**, *46*, 63–70. [CrossRef] [PubMed]
5. Ødegaard, H.; Paulsrud, B.; Karlsson, I. Wastewater sludge as a resource: Sludge disposal strategies and corresponding treatment technologies aimed at sustainable handling of wastewater sludge. *Water Sci. Technol.* **2002**, *46*, 295–303. [CrossRef] [PubMed]
6. Singh, S.; Kumar, V.; Dhanjal, D.S.; Datta, S.; Bhatia, D.; Dhiman, J.; Samuel, J.; Prasad, R.; Singh, J. A sustainable paradigm of sewage sludge biochar: Valorization, opportunities, challenges and future prospects. *J. Clean. Prod.* **2020**, *269*, 122259. [CrossRef]
7. Goldan, E.; Nedeff, V.; Barsan, N.; Culea, M.; Tomozei, C.; Panainte-Lehadus, M.; Mosnegutu, E. Evaluation of the use of sewage sludge biochar as a soil amendment—A review. *Sustainability* **2022**, *14*, 5309. [CrossRef]
8. Zhao, L.; Sun, Z.-F.; Pan, X.-W.; Tan, J.-Y.; Yang, S.-S.; Wu, J.-T.; Chen, C.; Yuan, Y.; Ren, N.-Q. Sewage sludge derived biochar for environmental improvement: Advances, challenges, and solutions. *Water Res. X* **2023**, *18*, 100167. [CrossRef]
9. Ike, I.A.; Linden, K.G.; Orbell, J.D.; Duke, M. Critical review of the science and sustainability of persulphate advanced oxidation processes. *Chem. Eng. J.* **2018**, *338*, 651–669. [CrossRef]
10. Yan, Y.; Wei, Z.; Duan, X.; Long, M.; Spinney, R.; Dionysiou, D.D.; Xiao, R.; Alvarez, P.J. Merits and limitations of radical vs. nonradical pathways in persulfate-based advanced oxidation processes. *Environ. Sci. Technol.* **2023**, *57*, 12153–12179. [CrossRef]
11. Babuponnusami, A.; Muthukumar, K. A review on Fenton and improvements to the Fenton process for wastewater treatment. *J. Environ. Chem. Eng.* **2014**, *2*, 557–572. [CrossRef]
12. Liang, C.; Guo, Y.-Y.; Chien, Y.-C.; Wu, Y.-J. Oxidative degradation of MTBE by pyrite-activated persulfate: Proposed reaction pathways. *Ind. Eng. Chem. Res.* **2010**, *49*, 8858–8864. [CrossRef]
13. Fang, G.-D.; Dionysiou, D.D.; Wang, Y.; Al-Abed, S.R.; Zhou, D.-M. Sulfate radical-based degradation of polychlorinated biphenyls: Effects of chloride ion and reaction kinetics. *J. Hazard. Mater.* **2012**, *227*, 394–401. [CrossRef]
14. Saien, J.; Soleymani, A.; Sun, J. Parametric optimization of individual and hybridized AOPs of Fe^{2+}/H_2O_2 and $UV/S_2O_8^{2-}$ for rapid dye destruction in aqueous media. *Desalination* **2011**, *279*, 298–305. [CrossRef]
15. Kang, Z.; Jia, X.; Zhang, Y.; Kang, X.; Ge, M.; Liu, D.; Wang, C.; He, Z. A review on application of biochar in the removal of pharmaceutical pollutants through adsorption and persulfate-based AOPs. *Sustainability* **2022**, *14*, 10128. [CrossRef]
16. Wang, C.; Huang, R.; Sun, R.; Yang, J.; Sillanpää, M. A review on persulfates activation by functional biochar for organic contaminants removal: Synthesis, characterizations, radical determination, and mechanism. *J. Environ. Chem. Eng.* **2021**, *9*, 106267. [CrossRef]
17. Yu, J.; Tang, L.; Pang, Y.; Zhou, Y.; Feng, H.; Ren, X.; Tang, J.; Wang, J.; Deng, L.; Shao, B. Non-radical oxidation by N, S, P co-doped biochar for persulfate activation: Different roles of exogenous P/S doping, and electron transfer path. *J. Clean. Prod.* **2022**, *374*, 133995. [CrossRef]
18. Yu, J.; Gong, Z.; Wang, S.; Zhong, H.; Tao, Y.; Hou, Y.; Fu, Q.; Yang, H.; Li, J.; Wang, J. Two major deactivation mechanisms in carbon-based advanced oxidation processes (AOPs) dominated by electron-transfer pathway (ETP). *Appl. Catal. B Environ. Energy* **2025**, *364*, 124850. [CrossRef]
19. Feng, Y.; Liu, M.; Shi, Q.; Song, Y.; Yang, L.; Zhang, J.; Li, Z.; Zhu, W. Sludge-derived biochar applied in peroxymonosulfate (PMS) activation: Reactive oxygen species (ROS) dominated process and characteristics. *J. Environ. Chem. Eng.* **2023**, *11*, 111365. [CrossRef]
20. Wang, S.; Wang, J. Activation of peroxymonosulfate by sludge-derived biochar for the degradation of triclosan in water and wastewater. *Chem. Eng. J.* **2019**, *356*, 350–358. [CrossRef]
21. Udayanga, W.C.; Veksha, A.; Giannis, A.; Lisak, G.; Lim, T.-T. Effects of sewage sludge organic and inorganic constituents on the properties of pyrolysis products. *Energy Convers. Manag.* **2019**, *196*, 1410–1419. [CrossRef]
22. Zielińska, A.; Oleszczuk, P.; Charmas, B.; Skubiszewska-Zięba, J.; Pasieczna-Patkowska, S. Effect of sewage sludge properties on the biochar characteristic. *J. Anal. Appl. Pyrolysis* **2015**, *112*, 201–213. [CrossRef]
23. Ye, S.; Zeng, G.; Tan, X.; Wu, H.; Liang, J.; Song, B.; Tang, N.; Zhang, P.; Yang, Y.; Chen, Q. Nitrogen-doped biochar fiber with graphitization from Boehmeria nivea for promoted peroxymonosulfate activation and non-radical degradation pathways with enhancing electron transfer. *Appl. Catal. B Environ.* **2020**, *269*, 118850. [CrossRef]
24. Duan, X.; Sun, H.; Wang, Y.; Kang, J.; Wang, S. N-doping-induced nonradical reaction on single-walled carbon nanotubes for catalytic phenol oxidation. *Acs Catal.* **2015**, *5*, 553–559. [CrossRef]
25. Xu, L.; Wu, C.; Liu, P.; Bai, X.; Du, X.; Jin, P.; Yang, L.; Jin, X.; Shi, X.; Wang, Y. Peroxymonosulfate activation by nitrogen-doped biochar from sawdust for the efficient degradation of organic pollutants. *Chem. Eng. J.* **2020**, *387*, 124065. [CrossRef]
26. Byambaa, B.; Kim, E.-J.; Seid, M.G.; An, B.-M.; Cho, J.; Aung, S.L.; Song, K.G. Synthesis of N-doped sludge biochar using the hydrothermal route-enabled carbonization method for the efficient degradation of organic pollutants by peroxymonosulfate activation. *Chem. Eng. J.* **2023**, *456*, 141037. [CrossRef]
27. Peng, X.; Wu, J.; Zhao, Z.; Wang, X.; Dai, H.; Li, Y.; Wei, Y.; Xu, G.; Hu, F. High efficiency degradation of tetracycline by peroxymonosulfate activated with Fe/NC catalysts: Performance, intermediates, stability and mechanism. *Environ. Res.* **2022**, *205*, 112538. [CrossRef]

28. Wang, Z.; Gao, B.; Liu, J.; Sillanpää, M.; Kim, Y. The oxidation treatment of pharmaceutical wastewater in H_2O_2 and PMS system by Iron-containing biochar originated from excess sludge. *J. Water Process Eng.* **2024**, *58*, 104833. [CrossRef]
29. Wu, Q.; Zhang, Y.; Liu, H.; Liu, H.; Tao, J.; Cui, M.H.; Zheng, Z.; Wen, D.; Zhan, X. Fe(x)N produced in pharmaceutical sludge biochar by endogenous Fe and exogenous N doping to enhance peroxymonosulfate activation for levofloxacin degradation. *Water Res.* **2022**, *224*, 119022. [CrossRef] [PubMed]
30. Zeng, S.; Kan, E. FeCl3-activated biochar catalyst for heterogeneous Fenton oxidation of antibiotic sulfamethoxazole in water. *Chemosphere* **2022**, *306*, 135554. [CrossRef]
31. Xu, H.; Zhang, X.; Zhang, Y. Modification of biochar by Fe_2O_3 for the removal of pyridine and quinoline. *Environ. Technol.* **2018**, *39*, 1470–1480. [CrossRef]
32. Luo, J.; Yi, Y.; Fang, Z. Nitrogen-rich magnetic biochar prepared by urea was used as an efficient catalyst to activate persulfate to degrade organic pollutants. *Chemosphere* **2023**, *339*, 139614. [CrossRef]
33. Mian, M.M.; Liu, G.; Zhou, H. Preparation of N-doped biochar from sewage sludge and melamine for peroxymonosulfate activation: N-functionality and catalytic mechanisms. *Sci. Total Environ.* **2020**, *744*, 140862. [CrossRef] [PubMed]
34. Hu, X.; Ding, Z.; Zimmerman, A.R.; Wang, S.; Gao, B. Batch and column sorption of arsenic onto iron-impregnated biochar synthesized through hydrolysis. *Water Res.* **2015**, *68*, 206–216. [CrossRef] [PubMed]
35. Li, Z.; Zhong, X.; Gao, L.; Hu, J.; Peng, W.; Wang, X.; Zhou, G.; Xu, B. Asymmetric coordination of bimetallic Fe–Co single-atom pairs toward enhanced bifunctional activity for rechargeable zinc–air batteries. *ACS Nano* **2024**, *18*, 13006–13018. [CrossRef] [PubMed]
36. Wu, Y.; Chen, J.; Liu, J.; Zhang, L.; Abazari, R.; Li, T.-T.; Qian, J. Iron phthalocyanine coupled with Co-Nx sites in carbon nanostraws for Zn-Air batteries. *Chem. Eng. J.* **2025**, *503*, 158343. [CrossRef]
37. Lu, X.; Li, Y.; Yang, P.; Wan, Y.; Wang, D.; Xu, H.; Liu, L.; Xiao, L.; Li, R.; Wang, G. Atomically dispersed Fe-NC catalyst with densely exposed Fe-N4 active sites for enhanced oxygen reduction reaction. *Chem. Eng. J.* **2024**, *485*, 149529. [CrossRef]
38. Ahmed, S.; Yoon, W.; Jo, H.; Irshad, M.; Khan, M.K.; Kim, J. Structure-activity relationship and deactivation behavior of iron oxide during CO_2 hydrogenation. *Chem. Eng. J.* **2024**, *499*, 156104. [CrossRef]
39. Liang, C.; Sun, H.; Ling, C.; Liu, X.; Li, M.; Zhang, X.; Guo, F.; Zhang, X.; Shi, Y.; Cao, S.; et al. Pyrolysis temperature-switchable Fe-N sites in pharmaceutical sludge biochar toward peroxymonosulfate activation for efficient pollutants degradation. *Water Res.* **2023**, *228 Pt A*, 119328. [CrossRef]
40. Bayoka, H.; Snoussi, Y.; Bhakta, A.K.; El Garah, M.; Khalil, A.M.; Jouini, M.; Ammar, S.; Chehimi, M.M. Evidencing the synergistic effects of carbonization temperature, surface composition and structural properties on the catalytic activity of biochar/bimetallic composite. *J. Anal. Appl. Pyrolysis* **2023**, *173*, 106069. [CrossRef]
41. Urbonaite, S.; Hälldahl, L.; Svensson, G. Raman spectroscopy studies of carbide derived carbons. *Carbon* **2008**, *46*, 1942–1947. [CrossRef]
42. Ni, Z.; Fan, H.; Fan, X.; Wang, H.; Zheng, Z.; Feng, Y.; Wu, Y.; Shen, Z. High temperature Raman spectroscopy studies of carbon nanowalls. *J. Raman Spectrosc.* **2007**, *38*, 1449–1453. [CrossRef]
43. Chen, C.; Sun, K.; Huang, C.; Yang, M.; Fan, M.; Wang, A.; Zhang, G.; Li, B.; Jiang, J.; Xu, W. Investigation on the mechanism of structural reconstruction of biochars derived from lignin and cellulose during graphitization under high temperature. *Biochar* **2023**, *5*, 51. [CrossRef]
44. Liu, H.; Ye, C.; Xu, Y.; Wang, Q. Effect of activation conditions and iron loading content on the catalytic cracking of toluene by biochar. *Energy* **2022**, *247*, 123409. [CrossRef]
45. Yang, Y.; Banerjee, G.; Brudvig, G.W.; Kim, J.-H.; Pignatello, J.J. Oxidation of organic compounds in water by unactivated peroxymonosulfate. *Environ. Sci. Technol.* **2018**, *52*, 5911–5919. [CrossRef]
46. Zhu, R.; Shi, Y.; Zhou, Y.; Xia, Y.; Qi, Q.; Liang, X.; Kuang, M.; Jia, Z.; Wang, M.; Yu, C. Highly reactive iron/nickel bimetallic biochar composites for highly efficient remediation of Cr (vi). *New J. Chem.* **2025**, *49*, 4427–4437. [CrossRef]
47. Sun, Y.; Jing, Y.; Wang, Z.; Huang, M.; Oh, W.-D.; Wu, X.; Zhou, T. Regulating sulfur vacancies formation on mechanochemically modified pyrite to steer non-radical molecular oxygen activation for water purification. *Sep. Purif. Technol.* **2025**, *353*, 128572. [CrossRef]
48. Zhang, L.S.; Jiang, X.H.; Zhong, Z.A.; Tian, L.; Sun, Q.; Cui, Y.T.; Lu, X.; Zou, J.P.; Luo, S.L. Carbon Nitride Supported High-Loading Fe Single-Atom Catalyst for Activation of Peroxymonosulfate to Generate 1O2 with 100 % Selectivity. *Angew. Chem. Int. Ed.* **2021**, *60*, 21751–21755. [CrossRef]
49. Wang, B.-B.; Shi, X.; Liu, X.-T.; Zou, J.-T.; Li, H.-J.; Peng, D.-C.; He, F. Insight into the fenton-induced degradation process of extracellular polymeric substances (EPS) extracted from activated sludge. *Chemosphere* **2019**, *234*, 318–327. [CrossRef]

50. Zhang, X.; Liu, Y.; Li, J.; Wei, Z.; Duan, W.; Chen, F. Enhancing effects of sludge biochar on aerobic granular sludge for wastewater treatment. *Processes* **2022**, *10*, 2385. [CrossRef]
51. Liu, Y.; Tian, Q.; Chen, Y.; Guo, T.; Zhang, Y.; Huang, Z.; Hu, H.; Gan, T. Single-atom Fe catalysts anchored on graphitized chitin-derived carbon for improved anti-interference ability of Fenton-like reaction via non-radical pathway. *Appl. Surf. Sci.* **2024**, *660*, 160020. [CrossRef]

Disclaimer/Publisher's Note: The statements, opinions and data contained in all publications are solely those of the individual author(s) and contributor(s) and not of MDPI and/or the editor(s). MDPI and/or the editor(s) disclaim responsibility for any injury to people or property resulting from any ideas, methods, instructions or products referred to in the content.

catalysts

MDPI

Article

Ag-Cu Synergism-Driven Oxygen Structure Modulation Promotes Low-Temperature NO_x and CO Abatement

Ruoxin Li [1], Jiuhong Wei [1], Bin Jia [1], Jun Liu [2,3,*], Xiaoqing Liu [4], Ying Wang [1,5], Yuqiong Zhao [1,5], Guoqiang Li [1,5] and Guojie Zhang [1,5,*]

[1] State Key Laboratory of Clean and Efficient Coal Utilization, College of Chemistry and Chemical Engineering, Taiyuan University of Technology, Taiyuan 030024, China
[2] College of Chemistry and Chemical Engineering, Taiyuan University of Technology, Taiyuan 030024, China
[3] National Engineering Laboratory for Multi Flue Gas Pollution Control Technology and Equipment, School of Environment, Tsinghua University, Beijing 100084, China
[4] School of Environment and Safety Engineering, North University of China, Taiyuan 030051, China
[5] Key Laboratory of Coal Science and Technology, Ministry of Education, Taiyuan University of Technology, Taiyuan 030024, China
* Correspondence: liujun02@tyut.edu.cn (J.L.); zhangguojie@tyut.edu.cn (G.Z.)

Abstract

The efficient simultaneous removal of NO_x and CO from sintering flue gas under low-temperature conditions (110–180 °C) in iron and steel enterprises remains a significant challenge in the field of environmental catalysis. In this study, we present an innovative strategy to enhance the performance of CuSmTi catalysts through silver modification, yielding a bifunctional system capable of oxygen structure regulation and demonstrating superior activity for the combined NH_3-SCR and CO oxidation reactions under low-temperature, oxygen-rich conditions. The modified AgCuSmTi catalyst achieves complete NO conversion at 150 °C, representing a 50 °C reduction compared to the unmodified CuSmTi catalyst ($T_{100\%}$ = 200 °C). Moreover, the catalyst exhibits over 90% N_2 selectivity across a broad temperature range of 150–300 °C, while achieving full CO oxidation at 175 °C. A series of characterization techniques, including XRD, Raman spectroscopy, N_2 adsorption, XPS, and O_2-TPD, were employed to elucidate the Ag-Cu interaction. These modifications effectively optimize the surface physical structure, modulate the distribution of acid sites, increase the proportion of Lewis acid sites, and enhance the activity of lattice oxygen species. As a result, they effectively promote the adsorption and activation of reactants, as well as electron transfer between active species, thereby significantly enhancing the low-temperature performance of the catalyst. Furthermore, in situ DRIFTS investigations reveal the reaction mechanisms involved in NH_3-SCR and CO oxidation over the Ag-modified CuSmTi catalyst. The NH_3-SCR process predominantly follows the L-H mechanism, with partial contribution from the E-R mechanism, whereas CO oxidation proceeds via the MvK mechanism. This work demonstrates that Ag modification is an effective approach for enhancing the low-temperature performance of CuSmTi-based catalysts, offering a promising technical solution for the simultaneous control of NO_x and CO emissions in industrial flue gases.

Keywords: NH_3-SCR; CO oxidation; Ag-Cu interaction; oxygen structure regulation; bifunctional catalysis; low-temperature flue gas

1. Introduction

Flue gas generated during the fossil fuel sintering process in iron and steel enterprises contains harmful atmospheric pollutants, such as nitrogen oxides (NO_x) and carbon monoxide (CO) [1], which pose serious threats to both environmental quality and human health [2,3]. Among various NO_x removal technologies, ammonia-based selective catalytic reduction (NH_3-SCR) is widely recognized as the most effective denitrification method [4]. The V_2O_5-WO_3/TiO_2 catalyst, known for its excellent catalytic performance, has been extensively applied in industrial NH_3-SCR processes [5]. However, this catalyst operates optimally within a temperature range of 320–450 °C and involves the use of V_2O_5, which becomes highly toxic at elevated temperatures [6]. As a result, its application faces significant challenges when treating sintering flue gas at much lower temperatures (110–180 °C) [7]. In light of increasingly stringent environmental regulations, the development of high-performance denitrification catalysts suitable for low-temperature conditions has become an urgent priority. Meanwhile, catalytic CO oxidation, as a well-established technology for CO control, has been widely studied and implemented [8]. Nevertheless, the design and development of a bifunctional catalyst capable of simultaneously removing both NO_x and CO remains a key research focus and challenge in the field of environmental catalysis.

In theory, the selective catalytic reduction of NO_x using CO as a reductant (CO-SCR) offers a promising strategy for addressing the simultaneous removal of NO_x and CO [9]. However, in practical applications, the presence of a large excess of oxygen in flue gas causes CO to preferentially react with O_2 rather than NO_x [10], significantly limiting the effectiveness and applicability of the CO-SCR process. A promising alternative is the development of bifunctional catalysts capable of simultaneously promoting both CO oxidation and NH_3-SCR reactions under oxygen-rich conditions. These catalysts can utilize the heat generated during CO oxidation to enhance the performance of the NH_3-SCR reaction, thereby improving overall energy efficiency [11]. This dual-function strategy not only reduces energy consumption and operational costs but also provides a feasible technical pathway for the synergistic control of NO_x and CO emissions in low-temperature flue gas environments.

In recent years, transition metal catalysts such as Cu, Mn, and Fe have demonstrated significant potential in NH_3-SCR coupled with CO oxidation due to their excellent catalytic activity, superior thermal stability, and relatively low cost [12]. Among these, copper-based catalysts exhibit particular potential, owing to their multiple redox states and strong redox capabilities, which confer significant advantages in both NH_3-SCR [13] and CO oxidation [14] reactions. To further enhance the catalytic performance of copper-based catalysts, extensive modification and optimization efforts have been undertaken by researchers. Liu et al. [15] introduced phosphorus into a CuCeZr (CCZ) catalyst to achieve a balanced combination of acidity and redox properties, significantly enhancing the catalytic activity of the CCZ-P1 catalyst within the temperature range of 250–350 °C. Shen et al. [16] synthesized a molybdenum-doped $CuCeO_x$ bifunctional catalyst and found that Mo incorporation enhanced the catalyst's reducibility, promoted the adsorption and activation of reactant gases, and enabled the CCM3 catalyst to achieve a NO_x conversion rate of 91.2% at 225 °C, along with complete CO oxidation over a broad temperature window of 150–300 °C. Lv et al. [17] modified a Cu/TiO_2 catalyst with Sm, constructing asymmetric active sites of Cu^{+}-Sm^{3+}-O_v-Ti^{4+}, which effectively facilitated full NO conversion at 200 °C and efficient CO oxidation in the temperature range of 175–300 °C.

Although modified copper-based catalysts such as CuSmTi have exhibited relatively superior low-temperature activity, their performance still does not fully meet the practical requirements for the treatment of sintering flue gas at temperatures below 180 °C. Therefore, further modification strategies are required to enhance their catalytic performance at such

conditions. Liu et al. [18] prepared Ag-modified α-MnO_2 catalysts for efficient benzene oxidation. The Ag modification enriched the variety of oxygen species and increased the quantity and enhanced the reactivity of lattice oxygen, thereby promoting the reaction efficiency. Similarly, Rao et al. [19] reported that the incorporation of Ag could activate a substantial amount of lattice oxygen in CeO_2 nanoparticles. The lattice oxygen activated at the Ag-CeO_2 interface significantly improved the catalytic performance. These studies demonstrate that Ag modification plays a crucial role in regulating the structure and distribution of oxygen species, thereby effectively enhancing the overall catalytic performance of the material.

In this study, an Ag-modified AgCuSmTi bifunctional catalyst was successfully synthesized using the sol–gel method, which facilitated effective oxygen structure regulation. The catalyst exhibits excellent NO and CO conversion efficiencies at low temperatures while maintaining favorable N_2 selectivity. A suite of characterization techniques was employed to investigate the surface structure and internal chemical valence states, revealing pronounced Ag-Cu interactions within the AgCuSmTi catalyst. Further analysis indicated that these Ag-Cu interactions promote the optimization of oxygen structure and modulate the distribution of surface acid sites, thereby enhancing the low-temperature activity of the AgCuSmTi bifunctional catalyst. This study provides new insights into catalytic materials and a theoretical basis for the synergistic removal of multiple pollutants in sintering flue gas.

2. Results and Discussion

2.1. Evaluation of Catalytic Performance

To regulate the performance of the CuSmTi catalyst in the NH_3-SCR coupled with CO oxidation reaction, Ag species were introduced as dopants, and the influence of varying Ag doping levels on catalytic activity was systematically investigated. The catalytic performance of Ag_xCuSmTi catalysts with different Ag contents (x = 0.5, 0.8, 1.0, 1.2, 1.5) was evaluated to determine the optimal doping ratio, where x denotes the molar ratio of $AgNO_3$ to $Cu(NO_3)_2 \cdot 3H_2O$. As shown in Figure S1a, the NO_x conversion at 150 °C gradually increases with increasing Ag content, reaching 100% for the $Ag_{1.2}$CuSmTi catalyst. However, further increasing the Ag doping ratio to x = 1.5 results in a slight decline in catalytic activity. Figure S1b presents the variation in N_2 selectivity with Ag loading. With increasing Ag content, the N_2 selectivity decreases gradually, and this trend becomes more pronounced at higher doping levels. Nevertheless, the $Ag_{1.2}$CuSmTi catalyst still maintains a N_2 selectivity exceeding 90%, demonstrating a favorable combination of high activity and selectivity. As depicted in Figure S1c, all catalysts achieve complete CO conversion at 175 °C. Based on the overall performance analysis, the $Ag_{1.2}$CuSmTi catalyst exhibits the best catalytic performance among the series. For simplicity and consistency in subsequent discussions, the $Ag_{1.2}$CuSmTi catalyst is hereafter referred to as AgCuSmTi.

After determining the optimal silver doping ratio, the effect of Ag modification on catalytic performance was further investigated by comparing the NH_3-SCR and CO oxidation activities of AgCuSmTi, CuSmTi, and AgSmTi catalysts. Figure 1a presents the NO_x conversion profiles of the three catalysts. The CuSmTi catalyst achieves complete NO_x conversion at 200 °C; however, its activity declines significantly at temperatures above 250 °C. Notably, the introduction of Ag markedly enhances low-temperature performance, enabling the AgCuSmTi catalyst to reach 100% NO_x conversion at 150 °C ($T_{100\%}$ = 150 °C). In contrast, the AgSmTi catalyst, which lacks Cu species, exhibits poor performance, achieving full NO_x conversion only between 225 and 250 °C. These results indicate that Ag species strongly interact with CuSmTi and play a crucial role in promoting the NH_3-SCR reaction. Figure 1b shows the N_2 selectivity of the three catalysts. The AgSmTi catalyst exhibits a sharp de-

crease in N_2 selectivity above 150 °C. Although the addition of Ag slightly lowers the N_2 selectivity compared to CuSmTi, the AgCuSmTi catalyst maintains over 90% selectivity across the entire temperature range of 50–300 °C. This suggests that the interaction between Ag and Cu not only enhances catalytic activity but also contributes to the preservation of high N_2 selectivity. The CO oxidation performance, shown in Figure 1c, further confirms the beneficial effect of Ag modification. Among the three catalysts, AgCuSmTi exhibits the lowest $T_{100\%}$ value. At any given temperature within the tested range, its CO conversion rate is slightly higher than that of CuSmTi, whereas AgSmTi shows relatively poor performance. This indicates that the synergistic interaction between Ag and CuSmTi plays a key role in enhancing CO oxidation activity as well. The TOF values for NO and CO conversion over the AgCuSmTi and CuSmTi catalysts are presented in Figure S2a and Figure S2b, respectively. The results clearly demonstrate that the incorporation of Ag significantly enhances the TOF values associated with the Cu species. Consequently, the AgCuSmTi catalyst exhibits markedly higher catalytic efficiency compared to the CuSmTi catalyst.

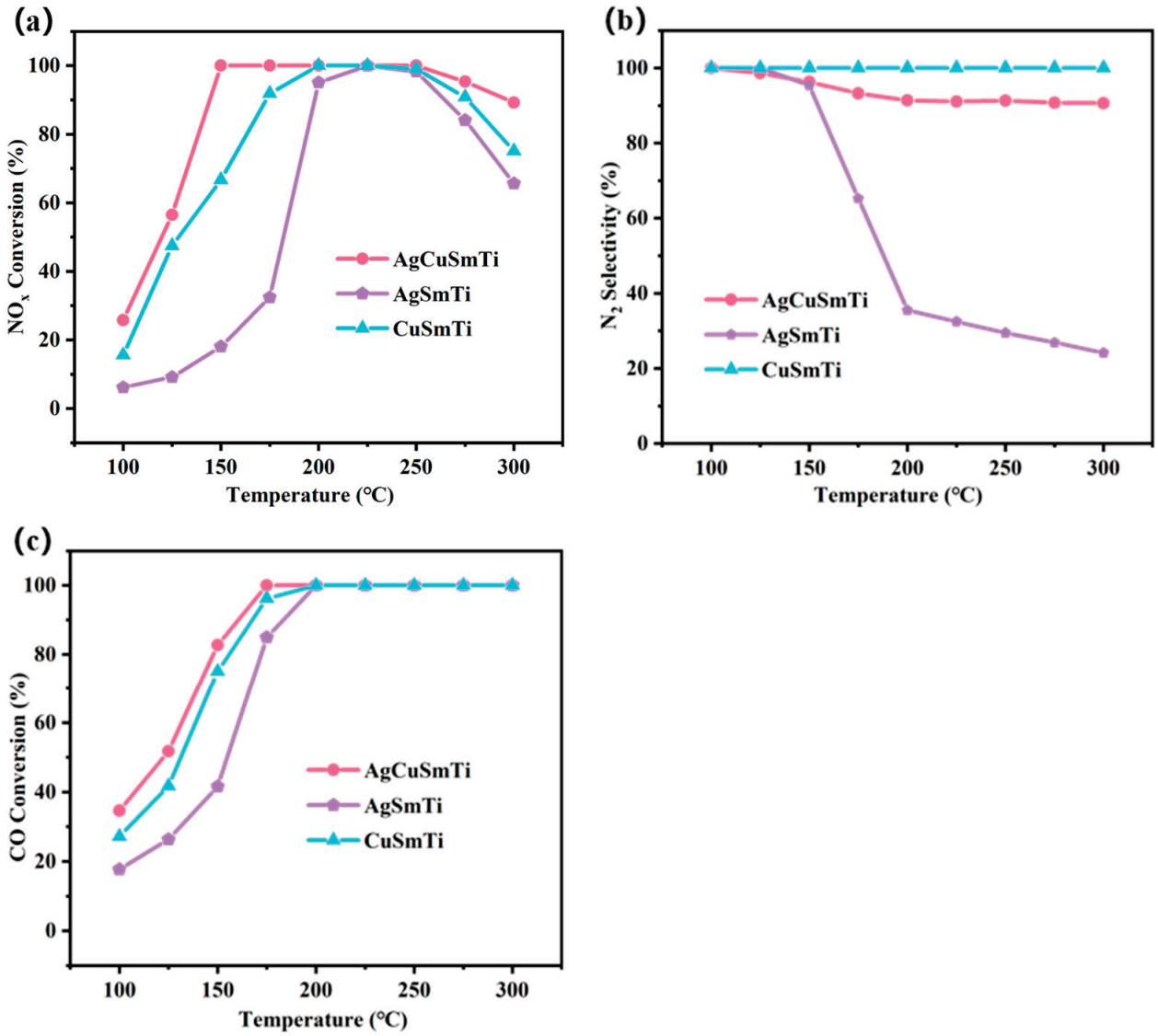


Figure 1. NO_x conversion (**a**), N_2 selectivity (**b**), and CO conversion (**c**) of catalyst. Gas composition: GHSV = 60,000·h^{-1}, [NO_x] = [NH_3] = 500 ppm, [CO] = 1000 ppm, O_2 = 5 vol%, N_2 as balance.

To further highlight the outstanding catalytic performance of the AgCuSmTi catalyst, Table S1 summarizes recent studies on Cu-based catalysts applied in NH_3-SCR coupled

with CO oxidation [15–17,19–24]. As shown, the α-MnO_2-Cu catalyst achieves a NO_x conversion rate of 85% at 150 °C and complete CO conversion at 175 °C [25]. In comparison, the AgCuSmTi catalyst developed in this study exhibits a 100% NO_x conversion rate at the same temperature of 150 °C. Moreover, the NO conversion rate over the CuO_x/α-MnO_2 catalyst reaches only 81% at 150 °C. Several other well-reported catalysts, such as $MnCuCeO_x$/γ-Al_2O_3 [26], CuMgFeO [20], V_2O_5-CuO/TiO_2 [22], CuO/VWTi [11], and CuW/CeZr, exhibit higher temperature requirements for achieving maximum NO and CO conversion. The results demonstrate that the AgCuSmTi catalyst not only exhibits competitive low-temperature catalytic activity compared to traditional systems, but in fact surpasses many of them, highlighting its significant potential for practical applications in low-temperature flue gas treatment.

To evaluate the stability of the AgCuSmTi catalyst, stability tests were carried out at 150 °C and 175 °C over a period of 20 h. The results presented in Figure S3a,b clearly indicate that during the 20 h reaction duration, the conversion rates of NO and CO, as well as the N_2 selectivity, remained relatively constant. This demonstrates that the AgCuSmTi catalyst exhibits excellent stability under reaction conditions. In summary, the synergistic interaction between Ag and CuSmTi significantly enhances the catalytic performance in both the NH_3-SCR and CO oxidation reactions. The AgCuSmTi catalyst displays outstanding low-temperature activity, excellent N_2 selectivity, strong CO conversion capability, and superior stability, highlighting its significant potential for practical applications.

2.2. Structural and Chemical Characterization of the Catalyst

2.2.1. Morphological Characterization of the Catalysts

The SEM images (Figure 2a–f) reveal that both the AgCuSmTi and CuSmTi catalysts exhibit irregular nanoparticle morphologies. The incorporation of Ag effectively suppresses nanoparticle agglomeration and promotes the uniform dispersion of active species, thereby enhancing the overall catalytic performance [27]. The particle size distribution of the AgCuSmTi catalyst is presented in Figure 2g. The results indicate that the particle sizes are predominantly within the range of 14–18 nm and are relatively uniformly distributed. However, the average particle size of AgCuSmTi is 16.77 nm, which is significantly larger than that of CuSmTi (6.22 nm; see Figure S4). This suggests that the introduction of Ag has somewhat altered the particle size characteristics of the catalyst. TEM images (Figure 2h,i) show a clear lattice fringe with an interplanar spacing of approximately 0.35 nm, consistent with the (101) plane of anatase TiO_2 [28]. Notably, no distinct lattice fringes corresponding to Ag, Cu, or Sm species were observed, indicating that these metal dopants are highly dispersed on the catalyst surface rather than forming large crystalline domains or aggregates.

To further investigate the elemental composition and surface distribution characteristics of the AgCuSmTi catalyst, energy-dispersive X-ray spectroscopy (EDX) mapping analysis was conducted. As shown in Figure 2j, elements such as Ag, Cu, Sm, Ti, and O are clearly present and exhibit a uniform spatial distribution, with no signs of agglomeration. This result indicates that all metallic components are highly dispersed on the catalyst surface. This uniform elemental distribution not only confirms the successful integration and dispersion of multiple metal components but also indicates the presence of well-distributed active sites, which are crucial for efficient catalytic performance. Additionally, the high dispersion of various elements suggests that there may be strong synergistic interactions between different active components, which could help enhance catalytic activity.

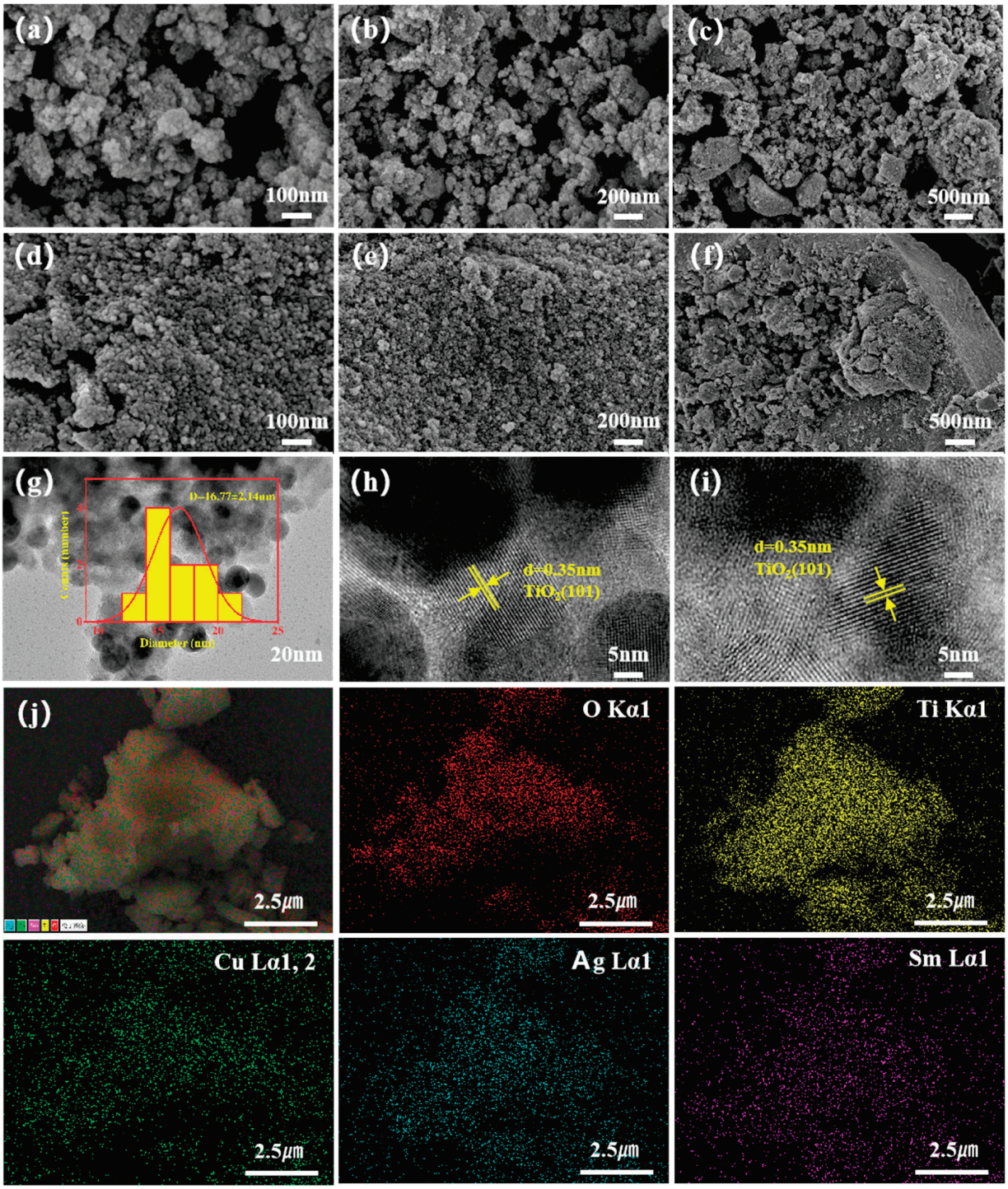


Figure 2. SEM (**a**–**c**) spectra of CuSmTi catalyst and SEM (**d**–**f**) and TEM (**g**–**i**) spectra and EDX mapping (**j**) of AgCuSmTi catalyst.

2.2.2. Evidence for Ag-Cu Interaction

To further investigate the structural characteristics of the catalysts, XRD analysis was conducted, and the results are presented in Figure 3a. All samples exhibited diffraction peaks corresponding to the anatase phase of TiO_2. Notably, no characteristic diffraction peaks associated with Sm, Cu, or Ag species were observed, indicating that these elements are either amorphous or highly dispersed within the matrix [29]. Compared to pure TiO_2, the intensity of the diffraction peaks in the SmTi sample was significantly reduced, suggesting that Sm doping inhibits the growth of TiO_2 crystallites. Upon further introduction of

Cu to form the CuSmTi catalyst, the peak intensities remained nearly unchanged relative to SmTi. However, upon co-doping with Ag, Cu, and Sm to obtain AgCuSmTi, the diffraction peak intensities decreased further, implying a further reduction in the average grain size of TiO_2. The smaller grain size facilitates the dispersion of active species, leading to an increased number of active sites and thereby enhancing the catalytic performance [30]. This phenomenon can be attributed to the lattice distortion and increased defect density resulting from the synergistic interaction among Ag, Cu, and Sm species, which collectively suppress the growth of TiO_2 grains.

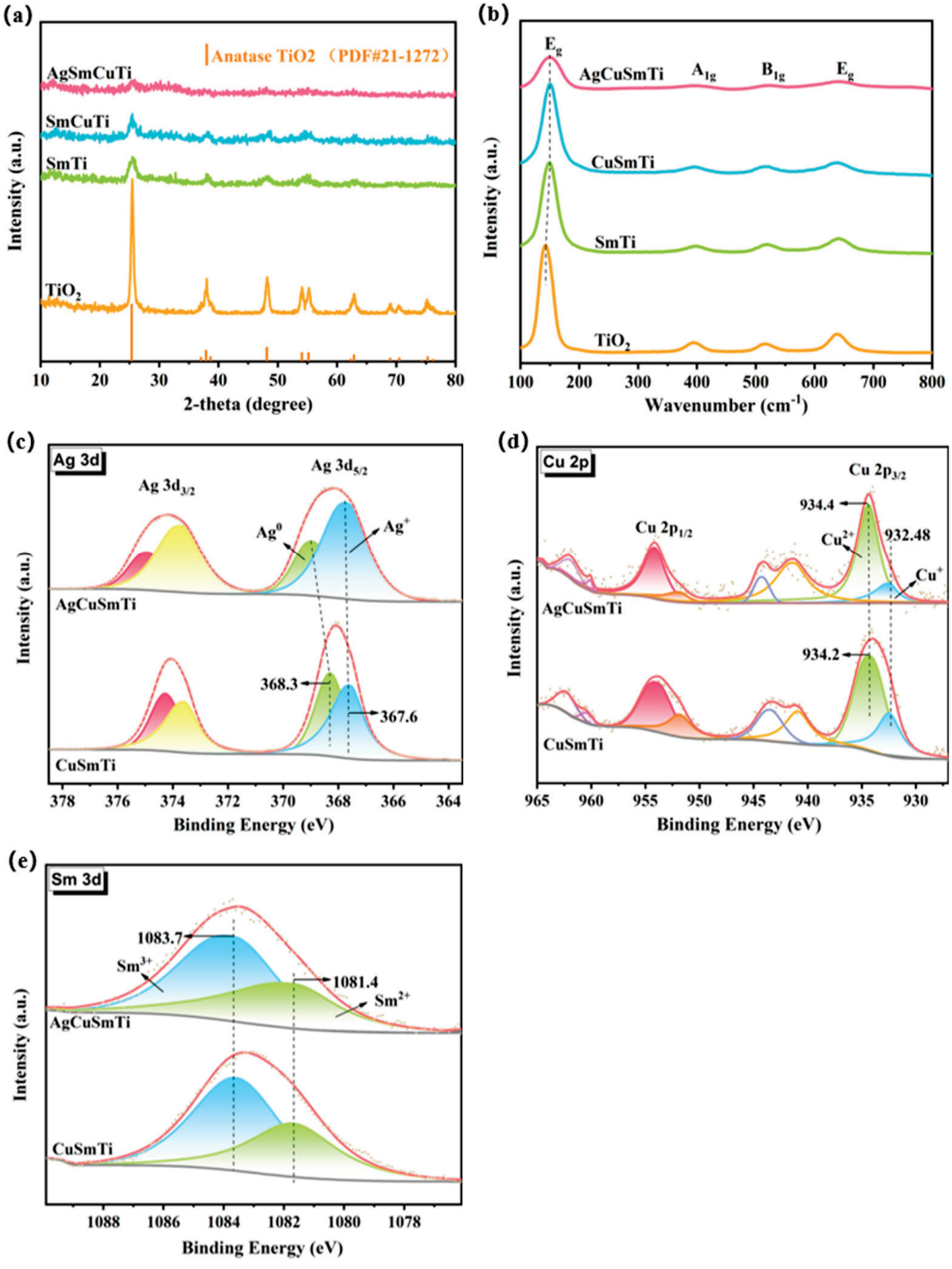


Figure 3. XRD (**a**), Raman (**b**), and XPS spectrum of (**c**) Ag 3d, (**d**) Cu2p, and (**e**) Sm 3d for catalysts.

The crystal structures of the samples were further analyzed using Raman spectroscopy. As shown in Figure 3b, all catalysts exhibit the characteristic Raman bands of anatase TiO_2 at approximately 143 cm^{-1} (E_g), 396 cm^{-1} (B_{1g}), 515 cm^{-1} (A_{1g}), and 638 cm^{-1} (E_g) [31]. These results confirm that doping does not induce any phase transformation of TiO_2 or lead to the formation of detectable secondary oxide phases, consistent with the XRD findings. However, after doping with Sm, Cu, and Ag, the Eg mode of TiO_2 undergoes noticeable blue shifts, exhibits reduced peak intensity, and shows an increased full width at half maximum (FWHM), reflecting enhanced local lattice distortions and internal stress within the TiO_2 lattice [32]. Further analysis of the changes in the E_g peak position, intensity, and FWHM reveals that the degree of lattice disturbance follows the order TiO_2 > SmTi > CuSmTi > AgCuSmTi. This trend indicates that the co-doping of Ag and Cu introduces the most significant structural perturbation. This effect is likely due to the large differences in ionic radii between Cu^{2+} (0.73 Å) and Ag^+ (1.26 Å) compared to Ti^{4+} (0.64 Å), which generate considerable lattice strain when incorporated into the TiO_2 structure [33]. Moreover, Cu doping tends to create localized stress fields, while the addition of Ag further weakens the Ti-O bond strength, thereby suppressing and broadening the Raman-active vibrational modes [33,34]. In particular, the most pronounced E_g peak broadening is observed for the AgCuSmTi sample. Therefore, the combined interaction of Ag, Cu, and Sm significantly disturbs the TiO_2 lattice, resulting in blue shifting of the E_g peak, reduced intensity, and increased peak width. These structural modifications provide a fundamental basis for the enhanced catalytic performance observed in the AgCuSmTi catalyst.

Figure S5 presents the nitrogen adsorption–desorption isotherms and corresponding pore size distribution curves of the samples. As shown in Figure S5a, all catalysts display IV-type nitrogen adsorption isotherms accompanied by H_2-type hysteresis loops, indicating that they possess typical mesoporous structural characteristics. The pore size distributions calculated from the desorption branches further support this conclusion [35]. As illustrated in Figure S5b, the pore size distribution of the SmTi catalyst is only slightly affected by Cu modification. However, upon co-doping with Ag and Cu, a noticeable change in the pore size distribution is observed. The data summarized in Table S2 indicate that the incorporation of Ag and Cu leads to an increase in average pore size and a broader pore size distribution. This suggests that the synergistic interaction among Ag, Cu, and Sm alters the aggregation behavior of the particles, thereby influencing both the pore structure and specific surface area. Moreover, by comparing the catalytic performance with the specific surface area data, it can be inferred that the specific surface area is not the dominant factor affecting catalytic performance.

To further investigate the chemical states of the elements in the AgCuSmTi catalyst and its reference samples, XPS analysis was carried out. As shown in Figure 3c, the Ag 3d spectrum exhibits two main peaks corresponding to the Ag $3d_{3/2}$ and Ag $3d_{5/2}$ spin–orbit components. The binding energies at 368.3 eV and 367.6 eV are assigned to metallic Ag^0 and oxidized Ag^+ species in the Ag $3d_{3/2}$ orbital, respectively [36]. According to the atomic ratio calculations presented in Table S3, the $Ag^+/(Ag^0 + Ag^+)$ ratio in the AgCuSmTi catalyst is higher than that in the AgSmTi catalyst upon Cu doping. Moreover, the binding energy of Ag^+ in the AgCuSmTi sample shifts toward a higher value compared to that in AgSmTi. These observations suggest that the introduction of Cu promotes the oxidation of Ag^0 to Ag^+, indicating possible electron transfer interactions among Ag, Cu, and Sm, which may enhance the electronic affinity of Ag.

The Cu 2p spectrum is displayed in Figure 3d. The peaks at 934.2 eV and 932.5 eV correspond to Cu^{2+} and Cu^+ species in the Cu $2p_{3/2}$ orbital, respectively [36,37]. Compared with the CuSmTi catalyst, the proportion of Cu^{2+} in the AgCuSmTi catalyst is significantly increased, as summarized in Table 1. This indicates that the incorporation of Ag improves

the stability of the Cu in its respective oxidation states, further supporting the presence of synergistic electronic interactions between Ag, Cu, and Sm.

Table 1. Surface elemental composition of the catalyst as determined by XPS analysis.

Sample	Surface Atomic Concentration (%)					Relative Concentration Ratio (%)		
	Ag	Cu	Sm	Ti	O	$Cu^{2+}/(Cu^{+} + Cu^{2+})$	$Sm^{3+}/(Sm^{2+} + Sm^{3+})$	$O_\beta/(O_\alpha + O_\beta)$
AgCuSmTi	8.79	2.61	5.50	24.63	58.46	82.51	60.98	77.77
CuSmTi	-	2.90	4.99	27.67	64.44	68.35	61.05	64.77

As shown in the Sm 3d spectrum (Figure 3e), all catalysts exhibit two fitted peaks at 1083.7 eV and 1081.4 eV, corresponding to Sm^{3+} and Sm^{2+} species, respectively [38]. Compared to the CuSmTi catalyst, the $Sm^{3+}/(Sm^{2+} + Sm^{3+})$ ratio in the AgCuSmTi catalyst remains nearly unchanged. This result suggests that the incorporation of Ag has little influence on the oxidation state of Sm, implying the absence of a strong direct interaction between Ag and Sm. Instead, the primary effect of Ag doping appears to be on its interaction with Cu species, rather than forming a direct synergistic relationship with Sm.

2.2.3. Structural Regulation of Oxygen

To gain deeper insight into the regulation of surface oxygen species and their role in catalytic performance, a comprehensive analysis of the oxygen structure in the catalyst was conducted. First, O 1s XPS was employed to qualitatively and quantitatively distinguish between lattice oxygen (O_{latt}) and surface-adsorbed oxygen (O_{ads}). As shown in Figure 4a, the O 1s spectrum can be deconvoluted into two characteristic peaks at 529.7–529.9 eV and 531.3–531.5 eV, corresponding to lattice oxygen (O_β) and surface-adsorbed oxygen (O_α), respectively [38]. The quantitative results summarized in Table 1 reveal that the AgCuSmTi catalyst exhibits a higher proportion of lattice oxygen compared to the CuSmTi catalyst. This enhancement may be attributed to the electronic synergy between Ag and Cu, which strengthens metal–oxygen bonding and increases the content of lattice oxygen within the crystal structure. The increased lattice oxygen content suggests that the AgCuSmTi catalyst possesses a greater reservoir of active oxygen species available during the initial reaction stage. This facilitates the rapid oxidation of reactant molecules and enhances the overall reaction rate. Concurrently, the consumption of lattice oxygen leads to the formation of oxygen vacancies, which can be readily replenished by gaseous oxygen, thereby sustaining efficient and continuous catalytic cycles [29].

Subsequently, O_2-TPD analysis was carried out on both the CuSmTi and AgCuSmTi catalysts to evaluate the mobility and desorption behavior of surface oxygen species, reflecting their potential involvement in oxidation reactions. As presented in Figure 4b, both catalysts exhibit two distinct desorption peaks: one in the low-temperature region (<300 °C), assigned to surface-adsorbed oxygen (O_α), and another in the medium-to-high temperature range (300–600 °C), corresponding to lattice oxygen (O_β) [20]. Notably, the AgCuSmTi catalyst shows a significant increase in lattice oxygen content, from 33.48% in CuSmTi to 48.25% after the introduction of Ag, indicating that Ag promotes the enrichment of lattice oxygen (Table S4). Therefore, the incorporation of Ag likely activates lattice oxygen through electronic interactions with Cu, enhancing both the reaction rate and stability of the catalyst.

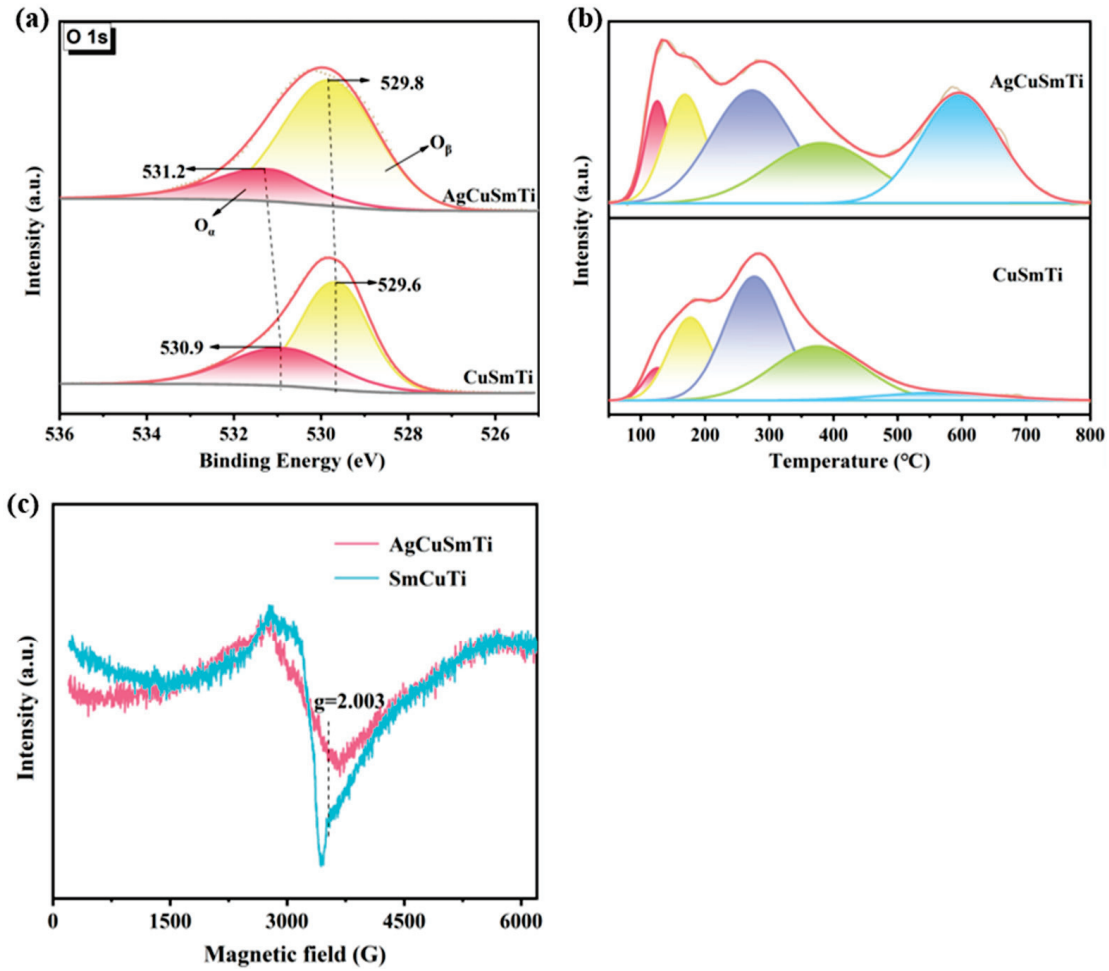


Figure 4. XPS (**a**), O_2-TPD (**b**), and EPR (**c**) spectrum of catalysts.

To further validate changes in oxygen vacancy concentration, EPR spectroscopy was employed for sample analysis. As illustrated in Figure 4c, all catalysts display a distinct EPR signal at g = 2.003, which is characteristic of oxygen vacancies [39]. Among them, the CuSmTi catalyst exhibits the strongest signal intensity, indicating a high concentration of oxygen vacancies on its surface. In contrast, the AgCuSmTi catalyst shows a significantly weakened EPR signal, suggesting a reduction in oxygen vacancy density. It can be inferred that the interaction between Ag and Cu contributes to the suppression of oxygen defects while simultaneously facilitating the mobilization and enrichment of lattice oxygen.

In summary, the synergistic effect between Ag and Cu drives the structural regulation of oxygen species, not only creating favorable conditions for oxygen migration and release but also improving the accessibility and utilization efficiency of reactive oxygen species during the reaction. These effects collectively enhance the catalytic activity of the AgCuSmTi system in low-temperature NH_3-SCR processes.

2.2.4. Redox Properties and Surface Acidity Characterization

To further investigate the influence of active species on the catalyst surface and their reduction behavior in relation to catalytic performance, H_2-TPR characterization was carried out on all catalysts, with the results presented in Figure 5a. The reduction profile of the CuSmTi catalyst can be divided into three distinct stages: the low-temperature peak (131 °C) corresponds to the reduction of Cu^{2+} to Cu^{+}; the medium-temperature peak (149 °C) is attributed to the reduction of Cu^{+} to Cu^{0}; and the high-temperature peak (178 °C) is associated with the reduction of CuO clusters [40]. These findings indicate that

Cu species exist in multiple oxidation states and undergo progressive reduction to the metallic state through sequential electron transfer processes. Upon Ag doping, all three reduction peaks in the AgCuSmTi catalyst shift toward lower temperatures, suggesting a notable enhancement in the reducibility of Cu species. This improvement can be attributed to the synergistic interaction between Ag and Cu, which facilitates electron transfer and promotes the activation of oxygen species. Consequently, Cu^{2+} becomes more readily reduced to Cu^{+} and ultimately to Cu^{0}. Additionally, a new reduction peak appears at approximately 228 °C for the AgCuSmTi catalyst, which is assigned to the reduction of Ag_2O to metallic Ag^{0} [41]. The enhanced Ag–Cu interaction accelerates the redox reaction kinetics at lower temperatures, thereby improving the overall redox activity of the catalyst.

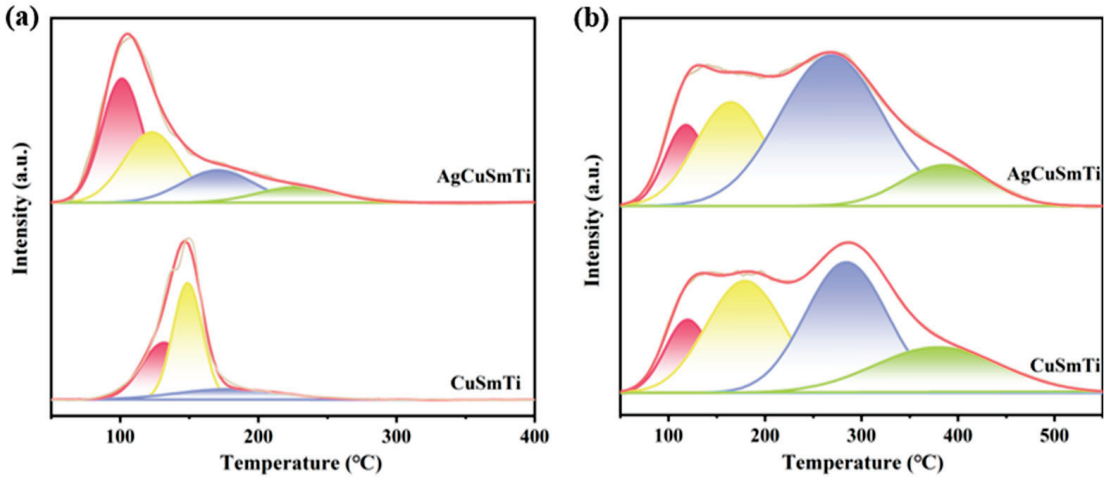


Figure 5. H_2-TPR (**a**) and NH_3-TPD (**b**) spectrum of catalysts.

The acid characteristics of the catalyst surfaces were investigated using NH_3-TPD analysis for the AgCuSmTi and CuSmTi samples. The results are shown in Figure 5b, with the desorption peak areas quantitatively analyzed and summarized in Table 2. Both catalysts exhibit three distinct NH_3 desorption peaks: the α peak (100–150 °C) corresponds to weak Lewis acid sites; the β peak (150–300 °C) represents strong Lewis acid sites; and the γ peak (>300 °C) is associated with Brønsted acid sites [42]. Comparative analysis reveals a significant increase in the proportion of the β peak in the AgCuSmTi catalyst, from 68.15% in CuSmTi to 76.86%, indicating that Ag incorporation substantially enhances the density of strong Lewis acid sites. This facilitates NH_3 adsorption and activation, providing abundant active sites for subsequent surface reactions. In contrast, the proportion of the γ peak decreases in AgCuSmTi, reflecting a reduction in Brønsted acidity. These observations suggest that the Ag-Cu interaction plays a crucial role in modulating the surface acidic structure, favoring the formation of strong Lewis acid sites that are more conducive to the NH_3-SCR reaction mechanism [43]. As a result, the catalytic performance is significantly improved.

Table 2. Acidic site distribution of catalysis.

Sample	α	β	γ
AgCuSmTi	11.25%	76.86%	11.89%
CuSmTi	11.5%	68.15%	20.35%

2.3. Proposed Reaction Mechanism Investigation

2.3.1. Proposed Reaction Mechanism of CO Oxidation

To elucidate the intermediate species and reaction mechanisms involved in CO oxidation over the AgCuSmTi composite metal oxide catalyst, in situ DRIFTS experiments were carried out under CO + O_2 co-adsorption conditions at various temperatures. The results are presented in Figure 6a. Upon exposure to CO and O_2, two main carbonate species formed via interactions between CO and surface oxygen species were observed: monodentate carbonate (1329 cm^{-1} and 1463 cm^{-1}) [16,44] and bidentate carbonate (1042 cm^{-1} and 1581 cm^{-1}) [45,46]. A distinct peak at 2113 cm^{-1} was assigned to Cu^{+}-CO, whose intensity decreased with increasing temperature and vanished entirely above 150 °C. A peak at 2163 cm^{-1} was attributed to Cu^{2+}-CO [47,48]. Additionally, broad bands in the range of 2285-2390 cm^{-1} corresponded to CO_2 molecules, indicating the formation of gaseous CO_2 as a result of CO oxidation [49]. As shown in the spectra, the band at 1581 cm^{-1}, associated with bidentate carbonate, along with the peak at 1329 cm^{-1}, representing monodentate carbonate, both diminished significantly with rising temperature. However, these features remained detectable even at 300 °C. In contrast, the peaks at 1463 cm^{-1} and 1042 cm^{-1} exhibited an opposite trend, showing increased intensity at higher temperatures. Considering the evolution of CO_2 and Cu^{+}-CO signals, it can be inferred that the thermal decomposition of carbonate species contributes significantly to the oxidation of CO at elevated temperatures.

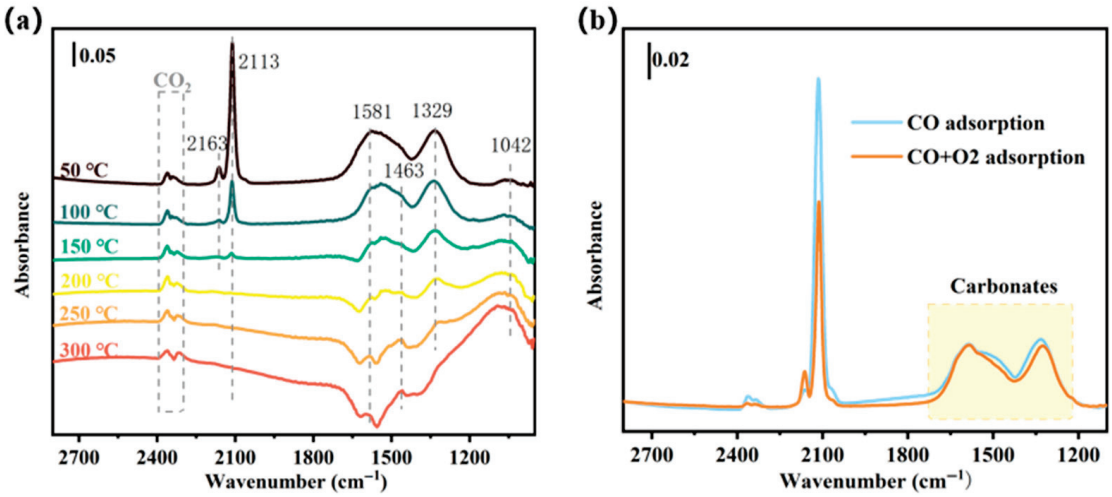


Figure 6. In situ DRIFTS analysis of the AgCuSmTi catalyst under different gas atmospheres: CO + O_2 adsorption across a temperature range of 50 to 300 °C (**a**) and CO adsorption alone versus co-adsorption with O_2 at 50 °C (**b**).

The involvement of molecular oxygen in the CO oxidation mechanism was examined by comparing DRIFTS spectra obtained at 50 °C under conditions with and without O_2, as shown in Figure 6b. Notably, the intensity of the Cu^{+}-CO peak at 2113 cm^{-1} is significantly lower under CO + O_2 co-adsorption compared to CO-only adsorption, suggesting that O_2 partially occupies the active sites responsible for CO adsorption. Meanwhile, the spectral region between 1200 and 1700 cm^{-1}, which includes the carbonate-related peaks, remains largely unchanged regardless of O_2 presence. This indicates that O_2 does not directly influence the formation of carbonate species [15]. Notably, without molecular oxygen present, CO reacts with lattice oxygen, resulting in the production of carbonate intermediates. Based on the above observations, the CO oxidation reaction over the AgCuSmTi catalyst proceeds primarily through the Mars–van Krevelen (MvK) mechanism.

2.3.2. Proposed Reaction Mechanism of NH_3-SCR

To investigate the acid sites and intermediate species formed on the catalyst upon incorporation of Ag species, NH_3 adsorption–desorption DRIFTS measurements were carried out at various temperatures. Figure 7a presents the in situ DRIFTS spectra of NH_3 adsorption on the AgCuSmTi catalyst as a function of surface temperature from 50 to 300 °C. The broad band observed in the range of 3000–3400 cm^{-1} is attributed to the N-H stretching of adsorbed NH_3 [50,51]. Additionally, two distinct peaks at 1668 cm^{-1} and 1479 cm^{-1} are assigned to NH_4^+ species formed via NH_3 protonation on Brønsted acid sites [52], whereas the bands at 1195 cm^{-1} and 1606 cm^{-1} correspond to NH_3 coordinated to Lewis acid sites [50,53]. It is evident that the intensity of the Lewis acid site-related peaks is significantly higher than that of the Brønsted acid site peaks, indicating the dominant role of Lewis acidity in NH_3 adsorption on the AgCuSmTi catalyst. As the temperature increases, the intensities of these NH_3 adsorption features gradually decrease, suggesting progressive desorption and activation of NH_3. Notably, the spectral at 1308 cm^{-1} and 1520 cm^{-1} can be assigned to the formation of -NH_2 species generated via dehydrogenation of NH_3 [54,55]. Furthermore, as the temperature increases, a new band emerges at 1429 cm^{-1} in the DRIFTS spectrum of the AgCuSmTi catalyst (Figure 7a), which is absent in the CuSmTi catalyst (Figure S6). This spectral feature can be attributed to the formation of -NH species on the Ag-doped catalyst surface [56]. -NH intermediates are likely involved in subsequent redox reactions with NO molecules, potentially leading to the formation of N_2O. This observation provides a plausible explanation for the reduced N_2 selectivity observed upon Ag doping.

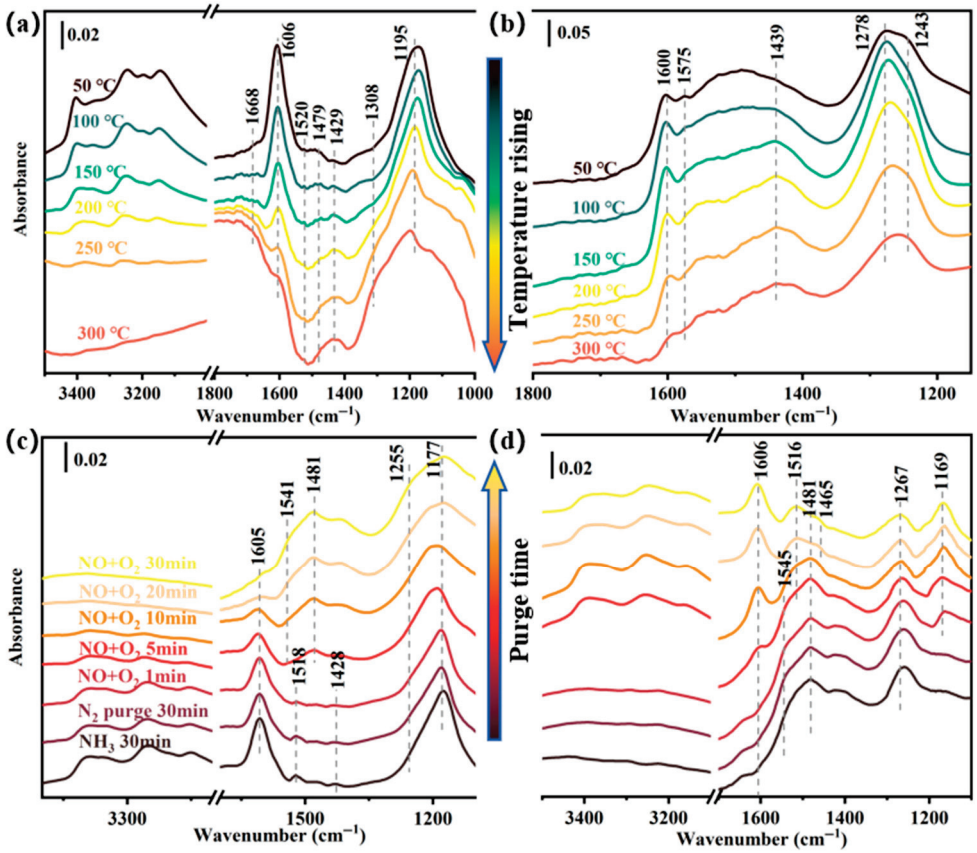


Figure 7. In situ DRIFTS sectra of AgCuSmTi catalyst under various reaction conditions: NH_3 adsorption (**a**) and NO + O_2 adsorption at temperatures ranging from 50 to 300 °C (**b**). Reaction between pre-adsorbed NH_3 species and NO + O_2 at 150 °C for 30 min (**c**) and reaction of NH_3 with pre-adsorbed NO_x species at 150 °C for 30 min (**d**). Gas composition: [NH_3] = [NO] = 500 ppm (when used), 5 vol% O_2 (when used), and N_2 as balance.

To further explore the interaction between NO and O_2 on the catalyst surface, in situ DRIFTS analysis of NO + O_2 adsorption was also conducted under the same temperature conditions. The results are shown in Figure 7b. Several nitrate species were identified based on their characteristic vibrational frequencies. The bands at 1600 cm^{-1} and 1243 cm^{-1} are attributed to bridged nitrate species [57,58], while the peak at 1575 cm^{-1} corresponds to bidentate nitrates [59]. The signals at 1439 cm^{-1} and 1278 cm^{-1} are associated with monodentate nitrate species [15,60]. As clearly observed in the spectra, the intensity of the monodentate nitrate peaks is significantly higher compared to that of bridged and bidentate nitrates. According to previous studies, the preferential formation of monodentate nitrates is beneficial for enhancing low-temperature NH_3-SCR performance [61,62]. This finding supports the conclusion that the AgCuSmTi catalyst exhibits excellent catalytic activity at low temperatures.

To elucidate the reaction mechanism of NH_3-SCR over the AgCuSmTi catalyst, in situ DRIFTS transient experiments were carried out. In the first set of experiments, NO + O_2 was introduced after NH_3 had been pre-adsorbed on the catalyst surface. The results are presented in Figure 7c. Following NH_3 pre-adsorption on the AgCuSmTi catalyst, characteristic peaks corresponding to Lewis acid sites (L-acid) were observed at 1177 cm^{-1} and 1605 cm^{-1}, along with a peak at 1518 cm^{-1} attributed to -NH_2 species and another at 1428 cm^{-1} assigned to -NH species. After 30 min of N_2 purging, the intensities of the L-acid-related peaks slightly decreased, indicating that weakly physisorbed NH_3 was partially desorbed. Upon introduction of NO + O_2 for 1 min, slight decreases in the intensities of the L-acid and -NH_3 peaks were observed, suggesting that gaseous NO and O_2 reacted with adsorbed NH_3 species, consistent with an Eley–Rideal (E-R) reaction mechanism. At 5 min after NO + O_2 exposure, new spectral features emerged corresponding to nitrate species, bridged nitrate (1255 cm^{-1}), monodentate nitrate (1481 cm^{-1}), and bidentate nitrate (1541 cm^{-1}), confirming successful adsorption of NO on the catalyst surface [16]. As the reaction time increased, the intensities of these nitrate-related peaks continued to rise, while the peak at 1605 cm^{-1} (attributed to L-acid sites) gradually diminished and eventually disappeared after 30 min. The reaction occurring 5 min after NO + O_2 introduction can be interpreted as the interaction between adsorbed NH_3 and adsorbed NO species, indicating that a Langmuir–Hinshelwood (L-H) mechanism also operates on the catalyst surface. In summary, the AgCuSmTi catalyst exhibits both the E-Rand L-H mechanisms during the NH_3-SCR process.

To further validate the above findings, a second set of experiments was conducted with a reversed reactant introduction order, where NH_3 was introduced after NO + O_2 had been pre-adsorbed on the catalyst. The results are shown in Figure 7d. Following 30 min of NO + O_2 pre-adsorption, characteristic peaks corresponding to bidentate nitrate (1545 cm^{-1}) and monodentate nitrate (1481 cm^{-1} and 1267 cm^{-1}) were clearly observed. After introducing NH_3 for 1 min, a new peak at 1169 cm^{-1} appeared, which is associated with L-acid centers. By 5 min, the intensities of the nitrate-related bands began to decrease, while signals corresponding to -NH_2 species and Brønsted acid (B-acid) centers emerged. This evolution indicates that the adsorbed NO species interacted with the incoming NH_3 via the L-H mechanism.

Figure 8 presents the proposed reaction pathway for the AgCuSmTi catalyst during the simultaneous removal of NO and CO. During the CO oxidation process, CO molecules adsorbed on the catalyst surface react with lattice oxygen to form either CO_2 or carbonate species. Upon desorption of CO_2, oxygen vacancies are generated, which are subsequently replenished by molecular oxygen, thereby facilitating continuous CO oxidation through lattice oxygen migration [63]. The detailed reaction mechanism is summarized as follows:

$$CO(gas) \rightarrow CO(ads)$$

$$CO(ads) + O^{2-}(latt) \rightarrow CO_2(g) + \square v$$

$$CO(ads) + 2O^{2-}(latt) \rightarrow CO_3^{2-} + \square v$$

$$CO_3^{2-} \rightarrow CO_2 + O^{2-}$$

$$O_2(g) + \square v \rightarrow 2O^{2-}(latt)$$

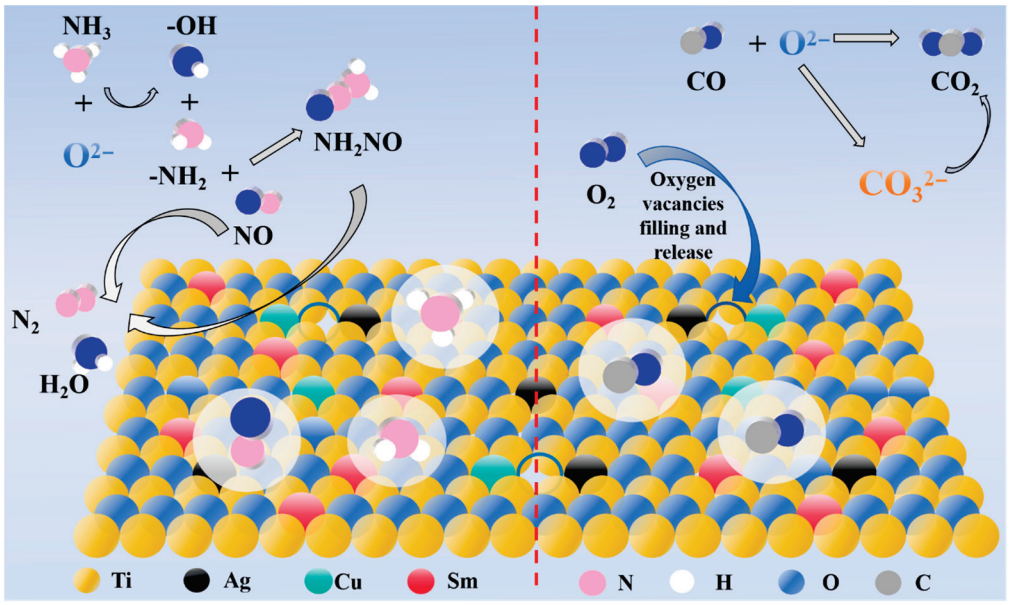


Figure 8. Schematic illustration of the NH_3-SCR and CO oxidation mechanisms occurring on the AgCuSmTi catalytic system.

Here, "□v" represents an oxygen vacancy.

The NH_3-SCR reaction mechanism over the AgCuSmTi catalyst is predominantly governed by the L-H mechanism, with the E-R mechanism playing a secondary role. In this process, gaseous NH_3 is adsorbed and activated on the catalyst surface to form -NH_2 intermediates (Equations (1)–(4)). Activated lattice oxygen facilitates the generation of -NH_2 species and enhances the redox cycling during the reaction. Subsequently, the -NH_2 intermediate reacts with either gaseous NO (Equation (5)) or adsorbed nitrate species (Equations (6) and (7)) to yield N_2 and H_2O. During the reaction, the -NH_2 species can undergo further dehydrogenation to form -NH intermediates, which then react with NO species to produce N_2O (Equations (8) and (9)). The formation of N_2O reduces the overall N_2 selectivity of the catalyst.

The detailed reaction mechanism is summarized as follows:

$$NH_3(g) \rightarrow NH_3(ads) \quad (1)$$

$$O_2(g) \rightarrow O_2(latt) \quad (2)$$

$$O_2(latt) \rightarrow 2O^{2-} \quad (3)$$

$$NH_3(ads) + O^{2-} \rightarrow -NH_2(ads) + -OH(ads) \quad (4)$$

$$-NH_2(ads) + NO(g) \rightarrow N_2 + H_2O \quad (5)$$

$$NO(g) \rightarrow NO(ads) \quad (6)$$

$$-NH_2(ads) + NO(ads) \rightarrow NH_2NO \rightarrow N_2 + H_2O \quad (7)$$

$$-NH_2(ads) + O^{2-} \rightarrow -NH(ads) + -OH(ads) \quad (8)$$

$$-NH(ads) + NO(g) \rightarrow N_2O + H^+ \quad (9)$$

3. Experimental Section

3.1. Catalyst Preparation

All catalysts were synthesized using the sol–gel method. In a typical procedure, 25.2 mL of n-butanol and 2.8 mL of glacial acetic acid were first mixed uniformly, followed by the gradual addition of 2.4 mL of deionized water under continuous stirring for 30 min to obtain solution A. Subsequently, 1.88 g of $Sm(NO_3)_3 \cdot 6H_2O$, 0.68 g of $Cu(NO_3)_2 \cdot 3H_2O$, and a precisely weighed amount of $AgNO_3$ were added to solution A. The mixture was stirred continuously until complete dissolution of all components. Then, 9.6 mL of titanium tetrabutyltitanate ($C_{16}H_{36}O_4Ti$) was slowly introduced into the homogeneous solution, which was further stirred at room temperature for 3 h to obtain a viscous gel-like solution. The obtained sol was then aged at ambient temperature until gelation occurred. Afterward, the gel was transferred to an oven and dried at 110 °C overnight. Finally, the dried precursor was calcined in a muffle furnace at 500 °C for 4 h to obtain the Ag_xCuSmTi composite metal oxide catalysts with different Ag loadings (x = 0.5, 0.8, 1.0, 1.2, 1.5).

For comparative analysis, other catalytic systems were prepared following similar procedures. In one case, 9.6 mL of $C_{16}H_{36}O_4Ti$ was added directly to solution A without incorporating any metal nitrates. The mixture was then dried and calcined under the same conditions to yield pure TiO_2. Additionally, three reference catalysts, SmTi, CuSmTi, and AgSmTi, were synthesized by sequentially adding the following combinations to solution A: (1) 1.88 g of $Sm(NO_3)_3 \cdot 6H_2O$, (2) 1.88 g of $Sm(NO_3)_3 \cdot 6H_2O$ and 0.68 g of $Cu(NO_3)_2 \cdot 3H_2O$, and (3) 1.88 g of $Sm(NO_3)_3 \cdot 6H_2O$ and a certain amount of $AgNO_3$. Each mixture was processed through the same drying and calcination steps as described above.

3.2. Catalyst Activity Test

The catalytic performance was evaluated using a fixed-bed reactor system. Detailed descriptions of the experimental setup, operating procedures, test conditions, and conversion rate calculations are provided in the Supporting Information.

3.3. Reagents and Gases

The reagents used in the preparation of the catalysts and the gases employed in the evaluation of their catalytic performance are listed in the Supporting Information.

3.4. Catalyst Characterization

The physical properties of the catalyst were investigated using a range of characterization techniques, including X-ray diffraction (XRD), N_2 adsorption, scanning electron microscopy (SEM), transmission electron microscopy (TEM), and Raman spectroscopy. Furthermore, the redox properties and acidic characteristics of the catalyst were systematically analyzed using X-ray photoelectron spectroscopy (XPS), H_2 temperature-programmed reduction (H_2-TPR), O_2 temperature-programmed desorption (O_2-TPD), NH_3 temperature-programmed desorption (NH_3-TPD), electron paramagnetic resonance (EPR), and in situ DRIFTS. Additional experimental details are provided in the Supporting Information.

4. Conclusions

This study presents an innovative approach in which Ag is introduced to modify the CuSmTi catalyst, resulting in the successful development of a dual-functional AgCuSmTi catalyst capable of effectively regulating oxygen structure. A combination of characterization techniques, including XRD, N_2 adsorption, and XPS, revealed a pronounced synergistic interaction between Ag and Cu, which plays a critical role in enhancing the

catalyst's low-temperature activity. Firstly, the Ag-Cu synergy significantly improves the physical properties of the catalyst by optimizing the dispersion of active sites, thereby establishing a structural foundation for its superior performance. Secondly, this synergistic effect markedly enhances the mobility of lattice oxygen. The highly active lattice oxygen not only facilitates redox cycling during the reaction but also accelerates electron transfer between metal species. Furthermore, the Ag-Cu interaction effectively modulates the acidic properties of the catalyst surface, increasing the density of Lewis acid sites, which are particularly favorable for the NH_3-SCR reaction. This enhancement promotes the adsorption and activation of reactant molecules, contributing to improved catalytic performance. These structural and chemical modifications significantly enhanced the performance of the AgCuSmTi catalyst, enabling complete conversion of NO and CO at temperatures as low as 150 °C and 175 °C, respectively, along with excellent N_2 selectivity. To further elucidate the underlying reaction mechanisms, in situ DRIFTS studies were conducted for both the NH_3-SCR and CO oxidation reactions. The results indicate that the NH_3-SCR process predominantly follows the L-H mechanism, with the E-R mechanism also playing a secondary role. Meanwhile, the CO oxidation reaction proceeds via the MvK mechanism. Overall, the results presented herein offer both a fundamental understanding and a promising theoretical foundation for the simultaneous elimination of nitrogen oxides and carbon monoxide from low-temperature industrial flue gases.

Supplementary Materials: The following supporting information can be downloaded at https://www.mdpi.com/article/10.3390/catal15070674/s1, Figure S1: NO_x conversion, N_2 selectivity, and CO conversion of catalysts with different proportions; Figure S2: TOF values for NO and CO conversions of the catalyst; Figure S3: Stability test (20 h) of AgCuSmTi catalyst at 150 °C and 175 °C; Figure S4: TEM spectrum of CuSmTi catalyst; Figure S5: N_2 adsorption and desorption isotherms and pore size distribution curves of catalysts; Figure S6: In situ DRIFTS on CuSmTi catalyst: changes in the NH_3 surface reaction with temperature when NH_3 is continuously introduced; Table S1: Summary of preparation methods, operating reaction conditions, catalytic performance metrics, and reaction mechanism for Cu-based catalysts in NO_x and CO abatement processes [11,15–17,21–26,38,64]; Table S2: Physical properties of catalysts; Table S3: Chemical state of Ag species on catalyst surface; Table S4: Distribution of desorbed oxygen species of catalyst.

Author Contributions: Conceptualization, R.L. and G.Z.; methodology, R.L. and J.W.; software, R.L.; validation, R.L., B.J. and X.L.; formal analysis, R.L.; investigation, R.L. and Y.W.; resources, G.Z. and J.L.; data curation, R.L. and G.L.; writing—original draft preparation, R.L.; writing—review and editing, G.Z. and J.L.; visualization, R.L. and Y.Z.; supervision, G.Z. and J.L.; project administration, G.Z. and J.L.; funding acquisition, J.L., G.Z., Y.Z. and Y.W. All authors have read and agreed to the published version of the manuscript.

Funding: This work was supported by the Key Technologies Research and Development Program, China (No. 2022YFC3701900) and Applied Basic Research Project of Shanxi Province (Nos. 202203021211178, 202303021211032, 202303021211034, and 202403021211217).

Data Availability Statement: The data presented in this study are available on request from the corresponding authors.

Conflicts of Interest: The authors declare no competing financial interest.

References

1. Li, C.; Han, Q.; Zhu, T.; Xu, W. Catalytic NO Reduction by CO over Ca–Fe Oxides in the Presence of O_2 with Sintering Flue Gas Circulation. *Ind. Eng. Chem. Res.* **2020**, *59*, 20624–20629. [CrossRef]
2. Gan, L.; Shi, W.; Li, K.; Chen, J.; Peng, Y.; Li, J. Synergistic Promotion Effect between NOx and Chlorobenzene Removal on MnOx–CeO_2 Catalyst. *ACS Appl. Mater. Interfaces* **2018**, *10*, 30426–30432. [CrossRef]

3. Qiao, B.; Wang, A.; Yang, X.; Allard, L.F.; Jiang, Z.; Cui, Y.; Liu, J.; Li, J.; Zhang, T. Single-atom catalysis of CO oxidation using Pt1/FeO_x. *Nat. Chem.* **2011**, *3*, 634–641. [CrossRef]
4. Jiang, L.; Xu, Y.; Jiang, W.; Pu, Y.; Yang, L.; Dai, Z.; Yao, L. The promotion of NH3-SCR performance by AC addition on Mn-Fe/Z catalyst. *Sep. Purif. Technol.* **2023**, *322*, 124274. [CrossRef]
5. Zhu, M.; Lai, J.-K.; Tumuluri, U.; Wu, Z.; Wachs, I.E. Nature of Active Sites and Surface Intermediates during SCR of NO with NH3 by Supported V_2O_5–WO_3/TiO_2 Catalysts. *J. Am. Chem. Soc.* **2017**, *139*, 15624–15627. [CrossRef]
6. Choi, J.-H.; Kim, J.-H.; Bak, Y.-C.; Amal, R.; Scott, J. Pt-V_2O_5-WO_3/TiO_2 catalysts supported on SiC filter for NO reduction at low temperature. *Korean J. Chem. Eng.* **2005**, *22*, 844–851. [CrossRef]
7. Wang, Y.-Z.; Zhang, J.-L.; Liu, Z.-J.; Du, C.-B. Recent Advances and Research Status in Energy Conservation of Iron Ore Sintering in China. *JOM* **2017**, *69*, 2404–2411. [CrossRef]
8. Dey, S.; Dhal, G.C.; Mohan, D.; Prasad, R. Advances in transition metal oxide catalysts for carbon monoxide oxidation: A review. *Adv. Compos. Hybrid. Mater.* **2019**, *2*, 626–656. [CrossRef]
9. Li, X.; Ren, S.; Jiang, Y.; Chen, Z.; Wang, L.; Liu, M.; Chen, T. In situ IR spectroscopy study of NO removal over CuCe catalyst for CO-SCR reaction at different temperature. *Catal. Today* **2023**, *418*, 114082. [CrossRef]
10. Hamada, H.; Haneda, M. A review of selective catalytic reduction of nitrogen oxides with hydrogen and carbon monoxide. *Appl. Catal. A Gen.* **2012**, *421–422*, 1–13. [CrossRef]
11. Zeng, Y.; Rong, W.; Zhang, S.; Wang, Y.; Zhong, Q. Promoting NH_3-SCR denitration via CO oxidation over CuO promoted V_2O_5-WO_3/TiO_2 catalysts under oxygen-rich conditions. *Fuel* **2022**, *323*, 124357. [CrossRef]
12. Zhang, X.; Zhang, G.; Liu, J.; Li, G.; Zhao, Y.; Wang, Y.; Lv, Y. Effects of defective structure originating from N incorporation-evaporation of Co-based biomass carbon catalysts on methane dry reforming. *Fuel* **2024**, *357*, 129752. [CrossRef]
13. Wang, X.; Sun, Y.; Han, F.; Zhao, Y. Effect of Fe addition on the structure and SCR reactivity of one-pot synthesized Cu-SSZ-13. *J. Environ. Chem. Eng.* **2022**, *10*, 107888. [CrossRef]
14. Shen, Z.; Xing, X.; She, Y.; Wang, S.; Lv, M.; Li, J.; Li, H. Revealing of K and SO_2 poisoning mechanism on $CuCeO_x$ catalyst for low-temperature CO oxidation. *Chem. Eng. J.* **2024**, *485*, 149373. [CrossRef]
15. Liu, Q.; Mi, J.; Chen, X.; Wang, S.; Chen, J.; Li, J. Effects of phosphorus modification on the catalytic properties and performance of CuCeZr mixed metal catalyst for simultaneous removal of CO and NO_x. *Chem. Eng. J.* **2021**, *423*, 130228. [CrossRef]
16. Shen, Z.; Xing, X.; She, Y.; Guo, P.; Ren, S.; Niu, W.; Li, J.; Li, H.; Meng, H. Unveiling the promoting mechanism of Mo on the performance of $CuCeO_x$ catalyst for simultaneously NH_3-SCR denitration and CO oxidation under oxygen-rich conditions. *Sep. Purif. Technol.* **2025**, *355*, 129561. [CrossRef]
17. Lv, D.; Liu, J.; Zhang, G.; Wang, Y.; Zhao, Y.; Li, G. Novel insights for simultaneous NOx and CO Removal: Cu^+-Sm^{3+}-Ov-Ti^{4+} asymmetric active site promoting NH3-SCR coupled with CO oxidation reaction. *Chem. Eng. J.* **2024**, *481*, 148534. [CrossRef]
18. Liu, Y.; Zhou, X.; Zhan, J.; Zhang, X.; Lian, H.-Y.; Zhou, H.; Yi, X.; Yang, H.-H.; Shan, J. Enhancing water resistance of α-MnO_2 catalyst for efficient airborne benzene oxidation at mild temperatures via facile Ag incorporation. *J. Environ. Chem. Eng.* **2023**, *11*, 110725. [CrossRef]
19. Rao, R.; Liang, H.; Hu, C.; Dong, H.; Dong, X.; Tang, Y.; Fang, S.; Ling, Q. A melamine-assisted pyrolytic synthesis of Ag-CeO_2 nanoassemblys for CO oxidation: Activation of Ag-CeO_2 interfacial lattice oxygen. *Appl. Surf. Sci.* **2022**, *571*, 151283. [CrossRef]
20. Md Saad, S.K.; Ali Umar, A.; Ali Umar, M.I.; Tomitori, M.; Abd Rahman, M.Y.; Mat Salleh, M.; Oyama, M. Two-Dimensional, Hierarchical Ag-Doped TiO_2 Nanocatalysts: Effect of the Metal Oxidation State on the Photocatalytic Properties. *ACS Omega* **2018**, *3*, 2579–2587. [CrossRef]
21. Ren, S.; Li, X.; He, C.; Chen, L.; Wang, L.; Li, F. Surface tailoring on bifunctional CuO_x/MnO_2 catalyst to promote the selective catalytic reduction of NO with NH_3 and oxidation of CO with O_2. *Sep. Purif. Technol.* **2024**, *346*, 127471. [CrossRef]
22. Li, X.; Lai, C.; Zhang, Y.; Wang, S.; Ding, S. Bifunctional catalysts V-Cu/TiO_2 for selective catalytic reduction of NO_x and CO oxidation under oxygen-rich conditions. *Mol. Catal.* **2024**, *569*, 114574. [CrossRef]
23. Gui, R.; Xiao, J.; Gao, Y.; Li, Y.; Zhu, T.; Wang, Q. Simultaneously achieving selective catalytic reduction of NO_x with NH_3 and catalytic oxidation of CO with O_2 over one finely optimized bifunctional catalyst $Mn_2Cu_1Al_1O_x$ at low temperatures. *Appl. Catal. B Environ.* **2022**, *306*, 121104. [CrossRef]
24. Li, Z.; Cheng, H.; Zhang, X.; Ji, M.; Wang, S.; Wang, S. CuW/CeZr Catalysts: A Dual-Function Catalyst for Selective Catalytic Reduction of NO and CO Oxidation Under Oxygen-Rich Conditions. *Catal. Lett.* **2021**, *151*, 3361–3371. [CrossRef]
25. Wang, L.; Wang, B.; Guo, Y.; Zheng, Y.; Zhu, T. Interactions between CO oxidation and selective catalytic reduction of NO with NH_3 over Mn-based catalysts. *Catal. Sci. Technol.* **2022**, *12*, 4776–4788. [CrossRef]
26. Wang, J.; Xing, Y.; Su, W.; Li, K.; Zhang, W. Bifunctional Mn-Cu-CeOx/γ-Al_2O_3 catalysts for low-temperature simultaneous removal of NO_x and CO. *Fuel* **2022**, *321*, 124050. [CrossRef]
27. Resitoglu, I.A.; Keskin, A. Hydrogen applications in selective catalytic reduction of NOx emissions from diesel engines. *Int. J. Hydrog. Energy* **2017**, *42*, 23389–23394. [CrossRef]

28. Gao, C.; Shi, J.-W.; Fan, Z.; Wang, B.; Wang, Y.; He, C.; Wang, X.; Li, J.; Niu, C. "Fast SCR" reaction over Sm-modified MnO_x-TiO_2 for promoting reduction of NO_x with NH_3. *Appl. Catal. A Gen.* **2018**, *564*, 102–112. [CrossRef]
29. Wang, B.; Wang, M.; Han, L.; Hou, Y.; Bao, W.; Zhang, C.; Feng, G.; Chang, L.; Huang, Z.; Wang, J. Improved Activity and SO_2 Resistance by Sm-Modulated Redox of $MnCeSmTiO_x$ Mesoporous Amorphous Oxides for Low-Temperature NH_3-SCR of NO. *ACS Catal.* **2020**, *10*, 9034–9045. [CrossRef]
30. Sun, H.; Wang, H.; Qu, Z. Construction of CuO/CeO_2 Catalysts via the Ceria Shape Effect for Selective Catalytic Oxidation of Ammonia. *ACS Catal.* **2023**, *13*, 1077–1088. [CrossRef]
31. Djaoued, Y.; Badilescu, S.; Ashrit, P.V.; Bersani, D.; Lottici, P.P.; Robichaud, J. Study of Anatase to Rutile Phase Transition in Nanocrystalline Titania Films. *J. Sol-Gel Sci. Technol.* **2002**, *24*, 255–264. [CrossRef]
32. Alhomoudi, I.A.; Newaz, G. Residual stresses and Raman shift relation in anatase TiO_2 thin film. *Thin Solid. Film.* **2009**, *517*, 4372–4378. [CrossRef]
33. Choudhury, B.; Dey, M.; Choudhury, A. Defect generation, d-d transition, and band gap reduction in Cu-doped TiO_2 nanoparticles. *Int. Nano Lett.* **2013**, *3*, 25. [CrossRef]
34. Liu, H.; Fan, Z.; Sun, C.; Yu, S.; Feng, S.; Chen, W.; Chen, D.; Tang, C.; Gao, F.; Dong, L. Improved activity and significant SO_2 tolerance of samarium modified CeO_2-TiO_2 catalyst for NO selective catalytic reduction with NH_3. *Appl. Catal. B Environ.* **2019**, *244*, 671–683. [CrossRef]
35. Guo, X.; Lin, F.; Gao, M.; Dai, Q.; Zhan, W.; Wang, L.; Guo, Y.; Wang, A.; Guo, Y. Enhanced catalytic performance and N_2 yield of Ag/CeO_2 catalyst by Cu modification for NVOCs removal. *Chem. Eng. J.* **2024**, *488*, 151117. [CrossRef]
36. Chen, C.; Cao, Y.; Liu, S.; Chen, J.; Jia, W. SCR catalyst doped with copper for synergistic removal of slip ammonia and elemental mercury. *Fuel Process. Technol.* **2018**, *181*, 268–278. [CrossRef]
37. Wang, M.; Ren, S.; Jiang, Y.; Su, B.; Chen, Z.; Liu, W.; Yang, J.; Chen, L. Insights into co-doping effect of Sm and Fe on anti-Pb poisoning of Mn-Ce/AC catalyst for low-temperature SCR of NO with NH_3. *Fuel* **2022**, *319*, 123763. [CrossRef]
38. Zang, P.; Liu, J.; He, Y.; Zhang, G.; Li, G.; Wang, Y.; Lv, Y. LDH-derived preparation of CuMgFe layered double oxides for NH_3-SCR and CO oxidation reactions: Performance study and synergistic mechanism. *Chem. Eng. J.* **2022**, *446*, 137414. [CrossRef]
39. Liu, S.; Xue, W.; Ji, Y.; Xu, W.; Chen, W.; Jia, L.; Zhu, T.; Zhong, Z.; Xu, G.; Mei, D.; et al. Interfacial oxygen vacancies at Co_3O_4-CeO_2 heterointerfaces boost the catalytic reduction of NO by CO in the presence of O_2. *Appl. Catal. B: Environ.* **2023**, *323*, 122151. [CrossRef]
40. Yao, X.; Zhang, L.; Li, L.; Liu, L.; Cao, Y.; Dong, X.; Gao, F.; Deng, Y.; Tang, C.; Chen, Z.; et al. Investigation of the structure, acidity, and catalytic performance of $CuO/Ti_{0.95}Ce_{0.05}O_2$ catalyst for the selective catalytic reduction of NO by NH_3 at low temperature. *Appl. Catal. B Environ.* **2014**, *150–151*, 315–329. [CrossRef]
41. Qu, Z.; Wang, Z.; Quan, X.; Wang, H.; Shu, Y. Selective catalytic oxidation of ammonia to N_2 over wire–mesh honeycomb catalyst in simulated synthetic ammonia stream. *Chem. Eng. J.* **2013**, *233*, 233–241. [CrossRef]
42. Wang, X.; Qin, M.; Xu, Y.; Li, Q. Improvement of Cu-SAPO-34 hydrothermal stability by tuning P/Al ratio for selective catalytic reduction of NO by NH_3. *J. Colloid. Interface Sci.* **2023**, *638*, 686–694. [CrossRef] [PubMed]
43. Yang, B.; Li, Z.; Huang, Q.; Chen, M.; Xu, L.; Shen, Y.; Zhu, S. Synergetic removal of elemental mercury and NO over $TiCe_{0.25}Sn_{0.25}O_x$ catalysts from flue gas: Performance and mechanism study. *Chem. Eng. J.* **2019**, *360*, 990–1002. [CrossRef]
44. Kang, R.; Wei, X.; Bin, F.; Wang, Z.; Hao, Q.; Dou, B. Reaction mechanism and kinetics of CO oxidation over a $CuO/Ce_{0.75}Zr_{0.25}O_2$-δ catalyst. *Appl. Catal. A Gen.* **2018**, *565*, 46–58. [CrossRef]
45. Qi, L.; Yu, Q.; Dai, Y.; Tang, C.; Liu, L.; Zhang, H.; Gao, F.; Dong, L.; Chen, Y. Influence of cerium precursors on the structure and reducibility of mesoporous CuO-CeO_2 catalysts for CO oxidation. *Appl. Catal. B Environ.* **2012**, *119–120*, 308–320. [CrossRef]
46. Davó-Quiñonero, A.; Bailón-García, E.; López-Rodríguez, S.; Juan-Juan, J.; Lozano-Castelló, D.; García-Melchor, M.; Herrera, F.C.; Pellegrin, E.; Escudero, C.; Bueno-López, A. Insights into the Oxygen Vacancy Filling Mechanism in CuO/CeO_2 Catalysts: A Key Step Toward High Selectivity in Preferential CO Oxidation. *ACS Catal.* **2020**, *10*, 6532–6545. [CrossRef]
47. Lu, J.; Wang, J.; Zou, Q.; He, D.; Zhang, L.; Xu, Z.; He, S.; Luo, Y. Unravelling the Nature of the Active Species as well as the Doping Effect over Cu/Ce-Based Catalyst for Carbon Monoxide Preferential Oxidation. *ACS Catal.* **2019**, *9*, 2177–2195. [CrossRef]
48. Ma, Y.; Li, Y.; Liang, P.; Min, X.; Sun, T. SnO2-modified $CuMnO_x$ catalysts for humid CO oxidation at low temperature. *J. Ind. Eng. Chem.* **2024**, *138*, 300–310. [CrossRef]
49. Sasmaz, E.; Wang, C.; Lance, M.J.; Lauterbach, J. In situ spectroscopic investigation of a Pd local structure over Pd/CeO_2 and Pd/MnOx–CeO_2 during CO oxidation. *J. Mater. Chem. A* **2017**, *5*, 12998–13008. [CrossRef]
50. Dann, E.K.; Gibson, E.K.; Blackmore, R.H.; Catlow, C.R.A.; Collier, P.; Chutia, A.; Erden, T.E.; Hardacre, C.; Kroner, A.; Nachtegaal, M.; et al. Structural selectivity of supported Pd nanoparticles for catalytic NH_3 oxidation resolved using combined operando spectroscopy. *Nat. Catal.* **2019**, *2*, 157–163. [CrossRef]
51. Chen, Y.; Yan, H.; Teng, W.; Li, J.; Liu, W.; Ren, S.; Yang, J.; Liu, Q. Comparative study on N_2O formation pathways over bulk MoO_3 and MoO_{3-x} nanosheets decorated Fe_2O_3-containing solid waste NH_3-SCR catalysts. *Fuel* **2023**, *337*, 127210. [CrossRef]

52. Zhang, Z.; Li, R.; Wang, M.; Li, Y.; Tong, Y.; Yang, P.; Zhu, Y. Two steps synthesis of $CeTiO_x$ oxides nanotube catalyst: Enhanced activity, resistance of SO_2 and H_2O for low temperature NH_3-SCR of NO_x. *Appl. Catal. B Environ.* **2021**, *282*, 119542. [CrossRef]
53. Hao, Z.; Jiao, Y.; Shi, Q.; Zhang, H.; Zhan, S. Improvement of NH_3-SCR performance and SO_2 resistance over Sn modified $CeMoO_x$ electrospun fibers at low temperature. *Catal. Today* **2019**, *327*, 37–46. [CrossRef]
54. Wang, X.; Peng, J.; Wang, Y.; Guo, N.; Li, T.; Li, H.; Ren, D.; Gui, K. Poisoning mechanism of different Cd precursors on Fe-Ce/TiO_2 catalyst for selective catalytic reduction of NO_x with NH_3. *J. Environ. Chem. Eng.* **2023**, *11*, 109625. [CrossRef]
55. Jia, B.; Liu, J.; Kang, J.; Zhang, G.; Lv, D.; Wang, Y. Investigating NH_3-SCR coupled with CO oxidation reaction mechanisms on titanium nanotube-loaded CuMnFe composite metal catalysts. *Appl. Surf. Sci.* **2024**, *652*, 159299. [CrossRef]
56. Liu, Y.; Gu, T.; Weng, X.; Wang, Y.; Wu, Z.; Wang, H. DRIFT Studies on the Selectivity Promotion Mechanism of Ca-Modified Ce-Mn/TiO_2 Catalysts for Low-Temperature NO Reduction with NH_3. *J. Phys. Chem. C* **2012**, *116*, 16582–16592. [CrossRef]
57. Yao, W.; Wang, X.; Liu, Y.; Wu, Z. CeOP material supported CeO_2 catalysts: A novel catalyst for selective catalytic reduction of NO with NH_3 at low temperature. *Appl. Surf. Sci.* **2019**, *467–468*, 439–445. [CrossRef]
58. Liu, F.; He, H.; Zhang, C.; Shan, W.; Shi, X. Mechanism of the selective catalytic reduction of NO_x with NH_3 over environmental-friendly iron titanate catalyst. *Catal. Today* **2011**, *175*, 18–25. [CrossRef]
59. Wu, Z.; Jiang, B.; Liu, Y.; Wang, H.; Jin, R. DRIFT Study of Manganese/Titania-Based Catalysts for Low-Temperature Selective Catalytic Reduction of NO with NH_3. *Environ. Sci. Technol.* **2007**, *41*, 5812–5817. [CrossRef]
60. Chen, L.; Li, J.; Ge, M. DRIFT Study on Cerium−Tungsten/Titiania Catalyst for Selective Catalytic Reduction of NO_x with NH_3. *Environ. Sci. Technol.* **2010**, *44*, 9590–9596. [CrossRef]
61. Chen, Z.; Ren, S.; Wang, M.; Yang, J.; Chen, L.; Liu, W.; Liu, Q.; Su, B. Insights into samarium doping effects on catalytic activity and SO_2 tolerance of $MnFeO_x$ catalyst for low-temperature NH3-SCR reaction. *Fuel* **2022**, *321*, 124113. [CrossRef]
62. Han, L.; Cai, S.; Gao, M.; Hasegawa, J.Y.; Wang, P.; Zhang, J.; Shi, L.; Zhang, D. Selective Catalytic Reduction of NO_x with NH_3 by Using Novel Catalysts: State of the Art and Future Prospects. *Chem. Rev.* **2019**, *119*, 10916–10976. [CrossRef] [PubMed]
63. Ye, Z.; Liu, Y.; Nikiforov, A.; Ji, J.; Zhao, B.; Wang, J. The research on CO oxidation over Ce–Mn oxides: The preparation method effects and oxidation mechanism. *Chemosphere* **2023**, *336*, 139130. [CrossRef] [PubMed]
64. Li, X.; Ren, S.; Chen, Z.; Chen, L.; Wang, M.; Wang, L.; Wang, A. Promoting mechanism of CuO on catalytic performance of CeFe catalyst for simultaneous removal of NOx and CO. *Fuel* **2023**, *347*, 128435. [CrossRef]

Disclaimer/Publisher's Note: The statements, opinions and data contained in all publications are solely those of the individual author(s) and contributor(s) and not of MDPI and/or the editor(s). MDPI and/or the editor(s) disclaim responsibility for any injury to people or property resulting from any ideas, methods, instructions or products referred to in the content.

catalysts

MDPI

Review

Non-Noble Metal Catalysts for Efficient Formaldehyde Removal at Room Temperature

Yiqing Feng and Rui Wang *

School of Environmental Science and Engineering, Shandong University, Qingdao 266237, China
* Correspondence: wangrui@sdu.edu.cn

Abstract

This review examines the research progress on non-noble-metal-based catalysts for formaldehyde (HCHO) oxidation at room temperature. It begins with an introduction to the hazards of HCHO as an indoor pollutant and the urgency of its removal, comparing several HCHO removal technologies and highlighting the advantages of room-temperature catalytic oxidation. It delves into the classification, preparation methods, and regulation strategies for non-precious metal catalysts, with a focus on manganese-based, cobalt-based, and other transition metal-based catalysts. The effects of catalyst preparation methods, morphological structure, and specific surface area on catalytic performance are discussed, and the catalytic oxidation mechanisms of HCHO, including the Eley–Rideal, Langmuir–Hinshelwood, and Mars–van Krevelen mechanisms, are analyzed. Finally, the challenges faced by non-precious metal catalysts are summarized, such as issues related to the powder form of catalysts in practical applications, lower catalytic activity at room temperature, and insufficient research in the presence of multiple VOC molecules. Suggestions for future research directions are also provided.

Keywords: formaldehyde; non-noble metal catalyst; catalytic oxidation; room temperature; catalytic mechanism

1. Introduction

Formaldehyde (HCHO) is becoming one of the most concerning indoor pollutants, originating from building materials, decoration materials, furniture, and consumables [1–3]. Based on formaldehyde-inhalation-induced squamous cell carcinoma (SCC) in rats and human cancers, the International Agency for Research on Cancer (IARC) classifies HCHO as Group 1 (human carcinogens), because the carcinogenic disability adjusted life (DALY) factor of HCHO is much higher than that of indoor pollutants such as ammonia, benzene, or toluene [4,5]. Therefore, removing indoor HCHO is an urgent issue at present in order to ensure public health security. Currently, several approaches exist for eliminating HCHO, including adsorption [6–8], photocatalytic oxidation [9,10], plasma techniques [11,12], and thermal or low-temperature catalytic oxidation [13–15]. Among the above technologies, adsorption can only temporarily fix HCHO on the surface of porous materials, which may cause secondary pollution during desorption. For photocatalytic oxidation, plasma techniques, and thermal catalytic oxidation, external devices such as light sources, plasma emission devices, and heat sources may be used in practical operations, which may increase processing costs and energy consumption. For low-temperature catalysis, especially at room temperature, it is increasingly favored as it can efficiently convert HCHO into CO_2 and H_2O without the need for external devices.

The existing HCHO oxidation catalysts at room temperature are divided into two categories: noble metal catalysts and non-noble metal catalysts. Noble metal catalysts typically contain Au, Ag, and platinum group elements (such as Pt, Rh, Pd, Ru, etc.) [16–19], while noble metal catalysts are generally replaced by non-noble metals such as Co and Mn [1,2,20,21], or materials such as graphene [22,23] and carbon nanotubes [24,25]. Although the use of noble metal catalysts can achieve good results in HCHO removal, the low content in the Earth and high price of noble metals determine that noble metal catalysts cannot be widely applied. Non-noble metal catalysts, with their wide availability and low cost, are showing their potential in replacing noble metal catalysts for eliminating HCHO. In this work, a review on room temperature catalysts for HCHO oxidation, non-noble metal catalyst classification, preparation methods, and regulation strategies, the mechanism of room temperature catalytic oxidation of HCHO, current research progress, challenges, and research directions are systematically discussed.

2. Catalytic Materials

Sekine et al. [26] first used synthesized MnO_2 to efficiently degrade indoor HCHO. Subsequently, research on the use of transition metal oxides for HCHO oxidation has received widespread attention. Transition metal oxides have shown promising application prospects in the removal of volatile organic compounds due to their low cost and abundant reserves. So far, researchers have developed a large number of transition metal oxide-containing elements such as Mn, Co, and Cr. Among them, MnO_x and Co_3O_4 can be doped with other metal elements such as Ce, Sn, Cu, and Zr. As research deepens, the types of elements that can remove HCHO will become increasingly diverse.

2.1. Manganese-Based Catalysts

Mn-based catalysts have multiple valence states (+2, +3, +4, +6, +7, etc.), strong oxygen storage/release capacity, and excellent redox performance, and are considered among the most promising transition metal oxide catalysts [27]. Manganese compounds with different valence states have different physical and chemical properties and catalytic performance, and are therefore widely used in the removal of volatile organic compounds (VOCs) [28].

Since Sekine et al. [26] assembled activated carbon and MnO_x into a purification material, researchers have been more concerned with MnO_2 catalysts because their catalytic activity toward HCHO is stronger than that of other transition metal oxides. like Ag_2O, TiO_2, CeO_2, CoO, CuO, and V_2O_5 [29]. In fact, MnO_2 contains several structural forms, such as α, β, γ, δ, and ε. Among them, MnO_x catalysts with [MnO_6] octahedral structures have different physical and chemical properties, such as stronger adsorption desorption ability, more active sites, and larger surface area, which in turn determine the adsorption effect of the catalyst [3]. Zhang et al. [30] prepared α-, β-, γ-, and δ-MnO_2 catalysts and compared their activity in catalyzing HCHO. They found that the δ-MnO_2 catalyst had the best activity and could achieve almost complete HCHO conversion at lower temperatures. They also pointed out that it was the special two-dimensional layer tunnel structure, abundant active oxygen species, and lattice oxygen species on the δ-MnO_2 surface that led to the highest activity of the catalyst. Han et al. [31] synthesized a δ-MnO_2 catalyst for the catalytic oxidation of HCHO. Due to the highly defective structure of the catalyst, abundant hydroxyl groups, abundant lattice oxygen, and Mn^{3+} species, it has an almost 100% removal rate for HCHO. In addition to preparing the above structural forms, Wen et al. [32] prepared a MnO_x catalyst (MnO_x-PMMA-SSM) with 3D nanocomposite structure, which achieved a HCHO removal efficiency of up to 98.82% after 110 min at room temperature, and also had a long service life. The tunnel structure will also affect the catalytic effects of catalysts on HCHO to a certain extent. As shown in Figure 1, due to

different tunnel structures, there are some differences in the treatment effects of catalysts on HCHO, which are reflected in three completely different curves [33]. Except for regulating the tunnel structure, Tao et al. [34] prepared a special interconnected network structure M-MnO_2 for HCHO oxidation, consisting of δ-MnO_2 nanosheets and c-MnOOH nanowires, using a one-step hydrothermal method. After 10 h of oxidation of 100 ppm HCHO, its catalytic activity reached 50%. The special network structure provides sufficient surface active oxygen species and surface-adsorbed water, exhibiting excellent catalytic activity and stability toward HCHO at room temperature. It can be seen that for a single form of manganese-based catalyst, δ-MnO_2 has outstanding performance, with its unique structure and active oxygen species, and has become an excellent HCHO catalyst.

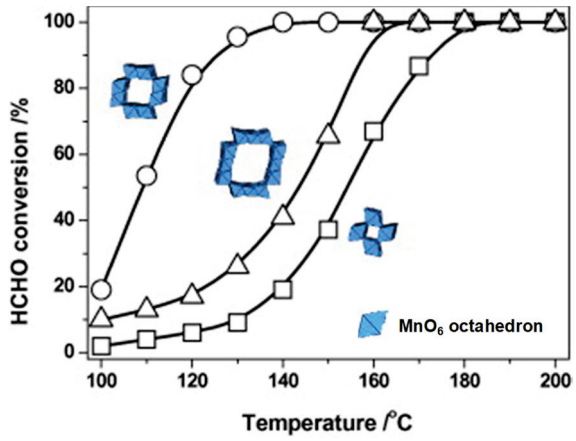


Figure 1. Tunnel effects of the 1 × 1, 2 × 2, and 3 × 3 tunnel manganese oxide catalysts (corresponding to right, middle, and left curves, respectively) on complete oxidation of HCHO. Reproduced with permission from [33].

In addition to single MnO_2-based catalysts, doping noble metals, rare earth elements, and transition or ordinary metal elements with MnO_2 to form a solid solution can increase the surface active sites, specific surface area, and redox ability of the catalyst, thereby enhancing the treatment effect on HCHO. Among them, CeO_2 is a good oxygen storage material. When CeO_2 is doped with MnO_2 in a certain proportion as a solid solution, this may change the oxidation state of Mn, thereby altering the physical and chemical properties of the catalyst itself. Zhang et al. [35] synthesized $MnCeO_x$ and analyzed the properties of the solid solution and the influence of water vapor on the catalytic effect of HCHO. As shown in Figure 2a, with the increase in processing time, $MnCeO_x$ has a significant improvement in the conversion rate of HCHO and ultimately stabilizes at around 80%. The results show that the catalytic performance of the $MnCeO_x$ catalyst is better than those of MnO_2 and CeO_2 alone, and even better than that of the mixture of MnO_2 and CeO_2. This is because the solid solution exhibits relatively abundant oxygen vacancies and the most surface lattice oxygen species, significantly enhancing the adsorption and redox performance. Additionally, from Figure 2b, we can observe that the catalyst can completely convert HCHO into CO_2 under conditions of relative humidity above 50%, which may be suitable for indoor air purification. In addition to combining Mn and Ce elements, Duan et al. [36] added Ag to prepare an Ag/Mn/CeO_2 catalyst for catalytic oxidation of low-concentration HCHO at room temperature. They showed that the introduction of Ag did not change the mesoporous structure of the Mn/CeO_2 catalyst, but reduced the pore size and specific surface area; meanwhile, the introduction of Ag increased the lattice defects and oxygen vacancies generated by the interaction between Ag and Mn/CeO_2. Therefore, the catalyst achieved a removal efficiency of 96.76% within 22 h, exhibiting high catalytic activity toward HCHO at room temperature.

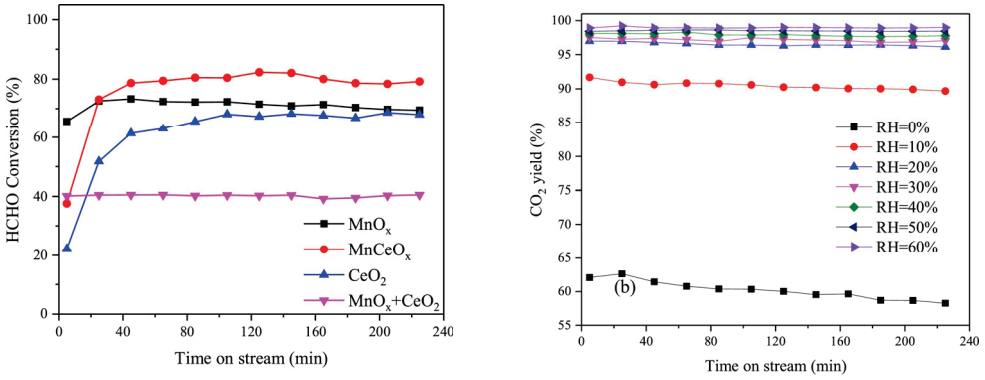


Figure 2. The effect of relative humidity on the $MnCeO_x$ catalyst: (**a**) Effect of catalyst type on HCHO conversion; (**b**) CO_2 yield of $MnCeO_x$ catalyst at different humidity. Reproduced with permission from [35].

Also, Xing et al. [37] synthesized a new type of K-Mn_3O_4@CeO_2 catalyst. It achieved a conversion rate of 99.3% for 10 mL of 40 mg/L HCHO solution at 30 °C, while also exhibiting strong cycling stability. Based on DFT calculations, it was found that K provides more active oxygen species and richer oxygen vacancies on the catalyst surface, enhancing the fluidity of lattice oxygen and the room temperature reduction performance of oxygen species, resulting in lower oxygen vacancy formation and HCHO adsorption energy in aqueous solution. Liu et al. [38] prepared MnCeNiOx (MCN) and treated it with FeO_x using the impregnation method to form an F-MCN catalyst. The results showed that under dry conditions, the F-MCN catalyst exhibited better HCHO conversion ability than the MCN and M_2CN catalysts, due to the rich Mn^{3+} and Ce^{3+} increasing the oxygen vacancies, surface adsorption strength, and S_{BET}, as well as strong interactions between Mn-Ce, Ce-Ni, and Fe-Mn mixed crystals. In addition, under wet conditions, the addition of water vapor enhances surface hydroxyl radicals, leading to complete oxidation of HCHO on the F-MCN catalyst at room temperature. Furthermore, the stability demonstrated by the 72 h continuous experiment shows the enormous potential for application of this new catalyst.

Mn can also be mixed with more components to synthesize more diverse HCHO catalysts. For instance, Jia et al. [39] developed a three-dimensional radiation nanostructure catalyst (Pt_{SA}-MnOOH/MnO_2) self-assembled by Pt single-atom anchored MnOOH/MnO_2 nanosheets using a two-step electrochemical method. Through the synergistic effect of active hydroxyl groups (OH*) and active oxygen species (O_2*) and the decomposition of intermediates, a long-term continuous HCHO removal rate (about 98%) was achieved within 100 h in a 15 ppm HCHO atmosphere at 25 °C and an hourly rate of 30000 mL/g_{cat}·h. Also, Zhu et al. [40] synthesized a series of CeO_2-x-MnO_x catalysts using Ce metal organic frameworks (MOFs) as precursors, and found that the gases released during the MOF pyrolysis process significantly affect the valence states of Ce and Mn, which is a key factor in catalytic activity. Furthermore, DFT results indicate that oxygen vacancies not only effectively suppress the charge loss of Mn and Ce atoms, but also significantly enhance the adsorption strength of CeO_2-x-MnO_x-2.5 for HCHO and O_2, thereby achieving a catalytic conversion rate of 63% at room temperature. In addition, Wang et al. [41] synthesized a Mn/HZSM-5 catalyst using an HZSM-5 molecular sieve as a carrier. The activity test results showed that the catalyst with 0.4% Mn/HZSM-5 had an HCHO removal rate close to 100% under stable conditions of 30 °C and 20 h. The analysis results also showed that Mn^{4+} and hydroxyl groups can provide more active sites for HCHO oxidation, and the interaction between the two enables HCHO to have good activity during the reaction process, effectively activating HCHO and oxygen. In addition, Mn^{4+} increases the concentration of

-OH on the catalyst surface, making it easier for the catalyst to adsorb and oxidize HCHO. Another interesting case is the one in which Wang et al. [42] used Al-Si-fiber-woven ceramic filter paper (CFP) as the substrate, $Mn(NO_3)_2$ as the oxidant, and glycine as the fuel, and in situ-coated Mn_2O_3 on it to prepare a Mn_2O_3/CFP catalyst. The Mn_2O_3/CFP catalyst was characterized by its more porous structure, higher oxidation-reduction ability, abundant surface active oxygen, and enhanced surface lattice oxygen mobility. The Mn_2O_3/CFP catalyst exhibits excellent HCHO oxidation performance with a high conversion rate (90%) of HCHO at room temperature. In addition, in the durability test conducted under room temperature dynamic flow mode, the Mn_2O_3/CFP catalyst maintained a high HCHO conversion rate of 66% within 11 days, demonstrating its potential in practical indoor air purification applications.

Generally speaking, manganese-based catalysts have shown great potential in the field of HCHO catalytic oxidation. Manganese's variable valence state and rich redox performance provide a broad space for catalyst design. From a single form of MnO_2 to doping modification and then to special preparation methods, by accurately adjusting the composition and structure of Mn-based catalysts, the catalytic oxidation efficiency of HCHO at room temperature can be effectively improved, providing an efficient solution for indoor air HCHO pollution control.

2.2. Cobalt-Based Catalysts

Cobalt, as a common transition metal, has been explored by researchers for its potential application in low-temperature HCHO catalytic oxidation. Co_3O_4, as a common cobalt oxide, has various forms including tubular, sheet-like, strip, rod, spherical, and porous [43–45]. It is precisely its diverse forms and structures that promote different chemical reactions and catalytic abilities due to the surface exposure of active sites. Bai et al. [46] synthesized nano-Co_3O_4, 2D-Co_3O_4, and 3D-Co_3O_4 catalysts and compared their performance in oxidizing HCHO. From the TEM image in Figure 3, it can be seen that nano-Co_3O_4 is composed of single crystals without pores, while 2D-Co_3O_4 and 3D-Co_3O_4 have polycrystalline pore walls, and all catalysts exhibit ordered mesopores while retaining the template structure during synthesis. Therefore, the catalytic activity order is 3D-Co_3O_4 > 2D-Co_3O_4 > nano-Co_3O_4, because 2D-Co_3O_4 and 3D-Co_3O_4 retain the mesoporous characteristics and channel structure of the hard template, and have a large specific surface area. In particular, 3D-Co_3O_4 contains abundant surface active oxygen species and the surface contains more Co^{3+}, which improves HCHO oxidation ability. Additionally Jiao et al. [47] synthesized Co_3O_4 porous nanofiber monolithic catalysts using heat-resistant polyacrylonitrile (PAN) as a template through electrospinning. At room temperature (10–12 ppm, 25 °C) and with a gas space velocity of 60000 $mL \cdot g^{-1}$ h^{-1}, the catalytic activity for HCHO exceeded 99%. At the same time, the authors used catalysts prepared by direct calcination as controls to further demonstrate the catalytic oxidation ability and stability of porous nanofiber catalysts. In general, for Co_3O_4, its different morphologies and structures (such as nano, two-dimensional, three-dimensional, etc.) have a significant impact on the catalytic activity. Studies show that Co_3O_4 catalysts with porous structures and high specific surface areas have higher HCHO oxidation ability.

In addition to utilizing Co_3O_4, synthesizing cobalt single atom catalysts (SACs) is also an interesting strategy, as SACs can achieve 100% atomic utilization and possess unique electronic/geometric structures [48]. Du et al. [49] synthesized a single Co atom on ultra-thin carbon nanosheets (Co-SAs/NCS), which has a two-dimensional graphene-like morphology, high specific surface area, and enhanced nitrogen doping level, providing many active sites to firmly fix separated Co atoms. Figure 4 intuitively demonstrates the excellent ability of the Co-SAs/NCS catalyst in both HCHO conversion rate and catalytic

activity, showing excellent application prospects. Mechanism studies also indicate that the planar structure of Co-N_4 enhances the ability to activate molecular oxygen, resulting in a removal rate of 86% for 500 ppm HCHO at room temperature. Zhang et al. [50] prepared a novel Co-SAC that can completely convert 50 ppm of HCHO at room temperature, and the catalyst remains stable for at least 120 h. DFT calculations and isotope experiments reveal that the excellent formic acid intermediate decomposition ability of Co-SACs is a key factor in obtaining excellent HCHO oxidation performance, which determines the kinetic rate of HCHO catalytic oxidation reactions. In conclusion, cobalt SACs have attracted much attention due to their 100% atomic utilization and unique electronic/geometric structure. Their special planar structure can enhance the activation ability of molecular oxygen, showing high removal rate and good stability for HCHO at room temperature.

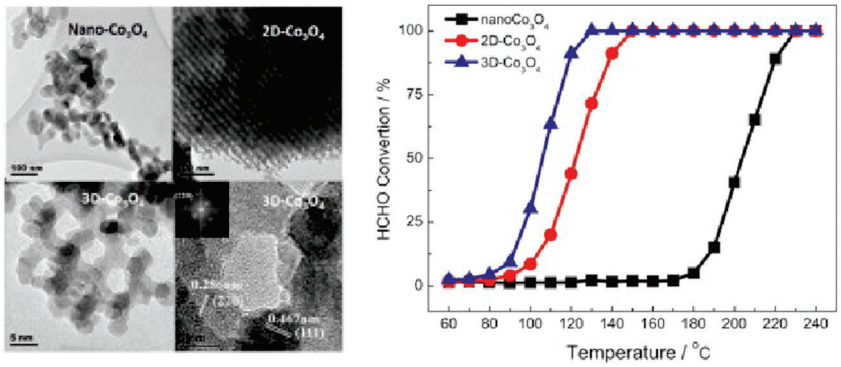


Figure 3. TEM images and HCHO conversions over 3D Co_3O_4 catalyst. Reproduced with permission from [46].

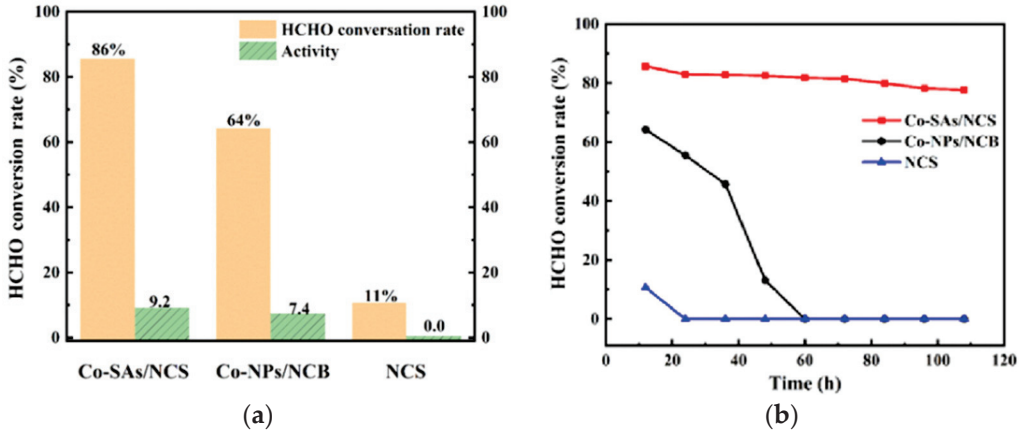


Figure 4. (**a**) HCHO conversion and specific activity of the catalysts tested after 12 h of reaction; and (**b**) stability of the as-prepared catalysts. Reproduced with permission from [49].

In summary, cobalt-based catalysts have great application potential in the field of low-temperature HCHO catalytic oxidation. The above studies show that the catalytic oxidation performance of cobalt-based catalysts for HCHO can be effectively improved by adjusting the morphology, structure, and composition of cobalt-based catalysts, which provides a variety of options for cobalt's application in indoor air HCHO purification.

2.3. Other Transition Metal-Based Catalysts

Besides Mn-based and Co-based catalysts, other transition metal-based catalysts are gradually receiving attention from researchers. The addition of other transition non-noble metals, such as Fe, Ni, Zn, etc., can not only replace the use of noble metals, but also enhance catalytic performance. Another reason is that they are easy to obtain and reduce

costs. For example, Chen et al. [1] synthesized a series of layered double hydroxides (LDHs) containing multiple bimetallic species (MgAl, ZnAl, NiAl, NiFe, and NiTi), among which the NiTi-LDH catalyst exhibited a nearly 100% HCHO removal rate and excellent water resistance and chemical stability. The abundant hydroxyl groups in LDH directly bind with HCHO to generate CO_2 and H_2O, even in the absence of O_2 and H_2O. Additionally, the coexistence of O_2 effectively reduces the reaction barrier for the dissociation of H_2O molecules, facilitating the formation of hydroxyl groups and their subsequent backfilling on the catalyst surface. Yang et al. [51] synthesized P-$Ce_xZr_{1-x}O_y$ (PCZ) mesoporous nanoparticle catalysts using Pluronic P123 as a template. The templating caused by P123 and the effective doping of Zr atoms adjusted the oxygen vacancies in the catalyst, changed the reduction characteristics and chemical state of cerium, and formed a Ce^{3+}/Ce^{4+} redox ring pair, successfully achieving a 100% conversion rate of HCHO at room temperature. Furthermore, it is also a good idea to synthesize catalysts using transition metals or non-metals as carriers. Wang et al. [52] developed a Pt-Ni bimetallic catalyst using γ-Al_2O_3 as a carrier, with a conversion rate of 97% at room temperature and a stability of 100 h. The presence of Pt sites stimulated more surface-adsorbed oxygen, improving the conversion rate of HCHO, and the doping of Ni helps to adsorb hydroxyl groups, thereby providing sustained activity. In addition, Zhou et al. [53] synthesized CuNi alloy carbon layer core–shell nanoparticles (CuNi@C) to achieve efficient conversion from formaldehyde to hydrogen. The H_2 generation rate of $CN_{(1:1)}$ is 110.98 mmol·g^{-1}. For H_2, the values for Cu@C and Ni@C are 1.47 times and 4.93 times, respectively. On the one hand, this is due to the synergistic effects of Cu and Ni metals on the alloy resulting in very high catalytic performance, with Cu generating a large number of active substances for the decomposition of HCHO, and Ni having excellent H_2 evolution performance. On the other hand, the carbon layer of CuNi@C protects Cu and Ni from excessive oxidation, greatly enhancing their stability.

The synthesis of HCHO catalysts using MOFs materials as carriers is also receiving more attention. For example, Duan et al. [54] added MOF UiO-66 to synthesize an Ag@Zr-TiO_2-1000U6 catalyst during the process of doping TiO_2 with Zr and achieved a degradation rate of 83.4% for HCHO. The doped Zr replaced Ti^{4+} in TiO_2 in the form of Zr^{4+}, resulting in a left shift of the TiO_2 peak and a decrease in bandgap energy. The composite material of Zr-TiO_2 and ZrO_2 effectively increases the pore volume of the catalyst and provides more active sites. Furthermore, Zhang et al. [55] used defective MIL-88B (Fe) nanorods as Fe-containing MOFs catalysts to activate molecular oxygen and trigger effective catalytic oxidation of HCHO. Defective MIL-88B (Fe) nanorods grow along the [001] direction, exposing a large number of coordinated unsaturated iron sites (Fe-cuss), sufficient for the diffusion of HCHO and O_2. The Lewis acid–base interaction between Fe-cuss and HCHO, as well as the Fenton-like catalysis of O_2, enable the adsorbed HCHO to be oxidized to CO_2, with a relatively high mineralization efficiency (over 80%). These studies show that reasonable selection and modification of other transition metal-based catalysts can further improve the catalytic oxidation efficiency of HCHO at room temperature, and provide more possibilities for HCHO pollution control.

3. Factors Affecting Catalytic Performance

The catalytic oxidation process of HCHO largely depends on the activity of the catalyst, which in turn is related to factors such as preparation methods, morphological structure, and specific surface area.

3.1. Preparation Methods

The physicochemical properties of the catalyst determine its ability to catalyze the oxidation of HCHO at room temperature, while the synthesis method and reaction conditions also affect the physicochemical properties of catalysts. At present, the synthesis methods for HCHO catalytic oxidants include the sol-gel method [56], the hydrothermal method [57], electrostatic spinning [58], the electrochemical method [39], the precipitation and coprecipitation method [59], template casting [60], etc. Different improvement methods have different effects on the valence state, morphology, and specific surface area of catalyst elements (as shown in Figure 5), thereby affecting the activity of catalysts.

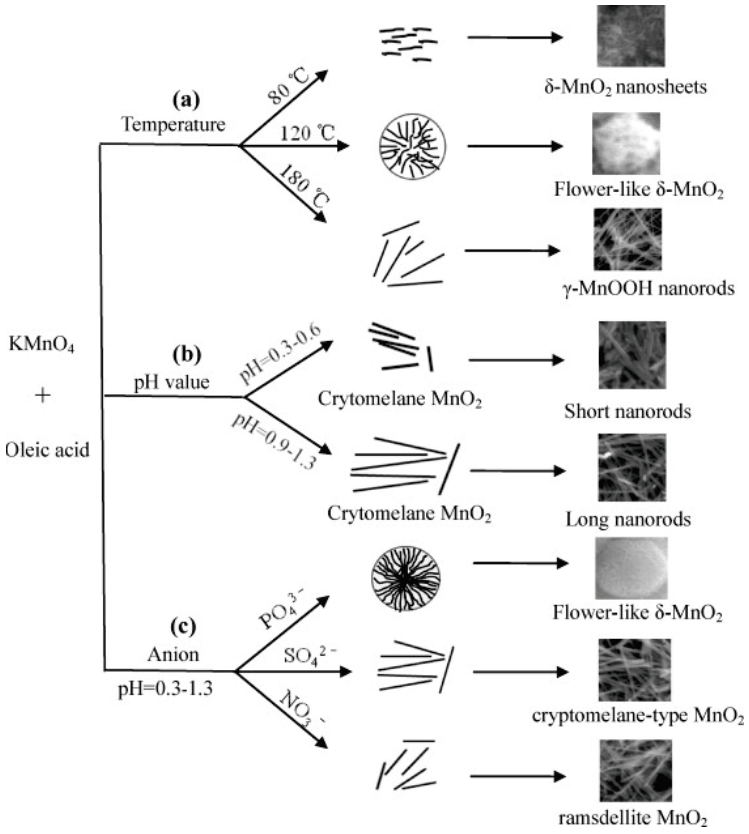


Figure 5. Schematic illustration of the growth of different manganese oxide nanostructures under varied conditions. Reproduced with permission from [61].

For example, Liu et al. [62] used an impregnation/carbonization process to synthesize PdZn alloy and a Pd-catalyst-modified 3D layered porous carbon (HPC) network catalyst from energetic MOFs of MET-6 as raw material. The extremely fine PdZn and Pd nanoparticles were uniformly distributed on or derocated in the HPC network, creating strong interaction between metal nanoparticles and HPC. The prepared HPC-PdZn has excellent HCHO catalytic performance at room temperature, and its hydrogen production rate is four times that of the pure Pd catalyst. Wang et al. [63] used freeze-drying-pyrolysis technology to prepare alkali-modified hierarchical porous Na-CoOx/CN materials using SAP/ZIF-67 composite materials as templates, achieving engineering of the pore structure and surface properties. The presence of Na^+ and CO_3^{2-} plays a crucial role in the formation of the layered porous structure of the catalyst, the enhancement of the surface area, and the formation of active hydroxyl groups, enabling the complete conversion of 1 mg/m^3 HCHO at room temperature at a high air velocity of 240000 mL/(g_{cat} h), and outstanding catalytic stability at higher air velocities (480000 mL/(g_{cat} h)). Furthermore, Sun et al. [64] prepared a series of MnO_x/γ-Al_2O_3 catalysts by the impregnation method and treated them with

acid, alkali, and H_2O_2 to study the effects of different treatment conditions on the catalytic activity. The results showed that the conversion rate of the MnAl-II catalyst to HCHO after the acid treatment was close to 100% (O_3/HCHO=2.0), because after the acid treatment, the better metal dispersion, smaller particle size, and surface microporous structure increased the surface area of the MnAl-II, and the corresponding active sites promoted the deep oxidation of the HCHO. In addition, the high Mn^{3+} and O_{ad} content of the catalyst is conducive to the formation of oxygen vacancies, accelerating the decomposition of O_3 and the ozonation process of HCHO.

Except for different reaction conditions, Liu et al. [65] synthesized a series of ε-MnO_2/$Mn_2V_2O_7$ composite catalysts at different V/Mn ratios. Different V/Mn ratios have a significant impact on catalytic performance: when the V/Mn molar ratio is 0.03, the degradation rate of 10 mL of 10 mg/L HCHO by the catalyst is 37.0%; when the V/Mn molar ratio is 0.06, the degradation rate of HCHO by the catalyst increases to 72.0%, which is attributed to the addition of a certain amount of V increasing the specific surface area of the catalyst. The reaction temperature can also affect the effectiveness of HCHO catalysts. Wang et al. [66] synthesized a series of layered MnO catalysts at different calcination temperatures. When the calcination temperature was below 300 °C, the catalyst took on a spherical shape, and when the calcination temperature was increased to 500 °C, the morphology of the catalyst transformed into a flower-like structure composed of nanorod clusters. Although the change in shape increased the specific surface area of the catalyst, evaluation experiments showed that an increase in calcination temperature led to a decrease in the internal water content of the catalyst, resulting in a decrease in the conversion rate of formaldehyde from 83.7% (S-30) to 43.1% (S-300).

Therefore, the preparation method has a significant effect on the performance of non-noble metal catalysts. Common methods include the impregnation method, precipitation method, hydrothermal method, and so on. Each method optimizes the catalytic performance by affecting the physical and chemical properties of the catalysts. These methods can improve the catalytic oxidation efficiency of HCHO by accurately controlling the preparation conditions and adjusting the active sites and redox performance of the catalysts.

3.2. Catalyst Morphological Structure

The morphology and structure of catalysts are of great significance for improving their activity. By regulating the morphology and structure of catalysts, various factors such as pore size, specific surface area, and surface active sites can be changed. So far, various forms such as nanotubes, nanofibers, nanosheets, nanobelts, nanoflowers, and nanoscale prism structures have been developed. Wang et al. [67] prepared nanorod-like, wire-like, tubular α-MnO_2, and flower-like spherical Mn_2O_3 using hydrothermal and CCl_4 solution methods. The oxygen radical concentration and low-temperature reducibility were in the order of rod-like α-MnO_2 > tubular α-MnO_2 > flower-like Mn_2O_3 > filamentous α-MnO_2, consistent with the catalytic performance of the samples. Meanwhile, surface active sites can affect the catalytic activity of catalysts. Li et al. [68] prepared MnO_x/C composite catalysts with abundant oxygen vacancies. After adding fructose to the synthesized raw materials, the crystal structure of the catalyst changed and the oxygen vacancies increased, providing more adsorption sites.

Changing the catalyst structure or constructing crystal defects can also enhance the catalytic activities of catalysts. Liao et al. [69] prepared six prisms (SP), short six pyramids (SSP), and long six pyramids (LSP) ZnO with different defect contents using low-temperature liquid-phase method. The results showed that due to the presence of donor defects, LSP ZnO had a high degradation efficiency for HCHO after 10 h. At the same time,

crystal morphology also had an impact on catalysis, and the differences in morphology and defect content jointly led to different catalytic performances for ZnO. In addition, Yu et al. [70] synthesized MnO_2 nanostructured catalysts with cocoon-like, urchin-like, and nest-like morphologies using a simple method. For example, Figure 6 shows TEM images of different Pt/urchin-like MnO_2 catalysts with varied Pt loadings. It can be observed that as the Pt content increases, the overall size of the catalyst increases (Figure 6c,f,i,l). This is due to the increase in precursor concentration ($H_2PtCl_6 \cdot 6H_2O$) during the loading process, which causes changes in the formation process. Compared with mesoporous cocoon-like and sea urchin-like MnO_2, nest-like MnO_2 has higher catalytic oxidation activity due to its higher dispersion of metal ions and specific surface area.

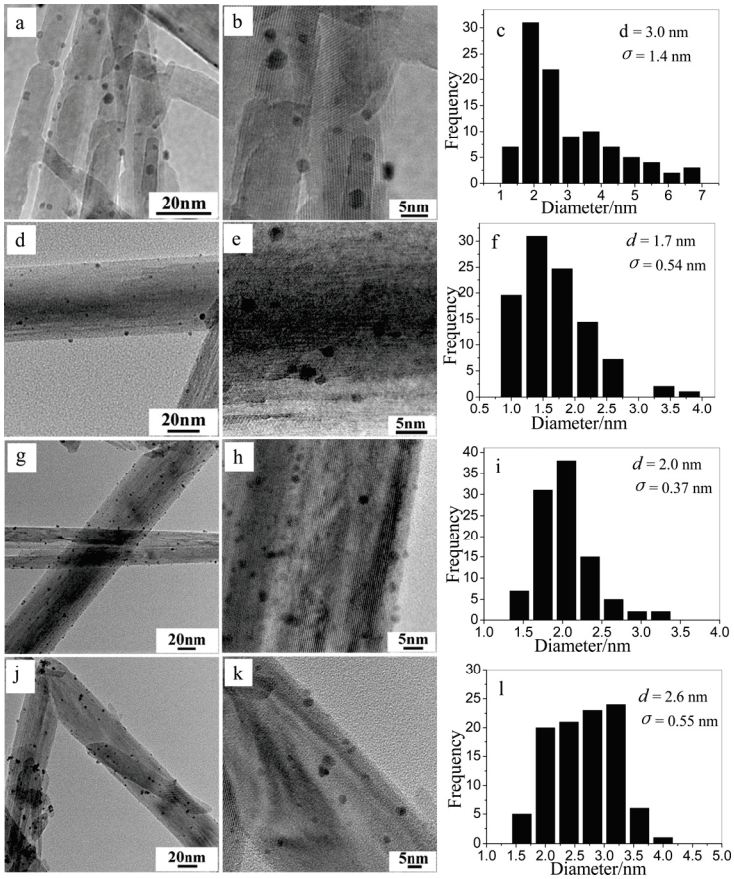


Figure 6. TEM images and histograms of Pt nanoparticles in Pt/urchin-like MnO_2 catalysts. Pt loading: (**a**–**c**) 0.5 wt%; (**d**–**f**) 1 wt%; (**g**–**i**) 2 wt%; (**j**–**l**) 3 wt%. Reproduced with permission from Elsevier from [70].

So, the morphological structure of HCHO catalysts has an important influence on their catalytic performance. A variety of catalysts have been developed, such as nanotubes, nanofibers, and so on. The pore size, specific surface area, and surface active sites can be changed by adjusting the structure. The common point of these studies is to enhance the adsorption capacity of HCHO and the number of active sites by reasonably designing the morphology and structure of the catalysts, so as to improve the catalytic oxidation performance.

3.3. Specific Surface Area

The specific surface area has a significant impact on catalysts' ability to oxidize HCHO. A higher specific surface area can increase the probability of capturing HCHO and provide more active sites and oxygen vacancies, which to some extent determines the catalytic

conversion rate of HCHO, so an important regulatory strategy is to develop HCHO catalysts with high specific surface area. Tian et al. [56] showed that compared with other catalysts synthesized in their experimental system, Mn-based catalysts with a birnesite (sodalite) structure and high specific surface area (154 m^2/g) exhibited better catalytic activity. Similarly, the MnO_2 catalyst synthesized by Sekine et al. [26] with a specific surface area of 163 m^2/g exhibited higher HCHO oxidation activity.

Fang et al. [71] prepared porous manganese oxide nanowires (MnO_x NWs) with large surface area and multiple manganese valence states using a simple electrospinning thermal calcination potassium permanganate solution post-treatment (C/S process) method. Subsequently, silver-oxide-coated silver nanowires were synthesized with the assistance of oxygen plasma (Ag@Ag_2O NWs). The nanowire diameters and BET surface areas of untreated MnO_x NWs, C-MnO_x NWs, S-MnO_x NWs, and C/S-MnO_x NWs were measured under the experimental conditions. It was found that the specific surface areas of C-MnO_x NWs and C/S-MnO_x NWs are higher than those of other nanowires. Generally speaking, a higher specific surface area can provide more oxidation reaction sites and improve the activity of the catalyst. Experimental results also showed that the catalytic conversion rate of HCHO is positively correlated with the specific surface area of the catalyst. Wu et al. [72] prepared Co_3O_4 nano necklaces and studied the state of the mesoporous structure by regulating calcination conditions. It was found that when the temperature exceeded 500 °C, the mesoporous structure and high specific surface area of the catalyst were disrupted, resulting in a decrease in catalyst activity. Additionally, Tian et al. [73] synthesized different forms of MnO_x of cryptomelane and tested the catalytic activity of a catalyst with a specific surface area of 206 m^2/g. They found that the catalytic ability was higher than that of a nanorod cryptomelane catalyst with a specific surface area of 68 m^2/g, indicating that an increase in specific surface area has a certain promoting effect on the improvement of catalytic ability.

4. Catalytic Oxidation Mechanism of HCHO

Understanding the catalytic oxidation mechanism of HCHO is of great significance for developing low-cost, high-stability, and high-activity catalysts. To understand the mechanism of HCHO catalytic oxidation, it is necessary to detect the distribution of reactive oxygen species on the reaction intermediates and catalyst surfaces. Generally, changes in the type and content of reactive oxygen species are detected by electron paramagnetic resonance (EPR) or electron spin resonance (ESR) [74]. Additionally, the formation of oxygen vacancies and oxygen mobility are determined by H_2 temperature programmed reduction (H_2-TPR), O_2 temperature programmed desorption (O_2-TPD), and X-ray photoelectron spectroscopy (XPS), in order to infer the generation of active substances [75]. In addition, in situ Fourier transform infrared spectroscopy (In-suit FTIR) or in situ diffuse reflectance infrared Fourier transform spectroscopy (In-suit DRIFTS) are also commonly used to analyze the intermediates produced by catalytic reactions [76,77]. According to these characterization analysis methods, the catalytic oxidation mechanism of HCHO can be divided into the Eley–Rideal mechanism (E-R), Langmuir–Hinshelwood mechanism (L-H), and Mars–Van Krevelen mechanism (MVK) [78–80].

4.1. Eley–Rideal Mechanism

Firstly, the oxidation process takes place between the oxygen that is adsorbed on the catalyst surface and the gaseous reactants, and during this process, chemisorption occurs on the catalyst surface. Then, the products that are formed when the reactive oxygen species react with the reactants are desorbed from the catalyst surface. The above is a typical E−R reaction process. In line with the E−R reaction model, HCHO is capable of dissociating

in the presence of reactive oxygen species that are produced by molecular oxygen on the catalyst surface. Zhou et al. [81] studied the Eley–Rideal (ER) mechanism of HCHO oxidation on the $Ti/Ti_3C_2O_2$ catalyst through DFT calculation. In the ER mechanism, O_2 molecules are first adsorbed and activated into two O atoms, and then HCHO molecules approach the activated O atoms. HCHO spontaneously dissociates into CO molecules on the $Ti/Ti_3C_2O_2$ surface, releasing 4.05 eV of energy, which helps overcome the energy barrier (1.04 eV) of subsequent reaction steps. Key steps include O-O bond cleavage, HCHO dissociation into CO and H atoms, H atoms combining with O atoms to form *OH groups, hydrogen transfer between *OH groups to form H_2O, and CO combining with O atoms to form CO_2. The ER mechanism has a low energy span of 1.04 eV, showing good catalytic cycle efficiency. The significant energy released in the initial step can promote subsequent reactions even without external heating. Liu et al. [80] used density functional theory (DFT) to study the mechanism of the oxidation of HCHO by three doped-carbon-based single-atom catalysts, $Fe/DV\text{-}N_4$, $Co/DV\text{-}N_4$, and $Pd/DV\text{-}N_4$. They found that the oxidation mechanism of HCHO is basically consistent with the Eley–Rideal (E-R) mechanism, as shown in Figure 7.

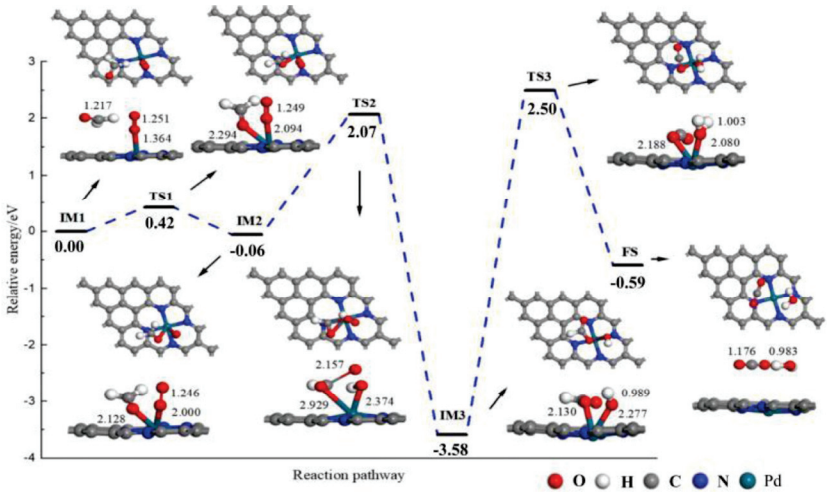


Figure 7. Optimized structures of intermediates, transition states, and final states of HCHO oxidation on Pd/DV-N4 surface and energy distribution of each reaction path. Reproduced with permission from [80].

4.2. Langmuir–Hinshelwood Mechanism

In the L−H catalytic mechanism, the reaction between adsorbed oxygen species and HCHO molecules on the surface serves as the rate-controlling step. In order to clarify the specific process of this mechanism, many researchers have put forward their own insights. Mang et al. [82] proposed five possible reaction pathways (including three L-H mechanisms and two E-R mechanisms), and using the transition state search method and other thermodynamic and kinetic analyses, they found that pathway 1 of the L-H mechanism ($HCHO+O_2 \rightarrow HCOOOH \rightarrow HCOH+OH \rightarrow CO_2+H_2O$) is the most likely reaction pathway to occur because it requires the lowest reaction energy barrier. During the entire catalytic process, IM-Co-2 to IM-Co-5 in $Co\text{-}MnO_2$, IM-Fe-2 to IM-Fe-5 in $Fe\text{-}MnO_2$, and IM-Ni-2 to IM-Ni-5 in $Ni\text{-}MnO_2$ have the highest energy barriers, and pathway 1 is considered the rate controlling step. In addition, Ding et al. [83] studied the L-H reaction mechanism of Pt/TiO_2 catalyst and found five basic steps: $HCHO^* \rightarrow HCO^*$, $HCO^* \rightarrow CO^*$, H_2O desorption, $CO^* \rightarrow CO_2^*$, and CO_2 desorption. The potential energy diagram is shown in Figure 8. In the first step (IM1 → TS1 → IM2), the H atom on HCHO transfers to form HOO species, which overcomes the 412.5 KJ/mol energy barrier

and releases 20.05 KJ/mol of heat. Second, HCO reacts with HOO to generate H_2O and activated O in step IM2 → TS2 → IM3, which requires overcoming an energy barrier of 146.09 kJ/mol and releasing a reaction heat of −217.71 kJ/mol. Then, H_2O desorbs directly from the surface with a desorption energy of 1.72 kJ/mol (IM3 → IM4). In the following step, CO reacts with adjacent O atoms to generate CO_2, releasing 57.29 kJ/mol of heat (IM4 → TS3 → IM5). Finally, CO_2 desorption from the catalyst surface (IM5 → TS) takes place. This reaction process shows that the HCHO* → HCO* step has the highest activation energy, of 412.50 kJ/mol, indicating that the reaction between adsorbed HCHO and O_2 is the rate-determining step in HCHO oxidation.

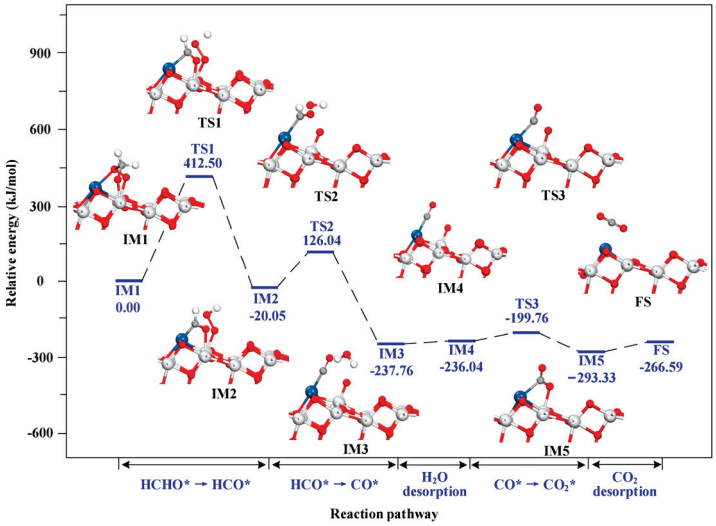


Figure 8. The energy profile and optimized structures of HCHO oxidation through the Langmuir–Hinshelwood mechanism over the Pt/TiO_2 (101) surface. Reproduced with permission from [83].

4.3. Mars–Van Krevelen Mechanism

Compared with the previous two reaction mechanisms, the MVK mechanism, also known as the two-step oxidation-reduction model, appears more frequently in the process of metal oxide catalysts catalyzing HCHO. This reaction consists of two steps: the catalyst surface is oxidized by gas-phase molecular oxygen to form surface-adsorbed oxygen, and the surface-adsorbed oxygen subsequently reduces pollutants. Sekine et al. [26] believed that HCHO first adsorbs and oxidizes on metal oxide catalysts, and then forms formic acid intermediates on the surface and decomposes, before, finally, the intermediates decompose into H_2O and CO_2, as shown in the following formulas:

$$HCHO\ (g) + O\ (a) \rightarrow HCHOO\ (a) \quad (1)$$

$$HCHOO\ (a) \rightarrow O\ (a) + HCHO\ (g) \quad (2)$$

$$HCOO\ (a) \rightarrow H\ (a) + CO_2\ (g) \quad (3)$$

$$2H\ (a) + O\ (a) \rightarrow H_2O\ (g) \quad (4)$$

where (g) represents the gaseous state, (a) represents the adsorbed state.

Through the above formulas, it can be found that formic acid intermediate is produced in the catalytic oxidation process of HCHO, which can be seen in many articles. For instance, Qian et al. [84] found that oxygen first adsorbed on the catalyst surface and reacted with acid sites and oxygen vacancies to generate superoxide radicals, which then reacted with water molecules adsorbed on the surface to generate hydroxyl radicals. Under the action of ·OH, HCHO decomposed into formate, which is gradually deeply oxidized into CO_2

and H_2O. Zhao et al. [85] found that doping alkali metal ions significantly increased the amount of surface -OH in MnO_x catalysts. The -OH groups can form hydrogen bonds with hydrogen atoms in HCHO and react with intermediate products such as formate, accelerating the decomposition of formate and promoting the generation of bridging formic acid intermediate products, thereby improving the catalytic oxidation activity of HCHO.

The properties of surface active substances have a significant impact on catalytic activity and, therefore, the forms of active substances have received high levels of attention in analyzing reaction mechanisms. Zhang et al. [30] showed that the catalytic activity of four MnO_2 catalysts (i.e., α, β, γ, and δ-MnO_2) is closely related to the amount of surface lattice oxygen (relative to surface-adsorbed oxygen) on each of them. Zhang's team [86] synthesized a range of zirconia quadrilateral monoclinic (TMZ) catalysts and clarified the HCHO catalytic oxidation mechanism using DFT calculations and DRIFTS measurements. Initially, active *H atoms transfer from HCHO to O_2, forming OOH groups. Then, lattice O atoms and OOH groups from TMZ dissociate into active *O and *H atoms, generating HCOOH. Finally, active O atoms from the OOH group facilitate HCOOH's conversion to CO_2 and H_2O. This reaction follows a novel D-H and MVK pathway, with the rate-determining step being the transfer of the H atom of HCHO to the O-Zr bond's lattice O atom in TMZ.

Wang et al. [87] analyzed the catalytic cycle of HCHO oxidation on black manganese ore, as shown in Figure 9. The water contained in birnite forms hydrogen bonds with HCHO, and the adsorbed HCHO and its hydrate ($CH_2(OH)_2$) are oxidized by surface reactive oxygen species (O_2^-, O^-, or terminal OH groups), producing oxygen vacancies (V_0). Then, the dioxygen molecules in the air are adsorbed on V_0 and dissociated ($O_2 + V_0 \rightarrow O_2^-, O^-$), and finally, O_2^- reacts with H_2O ($O_2^- + H_2O \rightarrow 2OH$) to supplement the surface OH. In this cyclic reaction, K^+ can compensate for the charge imbalance caused by the presence of manganese vacancies, promote the formation of surface reactive oxygen species, and become active sites for formaldehyde oxidation.

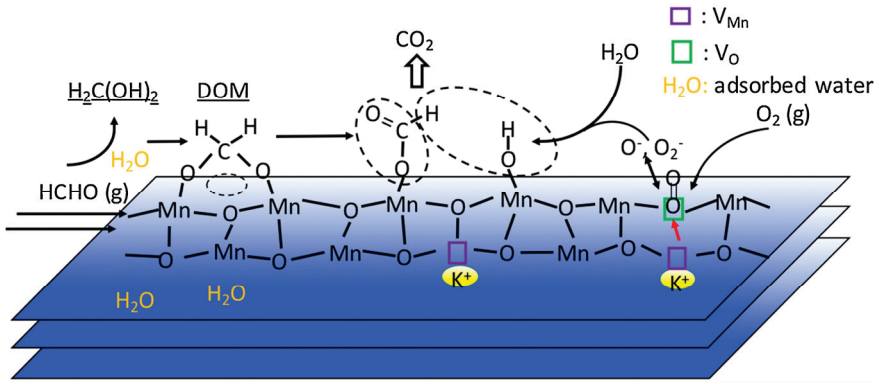


Figure 9. Reaction pathway of HCHO on layered manganese dioxide with K^+-compensated manganese vacancies. Reproduced with permission from [87].

In summary, three main catalytic oxidation mechanisms are discussed: Eley–Rideal (E-R), Langmuir–Hinshelwood (L-H), and Mars van–Krevelen (MVK). These mechanisms explain the oxidation process of HCHO on the surfaces of the catalysts from different perspectives. They jointly reveal the complex reaction path of HCHO catalytic oxidation, and provide theoretical guidance for the design of the catalysts. Through the in-depth understanding of these mechanisms, the composition and structure of the catalysts can be more targeted and optimized, and their performance and stability in practical applications can be improved.

5. Deactivation and Regeneration of HCHO Catalysts

The long-term use of HCHO catalysts will change their activity and selectivity, leading to deactivation. The catalyst presents a large cost in the operation of a catalytic device, and deactivation undoubtedly incurs many additional expenses [88]. Bartholomew summarized the deactivation process of a catalyst and divided it into the following six situations: pollution or coking, poisoning, gas–solid and/or solid–solid reaction, thermal degradation, crushing, and vapor compound formation [89]. Coking is due to the side reactions on the catalyst surface, and the carbon-containing by-products generated cover the catalysts' surface or block the pores of the catalysts. Poisoning is mostly caused by the loss of active sites due to the chemical adsorption of catalyst impurities [90,91]. Poisons can block the active sites or change the catalyst activity. At the same time, because the adsorption coefficient of poisons is higher than that of reactants, it is difficult for reactants to approach the active sites [91].

Of course, the catalyst for the catalytic oxidation of HCHO may also be deactivated due to other uncommon factors. For example, when dealing with HCHO gas containing chlorine, the interaction between chlorine and catalyst will make chlorine deposit on the surface of the catalyst, resulting in the deactivation of the catalyst. Unfortunately, almost all catalysts are affected by chlorine deposition [92], such as cerium oxide catalysts [93], vanadium-based catalysts [94], transition metal oxides, perovskite [95], and mixed metal catalysts. The presence of water may also lead to catalyst deactivation. Such as the competition between HCHO and H_2O for active sites caused by high gas humidity. Once H_2O molecules form a stable hydroxyl structure with the active site, the catalytic effect of HCHO is affected. Temperature and space velocity may also lead to catalyst deactivation.

In order to ensure the activity of the catalyst and reduce unnecessary cost consumption, the regeneration of the catalyst is an effective method. The regeneration of the catalyst is determined by the reversibility of the deactivation process. For example, deactivation caused by coking can be reversed, while that caused by sintering cannot. Toxicants can be selectively removed by mechanical, oxidation, or chemical washing [96]. Therefore, there are many methods for catalyst regeneration [78], such as heat treatment, pressure swing, chemical regeneration, and plasma [97,98]. For example, oxygen plasma and ozone injection can effectively regenerate Au/TiO_2 catalysts [99]. Considering the cost, although it is feasible to use air as the discharge gas for plasma regeneration, the presence of N_2 will generate nitrogen oxides and cause new poisoning. In order to solve this problem, the cold plasma technology of moist air came into being [98]. In a word, modern regeneration technology is gradually replacing the conventional heat treatment or mechanical treatment techniques.

6. Conclusions and Outlook

The catalytic oxidation of HCHO at room temperature is one of the major topics in the field of environmental catalysis. This article discusses the application of non-noble metal catalysts in the catalytic oxidation of HCHO, and summarizes the influence of experimental conditions and catalytic machines on the catalytic oxidation ability of HCHO. Among the reported non-precious-metal catalysts, Mn has attracted widespread attention due to its unique properties, such as abundant valence states, strong oxidation adsorption capacity, high abundance, acid resistance, low toxicity, low cost, and high environmental compatibility. There are currently three possible mechanisms for the catalytic oxidation of formaldehyde, among which the MVK mechanism is the most frequently discovered and widely accepted theory among researchers. An important feature of this mechanism is the conversion of HCHO carbonyl (-C=O) to carboxyl (-COOH), and the intermediate products are known to be formate, DOM, CO, etc., after in situ DRIFTS analysis. At the same time,

hydroxyl (-OH) groups are generated on the surface of the catalyst with the participation of water vapor, promoting the adsorption of HCHO by the catalyst and, thus, improving the catalytic oxidation activity. The surface structure and properties of the catalyst also affect its catalytic ability.

Many catalysts for HCHO catalytic oxidation are often prepared as powders. However, in practical applications, powder catalysts can encounter significant air resistance, which affects their catalytic efficiency. To mitigate this, they are typically pressed into pellets or flakes. This process not only complicates the preparation method but also leads to the agglomeration of active component particles and their attachment to the carrier surface, thereby reducing the effective surface area. Additionally, non-noble metal oxide catalysts often exhibit low catalytic activity for HCHO oxidation at room temperature. Moreover, there is a lack of studies on the catalytic activity, deactivation, and regeneration of catalysts for HCHO catalytic oxidation in the presence of multiple VOC molecules.

Although non-precious-metal catalysts have made progress in catalyzing HCHO at room temperature, there are still some challenges that can be studied in the following areas:

1. Improve materials and prepare catalysts with higher specific surface area. At present, a considerable portion of catalysts exist in powder form, and the agglomeration of powders can reduce catalytic efficiency. Using nanomaterials as carriers or preparing catalysts at the nanoscale is a potential development direction. At the same time, when preparing novel catalysts, it is important to actively consider their feasibility for practical applications. Some current catalysts suffer from problems such as high pressure drop, low mechanical strength, and poor physical or chemical stability. Although some catalysts contain non-noble metal components, they only partially replace noble metal elements, which still results in high costs. Overall, the preparation of catalysts with low pressure loss, good mechanical strength and stability, and low cost is of great significance.

2. Change the experimental conditions to gain a deeper understanding of the mechanism of HCHO catalytic oxidation. It is of great significance to design HCHO catalysts for room temperature oxidation, and to gain a deeper understanding of the catalytic steps through appropriate experimental design, in order to regulate the quantity and structural defect morphology of surface active substances in the future. In addition, the deactivation mechanism of catalysts can be further explored. Many factors, such as the nature of the catalyst, other components in the mixed gas, humidity, temperature, etc., will affect the activity and selectivity of the HCHO catalysts. Therefore, by combining these possible causes and conducting in-depth research using mixed gases, not only can the effectiveness of the catalyst be improved in a targeted manner, but the approach can also have positive significance for future large-scale applications.

3. Develop efficient materials to pave the way for future practical applications. At present, most of the reported catalysts are tested under laboratory conditions, but the concentration changes of HCHO in the actual environment and the interactions between HCHO and other atmospheric pollutants can complicate the catalytic process. Therefore, by combining theory with practice to develop catalysts that can be truly applied, contributions to human health can be made.

Author Contributions: R.W.: Conceptualization, methodology, validation, writing—review and editing, funding acquisition, supervision, project administration. Y.F.: investigation, writing—original draft preparation. All authors have read and agreed to the published version of the manuscript.

Funding: This research was funded by Natural Science Foundation of Shandong Province (ZR2018MEE048), China.

Data Availability Statement: No new data were created or analyzed in this study. Data sharing is not applicable to this article.

Conflicts of Interest: The authors declare no conflicts of interest.

References

1. Chen, L.; Li, K.; Xue, T.; Yang, Y.; Gong, Z.; Dong, F. Efficient and Durable Oxidation Removal of Formaldehyde over Layered Double Hydroxide Catalysts at Room Temperature. *Environ. Sci. Technol.* **2024**, *58*, 10378–10387. [CrossRef]
2. Huang, X.; Chen, M.; Li, G.; Wang, P. Constructing α-MnO_2/Mn_2O_3 Heterojunction for Formaldehyde Oxidation. *Chemosphere* **2024**, *349*, 140959. [CrossRef] [PubMed]
3. Chai, L.; Zhai, W.; Liu, X.; Xing, G.; Zhang, B.; Zang, J.; Yang, Y.; Ma, K.; Zhang, J. Room Temperature Catalysts for High Effective Degradation of Formaldehyde: Research Progresses and Challenges. *ChemistrySelect* **2024**, *9*, e202304418. [CrossRef]
4. Nielsen, G.D.; Larsen, S.T.; Wolkoff, P. Recent Trend in Risk Assessment of Formaldehyde Exposures from Indoor Air. *Arch. Toxicol.* **2013**, *87*, 73–98. [CrossRef]
5. La Torre, G.; Vitello, T.; Cocchiara, R.A.; Della Rocca, C. Relationship between Formaldehyde Exposure, Respiratory Irritant Effects and Cancers: A Review of Reviews. *Public Health* **2023**, *218*, 186–196. [CrossRef] [PubMed]
6. de Falco, G.; Li, W.; Cimino, S.; Bandosz, T.J. Role of Sulfur and Nitrogen Surface Groups in Adsorption of Formaldehyde on Nanoporous Carbons. *Carbon* **2018**, *138*, 283–291. [CrossRef]
7. Becker, A.; Israfilov, N.; Ehrstein, E.; Lara-Ibeas, I.; Planeix, J.-M.; Louis, B.; Le Calvé, S. Adsorption of Gaseous Formaldehyde on Y Zeolites and on Metal-Organic Frameworks. *Microporous Mesoporous Mater.* **2022**, *343*, 112136. [CrossRef]
8. Su, G.; Xiong, J.; Li, Q.; Luo, S.; Zhang, Y.; Zhong, T.; Harper, D.P.; Tang, Z.; Xie, L.; Chai, X.; et al. Gaseous Formaldehyde Adsorption by Eco-Friendly, Porous Bamboo Carbon Microfibers Obtained by Steam Explosion, Carbonization, and Plasma Activation. *Chem. Eng. J.* **2023**, *455*, 140686. [CrossRef]
9. Li, X.; Huang, Y.; Ho, W.; Han, S.; Wang, P.; Lee, S.; Zhang, Z. Modulation of Sulfur Vacancies at $ZnIn_2S_4$-δ/g-C_3N_4 Heterojunction Interface for Successive C-H Secession in Photocatalytic Gaseous Formaldehyde Complete Oxidation. *Appl. Catal. B Environ.* **2023**, *338*, 123048. [CrossRef]
10. Chen, M.; Wang, H.; Chen, X.; Wang, F.; Qin, X.; Zhang, C.; He, H. High-Performance of Cu-TiO_2 for Photocatalytic Oxidation of Formaldehyde under Visible Light and the Mechanism Study. *Chem. Eng. J.* **2020**, *390*, 124481. [CrossRef]
11. Zhu, X.; Gao, X.; Qin, R.; Zeng, Y.; Qu, R.; Zheng, C.; Tu, X. Plasma-Catalytic Removal of Formaldehyde over Cu–Ce Catalysts in a Dielectric Barrier Discharge Reactor. *Appl. Catal. B Environ.* **2015**, *170–171*, 293–300. [CrossRef]
12. Yuan, M.; Jiang, J.; Xue, F.; Deng, J.; Dai, Y.; Li, L.; Cui, M.; Qiao, X.; Fei, Z. Plasma-Engraved Co_3O_4 Nanostructure toward Improved Formaldehyde Oxidation Performance: Insight into the Structure–Activity Relationship. *Appl. Surf. Sci.* **2022**, *600*, 154183. [CrossRef]
13. Gao, E.; Jin, Q.; Zhang, T.; Han, L.; Li, N.; Xu, J.; Yao, S.; Wu, Z.; Li, J.; Zhu, J.; et al. Unraveling the Promotional Effects of K-Doping on the Mobility of Surface Oxygen Species of $CoCr_2O_4$ for Improved Formaldehyde Catalytic Oxidation: The Weakened Metal-Oxygen Bond Strength. *Chem. Eng. J.* **2023**, *474*, 145618. [CrossRef]
14. Yuan, X.; Zheng, C.; Zhang, T.; Li, L.; Yang, Q.; Zhao, H. Sodium Doped SrTi1-xBxO3 (BMn, Co) for Formaldehyde Catalytic Oxidation: Flame Spray Pyrolysis Fabrication and Reaction Mechanism Elaboration. *Fuel Process. Technol.* **2023**, *247*, 107763. [CrossRef]
15. Chen, D.; Zhang, G.; Wang, M.; Li, N.; Xu, Q.; Li, H.; He, J.; Lu, J. Pt/MnO_2 Nanoflowers Anchored to Boron Nitride Aerogels for Highly Efficient Enrichment and Catalytic Oxidation of Formaldehyde at Room Temperature. *Angew. Chem. Int. Ed.* **2021**, *60*, 6377–6381. [CrossRef] [PubMed]
16. Wang, C.; Li, Y.; Zheng, L.; Zhang, C.; Wang, Y.; Shan, W.; Liu, F.; He, H. A Nonoxide Catalyst System Study: Alkali Metal-Promoted Pt/AC Catalyst for Formaldehyde Oxidation at Ambient Temperature. *ACS Catal.* **2021**, *11*, 456–465. [CrossRef]
17. Ye, J.; Zhu, B.; Cheng, B.; Jiang, C.; Wageh, S.; Al-Ghamdi, A.A.; Yu, J. Synergy between Platinum and Gold Nanoparticles in Oxygen Activation for Enhanced Room-Temperature Formaldehyde Oxidation. *Adv. Funct. Mater.* **2022**, *32*, 2110423. [CrossRef]
18. Zhuo, Y.; Guo, X.; Cai, W.; Shao, T.; Xia, D.; Li, C.; Liu, S. Synergetic Modulation of Molecular Oxygen Activation and Surface Acidity/Basicity on Defective M/UiO-66m (M = Pt, Pd) for Advanced Oxidation of Gaseous Formaldehyde at Room Temperature. *Appl. Catal. B Environ. Energy* **2023**, *333*, 122789. [CrossRef]
19. Vikrant, K.; Chung, M.W.; Boukhvalov, D.W.; Heynderickx, P.M.; Kim, K.-H.; Weon, S. A Platinum Ensemble Catalyst for Room-Temperature Removal of Formaldehyde in the Air. *Chem. Eng. J.* **2023**, *475*, 146007. [CrossRef]
20. Gravvani, K.; Solakidou, M.; Louloudi, M. Highly-Efficient Reusable [Silica@Iminophosphine-FeII] Hybrids for Hydrogen Production via Formic Acid and Formaldehyde Dehydrogenation. *Chem.—Eur. J.* **2025**, *31*, e202404440. [CrossRef]
21. Meng, W.; Song, X.; Bao, L.; Chen, B.; Ma, Z.; Zhou, J.; Jiang, Q.; Wang, F.; Liu, X.; Shi, C.; et al. Synergistic Doping and De-Doping of Co_3O_4 Catalyst for Effortless Formaldehyde Oxidation. *Chem. Eng. J.* **2024**, *494*, 153028. [CrossRef]
22. Chen, Z.; Yang, W.; Wu, Y.; Zhang, C.; Luo, J.; Chen, C.; Li, Y. Atomic Iron on Mesoporous N-Doped Carbon to Achieve Dehydrogenation Reaction at Room Temperature. *Nano Res.* **2020**, *13*, 3075–3081. [CrossRef]

23. Lu, L.; Tian, H.; He, J.; Yang, Q. Graphene–MnO_2 Hybrid Nanostructure as a New Catalyst for Formaldehyde Oxidation. *J. Phys. Chem. C* **2016**, *120*, 23660–23668. [CrossRef]
24. Sun, Y.; Xiao, Y.; Ren, L.; Cheng, Z.; Niu, Y.; Li, Z.; Zhang, S. Pyrrolic Nitrogen Boosted H2 Generation from an Aqueous Solution of HCHO at Room Temperature by Metal-Free Carbon Catalysts. *J. Phys. Chem. Lett.* **2024**, *15*, 4538–4545. [CrossRef] [PubMed]
25. Wang, X.; Ying, J.; Mai, Y.; Zhang, J.; Chen, J.; Wen, M.; Yu, L. MOF-Derived Metal Oxide Composite $Mn_2Co_1O_x$/CN for Efficient Formaldehyde Oxidation at Low Temperature. *Catal. Sci. Technol.* **2019**, *9*, 5845–5854. [CrossRef]
26. Sekine, Y.; Nishimura, A. Removal of Formaldehyde from Indoor Air by Passive Type Air-Cleaning Materials. *Atmos. Environ.* **2001**, *35*, 2001–2007. [CrossRef]
27. Li, J.; Li, L.; Cheng, W.; Wu, F.; Lu, X.; Li, Z. Controlled Synthesis of Diverse Manganese Oxide-Based Catalysts for Complete Oxidation of Toluene and Carbon Monoxide. *Chem. Eng. J.* **2014**, *244*, 59–67. [CrossRef]
28. Lyu, Y.; Li, C.; Du, X.; Zhu, Y.; Zhang, Y.; Li, S. Catalytic Removal of Toluene over Manganese Oxide-Based Catalysts: A Review. *Environ. Sci. Pollut. Res.* **2020**, *27*, 2482–2501. [CrossRef]
29. Sekine, Y. Oxidative Decomposition of Formaldehyde by Metal Oxides at Room Temperature. *Atmos. Environ.* **2002**, *36*, 5543–5547. [CrossRef]
30. Zhang, J.; Li, Y.; Wang, L.; Zhang, C.; He, H. Catalytic Oxidation of Formaldehyde over Manganese Oxides with Different Crystal Structures. *Catal. Sci. Technol.* **2015**, *5*, 2305–2313. [CrossRef]
31. Han, Z.; Wang, C.; Zou, X.; Chen, T.; Dong, S.; Zhao, Y.; Xie, J.; Liu, H. Diatomite-Supported Birnessite–Type MnO_2 Catalytic Oxidation of Formaldehyde: Preparation, Performance and Mechanism. *Appl. Surf. Sci.* **2020**, *502*, 144201. [CrossRef]
32. Kang Zhao, W.; Yu Zheng, J.; Bao Han, C.; Ruan, J.; Lu, Y.; Ling Zhou, K.; Rui Zhai, T.; Wang, H.; Yan, H. MnO_x-PMMA Self-Powered Triboelectric Catalysts Based on Three-Dimensional Nanocomposite Structures for Formaldehyde Degradation at Room Temperature. *Chem. Eng. J.* **2022**, *440*, 135877. [CrossRef]
33. Chen, T.; Dou, H.; Li, X.; Tang, X.; Li, J.; Hao, J. Tunnel Structure Effect of Manganese Oxides in Complete Oxidation of Formaldehyde. *Microporous Mesoporous Mater.* **2009**, *122*, 270–274. [CrossRef]
34. Tao, Y.; Li, R.; Huang, A.-B.; Ma, Y.-N.; Ji, S.-D.; Jin, P.; Luo, H.-J. High Catalytic Activity for Formaldehyde Oxidation of an Interconnected Network Structure Composed of δ-MnO_2 Nanosheets and γ-MnOOH Nanowires. *Adv. Manuf.* **2020**, *8*, 429–439. [CrossRef]
35. Zhang, Y.; Chen, M.; Zhang, Z.; Jiang, Z.; Shangguan, W.; Einaga, H. Simultaneously Catalytic Decomposition of Formaldehyde and Ozone over Manganese Cerium Oxides at Room Temperature: Promotional Effect of Relative Humidity on the $MnCeO_x$ Solid Solution. *Catal. Today* **2019**, *327*, 323–333. [CrossRef]
36. Duan, C.; Zhou, Y.; Meng, M.; Huang, H.; Ding, H.; Zhang, Q.; Huang, R.; Yan, M. Research on the Elimination of Low-Concentration Formaldehyde by Ag Loaded onto Mn/CeO_2 Catalyst at Room Temperature. *Phys. Chem. Chem. Phys.* **2023**, *25*, 24495–24507. [CrossRef]
37. Xing, G.; Liu, X.; Jia, Y.; Wu, J.; Chai, L.; Zhai, W.; Wu, Z.; Kong, J.; Zhang, J. Oxygen Vacancy–Rich K-Mn_3O_4@CeO_2 Catalyst for Efficient Oxidation Degradation of Formaldehyde at near Room Temperature. *J. Colloid Interface Sci.* **2025**, *677*, 417–428. [CrossRef]
38. Liu, R.Y.; Man Trinh, M.; Chuang, H.T.; Chang, M.B. Ozone Catalytic Oxidation of Low-Concentration Formaldehyde over Ternary Mn-Ce-Ni Oxide Catalysts Modified with FeO_x. *Environ. Sci. Pollut. Res.* **2023**, *30*, 32696–32709. [CrossRef]
39. Zheng, J.Y.; Zhou, K.L.; Zhao, W.K.; Wang, Y.; He, J.; Wang, X.; Wang, H.; Yan, H.; Han, C.B. Enhanced the Synergistic Degradation Effect between Active Hydroxyl and Reactive Oxygen Species for Indoor Formaldehyde Based on Platinum Atoms Modified MnOOH/MnO_2 Catalyst. *J. Colloid Interface Sci.* **2022**, *628*, 359–370. [CrossRef]
40. Zhu, M.; Liu, W.; Li, W.; Cong, P.; Gao, D.; Jiang, X.; Hu, R.; Wang, R.; Chen, G. Insight into Formaldehyde Decomposition over MOFs-Derived CeO_2-MnO_x Bimetallic Oxides. *Sep. Purif. Technol.* **2025**, *358*, 130287. [CrossRef]
41. Wang, X.; Xu, Z.; Li, J.; Zhang, M.; Li, K.; Zheng, Y.; Ji, H. Mn/HZSM-5 Catalyst with High Content of Mn^{4+} and Surface Hydroxyls for Formaldehyde Oxidation at Room Temperature. *Appl. Surf. Sci.* **2023**, *637*, 157917. [CrossRef]
42. Wang, X.; Zhao, J.; Zhao, C.; Zhang, Y.; Mahmud, S.; Zhang, J. Ceramic Fiber Paper-Based Manganese Oxides Catalyst for Room Temperature Formaldehyde Oxidation. *Catal. Lett.* **2025**, *155*, 65. [CrossRef]
43. Hu, L.; Peng, Q.; Li, Y. Selective Synthesis of Co_3O_4 Nanocrystal with Different Shape and Crystal Plane Effect on Catalytic Property for Methane Combustion. *J. Am. Chem. Soc.* **2008**, *130*, 16136–16137. [CrossRef]
44. Yang, J.; Sasaki, T. Morphological Control of Single Crystalline Co_3O_4 Polyhedrons: Selective and Nonselective Growth of Crystal Planes Directed by Differently Charged Surfactants and Solvents. *Cryst. Growth Des.* **2010**, *10*, 1233–1236. [CrossRef]
45. Ma, C.Y.; Mu, Z.; Li, J.J.; Jin, Y.G.; Cheng, J.; Lu, G.Q.; Hao, Z.P.; Qiao, S.Z. Mesoporous Co_3O_4 and Au/Co_3O_4 Catalysts for Low-Temperature Oxidation of Trace Ethylene. *J. Am. Chem. Soc.* **2010**, *132*, 2608–2613. [CrossRef]
46. Bai, B.; Arandiyan, H.; Li, J. Comparison of the Performance for Oxidation of Formaldehyde on Nano-Co3O4, 2D-Co3O4, and 3D-Co_3O_4 Catalysts. *Appl. Catal. B Environ.* **2013**, *142–143*, 677–683. [CrossRef]

47. Jiao, Y.; Jing, C.; Wang, Y.; Yao, F.; Ye, G.; Wang, X.; Zhao, G.; Peng, W.; Huang, H.; Ye, D. Electrospinning Synthesis of Co_3O_4 Porous Nanofiber Monolithic Catalysts for the Room-Temperature Indoor Catalytic Oxidation of Formaldehyde at Low Concentrations. *Appl. Surf. Sci.* **2023**, *639*, 158215. [CrossRef]
48. Wang, A.; Li, J.; Zhang, T. Heterogeneous Single-Atom Catalysis. *Nat. Rev. Chem.* **2018**, *2*, 65–81. [CrossRef]
49. Du, B.; Wen, F.; Zhao, Y.; Yang, H.; Zhang, C. Efficient and Long-Lasting Removal of High-Level Formaldehyde at Room Temperature over a Cobalt Single-Atom Catalyst Anchored on Graphene-like Carbon Nanosheets. *ACS EST Eng.* **2025**, *5*, 1868–1878. [CrossRef]
50. Zhang, H.; Guo, G.; Wang, Z.; He, Q.; He, X.; Ji, H. Superior Performance of Formaldehyde Complete Oxidation at Ambient Temperature over Co Single-Atom Catalysts. *Appl. Catal. B Environ. Energy* **2023**, *333*, 122774. [CrossRef]
51. Yang, Z.; Liu, X.; Jia, L.; Wang, F.; Liu, T.; Xia, Y.; Xue, H. Regulation of Oxygen Vacancies in Ceria-Zirconia Nanocatalysts by Pluronic P123-Templated for Room Temperature Formaldehyde Total Oxidation. *Catal. Lett.* **2024**, *154*, 503–512. [CrossRef]
52. Wang, X.; Yang, F.; Yi, J.; Kong, J.; Gong, J.; Yuan, A.; Rui, Z.; Ji, H. Constructing Synergy of Sufficient Hydroxyl and Oxygen in PtNi/AlO Enables Room-Temperature Catalytic HCHO Oxidation. *AIChE J.* **2023**, *69*, e17895. [CrossRef]
53. Zhou, Z.; Ng, Y.H.; Xu, S.; Yang, S.; Gao, Q.; Cai, X.; Liao, J.; Fang, Y.; Zhang, S. A CuNi Alloy–Carbon Layer Core–Shell Catalyst for Highly Efficient Conversion of Aqueous Formaldehyde to Hydrogen at Room Temperature. *ACS Appl. Mater. Interfaces* **2021**, *13*, 37299–37307. [CrossRef] [PubMed]
54. Duan, J.; He, X.; Ma, Z.; Yue, J.; Wang, W.; Li, C. The Composite of Zr-Doped TiO_2 and MOF-Derived Metal Oxide for Oxidative Removal of Formaldehyde at the Room Temperature. *Microporous Mesoporous Mater.* **2022**, *336*, 111892. [CrossRef]
55. Zhang, S.; Zhuo, Y.; Ezugwu, C.I.; Wang, C.; Li, C.; Liu, S. Synergetic Molecular Oxygen Activation and Catalytic Oxidation of Formaldehyde over Defective MIL-88B(Fe) Nanorods at Room Temperature. *Environ. Sci. Technol.* **2021**, *55*, 8341–8350. [CrossRef]
56. Tian, H.; He, J.; Liu, L.; Wang, D.; Hao, Z.; Ma, C. Highly Active Manganese Oxide Catalysts for Low-Temperature Oxidation of Formaldehyde. *Microporous Mesoporous Mater.* **2012**, *151*, 397–402. [CrossRef]
57. Bathla, A.; Kukkar, D.; Heynderickx, P.M.; Younis, S.A.; Kim, K.-H. Removal of Gaseous Formaldehyde by Portable Photocatalytic Air Purifier Equipped with Bimetallic Pt@Cu-TiO_2 Filter. *Chem. Eng. J.* **2023**, *469*, 143718. [CrossRef]
58. Boyjoo, Y.; Rochard, G.; Giraudon, J.-M.; Liu, J.; Lamonier, J.-F. Mesoporous MnO_2 Hollow Spheres for Enhanced Catalytic Oxidation of Formaldehyde. *Sustain. Mater. Technol.* **2019**, *20*, e00091. [CrossRef]
59. Wu, Y.; Guo, Q.; Liu, H.; Wei, S.; Wang, L. Effect of Fe Doping on the Surface Properties of δ-MnO_2 Nanomaterials and Its Decomposition of Formaldehyde at Room Temperature. *J. Environ. Chem. Eng.* **2022**, *10*, 108277. [CrossRef]
60. Bai, B.; Qiao, Q.; Li, J.; Hao, J. Synthesis of Three-Dimensional Ordered Mesoporous MnO_2 and Its Catalytic Performance in Formaldehyde Oxidation. *Chin. J. Catal.* **2016**, *37*, 27–31. [CrossRef]
61. Zhou, L.; Zhang, J.; He, J.; Hu, Y.; Tian, H. Control over the Morphology and Structure of Manganese Oxide by Tuning Reaction Conditions and Catalytic Performance for Formaldehyde Oxidation. *Mater. Res. Bull.* **2011**, *46*, 1714–1722. [CrossRef]
62. Liu, X.; Chen, W.; Wang, W.; Jiang, Y.; Cao, K. PdZn Alloys Decorated 3D Hierarchical Porous Carbon Networks for Highly Efficient and Stable Hydrogen Production from Aldehyde solution. *Int. J. Hydrogen Energy* **2021**, *46*, 33429–33437. [CrossRef]
63. Wang, X.; Jiang, T.; Chen, J.; Zhang, J.; Mai, Y. Hydroxy-Modified Hierarchical Porous Na-CoOx/CN Material for Low-Concentration High-Throughput Formaldehyde Oxidation at Room Temperature. *ChemPlusChem* **2022**, *87*, e202200218. [CrossRef]
64. Sun, Y.; Zhang, Y.; Hou, B.; He, Y.; Weng, W.; Zhu, Y.; Wang, Z. Catalytic Ozonation of Formaldehyde with an Oxygen-Vacancy-Rich MnO_x/γ-Al_2O_3 Catalyst at Room Temperature. *Catalysts* **2024**, *14*, 885. [CrossRef]
65. Liu, X.; Wu, J.; Zhang, S.; Li, Q.; Wu, Z.; Zhang, J. Evaluation of an ε-Manganese (IV) Oxide/Manganese Vanadium Oxide Composite Catalyst Enriched with Oxygen Vacancies for Enhanced Formaldehyde Removal. *Appl. Catal. B Environ.* **2023**, *320*, 121994. [CrossRef]
66. Wang, J.; Zhang, P.; Li, J.; Jiang, C.; Yunus, R.; Kim, J. Room-Temperature Oxidation of Formaldehyde by Layered Manganese Oxide: Effect of Water. *Environ. Sci. Technol.* **2015**, *49*, 12372–12379. [CrossRef]
67. Wang, F.; Dai, H.; Deng, J.; Bai, G.; Ji, K.; Liu, Y. Manganese Oxides with Rod-, Wire-, Tube-, and Flower-Like Morphologies: Highly Effective Catalysts for the Removal of Toluene. *Environ. Sci. Technol.* **2012**, *46*, 4034–4041. [CrossRef]
68. Li, M.; Xu, H.; Hou, Y.; Fu, X.; Yang, J.; Li, Q. The Catalytic and Adsorptive Synergistic Effect of Oxygen-Vacancy-Rich MnO_x/C Catalysts for HCHO Oxidation at Room Temperature. *Ind. Eng. Chem. Res.* **2024**, *63*, 5125–5134. [CrossRef]
69. Liao, Y.; Xie, C.; Liu, Y.; Huang, Q. Enhancement of Photocatalytic Property of ZnO for Gaseous Formaldehyde Degradation by Modifying Morphology and Crystal Defect. *J. Alloys Compd.* **2013**, *550*, 190–197. [CrossRef]
70. Yu, X.; He, J.; Wang, D.; Hu, Y.; Tian, H.; He, Z. Facile Controlled Synthesis of Pt/MnO_2 Nanostructured Catalysts and Their Catalytic Performance for Oxidative Decomposition of Formaldehyde. *J. Phys. Chem. C* **2012**, *116*, 851–860. [CrossRef]
71. Fang, H.; Wang, C.; Li, D.; Zhou, S.; Du, Y.; Zhang, H.; Hang, C.; Tian, Y.; Suga, T. Fabrication of Ag@Ag_2O-MnO_x Composite Nanowires for High-Efficient Room-Temperature Removal of Formaldehyde. *J. Mater. Sci. Technol.* **2021**, *91*, 5–16. [CrossRef]

72. Wu, Y.; Ma, M.; Zhang, B.; Gao, Y.; Lu, W.; Guo, Y. Controlled Synthesis of Porous Co_3O_4 Nanofibers by Spiral Electrospinning and Their Application for Formaldehyde Oxidation. *RSC Adv.* **2016**, *6*, 102127–102133. [CrossRef]
73. Tian, H.; He, J.; Liu, L.; Wang, D. Effects of Textural Parameters and Noble Metal Loading on the Catalytic Activity of Cryptomelane-Type Manganese Oxides for Formaldehyde Oxidation. *Ceram. Int.* **2013**, *39*, 315–321. [CrossRef]
74. Zeng, L.; Song, W.; Li, M.; Zeng, D.; Xie, C. Catalytic Oxidation of Formaldehyde on Surface of $HTiO_2/HCTiO_2$ without Light Illumination at Room Temperature. *Appl. Catal. B Environ.* **2014**, *147*, 490–498. [CrossRef]
75. Zhao, W.K.; Zheng, J.Y.; Wang, X.; Ma, T.; Zhou, K.L.; Wang, H.; Yan, H.; Han, C.B. Removal of Formaldehyde by Triboelectric Charges Enhanced MnO_x-PI at Room Temperature. *Appl. Surf. Sci.* **2021**, *541*, 148430. [CrossRef]
76. Ahmad, W.; Park, E.; Lee, H.; Kim, J.Y.; Kim, B.C.; Jurng, J.; Oh, Y. Defective Domain Control of TiO_2 Support in Pt/TiO_2 for Room Temperature Formaldehyde (HCHO) Remediation. *Appl. Surf. Sci.* **2021**, *538*, 147504. [CrossRef]
77. Huang, Y.; Liu, Y.; Wang, W.; Chen, M.; Li, H.; Lee, S.; Ho, W.; Huang, T.; Cao, J. Oxygen Vacancy–Engineered δ-MnO_x/Activated Carbon for Room-Temperature Catalytic Oxidation of Formaldehyde. *Appl. Catal. B Environ.* **2020**, *278*, 119294. [CrossRef]
78. Kamal, M.S.; Razzak, S.A.; Hossain, M.M. Catalytic Oxidation of Volatile Organic Compounds (VOCs)—A Review. *Atmos. Environ.* **2016**, *140*, 117–134. [CrossRef]
79. Chen, R.; Li, J.; Wang, H.; Chen, P.; Dong, X.; Sun, Y.; Zhou, Y.; Dong, F. Photocatalytic Reaction Mechanisms at a Gas–Solid Interface for Typical Air Pollutant Decomposition. *J. Mater. Chem. A* **2021**, *9*, 20184–20210. [CrossRef]
80. Liu, S.; Niu, S.; Liu, J.; Wang, D.; Wang, Y.; Han, K. Mechanism of Formaldehyde Oxidation Catalyzed by Doped Graphene Single Atom Catalysts: Density Functional Theory Study. *Mol. Catal.* **2022**, *528*, 112516. [CrossRef]
81. Zhou, J.; Liu, G.; Jiang, Q.; Zhao, W.; Ao, Z.; An, T. Density Functional Theory Calculations on Single Atomic Catalysis: Ti-Decorated $Ti_3C_2O_2$ Monolayer (MXene) for HCHO Oxidation. *Chin. J. Catal.* **2020**, *41*, 1633–1644. [CrossRef]
82. Mang, C.; Li, G.; Rao, M.; Zhang, X.; Luo, J.; Jiang, T. An Ab Initio Investigation on the Mechanism of Formaldehyde Oxidation: A Case of Heterogeneous Catalytic Reaction over Graphene-like MnO_2 Monolayer Anchored Different Single Atoms (Fe, Co, and Ni). *Appl. Surf. Sci.* **2023**, *608*, 154964. [CrossRef]
83. Ding, J.; Yang, Y.; Liu, J.; Wang, Z. Catalytic Reaction Mechanism of Formaldehyde Oxidation by Oxygen Species over Pt/TiO_2 Catalyst. *Chemosphere* **2020**, *248*, 125980. [CrossRef] [PubMed]
84. Qian, J.; Mo, J.; Zhou, Y.; Fan, M.; Chen, Y.; Liu, J.; Xu, Y.; Shen, S. Study of Manganese–Cerium Composite Oxide Catalysed Oxidation for Low Concentration Formaldehyde at Room Temperature. *Mater. Chem. Phys.* **2022**, *285*, 126151. [CrossRef]
85. Zhao, H.; Liu, H.; Liu, Y.; Chu, X. Alkali Metal Doped MnO_x Catalysts for Formaldehyde Oxidation. *Catal. Lett.* **2024**, *155*, 40. [CrossRef]
86. Zhang, Y.; Huang, Y.; Lee, S.C.; Cao, J. The Mechanism of Room Temperature Catalytic C–H Dissociation and Oxygenation of Formaldehyde over Nano-Zirconia Phase-Junction. *Chem. Eng. J.* **2020**, *380*, 122498. [CrossRef]
87. Wang, J.; Li, J.; Jiang, C.; Zhou, P.; Zhang, P.; Yu, J. The Effect of Manganese Vacancy in Birnessite-Type MnO_2 on Room-Temperature Oxidation of Formaldehyde in Air. *Appl. Catal. B Environ.* **2017**, *204*, 147–155. [CrossRef]
88. Gallastegi-Villa, M.; Aranzabal, A.; Romero-Sáez, M.; González-Marcos, J.A.; González-Velasco, J.R. Catalytic Activity of Regenerated Catalyst after the Oxidation of 1,2-Dichloroethane and Trichloroethylene. *Chem. Eng. J.* **2014**, *241*, 200–206. [CrossRef]
89. Bartholomew, C.H. Mechanisms of Catalyst Deactivation. *Appl. Catal. A Gen.* **2001**, *212*, 17–60. [CrossRef]
90. Forzatti, P.; Lietti, L. Catalyst Deactivation. *Catal. Today* **1999**, *52*, 165–181. [CrossRef]
91. Neyestanaki, A.K.; Klingstedt, F.; Salmi, T.; Murzin, D.Y. Deactivation of Postcombustion Catalysts, a Review. *Fuel* **2004**, *83*, 395–408. [CrossRef]
92. Abbas, N.; Hussain, M.; Russo, N.; Saracco, G. Studies on the Activity and Deactivation of Novel Optimized TiO_2 Nanoparticles for the Abatement of VOCs. *Chem. Eng. J.* **2011**, *175*, 330–340. [CrossRef]
93. Dai, Q.; Wang, X.; Lu, G. Low-Temperature Catalytic Combustion of Trichloroethylene over Cerium Oxide and Catalyst Deactivation. *Appl. Catal. B Environ.* **2008**, *81*, 192–202. [CrossRef]
94. Kułażyński, M.; van Ommen, J.G.; Trawczyński, J.; Walendziewski, J. Catalytic Combustion of Trichloroethylene over TiO_2-SiO_2 Supported Catalysts. *Appl. Catal. B Environ.* **2002**, *36*, 239–247. [CrossRef]
95. Kießling, D.; Schneider, R.; Kraak, P.; Haftendorn, M.; Wendt, G. Perovskite-Type Oxides—Catalysts for the Total Oxidation of Chlorinated Hydrocarbons. *Appl. Catal. B Environ.* **1998**, *19*, 143–151. [CrossRef]
96. Argyle, M.D.; Bartholomew, C.H. Heterogeneous Catalyst Deactivation and Regeneration: A Review. *Catalysts* **2015**, *5*, 145–269. [CrossRef]
97. HafezKhiabani, N.; Fathi, S.; Shokri, B.; Hosseini, S.I. A Novel Method for Decoking of $Pt–Sn/Al_2O_3$ in the Naphtha Reforming Process Using RF and Pin-to-Plate DBD Plasma Systems. *Appl. Catal. A Gen.* **2015**, *493*, 8–16. [CrossRef]

98. Zhu, B.; Li, X.-S.; Liu, J.-L.; Liu, J.-B.; Zhu, X.; Zhu, A.-M. In-Situ Regeneration of Au Nanocatalysts by Atmospheric-Pressure Air Plasma: Significant Contribution of Water Vapor. *Appl. Catal. B Environ.* **2015**, *179*, 69–77. [CrossRef]
99. Kim, H.H.; Tsubota, S.; Daté, M.; Ogata, A.; Futamura, S. Catalyst Regeneration and Activity Enhancement of Au/TiO_2 by Atmospheric Pressure Nonthermal Plasma. *Appl. Catal. A Gen.* **2007**, *329*, 93–98. [CrossRef]

Disclaimer/Publisher's Note: The statements, opinions and data contained in all publications are solely those of the individual author(s) and contributor(s) and not of MDPI and/or the editor(s). MDPI and/or the editor(s) disclaim responsibility for any injury to people or property resulting from any ideas, methods, instructions or products referred to in the content.

catalysts

MDPI

Article

Metal-Free Cellulose Carbon Nanofiber Supported Graphitic Carbon Nitride for High-Efficient BPA Degradation by Photocatalytic Peroxymonosulfate Activation

Jingjing Liu, Guilong Gao and Lu Gan *

College of Materials Science and Engineering, Nanjing Forestry University, Nanjing 210037, China; liujingjing200503@163.com (J.L.); gaoguilong@njfu.edu.cn (G.G.)
* Correspondence: ganlu@njfu.edu.cn

Abstract

Herein, carbon nanofiber (CNF) was prepared by pyrolyzing electrospun cellulose nanofiber, which was further used to incorporate with graphitic carbon nitride (g-C_3N_4) to prepare metal-free photocatalyst (CNF/g-C_3N_4). CNF/g-C_3N_4 was then used to degrade bisphenol A (BPA) under visible light with the assistance of peroxymonosulfate (PMS). It was illustrated from the results that CNF with conjugated aromatic structure could significantly enhance the light absorption range and capability. At the existence of PMS, 0.5 g/L of CNF/g-C_3N_4 could efficiently degrade 0.05 mM of BPA within 45 min with a high total organic carbon removal rate of >70% under visible light. It was found that the reaction system could generate various reactive oxygen species (ROSs) including hydroxyl radical, superoxide radical and singlet oxygen for BPA degradation. Due to the existence of these species, the reaction system exhibited high performance adaptability towards abundant water matrices and high stability under consecutive runs. This work prospects a new strategy to develop a high-performance advanced oxidation system for quick organic pollutant degradation and mineralization.

Keywords: cellulose; carbon nanofiber; graphitic carbon nitride; composite photocatalyst; peroxymonosulfate; organic pollutant degradation

1. Introduction

Water contamination caused by excessive discharge of refractory organic pollutants (ROPs) such as drugs and personal care products, endocrine disruptors, and pesticides has been regarded as a serious threat to the ecosystem of humans recently [1]. ROPs generally are hard to remove by traditional sewage treatment means due to their stable structures [2]. Moreover, trace concentration of ROPs can cause severe damage to the human body, since most of these ROPs are highly toxic, which can easily accumulate in human organs and cause serious diseases [3]. Bisphenol A (BPA) as a typical endocrine-disrupting ROP has received tremendous attention since it has been frequently detected in various water bodies all over the world. More seriously, the concentrations of the detected BPA were much higher than that of the regulated standards in many countries [4]. Numerous studies have illustrated that BPA can affect the growth, development and reproduction of humans by destroying sex hormones. Advanced oxidation processes (AOPs) have received tremendous research interest in the area of prompt ROP removals since most AOPs can generate a variety of highly reactive oxygenated species (ROSs), including radicals and

non-radicals, which are able to quickly attack ROPs in water with a high mineralization rate [5]. Amongst all AOPs, semiconductor-based photocatalysis is a feasible solution for solving ROP pollution in water by harvesting solar energy to initiate electron–hole pair separations and subsequently produce abundant ROSs [6]. Graphitic carbon nitride (g-C_3N_4), a metal-free photocatalyst with a proper band gap energy of 2.70 eV, has shown enormous potential in ROP degradation since it can absorb visible light as energy and does not bring about secondary pollution to the water matrix during the whole process [7]. However, its practical applications have been significantly restricted due to the nature of slow charge mobility and fast recombination of photogenerated electron–hole pairs, which result in a low quantum utilization rate under light irradiations [8].

Many strategies have been proposed to overcome the defects. One of the applicable approaches is to incorporate carbonaceous materials with g-C_3N_4 [9]. Carbonaceous materials usually have a large specific area, which can promote the dispersion of g-C_3N_4 sheets and subsequently accelerate its quantum absorption capacity by exposing more active sites to irradiated light [10]. In addition, the conjugated aromatic structures within the carbon skeleton can also help to stabilized photogenerated electrons (e^-) and holes (h^+), which prolongs their lifetimes for higher ROS generation possibility [11]. Cellulose nanofiber derived carbon nanofiber (CNF) is a promising carbon candidate for g-C_3N_4 incorporation since cellulose can be easily obtained from abundant available wood biomass, and can be quickly converted to CNF with a high graphitization degree due to its inherent high carbon content [12]. Another way to enhance the photocatalytic performance of g-C_3N_4 is to employ persulfate into the system [13]. With the assistance of persulfate, more types of ROSs can be produced to boost ROP degradations.

Herein, composite photocatalysts based on cellulose carbon nanofiber incorporated g-C_3N_4 (CNF/g-C_3N_4) was prepared and used for BPA degradation under visible light with the assistance of peroxymonosulfate (PMS). The function of CNF and PMS in the reaction system and their synergistic impact on the performance of g-C_3N_4 were systematically studied. It is hypothesized that the reaction system established in this study can provide a new approach for highly efficient ROP degradation in aquatic environments.

2. Results and Discussion

2.1. Characterization of g-C_3N_4/CNF

Figure 1 shows the SEM images of cellulose nanofiber, CNF, g-C_3N_4 and CNF/g-C_3N_4. As illustrated in Figure 1a, the as-prepared cellulose nanofiber exhibited uniform filiform appearance with an average diameter of ~200–300 nm. After pyrolysis, the CNF still maintained the pristine morphology of its mother precursor with an average diameter of ~100–200 nm, except that the nanofibers were somehow curled and cracked due to the decomposition of the cellulose during high-temperature treatment (Figure 1b) [14]. Pristine g-C_3N_4 showed randomly distributed particle structure containing numerous small crystals (Figure 1c). When CNF was incorporated with g-C_3N_4, it was clearly observed from Figure 1d that two components adhered homogeneously with each other, in which the g-C_3N_4 sheets and CNF fibers were clearly revealed.

The fine morphology of CNF/g-C_3N_4 could be further investigated in terms of TEM with the results shown in Figure 2. Two components were clearly observed in Figure 2a which exhibited a uniform structure, indicating strong interactions between two components. From the magnified TEM shown in Figure 2b, it was also distinctly found that CNF integrated with g-C_3N_4, in which the nanofibers intercalated within the g-C_3N_4 sheets.

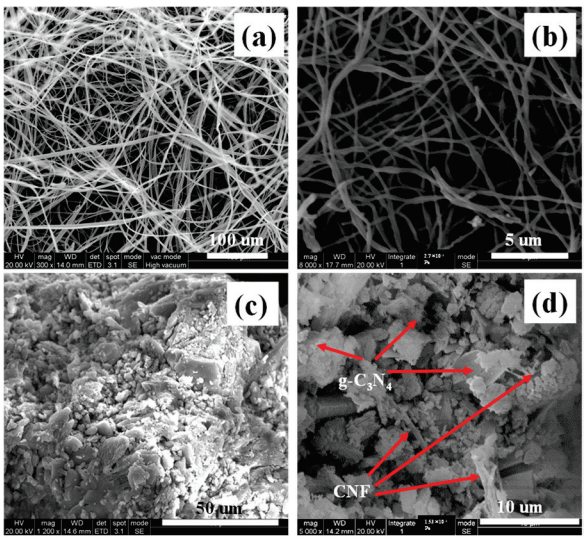


Figure 1. SEM images of (**a**) cellulose nanofiber, (**b**) CNF, (**c**) g−C_3N_4 and (**d**) CNF/g−C_3N_4.

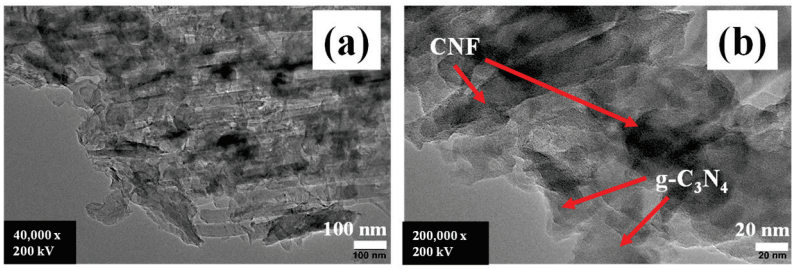


Figure 2. (**a**) TEM and (**b**) magnified TEM images of CNF/g-C_3N_4.

Figure 3a shows the XRD patterns of the prepared catalysts. As demonstrated, cellulose nanofiber contained four typical peaks located at ~12.2°, 20.1°, 22.4° and 35.6°, which were associated with the (1$\bar{1}$0), (110), (200), and (040) planes of cellulose II [15]. This meant the electrospun cellulose was regenerated cellulose instead of raw cellulose. After cellulose nanofibers were pyrolyzed, four peaks all disappeared in the pattern of the resulting CNF. Instead, two new broad peaks located at ~24° and 42° appeared, which were associated with the (002) and (100) lattice planes of a carbonaceous material [16]. This indicated that the skeleton of the carbohydrate polymer precursor was gradually converted to carbon with conjugated aromatic structures after the process was finished [17]. Figure 2a also illustrates that pristine g-C_3N_4 contained two main peaks located at ~13.4°, and 27.3°, which were indexed to the (100) and (002) planes of the hexagonal phase of g-C_3N_4 (JCPDS 87–1526) [18]. After CNF was incorporated, the CNF/g-C_3N_4 still maintained the peaks of g-C_3N_4, indicating that the incorporation of CNF did not break the structure of g-C_3N_4.

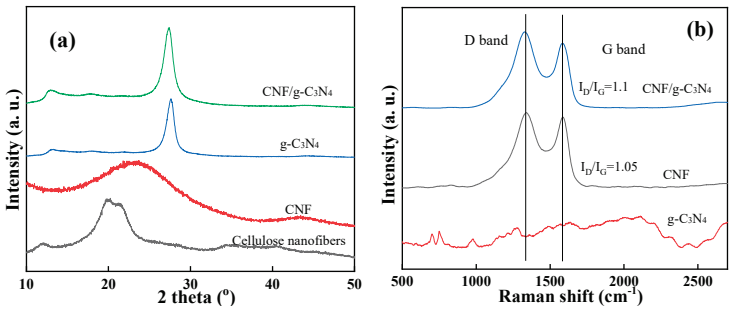


Figure 3. (**a**) XRD patterns of cellulose nanofiber, g−C_3N_4 and CNF/g−C_3N_4; (**b**) Raman spectra of CNF, g−C_3N_4 and CNF/g−C_3N_4.

The existence of CNF in CNF/g-C_3N_4 could be further investigated with Raman spectra with the results shown in Figure 3b. It was presented that the spectrum of pristine g-C_3N_4 contained many small peaks, assigning to the vibration modes of CN heterocycles. Specifically, the peaks at ~700 cm^{-1} were ascribed to the breathing modes of the s-triazine ring in g-C_3N_4. Meanwhile, the peaks located at ~1200–1300 cm^{-1} were corresponded to the lattice vibration of g-C_3N_4 crystal [19]. Furthermore, both CNF and CNF/g-C_3N_4 contained two characteristic peaks at ~1370 cm^{-1} and 1550 cm^{-1}. Generally, these two peaks represented the sp^3 bonding and sp^2 bonding in a carbonaceous material with aromatic structures, which were also named as D band and G band peaks [20]. Moreover, the intensity ratio of these two peaks (I_D/I_G) indicated the graphitization degree of the carbonaceous material [21]. As revealed in Figure 3b, the I_D/I_G value of pristine CNF was 1.05. After it was incorporated with g-C_3N_4, the I_D/I_G value of CNF/g-C_3N_4 was similar (1.10), indicating CNF was uniformly distributed within the CNF/g-C_3N_4 matrix and the graphitic structure of CNF was maintained in the composite. A high degree of the graphitic structure was helpful for accelerating the electron transfer rate during photocatlytic and PMS activation processes, thereby boosting the ROP degradation rate as a result [22].

The light response properties of the prepared photocatalysts were then studied by diffuse reflection spectrum (DRS) with the results shown in Figure 4. It was observed that pristine g-C_3N_4 had adsorption to the light from UV region to the visible region, in which the adsorption edge was located at ~440 nm. This meant that it could generate photo-energy from the visible light, which was in accordance with the previous studies [23]. After CNF was dosed with g-C_3N_4, it was clearly seen that the resulting CNF/g-C_3N_4 had a stronger response to the irradiated light, and the light adsorption edge was further extended. The involvement of CNF significantly enhanced the light absorption capability of g-C_3N_4 [24].

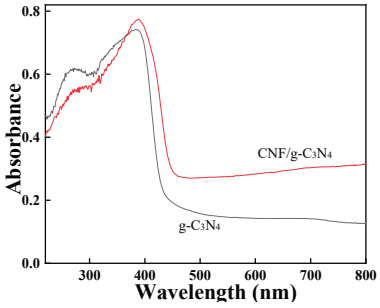


Figure 4. DRS spectra of g−C_3N_4 and CNF/g−C_3N_4.

2.2. Performance of g-C_3N_4/CNF for BPA Degradation

The catalytic activity of different systems was investigated through degrading BPA in water, with the results shown in Figure 5. The pseudo-first-order kinetic constant values (k) and their coefficients of determination (R^2) are also listed in Table 1. Since had relatively low adsorptive capability, the pre-adsorption/desorption process was omitted. Figure 5a first illustrates the performance of different prepared catalysts under the irradiation of visible light. Without the introduction of a photocatalyst, BPA was inert to irradiated light. Moreover, CNF did not show much BPA removal capability with light irradiation (k = 0.001 min^{-1}). No more than 20% of BPA was removed when the reaction time reached 120 min. Since CNF was a zero band gap conductor, the removal of BPA by CNF was mainly triggered by adsorption [25]. As a visible light photocatalyst, g-C_3N_4 was capable of degrading more than 90% of BPA within 120 min (k = 0.018 min^{-1}). When CNF was incorporated, CNF/g-C_3N_4 exhibited significantly enhanced BPA degradation capability,

in which all BPA could be removed within 90 min (k = 0.048 min^{-1}), indicating remarkable electron transfer accelerating capability of CNF.

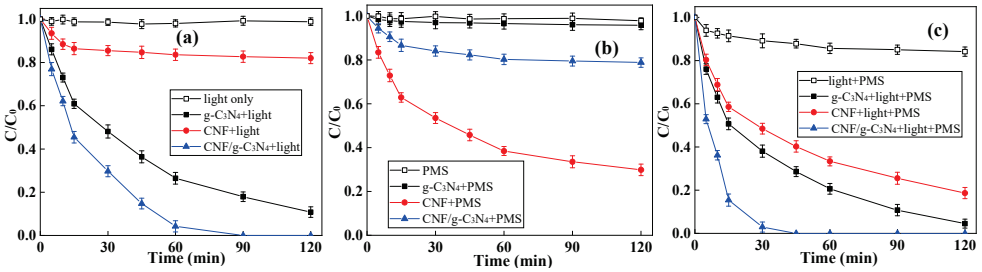


Figure 5. Catalytic performance of CNF, g-C_3N_4 and CNF/g-C_3N_4 under different reaction conditions: (**a**) visible irradiation, (**b**) PMS (2.0 mM) dosage and (**c**) visible irradiation plus PMS dosage (2.0 mM). ($[catalyst]_0$ = 0.5 g/L, $[BPA]_0$ = 0.05 mM).

Table 1. Performances of the prepared catalysts for BPA degradation.

Catalyst	Reaction System	k Value (min^{-1})	R^2
g-C_3N_4	light	0.018	0.98
	PMS	0.001	0.88
	light + PMS	0.022	0.97
CNF	light	0.001	0.96
	PMS	0.013	0.92
	Light + PMS	0.014	0.97
CNF/g-C_3N_4	light	0.048	0.97
	PMS	0.005	0.95
	Light + PMS	0.12	0.99

When light energy was changed to PMS dosing, the performances of different catalysts changed obviously. As illustrated in Figure 5b, both pure PMS and g-C_3N_4/PMS showed negligible BPA degradation activity since g-C_3N_4 did not have active sites for PMS activation on its surface. Conversely, CNF exhibited the optimal BPA degradation capability with the assistance of PMS (k = 0.013 min^{-1}). It has been reported that carbonaceous materials are capable of activating PMS with inherent oxygen containing groups [26]. Therefore, CNF was also able to activate PMS and generate ROSs for BPA degradation. Similarly, CNF/g-C_3N_4 under such circumstances could also degrade ~20% of BPA due to the existence of CNF.

When light irradiation was accompanied by PMS dosage, the BPA removal rate boosted as a result. It was first illustrated in Figure 5c that without the introduction of a catalyst, ~15% of BPA could be degraded by light plus PMS, indicating that light energy could activate a certain degree of PMS in the solution, which was in accordance with the previous studies. In addition, CNF/g-C_3N_4 was capable of degrading all BPA within 40 min under visible light irradiation with the assistance of PMS (k = 0.12 min^{-1}). Compared with the other two samples, CNF/g-C_3N_4 could integrate both high visible light absorption capability and PMS activation capability. Compared with g-C_3N_4 based photocatalyst for BPA degradation, CNF/g-C_3N_4 still exhibited remarkable BPA degradation performance (Table 2). Therefore, CNF/g-C_3N_4 was selected as the probe to investigate the mechanism in the reaction system.

Table 2. Performance comparison of g-C_3N_4 based photocatalysts for BPA degradation.

Catalyst	Light Source	Catalyst Dosage	BPA Concentration	Removal Time	Reference
CNF/g-C_3N_4+PMS	300 W Xenon lamp (CEL-PF300-T6, ZhongJiao jinyuan, Beijing, China)	0.5 g/L	0.05 mM	100%@40 min	This work
Carbon/g-C_3N_4	300 W Xenon lamp (Perfect light, Beijing, China)	0.2 g/L	0.05 mM	100%@75 min	[27]
Ag/S-g-C_3N_4	155 W Xe arc lamp (Newport 67005, Wuxi, China)	0.4 g/L	0.05 mM	80%@180 min	[28]
Fe_2O_3/g-C_3N_4+PDS	LED lamp (Yaming, Shenzhen, China)	0.5 g/L	0.05 mM	95%@60 min	[29]

The generated ROSs in the CNF/g-C_3N_4/visible light/PMS system was investigated first. Figure 6a revealed the performance of CNF/g-C_3N_4 at the existence of different classical scavengers. It was first seen that EDTA did not show inhibition on the performance of the reaction system, indicating that h^+ was not responsible for BPA degradation [22]. Under such conditions, it could be inferred that the photo-generated h^+ was quickly transferred to other ROSs. It was further illustrated from Figure 6a that TBA and MeOH provided similar impediment effects to the reaction system. Since TBA was a typical trapping agent for hydroxyl radical (·OH, k = ~6 × 10^8 $M^{-1}s^{-1}$) instead of sulfate radical ($SO_4^{2-\cdot}$, k = ~4 × 10^5 $M^{-1}s^{-1}$), whereas MeOH was the trapper for both ·OH (~9 × 10^8 $M^{-1}s^{-1}$) and $SO_4^{2-\cdot}$ (~3 × 10^7 $M^{-1}s^{-1}$) [30], the results indicated that only ·OH participated in BPA degradation; h^+ generated under visible light and $SO_4^{2-\cdot}$ generated by PMS activation were both promptly changed to ·OH right after they were produced. It was also seen that L-his exhibited obvious inhibition capability towards BPA degradation, indicating the existence of singlet oxygen ($^1O_2$) in the reaction system [31]. Furthermore, the BPA degradation rate was also impeded by both Cr(VI) and p-BQ, in which the inhibition degrees by these two agents were similar. This meant the photo-generated e^- quickly reacted with dissolved oxygen in the solution and were changed to superoxide radicals ($\cdot O_2^-$) for BPA degradation [32]. Therefore, it could be verified that ·OH and $^1O_2$ were two dominant ROSs which participated in BPA degradation, and $\cdot O_2^-$ was also slightly involved in the degradation reaction.

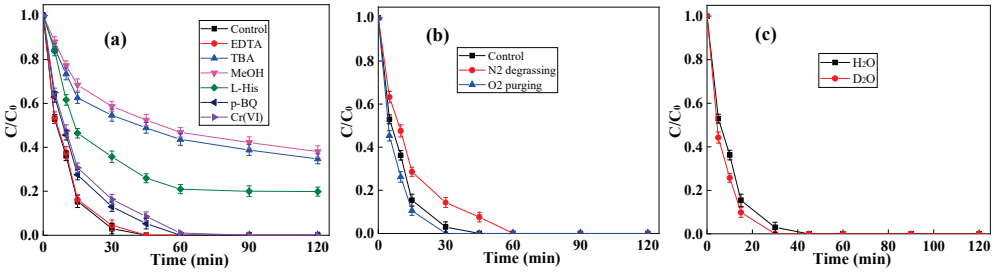


Figure 6. Performance of the CNF/g-C_3N_4/visible light/PMS system (**a**) at the existence of different scavengers, (**b**) at the existence of different gases, and (**c**) when H_2O was changed to D_2O ([catalyst]$_0$ = 0.5 g/L, [BPA]$_0$ = 0.05 mM, [PMS]$_0$ = 2.0 mM).

To confirm the deduction, the performance of the catalyst purged by different gases was then investigated, with the results shown in Figure 6b. It was seen that when the reaction solution was degassed by N_2, the BPA degradation rate slightly decreased, and the decreasing rate was similar to that at the existence of p-BQ and Cr(VI). The results implied that the e^- generated by light irradiation indeed reacted with dissolved oxygen and generated $\cdot O_2^-$ [33]. Therefore, it was further investigated in Figure 6b that when the gas was changed to oxygen, the performance of the CNF/g-C_3N_4/visible light/PMS system increased, since more $\cdot O_3^-$ could be produced for BPA degradation [34]. The existence of $^1O_2$ could be further detected by a solvent changing test. It was illustrated in Figure 6c that when H_2O was changed to D_2O, the BPA degradation rate obviously increased. Since $^1O_2$ had a longer lifetime in D_2O than H_2O [35], the results verified the generation of large amounts of $^1O_2$ which participated in BPA degradation.

The adaptability of the CNF/g-C_3N_4/visible light/PMS system was then investigated. Figure 7a shows the impact of solution pH value fluctuation on the BPA degradation rate in the reaction solution. It was clearly seen that the reaction solution could maintain its high BPA degradation activity at a wide pH range due to the existence of a variety of ROSs. The BPA degradation rate was only impeded a little when the pH value increased to 9. According to the previous studies, the pKa value of PMS was 9.4, which indicated that the activation of PMS was inhibited when the solution pH reached to 9 or higher. In addition, the BPA molecule (pKa = 9.6–10.2) was possibly deprotonated at a pH value of 9. Therefore, both BPA and PMS were not easy to attach onto the surface of CNF/g-C_3N_4 at basic condition [36]. Meanwhile, the reaction system also exhibited stable performance under the interference of different foreign inorganic ions and organic matters. It is clearly seen in Figure 7b that all BPA could be completely degraded in the reaction system within 120 min at the existence of multifarious foreign matters, indicating promising adaptability. The application potential of the CNF/g-C_3N_4/visible light/PMS system was further investigated by degrading BPA in real water matrices with results shown in Figure 7c. When deionized water was changed to tap water or lake water, 0.02 mM of BPA could still be completely degraded in the reaction system within 60 min, which implied significant implications of the reaction system for real-world water treatment.

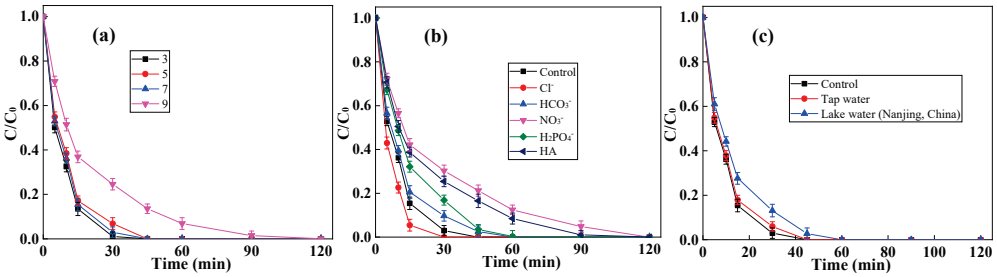


Figure 7. Impact of (**a**) pH value and (**b**) existence of foreign inorganic ions and humic acid, and (**c**) natural water matrices on the performance of the CNF/g−C_3N_4/visible light/PMS system ([catalyst]$_0$ = 0.5 g/L, [BPA]$_0$ = 0.05 mM, [PMS]$_0$ = 2.0 mM).

The long-time use stability of CNF/g-C_3N_4 was further studied by degrading BPA for consecutive cycles. Figure 8a illustrates the BPA degradation capability of the reaction system for four cycles. As revealed, all BPA could be completely degraded even at the fourth run. The performance missing might be ascribed to the gradual consumption of oxygen functional groups on CNF by continuous PMS activation [37]. Due to the existence of multiple ROSs, the reaction system also had a high TOC removal rate. Figure 8b illustrates that total organic carbon (TOC) removal rates were all higher than 60% for four runs, indicating that the CNF/g-C_3N_4/visible light/PMS system was able to mineralize

BPA without bringing about secondary pollution to the reaction solution. Furthermore, it was found from Figure 8c that recycled g-C_3N_4 still maintained its pristine structure, indicating promising long-time use stability.

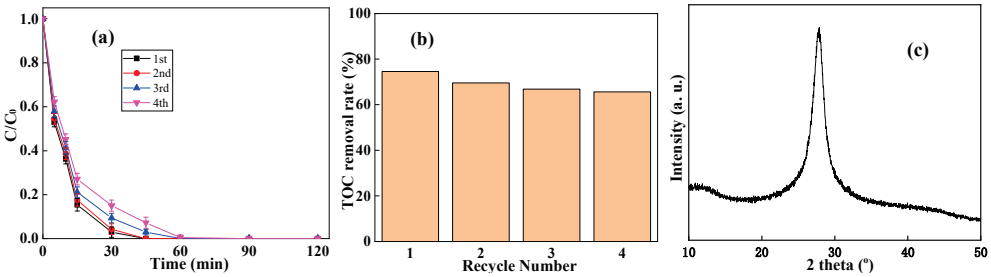


Figure 8. (**a**) Performance and (**b**) TOC removal rates of the CNF/g-C_3N_4/visible light/PMS system for four consecutive BPA degradation cycles ([catalyst]$_0$ = 0.5 g/L, [BPA]$_0$ = 0.05 mM, [PMS]$_0$ = 2.0 mM), (**c**) XRD pattern of recycled g-C_3N_4.

Based on the above results, the photocatalytic PMS activation by CNF/g-C_3N_4 for BPA degradation was proposed, which is schematically illustrated in Figure 9. When CNF/g-C_3N_4 was irradiated by visible light, the e^- at the valance band exited to the conduction band, which then either reacted with the dissolved O_2 and generated $\cdot O_2^-$, or reacted with PMS and produced $SO_4^{2-\cdot}$. $SO_4^{2-\cdot}$ was quickly transferred to ·OH by reacting with hydroxyl ion (OH^-). The h+ left on the valance band also reacted with OH^- to produce more ·OH. Simultaneously, CNF was also able to activate PMS and generate $^1O_2$. All the generated ROSs then oxidized BPA, which was finally mineralized to CO_2 and H_2O.

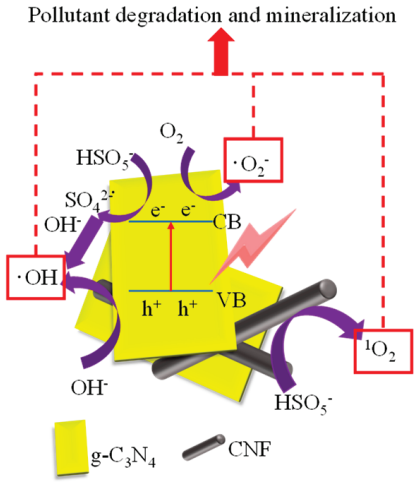


Figure 9. Schematic illustration of the BPA degradation mechanism in the CNF/g−C_3N_4/visible light/PMS system.

The impact of reaction parameters on the performance of CNF/g-C_3N_4 was finally investigated. As illustrated in Figure 10a, 0.02 mM of BPA could be promptly removed within 15 min when the dosage of the catalyst reached 0.8 g/L or higher. Even when the concentration of BPA in the solution reached as high as 0.15 mM, 0.5g/L of CNF/g-C_3N_4 could still degrade more than 90% of BPA within 120 min (Figure 10b). Both results manifested that with the assistance of PMS, CNF/g-C_3N_4 was capable of degrading BPA under visible light irradiations, which exhibited high practical application potentials.

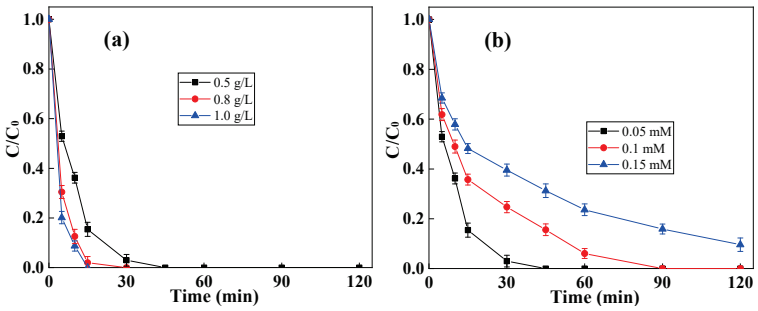


Figure 10. Impact of (**a**) catalyst dosage ($[BPA]_0$ = 0.05 mM, $[PMS]_0$ = 2.0 mM) and (**b**) BPA concentration ($[catalyst]_0$ = 0.5 g/L, $[PMS]_0$ = 2.0 mM) on the performance of the CNF/g−C_3N_4/visible light/PMS system.

3. Materials and Methods

3.1. Reagents and Chemicals

Cellulose acetate (Acetyl 39.8 wt%, hydroxyl 3.5 wt%), melamine (≥99%), Bisphenol A (BPA, ≥99%), L-histidine (L-his, 99%), humic acid (HA, AR), methanol (MeOH), t-butanol (TBA), potassium dichromate (Cr(VI), ≥99.5%) and p-benzoquinone (p-BQ, ≥99%) were purchased from Aladdin (Shanghai, China). Peroxymonosulfate $2KHSO_5 \cdot KHSO_4 \cdot K_2SO_4$, PMS) was purchased from Sigma Aldrich Inc. (Burlington, VT, USA). Other reagents and solvents were of analytical grade and used as received. The double distilled deionized water (H_2O) is used throughout the study.

3.2. Preparation of CNF/g-C_3N_4

The preparation of cellulose nanofibers was described in our previous study [38]. The prepared cellulose nanofiber was pyrolyzed in a tube furnace with a heating rate of 5 °C/min under N_2 atmosphere from room temperature to 800 °C, and stayed at 800 °C for 3 h. After being cooled to room temperature, CNF was obtained. The preparation of CNF/g-C_3N_4 was described as follows: based on our previous study, the yield of g-C_3N_4 produced from melamine was ~60%, and to achieve high photocatalytic performance plus high PMS activation capability [39], the incorporation amount of CNF was set at ~25 wt%. Here, 1 g melamine and 200 mg of CNF were added into 20 mL of H_2O. The solution was sonicated for 30 min and dried under magnetic stirring at 60 °C until all the H_2O was evaporated. The mixture was then transferred into a tube furnace. The tube furnace was heated to 550 °C at a heating rate of 10 °C/min under N_2 atmosphere and maintained at 550 °C for 3 h. After being cooled to room temperature, CNF/g-C_3N_4 was finally obtained. g-C_3N_4 was also prepared by pryolyzing melamine at 550 °C for 3 h following similar procedures.

3.3. Characterizations

The microstructure of the samples was observed by a scanning electron microscope (SEM, JEOL SEM 6490, Tokyo, Japan), and a transmission electron microscope (TEM, FEI F20, Hillsboro, OR, USA). An X-ray diffraction diffractometer (XRD, Rigaku Smartlab, Tokyo, Japan) was employed to analyze the crystalline structure. The graphitic structure of the samples was studied using Raman spectroscopy (Raman, Horiba Jobin Yvon HR800, Kyoto, Japan). The diffuse reflectance spectra (DRS) were conducted by a UV/Vis/NIR spectrophotometer (Perkin Elmer Lambda 950, Waltham, MA, USA). The concentration of the BPA was analyzed by high performance liquid chromatography (HPLC, Dionex Ultimate 3000, Sunnyvale, CA, USA). The total organic carbon (TOC) removal rate was determined with a TOC analyzer (Shimadzu TOC-VCPH, Tokyo, Japan).

3.4. Degradation of BPA in the CNF/g-C_3N_4/Visible Light/PMS System

If not specified, all the experiments were conducted in a 100 mL beaker with magnetic stirring containing 50 mL BPA solution with a concentration of 0.05 mM at room temperature (25 °C). A 300 W Xenon lamp (CEL-PF300-T6, ZhongJiao jinyuan, Beijing, China) with visible a light glass filter (400–700 nm, T% > 95%) at a distance 15 cm from the beaker was used as the light source. After 0.5 g/L of the catalyst and 2.0 mM of PMS was added into the BPA solution, the light was turned on. A total of 1.5 mL of the solution was taken out at pre-determined time intervals, filtered with a 0.22 μm polytetrafluoroethylene membrane and injected into 0.5 mL of fufuryl alcohol to cease the reaction. All the experiments were conducted three times, and all the data points were the average of the experiments. The photocatalytic test and PMS activation test were conducted following similar procedures in the absence of PMS or light irradiation.

4. Conclusions

To conclude, metal-free CNF/g-C_3N_4 photocatalyst was prepared in this study, which was further used for BPA degradation under visible light with the assistance of PMS. The results indicated that the incorporation of CNF significantly improved the photo-absorption capability of g-C_3N_4. Compared with g-C_3N_4, CNF/g-C_3N_4 exhibited better BPA degradation performance under visible light. When PMS was introduced into the reaction system, the CNF/g-C_3N_4/visible light/PMS system exhibited prominent BPA degradation capability, in which 0.05 mM of BPA could be completely degraded within 45 min with a high TOC removal rate (>70%). A scavenging test indicated that $\cdot OH$ and $^1O_2$ were two dominant ROSs involved in BPA degradation. In addition, the reaction system also exhibited high adaptability towards various water matrices. This study demonstrates a novel way to degrade organic pollutants in water with high performance, high mineralization efficiency and high adaptability in real aquatic environments.

Author Contributions: Investigation, J.L. and G.G.; data curation, J.L. and G.G.; formal analysis, J.L.; writing—original draft preparation, J.L.; writing—review and editing, L.G.; supervision, L.G.; project administration, L.G. All authors have read and agreed to the published version of the manuscript.

Funding: This research was funded by Qinglan Project of China (2023).

Data Availability Statement: Data is available upon request.

Acknowledgments: The Advanced Analysis and Testing Center of Nanjing Forestry University is acknowledged.

Conflicts of Interest: The authors declare no conflicts of interest.

References

1. Xu, L.; Qi, L.; Han, Y.; Lu, W.; Han, J.; Qiao, W.; Mei, X.; Pan, Y.; Song, K.; Ling, C.; et al. Improvement of Fe2+/peroxymonosulfate oxidation of organic pollutants by promoting Fe2+ regeneration with visible light driven g-C3N4 photocatalysis. *Chem. Eng. J.* **2022**, *430*, 132828. [CrossRef]
2. Kim, K.-H.; Ihm, S.-K. Heterogeneous catalytic wet air oxidation of refractory organic pollutants in industrial wastewaters: A review. *J. Hazard. Mater.* **2011**, *186*, 16–34. [CrossRef]
3. Ruan, Y.; Kong, L.; Zhong, Y.; Diao, Z.; Shih, K.; Hou, L.a.; Wang, S.; Chen, D. Review on the synthesis and activity of iron-based catalyst in catalytic oxidation of refractory organic pollutants in wastewater. *J. Clean. Prod.* **2021**, *321*, 128924. [CrossRef]
4. Jin, H.; Zhu, L. Occurrence and partitioning of bisphenol analogues in water and sediment from Liaohe River Basin and Taihu Lake, China. *Water Res.* **2016**, *103*, 343–351. [CrossRef] [PubMed]
5. Lado Ribeiro, A.R.; Moreira, N.F.F.; Li Puma, G.; Silva, A.M.T. Impact of water matrix on the removal of micropollutants by advanced oxidation technologies. *Chem. Eng. J.* **2019**, *363*, 155–173. [CrossRef]

6. Wu, Y.; Fang, X.; Shen, X.; Yu, X.; Xia, C.; Xu, L.; Zhang, Y.; Gan, L. Synergetic effect of photocatalytic oxidation plus catalytic oxidation on the performance of coconut shell fiber biochar decorated α-MnO_2 under visible light towards BPA degradation. *J. Environ. Manag.* **2023**, *345*, 118911. [CrossRef] [PubMed]
7. Wen, J.; Xie, J.; Chen, X.; Li, X. A review on g-C3N4-based photocatalysts. *Appl. Surf. Sci.* **2017**, *391*, 72–123. [CrossRef]
8. Xiong, T.; Cen, W.; Zhang, Y.; Dong, F. Bridging the g-C3N4 Interlayers for Enhanced Photocatalysis. *ACS Catal.* **2016**, *6*, 2462–2472. [CrossRef]
9. Inagaki, M.; Tsumura, T.; Kinumoto, T.; Toyoda, M. Graphitic carbon nitrides (g-C3N4) with comparative discussion to carbon materials. *Carbon* **2019**, *141*, 580–607. [CrossRef]
10. Woan, K.; Pyrgiotakis, G.; Sigmund, W. Photocatalytic Carbon-Nanotube–TiO_2 Composites. *Adv. Mater.* **2009**, *21*, 2233–2239. [CrossRef]
11. Kim, J.R.; Kan, E. Heterogeneous photocatalytic degradation of sulfamethoxazole in water using a biochar-supported TiO_2 photocatalyst. *J. Environ. Manag.* **2016**, *180*, 94–101. [CrossRef] [PubMed]
12. Gan, L.; Zhong, Q.; Geng, A.; Wang, L.; Song, C.; Han, S.; Cui, J.; Xu, L. Cellulose derived carbon nanofiber: A promising biochar support to enhance the catalytic performance of $CoFe_2O_4$ in activating peroxymonosulfate for recycled dimethyl phthalate degradation. *Sci. Total Environ.* **2019**, *694*, 133705. [CrossRef] [PubMed]
13. Xu, G.; Wu, Y.; Fang, X.; Li, J.; Xu, L.; Han, S.; Cui, J.; Gan, L. One-step solvothermal synthesis of wood flour carbon fiber/BiOBr composites for photocatalytic activation of peroxymonosulfate towards sulfadiazine degradation: Mechanisms comparison between photo, chemical and photo-chemical oxidation processes. *Sep. Purif. Technol.* **2022**, *297*, 121399. [CrossRef]
14. Lédé, J. Cellulose pyrolysis kinetics: An historical review on the existence and role of intermediate active cellulose. *J. Anal. Appl. Pyrolysis* **2012**, *94*, 17–32. [CrossRef]
15. Liu, Z.; Sun, X.; Hao, M.; Huang, C.; Xue, Z.; Mu, T. Preparation and characterization of regenerated cellulose from ionic liquid using different methods. *Carbohydr. Polym.* **2015**, *117*, 99–105. [CrossRef]
16. Yu, X.; Wang, L.; Shen, X.; Wu, Y.; Xu, L.; Zhang, Y.; Shi, J.; Gan, L. New insight into the S and N co-doped poplar biochar for efficient BPA removal via peroxymonosulfate activation: S for adsorptive removal and N for catalytic removal. *Sep. Purif. Technol.* **2025**, *354*, 128809. [CrossRef]
17. Shi, J.; Dai, B.; Shen, X.; Xu, L.; Zhang, Y.; Gan, L. Wood induced preparation of Fe3C decorated biochar for peroxymonosulfate activation towards bisphenol a degradation with low ion leaching. *J. Environ. Manag.* **2023**, *340*, 117978. [CrossRef]
18. Orooji, Y.; Ghanbari, M.; Amiri, O.; Salavati-Niasari, M. Facile fabrication of silver iodide/graphitic carbon nitride nanocomposites by notable photo-catalytic performance through sunlight and antimicrobial activity. *J. Hazard. Mater.* **2020**, *389*, 122079. [CrossRef]
19. Zinin, P.V.; Ming, L.-C.; Sharma, S.K.; Khabashesku, V.N.; Liu, X.; Hong, S.; Endo, S.; Acosta, T. Ultraviolet and near-infrared Raman spectroscopy of graphitic C3N4 phase. *Chem. Phys. Lett.* **2009**, *472*, 69–73. [CrossRef]
20. Guizani, C.; Haddad, K.; Limousy, L.; Jeguirim, M. New insights on the structural evolution of biomass char upon pyrolysis as revealed by the Raman spectroscopy and elemental analysis. *Carbon* **2017**, *119*, 519–521. [CrossRef]
21. Xu, W.; Wang, L.; Shen, X.; Wu, Y.; Xu, L.; Zhang, Y.; Shi, J.; Gan, L. Lignin regulating the active sites and peroxymonosulfate activation capacities of iron incorporated 1D carbon nanofiber for efficient organic pollutant degradation. *Sep. Purif. Technol.* **2025**, *354*, 129156. [CrossRef]
22. Gan, L.; Geng, A.; Song, C.; Xu, L.; Wang, L.; Fang, X.; Han, S.; Cui, J.; Mei, C. Simultaneous removal of rhodamine B and Cr(VI) from water using cellulose carbon nanofiber incorporated with bismuth oxybromide: The effect of cellulose pyrolysis temperature on photocatalytic performance. *Environ. Res.* **2020**, *185*, 109414. [CrossRef]
23. Yang, X.; Qian, F.; Zou, G.; Li, M.; Lu, J.; Li, Y.; Bao, M. Facile fabrication of acidified g-C3N4/g-C3N4 hybrids with enhanced photocatalysis performance under visible light irradiation. *Appl. Catal. B Environ.* **2016**, *193*, 22–35. [CrossRef]
24. Tang, R.; Gong, D.; Deng, Y.; Xiong, S.; Zheng, J.; Li, L.; Zhou, Z.; Su, L.; Zhao, J. π-π stacking derived from graphene-like biochar/g-C3N4 with tunable band structure for photocatalytic antibiotics degradation via peroxymonosulfate activation. *J. Hazard. Mater.* **2022**, *423*, 126944. [CrossRef] [PubMed]
25. Cheng, N.; Wang, B.; Wu, P.; Lee, X.; Xing, Y.; Chen, M.; Gao, B. Adsorption of emerging contaminants from water and wastewater by modified biochar: A review. *Environ. Pollut.* **2021**, *273*, 116448. [CrossRef] [PubMed]
26. Wu, Q.; Zhang, Y.; Liu, H.; Liu, H.; Tao, J.; Cui, M.-H.; Zheng, Z.; Wen, D.; Zhan, X. FexN produced in pharmaceutical sludge biochar by endogenous Fe and exogenous N doping to enhance peroxymonosulfate activation for levofloxacin degradation. *Water Res.* **2022**, *224*, 119022. [CrossRef]
27. Wu, M.; He, X.; Jing, B.; Wang, T.; Wang, C.; Qin, Y.; Ao, Z.; Wang, S.; An, T. Novel carbon and defects co-modified g-C3N4 for highly efficient photocatalytic degradation of bisphenol A under visible light. *J. Hazard. Mater.* **2020**, *384*, 121323. [CrossRef]
28. Oh, W.-D.; Lok, L.-W.; Veksha, A.; Giannis, A.; Lim, T.-T. Enhanced photocatalytic degradation of bisphenol A with Ag-decorated S-doped g-C3N4 under solar irradiation: Performance and mechanistic studies. *Chem. Eng. J.* **2018**, *333*, 739–749. [CrossRef]
29. Yan, S.; Shi, Y.; Tao, Y.; Zhang, H. Enhanced persulfate-mediated photocatalytic oxidation of bisphenol A using bioelectricity and a g-C3N4/Fe2O3 heterojunction. *Chem. Eng. J.* **2019**, *359*, 933–943. [CrossRef]

30. Li, S.; Huang, J.; Li, X.; Li, L. The relation of interface electron transfer and PMS activation by the H-bonding interaction between composite metal and MCM-48 during sulfamethazine ozonation. *Chem. Eng. J.* **2020**, *398*, 125529. [CrossRef]
31. Hua, L.-C.; OuYang, R.-C.; Zhao, Z.; Nguyen, T.N.A.; Huang, C. Homogeneous versus heterogeneous Mn(II) oxidation in peroxymonosulfate assisting chlorination: Synergistic role for enhanced Mn(II) oxidation in water treatment. *Water Res.* **2024**, *265*, 122265. [CrossRef]
32. Xiao, H.; Wang, Y.; Lv, K.; Zhu, C.; Guan, X.; Xie, B.; Zou, X.; Luo, X.; Zhou, Y. N-doped biochar-Fe/Mn as a superior peroxymonosulfate activator for enhanced bisphenol a degradation. *Water Res.* **2025**, *278*, 123399. [CrossRef] [PubMed]
33. Gu, J.; Song, Y.; Yang, Y.; Guan, C.; Jiang, J. Theoretical investigation into activation of hydroperoxides by excited quinones under ultraviolet irradiation. *Chem. Eng. J.* **2023**, *463*, 142423. [CrossRef]
34. Xie, J.; Pan, X.; Jiang, C.; Zhao, L.; Gong, X.; Liu, Y. Enhanced conversion of superoxide radical to singlet oxygen in peroxymonosulfate activation by metal-organic frameworks derived heteroatoms dual-doped porous carbon catalyst. *Environ. Res.* **2023**, *236*, 116745. [CrossRef] [PubMed]
35. Lu, H.; Gan, L. Catalytic Degradation of Bisphenol A in Water by Poplar Wood Powder Waste Derived Biochar via Peroxymonosulfate Activation. *Catalysts* **2022**, *12*, 1164. [CrossRef]
36. Guan, Y.-H.; Ma, J.; Li, X.-C.; Fang, J.-Y.; Chen, L.-W. Influence of pH on the Formation of Sulfate and Hydroxyl Radicals in the UV/Peroxymonosulfate System. *Environ. Sci. Technol.* **2011**, *45*, 9308–9314. [CrossRef]
37. Ding, H.; Zhu, Y.; Wu, Y.; Zhang, J.; Deng, H.; Zheng, H.; Liu, Z.; Zhao, C. In Situ Regeneration of Phenol-Saturated Activated Carbon Fiber by an Electro-peroxymonosulfate Process. *Environ. Sci. Technol.* **2020**, *54*, 10944–10953. [CrossRef]
38. Geng, A.; Meng, L.; Han, J.; Zhong, Q.; Li, M.; Han, S.; Mei, C.; Xu, L.; Tan, L.; Gan, L. Highly efficient visible-light photocatalyst based on cellulose derived carbon nanofiber/BiOBr composites. *Cellulose* **2018**, *25*, 4133–4144. [CrossRef]
39. Han, Y.; Gan, L.; Gong, H.; Han, J.; Qiao, W.; Xu, L. Photoactivation of peroxymonosulfate by wood pulp cellulose biochar/g-C3N4 composite for diclofenac degradation: The radical and nonradical pathways. *Biochar* **2022**, *4*, 35. [CrossRef]

Disclaimer/Publisher's Note: The statements, opinions and data contained in all publications are solely those of the individual author(s) and contributor(s) and not of MDPI and/or the editor(s). MDPI and/or the editor(s) disclaim responsibility for any injury to people or property resulting from any ideas, methods, instructions or products referred to in the content.

catalysts

MDPI

Article

$Zn_{0.8}Cd_{0.2}S$ Photocatalyst Modified with $Ni(OH)_2$ for Enhanced Photocatalytic Hydrogen Production

Qianran Feng, Xiaoting Yu, Jinlian Peng, Siying Du, Liuyun Chen, Xinyuan Xu and Tongming Su *

Guangxi Key Laboratory of Petrochemical Resource Processing and Process Intensification Technology, School of Chemistry and Chemical Engineering, Guangxi University, Nanning 530004, China; qianranfeng@163.com (Q.F.); alkaid0331@163.com (X.Y.); l13976060612@163.com (J.P.); dsy3322156148@163.com (S.D.); zjgxuxu@163.com (X.X.)
* Correspondence: sutm@gxu.edu.cn

Abstract

Sustainable production of hydrogen is currently a global research hotspot. In this study, a $Ni(OH)_2$ cocatalyst was loaded on $Zn_{0.8}Cd_{0.2}S$ to form $Ni(OH)_2$/ZCS composites and achieve highly efficient photocatalytic hydrogen production. After $Ni(OH)_2$ loading, a close contact interface was established between $Ni(OH)_2$ and $Zn_{0.8}Cd_{0.2}S$, which increased the separation efficiency of the photogenerated electrons and holes. Moreover, the addition of $Ni(OH)_2$ increases the specific surface area and light absorption of $Ni(OH)_2/Zn_{0.8}Cd_{0.2}S$, and the $Ni(OH)_2$ can act as active sites for photocatalytic hydrogen production. The photocatalytic H_2 production rate of $Ni(OH)_2$/ZCS composites increases with the increase in the Ni amount. 9$Ni(OH)_2$/ZCS exhibited the optimum H_2 production rate of 12.88 mmol h^{-1} g^{-1}, which was 9.9 times higher than that of $Zn_{0.8}Cd_{0.2}S$. When the amount of $Ni(OH)_2$ is further increased, the excess $Ni(OH)_2$ covers the active site of $Zn_{0.8}Cd_{0.2}S$ and reduced the light absorption of $Zn_{0.8}Cd_{0.2}S$, resulting in a decrease in the H_2 production rate. Furthermore, the H_2 production rate of 9$Ni(OH)_2$/ZCS decreased from 12.88 to 5.15 mmol g^{-1} h^{-1} after 3 cycles. The main reason for the decline in the photocatalytic performance of $Ni(OH)_2$/ZCS is the photocorrosion of $Zn_{0.8}Cd_{0.2}S$. This study provides an innovative design for loading $Ni(OH)_2$ cocatalysts on $Zn_{0.8}Cd_{0.2}S$ to improve the performance of photocatalysts.

Keywords: $Zn_{0.8}Cd_{0.2}S$; $Ni(OH)_2$; cocatalyst; photocatalytic; hydrogen

1. Introduction

In recent years, global energy scarcity and environmental pollution caused by the burning of fossil fuels have become increasingly serious problems [1,2]. Therefore, there is an urgent need to find a clean energy source [3,4]. Hydrogen, as an ideal clean energy source, is an alternative to fossil energy sources [5]. Among the various methods of hydrogen production, the use of solar energy to produce hydrogen is regarded as a promising strategy [6,7]. Since 1972, when Professors Fujishima A and Honda K discovered that TiO_2 possesses photocatalytic activity [8], researchers have developed various semiconductor photocatalysts, such as metal sulfides, (oxy)nitrides, and metal oxides, in recent decades [9–12].

Among the various types of metal sulfides, ZnCdS is a typical ternary sulfide that has wide spectral absorption and appropriate redox potentials [13,14]. Previous studies have shown that the separation efficiency of photoelectrons and holes is greatly improved when the Zn/Cd molar ratio is 0.8:0.2 [14]. Compared with other $Zn_{(1-x)}Cd_xS$ materials,

$Zn_{0.8}Cd_{0.2}S$ has more surface defect states, which can serve as active sites to improve the performance of photocatalytic hydrogen production. Moreover, the photocatalytic hydrogen production efficiency of $Zn_{0.8}Cd_{0.2}S$ is much greater than that of ZnS and CdS under visible light [15]. However, the fast recombination of photoexcited charge carriers and severe photocorrosion limit their photocatalytic activity [16,17]. The addition of suitable cocatalysts is an effective means to improve the performance and stability of $Zn_{0.8}Cd_{0.2}S$ in photocatalytic hydrogen production reactions [18].

Noble metals, such as Pt, Pd, Ag, and Au, have been widely used to improve the performance of photocatalytic hydrogen production. However, most noble metal cocatalysts are scarce and expensive. To reduce the cost of photocatalytic hydrogen production, finding alternative cocatalysts to replace precious metals has become a popular research topic. More recently, researchers have reported that Ni-based cocatalysts have the advantages of low cost, easy access, and high stability and can be used as ideal cocatalysts for photocatalysts [19–21]. For example, Lei et al. prepared a NiS@ZnCdS z-scheme heterostructure via a hydrothermal method, which enhances the separation of photogenerated electron–hole pairs and increases the photocatalytic activity [22]. In addition, Pan et al. prepared $Zn_{0.3}Cd_{0.7}S/NiS_{1.97}$ nanocomposites [23], in which $NiS_{1.97}$ nanosheets are tightly coupled to the inner surface of $Zn_{0.3}Cd_{0.7}S$ hollow spheres as cocatalysts. The hollow spherical shell structure decreases the distance of charge transfer to the surface, promotes the absorption of incident light, and significantly improves the photocatalytic hydrogen production performance [24,25].

However, the photocatalytic performance of ZnCdS is still relatively low; therefore, more Ni-based cocatalysts need to be developed to increase the stability and activity of the photocatalysts [26,27]. In recent years, $Ni(OH)_2$ has received widespread attention because of its low cost, high stability, and simple preparation method. According to previous reports, $Ni(OH)_2$ loaded on photocatalysts can efficiently inhibit the recombination of photogenerated electrons and holes, making it a promising noble metal-free cocatalyst [28,29]. Moreover, the formation of an interface between the $Ni(OH)_2$ cocatalyst and the photocatalyst is utilized to facilitate charge carrier separation, and the $Ni(OH)_2$ cocatalyst can also be used as an active site for surface reactions [29]. For example, the photocatalytic hydrogen evolution rate of a $Ni(OH)_2$-modified two-dimensional $ZnIn_2S_4$ heterostructure reached 4640 μmol h^{-1} g^{-1} under visible light irradiation ($\lambda > 420$ nm) [30], which can be attributed to the synergistic effect between $Ni(OH)_2$ and $ZnIn_2S_4$. Compared with those on pristine $ZnIn_2S_4$, the assembled β-$Ni(OH)_2$ nanosheets on the surface of exfoliated $ZnIn_2S_4$ nanosheets significantly promoted charge separation, water oxidation kinetics, and photocatalytic performance [31,32].

Although $Ni(OH)_2$ has been widely researched as a co-catalyst for photocatalytic H_2 production, its practical application is still limited by the low photocatalytic efficiency. The morphology, proportion, and contact interface in $Ni(OH)_{2\text{-based}}$ composite photocatalysts are the key factors influencing the H_2 production rate. In this work, $Ni(OH)_2$ nanosheets were successfully loaded on $Zn_{0.8}Cd_{0.2}S$ nanospheres by a simple method. The influence of the $Ni(OH)_2$ content on the photocatalytic activity of $Zn_{0.8}Cd_{0.2}S$ was investigated. Under visible light irradiation, the H_2 production rate of $9Ni(OH)_2/ZCS$ is significantly higher than that of other $Ni(OH)_{2\text{-based}}$ photocatalysts. In addition, the mechanism of photogenerated carrier transfer between $Ni(OH)_2$ and $Zn_{0.8}Cd_{0.2}S$ was revealed, and a mechanism for photocatalytic hydrogen production over $Ni(OH)_2/Zn_{0.8}Cd_{0.2}S$ composites was proposed.

2. Results and Discussion

The XRD patterns of $Zn_{0.8}Cd_{0.2}S$, $Ni(OH)_2$, and the $Ni(OH)_2$/ZCS composite are shown in Figure 1a. The peaks at 27.3°, 28.7°, and 30.7° in the XRD patterns of $Zn_{0.8}Cd_{0.2}S$ can be attributed to the (100), (002), and (101) crystal planes of $Zn_{0.8}Cd_{0.2}S$, respectively [14]. The position of these peaks of $Zn_{0.8}Cd_{0.2}S$ is completely consistent with the standard wurtzite structure, which confirms that the synthesized material has a typical hexagonal wurtzite crystal structure [33]. The diffraction peaks at 19.1°, 33.0°, 38.8°, 51.9°, 59.0°, and 62.6° can be attributed to the (001), (100), (011), (012), (110), and (111) crystal planes of β-$Ni(OH)_2$, respectively [34]. According to Equation (1), the Coherent Scattering Domain (CSD) size of $Zn_{0.8}Cd_{0.2}S$ and Ni(OH) is 13.7 and 4.34 nm, respectively.

$$CSD = \frac{K\lambda}{\beta cos\theta} \quad (1)$$

where K is the shape factor (value is 0.9), λ is the X-ray wavelength, and β is the full width at half maximum of the diffraction peak, θ is the diffraction angle.

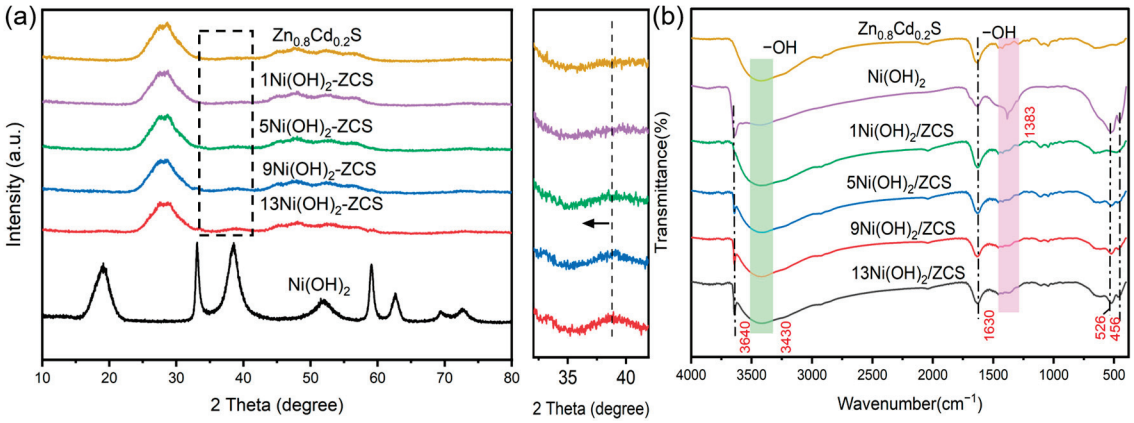


Figure 1. XRD patterns (**a**) and FT-IR spectra (**b**) of the $Zn_{0.8}Cd_{0.2}S$, $Ni(OH)_2$, and $Ni(OH)_2$/ZCS composites. (The figure on the right side of (**a**) shows the enlarged patterns of the dash box in (**a**)).

After loading $Ni(OH)_2$ on the surface of $Zn_{0.8}Cd_{0.2}S$, the XRD peak of the $Ni(OH)_2$/ZCS composite catalyst was consistent with that of the original $Zn_{0.8}Cd_{0.2}S$, indicating that β-$Ni(OH)_2$ did not change the structure of $Zn_{0.8}Cd_{0.2}S$. When the loading content of $Ni(OH)_2$ was greater than 5 wt%, the $Ni(OH)_2$/ZCS composites presented a weak diffraction peak at 38.8°, which was attributed to the (011) plane of $Ni(OH)_2$ [9]. These results confirm the successful synthesis of the $Ni(OH)_2$/ZCS composites.

The FT-IR spectra of the $Zn_{0.8}Cd_{0.2}S$, $Ni(OH)_2$, and $Ni(OH)_2$/ZCS composites are shown in Figure 1b. The broad peak at 3430 cm^{-1} corresponded to the bending vibration of O-H, and the peak at 1630 cm^{-1} was attributed to the stretching vibration of O-H, which was derived from the water absorbed on the photocatalyst surface. The peak at 3640 cm^{-1} is attributed to the stretching vibration mode of nonhydrogen-bonded hydroxyl groups in $Ni(OH)_2$, indicating that the hydroxyl groups in $Ni(OH)_2$ were arranged freely and existed in the form of β-$Ni(OH)_2$ [35], which was consistent with the XRD results. Notably, there were peaks at 3640 cm^{-1} in the $Ni(OH)_2$/ZCS composite, indicating the presence of $Ni(OH)_2$ in the composite. The absorption peak of $Ni(OH)_2$ at 1383 cm^{-1} corresponded to the vibration of the interlayer NO_3^-, which originated from nitrate during the preparation process. Moreover, $Ni(OH)_2$ and $Ni(OH)_2$/ZCS have two infrared peaks at 526 cm^{-1} and 456 cm^{-1}, which are attributed to the Ni–O stretching vibration in β-$Ni(OH)_2$ and the bending vibration of Ni–O–H [36], respectively. The above results further indicate the successful synthesis of the $Ni(OH)_2$/ZCS composites.

N_2 adsorption–desorption isotherms of the $Ni(OH)_2$/ZCS composites are shown in Figure S1a. Figure S1a shows that the N_2 adsorption–desorption isotherms of the $Ni(OH)_2$/ZCS composites and $Zn_{0.8}Cd_{0.2}S$ are type IV. The pore size distribution curve in Figure S1b shows that the pore size distributions of the $Zn_{0.8}Cd_{0.2}S$ and $Ni(OH)_2$/ZCS composites range from 1~5 nm. The specific surface area and average pore size of the $Zn_{0.8}Cd_{0.2}S$ and $Ni(OH)_2$/ZCS composites are shown in Table S1. The specific surface area of the $Ni(OH)_2$/ZCS composites was slightly greater than that of $Zn_{0.8}Cd_{0.2}S$. The specific surface areas of $Zn_{0.8}Cd_{0.2}S$, 1$Ni(OH)_2$/ZCS, 5$Ni(OH)_2$/ZCS, 9$Ni(OH)_2$/ZCS, and 13$Ni(OH)_2$/ZCS were 204.6, 204.9, 209.2, 212.4, and 212.8 $m^2\ g^{-1}$, respectively. Notably, the specific surface area of the $Ni(OH)_2$/ZCS composites gradually increased with increasing $Ni(OH)_2$ content. In general, an increase in the specific surface area of a photocatalyst can provide more surface active sites, which is beneficial for photocatalytic hydrogen production. In addition, the average pore size of the $Ni(OH)_2$/ZCS composites (~3 nm) was slightly greater than that of $Zn_{0.8}Cd_{0.2}S$ (2.81 nm), indicating that the addition of $Ni(OH)_2$ can regulate the pore structure of the $Ni(OH)_2$/ZCS composites.

The morphologies of the $Zn_{0.8}Cd_{0.2}S$, $Ni(OH)_2$, and $Ni(OH)_2$/ZCS composites were characterized by scanning electron microscopy (SEM). As shown in the SEM images of $Zn_{0.8}Cd_{0.2}S$ (Figure 2a), $Zn_{0.8}Cd_{0.2}S$ has a microsphere shape with a diameter of approximately 100 nm. In addition, the surface of the $Zn_{0.8}Cd_{0.2}S$ nanospheres was rough, with small nanoparticles uniformly distributed on the surface. As shown in Figure 2b, $Ni(OH)_2$ has a nanosheet structure. The SEM images of the $Ni(OH)_2$/ZCS composites (Figure 2c–f) are similar to those of the $Zn_{0.8}Cd_{0.2}S$ nanospheres, and no $Ni(OH)_2$ nanosheets can be clearly observed in the $Ni(OH)_2$/ZCS composites, indicating that the $Ni(OH)_2$ nanosheets were uniformly distributed on the surface of the small $Zn_{0.8}Cd_{0.2}S$ nanospheres.

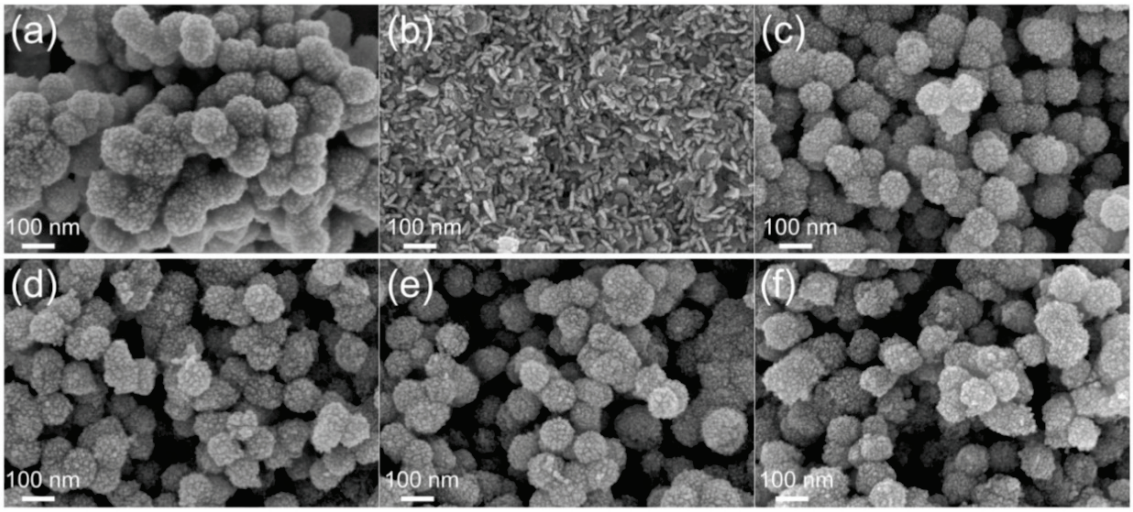


Figure 2. SEM images of $Zn_{0.8}Cd_{0.2}S$ (**a**), $Ni(OH)_2$ (**b**), 1$Ni(OH)_2$/ZCS (**c**), 5$Ni(OH)_2$/ZCS (**d**), 9$Ni(OH)_2$/ZCS (**e**), and 13$Ni(OH)_2$/ZCS (**f**).

Figure 3a confirmed that the $Zn_{0.8}Cd_{0.2}S$ nanospheres consisted of small nanoparticles. Figure 3b shows that the lattice fringe spacings of 0.31 nm and 0.19 nm are attributed to the (002) and (110) crystal planes of hexagonal $Zn_{0.8}Cd_{0.2}S$, respectively. The TEM images of $Ni(OH)_2$ (Figure 3d,e) further confirmed the nanosheet shape of $Ni(OH)_2$, and the lattice fringes of 0.23 and 0.46 nm were attributed to the (011) and (001) crystal planes of β-phase $Ni(OH)_2$, respectively [37]. Figure 3c,f show that the diffraction rings of the $Zn_{0.8}Cd_{0.2}S$ and $Ni(OH)_2$ samples correspond to the (100) and (110) crystal planes of $Zn_{0.8}Cd_{0.2}S$ and the (011) and (004) crystal planes of $Ni(OH)_2$, respectively. The above results indicated that $Zn_{0.8}Cd_{0.2}S$ and $Ni(OH)_2$ were successfully prepared.

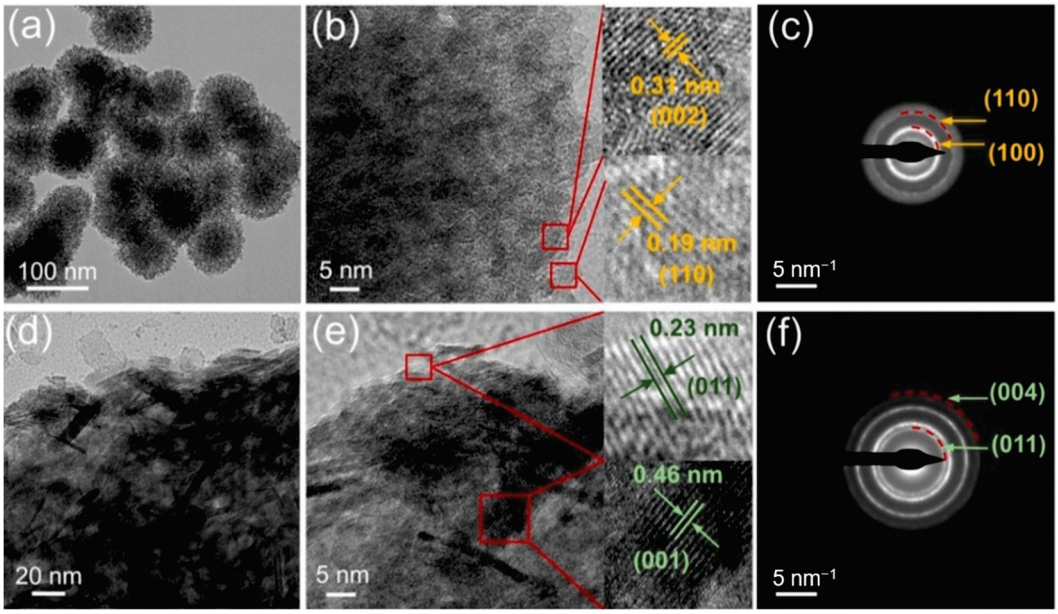


Figure 3. TEM images, HRTEM images, and SAED patterns of $Zn_{0.8}Cd_{0.2}S$ (**a**–**c**) and $Ni(OH)_2$ (**d**–**f**).

The TEM, SAED, and EDS element distribution maps of $9Ni(OH)_2/ZCS$ are shown in Figure 4. After the $9Ni(OH)_2/ZCS$ composite was synthesized, the morphology of the nanospheres was still maintained, and several $9Ni(OH)_2$ nanosheets were observed on the surface of the nanospheres (Figure 4a). As shown in the HRTEM images of $9Ni(OH)_2/ZCS$ (Figure 4b), the lattice spacings of 0.32 and 0.23 nm correspond to the (100) crystal plane of $Zn_{0.8}Cd_{0.2}S$ and the (011) crystal plane of $Ni(OH)_2$, respectively, indicating that close contact interfaces formed between $Ni(OH)_2$ and $Zn_{0.8}Cd_{0.2}S$. In addition, two diffraction rings in the SAED patterns (Figure 4c) of $9Ni(OH)_2/ZCS$ correspond to the (100) plane of $Zn_{0.8}Cd_{0.2}S$ and the (012) plane of $Ni(OH)_2$. The EDS results (Figure 4d) corresponding to the HAADF-STEM image show that Zn, Cd, S, Ni, and O were evenly distributed in the $9Ni(OH)_2/ZCS$ sample. The above results show that the $9Ni(OH)_2/ZCS$ composite was successfully constructed.

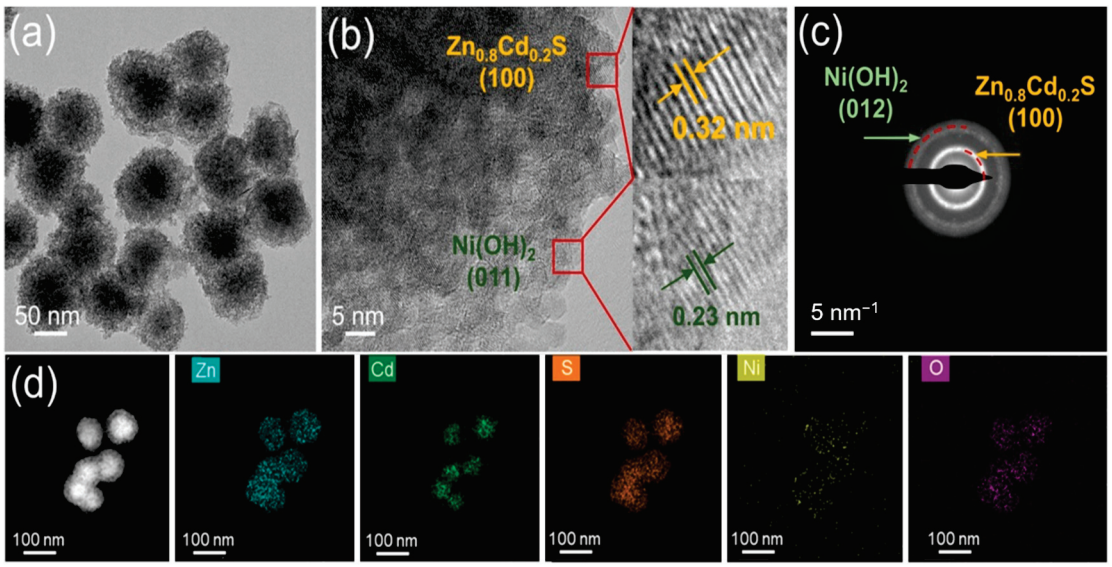


Figure 4. TEM images (**a**), HRTEM images (**b**), SAED patterns (**c**), HAADF-STEM images and corresponding elemental (Zn, Cd, S, Ni, O) mappings (**d**) of $9Ni(OH)_2/ZCS$.

To reveal the valence state of the elements in the $Ni(OH)_2$/ZCS composites, the surface chemical states of the $Zn_{0.8}Cd_{0.2}S$, $Ni(OH)_2$, and $9Ni(OH)_2$/ZCS composites were analyzed via XPS (Figure 5). As shown in Figure 5a, the XPS survey spectra of $9Ni(OH)_2$/ZCS reveal that Zn, Cd, S, Ni, and O are present in $9Ni(OH)_2$/ZCS. As shown in Figure 5b–d, the peaks of Zn 2p (1045.31 and 1022.31 eV), Cd 3d (411.89 and 405.17 eV), and S 2p (163.10 and 161.85 eV) of $Zn_{0.8}Cd_{0.2}S$ were attributed to Zn^{2+}, Cd^{2+}, and S^{2-} [38], respectively. Compared with those of $Zn_{0.8}Cd_{0.2}S$, the XPS peaks of Zn 2p, Cd 3d, and S 2p in $9Ni(OH)_2$/ZCS shifted to higher binding energies. Zn $2p_{1/2}$ and Zn $2p_{3/2}$ shifted to 1045.37 and 1022.41 eV, Cd $3d_{3/2}$ and Cd $3d_{5/2}$ shifted to 412.11 and 405.38 eV, and S $2p_{1/2}$ and S $2p_{3/2}$ shifted to 163.43 and 162.08 eV, respectively.

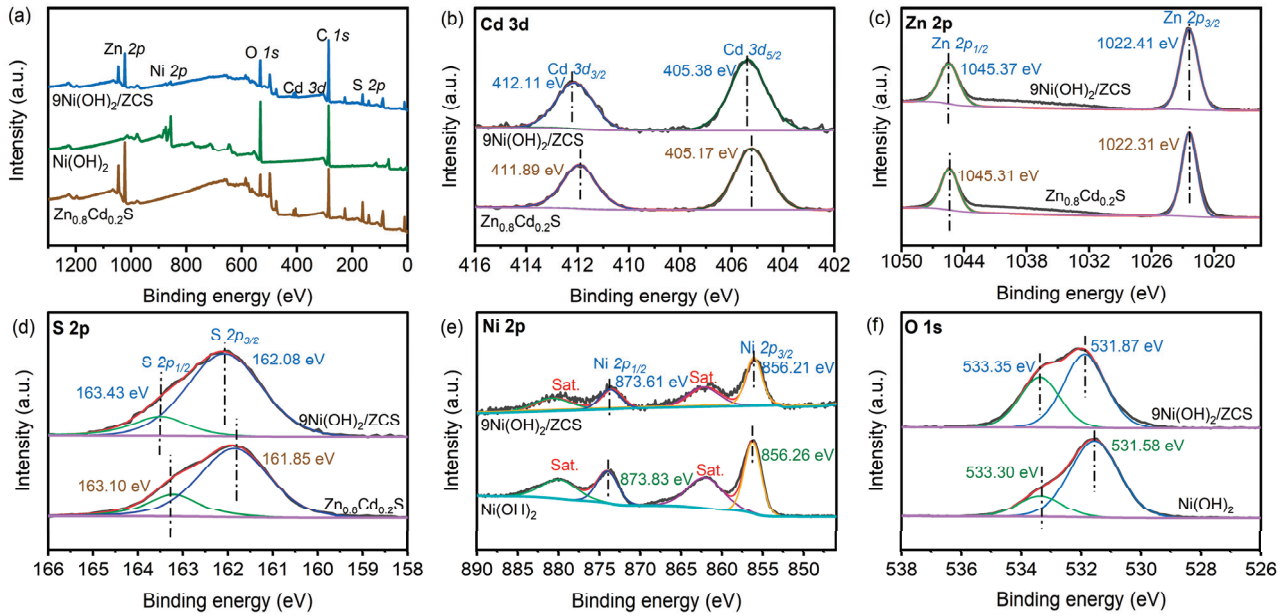


Figure 5. XPS survey spectra (**a**) and high-resolution XPS spectra of Cd 3d (**b**), Zn 2p (**c**), S 2p (**d**), Ni 2p (**e**), and O 1s (**f**) in $Zn_{0.8}Cd_{0.2}S$, $Ni(OH)_2$, and $9Ni(OH)_2$/ZCS.

The high-resolution XPS spectra of Ni 2p are shown in Figure 5e. The binding energies of Ni $2p_{1/2}$ and Ni $2p_{3/2}$ of $Ni(OH)_2$ were located at 873.71 and 856.26 eV, respectively, and two adjacent peaks at 879.92 and 861.90 eV were attributed to satellite peaks [39]. Notably, the Ni 2p peak of $9Ni(OH)_2$/ZCS was located at 873.61 and 856.21 eV, which shifted to lower binding energies by 0.1 and 0.05 eV, respectively, than that of $Ni(OH)_2$. As shown in Figure 5f, the O 1 s peaks of $9Ni(OH)_2$/ZCS exhibit two peaks at 533.54 and 532.07 eV, which are attributed to hydroxide and water adsorbed on the surface, respectively. Compared with the O 1s peak of $Ni(OH)_2$ (533.39 and 531.58 eV), the O 1s peak of $9Ni(OH)_2$/ZCS shifted to higher binding energies by 0.15 and 0.49 eV. These results revealed that there is a strong interaction between $Ni(OH)_2$ and $Zn_{0.8}Cd_{0.2}S$ composites and that the electron can transfer from $Zn_{0.8}Cd_{0.2}S$ to $Ni(OH)_2$ after $Ni(OH)_2$ contacts $Zn_{0.8}Cd_{0.2}S$. In addition, in $Ni(OH)_2$, electrons gather at the Ni site, which might be the active site for photocatalytic hydrogen production.

The light absorption of the $Zn_{0.8}Cd_{0.2}S$, $Ni(OH)_2$, and $Ni(OH)_2$/ZCS composites was analyzed via UV–vis diffuse reflectance spectroscopy. As shown in Figure 6a, the UV–vis diffuse reflectance spectra of $Ni(OH)_2$ show strong absorption in the range of 230~800 nm [40]. Notably, the absorption at 600~800 nm of the $Ni(OH)_2$/ZCS composites gradually increased with increasing content of $Ni(OH)_2$. Notably, the absorption edge of the $Ni(OH)_2$/ZCS did not shift, indicating that $Ni(OH)_2$ did not change the band structure

of $Zn_{0.8}Cd_{0.2}S$. In addition, the band gap of $Zn_{0.8}Cd_{0.2}S$ was estimated to be 2.65 eV (Figure 6b).

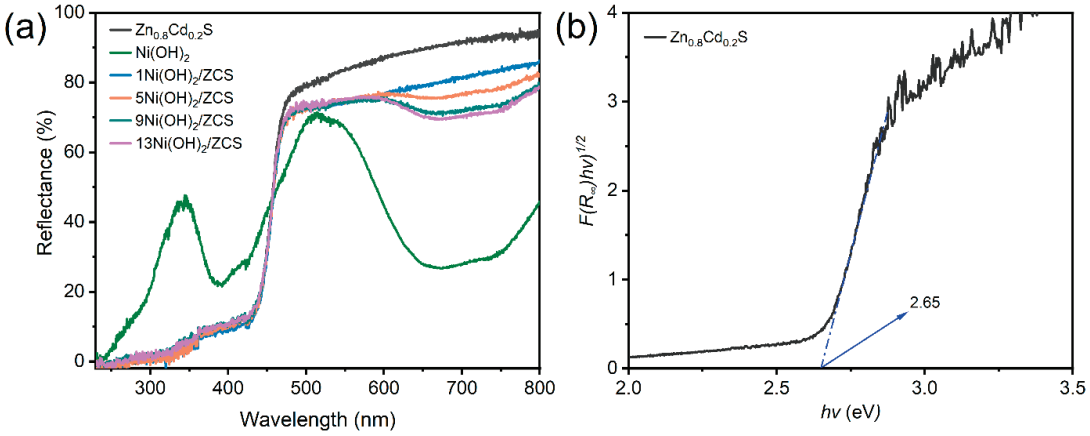


Figure 6. UV–vis diffuse reflectance spectra of the $Zn_{0.8}Cd_{0.2}S$, $Ni(OH)_2$, and $Ni(OH)_2$/ZCS composites (**a**), band gap (**b**) of $Zn_{0.8}Cd_{0.2}S$.

The separation efficiencies of the photogenerated charge carriers of the $Zn_{0.8}Cd_{0.2}S$ and $Ni(OH)_2$/ZCS composites were investigated via PL spectra [41]. Figure 7a shows that the PL intensity of the $Ni(OH)_2$/ZCS composites was significantly lower than that of $Zn_{0.8}Cd_{0.2}S$, indicating that the loading of $Ni(OH)_2$ on the surface of $Zn_{0.8}Cd_{0.2}S$ effectively inhibited the recombination of photogenerated electrons and holes. TRPL spectra were used to further analyze the separation of photogenerated electrons and holes. As shown in Figure 7b, the average fluorescence lifetime of $9Ni(OH)_2$/ZCS was 5.19 ns, which was longer than that of $Zn_{0.8}Cd_{0.2}S$ (4.37 ns), further demonstrating that the $Ni(OH)_2$ cocatalyst can effectively inhibit the recombination of photogenerated electrons and holes [42].

To further clarify the separation of the photogenerated electrons and holes in the catalyst, the photoelectrochemical properties of $Zn_{0.8}Cd_{0.2}S$ and $9Ni(OH)_2$/ZCS were investigated. As shown in Figure 7c, the transient photocurrent of $9Ni(OH)_2$/ZCS was significantly greater than that of $Zn_{0.8}Cd_{0.2}S$, indicating that the separation of photogenerated charge carriers was enhanced by the addition of the $Ni(OH)_2$ cocatalyst. In addition, to study the electron transfer resistance of the catalyst, the EIS data of $Zn_{0.8}Cd_{0.2}S$ and $9Ni(OH)_2$/ZCS were obtained. As shown in Figure 7d, the arc radius of $9Ni(OH)_2$/ZCS was smaller than that of $Zn_{0.8}Cd_{0.2}S$, indicating that the charge transfer resistance in $9Ni(OH)_2$/ZCS was lower. The above analysis indicates that the loading of $Ni(OH)_2$ on $Zn_{0.8}Cd_{0.2}S$ promoted the separation of photogenerated electrons and holes, which is beneficial for the photocatalytic hydrogen production reaction.

The performance of the photocatalysts for photocatalytic hydrogen production under visible light ($\lambda > 400$ nm) was investigated with Na_2S (0.35 M)/Na_2SO_3 (0.25 M) mixed aqueous solutions as sacrificial agents. As shown in Figures 8a and S2, the photocatalytic H_2 production rate of $Zn_{0.8}Cd_{0.2}S$ was 1.30 mmol h^{-1} g^{-1}. After $Ni(OH)_2$ was loaded on $Zn_{0.8}Cd_{0.2}S$, the H_2 production rate significantly increased. When the $Ni(OH)_2$ content was 9 wt%, the H_2 production rate of $9Ni(OH)_2$/ZCS reached the highest value of 12.88 mmol h^{-1} g^{-1}, which was 9.9 times greater than that of $Zn_{0.8}Cd_{0.2}S$. However, when the $Ni(OH)_2$ content increased to 13 wt%, the H_2 production rate decreased to 12.30 mmol h^{-1} g^{-1}, possibly because excessive $Ni(OH)_2$ covered the surface of $Zn_{0.8}Cd_{0.2}S$ and reduced the light absorption of $Zn_{0.8}Cd_{0.2}S$. Notably, no H_2 product can be detected over $Ni(OH)_2$ after photocatalytic reaction for 4 h, indicating that $Ni(OH)_2$ only acts as a cocatalyst of $Zn_{0.8}Cd_{0.2}S$ to enhance its photocatalytic performance. The performance comparison is shown in Table S2. The H_2 production rate of $9Ni(OH)_2$/ZCS is signifi-

cantly higher than that of other reported photocatalysts. In pure water, 9Ni(OH)$_2$/ZCS exhibits a low photocatalytic H_2 production rate of 49.86 μmol·g^{-1}·h^{-1}. The extremely low H_2 production efficiency of photocatalytic overall water splitting severely hinders its practical application. Constructing heterojunctions and redox-active sites can promote the separation of photogenerated electron-hole pairs and the hydrogen/oxygen evolution, thereby achieving efficient photocatalytic overall water splitting. In addition, the catalytic performances normalized on surface area and mass are shown in Table S3. 9Ni(OH)$_2$/ZCS shows the highest H_2 production rate normalized on surface area or mass.

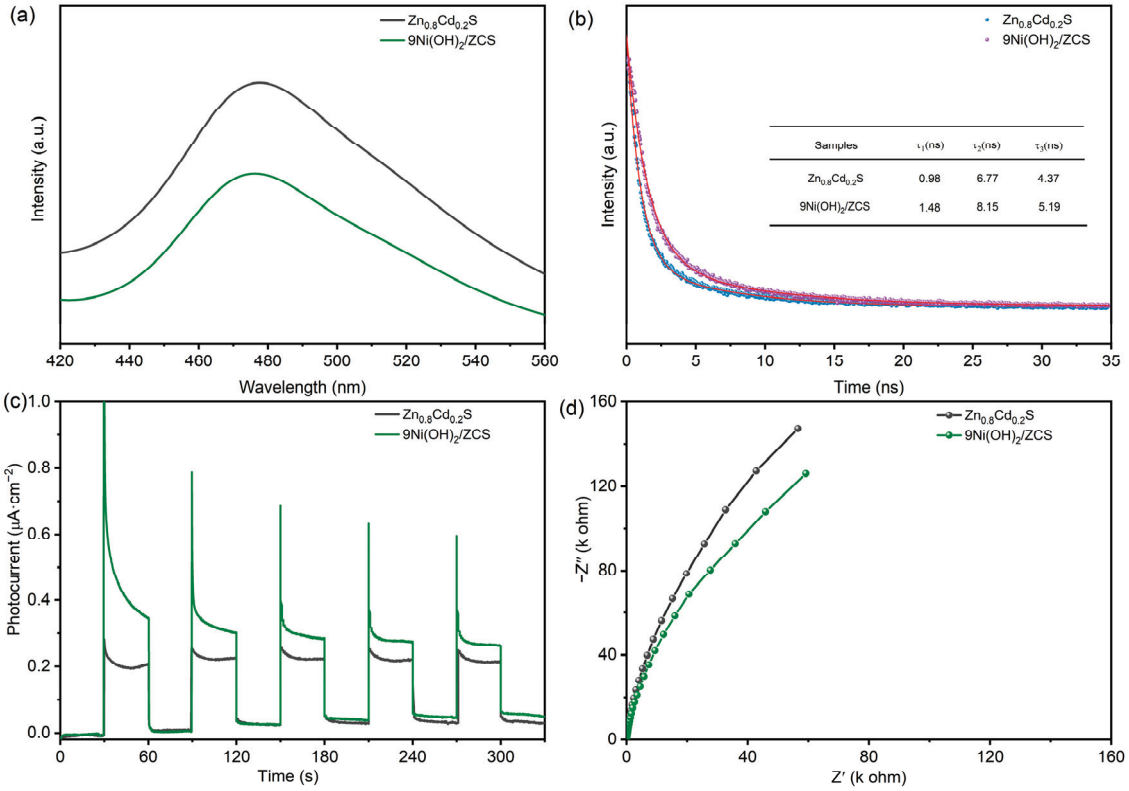


Figure 7. PL spectra (**a**), TRPL spectra (**b**), transient photocurrent response (**c**), and EIS Nyquist plots of $Zn_{0.8}Cd_{0.2}S$ and 9Ni(OH)$_2$/ZCS (**d**).

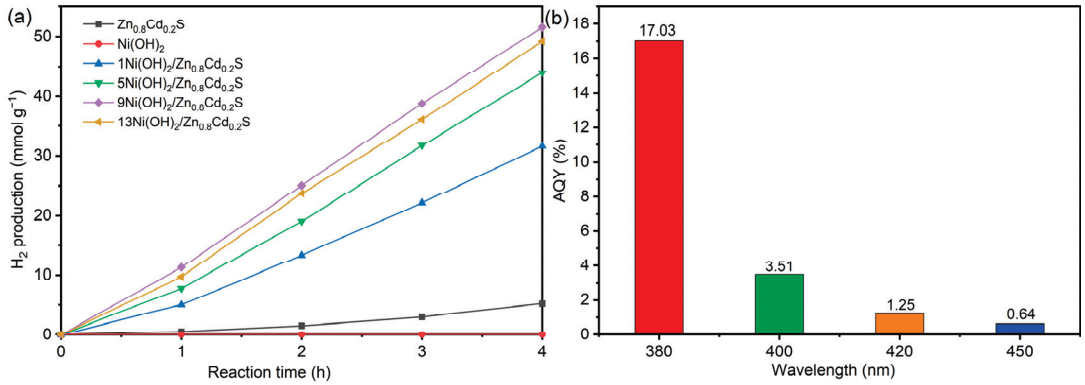


Figure 8. Photocatalytic H_2 production performance of the $Zn_{0.8}Cd_{0.2}S$, Ni(OH)$_2$, and Ni(OH)$_2$/ZCS composites (**a**) and the AQY of 9Ni(OH)$_2$/ZCS at different wavelengths of 380, 400, 420, and 450 nm (**b**).

To reveal the utilization efficiency of optical energy, the apparent quantum yield (AQY) of 9Ni(OH)$_2$/ZCS at different wavelengths (380 nm, 400 nm, 420 nm, and 450 nm) was tested. As shown in Figure 8b, the AQYs of 9Ni(OH)$_2$/ZCS are 17.03%, 3.51%, 1.25%, and

0.64% at 380 nm, 400 nm, 420 nm, and 450 nm, respectively. On the basis of our previous research on $Zn_{0.8}Cd_{0.2}S$ [14], the AQY of 9Ni(OH)$_2$/ZCS at 400 nm was greater than that of $Zn_{0.8}Cd_{0.2}S$ (2.05%), which demonstrated that the addition of the Ni(OH)$_2$ cocatalyst significantly improved the utilization of visible light by $Zn_{0.8}Cd_{0.2}S$.

To evaluate the reusability of the 9Ni(OH)$_2$/ZCS photocatalysts, cyclic experiments were carried out on 9Ni(OH)$_2$/ZCS. As shown in Figure S2b, after 3 cycles, the stability of 1Ni(OH)$_2$/ZCS, 5Ni(OH)$_2$/ZCS, 9Ni(OH)$_2$/ZCS, and 13Ni(OH)$_2$/ZCS decreased by 59.84%, 58.71%, 58.13%, and 62.09%, respectively. After 5 cycles, the stability of 1Ni(OH)$_2$/ZCS, 5Ni(OH)$_2$/ZCS, 9Ni(OH)$_2$/ZCS, and 13Ni(OH)$_2$/ZCS decreased by 82.12%, 78.25%, 74.11%, and 78.67%, respectively. To determine the reason for the decrease in hydrogen production, the sacrificial agent was supplemented in the sixth cycle of the reaction. After the addition of the sacrificial agent, the H_2 production rate of 9Ni(OH)$_2$/ZCS only slightly improved. This result indicated that the main reason for the decrease in the H_2 production rate of 9Ni(OH)$_2$/ZCS was not the consumption of sacrificial agents.

To further investigate the stability of 9Ni(OH)$_2$/ZCS, 9Ni(OH)$_2$/ZCS after the reaction was characterized via XRD, XPS, SEM, and TEM. As shown in Figure S3a, the XRD patterns of the 9Ni(OH)$_2$/ZCS photocatalyst before and after the reaction indicated that the crystal structure of 9Ni(OH)$_2$/ZCS was stable. The CSD size of 9Ni(OH)$_2$/ZCS is 12.76 nm, which is similar to that of 9Ni(OH)$_2$/ZCS before reaction (13.58 nm) and $Zn_{0.8}Cd_{0.2}S$ (13.70 nm). However, the high-resolution XPS spectra of 9Ni(OH)$_2$/ZCS after the reaction (Figure S3b–f) revealed that the XPS peaks of Zn 2p, Cd 3d, S 2p, and O 1s in 9Ni(OH)$_2$/ZCS shifted to higher binding energies, whereas the XPS peaks of Ni 2p shifted to lower binding energies. That is, the electronic structure of 9Ni(OH)$_2$/ZCS changed after the reaction, which may be attributed to the photocorrosion of $Zn_{0.8}Cd_{0.2}S$. In addition, as shown in Figure S4a, SEM images of 9Ni(OH)$_2$/ZCS after the reaction revealed that 9Ni(OH)$_2$/ZCS still maintained the nanosphere morphology after the reaction. Moreover, the Ni(OH)$_2$ nanosheet can still be observed in the TEM image (Figure S4b). In Figure S4c, the (002) plane of $Zn_{0.8}Cd_{0.2}S$ and the (011) plane of Ni(OH)$_2$ can be observed in the HRTEM image of 9Ni(OH)$_2$/ZCS after the reaction. Moreover, the element mapping corresponding to the HAADF-STEM image (Figure S4c) shows that Zn, Cd, S, Ni, and O were uniformly distributed in 9Ni(OH)$_2$/ZCS. The above results demonstrated that the composition and structure of 9Ni(OH)$_2$/ZCS remain unchanged after the reaction, and the possible reason for the decreased photocatalytic performance of 9Ni(OH)$_2$/ZCS might be the photocorrosion of $Zn_{0.8}Cd_{0.2}S$. To enhance the stability of Ni(OH)$_2$/ZCS, some potential strategies are believed to effectively prevent the photocorrosion of $Zn_{0.8}Cd_{0.2}S$. Firstly, the photogenerated holes on $Zn_{0.8}Cd_{0.2}S$ transfer or consumption via a reasonable heterojunction (e.g., S-scheme heterojunction, Z-scheme heterojunction, etc.). Secondly, anchoring photo-oxidation active sites (e.g., CoO_x, MnO_x, etc.) accelerates the photocatalytic oxidation reaction and the consumption of photogenerated holes. Finally, constructing core–shell structures (e.g., surface passivation layers, shell structures) restricts the detachment of S.

From Figure 9a, the E_{cutoff} value of $Zn_{0.8}Cd_{0.2}S$ is 7.71 eV. According to Equations (2)–(4), the work function of $Zn_{0.8}Cd_{0.2}S$ is calculated as 3.51 eV, and the Fermi level of $Zn_{0.8}Cd_{0.2}S$ is determined to be −3.51 eV (vs. vacuum level). Furthermore, the VB potential of $Zn_{0.8}Cd_{0.2}S$ is determined to be 1.80 eV (vs. Fermi level), which is converted to −5.31 eV (vs. vacuum level). Combined with the bandgap, the CB potential of $Zn_{0.8}Cd_{0.2}S$ is derived via Equation (5) as −2.66 eV (vs. vacuum level). The energy level structure of $Zn_{0.8}Cd_{0.2}S$ is shown in Figure 9b.

$$\phi = hv - E_{cutoff} \quad (2)$$

$$E_F = E_{vac} - \phi \quad (3)$$

$$E_{VB} = E_F - E_{VB}(vs\ \text{Fermi level}) \quad (4)$$

$$E_g = E_{CB} - E_{VB} \quad (5)$$

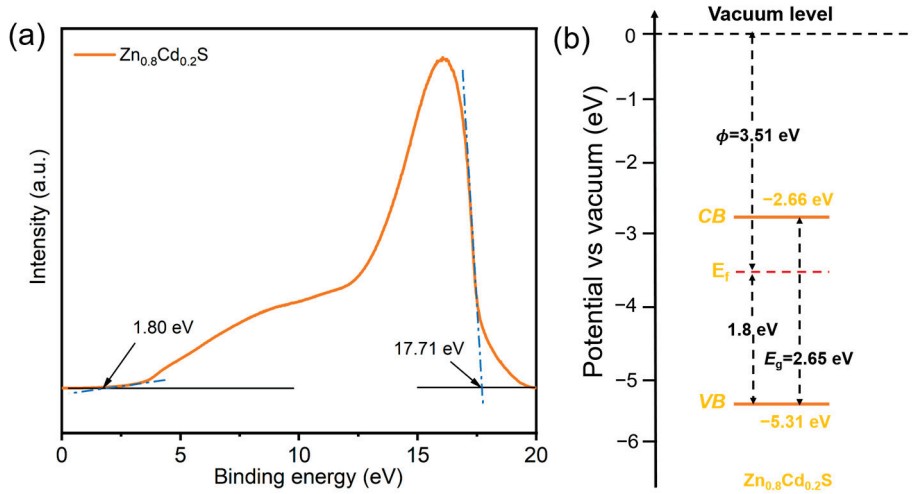


Figure 9. UPS spectrum (**a**) and energy level structures of $Zn_{0.8}Cd_{0.2}S$ (**b**).

Combining the above results, a possible mechanism for photocatalytic hydrogen production over $Ni(OH)_2$/ZCS composites was proposed. As shown in Figure 10, the electrons in the valence band (VB) of $Zn_{0.8}Cd_{0.2}S$ were stimulated to the conduction band (CB) under visible light. The photogenerated electrons of $Zn_{0.8}Cd_{0.2}S$ can then transfer to $Ni(OH)_2$ through the close contact interfaces between $Zn_{0.8}Cd_{0.2}S$ and $Ni(OH)_2$. Moreover, the photogenerated electrons can rapidly migrate to the surface of $Ni(OH)_2$, and $Ni(OH)_2$ can act as the active site for reducing H^+ to H_2. In addition, the photogenerated holes in the valence band of $Zn_{0.8}Cd_{0.2}S$ are consumed by the hole sacrificial agent, which effectively promotes the separation of photogenerated electrons and holes. Thus, the photocatalytic H_2 production performance of the $Ni(OH)_2$/ZCS composites was greatly improved.

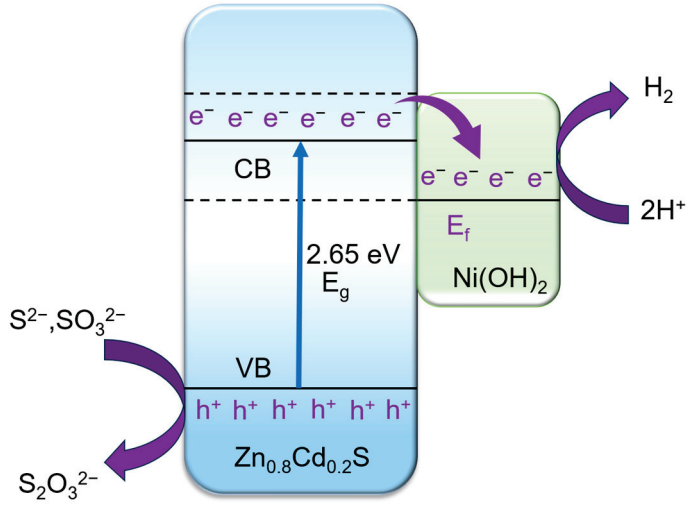


Figure 10. Charge transfer pathway and mechanism of photocatalytic hydrogen production over $Ni(OH)_2$/ZCS composites under visible light irradiation.

3. Experimental Section

3.1. Materials

All the chemicals used during the experiments were of analytical grade and were used without further purification and processing. Zinc acetate dihydrate ($Zn(CH_3COO)_2{\cdot}2H_2O$,

Damao Chemical Reagent Factory, Tianjin, China, >99%), cadmium acetate dihydrate ($Cd(CH_3COO)_2 \cdot 2H_2O$, Komeo Chemical Reagent Co., Ltd., Tianjin, China, >99.5%), polyvinylpyrrolidone ($(C_6H_9NO)_n$, PVP, Shanghai Aladdin Biochemical Technology Co., Ltd., Shanghai, China, Mr = 1,300,000), thiourea (CH_4N_2S, Guanghua Sci-Tech Co., Ltd., Shantou, China, >99%), sodium sulfide nonahydrate ($Na_2S \cdot 9H_2O$, Xilong Scientific Co., Ltd., Shantou, China, >98%), sodium sulfite (Na_2SO_3, Xilong Scientific Co., Ltd., Shantou, China, >97%), nickel nitrate ($Ni(NO_3)_2$, Komeo Chemical Reagents Ltd., Tianjin, China, >99%), nickel nitrate (NaOH, Komeo Chemical Reagents Ltd., Tianjin, China, >98%), ethylene glycol ($(CH_2OH)_2$, Kemao Chemical Reagent Co., Ltd., Tianjin, China, >99%), triethanolamine ($C_6H_{15}NO_3$, Xilong Scientific Co., Ltd., Shantou, China, ≥98%), methanol (CH_4O, Sinopharm Chemical Reagent Co., Ltd., Shanghai, China, ≥99.5%), lactic acid ($CH_3CH(OH)COOH$, Tianjin Fuyu Fine Chemical Co., Ltd., Tianjin, China, 85.0–90.0%).

3.2. Synthesis of $Zn_{0.8}Cd_{0.2}S$

1.2 mmol of $Cd(CH_3COO)_2 \cdot 2H_2O$ and 4.8 mmol of $Zn(CH_3COO)_2 \cdot 2H_2O$ were dissolved in 60 mL of ethylene glycol while stirring, and then, 1.08 g of PVP and 7.5 mmol of CH_4N_2S were added to the solution. The above solution was subsequently transferred to a 100 mL stainless steel high-pressure reactor with Teflon lining, which was heated at 180 °C and maintained for 12 h. After the reactants cooled, the obtained precipitates were centrifuged and washed 5 times with deionized water and anhydrous ethanol. After that, the precipitate was dried in an oven at 60 °C for 12 h, and $Zn_{0.8}Cd_{0.2}S$ was obtained.

3.3. Synthesis of $Ni(OH)_2$

1.9 g of $Ni(NO_3)_2$ was dissolved in 30 mL of deionized water, and 15 mL of 5 M $Ni(OH)_2$ solution was added to it while stirring. The solution was stirred for 1.5 h, centrifuged, washed 8 times with deionized water, and placed in a vacuum drying oven. The temperature was raised to 60 °C and maintained for 12 h to obtain $Ni(OH)_2$.

3.4. Synthesis of $Ni(OH)_2$/ZCS

$Zn_{0.8}Cd_{0.2}S$ (200 mg) was dispersed in 30 mL of deionized water, and 108 μL of 2 M $Ni(NO_3)_2$ solution was added and stirred evenly. The solution was ultrasonically dispersed for 20 min, 3 mL of 5 M NaOH was added dropwise while stirring, and the mixture was stirred for 5.5 h. After the reaction, the mixture was centrifuged to obtain the precipitate, which was then washed with deionized water until the supernatant was neutral. After that, the precipitate was placed in a vacuum drying oven at 60 °C and maintained for 12 h to obtain $Ni(OH)_2/Zn_{0.8}Cd_{0.2}S$ composites with a mass fraction of 1% $Ni(OH)_2$, labeled $1Ni(OH)_2$/ZCS. When the amount of added $Ni(NO_3)_2$ solution was changed, $Ni(OH)_2$/ZCS composites with different amounts (5 wt%, 9 wt%, and 13 wt%) of $Ni(OH)_2$ were obtained, labeled $5Ni(OH)_2$/ZCS, $9Ni(OH)_2$/ZCS, and $13Ni(OH)_2$/ZCS, respectively.

3.5. Characterization of the Catalysts

The crystal structure of the catalyst was examined by X-ray diffraction (XRD) using a Rigaku SMARTLAB 3KW diffractometer (Tokyo, Japan, Cu Kα radiation). Fourier-transform infrared (FT-IR) spectroscopy was conducted on a Bruker TENSOR II spectrometer (Bremen, Germany) to investigate chemical bonding. Morphological analysis was performed using a Carl Zeiss Sigma 300 field-emission scanning electron microscope (FE-SEM, Oberkochen, Germany) operated at 10 kV acceleration voltage. For detailed crystallographic analysis, high-resolution transmission electron microscopy (HRTEM), energy-dispersive X-ray spectroscopy (EDS), high-angle annular dark-field scanning TEM (HAADF-STEM), and elemental mapping were carried out using a Thermo Fisher Scientific

Talos F200X TEM (Santa Clara, CA, USA). N_2 adsorption–desorption isotherms were measured with a Micromeritics TriStar II analyzer (Norcross, GA, USA) to determine the specific surface area and pore size distribution. Surface chemical states were analyzed by X-ray photoelectron spectroscopy (XPS, Thermo Scientific, Waltham, MA, USA) on a Thermo Fisher Scientific K-Alpha spectrometer. Steady-state photoluminescence (PL, Thermo Fisher Scientific, USA) spectra were recorded on a Thermo Fisher Lumina fluorescence spectrometer, while time-resolved fluorescence decay was measured using an Edinburgh Instruments FLS 1000 spectrometer (Edinburgh, UK, excitation: 365 nm laser). Optical absorption properties were evaluated via UV-Vis diffuse reflectance spectroscopy (UV-Vis DRS) using a Beijing General Instrument TU-19 spectrophotometer (Beijing, China) equipped with an IS19-1 integrating sphere. Ultraviolet photoelectron spectroscopy (UPS) was performed on a PHI5000 Versa Probe III system (ULVAC-PHI, Inc., Fujisawa-shi, Japan, equipped with a spherical analyzer) to determine the surface work function and electronic structure.

3.6. Photoelectrochemical Measurements

The photoelectrochemical experiments were conducted using a CHI760E electrochemical workstation with a standard three-electrode system (Shanghai Chenhua Instrument Co., Ltd., Shanghai, China). The system consisted of a reference electrode (Ag/AgCl), a counter electrode (Pt mesh), and a working electrode (photocatalyst). A 0.5 M Na_2SO_4 solution serves as the electrolyte. 20 mg of photocatalyst was added to 400 μL anhydrous ethanol with 20 μL Nafion solution, followed by 90 min ultrasonication to achieve homogeneous dispersion. Subsequently, 0.1 mL of the suspension was uniformly drop-cast onto a 1 cm × 1 cm FTO substrate and dried at room temperature. A 300 W xenon lamp with a 400 nm cut-off filter is used as the light source. Electrochemical impedance spectroscopy (EIS) was tested at an alternating amplitude of 5 mV and a frequency of 0.01 Hz–1000 kHz.

3.7. Photocatalytic Hydrogen Evolution

The hydrogen production performance was evaluated in a 167 mL top-irradiation quartz reactor. A 300 W xenon lamp (CEL-HXF300-T3, Beijing China Education Au-light Co., Ltd., Beijing, China) equipped with a 400 nm cut-off filter served as the light source, providing an irradiation intensity of 103 mW cm^{-2}. The photocatalytic reaction system consisted of 20 mg photocatalyst dispersed in 50 mL of aqueous solution containing 0.35 M Na_2S and 0.25 M Na_2SO_3 as sacrificial agents. The mixture was ultrasonicated for 10 min to ensure homogeneous dispersion. Prior to illumination, the system was purged with ultra-high purity argon for 30 min to eliminate air. Subsequently, the suspension was continuously stirred during the reaction, and the temperature of the reactor was maintained at 25 °C using circulating cooling water. After the reaction began, the gaseous products were quantitatively detected by gas chromatography (GC-2018, SHIMADZU, Kyoto, Japan) with argon as the carrier gas. The AQY was measured using monochromatic filters (380, 400, 420, and 450 nm) and calculated according to the following equation:

$$\begin{aligned} AQY &= \frac{2\times \textit{the number of evolved } H_2 \textit{ Molecules}}{\textit{the number of incident photos}} \times 100\% \\ &= \frac{2\times r\times N_A\times h\times c}{S\times I\times t\times \lambda} \end{aligned} \quad (6)$$

where r is the yield of hydrogen, N_A is the Avogadro constant, h is the Planck constant, c is the speed of light, S is the illumination area, I is the average optical power density, t is the illumination time, and λ is the wavelength of the monochromatic light source.

The reusability tests of the catalysts were carried out using the following experimental procedure: each cycle was carried out under visible light ($\lambda \geq 400$ nm) for 4 h. After a single cycle reaction, the system was purged with ultra-high purity argon gas for 30 min

to remove the H_2 generated in the previous cycle. During the 5-cycle tests, no additional sacrificial agent was added, and the photocatalyst was not washed. To reveal the role of the sacrificial agent, 17.5 mmol Na_2S and 12.5 mmol Na_2SO_3 were added in the sixth cycle tests.

4. Conclusions

In summary, $Ni(OH)_2/Zn_{0.8}Cd_{0.2}S$ composites were synthesized to increase photocatalytic hydrogen production. After loading with $Ni(OH)_2$, close contact interfaces formed between $Ni(OH)_2$ and $Zn_{0.8}Cd_{0.2}S$, which was beneficial for the transfer and separation of charge carriers. In addition, the addition of $Ni(OH)_2$ increases the specific surface area, enhances light absorption, and increases the separation efficiency of the photogenerated electrons and holes of $Ni(OH)_2/Zn_{0.8}Cd_{0.2}S$. The photocatalytic H_2 production rate of $Ni(OH)_2$/ZCS composites increases with the increase in the Ni amount. $9Ni(OH)_2$/ZCS exhibited the optimum H_2 production rate of 12.88 mmol h^{-1} g^{-1}, which was 9.9 times higher than that of $Zn_{0.8}Cd_{0.2}S$. When the amount of $Ni(OH)_2$ is further increased, the excess $Ni(OH)_2$ covers the active site of $Zn_{0.8}Cd_{0.2}S$ and reduces the light absorption of $Zn_{0.8}Cd_{0.2}S$, resulting in a decrease in the H_2 production rate. Furthermore, the H_2 production rate of $9Ni(OH)_2$/ZCS decreased from 12.88 to 5.15 mmol g^{-1} h^{-1} after 3 cycles. The main reason for the decline in the photocatalytic performance of $Ni(OH)_2$/ZCS is the photocorrosion of $Zn_{0.8}Cd_{0.2}S$. In pure water, $9Ni(OH)_2$/ZCS exhibits a low photocatalytic H_2 production rate of 49.86 $\mu mol \cdot g^{-1} \cdot h^{-1}$. The extremely low H_2 production efficiency of photocatalytic overall water splitting severely hinders its practical application. Constructing heterojunctions and redox-active sites can promote the separation of photogenerated electron-hole pairs and the hydrogen/oxygen evolution, thereby achieving efficient photocatalytic overall water splitting. The high activity of the $Ni(OH)_2/Zn_{0.8}Cd_{0.2}S$ composite was attributed mainly to the increased separation efficiency of photogenerated electrons and holes and the addition of $Ni(OH)_2$ active sites. This work reveals the effects of $Ni(OH)_2$ cocatalysts on the photocatalytic H_2 production reaction, which is highly important for the development of efficient photocatalysts.

Supplementary Materials: The following supporting information can be downloaded at: https://www.mdpi.com/article/10.3390/catal15090886/s1, Refs. [27,28,30,43–54] are cited in Supplementary Materials.

Author Contributions: Conceptualization, T.S.; methodology, L.C. and S.D.; validation, T.S.; formal analysis, L.C. and T.S.; investigation, Q.F., X.Y., J.P., and S.D.; resources, T.S.; data curation, Q.F. and S.D.; writing—original draft, Q.F.; writing—review and editing, X.X. and T.S.; visualization, Q.F. and S.D.; supervision, T.S.; project administration, T.S.; funding acquisition, T.S. All authors have read and agreed to the published version of the manuscript.

Funding: This work was supported by the National Natural Science Foundation of China (22208065), the Opening Project of Guangxi Key Laboratory of Petrochemical Resource Processing and Process Intensification Technology (2023K012), and Guangxi Students' Innovation and Entrepreneurship Training Programs (202410593095).

Data Availability Statement: Data are contained within the article and Supplementary Materials.

Conflicts of Interest: The authors declare no conflicts of interest.

References

1. Zhong, W.; Xu, J.; Wang, P.; Zhu, B.; Fan, J.; Yu, H. Novel core-shell Ag@AgSe nanoparticle co-catalyst: In situ surface selenization for efficient photocatalytic H_2 production of TiO_2. *Chin. J. Catal.* **2022**, *43*, 1074–1083. [CrossRef]
2. Wang, J.; Niu, X.; Wang, R.; Zhang, K.; Shi, X.; Yang, H.Y.; Ye, J.; Wu, Y. High-entropy alloy-enhanced ZnCdS nanostructure photocatalysts for hydrogen production. *Appl. Catal. B Environ. Energy* **2025**, *362*, 124763. [CrossRef]

3. Huang, C.; Liu, N.; Zhou, Y.; Mao, H.; Qi, F.; Ouyang, X. Construction of 3D/0D Sv-ReS_2/ZnCdS hierarchical structure with improved interfacial charge transfer for enhanced photocatalytic hydrogen evolution. *Sep. Purif. Technol.* **2025**, *354*, 128838. [CrossRef]
4. Hiragond, C.B.; Powar, N.S.; Kim, H.; In, S.-I. Unlocking solar energy: Photocatalysts design for tuning the CO_2 conversion into high-value (C_{2+}) solar fuels. *EnergyChem* **2024**, *6*, 100130. [CrossRef]
5. Lian, Z.; Qu, M.; Xiao, H.; Wang, L.; Wu, H.; Zi, J.; Wang, W.; Li, H. Direct Observation of Z-Scheme Route in $Cu_{31}S_{16}/Zn_xCd_{1-x}S$ Heteronanoplates for Highly Efficient Photocatalytic Hydrogen Evolution. *Small* **2024**, *20*, 2400611. [CrossRef]
6. He, J.; Chen, L.; Xie, X.; Qin, Z.; Ji, H.; Su, T. Construction of ZnCoP/$CdLa_2S_4$ Schottky Heterojunctions for Enhancing Photocatalytic Hydrogen Evolution. *Acta Phys. Chim. Sin.* **2024**, *40*, 2404030. [CrossRef]
7. Kim, H.; Seo, J.W.; Chung, W.; Narejo, G.M.; Koo, S.W.; Han, J.S.; Yang, J.; Kim, J.Y.; In, S.I. Thermal Effect on Photoelectrochemical Water Splitting Toward Highly Solar to Hydrogen Efficiency. *ChemSusChem* **2023**, *16*, e202202017. [CrossRef]
8. HONDA, A.F.K. Electrochemical Photolysis of Water at a Semiconductor Electrode. *Nature* **1972**, *238*, 37–38. [CrossRef]
9. Han, M.; Guo, B.; Zhang, Z.; Hu, X.; Wang, Z. Hollow $Bi_4Ti_3O_{12}/TiO_2$ nanocakes for photocatalytic hydrogen generation. *J. Alloys Compd.* **2023**, *963*, 171192. [CrossRef]
10. Ren, T.; Dang, Y.; Xiao, Y.; Hu, Q.; Deng, D.; Chen, J.; He, P. Depositing Ag nanoparticles on g-C_3N_4 by facile silver mirror reaction for enhanced photocatalytic hydrogen production. *Inorg. Chem. Commun.* **2021**, *123*, 108367. [CrossRef]
11. Xiao, Y.; Liu, J.; Leng, J.; Yin, Z.; Yin, Y.; Zhang, F.; Sun, C.; Jin, S. Long-Lived Internal Charge-Separated State in Two-Dimensional Metal–Organic Frameworks Improving Photocatalytic Performance. *ACS Energy Lett.* **2022**, *7*, 2323–2330. [CrossRef]
12. Zhang, Y.; Liu, D.; Shi, J.; Chen, P.; Zong, S.; Cheng, C.; Chen, K.; Chen, Y.; Ma, L. (Oxy)nitride heterojunction-strengthened separation of photogenerated carriers in g-C_3N_4 towards enhanced photocatalytic H_2 evolution. *Appl. Catal. A Gen.* **2022**, *643*, 118746. [CrossRef]
13. Yang, H.; Li, C.; Mao, M.; Sun, H.; Zhu, X.; Zhang, Y.; Li, Y.; Jiang, Z. Synthesis of Type-S Ni_3S_4/ZnCdS Quantum Dots via Constitution Controller l-Cysteine for Photocatalytic H_2 Evolution. *ACS Appl. Nano Mater.* **2024**, *7*, 22093–22103. [CrossRef]
14. Du, S.; Chen, L.; Men, C.; Ji, H.; Su, T.; Qin, Z. Effect of surface defect states on $Zn_{(1-x)}Cd_xS$ for enhanced photocatalytic hydrogen evolution. *J. Alloys Compd.* **2023**, *955*, 170265. [CrossRef]
15. Zhang, L.; Jiang, T.; Li, S.; Lu, Y.; Wang, L.; Zhang, X.; Wang, D.; Xie, T. Enhancement of photocatalytic H_2 evolution on $Zn_{0.8}Cd_{0.2}S$ loaded with CuS as cocatalyst and its photogenerated charge transfer properties. *Dalton Trans.* **2013**, *42*, 12998. [CrossRef]
16. Li, S.; Li, Y.; Yin, W.; Su, K.; He, P.; Chen, J.; Si, Y.; Xiao, Y.; Ren, T. Boosting the photocatalytic hydrogen production activity of marigold-like $Zn_2In_2S_5$ by using noble-metal-free Ni_2P as cocatalyst. *Int. J. Hydrogen Energy* **2024**, *56*, 596–603. [CrossRef]
17. Li, Y.; Jin, Z.; Tsubaki, N. Hollow ZnCdS and NiCoP Nanostructures for Photocatalytic Hydrogen Generation. *ACS Appl. Nano Mater.* **2022**, *5*, 14677–14688. [CrossRef]
18. Li, M.; Chen, F.; Xu, Y.; Tian, M. $Ni(OH)_2$ Nanosheet as an Efficient Cocatalyst for Improved Photocatalytic Hydrogen Evolution over $Cd_{0.9}Zn_{0.1}S$ Nanorods under Visible Light. *Langmuir* **2024**, *40*, 3793–3803. [CrossRef]
19. Kong, Z.; Kong, Z.; Zhang, D.; Liu, J.; Ji, X.-Y.; Cai, P.; Pu, X. Magnetic separable non-precious metal Schottky heterojunction photocatalyst toward photothermal-assisted photocatalytic hydrogen evolution. *Sep. Purif. Technol.* **2025**, *361*, 131429. [CrossRef]
20. Zhang, Q.; Wang, Z.; Song, Y.; Fan, J.; Sun, T.; Liu, E. S-scheme regulated Ni_2P-NiS/twinned $Mn_{0.5}Cd_{0.5}S$ hetero-homojunctions for efficient photocatalytic H_2 evolution. *J. Mater. Sci. Technol.* **2024**, *169*, 148–157. [CrossRef]
21. Ma, F.; Wen, Y.; Fu, P.; Zhang, J.; Tang, Q.; Chen, T.; Luo, W.; Zhou, Y.; Wang, J. Engineering 0D/2D Architecture of $Ni(OH)_2$ Nanoparticles on Covalent Organic Framework Nanosheets for Selective Visible-Light-Driven CO_2 Reduction. *Small* **2023**, *20*, 2305767. [CrossRef]
22. Zuo, L.; Yang, N.; Xia, W.; Zeng, X.; Cao, R. Z-scheme NiS@ZnCdS heterostructures and their boosted photocatalytic H_2 evolution. *Appl. Surf. Sci.* **2025**, *689*, 162447. [CrossRef]
23. Lu, L.; Ma, Y.; Liu, H.; Dong, R.; Tan, P.; Yang, L.; Pan, J. Controlled preparation of hollow $Zn_{0.3}Cd_{0.7}S$ nanospheres modified by $NiS_{1.97}$ nanosheets for superior photocatalytic hydrogen production. *J. Colloid Interface Sci.* **2022**, *606*, 1–9. [CrossRef] [PubMed]
24. Zhu, X.; Wang, Z.; Zhong, K.; Li, Q.; Ding, P.; Feng, Z.; Yang, J.; Du, Y.; Song, Y.; Hua, Y.; et al. Mo-O-Bi Bonds as interfacial electron transport bridges to fuel CO_2 photoreduction via in-situ reconstruction of black Bi_2MoO_6/BiO_{2-x} heterojunction. *Chem. Eng. J.* **2022**, *429*, 132204. [CrossRef]
25. Gao, L.; Chen, Z.; Zheng, H.; Hu, J. A distinct hollow spindle-like $CdIn_2S_4$ photocatalyst for high-efficiency tetracycline removal. *Mater. Today Chem.* **2022**, *24*, 100800. [CrossRef]
26. Moridon, S.N.F.; Arifin, K.; Mohamed, M.A.; Minggu, L.J.; Mohamad Yunus, R.; Kassim, M.B. Improving photoelectrochemical performance of transferred TiO_2 nanotubes onto FTO substrate with Mo_2C and NiS as Co-catalyst. *Int. J. Hydrogen Energy* **2024**, *88*, 1196–1206. [CrossRef]
27. Bai, X.; Yang, T.; Zhao, M.; Fan, H.; Li, C.; Liu, E. Novel N-deficient g-C_3N_4 /$Ni(OH)_2$ 2D heterojunction design for efficient photocatalytic H_2 evolution. *J. Environ. Chem. Eng.* **2025**, *13*, 115447. [CrossRef]

28. Zhan, D.; Tian, J.; Fu, Q.; Liu, P.; Zhao, Y.; Liu, W.; Li, D.; Huang, Y.; Han, C. In situ photodeposition of Cu and $Ni(OH)_2$ dual cocatalyst: Synergistic effect on enhancing g-C_3N_4 photocatalytic H_2 evolution. *Appl. Surf. Sci.* **2023**, *641*, 158463. [CrossRef]
29. Nair, M.M.; Iacoban, A.C.; Neaţu, F.; Florea, M.; Neaţu, Ş. A comparative overview of MXenes and metal oxides as cocatalysts in clean energy production through photocatalysis. *J. Mater. Chem. A* **2023**, *11*, 12559–12592. [CrossRef]
30. Wang, H.; Shao, B.; Chi, Y.; Lv, S.; Wang, C.; Li, B.; Li, H.; Li, Y.; Yang, X. Engineering of $Ni(OH)_2$ Modified Two-Dimensional $ZnIn_2S_4$ Heterostructure for Boosting Hydrogen Evolution under Visible Light Illumination. *Nanomaterials* **2022**, *12*, 946. [CrossRef] [PubMed]
31. Wang, J.; Huang, L.; Sun, B.; Zhang, H.; Hou, D.; Qiao, X.-q.; Ma, H.; Li, D.-S. Efficient photothermal catalytic CO_2 reduction over in situ construction $ZnIn_2S_4$@$Ni(OH)_2$/NiO Z-scheme heterojunction. *Chem. Eng. J.* **2024**, *479*, 147719. [CrossRef]
32. Chen, R.; Zhu, H.; Liu, W.; Zhan, D.; Fu, Q.; Tian, J.; Huang, Y.; Han, C. Facile photodeposition $Ni(OH)_2$ anchored $ZnIn_2S_4$ as an efficient 1D/2D heterojunctions for photocatalytic H_2 evolution. *J. Am. Ceram. Soc.* **2024**, *107*, 5201–5211. [CrossRef]
33. Siang, T.J.; Zhang, P.; Chen, B.; Ong, W.-J. Surface defect engineering of ZnCoS in ZnCdS with twin crystal structure for visible-light-driven H_2 production coupled with benzyl alcohol oxidation. *Chin. J. Catal.* **2025**, *69*, 84–98. [CrossRef]
34. Guan, C.; Zhou, H.; Liao, Y.; Xiang, Q. 2D/2D g-C_3N_4/$Zn_xCd_{1-x}S$ Van der Waals heterojunctions modulation: Interfacial chemical bond accelerating charge separation for enhanced photocatalytic CO_2 reduction. *Appl. Surf. Sci.* **2023**, *619*, 156734. [CrossRef]
35. Govindarajan, D.; Murugadoss, G.; Kirubaharan, K.; Manavalan, R.K.; Manibalan, G.; Shaikh, J.; Etesami, M.; Kheawhom, S. Improved electrochemical supercapacitive properties of CuO-$Ni(OH)_2$ nanocomposites by eco-friendly low-temperature synthesis. *J. Alloys Compd.* **2023**, *942*, 169130. [CrossRef]
36. Sekar, S.; Lee, S.; Kim, D.Y.; Preethi, V.; Kalirajan, K.M.; Sutha, S.; Saravanan, S.; Therli, A.; Roy, M.; Jagannathan, K. Biomass activated carbon-decorated spherical β-$Ni(OH)_2$ nanoparticles for enhanced hydrogen production from sulphide wastewater. *J. Water Process Eng.* **2020**, *38*, 101669. [CrossRef]
37. Li, D.; Shen, C.; Lu, Q.; Yan, R.; Xiao, B.; Zi, B.; Zhang, J.; Lu, Q.; Liu, Q. Excellent performance supercapacitors with the compounding of $Ni(OH)_2$ and ZIF-67 derived Co–C–N nanosheets as flexible electrode materials. *Nanoscale Adv.* **2022**, *4*, 4381–4390. [CrossRef]
38. Yang, D.; Li, Z.-G.; Lang, F.; Zhang, X.; Li, H.; Zhang, J.; Bu, X.-H. Molecular Adsorption–An Effective Modification for a ZnCdS Photocatalyst in a Hydrogen Production Reaction. *ACS Mater. Lett.* **2024**, *6*, 2837–2845. [CrossRef]
39. Parvin, S.; Aransiola, E.; Ammar, M.; Lee, S.; Zhang, L.; Weber, J.; Baltrusaitis, J. Tailored $Ni(OH)_2$/CuCo/$Ni(OH)_2$ Composite Interfaces for Efficient and Durable Urea Oxidation Reaction. *ACS Appl. Mater. Interfaces* **2024**, *16*, 67715–67729. [CrossRef]
40. Liu, X.; Zhou, Z.; Han, D.; Wang, T.; Ma, C.; Huo, P.; Yan, Y. Interface engineered 2D/2D $Ni(OH)_2$/$Bi_4Ti_3O_{12}$ nanocomposites with higher charge transfer towards improving photocatalytic activity. *J. Alloys Compd.* **2020**, *816*, 152530. [CrossRef]
41. Hu, Q.; Chen, L.; Xie, X.; Qin, Z.; Ji, H.; Su, T. Construction of Electron Bridge and Activation of MoS_2 Inert Basal Planes by Ni Doping for Enhancing Photocatalytic Hydrogen Evolution. *Acta Phys.-Chim. Sin.* **2024**, *40*, 2406024. [CrossRef]
42. Liu, S.; Wang, W.; Shi, S.; Liao, S.; Zhong, M.; Xiao, W.; Wang, S.; Wang, X.; Chen, C. Hydrogen-bonded organic framework derived ultra-fine ZnCdS/ZnS heterojunction with high-porosity for efficient photocatalytic hydrogen production. *Appl. Surf. Sci.* **2024**, *657*, 159795. [CrossRef]
43. Serpone, N.; Borgarello, E.; Barbeni, M.; Pelizzetti, E. Effect of CdS Preparation on the Photo-catalyzed Decomposition of Hydrogen. *Inorganica Chim. Acta* **1984**, *90*, 191–196.
44. Li, Z.; Liu, F.; Yan, X.; Wang, Y.; Lu, K.; Liu, J.; Qiao, Y.; Liu, M. Photoreforming lignocellulose to hydrogen over noble-metal-free $Ni(OH)_2$/$Cd_{0.5}Zn_{0.5}S$ nanotwins. *Int. J. Hydrogen Energy* **2024**, *69*, 234–241. [CrossRef]
45. Gao, X.; Zeng, D.; Yang, J.; Ong, W.-J.; Fujita, T.; He, X.; Liu, J.; Wei, Y. Ultrathin $Ni(OH)_2$ nanosheets decorated with $Zn_{0.5}Cd_{0.5}S$ nanoparticles as 2D/0D heterojunctions for highly enhanced visible light-driven photocatalytic hydrogen evolution. *Chin. J. Catal.* **2021**, *42*, 1137–1146. [CrossRef]
46. Xia, Y.; Chen, W.; Liang, S.; Bi, J.; Wu, L.; Wang, X. Engineering a highly dispersed co-catalyst on a few-layered catalyst for efficient photocatalytic H2 evolution: A case study of $Ni(OH)_2$/HNb_3O_8 nanocomposites. *Catal. Sci. Technol.* **2017**, *7*, 5662–5669. [CrossRef]
47. Wang, C.; Xiong, J.; Wen, Z.; Cheng, G. Integrated $Ni(OH)_2$-TiO_2-Cu_2O Hybrids with a Synergic Impact of the p–n Heterojunction/Cocatalyst for Enhanced Photocatalytic Hydrogen Production. *Ind. Eng. Chem. Res.* **2023**, *62*, 11402–11413. [CrossRef]
48. Liu, H.; Su, P.; Jin, Z.; Ma, Q. Enhanced Hydrogen Evolution over Sea-Urchin-Structure NiCoP Decorated ZnCdS Photocatalyst. *Catal. Lett.* **2020**, *150*, 2937–2950. [CrossRef]
49. Li, Q.; Jin, F.; Liu, J.; Wang, P.; Yang, B.; Jin, Z. Construction of S-scheme $CoMn_2O_4$/ZnCdS p–n heterojunction for enhanced photocatalytic hydrogen production. *J. Mater. Chem. C* **2025**, *13*, 7380–7392. [CrossRef]
50. Chen, C.; Xia, Q.; Li, Z.; Wang, Y. Microwave synthesis and photocatalytic H2 production performance of SiO_2 aerogel/ZnCdS solid solution catalyst. *Inorg. Chem. Commun.* **2024**, *168*, 112874. [CrossRef]

51. Zou, Y.; Guo, C.; Cao, X.; Chen, T.; Kou, Y.; Zhang, L.; Wang, T.; Akram, N.; Wang, J. Photocatalytic performance and mechanism of hydrogen evolution from water over ZnCdS/Co@CoO in sacrificial agent-free system. *Int. J. Hydrogen Energy* **2022**, *47*, 25289–25299. [CrossRef]
52. Li, L.; Su, J.; Qiu, Y.; Gao, Y.; Li, N.; Ge, L. Design and fabrication of ternary Au/Co_3O_4/ZnCdS spherical composite photocatalyst for facilitating efficient photocatalytic hydrogen production. *Chin. J. Struct. Chem.* **2024**, *43*, 100472. [CrossRef]
53. Bai, T.; Shi, X.; Liu, M.; Huang, H.; Zhang, J.; Bu, X.-H. g-C_3N_4/ZnCdS heterojunction for efficient visible light-driven photocatalytic hydrogen production. *RSC Adv.* **2021**, *11*, 38120–38125. [CrossRef] [PubMed]
54. Xiao, Q.; Yang, T.; Guo, X.; Jin, Z. S-scheme heterojunction constructed by ZnCdS and $CoWO_4$ nano-ions promotes photocatalytic hydrogen production. *Surf. Interfaces* **2023**, *43*, 103577. [CrossRef]

Disclaimer/Publisher's Note: The statements, opinions and data contained in all publications are solely those of the individual author(s) and contributor(s) and not of MDPI and/or the editor(s). MDPI and/or the editor(s) disclaim responsibility for any injury to people or property resulting from any ideas, methods, instructions or products referred to in the content.

catalysts

MDPI

Article

Promotional Effect of Semiconductor-Supported Plasmonic Copper Nanoparticles in Visible-Light-Driven Photocatalytic Oxidative Homocoupling of Alkynes

Nan Deng †, Yaqi Wu †, Yi Sun and Peng Liu *

Key Laboratory of Material Chemistry for Energy Conversion and Storage (Ministry of Education), Hubei Key Laboratory of Material Chemistry and Service Failure, School of Chemistry and Chemical Engineering, Huazhong University of Science and Technology, Wuhan 430074, China

* Correspondence: pengliu@hust.edu.cn

† These authors contributed equally to this work.

Abstract

Enhancing the oxidation resistance of copper nanoparticles (CuNPs) is a crucial objective in plasmonic photocatalytic reactions. In this study, a series of Cu/X catalysts was synthesized using semiconductor nanomaterials (X = TiO_2, ZnO, BN, TiN, SiC, and C_3N_4) as supports for CuNPs. These catalysts were systematically evaluated in visible-light-driven photocatalytic oxidative homocoupling of phenylacetylene (OHA). Comprehensive characterization revealed distinct metal-support interactions and nanostructure evolution during repeated catalytic cycles. The photocatalytic performance, copper leaching, and structural stability of the catalysts were compared. Cu/TiO_2 achieved the highest 1,3-diyne yield (up to 93%) in the first two cycles. In contrast, Cu/ZnO showed minimal copper leaching and excellent recyclability, retaining high activity over three consecutive cycles without the need for reduction pretreatment. Comparative studies revealed that the combination of localized surface plasmon resonance (LSPR) and efficient electron transfer within the Cu^0-Cu_2O-CuO composite was a key factor in enhancing the photocatalytic activity and stability. These findings provide new insights into the rational design of durable CuNP-based photocatalysts for visible-light-driven organic transformations.

Keywords: copper nanoparticles; oxidative homocoupling; alkynes; semiconductors; heterojunction

1. Introduction

Sunlight-driven photocatalytic reactions offer significant potential for carbon-neutralization and for addressing environmental concerns [1–3]. Plasmonic metal nanomaterials are particularly promising due to their strong visible-light absorption via the localized surface plasmon resonance (LSPR) effect, making them effective photocatalysts for diverse chemical transformations [4,5]. Plasmonic catalysis enables enhanced catalytic activity at lower reaction temperatures, overcoming the equilibrium limits typically encountered in thermocatalytic processes [6]. Among the different plasmonic metals, inexpensive copper stands out as a viable alternative to noble metals like silver and gold. Copper nanoparticle (CuNP)-based plasmonic catalysts have been successfully utilized in applications such as CO_2 reduction, N_2 photofixation, pollutant degradation, and selective organic synthesis [7,8]. However, a significant challenge in developing oxidation-stable

CuNP-based plasmonic catalysts for oxidation reactions is the susceptibility of metallic Cu to oxidation in air.

Copper-catalyzed oxidative homocoupling of alkynes (OHA) is a crucial organic transformation for producing conjugated 1,3-diynes [9], which are valuable building blocks in the synthesis of natural products, pharmaceuticals, optoelectronic materials, and polymers [10]. While various homogeneous and heterogeneous Cu-based catalytic systems have been developed for the OHA reaction [11–19], many of these systems raise concerns about corrosion and environmental pollution due to the use of harmful solvents and base additives at elevated temperatures. Therefore, there is a strong demand for synthesizing 1,3-diynes at room temperature (RT) under green and base additive-free conditions. Hwang's group reported a photocatalytic OHA reaction at RT using CuCl as a homogeneous catalyst in CH_3CN, induced by blue LED irradiation [20]. Our group demonstrated that partially reduced copper ferrite (Cu/Fe_3O_4-$CuFe_2O_4$) exhibited comparable catalytic efficiency in photocatalytic OHA at RT and thermocatalytic OHA at 120 °C [21]. Despite advancements in CuNPs-mediated photocatalytic OHA, CuNPs-based plasmonic catalysts exhibit low LSPR stability and poor activity due to the oxidation of metallic Cu in oxidative environments [21–25]. Consequently, developing efficient and recyclable plasmonic photocatalytic OHA systems with improved stability remains a significant challenge.

Semiconductor-supported CuNPs have emerged as promising candidates for visible-light-driven catalysis, utilizing the LSPR effect to enhance light absorption and facilitate the efficient separation and transfer of photoinduced charge carriers at the metal-semiconductor interface [26–34]. For example, $Cu@TiO_2$ [26] and $Cu/SrTiO_3$ [34] have demonstrated effective performance in CO_2 photoreduction. Additionally, Cu/TiO_2 has shown high activity in both the photocatalytic degradation of Sarin [27] and the generation of H_2 from water [28,29]. Cu/TiN can selectively catalyze the epoxidation of alkenes with O_2 under visible light irradiation [30], while Cu/ZnO exhibits enhanced activity in photocatalytic H_2 evolution [31] and uranium photoreduction [32]. However, to our knowledge, simple semiconductor-supported CuNPs have not yet been explored in plasmonic photocatalytic OHA, leaving their potential advantages unverified. While fundamental aspects such as Mie-resonance tuning, dielectric screening, and photothermal effects have been discussed in other copper-based systems [7,8], the structure–performance relationships governing photocatalytic OHA activity are still unclear. In this work, representative semiconductors (X = TiO_2, ZnO, BN, TiN, SiC, and C_3N_4) were employed as supports for CuNPs to construct a series of Cu/X catalysts. These catalysts were applied for the first time in visible-light-driven photocatalytic OHA reactions, with the aim of leveraging the synergistic effects between plasmonic excitation and semiconductor-mediated charge transfer to prevent the complete oxidation of metallic Cu. The influence of the support and the structure-performance relationship of the Cu/X catalysts was systematically investigated. Our results underscore the critical role of metal-support interactions and identify Cu/ZnO as a promising catalyst for achieving stable plasmonic photocatalytic OHA reactions.

2. Results and Discussion

2.1. Characterization of Cu/X Composite Photocatalysts

Various Cu/X catalysts were prepared using a deposition-reduction procedure, with a target Cu loading of 5 wt% (see Section 3 for details). Except for the Cu/ZnO and Cu/C_3N_4 catalysts, which were reduced with $NaBH_4$ in aqueous solution, the other Cu/X catalysts were reduced with H_2 at 250 °C. The structural, textural, and chemical properties of the Cu/X catalysts were thoroughly characterized using X-ray diffraction (XRD), ultraviolet-visible spectroscopy (UV-vis), scanning electron microscopy (SEM), high-resolution transmission electron microscopy (HRTEM), nitrogen physisorption, atomic absorption spec-

trometer (AAS), Fourier transform infrared (FT-IR), and X-ray photoelectron spectroscopy (XPS). Figure 1 displays the XRD results. The XRD patterns of the bare semiconductors and the SEM images of the Cu/X catalysts are presented in Figures S1 and S2. Notably, the copper-loading procedure did not alter the structure and morphology of the semiconductors. While Cu/TiO_2 and Cu/SiC exhibit highly porous nanostructures, the other Cu/X catalysts are composed of irregular nanoaggregates.

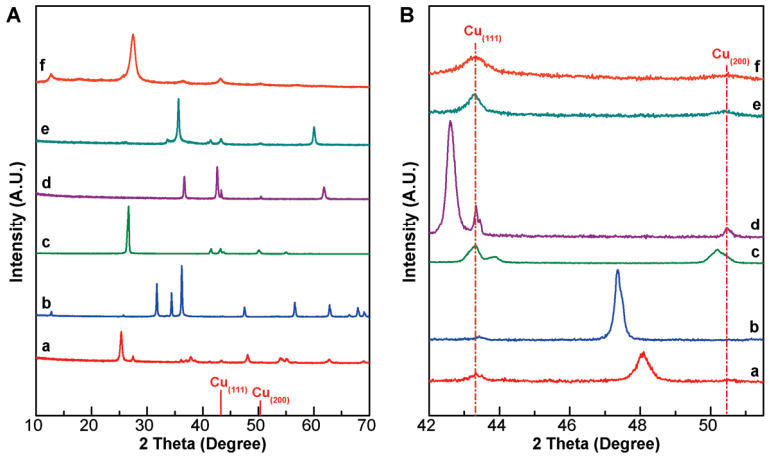


Figure 1. XRD patterns of (**a**) Cu/TiO_2, (**b**) Cu/ZnO, (**c**) Cu/BN, (**d**) Cu/TiN, (**e**) Cu/SiC, (**f**) Cu/C_3N_4. (**A**) wide 2θ range, (**B**) enlarged view of selected narrow 2θ region.

The diffraction peak corresponding to the metallic Cu (111) plane at 2θ = 43.3° is weak in all Cu/X catalysts (Figure 1B), indicating a well-dispersed distribution of CuNPs. This observation is further supported by HRTEM images shown in Figure 2, which reveal that the CuNPs are small, with sizes ranging from 2 to 6 nm. Characteristic lattice fringes corresponding to the (111) and (200) planes of metallic Cu^0, with spacings of 0.21 nm and 0.18 nm, respectively [23,28], are observed in all Cu/X catalysts. For Cu/C_3N_4, which possesses a larger CuNP size (>5 nm), the (111) plane of Cu_2O with a lattice fringe of 0.25 nm is found in close proximity to the planes of metallic Cu^0 [22,25]. In contrast, for other Cu/X catalysts with smaller CuNP sizes (<3 nm), the edge lattices of the metallic CuNPs appear disordered, indicating partial oxidation of the CuNPs. This observation aligns with previous reports that an inherent surface Cu_2O layer rapidly forms on metallic CuNPs upon exposure to ambient conditions [8]. Additionally, HRTEM images clearly reveal the formation of heterojunctions at the metal-semiconductor interfaces, which can facilitate charge carrier transfer between the CuNPs and the semiconductor supports [7,8].

The average CuNP sizes, copper loadings, and specific surface areas of the copper catalysts are summarized in Table 1. Although the surface area increases significantly from 2.3 m^2/g for Cu/TiN to 46.8 m^2/g for Cu/TiO_2, the copper loadings are close to the targeted value of 5.0 wt%. The relatively lower copper loadings observed for Cu/ZnO (4.3 wt%) and Cu/C_3N_4 (3.7 wt%) may be attributed to the liquid-phase reduction method, which tends to cause leaching of copper. Notably, the surface area of the semiconductor supports does not directly affect the copper loadings or CuNP size. The larger average CuNP sizes observed for Cu/SiC (4.7 nm) and Cu/C_3N_4 (5.5 nm) are likely due to weaker metal-support interactions between CuNPs and the SiC or C_3N_4 supports [35,36]. In contrast, the smallest average CuNP size, found in Cu/ZnO (2.0 nm), is consistent with the XRD results and suggests a stronger metal-support interaction.

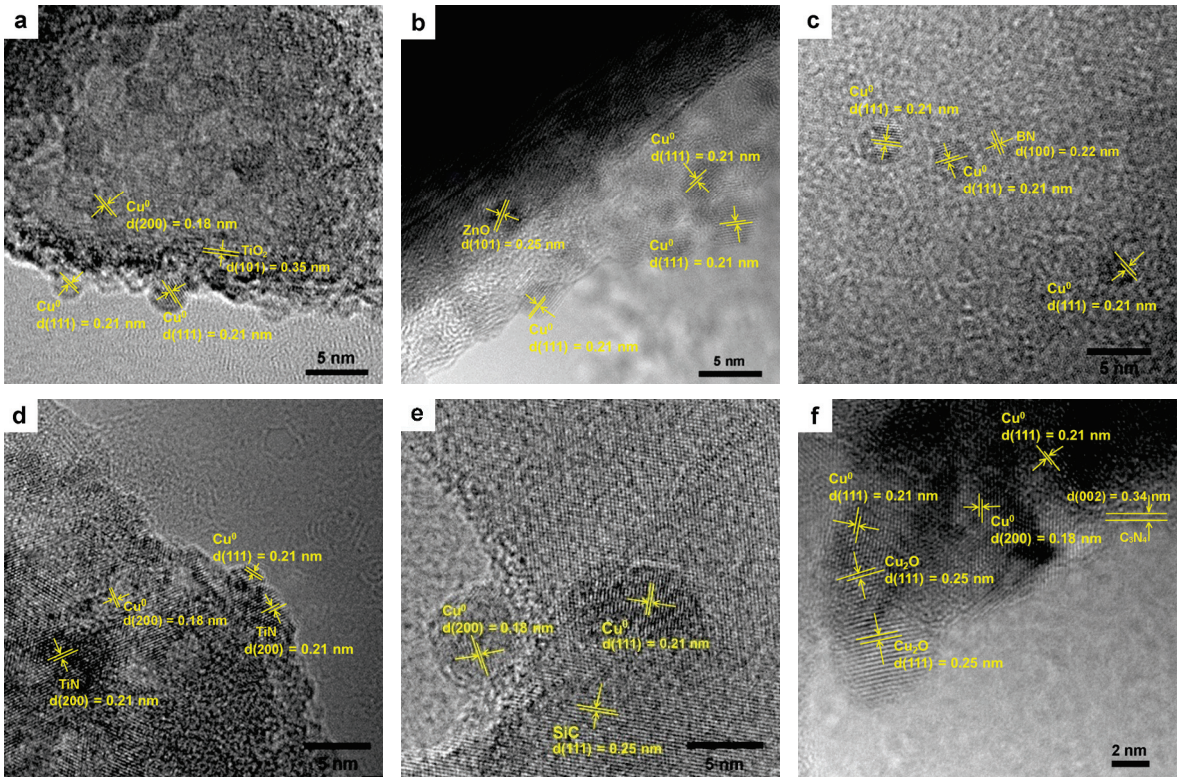


Figure 2. HRTEM images of (**a**) Cu/TiO_2, (**b**) Cu/ZnO, (**c**) Cu/BN, (**d**) Cu/TiN, (**e**) Cu/SiC, (**f**) Cu/C_3N_4.

Table 1. Textural, physicochemical, and optical properties of various Cu/X catalysts.

Catalyst	d_{Cu} [a] (nm)	[Cu] [b] (wt%)	S_{BET} (m^2/g)	XPS Peak Area Ratio (%)				E_g [c] (eV)
				Cu^0/Cu	Cu^+/Cu	O_L/O	O_A/O	
Cu/TiO_2	2.3	4.9	46.8	38	62	88	12	2.90 (3.18)
Cu/ZnO	2.2	4.3	16.8	14	38	60	40	3.09 (3.16)
Cu/BN	2.5	5.1	6.8	17	83	0	74	4.42 (5.20)
Cu/TiN	3.3	5.0	2.3	12	88	49	37	0.79 (0.90)
Cu/SiC	4.7	5.2	43.0	15	85	0	100	1.96 (2.10)
Cu/C_3N_4	5.5	3.7	20.4	24	45	14	86	2.53 (2.70)

[a] Based on the HRTEM result. [b] Based on the AAS result. [c] Calculated band gap E_g from UV-vis spectra, data in parentheses is the value for bare semiconductor.

XPS analysis was conducted to study the surface chemical states of copper and oxygen species in the Cu/X catalysts. In the Cu $2p_{3/2}$ spectra (Figure 3A), the main peak at a binding energy (BE) of approximately 932.2 eV is attributed to either Cu^0 or Cu^+ species [37–39]. Notably, except for Cu/ZnO and Cu/C_3N_4, the Cu^{2+} shakeup satellite peaks (938–946 eV) are absent in the other Cu/X catalysts, indicating the lack of Cu^{2+} species in these samples. Since the Cu $2p_{3/2}$ XPS cannot distinguish between Cu^0 and Cu^+, Auger Cu LMM spectra were utilized to quantify the fractions of Cu^0 (BE ~ 566.7 eV) and Cu^+ (BE ~ 569.3 eV) [21,39]. As shown in Figure 3B and Table 1, the fraction of Cu^+ decreases from 88% for Cu/TiN to 38% for Cu/ZnO, while the fraction of Cu^0 increases from 12% for Cu/TiN to 38% for Cu/TiO_2. These results confirm that the supported metallic CuNPs undergo rapid oxidation to form a surface Cu_2O layer upon brief exposure to air, in agreement with previous reports [8,40]. In the O 1s spectra (Figure 3C), peaks at BE ~ 530.0, 531.7, and 533.0 eV are assigned to lattice oxygen (O_L), surface oxygen vacancy or adsorbed oxygen (O_A), and adsorbed water (O_W), respectively [41,42]. The

fractions of O_L and O_A are listed in Table 1. Cu/TiO_2 and Cu/ZnO exhibit a majority of O_L species due to their oxide semiconductor nature, whereas Cu/BN and Cu/SiC show no O_L species [35,43]. For Cu/C_3N_4, the 14% fraction of O_L is due to the presence of CuO_x, which is consistent with the HRTEM (Figure 2f) and Cu LMM (Figure 3B) results. The similar O_L fraction (49%) observed for Cu/TiN and the TiN support suggests that the O_L species originate from minor TiO_2 impurities. Correspondingly, the O_A fraction increases in the order: Cu/TiO_2 (12%) < Cu/TiN (37%) < Cu/ZnO (40%) < Cu/BN (74%) < Cu/C_3N_4 (86%) < Cu/SiC (100%). Given the absence of O_L and Cu^{2+} species in the Cu/BN and Cu/SiC catalysts, the O_A species are most likely due to O_2 adsorbed on support defects or on the surface of CuNPs. Notably, the presence of an inherent surface Cu_2O layer and the lack of O_L species in several Cu/X catalysts suggest the formation of Cu^+-O_2^- species on the surface of plasmonic CuNPs, which can be restored under photocatalytic reaction conditions [8]. Therefore, it is plausible that O_2 can be activated on Cu^0 surfaces to produce Cu^+-O_2^- species via LSPR-assisted electron transfer from Cu to O_2 [44,45].

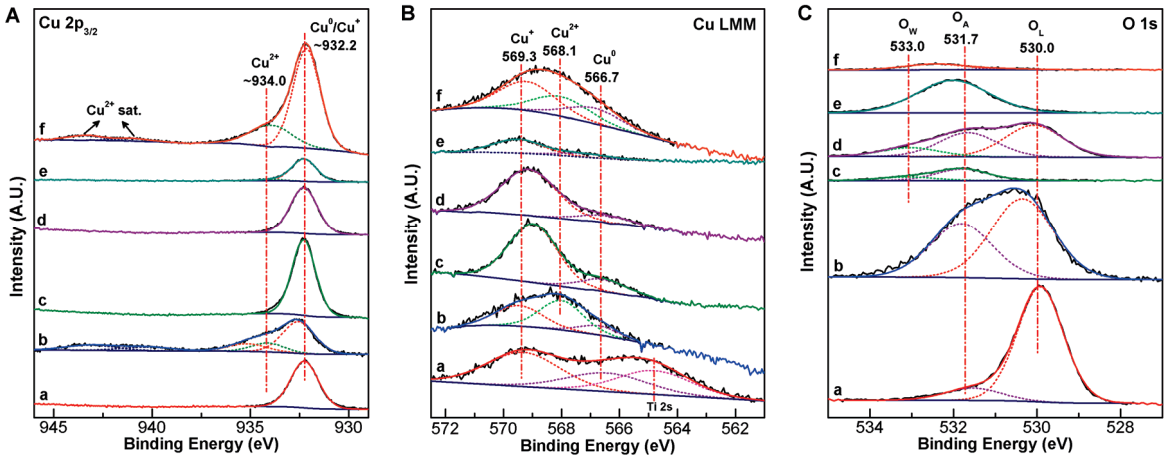


Figure 3. Cu $2p_{3/2}$ (**A**), Auger Cu LMM (**B**), and O 1s (**C**) XPS spectra of various Cu/X samples: (a) Cu/TiO_2, (b) Cu/ZnO, (c) Cu/BN, (d) Cu/TiN, (e) Cu/SiC, and (f) Cu/C_3N_4.

The light absorption properties of the Cu/X catalysts were investigated using diffuse reflectance UV-vis spectroscopy (Figure 4A). Comparative absorption spectra of the Cu/X catalysts and their corresponding supports are presented in Figure S3. After the deposition of CuNPs, all Cu/X catalysts exhibit significantly enhanced absorption in the visible light region. Notably, for Cu/TiO_2, Cu/ZnO, and Cu/BN, the absorption range extends from the ultraviolet region (<400 nm) for the bare supports to the near-infrared region (>800 nm) upon CuNP deposition. To further elucidate the contribution of CuNPs, the UV-vis spectra of the Cu/X catalysts were analyzed using the spectra of the semiconductor supports as background, isolating the absorption features attributable to CuNPs (inset in Figure S3). For Cu/BN, Cu/TiN, and Cu/SiC catalysts, the CuNPs display strong visible light absorption with a characteristic LSPR peak in the range of 560–630 nm [46]. In contrast, the LSPR absorption bands for Cu/TiO_2, Cu/ZnO, and Cu/C_3N_4 are red-shifted. This shift and broadening of the LSPR band have been reported to correlate with an increased proportion of Cu_2O and CuO [28,31], which is consistent with the HRTEM and XPS results.

The optical bandgap energies (E_g) of the semiconductor supports and Cu/X catalysts were determined from Tauc plots (Figures 4B and S4) derived using the Kubelka–Munk function [47]. In addition, valence band (VB) XPS measurements were employed to estimate the VB positions of the semiconductor supports (Figure 4C). Among the various supports, E_g values range from 0.9 eV for TiN to 5.2 eV for BN, while the estimated VB potentials increase from 1.61 V for C_3N_4 to 2.74 V for ZnO. Based on

these values, the conduction band (CB) potentials were calculated using the formula $E_{CB} = E_{VB} - E_g$ [48], resulting in CB potentials ranging from −2.46 V for BN to 1.18 V for TiN. The corresponding band structure diagram is illustrated in Figure 4D, and these results are consistent with previous reports for the bare semiconductor supports [32,43,47–51].

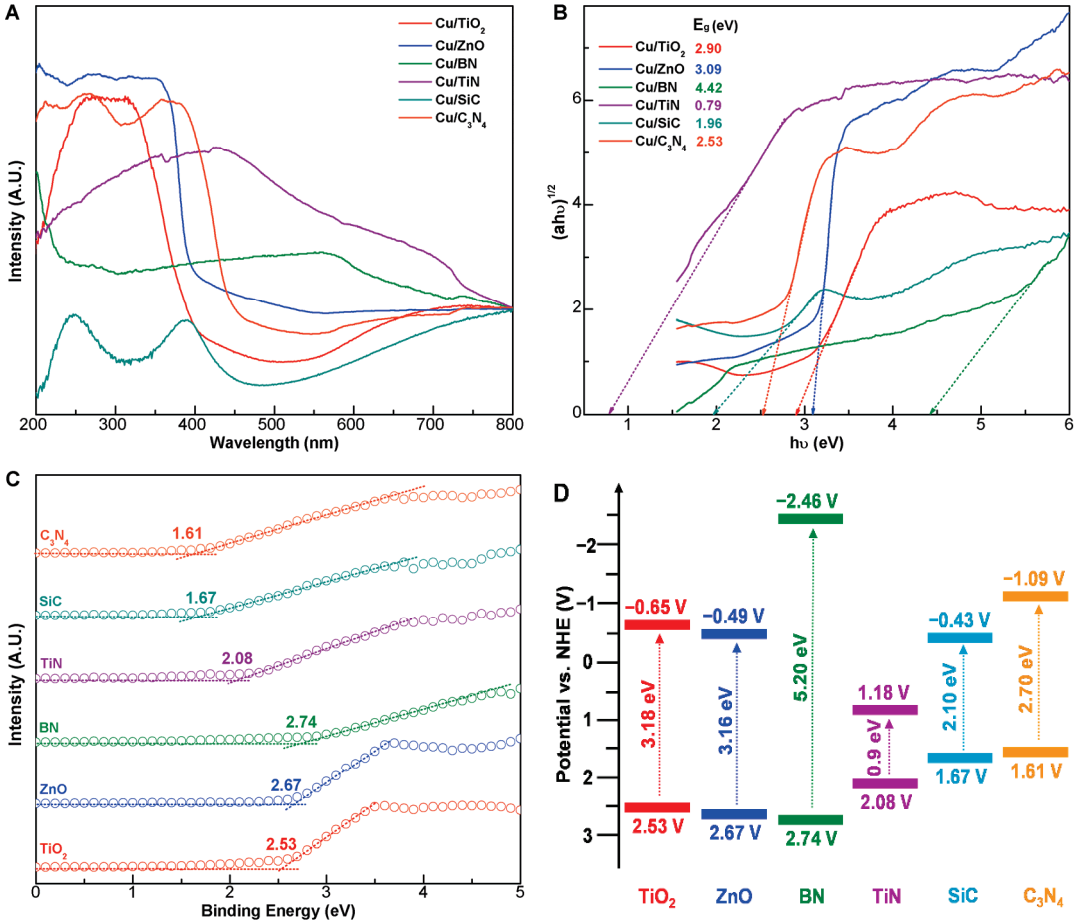


Figure 4. UV-vis spectra (**A**) and optical bandgap energy derived from Tauc plots (**B**) for various Cu/X samples. Valence band XPS spectra of various X samples (**C**). Plausible band structure diagrams for various X samples (**D**).

Under visible light irradiation, supports with narrower bandgaps (TiN, SiC, C_3N_4) can be photoexcited, whereas those with lager bandgaps (TiO_2, ZnO, BN) cannot. As shown in Figure 4B and Table 1, the optical bandgaps of all Cu/X catalysts are narrower than those of the pristine supports. The pronounced enhancement in light absorption within the 500–800 nm range for Cu/X catalysts is attributed to the synergetic effects of Cu/Cu_2O/X heterojunction formation and the LSPR of metallic CuNPs [28,29]. Given the small sizes of the CuNPs (2–6 nm), their LSPR is expected to decay primarily via Landau damping, whereby collective plasmon oscillations are non-radiatively converted into energetic electron–hole pairs that can be injected into the support or directly drive surface reactions [7,8,45]. The narrowing of the bandgap is expected to prolong the lifetime of photogenerated charge carriers and facilitate charge transfer between the CuNPs and the semiconductor supports [31], thereby improving the efficiency of visible-light-driven plasmonic photocatalytic reactions. It should be noted that, due to the complexity of the Cu/X nanostructures, a comprehensive understanding of their band structures would require more detailed photoelectrochemical characterization, which is beyond the scope of this study.

2.2. Photocatalytic Performance of the Cu/X Catalysts

The photocatalytic performance of Cu/X catalysts in the OHA reaction was systematically investigated (Figure 5). Phenylacetylene was chosen as the model substrate for the OHA reaction, which was carried out under white LED irradiation (λ > 400 nm, 0.2 W/cm^2) and an O_2 atmosphere at room temperature (RT ~ 30 °C) for 3h. Initially, the effect of solvent on the Cu/TiO_2-photocatalyzed OHA reaction was examined to identify the optimal reaction medium (Figure 5B). Overall, alcohol-based protonic solvents outperformed other polar and nonpolar solvents. Methanol, in particular, afforded the highest yield of 1,3-diyne (93%). To confirm the solvent effect, Cu/ZnO and Cu/BN catalysts were tested in both methanol and ethanol, with methanol consistently providing superior results. Consequently, methanol was selected as the solvent for subsequent heterogeneous photocatalytic OHA reactions.

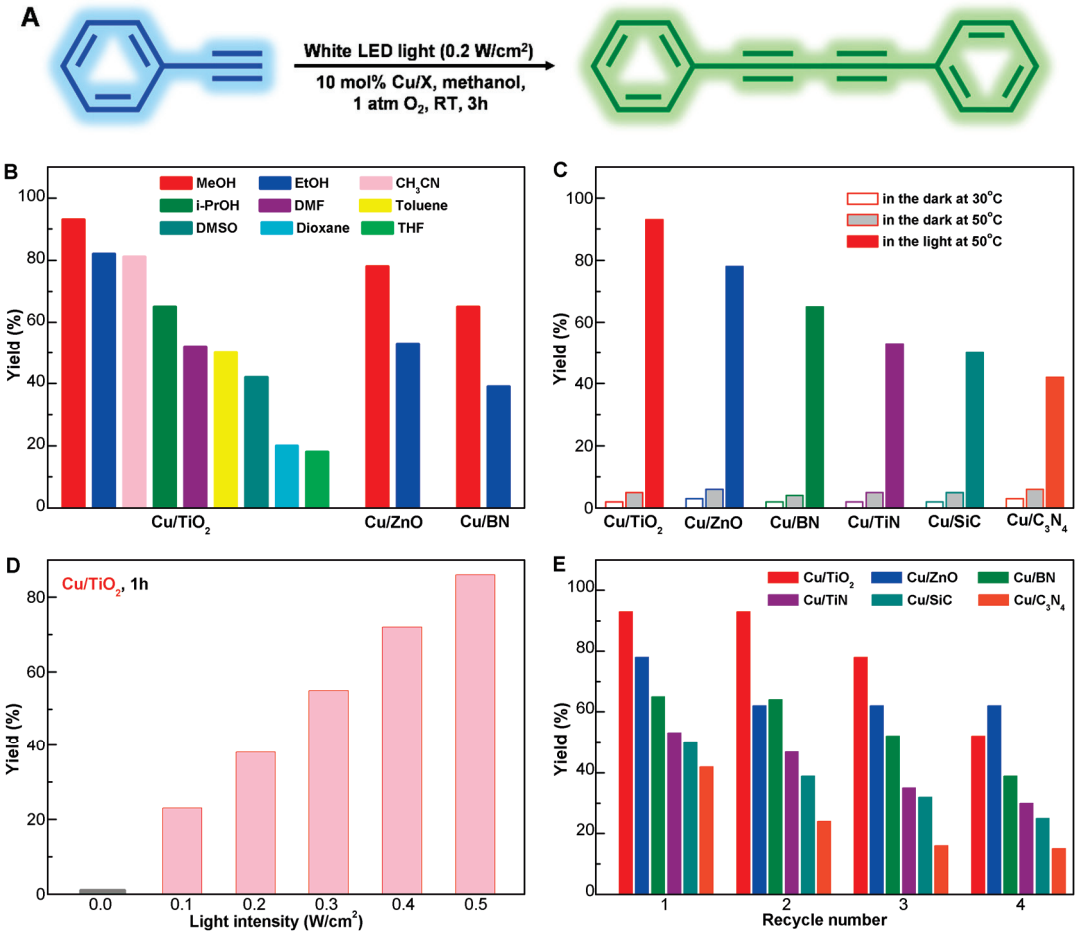


Figure 5. (**A**) Photocatalytic equation and reaction conditions. (**B**) Solvent effect on the yield of photocatalytic oxidative homocoupling of phenylacetylene using Cu/TiO_2, Cu/ZnO, and Cu/BN as catalysts. (**C**) Comparison of the catalytic activity of Cu/X catalysts in dark and light. (**D**) Influence of light intensity on the Cu/TiO_2-photocatalyzed OHA reaction. (**E**) Recyclability of Cu/X catalysts.

To clarify whether the photocatalytic activity enhancement originated primarily from the LSPR effect or from photothermal heating of CuNPs, we monitored the reaction temperature under visible-light irradiation and found it to rise to approximately 50 °C. Control experiments conducted without light at ~30 °C yielded less than 3% of the 1,3-diyne product for all Cu/X catalysts, while dark reactions at 50 °C produced slightly higher yields but still below 7% (Figure 5C). These clearly show that localized heating alone is insufficient to explain the high photocatalytic activity observed under illumination. In stark

contrast, under identical visible-light irradiation, the yields followed the order: Cu/C_3N_4 (42%) < Cu/SiC (50%) < Cu/TiN (53%) < Cu/BN (65%) < Cu/ZnO (78%) < Cu/TiO_2 (93%), far exceeding those under purely thermal conditions. Given that Cu^+ is recognized as the thermocatalytic active species in OHA [21], the low dark activity is mainly due to the absence of base additives and the relatively low reaction temperature, which are insufficient to activate the reactants and to promote the formation of Cu^+–phenylacetylide (Cu-PhAC) intermediates [52,53]. Therefore, the significantly enhanced yields under illumination suggest that LSPR excitation in CuNPs predominantly contributes to the reaction through Landau damping–induced hot-carrier generation, which efficiently activates O_2 and drives the oxidative homocoupling process, rather than from phonon-mediated photothermal heating.

Although Cu/TiN (E_g = 0.79 eV), Cu/SiC (E_g = 1.96 eV), and Cu/C_3N_4 (E_g = 2.53 eV) possess bandgaps suitable for visible-light photoexcitation of the supports, their photocatalytic activities were relatively poor. In contrast, the supports of Cu/TiO_2 (E_g = 2.90 eV), Cu/ZnO (E_g = 3.09 eV), and Cu/BN (E_g = 4.42 eV) cannot be directly photoexcited by visible light, yet these catalysts exhibited higher photocatalytic activity. Control experiments with bare semiconductor supports (without Cu loading) confirmed negligible activity (<1% yield) under visible-light irradiation, indicating that the supports alone do not drive the reaction. The low activity of Cu/C_3N_4 and Cu/SiC may be attributed to weak metal–support interactions, resulting in larger CuNP sizes (>4 nm) and excessive Cu_2O/CuO species (see Figures 2f and 3B). These factors can weaken the LSPR effect and hinder efficient electron transfer from the C_3N_4/SiC support to the CuNPs [7]. In contrast, the smaller CuNP sizes (<3 nm) in Cu/TiO_2, Cu/ZnO, and Cu/BN can induce a stronger LSPR effect and facilitate charge separation and transfer within the Cu^0/Cu_2O heterojunctions [31]. Overall, the photocatalytic activity of Cu/X catalysts mainly depends on the size-dependent LSPR effect and the stable Cu^0/Cu_2O heterojunction of CuNPs. In this system, the wide-bandgap supports (TiO_2, ZnO, BN) play a primarily structural and electronic-modulation role, providing strong Cu–support interactions that stabilize small-sized CuNPs and enhance hot-carrier utilization, rather than contributing directly via visible-light photoexcitation.

Since the LSPR effect is triggered when metallic CuNPs absorb photons from visible light [7], the photoinduced hot electron-driven OHA reaction is expected to be influenced by light intensity. To investigate this, the dependence of the photocatalytic activity of Cu/TiO_2 on light intensity was examined. As shown in Figure 5D, the yield of 1,3-diyne increased linearly with the intensity of the white LED, which serves as experimental evidence for a photoexcited electron-driven reaction mechanism [21]. Generally, higher irradiance leads to higher yields, likely due to enhanced photoexcitation of the CuNPs [30].

A key advantage of heterogeneous photocatalytic OHA reactions is the catalyst recyclability. To assess the reusability of the Cu/X catalysts, they were separated by centrifugation, thoroughly washed with ethyl acetate and ethanol, dried under vacuum at 60 °C, and then directly reused in subsequent OHA reactions (Figure 5E). Remarkably, all Cu/X catalysts could be recycled and reused at least four times without additional reduction treatment. Although some degree of deactivation was observed, these catalysts still outperformed the previously reported $Cu/Fe_3O_4/CuFe_2O_4$ composite catalyst [21], which exhibited a dramatic decline in 1,3-diyne yield from 95% in the first cycle to 26% in the second cycle. Cu/TiO_2 and Cu/BN maintained stable yields during the first two cycles, with slight deactivation occurring from the third cycle onward. In contrast, Cu/TiN, Cu/SiC and Cu/C_3N_4 showed gradual deactivation starting from the first cycle. Notably, Cu/ZnO demonstrated the best stability, with the yield of 1,3-diyne remaining constant at 62% over the last three cycles. The varying activity and stability of the Cu/X catalysts are likely

related to the intrinsic metal-support interactions, which influence both the LSPR effect and the formation of heterojunctions.

2.3. Evidence for Metal-Support Interactions

The recycled Cu/X catalysts were characterized by HRTEM, AAS, and XPS to elucidate the differences in their activity and stability, and to provide evidence for metal-support interactions. HRTEM images of the recycled Cu/X catalysts after the first use are shown in Figure 6, and the average CuNP sizes are summarized in Table 2. Notably, both the (111) plane of Cu_2O (lattice fringe of 0.25 nm) and the (111) plane of CuO (lattice fringe of 0.23 nm) were observed in close proximity to the (111) and (200) planes of metallic Cu^0, indicating oxidation of the CuNPs during the photocatalytic OHA reaction. After recycling, the average CuNP sizes of Cu/TiO_2, Cu/ZnO, and Cu/BN increased slightly, while those of Cu/TiN, Cu/SiC, and Cu/C_3N_4 decreased significantly. With the exception of Cu/C_3N_4 (4.3 nm), the other recycled Cu/X catalysts exhibited similar CuNP sizes (2.5~3.0 nm). This convergence in CuNP size suggests that the nanostructures are reconstructed during the photocatalytic OHA reaction. These findings are consistent with previous reports: (i) surface Cu^+ species can undergo phenylacetylene-induced leaching from Cu_2O nanoparticles, forming homogeneous copper catalytic species [53]; and (ii) soluble Cu^+ species can be reduced back to metallic CuNPs by photogenerated electrons [8].

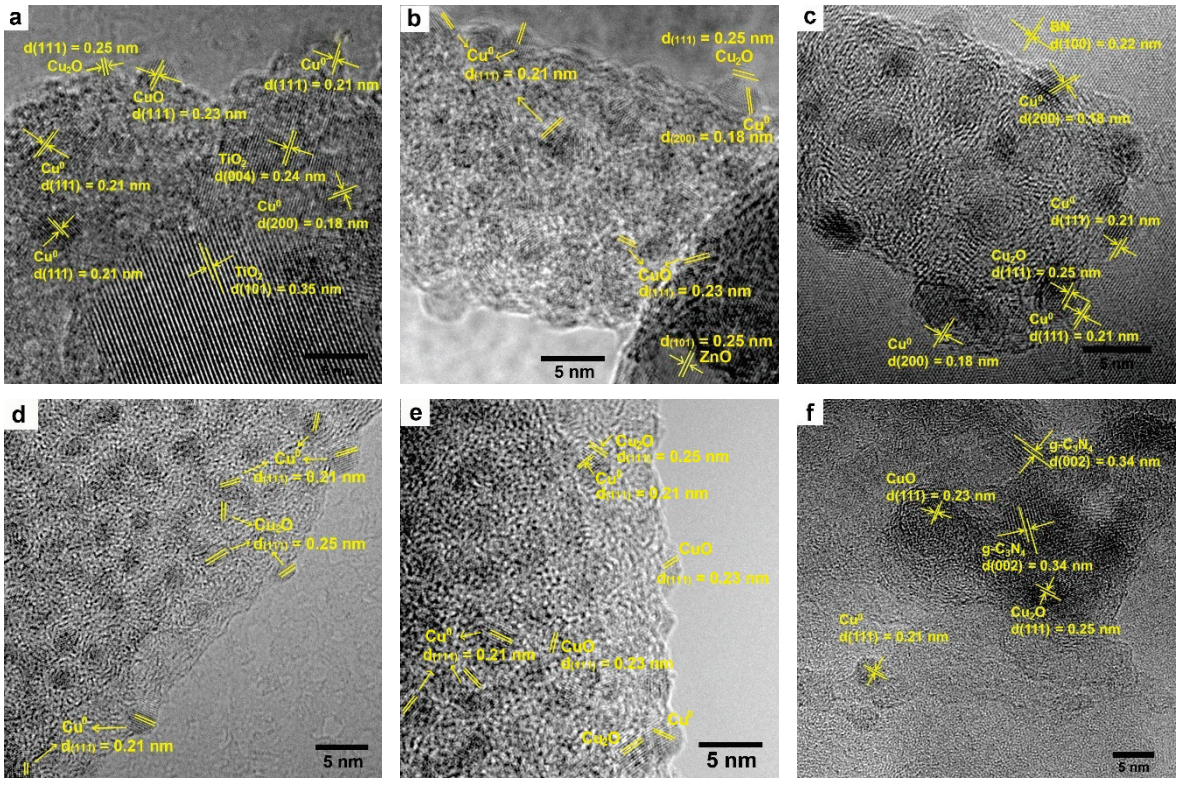


Figure 6. HRTEM images of the recycled Cu/X catalysts: (**a**) Cu/TiO_2, (**b**) Cu/ZnO, (**c**) Cu/BN, (**d**) Cu/TiN, (**e**) Cu/SiC, and (**f**) Cu/C_3N_4.

Copper contents of the recycled catalysts after the first and fourth cycles are listed in Table 2. Copper leaching was observed in each reaction cycle, with the most pronounced loss occurring during the first use. After four cycles, the percentage of Cu leaching increased in the following order: Cu/ZnO (23%) < Cu/TiO_2 (35%) < Cu/BN (39%) < Cu/TiN (44%) < Cu/SiC (60%) < Cu/C_3N_4 (70%). This trend indicates that the Cu-support interactions are stronger in the first three catalysts compared to the latter three, aligning well with

their activity and stability profiles. To elucidate the relationship between Cu leaching and the formation of the soluble Cu-PhAC complex, the Cu/TiO_2 catalyst was separated after 1–3 h of reaction and analyzed by UV-vis and FT-IR spectroscopy (Figure S5). Both the UV-vis absorption at ~460 nm [54] and the FT-IR peaks at 1930 cm^{-1} (C≡C-Cu) and 1595, 1481, 1438 cm^{-1} (C=C of phenyl) [55] first increased and then decreased with reaction time. This consistent trend indicates initial accumulation of Cu-PhAC complexes on the catalyst surface, followed by their coupling and transformation into diyne products in the later reaction stages.

Table 2. Structural, chemical, and photocatalytic properties of recycled Cu/X catalysts.

Catalyst	d_{Cu} [a] (nm)	Cu Content (wt%) [b]			XPS Peak Area Ratio (%) [c]				Yield [d] (%)	TOF [e] (h^{-1})
		Fresh	1st	4th	Cu^0/Cu	Cu^+/Cu	O_L/O	O_A/O		
Cu/TiO_2	2.8	4.9	4.3	3.2	23	68	63	28	52	3.4
Cu/ZnO	2.7	4.3	3.7	3.3	21	18	57	43	62	4.0
Cu/BN	3.0	5.1	4.4	3.1	18	75	0	91	39	2.7
Cu/TiN	2.6	5.0	3.8	2.8	9	82	50	40	30	2.3
Cu/SiC	2.8	5.2	3.5	2.1	10	52	3	97	25	2.5
Cu/C_3N_4	4.3	3.7	2.7	1.1	20	21	7	93	15	2.9

[a] Based on the HRTEM images after the 1st cycle. [b] Based on the AAS result. [c] Calculated from the XPS spectra after the 1st cycle. [d] Yield of 1,3-diyne in the 4th cycle. Photocatalytic conditions: phenylacetylene (0.2 mmol), n-dodecane (0.1 mmol, internal standard), catalyst (20 mg), methanol (2mL), white LED (λ > 400 nm, 0.2 W/cm^2), stirred 3 h under O_2 balloon at room temperature. [e] Turnover frequency (TOF) = (moles of 1,3-diyne produced)/(moles of Cu)/(reaction time, h), calculated from the 4th cycle.

To examine whether homogeneous Cu-PhAC species in solution contribute significantly to the overall activity, a hot-filtration test was conducted using the Cu/TiO_2 catalyst (Figure S6). In the second reuse cycle, the catalyst was removed by filtration after 1 h of visible-light irradiation, at which point the yield of 1,3-diyne was 49%. The filtrate was further irradiated for 2 h in the absence of the catalyst, and the yield only increased marginally to 55%. This slight yield increase indicates that leached Cu-PhAC species in the filtrate are unable to sustain the coupling reaction efficiently, confirming that the photocatalytic oxidative homocoupling primarily occurs on the catalyst surface via a heterogeneous pathway.

Based on the 1,3-diyne yield and copper content after the fourth cycle, the turnover frequencies (TOF) of the recycled Cu/X catalysts were calculated to be in the range of 2.3–4.0 h^{-1}. Notably, the most stable Cu/ZnO catalyst achieved the highest photocatalytic activity even after four cycles (TOF ~ 4.0 h^{-1}), which is 2.4-fold that of the freshly reduced $CuFe_2O_4$ catalyst [21]. These results demonstrate that the ZnO support exerts a unique stabilizing effect on the visible-light-activated Cu^0-Cu_2O-CuO composite (see Figure 6b), effectively retarding Cu leaching and facilitating the reduction in Cu^+/Cu^{2+} back to Cu^0. This stabilization helps maintain a balanced LSPR effect and ensures sustained photocatalytic activity.

XPS spectra of the recycled Cu/X catalysts (Figure 7) reveal that Cu^{2+} species are present in all recycled samples, consistent with the HRTEM observations. The XPS peak area ratios of Cu^0/Cu, Cu^+/Cu, O_L/O, and O_A/O are summarized in Table 2. The fraction of Cu^0 in the recycled Cu/X catalysts decreases in the order: Cu/TiO_2 (23%) > Cu/ZnO (21%) > Cu/C_3N_4 (20%) > Cu/BN (18%) > Cu/SiC (10%) > Cu/TiN (9%). The highest Cu^0 fraction in recycled Cu/TiO_2 correlates well with its superior photocatalytic activity in the second reaction cycle. Although the recycled Cu/C_3N_4 catalyst remains a relatively high Cu^0 fraction, its activity drops sharply in the second cycle, likely due to significant Cu leaching. For both fresh and recycled Cu/SiC and Cu/TiN catalysts, the low Cu^0 fractions

(~10%) and high Cu leaching rates (>40%) explain their poor photocatalytic activity and stability. Notably, the Cu^0 fraction in recycled Cu/ZnO increases from 14% (fresh) to 21% (recycled), whereas other recycled Cu/X catalysts show either a decrease or no change in Cu^0 fraction. This unusual increase in Cu^0 content further highlights the stabilizing effect of the ZnO support, which is also supported by the nearly unchanged O_A and O_L fractions. It is noteworthy that the successful identification of Cu^0, Cu^+, and Cu^{2+} species in this study was achieved through the combined use of HRTEM, Cu 2p XPS, and Auger Cu LMM XPS techniques. In contrast, most previous reports lacked Auger Cu LMM XPS analysis [23–34], which limited the accurate differentiation of copper oxidation states.

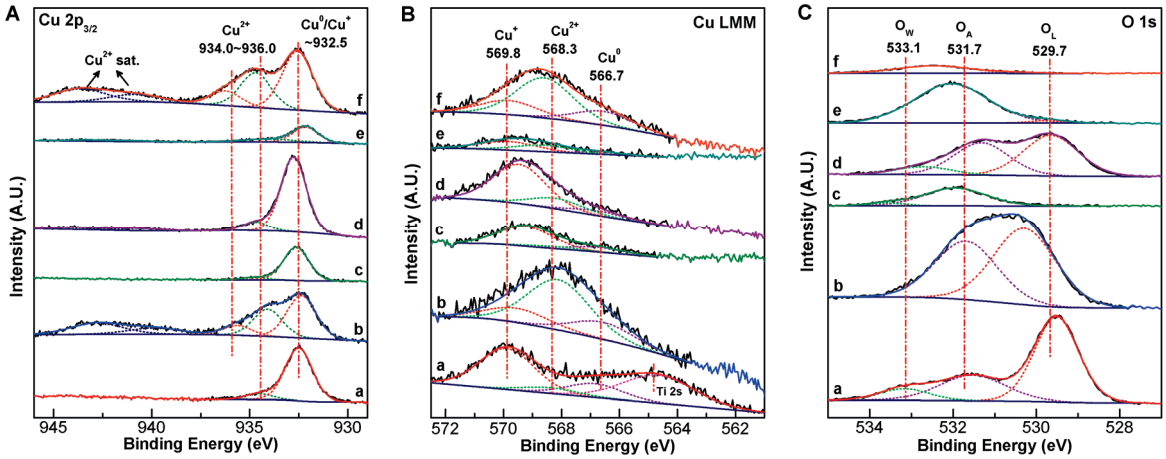


Figure 7. Cu $2p_{3/2}$ (**A**), Auger Cu LMM (**B**), and O 1s (**C**) XPS spectra of the recycled Cu/X catalyst after the 1st cycle: (a) Cu/TiO_2, (b) Cu/ZnO, (c) Cu/BN, (d) Cu/TiN, (e) Cu/SiC, and (f) Cu/C_3N_4.

To elucidate the role of metal–support interactions in photocatalytic stability, XPS analysis was conducted to examine the electronic interactions between CuNPs and various supports before and after the OHA reaction. The Cu 2p spectra revealed that oxidation during the reaction caused discernible binding-energy shifts for all samples (Figure S7). Notably, the overlapping Cu^0/Cu^+ $2p_{3/2}$ feature at ~932.0 eV shifted toward lower binding energies for Cu/ZnO and Cu/SiC, whereas the corresponding feature for the other catalysts shifted toward higher binding energies. In addition, the core-level binding energies of both metal and non-metal elements in the TiO_2, ZnO, and BN supports changed markedly after the reaction, while those in TiN, SiC, and C_3N_4 supports remained essentially unchanged. These observations indicate that TiO_2, ZnO, and BN exhibit stronger electronic metal–support interactions with CuNPs, which are likely responsible for the superior stability of these catalysts during photocatalysis.

Building on the above findings, two crucial observations can be made: (i) SiC, TiN, and C_3N_4 semiconductors, with narrower bandgaps (<2.7 eV), can be photoexcited by visible light to generate conduction band electrons; (ii) however, their corresponding Cu/X catalysts exhibit lower Cu^0 fractions and higher Cu leaching rates. This suggests that the conduction band electrons generated in these supports may not efficiently transfer to the CuNPs, thus failing to enhance the visible-light-driven photocatalytic OHA reactions. Excess photoexcited electrons may preferentially decompose the surface-bound Cu-PhAC complex, leading to a further decrease in catalytic efficiency. In contrast, TiO_2, ZnO, and BN, with wider bandgaps (>3.0 eV), cannot be excited by visible light, yet their corresponding Cu/X catalysts display lower Cu leaching, higher Cu^0 fraction, and superior photocatalytic activity. These results indicate that the photocatalytic activity in the OHA reaction is primarily governed by the synergistic effect of Cu^0-induced LSPR and efficient electron transfer within the $Cu^0/Cu_2O/X$ heterojunctions. Among them, ZnO demonstrates the

strongest interaction with the Cu^0-Cu_2O-ZnO composite, making Cu/ZnO a particularly promising catalyst. While more complex nanostructured catalysts such as Cu@C-TiO_2 [28], Cu-MOF/TiO_2 [29], Cu@Cu_2O/ZnO [31], and Cu_xO@TiO_2 [56] have shown higher stability, the structure-performance relationships revealed by these simple Cu/X catalysts highlight the need for deeper mechanistic understanding to guide the rational design of more efficient and stable CuNP-based systems.

Based on the above discussion, the plausible mechanism for the visible-light photocatalytic OHA over various semiconductor-supported CuNPs mainly involves a LSPR-induced hot-electron process. Under visible-light irradiation, the LSPR effect of CuNPs generates energetic electrons that activate molecular oxygen to form superoxide anions (O_2^-, as indicated in Figure S8) [57,58], which act as a Lewis base to abstract the terminal alkyne hydrogen from phenylacetylene. The resulting deprotonated alkyne species subsequently binds to surface Cu^+ centers, yielding Cu–PhAC intermediates. Coupling between two adjacent Cu–PhAC intermediates on the catalyst surface produces the 1,3-diyne product. The remaining isolated Cu^+ species can be reduced back to Cu^0 either by photogenerated electrons from the semiconductor (e.g., Cu_2O) or by electrons supplied from the methanol sacrificial agent, thereby completing the catalytic cycle.

Metallic Cu within the Cu/X composites can induce pronounced LSPR effects, whereas Cu_2O and CuO phases act as semiconductors capable of multifaceted electron-transfer interactions with the supports, resulting in a complex carrier-migration network. Previous studies have shown that metal-oxide-metal hybrid catalysts based on crystalline Cu_2O (e.g., Cu_2O-Pd) exhibit enhanced C-C coupling under visible light owing to more efficient charge separation [59]. This raises an important mechanistic question: how can the plasmonic enhancements from metallic Cu^0, the semiconductor contributions from Cu_2O, and potential photothermal effects during illumination be disentangled? In our present CuNP systems, Cu_2O exists only as a few-atomic-layer-thick surface oxide, rather than the large crystalline nanoparticles typically used as photocatalysts [60,61], and its role in oxidative homocoupling may differ substantially. Ex situ XPS analyses before and after reaction suggest interphase charge transfer; however, the lack of in situ spectroscopic and photoelectrochemical data limits a definitive mechanistic deconvolution. Moreover, methanol produced a more pronounced promoting effect than ethanol, yet the underlying causes—whether acting as a sacrificial electron donor, stabilizing the Cu-PhAC intermediate, or engaging in other specific interactions—remain speculative. Future work will focus on the Cu/ZnO catalyst, integrating advanced photoelectrochemical studies, in situ spectroscopic characterization, and kinetic analyses to separately quantify LSPR-induced hot-carrier contributions, Cu_2O-mediated semiconductor effects, and the promoting role of methanol. Such efforts will directly link mechanistic insight to structure-performance relationships, enabling the design of next-generation CuNP-based photocatalysts with improved stability and activity.

3. Methods

3.1. Catalyst Preparation

All chemicals and semiconductor nanomaterials (X = TiO_2, ZnO, BN, TiN, SiC, and C_3N_4) used in this study were of analytical grade and purchased from Adamas Reagent Co., Ltd. The Cu/X catalysts, with a theoretical loading of 5 wt%, were prepared via a deposition-reduction method. For the preparation of Cu/TiO_2, Cu/BN, Cu/TiN, and Cu/SiC catalysts, 0.5 g of the respective X powder was dispersed in an aqueous solution of $Cu(NO_3)_2 \cdot 3H_2O$ (0.1g mL^{-1}) at RT. After impregnation for 1 h, the mixture was dried under vacuum at 50 °C for 12 h. The resulting solid was then reduced under a flow of 10 vol% H_2 balanced with N_2 at 250 °C for 2 h to obtain the final catalyst. For Cu/ZnO

and Cu/C_3N_4 catalysts, a modified procedure was employed. Specifically, 0.5 g of ZnO or C_3N_4 powder was dispersed into 50 mL of an aqueous $Cu(NO_3)_2 \cdot 3H_2O$ solution (7 mM) under vigorous stirring for 30 min. Subsequently, $NH_3 \cdot H_2O$ aqueous solution (5 wt%) was added dropwise until the pH reached 9.0. The suspension was stirred for an additional 12 h at RT, after which the solid was separated by centrifugation and washed several times with deionized water. The precursor was then redispersed in 60 mL of deionized water, and 30 mL of $NaBH_4$ aqueous solution (70 mM) was added dropwise to completely reduce Cu^{2+} to metallic CuNPs. The final product was washed repeatedly with deionized water and ethanol and dried under vacuum at 50 °C overnight.

3.2. Catalyst Characterization

The crystalline phases of the catalyst were identified by XRD (Empyrean apparatus, 40 kV, 30 mA, PANalytical B.V., Almelo, The Netherlands) using Cu K_α radiation [62–64]. The structure and morphology of the catalyst were examined by SEM (FEI Nova NanoSEM 450, Eindhoven, the Netherlands) and HRTEM (FEI Tecnai G2 F30, Eindhoven, the Netherlands). Diffuse reflectance UV-vis spectra of the catalysts were collected with a Varian Cary 5000 spectrophotometer (Santa Clara, CA, USA) using $BaSO_4$ as a blank reference. XPS was performed on an AXISULTRA DLD-600 W spectrometer (Shimazu-Kratos, Tokyo, Japan) with Al K_α irradiation, and the binding energies were calibrated by using the C 1s peak of contaminant carbon at 284.5 eV as an internal standard. Nitrogen adsorption–desorption isotherms were analyzed by a Micromeritics ASAP 2020V3.04 H nitrogen adsorption apparatus (Norcross, GA, USA). Copper content of the fresh and recycled Cu/X catalysts was detected by AAS (Perkin Elmer AA-300, Waltham, MA, USA) after treating the samples in nitric acid. FT-IR spectra were recorded on a Bruker VERTEX 70 FT-IR spectrometer (Dresden, Germany), using the KBr pellet method at a resolution of 4 cm^{-1}. Electronic spin resonance (ESR) measurements were performed on a Bruker E500 spectrometer (Dresden, Germany) using 5, 5-dimethyl-1-pyrroline N-oxide (DMPO) as the spin-trapping agent to detect $O_2^{-\bullet}$ radical generated in the photocatalytic reaction system under visible-light irradiation (see Supporting Information for details).

3.3. Photocatalytic Oxidative Coupling of Phenylacetylene

All photocatalytic OHA experiments were conducted using a white light-emitting diode (PLS-LED 100, $\lambda > 400$ nm, Beijing Perfectlight Technology Co. Ltd., Beijing, China) as the light source, with the light intensity set at 0.2 W/cm^2 unless otherwise specified. Typically, phenylacetylene (0.2 mmol), n-dodecane (0.1 mmol, used as an internal standard), and Cu/X catalyst (10 mol% Cu) were mixed with methanol (2 mL) and transferred into a 15 mL Pyrex glass tube (φ 15 mm) equipped with an oxygen balloon. The reaction mixture was irradiated with visible light under stirring for 3 h at ambient temperature. To terminate the reaction, ethyl acetate (5 mL) was added to the mixture. A portion of the diluted reaction mixture (2 mL) was then filtered through a Titan filter (pore size 0.22 μm) to remove catalyst particles. The products were qualitatively analyzed using an Agilent 7890A/5975C GC-MS (Santa Clara, CA, USA), and quantitatively determined by a Fuli 9070 GC-FID (Taizhou, China) employing the internal standard method. Notably, 1,3-diyne was obtained as the sole product with 100% selectivity, and the carbon balance was maintained at 100 ± 3% in all experiments.

4. Conclusions

In summary, a series of Cu/X catalysts was successfully constructed using representative semiconductor nanomaterials (X = TiO_2, ZnO, BN, TiN, SiC, and C_3N_4) as supports for CuNPs and applied in visible-light-driven photocatalytic oxidative homocoupling of

phenylacetylene. The study revealed that the photocatalytic activity and stability of these catalysts are closely related to the nature of the metal-support interactions. Supports with stronger interactions, such as ZnO and TiO_2, effectively stabilized the Cu^0 species, suppressed copper leaching, and maintained high photocatalytic performance. In particular, the Cu/ZnO catalysts demonstrated remarkable photocatalytic activity and durability, attributed to their unique ability to balance the LSPR effect and facilitate electron transfer within the Cu^0-Cu_2O-ZnO composite. This structural synergy minimized copper leaching and enabled excellent recyclability, preserving high activity across four successive cycles without requiring reduction treatment before reuse. Notably, after the fourth cycle, the Cu/ZnO catalyst still achieved a TOF of ~4.0 h^{-1}, which is 2.4-fold higher than that of the freshly reduced $CuFe_2O_4$ catalyst reported in the literature, underscoring its superior long-term performance. These findings highlight the importance of rational support selection and structure-performance relationships in designing efficient and durable CuNP-based photocatalysts. The insights gained from this work provide valuable guidance for the future development of advanced heterogeneous photocatalysts for visible-light-driven organic transformations.

Supplementary Materials: The following supporting information can be downloaded at: https://www.mdpi.com/article/10.3390/catal15111045/s1. Figure S1: XRD patterns of various semiconductor supports; Figure S2: SEM images of (a) Cu/TiO_2, (b) Cu/ZnO, (c) Cu/BN, (d) Cu/TiN, (e) Cu/SiC, and (f) Cu/C_3N_4; Figure S3: Diffuse reflectance UV-vis spectra of various X, Cu/X, and isolated CuNPs (insert). The isolated spectra of CuNPs were obtained by measuring Cu/X using X as background; the band at ~570 nm is attributed to the LSPR peak of CuNPs; Figure S4. Optical bandgap energy derived from Tauc plots for various semiconductor supports. Figure S5. UV-vis (A) and FT-IR (B) spectra of in situ-generated Cu^+-phenylacetylide on the surface of Cu/TiO_2 catalyst; Figure S6. Hot filtration test by using fresh and recycled Cu/TiO_2 catalysts with removal of the catalyst in the second cycle; Figure S7. XPS spectra of the fresh and recycled Cu/X catalysts: (A) Cu/TiO_2, (B) Cu/ZnO, (C) Cu/BN, (D) Cu/TiN, (E) Cu/SiC, and (F) Cu/C_3N_4; Figure S8. DMPO spin-trapping ESR spectra of Cu/ZnO recorded at ambient temperature in methanol for DMPO-$O_2^{-\bullet}$ detection.

Author Contributions: Investigation, validation, writing—original draft, N.D.; investigation, data curation, editing, Y.W.; data curation, editing, Y.S.; conceptualization, resources, writing—review and editing, supervision, funding acquisition, P.L. All authors have read and agreed to the published version of the manuscript.

Funding: This work was supported by the National Natural Science Foundation of China (21972050).

Data Availability Statement: The data supporting the findings of this study are available in the paper and its Supplementary Materials.

Conflicts of Interest: The authors declare no conflicts of interest.

References

1. Wang, H.; Tian, Y.M.; König, B. Energy- and Atom-Efficient Chemical Synthesis with Endergonic Photocatalysis. *Nat. Rev. Chem.* **2022**, *6*, 745–755. [CrossRef]
2. Wang, S.; Wang, J.; Wang, Y.; Sui, X.; Wu, S.; Dai, W.; Zhang, Z.; Ding, Z.; Long, J. Insight into the Selectivity-Determining Step of Various Photocatalytic CO_2 Reduction Products by Inorganic Semiconductors. *ACS Catal.* **2024**, *14*, 10760–10788. [CrossRef]
3. Ban, L.; Zhang, Y.; Sun, D.; Zhou, Y.; Li, Y.; Xu, C.; Yang, S.; Zhang, H. Photocatalytic Hydrogen Evolution Driven by Advanced Metal Sulfides from Sustainable Multilevel Biomass and Waste Plastics. *Adv. Funct. Mater.* **2025**, *35*, 2506114. [CrossRef]
4. Linic, S.; Christopher, P.; Ingram, D.B. Plasmonic-Metal Nanostructures for Efficient Conversion of Solar to Chemical Energy. *Nat. Mater.* **2011**, *10*, 911–921. [CrossRef] [PubMed]
5. Zhang, Y.; He, S.; Guo, W.; Hu, Y.; Huang, J.; Mulcahy, J.R.; Wei, W.D. Surface-Plasmon-Driven Hot Electron Photochemistry. *Chem. Rev.* **2018**, *118*, 2927–2954. [CrossRef] [PubMed]

6. Mao, C.; Li, H.; Gu, H.; Wang, J.; Zou, Y.; Qi, G.; Xu, J.; Deng, F.; Shen, W.; Li, J.; et al. Beyond the Thermal Equilibrium Limit of Ammonia Synthesis with Dual Temperature Zone Catalyst Powered by Solar Light. *Chem* **2019**, *5*, 2702–2717. [CrossRef]
7. Xin, Y.; Yu, K.; Zhang, L.; Yang, Y.; Yuan, H.; Li, H.; Wang, L.; Zeng, J. Copper-Based Plasmonic Catalysis: Recent Advances and Future Perspectives. *Adv. Mater.* **2021**, *33*, 2008145. [CrossRef]
8. Sayed, M.; Yu, J.; Liu, G.; Jaroniec, M. Non-Noble Plasmonic Metal-Based Photocatalysts. *Chem. Rev.* **2022**, *122*, 10484–10537. [CrossRef]
9. Siemsen, P.; Livingston, R.C.; Diederich, F. Acetylenic Coupling: A Powerful Tool in Molecular Construction. *Angew. Chem. Int. Ed.* **2000**, *39*, 2632–2657. [CrossRef]
10. Shi, W.; Lei, A. 1,3-Diyne Chemistry: Synthesis and Derivations. *Tetrahedron Lett.* **2014**, *55*, 2763–2772. [CrossRef]
11. Stefani, H.A.; Guarezemini, A.S.; Cella, R. Homocoupling Reactions of Alkynes, Alkenes and Alkyl compounds. *Tetrahedron* **2010**, *66*, 7871–7918. [CrossRef]
12. Alonso, F.; Yus, M. Heterogeneous Catalytic Homocoupling of Terminal Alkynes. *ACS Catal.* **2012**, *2*, 1441–1451. [CrossRef]
13. Lei, J.; Su, L.; Zeng, K.; Chen, T.; Qiu, R.; Zhou, Y.; Au, C.-T.; Yin, S.-F. Recent Advances of Catalytic Processes on the Transformation of Alkynes into Functional Compounds. *Chem. Eng. Sci.* **2017**, *171*, 404–425. [CrossRef]
14. Chaabane, L.; Beyou, E.; Luneau, D.; Baouab, M.H.V. Functionalization of Graphene Oxide Sheets with Magnetite Nanoparticles for the Adsorption of Copper Ions and Investigation of its Potential Catalytic Activity toward the Homocoupling of Alkynes under Green Conditions. *J. Catal.* **2020**, *388*, 91–103. [CrossRef]
15. Wan, W.; Lin, C.; Qiao, Y.; Chen, L.; Chen, J. Cu Catalyst Supported on Nitrogen and Phosphorus Co-Doped Carbon Nanosheets for Homocoupling of Terminal Alkynes Using CO_2 as a Soft Oxidant. *ACS Appl. Nano Mater.* **2021**, *4*, 4839–4852. [CrossRef]
16. Tang, J.; Jiao, B.; Chen, W.; Ruan, F.; Li, F.; Cui, P.; Wan, C.; Ha, M.N.; Nguyen, V.N.; Ke, Q. Revealing Efficient Catalytic Performance of N-CuOx for Aerobic Oxidative Coupling of Aliphatic alkynes: A Langmuir-Hinshelwood Reaction Mechanism. *Nano Res.* **2022**, *15*, 6076–6083. [CrossRef]
17. Shen, Q.; Jin, C.; Xing, Y.; Jia, Z.; Zhang, Y.; Feng, G.; Wen, X. Oxidation Coupling of Terminal Alkynes over CuPd Bimetallic Alloy Enhanced by Optimized Charge Transfer and Alloy Structure. *Chem. Eng. J.* **2023**, *470*, 144193. [CrossRef]
18. Muzalevskiy, V.M.; Shastin, A.V.; Tirkasheva, S.I.; Ziyadullaev, O.E.; Parmanov, A.B.; Nenajdenko, V.G. CCl_4-TMEDA-CuCl—A Novel Convenient Catalytic System for Dimerization of Terminal Acetylenes in Mild Conditions. *Catalysts* **2023**, *13*, 1330. [CrossRef]
19. Ding, R.; Xia, H.; Wu, Y.; Li, Y.; Yang, W.; Xu, H. Ultrafine Copper Oxide Nanoparticles Immobilized on Poly(4-vinylpyridine)-grafted UiO-66-NH2 as Heterogeneous Catalyst for Oxidative Homocoupling of Terminal Alkynes. *Colloids Surf. A* **2024**, *703*, 135328. [CrossRef]
20. Sagadevan, A.; Charpe, V.P.; Hwang, K.C. Copper(I) Chloride Catalysed Room Temperature C_{sp}-C_{sp} Homocoupling of Terminal Alkynes Mediated by Visible Light. *Catal. Sci. Technol.* **2016**, *6*, 7688–7692. [CrossRef]
21. Zhu, Y.; Deng, N.; Feng, M.; Liu, P. On the Comparable Activity in Plasmonic Photocatalytic and Thermocatalytic Oxidative Homocoupling of Alkynes over Prereduced Copper Ferrite. *Chin. J. Catal.* **2019**, *40*, 1505–1515. [CrossRef]
22. Cai, J.; Li, Y.; Zhang, M.; Li, Z. Cooperation in Cu-MOF-74-Derived Cu-Cu_2O-C Nanocomposites To Enable Efficient Visible-Light-Initiated Phenylacetylene Coupling. *Inorg. Chem.* **2019**, *58*, 7997–8002. [CrossRef] [PubMed]
23. Yuan, Y.; Wang, Y.-Q.; Zhuang, G.; Li, Q.; Yang, F.-L.; Wang, X.; Han, X. Supporting a Cu@In_2O_3 Core-Shell Structure on N-doped Graphitic Carbon Cuboctahedral Cages for Efficient Photocatalytic Homo-Coupling of Terminal Alkynes. *J. Mater. Chem. A* **2021**, *9*, 24909–24914. [CrossRef]
24. Liu, H.; Zhao, J.; Zhang, M. Dual Photoactive Species in CuPd for Light-switched Homo-coupling of Alkynes in Anaerobic and Base Free Condition. *ChemCatChem* **2024**, *16*, e202400715. [CrossRef]
25. Yan, X.; Xu, T.; Zhan, W.; Yang, Y.; Yu, Y.; Yi, J.; He, X.; Yang, L.; Zhao, J.; Sun, L.; et al. Engineering Cu_2O/Cu/N-C Interface to Induce Directional Migration of Charge for Driving Photocatalytic Homo-Coupling of Terminal alkynes. *Nano Res.* **2024**, *17*, 6895–6902. [CrossRef]
26. Zhao, J.; Li, Y.; Zhu, Y.; Wang, Y.; Wang, C. Enhanced CO_2 Photoreduction Activity of Black TiO_2-Coated Cu Nanoparticles under Visible Light Irradiation: Role of Metallic Cu. *Appl. Catal. A Gen.* **2016**, *510*, 34–41. [CrossRef]
27. DeSario, P.A.; Gordon, W.O.; Balboa, A.; Pennington, A.M.; Pitman, C.L.; McEntee, M.; Pietron, J.J. Photoenhanced Degradation of Sarin at Cu/TiO_2 Composite Aerogels: Roles of Bandgap Excitation and Surface Plasmon Excitation. *ACS Appl. Mater. Interfaces* **2021**, *13*, 12550–12561. [CrossRef]
28. Liu, P.; Dörfler, A.; Tabrizi, A.A.; Skokan, L.; Rawach, D.; Wang, P.; Peng, Z.; Zhang, J.; Ruediger, A.P.; Claverie, J.P. In Operando Photoswitching of Cu Oxidation States in Cu-Based Plasmonic Heterogeneous Photocatalysis for Efficient H_2 Evolution. *ACS Appl. Mater. Interfaces* **2023**, *15*, 27832–27844. [CrossRef]
29. Khan, A.; Pivert, M.L.; Ranjbari, A.; Dragoe, D.; Bahena-Uribe, D.; Colbeau-Justin, C.; Herrero, C.; Rutkowska-Zbik, D.; Deschamps, J.; Remita, H. Cu-Based MOF/TiO_2 Composite Nanomaterials for Photocatalytic Hydrogen Generation and the Role of Copper. *Adv. Funct. Mater.* **2025**, 2501736. [CrossRef]

30. Huang, Y.; Liu, Z.; Gao, G.; Xiao, G.; Du, A.; Bottle, S.; Sarina, S.; Zhu, H. Stable Copper Nanoparticle Photocatalysts for Selective Epoxidation of Alkenes with Visible Light. *ACS Catal.* **2017**, *7*, 4975–4985. [CrossRef]
31. Lou, Y.; Zhang, Y.; Cheng, L.; Chen, J.; Zhao, Y. A Stable Plasmonic Cu@Cu_2O/ZnO Heterojunction for Enhanced Photocatalytic Hydrogen Generation. *ChemSusChem* **2018**, *11*, 1505–1511. [CrossRef] [PubMed]
32. Yu, K.; Jiang, P.; Yuan, H.; He, R.; Zhu, W.; Wang, L. Cu-Based Nanocrystals on ZnO for Uranium Photoreduction: Plasmon-Assisted Activity and Entropy-Driven Stability. *Appl. Catal. B Environ.* **2021**, *288*, 119978. [CrossRef]
33. Zhang, S.-W.; Li, S.; Zhang, B.-P.; Yu, D.; Zhang, Z.; Li, J.-F. Copper-Nanoparticle-Dispersed Amorphous $BaTiO_3$ Thin Films as Hole-Trapping Centers: Enhanced Photocatalytic Activity and Stability. *RSC Adv.* **2019**, *9*, 5045–5052. [CrossRef] [PubMed]
34. Li, Z.; Zhu, G.; Zhang, W.; Zhu, L.; Cao, B.; Gao, J.; Shi, X.; Huang, Y.; Liu, P.; Hojamberdiev, M. Dual-Functional Copper (Cu^0/Cu^{2+})-Modified $SrTiO_{3-\delta}$ Nanosheets with Enhanced Photothermal Catalytic Performance for CO_2 Reduction and H_2 Evolution. *Chem. Eng. J.* **2023**, *452*, 139378. [CrossRef]
35. Li, M.-Y.; Lu, W.-D.; He, L.; Schüth, F.; Lu, A.-H. Tailoring the Surface Structure of Silicon Carbide Support for Copper Catalyzed Ethanol Dehydrogenation. *ChemCatChem* **2019**, *11*, 481–487. [CrossRef]
36. Zhou, G.; Yang, F.; Zhu, X.; Feng, W.; Chen, D.; Fang, J. Copper-Copper Oxide Heterostructural Nanocrystals Anchored on g-C_3N_4 Nanosheets for Efficient Visible-Light-Driven Photo-Fenton-like Catalysis. *Molecules* **2025**, *30*, 144. [CrossRef]
37. Liu, P.; Hensen, E.J.M. Highly Efficient and Robust Au/$MgCuCr_2O_4$ Catalyst for Gas-Phase Oxidation of Ethanol to Acetaldehyde. *J. Am. Chem. Soc.* **2013**, *135*, 14032–14035. [CrossRef]
38. Yue, L.; Wang, J.; Liu, P. Promoting Effect of Copper Doping on $LaMO_3$ (M = Mn, Fe, Co, Ni) Perovskite-Supported Gold Catalysts for Selective Gas-Phase Ethanol Oxidation. *Catalysts* **2025**, *15*, 176. [CrossRef]
39. Wang, J.; Chen, L.; Yue, L.; Filot, I.A.W.; Hensen, E.J.M.; Liu, P. Unveiling the Au-Mn-Cu Synergy in Au/$LaMnCuO_3$ Catalysts for Selective Ethanol Oxidation. *Chin. J. Catal.* **2025**, *75*, 34–48. [CrossRef]
40. Dabera, G.D.M.R.; Walker, M.; Sanchez, A.M.; Pereira, H.J.; Beanland, R.; Hatton, R.A. Retarding Oxidation of Copper Nanoparticles Without Electrical Isolation and the Size Dependence of Work Function. *Nat. Commun.* **2017**, *8*, 1894. [CrossRef]
41. Liu, P.; Li, T.; Chen, H.; Hensen, E.J.M. Optimization of Au^0-Cu^+ Synergy in Au/$MgCuCr_2O_4$ Catalysts for Aerobic Oxidation of Ethanol to Acetaldehyde. *J. Catal.* **2017**, *347*, 45–56. [CrossRef]
42. Hu, W.; Li, D.; Yang, Y.; Li, T.; Chen, H.; Liu, P. Copper Ferrite Supported Gold Nanoparticles as Efficient and Recyclable Catalyst for Liquid-Phase Ethanol Oxidation. *J. Catal.* **2018**, *357*, 108–117. [CrossRef]
43. Liu, Q.; Chen, C.; Du, M.; Wu, Y.; Ren, C.; Ding, K.; Song, M.; Huang, C. Porous Hexagonal Boron Nitride Sheets: Effect of Hydroxyl and Secondary Amino Groups on Photocatalytic Hydrogen Evolution. *ACS Appl. Nano Mater.* **2018**, *1*, 4566–4575. [CrossRef]
44. Huang, Y.-F.; Zhang, M.; Zhao, L.-B.; Feng, J.-M.; Wu, D.-Y.; Ren, B.; Tian, Z. Activation of Oxygen on Gold and Silver Nanoparticles Assisted by Surface Plasmon Resonances. *Angew. Chem. Int. Ed.* **2014**, *53*, 2353–2357. [CrossRef] [PubMed]
45. Linic, S.; Aslam, U.; Boerigter, C.; Morabito, M. Photochemical Transformations on Plasmonic Metal Nanoparticles. *Nat. Mater.* **2015**, *14*, 567–576. [CrossRef]
46. DeSario, P.A.; Pietron, J.J.; Brintlinger, T.H.; McEntee, M.; Parker, J.F.; Baturina, O.; Stroud, R.M.; Rolison, D.R. Oxidation-Stable Plasmonic Copper Nanoparticles in Photocatalytic TiO_2 Nanoarchitectures. *Nanoscale* **2017**, *9*, 11720–11729. [CrossRef]
47. Zhou, T.; Wang, J.; Chen, S.; Bai, J.; Li, J.; Zhang, Y.; Li, L.; Xia, L.; Rahim, M.; Xu, Q.; et al. Bird-Nest Structured ZnO/TiO_2 as a Direct Z-Scheme Photoanode with Enhanced Light Harvesting and Carriers Kinetics for Highly Efficient and Stable Photoelectrochemical Water Splitting. *Appl. Catal. B Environ.* **2020**, *267*, 118599. [CrossRef]
48. Yang, Y.; Zhang, C.; Huang, D.; Zeng, G.; Huang, J.; Lai, C.; Zhou, C.; Wang, W.; Guo, H.; Xue, W.; et al. Boron Bitride Quantum Dots Decorated Ultrathin Porous g-C_3N_4: Intensified Exciton Dissociation and Charge Transfer for Promoting Visible-Light-Driven Molecular Oxygen Activation. *Appl. Catal. B Environ.* **2019**, *245*, 87–99. [CrossRef]
49. Yu, W.; Difa Xu, D.; Peng, T. Enhanced Photocatalytic Activity of g-C_3N_4 for Selective CO_2 Reduction to CH_3OH via Facile Coupling of ZnO: A Direct Z-Scheme Mechanism. *J. Mater. Chem. A* **2015**, *3*, 19936–19947. [CrossRef]
50. Hao, C.-H.; Guo, X.-N.; Pan, Y.-T.; Chen, S.; Jiao, Z.-F.; Yang, H.; Guo, X.-Y. Visible-Light-Driven Selective Photocatalytic Hydrogenation of Cinnamaldehyde over Au/SiC Catalysts. *J. Am. Chem. Soc.* **2016**, *138*, 9361–9364. [CrossRef]
51. Liu, Y.; Peng, M.; Gao, K.; Fu, R.; Zhang, S.; Xiao, Y.; Guo, J.; Wang, Z.; Wang, H.; Zhao, Y.; et al. Boosting Photocatalytic Degradation of Levofloxacin over Plasmonic TiO_{2-x}/TiN Heterostructure. *Appl. Surf. Sci.* **2024**, *655*, 159516. [CrossRef]
52. Madasu, M.; Huang, M.H. Cu_2O Polyhedra for Aryl Alkyne Homocoupling Reactions. *Catal. Sci. Technol.* **2020**, *10*, 6948–6952. [CrossRef]
53. Pary, F.F.; Tirumala, R.T.A.; Andiappan, M.; Nelson, T.L. Copper(I) Oxide Nanoparticle-Mediated C–C Couplings for Synthesis of Polyphenylenediethynylenes: Evidence for a Homogeneous Catalytic Pathway. *Catal. Sci. Technol.* **2021**, *11*, 2414–2421. [CrossRef]
54. Shanmugam, M.; Sagadevan, A.; Charpe, V.P.; Pampana, V.K.K.; Hwang, K.C. Cu_2O Nanocrystals-Catalyzed Photoredox Sonogashira Coupling of Terminal Alkynes and Arylhalides Enhanced by CO_2. *ChemSusChem* **2020**, *13*, 287–292. [CrossRef]

55. Lin, Z.; Xiao, Z.; Liu, Y.; Wang, Y.; Chen, S.; Zhang, J.; Chen, Y.; Zhang, X.; Zhang, G.; Li, D.; et al. Insights into Copper(I) Phenylacetylide with in-situ Transformation of Oxygen and Enhanced Visible-Light Response for Water Decontamination: Cu–O Bond Promotes Exciton Dissociation and Charge Transfer. *J. Colloid Interf. Sci.* **2024**, *671*, 1–14. [CrossRef]
56. Wang, K.; Bielan, Z.; Endo-Kimura, M.; Janczarek, M.; Zhang, D.; Kowalski, D.; Zielinska-Jurek, A.; Markowska-Szczupak, A.; Bunsho Ohtani, B.; Kowalska, E. On the Mechanism of Photocatalytic Reactions on Cu_xO@TiO_2 Core-Shell Photocatalysts. *J. Mater. Chem. A* **2021**, *9*, 10135–10145. [CrossRef]
57. Quan, X.; Guo, F.; Li, R.; Zhang, H.; Shen, Z.; Zhang, J. Palladium−Copper Alloy Nanoparticles Supported on Carbon Nitride Nanosheets as a Photocatalyst for Degradation of Ciprofloxacin. *ACS Appl. Nano Mater.* **2024**, *7*, 23228–23239. [CrossRef]
58. Hu, T.; Yue, Z.; Wang, Y.; Yu, Y.; Chang, Y.; Pei, L.; Chen, W.; Han, P.; Martens, W.; Waclawik, E.R.; et al. Cu@CuO_x/WO_3 with Photo-Regulated Singlet Oxygen and Oxygen Adatoms Generation for Selective Photocatalytic Aromatic Amines to Imines. *J. Colloid Interf. Sci.* **2024**, *663*, 632–643. [CrossRef]
59. Tirumala, R.T.A.; Gyawali, S.; Le, T.; Kumar, S.; Tan, S.; Wang, B.; Bristow, A.D.; Andiappan, M. Visible-Light-Driven Photocatalytic Carbon-Carbon Coupling Reaction under Atmospheric Temperature and Pressure Conditions Using Hybrid Cu_2O-Pd Nanostructures. *ACS Appl. Mater. Interfaces* **2025**, *17*, 26651–26660. [CrossRef]
60. Tirumala, R.T.A.; Ramakrishnan, S.B.; Mohammadparast, F.; Khatri, N.; Arumugam, S.M.; Tan, S.; Kalkan, A.K.; Andiappan, M. Structure-Property-Performance Relationships of Dielectric Cu_2O Nanoparticles for Mie Resonance-Enhanced Dye Sensitization. *ACS Appl. Nano Mater.* **2022**, *5*, 6699–6707. [CrossRef]
61. Tirumala, R.T.A.; Khatri, N.; Ramakrishnan, S.B.; Mohammadparast, F.; Khan, M.T.; Tan, S.; Wagle, P.; Puri, S.; McIlroy, D.N.; Kalkan, A.K.; et al. Tuning Catalytic Activity and Selectivity in Photocatalysis on MieResonant Cuprous Oxide Particles: Distinguishing Electromagnetic Field Enhancement Effect from the Heating Effect. *ACS Sustainable Chem. Eng.* **2023**, *11*, 15931–15940. [CrossRef]
62. Simukaitis, M.; Stewart, S.; Sun, Y. Visible-Light-Driven Desulfurization Reaction Using Partially Oxidized TiN Nanoparticles as Photocatalysts. *J. Phys. Chem. C* **2025**, *129*, 7780–7786. [CrossRef]
63. Jiang, L.; Yuan, X.; Zeng, G.; Wu, Z.; Liang, J.; Chen, X.; Leng, L.; Wang, H.; Wang, H. Metal-Free Efficient Photocatalyst for Stable Visible-Light Photocatalytic Degradation of Refractory Pollutant. *Appl. Catal. B Environ.* **2018**, *221*, 715–725. [CrossRef]
64. Wang, B.; Wang, Y.; Li, J.; Guo, X.; Bai, G.; Tong, X.; Jin, G.; Guo, X. Photocatalytic Sonogashira Reaction over Silicon Carbide Supported Pd–Cu Alloy Nanoparticles under Visible Light Irradiation. *Catal. Sci. Technol.* **2018**, *8*, 3357–3362. [CrossRef]

Disclaimer/Publisher's Note: The statements, opinions and data contained in all publications are solely those of the individual author(s) and contributor(s) and not of MDPI and/or the editor(s). MDPI and/or the editor(s) disclaim responsibility for any injury to people or property resulting from any ideas, methods, instructions or products referred to in the content.

catalysts

MDPI

Article

Efficient Water Disinfection via Photocatalytic Oxidation Process Mediated by WO_3/BiOBr@Si Composite

Xiaoxia Ye [1], Qiu Wu [1], Guifang Yang [2,*], Yuancai Lv [1,*] and Minghua Liu [1,2]

[1] Fujian Provincial Engineering Research Center of Rural Waste Recycling Technology, College of Environment & Safety Engineering, Fuzhou University, Fuzhou 350116, China; yexiaoxia@fzu.edu.cn (X.Y.); 230620061@fzu.edu.cn (Q.W.); mhliu2000@fzu.edu.cn (M.L.)
[2] Fujian Provincial Key Laboratory of Ecology-Toxicological Effects & Control for Emerging Contaminants, Putian University, Putian 351100, China
* Correspondence: abc396550322@ptu.edu.cn (G.Y.); yclv@fzu.edu.cn (Y.L.)

Abstract

Developing green water disinfection technology has been attracting much attention all over the world. In this work, a WO_3/BiOBr@Si composite was obtained through the solvothermal process, which exhibited denser and fuller intersecting petal-like spheres (1–3 μm in diameter) and retained its 3D sheet-like pore structure. The optical and electrochemical analysis demonstrated that the doped Si showed insignificant improvement in UV-Vis light absorption but greatly promoted the electron-hole separation efficiency and charge transfer capability on the surface of the catalyst at a 4.6 wt% Si doping dosage, resulting in an excellent performance in the inactivation of *Escherichia coli* (*E. coli*) under the irradiation of visible light. Under the optimal conditions (0.5 g/L of WO_3/BiOBr@Si dosage, 10^7 CFU mL^{-1} of *E. coli* concertation, and 30 min of treating time), the largest log value decline (6.6) occurred with WO_3/BiOBr@1.0Si, which was 3.3 and 1.8 times larger than those of BiOBr (2.0) and WO_3/BiOBr (3.7). According to the TEM, SEM, EDS, XRD, FTIR, and XPS analyses, in the photocatalytic system, the hole (h^+) and •OH were the main species for inactivating *E. coli* cells. These oxidizing species could attack the components on the surface of cells (such as the hydroxyl, carbonyl, ester, and amide groups of polysaccharides (PS) and proteins (PT)), resulting in the inactivation and destruction of the cell membranes and leakage of intracellular substances. The findings will provide a significant guide for developing an efficient catalyst for the green water disinfection process.

Keywords: water disinfection; photocatalysis; *Escherichia coli*; mechanism

1. Introduction

Against the backdrop of worsening global water pollution and pathogenic transmission risks, efficient elimination of pathogenic bacteria, viruses, and other microbes from water is pivotal for safeguarding public health and ecological health [1,2]. Notably, the exceedance of regulatory limits for typical pathogens such as *Escherichia coli* poses a critical hazard to water safety and drives disease spread. As an emerging green, high-efficiency sterilization technology for water and environmental media, photocatalytic disinfection serves as a core approach to overcoming conventional disinfection limitations, featuring mild reaction conditions, no secondary pollution, broad sterilization spectrum, and excellent energy efficiency [2]. Owing to highly oxidizing reactive species via semiconductors under light irradiation, it non-selectively disrupts microbial cells and degrades key intracellular biomacromolecules, realizing complete sterilization without inducing

drug resistance [2]. Therefore, developing high-performance photocatalytic disinfection materials and clarifying their sterilization mechanisms is of great theoretical and practical significance for upgrading environmental disinfection technologies.

To date, numerous semiconductor materials have exhibited exceptional photocatalytic performance, including titanium dioxide (TiO_2) [3], metal oxides [4,5], metal sulfides [6], and bismuth-baseds catalysts [7]. Among these, bismuth oxyhalides (BiOX, X = Cl, Br, I, and F), the typical bismuth-based photocatalysts, have unique layered structures and tunable band gaps and have demonstrated substantial application potential in environmental remediation and energy conversion. For instance, according to Zhang et al.'s findings [8], synthesized BiOCl with a band gap of 3.46 eV displayed superior photodegradation activity compared to commercial TiO_2 (P25) during the degradation of methyl orange, which has attracted widespread attention toward bismuth-oxyhalide-based materials. Notably, as a typical p-type semiconductor, BiOBr possesses a narrower band gap (2.7 eV) than BiOCl, which means that BiOBr has better visible-light absorption capability than BiOCl and promising application prospects in the field of visible-light-driven photocatalysis. For example, ultrathin BiOBr nanosheets have been reported to achieve high efficiency and long-term stability in CO_2 photoreduction under visible light [9]. However, due to its relatively narrow band gap, the pristine BiOBr has been plagued by insufficient visible-light utilization efficiency and rapid photogenerated electron-hole recombination during practical applications [9,10]. Therefore, improving the catalytic performance of BiOBr has become an urgent issue to address for its widespread practical application.

To address this issue, various strategies have been adopted, including extending the spectral response range via dye sensitization [11], tuning the band edge positions through co-doping [2], facilitating charge separation by integrating plasmonic metals [12], and reducing charge recombination rates via the construction of heterojunction structures [6,13]. Recently, artificial heterogenous Z-scheme systems, which mimic the natural photosynthetic process of green plants, have been developed for overall water splitting under visible light illumination [13,14]. Typically, a standard Z-scheme system comprises two narrow-bandgap semiconductors in the presence of a suitable redox mediator. When three components are integrated, the electrons generated in the oxygen-evolving semiconductor can transfer and recombine with holes excited in the hydrogen-evolving photocatalyst. Consequently, the photogenerated electrons and holes are, ultimately, localized in separate semiconductors with more negative conduction band (CB) and more positive valence band (VB) potentials, enabling efficient separation of photoinduced electron-hole pairs. Therefore, appropriate narrow-bandgap semiconductors and an optimal redox mediator are essential for constructing high-efficiency Z-scheme systems.

During the photocatalytic disinfection process, reactive oxygen species (especially •OH with strong oxidizing properties) play a crucial role in bacterial inactivation [15,16]. For BiOBr, its relatively low valence-band potential results in a weak capacity for •OH generation during photocatalysis. Thus, selecting a suitable semiconductor to enhance ROS production is of great significance. Extensive studies have demonstrated that transition metal oxides (such as ZnO, SnO_2, and WO_3) exhibit excellent stability and low cost, and they have been widely employed for the modification of photocatalysts [4,6,17]. The semiconductors modified by transition metal oxides show low recombination of photogenerated charge carriers. For example, the porous ZnO-modified ZnSe nanocomposites exhibit much higher activities than ZnSe nanostructures due to the wide light absorption and high separation efficiency of photogenerated electrons and holes [18]. Meanwhile, our previous work also found the SnO_2 was able to enhance the generation of ROS, achieving the rapid degradation of organic pollutants [6]. Notably, tungsten oxide (WO_3) features a narrow band gap (2.4–2.8 eV) and high oxidation capacity of valence band (VB) holes (+3.1–3.2 eV) [19,20]. Hence, WO_3 could

https://doi.org/10.3390/catal16020199

serve as an ideal candidate to couple with BiOBr for constructing a Z-scheme heterojunction system, which could significantly boost the generation of •OH.

Beyond semiconductors, exploring a suitable shuttle redox mediator also plays a vital role in enhancing photocatalytic performance. Generally, reversible redox mediators (redox pairs (Fe^{3+}/Fe^{2+})) and noble metals (Ag, Au, Pt, etc.) have been employed as electron mediators in Z-scheme water-splitting systems [21,22]. However, backward reactions readily occur in Z-scheme systems based on reversible redox mediators, while noble metal-based systems suffer from inherent drawbacks like the surface plasmon resonance (SPR) effect. Recently, doping nonmetallic materials or elements has emerged as an effective strategy to overcome these limitations associated with ionic or noble metal mediators. For example, since carbon materials like graphene and carbon nitride possess high charge carrier mobility, the Z-scheme systems constructed with them exhibit strong oxidizing capacity in pollutant degradation and water purification [23,24]. Meanwhile, certain nonmetallic elements (B and Si) have also been proven to facilitate the separation of photoinduced electron-hole pairs [25,26], among which silicon (Si) exhibits a suitable band structure and excellent charge transfer properties, as well as can readily form heterojunctions or Schottky junctions with metals and metal oxides [27], thereby facilitating the separation of photogenerated electron-hole pairs. In this work, it was hypothesized that Si could act as a solid-state electron mediator to transport photoexcited charges between BiOBr and WO_3. Importantly, it was found that the WO_3/BiOBr@Si composite exhibited enhanced electron-hole separation efficiency and charge transfer capability when WO_3 and Si were both introduced, resulting in strong inactivation on Gram-negative bacteria under visible photocatalytic process, which strongly confirmed our hypothesis.

In this work, a WO_3/BiOBr@Si composite was prepared using BiOBr and WO_3 as semiconductors and Si as shuttle redox mediator. The microstructure and surface composition of the WO_3/BiOBr@Si composite was well characterized by SEM, TEM, XRD, XPS, etc. Then, the bacterial inactivation resulting from the photocatalytic system mediated by the WO_3/BiOBr@Si composite was discussed, choosing *Escherichia coli* (*E. coli*) as the test organism. Meanwhile, the variation in the cell internal structure was analyzed. Furthermore, TEM, SEM, EDS, FT-IR, XRD, and XPS were used to further elaborate the microscopical interface analysis between WO_3/BiOBr@Si and the cell surface and, finally, the special inactivation mechanism of the photocatalytic process.

2. Results and Discussion

2.1. Characterization of WO_3/BiOBr@Si Composites

2.1.1. Morphology Observation and Structural Analysis of Different Catalysts

The morphology analysis of WO_3, BiOBr, WO_3/BiOBr, and WO_3/BiOBr@Si was conducted via SEM. As shown in Figure 1a–c, the synthesized WO_3 was composed of a large number of irregular aggregates of intertwined flat 2D nanosheets (~20 nm thick and 100–200 nm in size) with a smooth surface, while the BiOBr (Figure 1d–f) showed flower-like spheres composed of numerous nanosheets, with a ~3 μm diameter and numerous uniform petal-like 2D nanosheets (~20 nm thick). After being combined with WO_3 (Figure 1f,g,i), the WO_3/BiOBr still displayed the flower-like spheres but with looser stacking and distinct morphological changes. The diameter was 2–3 μm, and the petal-like 2D nanosheets were fuller than pure BiOBr. In contrast, WO_3/BiOBr@Si (Figure 1j–l) exhibited denser and fuller intersecting petal-like spheres (1–3 μm in diameter) and retained the 3D sheet-like pore structure. Meanwhile, due to the increased number of pores and the unique pore structure of the WO_3/BiOBr@Si material, light was prone to multiple scattering when irradiating the material's surface [28], leading to the accumulation of surface charges and a decline in the recombination rate of photogenerated electrons and holes. In addition, the EDS mapping

https://doi.org/10.3390/catal16020199

photos of WO_3/BiOBr@Si (Figure S1) confirmed a uniform surface distribution of W, O, Bi, Br, and Si on the surface of the catalyst. To observe the details of the WO_3/BiOBr@Si catalyst, HRTEM images (Figure 1m–r) displayed that the WO_3/BiOBr@Si composite was composed of three different crystal grains stacked in a certain direction. Among them, the red lattice fringes 0.31 nm in width were assigned to the (200) plane of the WO_3 [13], while the yellow lattice fringe 0.27 nm in width belonged to the BiOBr (110) plane [29].

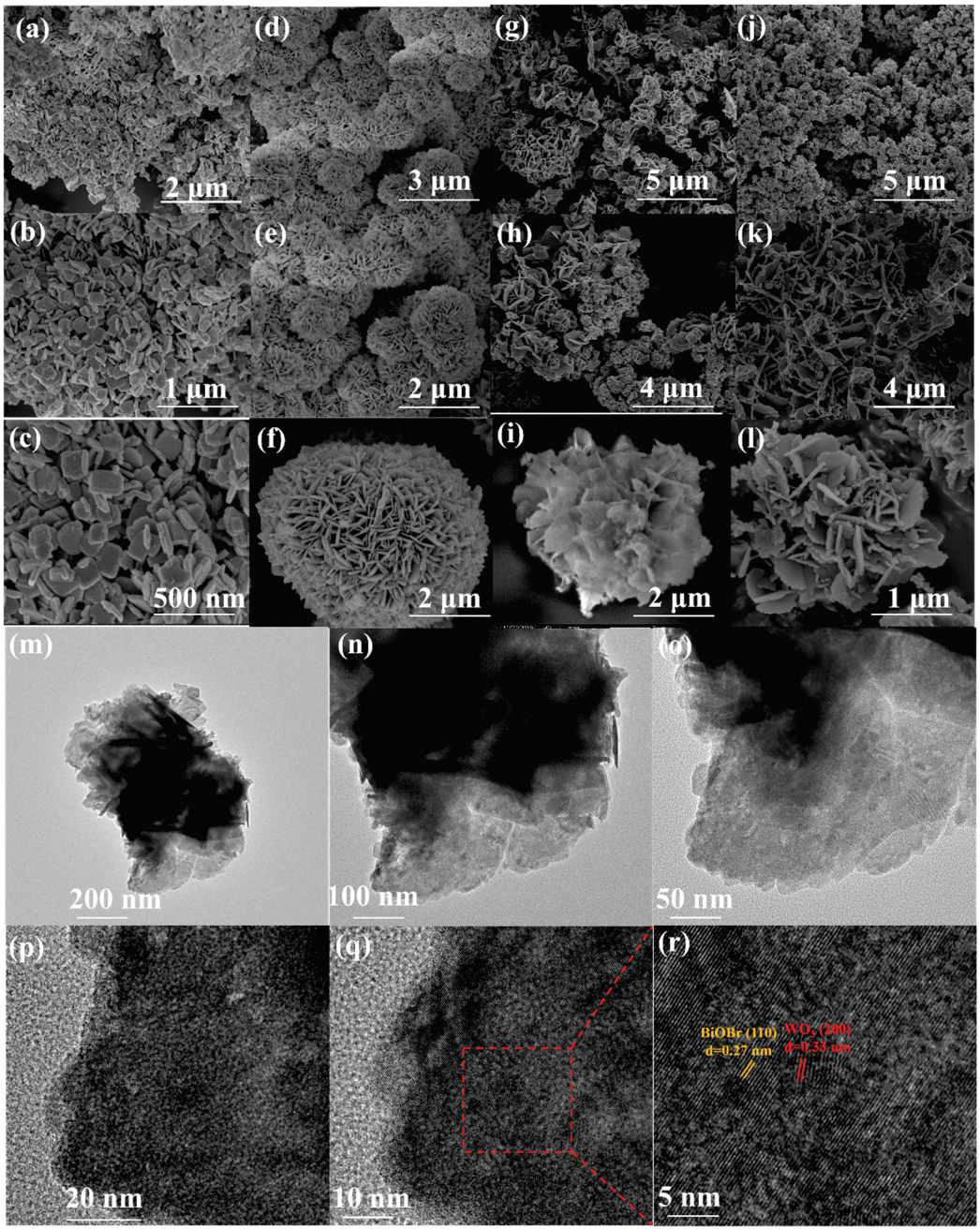


Figure 1. SEM images of samples of pure WO_3 (**a**–**c**), BiOBr (**d**–**f**), WO_3/BiOBr (**g**–**i**), and WO_3/BiOBr@Si (**j**–**l**); TEM images of WO_3/BiOBr@Si (**m**–**r**).

2.1.2. Surface Composition Analysis of WO_3/BiOBr@Si

The crystal structures of WO_3, BiOBr, WO_3/BiOBr, and WO_3/BiOBr@Si were analyzed by XRD. As shown in Figure 2a, the as-synthesized WO_3/BiOBr and WO_3/BiOBr@Si composites retained the characteristic diffraction peaks of BiOBr (PDF No. 78-0848) and the 200-plane characteristic peak of WO_3 at 40.86° (PDF No. 87-2385), indicating the successful combination

of WO_3 and BiOBr. Meanwhile, the XRD patterns of WO_3/BiOBr@Si and WO_3/BiOBr were basically consistent. In addition, no characteristic peaks of Si were observed in the pattern of WO_3/BiOBr@Si, which was attributed to the obvious overlap between the diffraction peaks of Si and the ultra-low loading percentage of Si on WO_3/BiOBr.

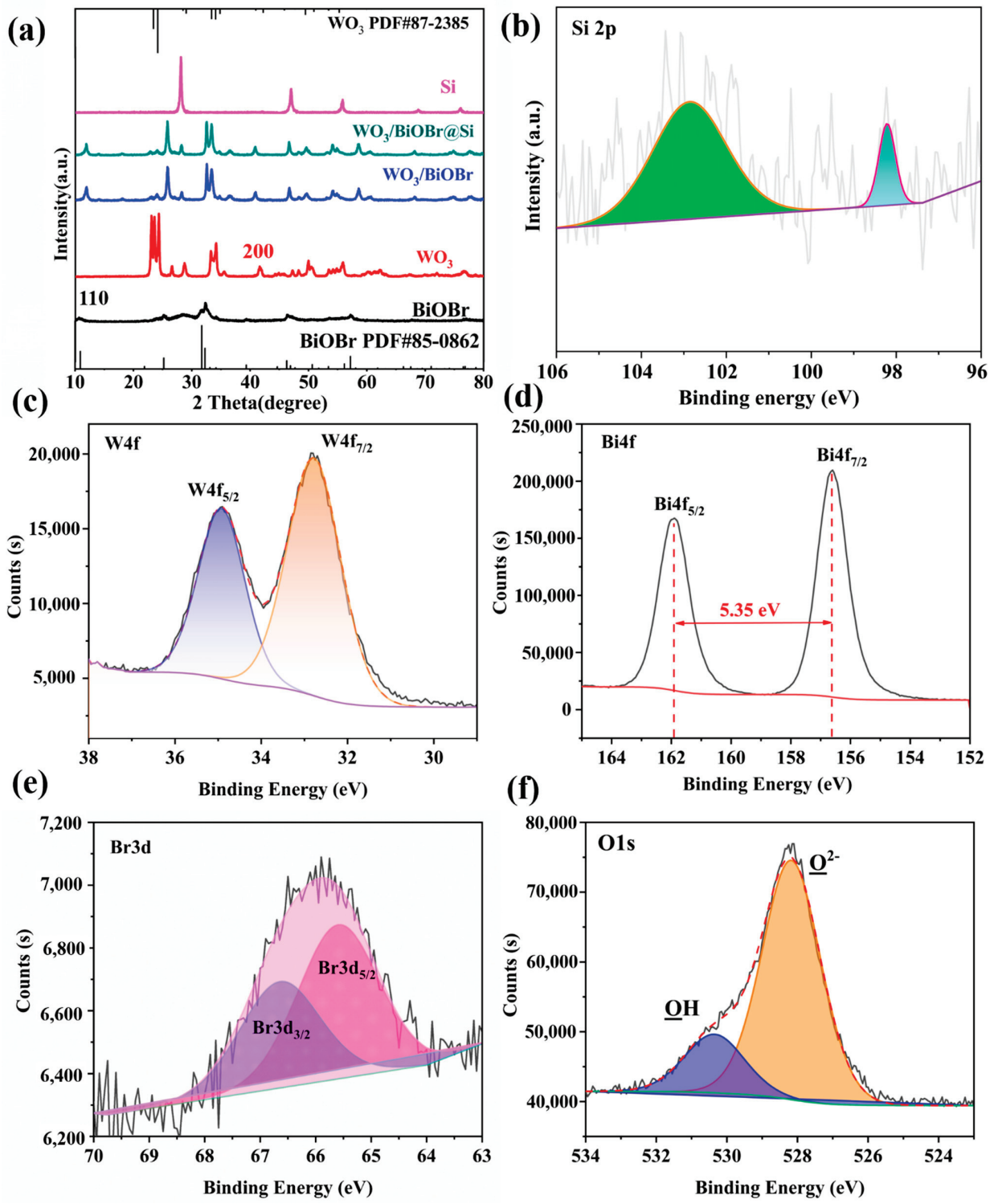


Figure 2. XRD patterns of (**a**) Si, WO_3, BiOBr, WO_3/BiOBr, and WO_3/BiOBr@Si; XPS high-resolution spectra of Si2p (**b**), W4f (**c**), Bi4f (**d**), Br3s (**e**), and O1s (**f**).

In addition, the surface element composition and valence states were analyzed via XPS. As demonstrated in the XPS survey spectrum of the WO_3/BiOBr@Si composite (Figure S2),

https://doi.org/10.3390/catal16020199

the composite was mainly composed of five elements, namely, Bi, O, Br, W, and Si. In the high-resolution XPS spectrum of Si2p (Figure 2b), it was composed of two peaks corresponding to the Si-Si bond in pure Si at 98 eV and the Si-O bond in the SiOx phase ($0 < x < 2$) at around 103 eV, indicating that that Si was present in two forms (Si and SiOx) in the composite [30]. Notably, considering the excellent conductivity of Si and poor conductivity of SiOx, only Si acted as an electron shuttle in the WO_3/BiOBr@Si composite. As seen in Figure 2c, the W4f XPS spectrum showed that two characteristic peaks of $W4f_{7/2}$ and $W4f_{5/2}$ orbitals were observed at 32.75 eV and 34.95 eV, suggesting the presence of W^{6+} in the composite nanomaterial, which is in line with the previous literature [31]. Meanwhile, two characteristic peaks appeared at binding energies of 156.6 eV and 161.95 eV in the XPS spectrum of Bi4f (Figure 2d), which is attributed to the $4f_{7/2}$ and $4f_{5/2}$ spin-orbitals of Bi, verifying the existence of Bi^{3+} in the composite [32]. As depicted in the Br3d's XPS spectrum (Figure 2e), characteristic peaks of $3d_{3/2}$ and $3d_{5/2}$ orbitals appeared at binding energies of 66.5 eV and 66.15 eV, respectively, confirming the presence of Br in the form of Br^- in the composite. For the O1s XPS spectrum (Figure 2f), the two peaks at approximately 528.20 eV and 530.35 eV corresponded to lattice oxygen and hydroxyl groups, respectively [32].

Furthermore, the FTIR was also employed to analyze the surface groups on the WO_3/BiOBr@Si composite. As shown in Figure S3, the adsorption peaks at 1057 cm^{-1} and 1001 cm^{-1} were attributed to the stretching vibration of the Si-O bond. According to previous findings [33], the adsorption peaks in the range 1000~1100 cm^{-1} were related to silicate substances. Based on the SEM, TEM, XRD, XPS, and FTIR results, the WO_3/BiOBr@Si composite was successfully synthesized.

2.1.3. Optical and Electrochemical Analyses of the WO_3/BiOBr@Si Composites

The optical properties of WO_3, BiOBr, WO_3/BiOBr, and WO_3/BiOBr@Si were analyzed by UV-Vis DRS. As observed in Figure 3a, both WO_3/BiOBr and WO_3/BiOBr@Si displayed better light absorption capacity than WO_3 and BiOBr. Notably, when the silicon element was doped, the absorption peaks of the WO_3/BiOBr@Si composite did not undergo significant changes. To well elevate the light-absorption capacity, the band-gap energies of WO_3, BiOBr, WO_3/BiOBr, and WO_3/BiOBr@Si were calculated based on the UV-Vis DRS spectra using Tauc's plot [34] and were 2.81 eV, 2.46 eV, 2.03 eV, and 2.01 eV, respectively (Figure S4). Meanwhile, based on the optical band gap, the refractive index (η) values of WO_3, BiOBr, WO_3/BiOBr, and WO_3/BiOBr@Si were also calculated according to previous findings [35,36] and were 2.08, 2.16, 2.30, and 2.31, respectively. The refractive index generally dictates the reflection, refraction, and scattering behaviors of incident light within semiconductor materials. Specifically, high-refractive-index substances (e.g., anatase TiO_2, $\eta \approx 2.5$) would enhance multiple internal reflections and light scattering, which prolongs the travel path of photons in the catalyst, leading to the likelihood of photon absorption and the production of more photo-induced electron-hole pairs [36].

Moreover, the electrochemical properties (electrochemical impedance and transient photocurrent responses) of WO_3, BiOBr, WO_3/BiOBr, and WO_3/BiOBr@Si composites were analyzed at a 1 g L^{-1} catalyst dosage. For the electrochemical impedance, an important indicator of electron-hole separation efficiency and charge transfer capability on the surface of the catalyst, the smaller radius of the semicircle meant a lower impedance value of the material and a high electron-hole separation efficiency [37]. As shown in Figure 3b, the WO_3/BiOBr@Si composites exhibited a smaller radius than WO_3, BiOBr, and WO_3/BiOBr, indicating that the doped Si significantly enhanced the electron-hole separation efficiency and charge transfer capability. Notably, the doping percentage of Si greatly affected the electrochemical impedance of the WO_3/BiOBr@Si composites, and the best mole ratio of Si was 1.0 mmol (4.6 wt%).

https://doi.org/10.3390/catal16020199

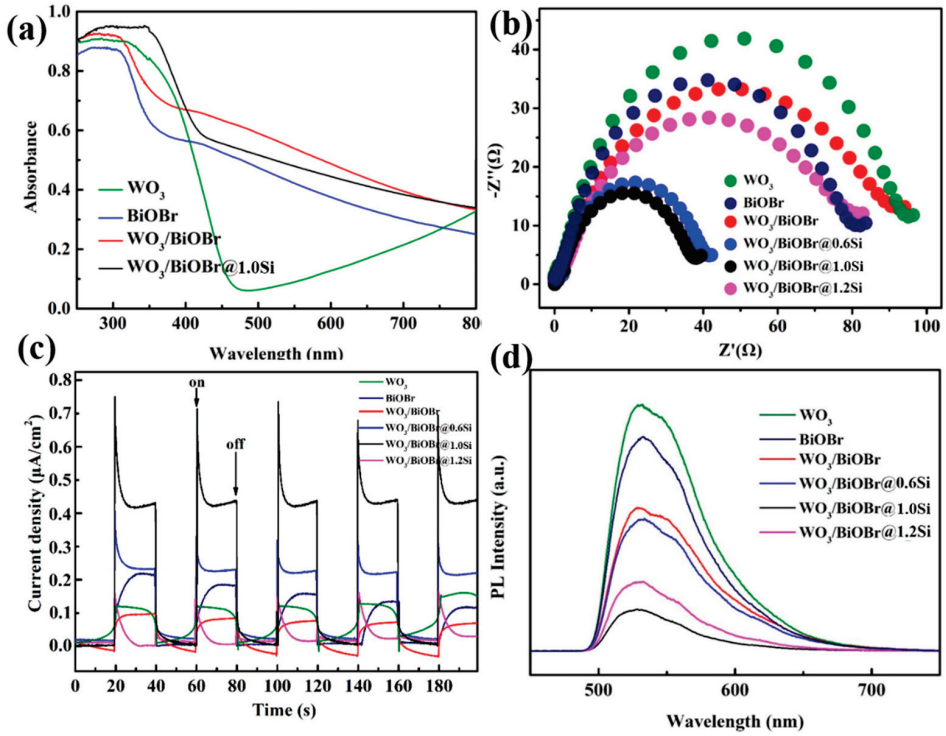


Figure 3. UV-Vis diffuse reflectance absorption spectra (**a**), electrochemical impedance (**b**), transient photocurrent responses (**c**), and fluorescence spectra (**d**) of WO_3, BiOBr, WO_3/BiOBr, and WO_3/BiOBr@Si composites.

Meanwhile, a photocurrent was employed to evaluate the electron separation efficiency of the WO_3, BiOBr, WO_3/BiOBr, and WO_3/BiOBr@Si composites. Generally, a higher photocurrent value means a larger amount of the transferred charge, a better electron-hole separation efficiency, and a stronger photocatalytic performance [37]. As shown in Figure 3c, the WO_3/BiOBr@1.0Si composites exhibited a higher photocurrent value than WO_3, BiOBr, and WO_3/BiOBr, indicating that the doped Si significantly restrained the recombination of the electron and hole and improved the charge transfer capability. Similarly, the highest photocurrent intensity also occurred with WO_3/BiOBr@1.0Si, which is in line with the results for the electrochemical impedance.

Furthermore, the fluorescence spectra of the WO_3, BiOBr, WO_3/BiOBr, and WO_3/BiOBr@Si composites (Figure 3d) were also collected to analyze the recombination rate of the photo-induced electron and hole. In the fluorescence spectra of bare WO_3 and BiOBr, a strong emission ranging from 500 to 600 nm was observed, manifesting the high photo-induced electron and hole recombination rate. Although the WO_3/BiOBr and WO_3/BiOBr@Si composites still displayed an emission in the same region, a rapid decline in fluorescence signals revealed the heterojunction was able to restrained the recombination of electron. Moreover, the lowest fluorescence signal was also observed in the spectra of WO_3/BiOBr@1.0Si, suggesting the lowest photo-induced electron and hole recombination rate, which is also in line with the results of the electrochemical impedance and photocurrent analyses.

Based on the characterization results, Si was successfully doped into the WO_3/BiOBr, and the optimal dosage was 1.0 mmol (4.6 wt%).

2.2. Bacteria Activation Under Visible Light Irradiation

Figure 4a illustrates the photocatalytic activation of *E. coli* with different photocatalysts at 10^7 CFU mL^{-1} (7 of log concentration) of the initial bacteria concentration. In the dark control and light control groups, no significant changes in the *E. coli* concentration over

time revealed a negligible bacteria inactivation of visible light and catalysts. Instead, when the visible light and catalysts coexisted in the solution, the concentration of live *E. coli* cells tended to decline along the treating time, suggesting the significant bacteria inactivation under photocatalysis. After 30 min, the *E. coli* log concentrations for BiOBr, WO_3/BiOBr and WO_3/BiOBr@1.0Si were 5.0 ± 0.7, 3.3 ± 0.4 and 0.4 ± 0.3, which suggests the introduced WO_3 and Si could greatly enhance the photocatalytic sterilization performance. In addition, the mole doping dosage of Si also greatly affected the photocatalytic performance of the WO_3/BiOBr@Si composites. When the Si doping dosages were 0.6, 1.0, and 1.2, the *E. coli* log concentrations were 2.2 ± 0.6, 0.4 ± 0.3, and 1.4 ± 0.4, respectively, indicating that the optimal mole doping dosage of Si was 1.0, which is in line with the analyses of the EIS, photocurrent responses, and fluorescence spectra (Figure 3).

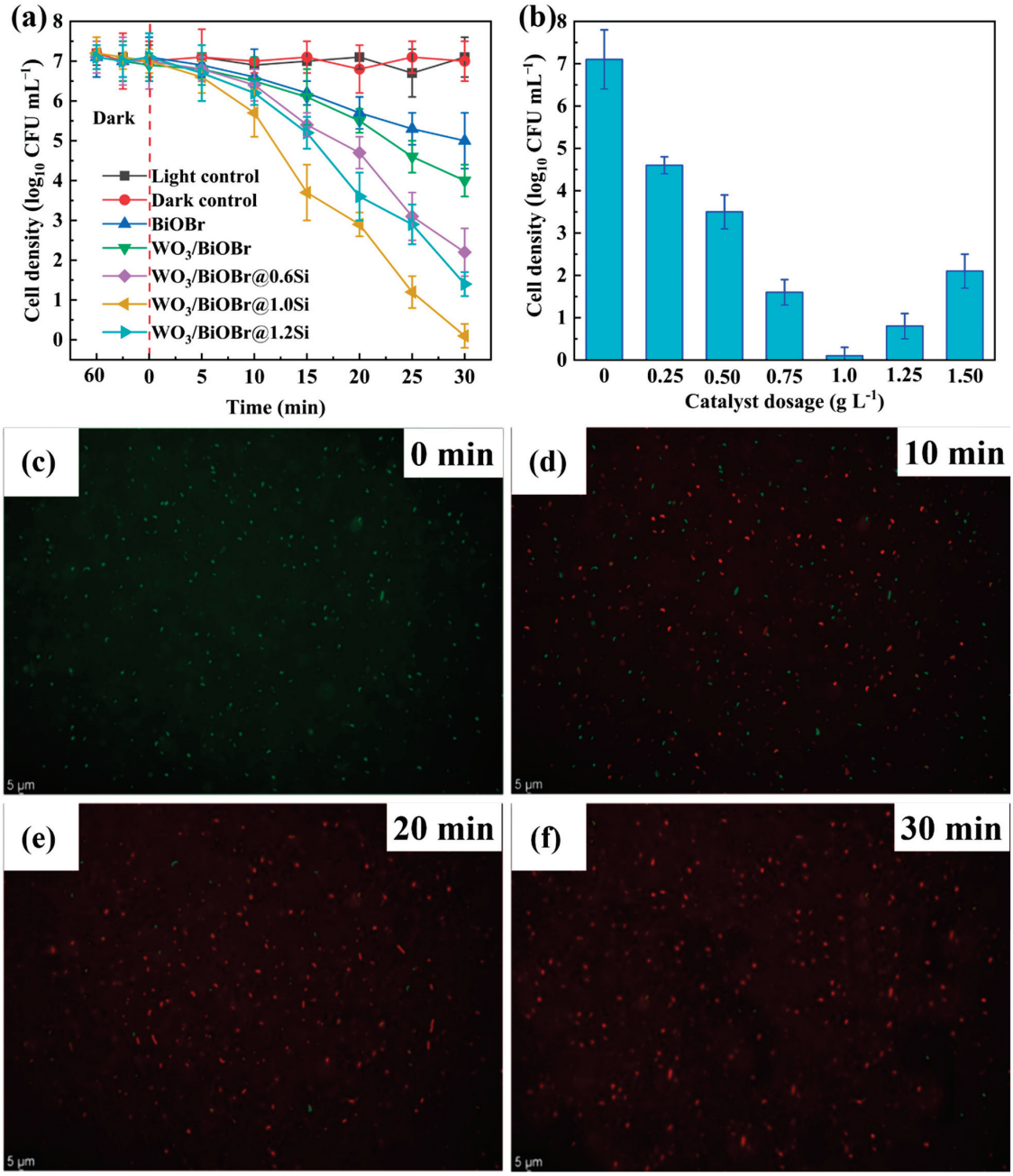


Figure 4. *E. coli* inactivation under a visible light photocatalytic system with different catalysts (**a**); catalyst dosage on the inactivation efficiency (**b**); observed fluorescence microscope images of the bacteria suspension at various treating times (0–30 min) after staining with a dead/live kit (**c**–**f**).

In addition, the photocatalyst dosage also demonstrated great effects on the bacteria inactivation. As shown in Figure 4b, the *E. coli* inactivation efficiency rose quickly along with the increase in the WO_3/BiOBr@Si dosage (from 0 to 1.0 g L^{-1}) and reached a peak at 1.0 g L^{-1} and then dropping with a further increase in the catalyst dosage. According to previous studies [6], a high-concertation catalyst caused high turbidity in the solution, which severely impacted the absorption of light, resulting in a significant decline in the photocatalytic performance.

To visually observe the variation of the *E. coli* cells during the photocatalytic process, a fluorescence microscope was employed to analyze the stained cells with dead/live kits. The dead/live kit included two dyes (SYTO-9 and propidium iodide (PI)). SYTO-9 could freely go through the cell membrane and combine with DNA, leading to a green signal under the fluorescence microscope, while the PI could only enter the dead cells and then mark the DNA in a red fluorescence signal. As shown in Figure 4c–f, at the beginning, most cells were alive and could be stained by SYTO-9, resulting in strong green signals and no red signals in the image (Figure 4c). With a prolonged irradiation time, the green signals gradually became weak and vanished after 30 min. At this time, the red signals greatly heightened, suggesting an increase in dead cells in the solution. All the results strongly proved the excellent *E. coli* inactivation efficiency under the photocatalysis mediated by the WO_3/BiOBr@Si composite.

2.3. Variation of the Cells

The changes in the surface morphology and interior structure of the cells before and after treatment were analyzed by TEM and SEM. As depicted in Figure 5a,b,e, the fresh *E. coli* cells had a rather smooth surface and no evident collapse on the surface. After treatment, the SEM images (Figure 5c–d,f–h) also clearly displayed the ample collapse on the cells' surface, suggesting serious destruction of the cell membrane during photocatalysis.

In addition, the intracellular variation in the *E. coli* cells before and after the photocatalytic process was also analyzed based the observation of ultrathin biological slices via TEM. As demonstrated in Figure 5i–j, the untreated cells had a whole membrane on the outside, and the cytoplasm inside was uniform. Once treated via the photocatalytic process, the cytoplasm inside the cell became inhomogeneous, and some cells' membrane was severely broken, suggesting the cell inactivation during the photocatalytic process was probably attributed to the inactivation of the cell membrane and a change in intracellular substances. In addition, it is worth noting that there were plentiful black particles surrounding the membrane and inside the broken cell, indicating that the catalyst might destroy the cell membrane. Due to the sharp edges of the nanoparticles, they can destroy the membrane, resulting in the leakage of substances inside the cell and then inactivation [38,39]. However, the physical disruption of bacterial membranes by sharp-edged catalyst particles was limited (Figure 4a).

As mentioned above, SEM and TEM images clearly showed the evident destruction of the membrane of the *E. coli* cells, which also meant that the permeability of the cell membrane had greatly changed. Here, K^+ and extracellular protein concentrations were monitored to estimate the permeability of the cell membrane. The K^+ plays an important role in the intracellular protein synthesis and polysaccharide cycle and is often used as an important indicator for assessing the permeability of a membrane [38]. In the control (Figure 6a), after 30 min, the K^+ concentration rose from 1451 $\pm$ 23 to 1502 $\pm$ 31 μg L^{-1}, while in the experimental groups, the K^+ concentrations increased from 1455 $\pm$ 73, 1450 $\pm$ 54, 1461 $\pm$ 88, and 1468 $\pm$ 46 μg L^{-1} to 1753 $\pm$ 35, 1911 $\pm$ 61, 2254 $\pm$ 42, and 2753 $\pm$ 52 μg L^{-1} for WO_3, BiOBr, WO_3/BiOBr, and WO_3/BiOBr@Si, respectively, revealing an increasing in the permeability of the cell membrane. This is attributed to the destruction of the cell

https://doi.org/10.3390/catal16020199

membrane, leading to the release of intracellular K^+. In addition, the extracellular protein was also monitored using the BCA method [40]. As shown in Figure 6b's inset, the color of the protein extract in the tubes gradually became darker over the reaction time, revealing an evident increase in extracellular protein. Meanwhile, after 30 min, the protein concentration of the solution increased from 31.2 to 132.4 μg mL^{-1}, which also confirms the increase in permeability of the cell membrane. Similar results were also observed in previous works [38,40].

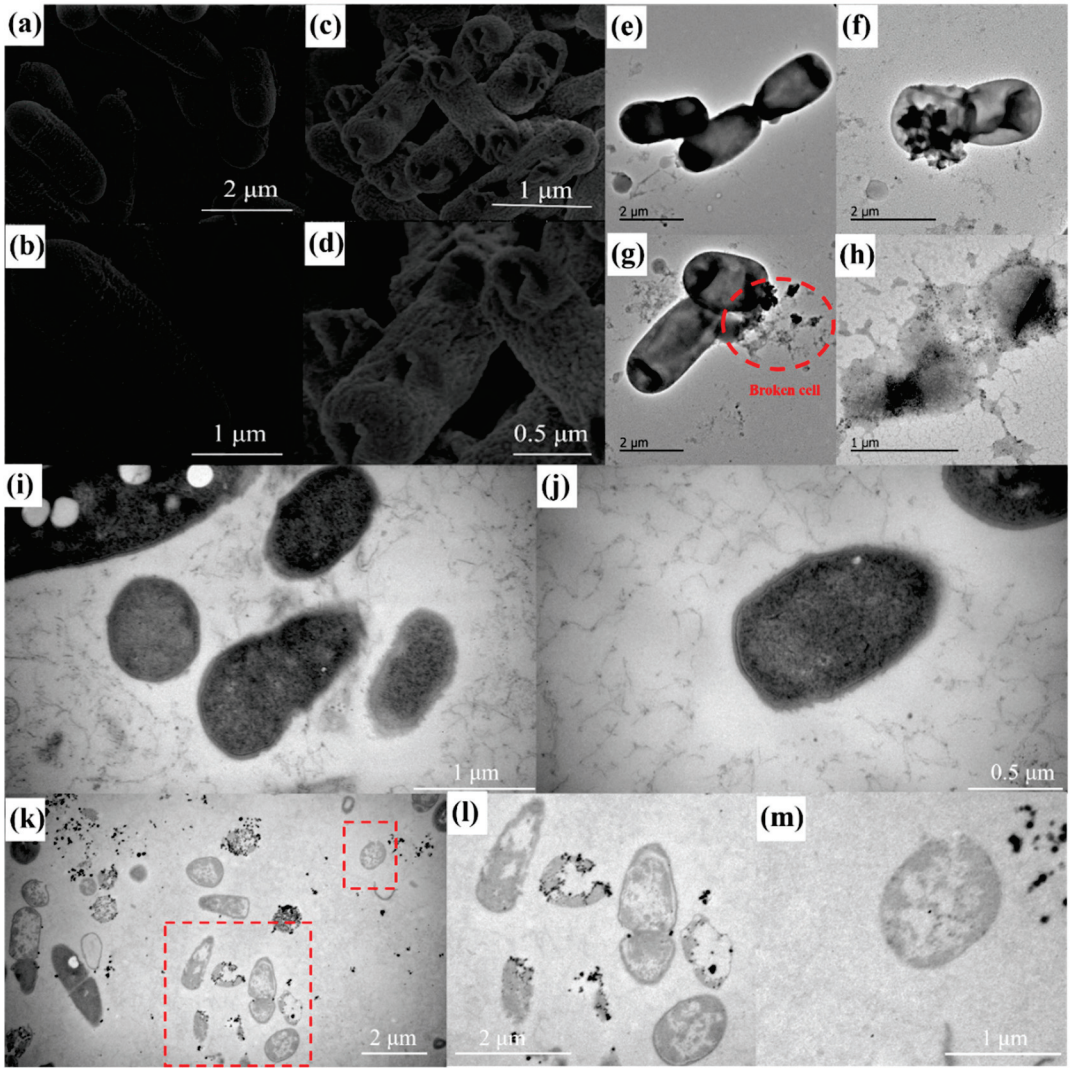


Figure 5. Morphologic observation of *E. coli* before and after photocatalytic treatment (SEM (**a**–**d**); TEM (**e**–**h**)) and intracellular changes in the *E. coli* before and after treatment (**i**–**m**).

In addition, the ROS level is vital for maintaining the metabolic activity of cells. In this work, the variation in the ROS level inside the cells was monitored with fluorospectrophotometer by staining the cells with dichlorodihydrofluorescein diacetate (DCFH-DA) [39,41]. At the beginning (Figure 6c), the ROS level was rather low (28.1 ± 3.4), while the fluorescence intensity greatly increased with the photocatalysis, being 41.3 ± 6.1, 89.1 ± 5.8, 152.1 ± 8.2, and 187.2 ± 2.7 at 5, 10, 20, and 30 min, respectively, indicating a significant increase in the ROS level inside the cell. Since ample ROS ($^1O_2$, $\bullet O_2^-$, and •OH) were generated during the photocatalytic process [16,42], they would enter the cells and oxidize DCFH-DA and cause an enhanced fluorescence intensity, which also means that the oxidative stress is probably an important mechanism for bacterial inactivation during the photocatalytic process.

https://doi.org/10.3390/catal16020199

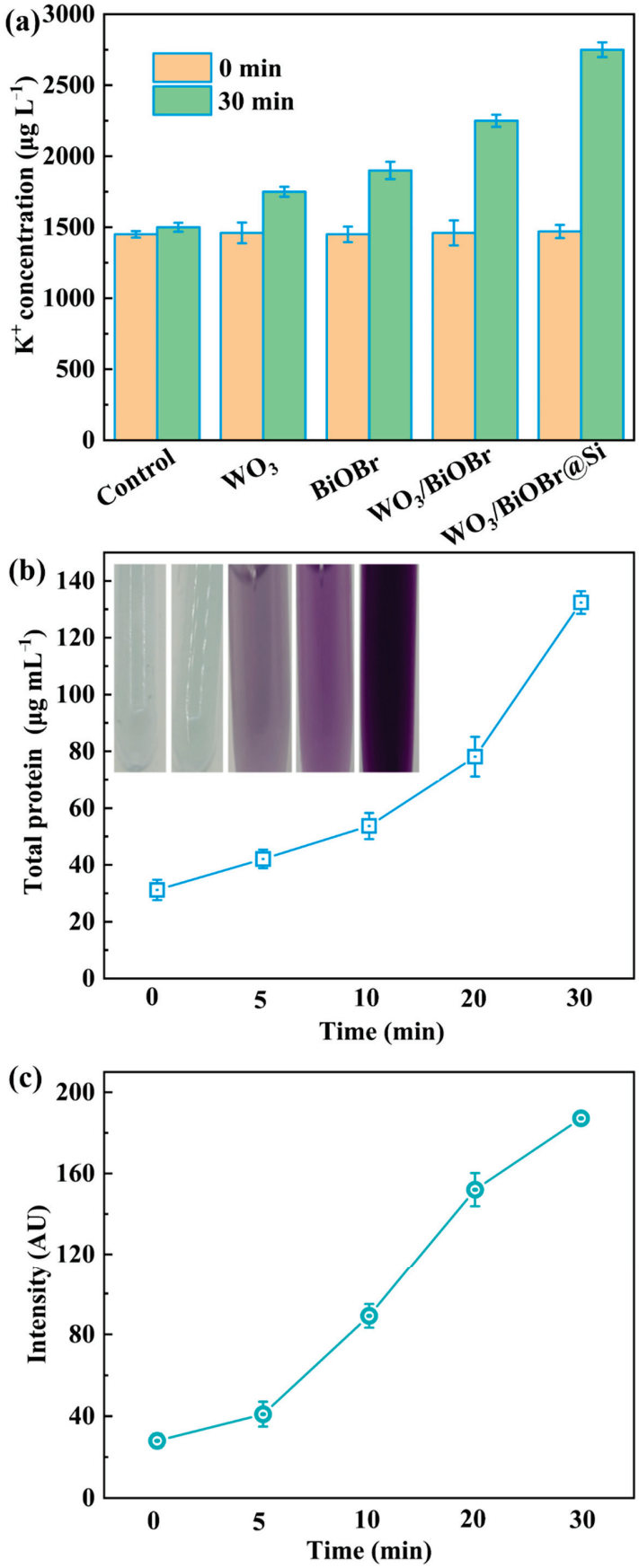


Figure 6. Released K^+ detection in the different systems (**a**); the total protein concentration (**b**) in the bacteria suspension; and ROS levels in inside cells (**c**) at various treatment times in the photocatalytic system.

https://doi.org/10.3390/catal16020199

Changes in the Chemical Composition of the Membrane

The chemical composition of the membrane before and after photocatalytic treatment was analyzed by FT-IR and XPS. The FT-IR spectra (Figure S5) displayed a variation in the untreated and treated *E. coli* cells. Based on the cellular components, each spectrum can be classified into the following four regions [43]: (I) fatty acid region (3000~2800 cm^{-1}), corresponding to the asymmetric stretching vibrations of the $=CH_2$ and $-CH_3$ groups in fatty acids; (II) protein/amide region (1700~1500 cm^{-1}), which encompasses the C=O, N-H, and C-N vibrational modes of the amide I and amide II protein bands [44]; (III) mixed region (1500~1200 cm^{-1}), containing carboxylic groups of proteins, free amino acids, nucleic acids (RNA/DNA), and phospholipids [45]; and (IV) polysaccharide region (1200~900 cm^{-1}), characterized by the stretching vibrations of phosphate groups and vibrational modes of polysaccharides [39]. A characteristic signal was observed around 1739~1725 cm^{-1}, which corresponds to the C=O stretching vibrations of carboxylic groups derived from membrane lipids and fatty acids [46]. Drawing on the vibrational patterns of bacteria reported in previous studies [39,47], the functional groups assigned to the infrared bands and their corresponding frequencies are summarized in Table S1.

Under light irradiation, the types of substances on the surface of *E. coli* cells remained basically unchanged after treatment with the WO_3/BiOBr@Si composite, whereas the characteristic signals of some surface functional groups were attenuated due to the photocatalytic treatment. Notably, the absorbance ratio corresponding to the C=O stretching vibration of amide bonds at 1630 cm^{-1} decreased significantly, indicating a reduction in the content of polypeptide substances on the surface of *E. coli* cells. During the photocatalytic process mediated by WO_3/BiOBr@Si composite, the generated oxidizing reactive species (•OH, $•O_2^-$, and H_2O_2) under visible light irradiation attacked and destroyed the amide bonds in polypeptide substances, leading to the cleavage of amide bonds and, ultimately, a decrease in peptide substances.

As demonstrated in Figure S6, in addition to the C, O, N, and P elements, the XPS survey after treatment also showed Bi, Br, and W, confirming the adsorption of WO_3/BiOBr@Si on the *E. coli* cells. In the C1s high-solution spectra (Figure 7a), after treatment, the C-C/C-H (284. 80 eV) species dropped from 69.82% to 54.01%, while the C-O (286.25 eV), C=O (287.85 eV), and O-C=O (289.07 eV) species rose from 19.70%, 8.06%, and 2.42% to 26.52%, 16.33%, and 3.14%, respectively. Meanwhile, the O1s spectra also confirmed the increase in the C=O group (C=O at 530.38 eV) from 9.97% to 14.26%, while the increase in O^{2-} (529.28 eV) species was ascribed to the adsorbed catalyst. Moreover, the N1s illustrated a variation in the N-contained groups during the photocatalysis, and two peaks at 399.77 and 401.05 eV were assigned to the amide (C-O-N-H) and amino (NH_2) species, respectively. After photocatalysis treatment, the amide percentage dropped from 87.01% to 81.90%, while the amino percentage rose from 12.99% to 18.10%, which suggests that the amide (C-O-N-H) group was probably related to cell inactivation.

Based on the XPS data, the mass percentages of the main compositions (polysaccharides (PS), proteins (PT), and lipidic compounds (mainly composed of hydrocarbon-like compounds, HCs)) on the cell membrane were calculated through equations (Equations (1)–(3)) [39]. As reported in the previous literature [39,48], the PS was mainly composed of $(C_6H_{10}O_5)_n$, with 0.833 O/C, 0.000 N/C, and a 37.0 mmol g^{-1} carbon concentration. Similarly, for the hydrocarbon-like products ($(CH_2)_n$), both the O/C and N/C were 0, while the carbon concentration was 71.4 mmol g^{-1}. For the proteins, the O/C, N/C, and carbon concentration were 0.325, 0.279, and 43.5 mmol g^{-1}, respectively.

$$O/C = 0.325\ (C_{PT}/C) + 0.833\ (C_{PS}/C) \quad (1)$$

https://doi.org/10.3390/catal16020199

$$N/C = 0.279\ (C_{PT}/C) \quad (2)$$

$$1 = (C_{PT}/C) + (C_{PS}/C) + (C_{HC}/C) \quad (3)$$

where both O/C and N/C are related to the atomic ratios of the oxygen and nitrogen obtained from the XPS data, while C_{PT}, C_{PS}, and C_{HC} represent the total carbon atomic concentrations in the proteins, polysaccharides, and hydrocarbon-like products, respectively.

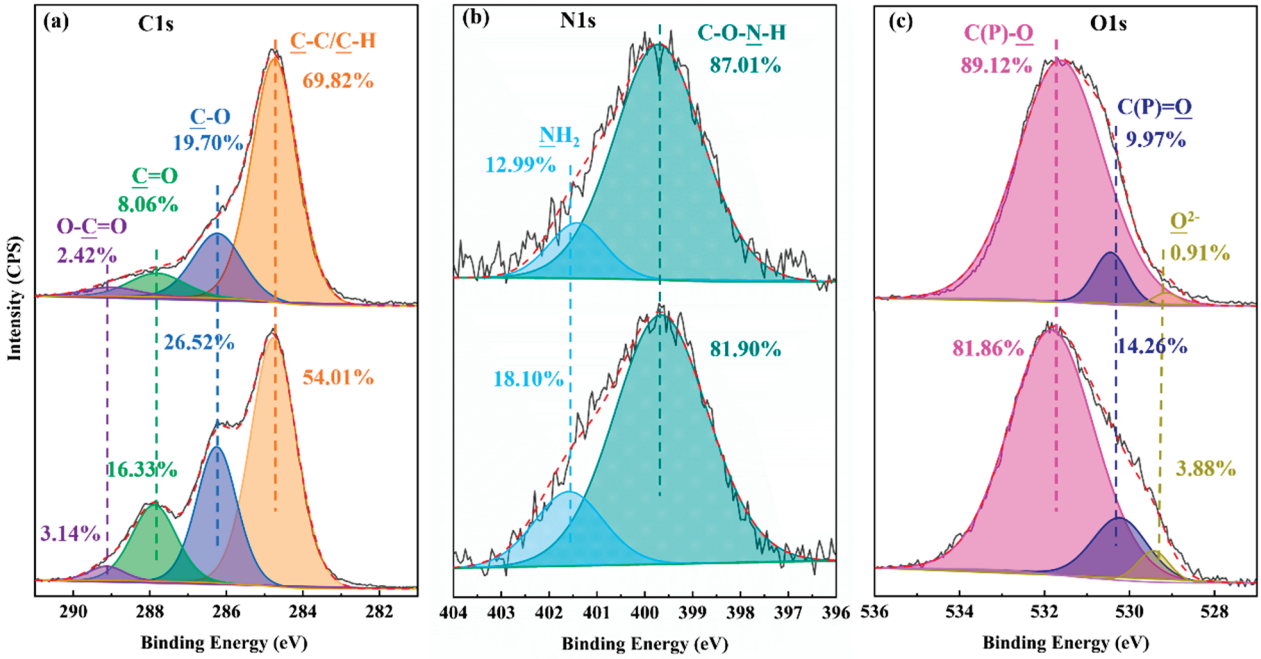


Figure 7. Variation in the high-resolution XPS spectra of C1s (**a**), N1s (**b**), and O1s (**c**) of *E. coli* before and after photocatalytic treatment.

The calculated results listed in Table 1 reveal that the mass percentages of the PT, PS, and HCs on the surface of the fresh *E. coli* cells were 27.26%, 23.38%, and 49.36%, respectively. After photocatalytic treatment, it could be observed that the PS percentage of the cell surface significantly increased to 37.54%, while the percentages of PT and HC dropped to 21.20% and 41.26, which indicates that the ROS probably reacted with the substances on the cell surface.

Table 1. Binding energies, assignments, and quantitation of chemical groups and substances on the cell surface before and after photocatalytic treatment.

Species	Peak Location (eV)	Percentage (%)		Assigned Group
		Untreated	Treated	
Total C [a]	**-**	70.25	66.53	
Total N [a]	-	9.14	6.67	
Total O [a]	-	19.64	25.99	
Total P [a]	-	0.97	0.81	
C1s	284.80	69.82	54.01	C-C/C-H
	286.25	19.70	26.52	C-O
	287.85	8.06	16.33	C=O
	289.07	2.42	3.14	O-C=O

Table 1. *Cont.*

Species	Peak Location (eV)	Percentage (%)		Assigned Group
		Untreated	Treated	
N1s	399.77	87.01	81.90	C-O-<u>N</u>-H
	401.05	12.99	18.10	<u>N</u>H_2
O1s	529.28	0.91	3.88	<u>O</u>$^{2-}$
	530.38	9.97	14.26	C(P)=<u>O</u>
	531.61	89.12	81.86	C(P)-<u>O</u>
N/C [b]	-	5.93	4.89	-
O/C [b]	-	19.84	27.71	-
C_{PT}/C [b]	-	21.27	17.54	-
C_{PS}/C [b]	-	15.52	26.42	-
C_{HC}/C [b]	-	63.21	56.04	-
PT [a]	-	27.26	21.20	-
PS [a]	-	23.38	37.54	-
HC [a]	-	49.36	41.26	-

[a] Mass percentage; [b] atomic percentages.

2.4. Mechanism

It was reported that both the physical disruption caused by the nanoparticles and the oxidative stress caused by the generated ROS were the main mechanisms during the sterilization with the AOP mediated by the nanoparticles [39,42]. In the blank group (no catalyst and light, Figure 8a), the lack of change in the cell concentration revealed that the inactivation caused by the PBS could be ignored. In the control group (no light but with catalyst), the slight log reduction (0.2) of the cell concentration suggests that the inactivation efficiency caused by the direct physical contact was rather low. Therefore, although some rupture in the cell membrane was observed in the TEM and SEM images, the contribution of physical disruption was extremely limited.

Since various ROS are usually generated during the photocatalytic process, the role of each free radical in bacterial inactivation is estimated by selecting the sodium oxalate (SO); isopropanol (IPA); 4-amino-2,2,6,6-tetramethylpiperidinooxy (TEMPOL); and L-histidine (L-H) as the scavengers for the h^+, •OH, $•O_2^-$, and $^1O_2$, respectively. As depicted in Figure 8a, after 30 min, no change occurred to TEMPOL, indicating that $•O_2^-$ was not the main ROS species, while a slight decline in the cell density of the L-H group revealed that $^1O_2$ participated in the cell inactivation but not the main species. Instead, the significant log reduction in the SO and IPA systems suggests that both h^+ and •OH played vital roles in the *E. coli* inactivation. To quantify the role of these species during the cell inactivation, their contribution to the cell inactivation was calculated, as shown in Figure 8b. The contribution percentages of the four species were 42.55% (•OH), 36.17% (h^+), 15.96% ($^1O_2$), and 5.32% ($•O_2^-$), respectively, which also confirms that the cell inactivation during photocatalysis was mainly ascribed to h^+ and •OH species. Furthermore, the EPR spectra visibly displayed the presence of •OH (Figure 8c) and $^1O_2$ (Figure 8d) during the photocatalysis.

https://doi.org/10.3390/catal16020199

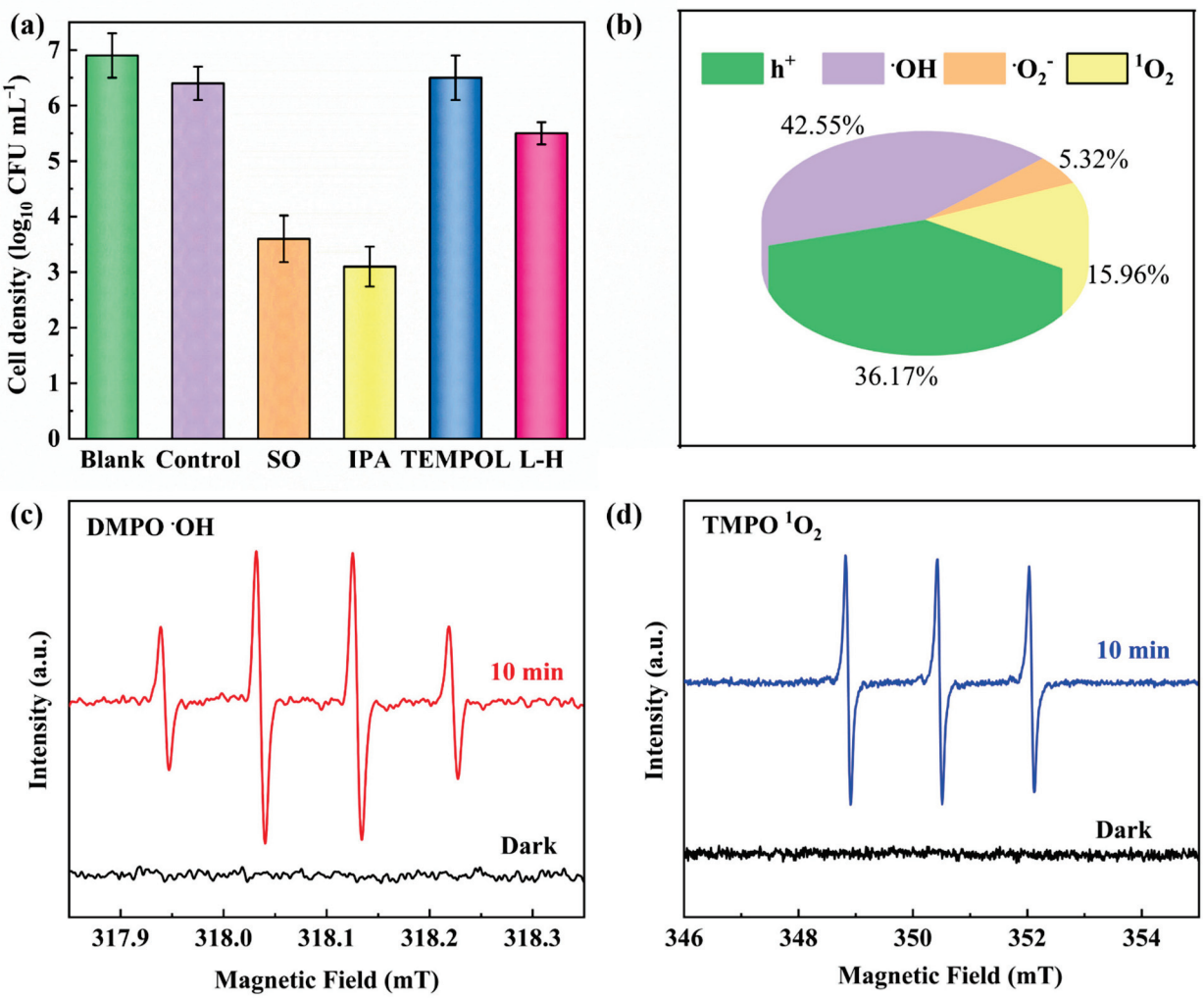


Figure 8. Inactivation efficiency (**a**) under different scavengers and contribution percentage (**b**) of the reactive oxygen species (ROS) in the photocatalytic system; EPR spectra of the DMPO-•OH (**c**) and TMPO-$^1O_2$ (**d**) species.

In order to calculate the valence band (VB) and conduction band (CB) of the catalysts, Mott–Schottky plots of pure BiOBr and WO_3 were generated at different frequencies (Figure S7). The tangent intercept clearly reveals that the flat band potentials of BiOBr and WO_3 were −0.43 eV and 0.17 eV (v.s. SCE), respectively. Generally, for semiconductors, the flat band potential is considered the conductor band potential (CB) [6]. Therefore, the CB potentials of pure BiOBr and WO_3 were −0.19 eV and 0.41 eV vs. NHE (NHE = 0.24 eV + SCE). Since the band gap energy (2.46 eV for BiOBr and 2.82 eV for WO_3, Figure 3a inset) is the difference between CB and VB (E_{bg} = E_{VB} − E_{CB}), the VB of BiOBr and WO_3 was 2.65 and 3.23 eV (vs. NHE), respectively. According to the ROS results, the generation of $^1O_2$ and $•O_2^-$ clearly revealed that the CB of WO_3/BiOBr@Si was kept at BiOBr. Meanwhile, the larger contribution percentages of •OH and h^+ evidently confirmed that VB remained at WO_3. Thus, it could be inferred that WO_3/BiOBr@Si was a Z-scheme photocatalyst. Based on these results, the catalytic and mechanism of WO_3/BiOBr@Si composite under visible light and the related bacteria inactivation mechanism are explored in Figure 9.

Under the irradiation of visible light, both WO_3 and BiOBr in the composite were excited and produced the electrons (e^-) and holes (h^+) on their CB and VB, respectively (Equation (4)). Due to the good electrical conductivity of Si, the electrons on the CB of WO_3 could quickly migrate to the VB of BiOBr through Si and then recombine with the holes, causing the efficient separation of the reductive e^- on the CB of BiOBr and the oxidative h^+

https://doi.org/10.3390/catal16020199

on the VB of WO_3 (Equation (5)). As reported in previous works [49], when materials with good electrical conductivity like biochar or other carbon-based materials are coupled with a semiconductor like TiO_2, it can act as a charge sink or shuttle, improving the photocatalytic separation efficiency. At the same time, the e^- can react with oxygen and produce $^1O_2$ (Equation (6)), while the h^+ can oxidize OH^- or H_2O to •OH (Equation (7)) due to the much higher standard redox potential (3.23 eV) than that of $H_2O(OH^-)$/•OH (2.40 eV).

$$WO_3/BiOBr@Si \xrightarrow{hv} WO_3(e^-/h^+)/Si/BiOBr(e^-/h^+) \quad (4)$$

$$WO_3(e^-/h^+)/Si/BiOBr(e^-/h^+) \xrightarrow{\text{Z-scheme}} WO_3(h^+)Si(e^-_{WO_3}/h^+_{BiOBr}) + BiOBr(e^-) \quad (5)$$

$$BiOBr(e^-) + O_2 \rightarrow {}^1O_2 \quad (6)$$

$$WO_3(h^+) + H_2O/OH^- \rightarrow \bullet OH \quad (7)$$

$$\text{OH group (PS or PT)} + \bullet OH/{}^1O_2/h^+ \rightarrow C=O \text{ or COOH groups} \quad (8)$$

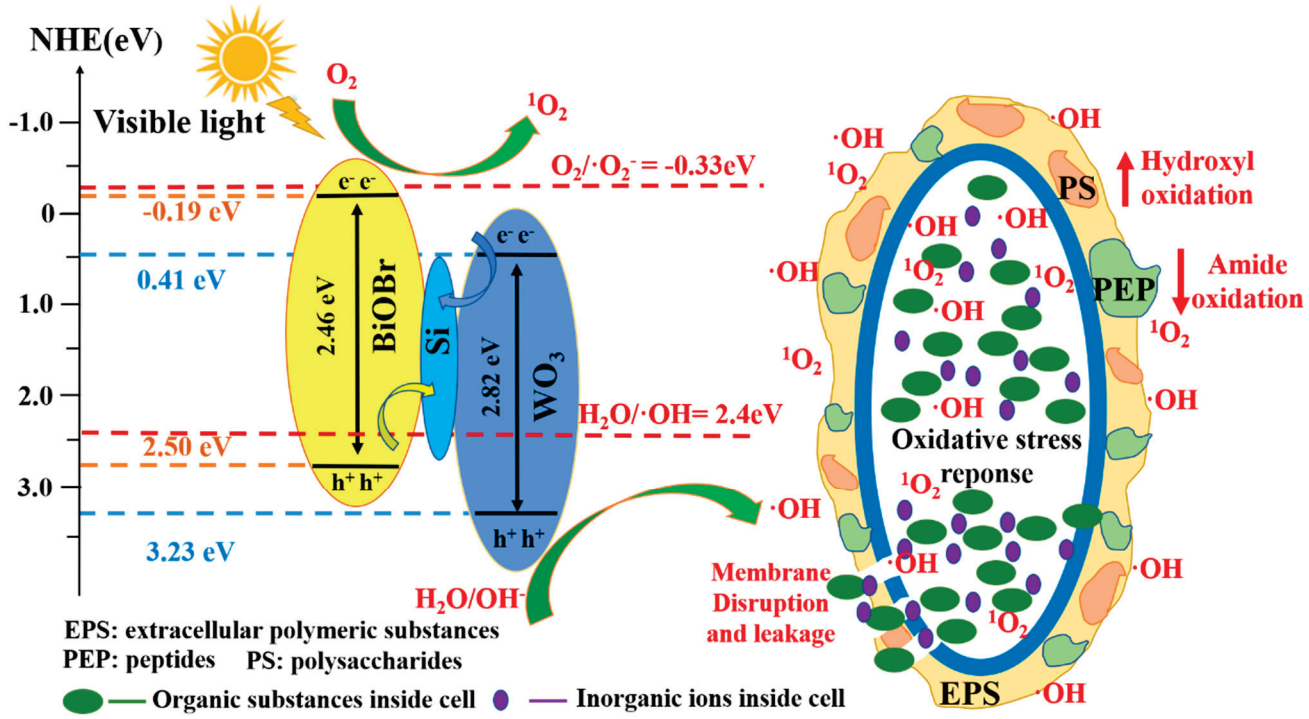


Figure 9. Inactivation mechanism of *E. coli* under a photocatalytic process mediated by WO_3/BiOBr@Si composite.

The ROS level inside a cell plays a vital role in maintaining the activities of the enzymes. In the photocatalytic system, the generated ROS ($^1O_2$ and •OH) were strong oxidative species and could cause a severe oxidative stress response in the cells when they entered inside, resulting in a rapid increase in the intracellular ROS level (Figure 6c) and then the inactivation of the *E. coli* cells. According to previous reports, a high ROS level inside a cell would inhibit the expression of the enzyme system, as well as the inactivation of the cell membrane [50,51]. In addition, the produced $^1O_2$ and •OH also could oxidize the PS and PT on the membrane, causing a great change in the predominant constituents on the membrane or membrane disruption (Figures 5–7). Furthermore, when the photocatalyst was added to the system, the photocatalyst could be adsorbed on the surface of the cells (Figures 5 and S5). At this time, the h^+ on the VB also has a strong oxidation capacity and can oxidize the OH group in the PS and PT on the membrane into C=O or COOH groups

(Equation (8)), resulting in the inactivation of *E. coli* cells. Similar results were also observed in previous reports [39,42].

3. Material and Methods

3.1. Materials

The sodium tungstate dihydrate, citric acid monohydrate, bismuth (III) nitrate pentahydrate, potassium bromide, silicotungstic acid hydrate, and glucose were of pure analytical grade and obtained from Shanghai Aladdin Biochemical Technology Co., Ltd. (Shanghai, China). Luria-Bertani (LB) nutrient broth and agar were purchased from Sigma-Aldrich (St. Louis, MO, USA).

3.2. Preparation of WO_3/BiOBr@Si

The synthesis of the WO_3/BiOBr@Si composite was as follows: Firstly, 1 mmol sodium tungstate dihydrate was dissolved in 30 mL of deionized water and then 5 mmol glucose and 1.5 mmol citric acid monohydrate were, in turn, added to the solution at 400 rpm of magnetic stirring. After 10 min, 3 mL of HCl solution (6 mol L^{-1}) was added and then continuously stirred until the appearance of some yellow precipitate in the solution. At this time, the solution was marked solution A. Secondly, 1 mmol bismuth (III) nitrate pentahydrate was dispersed in 20 mL of glycol and then 5 mL of KBr solution (0.2 mol L^{-1}) was added. After that, the solution was magnetically stirred till a milky white solution was obtained, which was marked as solution B.

After that, solution A and solution B were combined and then 5 mL of silicotungstic acid hydrate solution (0.2 mol L^{-1}) was added to the mixture. After stirring for 30 min at 400 rpm, the mixture was transferred to a hydrothermal reactor and kept in an oven at 180 °C for 24 h. Once the reactor cooled down, the brown precipitate was obtained after being washed with absolute ethyl alcohol and deionized water 3 times. Finally, the WO_3/BiOBr@Si was freeze-dried and stored in a vacuum container for further use.

The WO_3/BiOBr was prepared according to the same operation by replacing the silicotungstic acid hydrate solution with deionized water. The WO_3 and BiOBr were obtained by separately treating solutions A and B in a hydrothermal reactor at 180 °C for 24 h. To study the effects of the Si dosage on the catalytic performance, the WO_3/BiOBr@xSi composites were synthesized by adding different silicotungstic acid hydrate (0.6, 1.0, and 1.2 mmol).

3.3. Bacteria Activation Batch Experiments

The visible photocatalytic sterilization experiments were performed in a double-walled quartz reactor on a clean bench and tap water was pumped into the gap between the inside and outside walls to maintain a constant temperature during the whole process. The visible light source was a 300 W xenon lamp (Beijing China Education Au-light Co., Ltd., Beijing, China) with an optical filter ($\lambda > 420$ nm), and the distance between the lamp and solution was set at 5 cm. Typically, 100 mL of the *E. coli* cell suspension (*E. coli* cells in sterile PBS solution (pH 7.0)) with ~10^7 CFU mL^{-1} of the initial cell concentration was firstly added into the sterilized quartz reactor (121 °C for 30 min in autoclave), and then 100 mg of the WO_3/BiOBr@Si composite was dispersed in the cell suspension under magnetic stirring at 400 rpm. After 60 min of treatment in dark conditions, the visible light was turned on. At the scheduled sampling points, 1 mL solution was sampled for analysis. The system without both catalyst and visible light was set as the blank group, while the system with catalyst but without visible light was set as the control group.

https://doi.org/10.3390/catal16020199

3.4. Analytical Methods

The WO_3/BiOBr@Si composite was characterized by scanning electron microscope (SEM, Quanta250, FEI, Columbia, MD, USA), transmission electron microscope (TEM, Tecnai G2 Spirit, FEI, Columbia, MD, USA), X-ray diffractometer (XRD, minFlex600, Rigaku, Japan), and x-ray photoelectron spectrometer (XPS, ESCALAB 250). The optical and electrochemical properties of the WO_3/BiOBr@Si composites were analyzed via UV-visible diffuse reflectance spectrum (UV-DRS, Carry 5000, Agilent, CA, USA), fluorescence spectra (Cary Eclipse, Agilent, Santa Clara, CA, USA), electrochemical impedance spectroscopy (EIS, CHI650E, China), and transient photocurrent response (Zennium, Zahner, DE). The reactive oxygen species (ROS) during photocatalytic process was measured by the electron paramagnetic resonance (EPR, A300, Bruker, MA, USA).

The microscopic morphology of the cells was observed by SEM (Quanta250, FEI, Columbia, MD, USA) and TEM (JEM-2100F, JEOL, Japan), while the biological slices were performed via TEM (TECNAI 10, FEI, Columbia, MD, USA). The chemical groups on the cell surface were analyzed with a Fourier infrared spectrometer (FT-IR, Nicolet iS 50, Thermo, Waltham, MA, USA) and X-ray photoelectron spectroscopy (XPS, PHI X-tool, DE). The cell density was analyzed via the spread plate method, while stained cells were observed with a fluorescence microscope (DM2500, Agilent, CA, USA) using a LIVE/DEAD kit (FilmTracer, Thermo, Waltham, MA, USA). The K^+ concentration was determined with ICP-MS (XSERIES 2, Thermo, Waltham, MA, USA). The protein concentration was measured by BCA (bicinchoninic acid) protein assay.

4. Conclusions

As noted in our study, the WO_3/BiOBr@Si composite displayed strong inactivation on Gram-negative bacteria under a visible photocatalytic process. The present WO_3 and Si significantly enhanced the electron-hole separation efficiency and charge transfer capability, resulting in an excellent photocatalytic performance. The main inactivation mechanism was related to the oxidative stress caused by the hole (h^+) and •OH generated during the photocatalytic process. These oxidizing species could attack the components on the surface of cells (such as the hydroxyl, carbonyl, ester, and amide groups of polysaccharides (PS) and proteins (PT)), resulting in the inactivation and destruction of the cell membrane and leakage of intracellular substances. All of the findings provide a significant guide for the development of an efficient catalyst for the green water disinfection process. However, this work also suffers from some issues for future practice, such as catalyst stability, reusability, and potential leaching of components over long-term treatment.

Supplementary Materials: The following supporting information can be downloaded at https://www.mdpi.com/article/10.3390/catal16020199/s1: Figure S1: EDS mapping images of the WO_3/BiOBr@Si composite; Figure S2: XPS survey spectrum of the WO_3/BiOBr@Si composite; Figure S3: Infrared spectrogram of WO_3/BiOBr and WO_3/BiOBr@Si; Figure S4: Band-gap energies of WO3, BiOBr, WO_3/BiOBr, and WO_3/BiOBr@Si calculated based on the UV-Vis DRS spectra using Tauc's plot; Figure S5: FT-IR spectra of *E. coli* cells left untreated and after 30 min of photocatalyst irradiation; Figure S6: XPS survey spectra of *E. coli* cells left untreated (a) and after 30 min of photocatalyst irradiation (b); Figure S7: Mott–Schottky plots of WO_3 (a) and BiOBr(b); Table S1: Absorption bands of functional groups on the *E. coli* cell surface.

Author Contributions: Conceptualization, G.Y. and Y.L.; Methodology, Q.W.; Software, Q.W.; Formal analysis, Q.W.; Investigation, Q.W.; Resources, Q.W. and M.L.; Writing—original draft, X.Y.; Writing—review and editing, Y.L., X.Y. and M.L.; Supervision, M.L. and G.Y.; Funding acquisition, X.Y. All authors have read and agreed to the published version of the manuscript.

https://doi.org/10.3390/catal16020199

Funding: This work was financed by the Fujian Province University Industry–University Cooperation Project (No. 2025Y4016) and the University–Industry Cooperation Project of Fujian (No. 2025Y4004).

Data Availability Statement: The original contributions presented in this study are included in the article/Supplementary Material. Further inquiries can be directed to the corresponding authors.

Conflicts of Interest: The authors declare no conflicts of interest.

References

1. Martín-Sómer, M.; Pablos, C.; Adán, C.; Grieken, R.V.; Marugán, J. A review on led technology in water photodisinfection. *Sci. Total. Environ.* **2023**, *885*, 163963. [CrossRef]
2. Sun, Y.; Rao, S.; Liu, Q.; Zhi, C.; Lu, Z.; Ma, R.; Sun, Z.; Yang, J. Zn-N bonds boost interfacial charge transfer in ZnO/Nitrogen-Doped porous carbon Schottky heterojunction for enhanced photocatalytic sterilization. *Appl. Surf. Sci.* **2024**, *655*, 159624. [CrossRef]
3. Rizzo, L.; Della Sala, A.; Fiorentino, A.; Li Puma, G. Disinfection of urban wastewater by solar driven and UV lamp-TiO_2 photocatalysis: Effect on a multi drug resistant *Escherichia coli* strain. *Water Res.* **2014**, *53*, 145–152. [CrossRef]
4. Ramos, P.; Sánchez, L.; Rodríguez, J. Mechanisms of ZnO Photocatalysis. In *Enhancing Photocatalytic Water Decontamination: Exploring the Efficacy of ZnO Nanorods in Advanced Treatment Processes; SpringerBriefs in Materials*; Springer: Cham, Switzerland, 2025; pp. 15–16.
5. Wu, S.; Cao, H.; Yin, S.; Liu, X.; Zhang, X. Amino Acid-Assisted Hydrothermal Synthesis and Photocatalysis of SnO_2 Nanocrystals. *J. Phys. Chem. C Nanomater. Interfaces* **2009**, *113*, 17893–17898. [CrossRef]
6. Weng, R.; Tian, F.; Yu, Z.; Ma, J.; Xi, B. Efficient mineralization of TBBPA via an integrated photocatalytic reduction/oxidation process mediated by MoS_2/$SnIn_4S_8$ photocatalyst. *Chemosphere* **2021**, *285*, 131542. [CrossRef]
7. Tian, N.; Hu, C.; Wang, J.; Zhang, Y.; Ma, T.; Huang, H. Layered bismuth-based photocatalysts. *Coord. Chem. Rev.* **2022**, *463*, 214515. [CrossRef]
8. Zhang, K.; Liu, C.; Huang, F.; Zheng, C.; Wang, W. Study of the electronic structure and photocatalytic activity of the BiOCl photocatalyst. *Appl. Catal. B Environ.* **2006**, *68*, 125–129. [CrossRef]
9. Kong, X.Y.; Ng, B.J.; Tan, K.H.; Chen, X.; Wang, H.; Mohamed, A.R.; Chai, S.P. Simultaneous Generation of Oxygen Vacancies on Ultrathin BiOBr Nanosheets during Visible-Light-Driven CO_2 Photoreduction Evoked Superior Activity and Long-Term Stability. *Catal. Today* **2018**, *314*, 20–27. [CrossRef]
10. Guo, Y.; Wen, H.; Zhong, T.; Huang, H.; Lin, Z. Core-shell-like BiOBr@BiOBr homojunction for enhanced photocatalysis. *Colloids Surf. A Physicochem. Eng. Asp.* **2022**, *644*, 128829. [CrossRef]
11. Kuo, W.S.; Chiang, Y.H.; Lai, L.S. Solar photocatalysis of carbaryl rinsate promoted by dye photosensitization. *Dye. Pigment.* **2008**, *76*, 82–87. [CrossRef]
12. Henrotte, O.; Kment, S.; Naldoni, A. Mass Transport Limitations in Plasmonic Photocatalysis. *Nano Lett.* **2024**, *24*, 8851–8858. [CrossRef] [PubMed]
13. Zhou, J.; Li, X.; Wang, J.; Wei, T.; Liu, Z.; An, X.; Yuan, B. A defect-mediated WO_3/FeOOH heterostructure as Z-scheme photocathode for efficient water purification via persulfate activation. *Appl. Surf. Sci.* **2025**, *688*, 162403. [CrossRef]
14. Zhou, P.; Yu, J.; Jaroniec, M. All-Solid-State Z-Scheme Photocatalytic Systems. *Adv. Mater.* **2014**, *26*, 4920–4935. [CrossRef]
15. Melián, J.A.H.; Rodríguez, J.M.D.A.; Suárez, A.V.; Rendón, E.T.; Campo, C.V.D.; Arana, J.; Peña, J.P. The photocatalytic disinfection of urban waste waters. *Chemosphere* **2000**, *41*, 323–327. [CrossRef] [PubMed]
16. Leung, T.Y.; Chan, C.Y.; Hu, C.; Yu, J.C.; Wong, P.K. Photocatalytic disinfection of marine bacteria using fluorescent light. *Water Res.* **2008**, *42*, 4827–4837. [CrossRef] [PubMed]
17. Alina, A.K.; Kadyrzhanov, K.K.; Kozlovskiy, A.A.; Shlimas, D.D.; Borgekov, D.B.; Konuhova, M.; Popov, A.I. WO_3/$ZnWO_4$ microcomposites with potential application in photocatalysis. *Opt. Mater.* **2024**, *150*, 115280. [CrossRef]
18. Cho, S.; Jang, J.W.; Lee, J.S.; Lee, K.H. Porous ZnO-ZnSe nanocomposites for visible light photocatalysis. *Nanoscale* **2012**, *4*, 2066–2071. [CrossRef]
19. Liu, Y.; Xie, C.; Li, H.; Chen, H.; Zou, T.; Zeng, D. Improvement of gaseous pollutant photocatalysis with WO_3/TiO_2 heterojunctional-electrical layered system. *J. Hazard. Mater.* **2011**, *196*, 52–58. [CrossRef]
20. Xu, P.; Huang, S.; Liu, M.; Lv, Y.; Wang, Z.; Long, J.; Zhang, W.; Fan, H. Z-Schemed WO_3/rGO/$SnIn_4S_8$ Sandwich Nanohybrids for Efficient Visible Light Photocatalytic Water Purification. *Catalysts* **2019**, *9*, 187. [CrossRef]
21. Sayama, K.; Yoshida, R.; Kusama, H.; Okabe, K.; Abe, Y.; Arakawa, H. Photocatalytic decomposition of water into H_2 and O_2 by a two-step photoexcitation reaction using a WO_3 suspension catalyst and an Fe^{3+}/Fe^{2+} redox system. *Chem. Phys. Lett.* **1997**, *277*, 387–391. [CrossRef]
22. Zhang, L.; Wong, K.H.; Chen, Z.; Yu, J.C.; Zhao, J.; Hu, C.; Chan, C.Y.; Wong, P.K. AgBr-Ag-Bi_2WO_6 nanojunction system: A novel and efficient photocatalyst with double visible-light active components. *Appl. Catal. A Gen.* **2009**, *363*, 221–229. [CrossRef]

23. Liao, G.; Li, C.; Li, X.; Fang, B. Emerging polymeric carbon nitride Z-scheme systems for photocatalysis. *Cell Rep. Phys. Sci.* **2021**, *2*, 100355. [CrossRef]
24. Iwase, A.; Ng, Y.H.; Ishiguro, Y.; Kudo, A.; Amal, R. Reduced Graphene Oxide as a Solid-State Electron Mediator in Z-Scheme Photocatalytic Water Splitting under Visible Light. *J. Am. Chem. Soc.* **2011**, *133*, 11054–11057. [CrossRef]
25. Ling, Q.; Sun, J.; Zhou, Q.; Ren, H.; Zhao, Q. Visible-light-driven titania/silica photocatalyst co-doped with boron and ferrum. *Appl. Surf. Sci.* **2008**, *254*, 6731–6735. [CrossRef]
26. Islam, A.; Teo, S.H.; Islam, M.T.; Mondal, A.H.; Mahmud, H.; Ahmed, S.; Ibrahim, M.; Taufiq-Yap, Y.H.; Abdulkareem-Alsultan, G.; Hossain, M.L. Harnessing visible light for sustainable biodiesel production with Ni/Si/MgO photocatalyst. *Renew. Sustain. Energy Rev.* **2025**, *208*, 115033. [CrossRef]
27. He, Q.W.; Wu, Y.; Yang, C.; Zhang, H.N.; Tang, D.S.; Shang, X.; Wang, X.C. Switch effect on controlled water splitting by biaxial strain regulating the promising two-dimensional Janus X_2PAs (X = Si, Ge and Sn) photocatalyst. *Nanoscale* **2023**, *15*, 10458–10464. [CrossRef] [PubMed]
28. Allen, A.J.; Berk, N.F. Analysis of small-angle scattering data dominated by multiple scattering for systems containing eccentrically shaped particles or pores. *J. Appl. Crystallogr.* **2010**, *27*, 878–891. [CrossRef]
29. Tian, J.; Wang, X.; Liu, W. Cr(VI), Pb(II), Cd(II) adsorption properties of nanostructured BiOBr microspheres and their application in a continuous filtering removal device for heavy metal ions. *J. Mater. Chem. A Mater. Energy Sustain.* **2014**, *2*, 2599–2608.
30. Hayashi, T.; Maeyama, S.; Yoshii, S. TEM, AES and XPS Studies of Si Layer on Buried SiO_2 Layer Formed by High-Dose Oxygen Ion-Implantation. *Jpn. J. Appl. Phys.* **1980**, *19*, 1111. [CrossRef]
31. Wang, P.; Huang, B.; Qin, X.; Zhang, X.; Whangbo, M.H. Ag/AgBr/$WO_3{\cdot}H_2O$: Visible-light photocatalyst for bacteria destruction. *Inorg. Chem.* **2009**, *48*, 10697–10702. [CrossRef] [PubMed]
32. Xu, J.; Meng, W.; Zhang, Y.; Li, L.; Guo, C. Photocatalytic degradation of tetrabromobisphenol A by mesoporous BiOBr: Efficacy, products and pathway. *Appl. Catal. B Environ.* **2011**, *107*, 355–362. [CrossRef]
33. Shoval, S.; Nathan, Y. Analyzing the calcination of sulfur-rich calcareous oil shales using FT-IR spectroscopy and applying curve-fitting technique. *J. Therm. Anal. Calorim.* **2011**, *105*, 883–896. [CrossRef]
34. Tauc, J. Band tails in amorphous semiconductors. *J. Non-Cryst. Solids* **1987**, *97–98*, 149–154. [CrossRef]
35. Hervé, P.; Vandamme, L.K.J. General relation between refractive index and energy gap in semiconductors. *Infrared Phys. Technol.* **1994**, *35*, 609–615. [CrossRef]
36. Ravindra, N.M.; Ganapathy, P.; Choi, J. Energy gap–refractive index relations in semiconductors—An overview. *Infrared Phys. Technol.* **2007**, *50*, 21–29. [CrossRef]
37. Yuan, Y.J.; Chen, D.; Zhong, J.; Yang, L.X.; Zou, Z. Interface engineering of a noble-metal-free 2D–2D MoS_2/Cu-$ZnIn_2S_4$ photocatalyst for enhanced photocatalytic H_2 production. *J. Mater. Chem. A Mater.* **2017**, *5*, 15771–15779. [CrossRef]
38. Liu, S.; Ng, A.K.; Xu, R.; Wei, J.; Tan, C.M.; Yang, Y.; Chen, Y. Antibacterial action of dispersed single-walled carbon nanotubes on *Escherichia coli* and *Bacillus subtilis* investigated by atomic force microscopy. *Nanoscale* **2010**, *2*, 2744–2750. [CrossRef]
39. Lv, Y.; Niu, Z.; Chen, Y.; Hu, Y. Bacterial effects and interfacial inactivation mechanism of nZVI/Pd on *Pseudomonas putida* strain. *Water Res.* **2017**, *115*, 297–308. [CrossRef] [PubMed]
40. Sun, H.; Li, G.; Nie, X.; Shi, H.; Wong, P.K.; Zhao, H.; An, T. Systematic Approach to In-Depth Understanding of Photoelectrocatalytic Bacterial Inactivation Mechanisms by Tracking the Decomposed Building Blocks. *Environ. Sci. Technol.* **2014**, *48*, 9412–9419. [CrossRef]
41. Mondal, S.; Gupta, A.; Tiwari, S.; Maurya, P.K.; Pandey, P.; Singh, S.P. Reactive Oxygen Species Measurement in Cyanobacteria Using 2′,7′-Dichlorodihydrofluorescein Diacetate (DCFH-DA) Dye and Fluorescence Microscope or Flow Cytometer. In *Methods in Cyanobacterial Research*; CRC Press: Boca Raton, FL, USA, 2024; pp. 122–129.
42. Zhang, H.; Huang, C.H. Oxidative transformation of fluoroquinolone antibacterial agents and structurally related amines by manganese oxide. *Environ. Sci. Technol.* **2005**, *39*, 4474–4483. [CrossRef]
43. Naumann, D.; Helm, D.; Labischinski, H. Microbiological characterizations by FT-IR spectroscopy. *Nature* **1991**, *351*, 81–82. [CrossRef]
44. Baker, M.J.; Hussain, S.R.; Lovergne, L.; Untereiner, V.; Hughes, C.; Lukaszewski, R.A.; Thiéfin, G.; Sockalingum, G.D. Developing and understanding biofluid vibrational spectroscopy: A critical review. *Chem. Soc. Rev.* **2016**, *45*, 1803–1818. [CrossRef]
45. Auffan, M.; Achouak, W.; Rose, J.; Roncato, M.A.; Chaneac, C.; Waite, D.T.; Masion, A.; Woicik, J.C.; Wiesner, M.R.; Bottero, J.Y. Relation between the Redox State of Iron-Based Nanoparticles and Their Cytotoxicity toward *Escherichia coli*. *Environ. Sci. Technol.* **2008**, *42*, 6730–6735. [CrossRef]
46. Ojeda, J.J.; Romero-Gonzalez, M.E.; Bachmann, R.T.; Rgj, E.; Banwart, S.A. Characterization of the cell surface and cell wall chemistry of drinking water bacteria by combining XPS, FTIR spectroscopy, modeling, and potentiometric titrations. *Langmuir ACS J. Surf. Colloids* **2008**, *24*, 4032–4040. [CrossRef]
47. Dittrich, M.; Sibler, S. Cell surface groups of two picocyanobacteria strains studied by zeta potential investigations, potentiometric titration, and infrared spectroscopy. *J. Colloid Interface Sci.* **2005**, *286*, 487–495. [CrossRef]

48. van der Mei, H.C.; de Vries, J.; Busscher, H.J. X-ray photoelectron spectroscopy for the study of microbial cell surfaces. *Surf. Sci. Rep.* **2000**, *39*, 1–24. [CrossRef]
49. Rosa, D.; Remmani, R.; Bavasso, I.; Bracciale, M.P.; Di Palma, L. Biochar supported Fe-TiO_2 composite for wastewater treatment: Solid-state synthesis and mechanistic insights. *Chem. Eng. Sci.* **2025**, *317*, 122076. [CrossRef]
50. Shantz, L.M.; Stanley, B.A.; Secrist, J.A.; Pegg, A.E. Purification of human S-adenosylmethionine decarboxylase expressed in *Escherichia coli* and use of this protein to investigate the mechanism of inhibition by the irreversible inhibitors, 5′-deoxy-5′-[(3-hydrazinopropyl)methylamino]adenosine and 5′-{[(Z)-4-amino-2-butenyl]methylamino}-5′-deoxyadenosine. *Biochemistry* **1992**, *31*, 6848–6855. [CrossRef] [PubMed]
51. Sch Nbrunn, E.; Eschenburg, S.; Krekel, F.; Luger, K.; Amrhein, N. Role of the loop containing residue 115 in the induced-fit mechanism of the bacterial cell wall biosynthetic enzyme MurA. *Biochemistry* **2000**, *39*, 2164–2173. [CrossRef]

Disclaimer/Publisher's Note: The statements, opinions and data contained in all publications are solely those of the individual author(s) and contributor(s) and not of MDPI and/or the editor(s). MDPI and/or the editor(s) disclaim responsibility for any injury to people or property resulting from any ideas, methods, instructions or products referred to in the content.

catalysts

MDPI

Article

Facile Aqueous Synthesis of High-Entropy Metal Sulfides for Sulfion Oxidation-Assisted Energy-Saving Hydrogen Production

Linwei Jiang [1], Poh Lin Lau [1], Huaiyuan Kang [1], Bosong Duan [1], Aixiang Wang [2,*], Hsien-Yi Hsu [3,*], Zongyou Yin [4] and Guohua Jia [1,*]

[1] School of Molecular and Life Sciences, Curtin University, Perth, WA 6102, Australia
[2] School of Chemistry and Chemical Engineering, Linyi University, Linyi 276005, China
[3] School of Energy and Environment & Department of Materials Science and Engineering, City University of Hong Kong, Hong Kong 999077, China
[4] Research School of Chemistry, Australian National University, Canberra, ACT 2600, Australia
* Correspondence: wangaixiang1974@163.com (A.W.); sam.hyhsu@cityu.edu.hk (H.-Y.H.); guohua.jia@curtin.edu.au (G.J.)

Abstract

The high energy consumption of water electrolysis is primarily limited by the sluggish oxygen evolution reaction (OER). Replacing the OER with thermodynamically favorable anodic reactions provides an effective strategy to improve energy efficiency. Among these reactions, the sulfide oxidation reaction (SOR) offers both low thermodynamic potential and environmental relevance. In this work, we develop a high-entropy metal sulfide catalyst, CuNiCoFeMnS, via a facile aqueous synthesis route, achieving homogeneous elemental dispersion and a highly disordered structure. The catalyst exhibits excellent SOR activity, delivering a low potential of 0.396 V to achieve a current density of 10 mA cm^{-2}. In addition, it enables a significant reduction of 1.05 V in cell voltage at 50 mA cm^{-2} compared with conventional water electrolysis. Furthermore, by integrating solar energy, the system enables simultaneous upgrading of sulfide-containing wastewater and energy-efficient hydrogen production. These results demonstrate a promising pathway toward coupling waste remediation with sustainable hydrogen generation.

Keywords: high-entropy metal sulfides; aqueous synthesis; sulfion oxidation reaction; sustainable hydrogen production

1. Introduction

The urgent need to replace depleting fossil fuels and alleviate environmental damage has driven a global shift toward sustainable energy [1–4]. Hydrogen has emerged as a leading contender in this transition, offering high energy density with zero carbon emissions [5–8]. Although electrochemical water splitting represents a clean and renewable-compatible strategy for high-purity hydrogen production, it is fundamentally constrained by intrinsic sluggish kinetic limitations [9–11]. The process is severely constrained by the oxygen evolution reaction (OER) at the anode [12–14]. As the anodic half-reaction in water electrolysis, the OER involves a four-electron transfer process with inherently sluggish kinetics, resulting in high energy consumption [15,16].

A promising approach to enhancing electrolysis efficiency is to substitute the sluggish OER with alternative anodic reactions [17–20]. Instead of conventional water oxidation, the anode can be engineered to oxidize value-added substrates with substantially lower oxidation potentials, thereby reducing the overall energy input [21–23]. These substrates,

ranging from biomass derivatives to industrial byproducts, not only lower the voltage requirements for the hydrogen evolution reaction (HER) but also potentially treat waste simultaneously [24,25]. For instance, Li et al. reported a template-directed strategy to synthesize programmable nanoscale high-entropy alloys (HEA) with tunable morphology and composition. The HEA-PdPtCuPbBi catalyst shows superior ethanol oxidation reaction (EOR) activity and durability compared with commercial Pd/C and Pt/C. Replacing the OER with the EOR lowers the operating voltage and produces value-added acetate, reducing overall energy consumption [26]. Gu et al. reported a low-temperature plasma-assisted synthetic approach to preparing defect-rich, high-surface-area high-entropy oxide (HEO) nanosheets. The quinary $(FeCrCoNiCu)_3O_4$ nanosheets exhibit superior electrocatalytic performance for 5-hydroxymethylfurfural oxidation, delivering lower onset potential and faster kinetics than conventionally synthesized HEOs. This approach opens new opportunities for designing nanostructured HEOs with enhanced catalytic activity [27]. Among the various anodic alternatives, the sulfion oxidation reaction (SOR) has attracted growing interest because of its exceptionally low thermodynamic potential ($S^{2-} \rightarrow S + 2e^-$, -0.48 V vs. RHE) [28–30]. In addition to its favorable energetics, the SOR is highly relevant to practical applications across environmental and industrial fields [31]. Specifically, it offers a promising solution for managing sulfide-containing wastewater from industries like dyeing, petroleum refining, mining, and metallurgy, which otherwise poses significant threats to the environment and human health. Unlike the gas-phase Claus process, electrochemical sulfide oxidation provides a streamlined, oxidant-free solution for wastewater [32]. By replacing water oxidation with a thermodynamically favorable SOR, this method simultaneously treats pollutants and lowers the energy barrier for hydrogen production [33–35].

In the aqueous synthesis of high-entropy metal sulfides, configurational entropy dominates multicomponent systems by stabilizing disordered high-entropy sulfides under ambient conditions [36]. Based on a previous study, we report a facile aqueous co-precipitation strategy for the synthesis of high-entropy sulfide electrocatalysts. The CuNiCoFeMnS catalyst exhibits remarkable catalytic performance, delivering a low potential of 0.472 V at a current density of 50 mA cm^{-2} for the SOR. Furthermore, the assembled CuNiCoFeMnS-based hybrid electrolysis system coupled with the SOR exhibits a 1.05 V reduction in cell voltage relative to conventional water electrolysis at a practical current density of 50 mA cm^{-2}. This significantly lowered operating voltage enables substantially more energy-efficient hydrogen production. Additionally, a solar-driven hybrid electrolysis system was constructed under laboratory conditions, in which the incorporation of the SOR enabled operation at substantially lower cell voltages, thereby improving overall solar-to-hydrogen energy conversion efficiency. The coupled solar–hydrogen–electricity conversion processes were further simulated to evaluate its practical feasibility and energy-saving potential.

2. Results and Discussion

The synthesis of the CuNiCoFeMnS sample is simple and straightforward, as illustrated in Figure 1a. The metal chloride precursors were first mixed together (Figure S1a). This precursor solution was then rapidly injected into a Na_2S solution using a syringe. A black suspension formed immediately within one second (Figure S1b, Movie S1). This rapid precipitation indicates fast reaction kinetics. It also demonstrates the high efficiency of the aqueous coprecipitation strategy. The reaction conditions are mild, the operation is simple and the product forms instantaneously. Therefore, this method is highly suitable for large-scale production. XRD analysis (Figure S2) was first conducted to investigate the crystallographic structure of the CuNiCoFeMnS sample. The XRD pattern shows no discernible diffraction peaks, suggesting an amorphous or highly disordered structure, which is a typical characteristic of high-entropy systems. To gain insight into the structural

https://doi.org/10.3390/catal16060525

features of the as-synthesized sample, the TEM image in Figure 1b reveals that the sample consists of irregularly aggregated nanoparticles without a well-defined morphology. At higher magnification (Figure 1c), no distinct lattice fringes are observed, implying the lack of long-range crystalline order. This observation is consistent with the XRD results, further supporting the highly disordered structural nature of the sample. The corresponding selected-area electron diffraction (SAED) pattern in Figure 1d exhibits diffuse rings rather than sharp diffraction spots, further confirming the disordered nature of the CuNiCoFeMnS sample. To enable structural comparison, TEM, HRTEM, SAED and EDS mapping characterizations of the ternary sulfide CuNiCoS (Figures S3 and S4) were carried out, confirming a similar nanonet morphology and comparable crystalline features. Furthermore, elemental mapping analysis and EDS spectra (Figure 1e,f) reveal a uniform spatial distribution of Cu, Ni, Co, Fe, Mn and S throughout the sample, indicating homogeneous compositional dispersion. EELS analysis (Figure 1g) clearly identifies the characteristic energy-loss edges of different metal, confirming the coexistence of these metal elements within the sample. ICP-OES analysis (Figure S5) was performed to determine the metal elemental composition of CuNiCoFeMnS. The corresponding atomic percentages (Figure 1h) were calculated from the ICP data, revealing that the five constituent metals are distributed in near-equimolar ratios, consistent with the design principle of high-entropy materials. Collectively, the above results validate the homogeneous integration of multiple elements into the nanostructured high-entropy framework.

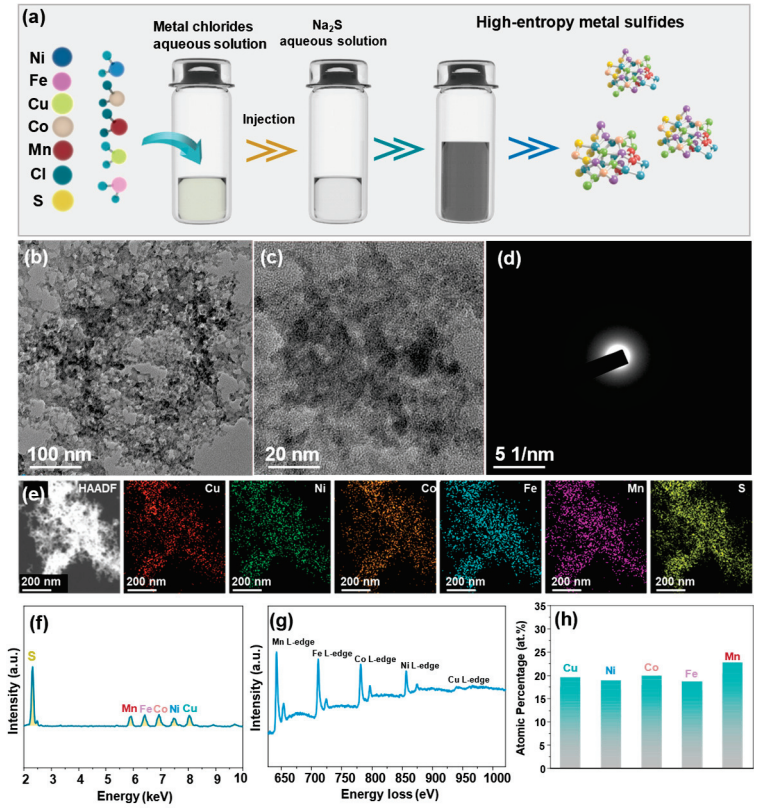


Figure 1. Structural characterization and compositional analysis of the CuNiCoFeMnS high-entropy sulfide. (**a**) Schematic illustration of the synthesis process. (**b**) TEM image showing irregularly aggregated nanoparticles. (**c**) High-resolution TEM image without discernible lattice fringes. (**d**) SAED pattern displaying diffuse diffraction rings. (**e**) HAADF-STEM image and corresponding elemental mappings of Cu, Ni, Co, Fe, Mn and S, demonstrating uniform elemental distribution. (**f**) EDS spectrum confirming the presence of all constituent elements. (**g**) EELS spectrum showing characteristic L-edge signals of the metal elements. (**h**) Quantitative atomic percentages determined by ICP analysis, indicating a near-equiatomic composition.

https://doi.org/10.3390/catal16060525

X-ray photoelectron spectroscopy (XPS) was conducted to investigate the surface composition, as presented in Figure 2. The survey spectrum (Figure 2a) and corresponding deconvoluted high-resolution spectra reveal the coexistence of five metal elements (Ni, Co, Fe, Mn and Cu) together with sulfur, confirming the successful integration of the target components into the HEMS framework. As shown in Figure 2b, the Cu 2p spectrum of Cu-NiCoFeMnS displays two prominent peaks centered at 935.3 and 955.1 eV, corresponding to Cu $2p_{3/2}$ and Cu $2p_{1/2}$, respectively [37]. The Ni 2p spectrum can be deconvoluted into two sets of spin–orbit doublets. The peaks at 856.5 and 874.1 eV are attributed to Ni^{2+}, while the peaks at 858.7 and 876.1 eV correspond to Ni^{3+} species (Figure 2c) [38]. In addition, prominent satellite features are observed at 863.6 and 881.4 eV. The high-resolution Co 2p XPS spectrum (Figure 2d) can be deconvoluted into multiple characteristic components, indicating the coexistence of different cobalt oxidation states. The main peaks located at 781.9 and 783.4 eV are assigned to the Co $2p_{3/2}$ signals of Co^{3+} and Co^{2+} species, respectively. The peak centered at 785.4 eV is attributed to the satellite peak. Correspondingly, the Co $2p_{1/2}$ signals appear at 796.9 and 799.3 eV, corresponding to Co^{3+} and Co^{2+} species, respectively, along with a satellite peak at 804.6 eV [39]. The Fe 2p spectrum exhibits three characteristic peaks at approximately 714.8, 722.0, and 727.6 eV, corresponding to Fe $2p_{3/2}$, Fe $2p_{1/2}$, and the associated satellite feature, respectively (Figure 2e) [40]. As shown in Figure 2f, the Mn 2p spectrum displays two characteristic peaks at 644.1 and 656.1 eV, corresponding to Mn $2p_{3/2}$ and Mn $2p_{1/2}$, respectively, accompanied by a satellite feature at 650.7 eV [41]. Further, the S 2p spectrum in Figure 2g can be deconvoluted into a doublet at 165.3 and 166.3 eV corresponding to S species, along with an additional peak at 171.5 eV, which is attributed to oxidized sulfur species [42]. Furthermore, the corresponding XPS data is summarized in Table S1 in the Supporting Information.

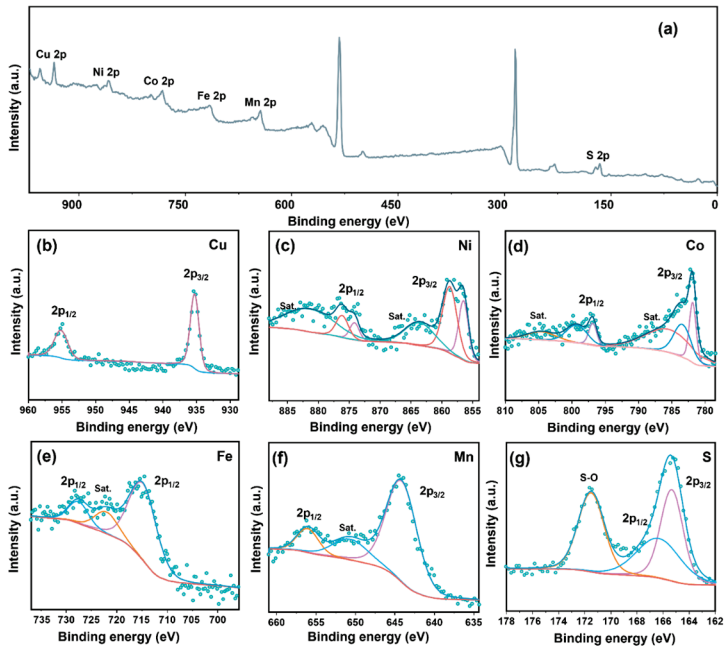


Figure 2. XPS analysis of high-entropy CuNiCoFeMnS metal sulfide sample. (**a**) Full survey spectrum confirming the presence of Cu, Ni, Co, Fe, Mn and S elements. High-resolution spectra of (**b**) Cu 2p, (**c**) Ni 2p, (**d**) Co 2p, (**e**) Fe 2p, (**f**) Mn 2p, and (**g**) S 2p regions.

The dots denote the raw XPS data points, whereas the colored lines represent the corresponding peak-fitting curves. Initially, to demonstrate the energy-saving advantages of SOR-assisted water electrolysis over conventional OER systems, the SOR performance of CuNiCoFeMnS was systematically evaluated in an alkaline sulfion electrolyte (1.0 M NaOH

https://doi.org/10.3390/catal16060525

+ 1.0 M Na_2S) within a conventional three-electrode configuration. Figure 3a presents a schematic comparison of the thermodynamic oxidation potentials of the SOR and OER. The much lower potential of the SOR (−0.48 V vs. RHE) compared with the OER (1.23 V vs. RHE) demonstrates its inherent thermodynamic advantage and energy-saving potential in electrolysis systems. As shown in Figure 3b, the linear sweep voltammetry (LSV) curves demonstrate that CuNiCoFeMnS exhibits a significantly lower potential at different current density at in 1 M KOH + 1 M Na_2S sulfion-containing solution compared with that in 1 M KOH alone. Figure 3c summarizes the potentials required to achieve current densities of 50, 100 and 200 mA·cm^{-2} in the form of a bar chart, enabling a direct quantitative comparison between the SOR and OER systems. Notably, CuNiCoFeMnS reaches 50 mA·cm^{-2} at a relatively low potential of 0.472 V vs. RHE, which is substantially lower than that required for the OER system (1.62 V) under the same conditions. As the current density increases to 200 mA·cm^{-2}, the SOR-driven system maintains a relatively low operating potential of 0.559 V, whereas the OER system requires 1.697 V under the same current density, demonstrating the superior capability of the SOR pathway to sustain high-rate electrolysis with reduced energy input. Subsequently, the SOR activities of CuNiCoFeMnS, CuNiCoS, and bare Ni foam were evaluated under identical conditions, and the LSV curves are presented in Figure 3d. As illustrated in Figure S6, at lower current densities of 50 mA cm^{-2}, the potential required by CuNiCoFeMnS is only 0.472 V, which remains markedly lower than those of CuNiCoS (0.58 V) and Ni foam (0.853 V). Even at higher current densities such as 200 and 300 mA cm^{-2}, CuNiCoFeMnS maintains favorable overpotentials of 0.559 and 0.6 V, respectively, consistently surpassing the performance of the comparison catalysts. The CuNiCoFeMnS electrocatalyst shows an excellent SOR activity, delivering a low potential of 0.396 V to achieve a current density of 10 mA cm^{-2}, as compared with the other reported SOR electrocatalyst shown in Table S2. Tafel slope analysis in Figure S7 reveals exceptionally fast reaction kinetics for CuNiCoFeMnS (36.5 mV dec^{-1}), outperforming that of CuNiCoS (54.8 mV dec^{-1}) and bare Ni foam (87.1 mV dec^{-1}). This enhanced activity demonstrates the superiority of the five-component catalyst over the ternary counterpart, arising from strengthened synergistic electronic interactions among the multiple metal species. Electrochemical impedance spectroscopy (EIS) was performed to probe the charge-transfer kinetics. The Nyquist plots in Figure 3e reveal that CuNiCoFeMnS possesses the lowest charge-transfer resistance (Rct, 1.84 Ω) among the tested catalysts, significantly lower than CuNiCoS (2.9 Ω) and Ni foam (6.27 Ω), reflecting accelerated electron-transfer dynamics. Furthermore, UV–visible absorption spectroscopy was employed to monitor the evolution of electrolyte composition during electrolysis. In addition, the electrochemically active surface area (ECSA) was evaluated by measuring the double-layer capacitance (C_{dl}) using cyclic voltammetry within the potential range of 0.35–0.40 V vs. RHE at different scan rates (Figure S8). Among the tested catalysts, (NiCoFeMnCr)S exhibits the highest C_{dl} value of approximately 8.51 mF cm^{-2} (Figure S8), indicating a larger electrochemically active surface area (ECSA). As shown in Figure 3f, after 1 h of galvanostatic operation, the electrolyte exhibits a pronounced increase in absorbance around 300 nm, accompanied by a secondary absorption feature near 370 nm. With the current density increasing from 10 to 200 mA cm^{-2}, the overall absorbance intensity gradually rises, indicating the continuous generation and accumulation of polysulfide species during electrolysis. These spectral changes provide compelling evidence for the formation of lower-order polysulfides (S_x^{2-}), thereby offering important mechanistic insight into the intermediate processes of the SOR pathway [25]. Although a gradual decrease in current density is observed during the 130 h stability test, the current is completely restored after refreshing the electrolyte. This recovery confirms that the minor performance loss is associated with reactant depletion instead

https://doi.org/10.3390/catal16060525

of intrinsic catalyst instability, demonstrating the outstanding durability of CuNiCoFeMnS (Figure 3g).

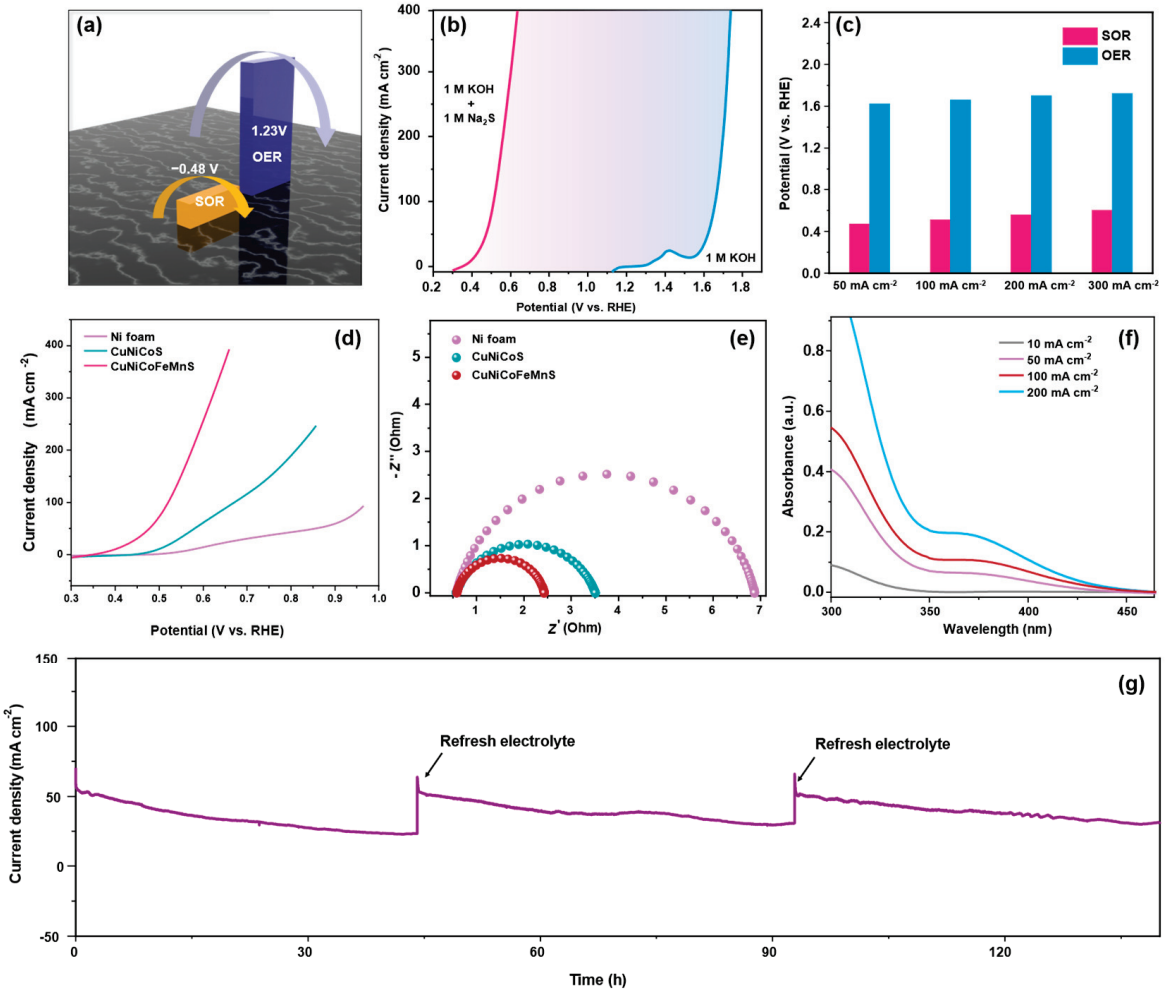


Figure 3. (**a**) Comparison of theoretical oxidation potentials between SOR and OER. (**b**) LSV curves of CuNiCoFeMnS in 1 M KOH + 1 M Na_2S and 1 M KOH electrolyze solutions. (**c**) Overpotentials at 50, 100, 200 and 300 mA·cm^{-2} for SOR and OER. (**d**) LSV curves of CuNiCoFeMnS, CuNiCoS and Ni foam in 1 M KOH + 1 M Na_2S. (**e**) Nyquist plots from EIS analysis. (**f**) UV-Vis spectra of the electrolyte recorded at various current density intervals. (**g**) Continuous current-time measurement of the CuNiCoFeMnS.

To further assess the practical electrocatalytic performance of the CuNiCoFeMnS catalyst, overall sulfion electrolysis was evaluated in a two-electrode configuration, as illustrated in Figure 4a. A two-electrode electrolyzer was constructed using CuNiCoFeMnS supported on nickel foam as the anode and commercial Pt/C as the cathode. As shown in Figure 4b, in the absence of sulfide ions, the CuNiCoFeMnS electrode requires relatively high cell voltages to deliver practical current densities in 1.0 M KOH. Specifically, as illustrated in Figure 4c, voltages of 1.7, 1.743, and 1.794 V are needed to reach current densities of 50, 100, and 200 mA cm^{-2}, respectively. In contrast, the SOR-coupled system requires only 0.653, 0.743, and 0.812 V to achieve the same current densities, demonstrating a substantial reduction in energy input across the entire current range. The continuous increase in cell voltage with rising current density under OER conditions reflects the pronounced kinetic limitations and high energy demand associated with oxygen evolution in alkaline media. These results clearly underscore the intrinsic thermodynamic and kinetic barriers of conventional OER-driven electrolysis, particularly at elevated current

https://doi.org/10.3390/catal16060525

densities. To assess the long-term electrochemical durability of CuNiCoFeMnS under practical operating conditions, a prolonged 50 h stability test was performed. Consistent with the SOR stability evaluation, the current fully recovered to its initial level upon electrolyte replacement.

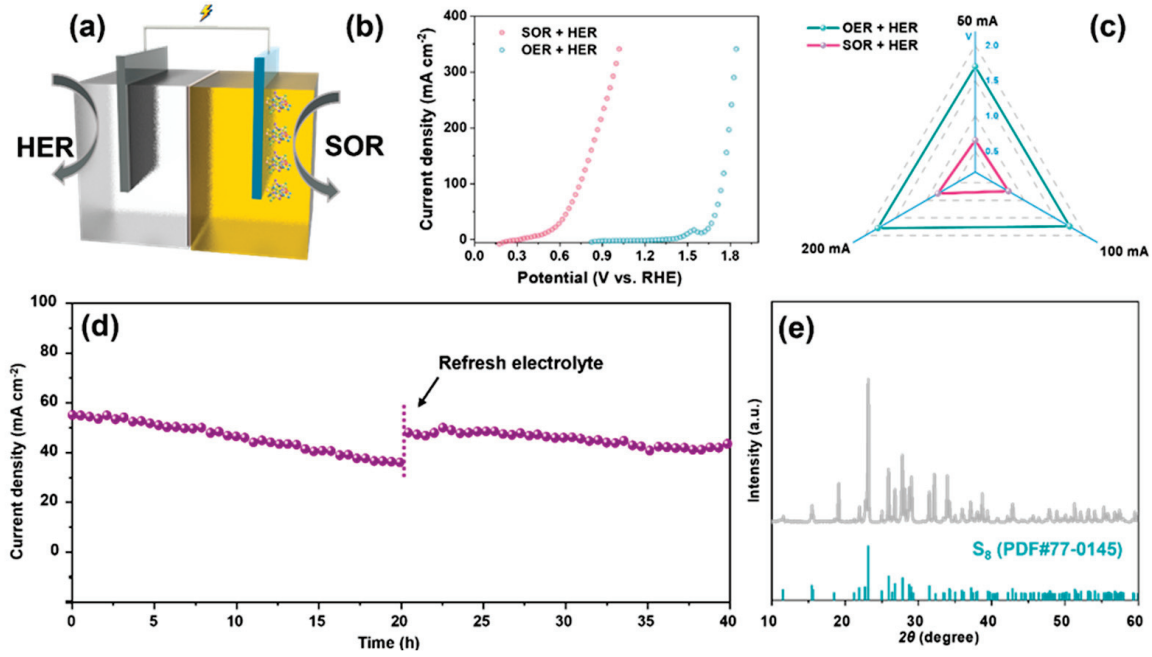


Figure 4. (**a**) Schematic illustration of the SOR-coupled HER electrolysis system. (**b**) LSV curves of the SOR-coupled HER and the conventional OER-coupled HER systems. (**c**) Comparison of the operating voltages at different current densities. (**d**) Long-term stability test of the SOR-coupled HER system. (**e**) XRD analysis of the sulfur products obtained after the reaction. In (**e**), the grey line represents the experimental XRD pattern of the sulfur products, while the turquoise bars correspond to the standard diffraction peaks of S_8 (PDF#77-0145).

Proton exchange membrane systems are widely recognized as efficient platforms for hydrogen–electricity conversion [43,44]. By integrating renewable solar energy with sulfide oxidation reaction assisted hydrogen production, a sustainable solar–hydrogen–electricity coupling strategy can be established. As illustrated in Figure 5a, sulfur-containing wastewater (S^{2-}) is selectively oxidized to elemental sulfur (S_8), while the cathodic reaction produces hydrogen, enabling energy-saving hydrogen generation under mild conditions. The conceptual scheme highlights the transformation of sulfion pollution into value-added sulfur products while simultaneously supporting clean hydrogen production. To experimentally validate this integrated strategy, a laboratory-scale solar-driven energy conversion system was constructed (Figure 5b). The setup consists of a photovoltaic (PV) panel, an electrolysis cell, a PEMFC unit and an electric fan as the external load. A more detailed photograph of the PEMFC device is provided in Figure S9 for clearer visualization of the fuel cell configuration. As shown in Movie S2, under simulated solar irradiation, the electrolysis cell generated visible hydrogen bubbles at the cathode, confirming efficient hydrogen evolution. The generated hydrogen was subsequently fed into the PEMFC, which successfully powered an electric fan as a proof of concept. The continuous and stable operation of the fan demonstrates the feasibility of sustained solar-driven hydrogen production and electricity generation, thereby verifying the practical applicability of the integrated sulfion-oxidation-assisted energy conversion pathway.

https://doi.org/10.3390/catal16060525

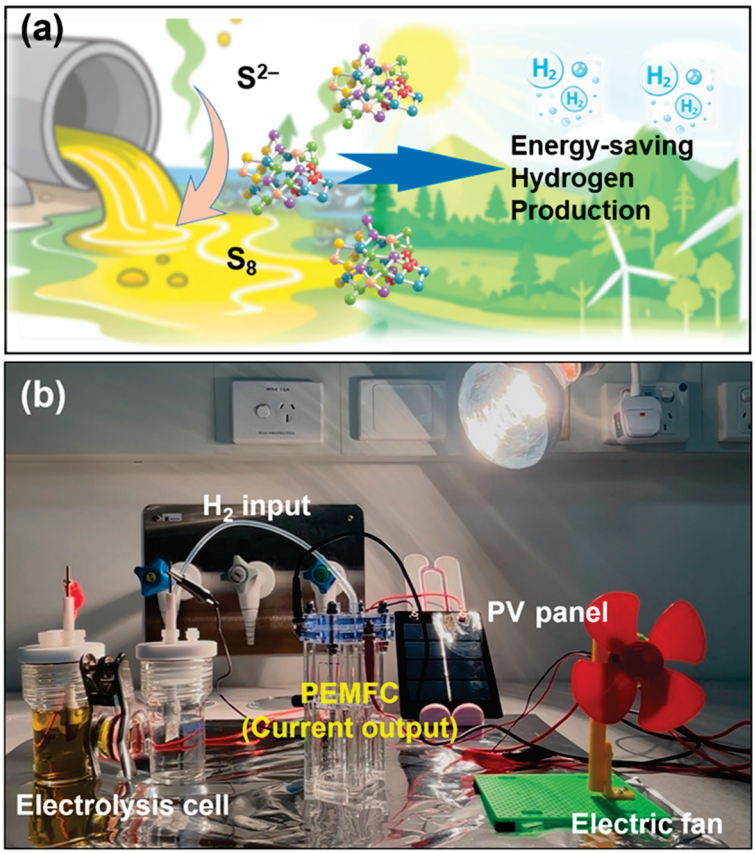


Figure 5. (**a**) Schematic diagram illustrating the SOR-assisted water electrolysis system. (**b**) Photograph of the integrated solar–hydrogen–electricity energy conversion system. These results validate the practical feasibility of the solar-coupled hydrogen energy conversion system and highlight its potential for sustainable energy applications.

3. Experiment

3.1. Reagents

Chemicals of analytical grade were used throughout the experiments without any purification steps. Sodium sulfide hydrate ($Na_2S{\cdot}xH_2O$, ≥60%) and a series of transition metal chlorides, namely $CuCl_2{\cdot}2H_2O$, $MnCl_2{\cdot}4H_2O$, $CoCl_2{\cdot}6H_2O$, $NiCl_2{\cdot}6H_2O$, and $FeCl_2{\cdot}4H_2O$, were sourced from Sigma-Aldrich (St. Louis, MO, USA). Sodium hydroxide (NaOH, >98.0%) was provided by TCL Chemicals (Chennai, India). A commercial Nafion solution (5 wt%, dispersed in a mixture of lower aliphatic alcohols and water) was purchased from Fuel Cell Store (Bryan, TX, USA).

3.2. Synthesis Method of CuNiCoFeMnS Electrocatalyst

A multimetal precursor solution was first prepared by dissolving $CuCl_2{\cdot}2H_2O$, $MnCl_2{\cdot}4H_2O$, $CoCl_2{\cdot}6H_2O$, $NiCl_2{\cdot}6H_2O$, and $FeCl_2{\cdot}4H_2O$ (each 0.5 mmol) in 25 mL of ultrapure water, yielding a homogeneous dark-colored solution. In parallel, $Na_2S{\cdot}xH_2O$ (500 mg) was dissolved in 25 mL of ultrapure water to serve as the sulfide source. All synthesis steps were carried out under ambient conditions without external heating or inert atmosphere. Subsequently, 5 mL of the metal precursor solution was rapidly injected into 5 mL of the Na_2S solution using a syringe under continuous stirring, leading to the instantaneous formation of a black precipitation. The reaction proceeded at room temperature for a short period to ensure complete conversion. The resulting suspension was then treated with 10 mL of ethanol to facilitate precipitation, followed by centrifugation at 7000 rpm for 5 min. The collected solid was washed twice with ethanol to remove residual ions and

https://doi.org/10.3390/catal16060525

impurities, and finally dried under vacuum at 60 °C overnight. For the preparation of the CuNiCoS electrocatalyst, the same procedure was employed, except that Mn and Fe precursors were omitted from the initial solution.

3.3. Materials Characterization

Powder X-ray diffraction (XRD) measurements were performed using a Panalytical Empyrean diffractometer (Malvern, UK) equipped with Cu Kα radiation (λ = 1.54 Å), operated at 40 kV and 40 mA. X-ray photoelectron spectroscopy (XPS) measurements were carried out using a Kratos Axis Ultra-XPS system (Manchester, UK) equipped with a hybrid lens and a monochromatic Al Kα radiation source (hν = 1486.6 eV). The instrument was operated at 10 kV and 10 mA, corresponding to a power of 100 W. All spectra were collected under ultra-high vacuum conditions. Transmission electron microscopy (TEM), high-angle annular dark-field scanning transmission electron microscopy (HAADF-STEM), energy-dispersive X-ray spectroscopy (EDS) mapping, and electron energy-loss spectroscopy (EELS) were performed at the Centre for Microscopy, Characterisation and Analysis (CMCA), The University of Western Australia. All measurements were carried out using an FEI Titan G2 80–200 kV transmission electron microscope (Hillsboro, OR, USA). To avoid possible interference from copper support grids during Cu elemental analysis, EDS measurements were conducted using a gold grid. The elemental compositions of Ni, Co, Fe, Mn and Cu were quantified by inductively coupled plasma optical emission spectroscopy and mass spectrometry (ICP-OES/MS) at ChemCentre (Perth, WA, Australia). UV–vis absorption spectra were recorded on an Agilent Cary 4000 spectrophotometer (Santa Clara, CA, USA) using quartz cuvettes with a 1 cm path length.

3.4. Electrochemical Measurements

Electrochemical measurements were conducted on a CS2350M workstation (Wuhan Corrtest Instruments Co., Ltd., Wuhan, China) using a standard three-electrode configuration. A graphite rod served as the counter electrode, while a Hg/HgO electrode was used as the reference electrode. All measurements were performed at ambient temperature. The recorded potentials were converted to the reversible hydrogen electrode (RHE) scale using the equation: $E_{RHE} = E_{Hg/HgO} + 0.0591\ pH + 0.098\ V$. For electrode preparation, the catalyst was dispersed to form a uniform ink by ultrasonically mixing 5 mg of powder in a solvent composed of deionized water (200 μL), ethanol (280 μL), and Nafion solution (20 μL, 5 wt%). The dispersion was sonicated for 1 h to ensure complete homogenization. A fixed volume (50 μL) of the resulting ink was then deposited onto a pretreated nickel foam substrate (1 × 1 cm^2) and dried naturally under ambient conditions, yielding a catalyst loading of approximately 0.5 mg cm^{-2}. Electrocatalytic performance was evaluated by linear sweep voltammetry (LSV) at a scan rate of 5 mV s^{-1}. To account for ohmic losses, 95% iR compensation was applied to all polarization curves. Electrochemical impedance spectroscopy (EIS) was carried out over a frequency range of 0.05 Hz to 10 kHz with a perturbation amplitude of 5 mV under working conditions. In addition, cyclic voltammetry (CV) was performed at various scan rates (80–160 mV s^{-1}) to assess the electrochemically active surface area.

4. Conclusions

To conclude, a CuNiCoFeMnS high-entropy sulfide electrocatalyst was synthesized via a rapid aqueous coprecipitation method. An effective strategy is proposed to reduce the energy consumption of conventional water electrolysis by coupling hydrogen evolution with the thermodynamically favorable sulfion oxidation reaction. The resulting high-entropy material demonstrates superior electrocatalytic performance for the sulfion

https://doi.org/10.3390/catal16060525

oxidation reaction. It delivers a low overpotential of 0.472 V at a current density of 50 mA cm^{-2}. Implementing this catalyst in a hybrid electrolysis cell drastically reduces the overall energy input. The system achieves a practical current density of 50 mA cm^{-2} at a cell voltage of only 0.65 V. This approach successfully bypasses the sluggish oxygen evolution reaction. It enables simultaneous pollutant degradation and energy-efficient hydrogen generation. Device integration and process simulations confirm that this solar-driven hybrid system holds immense promise for sustainable scalable industrial applications.

Supplementary Materials: The following supporting information can be downloaded at: https://www.mdpi.com/article/10.3390/catal16060525/s1, Figure S1: Photographs of the aqueous synthesis process: (a) Precursor solutions before mixing; (b) Immediate formation of a black suspension after injection; Figure S2: XRD pattern of the CuNiCoFeMnS sample. Figure S3: Structural characterization of CuNiCoS ternary sulfides. (a,b) TEM images demonstrate a network structure formed by interconnected nanoscale domains. (c) HRTEM image shows no discernible lattice fringes, suggesting short-range order with suppressed long-range crystallinity. (d) SAED pattern exhibiting broad diffuse rings, indicative of a highly disordered structural framework. Figure S4: EDS mapping results of CuNiCoS sulfides. Figure S5: ICP-OES results. Figure S6: Comparison of the SOR potentials of CuNiCoFeMnS and CuNiCoS at different current densities. Figure S7: Tafel plots of CuNiCoFeMnS, CuNiCoS and Ni foam. Figure S8: Cyclic voltammetry curves of (a) Ni foam, (b) CuNiCoS, and (c) CuNiCoFeMnS at different scan rates. (d) Linear fitting of $\Delta j/2$ versus scan rates. Figure S9: Photographs of the front and back sides of the proton exchange membrane fuel cell (PEMFC). Table S1: Summary of XPS analysis for CuNiCoFeMnS catalyst. Table S2: Comparison of the reported catalysts for sulfion oxidation reaction in alkaline media. Movie S1: Synthesis process of CuNiCoFeMnS. Movie S2: Demonstration of the solar–hydrogen–electricity energy conversion system [45–51].

Author Contributions: L.J.: Methodology, experiment, data analysis and writing the manuscript. P.L.L.: Data analysis. H.K.: Formal analysis. B.D.: Data analysis. A.W.: Supervision. H.-Y.H.: Writing—review and editing. Z.Y.: Formal analysis. G.J.: Writing—review and editing, supervision and funding acquisition All authors have read and agreed to the published version of the manuscript.

Funding: This work was supported by the Australian Research Council (ARC) Discovery Projects, grant numbers DP260101246 and DP220101959; the Australian Research Council (ARC) Future Fellowship Scheme, grant number FT210100509; and the Hebrew University of Jerusalem–Zelman Cowen Academic Initiatives (ZCAI) Joint Projects 2021.

Data Availability Statement: The data presented in this study are available on request from the corresponding author.

Conflicts of Interest: The authors declare no conflicts of interest.

References

1. Chu, S.; Majumdar, A. Opportunities and challenges for a sustainable energy future. *Nature* **2012**, *488*, 294–303. [CrossRef]
2. Scott, V.; Haszeldine, R.S.; Tett, S.F.B.; Oschlies, A. Fossil fuels in a trillion tonne world. *Nat. Clim. Change* **2015**, *5*, 419–423. [CrossRef]
3. McGlade, C.; Ekins, P. The geographical distribution of fossil fuels unused when limiting global warming to 2 °C. *Nature* **2015**, *517*, 187–190. [CrossRef]
4. Montzka, S.A.; Dlugokencky, E.J.; Butler, J.H. Non-CO_2 greenhouse gases and climate change. *Nature* **2011**, *476*, 43–50. [CrossRef]
5. Chu, S.; Cui, Y.; Liu, N. The path towards sustainable energy. *Nat. Mater.* **2017**, *16*, 16–22. [CrossRef]
6. Lu, Z.; Huang, J.; Chen, K.; Cai, P.; Zhang, H.; Chen, J.; Wen, Z. Amorphous–Crystalline High-Entropy Electrocatalysts for H_2 Evolution in High-Power Aluminum-Based Fuel Cells. *J. Am. Chem. Soc.* **2026**, *148*, 4317–4328. [CrossRef]
7. Li, S.; Hou, Y.; Feng, G.; Li, Q.; Zhai, H.; Hua, Q.; Hu, R.; Xu, M.; Zhang, C.; Huang, Z.; et al. High-Entropy Alloy Nanoflower Array Electrodes with Optimizable Reaction Pathways for Low-Voltage Hydrogen Production at Industrial-Grade Current Density. *Adv. Mater.* **2025**, *37*, 2416200. [CrossRef]
8. Guo, S.-N.; Zhang, S.-W.; Qiao, M.; Wang, J.-X. PtRuCoNiCu High-Entropy Alloy Nanodendrites for Efficient Electrocatalytic Reactions. *Chem. Mater.* **2026**, *38*, 1415–1424. [CrossRef]

9. Dey, G.R.; Teklu, S.; Shi, Z.; Hu, M.; Thompson, K.L.; Soliman, S.S.; Lord, R.W.; Abruña, H.D.; Muller, D.A.; Schaak, R.E. Structural, Compositional, and Morphological Interrelationships in Rocksalt (FeCoMnMgZn)O High Entropy Oxide Nanocrystals for Oxygen Evolution Electrocatalysis. *J. Am. Chem. Soc.* **2025**, *147*, 24230–24234. [CrossRef] [PubMed]
10. Chen, X.; Jiang, L.; Guo, W.; Shen, S.; Wang, Z.; Shao, K.; Wang, Z.; Li, C. Spontaneous Cation Exchange-Induced Iron Doping in $Ni(OH)_2$ for Enhanced Oxygen Evolution Reaction. *ACS Appl. Energy Mater.* **2025**, *8*, 751–758. [CrossRef]
11. Jiang, L.; Wang, C.; Shao, Z.; Jia, G. Synthesis and catalytic behaviour of IrO_2 nanostructures in acidic water oxidation. *Adv. Nanocompos.* **2026**, *3*, 149–179. [CrossRef]
12. Chong, L.; Gao, G.; Wen, J.; Li, H.; Xu, H.; Green, Z.; Sugar, J.D.; Kropf, A.J.; Xu, W.; Lin, X.-M.; et al. La- and Mn-doped cobalt spinel oxygen evolution catalyst for proton exchange membrane electrolysis. *Science* **2023**, *380*, 609–616. [CrossRef] [PubMed]
13. He, R.; Wang, S.; Yang, L.; Horta, S.; Ding, Y.; Di, C.; Zhang, X.; Xu, Y.; Ibáñez, M.; Zhou, Y.; et al. Active site switching on high entropy phosphides as bifunctional oxygen electrocatalysts for rechargeable/robust Zn–air battery. *Energy Environ. Sci.* **2024**, *17*, 7193–7208. [CrossRef]
14. Hu, C.; Yue, K.; Han, J.; Liu, X.; Liu, L.; Liu, Q.; Kong, Q.; Pao, C.-W.; Hu, Z.; Suenaga, K.; et al. Misoriented high-entropy iridium ruthenium oxide for acidic water splitting. *Sci. Adv.* **2023**, *9*, eadf9144. [CrossRef]
15. Jiang, L.; Yang, N.; Yang, C.; Zhu, X.; Jiang, Y.; Shen, X.; Li, C.; Sun, Q. Surface wettability engineering: CoSx-Ni_3S_2 nanoarray electrode for improving overall water splitting. *Appl. Catal. B Environ.* **2020**, *269*, 118780. [CrossRef]
16. Ding, Y.; Wang, Z.; Liang, Z.; Sun, X.; Sun, Z.; Zhao, Y.; Liu, J.; Wang, C.; Zeng, Z.; Fu, L.; et al. A Monolayer High-Entropy Layered Hydroxide Frame for Efficient Oxygen Evolution Reaction. *Adv. Mater.* **2023**, *37*, e2302860. [CrossRef]
17. Du, L.; Sun, Y.; You, B. Hybrid water electrolysis: Replacing oxygen evolution reaction for energy-efficient hydrogen production and beyond. *Mater. Rep. Energy* **2021**, *1*, 100004. [CrossRef]
18. Wang, H.-Y.; Sun, M.-L.; Ren, J.-T.; Yuan, Z.-Y. Circumventing Challenges: Design of Anodic Electrocatalysts for Hybrid Water Electrolysis Systems. *Adv. Energy Mater.* **2023**, *13*, 2203568. [CrossRef]
19. Li, Y.; Duan, Y.; Zhang, K.; Yu, W. Efficient anodic chemical conversion to boost hydrogen evolution with low energy consumption over cobalt-doped nickel sulfide electrocatalyst. *Chem. Eng. J.* **2022**, *433*, 134472. [CrossRef]
20. Qian, Q.; Zhu, Y.; Ahmad, N.; Feng, Y.; Zhang, H.; Cheng, M.; Liu, H.; Xiao, C.; Zhang, G.; Xie, Y. Recent Advancements in Electrochemical Hydrogen Production via Hybrid Water Splitting. *Adv. Mater.* **2024**, *36*, 2306108. [CrossRef]
21. Qin, Q.; Li, T.; Sun, X.; Pei, A.; Jia, Y.; He, H.; Gao, F.; Wang, P.; Wu, Q.; Liu, R.; et al. Unveiling the Gold Facet Effect in Selective Oxidation of 5-Hydroxymethylfurfural and Hydrogen Production. *Nano Lett.* **2024**, *24*, 16351–16359. [CrossRef]
22. Pei, A.; Li, G.; Zhu, L.; Huang, Z.; Ye, J.; Chang, Y.-C.; Osman, S.M.; Pao, C.-W.; Gao, Q.; Chen, B.H.; et al. Nickel Hydroxide-Supported Ru Single Atoms and Pd Nanoclusters for Enhanced Electrocatalytic Hydrogen Evolution and Ethanol Oxidation. *Adv. Funct. Mater.* **2022**, *32*, 2208587. [CrossRef]
23. Hu, S.M.; Chen, Y.N.; Liu, J.K.; Zhang, X.Y.; Jiang, W.H.; Zhou, Y.; Yuan, H.Y.; Liu, P.F.; Guo, Q.; Yang, H.G.; et al. Inhibiting the peroxidation of Co(III) oxyhydroxide for stable and ampere-level glycerol oxidation. *Appl. Catal. B Environ. Energy* **2026**, *381*, 125811. [CrossRef]
24. Jiang, L.; Pan, Y.; Zhang, J.; Chen, X.; Ye, X.; Li, Z.; Li, C.; Sun, Q. Mo propellant boosting the activity of Ni-P for efficient urea-assisted water electrolysis of hydrogen evolution. *J. Colloid Interface Sci.* **2022**, *622*, 192–201. [CrossRef]
25. Sun, H.; Wangzi, C.; Yang, Z.; Zhang, J.; Liang, Y.; Wang, J.; Zheng, Y.; Pan, J.; Li, C.; Cao, J. Oxygen adsorption on undercoordinated sites modulates electronic structure of Pd metallene for enhanced reaction kinetics in sulfur oxidation-assisted water splitting. *Appl. Catal. B Environ. Energy* **2026**, *381*, 125888. [CrossRef]
26. Li, M.; Huang, C.; Yang, H.; Wang, Y.; Song, X.; Cheng, T.; Jiang, J.; Lu, Y.; Liu, M.; Yuan, Q.; et al. Programmable Synthesis of High-Entropy Nanoalloys for Efficient Ethanol Oxidation Reaction. *ACS Nano* **2023**, *17*, 13659–13671. [CrossRef] [PubMed]
27. Gu, K.; Wang, D.; Xie, C.; Wang, T.; Huang, G.; Liu, Y.; Zou, Y.; Tao, L.; Wang, S. Defect-Rich High-Entropy Oxide Nanosheets for Efficient 5-Hydroxymethylfurfural Electrooxidation. *Angew. Chem. Int. Ed.* **2021**, *60*, 20253–20258. [CrossRef]
28. Li, F.; NG, W.K.; Qiao, W.; Yang, Y.; Li, X.; Xi, B.; Yu, Y.; Fang, J.; Li, P.; Xiong, S. Intercalation Chemistry Awakens Transition Metal Hydroxide for Boosted and Sustained Electrocatalytic Sulfion Oxidation. *Angew. Chem. Int. Ed.* **2025**, *64*, e202511402. [CrossRef]
29. Pei, Y.; Li, D.; Qiu, C.; Yan, L.; Li, Z.; Yu, Z.; Fang, W.; Lu, Y.; Zhang, B. High-Entropy Sulfide Catalyst Boosts Energy-Saving Electrochemical Sulfion Upgrading to Thiosulfate Coupled with Hydrogen Production. *Angew. Chem. Int. Ed.* **2024**, *63*, e202411977. [CrossRef]
30. Zhang, L.; Chen, M.; Xiao, L.; Wu, Y.; Liu, Q.; Hu, G.; Liu, X. Recent Advancement in Electrocatalytic Water Splitting Facilitated by the Sulfide Oxidation Reaction. *ACS Appl. Energy Mater.* **2025**, *8*, 5612–5624. [CrossRef]
31. Wang, J.; Liu, X.; Ma, C.; Duan, X.; Li, S.; Li, N.; Liu, W.; Li, Y.; Fan, X.; Peng, W. Asymmetric S Heteroatom Coordinated Dual-Atom Catalysts and Coupled Anodic Sulfion Oxidation to Boost Electrocatalysis Oxygen Reduction. *Adv. Funct. Mater.* **2025**, *35*, 2420157. [CrossRef]
32. Mohammed, S.; Raj, A.; Al Shoaibi, A.; Sivashanmugam, P. Formation of polycyclic aromatic hydrocarbons in Claus process from contaminants in H_2S feed gas. *Chem. Eng. Sci.* **2015**, *137*, 91–105. [CrossRef]

33. Zhang, L.; Wang, Z.; Qiu, J. Energy-Saving Hydrogen Production by Seawater Electrolysis Coupling Sulfion Degradation. *Adv. Mater.* **2022**, *34*, 2109321. [CrossRef]
34. Li, R.-Q.; Wang, X.; Xie, S.; Guo, S.; Cao, Z.; Yan, Z.; Zhang, W.; Wan, X. Vanadium-regulated nickel phosphide nanosheets for electrocatalytic sulfion upgrading and hydrogen production. *Chem. Sci.* **2025**, *16*, 809–815. [CrossRef] [PubMed]
35. Shi, M.-X.; Yang, H.-Y.; Xiao, X.; Jin, P.-J.; Chen, Y. Bifunctional Au@MoS_2 nanoflowers for solar-enhanced sulfur ion oxidation coupled nitrite reduction electrochemical purification system. *Chem. Eng. J.* **2025**, *522*, 167474. [CrossRef]
36. Jiang, L.; Duan, B.; Lin, S.; Jones, F.; Li, Y.; Wen, Z.; Jia, G. High-entropy chalcogenides via ambient and scalable synthesis for efficient OER catalysis. *Nano Energy* **2026**, *148*, 111634. [CrossRef]
37. Liu, L.; Zhang, Y.; Gu, Y.; Qu, J.; Wang, N.; Ge, S.; Li, J. Trace copper and bi-nonmetallic (N/S) modified ketjenblack (KB) as advanced electrocatalysts for oxygen reduction reactions. *J. Mater. Sci.* **2024**, *59*, 9250–9264. [CrossRef]
38. Yang, C.; Wang, Z.; Li, Z.; Pan, Y.; Jiang, L.; Li, C.; Wang, C.; Sun, Q. Nitrogen Disturbance Awakening the Intrinsic Activity of Nickel Phosphide for Boosted Hydrogen Evolution Reaction. *ChemSusChem* **2022**, *15*, e202200072. [CrossRef]
39. Wang, T.; Wang, P.; Zang, W.; Li, X.; Chen, D.; Kou, Z.; Mu, S.; Wang, J. Nanoframes of Co_3O_4–Mo_2N Heterointerfaces Enable High-Performance Bifunctionality toward Both Electrocatalytic HER and OER. *Adv. Funct. Mater.* **2022**, *32*, 2107382. [CrossRef]
40. Zhang, J.; Shang, X.; Ren, H.; Chi, J.; Fu, H.; Dong, B.; Liu, C.; Chai, Y. Modulation of Inverse Spinel Fe_3O_4 by Phosphorus Doping as an Industrially Promising Electrocatalyst for Hydrogen Evolution. *Adv. Mater.* **2019**, *31*, 1905107. [CrossRef]
41. Jiang, L.; Seow, Y.X.; Hsu, H.-Y.; Buntine, M.A.; Jia, H.; Yin, Z.; Jia, G. Rapid synthesis of high-entropy metal sulfides under ambient conditions as efficient catalysts for the urea oxidation reaction. *Chem. Commun.* **2026**, *62*, 4063–4066. [CrossRef]
42. Yang, C.; Wang, Z.; Jiang, L.; Zhang, J.; Li, Z.; Pan, Y.; Ye, X.; Chen, X.; Li, C.; Sun, Q. Modulation of Water Dissociation Kinetics with a "Breathable" Wooden Electrode for Efficient Hydrogen Evolution. *ACS Appl. Mater. Interfaces* **2022**, *14*, 6818–6827. [CrossRef]
43. Guan, P.; Jiang, M.; Li, W.; Zhang, W.; Zhang, L.; Long, K.; Yuan, D.; Ma, T.; Wang, D.; Liu, H.K.; et al. Strategies for Lowering Hydrogen Permeation in Membranes for Proton Exchange Membrane Water Electrolyzers and Fuel Cells. *Adv. Mater.* **2026**, *38*, e08400. [CrossRef]
44. Li, J.; Ma, Q.; Dong, S.; Zhao, S.; Wang, B.; Feng, X. Three-phase microenvironment modification by optimizing ionomer towards high-performance proton exchange membrane fuel cells. *Chem. Soc. Rev.* **2025**, *54*, 8555–8581. [CrossRef]
45. Lyu, C.; Li, Y.; Cheng, J.; Yang, Y.; Wu, K.; Wu, J.; Wang, H.; Lau, W.-M.; Tian, Z.; Wang, N.; et al. Dual Atoms (Fe, F) Co-Doping Inducing Electronic Structure Modulation of NiO Hollow Flower-Spheres for Enhanced Oxygen Evolution/Sulfion Oxidation Reaction Performance. *Small* **2023**, *19*, 2302055. [CrossRef] [PubMed]
46. Feng, W.; Cheng, M.; Du, R.; Wang, Y.; Wang, P.; Li, H.; Song, L.; Wen, X.; Yang, J.; Li, X.; et al. Gram-Scale Synthesized Two-Dimensional VSe_2 and $SnSe_2$ for Ultrahigh Electrocatalytic Sulfion Recycling. *Adv. Mater. Interfaces* **2022**, *9*, 2200060. [CrossRef]
47. Gao, K.; Zhou, M.; Liu, Y.; Wang, S.; Fu, R.; Wang, Z.; Guo, J.; Liu, Z.; Wang, H.; Zhao, Y.; et al. The dual built-in electric fields across CoS/MoS_2 heterojunctions for energy-saving hydrogen production coupled with sulfion degradation. *J. Colloid Interface Sci.* **2024**, *657*, 290–299. [CrossRef]
48. Wang, W.; Mao, Q.; Jiang, S.; Deng, K.; Yu, H.; Wang, Z.; Xu, Y.; Wang, L.; Wang, H. Hetero-phase Pd_4S metallene nanoribbons with Pd-rich vacancies for sulfur ion degradation-assisted hydrogen production. *Appl. Catal. B* **2024**, *340*, 123194. [CrossRef]
49. Zhang, S.; Zhou, Q.; Shen, Z.; Jin, X.; Zhang, Y.; Shi, M.; Zhou, J.; Liu, J.; Lu, Z.; Zhou, Y.-N.; et al. Sulfophobic and Vacancy Design Enables Self-Cleaning Electrodes for Efficient Desulfurization and Concurrent Hydrogen Evolution with Low Energy Consumption. *Adv. Funct. Mater.* **2021**, *31*, 2101922. [CrossRef]
50. Yi, L.; Ji, Y.; Shao, P.; Chen, J.; Li, J.; Li, H.; Chen, K.; Peng, X.; Wen, Z. Scalable Synthesis of Tungsten Disulfide Nanosheets for Alkali-Acid Electrocatalytic Sulfion Recycling and H_2 Generation. *Angew. Chem. Int. Ed.* **2021**, *60*, 21550–21557. [CrossRef] [PubMed]
51. Yu, Z.; Boukhvalov, D.W.; Tan, H.; Xiong, D.; Feng, C.; Wang, J.; Wang, W.; Zhao, Y.; Xu, K.; Su, W.; et al. Sulfur and phosphorus co-doped FeCoNiCrMn high-entropy alloys as efficient sulfion oxidation reaction catalysts enabling self-powered asymmetric seawater electrolysis. *Chem. Eng. J.* **2024**, *494*, 153094. [CrossRef]

Disclaimer/Publisher's Note: The statements, opinions and data contained in all publications are solely those of the individual author(s) and contributor(s) and not of MDPI and/or the editor(s). MDPI and/or the editor(s) disclaim responsibility for any injury to people or property resulting from any ideas, methods, instructions or products referred to in the content.

MDPI AG
Grosspeteranlage 5
4052 Basel
Switzerland
Tel.: +41 61 683 77 34

Catalysts Editorial Office
E-mail: catalysts@mdpi.com
www.mdpi.com/journal/catalysts



Disclaimer/Publisher's Note: The title and front matter of this reprint are at the discretion of the Guest Editor. The publisher is not responsible for their content or any associated concerns. The statements, opinions and data contained in all individual articles are solely those of the individual Editor and contributors and not of MDPI. MDPI disclaims responsibility for any injury to people or property resulting from any ideas, methods, instructions or products referred to in the content.





Academic Open
Access Publishing

mdpi.com

ISBN 978-3-7258-8396-7